V. 123, NO. 3
MAY 2026

ACI STRUCTURAL JOURNAL

A JOURNAL OF THE AMERICAN CONCRETE INSTITUTE

(a) Underground parking

(b) PC bearing walls

American Concrete Institute

CONTENTS

Editorial Board
Sergio Brena, Editor-in-Chief
University of Massachusetts Amherst
Robert W. Bames
Mary Beth Hueste,
Texas A&M University
Rémy Lequesne,
University of Kansas
Gustavo J. Parra-Montesinos,
University of Wisconsin-Madison

Board of Direction

President
Scott M. Anderson

Vice Presidents
Anton K. Schindler
Matthew R. Sherman

Directors
Matthew P. Adams
Michael Ahern
Corina-Maria Aldea
Tara Cavalline
James H. Hanson
Werner K. Hellmer
Mary Beth Deisz Hueste
Kimberly Waggle Kramer
John J. Myers
Enrique Pasquel
Xiomara Sapón-Roldán
Fouad H. Yazbeck

Past President Board Members
Maria Juenger
Antonio Nanni
Michael J. Paul

Executive Vice President
Frederick H. Grubbe

Staff
Publisher
John C. Glumb

Managing Director, Engineering and Professional Development
Michael L. Tholen

Engineers
Will J. Gold
Matthew R. Senecal
Michael L. Tholen
Gregory M. Zeisler

Managing Editor
Lauren E. Mentz

Associate Editor
Kimberly K. Olesky

Editors
Erin N. Azzopardi
Lauren C. Brown
Kaitlyn J. Dobberteen
Tiesha Elam
Angela R. Noelker
Kelli R. Slayden

ACI Structural Journal

May 2026, V. 123, No. 3

A JOURNAL OF THE AMERICAN CONCRETE INSTITUTE
AN INTERNATIONAL TECHNICAL SOCIETY

3 **Shear Capacity Prediction for Fiber-Reinforced Polymer Bar-Reinforced Concrete Beams Based on Gray Correlation Analysis**, by Yunxing Du, Baoqiang Liao, Rui Zhou, and Deju Zhu

17 **Lateral Response of Repaired Conventional and Hybrid Reinforced Concrete Bridge Piers**, by Sherif M. S. Osman, M. Shahria Alam, and Shamim A. Sheikh

33 **Effects of Slab Characteristics on Long-Term Deflections of One-Way Reinforced Concrete Slabs**, by John Ardila-Gonzalez, Matías A. Hube, and Julian Carrillo

45 **Flexural Performance of Glass Fiber-Reinforced Polymer and Highly Ductile Stainless-Steel Bar Hybrid-Reinforced Concrete Beams**, by Qi Cao, Teng Zhang, Shu Cao, Zhimin Wu, and Jinjin Xu

59 **Flexural Behavior of Preloaded Reinforced Concrete Beams Strengthened with Prestressed Carbon Textile-Reinforced Concrete Plates**, by Shujun Zhou, Yunxing Du, Yanqiu Li, Ziwei Li, and Xionggang Shi

71 **Pullout Behavior and Acoustic Emission Analysis of Large-Size Reinforcing Bars (D43 and D57) in Concrete**, by Yu-Cheng Kan, Kuang-Chih Pei, and Jyun-Ruei Wu

81 **Sensing-Based Simulation of Bending Moments in Reinforced Concrete Columns**, by Amir Iranmanesh, Mahsa Panahi, and Farhad Ansari

95 **Flexural Behavior of Ultra-High-Performance Seawater Sea-Sand Concrete Beams Reinforced with Fiber-Reinforced Polymer Bars**, by Fen Zhou, Lijuan Li, Yunxing Du, Fei Peng, and Deju Zhu

111 **Mathematical Framework for Computing Polar Moments of Inertia for Use with Traditional 'ACI Commentary Jc Method'**, by Hugo Esquivel and Guang Lin

123 **Effects of Axial Compression on Shear Strengths of Anchors**, by S.-C. Chun, S. Han, S.-H. Yun, M.-G. Kim, J.-H. Lee, C.-H. Park, and I.-H. Kim

133 **Interface Shear between Ordinary Concrete and Ultra-High-Performance Concrete with Glass Fiber-Reinforced Polymer Reinforcing Bars**, by Yail J. Kim and Ali Alatify

149 **Anchorage Zones Reinforced with Discrete Reinforcing Bars and Continuous Meshes**, by Yail J. Kim and Thi Ha

Contents continued on next page

ACI Structural Journal
© 2026 American Concrete Institute. All rights reserved.

This material may not be reproduced or copied, in whole or in part, in any form or by any means, including making copies by any photo process, or by electronic or mechanical device, printed, written, graphic, or oral, or recording for sound or visual reproduction for use in any knowledge or retrieval system or device, without the written consent of ACI. This material may not be used by data mining, robots, screen scraping, or similar data gathering and extraction tools such as artificial intelligence ("AI") for purposes of developing or training a machine learning or AI model, conducting computer analysis or creating derivatives of this material, without the written consent of ACI.

American Concrete Institute®, ACI®, Always Advancing®, *ACI Structural Journal*®, and *ACI Materials Journal*® are registered trademarks of American Concrete Institute.

The *ACI Structural Journal* (ISSN 0889-3241) is published bimonthly by the American Concrete Institute. Publication office: 38800 Country Club Drive, Farmington Hills, MI 48331. Periodicals postage paid at Farmington, MI, and at additional mailing offices. Subscription rates: $229 per year, payable in advance. POSTMASTER: Send address changes to: *ACI Structural Journal*, 38800 Country Club Drive, Farmington Hills, MI 48331.

Canadian GST: R 1226213149.

Direct correspondence to 38800 Country Club Drive, Farmington Hills, MI 48331. Telephone: +1.248.848.3700. Facsimile (FAX): +1.248.848.3701. **Website: http://www.concrete.org.**

PRINTED WITH SOY INK®

CONTENTS

165 **Confinement Reinforcement of Cyclically Loaded Normal-Strength Concrete Tied Columns under High Axial Loads**, by Wen-Cheng Shen and Shyh-Jiann Hwang

179 **Novel Small-Scale Accelerated Load Test for Assessing Dowel Performance**, by Charles A. Donnelly and Julie M. Vandenbossche

195 **Seismic Design of Intermediate Precast Group-Coupled Shear Walls**, by Won-Jun Lee, Deuckhang Lee, Min-Su Kim, and Xianze Jin

211 **Innovative Reinforced Concrete Deep Beam Analysis Using Improved Strut-and-Tie Method**, by Ali H. Alqarni, Hayder A. Rasheed, and Krishna Ghimire

225 **Optimized Slant Shear Interface between Steel-Fiber Concretes**, by Aaron Nzambi, Victória Seixas, and Dênio Oliveira

239 **Seismic Behavior of External Socket Connections for Reinforced Concrete Columns**, by Julio A. Samayoa, Giorgio T. Proestos, and Mervyn J. Kowalsky

253 **Seismic Performance of Precast Concrete Full-Scale Wide Beam-Column Connections with Emulative Detailing**, by Seon-Hoon Kim, Deuckhang Lee, Wei Zhang, and Thomas H.-K. Kang

269 **Component Model-Based Method for Damage Assessment of Reinforced Concrete Structures Subjected to Blast Loads**, by Ren Jiang

281 **Post-Cracking Shear Capacity of Precast Hollow-Core Floor Units**, by Mohamed Mostafa, Richard S. Henry, and Kenneth J. Elwood

295 **Comprehensive Multi-Metric Comparison of One-Way Shear Models for Reinforced Concrete Beams without Shear Reinforcement**, by Amir Mofidi, Sara Mirzabagheri, Kourosh Nasrollahzadeh, and Shahryar Rahnamayan

309 **Long-Term Field Monitoring and Analysis of Post-Tensioned Flat Slab System**, by Kwanwoo Yi, Ah Sir Cho, and Thomas H.-K. Kang

ACI CONCRETE CONVENTION: FUTURE DATES

2026—Oct. 11-14, Hilton Atlanta, Atlanta, GA
2027—Mar. 21-24, Caesars Palace Las Vegas, Las Vegas, NV
2027—Oct. 24-27, Caribe Royale Orlando, Orlando, FL

For additional information, contact:
Event Services, ACI
38800 Country Club Drive
Farmington Hills, MI 48331
Telephone: +1.248.848.3795
email: conventions@concrete.org

ON FRONT COVER: 123-S54, p. 196, Fig. 1—Typical precast concrete projects in multi-story building.

Permission is granted by the American Concrete Institute for libraries and other users registered with the Copyright Clearance Center (CCC) to photocopy any article contained herein for a fee of $3.00 per copy of the article. Payments should be sent directly to the Copyright Clearance Center, 21 Congress Street, Salem, MA 01970. ISSN 0889-3241/98 $3.00. Copying done for other than personal or internal reference use without the express written permission of the American Concrete Institute is prohibited. Requests for special permission or bulk copying should be addressed to the Managing Editor, *ACI Structural Journal*, American Concrete Institute.

The Institute is not responsible for statements or opinions expressed in its publications. Institute publications are not able to, nor intend to, supplant individual training, responsibility, or judgment of the user, or the supplier, of the information presented.

Papers appearing in the *ACI Structural Journal* are reviewed according to the Institute's Publication Policy by individual experts in the subject area of the papers.

Contributions to *ACI Structural Journal*

The *ACI Structural Journal* is an open forum on concrete technology and papers related to this field are always welcome. All material submitted for possible publication must meet the requirements of the "American Concrete Institute Publication Policy" and "Author Guidelines and Submission Procedures." Prospective authors should request a copy of the Policy and Guidelines from ACI or visit ACI's website at **www.concrete.org** prior to submitting contributions.

Papers reporting research must include a statement indicating the significance of the research.

The Institute reserves the right to return, without review, contributions not meeting the requirements of the Publication Policy.

All materials conforming to the Policy requirements will be reviewed for editorial quality and technical content, and every effort will be made to put all acceptable papers into the information channel. However, potentially good papers may be returned to authors when it is not possible to publish them in a reasonable time.

Discussion

All technical material appearing in the *ACI Structural Journal* may be discussed. If the discussion is received within four months of the paper's print publication, it will appear in the issue dated ten months from this journal's date. Discussion material received after specified dates will be considered individually for publication or private response. ACI Standards published in ACI Journals for public comment have discussion due dates printed with the Standard. Discussion should be complete and ready for publication, including finished, reproducible illustrations. Discussion must be confined to the scope of the paper and meet the ACI Publication Policy.

Follow the style of the current issue. Discussions should not exceed 1800-word equivalents (illustrations and tables count as 300 words each). References should be complete. Do not repeat references cited in original paper; cite them by original number. Numbering of additional references, figures, tables, and equations should follow sequentially from the original manuscript throughout the discussion. The discusser must indicate the month, year, volume number, issue number, authors' names, and manuscript number of the original manuscript. Closures responding to a single discussion should not exceed 1800-word equivalents in length, and to multiple discussions, approximately one half of the combined lengths of all discussions. Closures are published together with the discussions.

Discuss the paper, not some new or outside work on the same subject. Use references wherever possible instead of repeating available information.

Discussion offered for publication should offer some benefit to the general reader. Discussion which does not meet this requirement will be returned or referred to the author for private reply.

Send manuscripts to:
http://mc.manuscriptcentral.com/aci
Send discussions to:
Journals.Manuscripts@concrete.org

ACI STRUCTURAL JOURNAL TECHNICAL PAPER

Title No. 123-S40

Shear Capacity Prediction for Fiber-Reinforced Polymer Bar-Reinforced Concrete Beams Based on Gray Correlation Analysis

by Yunxing Du, Baoqiang Liao, Rui Zhou, and Deju Zhu

The existing design standards of fiber-reinforced polymer bar-reinforced concrete (FRP-RC) beams provide conservative shear capacity and fail to accurately reflect the effects of various factors. In this study, a comprehensive analysis was conducted on 174 sets of shear capacity data for FRP-RC beams with stirrups. Gray correlation analysis was used to investigate the correlations between the longitudinal reinforcement ratio, stirrup spacing, shear span-depth ratio, and shear capacity of FRP-RC beams with stirrups. The results show that stirrup spacing and shear span-depth ratio significantly influence the shear capacity of FRP-RC beams with stirrups, and thus must be considered in shear design. Based on the results of gray correlation analysis, recommendations were proposed for modifying the shear contribution of concrete and stirrups in the calculation formula of shear capacity for FRP-RC beams with stirrups in five design standards. The accuracy of modified formulas was verified with the experimental data, which show significant improvement in the shear capacity prediction in terms of mean value, coefficient of variation, and safety factor. By incorporating a database comprising 23 FRP-RC beams with stirrups, the revised formula was comprehensively validated for its sufficient applicability in shear design of three types of FRP-RC beams with stirrups.

Keywords: fiber-reinforced polymer (FRP) bars; gray correlation analysis method; shear capacity; stirrups.

INTRODUCTION

The increasing prevalence of deicing salts and antifreeze agents has exacerbated the corrosion of steel bars in concrete structures. Previous research[1] has suggested that fiber-reinforced polymer (FRP) bars, exhibiting elevated corrosion resistance, lightness, and strength, hold potential as a substitute for steel bars in addressing the electrochemical corrosion of steel bars within concrete structures. However, the lower elastic modulus and transverse shear strength of FRP bars result in larger deformations and cracks in FRP-reinforced concrete (RC) beams relative to steel bar-RC beams. This also leads to a reduced height of the concrete compression zone, resulting in a lower shear capacity of FRP-RC beams, as compared to steel bar-RC beams with the same reinforcement ratio.[2] Hence, the calculation theory for the shear capacity of steel bar-RC beams is unsuitable for FRP-RC beams. The mechanisms of shear failure in concrete beams are intricate, and as of present, there is no unified shear theory for FRP-RC beams with stirrups established, and a comprehensive design method considering the influence of various factors on the shear capacity of FRP-RC beams with stirrups remains inadequate. Consequently, it is imperative to establish a scientific and reasonable design method for FRP-RC beams with stirrups to ensure its practical application.

The shear behavior of FRP-RC beams has been thoroughly investigated by scholars.[3-7] The findings indicate that the primary factors influencing the shear capacity of FRP-RC beams are stirrup spacing, shear span-depth ratio, and longitudinal reinforcement ratio. Al-Hamrani et al.[4] discovered that decreasing the stirrup spacing from 350 to 250 mm resulted in a 55% increase in the shear capacity of basalt FRP (BFRP)-RC beams. Fan et al.[6] determined that as the shear span-depth ratio increased from 1.5 to 2.5, the shear capacity of BFRP-RC beams decreased by 29%. Abed et al.[7] observed that increasing the longitudinal reinforcement ratio from 0.3 to 5.3% led to a 4.5-fold increase in the shear capacity of BFRP-RC beams. Therefore, incorporating stirrup spacing, shear span-depth ratio, and longitudinal reinforcement ratio in the shear capacity calculation formula for FRP-RC beams with stirrups is more scientifically and logically appropriate.

Gray correlation analysis is a method to determine the correlation degree between variables by analyzing the similarities or differences of their development trends.[8] This method requires relatively minimal data and computational resources. The gray correlation analysis method has been widely applied in the evaluation and analysis of concrete performance.[9-14] This study collated existing related literature and analyzed 174 sets of shear capacity data of FRP-RC beams with stirrups (seven sets of aramid FRP [AFRP] bars, 59 sets of BFRP bars, 45 sets of carbon FRP [CFRP] bars, and 63 sets of glass FRP [GFRP] bars) using the gray correlation degree analysis method to investigate the influence of various factors on the shear capacity of FRP-RC beams with stirrups based on the selected data. Despite the increasing use of FRP composites, there is still limited systematic research on BFRP composites, resulting in a lack of detailed regulations and technical guidance for this material in relevant design standards for FRP composites. Moreover, several studies[5,15-17] have concluded that the current design standards' shear capacity equations for FRP-RC beams provide relatively conservative calculation results, resulting in high reinforcement ratios in shear design. To enrich

ACI Structural Journal, V. 123, No. 3, May 2026.
MS No. S-2023-091.R2, doi: 10.14359/51742136, received March 31, 2024, and reviewed under Institute publication policies. Copyright © 2026, American Concrete Institute. All rights reserved, including the making of copies unless permission is obtained from the copyright proprietors. Pertinent discussion including author's closure, if any, will be published ten months from this journal's date if the discussion is received within four months of the paper's print publication.

Table 1—Descriptive statistics of experimental test database

Parameters	b, mm	d, mm	f_c', MPa	ρ_f, %	E_f, GPa	ρ_f, % $q_1(k)$	s, mm $q_2(k)$	λ $q_3(k)$	τ, MPa $q_0(k)$
Minimum	100	115	20.0	0.08	28.00	0.39	24	0.67	0.56
Maximum	450	937	73.4	1.50	181.00	3.98	400	4.49	5.72
Mean	190.33	257.56	35.6	0.60	64.21	1.59	121.96	2.34	2.61
SD	58.56	97.98	10.5	0.40	32.95	0.70	78.89	0.91	1.14
CV	0.31	0.38	0.3	0.66	0.51	0.44	0.65	0.39	0.44

Note: SD is standard deviation; CV is coefficient of variation.

the design standards for FRP-RC beams with stirrups and enhance the accuracy of shear design, this study compared the 174 selected sets of experimental shear capacity data for FRP-RC beams with stirrups to the calculation results of the shear capacity design formulas in five design standards and proposed modifications to the shear design formulas for FRP-RC beams with stirrups in these design standards. The revised shear formulas for three different types of FRP-RC beams with stirrups were extensively validated by introducing a comprehensive database consisting of 23 FRP-RC beams with stirrups. The findings of this study provide a scientific and reliable design method for the FRP-RC beams and promote their engineering application.

RESEARCH SIGNIFICANCE

This study provides a scientific and reliable design method for FRP-RC beams with stirrups, addressing the limitations of existing design standards. The findings demonstrate the significant influence of stirrup spacing and shear span-depth ratio on the shear capacity of FRP-RC beams with stirrups, which must be considered in shear design. The proposed modifications to the shear contribution of concrete and stirrups in the calculation formula of shear capacity in the design standards show significant improvement in prediction accuracy. This study enriches design standards for FRP-RC beams and promotes their engineering application, enhancing the safety and efficiency of FRP-RC structures.

GRAY CORRELATION ANALYSIS OF SHEAR CAPACITY FACTORS IN FRP-RC BEAMS

The present study employed the nominal shear capacity τ as an indicator of the shear capacity of FRP-RC beams, defined in Eq. (1),[18] where V_u represents the beam's shear capacity, b stands for the beam width, and d is the beam's effective depth.

$$\tau = \frac{V_u}{b_w d} \tag{1}$$

A total of 174 FRP-RC beams with stirrups were collected as specimens and their mathematical characteristics are presented in Table 1, with the proportion of each type of FRP bar shown in Fig. 1. A gray correlation analysis was performed on the nominal shear capacity (τ) of the test specimens with respect to the longitudinal reinforcement ratio (ρ_f), stirrup spacing (s), and shear span-depth ratio (λ) to investigate the significance of various influencing factors. The analysis procedure is described as follows.[8]

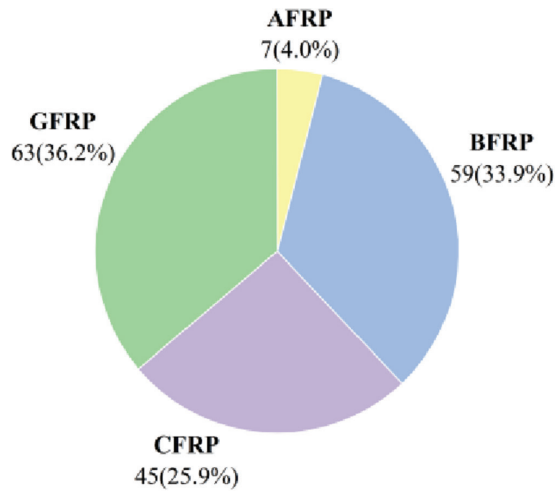

Fig. 1—Proportion of each type of FRP bar in 174 sets of selected data.

1. To assess the interrelation among the factors of interest through gray correlation analysis, the nominal shear capacity series (τ) denoted by $q_0(k)$ is taken as the parent factor sequence, while the longitudinal reinforcement ratio (ρ_f) represented by $q_1(k)$, stirrup spacing (s) represented by $q_2(k)$, and shear span-depth ratio (λ) represented by $q_3(k)$ are regarded as the subfactor sequences, as shown in Table 1.

2. In preparation for the gray correlation analysis, it is essential to standardize the factor sequences. The non-dimensional factor sequences, denoted by $q_1'(k)$, are obtained by dividing each factor sequence $q_i(k)$ by its corresponding mean value q_i, as expressed in Eq. (2). Herein, $q_i = (1/n)\sum_k^n q_i(k)(i = 0, 1, \ldots, m; k = 1, 2, \ldots, n)$, where m represents the number of influencing factors, which is three in this study, and n denotes the total number of samples, which is 174.

$$q_i'(k) = \frac{q_i(k)}{\overline{q}_i} \tag{2}$$

3. The standardized dimensionless sequence $q_1'(k)$ of each factor is substituted into Eq. (3) to compute the corresponding absolute difference sequence $\Delta_i(k)$ for each subfactor, where $q_0'(k)$ denotes the dimensionless sequence of the parent factor. Subsequently, the absolute difference sequence of each subfactor is substituted into Eq. (4) to determine the

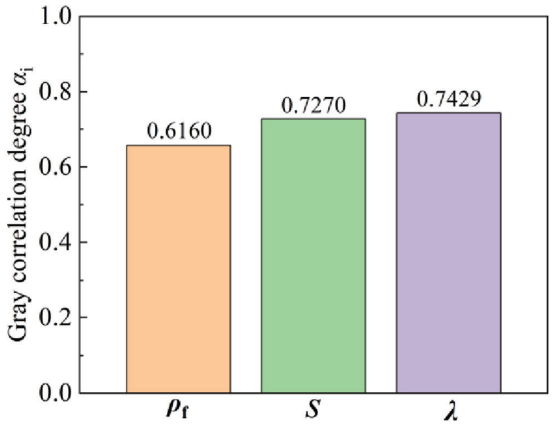

Fig. 2—Gray correlation degree α_i *of all factors.*

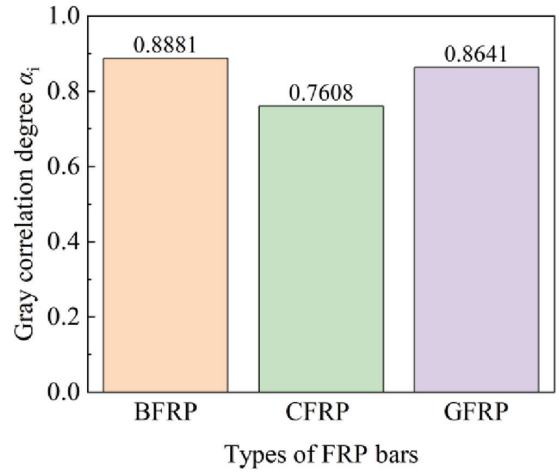

Fig. 3—Gray correlation degree α_i *of all types of FRP bars.*

gray correlation coefficient $r_i(k)$ for each subfactor, where Δ_{max} signifies the maximum value in the absolute difference sequence $\Delta_i(k)$, Δ_{min} denotes the minimum value in the absolute difference sequence $\Delta_i(k)$, and ξ is the discrimination coefficient, set to 0.5.

$$\Delta_i(k) = |q_0'(k) - q_i'(k)| \tag{3}$$

$$r_i(k) = \frac{\Delta_{min} + \xi\Delta_{max}}{\Delta_i(k) + \xi\Delta_{max}} \tag{4}$$

4. The correlation degree between each subfactor sequence and the parent factor sequence is evaluated by calculating the average α_i of the gray correlation coefficients $r_i(k)$ using Eq. (5), where i ranges from 0 to m, k ranges from 1 to n, and $n = 174$ in this study. The greater the gray correlation degree α_i, the more significant the influence of this factor on the shear capacity of FRP-RC beams.

$$\alpha_i = \frac{1}{n}\sum_k^n r_i(k) \tag{5}$$

According to the data presented in Fig. 2, there exists a gray correlation degree (α_i) between the shear span-depth ratio (λ), transverse reinforcement spacing (s), and longitudinal reinforcement ratio (ρ_f) in relation to the shear capacity of FRP-RC beams. The specific numerical values are 0.7429, 0.7270, and 0.6160, respectively. Therefore, the correlation magnitude, concerning the shear capacity of beams, follows the order: shear span-depth ratio, stirrup spacing, and longitudinal reinforcement ratio. In comparison with the other two factors, the gray correlation degree of the longitudinal reinforcement ratio is relatively lower, amounting to only 79% of that of the shear span-depth ratio. These variations encompass alterations in the critical oblique crack inclination and tensile stress within the beam, leading to variations in aggregate interlocking force between cracks and shear contribution of the compressed concrete region. Moreover, alterations in the stirrup spacing also exert a significant influence on the shear capacity of the beams. In contrast, the influence of the longitudinal reinforcement ratio is relatively minor, consistent with recent research findings.[4] Therefore, when revising the formula for shear capacity, the emphasis is placed on the influence of shear span-depth ratio and stirrup spacing in this study.

In this study, gray correlation analysis was conducted to evaluate the impact of three types of FRP bars (CFRP, BFRP, and GFRP) on a beam's shear capacity. The elastic modulus, design tensile strength of FRP bars, and shear capacity of beams were collected and analyzed. Figure 3 illustrates that BFRP bars exhibit the highest gray correlation coefficient, followed by GFRP bars, while CFRP bars exhibit the lowest correlation. This indicates varying degrees of influence by different FRP bar types on shear capacity. Strong correlations exist between BFRP bars and shear capacity, followed by GFRP bars, with minimal impact from CFRP bars. This finding has significant implications for shear design of FRP-RC beams. BFRP bars are preferred due to their strong correlation with shear capacity. Despite minimal influence, CFRP bars still play a role in situations requiring higher stiffness and strength. GFRP bars, despite lower correlation, can still be an alternative when lower shear capacity is required. Therefore, the gray correlation analysis results enable engineers to accurately select suitable FRP materials for shear design, based on project requirements. Additionally, these findings provide theoretical support and a reference basis for future research on different FRP bar types and their application in concrete structures.

COMPARISON OF DIFFERENT DESIGN STANDARDS

The methodologies used for assessing the shear capacity of FRP-RC beams differ across countries, including the United States, China, and Canada, as described in Appendix A.* Presently, five design standards[19-23] commonly divide the shear capacity of concrete beams into two separate parts: concrete and stirrups, as depicted in Eq. (6), where V_c denotes the shear contribution of concrete and V_f represents the shear contribution of FRP stirrups. Regarding the shear contribution of concrete, the five design standards consider the influence of the elastic modulus (E_f) and the

*The Appendix is available at **www.concrete.org/publications** in PDF format, appended to the online version of the published paper. It is also available in hard copy from ACI headquarters for a fee equal to the cost of reproduction plus handling at the time of the request.

longitudinal reinforcement ratio (ρ_f), which differs from the steel bar-RC structure standard GB 50010-2010.[24] Because the elastic modulus of steel bars is essentially identical, the steel bar-RC structure standard only needs to consider the effect of the longitudinal reinforcement ratio (ρ_f) on the shear contribution of concrete. The formulas used for computing the shear contribution of FRP stirrups in the five design standards are usually consistent, and it is assumed that the design tensile strength of stirrups is regulated by the tensile strength at the bend and strain limit, given that the stirrup stress may be considerably smaller than its longitudinal tensile strength when FRP-RC beams with stirrups fail in shear.

$$V_{exp} = V_c + V_f \tag{6}$$

These five design standards exhibit discrepancies in the shear design of FRP-RC beams. For instance, regarding the shear contribution of concrete, ACI 440.1R-15[19] uses a calculation formula based on the research findings of Tureyen and Frosch.[25] This formula assumes that the shear force of FRP-RC beams is transferred by the concrete located in the shear zone above the neutral axis. By analyzing the stress state of the concrete in the shear compression zone, the shear capacity model of FRP-RC beams is derived, and the existing test data is used to simplify the model. ACI CODE-440.11-22[23] further considers the influence of beam's cross-sectional size effects on this basis. On the other hand, the shear capacity formula for FRP-RC beams without stirrups in CSA S806-12[20] refers to research findings of Razaqpur and Isgor[26] and Razaqpur and Spadea.[27] This formula divides the shear capacity of FRP-RC beams without stirrups into two parts: the contribution of intact concrete and the contribution of aggregate bite force. The correlation between bending moment and shear force, as well as the effect of component size on shear capacity are also considered. For beams with a shear span-depth ratio of less than 2.5, the effect of arch action is also considered. Furthermore, the shear calculation formula of GB 50608-2010[21] is mainly derived from ACI 440.1R-15,[19] and on this basis, the tensile strength of concrete is employed to express the shear contribution of concrete in the compression zone.

According to ACI 440.1R-15,[19] CSA-S806-12,[20] GB 50608-2010,[21] SIMTReC Design Manual No. 3,[22] and ACI CODE-440.11-22,[23] the strain limits of FRP stirrups show differences in the five design standards, and their values range from 0.0025ε to 0.005ε. Table 2 summarizes the consideration of various factors in each design standard based on the forms of their respective formulas. However, it is worth noting that four of the standards do not account for the influence of shear span-depth ratio, which has a significant effect on the shear capacity of FRP-RC beams with stirrups, as confirmed by gray correlation analysis and relevant studies.[5,6] Neglecting this effect could result in over-conservative calculations for beams with small shear span-depth ratio and insufficient safety for beams with large shear span-depth ratio. Therefore, this study proposes modifications to the shear capacity formula of these standards to address this issue by considering the effect of shear span-depth ratio.

Table 2—Consideration of influencing factors in shear design formula in different design standards

Standards	ρ_f	s	λ	$\varepsilon_{fv,lim}$ (ε)
ACI 440.1R-15[19]	○	○	×	0.004
CSA-S806-12[20]	○	○	○	0.005
GB 50608-2010[21]	○	○	×	0.004
SIMTReC[22]	×	○	×	0.0025
ACI CODE-440.11-22[23]	○	○	×	0.005

Note: ○ denotes that the influencing factor has been considered; × denotes that the influencing factor has not been considered.

MODIFICATION TO SHEAR CAPACITY CALCULATION FORMULA

This study used 174 data sets of FRP-RC beams with stirrups to conduct a comparative analysis of shear equations in five design standards, namely ACI 440.1R-15,[19] CSA-S806-12,[20] GB 50608-2010,[21] SIMTReC Design Manual No. 3,[22] and ACI CODE-440.11-22.[23] Figure 4 illustrates the specific results of experimental and predicted shear capacity for FRP-RC beams in the literature,[3-6,28-54] where V_{exp} and V_p denote the measured and theoretical shear capacity of the beam, respectively. The findings reveal that the shear equation in ACI 440.1R-15[19] provides the most accurate results (mean = 1.52, standard deviation [SD] = 0.58, and coefficient of variation [CV] = 0.38) among the five design standards, while ACI CODE-440.11-22[23] shows the poorest prediction (mean = 0.77, SD = 0.25, and CV = 0.32). Subsequently, modifications to the shear capacity calculation formulas of all design standards were proposed, and a comparative evaluation was conducted on the results of the formulas before and after modification.

Modification to shear span-depth ratio in calculation formula

Based on Fig. 4, a data set solely containing variations in the shear span-depth ratio was chosen. The screened experimental data is presented in Fig. 5(a), which illustrates that the nominal shear capacity of FRP-RC beams with stirrups decreases as the shear span-depth ratio increases, and this finding is consistent with recent research.[4,6] This decline can be attributed to a gradual reduction in the angle of the critical shear crack, leading to less shear contribution of interlocking force between inclined cracks. Additionally, the arch truss model, which explains the shear mechanism of simply supported beams in inclined sections, suggests that the concrete teeth between cracks serve as compression diagonal web members. The reduction in the angle of the critical shear crack weakens the compressive effect of the concrete between inclined cracks, ultimately decreasing the shear contribution of concrete for beams and effecting their shear capacity. Therefore, neglecting the influence of shear span-depth ratio in the shear capacity calculation formula may result in overly conservative calculations for small shear span-depth ratio beams and insufficient safety for large shear span-depth ratio beams. To address this issue, the correction

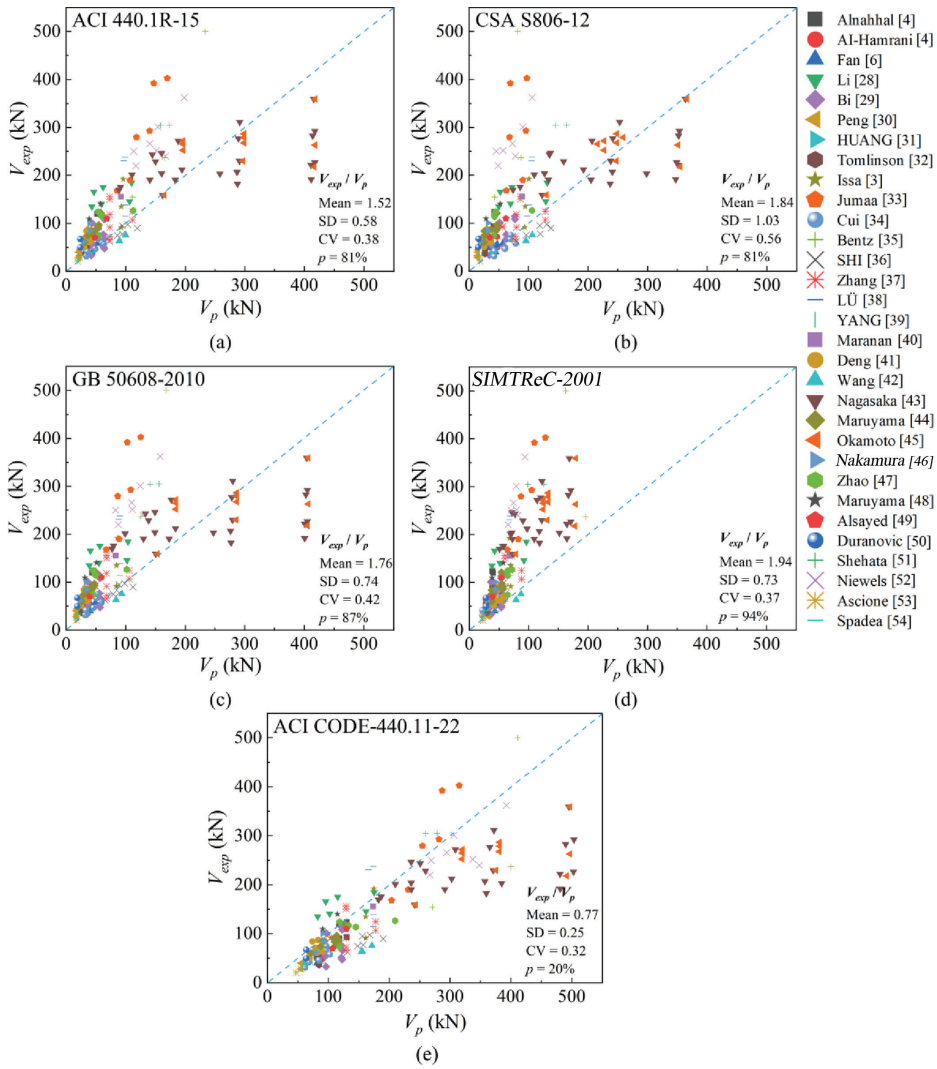

Fig. 4—Comparison of experimental and predicted shear capacity for FRP-RC beam in literature.[3-6,28-54]

coefficient of shear span-depth ratio α is introduced into the calculation formula for shear contribution of concrete in the five design standards.

In the present investigation, it is postulated that a certain correlation exists between the pre-modification and post-modification shear contribution formula of concrete in the design standard, as expressed in Eq. (7). Herein, V_{cm} denotes the concrete shear contribution accounting for the effect of the shear span-depth ratio. Subsequently, the points on the same shear span-depth ratio in the selected data set that solely underwent variations in shear span-depth ratio are averaged using $V_c/(V_{exp} - V_f)$ as the y-coordinate axis, and any points that deviate significantly from the trend are removed. The resulting processed test data is presented in Fig. 6, and a polynomial curve fitting is carried out based on the trend of the scatter plot as explicated in Eq. (8). Finally, the formula for the shear contribution of concrete for FRP-RC beams with stirrups, considering the effect of shear span-depth ratio, is presented in Table 3. The meanings of the symbols employed in the table are detailed in Appendix B.†

$$V_{cm} = \alpha V_c = V_{exp} - V_f \tag{7}$$

$$\alpha = \frac{1}{A\lambda^2 + B\lambda + C} \tag{8}$$

Modification to stirrup spacing in calculation formula

Based on Fig. 4, the data set solely comprising variations in stirrup spacing is selected. Experimental data are processed and exhibited in Fig. 5(b). It is noteworthy that the shear contribution of stirrups decreases with the increase of stirrup spacing for different FRP-RC beams with stirrups. Reduced stirrup spacing implies that more stirrups can bear the shear force, thus improving the shear capacity of beams. Moreover, increased stirrup spacing can further constrain the development of inclined cracks. According to Fig. 5(b), the relationship between stirrup spacing and the shear contribution of the stirrup is inconsistent with the linear correlation presented by the shear equation in the five design standards. In view of the remarkable influence of stirrup spacing on

†The Appendix is available at **www.concrete.org/publications** in PDF format, appended to the online version of the published paper. It is also available in hard copy from ACI headquarters for a fee equal to the cost of reproduction plus handling at the time of the request.

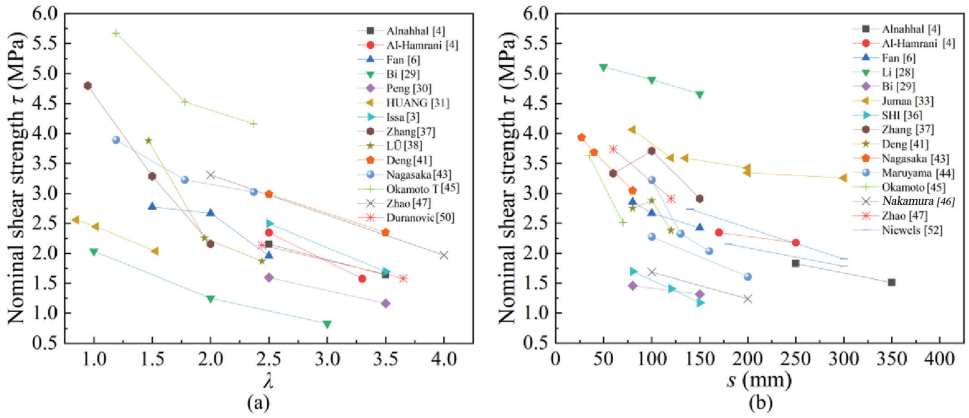

Fig. 5—Effects of: (a) shear span-depth ratio; and (b) stirrup spacing on τ.

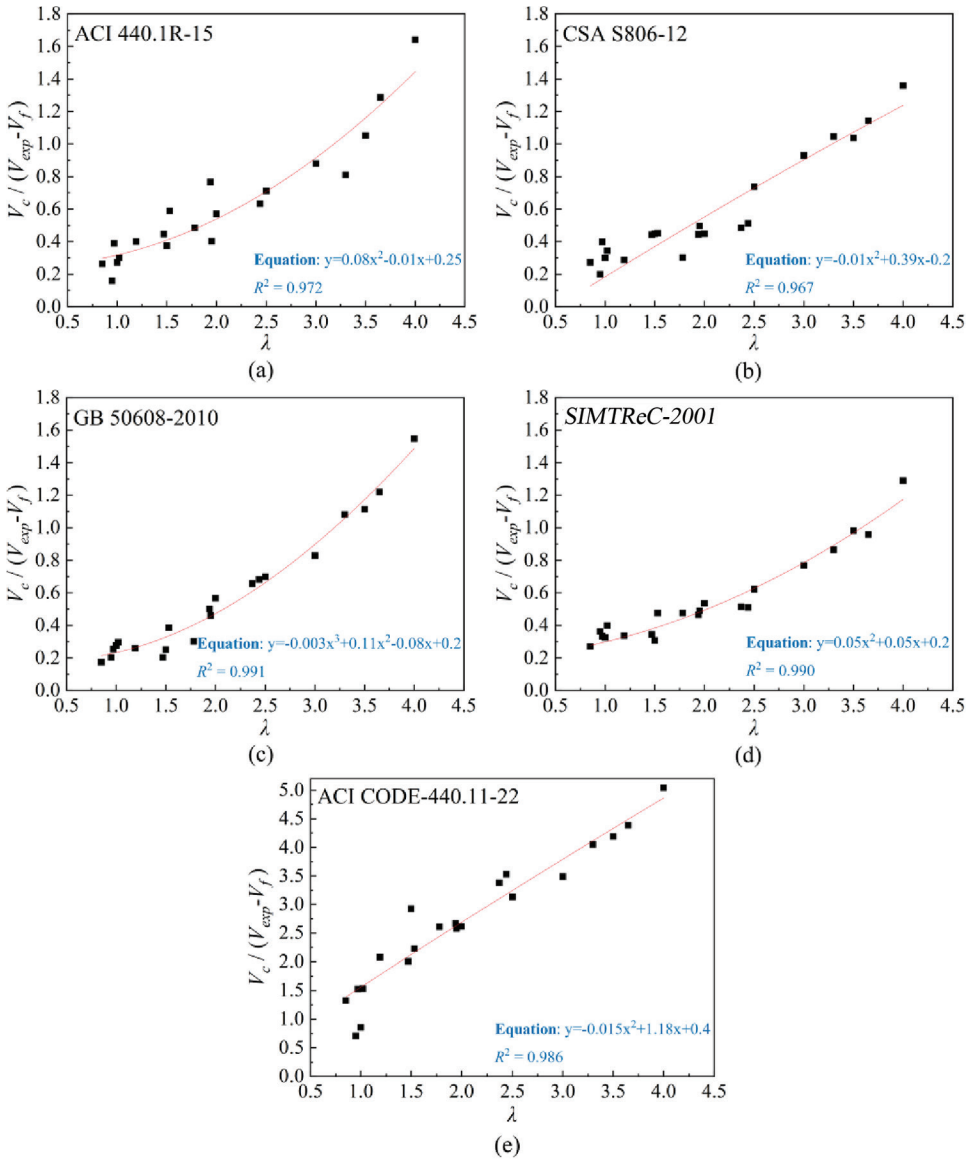

Fig. 6—Fitting results of shear span-depth ratio on shear contribution of concrete in all design standards.

the shear capacity of beams, it is imperative to modify the stirrup spacing in the shear equation.

It is assumed that there is a correlation between the stirrup shear contribution formula in design standards before and after modification, as illustrated in Eq. (9). Here, s_m represents the modified stirrup spacing, V_{exp} denotes the actual shear capacity of the beam, V_{fm} refers to the shear contribution of stirrup considering the modification to stirrup spacing, and V_f indicates the theoretical shear contribution of stirrup calculated according to the original shear capacity

formula of the beam in the design standards. Next, taking $sV_f/(V_{exp} - V_{cm})$ as the y-coordinate axis, the points with the same stirrup spacing in the selected data set with only stirrup spacing changes are averaged. The purpose of this averaging process is to capture the overall behavior and trend represented by the data points. However, not all data points may conform to this overall trend. Some data points may exhibit noticeable deviations or anomalies, indicating that they do not align with the expected pattern or behavior of most data. To ensure the integrity and accuracy of the analysis, these data points that significantly diverge from the expected trend are deliberately excluded from further consideration. This exclusion aims to enhance the reliability of the analysis results by focusing on data points that are consistent with the anticipated behavior and trends. As a result, the analysis is focused on the more representative and meaningful data, thus yielding more accurate insights and conclusions. The processed test data is depicted in Fig. 7. By analyzing the scatter plot trend, a power function is employed for fitting, and its specific form is shown in Eq. (10). Finally, the stirrup shear contribution expression for FRP-RC beams with stirrups in various design standards, considering stirrup spacing modification, is presented in Table 4. The detailed explanation of the symbols is provided in Appendix B.

Table 3—Summary of calculation formulas for shear contribution of concrete in design standards

Design standards	Modification of concrete contribution V_{cm}
Modified ACI 440.1R-15	$\frac{2}{5\times(0.08\lambda^2-0.01\lambda+0.25)}\sqrt{f_c'}\,b_w kd$
Modified CSA S806-12	$\frac{0.05}{-0.01\lambda^2+0.39\lambda-0.2}\phi_c k_r k_s \sqrt[3]{f_c'}\,b_w d_v$
Modified GB 50608-2010	$\frac{0.86}{-0.003\lambda^3+0.11\lambda^2-0.08\lambda+0.2}f_t b_w k h_{of}$
Modified SIMTReC-2001	$\frac{0.2}{0.05\lambda^2+0.05\lambda+0.2}\phi_c\sqrt{f_c'}\,b_w d\sqrt{\frac{E_{frp}}{E_s}}$
Modified ACI CODE-440.11-22	$\max\begin{cases}\frac{5}{-0.015\lambda^2+1.18\lambda+0.4}\lambda_s k_{cr}\sqrt{f_c'}\,b_w d\\ \frac{0.8}{-0.015\lambda^2+1.18\lambda+0.4}\lambda_s\sqrt{f_c'}\,b_w d\end{cases}$

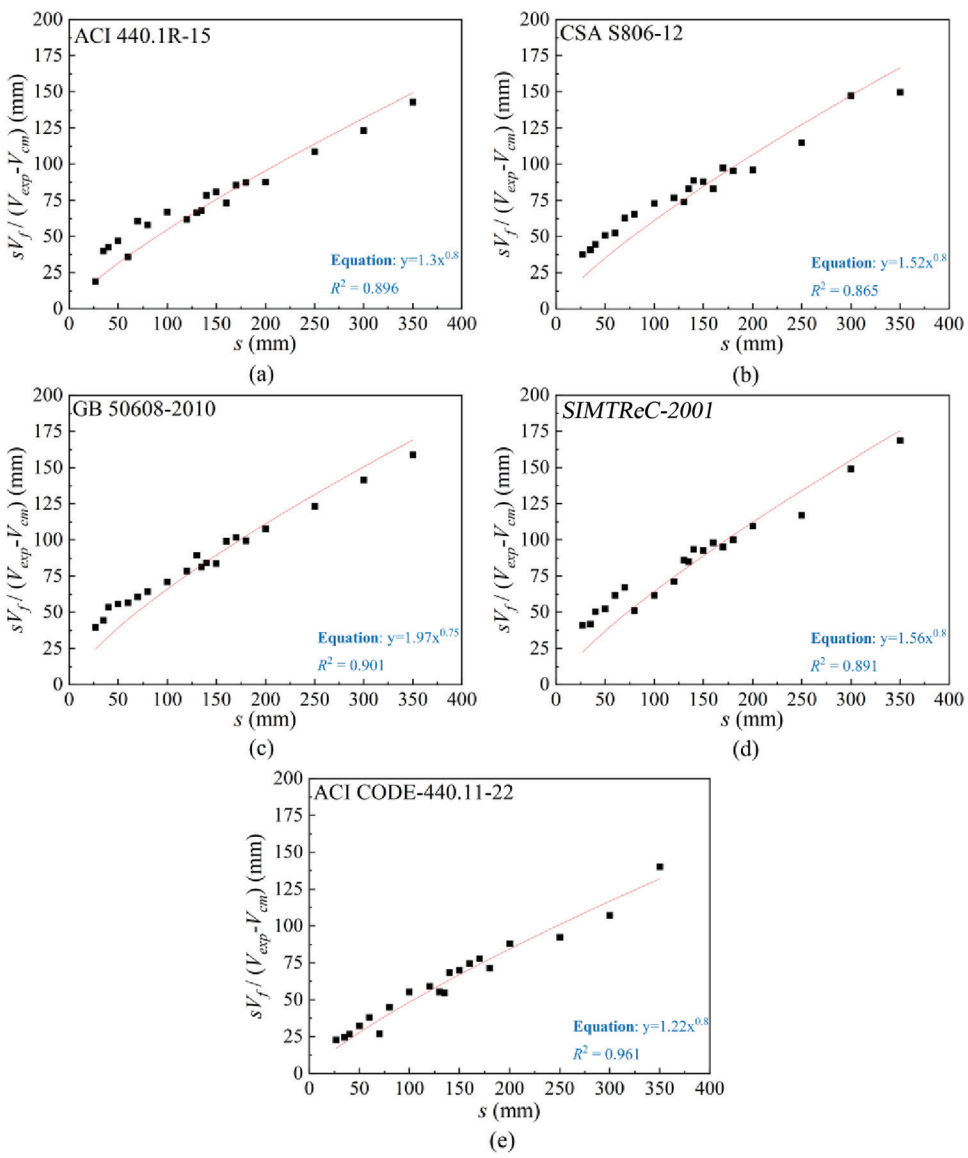

Fig. 7—Fitting results of stirrup spacing on shear contribution of stirrup in all design standards.

Table 4—Summary of modified shear contribution for stirrups in design standards

Design standards	Modified shear contribution for stirrup considering modification to stirrup spacing V_{fm}
Modified ACI 440.1R-15	$\frac{A_{fv} f_{fv} d}{1.3 s^{0.8}}$
Modified CSA S806-12	$\frac{A_{fv} f_{fv} d_v}{1.52 s^{0.8}}$
Modified GB 50608-2010	$\frac{A_{fv} f_{fv} h_{of}}{1.97 s^{0.75}}$
Modified SIMTReC-2001	$\frac{A_{fv} f_{fv} d}{1.56 s^{0.8}}$
Modified ACI CODE-440.11-22	$\frac{A_{fv} f_{ft} d}{1.22 s^{0.8}}$

$$V_{fm} = V_{\exp} - V_{cm} = \frac{s V_f}{s_m} \tag{9}$$

$$s_m = a s^b \tag{10}$$

Modification to stirrup strain in calculation formula

Due to the relatively low elastic modulus of FRP composites, the relevant FRP composite material standards impose restrictions on the maximum allowable stress and strain in FRP stirrups to maintain the structural integrity of components by controlling crack width and preserving the interlocking force of aggregates. The design standards under scrutiny in this study limit the strain of FRP stirrups between 2500 and 5000 με, as demonstrated in Table 2. Considering the relatively conservative restrictions of these design standards on stirrup strain, Said et al.[55] proposed an equation for correcting stirrup strain that accounts for the concrete compressive strength, longitudinal reinforcement axial stiffness ($\rho_f E_f$), and stirrup axial stiffness ($\rho_{fv} E_{fv}$), as expressed in Eq. (11). Therefore, the design value of stirrup tensile strength (f_{fv}) for FRP-RC beams with stirrups in the five design standards was uniformly revised to the form shown in Eq. (12).

$$\varepsilon_{fv} = 0.000396 \sqrt{f_c' \left(\frac{\rho_f E_f}{\rho_{fv} E_{fv}} \right)} \tag{11}$$

$$f_{fv} = 0.000396 E_{fv} \sqrt{f_c' \left(\frac{\rho_f E_f}{\rho_{fv} E_{fv}} \right)} \tag{12}$$

Correction coefficient of stirrup shear contribution in calculation formula

The tensile strength of FRP bars is relatively high. However, in the actual situations, FRP stirrups are unable to achieve their tensile strength when shear failure occurs in FRP-RC beams with stirrups. Therefore, all the design standards considered in this study limit the stress level of FRP stirrups for design purposes. For instance, in ACI 440.1R-15,[19] the design value of stirrup tensile strength $f_{fv} = \min\{0.004E_{fv}, (0.05r_b/d_b + 0.3)f_{fu}\}$ is adopted. Despite the correction of stirrup strain in the previous chapter, this approach still overestimates the effect of FRP stirrups on the shear capacity of beams. Based on the aforementioned reasons, the shear contribution correction coefficient for φ_{fv} of stirrups is put forward to ensure the safety of shear design.

The expression for the actual shear contribution of stirrups is formulated as Eq. (13), where V_{exp} signifies the measured shear capacity of FRP-RC beams, $V_{exp,f}$ represents the actual shear contribution of stirrups in the beams, V_{cm} denotes the shear contribution of concrete in the beams, considering the influence of shear span-depth ratio, and V_{fm} refers to the theoretical shear contribution of stirrups after adjusting for stirrup spacing and stirrup strain. Using the data from 174 FRP-RC beams with stirrups, a scatter plot of the stirrup ratio $\rho_{fv} - V_{exp,f}/V_{fm}$ is depicted in Fig. 8. When $V_{exp,f}/V_{fm} \geq 1$, it is indicative of safe calculated results for the shear contribution of stirrup; however, $V_{exp,f}/V_{fm} < 1$ implies unsafe calculated results for the shear contribution of stirrup. Figure 8 presents a significant number of unsafe results, indicating that the contribution of stirrups to the shear capacity of beams may be overestimated if the theoretical shear contribution of stirrups is not reduced, thereby posing potential safety hazards to the shear design of beams. Therefore, it is imperative to propose the shear contribution coefficient of stirrups, and the corresponding shear contribution coefficient of stirrups φ_{fv} can be obtained from a quantile value of the corresponding scatter plot in each design guideline. Table 5 summarizes the shear contribution coefficient of stirrup, along with its corresponding quantile values in the calculation formulas of shear contribution for stirrup in various design standards, as well as the calculation formula of shear contribution for stirrup V_f, which takes the shear contribution coefficient of stirrups, modification to stirrup strain, and stirrup spacing into account.

$$V_{exp,f} = V_{exp} - V_{cm} \tag{13}$$

COMPARISON OF SHEAR CAPACITY FORMULA BEFORE AND AFTER MODIFICATION

Table 6 presents the modified shear capacity calculation formula for FRP-RC beams with stirrups in five design standards. In this regard, V_{pm} signifies the modified theoretical shear capacity, and the expression of f_{fv} is presented in Eq. (12). This study introduces a safety index, denoted by p, to assess the precision of modified equations. This index represents the percentage of samples with $V_{exp}/V_{pm} > 0.95$ among the total number of samples. Table 7 and Fig. 9 summarize the results of the shear capacity calculation formula before and after modification for the design standards considered in this study. The results show that the modified shear capacity equations have lower mean values and CV, and higher safety indices than all the original equations. These findings demonstrate that the modified equations significantly enhance the accuracy of the shear capacity calculation results for FRP-RC beams with stirrups, improve the safety of the shear design, and decrease the fluctuation of the results.

Table 8 summarizes the predictive performance of the formulas before and after modification concerning the shear capacity of concrete beams reinforced with FRP bars and stirrups, aiming to demonstrate the influence of FRP bar types on predictive performance of modified formulas. The

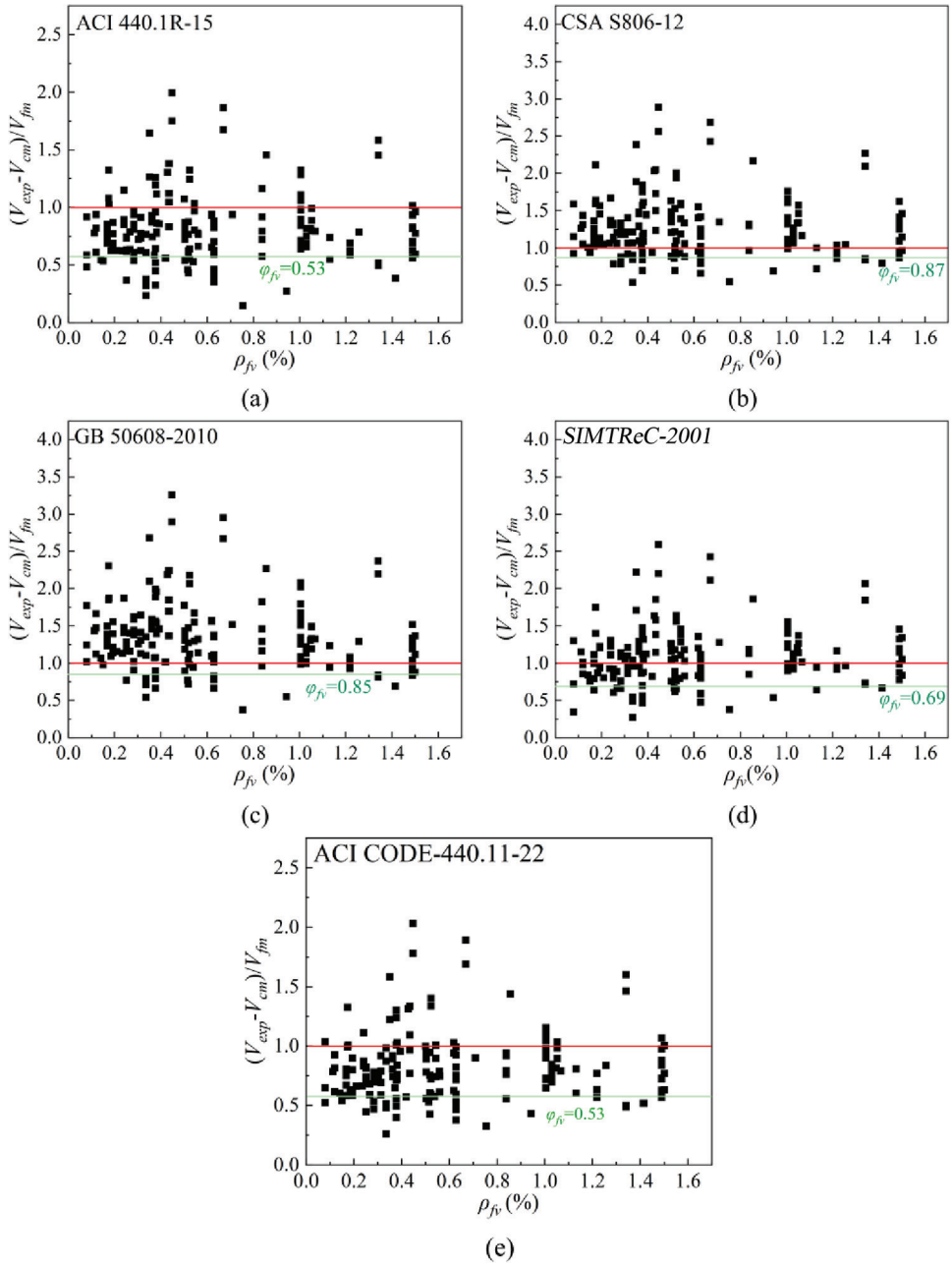

Fig. 8—Summarization of shear contribution coefficient for stirrups φ_{fv}.

Table 5—Summarization of modification to shear contribution of stirrups in all design standards

Design standards	Quantile values of φ_{fv}	Shear contribution coefficient of stirrups	Modified shear contribution of stirrups V_f
Modified ACI 440.1R-15	88%	0.53	$0.53\frac{A_{fv}f_{fv}d}{1.3s^{0.8}}$
Modified CSA S806-12	95%	0.87	$0.87\frac{A_{fv}f_{fv}d_v}{1.52s^{0.8}}$
Modified GB 50608-2010	89%	0.85	$0.85\frac{A_{fv}f_{fv}h_{of}}{1.97s^{0.75}}$
Modified SIMTReC-2001	87%	0.69	$0.69\frac{A_{fv}f_{fv}d}{1.56s^{0.8}}$
Modified ACI CODE-440.11-22	88%	0.53	$0.53\frac{A_{fv}f_{ft}d}{1.22s^{0.8}}$

table illustrates a substantial improvement in the predictive performance of the modified formulas across all three types of FRP-RC beams compared to the original formulas. Moreover, the modified formulas effectively maintain the ratio of shear capacity experimental values to theoretical values within a reasonable range for three types of beams. Additionally, the predictive performance of the modified formulas is found to be the highest for beams reinforced with CFRP bars

Table 6—Summary of modified shear equations in design standards

Design standards	Modified shear capacity V_{pm}
Modified ACI 440.1R-15	$\frac{2}{5\times(0.08\lambda^2-0.01\lambda+0.25)}\sqrt{f_c'}\,b_w kd+0.53\frac{A_{fv}f_{fv}d}{1.3s^{0.8}}$
Modified CSA S806-12	$\frac{0.05}{-0.01\lambda^2+0.39\lambda-0.2}\phi_c k_r k_s\sqrt[3]{f_c'}\,b_w d_v+0.87\frac{A_{fv}f_{fv}d_v}{1.52s^{0.8}}$
Modified GB 50608-2010	$\frac{0.86}{-0.003\lambda^3+0.11\lambda^2-0.08\lambda+0.2}f_t b_w k h_{of}+0.85\frac{A_{fv}f_{fv}h_{of}}{1.97s^{0.75}}$
Modified SIMTReC-2001	$\frac{0.2}{0.05\lambda^2+0.05\lambda+0.2}\phi_c\sqrt{f_c'}\,b_w d\sqrt{\frac{E_{frp}}{E_s}}+0.69\frac{A_{fv}f_{fv}d}{1.56s^{0.8}}$
Modified ACI CODE-440.11-22	$\max\begin{cases}\frac{5}{-0.015\lambda^2+1.18\lambda+0.4}\lambda_s k_{cr}\sqrt{f_c'}\,b_w d\\ \frac{0.8}{-0.015\lambda^2+1.18\lambda+0.4}\lambda_s\sqrt{f_c'}\,b_w d\end{cases}+0.53\frac{A_{fv}f_{ft}d}{1.22s^{0.8}}$

Table 7—Prediction results of shear equation before and after modification

Design standards	Mean	SD	CV	Safety factor p, %
ACI 440.1R-15[19]	1.52	0.58	0.38	81
CSA S806-12[20]	1.84	1.03	0.56	81
GB 50608-2010[21]	1.76	0.74	0.42	87
ISIS-2001[22]	1.94	0.73	0.37	94
ACI CODE-440.11-22[23]	0.77	0.25	0.32	20
Modified ACI 440.1R-15	1.31	0.30	0.23	92
Modified CSA S806-12	1.36	0.34	0.25	93
Modified GB 50608-2010	1.39	0.33	0.23	95
Modified SIMTReC-2001	1.33	0.29	0.22	92
Modified ACI CODE-440.11-22	1.36	0.33	0.24	94

and stirrups, followed by GFRP bars, and relatively lower for BFRP bars. These findings hold immense significance in the research field of FRP-RC beams with stirrups as they augment the comprehension of the influence of distinct FRP bar types on the predictive precision of modified formulas and offer invaluable insights to design engineers regarding the practical implementation of formulas for shear design of FRP-RC beams with stirrups.

The applicability of the revised shear formula for three types of FRP-RC beams with stirrups has been comprehensively validated through the introduction of a database comprising 23 FRP-RC beams with stirrups. The key parameters of the FRP-RC beams with stirrups included in this database are presented in Table 9. The verification results are summarized in Table 10, revealing that the experimental-to-theoretical shear capacity ratios of various types of FRP-RC beams with stirrups closely approximate the reference values corresponding to each revised formula in Table 8, indicating a high accuracy in the predictions provided by the revised formulas. It is noteworthy that the majority of the measured-to-theoretical values (V_{exp}/V_p) in the database for FRP-RC beams with stirrups exceed 0.95, demonstrating a high level of safety achieved by the revised formulas. These findings ascertain the sufficient applicability of the revised formulas in shear design of various types of FRP-RC beams with stirrups, consequently offering reliable guidance for engineering design, ensuring both structural safety and design economy. Moreover, they provide valuable references for future research, such as further enhancement of the formulas to cater to a broader range of engineering practices.

CONCLUSIONS

The experimental data, which consists of 174 sets of fiber-reinforced polymer-reinforced concrete (FRP-RC) beams with stirrups, was analyzed using gray correlation analysis to investigate the interrelationships between the longitudinal reinforcement ratio, stirrup spacing, shear span-depth ratio, and the shear capacity of FRP-RC beams with stirrups. Next, the similarities and differences of five design standards for FRP-RC beams were compared. Based on the analysis results mentioned herein, recommendations were proposed for modifying the shear contribution of concrete and stirrup in the calculation formula for shear capacity of FRP-RC beams with stirrups in the five design standards. The main findings are summarized as follows:

1. The gray correction analysis reveals that both the stirrup spacing and shear span-depth ratio exhibit a significant effect on the shear capacity of FRP-RC beams with stirrups. Thus, these parameters should be considered in shear design.

2. Comparing the five design standards regarding FRP-RC beams with stirrups, significant disparities in the shear capacity calculation formula are evident, specifically in relation to the concrete shear contribution, among different nations. Furthermore, four of these standards neglect the impact of shear span-depth ratio on the concrete shear contribution, leading to overly cautious calculations for beams with smaller ratios and compromised design safety for beams with larger ratios.

3. The modified shear capacity formulas improve the accuracy of shear capacity calculations for FRP-RC beams with stirrups. They result in smaller mean values, lower coefficients of variation, and a higher safety index compared to the original formulas. This enhancement of accuracy enhances the safety of shear design and reduces result fluctuations. The modified formulas were validated using a database of 23 FRP-RC beams with stirrups, demonstrating its suitability for shear design of these beams.

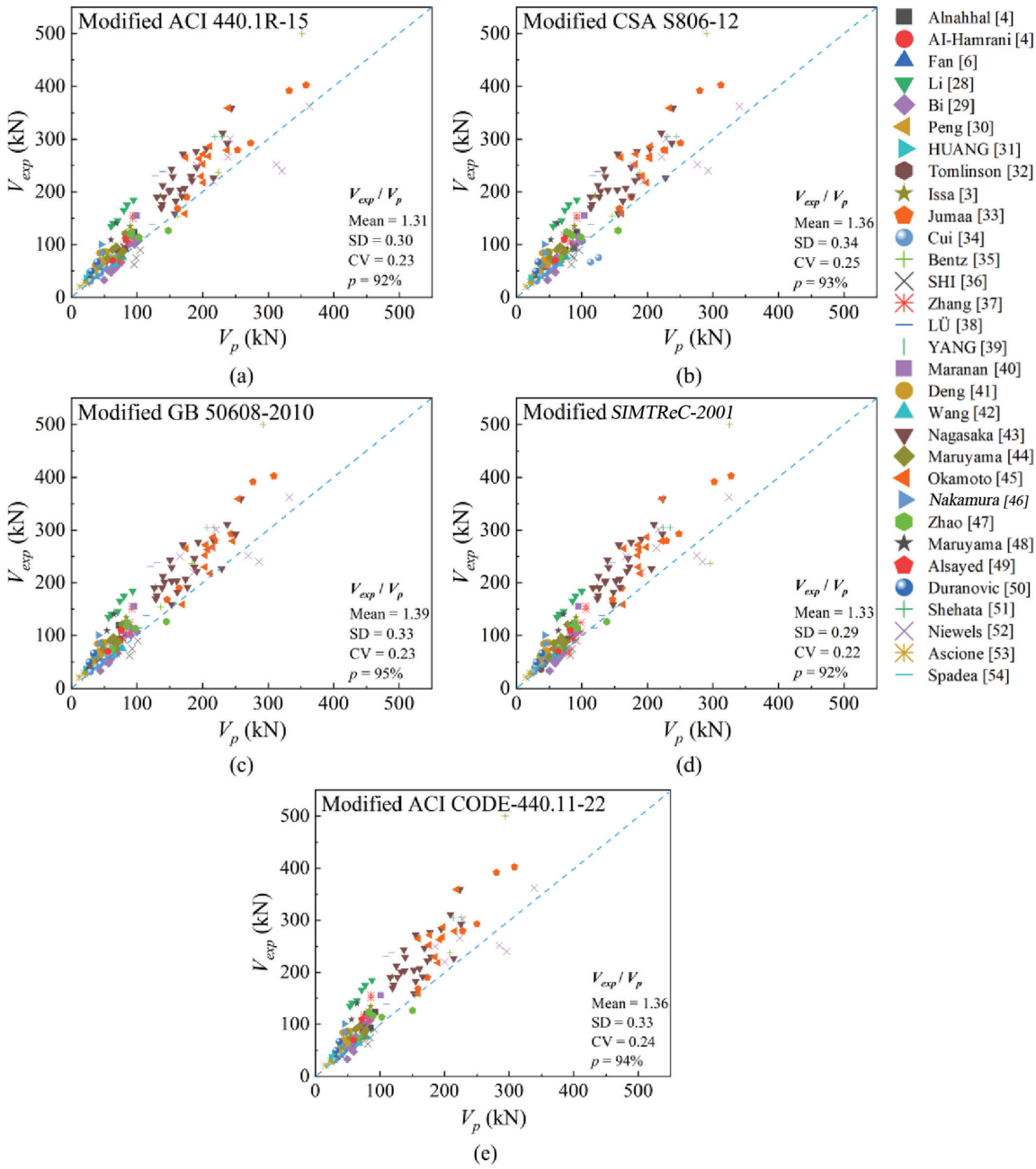

Fig. 9—Prediction results of modified shear equation in all design standards.

Table 8—Prediction performance of shear equations before and after modification about beams reinforced with three types of FRP bars

Types of FRP-RC beams	ACI 440.1R-15[19]		CSA S806-12[20]		GB 50608-2010[21]		SIMTReC-2001[22]		ACI CODE-440.11-22[23]	
	Original V_{exp}/V_p	Modified V_{exp}/V_p	Original V_{exp}/V_p	Modified V_{exp}/V_p	Original V_{exp}/V_p	Modified V_{exp}/V_p	Original V_{exp}/V_p	Modified V_{exp}/V_p	Original V_{exp}/V_p	Modified V_{exp}/V_p
BFRP	1.75	1.35	2.03	1.41	2.05	1.45	1.84	1.37	0.83	1.39
CFRP	1.20	1.25	1.37	1.29	1.33	1.28	1.84	1.25	0.72	1.31
GFRP	1.57	1.30	2.09	1.33	1.85	1.40	2.10	1.32	0.76	1.33

Note: V_{exp} /V_p signifies mean experimental-to-predicted shear capacity ratios for corresponding FRP-RC beam types.

AUTHOR BIOS

Yunxing Du *is a Professor at the Key Laboratory for Green & Advanced Civil Engineering Materials and Application Technology of Hunan Province, College of Civil Engineering, Hunan University, Changsha, China, where he received his BS, MS, and PhD in 1995, 2000, and 2003, respectively. His research interests include development and application of composites, structural strengthening, and steel structure.*

Table 9—Main parameters of FRP-RC beams with stirrups from references

Specimens		FRP type	b_w, mm	d, mm	l, mm	λ	ρ_f, %	ρ_{fv}, %	f_{cu}, MPa	V_{exp}, kN
Liao et al.[56]	10-125-1.95	BFRP	200	257	1000	1.95	1.17	0.63	55.0	186.0
	12-150-2.35		200	255	1200	2.35	1.18	0.75		105.7
	12-100-1.95		200	255	1000	1.95	1.18	1.13		203.9
	8-125-2.35		200	259	1200	2.35	1.16	0.40		113.1
	12-125-1.55		200	255	800	1.55	1.18	0.91		190.5
	10-100-2.35		200	257	1200	2.35	1.17	0.79		134.0
Chen[57]	L1	CFRP	200	319	2100	0.94	0. 90	0.15	33.4	215.0
	L2		200	319	2100	1.88	0. 90	0.15		197.5
	L3		200	319	2100	1.88	0. 90	0.20		207.5
Hou et al.[58]	L1		200	319	2100	1.88	0. 90	0.15	26.0	152.5
	L2		200	319	2100	1.88	0. 90	0.20		142.5
	L4		200	319	2100	1.88	0. 90	0.15	44.2	197.5
Zhou et al.[59]	B-1-Y-350-1.95-0.98		200	307	1800	1.95	1.00	0.52	37.6	138.5
	B-1-Y-350-2.44-0.98		200	307	1800	2.44	1.00	0.52		114.5
Krall and Polak[60]	BM12-220	GFRP	200	270	1810	2.50	2.50	0.51	59.8	191.2
	BM16-220		200	270	1930	2.50	2.20	0.51		154.7
	BM25-220		200	270	2470	2.50	1.80	0.51		180.1
	BM12-150		200	270	1810	2.50	2.50	0.75		202.6
	BM16-150		200	270	1930	2.50	2.20	0.75		208.3
	BM25-150		200	270	2470	2.50	1.80	0.75		207.9
	BM12-s230		230	270	1810	2.50	2.20	1.19		233.5
	BM16-s230		230	270	2110	2.50	1.90	1.19		225.1
	BM25-s230		230	270	2310	2.50	1.60	1.19		222.0

Table 10—Validation results of modified equations

Specimens	FRP type	V_{exp}/V_p				
		ACI 440.1R-15[19]	CSA S806-12[20]	GB 50608-2010[21]	SIMTReC-2001[22]	ACI CODE-440.11-22[23]
10-125-1.95	BFRP	1.72	1.84	1.84	1.69	1.87
12-150-2.35		0.95	0.95	1.02	0.94	0.99
12-100-1.95		1.68	1.71	1.75	1.67	1.79
8-125-2.35		1.28	1.38	1.40	1.25	1.38
12-125-1.55		1.45	1.54	1.53	1.45	1.61
10-100-2.35		1.33	1.35	1.40	1.31	1.39
Mean		1.40	1.46	1.49	1.38	1.50
Reference mean value		1.35	1.41	1.45	1.37	1.39
L1	CFRP	1.02	1.13	1.52	1.63	1.23
L2		1.20	1.39	1.40	1.50	1.37
L3		1.20	1.36	1.37	1.48	1.36
L1		1.03	1.20	1.19	1.31	1.18
L2		0.92	1.04	1.03	1.15	1.04
L4		1.02	1.21	1.22	1.30	1.17
Mean		1.06	1.22	1.29	1.40	1.23
Reference mean value		1.25	1.29	1.28	1.25	1.31

Table 10, cont.—Validation results of modified equations

Specimens	FRP type	V_{exp}/V_p				
		ACI 440.1R-15[19]	CSA S806-12[20]	GB 50608-2010[21]	ISIS-2001[22]	ACI CODE-440.11-22[23]
B-1-Y-350-1.95-0.98	GFRP	1.31	1.44	1.42	1.27	1.48
B-1-Y-350-2.44-0.98		1.20	1.24	1.31	1.16	1.29
BM12-220		1.19	1.19	1.31	1.29	1.23
BM16-220		0.98	1.00	1.09	1.05	1.02
BM25-220		1.31	1.35	1.44	1.36	1.36
BM12-150		1.16	1.14	1.25	1.25	1.20
BM16-150		1.22	1.21	1.31	1.30	1.26
BM25-150		1.39	1.40	1.50	1.45	1.44
BM12-s230		0.99	0.88	1.07	1.04	1.00
BM16-s230		0.98	0.88	1.06	1.02	0.99
BM25-s230		1.10	1.03	1.19	1.12	1.11
Mean		1.17	1.16	1.27	1.21	1.22
Reference mean value		1.30	1.33	1.40	1.32	1.33

Note: Reference mean value represents corresponding mean value of modified equation in Table 8.

Baoqiang Liao *is a Graduate Student in the College of Civil Engineering at Hunan University. He received his BS in civil engineering from Shantou University, Shantou, China, in 2016. His research interests include shear behavior of seawater sea-sand concrete (SSC) beams reinforced with basalt fiber-reinforced polymer (FRP) bar.*

Rui Zhou *is a Graduate Student in the College of Civil Engineering at Hunan University. He received his BS from China University of Geosciences, Wuhan, China, in 2016. His research interests include durability and shear behavior of SSC beams reinforced with basalt FRP bar and concrete structures reinforced with FRP.*

Deju Zhu *is a Professor at the Key Laboratory for Green & Advanced Civil Engineering Materials and Application Technology of the College of Civil Engineering, Hunan University. He received his BS and MS from Northeast Forestry University, Harbin, China, in 2003 and 2005, respectively, and his PhD from Arizona State University, Tempe, AZ, in 2009. His research interests include SSC; FRP bar-reinforced SSC structures in marine environments; high-performance textile-reinforced concrete (TRC); and multiscale behavior of biological and bio-inspired materials.*

ACKNOWLEDGMENTS

The work was financially supported by the National Natural Science Foundation of China-Shandong Joint Fund (U1806225). D. Zhu (dzhu@hnu.edu.cn) is the corresponding author.

REFERENCES

1. Huang, H.; Hao, R.-Q.; and Huang, M., "Research Status of FRP Reinforced Concrete Structures," *Glass Fiber Reinforced Plastics/Composite Materials*, V. 7, 2018, pp. 108-116. (in Chinese)

2. Omeman, Z.; Nehdi, M.; and El-Chabib, H., "Experimental Study on Shear Behavior of Carbon-Fiber-Reinforced Polymer Reinforced Concrete Short Beams without Web Reinforcement," *Canadian Journal of Civil Engineering*, V. 35, No. 1, 2008, pp. 1-10. doi: 10.1139/L07-080

3. Issa, M. A.; Ovitigala, T.; and Ibrahim, M., "Shear Behavior of Basalt Fiber Reinforced Concrete Beams with and without Basalt FRP Stirrups," *Journal of Composites for Construction*, ASCE, V. 20, No. 4, 2016, p. 04015083. doi: 10.1061/(ASCE)CC.1943-5614.0000638

4. Al-Hamrani, A.; Alnahhal, W.; and Elahtem, A., "Shear Behavior of Green Concrete Beams Reinforced with Basalt FRP Bars and Stirrups," *Composite Structures*, V. 277, 2021, p. 114619. doi: 10.1016/j.compstruct.2021.114619

5. Al-Hamrani, A., and Alnahhal, W., "Shear Behavior of Basalt FRC Beams Reinforced with Basalt FRP Bars and Glass FRP Stirrups: Experimental and Analytical Investigations," *Engineering Structures*, V. 242, 2021, p. 112612. doi: 10.1016/j.engstruct.2021.112612

6. Fan, X.; Zhou, Z.; Tu, W.; and Zhang, M., "Shear Behaviour of Inorganic Polymer Concrete Beams Reinforced with Basalt FRP Bars and Stirrups," *Composite Structures*, V. 255, 2021, p. 112901. doi: 10.1016/j.compstruct.2020.112901

7. Abed, F.; El-Refai, A.; and Abdalla, S., "Experimental and Finite Element Investigation of the Shear Performance of BFRP-RC Short Beams," *Structures*, V. 20, 2019, pp. 689-701. doi: 10.1016/j.istruc.2019.06.019

8. Uomoto, T.; Ishibashi, T.; Nobuta, Y.; Satoh, T.; Kawano, H.; and Uji, K., "Standard Specifications for Concrete Structures-2007 by Japan Society of Civil Engineers," *Concrete Journal*, V. 46, No. 7, 2008, pp. 3-14. doi: 10.3151/coj1975.46.7_3

9. Liu, J. X., and Liang, B. L., "Grey Correlation Analysis of Sensitive Factors of Concrete Structures Durability," *Key Engineering Materials*, V. 400-402, 2008, pp. 471-476. doi: 10.4028/www.scientific.net/KEM.400-402.471

10. Chou, J.-S., and Ongkowijoyo, C. S., "Reliability-Based Decision Making for Selection of Ready-Mix Concrete Supply Using Stochastic Superiority and Inferiority Ranking Method," *Reliability Engineering & System Safety*, V. 137, 2015, pp. 29-39. doi: 10.1016/j.ress.2014.12.004

11. Jiang, W.; Shen, X.; Xia, J.; Mao, L.; Yang, J.; and Liu, Q., "A Numerical Study on Chloride Diffusion in Freeze-Thaw Affected Concrete," *Construction and Building Materials*, V. 179, 2018, pp. 553-565. doi: 10.1016/j.conbuildmat.2018.05.209

12. Xu, J.-J.; Chen, Z.-P.; Ozbakkaloglu, T.; Zhao, X.-Y.; and Demartino, C., "A Critical Assessment of the Compressive Behavior of Reinforced Recycled Aggregate Concrete Columns," *Engineering Structures*, V. 161, 2018, pp. 161-175. doi: 10.1016/j.engstruct.2018.02.003

13. Zhou, C.; Cao, J.; and Chen, Z., "Bond Behavior of Steel-Recycled Aggregate Concrete Interface after High Temperatures and Spraying Water Cooling," *Frontiers in Materials*, V. 8, 2021, p. 643510. doi: 10.3389/fmats.2021.643510

14. Zhu, L.; Zhao, C.; and Dai, J., "Prediction of Compressive Strength of Recycled Aggregate Concrete Based on Gray Correlation Analysis," *Construction and Building Materials*, V. 273, 2021, p. 121750. doi: 10.1016/j.conbuildmat.2020.121750

15. Shahnewaz, M.; Machial, R.; Alam, M. S.; and Rteil, A., "Optimized Shear Design Equation for Slender Concrete Beams Reinforced with FRP Bars and Stirrups Using Genetic Algorithm and Reliability Analysis," *Engineering Structures*, V. 107, 2016, pp. 151-165. doi: 10.1016/j.engstruct.2015.10.049

16. El-Sayed, A. K.; El-Salakawy, E. F.; and Benmokrane, B., "Shear Strength of FRP-Reinforced Concrete Beams without Transverse Reinforcement," *ACI Structural Journal*, V. 103, No. 2, Mar.-Apr. 2006, pp. 235-243.

17. Kim, C. H., and Jang, H. S., "Concrete Shear Strength of Normal and Lightweight Concrete Beams Reinforced with FRP Bars," *Journal of Composites for Construction*, ASCE, V. 18, No. 2, 2014, p. 04013038. doi: 10.1061/(ASCE)CC.1943-5614.0000440

18. Jin, L.; Wang, T.; and Du, X.-L., "Size Effect Theory on Shear Strength of RC Cantilever Beams without Stirrups," *Chinese Journal of Computational Mechanics*, V. 37, No. 4, 2020, pp. 396-404. (in Chinese)

19. ACI Committee 440, "Guide for the Design and Construction of Structural Concrete Reinforced with Fiber-Reinforced Polymer (FRP) Bars (ACI 440.1R-15)," American Concrete Institute, Farmington Hills, MI, 2015, 88 pp.

20. CSA S806-12, "Design and Construction of Building Structures with Fiber-Reinforced Polymers," CSA Group, Toronto, ON, Canada, 2012.

21. GB 50608-2010, "Technical Code for Infrastructure Application of FRP Composites," China Planning Press, Beijing, China, 2010.

22. Design Manual No. 3, "Reinforcing Concrete Structures with Fibre Reinforced Polymers," SIMTReC, Winnipeg, MB, Canada, 2001.

23. ACI Committee 440, "Building Code Requirements for Structural Concrete Reinforced with Glass Fiber-Reinforced Polymer (GFRP) Bars—Code and Commentary (ACI CODE-440.11-22)," American Concrete Institute, Farmington Hills, MI, 2022, 260 pp.

24. GB 50010-2010, "Code for Design of Concrete Structures," Standardization Administration of China, Beijing, China, 2010.

25. Tureyen, A. K., and Frosch, R. J., "Concrete Shear Strength: Another Perspective," *ACI Structural Journal*, V. 100, No. 5, Sept.-Oct. 2003, pp. 609-615.

26. Razaqpur, A. G., and Isgor, O. B., "Proposed Shear Design Method for FRP-Reinforced Concrete Members without Stirrups," *ACI Structural Journal*, V. 103, No. 1, Jan.-Feb. 2006, pp. 93-102.

27. Razaqpur, A. G., and Spadea, S., "Shear Strength of FRP Reinforced Concrete Members with Stirrups," *Journal of Composites for Construction*, ASCE, V. 19, No. 1, 2015, p. 04014025. doi: 10.1061/(ASCE)CC.1943-5614.0000483

28. Li, S., "Experiment Studies on the Shear Performance of Sea Sand Concrete Beam with BFRP Tendons," master's thesis, School of Civil and Transportation Engineering, Guangdong University of Technology, Guangdong, China, 2014. (in Chinese)

29. Bi, Q., "Experimental Research on the Micro-Structure of Basalt Fiber Reinforced Concrete and the Oblique Section Bearing Capacity of the BFRP Bars Reinforced Fiber Concrete Beams," PhD dissertation, Dalian University of Technology, Dalian, China, 2012. (in Chinese)

30. Peng, J., "Research on Shear Performance of BFRP Reinforced Concrete Beams," master's thesis, Xiamen University, Xiamen, China, 2019. (in Chinese)

31. Huang, Z.-H.; Lin, J.-B.; Lu, J.-J.; and Guo, F.-B., "Influence of Shear Span Ratio on the Shearing Properties of BFRP Tendons Concrete Beams," *Journal of Taizhou University*, V. 35, No. 3, 2013, pp. 43-47. (in Chinese)

32. Tomlinson, D., and Fam, A., "Performance of Concrete Beams Reinforced with Basalt FRP for Flexure and Shear," *Journal of Composites for Construction*, ASCE, V. 19, No. 2, 2015, p. 04014036. doi: 10.1061/(ASCE)CC.1943-5614.0000491

33. Jumaa, G. B., and Yousif, A. R., "Size Effect on the Shear Failure of High-Strength Concrete Beams Reinforced with Basalt FRP Bars and Stirrups," *Construction and Building Materials*, V. 209, 2019, pp. 77-94. doi: 10.1016/j.conbuildmat.2019.03.076

34. Cui, Q., "Study on Shear Resistance Properties of the Oblique Section of GFRP Reinforced Concrete Members and its Designed Method," master's thesis, Southwest Jiaotong University, Chengdu, China, 2007. (in Chinese)

35. Bentz, E. C.; Massam, L.; and Collins, M. P., "Shear Strength of Large Concrete Members with FRP Reinforcement," *Journal of Composites for Construction*, ASCE, V. 14, No. 6, 2010, pp. 637-646. doi: 10.1061/(ASCE)CC.1943-5614.0000108

36. Shi, X.; Zhang, Z.; Li, Z.; and Lou, X., "Influencing Factors of Shear Capacity of Concrete Beam Reinforced with GFRP," *Journal of Southwest Jiaotong University*, V. 45, No. 6, 2010, pp. 898-903. (in Chinese)

37. Zhang, J., "Experimental Study on Shear Behavior of all Coral Concrete Beams Reinforced with CFRP Bars," master's thesis, Guilin University of Technology, Guilin, China, 2020. (in Chinese)

38. Lü, J.; Pan, J.; Di, B.; Zheng, Y.; Zhu, W.; Li, J.; Zhang, Z.; and Zhou, L., "Experimental Study on Shear Capacity of Seawater Sea-Sand and Self-Compacting Concrete Beams with GFRP Bars and Stirrups," *Concrete*, V. 11, 2021, pp. 53-57. (in Chinese)

39. Yang, F., "Deformation Behaviour of Beams Reinforced with Fibre Reinforced Polymer Bars under Bending and Shear," PhD dissertation, University of Sheffield, Sheffield, UK, 2015.

40. Maranan, G. B.; Manalo, A. C.; Benmokrane, B.; Karunasena, W.; Mendis, P.; and Nguyen, T. Q., "Shear Behaviour of Geopolymer-Concrete Beams Transversely Reinforced with Continuous Rectangular GFRP Composite Spirals," *Composite Structures*, V. 187, 2018, pp. 454-465. doi: 10.1016/j.compstruct.2017.12.080

41. Deng, S., "Research on Load-Bearing Mechanism and Shear Capacity Prediction of BFRP Reinforced Concrete Beams," master's thesis, Xiamen University, Xiamen, China, 2020. (in Chinese)

42. Wang, Z.; Xie, J.; Li, J.; Liu, P.; Shi, C.; and Lu, Z., "Flexural Behaviour of Seawater–Sea Sand Concrete Beams Reinforced with GFRP Bars: Effects of the Reinforcement Ratio, Stirrup Ratio, Shear Span Ratio and Prestress Level," *Journal of Building Engineering*, V. 54, 2022, p. 104566. doi: 10.1016/j.jobe.2022.104566

43. Nagasaka, T.; Fukuyama, H.; and Tanigaki, M., "Shear Performance of Concrete Beams Reinforced with FRP Stirrups," *Fiber-Reinforced-Plastic Reinforcement for Concrete Structures - International Symposium*, SP-138, A. Nanni and C. W. Dolan, eds., American Concrete Institute, Farmington Hills, MI, 1993, pp. 789-812.

44. Maruyama, K., and Zhao, W. J., "Flexural and Shear Behaviour of Concrete Beams Reinforced by FRP Rods," *Corrosion and Corrosion Protection of Steel in Concrete: Proceedings of International Conference*, Sheffield, UK, 1994.

45. Okamoto, T.; Nagasaka, T.; and Tanigaki, M., "Shear Capacity of Concrete Beams Using FRP Reinforcement," *Journal of Structural and Construction Engineering*, V. 59, No. 455, 1994, pp. 127-136. doi: 10.3130/aijs.59.127_1

46. Nakamura, H., and Higai, T., "Evaluation of Shear Strength of Concrete Beams Reinforced with FRP," *Doboku Gakkai Rombunshuu*, V. 1995, No. 508, 1995, pp. 89-100. doi: 10.2208/jscej.1995.508_89

47. Zhao, W.; Maruyama, K.; and Suzuki, H., "Shear Behavior of Concrete Beams Reinforced by FRP Rods as Longitudinal and Shear Reinforcement," *Non-Metallic (FRP) Reinforcement for Concrete Structures: Proceedings of the Second International RILEM Symposium*, CRC Press, Boca Raton, FL, 1995, pp. 352-359.

48. Maruyama, K., and Zhao, W., "Size Effect in Shear Behavior of FRP Reinforced Concrete Beams," *International Conference on Advanced Composite Materials in Bridges and Structures*, Montreal, QC, Canada, 1996, pp. 227-234.

49. Alsayed, S. H., "Flexural Behaviour of Concrete Beams Reinforced with GFRP Bars," *Cement and Concrete Composites*, V. 20, No. 1, 1998, pp. 1-11. doi: 10.1016/S0958-9465(97)00061-9

50. Duranovic, N.; Pilakoutas, K.; and Waldron, P., "Tests on Concrete Beams Reinforced with Glass Fibre Reinforced Plastic Bars," *Non-Metallic (FRP)*," *Reinforcement for Concrete Structure*, V. 2, 1997, pp. 479-486.

51. Shehata, E.; Morphy, R.; and Rizkalla, S., "Fibre Reinforced Polymer Shear Reinforcement for Concrete Members: Behaviour and Design Guidelines," *Canadian Journal of Civil Engineering*, V. 27, No. 5, 2000, pp. 859-872. doi: 10.1139/l00-004

52. Niewels, J., "Zum Tragverhalten von Betonbauteilen mit Faserverbundkunststoff-Bewehrung," dissertation, RWTH Aachen University, Aachen, Germany, 2008.

53. Ascione, L.; Mancusi, G.; and Spadea, S., "Flexural Behaviour of Concrete Beams Reinforced with GFRP Bars," *Strain*, V. 46, No. 5, 2010, pp. 460-469. doi: 10.1111/j.1475-1305.2009.00662.x

54. Spadea, S., "Comportamento di elmenti di calcestruzzo armato con barre di materiale compositeo fibroinforzato," University of Salerno, Fisciano, Italy, 2010.

55. Said, M.; Adam, M. A.; Mahmoud, A. A.; and Shanour, A. S., "Experimental and Analytical Shear Evaluation of Concrete Beams Reinforced with Glass Fiber Reinforced Polymers Bars," *Construction and Building Materials*, V. 102, 2016, pp. 574-591. doi: 10.1016/j.conbuildmat.2015.10.185

56. Liao, B.; Du, Y.; Zhou, R.; Rahman, M. Z.; and Zhu, D., "Shear Behavior of Seawater–Sea Sand Concrete Beams Reinforced with BFRP Bars and Stirrups," *Journal of Composites for Construction*, V. 28, No. 2, 2024, p. 04023077. doi: 10.1061/JCCOF2.CCENG-4332

57. Chen, Q.-J., "Experimental Study on Shear Performance of CFRP-Reinforced Concrete Beams," *Building Technology Development*, V. 49, No. 9, 2022, pp. 108-113.

58. Hou, M.; Yang, Y.; Jia, B.; Li, B.; and Yu, J., "Experiment Study of the Shear Performance of Coral Aggregate Concrete Beam with CFRP Bars," *Industrial Construction*, V. 46, No. 10, 2016, pp. 174-178.

59. Zhou, L.; Zheng, Y.; Di, B.; Lv, J.; and Taylor, S., "Shear Behaviour of SWSS-SCC Beams Reinforced with GFRP Bars and Stirrups: Experimental and Analytical Investigations," *Structures*, V. 56, 2023, p. 104946. doi: 10.1016/j.istruc.2023.104946

60. Krall, M., and Polak, M. A., "Concrete Beams with Different Arrangements of GFRP Flexural and Shear Reinforcement," *Engineering Structures*, V. 198, 2019, p. 109333 doi: 10.1016/j.engstruct.2019.109333

ACI STRUCTURAL JOURNAL TECHNICAL PAPER

Title No. 123-S41

Lateral Response of Repaired Conventional and Hybrid Reinforced Concrete Bridge Piers

by Sherif M. S. Osman, M. Shahria Alam, and Shamim A. Sheikh

This study examines the lateral cyclic response of a repaired damaged bridge pier originally reinforced with fiber-reinforced polymer (FRP) bars, particularly glass FRP (GFRP), as a corrosion-resistant and durable alternative to traditional steel. An as-built large-scale hybrid (GFRP-steel) reinforced concrete (RC) column had an outer cage reinforced with GFRP bars and an inner cage reinforced with steel reinforcing bars. The columns were first tested under cyclic lateral loading, where the hybrid specimen demonstrated ductility and energy dissipation capacity comparable to a conventional single-layer steel RC column. Following these initial tests, both specimens were repaired using FRP wraps and retested under the same loading protocol, resulting in a total of four tests. Enhanced structural integrity and energy dissipation demonstrate the effectiveness of innovative repair techniques in seismic engineering. These findings provide a blueprint for resilient infrastructure in earthquake-prone areas and contribute to advancements in bridge design and repair strategies.

Keywords: bridge piers; corrosion resistance; hybrid bridge piers; hybrid reinforcement; repair.

INTRODUCTION

Steel corrosion in bridge infrastructure is a significant challenge that substantially reduces the service life (Holland et al. 2023; Lau et al. 2023). To address this, new design methods focus on improving ductility and seismic resilience (Abbass et al. 2020; Rassoulpour et al. 2023). A key approach is the use of glass fiber-reinforced polymer (GFRP) bars, which offer strong corrosion resistance and help reduce cracking, enhancing structural durability (Dasgupta 2018; El-Sayed et al. 2023; Sheikh and Kharal 2018). GFRP bars, when used instead of internal steel in bridge slabs and beams, provide reliable strength and enhanced deformation capacity (Bakis et al. 2002; El-Salakawy et al. 2005; Ge et al. 2019; Kassem et al. 2011; Pecce et al. 2000; Soric et al. 2010; Tu et al. 2009). When adequate confinement is provided per North American codes and standards (CSA A23.3:19 [2019]; ACI 318-19 [ACI Committee 318 2019]), GFRP spirals can offer superior confinement compared to traditional steel lateral reinforcement (Kharal et al. 2021).

The increasing use of carbon and glass FRP bars in bridges in the United States, Japan, and Canada (Ahmed et al. 2010; Aidoo et al. 2006; Benmokrane et al. 2007; Grace et al. 2012; Lau et al. 2023; Pham et al. 2024; Vosooghi and Saiidi 2013) has paved the way for the recent integration of FRP spirals and bars in reinforced concrete (RC) columns, driving advancements in material technologies within the construction industry. Yet, the tendency of GFRP bars to fail in a brittle manner under tensile strain poses a threat to structural integrity, especially under seismic forces that can induce tensile strains close to the ultimate GFRP's capacity, potentially leading to cracking and collapse. In light of this challenge, researchers have developed hybrid configurations combining steel bars and GFRP spirals to reduce corrosion while preserving stiffness and ductility. Studies show that these hybrid columns offer greater ductility and energy dissipation, outperforming GFRP-only columns under cyclic loading (Kharal et al. 2021; Prajapati et al. 2022a,b), and drive interest in hybrid RC bridge piers (HRCBP) for improved seismic performance.

Further, RC columns with double stirrup layers have shown improved ductility and axial load-carrying capacity due to enhanced confinement (Chen et al. 2012; Sun et al. 2017a,b; Wu et al. 2016; Yang et al. 2015). The inner and outer spiral layers provide different levels of confinement. Several studies (Jia et al. 2020, 2023; Li et al. 2018; Sun et al. 2017a,b; Wu et al. 2016; Yang et al. 2015) have used the average effective confinement model. The lateral behavior of RC columns with double spiral layers has also been widely investigated, with a focus on their capacity to resist lateral loads (Jia et al. 2020; Kim 2022; Li et al. 2018). The use of two spiral layers has been shown to enhance lateral strength and stiffness significantly (Li et al. 2018; Sun and Li 2019). Meanwhile, the need to retrofit aging infrastructure has become more pressing, which has made FRP sheets a valuable solution. Used for repair and strengthening, they improve flexural and shear strength, ductility, and seismic performance. Their light weight, corrosion resistance, and cost-effectiveness make them ideal for externally confining RC bridge columns.

This study builds upon these insights by presenting a comparative performance analysis of a repaired full-scale HRCBP, originally constructed with separate reinforcing bar cages for GFRP and conventional steel bars, against a repaired traditional single-layer RC bridge pier subjected to quasi-static cyclic loading. The research begins by thoroughly evaluating the as-built performance of the HRCBP, focusing on the double-confined hybrid (DCH) configuration compared to traditional single-layer RC bridge piers. Afterward, both piers were repaired with FRP wraps and retested using the same loading protocol. The study compares the

ACI Structural Journal, V. 123, No. 3, May 2026.
MS No. S-2024-057.R4, doi: 10.14359/51749314, received September 18, 2025, and reviewed under Institute publication policies. Copyright © 2026, American Concrete Institute. All rights reserved, including the making of copies unless permission is obtained from the copyright proprietors. Pertinent discussion including author's closure, if any, will be published ten months from this journal's date if the discussion is received within four months of the paper's print publication.

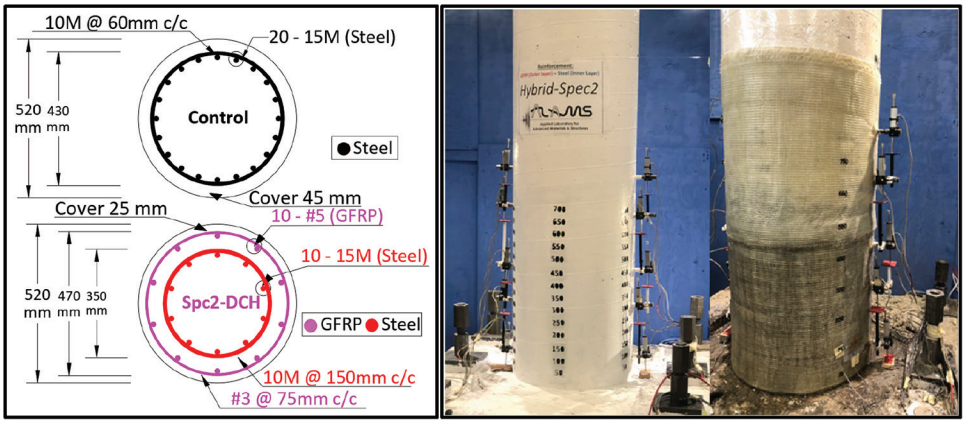

Fig. 1—Specimen cross section: Spc2-DCH as-built and after being repaired.

Table 1—Reinforcement details for specimens (Control and Spc2-DCH)

Description	Conventional bridge pier	Bridge pier (two layers)
Code	Control	Spc2-DCH
Number of layers of longitudinal reinforcement	1	2
Number of layers of transverse reinforcement	1	2
External layer: outer diameter, mm	430	470
Internal layer: outer diameter, mm	NA	350
External layer: number of longitudinal reinforcing bars	20	10
External layer: area of longitudinal reinforcing bars	200	199
External layer: longitudinal reinforcement ratio, %	1.901	0.946
Internal layer: number of longitudinal reinforcing bars	NA	10
Internal layer: area of longitudinal reinforcing bars		200
Internal layer: longitudinal reinforcement ratio, %		0.951
External layer: volumetric transverse reinforcement ratio, %	1.592	0.824
External layer: spacing of transverse reinforcement, mm	60	75
External layer: diameter of longitudinal reinforcing bar ϕ, mm	15.9	10.33
Internal layer: volumetric transverse reinforcement ratio, %	NA	0.787
Internal layer: spacing of transverse reinforcement, mm		150
Internal layer: diameter of longitudinal reinforcing bar ϕ, mm		11.3

Note: NA is not available.

as-built and repaired specimens in terms of damage mechanisms, hysteretic responses, energy dissipation, damping ratios, and reinforcement strains.

RESEARCH SIGNIFICANCE

This study examines the repair and post-repair seismic performance of large-scale HRCBP using FRP sheets. Through pioneering large-scale cyclic loading experiments, this study aimed to document the response of these piers to both original and subsequent lateral cyclic loads in their initial and repaired conditions, focusing on changes in damage patterns and structural integrity. Results revealed that repairs significantly enhanced the seismic resilience, making them an effective retrofit solution.

EXPERIMENTAL PROGRAM

Test specimens, setup, and procedure

This section examines the performance of HRCBP, designated as Spc2-DCH, compared to that of conventional single-layer RC bridge piers, referred to as Control. This section presents the geometry and design (Fig. 1 and Table 1) of the three-span continuous concrete-box girder bridge in Vancouver, BC, Canada (Siddiquee and Alam 2017). A spectral analysis that predicted demands at various hazard levels was conducted to design the bridge piers using elastic response. A performance-based design (PBD) approach was adopted, considering two different return periods—one with a 2% probability of exceedance in 50 years (corresponding to 2475 years) and another with a 5% probability of exceedance in 50 years (corresponding to 975 years). The site-specific spectral acceleration was determined based on the hazard level defined in the 2015

National Building Code of Canada (NBCC 2015). Half-scale models were constructed based on a prototype pier with a diameter of 914 mm and a height of 4.7 m. An axial load of 800 kN (approximately 10% of capacity) was applied using the tributary method. A column aspect ratio of 5 was used to ensure flexure-dominant behavior. Specimens were evaluated after initial testing, after repair, and post-retesting phases (Fig. 1). Data were collected using LabVIEW 2020, with load cells and linear variable differential transformers (LVDTs) ensuring consistent force and displacement measurements. Reverse cyclic loading followed two cycles per drift level (Fig. 2), increasing from $1\Delta_Y$ to $9\Delta_Y$ (1.04 to 9.35% drift). A service drift of 0.61% was applied before each increase, following the ACI Committee 374 Report's guidance and Ali and El-Salakawy (2016). The actuator (pull) side is labeled South (S-side), and the push direction is North (N-side), with positive drift indicating push (→) and negative indicating pull (←). Following the initial testing phase and damage assessment, a detailed repair procedure was implemented to restore and strengthen the specimens for subsequent retesting.

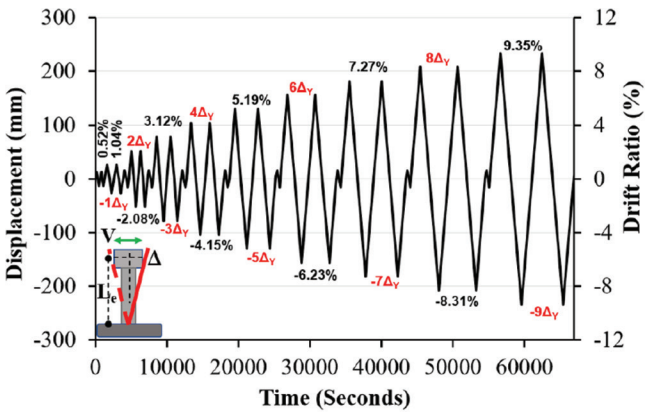

Fig. 2—Test procedure (loading protocol) applied.

The repair of damaged bridge piers was conducted using FRP wraps. The process included removing loose concrete, realigning the column, installing new strain gauges (SGs), and applying fresh concrete. The plastic hinge region and a portion beyond it were then wrapped with impregnated FRP sheets to ensure adequate confinement and restore structural integrity (Fig. 3 and 4). Material properties were evaluated through tensile tests on three-layer dog-bone specimens (Fig. 3) using a universal testing machine, following CSA-S806:12 (2021). Test results are shown in Table 2, and the full repair sequence is illustrated in Fig. 4.

EXPERIMENTAL RESULTS AND DISCUSSION

This section presents and compares the experimental results of HRCBP and Control piers (as-built and repaired), focusing on damage mechanisms and structural behavior. Despite the limited sample size, the findings offer valuable insights for seismic design, retrofit strategies, and future research directions. The following subsection examines the detailed hysteretic behavior and failure patterns of the tested specimens, highlighting key differences in seismic performance.

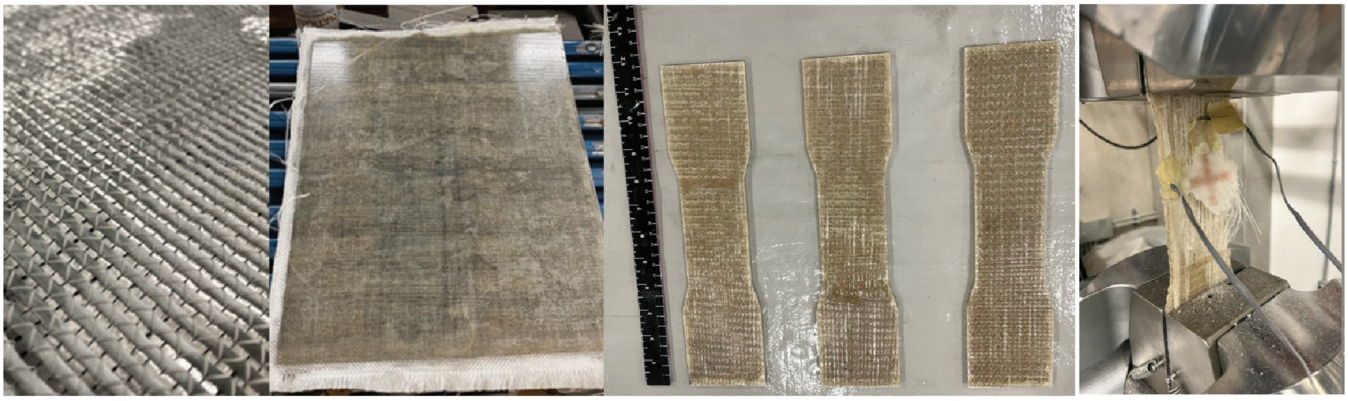

Fig. 3—(a) Preparation of FRP specimens before; and (b) instrumented for testing.

Fig. 4—Control and Spc2-DCH repairs: concrete removal, installing new instrumentation, placing new concrete, and wrapping three layers around specimens.

Table 2—FRP coupon tensile testing

Specimen	Width, mm	Thickness, mm	Stress σ, MPa	Strain ε, mm/mm	Young's modulus of elasticity E, GPa
Three layers of FRP (Specimens S1, S2, and S3)	W1 = W2 = W3 = 60	T1 = 4.51, T2 = 4.50, and T3 = 4.23	$\sigma1$ = 236.64, $\sigma2$ = 210.25, and $\sigma3$ = 220.24	$\varepsilon1$ = 0.0152, $\varepsilon2$ = 0.0125, and $\varepsilon3$ = 0.0132	E1 = 15.57, E2 = 16.82, and E3 = 16.68

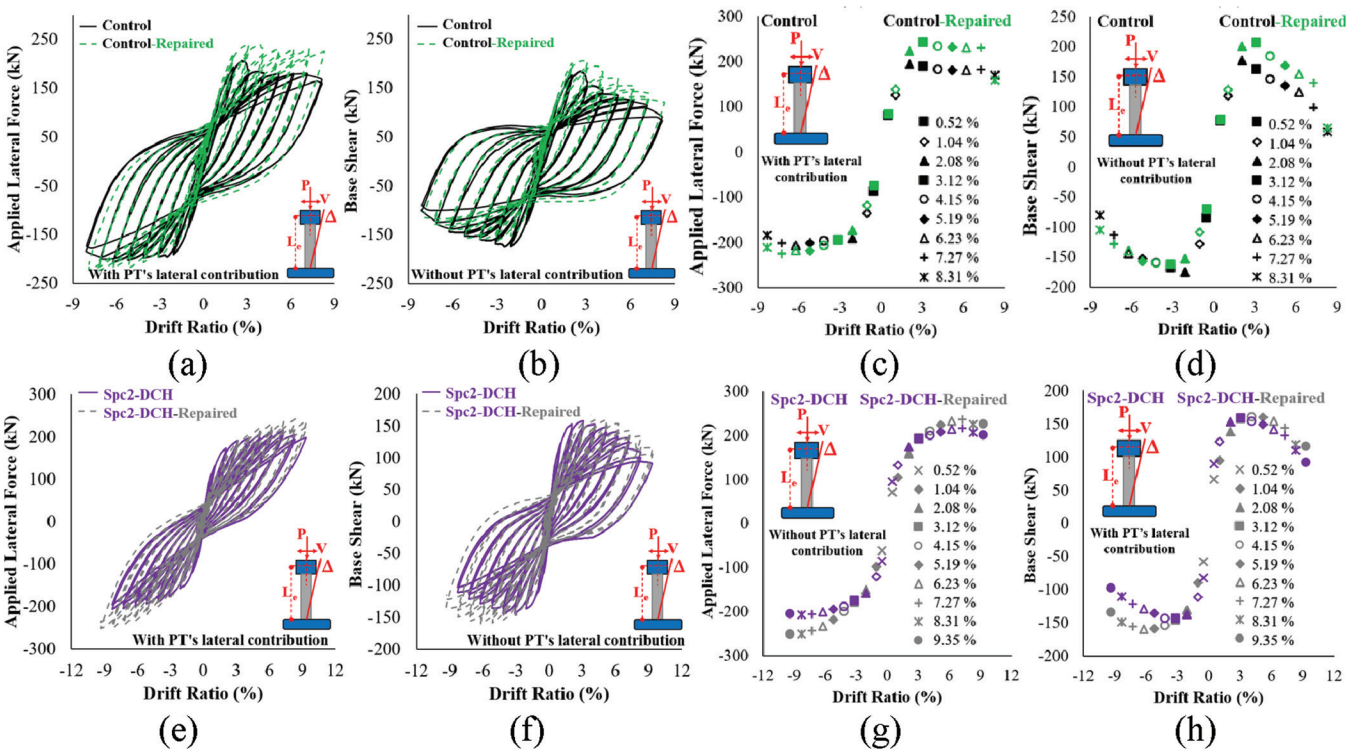

Fig. 5—Lateral force-drift and base shear-drift responses: (a) and (c) applied lateral force-drift and (b) and (d) base shear-drift for Control versus Control-Repaired specimens; (e) and (g) applied lateral force-drift and (f) and (h) base shear-drift for Spc2-DCH versus Spc2-DCH-Repaired specimens.

Hysteretic response relationships

This section evaluates the seismic behavior, failure patterns, and hysteretic response of four specimens, as illustrated in Fig. 5, which shows both the complete cyclic responses and the discrete maximum values at each drift cycle for RC bridge piers (Control, Control-Repaired, Spc2-DCH, and Spc2-DCH-Repaired). When subjected to high drift levels (for example, 8.31%), these piers exhibited stable lateral performance, avoiding significant pinching. As lateral drift increased during cyclic loading, the strain in the centrally post-tensioned (PT) reinforcing bar increased, resulting in an increased axial load applied to the column. This additional axial load resulted in a higher applied lateral force, which, including the axial load acting against the direction of loading, exceeded the base shear. Figures 5(a) to (d) present a comparison of Control and Control-Repaired, showing the applied lateral force alongside the lateral contribution of the PT and the base shear, excluding the PT's lateral input. Similarly, Fig. 5(e) to (h) display the corresponding comparison for Spc2-DCH and Spc2-DCH-Repaired. Table 3 summarizes the peak values at each drift level, including the applied lateral force, lateral force contributed by the PT system, base shear excluding PT effects, and the measured axial load. The data provided within Table 3 allow for easy comparison and quantification of the influence of post-tensioning and repair strategies on seismic performance.

This study first examined the behavior of the bridge pier in its original (Control) and repaired (Control-Repaired) states under lateral loads. When subjected to a 1.04% drift, the Control bridge pier exhibited an applied lateral load (AppLL) of 125.75 kN and a base shear of 118.33 kN on the push side (N-side), while the Control-Repaired bridge pier recorded higher values of 138.04 and 128.06 kN, respectively. On the pull side, Control and Control-Repaired achieved –135.62 and –118.71 kN in AppLL, and –128.03 and –108.87 kN in Base shear, respectively. The peak performance occurred between 2.08 and 3.12% drift intervals on the push side, with Control and Control-Repaired reaching 193.40 and 240.68 kN in AppLL, and 177.17 and 205.66 kN in base shear, respectively. On the pull side, peaks occurred at a later loading stage, between 6.23 and 7.27% drift intervals, with Control attaining –206.47 and –168.38 kN, and Control-Repaired achieving –224.72 and –162.42 kN in AppLL and base shear, respectively. By the 8.31% drift cycle, Control's AppLL and base shear were 169.12 and 58.59 kN on the push side, compared to Control-Repaired's 158.45 and 65.36 kN. On the pull side, Control registered –184.50 and –80.32 kN, showing lesser resilience compared

Table 3—Summary for Control versus Control-Repaired and SPC2-DCH versus SPC2-DCH-Repaired, kN

Drift (positive push →; negative pull←)	Control			Control-Repaired			SPC2-DCH			SPC2-DCH-Repaired		
	AppLL	Base shear	Axial load	AppLL	Base shear	Axial load	AppLL	Base shear	Axial load	AppLL	Base shear	Axial load
0.52% →	80.11	76.53	805.18	71.12	65.95	926.53	94.10	90.27	861.68	71.12	66.22	877.74
–0.52% ←	–88.50	–84.89	810.11	–62.14	–57.74	913.93	–86.23	–82.38	864.22	–62.14	–57.94	871.22
1.04% →	125.75	118.33	835.54	104.22	93.83	963.66	132.43	124.36	906.08	104.22	94.37	914.10
–1.04% ←	–135.62	–128.03	852.14	–98.38	–88.90	947.27	–121.05	–112.95	908.61	–98.38	–89.29	908.17
2.08% →	193.40	177.17	911.14	158.87	136.88	1039.50	173.59	155.96	989.85	158.87	137.79	996.28
–2.08% ←	–191.17	–174.43	939.78	–150.55	–129.91	1012.65	–157.54	–139.95	987.63	–150.55	–130.26	995.60
3.12% →	188.17	162.18	972.96	191.44	155.99	1123.90	190.72	162.49	1056.94	191.44	157.12	1088.30
–3.12% ←	–195.58	–168.38	1018.38	–179.10	–146.04	1074.13	–176.24	–148.12	1052.25	–179.10	–146.15	1070.58
4.15% →	181.76	145.74	1012.16	208.81	159.95	1165.65	198.34	159.16	1100.26	208.81	160.12	1161.56
–4.15% ←	–198.13	–159.77	1078.03	–200.53	–154.18	1126.64	–189.53	–150.33	1100.89	–200.53	–154.23	1125.46
5.19% →	180.87	134.90	1033.64	223.71	161.36	1192.37	207.62	157.20	1133.00	223.71	160.04	1217.56
–5.19% ←	–202.17	–151.95	1129.35	–218.65	–157.23	1192.12	–194.18	–144.03	1126.85	–218.65	–158.61	1165.24
6.23% →	179.96	124.43	1040.80	232.04	155.49	1221.67	213.08	151.64	1151.09	232.04	153.64	1251.33
–6.23% ←	–206.47	–143.85	1173.65	–233.77	–155.38	1266.81	–200.24	–139.22	1143.14	–233.77	–159.94	1193.10
7.27% →	189.03	98.40	1072.79	236.15	145.13	1246.63	216.17	144.18	1156.72	236.15	143.52	1268.58
–7.27% ←	–188.99	–113.31	1209.83	–243.59	–147.56	1329.17	–205.38	–133.43	1156.03	–243.59	–155.85	1214.46
8.31% →	216.03	58.95	1102.86	242.61	141.26	1215.69	205.71	123.55	1155.82	223.99	118.83	1261.56
–8.31% ←	–216.00	–80.32	1215.79	–251.32	–139.65	1351.96	–206.95	–124.58	1158.80	–251.32	–148.92	1222.55
9.35% →							199.02	107.09	1150.29	225.01	115.93	1267.01
–9.35% ←							–205.19	–113.63	1145.55	–251.82	–134.69	1240.11

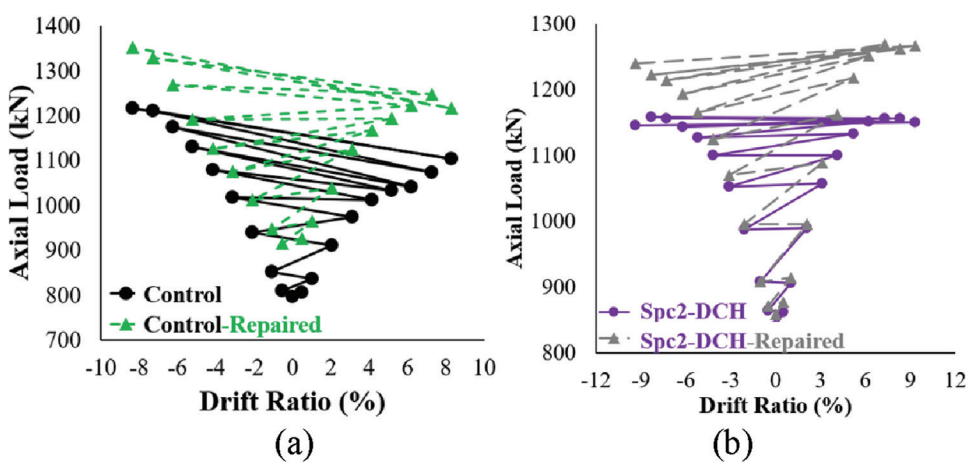

Fig. 6—Axial load with increased cyclic drift for: (a) Control and Control-Repaired specimens; and (b) Spc2-DCH and Spc2-DCH-Repaired specimens.

to Control-Repaired's –211.77 and –105.01 kN (Fig. 5). A detailed comparison revealed that Control performed better on the pull side. It was observed that during the casting of the Control specimen, a slight shift in the reinforcing bar cage occurred, leading to the uneven concrete cover thickness, and subsequently, more extensive damage on the N-side (push side). Consequently, this condition limited the axial load increase during push cycles relative to the pull cycles, as illustrated in Fig. 6. This issue was somewhat addressed in the Control-Repaired specimen, which provided better confinement and reversed the stronger side between Control and Control-Repaired. The pitch spacing remained largely unaffected, though it became narrower in certain areas where SGs were attached. During the fabrication of the original Control specimen, a construction discrepancy resulted in a localized pitch spacing of 40 mm instead of the intended 60 mm, which contributed to enhanced confinement at those locations and increased ductility on the pull side of the

control specimen. For the control specimen, the push side reached a peak base shear of 177.17 kN, which dropped to 124.43 kN at 6.23% drift—a 29.76% reduction on the deficient side. On the pull side, the peak base shear was 174.45 kN at 2.07% drift, decreasing slightly to 143.85 kN at 6.27% drift (17.54% reduction). After repair, the base shear capacity on the push side was restored to 155.49 kN, reflecting a 24.96% improvement, while the pull side reached 155.38 kN, benefiting from the good confinement (8.0% improvement). The FRP wrapping significantly enhanced ductility and post-peak performance, allowing the specimen to regain nearly the same base shear capacity, with values of 141.26 and 139.65 kN on the push and pull sides, respectively.

Having established the behavior of the Control and Control-Repaired piers, the study further explored the response of HRCBP, represented by the Spc2-DCH and Spc2-DCH-Repaired specimens, to identify key findings crucial for HRCBP design under lateral loads. At a 1.04% drift, Spc2-DCH registered an AppLL of 132.43 kN and a base shear of 124.36 kN on the push side (N-side), while Spc2-DCH-Repaired showed 104.22 and 94.37 kN, respectively. On the pull side, Spc2-DCH recorded –121.05 kN in AppLL and –112.95 kN in base shear, in contrast to Spc2-DCH-Repaired's –98.38 and –89.30 kN (Fig. 5). The peak performance of both specimens was observed at different drift levels. For AppLL, it was at 7.27% drift, with Spc2-DCH reaching 216.17 kN and Spc2-DCH-Repaired 236.15 kN on the push side, while on the pull side, Spc2-DCH registered –205.38 kN, 18.60% less than Spc2-DCH-Repaired's –243.60 kN. For base shear, the peak occurred at a 4.16% drift interval, with Spc2-DCH and Spc2-DCH-Repaired recording 159.16 and 160.12 kN, respectively, on the push side, and –150.33 and –154.23 kN on the pull side. Notably, the testing of the HRCBP specimens was extended to a higher drift level of 9.35%, compared to the maximum 8.31% drift level achieved by the Control specimens. By the 9.35% drift interval, Spc2-DCH's AppLL was 199.02 kN compared to Spc2-DCH-Repaired's 225.01 kN on the push side, while on the pull side, Spc2-DCH registered –205.19 kN, less resilient than Spc2-DCH-Repaired's –251.82 kN. In terms of base shear, Spc2-DCH recorded 107.09 kN, while Spc2-DCH-Repaired achieved 115.93 kN on the push side. On the pull side, the values were –113.63 kN for Spc2-DCH and –134.69 kN for Spc2-DCH-Repaired. A comprehensive comparison revealed that Spc2-DCH generally performed better on the push side, with a particularly noticeable improvement (8.85% higher on the push side) up to a 7.27% drift level. Although it displayed similar resistance during the pull cycle at 8.31% drift (109.80 and –110.79 kN), Spc2-DCH slightly improved (6.72% higher) on the last pull side of the 9.35% drift cycle. In contrast, Spc2-DCH-Repaired performed better on the push side up to 5.19% drift (Fig. 5), with greater resistance on the pull side emerging from 6.23% drift and showing notable improvement at higher drift levels, 20.21% higher at 8.31% drift.

Axial load-displacement relationships

Axial load development in the Control and Control-Repaired specimens increased consistently with drift levels. The Control specimen exhibited higher axial loads on the pull side, peaking at 1215.79 kN at 7.27% drift. In contrast, the Control-Repaired specimen showed greater axial loads on the push side, reaching 1351.96 kN at 8.31% drift, representing an 11.20% increase due to the repair. Overall, the improved performance on the push side for the Control-Repaired specimen can be attributed to better confinement and structural integrity achieved through the repair process, mitigating the initial weaknesses resulting from construction imperfections (Fig. 6(a)). Overall, the detailed comparison clearly shows that while the Control specimen performed better on the pull side, the Control-Repaired specimen, up to 6.23% drift, exhibited balanced performance on both sides, demonstrating the effectiveness of the repair in reversing the structural weaknesses of the original Control specimen (Fig. 6(a)). In the DCH specimens, Spc2-DCH demonstrated stronger performance during push cycles, up to 7.27% drift, with axial loads rising from 861.68 to 1156.72 kN. At higher drifts, performance was balanced, with a minor drop on the pull side. Spc2-DCH-Repaired also demonstrated push-side strength initially, peaking at 1268.58 kN at 7.27% drift before balancing between push and pull sides at higher drifts. These results suggest the repair improved structural resilience and balanced performance under varying load conditions (Fig. 6(b)).

Damage, curvature, and ductility analysis

In their as-built and repaired states, damage levels for both the Control and Spc2-DCH specimens were documented at each drift cycle. Curvature analysis using linear potentiometers up to 700 mm above the base was conducted to assess plastic deformation in Control and HRCBP specimens before and after repair (Fig. 7). Although localized damage occurred on the outer FRP wrap layer, the DCH specimen remained intact, highlighting the effectiveness of the FRP wraps, even when pushed to a higher drift magnitude (9.35%). This resilience is demonstrated by examples of damage at 2.08% and 6.23% drift cycles for the Control and Control-Repaired (Fig. 8), and for the Spc2-DCH and Spc2-DCH-Repaired (Fig. 9).

A detailed curvature analysis was carried out to understand the performance of the Control and HRCBP at the initial and repaired status, with a focus on determining the extent of plastic deformation. The comparison between the Control and Control-Repaired specimens under different drift cycles reveals a clear difference in their response to push-pull loading (Fig. 7). At each drift level, the Control-Repaired specimen consistently exhibited significantly higher curvature values than the Control specimen. For example, at 2.08% drift, the Control-Repaired specimen shows curvatures of 0.124 on the N-side and –0.075 on the S-side, approximately 4.6 times higher on the N-side and 3.2 times higher on the S-side than the Control specimen's curvatures of 0.027 on the N-side and –0.023 on the S-side. This pattern continues, with the largest difference observed at 8.31% drift, where the Control-Repaired specimen's curvatures are 0.449 on the

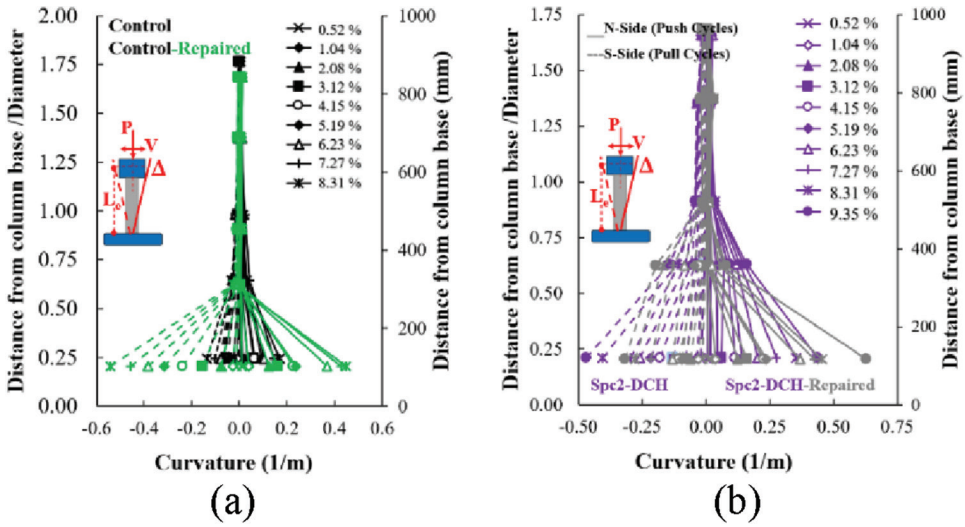

Fig. 7—Curvature profiles for as-built versus repaired: (a) Control; and (b) Spc2-DCH.

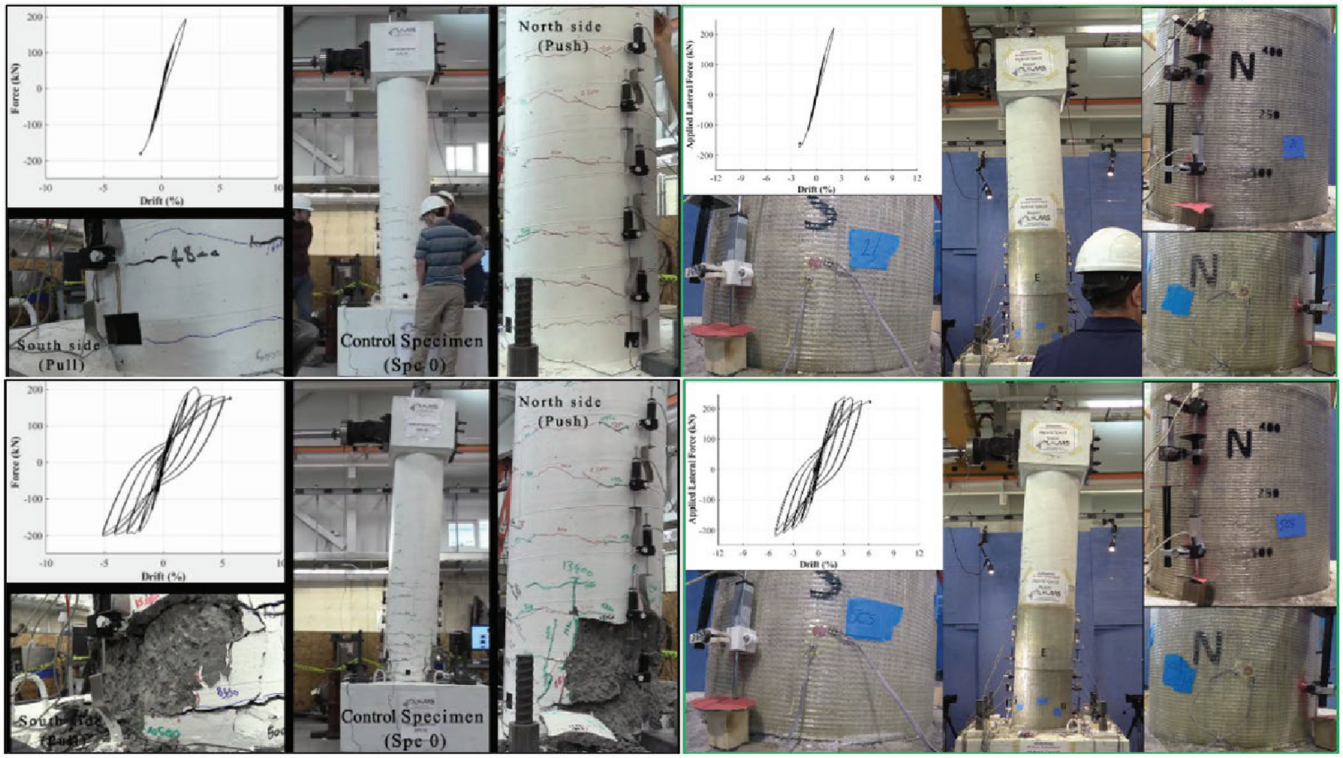

Fig. 8—Damage in Control (left) and Control-Repaired (right) at 2.08 and 6.23% drift.

N-side and –0.543 on the S-side, approximately 2.8 and 2.3 times higher than the Control's values of 0.160 on the N-side and –0.237 on the S-side. These findings suggest that the repairs result in a more pronounced deformation response, indicating changes in the structural behavior post-repair (Fig. 7(a)).

At low drift percentages, the HRCBP's curvature was relatively small and concentrated near the base of the Spc2-DCH and Spc2-DCH-Repaired. As the drift increased, the curvature region expands along the column height, indicating a more distributed deformation (Fig. 7(b)). There was a visible symmetry between the push and pull cycles at lower drifts, suggesting a consistent behavior of the column in both directions initially. However, as mentioned earlier, this symmetry started to diverge at higher drift values, with push cycles (N-side) exhibiting more pronounced curvatures. For instance, at 8.31% and 9.35% drifts, the curvature remainedmore pronounced than in the push cycles of the same magnitudes. This indicates that the column exhibits more deformation in the push cycles at higher drifts, which could be due to differences in load application or previous cycle effects.

Stiffness degradation and energy dissipation

The analysis of stiffness degradation post-drift cycles for the Control and Control-Repaired specimens, as presented in Fig. 10(a), reveals their differing responses to AppLLs during push-pull loading cycles. This behavior, observed

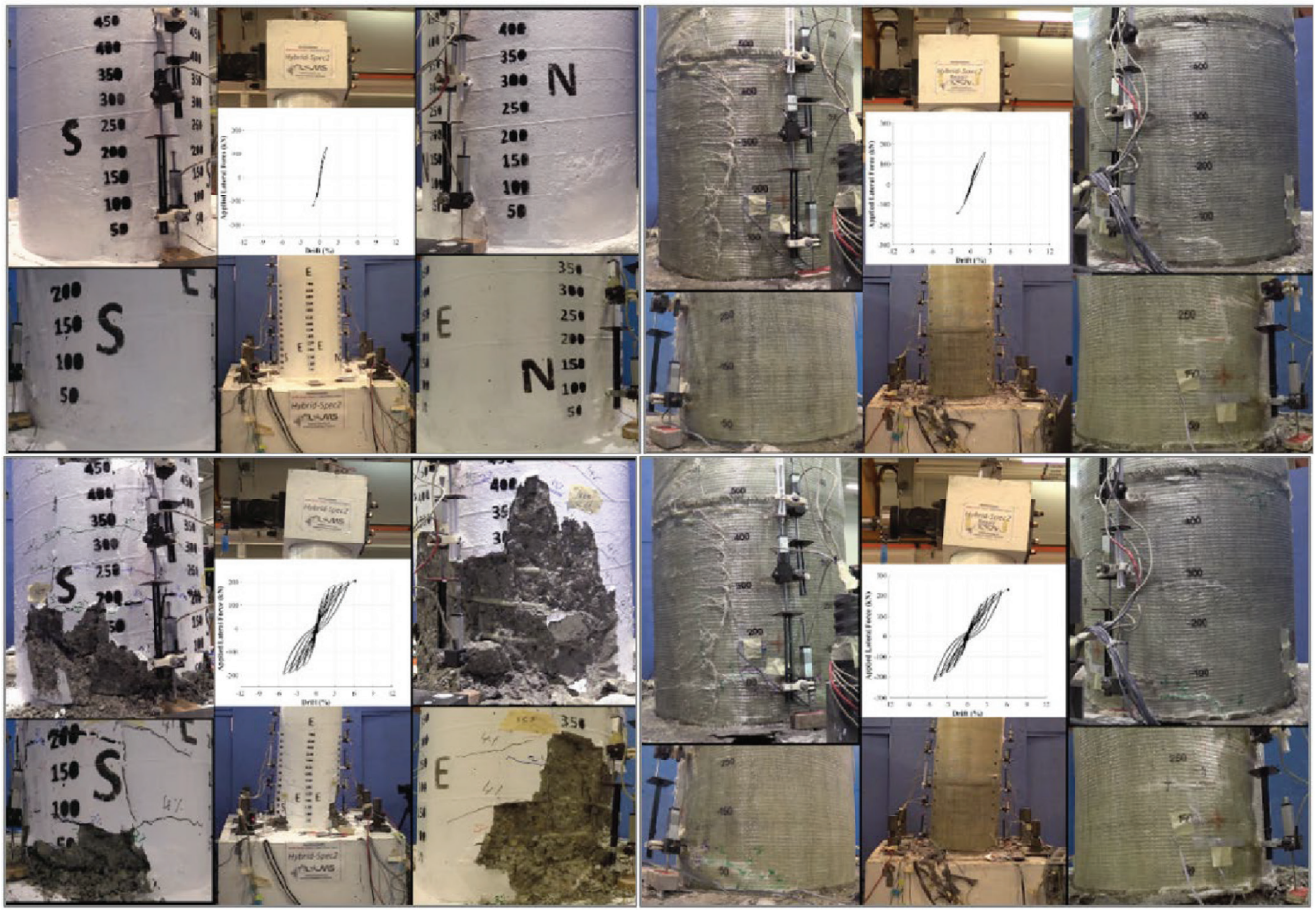

Fig. 9—Damage in Spc2-DCH (left) and Spc2-DCH-Repaired (right) at 2.08 and 6.23% drift.

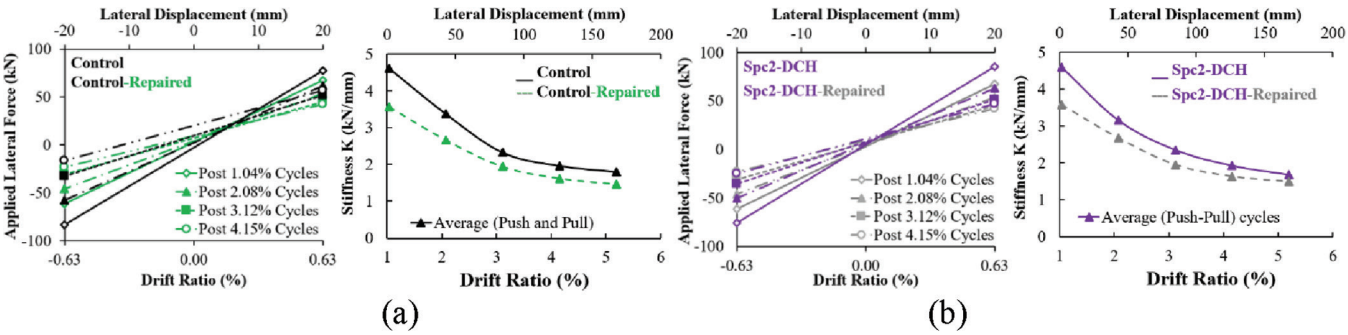

Fig. 10—Stiffness degradation for: (a) Control versus Control-Repaired; and (b) Spc2-DCH versus Spc2-DCH-Repaired.

at ±0.63% drift levels across all specimens examined in this study, is directly associated with the push-pull loading cycles that occur after each major drift cycle, such as post-1.04%, 2.08%, 3.12%, and so on. For the Control specimen, a notable reduction in stiffness was observed with successive drift cycles. Initially, after 1.04% cycles, the AppLL at 0.63% drift was 77.49 kN, while at –0.63% drift, it was –83.26 kN. As the drift cycles progressed, these values consistently decreased, underscoring a reduction in stiffness. After 2.08% cycles, the AppLL had reduced to 61.82 and –57.93 kN, and this trend continued with subsequent cycles. Notably, the reduction was more pronounced on the pull side (negative drift), where the values dropped significantly, reaching –5.04 kN post-5.19% cycles. This pattern demonstrated the structure's diminishing ability to resist lateral forces, indicating cumulative damage and a decline in structural integrity. Compared to the Control specimen, the Control-Repaired specimen, despite having preexisting damage prior to repair, exhibited a notably less severe pattern of stiffness degradation. Following the initial 1.04% drift cycles, the apparent lateral load (AppLL) reached 67.73 kN at +0.63% drift and –61.46 kN at –0.63% drift during the pull cycle. Although these values decreased in subsequent cycles, the rate of decline was more gradual than that observed in the unrepaired specimen. For instance, after the 2.08% drift cycles, the AppLL values remained relatively higher at 53.74 and –45.61 kN. By the 5.19% drift cycles, the Control-Repaired specimen still maintained 43.09 kN on the push

side and –17.19 kN on the pull side, indicating better stiffness retention, especially in the pull direction, despite the cumulative damage.

Moving to the analysis of stiffness degradation in Spc2-DCH and Spc2-DCH-Repaired specimens, as depicted in Fig. 10(b), showed there is a clear trend of decreasing stiffness with each drift cycle. After the initial 1.04% cycles, the lateral load at 0.63% drift was recorded at 85.53 kN in the push cycle and –75.45 kN in the pull one. However, these values steadily decreased with subsequent cycles, indicating progressive stiffness degradation. For example, after the 2.08% cycles, the AppLL values reduced to 62.9 and –50.36 kN, continuing to decline to 46.69 and –17.30 kN after the 5.19% cycles. The consistent decline in AppLL and base shear values highlighted the structure's cumulative damage and waning ability to resist lateral forces. In comparison, the Spc2-DCH-Repaired specimen showed a similar stiffness degradation trend but generally exhibited lower AppLL values due to its reduced section modulus. After the 1.04% cycles, the lateral loads were 67.73 and –61.46 kN at 0.63% drift. These values also decreased throughout the drift cycles, yet the rate of reduction is somewhat less pronounced than in the Spc2-DCH specimen. By the end of the 5.19% cycles, the lateral loads for the repaired specimen were measured at 43.09 and –17.62 kN. This indicated that, although the Spc2-DCH-Repaired specimen also experienced stiffness degradation, its decline was slightly less severe, suggesting that the repairs had somewhat mitigated the loss of structural integrity.

In general, the repaired specimens exhibited lower initial stiffness values compared to their original counterparts, primarily due to the accumulation of prior damage before the repair. For the Control-Repaired specimen, stiffness at the beginning of the loading cycles (post 1.04% drift) was 3.57 kN/mm, representing a 22.5% reduction compared to the original Control specimen (4.61 kN/mm). By the end of the test (post 5.19% drift), the Control-Repaired specimen maintained 1.47 kN/mm, approximately 18.7% lower than the Control's 1.81 kN/mm at the same drift level. Despite this reduction, the rate of stiffness degradation in the Control-Repaired specimen was more gradual, with a 58.8% drop from start to end, compared to a 60.8% drop in the Control specimen.

Similarly, the Spc2-DCH-Repaired specimen had an initial stiffness of 3.59 kN/mm, which is 21.8% lower than that of the original Spc2-DCH specimen (4.60 kN/mm). At the final drift cycle (post 5.19%), it retained 1.49 kN/mm, an 11.3% reduction compared to the original 1.68 kN/mm. The overall stiffness degradation from the first to last cycle was 58.5% in the repaired specimen, compared to 63.5% in the original Spc2-DCH. These findings suggest that while repaired specimens start with reduced stiffness due to pre-existing damage, they generally experience a more gradual rate of degradation, highlighting the positive impact of FRP repair in maintaining structural resilience under increasing drift demands. While stiffness degradation provides insight into the structural integrity and lateral capacity, it is also crucial to examine how well the specimens can absorb and dissipate energy during cyclic loading, as energy dissipation is a key factor in assessing the overall seismic performance of structures.

The analysis of energy dissipation in the Control and Control-Repaired specimens, based on the area within the hysteresis loops, provided a clear picture of their behavior under cyclic loading. Meanwhile, the equivalent viscous damping reflects the effectiveness of energy dissipation (computed as the ratio of the hysteretic loop area to the elastic energy stored in the system). In a comparative analysis of energy dissipation between the Control and Control-Repaired specimens, significant differences were observed at various drift stages (Fig. 11(a) to (c)). By beginning at a 1.04% drift, the Control-Repaired specimen exhibited a higher cumulative energy dissipation (ET) of 1.69 kN·m compared to the Control's 1.29 kN·m, indicating a greater capacity for energy absorption. However, the Control specimen showed a higher energy dissipation per drift cycle (EC) and equivalent viscous damping factor at this early stage. Moving to intermediate drift values, such as

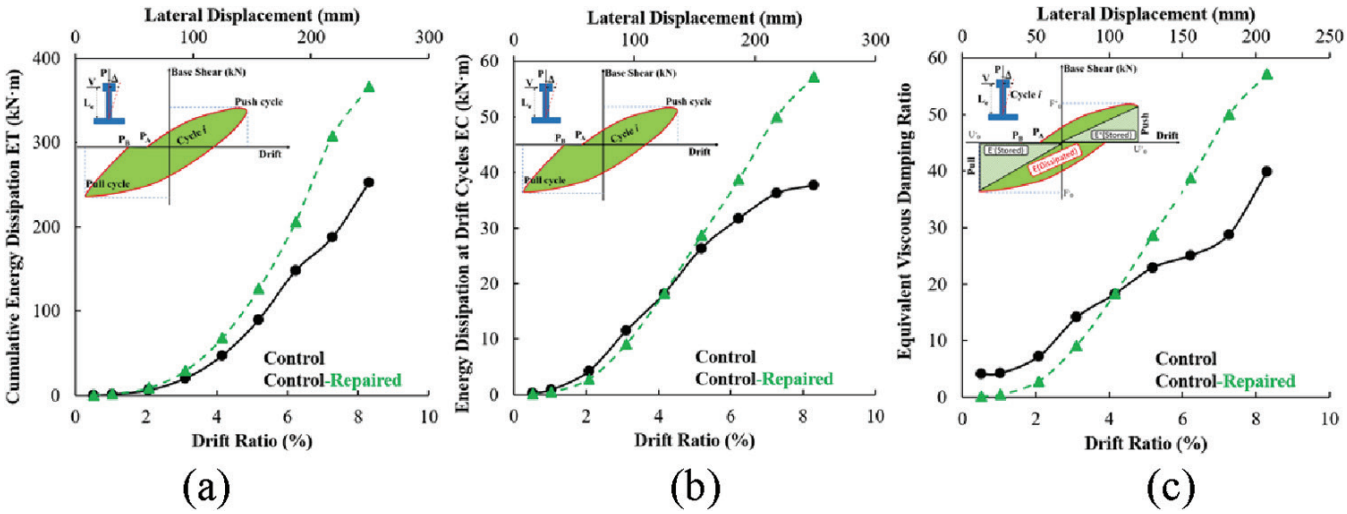

Fig. 11—(a) Cumulative energy; (b) energy at drift cycle; and (c) equivalent viscous damping for Control versus Control-Repaired.

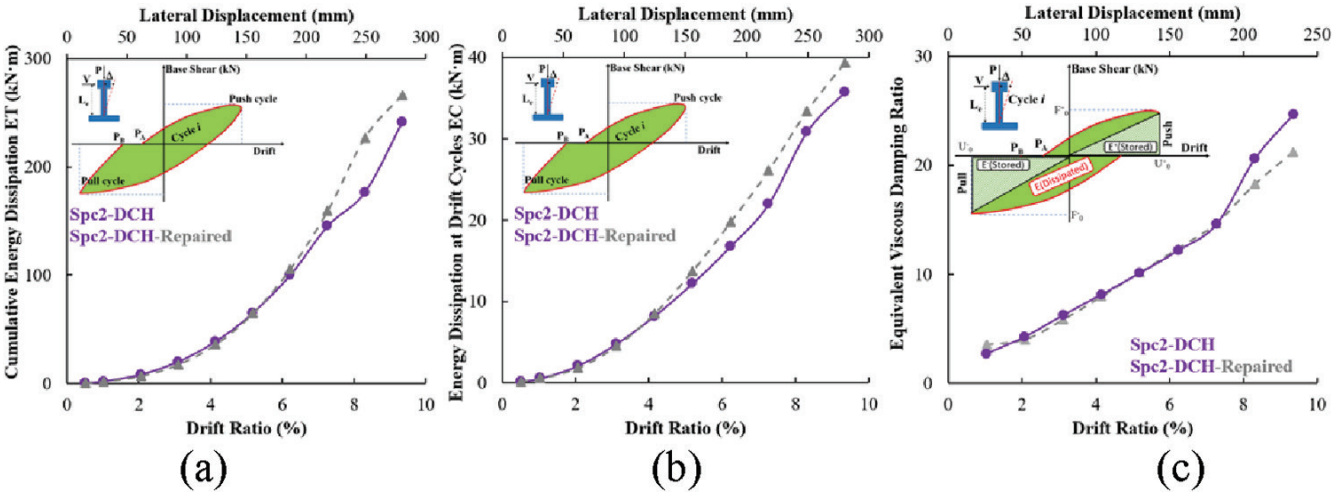

Fig. 12—(a) Cumulative energy; (b) energy at drift cycle; and (c) equivalent viscous damping for Spc2-DCH versus Spc2-DCH-Repaired.

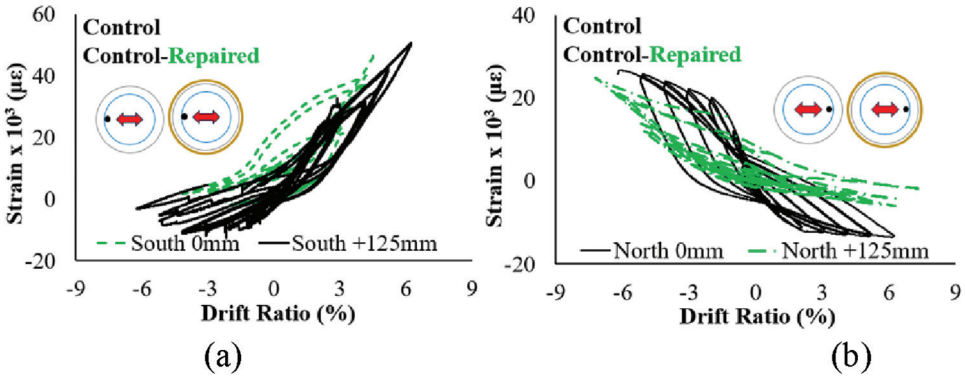

Fig. 13—Longitudinal steel strain on: (a) S-side; and (b) N-side for Control versus Control-Repaired.

at 4.15% and 5.19%, the Control-Repaired continued to demonstrate a consistently higher ET, reaching 67.82 and 126.56 kN·m, respectively, compared to the Control's 47.04 and 89.92 kN·m. This trend suggested a more robust energy dissipation capacity in the repaired specimen. The EC and damping factors in these intermediate stages are somewhat comparable, with only slight variations. The differences became more pronounced at the final drift stage of 8.31%. The Control-Repaired specimen significantly outperformed the Control, with an ET of 366.31 kN·m against the Control's 252.37 kN·m, and an EC of 57.24 kN·m compared to the Control's 37.67 kN·m. Moreover, the equivalent viscous damping factor for the Control-Repaired was substantially higher at 52.65, compared to the Control's 39.86. These values indicated a superior ability of the Control-Repaired specimen to dissipate energy, especially at higher levels of stress. Overall, the Control-Repaired specimen consistently showed an enhanced capacity for energy dissipation across all drift levels when compared to the Control specimen, highlighting the effectiveness of the repair in augmenting the structure's resilience and energy absorption capabilities under cyclic loading conditions.

An analysis comparing the energy dissipation behavior of the Spc2-DCH and Spc2-DCH-Repaired specimens highlighted noticeable differences across multiple drift intervals (Fig. 12). At an early drift of 1.04%, the Spc2-DCH specimen exhibited ET of 2.10 kN·m and EC of 0.54 kN·m, with an equivalent viscous damping factor of 2.74. The Spc2-DCH-Repaired, on the other hand, showed slightly lower ET at 1.79 kN·m but marginally higher EC at 0.55 kN·m and a higher damping factor of 3.54. While moving to intermediate drift values between 4.15% and 5.19%, both specimens demonstrated similar cumulative energy dissipations, with Spc2-DCH-Repaired displaying slightly higher ECs and comparable damping factors. However, in the final drift stages of 8.31% and 9.35%, the Spc2-DCH-Repaired specimen surpassed Spc2-DCH in cumulative energy dissipation, recording 227.28 and 266.79 kN·m, respectively. This analysis revealed that while Spc2-DCH maintained a steady increase in energy dissipation and damping factors, the Spc2-DCH-Repaired demonstrated higher cumulative energy dissipation but varied in efficiency and damping, especially at the peak drift levels.

Analysis of longitudinal reinforcement, transverse spirals, and external FRP wrap strains

Having analyzed the stiffness degradation and energy dissipation behaviors, it is now essential to focus on the longitudinal reinforcement strains, which provide further insight into the internal stress distribution and overall structural performance under cyclic loading. Figure 13 illustrates that the Control-Repaired specimen attained similar tensile

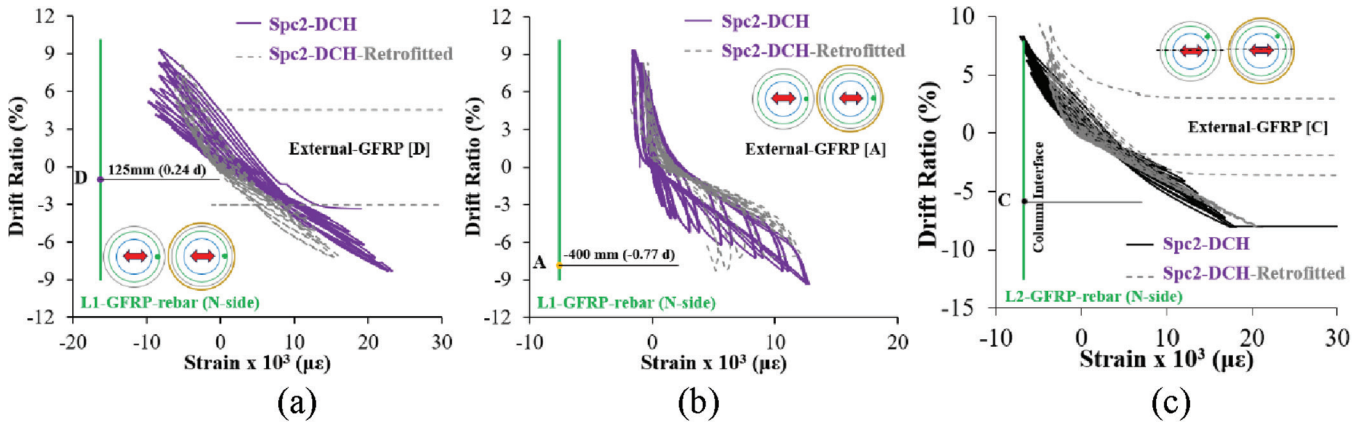

Fig. 14—Longitudinal GFRP strain (N-side) for Spc2-DCH versus Spc2-DCH-Repaired specimens: (a) L1-GFRP at [D]; (b) L1-GFRP at [A]; and (c) L2-GFRP at [C].

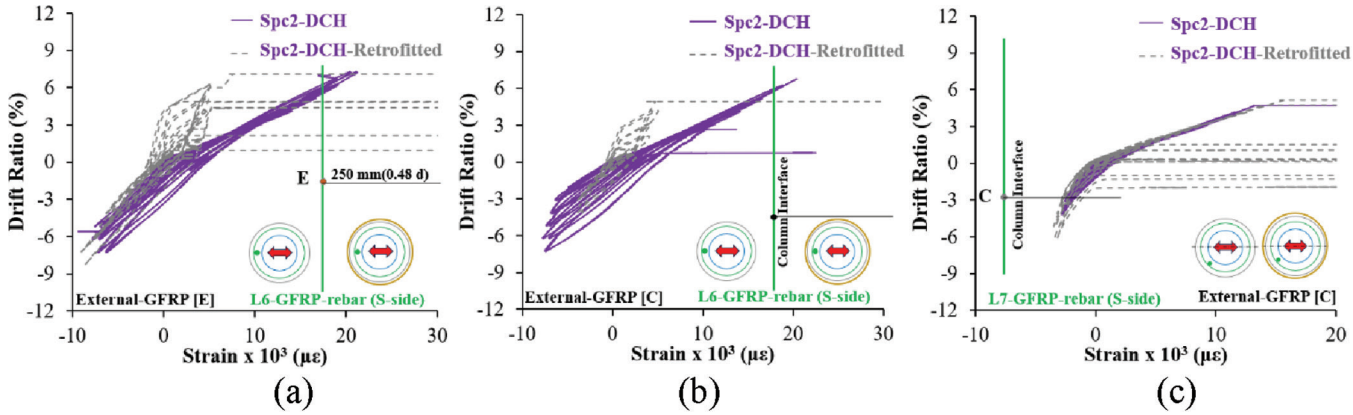

Fig. 15—Longitudinal GFRP strain (S-side) for Spc2-DCH versus Spc2-DCH-Repaired specimens: (a) L6-GFRP at [E]; (b) L6-GFRP at [C]; and (c) L7-GFRP at [C].

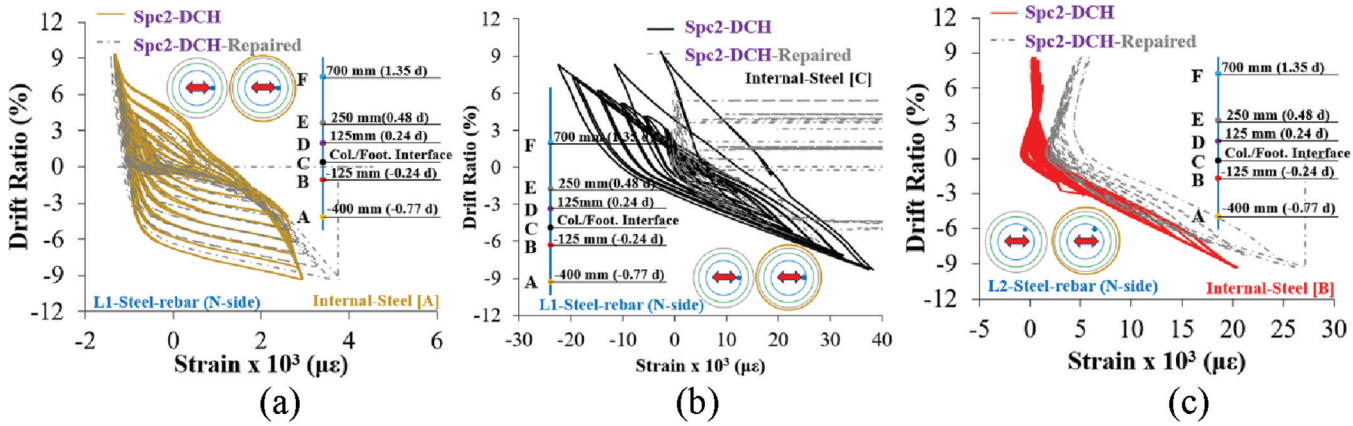

Fig. 16—Longitudinal steel strain (N-side) for Spc2-DCH versus Spc2-DCH-Repaired specimens: (a) L1-Steel at [A]; (b) L1-Steel at [C]; and (c) L2-Steel at [B].

strain levels as the initial Control specimen. However, due to buckling and repeated strain levels, the Control-Repaired specimen exhibited significantly lower compressive strains compared to those observed in the initial test of the Control specimen. On the other hand, the Spc2-DCH-Repaired managed to sustain both tensile and compressive strains at levels close to the original Spc2-DCH specimen, despite some SGs not surviving until the end of the 9.35% drift cycle (Fig. 14 to 19). Notably, the elasticity of GFRP reinforcing bars contributed to their ability to withstand high levels of repeated strains (up to 20 × 10^3 με), indicating the potential effectiveness of HRCBP in post-repair scenarios. The recorded tensile and compressive strains at the extreme reinforcing bars on both the S-side and N-side were approximately 18 to 22% lower compared to the original specimen; however, side bars such as L2 and L7 experienced higher strain levels. This observation emphasizes that adjacent GFRP reinforcing bars become more actively engaged (by

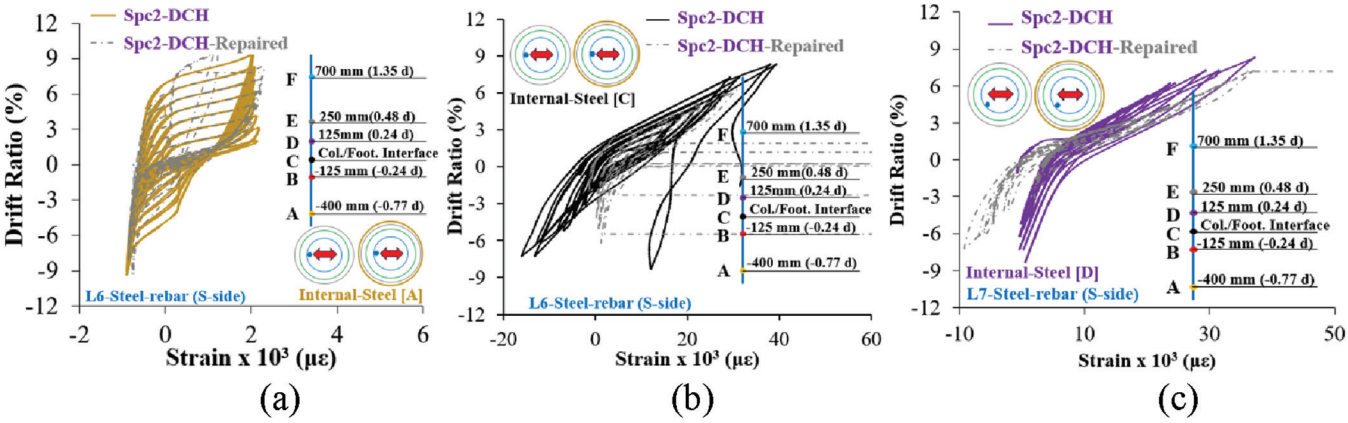

Fig. 17—Longitudinal steel strain (S-side) for Spc2-DCH versus Spc2-DCH-Repaired specimens: (a) L6-Steel at [A]; (b) L6-Steel at [C]; and (c) L7-Steel at [D].

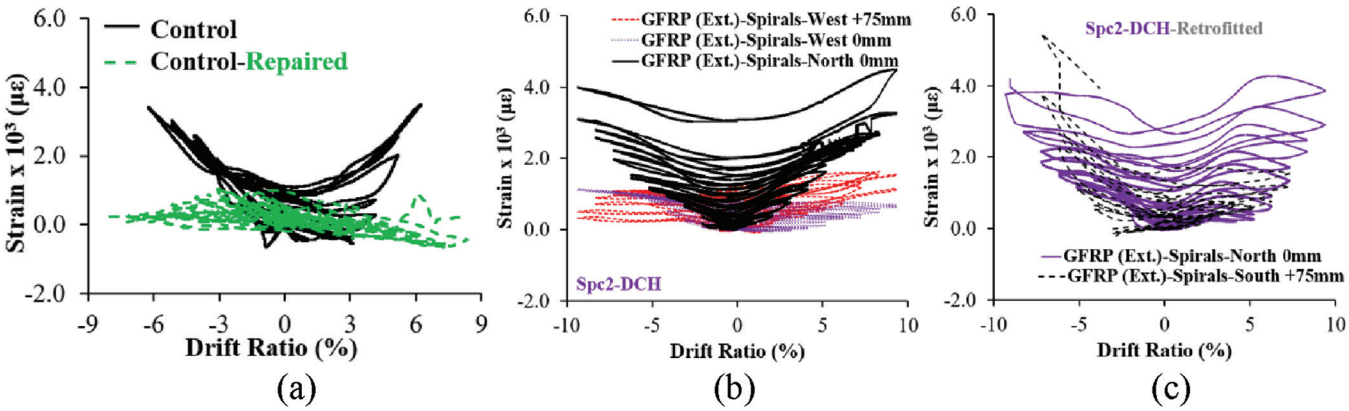

Fig. 18—Transverse reinforcement strain: (a) steel spirals in Control versus Control-Repaired; (b) GFRP spirals in Spc2-DCH; and (c) GFRP spirals in Spc2-DCH-Repaired.

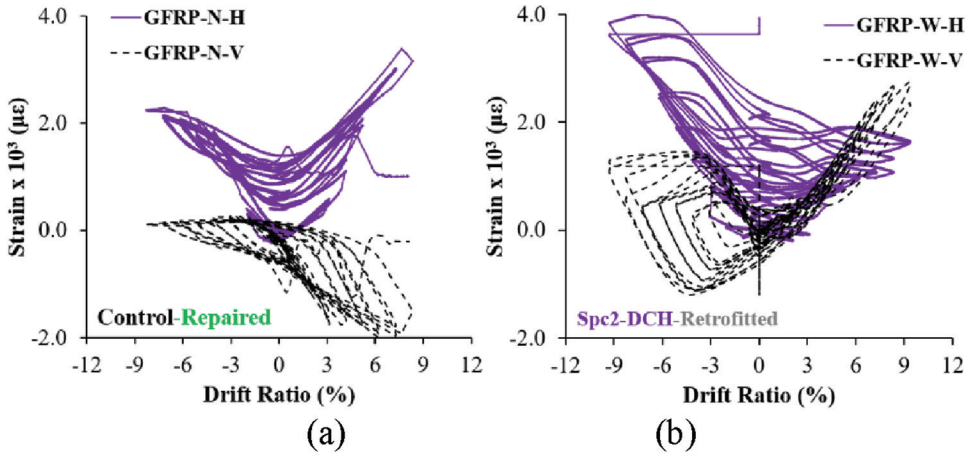

Fig. 19—FRP strain in external wraps: (a) Control-Repaired; and (b) Spc2-DCH-Repaired.

approximately 10 to 15%) following the repair procedure. The strain experienced by the internal steel reinforcing bars in Spc2-DCH-Repaired closely aligned with those in the initial Spc2-DCH, as seen in Fig. 16 and 17. This similarity, and occasional increase, was attributed to the intact condition of the internal bars, which did not experience significant out-of-plane deformation due to the effective confinement provided by the double-layer transverse reinforcement. This was especially clear in section [A], which was embedded in the footing. Original SGs were used there without adding new instrumentation. Although this section was inaccessible during the repair process and thus received no additional measurement devices, the strain readings still surpassed those recorded during the initial testing of the Spc2-DCH specimen. Strain readings for the bars adjacent to the extreme fibers (such as L2 and L7) are also shown in Fig. 16(c) and 17(c) to compare strain levels across different bars. Following the assessment of longitudinal reinforcement strain behavior, it was essential to evaluate transverse reinforcement strains, given their critical role in providing

confinement and maintaining structural integrity under cyclic loading.

The strain measured in the transverse steel spirals of the Control-Repaired specimen was significantly (66%) lower than that in the original Control specimen being enhanced by the extra confinement from the FRP wrapping (Fig. 18(a)). Conversely, the Spc2-DCH-Repaired specimen exhibited the same strain levels on its GFRP spirals (Fig. 18(b) and (c)). Additionally, within the steel spirals of the Spc2-DCH-Repaired, the SGs exhibited comparable performance to those in the initial Spc2-DCH until they ceased functioning, resulting in a 5.19% drift.

To further evaluate the effectiveness of external FRP wrapping under cyclic loading, SGs were installed on the external FRP wraps of both the Control-Repaired and Spc2-DCH-Repaired specimens. These gauges were identified based on their location and orientation: GFRP-N-H (north side, horizontal) and GFRP-S-V (south side, vertical). At an 8.31% drift level, strain measurements on the external FRP wrapping reached a peak of 3.25 με for the Control-Repaired specimen, whereas the Spc2-DCH-Repaired specimen experienced higher strain values of 4 με. The higher strain observed in the Spc2-DCH-Repaired specimen is attributed to the increased deformation demand associated with reaching a higher drift of 9.35%, compared to the maximum 8.31% drift achieved by the Control-Repaired specimen, demonstrating the enhanced contribution and effectiveness of the FRP wraps at elevated drift levels (Fig. 19).

POST-TEST DAMAGE ASSESSMENT

Post-test damage assessment is a crucial phase following the repair process of concrete bridge piers. This process involved several key steps, each aimed at evaluating the integrity and resilience of the materials and structures under test conditions. Initially, the assessment began with the careful removal of FRP wrapping from the tested specimens. This step was critical to examine the underlying concrete and reinforcing bars for indications of damage such as delamination, ruptures, or deformation in the FRP wraps, which could suggest overstressing or material failure during testing. Following the FRP removal, the next stage involved manually chipping away the concrete cover. This process revealed the internal reinforcement structure and allowed for a detailed inspection of the condition of the concrete. This examination helped to assess the extent of crack propagation, spalling, or any other forms of deterioration that the concrete may have undergone during the testing.

An integral part of the damage assessment was the evaluation of the spirals or the transverse reinforcement. This involved measuring any distortions or deformations, offering insights into the level of stress these components withstood and their effectiveness in maintaining structural integrity under seismic loadings. Furthermore, a thorough inspection of both GFRP and steel reinforcing bars was conducted. For GFRP bars, the focus was on identifying signs of fraying, delamination, or any reduction in bond strength with the concrete. Their ability to elastically recover or to sustain permanent deformation was also assessed. The steel bars, on the other hand, were examined for indications of buckling, yielding, or ruptures resulting from the repeated stress and conditions of the tests. The Spc2-DCH-Repaired specimen experienced the snapping of two spirals on both the N-side and S-side, whereas the Control-Repaired specimen did not undergo any similar ruptures (Fig. 20).

SUMMARY AND CONCLUSIONS

This study presents one of the first large-scale experimental evaluations of hybrid glass fiber-reinforced polymer (GFRP)-steel reinforced concrete (RC) bridge piers, tested both in their as-built and repaired states, under cyclic lateral loading. The findings establish that hybrid RC bridge piers (HRCBP), repaired with fiber-reinforced polymer (FRP) wraps, not only sustain higher drift levels but also preserve strength, stiffness, and ductility after severe damage—enhancements that were observed following repairs. The quantified performance gains—including up to 34% higher lateral strength retention, nearly 40% equivalent viscous damping (compared to ~25% as-built), and an 11 to 13% increase in axial load capacity—underscore the novelty of this work in demonstrating measurable resilience benefits of FRP repair. Furthermore, the observed reduction in spalling, delayed bar buckling, and improved confinement efficiency highlight the effectiveness of this combined reinforcement and repair strategy. Collectively, these outcomes not only confirm the robustness of FRP repair but also provide new benchmarks and design-oriented insights for performance-based seismic design and retrofit strategies, offering researchers and practitioners

(a) (b) (c) (d)

Fig. 20—Post-test condition on S-side: (a) Control-Repaired, and (b) Spc2-DCH-Repaired; after manual concrete removal: (c) Control-Repaired; and (d) Spc2-DCH-Repaired.

quantifiable targets to enhance the resilience of bridge piers in earthquake-prone regions.

The Control (conventional RC) and Spc2-DCH (HRCBP) specimens were thoroughly studied to quantify the piers' responses under both initial and repeated lateral cyclic loading in as-built and repaired states, focusing on variations in damage patterns, damage progression, structural integrity, structural degradation, energy dissipation, and resilience. Key conclusions from this research include:

- Experimental program: Both Control and Spc2-DCH specimens underwent quasi-static cyclic lateral load testing (beyond 8% drift), including service load cycles. Control specimens reached a maximum drift level of 8.31%, whereas Spc2-DCH was tested to a higher drift level of 9.35%, highlighting their enhanced deformation capacity and performance under extreme seismic loading conditions.
- Hysteretic pesponse: All repaired specimens demonstrated stable post-peak hysteresis with minimal pinching, indicating strong energy dissipation. FRP-wrapped specimens showed enhanced lateral performance, maintaining higher loads at large drifts. At 3.12% drift, the Control-Repaired specimen showed only a 3.82% drop in base shear compared to the original Control. By 7.27% drift, Control-Repaired retained 94.97% of peak strength, while the original Control lost 39.32%. Spc2-DCH-Repaired outperformed its original counterpart, achieving 34.42% higher lateral capacity and retaining 97.4% of its peak strength at 7.27% drift.
- The repaired specimens showed improved axial load-carrying capacity at increasing drift levels, attributed to the enhanced confinement from FRP wrapping. The Control-Repaired specimen exhibited an 11.2% increase in axial capacity compared to the original, while the Spc2-DCH-Repaired specimen sustained up to 13.0% higher axial loads at 9.35% drift. These results demonstrate the effectiveness of the repair strategy in promoting load redistribution and preserving structural integrity under large lateral deformations.
- Damage, curvature, and ductility analysis: Curvature and damage analyses confirmed the improved deformation capacity and resilience of the repaired specimens under cyclic loading. At 2.08% drift, the Control-Repaired specimen exhibited curvature values of 0.124 (N-side) and –0.075 (S-side), which are approximately 4.6 and 3.2 times higher, respectively, than the original Control (0.027 and –0.023). This trend persisted at higher drifts, with peak curvatures at an 8.31% drift of 0.449 and –0.543, representing increases of 2.8 and 2.3 times, respectively, over the Control specimen. In the hybrid series, the Spc2-DCH-Repaired specimen also demonstrated enhanced curvature performance, with values up to 0.311 (N-side) and –0.405 (S-side) at 8.31% drift—29% and 21% higher, respectively, than the original Spc2-DCH specimen (0.241 and –0.335). Despite localized FRP damage, the repaired hybrid column sustained curvature and structural integrity up to 9.35% drift, indicating more distributed plasticity and effective post-repair behavior.
- Stiffness degradation and energy dissipation: Despite having lower initial stiffness due to accumulated damage, the repaired specimens showed a more gradual degradation trend compared to their original counterparts. Control-Repaired and Spc2-DCH-Repaired exhibited 22.5% and 21.8% lower initial stiffness, respectively, yet maintained higher retention rates with 58.8% and 58.5% total stiffness loss, versus 60.8% and 63.5% in the original specimens. These trends indicate that FRP repair, although not fully restoring the initial stiffness, effectively slows degradation and enhances structural resilience under increasing lateral demands. Both Control-Repaired and Spc2-DCH-Repaired specimens exhibited increased cumulative energy dissipation, with equivalent viscous damping reaching up to 39.86%, compared to 25.45% in the original specimens, confirming enhanced performance under repeated lateral loading.
- Analysis of longitudinal reinforcement strains: The Control-Repaired specimen reached peak tensile strains of 13.6×10^3 με in the longitudinal steel, within 5% of the original Control (14.1×10^3 με), indicating effective repair. Compressive strains dropped from -10.4×10^3 to -7.4×10^3 με (~29% reduction) due to better confinement and less bar buckling. In the Spc2-DCH series, the repaired specimen achieved GFRP tensile strains up to 20×10^3 με, similar to the original. While extreme reinforcing bar locations (for example, L1 and L6) exhibited 18 to 22% lower strain, side reinforcing bars (for example, L2 and L7) showed 10 to 15% higher strain, indicating improved engagement. Internal steel bars reached 11.0 to 13.5×10^3 με, with a deep foundation section peaking at 14.2×10^3 με despite no direct repair. These results underscore the FRP wrapping in maintaining and redistributing strain demands under large drifts.
- Transverse spiral and FRP wrap strains: Repaired specimens showed reduced spiral strains—66% in Control-Repaired and 50% in Spc2-DCH-Repaired—due to FRP wrapping confinement. Strain gauges (SGs) on the FRP wraps confirmed active engagement, with Spc2-DCH-Repaired reaching 4 με versus 3.25 με in Control-Repaired, reflecting effective confinement under higher drift demands.
- Post-test damage assessment: Visual inspections showed reduced damage in repaired specimens. FRP wraps prevented major spalling and reinforcing bar buckling. Although some spiral ruptures occurred in hybrid specimens, overall damage was minimal, confirming the repair strategy's effectiveness.

AUTHOR BIOS

ACI member **Sherif M. S. Osman** *is a Postdoc at the School of Engineering at the University of British Columbia (UBC), Kelowna, BC, Canada, where he received his PhD in civil engineering. His research interests include advanced composite materials, large-scale testing, and the construction and design of concrete structures reinforced with fiber-reinforced polymers.*

ACI member **M. Shahria Alam** *is a Professor of Civil Engineering, the Tier 1 Principal's Research Chair in Resilient & Green Infrastructure in the School of Engineering, and Director of the Green Construction Research*

& Training Centre (GCRTC) at UBC Okanagan, Okanagan, BC, Canada. He is Chair of ACI Committee 441, Reinforced Concrete Columns, and ACI Subcommittee 341-C, Earthquake Resistant Concrete Bridges-Retrofit; and a member of ACI Committee 555, Concrete with Recycled Materials, and ACI Subcommittee 318-D, Members. His research interests include smart materials and their structural applications, seismic rehabilitation of deteriorated structures, and performance-based design of structures.

ACI member **Shamim A. Sheikh** *is a Professor in the Department of Civil & Mineral Engineering at the University of Toronto, Toronto, ON, Canada. He is a member of ACI Committees 374, Performance-Based Seismic Design of Concrete Buildings, and 441, Reinforced Concrete Columns. His research interests include the behavior and design of reinforced concrete structures, performance-based seismic design, confinement of concrete in columns, evaluation of structural integrity, repair and strengthening of concrete structures using traditional materials and fiber-reinforced polymers (FRP), and expansive cement and its applications.*

ACKNOWLEDGMENTS

Financial contributions of the Natural Sciences and Engineering Research Council (NSERC) of Canada through the Collaborative Research and Development (CRD) grant and S-FRAME Software Inc. (Altair) were critical for conducting this study and are gratefully acknowledged. Financial support from the Green Construction Research and Training Center (GCRTC) at the University of British Columbia is gratefully acknowledged. The authors also gratefully acknowledge V-ROD Canada (Pultrall Inc.), Advance Precast, and Pump Pro for donating the glass fiber-reinforced polymer (GFRP) composite reinforcing bar cages, steel reinforcing bar cages, and concrete pumping services, respectively.

REFERENCES

Abbass, A.; Attarnejad, R.; and Ghassemieh, M., 2020, "Seismic Assessment of RC Bridge Columns Retrofitted with Near-Surface Mounted Shape Memory Alloy Technique," *Materials*, V. 13, No. 7, p. 1701. doi: 10.3390/ma13071701

ACI Committee 318, 2019, "Building Code Requirements for Structural Concrete (ACI 318-19) and Commentary (ACI 318R-19) (Reapproved 2022)," American Concrete Institute, Farmington Hills, MI, 624 pp.

Ahmed, E. A.; El-Salakawy, E. F.; and Benmokrane, B., 2010, "Shear Performance of RC Bridge Girders Reinforced with Carbon FRP Stirrups," *Journal of Bridge Engineering*, ASCE, V. 15, No. 1, pp. 44-54. doi: 10.1061/(ASCE)BE.1943-5592.0000035

Aidoo, J.; Harries, K. A.; and Petrou, M. F., 2006, "Full-Scale Experimental Investigation of Repair of Reinforced Concrete Interstate Bridge Using CFRP Materials," *Journal of Bridge Engineering*, ASCE, V. 11, No. 3, pp. 350-358. doi: 10.1061/(ASCE)1084-0702(2006)11:3(350)

Ali, M. A., and El-Salakawy, E., 2016, "Seismic Performance of GFRP-Reinforced Concrete Rectangular Columns," *Journal of Composites for Construction*, ASCE, V. 20, No. 3, p. 04015074. doi: 10.1061/(ASCE)CC.1943-5614.0000637

Bakis, C. E.; Bank, L. C.; Brown, V.; Cosenza, E.; Davalos, J.; Lesko, J.; Machida, A.; Rizkalla, S.; and Triantafillou, T., 2002, "Fiber-Reinforced Polymer Composites for Construction—State-of-the-Art Review," *Journal of Composites for Construction*, ASCE, V. 6, No. 2, pp. 73-87. doi: 10.1061/(ASCE)1090-0268(2002)6:2(73)

Benmokrane, B.; El-Salakawy, E.; El-Gamal, S.; and Goulet, S., 2007, "Construction and Testing of an Innovative Concrete Bridge Deck Totally Reinforced with Glass FRP Bars: Val-Alain Bridge on Highway 20 East," *Journal of Bridge Engineering*, ASCE, V. 12, No. 5, pp. 632-645. doi: 10.1061/(ASCE)1084-0702(2007)12:5(632)

Chen, Y.; Feng, J.; and Yin, S., 2012, "Compressive Behavior of Reinforced Concrete Columns Confined by Multi-Spiral Hoops," *Computers and Concrete*, V. 9, No. 5, pp. 341-355. doi: 10.12989/cac.2012.9.5.341

CSA A23.3:19, 2019, "Design of Concrete Structures," CSA Group, Toronto, ON, Canada.

CSA-S806:12(R2021), 2012, "Design and Construction of Building Structures with Fibre-Reinforced Polymers (Reaffirmed 2021)," CSA Group, Toronto, ON, Canada.

Dasgupta, A., 2018, "Retrofitting of Concrete Structure with Fiber Reinforced Polymer," *International Journal*, V. 4, No. 9, pp. 42-49.

El-Salakawy, E.; Benmokrane, B.; El-Ragaby, A.; and Nadeau, D., 2005, "Field Investigation on the First Bridge Deck Slab Reinforced with Glass FRP Bars Constructed in Canada," *Journal of Composites for Construction*, ASCE, V. 9, No. 6, pp. 470-479. doi: 10.1061/(ASCE)1090-0268(2005)9:6(470)

El-Sayed, T. A.; Abdallah, K. S.; Ahmed, H. E.; and El-Afandy, T. H., 2023, "Structural Behavior of Ultra-High Strength Concrete Columns Reinforced with Basalt Bars under Axial Loading," *International Journal of Concrete Structures and Materials*, V. 17, No. 1, p. 43. doi: 10.1186/s40069-023-00600-9

Ge, W.-J.; Ashour, A. F.; Yu, J.; Gao, P.; Cao, D.-F.; Cai, C.; and Ji, X., 2019, "Flexural Behavior of ECC–Concrete Hybrid Composite Beams Reinforced with FRP and Steel Bars," *Journal of Composites for Construction*, ASCE, V. 23, No. 1, p. 04018069. doi: 10.1061/(ASCE)CC.1943-5614.0000910

Grace, N. F.; Jensen, E. A.; Eamon, C. D.; and Shi, X., 2012, "Life-Cycle Cost Analysis of Carbon Fiber-Reinforced Polymer Reinforced Concrete Bridges," *ACI Structural Journal*, V. 109, No. 5, Sept.-Oct., pp. 697-704.

Holland, B.; Alapati, P.; Kurtis, K. E.; and Kahn, L., 2023, "Effect of Different Concrete Materials on the Corrosion of the Embedded Reinforcing Steel," *Corrosion of Steel in Concrete Structures*, pp. 199-218.

Jia, D.; Mao, J.; Guo, Q.; Yang, Z.; and Xiang, N., 2020, "A Flexure-Capacity Design Method and Seismic Fragility Assessment of FRP/Steel Double-Reinforced Bridge Piers," *Structure and Infrastructure Engineering*, V. 16, No. 9, pp. 1311-1325. doi: 10.1080/15732479.2019.1703762

Jia, D.; Mao, J.; Lv, J.; Zhang, W.; and Sun, J., 2023, "Seismic Performance of Fibre-Reinforced Polymer and Steel Double-Reinforced Bridge Piers," *Structure and Infrastructure Engineering*, V. 19, No. 3, pp. 291-301. doi: 10.1080/15732479.2021.1944225

Kassem, C.; Farghaly, A. S.; and Benmokrane, B., 2011, "Evaluation of Flexural Behavior and Serviceability Performance of Concrete Beams Reinforced with FRP Bars," *Journal of Composites for Construction*, ASCE, V. 15, No. 5, pp. 682-695. doi: 10.1061/(ASCE)CC.1943-5614.0000216

Kharal, Z.; Carrette, J. K.; and Sheikh, S. A., 2021, "Large Concrete Columns Internally Reinforced with GFRP Spirals Subjected to Seismic Loads," *Journal of Composites for Construction*, ASCE, V. 25, No. 3, p. 04021014. doi: 10.1061/(ASCE)CC.1943-5614.0001121

Kim, T.-H., 2022, "Seismic Performance Assessment of RC Columns with Interlocking Hoops," *Canadian Journal of Civil Engineering*, V. 49, No. 4, pp. 579-589. doi: 10.1139/cjce-2020-0345

Lau, K.; Permeh, S.; and Lasa, I., 2023, "Corrosion of Prestress and Posttension Reinforced Concrete Bridges," *Corrosion of Steel in Concrete Structures*, pp. 81-105.

Li, W.; Sun, L.; Zhao, J.; Lu, P.; and Yang, F., 2018, "Seismic Performance of Reinforced Concrete Columns Confined with Two Layers of Stirrups," *Structural Design of Tall and Special Buildings*, V. 27, No. 12, p. e1484. doi: 10.1002/tal.1484

NBCC, 2015, "2015 - 2005 National Building Code of Canada Seismic Hazard Values," National Research Council of Canada, Ottawa, ON, Canada, http://www.earthquakescanada.nrcan.gc.ca/hazard-alea/interpolat/index_2015-en.php. (last accessed Mar. 12, 2026)

Pecce, M.; Manfredi, G.; and Cosenza, E., 2000, "Experimental Response and Code Models of GFRP RC Beams in Bending," *Journal of Composites for Construction*, ASCE, V. 4, No. 4, pp. 182-190. doi: 10.1061/(ASCE)1090-0268(2000)4:4(182)

Pham, N. V.; Ohgaki, K.; Miyashita, T.; and Pham, N. Q., 2024, "Experimental Study on Strengthening Steel-Truss Bridge Diagonal Members Using Carbon-Fibre-Reinforced Polymer Bonding Methods," *Advances in Structural Engineering*, V. 27, No. 15, pp. 2710-2732. doi: 10.1177/13694332241281545

Prajapati, G. N.; Farghaly, A. S.; and Benmokrane, B., 2022a, "Behavior of Reinforced Concrete Columns with Hybrid Reinforcement (Steel/Glass Fiber-Reinforced Polymer) under Reversed Cyclic Load," *ACI Structural Journal*, V. 119, No. 4, July, pp. 141-155.

Prajapati, G. N.; Farghaly, A. S.; and Benmokrane, B., 2022b, "Performance of Concrete Columns Longitudinally Reinforced with Steel and GFRP Bars and Confined with GFRP Spirals and Cross Ties under Reversed Cyclic Loading," *Engineering Structures*, V. 270, p. 114863. doi: 10.1016/j.engstruct.2022.114863

Rassoulpour, S.; Shiravand, M.; and Safi, M., 2023, "Proposed Seismic-Resistant Dual System for Continuous-Span Concrete Bridges Using Self-Centering Cores," *Engineering Structures*, V. 274, p. 115181. doi: 10.1016/j.engstruct.2022.115181

Sheikh, S. A., and Kharal, Z., 2018, "Replacement of Steel with GFRP for Sustainable Reinforced Concrete," *Construction and Building Materials*, V. 160, pp. 767-774. doi: 10.1016/j.conbuildmat.2017.12.141

Siddiquee, K., and Alam, M. S., 2017, "Highway Bridge Infrastructure in the Province of British Columbia (BC), Canada," *Infrastructures*, V. 2, No. 2, p. 7. doi: 10.3390/infrastructures2020007

Soric, Z.; Kisicek, T.; and Galic, J., 2010, "Deflections of Concrete Beams Reinforced with FRP Bars," *Materials and Structures*, V. 43, pp. 73-90. doi: 10.1617/s11527-010-9600-1

Sun, L., and Li, W., 2019, "Cyclic Behavior of Reinforced Concrete Columns Confined with Two Layers of Stirrups," *Structural Concrete*, V. 20, No. 4, pp. 1279-1291. doi: 10.1002/suco.201800229

Sun, L.-Z.; Wu, D.-Y.; Zhao, J.-L.; Yang, F.; and Li, W., 2017a, "Behavior of Circular RC Columns with Two Layers of Spirals," *KSCE Journal of Civil Engineering*, V. 21, No. 3, pp. 955-963. doi: 10.1007/s12205-016-0928-0

Sun, Z.; Wu, G.; Zhang, J.; Zeng, Y.; and Xiao, W., 2017b, "Experimental Study on Concrete Columns Reinforced by Hybrid Steel-Fiber Reinforced Polymer (FRP) Bars under Horizontal Cyclic Loading," *Construction and Building Materials*, V. 130, pp. 202-211. doi: 10.1016/j.conbuildmat.2016.10.001

Tu, Y.; Zhang, J.; and Qian, Y., 2009, "Experimental and Theoretical Investigation of Flexural Load-Carrying Capacity of Concrete Beams Reinforced with AFRP Tendons," *Journal of Southwest University (Natural Science Edition)*, V. 39, No. 3, pp. 563-568.

Vosooghi, A., and Saiidi, M. S., 2013, "Design Guidelines for Rapid Repair of Earthquake-Damaged Circular RC Bridge Columns Using CFRP," *Journal of Bridge Engineering*, ASCE, V. 18, No. 9, pp. 827-836. doi: 10.1061/(ASCE)BE.1943-5592.0000426

Wu, D.-Y.; Sun, L.-Z.; Yang, F.; Zhao, J.-L.; and Li, W., 2016, "Axial Compressive Behavior of Square Reinforced Concrete Columns Confined Using Two Layers of Stirrups," *Advances in Structural Engineering*, V. 19, No. 8, pp. 1345-1356. doi: 10.1177/1369433216643897

Yang, F.; Sun, L.; Zhao, J.; Wu, D.; and Li, W., 2015, "Behavior of a Novel Circular HSC Column with Double High Strength Spirals," *Advances in Structural Engineering*, V. 18, No. 9, pp. 1371-1382. doi: 10.1260/1369-4332.18.9.1371

ACI STRUCTURAL JOURNAL TECHNICAL PAPER

Title No. 123-S42

Effects of Slab Characteristics on Long-Term Deflections of One-Way Reinforced Concrete Slabs

by John Ardila-Gonzalez, Matías A. Hube, and Julian Carrillo

Controlling deflections in reinforced concrete (RC) flexural members under service loads is a serviceability requirement prescribed by design codes, such as ACI CODE-318. Serviceability requirements are challenged by productivity requirements, such as faster construction and longer span demands, among others. This paper summarizes a parametric analysis conducted to estimate long-term deflections of one-way RC slabs. The objective of this study is to assess the effect of geometrical, concrete, and construction parameters on the long-term deflections of one-way RC slabs. The effect of these parameters on immediate deflections is also analyzed. Results of this study show that increasing the slab thickness and the area of tension reinforcement proved to be the most effective strategies for reducing both immediate and long-term deflections of one-way RC slabs. Additionally, the results of the parametric study highlight the relative influence of each studied parameter in controlling deflections.

Keywords: creep; deflections; long-term; one-way slab; serviceability, shrinkage.

INTRODUCTION

Controlling deflections in reinforced concrete (RC) flexural members—beams and slabs under service load conditions—is a serviceability requirement prescribed by design codes such as ACI CODE-318.[1] However, faster construction and longer span demands appeal for improving productivity of the construction industry, challenging serviceability requirements.[2] Therefore, concern has been raised about appropriate design limits of flexural RC members to comply with both serviceability and productivity requirements.[3-5]

ACI CODE-318[1] provides two approaches to control deflections of RC flexural members. The first one consists of prescribing minimum depths for beams and minimum thickness for slabs. The second approach encompasses estimating immediate and long-term deflections and comparing those with deflection limits. Nevertheless, Bertero and Bertero[4] reported that minimum slab thickness provisions in ACI CODE-318[1] may result in deflections that exceed deflection limits in the Code,[1] for some specific cases. This discrepancy highlights the disparity between minimum slab thickness requirements and deflection limitations specified by ACI CODE-318.[1] Therefore, verifying immediate and long-term deflections becomes imperative as a serviceability requirement, even when the minimum slab thickness required by ACI CODE-318[1] is complied.

Long-term deflections of RC flexural members have been studied by several authors. Gilbert and Nejadi[6] conducted tests on RC beams and slabs, recording long-term deflections and cracking propagation. Results showed that increasing the tension reinforcement reduced both the width and spacing of cracks. Gilbert and Guo[7] highlighted the influence of stiffness reduction due to time-dependent cracking on the long-term deflections of two-way RC slabs tested at 470 and 776 days after casting. Hwang et al.[8] developed a numerical method to predict long-term deflections in two-way RC slabs, which was validated with on-site measurements. The method focuses on the influence of construction load, moment redistribution due to slab cracking, and long-term effect of creep and shrinkage.

The impact of emerging concrete technologies and innovative concrete mixtures on the long-term deflection of flexural members has also been studied by several authors. Aslani[9] compared the long-term deflections of one-way slabs constructed with self-consolidating concrete (SCC) and fiber-reinforced SCC (FRSCC). The experimental data showed that FRSCC helps to reduce the long-term deflections and generate narrower crack spacing over time when compared to SCC slabs. Tošić and Kurama[10] conducted a parametric analysis on long-term deflections of flexural RC beams and one-way slabs built with recycled aggregates. The parameters investigated included the ratio of recycled aggregate to coarse aggregate, the concrete compressive strength, the bottom and top reinforcement ratios, and the span-depth ratio. The parametric study showed that increasing the amount of recycled aggregate (up to 25% of the coarse aggregate by mass) increased the long-term deflection of beams and slabs. These authors also concluded that increasing the tensile reinforcement reduced deflection, particularly in the scenario where other parameters remain unaltered.

This study analyzes the effect of geometrical, concrete, and construction parameters on the long-term deflections of one-way RC slabs. The considered geometrical, material, and construction parameters are the slab thickness, area of tension reinforcement, area of compression reinforcement, concrete modulus of elasticity at loading time, concrete modulus of rupture at loading time, ultimate creep coefficient, ultimate shrinkage strain, loading time, initiation of concrete drying time, and external load level. Long-term deflections are estimated using the effective moment of inertia incorporating both creep and shrinkage effects based on ACI 209.2[11] equations. The parametric analysis incorporated both immediate and long-term deflections for meaningful comparisons.

ACI Structural Journal, V. 123, No. 3, May 2026.
MS No. S-2024-160.R2, doi: 10.14359/51749488, received September 12, 2025, and reviewed under Institute publication policies. Copyright © 2026, American Concrete Institute. All rights reserved, including the making of copies unless permission is obtained from the copyright proprietors. Pertinent discussion including author's closure, if any, will be published ten months from this journal's date if the discussion is received within four months of the paper's print publication.

RESEARCH SIGNIFICANCE

Long-term deflection assessment is essential in RC slab design, as excessive deflections can reduce serviceability and productivity indicators. Several factors affect long-term deflection of RC slabs. This paper quantifies the effects of geometric, concrete, and construction parameters, including the external applied load level, on long-term deflection of one-way RC slabs. Results of this study allow for the identification of parameters that mostly affect long-term deflections of RC slabs. This identification facilitates the modification of design and construction procedures for RC slabs to control long-term deflections.

LONG-TERM DEFLECTION ESTIMATION

The total long-term deflection δ_a of flexural RC members under service loads at a time t, described by Bischoff and Torres,[12] can be rewritten as shown in Eq. (1)

$$\delta_a(t, t_0, t_d) = \delta_m(t, t_0) + \delta_{cr}(t, t_0) + \delta_{sh}(t, t_d) \tag{1}$$

where t_0 is loading time; and t_d is the initiation of concrete drying time. The terms $\delta_m(t, t_0)$, $\delta_{cr}(t, t_0)$, and $\delta_{sh}(t, t_d)$ are the mechanical (immediate at loading time t_0), creep (from t_0), and shrinkage (from t_d) deflection components, respectively. The derivative of the total deflection with respect to the longitudinal axis x of the flexural member is presented in Eq. (2)

$$\frac{d}{dx}\delta_a(t, t_0 t_d) = \frac{d}{dx}[\delta_m(t, t_0) + \delta_{cr}(t, t_0) + \delta_{sh}(t, t_d)] \tag{2}$$

Because the derivative of the deflection is the slope of the flexural member, the total slope (θ_a) at time t of the member can be written as shown in Eq. (3)

$$\theta_a(t, t_0, t_d) = \theta_m(t, t_0) + \theta_{cr}(t, t_0) + \theta_{sh}(t, t_d) \tag{3}$$

Given that the derivative of the slope is the curvature, the total curvature (ϕ_a) of the flexural member at time t, at each location x of the flexural member, can be written as shown in Eq. (4)

$$\phi_a(t, t_0, t_d) = \phi_m(t, t_0) + \phi_{cr}(t, t_0) + \phi_{sh}(t, t_d) \tag{4}$$

The curvature of the first two terms in Eq. (4) can be written as shown in Eq. (5),[12] where M_a is the service load moment at each location x; $\bar{E}_c(t, t_0)$ is the effective modulus of elasticity of concrete computed as $E_c(t_0)/(1 + \phi_{cr}(t, t_0))$, where $E_c(t_0)$ is the concrete modulus of elasticity at t_0, and $\phi_{cr}(t, t_0)$ is the creep coefficient at time t relative to t_0.[11] Additionally, $\bar{I}_e$ is the effective moment of inertia, which results from an interpolation between the moment of inertia of the uncracked transformed section ($\bar{I}_{tr}$) and that of the cracked transformed section ($\bar{I}_{cr}$).[13] The effective moment of inertia $\bar{I}_e$ is computed as shown in Eq. (6)[12]

$$\phi_m(t, t_0) + \phi_{cr}(t, t_0) = \frac{M_a}{\bar{E}_c(t, t_0)\,\bar{I}_e(t, t_0)} \tag{5}$$

$$\bar{I}_e(t, t_0) = \frac{\bar{I}_{cr}(t, t_0)}{1 - \left(\frac{M'_{cr}}{M_a}\right)^2 \left[1 - \frac{\bar{I}_{cr}(t, t_0)}{\bar{I}_{tr}(t, t_0)}\right]} \tag{6}$$

In Eq. (6), $M_{cr}' = \sqrt{\beta}\,M_{cr}$, where M_{cr} is the cracking moment, and β is a coefficient accounting for the influence of the duration of loading or repeated loading on the average strain.[14] The Bischoff and Torres approach does not use the β coefficient but uses a reduced cracking moment to account for the tensile stresses generated in the concrete due to shrinkage. In this study, the β coefficient was introduced in the Bischoff and Torres approach to account for the reduced cracking moment (M_{cr}').

The shrinkage curvature in Eq. (4) is determined through interpolation between the shrinkage curvature associated with the uncracked transformed section ($\phi_{sh,tr}$) and that associated with the cracked transformed section ($\phi_{sh,cr}$),[12] as defined in Eq. (7). The terms $\phi_{sh,tr}$ and $\phi_{sh,cr}$ in Eq. (7) are detailed in Appendix A, and μ is a constant that depends on the adopted approach (ζ-Method[14] or Bischoff and Torres[12]).

$$\phi_{sh}(t, t_d) = \left(M_{cr}'/M_a\right)^{\mu} \phi_{sh,tr}(t, t_d) + \left[1 - \left(M_{cr}'/M_a\right)^{\mu}\right] \phi_{sh,cr}(t, t_d) \tag{7}$$

The curvatures given by Eq. (5) and (7) are equivalent to the curvatures proposed by the ζ-Method[14] and by Bischoff and Torres[12] approach. Furthermore, the effective moment of inertia in Eq. (6) is equivalent to that used in both the ζ-Method[14] and the approach proposed by Bischoff and Torres.[12] In both cases, the cracking moment is estimated as $M_{cr} = f_{r,t0}(y_t/I_g)$, where y_t is the distance from the centroid of the uncracked section to the tension face, I_g is the gross moment of inertia of the concrete section, and $f_{r,t0}$ is the modulus of rupture at the age of loading. For the ζ-Method in this study, $f_{r,t0}$ is taken as the axial tensile strength f_{ctm}, rather than the flexural tensile strength $f_{ctm,fl}$, as suggested in previous studies.[15,16] The distinctions between the ζ-Method and Bischoff and Torres approach are the values used for β, μ, $f_{r,t0}$, $\bar{I}_e(t, t_0)$, and $\phi_{sh}(t, t_d)$, as summarized in Table 1.

The long-term deflection of a flexural member is determined from the curvatures along the length of the element using flexural theory. The total curvature in Eq. (4) is integrated along the length of the member to calculate rotations and, subsequently, deflections.[17] Boundary conditions are considered into the integration process to account for kinematic restrictions.

VALIDATION OF SELECTED APPROACHES USING TEST RESULTS

The analytical estimation of long-term deflections was validated using the results of RC one-way slabs S1-a and S1-b previously tested by Gilbert and Nejadi.[6] The deflections were calculated using curvatures estimated with both the ζ-Method and the Bischoff and Torres approach described previously. The one-way slabs were 3500 mm long and were

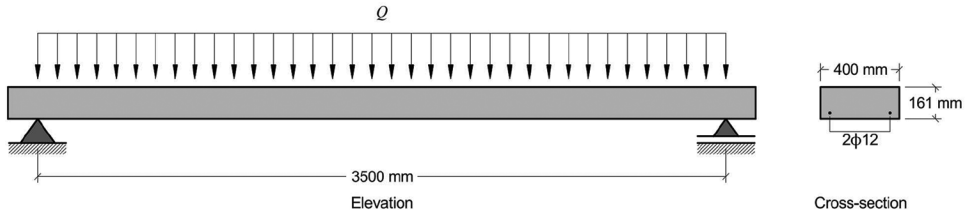

Fig. 1—Elevation and cross section of Slabs S1-a and S1-b tested by Gilbert and Nejadi.[6]

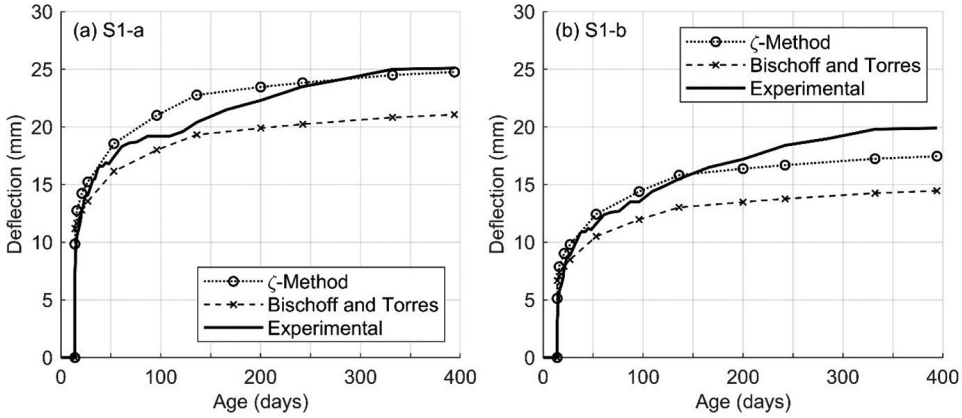

Fig. 2—Comparison of experimental and analytical long-term deflections of slabs tested by Gilbert and Nejadi.[6]

Table 1—Parameters of ζ-Method and Bischoff and Torres approach

	ζ-Method[14]	Bischoff and Torres[12]
β	1.0 for short-term loads 0.5 for sustained loads	$(2/3)^2$
μ	2	1
$f_{r,t0}$	$0.3(f_{c,t0})^{2/3}$ for $f_{c,t0} \leq 50$ MPa	$0.62\sqrt{f_{c,t0}}$
	$2.12\ln[1 + 0.1(f_{c,t0} + 8)]$ for $f_{c,t0} > 50$ MPa	
$\bar{T}_e(t,t_0)$	$\bar{T}_{tr}$ for $M_a \leq M_{cr}$	$\bar{T}_{tr}$ for $M_a \leq M_{cr}'$
	Eq. (6) for $M_a > M_{cr}$	Eq. (6) for $M_a > M_{cr}'$
$\phi_{sh}(t,t_d)$	$\phi_{sh,tr}(t,t_d)$ for $M_a \leq M_{cr}$	$\phi_{sh,tr}(t,t_d)$ for $M_a \leq M_{cr}'$
	Eq. (7) for $M_a > M_{cr}$	Eq. (7) for $M_a > M_{cr}'$

Note: $f_{c,t0}$ is measured compressive strength at loading time, in MPa.

simply supported (Fig. 1). The cross section of both slabs was 400 mm wide and 161 mm deep, and the reinforcement ratio $\rho = A_s/(bh) = 0.35\%$ (two bars of 12 mm diameter). The slabs were loaded with sustained uniformly distributed load Q, and their self-weight (24 kN/m^3). The load was applied at 14 days and sustained for 394 days. Slabs S1-a and S1-b were loaded with Q = 2.9 and 1.9 kN/m, respectively. Both slabs were exposed to identical environmental conditions and the reported temperatures ranged from 11 to 24°C, with an average of 20°C. Relative humidity data was not reported.

The mechanical properties of concrete and steel used in the numerical model in this study were those measured by Gilbert and Nejadi,[6] except for the modulus of rupture. The modulus of elasticity of the concrete at the age of loading (14 days) was 22.82 GPa. To estimate long-term deflections of these slabs, Gilbert[18] assumed the modulus of rupture at the age of loading as $0.6\sqrt{f_{c,t0}}$ = 2.6 MPa (where $f_{c,t0}$ = 18.3 MPa was the measured compressive strength at loading time, in MPa). For this study, the modulus of rupture at the age of loading ($f_{r,t0}$) used to estimate M_{cr} for both the ζ-Method and the Bischoff and Torres approach was estimated according to Table 1. The resulting modulus of rupture are 2.1 MPa and 2.7 for the ζ-Method and Bischoff and Torres approach, respectively. The long-term effects in the concrete were considered using the creep coefficients and shrinkage strain data measured by Gilbert and Nejadi[6] at ages of 16, 21, 27, 53, 96, 136, 200, 242, 332, and 394 days. Because the modulus of elasticity of the reinforcing steel was not reported by Gilbert and Nejadi,[6] a value of 200 GPa was assumed in this study, in accordance with ACI 318.[1] The yield stress of the reinforcing steel was assumed as 500 MPa.[18]

The estimated curvatures along the length of the flexural members were integrated to obtain the deflections of the slabs. The slab specimens were discretized along their length using 11 integration points. The midpoint integration rule was used with the boundary conditions of a simply supported element. The cross-sectional properties of the slabs were estimated using the equations detailed in Appendix A. Deflections of the slabs were calculated at ages varying from 14 to 394 days. The age of 14 days corresponds to both the age of load application (t_0) and the end of curing (t_d). The calculated immediate deflections are solely due to the effects of the superimposed sustained loads, as those caused by the self-weight of the slabs were not measured in the tests.

Figure 2 compares the experimental deflections at midspan of Slabs S1-a and S1-b, and the analytical deflections computed using both the ζ-Method[14] and the Bischoff and Torres[12] approach. Both analytical approaches accurately predict deflections of both slabs during the first 27 days.

Table 2—Comparison of experimental and analytical deflections for Slabs S1-a and S1-b

				Deflection, mm		
Specimen	Method	M_a/M_n	M_a/M_{cr}	at 14 days	at 394 days	Ana/Exp
S1-a	Experimental	—	—	7.14	25.10	—
	ζ-Method	0.50	1.89	9.84	24.76	0.99
	Bischoff and Torres	0.50	1.49	11.18	21.07	0.84
S1-b	Experimental	—	—	2.72	19.90	—
	ζ-Method	0.39	1.47	5.13	17.46	0.88
	Bischoff and Torres	0.39	1.15	6.68	14.46	0.73

Note: Ana/Exp is ratio of analytical to experimental deflections at 394 days.

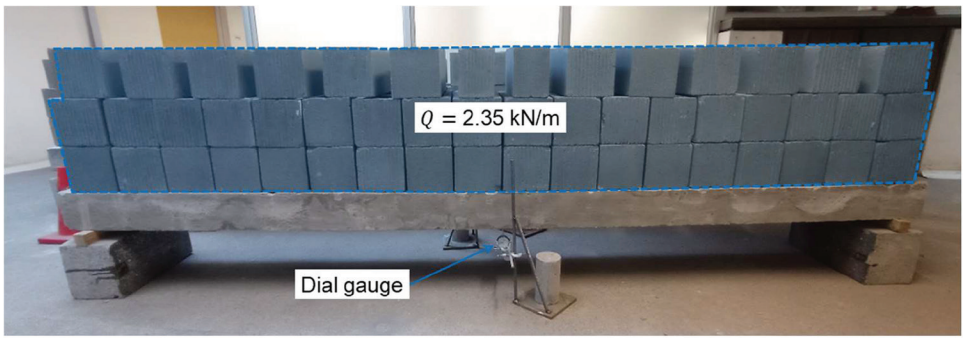

Fig. 3—General view of long-term test (Slab S1-CC).

Thereafter, larger differences between analytical and experimental deflections are observed for Slab S1-b. Table 2 shows the M_a/M_n ratios, where M_n is the nominal moment strength calculated with the measured material properties. Table 2 also shows the M_a/M_{cr} ratios obtained for the ζ-Method and the Bischoff and Torres approach, along with the experimental and analytical deflections at 14 and 394 days. Finally, Table 2 includes the ratios of analytical to experimental deflections at 394 days for both slabs. Results show that the deflection predictions with the ζ-Method are more accurate than those with the Bischoff and Torres approach. The lesser displacements prediction with the Bischoff and Torres approach are attributed to the larger modulus of rupture considered for this approach (2.7 MPa).

The analytical estimation of long-term deflections was also validated using the results of two RC one-way slabs tested in this research. Two simply supported one-way slabs with a span of 3500 mm and with different concrete properties were tested. The slabs were loaded with sustained uniformly distributed load $Q = 2.35$ kN/m (Fig. 3), and their self-weight (24 kN/m^3). The load was applied at 16 days and sustained for 245 days. The cross section of both slabs was identical to that of Blab S1-a tested by Gilbert and Nejadi,[6] measuring 400 mm in width and 161 mm in depth. The reinforcement ratio of the slabs was $\rho = A_s/bh = 0.35\%$ (two bars of 12 mm diameter).

Slab S1-CC was constructed with conventional concrete (CC), and Slab S1-SCC with SCC. Ready mixed concrete with a specified concrete strength of 35 MPa was used for casting the slabs. For the CC mixture, the water-cement ratio (w/c) was 0.58, and the percentages of coarse and fine aggregates were 48.2% and 51.8%, respectively. For the SCC, the w/c was 0.49, and the percentages of coarse and fine aggregates were 26.4% and 73.6%, respectively. The maximum aggregate size was 20 mm and 10 mm for the CC and SCC mixtures, respectively. The slab specimens were moist-cured for 16 days and were loaded at that age. The slab specimens were exposed to an external environment with temperatures ranging from 12 to 36°C and relative humidity levels between 26 and 73%.

The mechanical properties of CC, SCC, and steel used in the numerical model in this study were obtained experimentally, except for the modulus of rupture that was obtained from the equations of Table 1. The concrete strength at the age of loading ($f_{c,t0}$) for CC and SCC were 31.9 MPa and 53.6 MPa, respectively. The modulus of elasticity at the age of loading ($E_{c,t0}$) was 25.5 MPa for CC and 27.5 GPa for SCC. The modulus of rupture at the age of loading used to estimate M_{cr} for the ζ-Method was 3.0 for CC and 4.2 MPa for SCC. The modulus of rupture at the age of loading for the Bischoff and Torres approach was 3.5 for CC and 4.5 MPa for SCC. The measured modulus of elasticity of the reinforcing steel was $E_s = 192.2$ GPa and the measured yield stress 470.2 MPa. The shrinkage strains in the CC and SCC mixtures were determined by fitting experimental shrinkage data collected at various concrete ages. The adjusted shrinkage strains (ε_{sh}) at 245 days were 727 με for CC and 683 με for SCC. The creep coefficients for CC and SCC were not measured, and values reported by ICH[19] for concretes with similar characteristics were considered. The adjusted creep coefficient (ϕ_{cr}) at 245 days were 1.44 for CC and 1.23 for SCC.

Figure 4 compares the experimental deflection at midspan of Slabs S1-CC and S1-SCC, and the analytical deflections computed using both the ζ-Method[14] and the Bischoff and Torres[12] approach. Both approaches accurately predict the

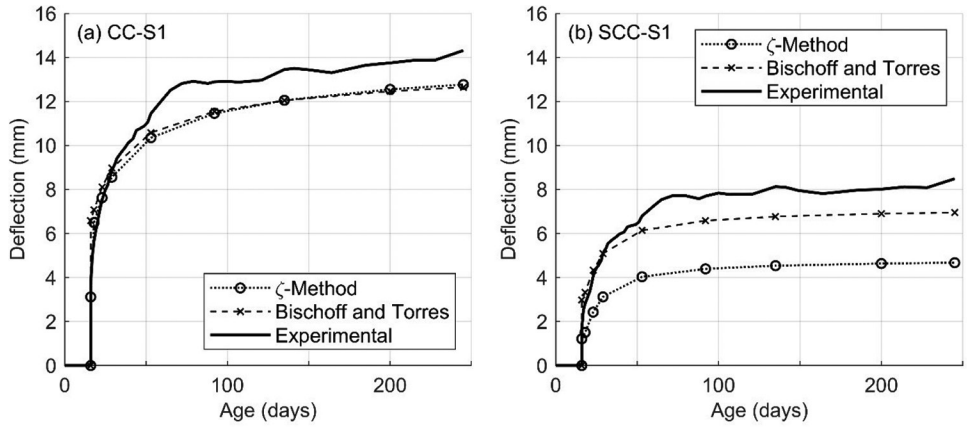

Fig. 4—Comparison of experimental and analytical long-term deflections of tested Slabs CC-S1 and SCC-S1.

Table 3—Comparison of experimental and analytical deflections for Slabs S1-CC and S1-SCC

				Deflection, mm		
Specimen	Method	M_a/M_n	M_a/M_{cr}	at 16 days	at 245 days	Ana/Exp
S1-CC	Experimental	—	—	3.69	14.32	—
	ζ-Method	0.46	0.80	3.12	12.77	0.89
	Bischoff and Torres	0.46	1.02	6.59	12.65	0.88
S1-SCC	Experimental	—	—	1.66	8.49	—
	ζ-Method	0.46	0.58	1.21	4.67	0.55
	Bischoff and Torres	0.46	0.78	2.99	6.95	0.82

Note: Ana/Exp is ratio of analytical to experimental deflections at 245 days.

deflections of Slab S1-CC within the first 27 days, and larger differences between experimental and analytical deflections are observed for Slab S1-SCC when using the ζ-Method. Table 3 shows the M_a/M_n ratios, the M_a/M_{cr} ratios, the immediate and long-term deflections obtained with the ζ-Method and the Bischoff and Torres approach, and the ratios of analytical to experimental deflections at 245 days for both slabs. The Bischoff and Torres approach provides better predictions of deflections than the ζ-Method, which contradicts the results in Fig. 2 and Table 2. This discrepancy is attributed to the modulus of rupture used in each model and the treatment of the effective moment of inertia. The Bischoff and Torres approach considers the effective moment of inertia for $M_a/M_{cr} > 2/3$, while the ζ-Method applies it for $M_a/M_{cr} > 1$. As a result, the Bischoff and Torres approach predicts larger displacement and is more accurate for lower M_a/M_{cr} ratio values than the ζ-Method.

Additionally, the comparison of the measured deflections for S1-CC and S1-SCC shows that a 7% increase in the concrete modulus of elasticity (from 25.5 to 27.5 GPa) and a 6% reduction in shrinkage strains (from 727 to 683 με) led to a 55% decrease in immediate deflections and a 41% decrease in long-term deflections.

PARAMETRIC STUDY

The parametric study was conducted considering Slab S-1a of Gilbert and Nejadi[6] as the benchmark case. The Bischoff and Torres[12] approach was implemented to estimate curvatures and deflections. Table 4 summarizes all the parameters considered to estimate deflections at any time t for the benchmark case, which can be classified as geometrical, concrete, and construction parameters. The parametric analysis was performed using different values

Table 4—Modeling parameters considered for benchmark case

Parameter	Unit	Values of benchmark case
Slab thickness (h)	mm	160
Area of tension reinforcement (A_s)	mm^2	226
Area of compression reinforcement (A_s')	mm^2	0
Modulus of elasticity at t_0 (E_{c,t_0})	GPa	23
Modulus of rupture at t_0 (f_{r,t_0})	MPa	2.7
Cracking moment reduction factor (β)	—	$(2/3)^2$
Ultimate creep coefficient ($\varphi_{cr,u}$)	—	2.0
First creep coefficient ($\psi_{cr,1}$)	—	1.0
Second creep coefficient ($\psi_{cr,2}$)	—	59
Ultimate shrinkage strain ($\varepsilon_{sh,u}$)	microstrain	950
First shrinkage coefficient ($\psi_{sh,1}$)	—	1.0
Second shrinkage coefficient ($\psi_{sh,2}$)	—	59
Loading time (t_0)	days	14
Initiation of concrete drying time (t_d)	days	14

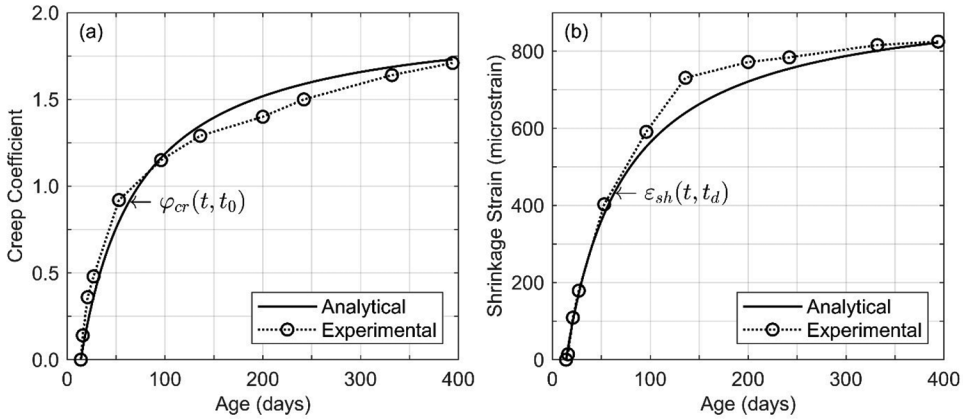

Fig. 5—Creep coefficient and shrinkage strain at different concrete ages.

Table 5—Modeling parameters used for parametric study

Parameters category	Parameter	Unit	Values
Geometrical	Slab thickness (h)	mm	**160**, 180, 200
	Area of tension reinforcement (A_s)	mm^2	**226**, 339, 452
	Area of compression reinforcement (A_s')	mm^2	**0**, 113, 226
Concrete	Modulus of elasticity at t_0 ($E_{c,t0}$)	GPa	**23**, 26, 29
	Modulus of rupture at t_0 ($f_{r,t0}$)	MPa	**2.7**, 3.0, 3.3
	Ultimate creep coefficient ($\varphi_{cr,u}$)	—	**2.0**, 1.7, 1.4
	Ultimate shrinkage strain ($\varepsilon_{sh,u}$)	με	**950**, 750, 550
Construction	Loading time (t_0)	days	**14**, 21, 28
	Initiation of concrete drying time (t_d)	days	**14**, 21, 28

of the slab thickness, area of tension reinforcement, area of compression reinforcement, concrete modulus of elasticity at loading time, concrete modulus of rupture at loading time, ultimate creep coefficient, ultimate shrinkage strain, loading time, and initiation of concrete drying time. Additionally, the external applied load level (Q) was considered as 1.9, 2.9, and 3.9 kN/m. The constant parameters were the assumed modulus of elasticity (E_s = 200 GPa) and the yield stress (f_y = 420 MPa) of the reinforcing steel, the cracking moment reduction factor (β), as well as the first and second creep and shrinkage coefficients ($\psi_{cr,1}$, $\psi_{cr,2}$, $\psi_{sh,1}$, and $\psi_{sh,2}$).

The creep coefficient used to estimate $\overline{E}_c(t, t_0)$ in Eq. (5), and the shrinkage strain used to estimate $\phi_{sh,tr}(t, t_d)$ and $\phi_{sh,cr}(t, t_d)$, are computed using Eq. (8) and (9), respectively.[11] The parameters $\psi_{cr,1}$, $\psi_{cr,2}$, $\psi_{sh,1}$, and $\psi_{sh,2}$ are considered constants for a given member shape and size.[11] The parameters $\psi_{cr,1}$ and $\psi_{sh,1}$ were assumed equal to 1.0.[11] The parameters $\psi_{cr,2}$ and $\psi_{sh,2}$ were estimated as $26e^{0.0142(V/S)} \approx 59$, where V/S represents the volume-to-surface ratio of the element.[11] The ultimate creep coefficient ($\varphi_{cr,u}$), and the ultimate shrinkage strain ($\varepsilon_{sh,u}$) were estimated from the experimental results reported by Gilbert and Nejadi.[6] Figures 5(a) and (b) show the creep coefficient and shrinkage strain, respectively, reported by Gilbert and Nejadi,[6] and the adjusted curves using Eq. (8) and (9). The estimated values of $\varphi_{cr,u}$ and $\varepsilon_{sh,u}$ were found to be 2.0 and 950 με (10^{-6} mm/mm), respectively. Finally, the age t_0 and t_d were assumed as 14 days, equivalent to Slab S1-a from Gilbert and Nejadi.[6]

$$\varphi_{cr}(t, t_0) = \frac{(t - t_0)^{\psi_{cr,1}}}{\psi_{cr,2} + (t - t_0)^{\psi_{cr,1}}} \cdot \varphi_{cr,u} \tag{8}$$

$$\varepsilon_{sh}(t, t_d) = \frac{(t - t_d)^{\psi_{sh,1}}}{\psi_{sh,2} + (t - t_d)^{\psi_{sh,1}}} \cdot \varepsilon_{sh,u} \tag{9}$$

Table 5 summarizes the parameters considered in the parametric study, where the values of the benchmark case are bolded. Each parameter was varied independently, with all other parameters held constant at their benchmark values, except in the cases of loading time and concrete drying, as explained in the following. The chosen slab thicknesses were 160 mm, 180 mm, and 200 mm, representing span ratios of approximately L/22, L/19, and L/17, respectively. According to ACI CODE-318,[1] the minimum thickness for solid nonprestressed simply supported one-way slabs is L/20. Using 226 mm^2 of tension reinforcement for the slab thicknesses of 160 mm, 180 mm, and 200 mm corresponds to a steel reinforcement area of $0.0035A_g$, $0.0031A_g$, and $0.0028A_g$, respectively. Moreover, for the 160 mm thick slab, 339 mm^2 of tension reinforcement corresponds to $0.0053A_g$ and 452 mm^2 corresponds to $0.0070A_g$. ACI CODE-318[1] specifies a minimum area of flexural reinforcement equal to $0.0018A_g$. The chosen values for the area of compression reinforcement were 0 mm^2 (no reinforcement), 113 mm^2 ($0.0018A_g$), and 226 mm^2 ($0.0035A_g$).

The additional values of the concrete modulus of elasticity at t_0 were those measured by Aslani[9] and the maximum considered value at 14 days was 29 GPa. The concrete modulus of rupture at t_0 was assumed to range from 2.7 to 3.3 MPa. The additional values for the ultimate creep coefficient for the parametric study were chosen considering that $\varphi_{cr,u} = 2.35\gamma_{cr}$, following ACI 209,[11] where γ_{cr} is a modification factor that depends on various parameters, including relative humidity (RH), as explained in Appendix B. The

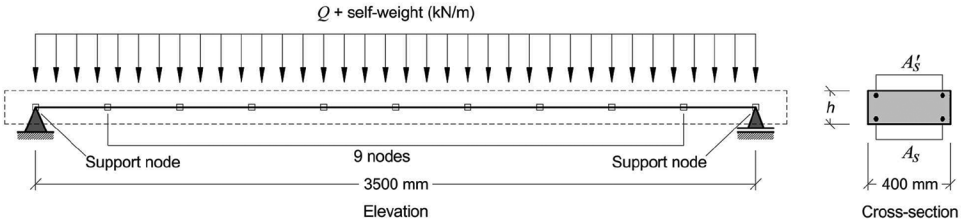

Fig. 6—Elevation and cross section of slab for parametric study.

values of $\varphi_{cr,u}$ were estimated considering RH of 40, 60, and 80%, whereas for the benchmark case, an RH of 40% was considered. The additional values for the ultimate shrinkage strain were computed as $\varepsilon_{sh,u} = 780\gamma_{sh}$ (με),[11] where γ_{sh} is a modification factor that was estimated for the same RH values used to estimate γ_{cr}.

The additional values for the loading time (t_0) were 21 and 28 days. The loading time affects $E_{c,t0}$ and $f_{r,t0}$ for this parametric study. The modulus of elasticity at the age of loading was estimated as $E_{c,t0} = 25\sqrt{t_0/(3.7 + 0.9t_0)}$ in GPa, following ACI 209.[11] The modulus of rupture at different loading ages was estimated using $f_{r,t0} = 2.39\sqrt{t_0/(3.7 + 0.52t_0)}$ in MPa, following ACI 209.[11] These equations result $E_{c,t0}$ = 23 GPa and $f_{r,t0}$ = 2.70 MPa at the age of 14 days, which are the values of the benchmark case at that age. At 21 days, the resulting values of $E_{c,t0}$ and $f_{r,t0}$ were 24.1 GPa and 2.9 MPa, respectively. At 28 days, the resulting values of $E_{c,t0}$ and $f_{r,t0}$ were 24.6 GPa and 3.0 MPa, respectively. The loading time also affects $\varphi_{cr,u}$ (Appendix B). At 21 and 28 days, the resulting values of $\varphi_{cr,u}$ were 1.88 (γ_{cr} = 0.80) and 1.81 (γ_{cr} = 0.77), respectively. Finally, the additional values for the initiation of concrete drying time (t_d) were also 21 and 28 days. The initiation of concrete drying time affects $\varepsilon_{sh,u}$ (Appendix B). At 21 and 28 days, the resulting values of $\varepsilon_{sh,u}$ were 911 με (γ_{sh} = 1.17) and 881 με (γ_{sh} = 1.13), respectively.

The slab used in the parametric study was modeled using 11 integration points along the element, as shown in Fig. 6. For estimating the deflections at different concrete ages, the midpoint integration rule was implemented. The total load (Q) was applied at concrete age t_0 considering both the uniform external load and the self-weight of the slab. The self-weight of the slab was included to estimate deflections considering a specific weight of 24 kN/m^3. The self-weight of the slab of the benchmark case, with a thickness of 160 mm, is 1.54 kN/m. The self-weights of the slabs with thicknesses of 180 and 200 mm are 1.73 and 1.92 kN/m, respectively. The deflections of the slabs were estimated from the loading time (t_0) through to a concrete age of 394 days.

RESULTS AND DISCUSSION

Figure 7 shows the time-dependent deflection at the midspan of the slabs of the parametric study for the applied load of Q = 2.9 kN/m. Figures 7(a) through (i) show the estimated deflection when each of the three values in Table 5 are considered. Table 6 summarizes the results of the parametric study for the three levels of external loading. The table shows the M_a/M_{cr} and M_a/M_{cr} ratios for each case. Additionally, Table 6 shows the normalized immediate (δ_I) and long-term (δ_L) deflections of each slab relative to the deflections of the benchmark case (δ_{IB} and δ_{LB}) at 14 and 394 days. For Q = 1.9 kN/m, the immediate and long-term deflections of the benchmark case are 7.61 and 15.43 mm, respectively; for Q = 2.9 kN/m, 12.20 and 22.17 mm; and for Q = 3.9 kN/m, 16.40 and 28.07 mm. Finally, Table 6 shows the multiplier for the additional deflection due to long-term effects (λ_Δ), which is calculated as δ_L/δ_I.

The load case Q = 2.9 kN/m was selected to compare results based on geometrical, concrete, and construction parameters. Figures 7(a) through (c) show the deflections of the one-way slabs when varying the geometrical parameters (slab thickness, area of tension reinforcement, and area of compression reinforcement). Table 6 and Fig. 7(a) show that increasing the slab thickness was the most effective strategy for reducing both the immediate and long-term deflections. The immediate and long-term deflections were reduced by 34% and 31%, respectively, when the slab thickness increases 13% (from 160 to 180 mm), and were reduced by 59% and 54%, respectively, when the slab thickness increases 25% (from 160 to 200 mm). Table 6 and Fig. 7(b) show that increasing the area of tension reinforcement was the second most effective strategy for reducing both the immediate and long-term deflections. The immediate and long-term deflections were reduced by 26% and 14%, respectively, when the area of tension reinforcement increases 50% (from 226 to 339 mm^2), and were reduced by 40% and 20%, respectively, when the area of tension reinforcement increases 100% (from 226 to 452 mm^2). Table 6 and Fig. 7(c) show that increasing the area of compression reinforcement was the least effective geometrical strategy for reducing deflections. These findings agree with those reported by Hollington,[20] where increasing tension reinforcement was more effective than increasing compression reinforcement to reduce deflections of lightly reinforced RC slabs. In this study, the increase in compression reinforcement led only to a reduction in long-term deflections, with no impact on immediate deflections. The long-term deflections were reduced by 6% and 10% when the area of compression reinforcement increases from 0 to 113 mm^2 (0.0018A_g), and to 226 mm^2 (0.0035A_g), respectively. Finally, Table 6 shows that the multiplier for additional deflection due to long-term effects (λ_Δ) decreased as the area of compression reinforcement increases, which aligns with the λ_Δ specified in ACI 318.[1] According to Branson,[21] λ_Δ is estimated as the product of the reduction factor (k_r) and the time dependent factor (ξ). The reduction factors, $k_r = 1/(1 + 50\rho')$, for ρ' values of 0, 0.0018 (A_s' = 113 mm^2), and 0.0035 (A_s' = 226 mm^2), are 1.00, 0.92, and 0.85, respectively. Using ACI CODE-318 expression with ξ = 1.4 (12 months), the resulting values of λ_Δ are 1.40, 1.29, and 1.19, respectively. These time-dependent values are smaller than the values of 1.82, 1.72, and 1.63 obtained for ρ'

Table 6—Slab deflections for three levels of applied load levels

	Parameter		Q = 1.9 kN/m					Q = 2.9 kN/m					Q = 3.9 kN/m				
			$\frac{M_a}{M_n}$	$\frac{M_a}{M_{cr}}$	$\frac{\delta_I}{\delta_{IB}}$	$\frac{\delta_L}{\delta_{LB}}$	λ_Δ	$\frac{M_a}{M_n}$	$\frac{M_a}{M_{cr}}$	$\frac{\delta_I}{\delta_{IB}}$	$\frac{\delta_L}{\delta_{LB}}$	λ_Δ	$\frac{M_a}{M_n}$	$\frac{M_a}{M_{cr}}$	$\frac{\delta_I}{\delta_{IB}}$	$\frac{\delta_L}{\delta_{LB}}$	λ_Δ
Geometrical parameters	h, mm	**160**	**0.46**	**1.14**	**1.00**	**1.00**	**2.03**	**0.59**	**1.47**	**1.00**	**1.00**	**1.82**	**0.72**	**1.81**	**1.00**	**1.00**	**1.71**
		180	0.41	0.95	0.59	0.65	2.22	0.53	1.22	0.66	0.69	1.90	0.64	1.48	0.69	0.71	1.76
		200	0.38	0.81	0.31	0.41	2.63	0.48	1.03	0.41	0.46	2.04	0.58	1.24	0.47	0.51	1.83
	A_s, mm^2	**226**	**0.46**	**1.14**	**1.00**	**1.00**	**2.03**	**0.59**	**1.47**	**1.00**	**1.00**	**1.82**	**0.72**	**1.81**	**1.00**	**1.00**	**1.71**
		339	0.31	1.14	0.75	0.90	2.43	0.41	1.47	0.74	0.86	2.13	0.50	1.81	0.73	0.84	1.97
		452	0.24	1.14	0.63	0.87	2.80	0.31	1.47	0.60	0.80	2.42	0.39	1.81	0.59	0.77	2.22
	A_s', mm^2	**0**	**0.46**	**1.14**	**1.00**	**1.00**	**2.03**	**0.59**	**1.47**	**1.00**	**1.00**	**1.82**	**0.72**	**1.81**	**1.00**	**1.00**	**1.71**
		113	0.51	1.14	1.00	0.92	1.87	0.66	1.47	1.00	0.94	1.72	0.81	1.81	1.00	0.95	1.63
		226	0.55	1.14	1.00	0.85	1.74	0.71	1.47	1.00	0.90	1.63	0.87	1.81	1.00	0.92	1.57
Concrete parameters	$E_{c,t0}$, GPa	**23**	**0.46**	**1.14**	**1.00**	**1.00**	**2.03**	**0.59**	**1.47**	**1.00**	**1.00**	**1.82**	**0.72**	**1.81**	**1.00**	**1.00**	**1.71**
		26	0.46	1.14	0.97	0.95	2.00	0.59	1.47	0.97	0.96	1.80	0.72	1.81	0.98	0.97	1.69
		29	0.46	1.14	0.94	0.92	1.98	0.59	1.47	0.95	0.93	1.78	0.72	1.81	0.96	0.94	1.68
	$f_{r,t0}$, MPa	**2.7**	**0.46**	**1.14**	**1.00**	**1.00**	**2.03**	**0.59**	**1.47**	**1.00**	**1.00**	**1.82**	**0.72**	**1.81**	**1.00**	**1.00**	**1.71**
		3.0	0.46	1.03	0.86	0.89	2.10	0.59	1.33	0.93	0.94	1.84	0.72	1.63	0.96	0.96	1.72
		3.3	0.46	0.93	0.74	0.81	2.20	0.59	1.21	0.86	0.88	1.87	0.72	1.48	0.91	0.92	1.73
	$\varphi_{cr,u}$	**2.0**	**0.46**	**1.14**	**1.00**	**1.00**	**2.03**	**0.59**	**1.47**	**1.00**	**1.00**	**1.82**	**0.72**	**1.81**	**1.00**	**1.00**	**1.71**
		1.7	0.46	1.14	1.00	0.96	1.95	0.59	1.47	1.00	0.97	1.76	0.72	1.81	1.00	0.97	1.66
		1.4	0.46	1.14	1.00	0.92	1.87	0.59	1.47	1.00	0.94	1.70	0.72	1.81	1.00	0.94	1.61
	$\varepsilon_{sh,u}$, με	**950**	**0.46**	**1.14**	**1.00**	**1.00**	**2.03**	**0.59**	**1.47**	**1.00**	**1.00**	**1.82**	**0.72**	**1.81**	**1.00**	**1.00**	**1.71**
		750	0.46	1.14	1.00	0.94	1.90	0.59	1.47	1.00	0.94	1.72	0.72	1.81	1.00	0.95	1.63
		550	0.46	1.14	1.00	0.87	1.77	0.59	1.47	1.00	0.89	1.61	0.72	1.81	1.00	0.90	1.54
Construction parameters	t_0, days	**14**	**0.46**	**1.14**	**1.00**	**1.00**	**2.03**	**0.59**	**1.47**	**1.00**	**1.00**	**1.82**	**0.72**	**1.81**	**1.00**	**1.00**	**1.71**
		21	0.45	1.06	0.94	0.89	1.93	0.58	1.36	0.99	0.93	1.72	0.71	1.67	1.00	0.95	1.62
		28	0.45	1.02	0.92	0.84	1.85	0.58	1.32	0.99	0.90	1.65	0.71	1.62	1.01	0.93	1.56
	t_d, days	**14**	**0.46**	**1.14**	**1.00**	**1.00**	**2.03**	**0.59**	**1.47**	**1.00**	**1.00**	**1.82**	**0.72**	**1.81**	**1.00**	**1.00**	**1.71**
		21	0.46	1.14	1.00	0.99	2.00	0.59	1.47	1.00	0.99	1.80	0.72	1.81	1.00	0.99	1.69
		28	0.46	1.14	1.00	0.98	1.98	0.59	1.47	1.00	0.98	1.78	0.72	1.81	1.00	0.98	1.68

Note: Bolded values correspond to benchmark (reference) case for each external load level and parameter.

of 0, 0.0018, and 0.0035, respectively (Table 5). The larger values of λ_Δ obtained in this study are mostly attributed to the loading time of 14 days for measuring immediate deflections, whereas ACI CODE-318 estimates immediate deflections at 28 days.

Figures 7(d) through (g) show the deflections of the one-way RC slabs when varying the concrete parameters (modulus of elasticity at t_0, modulus of rupture at t_0, ultimate creep coefficient, and ultimate shrinkage strain). The effect of concrete parameters on deflections is less significant than that of geometrical parameters, such as the slab thickness and the area of tension reinforcement. Table 6 shows that the modulus of rupture at t_0 and the ultimate shrinkage strain are the concrete parameters that mostly affect long-term deflections. Additionally, increasing the modulus of rupture also reduces the immediate deflection. The immediate and long-term deflections were reduced by 14% and 12%, respectively, when the modulus of rupture increases 22%. This finding is consistent with the experimental results of one-way RC slabs tested by Aslani,[9] in which a 16% increase (Slabs N-SCC-a and D-SCC-a) in the modulus of rupture reduced immediate and long-term deflections by 37% and 28%, respectively. However, both the modulus of elasticity and the modulus of rupture are related to the concrete compressive strength. Therefore, it is expected that both parameters increase simultaneously as the compressive strength increases. Table 6 also shows that the long-term deflection was reduced by only 11% when the ultimate shrinkage strain decreased 42% (from 950 to 550 με). Thus, reducing the ultimate shrinkage strain only had a limited effect on reducing long-term deflections. Moreover, Table 6 shows that immediate and long-term deflections were reduced by 5% and 7%, respectively, when the modulus of elasticity increased 26% (from 23 to 29 GPa). Finally, regarding the ultimate creep coefficient, Table 6 shows that the long-term deflection was reduced by

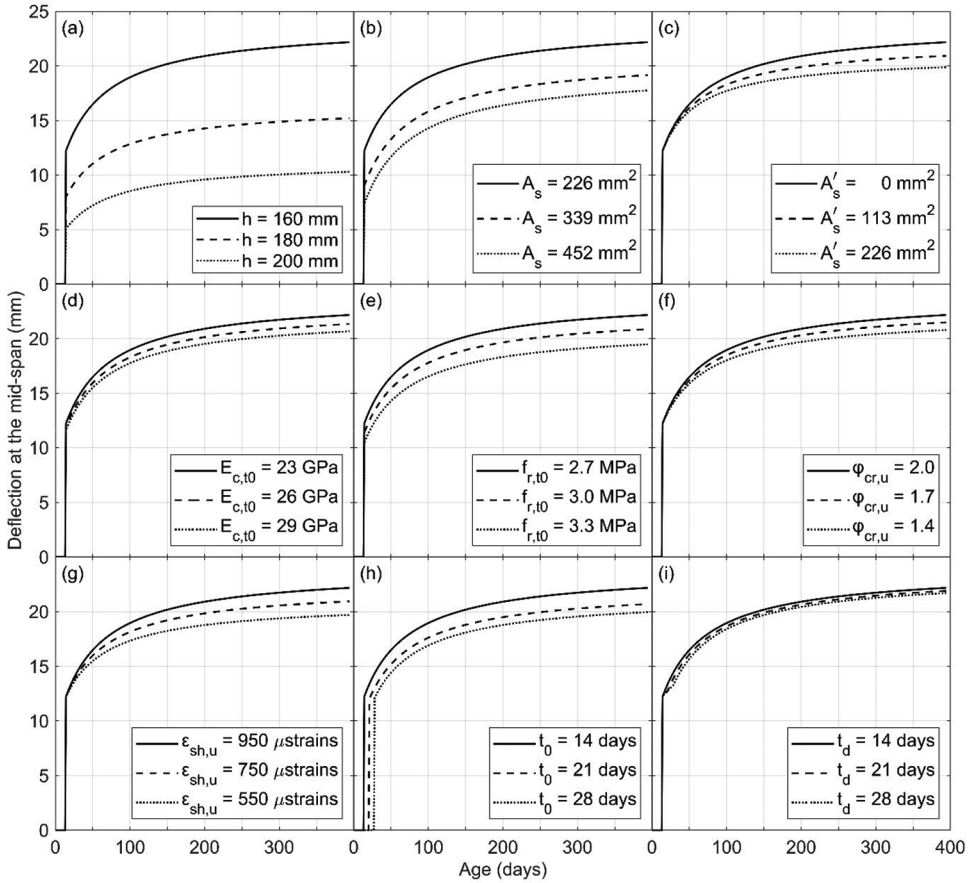

Fig. 7—Midspan deflections of slabs in parametric study for Q *= 2.9 kN/m.*

only 6%, when the ultimate creep coefficient decreased 30% (from 2.0 to 1.4).

Figures 7(h) and (i) show the deflections of the slabs when varying the construction parameters (loading time and initiation of concrete drying time). Figure 7(h) and Table 6 show that the loading time has a significant effect on long-term deflection but minimal impact on immediate deflection. The long-term deflection was reduced by 10% when the loading time increased from 14 to 28 days. Finally, Table 6 shows that the initiation of concrete drying time has only a minor effect on long-term deflection and no effect on immediate deflections. However, ensuring proper concrete hydration during the initial days guarantees adequate maturation that positively affects the modulus of elasticity, modulus of rupture, creep, and shrinkage parameters. This helps delay crack formation and reduce deflection, particularly in the long term.

Regarding the effects of the external load level, Table 6 shows that increasing the slab thickness and the area of compression reinforcement were more effective for reducing long-term deflections at lesser loads. Conversely, increasing the area of tension reinforcement was more effective for reducing long-term deflections at larger loads. Regarding concrete parameters, Table 6 shows that larger reductions of long-term deflections were obtained at lesser loads, and that the variation of the modulus of rupture was the most effective concrete parameter for reducing deflections. This finding suggests that the tensile strength can be optimized for different loading conditions to reduce deflections. Regarding construction parameters, Table 6 shows that the loading time plays a crucial role in reducing both immediate and long-term deflections, with greater effectiveness at lesser loads. Finally, Table 6 shows that the λ_Δ factor decreased as the load level increased. The average λ_Δ factor was 2.05 (range from 1.74 to 2.80) for Q = 1.9 kN/m, 1.82 (range from 1.61 to 2.42) for Q = 2.9 kN/m, and 1.71 (range from 1.54 to 2.21) for Q = 3.9 kN/m.

CONCLUSIONS AND RECOMMENDATIONS

The effects of geometry, concrete, and construction parameters, of one-way reinforced concrete (RC) slabs on the immediate and long-term deflections were assessed in this paper. This parametric study provides practical guidance for engineers and constructors to quantify how the studied parameters affect immediate and long-term deflection in one-way RC slabs. The main conclusions from this study are:

1. Geometrical parameters showed the greatest influence on the deflections of one-way RC slabs. As expected, increasing slab thickness and the area of tension reinforcement proved to be the most effective strategies for reducing both immediate and long-term deflections, whereas increasing the area of compression reinforcement affected only long-term deflections. Moreover, increasing the slab thickness and the area of compression reinforcement were more effective for reducing long-term deflections at lesser loads.

2. Concrete parameters had a comparatively minor effect on one-way RC slab deflections compared to slab thickness

and tension reinforcement. As expected, increasing the modulus of rupture and modulus of elasticity reduced both immediate and long-term deflections, with greater effectiveness observed at higher modulus of rupture values and under lower applied load levels. In contrast, ultimate shrinkage strain influenced only long-term deflections.

3. Loading time showed a significant influence on one-way RC slab deflections. As expected, delaying load application reduced both immediate and long-term deflections, while postponing the initiation of concrete drying produced a slight reduction in long-term deflections. These findings highlight the importance of proper construction scheduling to optimize structural performance.

The results of this study highlight that optimizing geometrical, concrete, and construction parameters is crucial for controlling deflections and ensuring long-term structural performance of one-way RC slabs.

AUTHOR BIOS

John Ardila-Gonzalez *is a Doctoral Student at the Department of Structural and Geotechnical Engineering, Pontificia Universidad Católica de Chile, Santiago, Chile. He received his BS and MEng from the Universidad Industrial de Santander, Bucaramanga, Colombia. His research interests include analysis, design, and laboratory testing of reinforced concrete (RC) structural elements.*

ACI member **Matías A. Hube** *is an Associate Professor in the Department of Structural and Geotechnical Engineering and the Co-Director of the Concrete Innovation Hub UC at Pontificia Universidad Católica de Chile. He is a member of ACI Committees 369, Seismic Repair and Rehabilitation, and 374, Performance-Based Seismic Design of Concrete Buildings, and ACI Subcommittee 318-D, Members. His research interests include analysis and design of RC buildings and bridges, and earthquake engineering.*

ACI member **Julian Carrillo** *is Professor in the Department of Civil Engineering at the Universidad Militar Nueva Granada, Bogota, Colombia. He is member of ACI Committees 133, Disaster Reconnaissance; 135, Machine Learning-Informed Construction and Design; 314, Simplified Design of Concrete Buildings; 318S, Spanish Translation; 369, Seismic Repair and Rehabilitation; 374, Performance-Based Seismic Design of Concrete Buildings; 440, Fiber-Reinforced Polymer Reinforcement; and 544, Fiber Reinforced Concrete, and ACI Subcommittee 445-B, Shear & Torsion-Seismic Shear. His research interests include the behavior and design of RC structures under seismic actions.*

ACKNOWLEDGMENTS

The authors wish to acknowledge the financial support provided by Becas VRI/Escuela de Graduados/Doctorados UC. In addition, the authors are thankful to the Concrete Innovation Hub UC and the Structural and Geotechnical Engineering Department of Pontificia Universidad Católica de Chile. J. Carrillo thanks Vicerrectoría de Investigaciones at Universidad Militar Nueva Granada for providing research grants.

REFERENCES

1. ACI Committee 318, "Building Code Requirements for Structural Concrete and Commentary (ACI CODE-318-25)," American Concrete Institute, Farmington Hills, MI, 2025, 702 pp.

2. Tošić, N.; Pecić, N.; Marí, A.; Torres, L.; Dragaš, J.; and Poliotti, M., "Development and Assessment of a Modified ζ-Method for Deflection Control of Two-Way Slabs," *Concrete Structure: New Trends for Eco-Efficiency and Performance*, 18th *fib* Symposium Proceedings, Lausanne, Switzerland, 2021, pp. 1549-1557.

3. Desalegne, A. S., and Lubell, A. S., "Deflection Control of Concrete Slabs Longitudinally Reinforced with ASTM A1035/A1035M-07 Steel," *ACI Structural Journal*, V. 109, No. 6, Nov.-Dec. 2012, pp. 867-877.

4. Bertero, R., and Bertero, A., "Statistical Evaluation of Minimum Thickness Provisions for Slab Deflection Control," *ACI Structural Journal*, V. 115, No. 6, Nov. 2018, pp. 1659-1670.

5. Aljazaeri, Z.; Alghazali, H.; and Myers, J., "Effectiveness of Using Carbon Fiber Grid Systems in Reinforced Two-Way Concrete Slab System," *ACI Structural Journal*, V. 117, No. 2, Mar. 2020, pp. 81-89.

6. Gilbert, I., and Nejadi, S., "An Experimental Study of Flexural Cracking in Reinforced Concrete Members Under Sustained Loads," UNICIV *Report* No. R-435, University of New South Wales, Sydney, NSW, Australia, 2004, 59 pp.

7. Gilbert, I., and Guo, X., "Time-Dependent Deflection and Deformation of Reinforced Concrete Flat Slabs—An Experimental Study," *ACI Structural Journal*, V. 102, No. 3, May-June 2005, pp. 363-373.

8. Hwang, H. J.; Park, H. G.; Hong, G. H.; Kim, J. Y.; and Kim, Y. N., "Time-Dependent Deflection of Slab Affected by Construction Load," *ACI Structural Journal*, V. 113, No. 3, Mar.-Apr. 2016, pp. 557-566.

9. Aslani, F., "Reinforced SCC One-Way Slabs: Time-Dependent Flexural Cracking Control," *Proceedings of the Institution of Civil Engineers. Structures and Buildings*, V. 172, No. 1, 2019, pp. 55-73. doi: 10.1680/jstbu.17.00127

10. Tošić, N., and Kurama, Y., "Parametric Numerical Study on Service-Load Deflections of Reinforced Recycled Aggregate Concrete Slabs and Beams Based on *fib* Model Code 2010," *Structural Concrete*, V. 21, No. 6, 2020, pp. 2854-2868. doi: 10.1002/suco.202000015

11. ACI Committee 209, "Guide for Modeling and Calculating Shrinkage and Creep in Hardened Concrete (ACI 209.2-08)," American Concrete Institute, Farmington Hills, MI, 2008, 45 pp.

12. Bischoff, P. H., and Torres, L., "Rational Approach for Computing Long-Term Deflection of Reinforced Concrete," *ACI Structural Journal*, V. 118, No. 2, Mar. 2021, pp. 215-224.

13. Bischoff, P. H., "Comparison of Existing Approaches for Computing Deflection of Reinforced Concrete," *ACI Structural Journal*, V. 117, No. 1, Jan. 2020, pp. 231-240.

14. *fib*, "fib Model Code for Concrete Structures 2010," Federation Internationale du Beton (*fib*), Lausanne, Switzerland, 2013, 434 pp.

15. Pecić, N.; Mašović, S.; and Stošić, S., "Span-to-Depth Ratio Limits for Deflection Control of Reinforced Concrete Elements," *Structural Concrete*, V. 24, No. 2, 2023, pp. 2547-2562. doi: 10.1002/suco.202200132

16. Tošić, N.; Pecić, N.; Poliotti, M.; Marí, A.; Torres, L.; and Dragaš, J., "Extension of the ζ-Method for Calculating Deflections of Two-Way Slabs Based on Linear Elastic Finite Element Analysis," *Structural Concrete*, V. 22, No. 3, 2021, pp. 1652-1670. doi: 10.1002/suco.202000558

17. Moehle, J., *Seismic Design of Reinforced Concrete Buildings*, first edition, McGraw-Hill Professional, Columbus, OH, 2014, 760 pp.

18. Gilbert, R. I., "The Serviceability Limit States in Reinforced Concrete Design," *Procedia Engineering*, V. 14, 2011, pp. 385-395. doi: 10.1016/j.proeng.2011.07.048

19. Holmberg, A., "Modulus of Elasticity and Creep in Self Compacting Concretes," webinar (in Spanish), Instituto del Cemento y del Hormigón de Chile (ICH), Santiago de Chile, Chile, Apr. 11, 2023, https://ich.cl/webinar/modulo-de-elasticidad-creep-en-hormigones-autocompactantes/. (last accessed Apr. 2, 2026)

20. Hollington, M., "A Series of Long-Term Tests to Investigate the Deflection of a Representative Precast Concrete Floor Component," *Cement and Concrete Association*, London, England, Tech. Rep. TRA 442, 1970, 43 pp.

21. Branson, D., "Compression Steel Effect on Long-Time Deflections," *ACI Journal Proceedings*, V. 68, No. 8, Aug. 1971, pp. 555-559.

22. ACI Committee 435, "Report on Deflection of Nonprestressed Concrete Structures (ACI 435R-20)," American Concrete Institute, Farmington Hills, MI, 2020, 56 pp.

APPENDIX A

Shrinkage curvature for uncracked transformed section and cracked transformed section

The shrinkage curvature, estimated with Eq. (7), comprises a shrinkage curvature for the uncracked (gross) transformed section and a shrinkage curvature for the cracked transformed section. Both components are estimated using Eq. (A1) and (A2), respectively.[12]

$$\phi_{sh,tr} = \frac{\bar{S}_{tr}}{\bar{I}_{tr}}\varepsilon_{sh} \tag{A1}$$

$$\phi_{sh,cr} = \frac{\bar{S}_{cr}}{\bar{I}_{cr}}\varepsilon_{sh} \tag{A2}$$

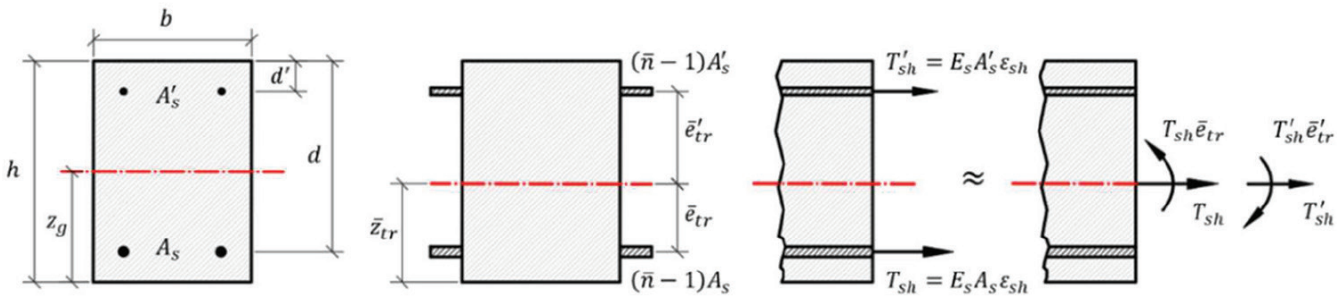

Fig. A1—Uncracked transformed section.

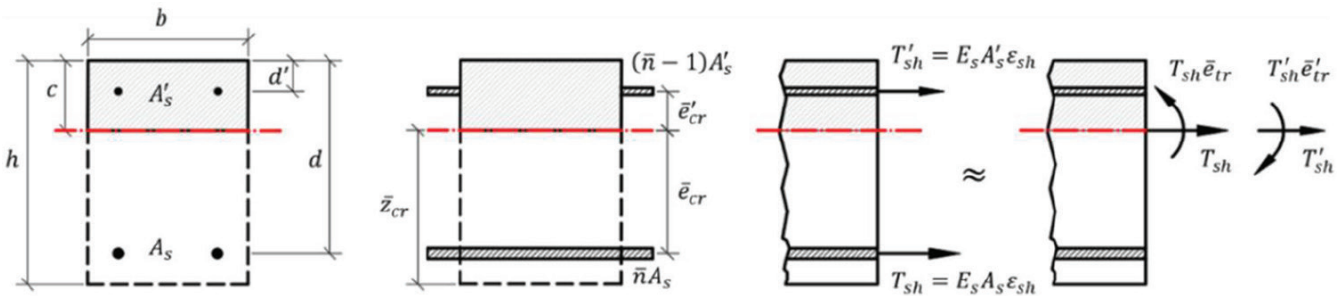

Fig. A2—Cracked transformed section.

where ε_{sh} is the shrinkage strain and $\bar{S}_{tr}$ and $\bar{I}_{tr}$ are the first moment of area and moment of inertia of the uncracked transformed section, respectively. In Eq. (A2), $\bar{S}_{cr}$ and $\bar{I}_{cr}$ are the first moment of area and the moment of inertia of the cracked transformed section, respectively.

Cross-sectional properties of uncracked transformed section

To estimate cross-sectional properties for the uncracked transformed section shown in Fig. A1, the cross section is transformed and the total uncracked transformed area is computed using Eq. (A3), following ACI 435R-20.[22] In this equation, A_g is the gross concrete area estimated as $A_g = bh$; A_s is the area of tension reinforcement; A_s' is the area of compression reinforcement; and $\bar{n}$ is the effective modular ratio computed as $\bar{n} = E_s/\bar{E}_c$.

$$\bar{A}_{tr} = A_g + (\bar{n}-1)A_s + (\bar{n}-1)A_s' \tag{A3}$$

The neutral axis of the cross section for the uncracked transformed concrete area is estimated using Eq. (A4), where $z_g = h/2$ is the neutral axis for the rectangular cross section of concrete. The transformed uncracked moment of inertia is estimated using Eq. (A5).

$$\bar{z}_{tr} = \frac{1}{\bar{A}_{tr}}\left[A_g z_g + (\bar{n}-1)A_s(h-d) + (\bar{n}-1)A_s'(h-d')\right] \tag{A4}$$

$$\bar{I}_{tr} = I_g + A_g(z_g - \bar{z}_{tr})^2 + (\bar{n}-1)A_s(\bar{e}_{tr})^2 + (\bar{n}-1)A_s'(\bar{e}'_{tr})^2 \tag{A5}$$

The gross moment of inertia in Eq. (A5) is estimated as $I_g = (bh^3)/12$. The eccentricities of the tension and compression reinforcements with respect to the neutral axis of the uncracked transformed concrete cross section are computed as $\bar{e}_{tr} = \bar{z}_{tr} - (h-d)$ and $\bar{e}'_{tr} = (h-d') - \bar{z}_{tr}$, respectively. Finally, the term $\bar{S}_{tr}$ to estimate the curvature in Eq. (A1), for the transformed uncracked section based on the shrinkage strain, is computed using Eq. (A6).

$$\bar{S}_{tr} = \bar{n}(A_s\bar{e}_{tr} - A'_s\bar{e}'_{tr}) \tag{A6}$$

Cross-sectional properties of cracked transformed section

To estimate cross-sectional properties for the cracked transformed section shown in Fig. A2, the cross section is transformed and the total cracked transformed area is computed using Eq. (A7) following ACI 435R-20.[22] The depth c of the concrete block subjected to compression is computed as $c = kd$, and the coefficient k is estimated using Eq. (A8).

$$\bar{A}_{cr} = bc + \bar{n}A_s + (\bar{n}-1)A'_s \tag{A7}$$

$$k = \sqrt{\left[\bar{n}\rho - (\bar{n}-1)\rho'\right]^2 + 2\left[\bar{n}\rho - (\bar{n}-1)\rho'\left(\frac{d'}{d}\right)\right]} - \left[\bar{n}\rho - (\bar{n}-1)\rho'\right] \tag{A8}$$

The tension and the compression reinforcement ratios in Eq. (A8) are computed as $\rho = A_s/(bd)$ and $\rho' = A'_s/(bd)$, respectively. For the RC slab, the tension and the compression reinforcement ratios are computed as $\rho = A_s/(bh)$ and $\rho' = A_s'/(bh)$, respectively.

The neutral axis of the cross section for the cracked transformed concrete area is estimated using Eq. (A9). The transformed cracked moment of inertia is estimated using Eq. (A10).

$$\bar{z}_{cr} = \frac{1}{\bar{A}_{cr}}\left[bc\left(h - \frac{c}{2}\right) + n A_s(h - d) + (n - 1)A'_s(h - d')\right] \tag{A9}$$

$$\bar{I}_{cr} = \frac{1}{12}bc^3 + bc\left[\left(h - \frac{c}{2}\right) - \bar{z}_{cr}\right]^2 + n A_s \bar{e}_{cr}^2 + (n - 1)A'_s \bar{e}'^2_{cr} \tag{A10}$$

The eccentricities of the tension and compression reinforcement with respect to the neutral axis of the cracked transformed concrete cross section are computed as $\bar{e}_{cr} = \bar{z}_{cr} - (h - d)$ and $\bar{e}'_{cr} = (h - d') - \bar{z}_{cr}$, respectively. Finally, the term $\bar{S}_{cr}$ to estimate the curvature of the Eq. (A2) for the transformed cracked section, based on the shrinkage strain, is computed using Eq. (A11).

$$\bar{S}_{cr} = n(A_s \bar{e}_{cr} - A'_s \bar{e}'_{cr}) \tag{A11}$$

APPENDIX B

Creep and shrinkage models

The ultimate creep coefficient, used in Eq. (8), can be modified by the modification factor (γ_{cr}) using Eq. (B1).[11]

$$\varphi_{cr,u} = 2.35\gamma_{cr} \tag{B1}$$

The modification factor (γ_{cr}) depends on loading time factor ($\gamma_{cr,t0}$), relative humidity factor ($\gamma_{cr,RH}$), volume-to-surface ratio factor ($\gamma_{cr,VS}$), slump factor ($\gamma_{cr,S}$), fine-coarse aggregate ratio factor ($\gamma_{cr,\psi}$), and air content factor ($\gamma_{cr,\alpha}$). The modification factor is computed using Eq. (B2).

$$\gamma_{cr} = \gamma_{cr,t0}\gamma_{cr,RH}\gamma_{cr,VS}\gamma_{cr,S}\gamma_{cr,\psi}\gamma_{cr,\alpha} \tag{B2}$$

Each factor can be estimated using Eq. (B3) to (B8).[11] In these equations t_0 is the loading time in days, h is the relative humidity in decimals, V/S is the volume-to-surface ratio in mm, S is the slump of the concrete mixture in mm, ψ is the fine-coarse aggregate ratio in percentage, and α is the air content in percentage.

$$\gamma_{cr,t0} = 1.25\,t_0^{-0.118} \tag{B3}$$

$$\gamma_{cr,RH} = \begin{cases} 1.27 - 0.67h & h \geq 0.40 \\ 1 & h < 0.40 \end{cases} \tag{B4}$$

$$\gamma_{cr,VS} = \frac{2}{3}(1 + 1.13\,e^{-0.0213V/S}) \tag{B5}$$

$$\gamma_{cr,S} = 0.82 + 0.00264S \tag{B6}$$

$$\gamma_{cr,\psi} = 0.88 + 0.0024\psi \tag{B7}$$

$$\gamma_{cr,\alpha} = 0.46 + 0.09\alpha \geq 1 \tag{B8}$$

The ultimate shrinkage coefficient, used in Eq. (9), can be modified by the modification factor (γ_{sh}) using Eq. (B9).[11]

$$\varepsilon_{sh,u} = 780\gamma_{sh} \times 10^{-6} \tag{B9}$$

The modification factor γ_{sh} depends on loading time factor ($\gamma_{sh,t0}$), relative humidity factor ($\gamma_{sh,RH}$), volume-to-surface ratio factor ($\gamma_{sh,VS}$), slump factor ($\gamma_{sh,S}$), fine-coarse aggregate ratio factor ($\gamma_{sh,\psi}$), cement content factor ($\gamma_{sh,C}$), and air content factor ($\gamma_{sh,\alpha}$). The modification factor is computed using Eq. (B10).

$$\gamma_{sh} = \gamma_{sh,td}\gamma_{sh,RH}\gamma_{sh,VS}\gamma_{sh,S}\gamma_{sh,\psi}\gamma_{sh,C}\gamma_{sh,\alpha} \tag{B10}$$

Each factor can be estimated by Eq. (B11) to (B17).[11] In these equations, t_d is the initiation of concrete drying time in days, where C is the cement content in kg/m^3.

$$\gamma_{sh,td} = 1.202 - 0.2337\log(t_d) \tag{B11}$$

$$\gamma_{sh,RH} = \begin{cases} 1.40 - 1.02h & 0.40 \leq h \leq 0.80 \\ 3.00 - 3.00h & 0.80 < h \leq 1 \end{cases} \tag{B12}$$

$$\gamma_{sh,VS} = 1.2\,e^{-0.00472V/S} \tag{B13}$$

$$\gamma_{sh,S} = 0.89 + 0.00161S \tag{B14}$$

$$\gamma_{sh,\psi} = \begin{cases} 0.30 + 0.014\psi & \psi \leq 50\% \\ 0.90 + 0.002\psi & \psi > 50\% \end{cases} \tag{B15}$$

$$\gamma_{sh,C} = 0.75 + 0.00061C \tag{B16}$$

$$\gamma_{sh,\alpha} = 0.95 + 0.008\alpha \geq 1 \tag{B17}$$

ACI STRUCTURAL JOURNAL TECHNICAL PAPER

Title No. 123-S43

Flexural Performance of Glass Fiber-Reinforced Polymer and Highly Ductile Stainless-Steel Bar Hybrid-Reinforced Concrete Beams

by Qi Cao, Teng Zhang, Shu Cao, Zhimin Wu, and Jinjin Xu

To improve the ductility of fiber-reinforced polymer-reinforced concrete structures, hybrid reinforcement with glass fiber-reinforced polymer (GFRP) and stainless steel (SS) was selected in this paper. Nine seawater sea-sand concrete (SSC) beams were designed and tested. The effects of concrete strength, effective reinforcement ratio ρ_2, and reinforcement type in the tensile zone on the flexural behavior of the beams were analyzed. The test results showed that with the same concrete strength and effective reinforcement ratio ρ_2, the ductility of hybrid-reinforced beams is higher than GFRP-reinforced beams. The comparison of midspan deflection of the GFRP bars and hybrid-reinforced beams not only depends on the reinforcement type but also on the total stiffness of reinforcement before SS bars yielded in the tensile zone and whether they yielded in the tensile zone. Meanwhile, theoretical analysis was conducted for cracking moments, ultimate flexural load-carrying capacity, and midspan deflections. A new ultimate flexural load-carrying calculation equation was proposed, which predicted the experimental values in good agreement.

Keywords: ductility; flexural behavior; glass fiber-reinforced polymer (GFRP) bars; hybrid reinforcement; stainless steel (SS) bars.

INTRODUCTION

The extensive construction of worldwide infrastructure has depleted significant freshwater and river sand resources, leading to resource shortage (Gagg 2014; Dhondy et al. 2020a). Marine resources, such as seawater and sea sand, have the potential to be used as substitutes for freshwater and river sand in concrete production. Scholars globally have conducted extensive research on seawater sea-sand concrete (SSC), including studies by Guo et al. (2018), Otsuki et al. (2012), Chen et al. (2021), and Dhondy et al. (2020b). This research indicates that there is no significant difference in mechanical properties between SSC and ordinary concrete; however, it is important to note that it contains a considerable amount of chloride ions, which can corrode the reinforcement bars (Xu and Li 2017). Fiber-reinforced polymer (FRP) reinforcement is a novel material that has excellent characteristics such as lightweight, high strength, and good corrosion resistance (Hawileh 2015). The application of FRP bars in SSC structures has become a popular research field. However, due to the low elastic modulus of FRP bars, the deformation of FRP bar-reinforced concrete beams in the range of the serviceability stage is greater than that of steel bar-reinforced concrete beams. At the same time, unlike the steel bar-reinforced concrete beams, which undergo significant deformation during failure stage due to the yielding of steel bars, the linear elastic characteristics of FRP bars make FRP bar-reinforced concrete beams prone to brittle failure (Alsayed et al. 2000; Zhu et al. 2015).

To reduce deformation in the range of serviceability stage and improve ductility during the failure phase of FRP bar-reinforced concrete beams, scholars have proposed a hybrid reinforcement method of FRP steel bars (Tan et al. 1997; Aiello and Ombres 2002), and studied the effects of concrete strength, effective reinforcement ratio, reinforcement type, and the area ratio of FRP bars to steel bars in tensile zone on the flexural behavior of the hybrid-reinforced beams (Lau and Pam 2010; Adam et al. 2015; Qin et al. 2017; Wang et al. 2022; Xu et al. 2022; Hussein et al. 2022).

To establish calculation equations applicable to the hybrid reinforcement system of FRP steel bars, scholars conducted extensive experimental research. Oh and Ahn (2008) designed and tested 12 FRP steel bars hybrid-reinforced concrete beams under a four-point bending experiment. By comparing the experimental results with the calculation results obtained using the calculation equations in ACI 440.1R-06 (ACI Committee 440 2006), it was concluded that the theory of ultimate limit state design for bearing capacity of FRP bars can accurately predict the ultimate flexural load-carrying capacity of hybrid-reinforced beams. Qu et al. (2009) conducted experiments on hybrid-reinforced beams and proposed a flexural capacity calculation model that effectively predicts the ultimate flexural load-carrying capacity of hybrid-reinforced beams under the under-reinforced failure state. Zhang et al. (2011) analyzed the flexural behavior of basalt fiber-reinforced polymer (BFRP) steel bar hybrid-reinforced concrete beams and proposed the ultimate flexural load-carrying capacity equation of hybrid-reinforced beams under the under-reinforced failure state (the steel bars in the tensile zone yield, the concrete in the compressive zone breaks, and the FRP bars in the tensile zone are not ruptured) based on the plane section assumption. Su et al. (2023) studied the flexural behavior of BFRP steel bar hybrid-reinforced beams and conducted numerical simulation. The theoretical calculation results of the ultimate flexural load-carrying capacity and midspan deflection of hybrid-reinforced concrete beams based on ACI, CSA, and GB codes were compared with the simulation results.

ACI Structural Journal, V. 123, No. 3, May 2026.
MS No. S-2024-189.R3, doi: 10.14359/51749489, received May 9, 2025, and reviewed under Institute publication policies. Copyright © 2026, American Concrete Institute. All rights reserved, including the making of copies unless permission is obtained from the copyright proprietors. Pertinent discussion including author's closure, if any, will be published ten months from this journal's date if the discussion is received within four months of the paper's print publication.

Yinghao and Yong (2013) proposed the boundary reinforcement ratio in the tensile zone corresponding to three failure modes of hybrid-reinforced beams and provided a method for calculating the inertia moment of section cracking based on the boundary reinforcement ratio in the tensile zone. Ruan et al. (2020) found that midspan deflections calculated based on the effective moment of inertia equations in ACI 318-14 (ACI Committee 318 2014) and ACI 440.1R-15 (ACI Committee 440 2015) were almost equal, and both underestimated the midspan deflections in the range of the serviceability stage.

The use of steel bars in SSC structures will cause corrosion of the steel bars, so it is necessary to replace them with stainless steel (SS) bars, which have stronger corrosion resistance. However, due to limited research on FRP-SS bar hybrid-reinforced beams both domestically and internationally, and the fact that SS bars are different from ordinary steel bars and do not have a distinct yield platform, it is still unknown whether the relevant calculation equations for the flexural behavior of FRP steel bar hybrid-reinforced beams obtained by previous scholars can be applied to FRP-SS bar hybrid-reinforced beams. This study investigates the effects of concrete strength, reinforcement type in tensile zone and effective reinforcement ratio ρ_2 in the tensile zone on the cracking moment, ultimate flexural load-carrying capacity, and midspan deflection and ductility of beams through experiments. In addition, this paper also calculated the flexural behavior of FRP-SS bar hybrid-reinforced beams by using the existing theoretical calculation methods for the flexural behavior of FRP steel bar hybrid-reinforced beams provided by existing design codes, the tensile zone, and effective reinforcement ratio 2 in the tensile zone on the cracking moment, ultimate flexural load-carrying capacity, and midspan deflection. The comparison between the theoretical calculation results and experimental results provides a reference for the theoretical calculation of the flexural behavior of FRP-SS bar hybrid-reinforced concrete beams.

RESEARCH SIGNIFICANCE

FRP bar-reinforced concrete structures have been observed with brittle failure due to the linear-elastic properties of FRP. SS bars have excellent corrosion resistance as well as good ductility. The objective of this paper is to study the flexural behavior of GFRP-SS bar hybrid-reinforced concrete beams. The findings of this paper will assist in understanding the effect of GFRP-SS bar hybrid reinforcing on improving the ductility of FRP-reinforced concrete structures, as well as overall flexural behavior. It will also provide detailed test data that assists further analysis and numerical studies in this area.

EXPERIMENTAL PROGRAM

Materials

Reinforcing bars—In this study, 12 mm (0.47 in.) diameter SS bars were used, with the symbol 304. The GFRP bars used in the experiment varied in diameter, ranging from 16, 18, 20, and 22 mm (0.63, 0.71, 0.79, and 0.87 in.), as shown in Fig. 1. The rib height of the 12 mm (0.47 in.) diameter SS bars is 2 mm (0.08 in.), and the rib distance is 7 mm (0.28 in.). The rib height of 16 mm (0.63 in.) diameter GFRP bars is 2 mm (0.08 in.), and the rib distance is 10 mm (0.39 in.). The rib height of GFRP bars with a diameter of 18 to 22 mm (0.71 to 0.87 in.) is 2 mm (0.08 in.), and the rib distance is 13 mm (0.51 in.). SS bars underwent tensile testing according to GB/T 228.1-2021 (2021), and FRP bars underwent tensile testing according to ASTM D7205/D7205M-21 (2021). Before the experiment, a computer-controlled electronic universal testing machine was used to determine the tensile mechanical properties. An extensometer with a gauge

Fig. 1—Reinforcing bars.

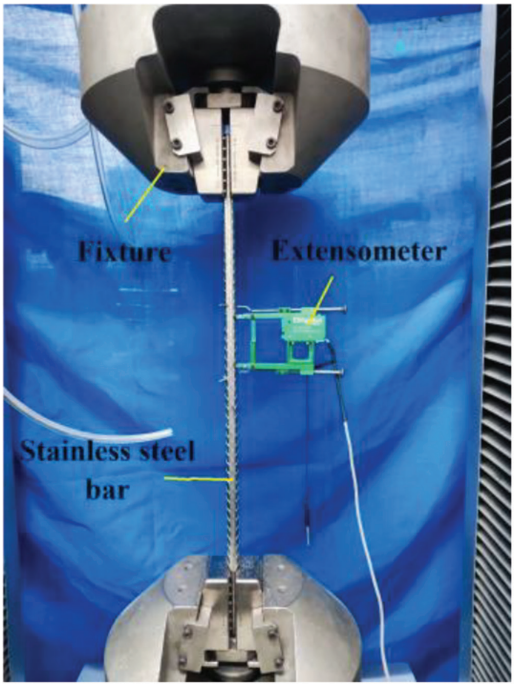

Fig. 2—Reinforcement tensile test setup.

length of 50 mm (1.97 in.) was attached to the reinforcing bar at its midpoint to measure strain. The experimental setup is illustrated in Fig. 2.

Due to the absence of an obvious yield platform in SS bars, the stress value corresponding to the residual strain of 0.2% is taken as the nominal yield strength of SS bars (Rasmussen 2003; Fernando et al. 2020). The stress-strain curve of SS bars and GFRP bars is shown in Fig. 3. Each mechanical property was measured three times. The average of the test results was taken as the actual material parameters. At the same time, the standard deviation was also provided. The mechanical properties of SS bars and FRP bars are shown in Tables 1 and 2, respectively.

Seawater sea-sand concrete—The seawater used in this study is natural seawater from the coastal area in Dalian city, and the sea sand is natural sea sand from the Qingdao city region. The coarse aggregate consists of crushed limestone with a continuous particle size of 5 to 10 mm (0.20 to 0.39 in.). According to GB 175-2023 (2023), three different concrete mixtures with varying strengths were designed using PO42.5 cement. The concrete mixture proportions can be found in Table 3. During specimen casting, 150 x 150 x 150 mm (5.91 x 5.91 x 5.91 in.) cubes and 150 x 150 x 300 mm (5.91 x 5.91 x 11.81 in.) prisms were prepared to measure the mechanical properties of the concrete. After 60 days from the date of casting specimens—that is, the date of testing the beams, the concrete strength was measured at the same time according to GB/T 50081-2019 (2019). Each mechanical property was measured three times. The average of the test results was taken as the actual material parameters. At the same time, the standard deviation was also provided. The concrete's mechanical performance parameters are provided in Table 4.

Hybrid reinforced concrete beams

A total of nine SSC beams were designed for this experiment to study their flexural behavior, comprising eight beams with a hybrid reinforcement of GFRP and SS bars and one beam with GFRP reinforcement. The dimensions of the beams are 200 mm (7.87 in.) wide, 300 mm (11.81 in.) high, and 2750 mm (108.27 in.) long with a 20 mm (0.79 in.)

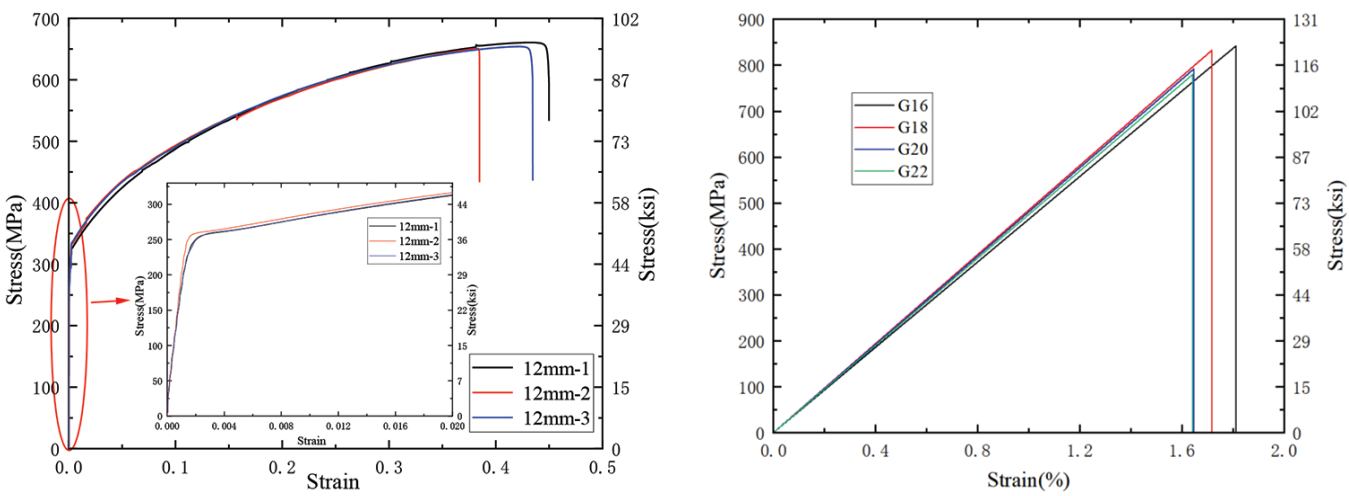

Fig. 3—Tensile stress-strain curves of reinforcing bars.

Table 1—Mechanical properties of stainless steel (SS) bars

Diameter, mm (in.)	Nominal yield strength, MPa (ksi)	Tensile strength, MPa (ksi)	Elastic modulus, GPa (ksi)	Yield strain, εμ	Rupture strain, εμ
12 (0.47)	270 ± 8 (39.16 ± 1.16)	663 ± 31 (96.16 ± 4.49)	191 ± 3 (27,702.26 ± 435.11)	1414 ± 17	420,000 ± 30,000

Table 2—Mechanical properties of GFRP bars

Diameter, mm (in.)	16 (0.63)	18 (0.71)	20 (0.79)	22 (0.87)
Tensile strength, MPa (ksi)	842 ± 11 (122.12 ± 1.60)	833 ± 15 (120.82 ± 2.18)	792 ± 7 (114.87 ± 1.02)	780 ± 19 (113.13 ± 2.76)
Elastic modulus, GPa (ksi)	46.5 ± 2.3 (6744.27 ± 333.59)	48.5 ± 1.9 (7034.34 ± 275.57)	48.1 ± 1.7 (6976.33 ± 246.56)	47.5 ± 2.1 (6889.31 ± 304.58)
Rupture strain, εμ	18,100 ± 402	17,200 ± 241	16,500 ± 275	16,300 ± 322

Table 3—Mixture proportion of SSC

Strength grade	Seawater, kg/m^3 (lb/ft^3)	Sea sand, kg/m^3 (lb/ft^3)	Cement, kg/m^3 (lb/ft^3)	Crushed limestone, kg/m^3 (lb/ft^3)
C30	195 (12.17)	774 (48.30)	270 (16.85)	1160 (72.38)
C40	195 (12.17)	696 (43.43)	325 (20.28)	1184 (73.88)
C50	195 (12.17)	550 (34.32)	487 (30.39)	1168 (72.88)

Table 4—Mechanical properties of SSC

Strength grade	f_t, MPa (ksi)	f_{cu}, MPa (ksi)	f_c, MPa (ksi)	E_c, GPa (ksi)
C30	2.64 ± 0.11 (0.38 ± 0.02)	34.38 ± 1.06 (4.99 ± 0.15)	22.99 ± 0.43 (3.33 ± 0.06)	30.02 ± 0.67 (4354.04 ± 97.18)
C40	2.71 ± 0.08 (0.39 ± 0.01)	46.38 ± 0.78 (6.73 ± 0.11)	31.02 ± 0.68 (4.50 ± 0.10)	32.89 ± (4770.30 ± 139.24)
C50	3.54 ± 0.13 (0.51 ± 0.02)	55.24 ± 1.44 (8.01 ± 0.21)	35.74 ± 0.81 (5.18 ± 0.12)	34.89 ± 0.53 (5060.38 ± 76.87)

Table 5—Reinforcement ratio of test beams

Beam identifier	A_f, mm^2 (in.^{2})	A_s, mm^2 (in.^{2})	A_s', mm^2 (in.^{2})	ρ_1	ρ_2
G16S12-S12-C30	402.12 (0.62)	226.19 (0.35)	226.19 (0.35)	2.24	0.62
G18S12-S12-C30	508.94 (0.79)	226.19 (0.35)	226.19 (0.35)	2.70	0.68
G16S12-S12-C40	402.12 (0.62)	226.19 (0.35)	226.19 (0.35)	2.24	0.62
G18S12-S12-C40	508.94 (0.79)	226.19 (0.35)	226.19 (0.35)	2.70	0.68
G20S12-S12-C40	628.32 (0.97)	226.19 (0.35)	226.19 (0.35)	3.09	0.74
G16S12-S12-C50	402.12 (0.62)	226.19 (0.35)	226.19 (0.35)	2.24	0.62
G18S12-S12-C50	508.94 (0.79)	226.19 (0.35)	226.19 (0.35)	2.70	0.68
G20S12-S12-C50	628.32 (0.97)	226.19 (0.35)	226.19 (0.35)	3.09	0.74
G22-S12-C40	1520.53 (2.36)	0	226.19 (0.35)	—	0.73

concrete cover. The stirrups are made of GFRP with a diameter of 12 mm (0.47 in.).

Zhang et al. (2011) proposed a hybrid reinforcement failure mode criterion with calculations in Eq. (1) and (2). To ensure that the hybrid reinforced beam undergoes the failure mode that the steel bars in the tensile zone yield, the concrete in the compressive zone breaks, and the FRP bars in the tensile zone are not ruptured. The reinforcement ratio in the tensile zone should meet the following equations.

$$\rho_1 = \rho_s + \frac{f_{fd}}{f_y}\rho_f > \frac{f_c}{f_y}\frac{2\varepsilon_0}{3(\varepsilon_{cu}' + \varepsilon_{fd})} \tag{1}$$

$$\rho_2 = \rho_s + \frac{E_f}{E_S}\rho_f < \frac{f_c}{f_y}\frac{2\varepsilon_0}{3(\varepsilon_{cu}' + \varepsilon_y)} \tag{2}$$

The reinforcement parameters for the beams are listed in Table 5. The influence of different effective reinforcement ratios ρ_2 under the same and different concrete strength under the same effective reinforcement ratio ρ_2 on the flexural behavior of hybrid-reinforced beams is studied. The effective reinforcement ratio ρ_2 is the reinforcement ratio of all longitudinal bars in the tensile zone obtained by equating the reinforcement ratio of FRP bars to SS bars in the tensile zone according to the stiffness principle. Meanwhile, the ρ_2 of G20S12-S12-C40 are approximately equal to G22-S12-C40, exploring the influence of the reinforcement type in the tensile zone on the flexural behavior of the beams under the condition that the total stiffness of reinforcement in the tensile zone is equal. Table 5 shows the calculated results for ρ_1 and ρ_2 according to Eq. (1) and (2). After verification, it was found that the reinforcement ratios in the tensile zone fall within the specified range of Eq. (1) and (2).

In the calculation process of the design phase, the concrete strength is obtained by precasting and testing according to the mixture proportions in Table 3, as described in the Section *Seawater sea-sand concrete*. By using the calculations from Eq. (3) and (4) proposed by Qu et al. (2009) to calculate the ultimate flexural load-carrying capacity of the beams, and then assuming the amount and spacing of stirrups, calculating the shear capacity of the beams according to ACI 440.1R-15 so that the shear capacity of the beams is greater than the ultimate flexural load-carrying capacity of the beams will ensure that the beams will not undergo shear failure. By calculation, when the spacing between stirrups is 80 mm (3.15 in.), it meets the requirement.

$$f_f = \sqrt{\frac{1}{4}\left(\frac{A_s f_y}{A_f} + E_f\varepsilon_{cu}\right)^2 + \left(0.85\frac{\beta_1 f_c'}{\rho_f} - \frac{A_s f_y}{A_f}\right)E_f\varepsilon_{cu}} - \frac{1}{2}\left(\frac{A_s f_y}{A_f} + E_f\varepsilon_{cu}\right) \le f_{fu} \tag{3}$$

$$M = (\rho_f f_f + \rho_s f_y)\left(1 - 0.59\frac{\rho_f f_f + \rho_s f_y}{f_c'}\right)bh_0^2 \tag{4}$$

In this paper, the beam labels are defined according to the reinforcement form of the test beam and the concrete strength grade, and G and S in the symbols represent GFRP bars and low-strength SS bars, respectively; C represents the cubic compressive strength of concrete. Take G16S12-S12-C30 as an example, where G16S12 represents that the diameter of the GFRP bar in the tensile zone is 16 mm (0.63 in.), and the diameter of the low-strength SS bar is 12 mm (0.47 in.). S12 represents that the diameter of the low-strength SS bar in the compression zone is 12 mm (0.47 in.). C30 represents the cubic compressive strength of concrete in the row corresponding to C30 in Table 4. The schematic diagrams of the beam cross section, the cross section dimension and configuration, are shown in Fig. 4 and 5, respectively.

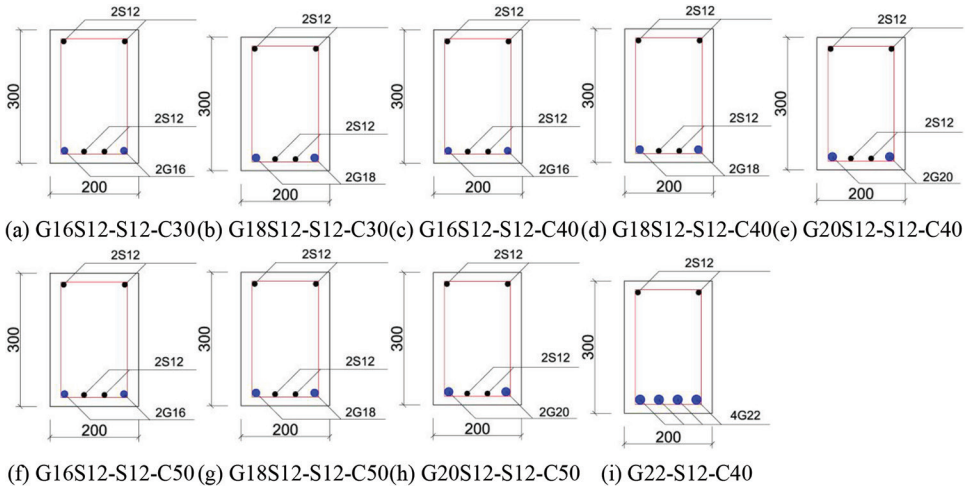

(a) G16S12-S12-C30 (b) G18S12-S12-C30 (c) G16S12-S12-C40 (d) G18S12-S12-C40 (e) G20S12-S12-C40

(f) G16S12-S12-C50 (g) G18S12-S12-C50 (h) G20S12-S12-C50 (i) G22-S12-C40

Fig. 4—Section reinforcements.

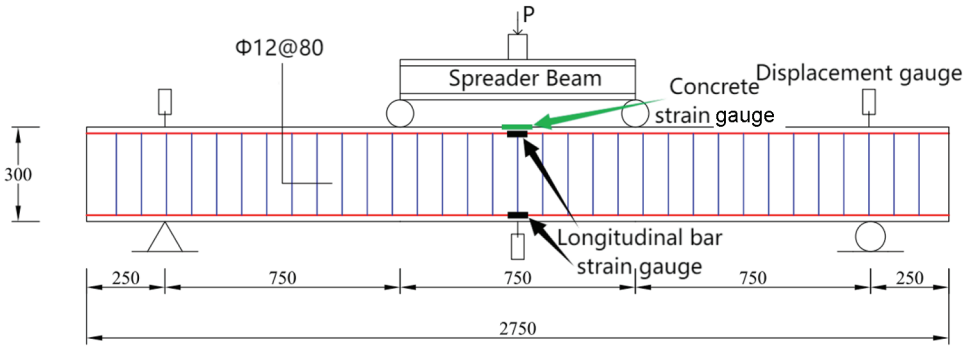

Fig. 5—Schematic diagram of test setup for tested beams. (Note: Dimensions in mm; 1 mm = 0.039 in.)

Test setup

The experimental setup is shown in Fig. 5. The test beam was loaded at four points on the 10,000 kN (2248 kip) testing machine. The strains of GFRP and SS bars in the middle of the span were measured through 3 mm (0.12 in.) long strain gauges. An 80 mm (3.15 in.) long strain gauge was pasted in the midspan of the beam on the compression side to measure the compressive strain of the concrete. First, the flexural region of the beam was sprayed with white paint. After the paint dried, it was uniformly sprayed with black paint, creating a visible spot. A camera was positioned in front of the beam to record crack changes. The strain gauge acquisition frequency was set at 50 Hz, and the camera automatically captured a photo every 10 seconds. This experiment was loaded according to GB/T 50152-12 (2012). The loading was carried out in a displacement control mode, starting with a loading speed of 0.2 mm/min (0.0079 in./min). The development of cracks in the beam was observed simultaneously. When the first crack appeared, the loading speed was increased to 0.4 mm/min (0.0157 in./min). The beam was unloaded upon reaching the ultimate flexural load-carrying capacity. Once the load value reached 0, the beam was reloaded at a speed of 0.4 mm/min (0.0157 in./min) until failure occurred.

EXPERIMENTAL RESULTS AND DISCUSSION

Failure modes

The failure modes of beams in the experiment are very similar. Specifically, when the beam was loaded to a certain extent, vertical cracks at the midspan position of the beam appeared first and developed rapidly in later stages. As the applied load continued to increase, the number of vertical cracks in the beam increased, and their widths gradually enlarged. Additionally, as the load approached the ultimate load-carrying capacity, slight transverse cracks gradually appeared along the length direction of the concrete beams in the compression zone of the pure flexural region of the beams, indicating that the compression zone of the concrete had entered a plastic state. When the load reached the ultimate load-carrying capacity of the beam, a continuous transverse crack occurred in the compression concrete and the crack width of the transverse crack further increased, as shown in Fig. 6. Finally, the specimen failed by the concrete crushing failure in the compression zone. After the experiment, strain gauges on the SS bars indicated that in the tensile zone, they yielded at the point of failure. Simultaneously, strain gauges on the GFRP bars showed that the strain values did not exceed 13,000 εμ, indicating that GFRP bars in the tensile zone were not ruptured. This indicated that all the hybrid-reinforced beams had reached the expected failure mode—that is, when the concrete in the compression zone was crushed, the SS bars in the tensile zone yielded, and the GFRP bars were not broken.

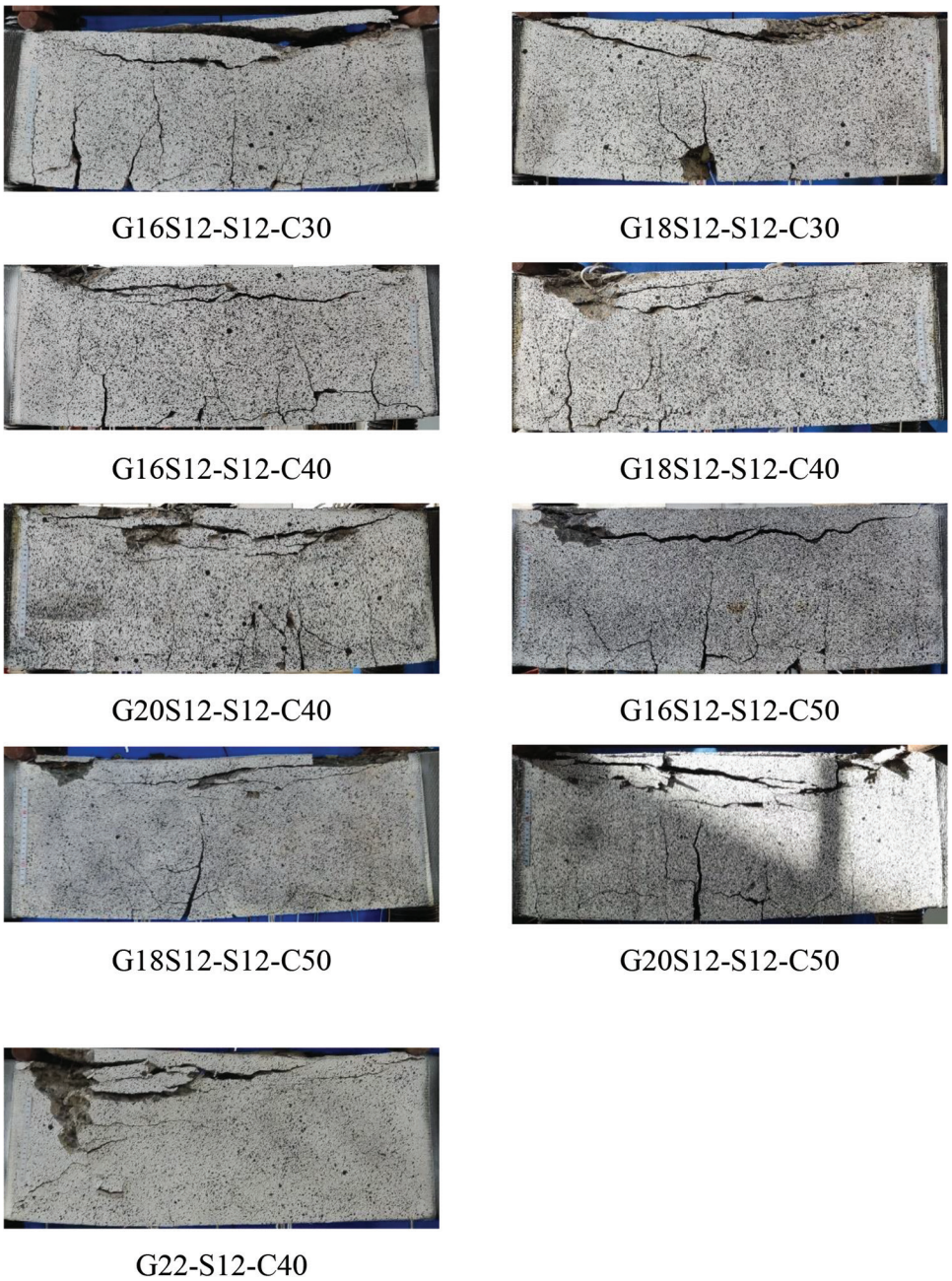

Fig. 6—Damage modes of test beams.

In terms of crack development before beam failure, there is no obvious difference between hybrid-reinforced beams and GFRP-reinforced beams due to the same total stiffness of the reinforcement in the tensile zone before the yield of SS bars.

Cracking moment

Digital image correlation (DIC) was adopted to process the data for reading. When using VIC 2D-7 software for processing, the virtual extensometer was arranged along the position of the principal strain in the tensile zone of the pure bending section of the beam at the crack, and the displacement and strain of the concrete was calculated by the changes between the marked points of the virtual extensometer. Considering the influence of the software noise, by experimental observation, it was found that when the strain at the crack position in the software reached 500 με, the beam was cracked. Five-hundred με was used as the basis for cracking, and the cracking moments of the test are shown in Table 6.

It was observed that the effective reinforcement ratio ρ_2 of beams has little impact on the cracking moment at the same concrete strength. Under the same effective reinforcement ratio ρ_2, the reinforcement type also has little effect on the cracking moment of concrete beams. Moreover, concrete strength has a significant effect on the cracking moment, especially compared to C30 and C40. However, the influence of concrete strength is smaller when it reaches C50.

Ultimate flexural load-carrying capacity

The maximum value of the load-displacement curve in Fig. 7 is the experimental value of the ultimate flexural

Table 6—Experimental results for beams

Beam identifier	ρ_2, %	$M_{cr,exp}$, kN·m (kip·ft)	$M_{u,exp}$, kN·m (kip·ft)	G
G16S12-S12-C30	0.62	10.69 (7.88)	69.51 (51.27)	15.81
G18S12-S12-C30	0.68	7.23 (5.33)	72.30 (53.33)	9.12
G16S12-S12-C40	0.62	9.11 (6.72)	73.92 (54.52)	13.26
G18S12-S12-C40	0.68	9.16 (6.76)	84.70 (62.47)	15.49
G20S12-S12-C40	0.74	8.45 (6.23)	102.45 (75.56)	14.98
G16S12-S12-C50	0.62	10.03 (7.40)	85.77 (63.26)	13.70
G18S12-S12-C50	0.68	11.96 (8.82)	87.73 (64.71)	13.43
G20S12-S12-C50	0.74	9.88 (7.29)	102.93 (75.92)	13.91
G22-S12-C40	0.73	8.20 (6.05)	127.50 (94.04)	15.32

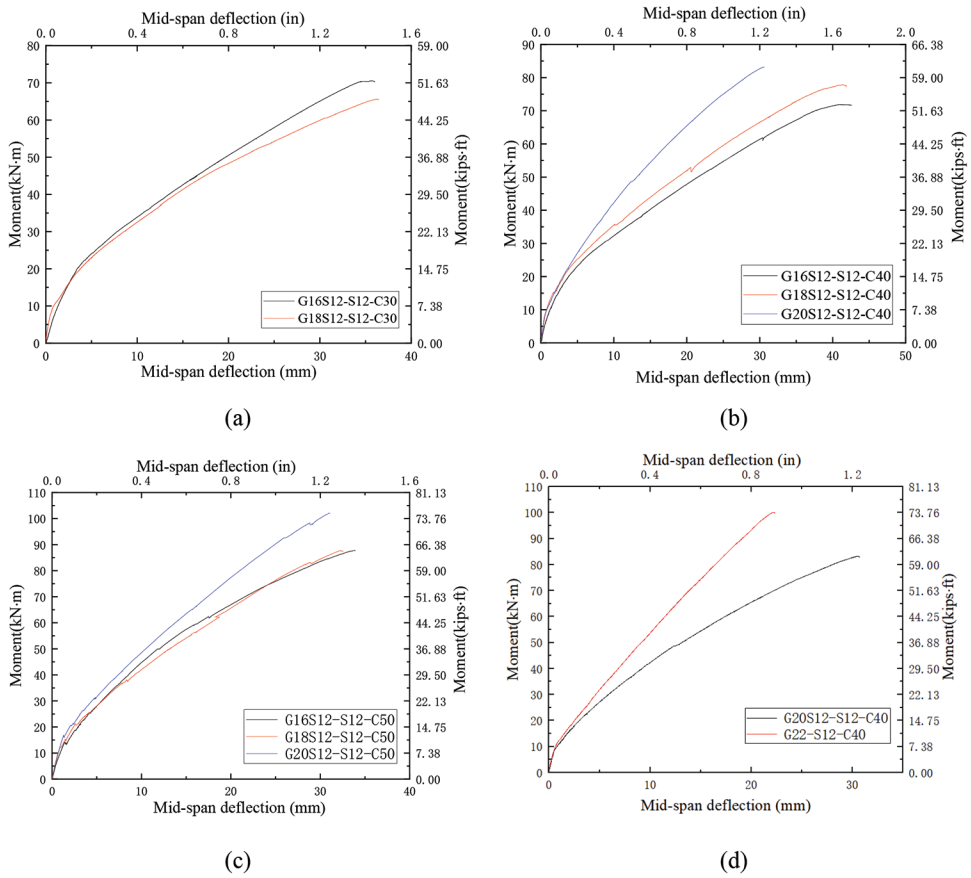

Fig. 7—Moment-deflection curves: (a) G16S12-S12-C30, G18S12-S12-C30; (b) G16S12-S12-C40, G18S12-S12-C40, G20S12-S12-C40; (c) G16S12-S12-C50, G18S12-S12-C50, G20S12-S12-C50; and (d) G20S12-S12-C40, G22-S12-C40.

load-carrying capacity. Figure 8 shows the relationship between the ultimate flexural load-carrying capacity and effective reinforcement ratio ρ_2 of the test beams. From the figure, it can be seen that the ultimate flexural load-carrying capacity of the hybrid-reinforced beams increases with the increase of the effective reinforcement ratio ρ_2 when the concrete strength is the same, and the ultimate flexural load-carrying capacity of the hybrid-reinforced beams increases by upgrading the strength grade of the concrete when the effective reinforcement ratio ρ_2 is the same.

As shown in Table 6, for the same effective reinforcement ratio ρ_2 and concrete strength grade, the ultimate flexural load-carrying capacity of G22-S12-C40 is larger than that of G20S12-S12-C40, which indicates that the use of hybrid reinforcement will reduce the ultimate flexural load-carrying capacity of pure GFRP bar's reinforced beams. This is because after the SS bars in the tensile zone of the hybrid-reinforced beam yield, the total stiffness of the reinforcement in the tensile zone decreases, resulting in the weakening of the load-carrying capacity of the hybrid-reinforced beam while the total stiffness of the reinforcement in the tensile zone of the GFRP bar's reinforced beam will remain unchanged due to the linear elasticity of the GFRP bars, resulting in the load-carrying capacity of the GFRP bar-reinforced beam being greater than that of the hybrid-reinforced beam.

Midspan deflections

From the load-displacement curves shown in Fig. 7, the slopes of each curve can be obtained in the initial elastic segment, which are represented by G in Table 6. It is apparent that the initial segments of the load-displacement curves for hybrid-reinforced beams are similar. This suggests that changing the effective reinforcement ratios ρ_2 in the tensile zone of hybrid-reinforced beams has little impact on the initial section stiffness of the beam, which aligns with the theoretically-calculated results. After further loading, when the bending moment is approximately 10 kN·m, the slope of all curves decreases compared with the initial segment, indicating that the beams begin to crack, resulting in the reduction of section stiffness. By comparison, it is evident that after the beam cracks, under the same concrete strength and the same bending moment, the higher the effective reinforcement ratio ρ_2 of the hybrid reinforcement, the lower the midspan deflection of the beam.

At the same concrete strength and the same effective reinforcement ratios ρ_2, as shown in Fig. 7(d), it can be observed that the early-stage curves of the two beams still overlap significantly. With further loading, under the same load, the deflection of the hybrid-reinforced beam is larger. This is because if the effective reinforcement ratios ρ_2 are equal, the total stiffness of the reinforcement is equal before SS bars yield in the tensile zone. Under the same bending moment, the deflection of the hybrid-reinforced beam in the range of the serviceability stage is similar to that of the GFRP bar-reinforced beam and will not be reduced. On the contrary, in the hybrid-reinforced beam, after the SS bars in the tensile zone yield, the deflection of the hybrid-reinforced beam is larger than that of the GFRP bar's reinforced beam under the same bending moment because the total stiffness of the reinforcement in the tensile zone is lower than that of the GFRP bar's reinforced beam. Therefore, the comparison of midspan deflection of the GFRP bars and hybrid-reinforced beams are not only dependent on the reinforcement type, but also depend on the total stiffness of reinforcement before SS bars yield in the tensile zone and whether the SS bars are yielding in the tensile zone.

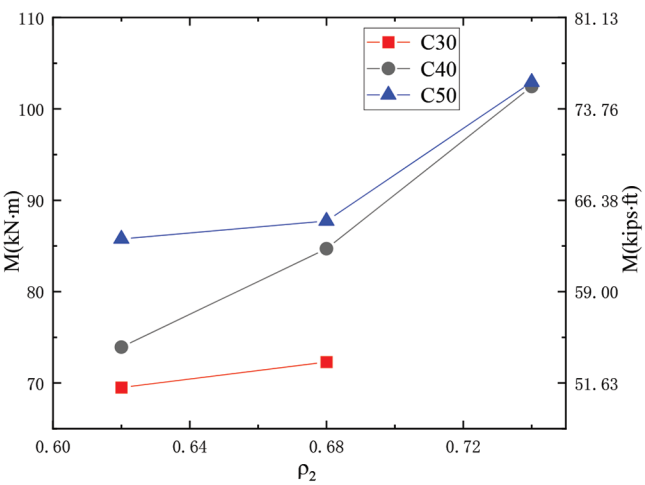

Fig. 8—Effect of reinforcement ratio on ultimate flexural load-carrying capacity.

THEORETICAL ANALYSIS

Cracking moment

In this paper, the equations specified in ACI 318-19 (ACI Committee 318 2019) are used for the theoretical calculations of cracking moment

$$M_{cr,c} = \frac{f_r I_g}{y_t} \tag{5}$$

$$I_g = bh^3/12 \tag{6}$$

From the data in Table 7, the mean value of $M_{cr,c}/M_{cr,exp}$ is 1.20, with a standard deviation of 0.14, which indicates that the theoretical calculations yielded slightly larger results compared to the experimental values. In terms of the neutral axis height, it can be considered that the neutral axis height of the hybrid-reinforced beam is approximately half of the height of the beam section.

Ultimate flexural load-carrying capacity

Like the design of conventional steel-reinforced concrete beams, the design philosophy for FRP-reinforced RC beams is based on force equilibrium and strain compatibility. Unlike steel-reinforced concrete beams, the design for FRP beams takes into consideration that FRP bars do not undergo a yielding stage.

When the reinforcement ratio in the compression zone is low, the steel bars in the compression zone are generally treated as erection steel bars and are not included in the stress

Table 7—Cracking moment results

Beam identifier	$M_{cr,c}$, kN·m (kip·ft)	$M_{cr,exp}$, kN·m (kip·ft)	$M_{cr,c}/M_{cr,exp}$
G16S12-S12-C30	9.71 (7.16)	10.69 (7.88)	0.91
G18S12-S12-C30	9.72 (7.17)	7.23 (5.33)	1.35
G16S12-S12-C40	11.28 (8.32)	9.11 (6.72)	1.24
G18S12-S12-C40	11.29 (8.32)	9.16 (6.76)	1.23
G20S12-S12-C40	11.29 (8.33)	8.45 (6.23)	1.34
G16S12-S12-C50	12.30 (9.07)	10.03 (7.40)	1.23
G18S12-S12-C50	12.31 (9.08)	11.96 (8.82)	1.03
G20S12-S12-C50	12.32 (9.08)	9.88 (7.29)	1.25
G22-S12-C40	10.90 (8.04)	8.20 (6.05)	1.33

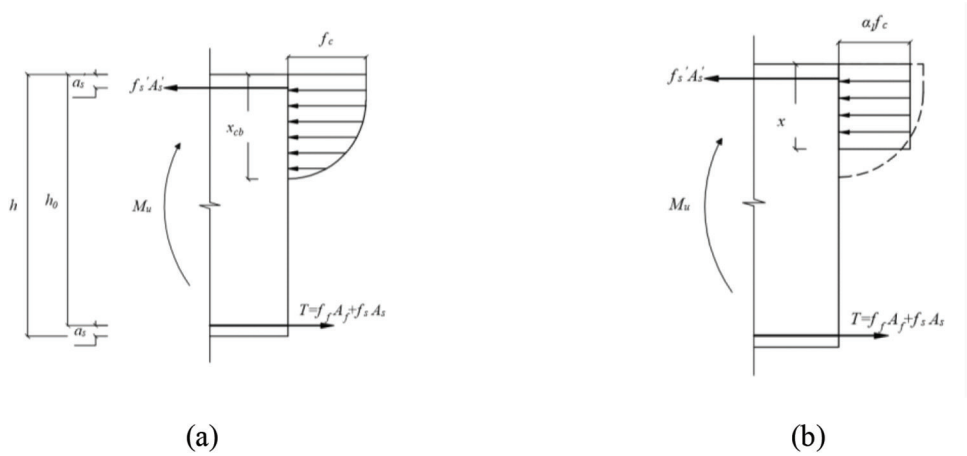

Fig. 9—Equivalent rectangular stress diagrams.

Table 8—Ultimate flexural load-carrying capacity results

Beam identifier	M_1, kN·m (kip·ft)	M_2, kN·m (kip·ft)	M_3, kN·m (kip·ft)	$M_{u,exp}$, kN·m (kip·ft)	$M_1/M_{u,exp}$	$M_2/M_{u,exp}$	$M_3/M_{u,exp}$
G16S12-S12-C30	56.51 (41.67)	56.53 (41.69)	62.21 (45.87)	69.51 (51.27)	0.81	0.81	0.89
G18S12-S12-C30	61.97 (45.70)	62.00 (45.72)	69.02 (50.90)	72.30 (53.33)	0.86	0.86	0.95
G16S12-S12-C40	66.80 (49.26)	66.82 (49.28)	71.17 (52.48)	73.92 (54.52)	0.90	0.90	0.96
G18S12-S12-C40	73.72 (54.36)	73.74 (54.38)	79.43 (58.58)	84.70 (62.47)	0.87	0.87	0.94
G20S12-S12-C40	79.12 (58.35)	79.15 (58.37)	85.83 (63.30)	102.45 (75.56)	0.77	0.77	0.84
G16S12-S12-C50	73.63 (54.30)	73.65 (54.31)	77.22 (56.95)	85.77 (63.26)	0.86	0.86	0.90
G18S12-S12-C50	81.52 (60.12)	81.55 (60.14)	86.46 (63.76)	87.73 (64.71)	0.93	0.93	0.99
G20S12-S12-C50	87.71 (64.68)	87.74 (64.71)	93.65 (69.06)	102.93 (75.92)	0.85	0.85	0.91
G22-S12-C40	100.79 (74.33)	100.84 (74.36)	109.31 (86.61)	127.50 (94.04)	0.79	0.79	0.86

analysis. The beam using this analytical model is called a single-reinforced beam.

Based on this idea, Qu et al. (2009) proposed that the calculations in Eq. (3) and (4) are applicable to a single-reinforced beam with hybrid reinforcement, following the guidelines of ACI 440.1R-06. The calculations in Eq. (3) and (4) introduce the steel bars in the tension zone into the stress analysis, assuming that the steel bars in tension reach the yield state, making the calculation equations in ACI 440.1R-06 applicable to the full FRP reinforcement in the tension zone become the calculation equations applicable to the hybrid reinforcement in the tension zone.

Zhang et al. (2011) also proposed equations for calculating the ultimate flexural load-carrying capacity of a single-reinforced beam with hybrid reinforcement, based on GB 50010-2010 (2015). For comparability, the assumptions based on GB 50010-2010 in the calculation equations have been replaced with the assumptions based on ACI 440.1R-15—that is, ε_{cu} = 0.0033 has been changed to ε_{cu} = 0.003, α_1 = 1.0 has been changed to α_1 = 0.85, and β_1 = 0.8 has been changed to β_1 = max(0.85 – 0.005 [27.6 – f_c'/6.9]; 0.85). The modified Eq. (7) and (8) are as follows

$$\xi = \frac{A - B + \sqrt{(A-B)^2 + 3.4\beta_1 B}}{1.7} \tag{7}$$

$$M_2 = \alpha_1 f_c' b h_0^2 \xi\,(1 - 0.5) \tag{8}$$

where $A = f_y\rho_s/f_c'$; and $B = \varepsilon_{cu}E_f\rho_f/f_c'$.

The experimental beams in this paper have two SS bars in the compression zone. To better conform the true stress model of the beams and obtain the calculation equations of the double-reinforced beams, the SS bars in the compression zone will no longer be considered as erection bars in the ultimate flexural load-carrying capacity calculation as follows. Figure 9 exhibits the stress state at the beam section. Based on the assumptions of a plane section and the equations of force equilibrium, the following relationship can be derived in Eq. (9) to (11)

$$\alpha_1\beta_1 f_c' bx + E_s'A_s'\varepsilon_s' = f_yA_s + E_fA_f\varepsilon_f \tag{9}$$

$$\frac{x_{cb}}{h_0} = \frac{\varepsilon_{cu}}{\varepsilon_{cu} + \varepsilon_f} \tag{10}$$

$$\frac{\varepsilon_s'}{x_{cb} - a_s'} = \frac{\varepsilon_{cu}}{x_{cb}} \tag{11}$$

Therefore, the modified Eq. (12) and (13) for calculating the ultimate flexural load-carrying capacity of double-reinforced beams with hybrid reinforcement are obtained based on the calculation equations proposed by Zhang et al. (2011). The assumptions based on GB 50010-2010 have also been replaced with the assumptions based on ACI 440.1R-15

$$\xi = \frac{A - B - C + \sqrt{(A-B-C)^2 + 3.4\beta_1(B + c'C)}}{1.7} \tag{12}$$

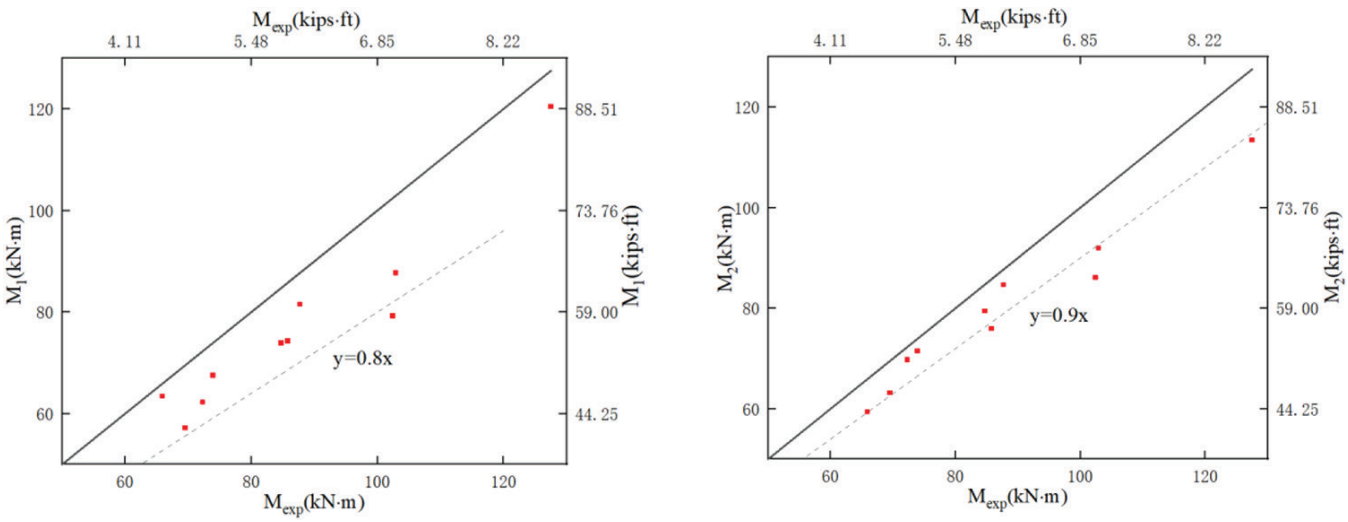

Fig. 10—Ratio of experimental to theoretical load-carrying capacity for tested beams: (a) ratio of M_1 *to* M_{exp} *and* M_2 *to* M_{exp}*; and (b) ratio of* M_3 *to* M_{exp}.

$$M_3 = \alpha_1 f_c' b h_0^2 \xi(1 - 0.5\xi) + E_s'\varepsilon_s' A_s'(h_0 - a_s') \tag{13}$$

where $A = f_y\rho_s/f_c'$; $B = \varepsilon_{cu}E_f\rho_f/f_c'$; $C = \varepsilon_{cu}E_s'\rho_s'/f_c'$; and $c' = a_s'/h_0$. When ε_s' reaches ε_y ($\varepsilon_y = 0.0014$), $E_s'\varepsilon_s'$ takes the value of f_y ($f_y = 270$ MPa [39 ksi]).

The theoretical ultimate flexural load-carrying capacity M_1, M_2, and M_3 of the beams can be obtained according to the previous three calculation methods, and the theoretical values and experimental results are shown in Table 8 and Fig. 10.

From the data in Table 8, the mean value of $M_1/M_{u,exp}$ is 0.85 with a standard deviation of 0.05; the mean value of $M_2/M_{u,exp}$ is 0.85 with a standard deviation of 0.05; and the mean value of $M_3/M_{u,exp}$ is 0.92 with a standard deviation of 0.05. Comparing the three calculation methods, it is evident that the results of M_1 and M_2 are the same, the results of M_1 and M_2 are smaller than the results of M_3, the results of M_1, M_2, and M_3 are smaller than the experimental values, and the results of M_3 are closer to the experimental values. This indicates that the essence of Eq. (3) and (4) and Eq. (7) and (8) is the same, only the expression form is different, and Eq. (3) and (4) and Eq. (7) and (8) tend to be conservative in estimating the ultimate flexural load-carrying capacity of the beam. The results from M_3 are closer to the experimental values, indicating that Eq. (12) and (13) for the double-reinforced beam can better estimate the ultimate flexural load-carrying capacity of the beam. However, due to the lack of a clear yield platform for SS bars, their strength will continue to increase after reaching the nominal yield strength, so the results calculated by Eq. (12) and (13) are also conservative.

Midspan deflections

Assuming a uniform inertia of moment along the span of the beam and employing linear elastic analysis, the equation for calculating the deflection at the midspan of a four-point bending beam can be obtained

$$\Delta_c = \frac{M_a}{24E_cI_e}(3L_0^2 - 4a^2) \tag{14}$$

For the calculation of I_e, ACI 440.1R-15 adopts the effective moment of inertia proposed by Bischoff and Gross (2011), which is recognized as suitable for steel bar-reinforced beams and FRP bar-reinforced beams. The calculations are shown in Eq. (15). The value of γ is determined by the load and boundary conditions

$$I_e = \frac{I_{cr}}{1 - \gamma\left(\frac{M_{cr,\exp}}{M_a}\right)^2\left[1 - \frac{I_{cr}}{I_g}\right]} \le I_g \tag{15}$$

$$\gamma = 1.7 - 0.7\frac{M_{cr,exp}}{M_a} \tag{16}$$

assuming that the tensile zone of the concrete in the cracked section is entirely ineffective and only the longitudinal bar is carrying the tensile force. To calculate the cracking moment of inertia I_{cr}, the area of GFRP bars and SS bars can be converted into the equivalent concrete area at the same height. For example, the area of the compressive zone's SS reinforcement can be converted into n_sA_s'. By assuming homogeneous material properties, the value of I_{cr} can be determined

$$I_{cr} = \frac{1}{3}bx_{cr}^3 + (n_sA_s + n_fA_f)(h_0 - x_{cr})^2 + (n_s - 1)A_s'(x_{cr} - a_s')^2 \tag{17}$$

where x_{cr} is the height of the neutralization axis in the compression zone of the section at the time of cracking, calculated from the plane section assumption

$$0.5bx_{cr}^2 + n_sA_s'(x_{cr} - a_s') = (n_sA_s + n_fA_f)(h_0 - x_{cr}) \tag{18}$$

Table 9—Midspan deflection results

Beam identifier	Δ_c, mm (in.)		Δ_{exp}, mm (in.)		Δ_c/Δ_{exp}	
	$0.3M_u$	$0.67M_u$	$0.3M_u$	$0.67M_u$	$0.3M_u$	$0.67M_u$
G16S12-S12-C30	2.75 (0.11)	7.97 (0.31)	3.34 (0.13)	15.71 (0.62)	0.82	0.51
G18S12-S12-C30	3.23 (0.13)	8.02 (0.32)	4.44 (0.17)	20.08 (0.79)	0.73	0.40
G16S12-S12-C40	3.23 (0.13)	8.55 (0.34)	4.63 (0.18)	21.17 (0.83)	0.70	0.40
G18S12-S12-C40	3.63 (0.14)	9.21 (0.36)	5.12 (0.20)	23.21 (0.91)	0.71	0.40
G20S12-S12-C40	4.40 (0.17)	10.59 (0.42)	6.12 (0.24)	21.59 (0.85)	0.72	0.49
G16S12-S12-C50	3.79 (0.15)	9.86 (0.39)	4.38 (0.17)	14.99 (0.59)	0.86	0.66
G18S12-S12-C50	3.38 (0.13)	9.27 (0.36)	4.46 (0.18)	17.18 (0.68)	0.76	0.54
G20S12-S12-C50	4.24 (0.17)	10.46 (0.41)	4.74 (0.19)	17.02 (0.67)	0.89	0.61
G22-S12-C40	5.76 (0.23)	13.45 (0.53)	6.47 (0.25)	17.84 (0.70)	0.89	0.75

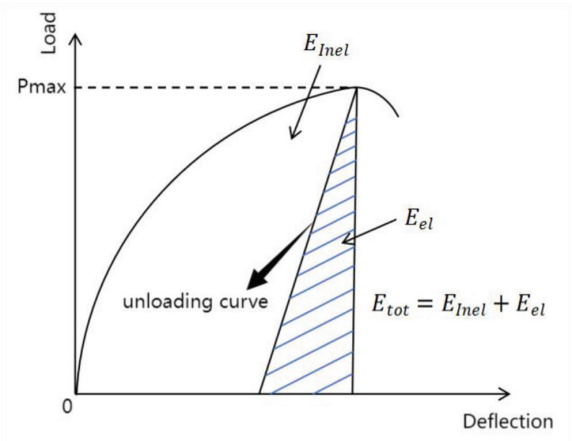

Fig. 11—Definition of ductility factor based on energy method.

assume $m = \dfrac{n_s A_s + n_f A_f}{b h_0}, n = \dfrac{(n_s - 1) A_s'}{b h_0}, p = \dfrac{a_s'}{h_0},$

$$q = \sqrt{(n+m)^2 + 2(np+m)} - (m+n)$$

then I_{cr} can be expressed as

$$I_{cr} = \frac{1}{3} b\,(q h_0)^3 + (n_s A_s + n_f A_f)(1-q)^2 h0^2 + n_s A_s'\,(q-p)^2 h_0^2 \tag{19}$$

Studies indicate that $0.3M_u$ is in the range of serviceability stage. When the load reaches $0.67M_u$, the crack distribution in the beam stabilizes and no new cracks appeared. In this study, $0.3M_u$ and $0.67M_u$ are selected as the two load levels for stiffness and deflection calculation according to the previous equations. The theoretical and experimental values of the midspan deflection for all beam specimens are compared in Table 9.

When the load level is $0.3M_u$, the average value of the ratio of Δ_c/Δ_{exp} is 0.79, with a standard deviation of 0.07. At a load level of $0.67M_u$, the average value of the ratio of Δ_c/Δ_{exp} is 0.56, with a standard deviation of 0.15. The results indicate that Eq. (15) and (16) in ACI 440.1R-15 are more suitable to calculate the midspan deflection under short-term loading at a load level of $0.3M_u$. The overall calculation results in the range of serviceability stages are relatively small, indicating that the further consideration should be given to stiffness reduction in the case of hybrid reinforcement.

Table 10—Ductility results

Beam label	μ_E
G16S12-S12-C30	1.71
G18S12-S12-C30	1.58
G16S12-S12-C40	1.68
G18S12-S12-C40	1.43
G20S12-S12-C40	1.39
G16S12-S12-C50	1.44
G18S12-S12-C50	1.38
G20S12-S12-C50	1.18
G22-S12-C40	1.18

Ductility

For traditional reinforced concrete structures, the ductility coefficient is typically defined as the ratio of ultimate deformation at the ultimate limit state for bearing capacity to the first yield point of the reinforcement. Due to the linear constitutive curve of FRP bars, there is no distinct yield point when FRP bars rupture. Thus, the traditional ductility coefficient used for the conventional reinforced concrete structures with steel bar reinforcement cannot be directly applied to FRP bar's reinforced concrete beams and hybrid-reinforced beams.

Naaman and Jeong (1995) proposed a ductility calculation based on the energy perspective, which divides the total absorbed energy of the structure into elastic and plastic energy. It reported that the ductility coefficient can be expressed as the ratio of the total dissipated energy (E_{tot}) to the elastic energy (E_{el}), as shown in Eq. (20)

$$\mu_E = 1/2\,(E_{tot}/E_{el} + 1) \tag{20}$$

where E_{tot} is the total energy, which is the area under the load-deflection curve up to the maximum load; and E_{el} is the elastic area, which is the area under the unloading curve from the maximum load. The schematic diagram for definitions of E_{tot} and E_{el} is shown in Fig. 11.

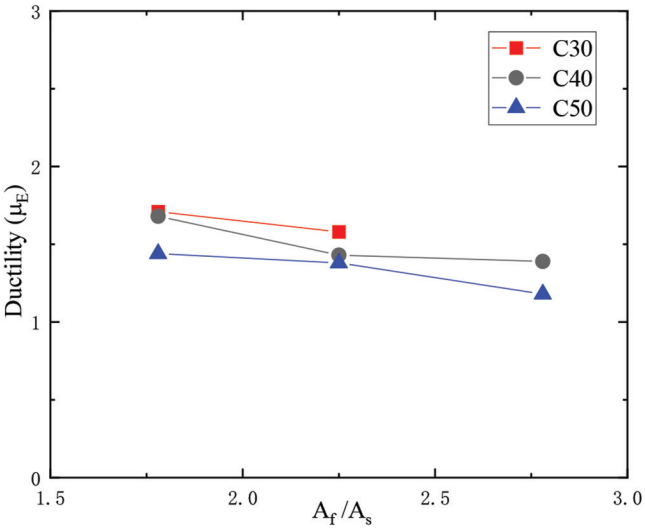

Fig. 12—Comparison of ductility of hybrid reinforced beams.

The calculation results of the ductility coefficient are listed in Table 10, as shown in Fig. 12. Under the same concrete strength, the ductility coefficient decreases with the increase in effective reinforcement ratio ρ_2. This indicates a reduction in the beams' ductility. As the area of GFRP bars in the hybrid-reinforced beams increases, it enhances the ultimate flexural load-carrying capacity but significantly decreases the ductility of the beams, making them prone to brittle failure. Additionally, it can be observed that higher concrete strength results in a smaller ductility coefficient for the beams. This indicates that high-strength concrete is also prone to causing brittle failure in beams. In addition, the data presented in Table 10 shows that for the same effective reinforcement ratio ρ_2, the value of the ductility coefficient for the hybrid reinforced beam G20S12-S12-C40 is 18% higher than that of the GFRP bar's reinforced beam G22-S12-C40, which shows that hybrid reinforcement can improve the ductility of the beams.

CONCLUSIONS

This paper examines the effect of parameters, including concrete strength, effective reinforcement ratio ρ_2, and reinforcement type in tensile zone on the mechanical properties of fiber-reinforced polymer-stainless steel (FRP-SS) bar's hybrid-reinforced seawater sea-sand concrete (SSC) beams. Through four-point bending tests and the use of digital image correlation (DIC) technology, the cracking moment, ultimate flexural load-carrying capacity, midspan deflection, maximum crack width, and ductility of the beams were investigated. The following conclusions can be drawn:

1. The hybrid reinforcement test beams in the experiment reached ultimate compressive strain in the concrete in the compression zone at failure, the SS bars in the tension zone yielded, and the glass fiber-reinforced polymer (GFRP) bars were not broken.

2. The ultimate flexural load-carrying capacity of the hybrid-reinforced test beams is positively correlated with the concrete strength; when the concrete strength is the same, the higher the effective reinforcement ratio ρ_2, the higher the ultimate flexural load-carrying capacity of the hybrid reinforced beams. When the effective reinforcement ratio ρ_2 and concrete strength are the same, the ultimate flexural load-carrying capacity of hybrid-reinforced beams is lower than that of GFRP bar-reinforced beams.

3. The comparison of midspan deflection of the GFRP bars and hybrid-reinforced beams not only depends on the reinforcement type, but also on the total stiffness of reinforcement before SS bars yield in the tensile zone, and whether the SS bars are yielding in the tensile zone.

4. With the increase in the effective reinforcement ratio ρ_2, the ultimate flexural load-carrying capacity of hybrid-reinforced beams increases, but the ductility decreases. Meanwhile, hybrid-reinforced beams exhibit higher ductility compared with GFRP bar-reinforced beams under the same effective reinforcement ratio ρ_2. This suggests that hybrid reinforcement can address the poor ductility issue observed in FRP-reinforced beams.

5. The theoretical values of ultimate flexural load-carrying capacity calculated using the methods for single reinforced beams proposed by Qu et al. (2009) and Zhang et al. (2011) are smaller than the experimental values. The results calculated from Eq. (14) and (15) presented in this study are closer to the experimental results.

AUTHOR BIOS

Qi Cao *is an Associate Professor at the State Key Laboratory of Coastal and Offshore Engineering, School of Infrastructure Engineering at Dalian University of Technology, Dalian, China. His research interests include fiber-reinforced polymer (FRP) reinforced concrete structures and composite materials and structures.*

Teng Zhang *is a Graduate Student at the State Key Laboratory of Coastal and Offshore Engineering, School of Infrastructure Engineering at Dalian University of Technology. His research interests include FRP bar-reinforced concrete structures and hybrid reinforced concrete structures.*

Shu Cao *is a Graduate Student at the State Key Laboratory of Coastal and Offshore Engineering, School of Infrastructure Engineering at Dalian University of Technology. His research interests include FRP bar-reinforced concrete structures and hybrid reinforcement in concrete structures.*

Zhimin Wu *is a Professor at the School of Civil Engineering and Architecture at Zhejiang University of Science and Technology, Hangzhou, China. His research interests include the fracture mechanics of concrete, FRP, and rehabilitated concrete structures.*

Jinjin Xu *is a Lecturer at the School of Civil Engineering, Tianjin Ren'ai College, Tianjin, China. Her research interests include hybrid FRP and steel bar-reinforced concrete structures.*

ACKNOWLEDGMENTS

The financial support provided by the National Natural Science Foundation of China (Grant No.52271264) is greatly appreciated.

DATA AVAILABILITY STATEMENT

Some or all data, models, or standards that support the findings of this study are available from the corresponding author upon reasonable request.

NOTATION

A_f = area of FRP bars in tensile zone of concrete cross section
A_s = area of SS bars in tensile zone of concrete cross section
A_s' = area of SS bars in compression zone of concrete cross section
a = distance from loading point to support
a_s = distance from centroid of tensile steel bar section to edge of tensile zone of beam

a_s' = distance from centroid of compression steel bar section to edge of compression zone of beam
b = width of beam's cross section
E_c = elastic modulus of concrete
E_{el} = elastic area, which is area under unloading curve from maximum load
E_f = elastic modulus of FRP bars in tensile zone
E_{Inel} = plastic energy
E_s = elastic modulus of SS bars in tensile zone
E_s' = elastic modulus of SS bars in compression zone; $E_s' = E_s$
E_{tot} = total energy, which is area under load-deflection curve up to maximum load
f_c = prism compressive strength of concrete
f_c' = cylinder compressive strength of concrete; according to GB/T 50081-2019, $f_c' = 0.79 \times f_{cu}$
f_{cu} = cubic compressive strength of concrete
f_f = stress in FRP bars at time of beam reaching ultimate flexural load-carrying capacity
f_{fd} = nominal yield strength of FRP reinforcement ($0.75 \times f_{fu}$ according to ACI 440.1R-15)
f_{fu} = ultimate tensile strength of FRP bar
f_r = modulus of rupture of concrete, $f_r = 0.62f_c'$ MPa ($f_r = 7.5f_c'$ psi)
f_t = splitting tensile strength of concrete
f_y = nominal yield strength of SS reinforcement
G = slope of each curve in initial elastic segment in Fig. 7
h = height of beam's cross section
h_0 = effective height of cross section, distance from centroid of tensile steel bar section to edge of compression zone of beam
I_{cr} = cracking moment of inertia
I_e = effective moment of inertia of section after cracking
I_g = moment of inertia of gross concrete section about centroidal axis, neglecting reinforcement
L_0 = length of beam span
M = calculated value of ultimate flexural load-carrying capacity of beams during specimen design phase
M_a = moment of midspan normal section of beam at any time during loading process
$M_{cr,c}$ = calculated value of cracking moment
$M_{cr,exp}$ = experimental value of cracking moment
$M_{u,exp}$ = experimental value of ultimate flexural load-carrying capacity
M_1 = calculated value of ultimate flexural load-carrying capacity of beams using Eq. (3) and (4)
M_2 = calculated value of ultimate flexural load-carrying capacity of beams using Eq. (7) and (8)
M_3 = calculated value of ultimate flexural load-carrying capacity of beams using Eq. (12) and (13)
n_f = ratio of elastic modulus of FRP bar to elastic modulus of concrete
n_s = ratio of elastic modulus of SS bar to elastic modulus of concrete
P = load applied to beam
x = height of rectangular stress diagram in compression zone
x_{cb} = height of compressive zone of concrete cross section
x_{cr} = height of neutralization axis in compression zone of section at time of cracking
y_t = distance between extreme fiber in tension and centroid axis of cross section
α_1 = ratio of stress value of rectangular stress diagram of concrete in compression zone to design value of axial compressive strength of concrete; according to ACI 440.1R-15, $\alpha_1 = 0.85$; according to GB 50010-2010, $\alpha_1 = 1.0$
β_1 = ratio of height of rectangular stress diagram in compression zone to height of neutral axis; according to ACI 440.1R-15 $\beta_1 = \max[0.85 - 0.005(27.6 - f_c'/6.9); 0.85]$; according to GB 50010-2010, $\beta_1 = 0.8$
Δ_c = calculated value of midspan deflection corresponding to M_a
Δ_{exp} = experimental value of midspan deflection corresponding to M_a
ε_{cu}' = ultimate compressive strain of concrete according to GB 50010-2010 and it assumes that $\varepsilon_{cu}' = 0.0033$
ε_{cu} = ultimate compressive strain of concrete according to ACI 440.1R-15 and it assumes that $\varepsilon_{cu} = 0.003$
ε_f = tensile strains of FRP bars in tension zone
ε_{fd} = design tensile strain of FRP bars ($\varepsilon_{fd = 0.01}$)
ε_s' = strain of SS bars in compression zone
ε_y = yield strain of SS bars; ε_y is taken as ratio of nominal yield strength and elastic modulus of SS bars ($\varepsilon_y = 0.0014$)
ε_0 = compressive strain of concrete when it just reaches its compressive strength ($\varepsilon_0 = 0.002$)
ξ = relative depth of compression zone; ratio of height of rectangular stress diagram in compression zone x to effective height of cross section h_0
ρ_f = FRP reinforcement ratio in tensile zone
ρ_s = SS reinforcement ratio in tensile zone
ρ_s' = SS reinforcement ratio in the compression zone
ρ_1 = reinforcement ratio of all longitudinal bars in tensile zone obtained by equating reinforcement ratio of FRP bars to SS bars in tensile zone according to strength principle $\rho_1 = \rho_s + f_{fd}/f_y\rho_f$
ρ_2 = reinforcement ratio of all longitudinal bars in tensile zone obtained by equating reinforcement ratio of FRP bars to SS bars in tensile zone according to stiffness principle $\rho_2 = \rho_s + E_s/E_f\rho_f$

REFERENCES

ACI Committee 318, 2014, "Building Code Requirements for Structural Concrete (ACI 318-14) and Commentary (ACI 318R-14)," American Concrete Institute, Farmington Hills, MI, 520 pp.

ACI Committee 318, 2019, "Building Code Requirements for Structural Concrete (ACI 318-19) and Commentary (ACI 318R-19) (Reapproved 2022)," American Concrete Institute, Farmington Hills, MI, 624 pp.

ACI Committee 440, 2006, "Guide for the Design and Construction of Structural Concrete Reinforced with Fiber-Reinforced Polymer (FRP) Bars (ACI 440.1R-06)," American Concrete Institute, Farmington Hills, MI, 44 pp.

ACI Committee 440, 2015, "Guide for the Design and Construction of Structural Concrete Reinforced with FRP Bars (ACI 440.1R-15)," American Concrete Institute, Farmington Hills, MI, 88 pp.

Adam, M.; Said, M.; Mahmoud, A. A.; and Shanour, A. S., 2015, "Analytical and Experimental Flexural Behavior of Concrete Beams Reinforced with Glass Fiber-Reinforced Polymer Bars," *Construction and Building Materials*, V. 84, pp. 354-366. doi: 10.1016/j.conbuildmat.2015.03.057

Aiello, M. A., and Ombres, L., 2002, "Structural Performances of Concrete Beams with Hybrid (Fiber-Reinforced Polymer-Steel) Reinforcements," *Journal of Composites for Construction*, ASCE, V. 6, No. 2, pp. 133-140. doi: 10.1061/(ASCE)1090-0268(2002)6:2(133)

Alsayed, S. H.; Al-Salloum, Y.; and Almusallam, T., 2000, "Performance of Glass Fiber Reinforced Plastic Bars as a Reinforcing Material for Concrete Structures," *Composites Part B: Engineering*, V. 31, No. 6-7, pp. 555-567. doi: 10.1016/S1359-8368(99)00049-9

ASTM D7205/D7205M, 2021, "Standard Test Method for Tensile Properties of Fiber Reinforced Polymer Matrix Composite Bars," ASTM International, West Conshohocken, PA, 13 pp.

Bischoff, P. H., and Gross, S. P., 2011, "Equivalent Moment of Inertia Based on Integration of Curvature," *Journal of Composites for Construction*, V. 15, No. 3, pp. 263-273. doi: 10.1061/(ASCE)CC.1943-5614.0000164

CAN/CSA-S6-19, 2019, "Canadian Highway Bridge Design Code," CSA Group, Toronto, ON, Canada, 1093 pp.

Chen, Z.; Mo, L.; Song, C.; and Zhang, Y., 2021, "Investigation on Compression Properties of Seawater-Sea Sand Concrete," *Advances in Concrete Construction*, V. 12, No. 2, pp. 93-103.

Dhondy, T.; Remennikov, A.; and Sheikh, M. N., 2020a, "Properties and Application of Sea Sand in Sea Sand–Seawater Concrete," *Journal of Materials in Civil Engineering*, ASCE, V. 32, No. 12.

Dhondy, T.; Xiang, Y.; Yu, T.; and Teng, J.-G., 2020b, "Effects of Mixing Water Salinity on the Properties of Concrete," *Advances in Structural Engineering*, V. 24, No. 6, pp. 1150-1160. doi: 10.1177/1369433220965272

Fernando, D.; Teng, J.; Quach, W.; and De Waal, L., 2020, "Full-Range Stress-Strain Model for Stainless Steel Alloys," *Journal of Constructional Steel Research*, V. 173, pp. 106266. doi: 10.1016/j.jcsr.2020.106266

Gagg, C. R., 2014, "Cement and Concrete as an Engineering Material: An Historic Appraisal and Case Study Analysis," *Engineering Failure Analysis*, V. 40, pp. 114-140. doi: 10.1016/j.engfailanal.2014.02.004

GB 175-2023, 2023, "Common Portland Cement," Standardization Administration of the People's Republic of China, Beijing, China. (in Chinese)

GB 50010-2010, 2015, "Code for Design of Concrete Structures," Standardization Administration of the People's Republic of China, Beijing, China. (in Chinese)

GB/T 228.1-2021, 2021, "Metallic Materials–Tensile Testing–Part 1: Method of Test at Room Temperature," Standardization Administration of the People's Republic of China, Beijing, China. (in Chinese)

GB/T 50081-2019, 2019, "Standard for Test Methods of Concrete Physical and Mechanical Properties," Standardization Administration of the People's Republic of China, Beijing, China. (in Chinese)

GB/T 50152-2012, 2012, "Standard for Test Method of Concrete Structures," Standardization Administration of the People's Republic of China, Beijing, China. (in Chinese)

Guo, Q.; Chen, L.; Zhao, H.; Admilson, J.; and Zhang, W., 2018, "The Effect of Mixing and Curing Sea Water on Concrete Strength at Different Ages," *MATEC Web of Conferences*. doi:10.1051/matecconf/201814202004

Hawileh, R. A., 2015, "Finite Element Modeling of Reinforced Concrete Beams with a Hybrid Combination of Steel and Aramid Reinforcement," *Materials & Design*, V. 65, pp. 831-839. doi: 10.1016/j.matdes.2014.10.004

Hussein, A. A.; Huang, H.; Okuno, Y.; and Wu, Z., 2022, "Experimental and Numerical Parametric Study on Flexural Behavior of Concrete Beams Reinforced with Hybrid Combinations of Steel and BFRP Bars," *Composite Structures*, V. 302, pp. 116230. doi: 10.1016/j.compstruct.2022.116230

Lau, D., and Pam, H., 2010, "Experimental Study of Hybrid FRP Reinforced Concrete Beams," *Engineering Structures*, V. 32, No. 12, pp. 3857-3865. doi: 10.1016/j.engstruct.2010.08.028

Naaman, A. E., and Jeong, S., 1995, "Structural Ductility of Concrete Beams Prestressed with FRP Tendons," *Proceedings of 2nd International Symposium, Non-Metallic (FRP) Reinforcement for Concrete Structures*, Ghent, Belgium, pp. 379-386.

Oh, H. S., and Ahn, K. Y., 2008, "Experimental Verification of Reinforced Concrete Beam with FRP Rebar," *Journal of the Korea Institute for Structural Maintenance and Inspection*, V. 12, No. 3, pp. 93-100.

Otsuki, N.; Saito, T.; and Tadokoro, Y., 2012, "Possibility of Sea Water as Mixing Water in Concrete," *Journal of Civil Engineering and Architecture*, V. 6, No. 11, 7 pp.

Qin, R.; Zhou, A.; and Lau, D., 2017, "Effect of Reinforcement Ratio on the Flexural Performance of Hybrid FRP Reinforced Concrete Beams," *Composites Part B: Engineering*, V. 108, pp. 200-209. doi: 10.1016/j.compositesb.2016.09.054

Qu, W.; Zhang, X.; and Huang, H., 2009, "Flexural Behavior of Concrete Beams Reinforced with Hybrid (GFRP and Steel) Bars," *Journal of Composites for Construction*, ASCE, V. 13, No. 5, pp. 350-359. doi: 10.1061/(ASCE)CC.1943-5614.0000035

Rasmussen, K. J. R., 2003, "Full-Range Stress-Strain Curves for Stainless Steel Alloys," *Journal of Constructional Steel Research*, V. 59, No. 1, pp. 47-61. doi: 10.1016/S0143-974X(02)00018-4

Ruan, X. J.; Lu, C. H.; Xu, K.; Xuan, J. Y.; and Ni, M. Z., 2020, "Flexural Behavior and Serviceability of Concrete Beams Hybrid-Reinforced with GFRP Bars and Steel Bars," *Composite Structures*, V. 235, p. 111772. doi: 10.1016/j.compstruct.2019.111772

Su, C.; Wang, X.; Ding, L.; Liu, S.; and Wu, Z., 2023, "Flexural Property and Design Method Evaluation of BFRP and Steel Bars Hybrid Reinforced Concrete Beams," *Structural Concrete*, V. 24, No. 4, pp. 4942-4959. doi: 10.1002/suco.202201140

Tan, H.; Hou, Z.; Li, Y.; and Xu, X., 2022, "A Flexural Ductility Model for UHPC Beams Reinforced with FRP Bars," *Structures*, V. 45, pp. 773-786. doi: 10.1016/j.istruc.2022.09.052

Wang, X.; Liu, S.; Shi, Y.; Wu, Z.; and He, W., 2022, "Integrated High-Performance Concrete Beams Reinforced with Hybrid BFRP and Steel Bars," *Journal of Structural Engineering*, ASCE, V. 148, No. 1, p. 04021235. doi: 10.1061/(ASCE)ST.1943-541X.0003207

Xu, J., and Li, F., 2017, "Analytical Model for Load Dependence of Chloride Penetration into Concrete," *Journal of Materials in Civil Engineering*, ASCE, V. 29, No. 5, p. 04016279. doi: 10.1061/(ASCE)MT.1943-5533.0001823

Xu, J.; Zhu, P.; and Qu, W., 2022, "Numerical and Analytical Study of Concrete Beams Reinforced with Hybrid Fiber-Reinforced Polymer and Steel Bars," *Journal of Composites for Construction*, ASCE, V. 26, No. 5, p. 04022045. doi: 10.1061/(ASCE)CC.1943-5614.0001230

Yinghao, L., and Yong, Y., 2013, "Arrangement of hybrid Rebars on Flexural Behavior of HSC Beams," *Composites. Part B, Engineering*, V. 45, No. 1, pp. 22-31. doi: 10.1016/j.compositesb.2012.08.023

Zhang, J.; Ge, W.; Dai, H.; and Tu, Y., 2011, "Study on the Flexural Capacity of Concrete Beam Hybrid Reinforced with FRP Bars and Steel Bars," *Springer eBooks*, pp. 304-307.

Zhu, H., Ge, Dong; Z. G.; and Wu, G., 2015, "Experimental Study and Theoretical Calculation of Stiffness of FRP Reinforced Concrete Beams," *Tumu Gongcheng Xuebao*, V. 48, No. 11, pp. 44-53. (in Chinese)

ACI STRUCTURAL JOURNAL TECHNICAL PAPER

Title No. 123-S44

Flexural Behavior of Preloaded Reinforced Concrete Beams Strengthened with Prestressed Carbon Textile-Reinforced Concrete Plates

by Shujun Zhou, Yunxing Du, Yanqiu Li, Ziwei Li, and Xionggang Shi

In practical engineering, beams requiring strengthening are usually preloaded, and research on their strengthening techniques directly affects structural safety and cost-effectiveness. This study investigated flexural behavior of preloaded reinforced concrete (RC) beams strengthened with prestressed carbon textile-reinforced concrete (CTRC) plates using four-point bending tests. Parameters included preload levels and whether to unload during strengthening. Results showed that strengthening with prestressed CTRC plates effectively improved the service moment, ultimate bending moment, and crack resistance, and preload level and whether to unload during strengthening had no significant effect on the strengthening effect. All strengthened beams failed by CTRC plate rupture, with post-failure moments reducing to the unstrengthened beam's ultimate moment level. Pre-cracking flexural stiffness decreased with increasing preload, and the stiffness after cracking was independent of the preload and strengthening method. Finally, the ultimate bending moments were evaluated using four current codes, with the Chinese code exhibiting the highest prediction accuracy.

Keywords: flexural behavior; preloaded reinforced concrete (RC) beam; prestressed carbon textile-reinforced concrete (CTRC) plates; strengthening; ultimate bending moment calculation.

INTRODUCTION

In the field of structural engineering, strengthening existing reinforced concrete (RC) beams is a critical technical approach to address increasing service loads or material degradation.[1,2] However, compared to unloaded members, strengthening preloaded RC beams often leads to a significant "strain lag" effect in strengthening materials due to the difficulty in fully recovering the original deformation. Even if strengthening occurs after unloading, this effect is hard to avoid and the unloading process itself is often costly and constructionally complex.[3,4] Strain lag not only reduces the strain development capacity and use efficiency of the strengthening materials, but may also adversely affect the overall load-bearing capacity and ductility of the strengthened structure.[5] Therefore, systematically studying the mechanical behavior of new strengthening materials in preloaded RC beams holds significant theoretical value and practical importance for promoting their engineering application.

This paper focused on the use of prestressed carbon textile-reinforced concrete (CTRC) plates for strengthening preloaded RC beams. Based on improvement over the traditional textile-reinforced concrete (TRC) material system, prestressed CTRC plates offer excellent fire resistance, durability, and good compatibility with concrete substrates.[6,7] More critically, fiber textile was effectively pretensioned during fabrication,[8,9] ensuring smoothness and establishing pre-compressive stresses within the matrix. This approach not only improved the plate's resistance to cracking but also enhanced the performance of the fiber textile. Furthermore, this material could be produced using prefabrication methods, which helped ensure consistent performance and facilitated efficient strengthening operations.

Existing research indicates that the performance of preloaded RC beams after strengthening is essentially the result of the complex interaction between the strengthening material, the existing concrete beam, and their interface. Among these, the mechanical characteristics of the strengthening material and preload level (manifested as damage states such as existing crack width and residual deflection) jointly determine the magnitude and distribution characteristics of the interfacial shear stress. When the interfacial bond performance is good and failure is controlled by the strengthening material, preload level has no impact on the ultimate load-bearing capacity of the strengthened beam.[10,11] When the failure mode is concrete crushing, the ultimate load-bearing capacity of the strengthened beam decreases with an increasing preload.[12,13] However, in practical engineering, due to insufficient interfacial bond or stress concentration, strengthened beams are more prone to non-ideal failure modes such as interfacial debonding or concrete cover separation, which prevents the full use of the strengthening material's strength.[14,15] Notably, as preload level increased, the failure modes of different strengthening systems could undergo transitions: for engineered cementitious composite (ECC)-strengthened beams, failure might shift from concrete crushing to interfacial debonding[16]; for carbon fiber-reinforced polymer (CFRP) plates or steel plates strengthened beams, it might transition from interfacial debonding to cover separation[10,17]; while for CFRP sheets-strengthened beam, it might degrade from fiber ruptured to interfacial failure.[5] These phenomena suggest that the stiffness, ductility, and deformation compatibility of the strengthening material with concrete are key factors influencing the evolution path of interfacial performance. However, for prestressed CTRC plates, which combine high stiffness,

ACI Structural Journal, V. 123, No. 3, May 2026.
MS No. S-2024-208.R4, doi: 10.14359/51749315, received September 29, 2025, and reviewed under Institute publication policies. Copyright © 2026, American Concrete Institute. All rights reserved, including the making of copies unless permission is obtained from the copyright proprietors. Pertinent discussion including author's closure, if any, will be published ten months from this journal's date if the discussion is received within four months of the paper's print publication.

prestressing effects, and good compatibility with concrete substrate, there is a lack of research on their interfacial load transfer mechanisms and collaborative performance with preloaded RC beams under different damage states.

To address the aforementioned issues, this paper investigated the flexural behavior of preloaded RC beams strengthened with prestressed CTRC plates through four-point bending tests. The study focused on the effects of three typical preload levels (corresponding to the cracking load, yield load, and serviceability limit state load) and two construction methods (strengthening under sustaining load and strengthening after unload) on the load-bearing capacity, stiffness, crack development, and failure modes of strengthened beams. The goal is to elucidate the working mechanism of prestressed CTRC plates in strengthening preloaded beams, and to provide a basis for establishing a flexural design method for this strengthening technique.

RESEARCH SIGNIFICANCE

Despite the increasing use of TRC in strengthening, the behavior of prestressed CTRC plates used in preloaded RC beams remains unexplored. Existing knowledge on fiber-reinforced polymer (FRP) or conventional TRC cannot be directly transferred due to fundamental differences in material system, bond mechanism, and preloading effects. This study first fills this gap by demonstrating that prestressed CTRC plates achieve consistent flexural capacity regardless of preload level or whether to unload during strengthening, with failure governed by plate rupture rather than interfacial debonding—indicating superior bond compatibility. Furthermore, code evaluations reveal that current FRP-based models are unsuitable for CTRC, while the Chinese code offers reasonable accuracy, underscoring the need for dedicated design provisions. These findings provide a critical foundation for the reliable application of prestressed CTRC in practical retrofitting.

EXPERIMENTAL PROGRAM

Materials

The fiber textile used in the prestressed CTRC plates was a bidirectional carbon-fiber grid with a spacing of 20 mm (0.79 in.) in both latitudinal and longitudinal directions, and the grid consisted of 12 K carbon-fiber bundles with a thickness of 0.167 mm (0.0066 in.). Carbon-fiber bundles were impregnated with epoxy resin adhesive; the carbon-fiber textile before and after impregnation is shown in Fig. 1. The longitudinal fiber was the main stress fiber, and the tensile test was carried out by using the longitudinal carbon-fiber bundle with a marking distance of 100 mm (3.94 in.); and the results are shown in Table 1. The short-cut steel fibers in the prestressed CTRC plates were copper-plated microfilament short-cut steel fibers, as shown in Fig. 1(c), which were 14 to 16 mm (0.55 to 0.63 in.) in length and approximately 0.2 mm (0.008 in.) in diameter. The high-performance cementitious materials used to fabricate and bond the CTRC plates had specific mortar compositions, as shown in Table 2. The mechanical properties of the materials used to fabricate the CTRC plates, and the materials used for the RC beams are shown in Table 3.

Prestressed CTRC plates

Three layers of carbon textile were layered and anchored in the homemade tensioning device, with the same spacing between each layer. A pretension force of 5.6 kN (1.26 kip)

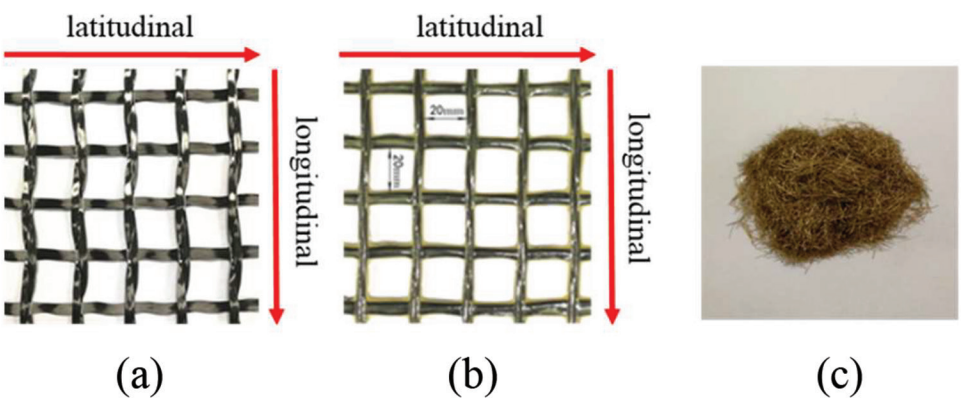

Fig. 1—(a) Carbon textile not impregnated with epoxy resin; (b) carbon textile impregnated with epoxy resin; and (c) short steel fibers. (Note: 1 mm = 0.0394 in.)

Table 1—Mechanical properties of impregnated carbon textile

Material	Tensile load-bearing capacity of one single bundle yarn, N (kip)	Tensile strength, MPa (ksi)	Elastic modulus, GPa (ksi)	Ultimate strain, %
Carbon textile yarn (12K)	1757 (0.39)	4900 (710.66)	250 (36,258.16)	1.96

Table 2—Constituents and mixture proportion of mortar

Material	Cement	Fly ash	Mineral ash	Silica fume	High-range water-reducing admixture	Sand	Water
Content, kg/m^3	800	100	50	50	2	120	286

Note: 1 kg/m^3 = 1.69 lb/yd^3.

Table 3—Mechanical properties of materials

Material	Elastic modulus, GPa (ksi)	Yield tensile strength, MPa (ksi)	Ultimate tensile strength, MPa (ksi)	Compressive strength, MPa (ksi)
Short steel fiber	200 (29,007.54)	—	2850 (413.36)	—
Mortar	30.75 (4459.91)	—	—	76.7 (11.12)
Concrete	30 (4351.13)	—	—	30.6 (4.44)
Steel bar	210 (30,457.92)	488 (70.78)	651 (94.42)	—

Table 4—Fabrication parameters of prestressed CTRC plate

Textile layer	Prestress level	Steel-fiber content	Length, mm (in.)	Width, mm (in.)	Depth, mm (in.)	Ultimate load, N (kip)
3	15%	1%	1900 (74.80)	150 (5.91)	16 (0.63)	79,200 (17.80)

Table 5—Detailed specifications of test beams

Name	Experimental program	Cracking state of RC beam	Crack width, mm (in.)	Midspan deflection, mm (in.)
R	Unstrengthened, undamaged beam	Undamaged	—	0
D	Strengthened, undamaged beam	Undamaged	—	0
U1	$0 \rightarrow F_{cr} \rightarrow 0$	Only one main crack formed, and crack nearly closed after unloading.	—	0.12 (0.005)
U2	$0 \rightarrow F_{y} \rightarrow 0$	Main cracks formed essentially, and most of them closed after unloading, but there were still some cracks visible.	0.10 (0.004)	1.26 (0.050)
U3	$0 \rightarrow F_{11} \rightarrow 0$	Main cracks formed essentially, and crack widths were reduced once unloading, but most of them were visible.	1.01 (0.040)	5.60 (0.220)
S1	$0 \rightarrow F_{cr}$	Only one main crack formed.	0.08 (0.003)	0.70 (0.028)
S2	$0 \rightarrow F_{y}$	Main cracks formed essentially.	0.30 (0.012)	4.56 (0.180)
S3	$0 \rightarrow F_{11}$	Main cracks formed essentially, and crack width was larger than Beam S-2.	1.60 (0.063)	11.06 (0.435)

Note: Crack widths and midspan deflections are corresponding values when strengthened.

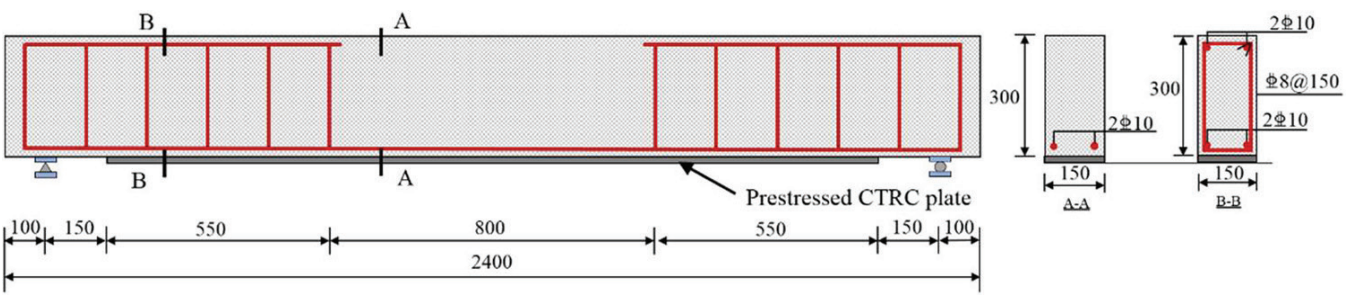

Fig. 2—Design details of RC beams.

was applied to the carbon textile with a prestressing level of approximately 15%.[9] After the prestressing value was basically stabilized, a high-performance cementitious matrix was cast and steel fibers with a volume fraction of 1% were incorporated during the casting process.[9] The fabrication parameters of the prestressed CTRC plates are shown in Table 4.

RC beams

Eight RC beams were designed as shown in Fig. 2—one of which an unstrengthened reference beam and the remaining seven were strengthened with prestressed CTRC plates. The beams were numbered R for unstrengthened and D for no preload strengthened. The numbering of beams with preloads consisted of two parts: the letters indicated the state of the beams and the numbers indicated the degree of preloading. U denoted unloading strengthened and S denoted sustaining load strengthened; and 1 denoted preloading up to F_{cr}, 2 denoted preloading up to F_y, and 3 denoted preloading up to F_{11}. The specific working conditions of the test beams are shown in Table 5.

Strengthening procedure

Strengthening was divided into four steps: 1) to enhance the interfacial bonding performance, the bonding surface of the concrete beam bottom was chiseled and diagonal marks 1 to 2 mm (0.04 to 0.08 in.) deep and were scored on the bonding surface of the CTRC plates and then washed with water; 2) RC beams were preloaded according to the conditions in Table 5; 3) the prestressed CTRC plates were bonded to the tensile surfaces of RC beams with high-performance mortar after unloading was completed or during sustaining load. The thickness of the bonding layer was approximately 4 to 5 mm (0.16 to 0.20 in.), noting that the thickness of the bonding layer could be slightly adjusted at different locations to ensure that the CTRC plate was completely straight;

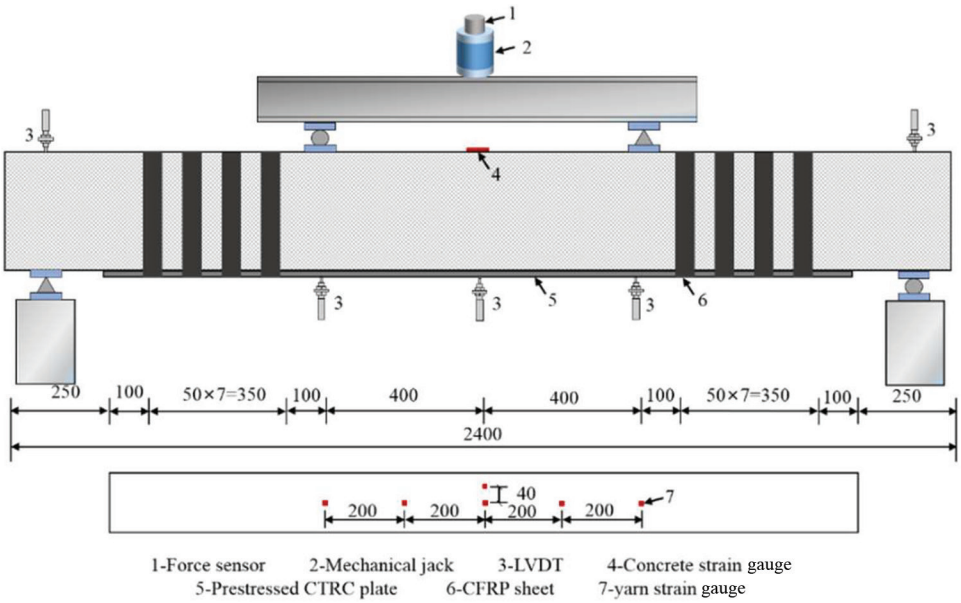

Fig. 3—Schematic drawing of test setup.

and 4) finally, CFRP sheets of 50 mm (1.97 in.) width and 900 mm (35.43 in.) length were pasted to the shear spans of the RC beams using an epoxy adhesive for anchoring,[18-20] as shown in Fig. 3.

Test setup

The test setup is shown in Fig. 3. The test was performed using a mechanical jack and a distributing beam for the four-point bending test, and the force sensor was attached between the jack and the distributing beam. A total of five linear variable differential transformers (LVDTs) were arranged at the top and bottom of the beam at the support and at the bottom of the beam at midspan, to measure the deflection of the beam and to calculate the curvature and stiffness of the beam. A strain gauge was attached at the midspan region of each of the two steel reinforcements at the bottom of the beam, and a concrete strain gauge was attached at the top surface of the beam in midspan. Five strain gauges were used to measure the longitudinal strain of the fiber bundle at the CTRC plate, all of which were distributed every 200 mm (7.88 in.) in the pure bending section, and one additional strain gauge was attached on the parallel fiber bundle at the midspan; the specific distribution is shown in Fig. 3. The arrangement of strain gauges could collect real-time strains so that it was easy to observe whether the steel reinforcements yield during the loading process, and whether the carbon fiber textile and concrete reached the ultimate strain. The purpose of arranging multiple strain gauges was to ensure that when a strain gauge failed, the strain at that location could still be effectively captured.

RESULTS AND DISCUSSIONS

Bending moment-midspan deflection curves

Typical curves—The bending moment-midspan deflection curve is shown in Fig. 4. For the reference beam *R*, the curve could be divided into three stages. Stage AB was the elastic stage, where the bending moment increased linearly with the increase of midspan deflection and the beam had a high flexural stiffness. This stage ended with the appearance of the first crack in the beam (point B). Stage BC was the crack development stage. In stage BC, concrete in the tensile zone quit working and the tensile force in the beam section was mainly borne by the tensile reinforcement, leading to a decrease in flexural stiffness. This stage ended with the yielding of steel reinforcement (point C). Stage CD was the failure stage. The steel reinforcement entered the plastic stage, and the beam eventually failed when the concrete in the compression zone crushed (point D).

There were five stages in the curve of a strengthened beam. Stage OA was the preloading stage, representing the beam's loading condition before strengthening. Stage AD (AB, BC, CD) was the loading stage. Stage AB was the elastic stage, which ended with the appearance of the first beam-plate penetration crack (point B). Stage BC was the crack development stage, both the steel reinforcement and the prestressed CTRC plate shared the beam section tension. This stage ended with the yielding of steel reinforcement (point C). Stage CD was the failure stage. Flexural stiffness decreased further due to the yielding of the steel reinforcement, and the tension was mainly borne by the prestressed CTRC plate. When the prestressed CTRC plate reached the ultimate tensile strength (point D), it ruptured, leading to the failure of the strengthened beam. Stage DE was the after-failure stage. Point E was the residual bending moment of the beam after unloading. In addition, S2 and S3 beams had no point C in stage AD because they were strengthened under sustaining load with a degree of preloading that reached (or exceeded) the yielding load of the steel reinforcement. The beams were not ever unloaded and the steel reinforcement did not yield twice under the always loaded condition.

From Fig. 4, the curves of the reference beam and the strengthened beam were nearly straight in the AB stage, indicating that both beams maintained high flexural stiffness. In stage BC, concrete in the tensile zone quit working. Because the strengthened beams had prestressed CTRC plates and steel reinforcement to share the tensile zone tension, the

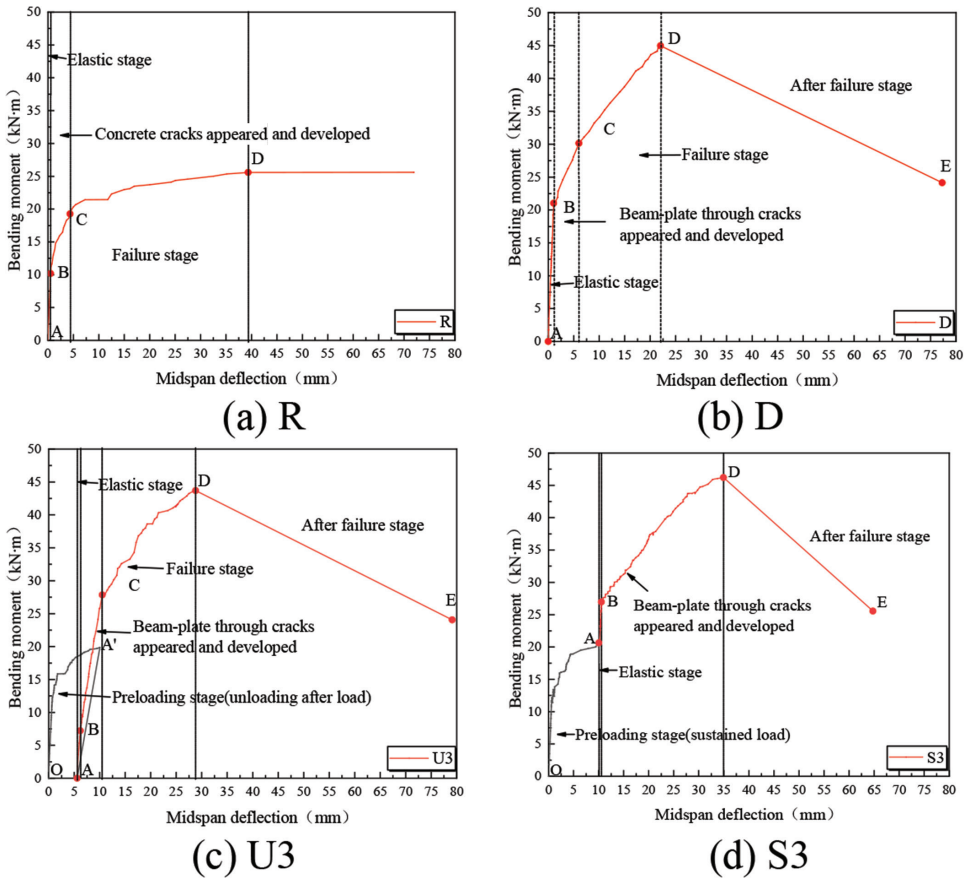

Fig. 4—Typical bending moment-midspan deflection curves. (Note: 1 kN·m = 8.86 kip·in.; 1 mm = 0.0394 in.)

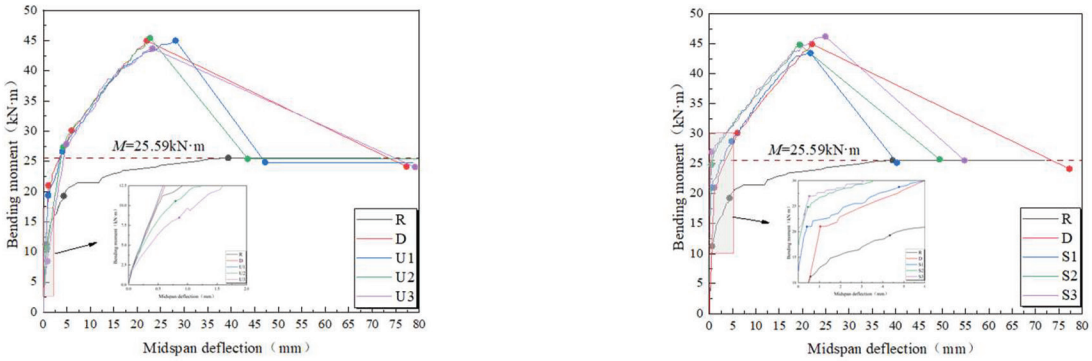

（a）beam strengthened under unloading （b）beam strengthened under sustained load

Fig. 5—Bending moment-midspan deflection curves. (Note: 1 kN·m = 8.86 kip·in.; 1 mm = 0.0394 in.)

slope of the bending moment-midspan deflection curve of the strengthened beams in the BC stage was larger and the flexural stiffness was improved. In stage CD, after the yielding of the steel reinforcement, the bending moment of the reference beam grew slowly, the deflection grew rapidly, and the flexural stiffness decreased significantly. The strengthened beams, on the other hand, still maintained high flexural stiffness until failure because the prestressed CTRC plates were continuing to take up the tension in the tension zone, and the bending moment continued to grow continuously with the growth of the deflection.

Effect of parameters on bending moment-midspan deflection curves—After strengthening, the deflection of the beams was reset, removing the preloading deflection. Deflection at point A for all beams was 0. Figure 5(a) shows the bending moment-deflection curves for the unloading strengthened beams. Figure 5(b) shows those for the sustaining load strengthened beams. Table 6 lists the bending moments and deflections at characteristic points for each beam.

The difference between M_B and M_A for strengthened beams decreased with increasing preload. After strengthening, positive stresses perpendicular to the interface were generated at locations with cracks, and the tensile stresses in the cracked section were transferred to the prestressed CTRC plate. As the preload increased, the initial cracks in the beams before strengthening increased and the crack width increased. After strengthening, the plates were more likely to crack and the cracks extended upwards, resulting

Table 6—Characteristic point bending moment and deflection

Beam	Point A	Point B		Point C			Point D			Point E	
	M_A, kN·m	M_B, kN·m	f_B, mm	M_C, kN·m	IR, %	f_C, mm	M_D, kN·m	IR, %	f_D, mm	M_E, kN·m	M_E/M_{DR}, %
R	0.0	11.24	0.58	19.29	—	4.34	25.59	—	39.37	—	—
D	0.0	21.04	1.04	30.14	56.3	6.03	44.98	75.8	22.05	24.15	94.37
U1	0.0	19.36	1.08	26.64	38.1	4.10	45.01	75.9	28.15	24.85	97.11
U2	0.0	10.57	0.82	27.37	42.0	4.24	45.43	77.6	22.74	25.41	99.30
U3	0.0	8.72	1.00	27.86	44.5	5.81	43.68	70.7	26.54	24.08	94.10
S1	12.04	21.07	0.49	28.63	48.5	5.31	43.47	69.9	21.24	25.69	100.4
S2	17.43	24.75	0.62	—	—	—	44.87	75.4	19.40	25.73	100.5
S3	20.62	26.95	0.52	—	—	—	46.20	80.6	23.90	25.69	100.4

Note: 1 kN·m = 8.86 kip·in.; 1 mm = 0.0394 in.

in the strengthened beams being more susceptible to beam-plate penetration cracks. The difference between M_B and M_A for the sustaining load strengthened beams was smaller than that for unloading strengthened beams for the same preload level. The difference was 9.03 kN·m (80 kip·in.) for beam S1, while the difference was 19.36 kN·m (171.53 kip·in.) for beam U1. The reason was that the unloading strengthened beams were unloaded before strengthening, the initial strain of the steel reinforcement was reduced, and the prestressed CTRC plates were stressed together with the steel reinforcement after strengthening to delay cracking. While in the sustaining load strengthened beams, the strain of the steel reinforcement was larger and there was obvious strain hysteresis between the carbon fibers and steel reinforcement. The prestressed CTRC plate could not effectively participate in the bearing at the initial stage of strengthening and could not effectively inhibit the expansion of cracks. At the same preload level, the sustaining load strengthened beams showed beam-plate penetration cracks under smaller bending moments.

Compared to the reference beam R, M_C of the strengthened beams increased by 38.1 to 48.5% and M_D increased by 69.9 to 80.6%, indicating that the prestressed CTRC plates were effective for strengthening RC beams. Moreover, the degree of preloading and whether unloading before strengthening had little effect on the yield moments and ultimate moments of the strengthening beams. This was due to the excellent interfacial bonding between the prestressed CTRC plates and the RC beams, which prevented interfacial failure due to the stress hysteresis between carbon fibers and steel reinforcement. The steel reinforcement in this study remained in plastic deformation when the strengthened beams failed, allowing the plasticity of the reinforcements to be fully used and ensuring the ductility of the beams. The failure of all strengthened beams was prestressed when CTRC plates ruptured, and the ultimate bending moment at failure was determined by the ultimate tensile strength of the prestressed CTRC plates. Because all the strengthened beams had the same reinforcement ratio and the same mesh ratio for the prestressed CTRC plates, the ultimate moments of the strengthened beams were essentially the same. In addition, the M_E of all strengthened beams after failure decreased to the ultimate moment level of the reference beam R. The reason was that the failure mode of all strengthened beams in this study was the rupture of the prestressed CTRC plates, and the beams were still in the yield stage of the reinforcement at the time of failure. The strengthened beams only lost the bending moment provided by the prestressed CTRC plates.

Table 7—Flexural stiffness and ductility factor of beam

Beam	B_{AB}, × 10^7 N·mm^2	B_{BC}, × 10^7 N·mm^2	B_{CD}, × 10^7 N·mm^2	M_{fa}, kN	IR, %	μ
R	1.53	0.11	0.01	21.46	0	9.07
D	2.09	0.12	0.04	35.21	64.1	3.66
U1	1.88	0.12	0.05	34.79	62.2	6.87
U2	1.05	0.23	0.08	35.46	65.3	5.36
U3	0.48	0.22	0.05	34.30	59.9	4.56
S1	1.95	0.12	0.08	35.95	67.5	4.00
S2	1.18	—	0.06	37.35	74.1	—
S3	1.01	—	0.04	37.84	76.3	—

Note: 1 mm = 0.0394 in.; 1 N = 0.0002 kip; 1 kN = 0.225 kip.

Combining Fig. 5 with Table 6, the f_D of both the unloading and sustaining load strengthened beams were smaller than that of the reference beam R. The deflection-changed values of U1, U2, and U3 at stage AB were basically the same as that of beam D, while S1, S2, and S3 were smaller. This was because the unloading-strengthened beams were unloaded prior to strengthened; the beams' deflection and cracking recovered, and they did not differ much from the initial state of the beams D when strengthening. But sustaining load-strengthened beams with large deflections and cracks already presented at the time of strengthening. Continuing to load, most of the tensile zone concrete quit working in the smaller deflection due to beam-plate penetration crack. The deflection change values at stage CD were essentially the same for all strengthened beams because when the steel reinforcement yielded, the deformation of the steel reinforcement was mainly dominated by plastic deformation, and the deformation characteristics were basically the same. The prestressed CTRC plates took up the major tensile forces and provided the main flexural stiffness of the beams, and prestressed CTRC plates with consistent mesh rates had essentially the same effect on stiffness enhancement.

Flexural stiffness—Table 7 showed the flexural stiffness values of the beams at each stage. In stage AB, only the

flexural stiffness of the strengthened beams D, U1, and S1 were higher than that of the reference beam R, while the flexural stiffness of other strengthened beams was significantly lower than R. The flexural stiffness of U3 was only 4.8×10^6 N·mm^2 (6.18×10^6 kip·in.^{2}), while the flexural stiffness of R was 1.53×10^7 N·mm^2 (1.97×10^6 kip·in.^{2}). This indicated that the B_{AB} of strengthened beams decreased gradually with increasing preload. Before strengthening, cracking of beams under preload significantly reduced the effective cross section of the beam, resulting in a lower moment of inertia of the cross section and a lower flexural stiffness. In this paper, the preload levels of the strengthened beams were cracking load, reinforcement yielding load, and normal service limit load, and their stiffness before strengthening corresponded to B_{AB}, B_{BC}, and B_{CD} of the reference beams, respectively. From Table 7, it could be seen that there was a significant difference in the stiffness of these three stages. Although the prestressed CTRC plate strengthening slightly increased the beam stiffness compared to the pre-strengthening, the stiffness of the beam before strengthening still had a significant impact.

After the appearance of beam-plate penetration crack, flexural stiffness of strengthened beams reduced. In stage BC, the flexural stiffness of strengthened beam was mainly provided by steel reinforcement and carbon fibers. Because the strengthened beams had the same reinforcement rate and mesh rate, the flexural stiffnesses B_{BC} of the strengthened beams D, S1, U1, U2, and U3 were essentially the same. In stage CD, the steel reinforcement yielded. Carbon fibers were mainly used to take up the tension in the tension zone, thus slowing down the upward shift of the neutral axis and providing flexural stiffness. As a result, the strengthened beam had a higher flexural stiffness B_{CD} compared to the reference beam R. Because the failure mode for all strengthened beams was plate ruptured, the prestressed CTRC plates fully used their tensile capacity, and all strengthened beams had the same mesh ratio. Therefore, the flexural stiffness B_{CD} was essentially the same for all strengthened beams. It was worth noting that S2 and S3 beams, because they were preloaded to (or above) the yield load of the reinforcement prior to strengthening, the steel reinforcement remained in the yield state after the sustaining load strengthened. As a result, the flexural stiffness significantly reduced after the strengthened beam cracked, and the flexural stiffness of the cracked S2 and S3 beams was provided only by carbon fibers. So, the flexural stiffness of S2 and S3 beams after cracking were essentially the same as the flexural stiffnesses B_{CD} of the other strengthened beams after yielding of the steel reinforcement.

Serviceability limit state bending moment and ductility—According to GB 50010-2010,[21] the deflection f_a was 11 mm (0.43 in.). The corresponding ultimate moments M_{fa} were shown in Table 7. It could be seen that M_{fa}, of all the strengthened beams in the normal service limit state were basically the same and were higher than those of the reference beam R. The range of increase was 59.9 to 76.3%. Showing that preload level and whether to unload during strengthened did not have any effect on the bending moments of the preloading strengthened beams at the limit state of normal service. By comparing M_C in Table 6 with M_{fa} in Table 7, it could be seen that the reinforcement yielded when the beam reached the limit state of normal service load. At this time, the tensile force of the beam section was mainly borne by the prestressed CTRC plate, so the increased bending moments in the strengthened beams were mainly provided by the prestressed CTRC plate. The strengthening of the prestressed CTRC plates slowed down the upward shift of the neutral axis of the strengthened beams and improved the flexural stiffness, thus providing higher bending moments in the normal service limit state compared to the reference beam R. Moreover, all strengthened beams were strengthened with the same prestressed CTRC plates, thus providing essentially the same increased moments under normal service conditions.

The beam ductility was determined by using the ductility factor μ. For S2 and S3 beams, because the reinforcement had yielded before strengthening and there was no reinforcement yield point C after strengthening, there was no deflection f_c corresponding to the point C, and it was not possible to calculate the ductility factor μ. The results are shown in Table 7. The ductility of all strengthened beams was lower than the ductility of beam R. The degree of preload and whether unloading when strengthened had no significant effect on the ductility of preloading strengthened beams. This indicated that though the strengthening of prestressed CTRC plates was effective in increasing the flexural stiffness of the beams, the improvement in ductility was limited. The ductility of the beam mainly relied on the plastic deformation capacity of the reinforcement, and because the prestressed CTRC plate took up most of the tensile force, the space for plastic deformation of the reinforcement was reduced, leading to a decrease in ductility. The degree of preload and whether unloading when strengthened had little effect on ductility factor, because the dominant effect of the prestressed CTRC plates was more significant on the ductility of the beams after strengthened.

Load-strain curves—Figure 6 shows the moment-strain curves of strengthened beams under load. For the sustaining load strengthened beams, except for the carbon-fiber tensile strain from 0, the steel tensile strain and concrete compressive strain had certain initial values that increased with preload level. This caused the carbon fiber strain to lag greatly behind the reinforcement as the preload increased. Unloading strengthened beams started at 0 for all strains.

Figure 6(a) shows beam D exhibited near-linear strain-moment relationships for reinforcement, carbon fiber, and concrete until cracking moment M_B, with minimal strain difference between reinforcement and carbon fiber. When bending moment reached M_B, the curve slope decreased significantly. As concrete cracked and tensile forces were shared by carbon fiber and reinforcement, they were strained at similar rates. After reinforcement yielding moment M_C, reinforcement strain accelerated while carbon fiber bore most tensile force, yielding a steeper moment-strain slope than reinforcement. Concrete compressive strain growth also slightly slowed. Figures 6(b) and (c) show the trends of the moment-strain curves of beam S1, U1, and D were basically the same.

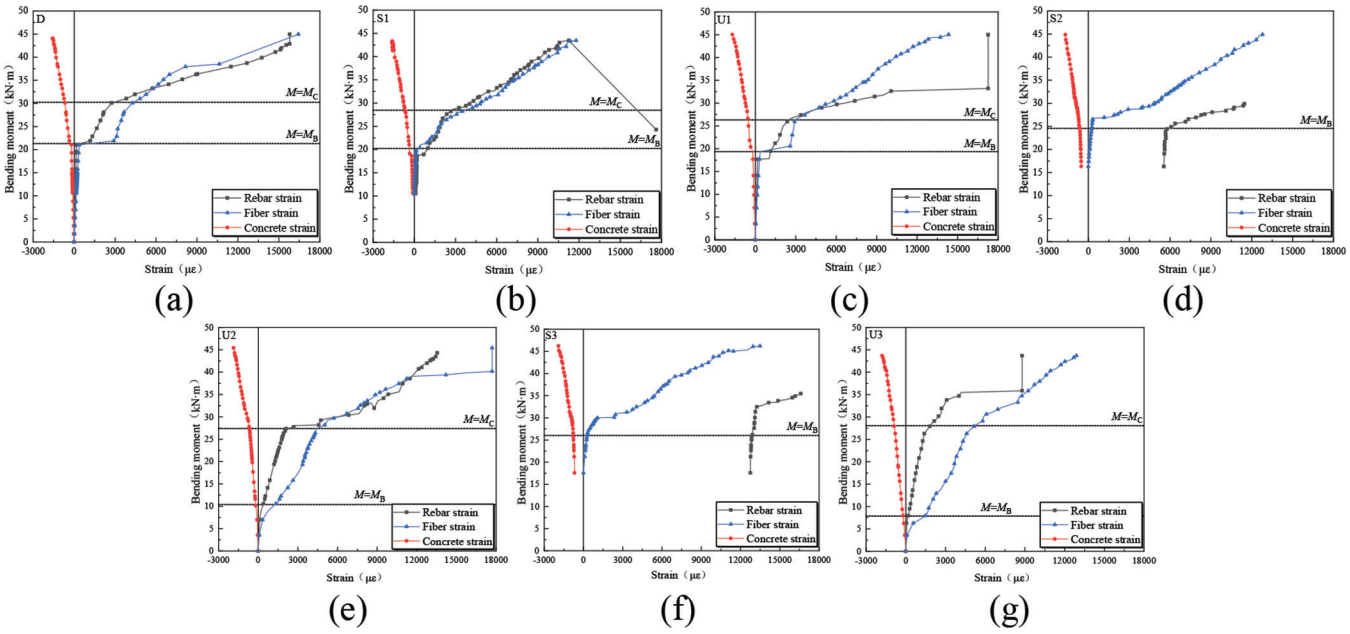

Fig. 6—Bending moment-strain curves. (Note: 1 kN·m = 8.86 kip·in.)

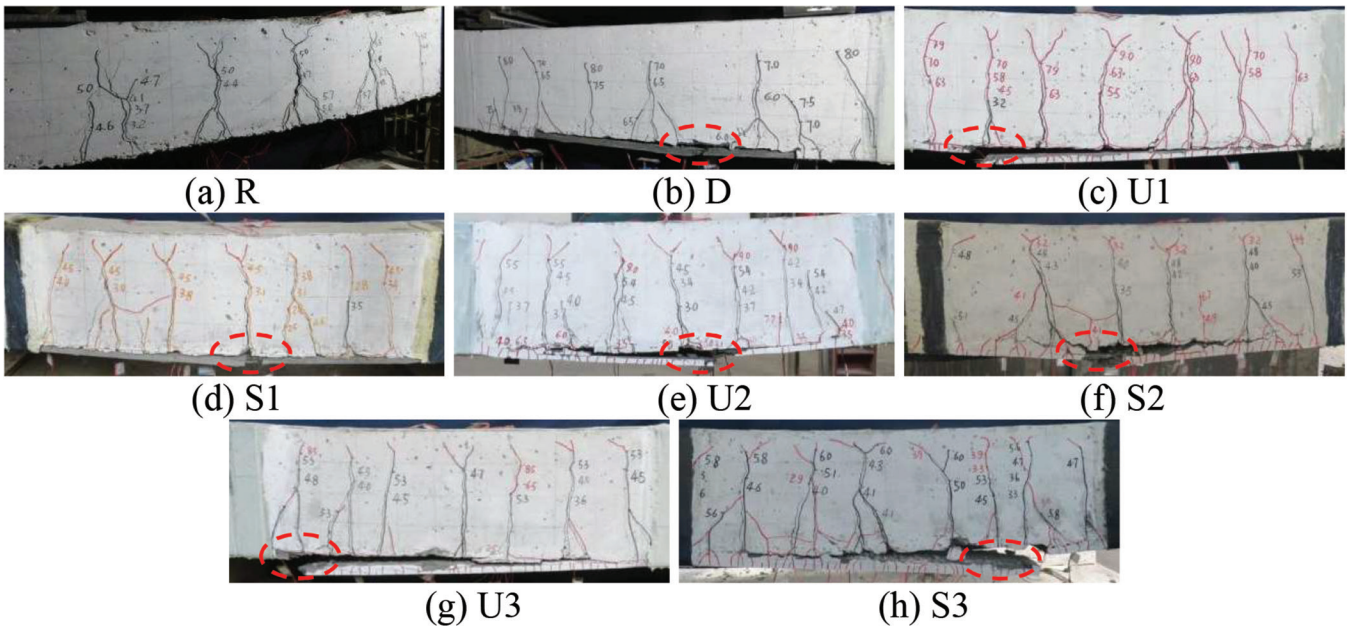

Fig. 7—Crack patterns of all beams at ultimate.

As shown in Fig. 6(d) through (g), carbon fiber exhibited significant strain lag relative to reinforcement at point A in S2 and S3 beams, with S3 showing higher reinforcement plastic strain at carbon fiber's ultimate tensile strain due to greater preload. Before, cracking moment strain progression mirrored beam D, but no distinct curve inflection occurred at S2 and S3 beams consistent with moment-deflection behavior since reinforcement had yielded pre-strengthening. In contrast, U2 and U3 beams showed a new reinforcement yield point after reloading, as unloading recovered elastic strains. Concrete compressive strain rose with preload in all beams yet never reached ultimate compressive strain at the edge. Consequently, all failure modes were carbon fiber ruptured.

Crack and failure—Figure 7 summarizes ultimate failure modes with plate ruptured locations circled. Pre-strengthening cracks are black; new cracks red. (Note: Full-color PDF is available at www.concrete.org.) Beam R failed by concrete crushing after reinforcement yielding (Fig. 7(a)). Before bending moment reached M_B (Table 6), beam D (Fig. 7(b)) developed small vertical cracks in the CTRC plate, with upward propagation inhibited by steel-fiber bridging. When the bending moment reached M_B, the crack in the CTRC plate developed upward in the direction of the height of the beam and penetrated the upper region of the beam, forming the first beam-plate penetration crack. Subsequent moment increase caused crack development. Finally, carbon-fiber textile ruptured within the pure bending section, and the strengthened beam failed.

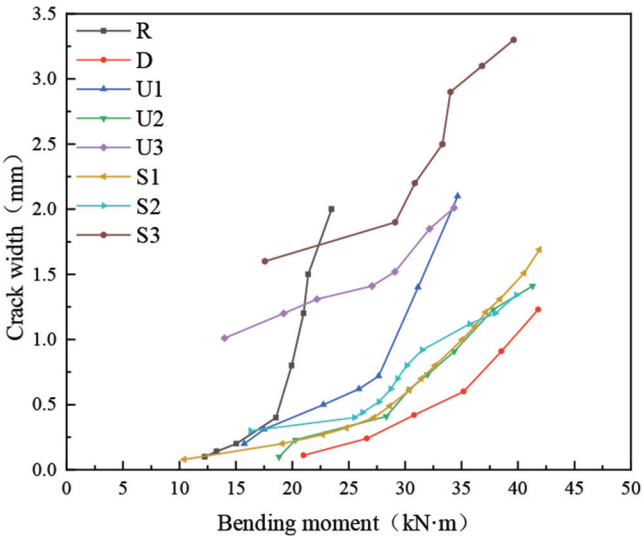

Fig. 8—Crack width-bending moment curves. (Note: 1 kN·m = 8.86 kip·in.; 1 mm = 0.0394 in.)

Figures 7(c) through (h) showed failure modes of preloaded strengthened beams. U1 and S1 beams had minor preloading cracks during preloading, while other beams developed main cracks. During unloading, crack widths reduced. The crack width of U2 before strengthening was 0.1 mm (0.004 in.), while the crack width of S2 was 0.3 mm (0.012 in.). Concrete at crack locations had failed during preloading, creating perpendicular interface stress and reducing section stiffness. After strengthening, cracking initiated at minimum stiffness areas. Therefore, the first CTRC plate crack aligned vertically below preloaded beam cracks. When bending moment reached M_B, additional vertical cracks emerged when plate cracks penetrated beam main cracks. Further loading eventually led to carbon textile ruptured within the pure bending section. Notably, rupture consistently occurred at the location of main flexural crack presented in the beam.

Crack width—Figure 8 shows crack width-bending moment curves measured from point A. The slope inversely indicated crack inhibition ability, the steeper slope being the lower inhibition. Beam R exhibited the steepest slope, confirming weakest crack control. All strengthened beams showed superior crack width suppression versus Beam R, with similar inhibition capacities due to identical CTRC strengthening. Maximum crack widths increased with preload levels due to higher initial tensile strains in concrete and reinforcement. At equivalent preloads, sustaining load beams developed wider cracks than unloaded beams owing to greater initial crack widths without unloading.

ULTIMATE FLEXURAL STRENGTH CALCULATION FORMULAS

Calculation of flexural strength after flexural strengthening

Currently, the only code that uses TRC to strengthen concrete structures is ACI 549.6R-20.[22] The bending strength calculation model specified in this code is shown in Eq. (1) and (2), and the assumptions associated with the model in the code were as follows:

1. Plane sections remain plane after loading;
2. The bond between the TRC and substrate remains effective;
3. The maximum usable compressive strain in concrete is 0.003;
4. TRC has a bilinear elastic behavior to failure; and
5. The tensile strength of concrete and mortar is not considered.

It could be seen that the tensile strength of the mortar was neglected in the calculation code for TRC, and thus the contribution of TRC to the ultimate bending moment of the strengthened beams was calculated by considering only the contribution of the fiber textile, which was similar to the calculation of the FRP material. Therefore, bending strength calculation models for concrete structures strengthened with FRP material were also presented. The calculation model specified in ACI 440.2R-17[23] is shown in Eq. (3) and (4), the calculation model specified in CNR-DT 200R1/2013[24] is shown in Eq. (5), and the calculation model specified in T/CECS 146-2022[25] is shown in Eq. (6). These three codes have similar assumptions as ACI 549.6R-20,[22] but the ultimate compressive strain of concrete was taken as 0.0033 in the Chinese and European codes. In addition, because the failure modes of all the strengthened beams in this paper were fiber ruptured, only the calculation models for each code in this failure mode are listed in the paper.

$$\phi M_n = \phi(M_s + M_f) \tag{1}$$

$$\phi = \begin{cases} 0.90 \text{ for } \varepsilon_t \geq 0.005 \\ 0.65 + \dfrac{0.25(\varepsilon_t - \varepsilon_{sy})}{0.005 - \varepsilon_{sy}} \quad \text{for } \varepsilon_{sy} < \varepsilon_t < 0.005 \\ 0.65 \text{ for } \varepsilon_t < \varepsilon_{sy} \end{cases} \tag{2}$$

$$\phi M_n \geq M \tag{3}$$

$$M_n = A_s f_s\left(d - \frac{\beta_1 c}{2}\right) + \psi_f A_f f_{fe}\left(h - \frac{\beta_1 c}{2}\right) \tag{4}$$

$$M = \frac{1}{\gamma_{Rd}}[\psi b x f_{cd}(d - \lambda \cdot x) + A_{s2}\sigma_{s2}(d - d_2) + A_f \sigma_f d_1] \tag{5}$$

$$M = f_y A_s (h_0 - a) + \sigma_{f,md} A_f (h_{fe} - a') \tag{6}$$

Comparison of calculation and experimental results

The calculation results are shown in Fig. 9(a) and Table 8. The calculated results of all codes were smaller than the experimental results, indicating that the code calculations were conservative in the failure mode of fiber ruptured. Among them, the average value of the ratio of the experimental value to the calculated value of the Chinese code was 1.07, and the calculated value was the closest to the experimental value. The standard deviation of the ratio of the experimental values to the calculated values of the European

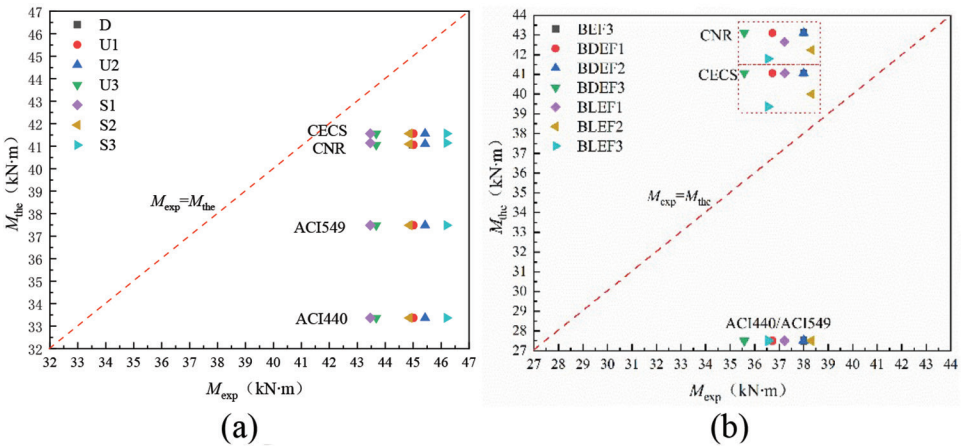

Fig. 9—Comparison of calculated and experimental results. (Note: 1 kN·m = 8.86 kip·in.)

Table 8—Related data of M_{exp}/M_{the}

Beam	ACI 549.6-20[22]		ACI 440.2-17[23]		CNR-DT 200R1/2013[24]		T/CECS 146-2022[25]	
	M_{exp}/M_{the}	σ	M_{exp}/M_{the}	σ	M_{exp}/M_{the}	σ	M_{exp}/M_{the}	σ
D	1.20	0.024	1.35	0.026	1.10	0.021	1.08	0.021
U1	1.20		1.35		1.10		1.08	
U2	1.21		1.36		1.09		1.09	
U3	1.17		1.31		1.05		1.05	
S1	1.16		1.30		1.05		1.05	
S2	1.20		1.34		1.08		1.08	
S3	1.23		1.38		1.12		1.11	
BEF3	1.38	0.033	1.38	0.033	0.88	0.024	0.93	0.027
BDEF1	1.33		1.34		0.85		0.89	
BDEF2	1.38		1.38		0.88		0.93	
BDEF3	1.29		1.29		0.83		0.87	
BLEF1	1.35		1.35		0.87		0.91	
BLEF2	1.39		1.39		0.91		0.96	
BLEF3	1.33		1.33		0.87		0.93	

and Chinese codes was 0.021, which resulted in better data stability. The European code and the two U.S. codes substituted the height of the RC beam for the effective depth of the fiber flexural strengthening in the calculation of the ultimate bending moment, without considering the distance of the fibers from the edge of the beam tensile zone. While the Chinese code took this into account, the effective depth of fiber flexural strengthening was the sum of the height of the RC beam and the distance from the center of the fibers to the edge of the tensile zone of the beam. Thus, the calculated values of the Chinese code were closer to the test values. Furthermore, two U.S. codes incorporated strength reduction factors for fibers in their calculations. As the test material in this paper was a prestressed CTRC plate, during the fabrication of prestressed CTRC plates, fiber textile got effective pretensioned, ensuring its smoothness. The strength of the fiber effective use rate was high. The strength reduction factors stipulated in U.S. codes were too high, resulting in large differences between calculated values and test values.

Precast prestressed CTRC plates exhibited high fiber use, requiring careful evaluation of code safety factors and adoption of rational strength coefficients to balance safety with economy. Additionally, mortar thickness should be considered in design to determine the effective depth (the center of the fiber textile to the edge of the concrete in the compression zone). It was worth noting that the European code considered the effect of preload; the calculated value of ultimate bending moments were slightly different for each beam. While the other three codes did not consider the effect of preload in the case of failure mode of fiber ruptured, they had the same calculated values for all the beams. In general, preload level and whether to unload during strengthening had little effect on the ultimate bending moment in the case of failure mode of fiber ruptured.

As the strengthened beams in this paper had a single failure mode, all of them were fiber ruptured and there was no concrete crushing failure. Consequently, the experimental results of Yan et al. paper,[16] which had a failure mode of concrete crushing in the compression zone, were selected. Results are shown in Fig. 9(b) and Table 8. The calculated results of the two U.S. codes were still very conservative and discounted the contribution to TRC too much, much less

than the experimental results. The calculated results of the Chinese and the European code were higher than the experimental results, but in comparison, the average value of the ratio of the experimental value to the calculated value for the Chinese code was 0.92, which was closer to the experimental value. The calculated results were all higher than the experimental results, indicating that the codes were not conservative in the case of failure of concrete crushing, which was due to an overestimation of the strain value of the fibers in this failure mode resulting in the calculated value of the bending moment provided by the fibers being too high. It is worth noting that in this failure mode, both the Chinese and European codes considered the effect of preloading, and at this point preload level and whether to unload during strengthened would influence the ultimate bending moment. In addition, in the case of failure of concrete crushing in the compression zone, the standard deviation between the ratio of experimental and calculated values calculated by the European code was the smallest, followed by the Chinese code, which indicated that these two codes had better predictive stability for the concrete crushing failure mode.

In summary, the calculation results of the Chinese code in both failure modes were closer to the experimental values, the calculation accuracy was higher, and it was more suggested to use the Chinese code for the prediction of the ultimate bending moment values of prestressed CTRC plate strengthened preloaded beams.

CONCLUSIONS

In this paper, the flexural behavior of preloaded reinforced concrete (RC) beams strengthened with prestressed carbon textile-reinforced concrete (CTRC) plates, was investigated through four-point bending tests and theoretical analysis, and the following conclusions were obtained.

Preloaded RC beams could be effectively strengthened with prestressed CTRC plates. Compared to the reference beam R, the steel reinforcement yield moment increased by 38.1 to 48.5%, the ultimate moment increased by 69.9 to 80.6%, and the bending moment at the normal service limit increased by 59.9 to 76.3%. Preload level and whether to unload during strengthening had little effect on the effectiveness of strengthening.

Cracking moments of strengthened beams decreased with increasing preloads. When the preload exceeded the cracking load, the cracking moment of the strengthened beam was lower than that of the reference beam. After the strengthened beams failed, the bending moment decreased and remained at 25.5 kN·m (226 kip·in.), which was consistent with the ultimate bending moment of the reference beam. This was because steel reinforcement was in the plastic yielding stage when the beam failed, and the bending moment provided by the reinforcement was maintained after the beam failed.

In the precracking stage, the flexural stiffness of only the unpreloaded strengthened beams and the strengthened beams which preloaded level was cracking load were higher than that of the reference beams. Flexural stiffness of strengthened beams decreased with increasing preload. After cracking, the stiffness reduced and carbon fiber and steel reinforcement worked together to provide stiffness. When the reinforcement yielded, the stiffness decreased again. Because only carbon fibers provided flexural stiffness at this point, the flexural stiffness of strengthened beams was all higher than those of the reference beams after yielding of the reinforcement.

Cracks on beams before strengthening increased with increasing preloads. After strengthening, the first crack in the prestressed CTRC plate appeared directly below the cracked area along the beam height direction during preloading. All the strengthened beams failed due to the rupture of the carbon-fiber textile in the CTRC plates in the pure bending section. Maximum crack width at failure increased with increasing preload. The crack widths of sustaining load strengthened beams were greater than those of unloading strengthened beams for the same degree of preloading.

In this paper, four current codes were selected to calculate the ultimate moments of preloaded RC beams strengthened with TRC. Comparison of calculated values with experimental values in this paper as well as with the experimental values in the references revealed that the Chinese code had the highest calculation accuracy in both failure modes.

AUTHOR BIOS

Shujun Zhou *is a PhD Student at Hunan University, Changsha, China. She received her BS from Nanjing Tech University, Nanjing, China. Her research interests include structural strengthening with composite materials.*

Yunxing Du *is a Professor in the Department of Civil Engineering at Hunan University. His research interests include the development and application of composite plates and structural strengthening.*

Yanqiu Li *is an Engineer in the China Construction First Group Fifth Construction Co., Ltd., Beijing, China. His research interests include structural strengthening.*

Ziwei Li *is an Engineer in the China Construction First Group Fifth Construction Co., Ltd. Her research interests include structural strengthening.*

Xionggang Shi *is an Engineer in the China Construction First Group Fifth Construction Co., Ltd. His research interests include structural strengthening.*

ACKNOWLEDGMENTS

This research was financially supported by the National Natural Science Foundation of China (Grant No. 52178206 and 52378299). The authors are grateful to the authorities for their support.

NOTATIONS

A_f = area of FRP external reinforcement, mm^2 (in.^{2})
A_s = area of nonprestressed reinforcement, mm^2 (in.^{2})
A_{s2} = area of steel reinforcement subjected to compression, mm^2 (in.^{2})
a' = distance from center of gravity of compression steel reinforcement section to edge of concrete compression zone, mm (in.)
B_{AB} = flexural stiffness during elastic stage, N·mm^2 (lb·in.^{2})
B_{BC} = flexural stiffness during crack development stage, N·mm^2 (lb·in.^{2})
B_{CD} = fexural stiffness after steel reinforcement yielding, N·mm^2 (lb·in.^{2})
b = width of the section, mm (in.)
c = distance from extreme compression fiber to neutral axis, mm (in.)
d = distance from extreme compression fiber to centroid of tension reinforcement, mm (in.)
d_1 = distance from center of gravity of tensile steel reinforcement section to edge of concrete compression zone, mm (in.)
d_2 = distance from center of gravity of compression steel reinforcement section to edge of concrete compression zone, mm (in.)
F_{cr} = during preloading, load at cracking, kN (kip)

F_y = during preloading, load at just yielding of steel reinforcement, kN (kip)
F_{11} = during preloading, load at midspan deflection of 11 mm (0.43 in.), kN (kip)
f_a = deflection limit of beams at limit state of normal service, mm (in.)
f_B = deflection at cracking of beam, mm (in.)
f_C = deflection at yielding of steel reinforcement of beam, mm (in.)
f_{cd} = design concrete compressive strength, MPa (psi)
f_D = deflection at failure of beam, mm (in.)
f_{fe} = effective stress in FRP; stress attained at section faliure, MPa (psi)
f_s = stress in nonprestressed steel reinforcement, MPa (psi)
f_y = design tensile strength of tension steel reinforcement, MPa (psi)
h = overall thickness of height of number, mm (in.)
h_{fe} = effective height from center of area of tensioned carbon fiber mesh to compression edge, mm (in.)
h_0 = distance from extreme compression fiber to centroid of tension reinforcement, mm (in.)
IR = increasing rate
M = design flexural strength, N·mm (lb·in.)
M_A = initial bending moment of beam, N·mm (lb·in.)
M_B = bending moment at beam-plate crack penetration of beam, N·mm (lb·in.)
M_C = bending moment at yielding of steel reinforcement of beam, N·mm (lb·in.)
M_D = bending moment at failure of beam, N·mm (lb·in.)
M_{DR} = bending moment at failure of beam R, N·mm (lb·in.)
M_E = residual bending moment of beam after failure, N·mm (lb·in.)
M_{exp} = experimental bending moment value of beam, N·mm (lb·in.)
M_f = contribution of FRCM to nominal flexural strength, N·mm (lb·in.)
M_{fa} = bending moments of beam in normal service limit state, N·mm (lb·in.)
M_n = nominal flexural strength, N·mm (lb·in.)
M_s = contribution of steel reinforcement to nominal flexural strength, N·mm (lb·in.)
M_{the} = calculated bending moment value of beam, N·mm (lb·in.)
x = distance from extreme compression fiber to neutral axis, mm (in.)
β_1 = ratio of depth of equivalent rectangular stress block to depth of neutral axis
ε_{sy} = steel tensile yield strain, mm/mm (in./in.)
ε_t = ultimate strain of fabric, mm/mm (in./in.)
ϕ = strength reduction factor for flexure
γ_{Rd} = partial factor for resistance models
λ = distance from extreme compression fiber divided by x
μ = ductility factor, $\mu = f_D/f_C$
σ = standard deviation of ratio of M_{exp}/M_{the}
σ_f = stress in FRP reinforcement, N/mm^2 (lb/in.^{2})
$\sigma_{f,md}$ = design tensile stress of CFRP plate when reaching limit state of bending load capacity, N/mm^2 (lb/in.^{2})
σ_{s2} = stress in tensile stress reinforcement, N/mm^2 (lb/in.^{2})
Ψ = resultant of compression stresses divided by $b \cdot x \cdot f_{cd}$
Ψ_f = FRP strength reduction factor is 0.85

REFERENCES

1. Hawileh, R. A.; Nawaz, W.; and Abdalla, J. A., "Flexural Behavior of Reinforced Concrete Beams Externally Strengthened with Hardwire Steel-Fiber Sheets," *Construction and Building Materials*, V. 172, 2018, pp. 562-573. doi: 10.1016/j.conbuildmat.2018.03.225

2. Nawaz, W.; Elchalakani, M.; Karrech, A.; Yehia, S.; Yang, B.; and Youssf, O., "Flexural Behavior of all Lightweight Reinforced Concrete Beams Externally Strengthened with CFRP Sheets," *Construction and Building Materials*, V. 327, 2022, p. 126966. doi: 10.1016/j.conbuildmat.2022.126966

3. Guo, L.; Deng, M.; Chen, H.; Li, R.; Ma, X.; and Zhang, Y., "Experimental Study on Pre-Damaged RC Beams Shear-Strengthened with Textile-Reinforced Mortar (TRM)," *Engineering Structures*, V. 256, 2022, p. 113956. doi: 10.1016/j.engstruct.2022.113956

4. Helal, K.; Yehia, S.; Hawileh, R.; and Abdalla, J., "Performance of Preloaded CFRP-Strengthened Fiber Reinforced Concrete Beams," *Composite Structures*, V. 244, 2020, p. 112262. doi: 10.1016/j.compstruct.2020.112262

5. Yu, F.; Zhou, H.; Jiang, N.; Fang, Y.; Song, J.; Feng, C.; and Guan, Y., "Flexural Experiment and Capacity Investigation of CFRP Repaired RC Beams under Heavy Pre-Damaged Level," *Construction and Building Materials*, V. 230, 2020, p. 117030. doi: 10.1016/j.conbuildmat.2019.117030

6. Elghazy, M.; El Refai, A.; Ebead, U.; and Nanni, A., "Post-Repair Flexural Performance of Corrosion-Damaged Beams Rehabilitated with Fabric-Reinforced Cementitious Matrix (FRCM)," *Construction and Building Materials*, V. 166, 2018, pp. 732-744. doi: 10.1016/j.conbuildmat.2018.01.128

7. Mandor, A., and El Refai, A., "Flexural Response of Reinforced Concrete Continuous Beams Strengthened with Fiber-Reinforced Cementitious Matrix (FRCM)," *Engineering Structures*, V. 251, 2022, p. 113557. doi: 10.1016/j.engstruct.2021.113557

8. Ebead, U.; Shrestha, K. C.; Afzal, M. S.; El Refai, A.; and Nanni, A., "Effectiveness of Fabric-Reinforced Cementitious Matrix in Strengthening Reinforced Concrete Beams," *Journal of Composites for Construction*, V. 21, No. 2, 2017, p. 04016084. doi: 10.1061/(ASCE)CC.1943-5614.0000741

9. Du, Y.; Zhang, X.; Liu, L.; Zhou, F.; Zhu, D.; and Pan, W., "Flexural Behaviour of Carbon Textile-Reinforced Concrete with Prestress and Steel Fibres," *Polymers*, V. 10, No. 1, 2018, p. 98. doi: 10.3390/polym10010098

10. Al-Ghrery, K.; Al-Mahaidi, R.; Kalfat, R.; Oukaili, N.; and Al-Mosawe, A., "Externally Bonded CFRP for Flexural Strengthening of RC Beams with Different Levels of Soffit Curvature," *Journal of Composites for Construction*, ASCE, V. 26, No. 1, 2022, p. 04021062. doi: 10.1061/(ASCE)CC.1943-5614.0001176

11. Al-Ghrery, K.; Al-Mahaidi, R.; Kalfat, R.; Oukaili, N.; and Al-Mosawe, A., "Experimental Investigation of Curved-Soffit RC Bridge Girders Strengthened in Flexure Using CFRP Composites," *Journal of Bridge Engineering*, ASCE, V. 26, No. 4, 2021, p. 04021009. doi: 10.1061/(ASCE)BE.1943-5592.0001691

12. Gao, P.; Gu, X. L.; and Mosallam, A. S., "Flexural Behavior of Preloaded Reinforced Concrete Beams Strengthened by Prestressed CFRP Laminates," *Composite Structures*, V. 157, 2016, pp. 33-50. doi: 10.1016/j.compstruct.2016.08.013

13. Xiong, X., and Xu, H., "Experimental Research and Parametric Analysis on Flexural Performance of Reinforced Concrete Beams Combination Strengthened with Bonded CFRP and Steel Plates Under Sustaining Load," *Building Structure*, V. 40, No. 5, 2010, pp. 37-41.

14. Al-Ghrery, K.; Kalfat, R.; Al-Mahaidi, R.; Oukaili, N.; and Al-Mosawe, A., "Prediction of Concrete Cover Separation in Reinforced Concrete Beams Strengthened with FRP," *Journal of Composites for Construction*, ASCE, V. 25, No. 4, 2021, p. 04021022. doi: 10.1061/(ASCE)CC.1943-5614.0001130

15. Al-Ghrery, K.; Al-Mahaidi, R.; Kalfat, R.; and Oukaili, N., "Near-Surface-Mounted CFRP for Strengthening Concavely-Curved Soffit RC Beams: Experimental and Analytical Investigation," *Journal of Composites for Construction*, ASCE, V. 26, No. 5, 2022, p. 04022051. doi: 10.1061/(ASCE)CC.1943-5614.0001239

16. Yan, Y.; Lu, Y.; Zhao, Q.; and Li, S., "Flexural Behavior of Pre-Damaged and Repaired Reinforced Concrete Beams with Carbon Fiber Reinforced Polymer Grid and Engineered Cementitious Composite," *Engineering Structures*, V. 277, 2023, p. 115390. doi: 10.1016/j.engstruct.2022.115390

17. Gao, R.; Cao, Q.; Hu, F.; Gao, Z.; and Li, F., "Experimental Study on Flexural Performance of Reinforced Concrete Beams Subjected to Different Plate Strengthening," *Composite Structures*, V. 176, 2017, pp. 565-581. doi: 10.1016/j.compstruct.2017.05.052

18. D'Ambrisi, A., and Focacci, F., "Flexural Strengthening of RC Beams with Cement-Based Composites," *Journal of Composites for Construction*, ASCE, V. 15, No. 5, 2011, pp. 707-720. doi: 10.1061/(ASCE)CC.1943-5614.0000218

19. Sneed, L. H.; Verre, S.; Carloni, C.; and Ombres, L., "Flexural Behavior of RC Beams Strengthened with Steel-FRCM Composite," *Engineering Structures*, V. 127, 2016, pp. 686-699. doi: 10.1016/j.engstruct.2016.09.006

20. Zhang, D.; Shi, H.; and Ueda, T., "Effect of U-Shaped Anchorages on Concrete Cover Separation in Carbon Fiber-Reinforced Polymer-Strengthened Beams with Notches at the Sheet End," *Structural Concrete*, V. 22, No. 1, 2021, pp. 50-68. doi: 10.1002/suco.201900388

21. GB 50010-2010, "Code for Design of Concrete Structures, "Ministry of Housing and Urban-Rural Development of the People's Republic of China, Beijing, China," 2010.

22. ACI Committee 549, "Guide to Design and Construction of Externally Bonded Fabric-Reinforced Cementitious Matrix and Steel-Reinforced Grout Systems for Repair and Strengthening of Concrete Structures, (ACI 549.6R-20)," American Concrete Institute, Farmington Hills, MI, 2020, 162 pp.

23. ACI Committee 440, "Guide for the Design and Construction of Externally Bonded FRP Systems for Strengthening Concrete Structures (ACI 440.2R-17)," American Concrete Institute, Farmington Hills, MI, 2017, 112 pp.

24. CNR-DT 200R1/2013, "Guide for the Design and Construction of Externally Bonded FRP Systems for Strengthening Existing Structures," Consiglio Nazionale delle Ricerche, Roma, Italy, 2013.

25. T/CECS 146-2022, "Technical Specification for Strengthening Concrete Structures with Carbon Fiber Reinforced Polymer Laminate," China Association for Engineering Construction Standardization, 2022.

ACI STRUCTURAL JOURNAL TECHNICAL PAPER

Title No. 123-S45

Pullout Behavior and Acoustic Emission Analysis of Large-Size Reinforcing Bars (D43 and D57) in Concrete

by Yu-Cheng Kan, Kuang-Chih Pei, and Jyun-Ruei Wu

This study investigates the bond behavior of large-diameter steel bars (D43 and D57) embedded in concrete using pullout tests coupled with acoustic emission (AE) monitoring. These large bars, commonly used in nuclear containment structures in the 1970s, were compared with conventional steel bars (D19 and D32) across three concrete strength levels. All tests were performed under displacement-controlled loading using a universal testing machine. Results indicate that ACI 408R provisions remain valid for large-diameter reinforcing bars. The test results showed that when specimens reached ultimate bond stress, the D57 bar developed only 12 to 16% of its yield strength, whereas the D19 bar reached at least 70%. AE monitoring effectively captured the debonding process, and cumulative AE hit counts correlated with the strain energy released at each loading stage, offering insight into bond failure mechanisms.

Keywords: acoustic emission (AE); bond; large reinforcing bar; pullout test.

RESEARCH SIGNIFICANCE

As the demand for carbon-free energy increases, many nuclear power plants that are about to be decommissioned in some countries are preparing for an extension of their operations. It is necessary to understand the characteristics of the bond behavior of these large-size steels used in the nuclear structures of concrete shielding containments built in the 1970s. The acoustic emission (AE) technique provides a viable method to monitor the bond behavior between concrete and steel bars during the replacement of tendons.

INTRODUCTION

Many studies have investigated the bond behavior of regular steel reinforcing bars in concrete; however, limited research has examined the bond behavior of large reinforcing bars (D43 and D57) in concrete. Large reinforcing bars are mostly used in the concrete shielding employed in nuclear power plants constructed in the 1970s. Degradation of the bond between concrete and large reinforcing bars causes the service life of the concrete shielding used in nuclear power plants to be reduced. Ferguson et al.[1] explored the development length of reinforced concrete containing embedded steel bars of varying sizes, including D57. They found that large reinforcing bars embedded in concrete exhibited different bond behavior to that exhibited by small reinforcing bars in concrete.

The factors affecting the bond between a deformed reinforcing bar and concrete include chemical adhesion, friction forces, and mechanical anchorage of the ribs against the surrounding concrete. These factors can be influenced by structural characteristics, bar properties, and concrete properties. For a given embedment length, larger bars achieve higher total bond forces, as concluded in ACI 408R-03.[2] Therefore, for a given bond length, the larger the bar is, the larger the force required to cause splitting or pullout failure. Orangun et al.[3] and Darwin et al.[4] have concluded that a larger embedment length is required for a certain amount of stress to develop in a larger bar. Soroushian and Choi[5] investigated the effects of bar diameter (No. 6 to No. 10) and found that the bond strength decreased as the bar diameter increased. Design codes such as ACI 349 and ACI 359,[6,7] first published in 1976, did not provide rigorous, detailed guidelines on the design of concrete containment for nuclear power plants. In consequence, the concrete containments built in the 1970s face the problem of degradation of the bond between concrete and reinforcing bars.

Bond characteristics of reinforced concrete

For concrete structures with an embedded steel bar, the bond between the concrete and the bar should be sufficiently strong for the bar to transfer stresses to the concrete. Adding ribs to the surface of the steel bar enhances the adhesive force between this bar and the concrete, generating an internal force that prevents the bar from being pulled out of the concrete. This internal acting force is referred to as the bond force. Many studies have explored the bond behavior between steel and concrete.[8-10] ACI 408R-03 defines bond stress as force transfer at the steel-concrete interface. Bond force varies along the bar length, influenced by adhesion, friction, and mechanical anchorage. These also affect the pullout failure of different types of reinforcing bars.

In general, the main factors affecting the strength of this bond are the chemical adhesion between the bar and concrete; the frictional forces caused by the roughness of the bar-concrete interface, forces transverse to the bar surface, and the relative slip between the bar and surrounding concrete; and the mechanical anchorage or bearing of the ribs against the concrete surface. These factors may also affect the pullout failure of concrete containing various types of embedded steel bars.

ACI Structural Journal, V. 123, No. 3, May 2026.
MS No. S-2024-234.R3, doi: 10.14359/51749301, received August 21, 2025, and reviewed under Institute publication policies. Copyright © 2026, American Concrete Institute. All rights reserved, including the making of copies unless permission is obtained from the copyright proprietors. Pertinent discussion including author's closure, if any, will be published ten months from this journal's date if the discussion is received within four months of the paper's print publication.

AE monitoring of concrete

Recently, AE monitoring technology has been widely used to investigate the fracture mechanics of concrete structures.[11-18] Cracking releases stress waves captured as AE signals, which reflect fracture behavior. Liu et al.[19] proposed an analysis to combine parameter analysis with fractal theory to assess the damage state and crack extension of the structure. Landis and Shah[20] explore how AE waves, generated by energy release from cracking, are affected by frequency-dependent material damping. Aggelis[21] proposed AE indexes to classify crack modes during bending. Ohtsu[22] classified cracks into tensile and shear cracks in accordance with the relationship of average frequency versus RA value (ratio of the rise time to the peak amplitude). RILEM Technical Committee 212-ACD[23] provided guidelines for AE damage assessment using AE parameters such as amplitude, rise time, and duration. AE frequency and RA value help distinguish tensile (low RA, high frequency) from shear (high RA, low frequency) cracks.[24,25] Several researchers dealing with the fracture mechanics of concrete have attempted to correlate the AE signal with the fracture energy. Carpinteri et al.[26] linked AE energy to crack growth for lifetime evaluation. Yuyama et al.[27] used moment tensor analysis to quantify fracture. Grosse and Finck[28] validated AE's ability to monitor fracture. However, most AE models focus on plain concrete. These may not sufficiently explain bond behavior signals between concrete and steel bars. Xiao and Falkner[29] studied AE in recycled aggregate concrete (RAC)-steel bar bonding, showing that recycled aggregate introduces more dispersed damage. Because AE reflects the cracking energy,[25] it is feasible to relate cumulative AE signals to energy released during concrete-reinforcing bar debonding.

Structural health monitoring for reinforced concrete structures

Over the past few decades, many reinforced concrete structures around the world, such as bridges and dams, have failed due to aging or construction defects. Structural health monitoring (SHM) can be used to identify the structural damage state and provide early warning before the structure collapses. SHM can be used to detect the current state of the structure, including damage detection and location, damage assessment, and prediction of the remaining life of the structure. AE is a viable SHM method for evaluating damaged or deteriorated concrete structures such as bridges,[11-14] dams,[15] tunnels,[16] and nuclear containment vessels.[17,18]

In Taiwan, nuclear power plants have been operating for 40 years, and their life extension is currently under evaluation. If approved, repairs and prestressing updates will be necessary. During tendon replacement in shielding concrete, AE can support SHM for safety. Pullout tests of large reinforcing bars (D43 and D57) can reveal information about mechanical bond behavior through AE signals.

EXPERIMENTAL PROGRAM

This study experimentally investigated the bond between concrete and steel bars (D19, D32, D43, and D57 [No. 6, No. 10, No. 14, and No. 18 in the U.S. equivalent sizes]) using pullout tests combined with AE monitoring to characterize bond failure signals.

Table 1—Concrete mixtures

Mixture	A	B	C
w/c	0.62	0.52	0.45
Cement	2.93* (18.6)	3.46 (22.0)	3.96 (25.2)
Water	1.81 (11.5)	1.80 (11.5)	1.79 (11.4)
Aggregate	11.09 (70.5)	11.03 (70.1)	10.12 (64.4)
Sand	7.36 (46.8)	7.02 (44.6)	7.38 (46.9)
HRWRA	0.01 (0.06)	0.01 (0.07)	0.02 (0.10)

*Unit of weight is kN/m^3 (lb/ft^3).

Note: HRWRA is high-range water-reducing admixture.

Specimen preparation

Three concrete mixtures were used to prepare specimens, as shown in Table 1. Mixtures with water-cement ratios (*w/c*) of 0.62, 0.52, and 0.45 were used to create concrete specimens with strengths of 30.2, 34.6, and 47.3 MPa (4.38, 5.02, and 6.86 ksi), respectively. Single D19, D32, D43, and D57 steel bars were then separately embedded into specimens with each of the aforementioned strengths. To meet the requirements for concrete shielding with the embedded large reinforcing bar (D57) considered in this study, cubic specimens with a concrete cover of 10 cm (3.93 in.) and dimensions of 260 x 260 x 260 mm (10.2 x 10.2 x 10.2 in.) were prepared. Cylindrical concrete specimens with dimensions of ϕ100 x 200 mm (3.93 x 7.86 in.) of the same batch were also cast to determine the compressive strength of the concrete.

Pullout test

This study conducted pullout tests in compliance with the guidelines of ASTM C234 to investigate the bond between steel bars and concrete. All concrete specimens were cured for 28 days and tested on a universal testing machine, as shown in Fig. 1. The anchoring arrangements for each reinforcing bar size were designed individually, as shown in Fig. 2. The yield strengths of the D19, D32, D43, and D57 steel bars were determined to be 469, 483, 442, and 439 MPa (68.1, 70.1, 64.2, and 63.7 ksi), respectively. The yield strengths of the D43 and D57 steel bars were particularly determined by performing the reinforcing bar tensile tests on the round bars with a diameter of 25.4 mm (1 in.) that were milled from the original reinforcing bars. A rubber plate was placed on the contact surface between the steel bearing plate and the concrete specimen surface to ensure uniform stress transmission and avoid stress concentration. In addition, a linear variable differential transformer (LVDT) was set up to measure the slippage of the loaded end of the steel bar relative to the concrete specimen. All tests were conducted on the universal testing machine by using displacement control. The loading rate was 0.01 mm/s (0.0004 in./s). A data acquisition controller was used to record load data from the universal testing machine and slip data from the LVDT. These data were employed to analyze the mechanical behaviors corresponding to different AE signal patterns.

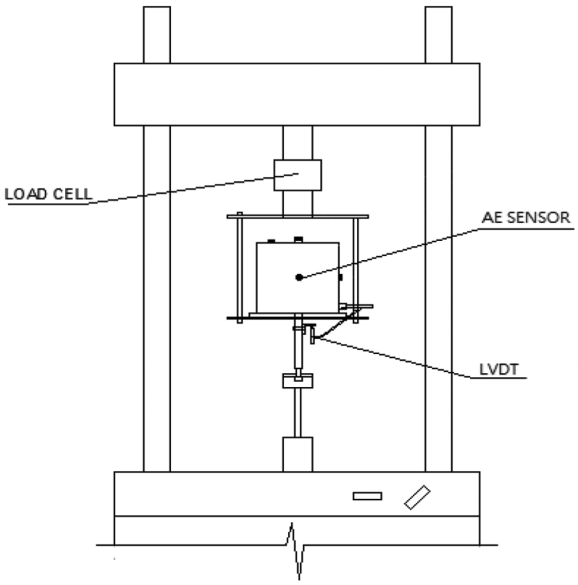

Fig. 1—Configuration of pullout test.

Fig. 2—D19, D32, D43, and D57 steel bars.

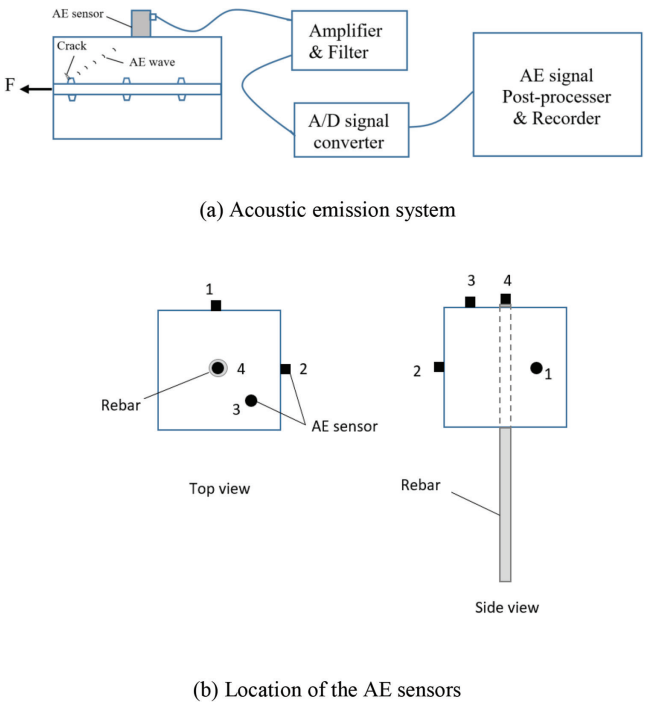

Fig. 3—Acoustic emission monitoring system.

AE monitoring

Throughout the testing process, AE monitoring was conducted to record the sound signals produced within the concrete. The AE monitoring system used in this study mainly comprised AE sensors, amplifiers, filters, and regulators, as shown in Fig. 3(a). The AE sensors received stress waves produced through the energy release caused by cracking, friction, or slippage at the interface between the steel and concrete. Amplifiers were used to amplify the very-low-amplitude signals received by the AE sensors into a usable form for analysis. In addition, AE signal filters were employed to eliminate noise from the detected waveforms. The acquired AE signals were subjected to analog-to-digital conversion, and both the original and converted signals were recorded. The AE system contained four AE sensors, each with a preamplifier gain of 40 dB and a resonant frequency of 150 kHz. These sensors were installed on different surfaces of each pullout specimen, as shown in Fig. 3(b): one sensor was placed on the top surface of the concrete, two other sensors were installed on different sides of the specimen, and the last sensor was installed on top of the steel bar protruding from the top face of the concrete specimen. Therefore, the differences in AE signal patterns for the concrete and steel bar could be compared. AE signals were recorded when the amplitude was higher than the 50 dB threshold. Furthermore, the received waveforms were digitized and converted into hit counts at a sampling rate of 800 kHz. The cumulative hit counts per second were recorded as the AE signal density. The recorded data could be compared with loading curves and analyzed.

RESULTS AND DISCUSSION

This study investigated the bond of concrete to embedded steel bars of different sizes in different loading stages. The bond properties of the prepared concrete specimens are summarized in Table 2.

Bond strength between concrete and steel bar

The stress acting on the steel bars in the pullout tests varied from zero at the free end to the maximum value at the loaded end.[30] The nominal bond strength was determined using one of the most widely used equations

$$U_u = \frac{P_u}{\pi DL} \tag{1}$$

where P_u is the critical tensile force in the pullout test; D is the diameter of the steel bar; and L is the length of embedment in the concrete specimen.

Table 2—Bond properties of concrete and steel bars of various sizes

f_c', MPa (ksi)	Reinforcing bar	P_u, kN (kip)	Bond strength		
			U_u^*, MPa (ksi)	$U_{u,OJB}$, MPa (ksi)	$U_u/\sqrt{f_c'}$
30.2 (4.38)	D19	92.8 (20.9)	5.98 (0.868)	10.9 (1.58)	1.09
	D32	118 (26.5)	4.52 (0.656)	8.21 (1.19)	0.82
	D43	125 (28.1)	3.55 (0.515)	7.75 (1.12)	0.65
	D57	139 (31.2)	2.98 (0.433)	7.96 (1.16)	0.54
34.6 (5.02)	D19	99.2 (22.3)	6.39 (0.927)	11.6 (1.68)	1.09
	D32	107 (24.0)	4.08 (0.592)	8.77 (1.27)	0.69
	D43	115 (25.8)	3.27 (0.475)	8.29 (1.20)	0.56
	D57	136 (30.6)	2.91 (0.422)	8.51 (1.24)	0.50
47.3 (6.82)	D19	106 (23.8)	6.82 (0.990)	13.6 (1.97)	0.99
	D32	131 (29.4)	5.00 (0.726)	10.3 (1.49)	0.73
	D43	153 (34.4)	4.36 (0.633)	9.70 (1.41)	0.63
	D57	179 (40.2)	3.84 (0.557)	9.97 (1.45)	0.56

*U_u was evaluated through a pullout test and by using Eq. (1), and $U_{u,OJB}$ was evaluated using Eq. (2).

The bond strength calculated from Eq. (2), provided by Orangun et al.,[3] which considers the effect of concrete cover and embedment length of the steel bar in concrete, was also evaluated (in MPa) for comparison.

$$U_{u,OJB} = \left(1.2 + 3\frac{c}{d_b} + 50\frac{d_b}{l_s}\right)\sqrt{f_c'} \tag{2}$$

where c is the thickness of the concrete cover; d_b is the diameter of the steel bar; and l_s is the length of embedment of the steel bar in concrete.

Table 2 shows that the bond strengths calculated using Eq. (2) were higher than those determined from the pullout tests and Eq. (1) for a given concrete strength and a reinforcing bar size. In addition, it also indicates that as the concrete strength increased by 56.6% from 30.2 to 47.3 MPa (4.38 to 6.86 ksi), the bond strengths of the specimens containing the D19, D32, D43, and D57 reinforcing bars increased by only 14.2%, 11.0%, 22.8%, and 28.8%, respectively. In addition, the nominal bond strength in terms of $U_u/\sqrt{f_c'}$ was strongly correlated with the steel bar diameter. However, the calculated bond strength in terms of $U_{u,OJB}/\sqrt{f_c'}$ is independent of the concrete strength for a given bar size. This is because the concrete cover, bar diameter, and embedment length are identical for a given bar in the specimen. The nominal bond strength and concrete strength decreased with increasing bar diameter. These results were attributable to changes in the concrete cover and geometry of the steel rib. At the same concrete strength, the ultimate bond stress decreased as the bar diameter was increased. Furthermore, for the same embedment length, smaller steel bars had a thicker concrete cover, a larger number of ribs, and smaller ribs, which reduced the likelihood of stress concentration. The test results, including those obtained from the D43 and D57 bars, basically comply with the provisions in ACI 408R-03.

The steel bar and concrete stresses at bond failure for various compressive strengths are shown in Table 3 and illustrated in Fig. 4. The ratio of the stress at bond failure to the yield strength was 70 to 80%, 27 to 34%, 18 to 24%, and 12 to 16% of the yield strength for the D19, D32, D43, and D57 steel bars, respectively. In general, the bond stress of the concrete reached the ultimate bond stress before the bar yielded.

Failure patterns of pullout specimens

The typical failure mechanism of a pullout specimen with a regular reinforcing bar is depicted in Fig. 5(a). This mechanism is divided into the following four phases: 1) loss of chemical adhesion; 2) splitting crack development; 3) concrete crushing near the ribs; and 4) shearing in the longitudinal direction. Among them, the splitting crack is the only phase induced by tensile stress, which involves the opening of a crack perpendicular to the direction of the applied tensile stress. It requires releasing much higher strain energy to overcome the cohesive forces holding the material together along the crack plane, as compared to those released by crushing and shear cracks. The first splitting crack dominates the sequent stress redistribution and failure mechanism of concrete.

For the specimens containing D43 and D57 steel bars, the failure mechanism was clearly affected by splitting rather than by loss of chemical bond and front rib crushing, as shown in Fig. 5(b). After the pullout test, it was observed that the area proportion of residual concrete attached to the surface of large steel bars (D43 and D57) appeared greater than that of small steel bars. The chemical adhesion and frictional resistance increased with increases in the area of the bar-concrete interface and the bearing from the ribs. Shear-off failure, a possible type of pullout failure, was not observed in this study because all the reinforcing bars used had a height-to-rib spacing that exceeded 0.10, according to Park and Paulay.[31]

Table 3—Bond stress of steel bars in pullout tests

f_c', MPa (ksi)	Reinforcing bar	Loading properties			
		P_u, kN (ksi)	f_{peak}, MPa (ksi)	f_y, MPa (ksi)	f_{peak}/f_y, %
30.2 (4.38)	D19	92.8 (20.9)	328 (47.6)	469 (68.1)	70
	D32	118 (26.5)	147 (21.3)	483 (70.1)	30
	D43	125 (28.1)	86 (12.5)	442 (64.2)	19
	D57	139 (31.2)	54 (7.80)	439 (63.7)	12
34.6 (5.02)	D19	99.2 (22.3)	350 (50.8)	469 (68.1)	75
	D32	107 (24.0)	132 (19.2)	483 (70.1)	27
	D43	115 (25.8)	79 (11.5)	442 (64.2)	18
	D57	136 (30.6)	53 (7.70)	439 (63.7)	12
47.3 (6.82)	D19	106 (23.8)	374 (54.3)	469 (68.1)	80
	D32	131 (29.4)	162 (23.5)	483 (70.1)	34
	D43	153 (34.4)	106 (15.4)	442 (64.2)	24
	D57	179 (40.2)	70 (10.2)	439 (63.7)	16

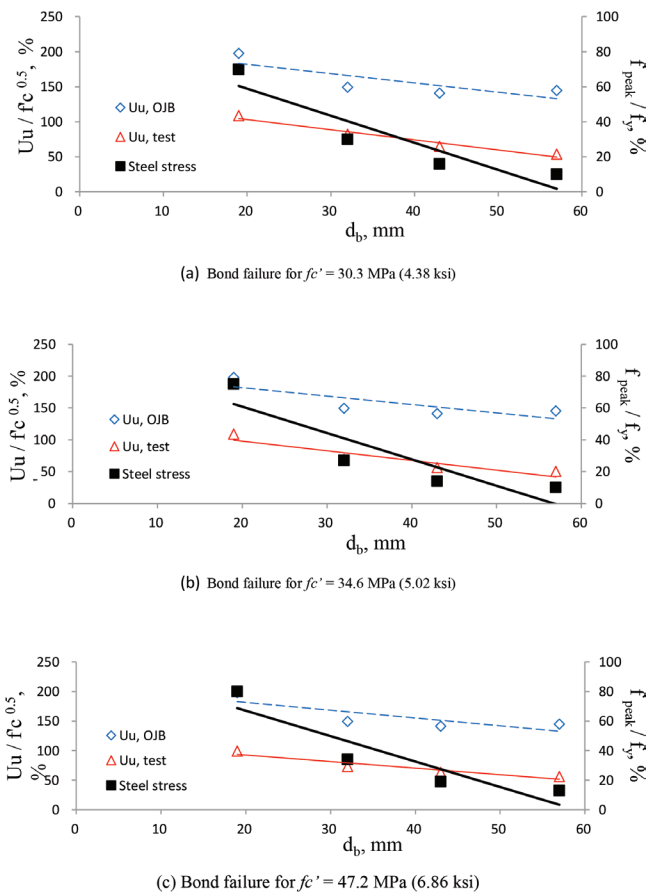

(a) Bond failure for fc' = 30.3 MPa (4.38 ksi)

(b) Bond failure for fc' = 34.6 MPa (5.02 ksi)

(c) Bond failure for fc' = 47.2 MPa (6.86 ksi)

Fig. 4—Stresses in steel and concrete at bond failure for various strengths.

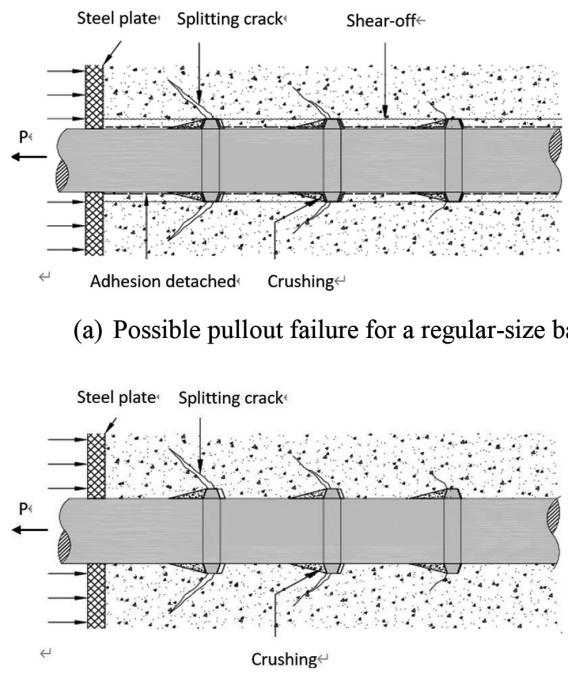

(a) Possible pullout failure for a regular-size bar

(b) Pullout failure for a large-size bar

Fig. 5—Pullout failure for steel bar embedded in concrete.

AE monitoring in pullout tests

In this study, the changes in the AE signal (expressed in hits per second) monitored for each pullout specimen during the load test revealed that the first peak (main peak) corresponds to the maximum load that causes the main splitting crack. Consequently, the entire loading process can be divided into three stages: Stage I, Stage II, and Stage III, corresponding to the three periods before, during, and after the generation of the first splitting crack, respectively. After Stage I, Stage II is measured starting from the rise time to the first valley after the first peak observed from the AE signal.

Concrete specimen with f_c' *= 30.2 MPa and embedded D19 steel bar*—The AE signal shown in Fig. 6 illustrates the behavior of a concrete specimen with a strength of 30.2 MPa (4.38 ksi) and a D19 steel bar during the pullout test. In the first stage (Stage I), the AE signal detected from the concrete appears to be weaker, which may be due to the loss of chemical adhesion resulting from the strain difference between the concrete and the steel bar. During this period, the signal detected from the steel bar appears to be stronger than that detected from the concrete. This is because the AE wave propagates faster and has less attenuation in the

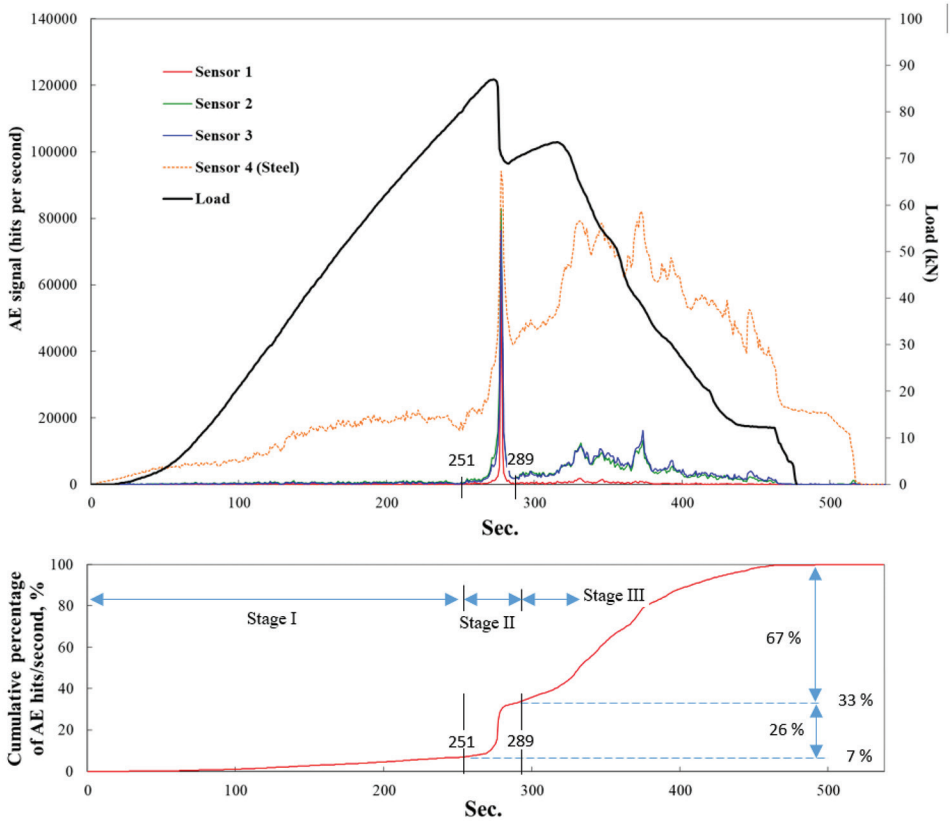

Fig. 6—AE analysis for specimen with D19 steel bar and f_c' *= 30.2 MPa (4.38 ksi). (Note: 1 kN = 0.225 kip.)*

steel bar.[21,28,32] The cumulated AE hit counts collected by four sensors from concrete in Stage I account for approximately 7% of the total signal calculated from the entire loading duration, which is approximately equivalent to the energy released in this stage. In the second stage (Stage II), the signal started to rise at 251 seconds, reached a peak at 277 seconds, and ended at 289 seconds. The main peak of the AE signal corresponds to the maximum load that causes the splitting crack to release the fracture energy. The released energy is much higher than that caused by friction, shear, and crushing cracks in concrete. The splitting (tensile) crack can produce an AE waveform with a shorter rise time, shorter duration, and higher frequency than a shear crack.[33] The rise time during this period is 26 seconds. The cumulative AE hit counts captured in Stages II and III account for 26% and 57% of the total hit counts, respectively.

Concrete specimen with f_c' *= 47.3 MPa and embedded D19 steel bar*—The AE signal shown in Fig. 7 illustrates the behavior of the specimen with a concrete strength of 47.3 MPa (6.86 ksi) and a D19 steel bar during the pullout test. During the first stage (Stage I), the AE signal detected from the concrete appeared to be stronger than that of concrete strength of 30.2 MPa (4.38 ksi), but the signal detected from the steel bars appeared to be weak. The phenomenon can be attributed to the higher concrete strength, which enhanced the adhesion at the interface and the shear resistance of concrete along the steel bar. These AE signals resulted from the microcracks formed by the concrete near the ribs, which was subjected to the stress transferred from the steel reinforcing bar. The ribs on the small bar can distribute the stresses more uniformly along the steel bar.[2] The ribs share the higher stresses transferred from the steel bar in this stage. The cumulated AE hit counts collected in Stage I account for approximately 35.2% of the total signal volume, approximately equal to the energy released in this stage. It was then observed that the signal in Stage II began to rise at 231 seconds, reached a peak at 273 seconds, and ended at 285 seconds. The cumulative AE hit counts captured in Stages II and III account for 26.0% and 38.8% of the total hit counts, respectively.

Concrete specimen with f_c' *= 30.2 MPa and embedded D57 steel bar*—The AE signal shown in Fig. 8 illustrates the behavior of a specimen with a concrete strength of 30.2 MPa (4.38 ksi) and a D57 reinforcing bar during the load test. In Stage I, the AE signal obtained from the concrete appeared to be stronger than that of the D19 reinforcing bar. This can be attributed to the fact that the D57 steel bar used in this study has a rougher surface (as shown in Fig. 2) and a larger area surrounded by concrete, as compared with the D19 steel bar. When the concrete at the interface is subjected to stresses transmitted from the steel bars, it is more likely that local stress concentration will occur in the concrete at the uneven places of the steel bars, resulting in increased strain or microcracks at those locations in the concrete. The AE signal detected from the steel bar still appears to be stronger than that from the concrete in this case. The cumulated AE hit counts captured in Stage I account for approximately 11% of the total hit counts, which is approximately equal to the energy released in this stage. The signal of Stage II started to rise at 224 seconds, reached the peak at 256 seconds,

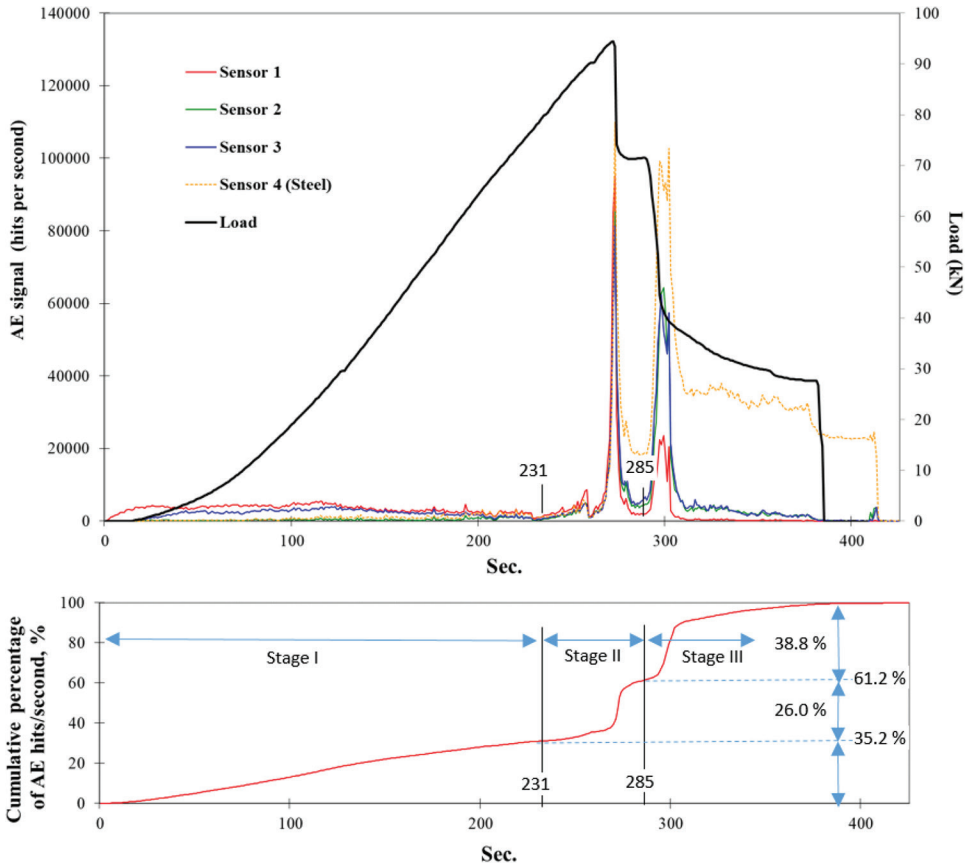

Fig. 7—AE analysis for specimen with D19 steel bar and f_c' *= 47.3 MPa (6.86 ksi). (Note: 1 kN = 0.225 kip.)*

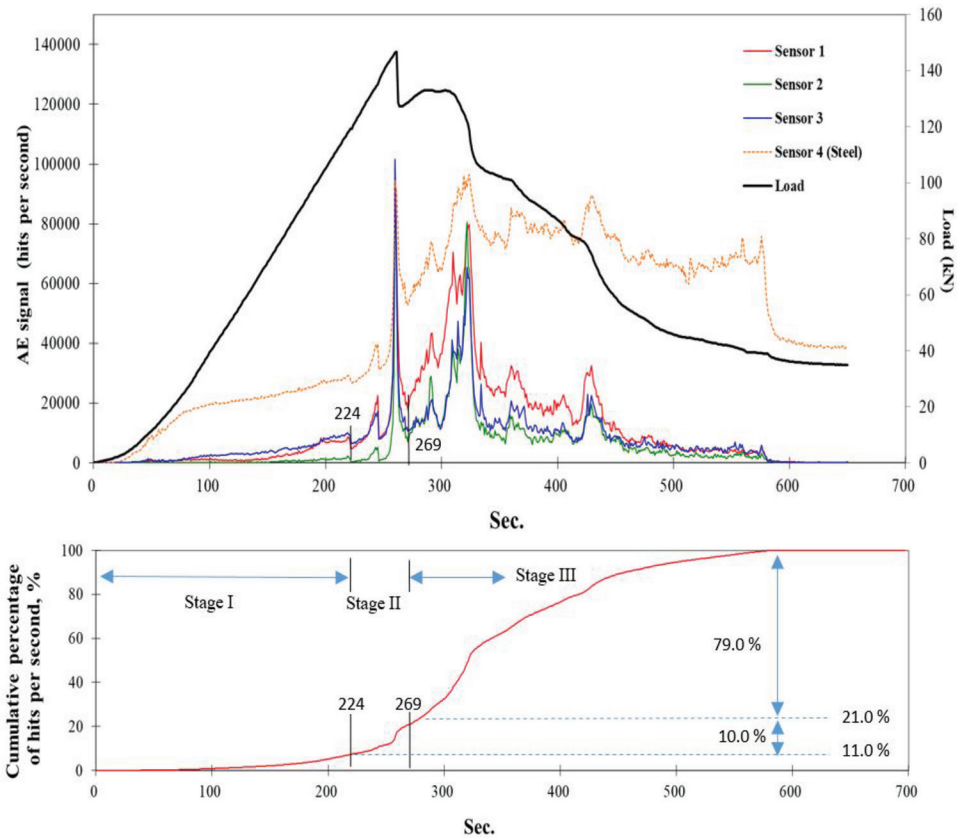

Fig. 8—AE analysis for specimen with D57 steel bar and f_c' *= 30.2 MPa (4.38 ksi). (Note: 1 kN = 0.225 kip.)*

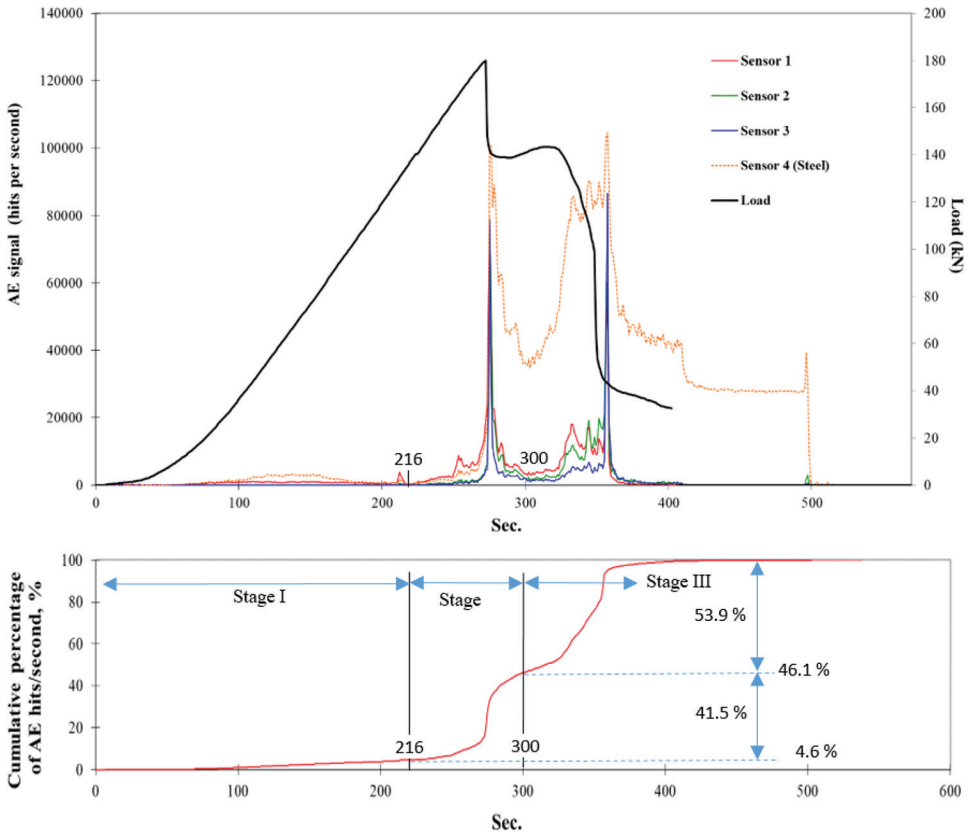

Fig. 9—AE analysis for specimen with D57 steel bar and f_c' *= 47.3 MPa (6.86 ksi). (Note: 1 kN = 0.225 kip.)*

and ended at 269 seconds, which corresponds to the main valley after the peak. The rise time during this period was 32 seconds. The cumulated AE hit counts captured in Stage II account for approximately 10% of the total hit counts. The cumulative AE hit counts captured in Stage III account for 79% of the total hit counts.

Concrete specimen with f_c' *= 47.3 MPa and embedded D57 steel bar*—The AE signal shown in Fig. 9 illustrates the behavior of the specimen with a concrete strength of 47.3 MPa (6.86 ksi) and a D57 steel bar during the pullout test. In Stage I, the AE signal appeared weak for both the concrete and steel as the load was increased. The higher concrete strength seems to enhance the adhesion at the interface between the concrete and steel bar. These signals resulted from the microcracks in concrete due to the roughness of the reinforcing bar surface, which led to stress concentration, as mentioned previously. Furthermore, the concrete embedded by the D57 steel bar had a larger surrounding area and bearing area of the ribs to sustain the stresses transferred from the steel bar. The stresses were then increased until the first splitting crack was induced when the radial tensile stress exceeded the tensile strength of concrete. The cumulated AE hit counts collected in Stage I account for approximately 4.6% of the total hit counts in this stage. The signal in Stage II began to rise at 216 seconds, reached a peak at 275 seconds, and ended at 300 seconds. The rise time during this period was 59 seconds. The cumulated AE hit counts captured in Stages II and III account for approximately 41.5% and 54.6% of the total hit counts, respectively.

CONCLUSIONS

This study examined the bond behavior of concrete embedded with steel reinforcing bars of various sizes using pullout tests and acoustic emission (AE) signal monitoring. The conclusions of this study are as follows:

1. For a given concrete strength, the bond strength decreased as the steel bar diameter increased. The results of large-size reinforcing bars (D43 and D57) are consistent with the provisions in ACI 408R-03. Furthermore, the crack width increased with an increase in the steel bar diameter.

2. Bond strengths calculated using the Orangun et al. equation, which considers cover and embedment, were higher than those from pullout tests.

3. At the ultimate bond force for a given concrete strength in the pullout test, the stress in the D19 steel bar reached 70 to 80% of the yield strength, while that in the D57 steel bar attained only 12 to 16% of the yield strength.

4. AE signals reveal three stages in a pullout test: Stage I (pre-splitting), Stage II (first splitting crack), and Stage III (post-crack stress redistribution). Higher concrete strength improves adhesion in Stage I, while Stage II dominates energy release and failure.

5. Cumulative AE hit counts can quantify energy released at each stage, influenced by concrete strength and reinforcing bar properties such as diameter, surface roughness, and rib geometry.

AUTHOR BIOS

Yu-Cheng Kan *is an Associate Professor in the Department of Construction Engineering at Chaoyang University of Technology, Taichung, Taiwan. He received his MS and PhD from Kansas State University, Manhattan,*

KS, in 1993. His research interests include fracture mechanics and crack repair of concrete.

Kuang-Chih Pei *is a Senior Engineer at the National Atomic Research Institute in Taiwan. He received his MS and PhD from Colorado State University, Fort Collins, CO, in 1997. His research interests include the application of the acoustic emission technique to concrete structures and nuclear power plant facilities.*

Jyun-Ruei Wu *is a Master's Student of the first author. He received his master's degree from Chaoyang University of Technology and is a Project Manager of a construction company in Taiwan.*

ACKNOWLEDGMENTS

This research fund is supported by the Ministry of Science and Technology (National Science Council) with Grant NSC-100-2211-E-324-018 and the Institute of Nuclear Energy Research with Grant NL 0991009, which are sincerely acknowledged. The authors wish to thank H.-Y. Wang and Y.-S. Yap, who provided technical assistance for the experimental work.

REFERENCES

1. Ferguson, P. M.; Breen, J. E.; and Thompson, J. N., "Pullout Tests on High Strength Reinforcing Bars, Part 1," *ACI Journal Proceedings*, V. 62, No. 8, Aug. 1965, pp. 933-950.

2. ACI Committee 408, "Bond and Development of Straight Reinforcing Bars in Tension (ACI 408R-03) (Reapproved 2012)," American Concrete Institute, Farmington Hills, MI, 2003, 49 pp.

3. Orangun, C. O.; Jirsa, J. O.; and Breen, J. E., "A Reevaluation of Test Data on Development Length and Splices," *ACI Journal Proceedings*, V. 74, No. 3, Mar. 1977, pp. 114-122.

4. Darwin, D.; McCabe, S. L.; Idun, E. K.; and Schoenekase, S. P., "Development Length Criteria: Bars Not Confined by Transverse Reinforcement," *ACI Structural Journal*, V. 89, No. 6, Nov.-Dec. 1992, pp. 709-720.

5. Soroushian, P., and Choi, K.-B., "Local Bond of Deformed Bars with Different Diameters in Confined Concrete," *ACI Structural Journal*, V. 86, No. 2, Mar.-Apr. 1989, pp. 217-222.

6. ACI Committee 349, "Code Requirements for Nuclear Safety-Related Concrete Structures (ACI 349-13) and Commentary," American Concrete Institute, Farmington Hills, MI, 2014, 196 pp.

7. Joint ACI-ASME Committee 359, "Code for Concrete Containments (ACI 359-01)," American Concrete Institute, Farmington Hills, MI, 2001.

8. Gambarova, P. G.; Rosati, G. P.; and Zasso, B., "Steel-to-Concrete Bond After Concrete Splitting: Test Results," *Materials and Structures*, V. 22, No. 1, Jan. 1989, pp. 35-47. doi: 10.1007/BF02472693

9. Goto, Y., "Cracks Formed in Concrete Around Deformed Tension Bars," *ACI Journal Proceedings*, V. 68, No. 4, Apr. 1971, pp. 244-251.

10. Lutz, L. A., and Gergely, P., "Mechanics of Bond and Slip of Deformed Bars in Concrete," *ACI Journal Proceedings*, V. 64, No. 11, Nov. 1967, pp. 711-721.

11. Yapar, O.; Basu, P. K.; Volgyesi, P.; and Ledeczi, A., "Structural Health Monitoring of Bridges with Piezoelectric AE Sensors," *Engineering Failure Analysis*, V. 56, Oct. 2015, pp. 150-169. doi: 10.1016/j.engfailanal.2015.03.009

12. Nair, A., and Cai, C. S., "Acoustic Emission Monitoring of Bridges: Review and Case Studies," *Engineering Structures*, V. 32, No. 6, June 2010, pp. 1704-1714. doi: 10.1016/j.engstruct.2010.02.020

13. Yuyama, S.; Yokoyama, K.; Niitani, K.; Ohtsu, M.; and Uomoto, T., "Detection and Evaluation of Failures in High-Strength Tendon of Prestressed Concrete Bridges by Acoustic Emission," *Construction and Building Materials*, V. 21, No. 3, Mar. 2007, pp. 491-500. doi: 10.1016/j.conbuildmat.2006.04.010

14. Shiotani, T.; Oshima, Y.; Goto, M.; and Momoki, S., "Temporal and Spatial Evaluation of Grout Failure Process with PC Cable Breakage by Means of Acoustic Emission," *Construction and Building Materials*, V. 48, Nov. 2013, pp. 1286-1292. doi: 10.1016/j.conbuildmat.2013.04.026

15. Li, S.; Chen, X.; and Zhang, J., "Acoustic Emission Characteristics in Deterioration Behavior of Dam Concrete Under Post-Peak Cyclic Test," *Construction and Building Materials*, V. 292, July 2021, Article No. 123324. doi: 10.1016/j.conbuildmat.2021.123324

16. Liu, F.; Guo, R.; Lin, X.; Zhang, X.; Huang, S.; Yang, F.; and Cheng, X., "Monitoring the Damage Evolution of Reinforced Concrete During Tunnel Boring Machine Hoisting by Acoustic Emission," *Construction and Building Materials*, V. 327, Apr. 2022, Article No. 127000. doi: 10.1016/j.conbuildmat.2022.127000

17. Hamdi, S. E.; Sbartaï, Z.-M.; Boniface, A.; Saliba, J.; and Henault, J.-M., "Pressure-Induced Damage Monitoring in Prestressed Concrete of Nuclear Containment Wall Segments Using Acoustic Emission Technique – Application to VeRCoRs Containment Building," *Engineering Fracture Mechanics*, V. 281, Mar. 2023, Article No. 109089. doi: 10.1016/j.engfracmech.2023.109089

18. Ebrahimkhanlou, A.; Choi, J.; Hrynyk, T. D.; Salamone, S.; and Bayrak, O., "Acoustic Emission Monitoring of Containment Structures During Post-Tensioning," *Engineering Structures*, V. 209, Apr. 2020, Article No. 109930. doi: 10.1016/j.engstruct.2019.109930

19. Liu, M.; Lu, J.; Ming, P.; and Song, J., "AE-Based Damage Identification of Concrete Structures Under Monotonic and Fatigue Loading," *Construction and Building Materials*, V. 377, May 2023, Article No. 131112. doi: 10.1016/j.conbuildmat.2023.131112

20. Landis, E. N., and Shah, S. P., "Frequency-Dependent Stress Wave Attenuation in Cement-Based Materials," *Journal of Engineering Mechanics*, ASCE, V. 121, No. 6, June 1995, pp. 737-743. doi: 10.1061/(ASCE)0733-9399(1995)121:6(737)

21. Aggelis, D. G., "Classification of Cracking Mode in Concrete by Acoustic Emission Parameters," *Mechanics Research Communications*, V. 38, No. 3, Apr. 2011, pp. 153-157. doi: 10.1016/j.mechrescom.2011.03.007

22. Ohtsu, M., ed., *Acoustic Emission (AE) and Related Non-destructive Evaluation (NDE) Techniques in the Fracture Mechanics of Concrete: Fundamentals and Applications*, Woodhead Publishing, Sawston, UK, 2015.

23. RILEM Technical Committee 212-ACD., "Recommendation of RILEM TC 212-ACD: Acoustic Emission and Related NDE Techniques for Crack Detection and Damage Evaluation in Concrete," *Materials and Structures*, V. 43, No. 9, Nov. 2010, pp. 1187-1189. doi: 10.1617/s11527-010-9640-6

24. JCMS-III B5706, "Monitoring Method for Active Cracks in Concrete by Acoustic Emission," Japan Construction Material and Housing Equipment Industries Federation, Tokyo, Japan, 2003.

25. Noorsuhada, M. N., "An Overview on Fatigue Damage Assessment of Reinforced Concrete Structures with the Aid of Acoustic Emission Technique," *Construction and Building Materials*, V. 112, June 2016, pp. 424-439. doi: 10.1016/j.conbuildmat.2016.02.206

26. Carpinteri, A.; Lacidogna, G.; and Pugno, N., "Structural Damage Diagnosis and Life-Time Assessment by Acoustic Emission Monitoring," *Engineering Fracture Mechanics*, V. 74, No. 1-2, Jan. 2007, pp. 273-289. doi: 10.1016/j.engfracmech.2006.01.036

27. Yuyama, S.; Okamoto, T.; Shigeishi, M.; and Ohtsu, M., "Quantitative Evaluation of Fracture Processes in Concrete Using Acoustic Emission," *Materials Evaluation*, V. 53, No. 6, 1995, pp. 882-889.

28. Grosse, C. U., and Finck, F., "Quantitative Evaluation of Fracture Processes in Concrete Using Signal-Based Acoustic Emission Techniques," *Cement and Concrete Composites*, V. 28, No. 4, Apr. 2006, pp. 330-336. doi: 10.1016/j.cemconcomp.2006.02.006

29. Xiao, J., and Falkner, H., "Bond Behaviour Between Recycled Aggregate Concrete and Steel Rebars," *Construction and Building Materials*, V. 21, No. 2, Feb. 2007, pp. 395-401. doi: 10.1016/j.conbuildmat.2005.08.008

30. MacGregor, J. G., and Wight, J. K., *Reinforced Concrete: Mechanics and Design*, fourth edition, Pearson Prentice Hall, Upper Saddle River, NJ, 2005.

31. Park, R., and Paulay, T., *Reinforced Concrete Structures*, John Wiley & Sons, Inc., New York, 1975.

32. Saliba, J., and Mezhoud, D., "Monitoring of Steel-Concrete Bond with the Acoustic Emission Technique," *Theoretical and Applied Fracture Mechanics*, V. 100, Apr. 2019, pp. 416-425. doi: 10.1016/j.tafmec.2019.01.034

33. Ospitia, N.; Korda, E.; Kalteremidou, K.-A.; Lefever, G.; Tsangouri, E.; and Aggelis, D. G., "Recent Developments in Acoustic Emission for Better Performance of Structural Materials," *Developments in the Built Environment*, V. 13, Mar. 2023, Article No. 100106. doi: 10.1016/j.dibe.2022.100106

JOIN AN ACI Chapter!

The American Concrete Institute has Chapters and Student Chapters located throughout the world. Participation in a local chapter can be extremely rewarding in terms of gaining greater technical knowledge and networking with leaders in the concrete community.

Because chapters are distinct and independent legal entities, membership includes both ACI members and non-ACI members and is made up of a diverse blend of architects, engineers, consultants, contractors, educators, material suppliers, equipment suppliers, owners, and students—basically anyone interested in concrete. Many active ACI members initially became involved in ACI through their local chapter. In addition to technical programs and publications, many chapters sponsor ACI Certification programs, ACI educational seminars, project award recognition programs, and social events with the goal of advancing concrete knowledge.

To find a chapter near you, go to: https://www.concrete.org/getinvolved/chapters.aspx

---

Student Chapters

Join or form an ACI Student Chapter to maximize your influence, knowledge sharing, and camaraderie! ACI has 240+ student chapters located throughout the world, each providing opportunities for students to:

- Connect with their peers and participate in concrete-related activities such as: student competitions, ACI Conventions, ACI Certification Programs, ACI Educational Seminars, local chapter meetings, social events, and community service projects;
- Network with members of local chapters, many of whom have been in the industry for decades and can help to develop professional relationships and offer career advice;
- Win recognition for their universities through the University Award; and
- Learn about the many scholarships and fellowships offered by the ACI Foundation and by ACI's local chapters.

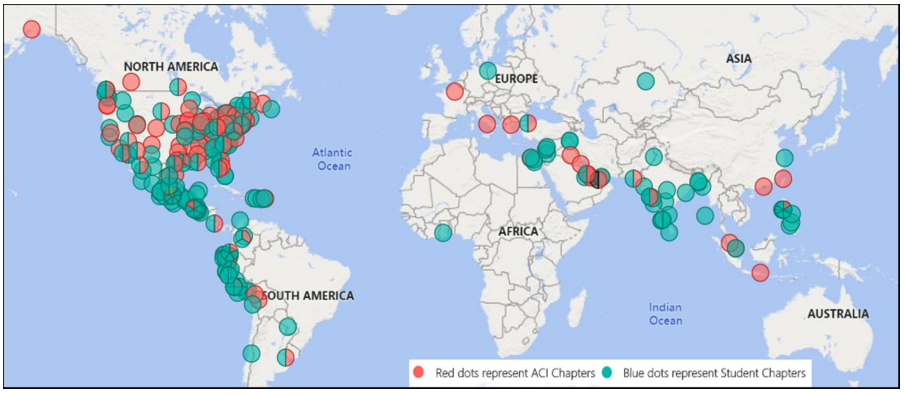

American Concrete Institute

www.concrete.org/getinvolved/chapters.aspx

ACI STRUCTURAL JOURNAL TECHNICAL PAPER

Title No. 123-S46

Sensing-Based Simulation of Bending Moments in Reinforced Concrete Columns

by Amir Iranmanesh, Mahsa Panahi, and Farhad Ansari

Integrating real-time sensor data with physics-based models enhances the accuracy and efficiency of structural simulation and prognosis. In this study, a sensing-based simulation method is introduced to compute bending moments in reinforced concrete bridge columns subjected to seismic motions, based on the measured strains continuously fed into plasticity models. The experimental program included hybrid testing of scaled reinforced concrete bridges under consecutive seismic events. The experimental columns were instrumented with embedded as well as surface-adhered fiber-optic Bragg grating (FBG) sensors for real-time monitoring of strains, reflecting degradation of the columns during the formation of damage. The fundamental assumption of strain compatibility in reinforced concrete members was investigated for the successive progression of damage in the cross sections of the columns. The stress distributions within the concrete core and cover were computed through the confined and unconfined concrete stress-strain relations for loading, unloading, and reloading scenarios. The bending moments in the cross section were computed and compared with the corresponding experimental values calculated based on direct measurements of forces. The results from this study revealed that the cross-sectional strains exhibit three primary features during the seismic events that need to be considered for the accurate calculation of bending moments. Computation of the bending moments requires consideration of the shifts in cyclic reference, post-event residual strains, and real steel strains. Using these features, the computed bending moments during the column tests mimicked the experimental results based on the measured seismic forces on the columns.

Keywords: columns; confined concrete; fiber-optic sensors; plasticity; reinforced concrete; seismic loading; sensing-based simulation; structural health monitoring; theoretical stress-strain model.

INTRODUCTION

Bridges form crucial links in the transportation network, especially in the aftermath of earthquakes. In high-seismic zones, bridges may experience accumulation of damage from a variety of seismic motions they may experience throughout their lifetime. Accumulation of low and moderate damage, which is barely visible, makes the reinforced concrete bridges structurally deficient.[1] Past experiences reveal that without proper monitoring and maintenance, catastrophic failures are inevitable. Real-time structural health monitoring can be an effective and affordable methodology to postpone costly repair and replacement tasks and prevent tragic events. In essence, structural health monitoring is the process of determining structural integrity by continuously collecting data using an array of sensors and making a prognosis by assessing certain structural quantities.[2] Piers, including reinforced concrete columns with circular cross sections, are common structural subsystems used in modern bridge construction.[3] In high-seismic zones, the piers are designed to undergo inelastic deformations through the formation of plastic hinges in the columns. The gradual formation of plastic hinges is a mechanism to dissipate energy. Under seismic motions with progressively increasing amplitudes, the damage begins with hairline cracks, continues with the formation of a local mechanism, and leads to the buckling of the longitudinal steel reinforcement and the crushing of the concrete core.[4] In small and moderate states, the damage is pronounced in the form of invisible or barely visible defects in the aftermath of earthquakes, such as residual crack openings, internal cracks, and voids, as well as debonding between the steel and concrete.[1] To properly monitor the seismic behavior of reinforced concrete members, in addition to the strains and displacements, the forces and bending moments must be continuously measured to provide relevant information on the loading history of the member.[5] Accurate real-time measurement of forces in reinforced concrete members, especially when they are subjected to seismic motions during earthquakes, is not always pragmatic. The proposed solution in this paper involves the indirect computation of stresses based on the directly measured strains using plasticity material models. The structural health monitoring methods for reinforced concrete members that have been investigated in the literature, such as smart aggregates,[6] long-gauge fiber optics,[7] and distributed optical fiber sensors,[8] are effective for detecting strain and cracking, but they do not quantify the evolution of internal forces under degradation and accumulation of damage. The proposed sensing-based simulation method addresses this gap by enabling continuous computation of bending moments. Long-gauge fiber-optic sensors are too large to be embedded within the circumference of the column. Fiber-optic distributed sensors are suitable for measuring internal strains and cracks when embedded in concrete. However, the dependency of noise levels on the spatial resolution of measurements for distributed sensors renders the method inferior to the approach presented herein.

For monitoring internal strains and cracking, fiber-optic sensors were the best choice because of their geometric compatibility with structural forms and high resolution for measuring small displacements. Their capability for serial

ACI Structural Journal, V. 123, No. 3, May 2026.
MS No. S-2024-240.R3, doi: 10.14359/51749316, received September 3, 2025, and reviewed under Institute publication policies. Copyright © 2026, American Concrete Institute. All rights reserved, including the making of copies unless permission is obtained from the copyright proprietors. Pertinent discussion including author's closure, if any, will be published ten months from this journal's date if the discussion is received within four months of the paper's print publication.

multiplexing makes them ideal for the synchronized acquisition of dynamic seismic-induced signals. A fiber-optic Bragg grating (FBG) sensor was employed to monitor strain and cracking at the surface of the concrete.[9] Internal strains in concrete were measured by an embedded FBG sensor,[10] and strains in the reinforcing bars were also monitored by FBG sensors.[11] Details about the attributes of optical fiber sensors in structural monitoring have been discussed in several studies.[10,12,13] FBG sensors have been used for embedment within reinforced concrete and in several bridges across the globe.[11,14,15]

The scope of this paper includes the development of a methodology to compute the bending moments in reinforced concrete columns by inputting real-time and continuous strain data. The methodology was examined in a reinforced concrete column subjected to five seismic events with progressively varying amplitudes. FBG sensors were used in the experiment to measure strains in the plastic hinge area. The proposed approach involves the determination of strain distribution throughout seismic events and highlights the importance of embedded sensing. The computed results were compared and validated by the bending moments, which were calculated based on the directly measured forces. Experimental details are briefly described next, followed by the formulation of the plasticity model and the computation of the force history of the pier due to several cycles of seismic motions.

RESEARCH SIGNIFICANCE

The study introduces a novel sensing-based simulation method to compute bending moments in reinforced concrete columns based on locally measured strain data continuously fed into plasticity models of concrete and steel. The method is validated through an experimental program that includes hybrid simulations of scaled reinforced concrete bridges subjected to consecutive seismic events. FBG sensors were used for real-time sensing of strains. The study highlights the importance of embedded sensing and continuous monitoring to achieve an accurate and computationally efficient sensing-based simulation method that can be used for real-time prognosis of reinforced concrete structures in earthquake-prone areas.

EXPERIMENTAL PROGRAM

Hybrid simulation-based experimental program

The reinforced column considered in this research was the physical part of a scaled hybrid model formerly studied by the authors.[1] The hybrid simulations were performed on scale models of a two-span bridge tested in an earlier study.[16] The bridge in the earlier study was a quarter-scale model of a two-span reinforced concrete highway bridge. The bridge was tested to failure using the multiple shake-table system under a series of progressively increasing ground motions of the 1994 Northridge earthquake in California. In the context of the present research, hybrid simulation refers to an experimental-numerical testing technique that combines physical testing of critical components with numerical modeling of the remainder of the structure. The details of the hybrid simulations can be found in the studies previously published by the authors.[1,17]

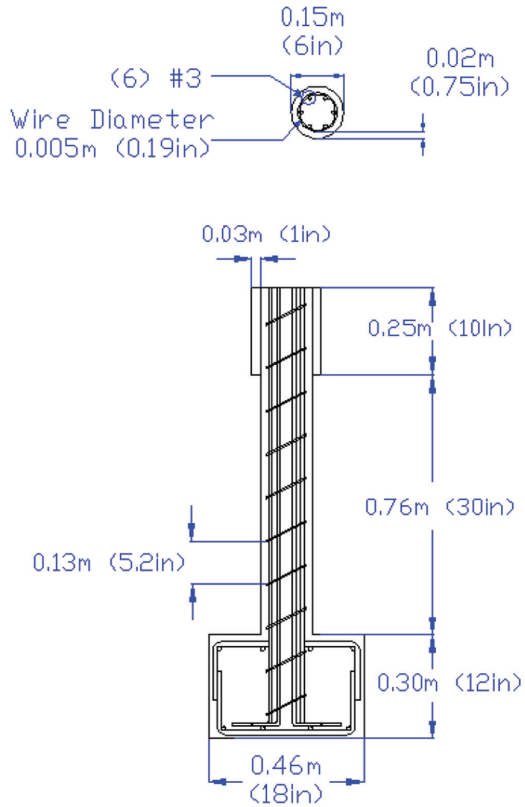

Fig. 1—Geometry and reinforcement of investigated concrete column.

The numerical part of the hybrid models includes all the components of the bridge structure, except for one column, which is simulated physically in the laboratory. The physical portion of the hybrid simulations consists of scaled, well-confined reinforced concrete columns instrumented with an array of fiber-optic sensors along the diameter of the circular cross section in the plastic hinge zone. The tests on the hybrid models of the bridge were carried out by applying earthquake excitations to the base of the hybrid models. To achieve the objectives of the present study, a one-eighth scale column, which served as an experimental element of a hybrid model, was investigated in detail. The column was subjected to five successive seismic motions with progressively increasing amplitudes, mimicking earthquake excitations with 0.075 to 1.00*g* peak ground accelerations. The geometry, dimensions, and reinforcement of the one-eighth concrete column are detailed in Fig. 1. A sample acceleration time history of the third seismic event inserted into the base of the hybrid models is presented in Fig. 2.

A self-equilibrium steel reaction frame was designed and manufactured to provide support for the concrete columns, and the actuator applied the loadings to the top end of the columns. A load cell with a capacity of ±490 kN connected the actuator to the specimens to measure the resisting forces. A linear variable differential transformer (LVDT) with a displacement range of ±76 mm was employed to measure the displacements at the top of the columns and to return the feedback required by the servo-hydraulic system and the

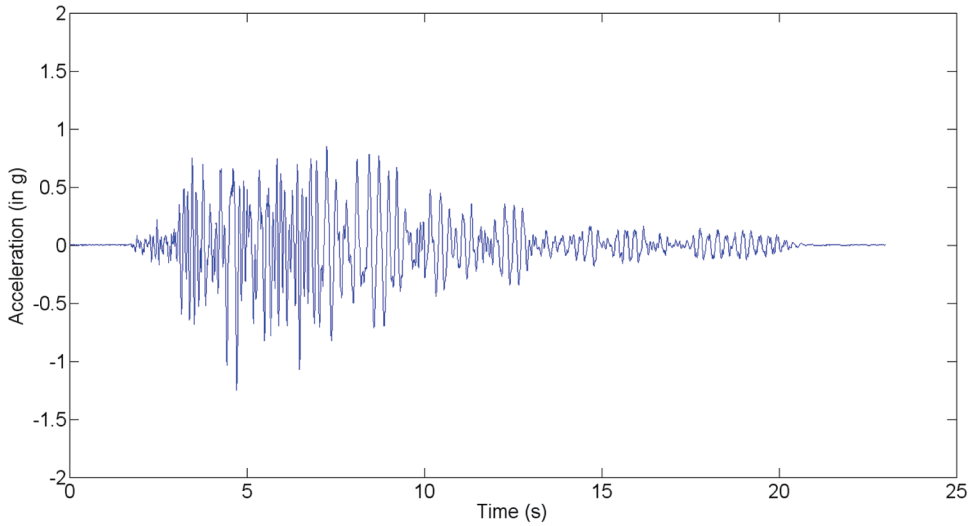

Fig. 2—Ground motion, transverse bridge direction, Event 5.

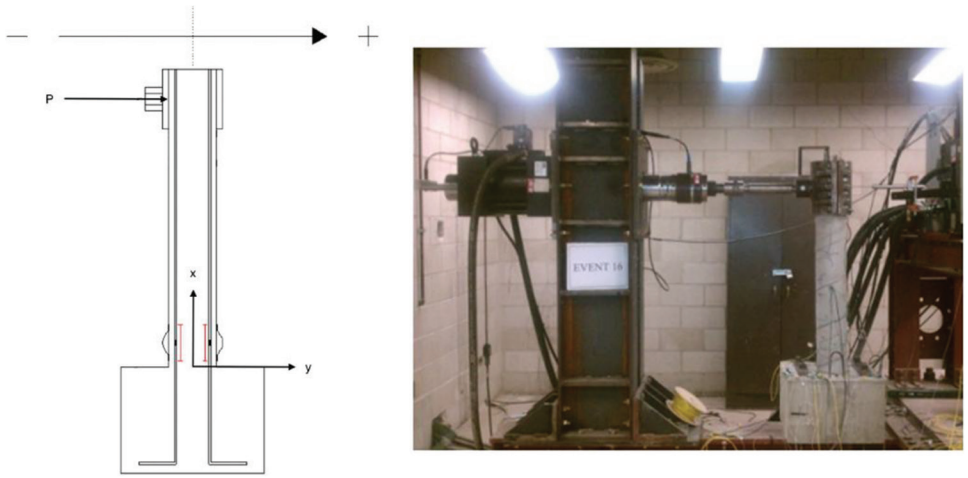

(a) (b)

Fig. 3—(a) Schematic; and (b) picture of test setup and actuator position for studied specimen.

hybrid models. Figure 3 displays the test setup and actuator positions for the studied reinforced concrete column.

The lateral response of the studied reinforced concrete column is dominated by the bending behavior. It was rationally expected that a plastic hinge, along with the majority of cracks, would form at the bottom of the column after the column undergoes large lateral displacements.[18] To thoroughly capture the dominant mechanics in the plastic hinge region, three types of FBG sensors were employed to continuously measure the deformations and strains in each distinct part of the reinforced concrete column section. Internal concrete sensors were embedded inside the column core, while the arch-shaped sensors were mounted on the external surface of the concrete cover. The FBG strain sensors were installed on the two longitudinal reinforcing bars on the opposite sides of the cross section. The sensors were installed across the diameter of the studied circular section in the direction of the applied loading. Figure 4 shows the arrangement of sensors across the circular section of the column. Pictures of the manufactured and installed sensors, including the concrete embedded sensor, arch sensor, and steel sensor, are shown in Fig. 5.

Measured strains

In this study, the displacements measured by the arch sensors and the concrete embedded sensors were divided by their corresponding gauge lengths to obtain the average normal strains. Figure 6 shows the first 800 data points of strains measured by all the sensors at the beginning of the test. In this paper, it is assumed that compressive strain and stress are positive and tensile strain and stress are negative. In the very first cycle, the left sensors show positive strains, indicating that the left side of the column undergoes compression first. The authors connected the points of intersections of the left and right signals from the same type of sensors by a line and called it the "cyclic reference." The cyclic reference represents the line around which the arch, steel, and concrete embedded sensors oscillate during seismic events. Herein, the observed phenomenon is that the cyclic reference lines for all three types of sensors are zero for the first couple of cycles, then gradually shift downward

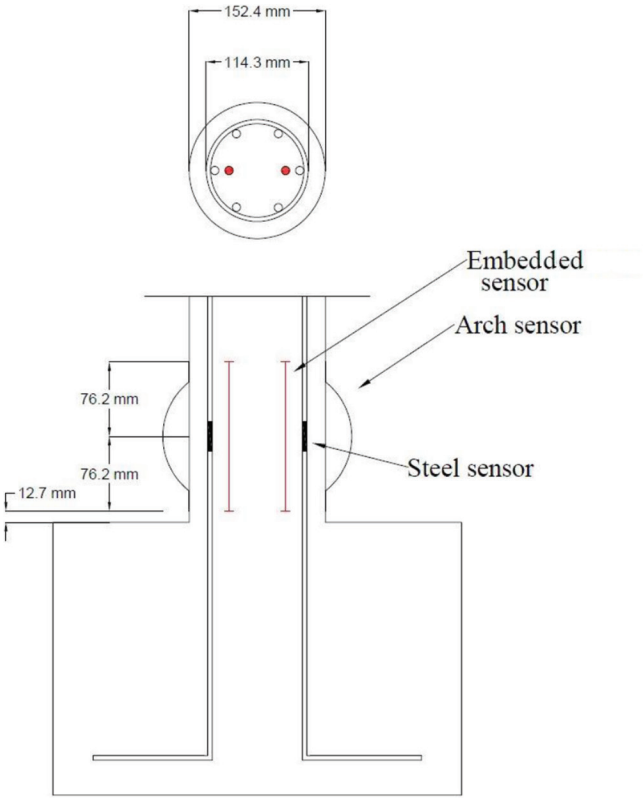

Fig. 4—Sensor arrangement across circular section of studied column.

for the next three cycles, and finally become stable for the rest of the event. As the amplitudes of seismic events progressively increase, the shift in the cyclic reference of the sensors becomes larger. Increases in the successive amplitudes of seismic events further damage the column, resulting in a more degraded reloading stiffness and a more nonlinear distribution of stresses. This phenomenon suggests a correlation between the shift in cyclic reference and the gradual degradation of stiffness and stress redistribution. It will be thoroughly demonstrated in a later section of this paper that capturing this phenomenon is essential for the predictive capability of the proposed sensing-based simulation method for long-term or future seismic events.

A similar trend is observable in the rest of the events, as depicted in Fig. 7. Figure 7 shows the strains measured by the arch and steel sensors throughout Events 1 through 5. In addition to the shift of cyclic reference, a second observable feature in this plot is the fact that the final strain point from every sensor in each event is considered as the initial strain point of the next event. Thus, the cyclic reference line is straight and does not shift up or down in transition from one event to the next. In other words, the post-event residual strains were not neglected.

Figure 8 shows the distribution of strains across the cross section at the instant when compressive strain is maximum on both the right and left sides of the column for Events 1 through 3. The distribution of strains across the cross section in other events is rather similar. A discernible commonality among all the events is that the values of strain measured on steel reinforcing bars are considerably smaller than the expected values based on the assumption of the linear

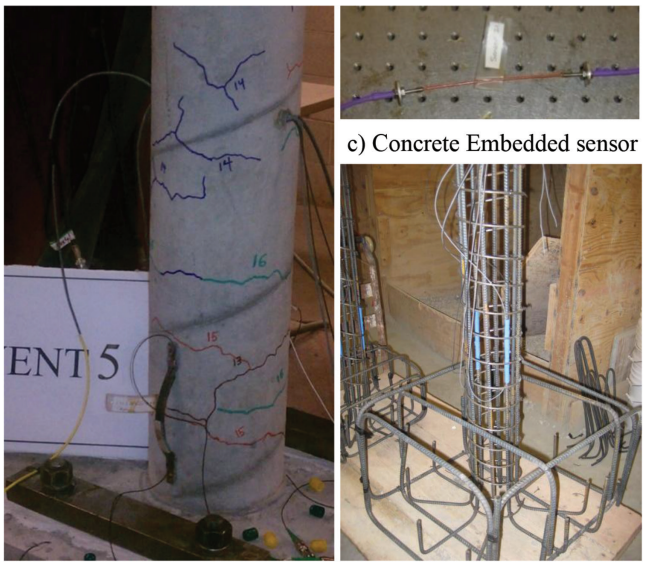

c) Concrete Embedded sensor

a) Arch sensor

b) Steel sensor

Fig. 5—Images of manufactured and installed sensors.

distribution of strains according to the Euler-Bernoulli theory for beams under small deformations. In other words, if the steel sensors had not been used, a linear assumption on the distribution of strains would have given higher strain values for steel bars. The fact that the real steel strains are lower than the expected values is the third observable feature that is common among all the events and can be attributed to the existence of bond stresses at the location of the steel sensor.

Computational plasticity method

Bending moments at the cross section of a reinforced concrete column can be calculated based on the availability of stress distribution. To obtain the stress distribution, the strain distribution and an appropriate stress-strain model are required. Then, the bending moments can be computed by satisfying the requirements of strain compatibility and equilibrium of forces. Thus, in the proposed method, three major steps were taken: 1) the strains were calculated throughout the cross section based on the strains measured by the sensors; 2) the stresses were calculated throughout the cross section by the adoption of appropriate hysteretic stress-strain models; and 3) the internal bending moment in the column cross section was computed by satisfying the equilibrium equation. The three steps are discussed as follows.

Strain distribution—The strains throughout the concrete part of the cross section ($\varepsilon_{concrete}$) were calculated based on the linear interpolation of strains measured by the arch sensors on the right side (ε_{archR}) and left side (ε_{archL}) of the column by using Eq. (1) for both the concrete cover and core

$$\varepsilon_{concrete} = \frac{(\varepsilon_{archR} - \varepsilon_{archL})(y - y_{arch})}{2y_{arch}} + \varepsilon_{archR} \tag{1}$$

where y_{arch} is the distance between the centerline of the column and the location of the arch sensors on the column surface (Fig. 9). The strains in the reinforcing steel bars (ε_{steel}) were calculated based on Eq. (2) by linear interpolation of the strains measured by the sensors on the two reinforcing

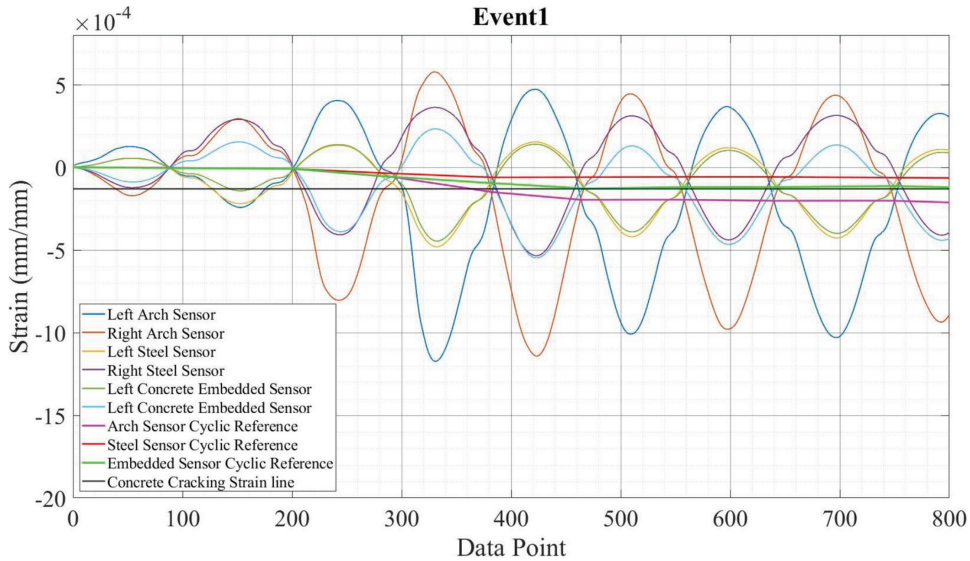

Fig. 6—First 800 data points of strains measured by all sensors at beginning of Event 1.

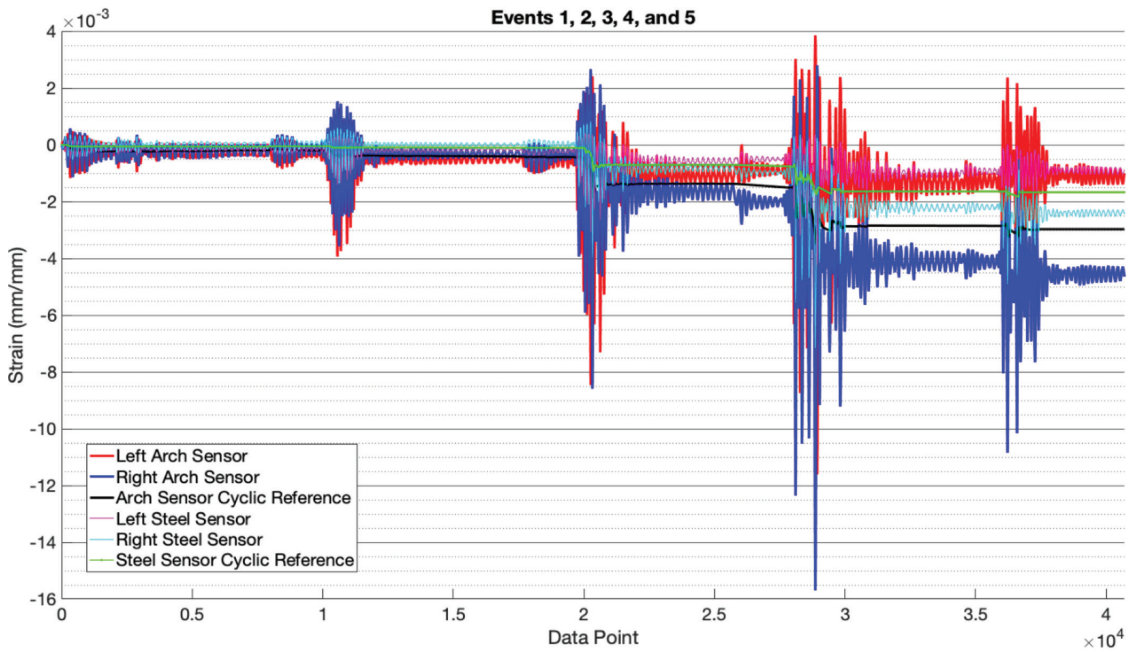

Fig. 7—Strains measured by arch and steel sensors throughout all events of one through five.

steel bars located on the opposite sides of the cross section. ε_{steelR} is the strain measured by the sensor mounted on the reinforcing bar on the right side of the cross section, and ε_{steelL} is the strain measured by the sensor mounted on the reinforcing bar on the left side of the cross section. In this equation, y_{steel} is the distance between the centerline of the column and the location of reinforcing steel bars (Fig. 9).

$$\varepsilon_{steel} = \frac{(\varepsilon_{steelR} - \varepsilon_{steelL})(y - y_{steel})}{2y_{steel}} + \varepsilon_{steelR} \qquad (2)$$

Hysteretic stress-strain model for concrete—In the seismic design of reinforced concrete columns, adequate ductility is imperative to prevent the structure from collapsing and to ensure that moment redistribution can occur. It has been widely proven by tests in the past decades that the confinement of concrete by sufficient transverse reinforcement in the form of spirals increases both the compressive strength and the ductility of the concrete core, while the cover concrete will be unconfined. In this paper, the uniaxial stress-strain models for both confined and unconfined concrete under cyclic loading, developed by Mander et al.,[19] were employed for the computation of stresses. The tensile stresses in concrete were considered to be zero because concrete tensile strains measured by the sensors early in the first event (Fig. 6) exceeded the cracking strain of 0.00013.[20]

To model the compressive stress-strain relation under cyclic loading in both concrete core and cover, three different states in the loading path were considered: loading, unloading, and reloading. A code was written in a strain-controlled fashion, where the stresses were calculated based on the measured strains, available in the form of an array of data points gathered continuously from the fiber-optic sensors. The code includes several MATLAB scripts that

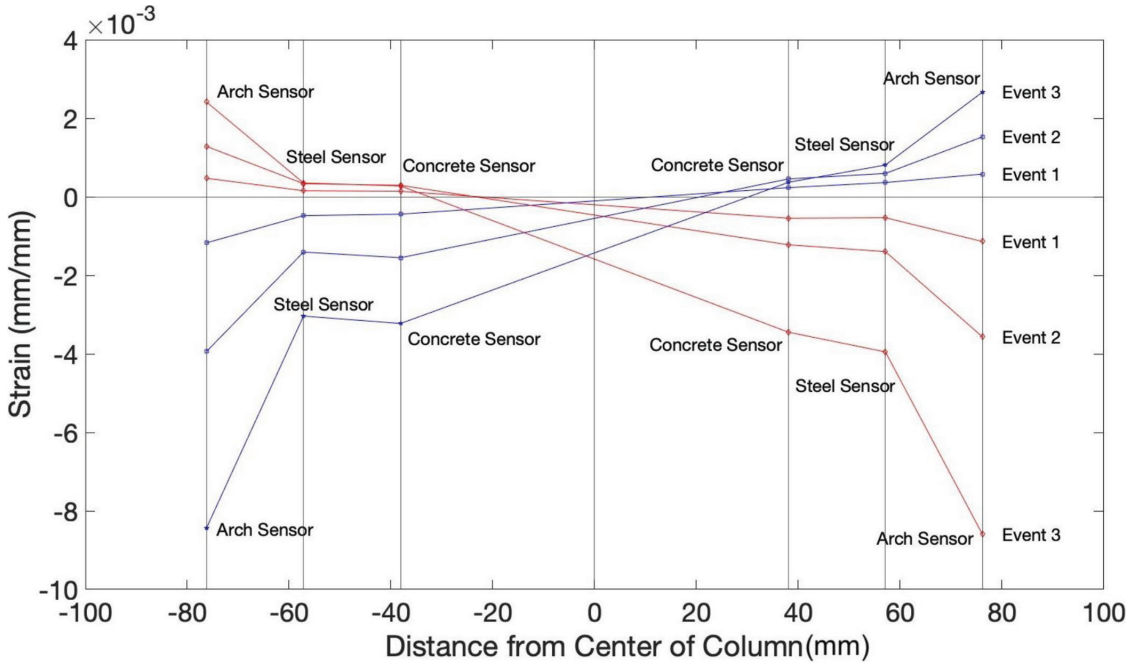

Fig. 8—Distribution of strains across cross section when compressive strain is maximum on both right and left sides of column for Events 1 through 3.

are available from the corresponding author upon request. The beginning of the loading path, where there is no loading history and the compressive strains increase with time, represents the loading state. After the loading state, there are unloading and reloading states. The unloading state pertains to the decrease in the compressive strain with time, while the reloading state represents the increase in the compressive strain with respect to time after the first unloading state. Figure 10 shows a compressive stress-strain curve, including loading, unloading, and reloading states for both confined and unconfined concrete. The stress-strain curve in Fig. 10 was generated by the developed code.

The mathematical equations modeling the three states are presented as follows.

Loading: The stress-strain model used for the loading state is based on the unified approach proposed by Mander et al.[21] In this model, the compressive stresses in the unconfined concrete (f_{uc}) and confined concrete (f_{cc}) for a slow strain rate, under monotonic loading, are calculated based on the compressive strains in unconfined concrete (ε_{cover}) and confined concrete (ε_{core}), respectively. This model involves the strain (ε_{uc}) corresponding to the compressive strength of unconfined concrete (f_{uc}') and the strain (ε_{cc}) corresponding to the compressive strength of confined concrete (f_{cc}'). The mixture design for the concrete in the column was in accordance with ACI's recommendations for producing a concrete with a compressive strength of 34.5 MPa. This value was employed for f_{uc}' in the study provided herein. The value of ε_{uc} was considered as 0.002, based on the well-established observation that, irrespective of compressive strength, normal-strength concretes typically attain their peak stress at a strain approximately 0.002.[19] This assumption is consistent with ACI 318-19, Appendix A, which cites, as an example of acceptance criteria for strain limits, that the unconfined concrete model reaches its peak stress at a compressive strain of 0.002.[20] f_{cc}' was assumed to be 45.2 MPa, consistent with Mander et al.'s equation for compressive strength of confined concrete core.[19]

The ε_{cc} was calculated based on (ε_{uc} = 0.003) through the following equation, as suggested by Richart et al.[22]

$$\varepsilon_{cc} = \varepsilon_{uc}\left[1 + 5\left(\frac{f_{cc}'}{f_{uc}'} - 1\right)\right] \tag{3}$$

For the confined concrete, the equations used for the calculation of the compressive stress (f_{cc}) based on the compressive strain in the confined concrete (ε_{core}) are as follows

$$f_{cc} = \frac{f_{cc}' r_{cc} x_{core}}{r_{cc} - 1 + x_{core}^{r_{cc}}} \tag{4}$$

where x_{core} and r_{cc} are two parameters that are calculated based on the following equations for confined concrete core

$$x_{core} = \frac{\varepsilon_{core}}{\varepsilon_{cc}} \tag{5}$$

$$r_{cc} = \frac{E_c}{E_c - E_{secc}} \tag{6}$$

where E_c is the tangent modulus of elasticity of the unconfined concrete, calculated based on the following equation in MPa

$$E_c = 5000\sqrt{f_{uc}'} \tag{7}$$

and E_{secc} is a stiffness modulus for confined concrete calculated based on the compressive strength of confined concrete (f_{cc}') and the strain (ε_{cc}) corresponding to the compressive strength of confined concrete through the following equation

$$E_{secc} = \frac{f_{cc}'}{\varepsilon_{cc}} \tag{8}$$

For the unconfined concrete, the same equations were used, replacing the f_{cc}' and ε_{cc} with f_{uc}' and ε_{uc}, respectively. In the unloading and reloading states, which will be discussed next, with the same replacement of f_{cc}' and ε_{cc} with f_{uc}' and ε_{uc}, the equations developed for confined concrete were used for the unconfined concrete.

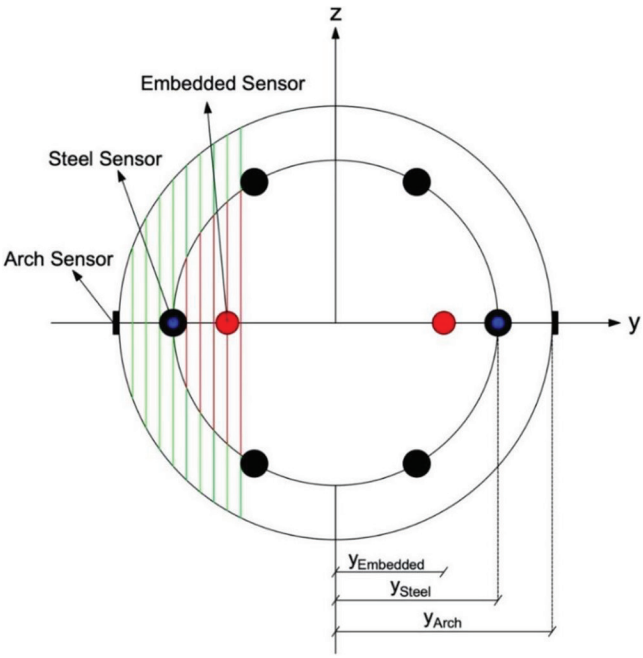

Fig. 9—Column cross section with location of sensors across diameter.

Unloading: Based on the equations developed by Mander et al.,[19] the compressive stress in confined concrete (f_{cc}) in the unloading branch is calculated for every compressive strain ε_{core} in the unloading branch. To do this, in addition to ε_{core}, the strain (ε_{uncc}) and the stress (f_{uncc}) at the beginning of the unloading branch should be known. Throughout the strain signals, the ε_{uncc} can be determined for every unloading branch by comparing every strain data point $\varepsilon_{core}(i)$ with the next strain data point $\varepsilon_{core}(i + 1)$. The stress ($f_{uncc}$) is determined based on the ε_{uncc} using the equations used in the loading branch or the equations that will be discussed in the reloading branch. To establish an equation for the compressive stress in the confined concrete (f_{cc}) in the unloading branch, a plastic strain ε_{plcc} should also be determined based on the strain and the stress at the beginning of the unloading branch (ε_{uncc}, f_{uncc}). Thus, in the following equations, ε_{core}, ε_{uncc}, and f_{uncc} are the input variables, and f_{cc} and ε_{plcc} are the output variables. ε_{uncc}, f_{uncc}, and ε_{plcc} have unique values for every single unloading branch, as long as $|\varepsilon_{core}(i + 1)|$ is smaller than $|\varepsilon_{core}(i)|$; however, f_{cc} is updated for every single ε_{core}. The equations used for the calculation of f_{cc} are as follows

$$f_{cc} = f_{uncc} - \frac{f_{uncc} r_{cc} x_{core}}{r_{cc} - 1 + x_{core}^{r_{cc}}} \tag{9}$$

where x_{core} and r_{cc} are two parameters that are calculated based on the following equations for confined concrete core

$$x_{core} = \frac{\varepsilon_{core} - \varepsilon_{uncc}}{\varepsilon_{plcc} - \varepsilon_{uncc}} \tag{10}$$

$$r_{cc} = \frac{E_{uc}}{E_{uc} - E_{secc}} \tag{11}$$

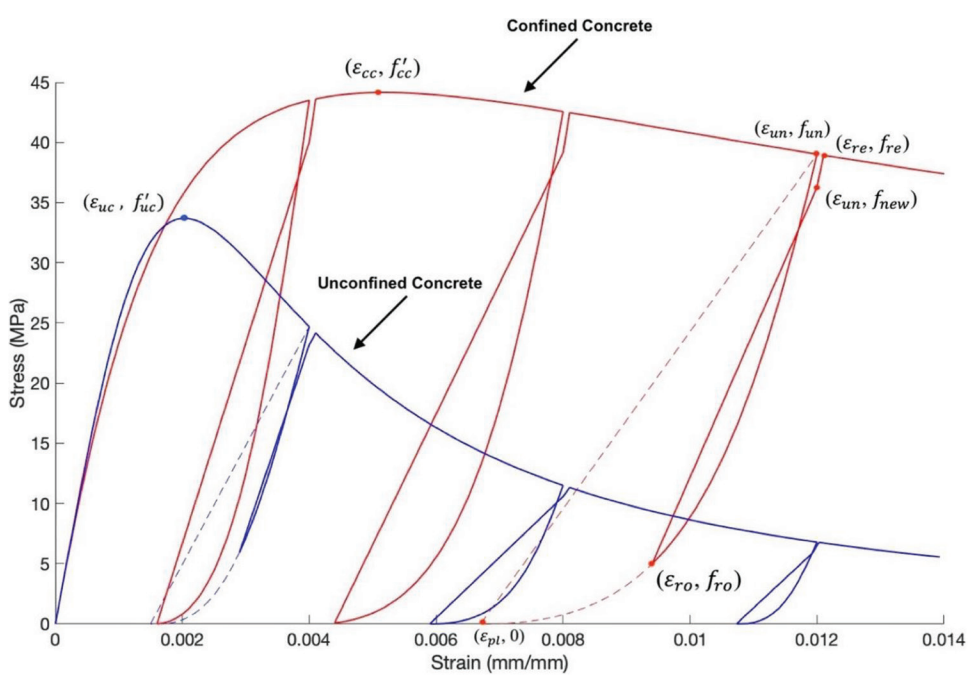

Fig. 10—Compressive stress-strain curve generated by developed code, including loading, unloading, and reloading states for both confined and unconfined concrete.

where E_{secc} and E_{uc} are stiffness moduli calculated through the following equations for the unloading branch of the confined concrete

$$E_{secc} = \frac{f_{uncc}}{\varepsilon_{uncc} - \varepsilon_{plcc}} \tag{12}$$

$$E_{uc} = bcE_c \tag{13}$$

where b and c are determined as follows

$$b = \frac{f_{uncc}}{f_{uc}'} \geq 1 \tag{14}$$

$$c = \left(\frac{\varepsilon_{cc}}{\varepsilon_{uncc}}\right)^{0.5} \leq 1 \tag{15}$$

The plastic strain ε_{plcc} required for the calculation of E_{secc} is determined as a function of the strain and the stress at the beginning of the unloading branch ($\varepsilon_{uncc}, f_{uncc}$) using the following equation

$$\varepsilon_{pl} = \varepsilon_{uncc} - \frac{(\varepsilon_{uncc} + \varepsilon_a)f_{uncc}}{(f_{uncc} + E_c\varepsilon_a)} \tag{16}$$

The parameter ε_a is the strain at the intersection of the plastic unloading secant and initial tangent slopes. The strain ε_a is calculated using the following equation

$$\varepsilon_a = a\sqrt{\varepsilon_{uncc}\varepsilon_{cc}} \tag{17}$$

where a is a parameter determined by the following equation developed by Mander et al.[19] as a modification of an original approach used by Takiguchi et al.[23]

$$a = \max\left(\frac{\varepsilon_{cc}}{\varepsilon_{cc} + \varepsilon_{uncc}}, \frac{0.09\varepsilon_{uncc}}{\varepsilon_{cc}}\right) \tag{18}$$

Reloading: Comprehensive stress-strain curves, including one loading branch and three branches of unloading and reloading for both confined and unconfined concrete, are plotted in Fig. 10. The coordinates of the point of reloading (ε_{ro}, f_{ro}) are either from the unloading curve in the fully compressive cycles or equal to ($\varepsilon_{ro} = \varepsilon_{pl}, f_{ro} = 0$) in the cycles including both compression and tension. As mentioned earlier, the tensile strength of concrete is neglected in this study. The stress-strain relation in the reloading branch starts from the point of reloading (ε_{ro}, f_{ro}) and linearly continues to a new point with the coordinates ($\varepsilon_{un}, f_{new}$). The stress at the end of the linear part of a reloading branch (f_{new}) has a value between f_{ro} and f_{new} and is calculated using the following equation

$$f_{new} = 0.92f_{un} + 0.08f_{ro} \tag{19}$$

As shown in Fig. 10, the slopes of the linear parts of the reloading branches throughout the cycles account for the cyclic degradation of stiffness. The slope of the linear part of the reloading branch (E_r) is calculated using the following equation

$$E_r = \frac{f_{ro} - f_{new}}{\varepsilon_{ro} - \varepsilon_{un}} \tag{20}$$

Thus, for strains on the reloading branch that are smaller than ε_{un}, the stress-strain relationship is as follows

$$f_{core} = f_{ro} + E_r x \tag{21}$$

where

$$x = \varepsilon_c - \varepsilon_{ro} \tag{22}$$

The second part of the reloading branch starts from the point at the end of the linear branch ($\varepsilon_{un}, f_{new}$) and parabolically transits to a point located on the monotonic loading branch with the coordinates (ε_{re}, f_{re}). The return strain (ε_{re}) is calculated by the following equation, suggested by Mander et al.,[19] based on the experimental data

$$\varepsilon_{re} = \varepsilon_{un} + \frac{f_{un} - f_{new}}{E_r\left(2 + \frac{f_{cc}'}{f_{co}'}\right)} \tag{23}$$

and the return stress (f_{re}) is calculated based on the return strain (ε_{re}) according to the monotonic compressive loading branch. For strains on the reloading branch that are larger than ε_{un}, the stress-strain relationship can be expressed as follows

$$f_{core} = f_{re} + E_{re}x + Ax^2 \tag{24}$$

where

$$E_{re} = \frac{f_{re} - f_{un}}{\varepsilon_{re} - \varepsilon_{un}} \tag{25}$$

and

$$A = \frac{E_r - E_{re}}{-4\left[(f_{new} - f_{re}) - E_r(\varepsilon_{un} - \varepsilon_{re})\right]} \tag{26}$$

Thus, throughout the reloading branch, ε_{core}, ε_{ro}, f_{ro}, ε_{uncc}, f_{uncc}, and ε_{plcc} are the input variables, and f_{cc} is the output variable. ε_{ro}, f_{ro}, ε_{uncc}, f_{uncc}, and ε_{plcc} have unique values for every single reloading branch, as long as $|\varepsilon_{core}(i + 1)|$ is larger than $|\varepsilon_{core}(i)|$; however, f_{cc} is updated for every single ε_{core}. Figure 11 depicts the distribution of computed concrete stresses across the diameter of the cross section at the instant that the compressive strain is maximum on the left of the cross section in Event 4.

Hysteretic stress-strain model for reinforcing steel—The hysteretic stress-strain behavior for reinforcing steel bars was modeled by using both isotropic and kinematic hardening plasticity models. The difference between the two models in predicting accurate results was minimal. Because the kinematic hardening model rendered results slightly closer to the experimental measurements, it was selected for the present study. The kinematic hardening model was used in this simulation with a bilinear curve with an initial slope of E_{steel} + 199,948 MPa; a yield stress of 413 MPa, consistent with the material properties of Grade 60 steel bars; and the hardening slope of E_{harden} = 1461 MPa. Figure 12 shows

the stress-strain curves, including loading, unloading, and reloading of reinforcing steel.

Calculation of bending moment—Upon the calculation of stresses along the diameter of the cross section, by assuming that stresses are distributed uniformly across the transverse direction, the stresses at all the points throughout the cross section are known. To calculate the resultant forces in concrete, the area of the cross section is divided into a series of finite areas along the diameter of the cross section with equal widths. In this study, 1905 elements with a width of 0.08 mm were used to calculate resultant forces in concrete. Selection of thinner elements (for example, a width of 0.06 mm) did not change the accuracy of the calculated results to the fourth decimal digit. In Fig. 9, vertical strips with red boundary lines schematically represent elements under compression in confined concrete core, and the vertical strips with green boundary lines schematically represent elements under compression in unconfined concrete cover (full-color version of this paper can be accessed at www.concrete.org).

At every instant, the bending moment (M) is calculated by multiplying the forces in both concrete and steel bars by their corresponding moment arms measured from the centerline of the cross section, as the centerline coincides with the plastic center of the cross section, because of the symmetrical shape and distribution of longitudinal bars. Figure 13 displays the forces in the steel bars and the equivalent distributed force applied to the compressive concrete at the instant that the compressive strain is maximum on the left of the cross section in Event 3. The resultant of all the forces in the cross section (F_{total}) was calculated, and it was assumed that it is applied at the line of the axis of the column. F_i (for i = 1 to 6) are the individual forces in the six reinforcing steel bars in the cross section. Because F_{total} is applied at the centerline of the column cross section and the bending moment is calculated about the center of the cross section, it was not incorporated in the calculation of the bending moment.

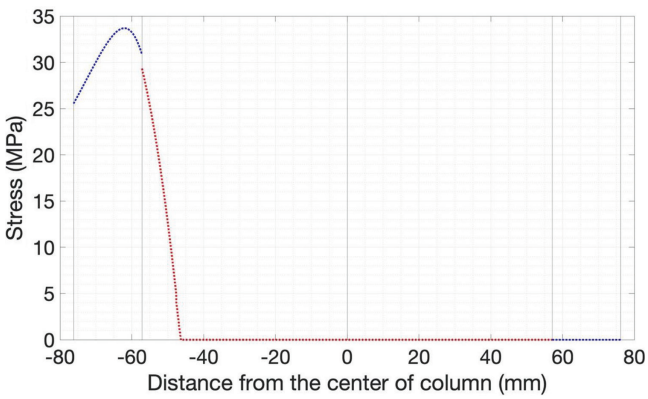

Fig. 11—Distribution of computed concrete stresses across diameter of cross section when compressive strain is maximum on left of cross section in Event 4.

RESULTS AND DISCUSSION

The bending moments that were continuously computed based on the strain measurements at the bottom of the column, according to the described method, were compared with those that were calculated based on the forces measured by the load cell at the top of the column. The results of the computed and measured bending moments for all five seismic events applied to the specimen are plotted in Fig. 14. The results illustrate the significance of embedded sensing and continuous monitoring for accurately computing bending moments in reinforced concrete columns.

The bending moments that were computed by including these three features for seismic Event 5 are depicted along with the corresponding measured bending moments in the same event in Fig. 15. Figure 16 shows the strains measured by the arch sensors mounted on opposite sides of the column during Event 5. In this plot, the cyclic reference initiates at a residual tensile strain of 0.002855 mm/mm, accumulated from Events 1 through 4, and gradually shifts downward, eventually becoming stable around a tensile strain of –0.002973 mm/mm.

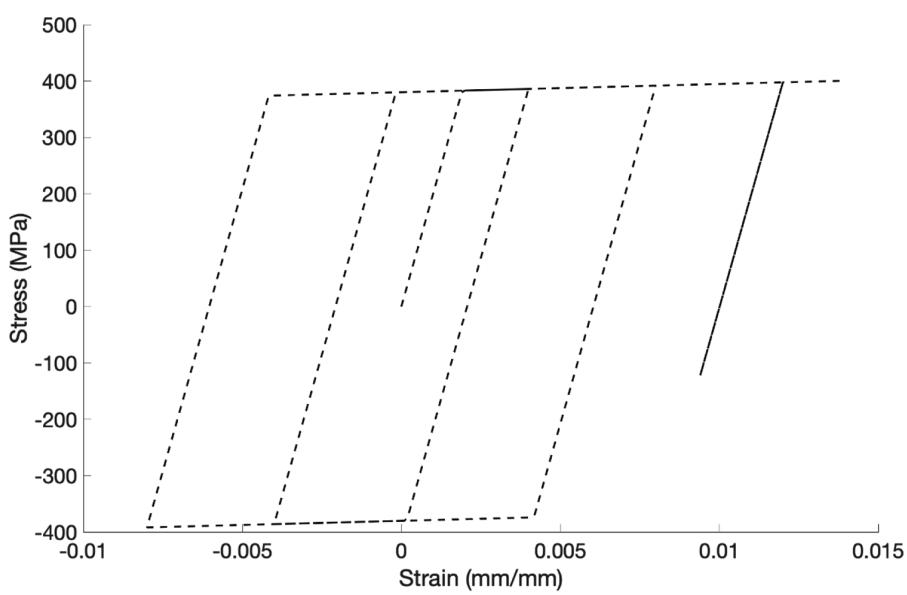

Fig. 12—Stress-strain curves, including loading, unloading, and reloading of reinforcing steel.

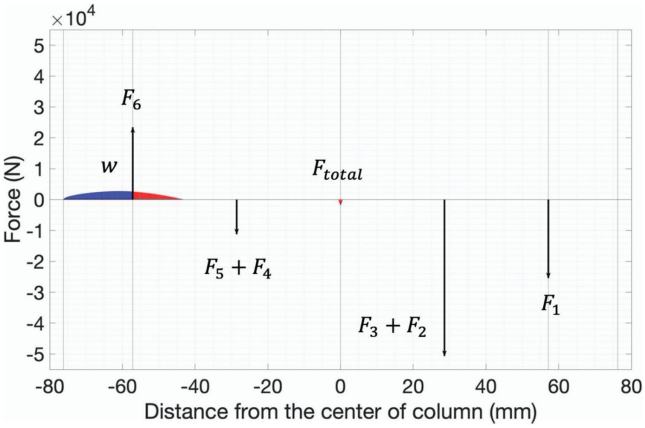

Fig. 13—Distribution of forces in steel bars and equivalent distributed force applied to compressive concrete, when compressive strain is maximum on left of cross section in Event 3.

Figures 17 to 19 demonstrate that the three features of post-event residual strains, the shift of cyclic reference, and real steel strains are essential for computing bending moments in the column. If the residual strain accumulated from previous events at the beginning of Event 5 is ignored, the strains measured by the arch sensors will resemble the plots in Fig. 17. Figure 18 demonstrates the computed and measured bending moments for Event 5, where post-event residual strains are ignored.

To obtain a comprehensive and quantitative measure of similarity between the computed and measured signals, the first 14 largest signal peaks of each event (both maximum and minimum peaks) were compared. The plots in Fig. 20 display 70 peak values of measured and computed bending moment signals, sorted from lowest to highest. The plots reveal how consideration of post-event residual strains, shift of cyclic reference, and real steel strains influences the accuracy of computations. Table 1 lists the computation errors for

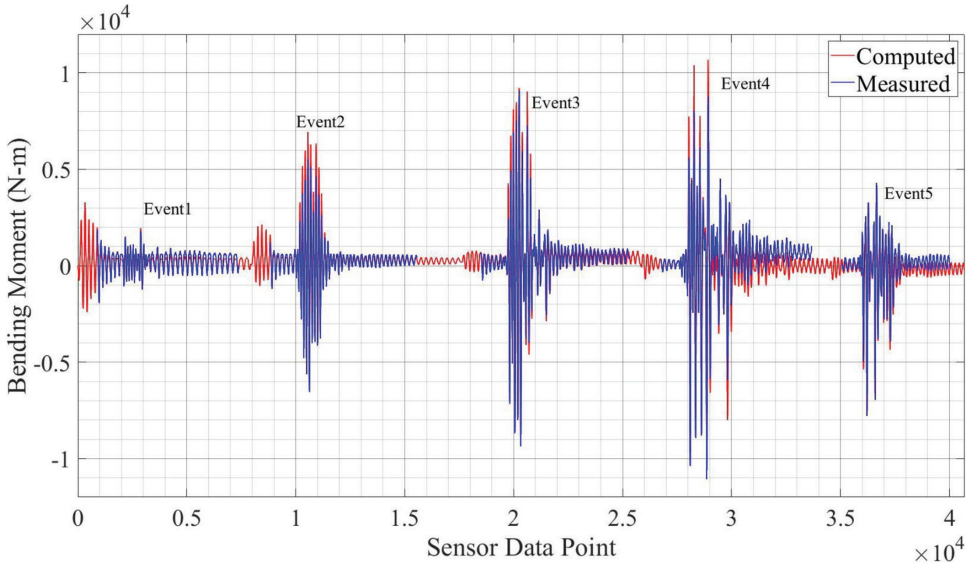

Fig. 14—Computed and measured bending moments for all five seismic events.

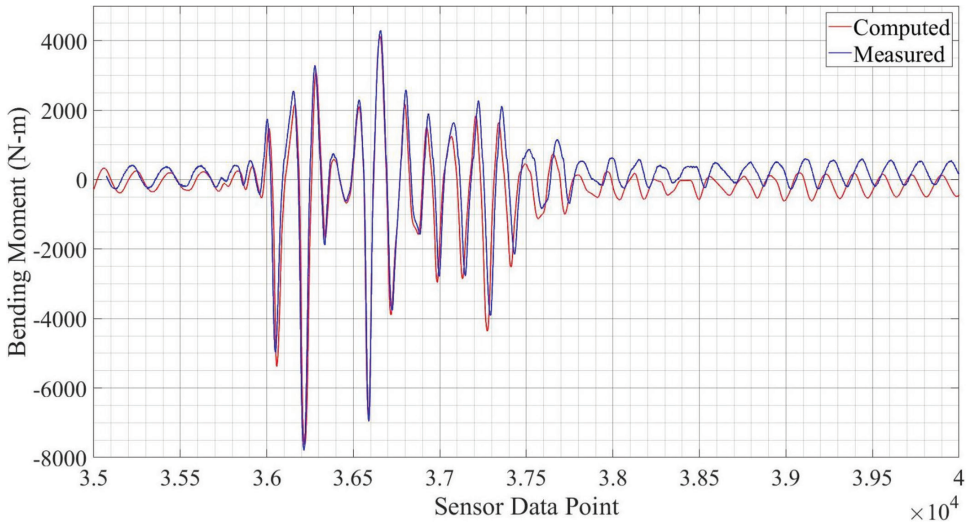

Fig. 15—Measured bending moments versus bending moments that were computed by including three features (shift of cyclic reference, post-event residual strains, and real steel strains) for seismic Event 5.

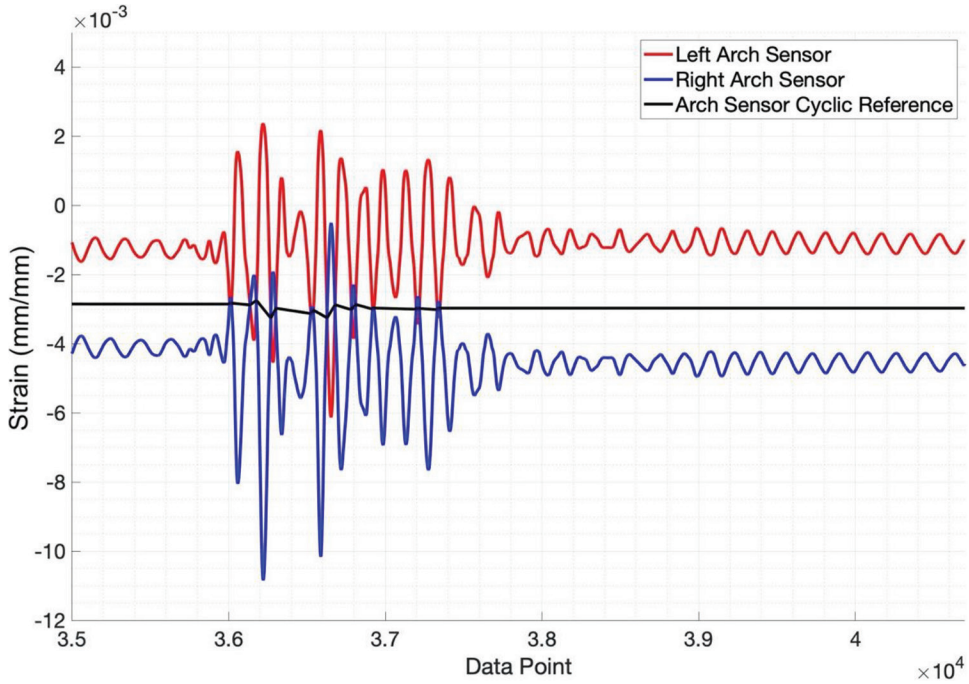

Fig. 16—Strains measured by arch sensors during Event 5.

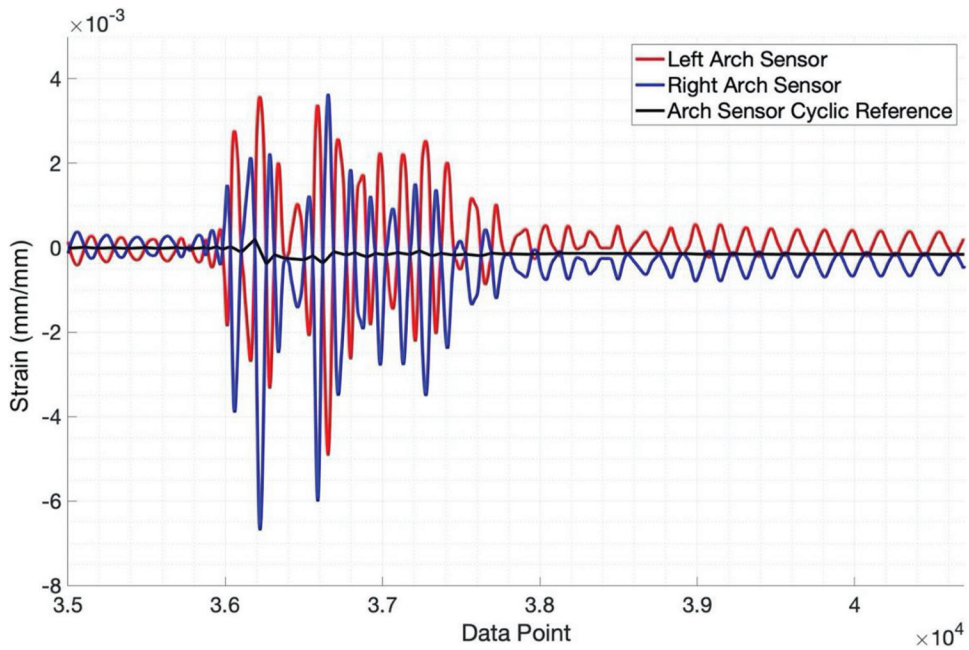

Fig. 17—Strains measured by arch sensors during Event 5, if residual strain accumulated from previous events is ignored.

the first 14 largest signal peaks of Event 5 (both maximum and minimum peaks). The computation error is considered as the average of the differences between computed and measured peak values, divided by the measured peak values. In Fig. 20 and Table 1, "SSR" refers to the consideration of the Shift of cyclic reference, real Steel strains, and post-event Residual strains.

Figure 21 provides a detailed summary of the results from one cycle of Event 3, demonstrating continuous monitoring in this study. Figure 21(a) illustrates the measured strain distribution across the cross section, considering the six attached sensors. Additionally, Fig. 21(b) shows the progression of strains for arch, embedded, and steel sensors, highlighting the cycle with the maximum and minimum peaks of Event 3. Furthermore, Fig. 21(c) displays the bending moment graphs, comparing the bending moment computed using the proposed method with the bending moment calculated based on the forces directly measured by the load cell. Notably, the computed and measured bending moment signals match, with an acceptable level of accuracy within this cycle.

CONCLUSIONS

This study proposes a sensing-based method to simulate bending moments in reinforced concrete columns by using plasticity models fed with continuous strain measurements. Bending moments at a cross section of a reinforced concrete

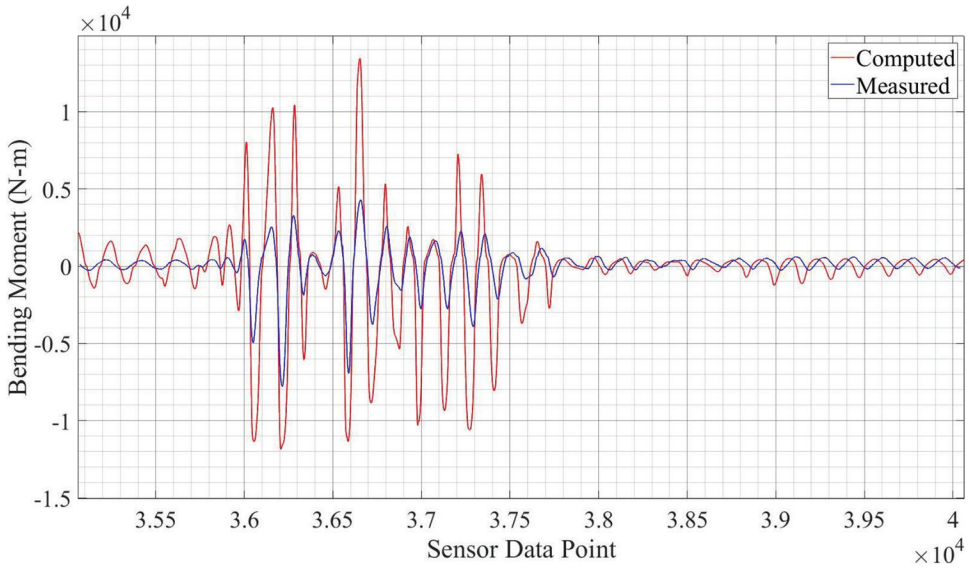

Fig. 18—Measured bending moments versus computed bending moments in Event 5, where post-event residual strains are ignored.

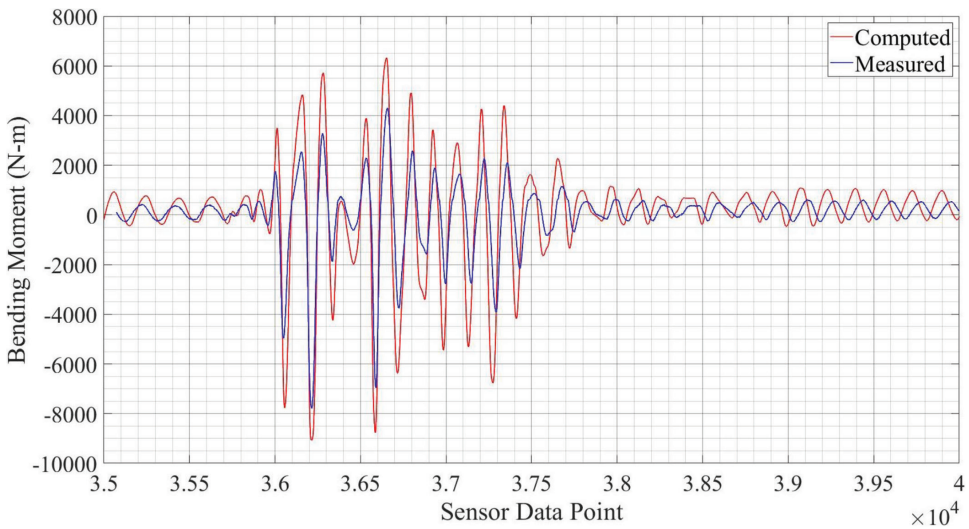

Fig. 19—Measured bending moments versus computed bending moments in Event 5, where real steel strains are ignored.

Table 1—Computation error of Event 5

Computation assumption	Error, %
With SSR	5.87
Without residual strains	177.68
Without real steel strains	72.24
Without shift of cyclic reference	247.19
Without SSR	283.54

column were computed based on stress distribution by satisfying equilibrium equations and proposed compatibility equations. The column was subjected to a series of progressively increasing ground motions of the 1994 Northridge earthquake in California. Six fiber-optic Bragg grating (FBG) sensors were employed to measure strains across the cross section of the column. Upon the availability of strain distribution across the concrete column cross section, the compressive stress distributions within the concrete core and cover were computed through the confined and unconfined concrete stress-strain relations for loading, unloading, and reloading scenarios. The tensile and compressive stresses in steel reinforcing bars were also determined using the kinematic hardening plasticity model, which considers the hysteretic stress-strain behavior. The paper demonstrated that concrete and steel plasticity stress-strain models for loading, unloading, and reloading can be successfully applied to calculate the history of bending moments in a reinforced concrete column subjected to several seismic motions. The history of bending moments experienced by a reinforced concrete member is essential to quantifying the damage and assessing its remaining lifetime. Besides, it was quantitatively proved that the accuracy of the computation of bending moments in a studied reinforced concrete column depends significantly on continuous internal and external measurements. It was shown that without deep access to the internal layers of the cross section and the continuous gathering of data, it would not be possible to capture the features

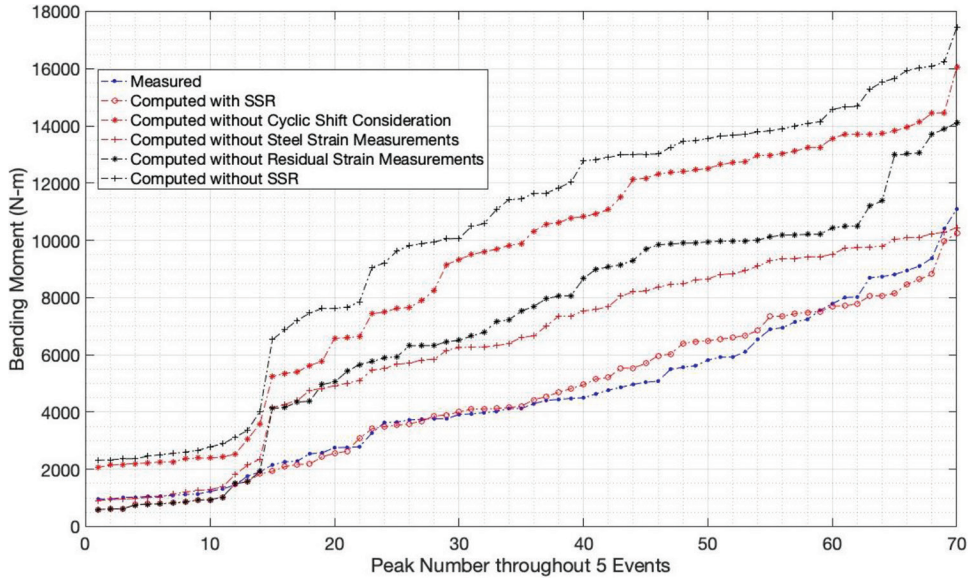

Fig. 20—Peak values of measured and computed bending moment signals for all five events.

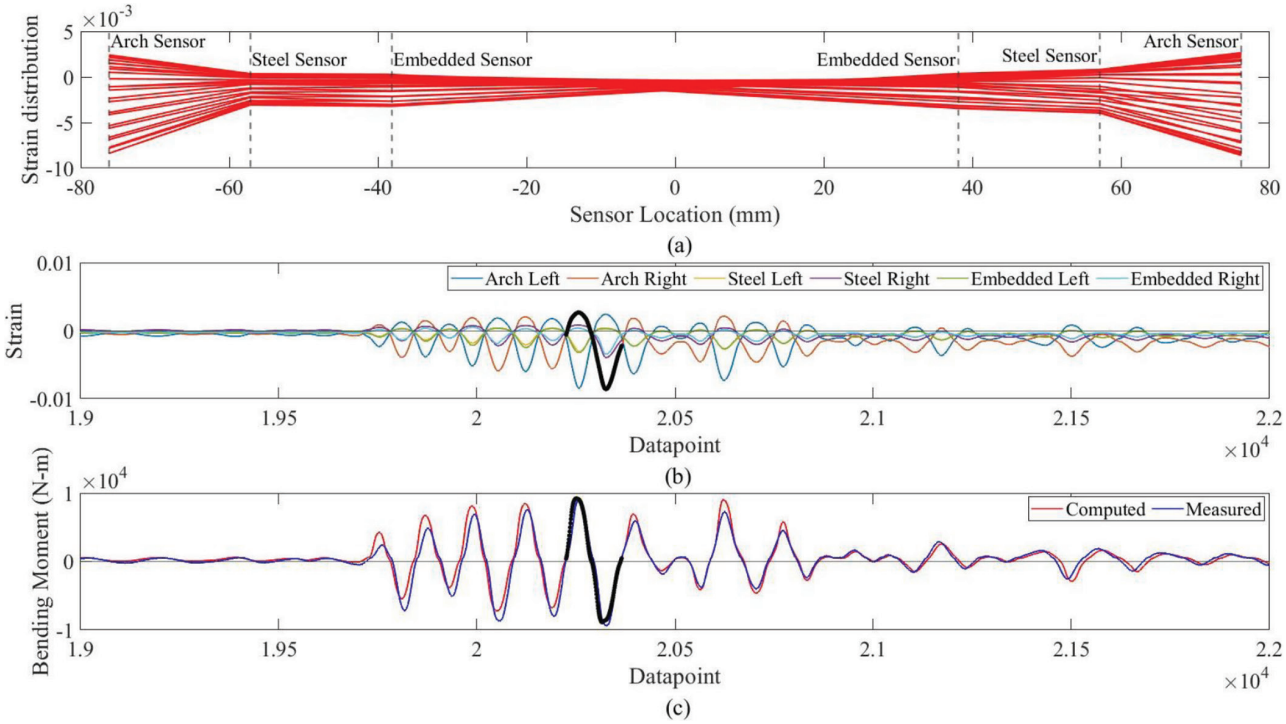

Fig. 21—(a) Strain distribution over cross section; (b) strains measured by all sensors; and (c) bending moment at Event 3.

of shift of cyclic reference, post-event residual strains, and real steel strains, which are extremely influential on the accuracy of continuous computation of bending moments.

AUTHOR BIOS

Amir Iranmanesh *is a Clinical Associate Professor of structural engineering at the University of Illinois Chicago, Chicago, IL, where he received his PhD in structural engineering in 2012. He received his BS in civil engineering and MS in structural engineering from the University of Tehran, Tehran, Iran, in 2002 and 2005, respectively. His research interests include structural health monitoring, sensing-based simulation, and structural digital twins.*

Mahsa Panahi *is a PhD Student in the Department of Civil, Materials, and Environmental Engineering at the University of Illinois Chicago. She received her BS in civil engineering from Isfahan University of Technology, Isfahan, Iran, and her MS in structural engineering from the University of Tehran. Her research interests include structural health monitoring and the prognosis of structures.*

Farhad Ansari *is a Distinguished Professor at the University of Illinois Chicago. He received his BS from the University of Illinois Urbana-Champaign, Champaign, IL; his MS from the University of Colorado Denver, Denver, CO; and his PhD from the University of Illinois Chicago, all in civil engineering. He was previously a member of ACI Committees 228, Nondestructive Testing of Concrete, and 446, Fracture Mechanics of Concrete. His research interests include structural health monitoring and fiber-optic sensor applications in civil structures.*

REFERENCES

1. Iranmanesh, A., and Ansari, F., "Energy-Based Damage Assessment Methodology for Structural Health Monitoring of Modern Reinforced Concrete Bridge Columns," *Journal of Bridge Engineering*, ASCE, V. 19, No. 8, Aug. 2014, p. A4014004. doi: 10.1061/(ASCE)BE.1943-5592.0000569

2. Chang, F.-K.; Markmiller, J. F. C.; Yang, J.; and Kim, Y., "Structural Health Monitoring," *System Health Management: With Aerospace Applications*, S. B. Johnson, T. J. Gormley, S. S. Kessler, C. D. Mott, A. Patterson-Hine, K. M. Reichard, and P. A. Scandura Jr., eds., John Wiley & Sons, Ltd., Chichester, UK, 2011, pp. 419-428.

3. Sezen, H., and Miller, E. A., "Experimental Evaluation of Axial Behavior of Strengthened Circular Reinforced-Concrete Columns," *Journal of Bridge Engineering*, ASCE, V. 16, No. 2, Mar. 2011, pp. 238-247. doi: 10.1061/(ASCE)BE.1943-5592.0000143

4. Lehman, D.; Moehle, J.; Mahin, S.; Calderone, A.; and Henry, L., "Experimental Evaluation of the Seismic Performance of Reinforced Concrete Bridge Columns," *Journal of Structural Engineering*, ASCE, V. 130, No. 6, June 2004, pp. 869-879. doi: 10.1061/(ASCE)0733-9445(2004)130:6(869)

5. Stewart, M. G., and Val, D. V., "Role of Load History in Reliability-Based Decision Analysis of Aging Bridges," *Journal of Structural Engineering*, ASCE, V. 125, No. 7, July 1999, pp. 776-783. doi: 10.1061/(ASCE)0733-9445(1999)125:7(776)

6. Moslehy, Y.; Gu, H.; Belarbi, A.; Mo, Y. L.; and Song, G., "Smart Aggregate Based Damage Detection of Circular RC Columns Under Cyclic Combined Loading," *Smart Materials and Structures*, V. 19, No. 6, June 2010, Article No. 065021. doi: 10.1088/0964-1726/19/6/065021

7. Lin, H.; Xu, Z.; Hong, W.; Yang, Z.; Wang, Y.; and Li, B., "Long-Gauge Fiber Optic Sensors: Strain Measurement Comparison for Reinforced Concrete Columns," *Sensors*, V. 25, No. 1, Jan. 2025, Article No. 220. doi: 10.3390/s25010220

8. Rodríguez, G.; Casas, J. R.; and Villaba, S., "Cracking Assessment in Concrete Structures by Distributed Optical Fiber," *Smart Materials and Structures*, V. 24, No. 3, Mar. 2015, Article No. 035005. doi: 10.1088/0964-1726/24/3/035005

9. Ansari, F., and Bassam, S. A., "High Resolution Large Displacement/Crack Sensor," U.S. Patent 9,109,883, filed May 28, 2010, and issued Aug. 18, 2015.

10. Ansari, F., "Practical Implementation of Optical Fiber Sensors in Civil Structural Health Monitoring," *Journal of Intelligent Material Systems and Structures*, V. 18, No. 8, Aug. 2007, pp. 879-889. doi: 10.1177/1045389X06075760

11. Iranmanesh, A.; Bassam, A.; and Ansari, F., "Post Earthquake Performance Monitoring of a Typical Highway Overpass Bridge," *Smart Structures and Systems*, V. 5, No. 4, July 2009, pp. 495-505. doi: 10.12989/sss.2009.5.4.495

12. Wu, T.; Liu, G.; Fu, S.; and Xing, F., "Recent Progress of Fiber-Optic Sensors for the Structural Health Monitoring of Civil Infrastructure," *Sensors*, V. 20, No. 16, Aug. 2020, Article No. 4517. doi: 10.3390/s20164517

13. Lin, T.-K.; Chang, K.-C.; and Lin, Y.-B., "Active Control with Optical Fiber Sensors and Neural Networks. II: Experimental Verification," *Journal of Structural Engineering*, ASCE, V. 132, No. 8, Aug. 2006, pp. 1304-1313. doi: 10.1061/(ASCE)0733-9445(2006)132:8(1304)

14. Ansari, F., "Fiber Optic Health Monitoring of Civil Structures Using Long Gage and Acoustic Sensors," *Smart Materials and Structures*, V. 14, No. 3, June 2005, pp. S1-S7. doi: 10.1088/0964-1726/14/3/001

15. Casas, J. R., and Cruz, P. J. S., "Fiber Optic Sensors for Bridge Monitoring," *Journal of Bridge Engineering*, ASCE, V. 8, No. 6, Nov. 2003, pp. 362-373. doi: 10.1061/(ASCE)1084-0702(2003)8:6(362)

16. Johnson, N.; Ranf, R. T.; Saiidi, M. S.; Sanders, D.; and Eberhard, M., "Seismic Testing of a Two-Span Reinforced Concrete Bridge," *Journal of Bridge Engineering*, ASCE, V. 13, No. 2, Mar. 2008, pp. 173-182. doi: 10.1061/(ASCE)1084-0702(2008)13:2(173)

17. Iranmanesh, A.; Panahi, M.; and Ansari, F., "Comparison of Scaled Hybrid Simulations and Shaking Table Tests on a 2-Span Reinforced Concrete Bridge," *Proceedings of the Twelfth International Structural Engineering and Construction Conference*, A. Karatas, A. Iranmanesh, A. Gurgun, S. Yazdani, and A. Singh, eds., V. 10, No. 1, Chicago, IL, Aug. 2023, 6 pp. doi: 10.14455/ISEC.2023.10(1).STR-89

18. Bae, S., and Bayrak, O., "Plastic Hinge Length of Reinforced Concrete Columns," *ACI Structural Journal*, V. 105, No. 3, May-June 2008, pp. 290-300.

19. Mander, J. B.; Priestley, M. J. N.; and Park, R., "Theoretical Stress-Strain Model for Confined Concrete," *Journal of Structural Engineering*, ASCE, V. 114, No. 8, Sept. 1988, pp. 1804-1826. doi: 10.1061/(ASCE)0733-9445(1988)114:8(1804)

20. ACI Committee 318, "Building Code Requirements for Structural Concrete (ACI 318-19) and Commentary (ACI 318R-19) (Reapproved 2022)," American Concrete Institute, Farmington Hills, MI, 2019, 624 pp.

21. Mander, J. B.; Priestley, M. J. N.; and Park, R., "Seismic Design of Bridge Piers," Research Report No. 84-2, University of Canterbury, Christchurch, New Zealand, 1984, 483 pp.

22. Richart, F. E.; Brandtzaeg, A.; and Brown, R. L., "The Failure of Plain and Spirally Reinforced Concrete in Compression," Bulletin No. 190, University of Illinois Engineering Experiment Station, Champaign, IL, Apr. 1929, 82 pp.

23. Takiguchi, K.; Kokusho, S.; and Kobayashi, K., "Analysis of Reinforced Concrete Sections Subjected to Biaxial Bending Moments," *Transactions of the Architectural Institute of Japan*, V. 250, 1976, pp. 1-8. doi: 10.3130/aijsaxx.250.0_1

ACI STRUCTURAL JOURNAL TECHNICAL PAPER

Title No. 123-S47

Flexural Behavior of Ultra-High-Performance Seawater Sea-Sand Concrete Beams Reinforced with Fiber-Reinforced Polymer Bars

by Fen Zhou, Lijuan Li, Yunxing Du, Fei Peng, and Deju Zhu

To promote the application of fiber-reinforced polymer (FRP) bar-reinforced ultra-high-performance seawater sea-sand concrete (FRP-UHPSSC) structures in marine construction, four-point static bending tests were carried out on 16 FRP-UHPSSC beams with different reinforcement ratios, cross-section heights, and types of FRP bars to investigate the ultimate load-carrying capacity, the midspan deflection, and the failure modes of the beams. The experimental results show that all the test beams had brittle failure, and the failure mode of the beams is shear failure when the ratio of the actual reinforcement ratio to the balanced one is higher than 2.73. Increasing the reinforcement ratio and the beam section height improve both bending moment at ultimate load and flexural stiffness at the service limit state. The steel-FRP composite bar (SFCB)-reinforced UHPSSC beams have the maximal bending moment at ultimate load, and the basalt fiber-reinforced polymer (BFRP) bar-reinforced UHPSSC beams have the optimal ductility. The deviation of ultimate bending moment and midspan deflection obtained by proposed calculation method is reduced from 7.5 to 2.8%, and from 15 to 3%, respectively, compared with current specifications for FRP-reinforced concrete structures.

Keywords: fiber-reinforced polymer (FRP); flexural behavior; ultra-high-performance seawater sea-sand concrete (UHPSSC).

INTRODUCTION

In the construction of island projects far from the inland, using seawater and sea sand locally to prepare seawater sea-sand concrete (SSC) can not only save costs but also alleviate the current shortage of freshwater resources. However, SSC contains a large amount of Cl^-, which can accelerate the corrosion of steel bars.[1] Compared with steel bars, fiber-reinforced polymer (FRP) bars are more suitable for SSC structures due to their excellent resistance to Cl^- corrosion.[2] However, over time, FRP bars will undergo chemical reactions with concrete, which greatly affects the connection between FRP bars and concrete.[3] To solve this problem, many scholars[4,5] have found that the hindering effect of the sand layer can enhance the bond durability between FRP bars and SSC. In addition, a subsequent comprehensive investigation also revealed that the mechanical properties of FRP bars deteriorate over prolonged exposure to the alkaline pore fluid present in SSC.[6]

To mitigate the degradation of FRP bars, it is imperative to employ an SSC variant characterized by smaller pores and a more compact internal structure. In this regard, ultra-high-performance seawater sea-sand concrete (UHPSSC) is a favorable option. Several scholars have successfully prepared UHPSSC with significantly greater compressive strength compared to traditional SSC.[7-9] They also confirmed that UHPSSC exhibits a reduced surface porosity and denser pore structure under marine conditions, forming a strong "protective layer" that effectively isolates external seawater intrusion, avoiding further chemical reactions of FRP reinforcement.[10] Furthermore, Li et al.[11] demonstrated that, in terms of Cl^- penetration resistance and overall durability, UHPSSC performs even better than ultra-high-performance concrete (UHPC) in short-term mechanical properties. Combining UHPSSC with FRP bars not only enhances the mechanical properties of the structures but also improves durability. However, due to the distinct mechanical properties of UHPSSC compared to ordinary concrete, the existing design specifications for FRP-reinforced concrete (FRP-RC) structures may not be suitable for FRP-UHPSSC structures. To advance the application of UHPSSC, extensive research focusing on the flexural behavior of FRP-UHPSSC beams is imperative. Presently, the available studies on the flexural behavior of such beams are limited, with only Liu[12] conducting a four-point bending test on basalt fiber-reinforced polymer (BFRP)-UHPSSC beams using reinforcement ratio as the sole research factor. Considering that the influencing factors of flexural behavior of FRP-UHPSSC beams go beyond just reinforcement ratio, further research analyzing additional influencing factors is necessary to fully elucidate the flexural behavior characteristics of FRP-UHPSSC beams.

RESEARCH SIGNIFICANCE

The innovation of this paper lies in the combination of FRP reinforcements and UHPSSC. By conducting four-point bending tests on FRP-UHPSSC beams, the influence of reinforcement ratio, beam section height, and FRP reinforcement type (carbon fiber-reinforced polymer [CFRP], BFRP, steel fiber composite bar [SFCB], and basalt/carbon fiber-reinforced polymer [B/CFRP]) on the flexural performance of FRP-UHPSSC beams is explored. The failure modes, cracking development trend, bending stiffness, and flexural capacity of FRP-UHPSSC beams are discussed. Based on

ACI Structural Journal, V. 123, No. 3, May 2026.
MS No. S-2024-248.R2, doi: 10.14359/51749490, received April 20, 2025, and reviewed under Institute publication policies. Copyright © 2026, American Concrete Institute. All rights reserved, including the making of copies unless permission is obtained from the copyright proprietors. Pertinent discussion including author's closure, if any, will be published ten months from this journal's date if the discussion is received within four months of the paper's print publication.

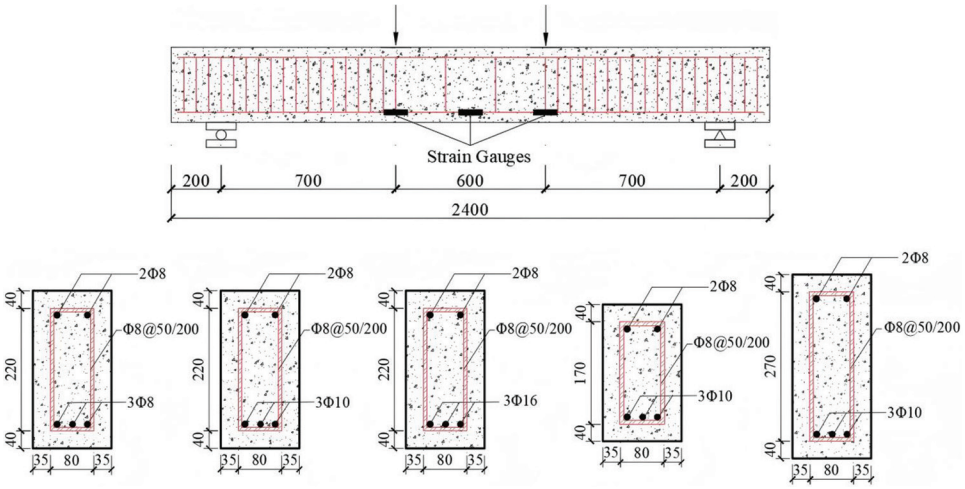

Fig. 1—Geometry and reinforcement details for UHPSSC beams.

Fig. 2—View of CFRP transverse reinforcements.

these results, the existing design specifications and a new calculation method proposed for FRP-RC structures were evaluated.

EXPERIMENTAL INVESTIGATION

Details of test specimen

The study examines the effect of the tensile FRP bar types, the reinforcement ratio, and the beam section height on the test beams. Sixteen test beams were designed according to GB 50608-2020.[13] Two CFRP bars with an 8 mm diameter were used in the compression zone of the beams. The cross-sectional width of the test beam is uniformly 150 mm, with three different heights: 250, 300, and 350 mm. The total length of the test beam is 2400 mm, and simply supported hinged supports are located 200 mm from each end, resulting in a clear span of 2000 mm. Two symmetrical concentrated loads are applied to the top of the simply supported beam, each at a distance of 700 mm from the nearest support, and the clear span between the two symmetrical concentrated loads is 600 mm. For more details, please refer to Fig. 1. The test beam numbers comprise three components. The first letter denotes the type of tensile longitudinal reinforcement: C, B/C, SF, and B indicates CFRP bars, B/CFRP bars, SFCB bars, and BFRP bars, respectively. The first value specifies the diameter of the longitudinal bars in the tension zone, while the second value indicates their quantity. The third value represents the beam section height. For instance, B/C8-3-300 implies that the tensile longitudinal bars are B/CFRP bars with a diameter of 8 mm, three bars are employed, and the beam section has a height of 300 mm.

Reinforcing bars

The longitudinal bars used in this study include CFRP bars, B/CFRP bars, SFCB bars, and BFRP bars. The transverse reinforcements are CFRP bars with a diameter of 8 mm, as shown in Fig. 2. The core of the SFCB bar is an HRB400 steel bar with a diameter of 6 mm, wrapped with CFRP fibers. The core of the B/CFRP bar is CFRP fibers, wrapped with BFRP fibers, and the two types of fibers are mixed in a ratio of 1:1, as shown in Fig. 3. The mechanical properties of the FRP bars were measured by GB/T 30022-2013.[14] An electronic universal testing machine with a maximum test force of 1000 kN and a loading speed of 4 mm/min was used. Each test group consisted of five specimens, and the average test results are presented in Table 1. The test specimens for mechanical properties are shown in Fig. 4(a). The diameter of the gripping section (D) at both ends of the specimen is related to the specimen diameter (d). When d is 8 or 10 mm, D is 20 mm; when d is 16 mm, D is 33 mm. Figures 4(b), (c), (d), and (e) show the states of CFRP, BFRP, B/CFRP, and SFCB bars at failure, respectively. Figures 5(a) to (d) present the stress-strain relationships of the four types of longitudinal bars, all of which exhibit a clear linear relationship. However, existing studies[15] have suggested that the stress-strain curve of SFCB bars is bilinear, which is inconsistent with the results shown in Fig. 5(c). The discrepancy arises because the core of the SFCB bar did not yield when the SFCB bar experienced tensile damage, as shown in Fig. 4(e). Additionally, the fluctuation observed in Fig. 5(d) is due to slippage at the end of the FRP test specimen.

UHPSSC

The UHPSSC raw materials comprised cementitious materials, including P.O 42.5 grade ordinary silicate cement, silica fume (with over 97% SiO_2 content), and Class II fly ash. The chemical compositions of these materials are detailed in the literature.[9] Raw sea sand served as the aggregate, and its primary parameters are outlined in literature.[9]

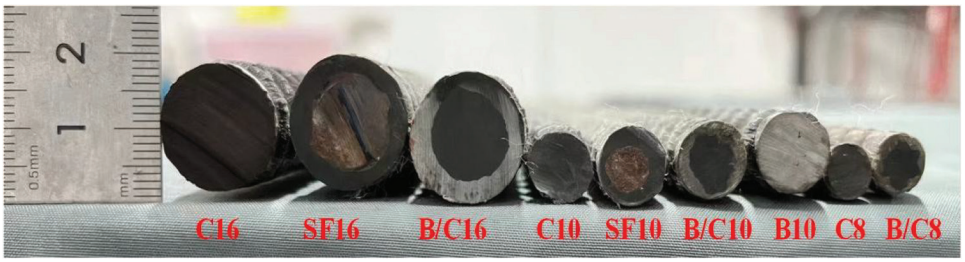

Fig. 3—Cross section of FRP bars.

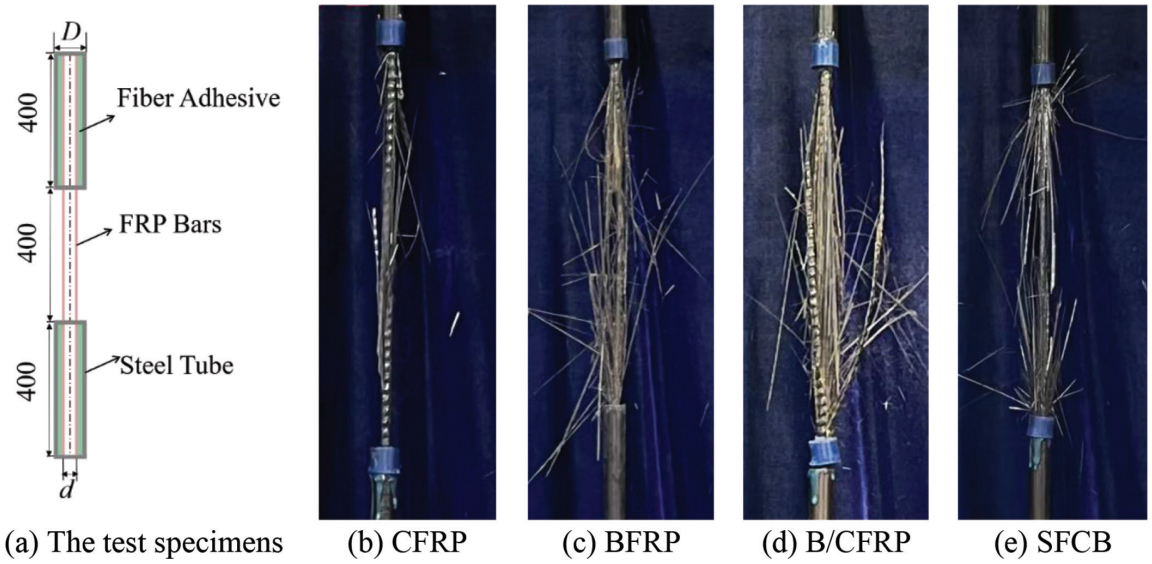

Fig. 4—Test specimens and FRP damage patterns.

Table 1—Mechanical properties of FRP bars

FRP bar types	d, mm	E_f, GPa	f_f, MPa	COVf_f	ε_{fu}	COVε_{fu}	s_r, mm	b_r, mm	h_r, mm
CFRP	8	83.48	952.2	0.10	0.011	0.07	2	8	1.0
	10	87.26	967.4	0.09	0.011	0.08			
	16	81.24	1028.1	0.08	0.013	0.08			
B/CFRP	8	136.52	1927.3	0.09	0.014	0.10	3	5	1.0
	10	123.62	2189.2	0.08	0.018	0.07			
	16	102.64	2016.4	0.10	0.020	0.08			
SFCB	10	137.32	1459.5	0.07	0.011	0.09	3	7	0.5
	16	114.78	1472.0	0.09	0.013	0.08			
BFRP	10	51.63	883.1	0.10	0.017	0.07	3	7	0.5

For admixtures, a polycarboxylic acid-type high-efficiency water-reducing agent (with a water reduction rate of 22%) and an organosilicon antifoam agent (with an activity content of 99%) were used. Additionally, due to the large difference in seawater composition in different sea areas, which has a significant impact on the performance of UHPSSC, this paper adopts ASTM D1141-98[16] for the preparation of artificial seawater to ensure the stability of seawater quality, and its primary chemical composition is presented in Table 2.

The preparation process of UHPSSC involved the following steps: first, cement, silica fume, fly ash, and sea sand were combined in the mixer and subjected to 3 minutes of low-speed dry mixing. Next, pre-configured artificial seawater, water reducer, and antifoam agent were added, and the materials were mixed at low speed for an additional 3 minutes. Finally, high-speed mixing was performed for 2 minutes. Referring to the UHPSSC mixture design proposed in the literature[9] based on orthogonal design, the optimum mixture design of UHPSSC for this test was obtained: 736.5 kg/m^3 cement, 168 kg/m^3 artificial seawater, 210 kg/m^3 silica fume, 105 kg/m^3 fly ash, 946.6 kg/m^3 sea sand, 8.41 kg/m^3 antifoam agent, and 21.03 kg/m^3 water-reducing agent. To ensure the durability of the concrete and mitigate risks related to the corrosion of steel fibers or the aging of polyethylene (PE) fibers,[17] no fibers were included in this particular test. The test beams in this paper were placed in the same batch and naturally cured for 28 days after placement, with a testing period of 1 month. Table 3 presents the

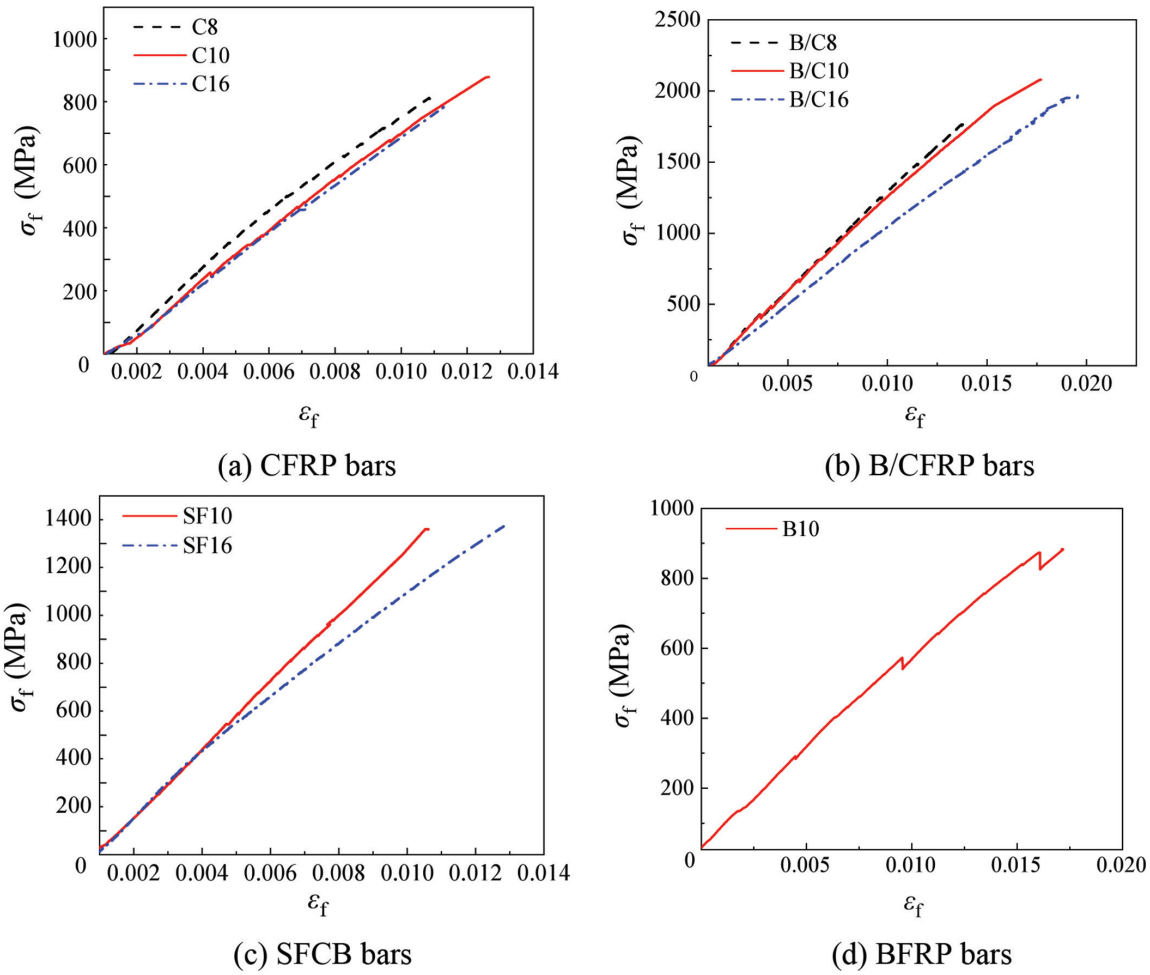

Fig. 5—Stress-strain curves of FRP bars.

Table 2—Chemical compositions of artificial seawater, g/L

Component	NaCl	$MgCl_2$	Na_2SO_4	$CaCl_2$	KCl	$NaHCO_3$
Concentration	24.530	5.200	4.090	1.160	0.695	0.201

mechanical properties of UHPSSC. All material parameters were tested using GB/T 50081-2019,[18] except for f_c', which was tested according to ASTM C39/C39M-18.[19]

Test setup and instrumentation

The experimental investigation employed a four-point bending loading configuration, as illustrated in Fig. 6. Each test beam featured a total length of 700 mm, with a 600 mm pure bending span between the loading points. Five high-precision linear variable differential transformers (LVDTs; accuracy: 0.01 mm) were strategically positioned to monitor vertical displacements at critical locations: midspan, two loading points, and both support ends. Concrete surface strains were measured using electrical strain gauges mounted on the midspan side face of the beams.

Loading was applied through a spreader beam system equipped with a manually operated hydraulic jack at midspan, connected to a reaction frame through a load cell for real-time force measurement. All displacement, load, and strain data were synchronously acquired using a dynamic data acquisition system and subsequently processed with analytical software, ensuring sampling rates above 10 Hz for transient response capture.

Table 3—Mechanical properties of UHPSSC

f_{cu}, MPa	f_c, MPa	E_c, GPa	f_t, MPa	ε_{cu}
107.33	78.08	43.40	4.50	0.0025

The loading procedure follows GB/T 50152-2012,[20] and the specific steps are as follows:

1. Before formal loading, the test beam should be preloaded to ensure that the test setup is correctly assembled and all experimental instruments are functioning properly. The preload is applied in a force-controlled manner, with the applied load not exceeding 0.7 times the calculated cracking load, keeping the test beam within the elastic range without generating cracks.

2. During formal loading, a force-controlled loading method is used. Based on the pre-test calculations of the cracking load and ultimate load of the test beam, a graded loading system is adopted to ensure that the holding time for each load level is 3 minutes. In the early stage of loading, each load increment is 10 kN. When the load approaches the calculated cracking load, the load increment is adjusted to 5 kN to facilitate the observation of initial microcrack development. After the initial cracks appear, the load increment is readjusted to 10 kN, and loading continues up to 0.85 times the calculated ultimate load. Subsequently, the loading

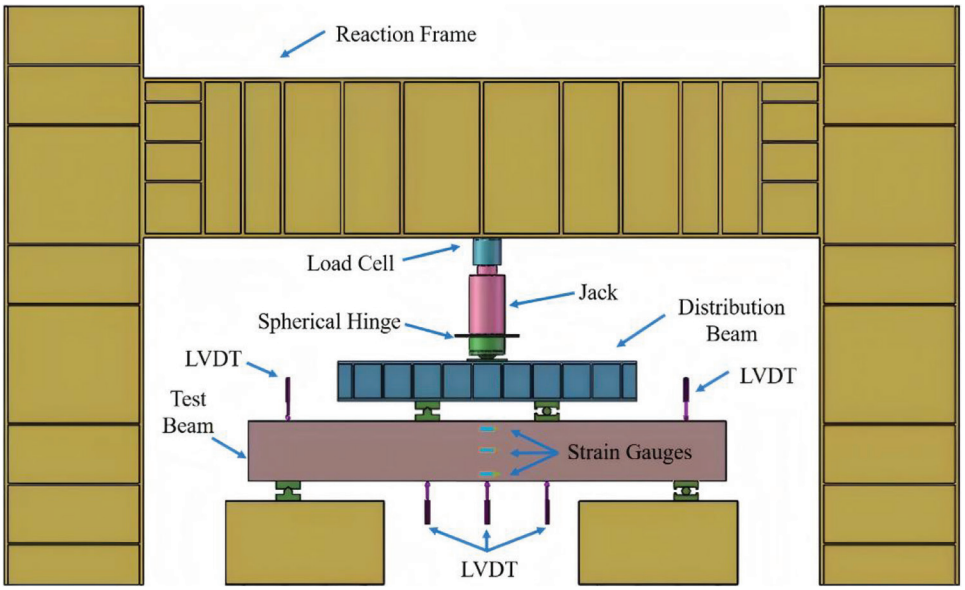

Fig. 6—Flexural test setup for FRP-UHPSSC beams.

method is switched to displacement-controlled loading, with each displacement increment being 1 mm, until the test beam fails and the test is terminated.

EXPERIMENTAL RESULTS

All test results are shown in Table 4, where P_s and M_s are the load and bending moments corresponding to the test beams reaching the service limit state (when the midspan deflection reaches $\Delta_s = l_0/360 = 5.56$ mm),[21] respectively. B_s is the service limit state stiffness (tangential stiffness) of the test beams, the values of which are the slopes corresponding to the bending moment-curvature curves at M_s. In this test, the displacement change of the purely curved section of the test beam was measured by a high-precision linear displacement meter, and then the section curvature of the purely curved section of the test beam could be calculated according to the displacement data for each level of loading. The curvature is obtained by geometrically calculating the displacements of the three LVDTs measured at the bottom of the beams. The ductility of RC beams is defined as the ratio of the ultimate deflection, or curvature of RC to the deflection or curvature when the steel reinforcement is at yield. Because FRP reinforcement is a linear elastic material without a yield stage, traditional methods for analyzing the ductility of RC beams will no longer be applicable. In this paper, the method of calculating the ductility factor μ_f for FRP beams proposed by Naaman and Jeong[22] based on the energy concept is used (Eq. (1)). E_{tot} is the total energy of the test beam, which means the area enclosed by the load-deflection curve when the ultimate load is reached ($A_1 + A_2$), and E_{el} is the energy stored in the elastic phase (A_2); refer to Fig. 7.

$$\mu_f = \frac{1}{2}\left(\frac{E_{tot}}{E_{el}} + 1\right) \tag{1}$$

Failure modes

The failure modes of the 16 FRP-UHPSSC beams were systematically categorized based on experimental observations and parametric thresholds. The dominant failure mechanisms (tensile, compression, or shear failure) exhibited strong correlations with the reinforcement ratio (ρ), beam height (h), and FRP bar type, detailed as follows.

1. Classification of failure modes—Three distinct failure modes were identified (Fig. 8): tensile failure—rupture of FRP bars in the tension zone, with intact concrete in the compression zone (for example, C10-3-300, Fig. 8(b)); compression failure—crushing of concrete in the compression zone, with FRP bars remaining intact (for example, B/C10-3-300, Fig. 8(k)); and shear failure—diagonal cracking in the shear span, accompanied by transverse reinforcement fracture (for example, B/C16-3-300, Fig. 8(n)).

2. Quantitative thresholds for failure mode transition—The failure mode transition was governed by the actual-to-balanced reinforcement ratio (ρ/ρ_{fb}) and FRP bar properties (Table 5). According to GB 50608-2020,[13] when the normalized reinforcement ratio $\rho/\rho_{fb} > 1.83$, the failure mode transitions from tension-controlled to compression-controlled. A representative example is Specimen B/C10-3-300 (ρ = 0.61%, ρ/ρ = 2.19), where the high modulus of FRP bars (E_f = 123.62 GPa) restricted tensile strain development (ε_{fu} = 18,000 με), leading to premature crushing of the concrete compression zone. Furthermore, experimental data indicate that when $\rho/\rho_{fb} > 2.73$, excessive reinforcement ratios trigger a secondary transition from compression-controlled to shear-dominated failure. For instance, Specimen B/C16-3-300 (ρ = 1.58%, ρ/ρ_{fb} = 5.73) exhibited a reduced shear span-depth ratio (a/h_0 = 2.80), which, combined with intensified stress concentration under high ρ, ultimately resulted in diagonal shear failure. These findings demonstrate that while increasing ρ enhances load-bearing capacity, surpassing critical thresholds induces multi-mechanistic degradation of ductility and embrittlement of failure modes.

Table 4—Results of four-point bending tests

Beam designation	ρ, %	P_{cr}, kN	M_{cr}, kN·m	P_s, kN	M_s, kN·m	P_u, kN	M_u, kN·m	Δ_u, mm	B_s, kN·m^2	μ_f	Failure mode
C8-3-300	0.39	15	5.4	40	14.0	97	34.0	23.9	650	3.768	T
C10-3-300	0.61	15	5.3	49	17.2	150	52.5	32.4	840	3.678	T
C16-3-300	1.58	16	5.8	95	33.3	280	98.0	31.2	1434	1.436	C
C10-3-250	0.76	10	3.5	29	10.2	115	40.3	39.0	532	2.552	T
C10-3-350	0.51	26	8.9	80	28.0	185	64.8	26.0	1447	3.003	T
B/C8-3-300	0.39	16	5.7	55	19.3	212	74.2	38.0	981	2.681	T
B/C10-3-300	0.61	15	5.3	68	23.8	242	84.7	35.8	1148	2.049	C
B/C16-3-300	1.58	20	7.0	136	47.6	340	119.0	27.0	1659	1.315	S
B/C10-3-250	0.76	10	3.6	43	15.1	165	57.8	34.3	889	1.305	S
B/C10-3-350	0.51	25	8.6	104	36.4	335	117.3	34.5	1789	2.340	C
SF10-2-300	0.39	20	7.0	61	21.4	188	65.8	34.0	1006	2.449	T
SF10-3-300	0.61	15	5.3	80	28.0	266	93.1	35.9	1385	2.300	T
SF16-3-300	1.58	20	7.0	156	54.6	358	125.3	29.5	1526	1.862	S
SF10-3-250	0.76	15	5.3	51	17.9	191	66.9	40.0	872	2.103	T
SF10-3-350	0.51	26	8.9	120	42.0	346	121.1	33.5	1732	2.482	T
B10-3-300	0.61	16	5.4	39	13.7	162	56.7	55.0	474	4.109	T

Note: T means tensile failure; C means compression failure; and S means shear failure.

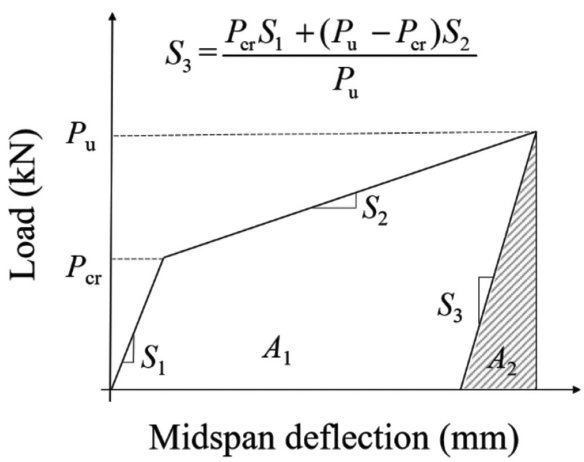

Fig. 7—Schematic diagram of μ_f *calculation.*

3. FRP bar performance and failure mechanism coupling—The performance and failure mechanisms of FRP bars exhibited significant type-dependent characteristics, as detailed later. CFRP bars predominantly failed in tensile-shear hybrid modes, where their high elastic modulus (E_f = 83.48 GPa) delayed concrete crack initiation but amplified interfacial shear stress concentrations. In contrast, BFRP bars demonstrated tensile-dominated failures owing to their lower modulus (E_f = 51.63 GPa), which permitted substantial ductile deformations (Δ_u = 55.0 mm) prior to rupture. SFCB bars exhibited compression-controlled failures, attributed to the elastic-plastic synergy between their steel core and CFRP outer layer, effectively stabilizing post-cracking stiffness through staged energy dissipation. Conversely, B/CFRP hybrid bars showed shear-critical failures due to abrupt stress redistribution caused by their ultra-high tensile strength (f_f = 2189.2 MPa), overwhelming the concrete's shear capacity. These observations underscore the critical role of FRP material properties in governing failure mode transitions and structural energy dissipation pathways.

4. Crack development and failure progression—Crack propagation patterns across different loading stages were systematically investigated for all beam specimens (Fig. 8, Table 4), revealing three distinct evolutionary phases.

Stage 1 (Pre-cracking, $P < P_{cr}$): Vertical flexural cracks initiated predominantly at midspan regions, with crack widths (w) ranging from 0.06 to 0.3 mm. Specimen C10-3-250 exemplified this stage, displaying uniform crack spacing (s = 120 mm) due to homogeneous stress distribution prior to cracking.

Stage 2 (Post-cracking, $P_{cr} < P < 0.8P_u$): Symmetrical diagonal cracks propagated within shear spans, widening to w = 0.1 to 0.5 mm. The hybrid stiffness of SFCB reinforcement in Specimen SF10-3-300 induced uniquely oriented inclined cracks at 45 degrees, demonstrating material-specific crack trajectory modulation.

Stage 3 (Ultimate failure, $P > 0.8P_u$): Failure modes diverged based on reinforcement configurations.

Tensile failure: Characterized by abrupt FRP rupture, as observed in B10-3-300 (ε_{fu} = 17,000 με).

Compression failure: Manifested as localized concrete crushing beneath loading points, reaching ultimate compressive strains (ε_{cu} = 0.0025).

Shear failure: Dominated by critical diagonal cracks splitting concrete into prismatic columns (Fig. 8(n)), indicative of shear-tension interaction failure.

Load-midspan deflection curves of FRP-UHPSSC beams

The load-midspan deflection response curves of test beams exhibit distinct bilinear characteristics (Fig. 9), with

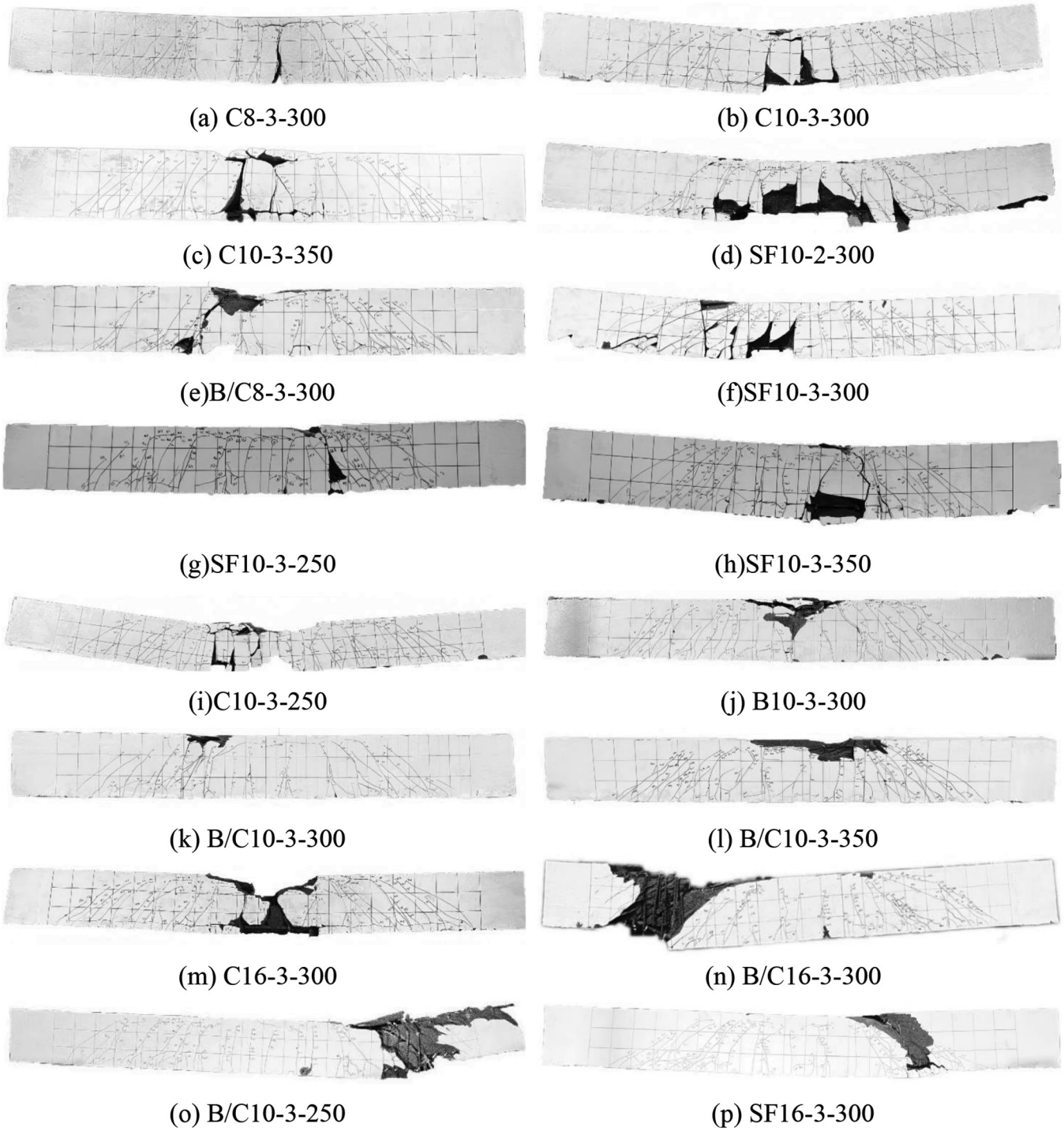

Fig. 8—Failure patterns of tested FRP-UHPSSC beams.

mechanical behavior systematically divided into two evolutionary phases:

1. Elastic phase (load < P_{cr}*)*—All specimens demonstrate linear elastic response during initial loading, with average initial stiffness B_0 = 43.4 GPa (consistent with UHPSSC elastic modulus E_c = 43.40 GPa; refer to Table 3). The concrete matrix remains intact without cracking in this phase, and the moment of inertia is calculated using full geometric parameters

$$I_g = \frac{1}{12} b h^3 \tag{2}$$

Initial stiffness is governed by material constitutive relationship and geometric parameters

$$B_0 = \frac{E_c I_g}{\psi_f} \tag{3}$$

where ψ_f = 0.87, denoting internal lever arm correction factor.

2. Post-cracking phase (load > P_{cr}*)*—Concrete bottom cracking induces drastic stiffness degradation to 18 to 35% of initial values, with degradation magnitude strongly correlated to FRP bar types. SFCB-reinforced beams

Table 5—ρ/ρ_{fb} and load-bearing capacity calculation of FRP-UHPSSC beams

Beam designation	Failure modes	GB 50608-2020[13]			ACI 440.1R-15[23]			CSA S806-12[24]	
		ρ/ρ_{fb}	x, mm	M_{upre}, kN·m	ρ/ρ_{fb}	x, mm	M_{upre}, kN·m	ρ/ρ_{fb}	M_{upre}, kN·m
C8-3-300	Tensile failure	0.42	18.0	34.3	0.44	21.0	51.4	0.45	33.1
C10-3-300		0.65	25.0	53.4	0.69	26.3	64.1	0.69	52.4
C10-3-250		0.81	23.6	42.2	0.86	23.3	45.2	0.86	41.8
C10-3-350		0.54	26.4	64.7	0.58	29.1	85.1	0.58	63.0
B/C8-3-300		1.02	29.1	67.8	1.07	26.4	65.1	1.08	62.9
SF10-2-300		0.61	24.6	53.8	0.64	26.9	65.5	0.64	52.7
SF10-3-300		1.11	34.7	79.0	1.03	32.3	78.6	1.01	75.6
SF10-3-250		1.18	33.2	62.0	1.25	28.4	54.8	1.26	52.0
SF10-3-350		0.79	36.2	95.9	0.84	35.8	104.7	0.84	95.0
B10-3-300		0.86	21.5	49.2	0.91	20.7	51.2	0.91	48.9
C16-3-300	Compression failure	2.00	38.5	95.1	2.11	38.5	91.1	2.13	83.4
B/C10-3-300		2.19	30.5	77.6	2.32	30.8	75.1	2.33	69.4
B/C10-3-350		1.83	33.8	103.5	1.94	34.1	100.4	1.95	94.3
B/C16-3-300	Shear failure	5.73	42.3	103.7	6.06	42.5	99.9	6.09	78.9
B/C10-3-250		2.73	26.8	54.5	2.89	27.2	52.5	2.98	47.2
SF16-3-300		2.90	45.0	109.5	3.06	44.5	104.3	3.08	90.5

benefit from the high elastic modulus of hybrid bars (E_f = 137.32 GPa), retaining 35% post-cracking stiffness (for example, Specimen SF10-3-300), while BFRP-reinforced beams are limited by lower elastic modulus (E_f = 51.63 GPa), so stiffness retention plummets to 18% (for example, Specimen B10-3-300).

Experimental evidence confirms that FRP elastic modulus is the dominant parameter controlling post-cracking stiffness degradation (Fig. 9(d)).

Load-strain curve of FRP bars

The load-strain response curves of FRP bars (Fig. 10) systematically reveal the evolution of mechanical behavior before and after concrete cracking, characterized by two distinct phases:

1. Pre-cracking phase (ε_f < 500 με)—Concrete matrix predominantly resists tensile stress, with gradual strain development in FRP bars governed by Eq. (9). Measured strains in this phase range from 200 to 500 με (Fig. 10(a) to (c)), indicating effective load transfer through interfacial bonding.

$$\sigma_f = \frac{M}{\eta A_f h_0} \tag{4}$$

where $\eta \approx 0.98$ denotes concrete-FRP strain compatibility coefficient.

2. Post-cracking phase (ε_f > 500 με)—After concrete loses tensile capacity, FRP strains surge nonlinearly to ultimate values (ε_{fu} =11,000 to 20,000 με) with type-dependent characteristics. In SFCB bars, synergy between steel core and CFRP fibers (Fig. 10(c)) retards strain growth, stabilizing at ε_{fu} = 11,000 με. In B/CFRP bars, carbon fiber dominance (Fig. 10(b)) drives rapid strain escalation to ε_{fu} = 20,000 με, yet with limited ductility (μ_f = 2.05, Table 4). In BFRP bars, despite the lowest modulus, maximum ultimate strain (ε_{fu} = 17,000 με) enables superior deformation capacity (μ_f = 4.11).

This mechanistic evolution confirms that post-cracking FRP bars act as sole tensile carriers, whose constitutive properties (elastic modulus E_f, ultimate strain ε_{fu}) directly govern beam failure modes (Fig. 8) and ductility performance.

DISCUSSION

Effect of reinforcement ratio

Figure 11 illustrates the impact of ρ on B_s and M_u. With constant beam height (h) and fixed FRP reinforcement type in the tension zone, increasing the reinforcement ratio (ρ) demonstrates significant positive regulatory effects on both beam stiffness (B_s) and ultimate load capacity (M_u). Taking CFRP-reinforced beams (h = 300 mm) as a representative case: when ρ rises from 0.39% to 0.61%, B_s increases from 649.6 to 839.8 kN·m^2 (+29.2%), while M_u surges from 33.95 to 52.5 kN·m (+54.4%). This enhancement stems from two synergistic mechanisms: 1) the increased flexural inertia moment (I) due to higher ρ; and 2) the interfacial cooperative working mechanism between FRP and UHPSSC that effectively restrains stable crack propagation. According to the balanced reinforcement ratio (ρ_{fb}) calculation formula specified in Table A, experimental findings reveal critical threshold effects: when ρ/ρ_{fb} exceeds 1.83 (for example, Specimen B/C10-3-300), the failure mode undergoes phase transition from tension-controlled to compression-controlled; further, exceeding ρ/ρ_{fb} > 2.73 (for example, Specimen B/C16-3-300) induces shear-dominated brittle failure, conclusively proving that excessive reinforcement disrupts ductile energy dissipation mechanisms.

The relationship between P_u and ρ demonstrates remarkable nonlinear characteristics, with its core originating from

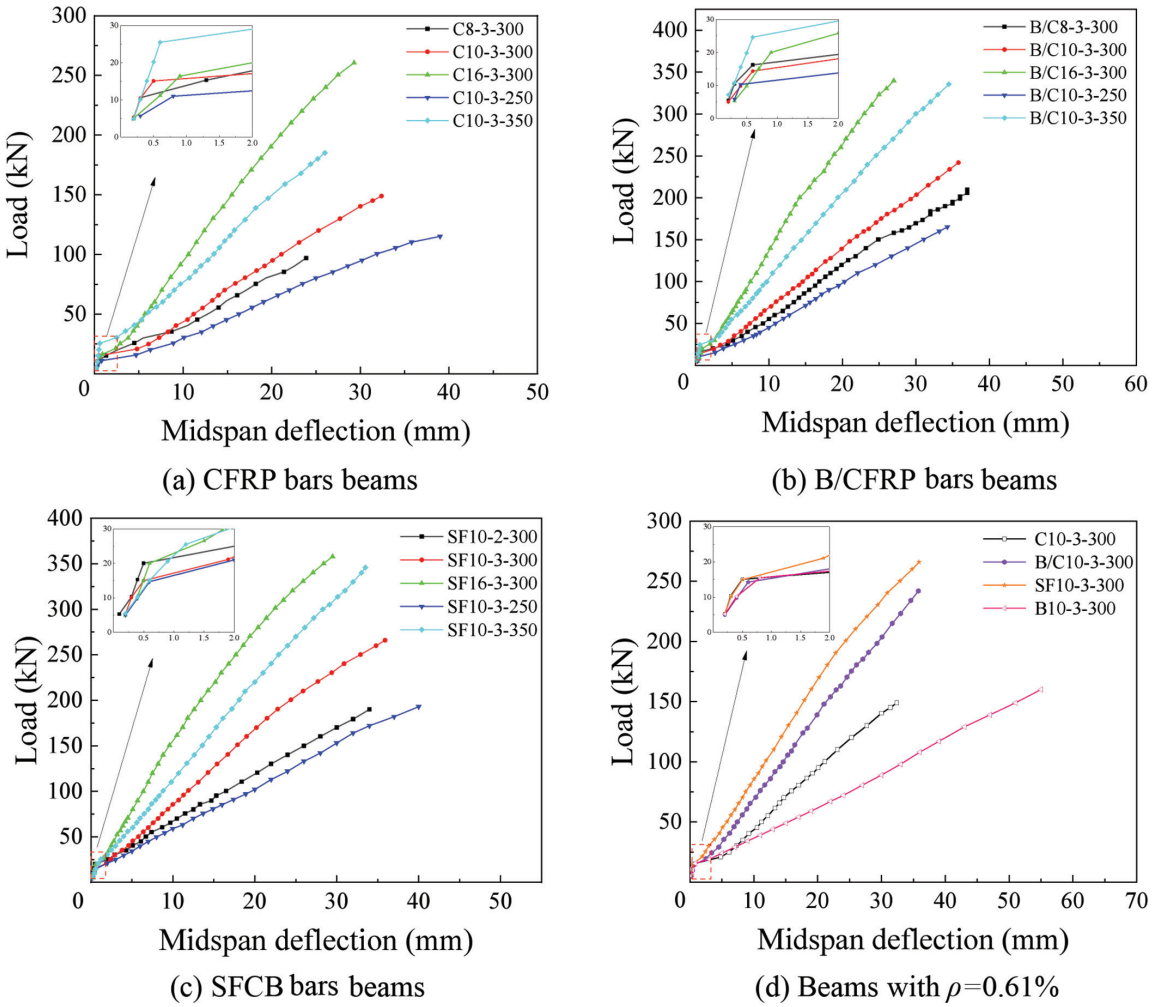

Fig. 9—Load-midspan deflection curves of FRP-UHPSSC beams.

the coupled effect of failure mode transition and size effect. Experiments indicate that: 1) during the stage dominated by tensile failure ($\rho/\rho_{fb} < 1.83$), P_u is approximately linearly and positively correlated with ρ. For instance, when the ρ of a CFRP beam increases from 0.39% to 0.61%, P_u increases by 55% concurrently; and 2) when ρ exceeds the balanced reinforcement ratio ($\rho/\rho_{fb} > 1.83$), the failure mode changes to compression or shear failure. For example, the B/C16-3-300 beam with ρ = 1.58% experiences shear failure. At this point, the growth rate of P_u significantly decreases or even halts. When the ρ of the CFRP beam increases to 1.58%, P_u only increases by 189%, which is far lower than the 259% increase in the reinforcement ratio. The size effect is particularly prominent in shear failure. For specimens with a high reinforcement ratio, the increase in cross-sectional height leads to the nonlinear attenuation of shear strength. For example, the P_u of the SF16-3-300 beam is only 125.3 kN. Moreover, the deviation in the actual mechanical properties of transverse FRP bars, such as the f_f of CFRP bars being 952.2 MPa, which is lower than the design value of 1800 MPa, exacerbates this nonlinearity.

Effect of FRP bar category

Figure 12 illustrates the impact of different types of FRP bars on B_s, M_u, and μ_f in the tension zone. When substituting the BFRP bar (E_f = 51.63 GPa) with the SFCB bar (E_f = 137.32 GPa) as the tensile reinforcement in the test beam, the value of B_s increases in line with the higher E_f of the FRP bar, similar to the behavior observed in the FRP-SSC beam case. Conversely, when replacing the SFCB bar (f_f = 1459.5 MPa) with B/CFRP bar (f_f = 2189.2 MPa) as the tensile reinforcement, M_u exhibited a 10% decrease instead of the expected 50% increase in f_f. This unexpected outcome can be attributed to the fact that when the B/C10-3-300 beam experienced compression failure, the concrete in its compression zone reached the ultimate compressive strain, resulting in diminished stresses on the FRP bars located in the tension zone. Consequently, these stresses were significantly lower than the f_f values of the B/CFRP bars. In addition, comparing B10-3-300 and C10-3-300, it can be found that M_u decreases with the increase of f_f, which is caused by the partial sliding of the tensile longitudinal bars of the test beam C10-3-300 at the end anchoring point, which prevents the tensile strength of the CFRP bars in this test beam from being fully used. In this case, even if the f_f of CFRP bars is greater than that of BFRP bars, the ultimate stress of CFRP bars is smaller than that of BFRP bars when the ultimate failure of the test beam is achieved. For tensile failure beams, the M_u depends on the ultimate stress of FRP bars, so the M_u of C10-3-300 is less than that of B10-3-300

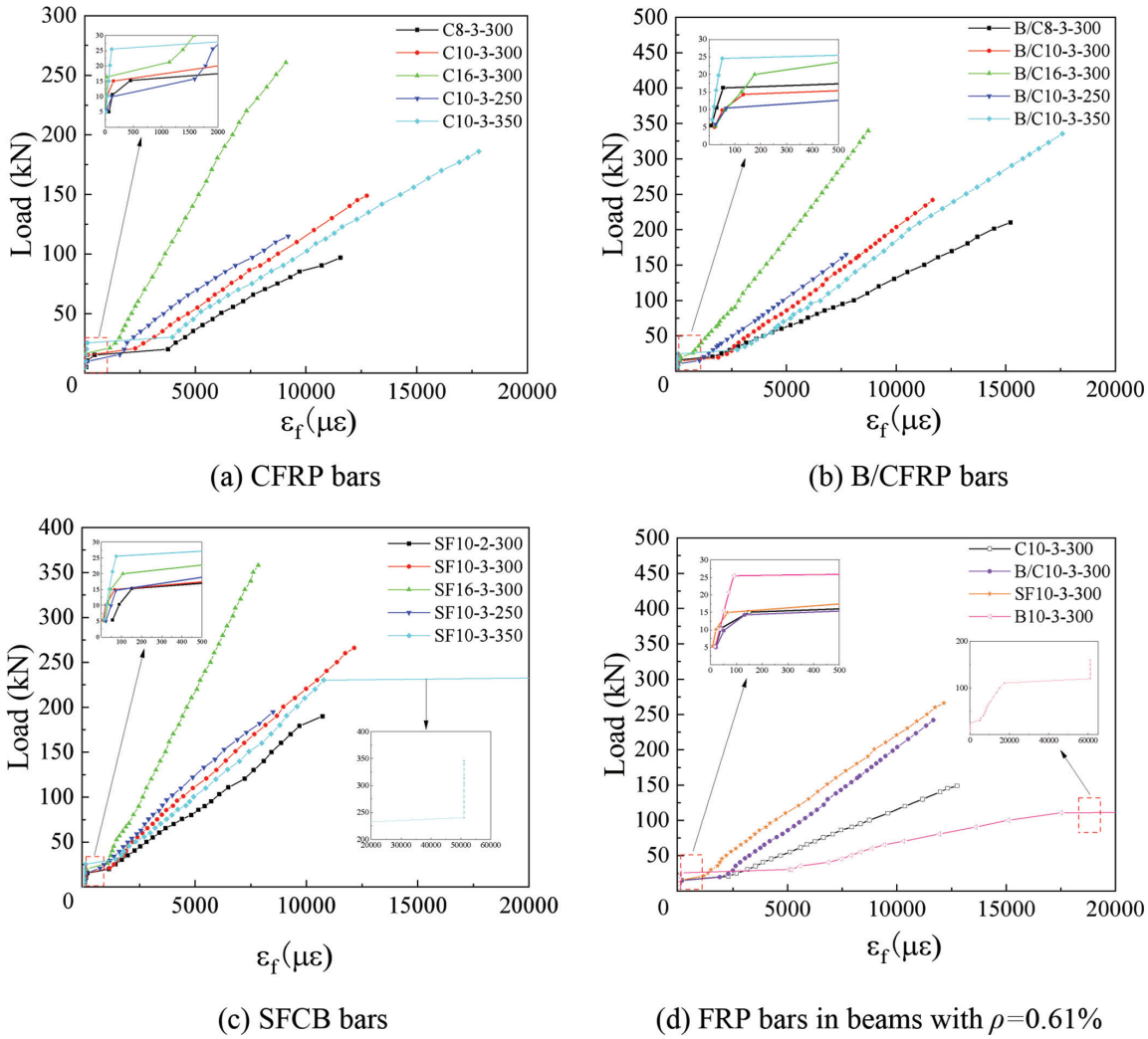

(a) CFRP bars (b) B/CFRP bars

(c) SFCB bars (d) FRP bars in beams with ρ=0.61%

Fig. 10—Load-strain curves of FRP bars.

in Fig. 12(b). From Fig. 12(d), it can be seen that the use of BFRP reinforcement is the largest (40.1%) and the use of B/CFRP reinforcement is the smallest (23.6%), which is due to the difference in ultimate tensile strength between FRP reinforcement and UHPSSC being too large; the larger the f_f, the lower the efficiency of the synergistic work between FRP reinforcement and UHPSSC. ε_{10} is the strain value of FRP reinforcement corresponding to the test beams reaching the service limit state (when the midspan deflection reaches $\Delta_s = l_0/360 = 5.56$ mm).[21]

With the transition of the main reinforcement in the tension zone of the test beam from BFRP bars to B/CFRP bars, the ductility of the test beam decreases as the f_f of the FRP reinforcement in the tension zone increases. This is attributed to the fact that the increased f_f of the FRP reinforcement leads to a higher relative height of the compressed zone. Consequently, this results in a reduction in the deformation capacity of the test beam.

Effect of beam section height

By examining the load-midspan deflection curves illustrated in Fig. 13, it is evident that the test beams, with ρ and the type of FRP bars in the tension zone remaining constant, exhibit an increase in B_s and M_u as the h_0 increases. Beam height (h) exerts significant regulatory effects on the mechanical performance of CFRP-UHPSSC composite beams. With a fixed reinforcement ratio (ρ = 0.61%), increasing h from 250 to 350 mm elevates the serviceability limit state stiffness (B_s) from 532 to 1447 kN·m^2 (+172%), while the ultimate bending moment (M_u) improves from 40.3 to 64.8 kN·m (+60.8%) (Table 4). This nonlinear enhancement mechanism can be theoretically explained through sectional inertia principles: the cubic relationship between beam height and moment of inertia ($I \propto h^3$) leads to exponential growth in flexural stiffness ($B_s \propto E_cI$). Concurrently, the reduced compression zone depth (x) significantly increases the internal lever arm ($z = h_0 - x/2$), driving quasi-linear growth of M_u with beam height (Table A). Crucially, when increased h reduces the shear span-depth ratio (a/h_0) below critical thresholds (for example, Specimen B/C10-3-250), it triggers transition to shear-induced brittle failure modes, necessitating co-optimization of stiffness enhancement and ductility preservation in structural design.

THEORETICAL ANALYSIS

Bending moment at ultimate limit state

In the calculation of bearing capacity for the flexural beams, GB 50608-2020,[13] ACI 440.1R-15,[23] and CSA S806-12[24] do

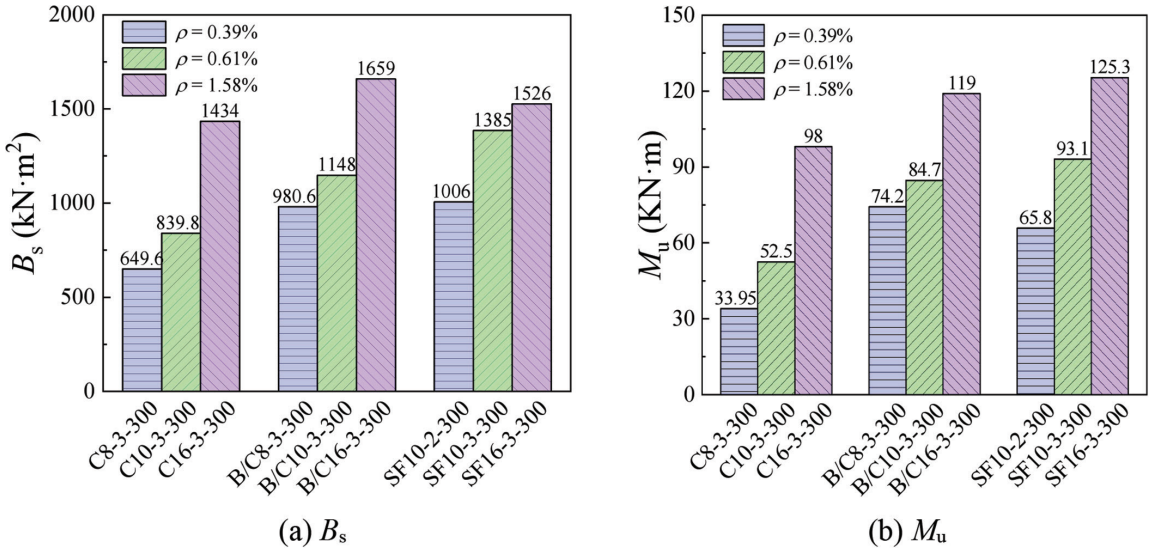

Fig. 11—Effect of reinforcement ratio on B_s *and* M_u.

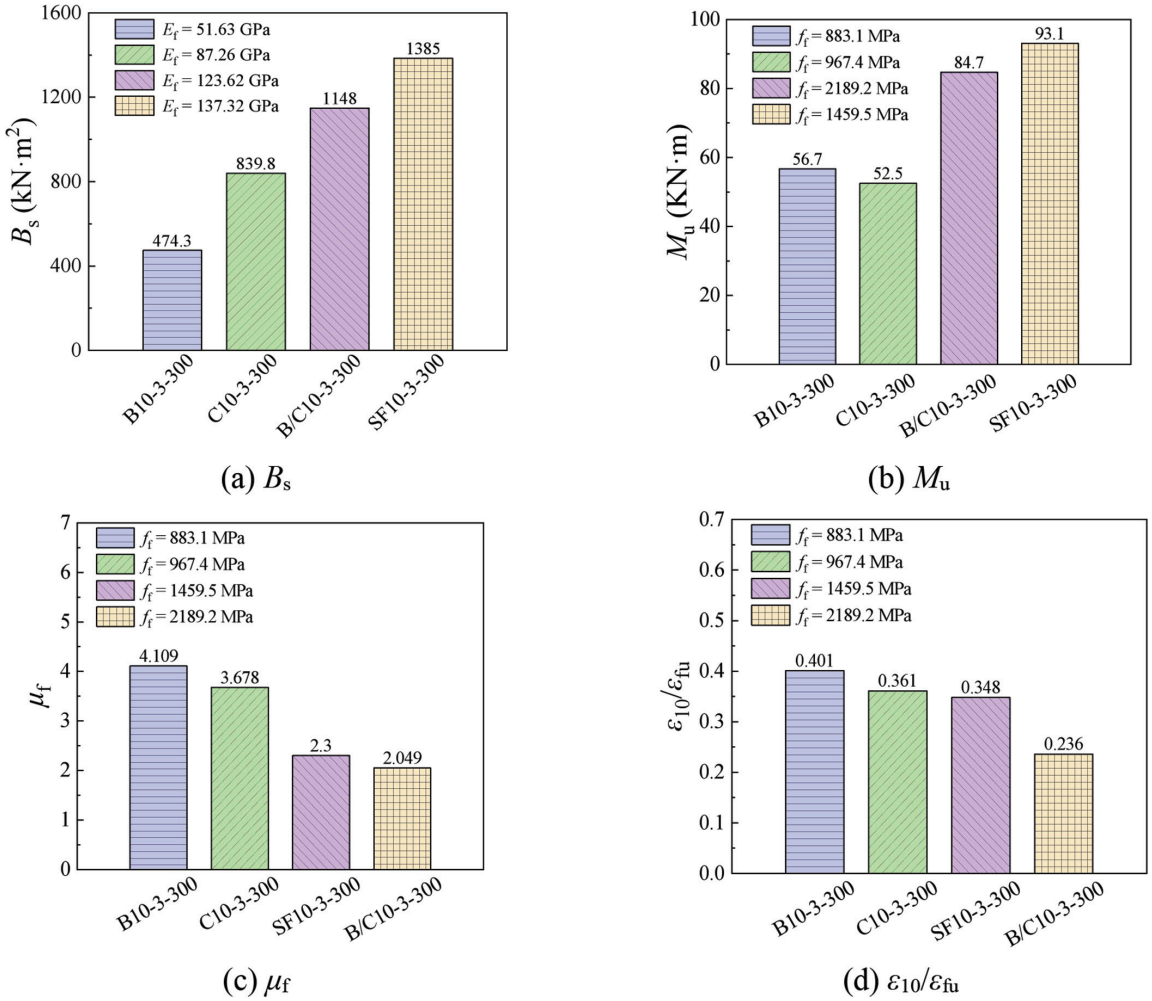

Fig. 12—Effect of FRP bar types on B_s, M_u, μ_f, *and* $\varepsilon_{10}/\varepsilon_{fu}$.

not consider the compression zone of the longitudinal reinforcement or the tensile area of the concrete. These codes categorize flexural damage modes into tensile failure and compression failure (the code specifies the ultimate bending moment calculation formula presented in Table A). In addition, Fig. 14(a) to (c) compare M_u obtained from the test beam experiment with the calculation result M_{upre} using the aforementioned code (excluding shear failure beams). The results show that the calculation according to CSA S806-12[24] is the most conservative, with M_u being approximately 1.129 times M_{upre}. Some calculated values exceed the test values, indicating a potential risk. The calculated value of

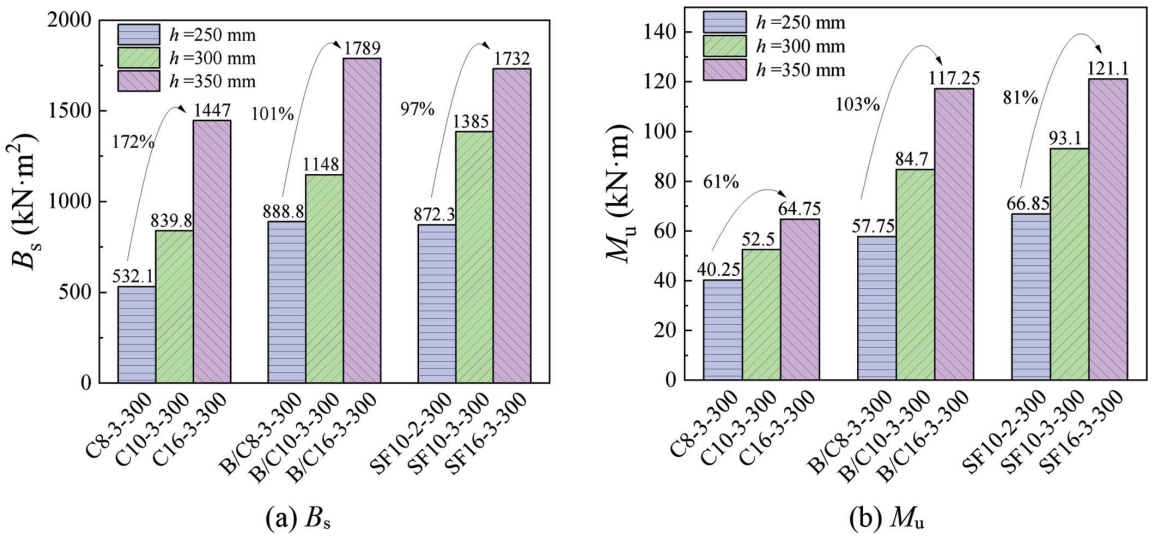

Fig. 13—Effect of beam section height on B_s *and* M_u.

GB 50608-2020[13] is closest to the test value, with M_u being approximately 1.075 times M_{upre}.

Xue et al.[25] conducted parametric analyses on approximately 150 FRP-RC beams and introduced formulas for determining FRP bars' nominal yield strength and flexural capacity under various failure modes. These formulas are presented in Table A. The findings reveal that this method exhibits higher accuracy in calculating tensile failure beams than the specified process mentioned earlier. However, the computed value for compression failure beams exceeds the test value by approximately 15%. This disparity can be attributed to the primary influence of the ultimate compressive strain of the concrete within the compression zone on compression failure. In the current test, the ε_{cu} of the unfiberized UHPSSC is only 0.0025, smaller than the ε_{cu} of concrete used in this method, which is 0.0033. To address this issue, the calculation of x is innovated. Because the flexural capacity is closely related to ρ, ρ is used to correspond to x and ρ_{fb} is used to correspond to c_b. The back-calculation method described in Eq. (5) is used to determine x_{exp} of the compression failure beam.[26] Furthermore, c_b is determined using Eq. (6). By fitting the ratio parameter (ρ/ρ_{fb}) with the parameter (x_{exp}/c_b), a quantitative relationship between the x and c_b of the compression failure beams can be established as shown in Eq. (7). Finally, the traditional calculation method shown in Eq. (8) is used for the calculation of the compression failure beam's M_u.

$$x_{exp} = h_0 \pm \sqrt{h_0^2 - \frac{2M_u}{0.9 f_c b}} \tag{5}$$

$$c_b = \left(\frac{\varepsilon_{cu}}{\varepsilon_{cu} + \varepsilon_{fu}}\right) h_0 \tag{6}$$

$$x = 0.826\, c_b \left(\frac{\rho}{\rho_{fb}}\right)^{0.676} \tag{7}$$

$$M_u = \alpha_1 f_c b x \left(h_0 - \frac{x}{2}\right) \tag{8}$$

This paper presents an improved calculation method for M_u of FRP-UHPSSC beams based on the approach proposed by Xue et al.,[25] shown in Table A. This method is used for calculating M_u of 18 flexural failure beams in the current test and the test conducted by Liu.[12] The results in Fig. 14(d) indicate that all calculated values obtained through the improved method exceed the experimental values. Furthermore, the calculation deviation is significantly smaller than the current FRP-RC design code. Specifically, M_u only exceeds M_{upre} by approximately 2.8%, and the dispersion of the calculated values closely matches that of GB 50608-2020.[13] To ensure the guaranteed rate of $M_u/\theta M_{upre} > 1$ is not less than 95%, θ is calculated as 1.049, and the formula is presented in Eq. (9)[26]

$$\theta = \mu_r + 1.645\sigma_r \tag{9}$$

Midspan deflection at service limit state

The GB 50608-2020[13] adopts the analytical solution method to establish the formula with the averaging idea—that is, the curvature, the strain on the bending cross section, and the neutralized axis position adopts the idea of averaging. Then, it considers the effect of the influence of the FRP reinforcement and the concrete inhomogeneity coefficient ψ_f, which gives the beam flexural stiffness B_s, and finally integrates it to derive the deflection calculation formula; refer to Table A. ACI 440.1R-15[23] adopts the effective moment of inertia method. The deflection is controlled by the gross moment of inertia section I_g when the FRP-RC beam is not cracked. After the initial crack appears in the test beam, the tensile effect of the concrete in the tension zone is neglected, and the FRP reinforcement bears the tensile force. For the elastic analysis of the FRP-reinforced member, the area of the FRP reinforcement can be equated to the area of the concrete at the same height ($n_f A_f$), and the integral coefficient (γ) of the change in stiffness along the length of the bar is taken into account. The deflection is controlled by the effective sectional moment of inertia (I_e), after cracking, and the calculation equations are shown in Table A. CSA S806-12[24] assumes that the section is fully cracked and the crack area of the beam does not contribute to the tensile stiffness; the deflection is calculated

by the integral of the moment-curvature along any point in the span, and the formula is shown in Table A.

Table 6 compares the Δ_s of the flexural failure beams under service limit state in this test and literature[12] with the calculated results of the aforementioned codes. It can be seen that the measured values are all larger than the calculated values of the codes, of which the calculated results of ACI 440.1R-15[23] and CSA S806-12[24] are pretty close to each other, and the computational deviation is approximately 15%. GB 50608-2020[13] has the largest computational deviation and dispersion, with Δ_s approximately 66% of Δ_{spre}, which indicates that the FRP-UHPSSC beams have a more extensive stiffness degradation after cracking compared to FRP-RC beams.

As the UHPSSC used in this paper does not contain fiber, compared with ordinary concrete, the brittleness becomes greater while the strength is increased, and the ultimate compressive strain is approximately 32% lower than that of ordinary concrete, which leads to the reduction of the stiffness of the UHPSSC beam. The existing calculation formula for the deflection of the FRP-RC beam is no longer applicable, so the existing deflection formula needs to be revised. The reason for the excessive calculation deviation of GB 50608-2020[13] is that the internal force arm coefficient η in the flexural stiffness calculation formula (Eq. (10)) and the integrated coefficient of average concrete strain at the edge of the compression zone ζ are empirical coefficients, which are derived from the regression analysis and fitting of the test data of FRP-RC beams, so they are no longer applicable for FRP-UHPSSC beams. For ordinary concrete, GB 50608-2020[13] takes $\eta = 0.87$ or 1/1.15. The actual height of the compression zone x_{exp} of the test beam is obtained by back-calculating in Eq. (2),[26] and the mean value of η is taken as 0.98 by calculating in Eq. (11). ζ reflects the combined effect of elasticity and plasticity of concrete, stress distribution, and cross-section force on the average strain of concrete at the edge of compression zone, which is affected very little by the change of bending moment in the service limit state, and mainly depends on ρ and the shape factor of the cross section of the compression zone α_E, which can be inverted to obtain ζ by Eq. (12), and fitted with $\rho\alpha_E$ to obtain $\zeta = 0.01 + 0.4\rho\alpha_E$. This paper proposes an improved calculation method for Δ_s of FRP-UHPSSC beams based on GB 50608-2020,[13] shown in Table A. The Δ_s of a total of 18 flexural failure beams in the present test and the test by Liu[12] are calculated by this method. As can be seen in Table 6, the computational deviation of this paper's improved calculation method is only 3%, which is much smaller than that of the current FRP-RC design code. It can accurately predict the Δ_s of FRP-UHPSSC beams

$$B_s = \frac{E_s A_s h_0^2}{\frac{\psi_f}{\eta} + \frac{\alpha_E \rho}{\zeta}} \tag{10}$$

$$\eta = \left(h_0 - \frac{x_{exp}}{2}\right) / h_0 \tag{11}$$

$$\bar{\varepsilon}_c = \psi_f \varepsilon_c = \psi_f \frac{\sigma_c}{\nu E_c} = \frac{M}{\zeta E_c b h_0^2} \tag{12}$$

Calculation of shear bearing capacity

GB 50608-2020[13] and ACI 440.1R-15[23] have the same formula for calculating the shear force V_f provided by the FRP reinforcement in calculating the shear bearing capacity, and there is a difference in the formula for calculating the shear force V_c provided by the concrete, which has a linear relationship of 1 power and 0.5 power with the f_t and f_c', respectively. The formulas for calculating shear capacity in GB 50608-2020[13] and ACI 440.1R-15[23] are shown in Table A.

Table 7 compares the measured ultimate loads V_u of the shear-damaged beams B/C16-3-300, B/C10-3-250, and SF16-3-300 in this paper, with the ultimate loads V_{upre} calculated through the aforementioned codes. From Table 7, it can be seen that both GB 50608-2020[13] and ACI 440.1R-15[23] underestimate the shear capacity of FRP-UHPSSC beams and V_{upre}/V_u decreases with decreasing a/h_0. This is because the a/h_0, as an important factor affecting the shear capacity of beams, is not reflected in the shear capacity formulas of GB 50608-2020[13] and ACI 440.1R-15.[23]

CONCLUSIONS

Through four-point bending tests, this study investigated the flexural stiffness, load-carrying capacity, cracking trends, and failure modes of 16 fiber-reinforced polymer (FRP) ultra-high-performance (UHP) seawater sea-sand concrete (SSC) beams. The experiments considered variables such as reinforcement ratio, beam section height, and type of FRP bars. The study yielded the following key findings:

1. With the increase of reinforcement ratio and the beam section height, the bending moment at ultimate limit state and flexural stiffness at the service limit state of FRP-UHPSSC beams both increase. The steel fiber composite bar (SFCB)-UHPSSC beams have the most considerable bending moment at ultimate limit state and the largest flexural stiffness at the service limit state and the basalt FRP (BFRP)-UHPSSC beams have optimal ductility.

2. The FRP-UHPSSC beams exhibit brittle failures, and the destruction is accompanied by a violent explosion. The specific failure mode is closely associated with ρ. A transition from tensile failure to compression failure takes place when $\rho/\rho_{fb} > 1.83$. Additionally, if $\rho/\rho_{fb} > 2.73$, the test beam transforms flexural failure to shear failure.

3. Compared to ACI 440.1R-15 and CSA S806-12, GB 50608-2020 exhibits the lowest computational deviation of the ultimate bending moment. The actual value exceeds the computed value of GB 50608-2020 by approximately 7.5%. In contrast, the computational method proposed in this paper for calculating M_u demonstrates higher computational accuracy, with the actual value exceeding the computed value of method proposed in this paper by approximately 2.8%. Furthermore, to ensure a certain safety margin in the calculated values, the safety coefficient θ should be considered, which takes the value of 1.049.

4. The calculated values of midspan deflection under the service limit state in the current FRP-reinforced concrete (RC) structural design code are smaller than the measured values, the calculation results of ACI 440.1R-15 and CSA S806-12 are pretty close to each other, and the calculation

Table 6—Δ_{spre}/Δ_s of FRP-UHPSSC beams

Beam designation	Δ_s, mm	Δ_{spre}/Δ_s			
		GB 50608-2020[13]	ACI 440.1R-15[23]	CSA S806-12[24]	Present study
C8-3-300	5.56	0.75	0.82	0.85	0.92
C10-3-300		0.62	0.67	0.67	0.86
C16-3-300		0.68	0.63	0.63	1.03
C10-3-250		0.56	0.63	0.63	0.84
C-10-3-350		0.72	0.73	0.75	0.94
B/C8-3-300		0.60	0.74	0.75	0.87
B/C10-3-300		0.62	0.68	0.69	0.94
B/C10-3-350		0.66	0.71	0.72	0.96
SF10-2-300		0.66	0.79	0.80	0.95
SF10-3-300		0.67	0.73	0.74	1.04
SF10-3-250		0.68	0.75	0.75	1.11
SF10-3-350		0.70	0.75	0.75	1.03
B10-3-300		1.00	0.85	0.86	1.03
BS1[12]	3.75	0.43	0.76	0.76	0.93
BS2[12]		0.61	0.90	0.90	0.97
BS3[12]		0.67	0.91	0.91	1.09
BS5[12]		0.54	0.71	0.71	1.01
BS6[12]		0.69	0.75	0.75	0.87
Mean	—	0.66	0.75	0.76	0.97
SD	—	0.11	0.08	0.08	0.08
COV	—	0.17	0.10	0.10	0.08

deviation of both of them is minimized, which is approximately 15%. In contrast, the calculation method proposed in this paper is more accurate, with a calculation deviation of only 3%.

5. The design codes for FRP-RC structures in both China and the United States underestimated the shear capacity of FRP-UHPSSC beams, and the computational deviation for the shear capacity varied depending on the a/h_0 of the test beams.

Table 7—V_{upre}/V_u of FRP-UHPSSC beams

Beam designation	a/h_0	V_u, kN	V_{upre}/V_u	
			GB 50608-2020[13]	ACI 440.1R-15[23]
B/C10-3-250	3.46	165.0	0.99	0.93
B/C16-3-300	2.80	340.0	0.79	0.72
SF16-3-300	2.80	358.0	0.80	0.75
Mean	—	—	0.86	0.80

AUTHOR BIOS

Fen Zhou *is an Associate Professor at the College of Civil Engineering, Hunan University, Changsha, China, where she received her BS and MS. Her research interests include high-performance textile-reinforced concrete (TRC), fiber-reinforced polymers (FRP), seawater sea-sand concrete (SSC), and FRP-reinforced SSC structures in marine environments.*

Lijuan Li *is a Master's Degree Candidate in the College of Civil Engineering, Hunan University. Her research interests include FRP, SSC, and FRP-reinforced SSC structures in marine environments.*

Yunxing Du *is a Professor at the College of Civil Engineering, Hunan University, where he received his BS, MS, and PhD. His research interests include structural strengthening, and the use of SSC and FRP-reinforced SSC structures in marine environments.*

Fei Peng *is an Associate Professor at the College of Civil Engineering, Hunan University, where he received his BS in 2013. He received his PhD from Tongji University, Shanghai, China, in 2019. His research interests include reinforced concrete structures with FRP and ultra-high-performance concrete structures.*

Deju Zhu *is a Professor at the College of Civil Engineering, Hunan University. He received his BS and MS from Northeast Forestry University, Harbin, Heilongjiang, China, and his PhD from Arizona State University, Tempe, AZ. His research interests include high-performance TRC and FRPs, and SSC and FRP-reinforced SSC structures in marine environments. Corresponding author: dzhu@hnu.edu.cn.*

ACKNOWLEDGMENTS

This work was supported by the funds from the National Natural Science Foundation of China-Shandong Joint Fund (U1806225) and the National Natural Science Foundation of China (52178206).

NOTATION

A_f = area of FRP bars
A_{fv} = total area of each limb of transverse reinforcement in cross section
a = shear span length, taken as 700 mm
B_s = flexural stiffness at service limit state
B_{spre} = computed value of B_s
b = beam width
b_r = width of FRP bar ribs
c_b = bounded compression zone height
D = outer diameter of steel pipe
d = diameter of FRP bar
E_c = static elastic modulus of UHPSSC

E_f = elastic modulus of FRP bar
E_{fv} = elastic modulus of transverse reinforcement
f_c = axial compressive strength of UHPSSC (150 x 150 x 300 mm)
f_{cu} = cubic compressive strength of UHPSSC (150 x 150 x 150 mm)
f_f = ultimate tensile strength of FRP bar
f_{fv} = calculated tensile strength value of transverse reinforcement
f_t = axial tensile strength of UHPSSC
f_{uv} = ultimate tensile strength of transverse reinforcement
h = beam height
h_r = height of FRP bar ribs
h_0 = beam effective height
k = $\sqrt{2\rho\alpha + (\rho\alpha)^2} - \rho\alpha$
M_{cr} = bending moment at cracking load
M_s = bending moment at service limit state
M_u = bending moment at ultimate load
M_{upre} = computed value of M_u
P_{cr} = cracking load
P_s = load at service limit state
P_u = ultimate load
r_{fv}/d_{fv} = taken as 3.5
s = spacing between reinforcement bars in encrypted area, taken as 50 mm
s_r = spacing of FRP bar ribs
x = calculation compression zone height
x_{exp} = actual compression zone height
α = E_f/E_c
Δ_s = midspan deflection at service limit state
Δ_{spre} = computed value of Δ_s
Δ_u = midspan deflection at ultimate load
ε_c = concrete strain
ε_{cu} = ultimate compressive strain of UHPSSC
ε_f = tensile strain of FRP bar
ε_{fu} = ultimate tensile strain of FRP bar
μ_f = ductility factor
μ_ρ = mean of M_u/M_{upre}, taken as 1.028
θ = safety factor
ρ = actual reinforcement ratio
ρ_{fb} = balanced reinforcement ratio
σ_c = compressive stress of UHPSSC
σ_f = tensile stress of FRP bar
σ_r = variance of M_u/M_{upre}, taken as 0.013
υ = Poisson's ratio of UHPSSC, taken as 0.2

REFERENCES

1. Hong, N. F., "Sea Sand Corrosion and Harm of Sea Sand House," *Industrial Construction*, V. 34, No. 11, 2004, pp. 65-67. (in Chinese)

2. Manalo, A. C.; Mendis, P.; Bai, Y.; Jachmann, B.; and Sorbello, C. D., "Fiber-Reinforced Polymer Bars for Concrete Structures: State-of-the-Practice in Australia," *Journal of Composites for Construction*, ASCE, V. 25, No. 1, 2021, p. 05020007. doi: 10.1061/(ASCE)CC.1943-5614.0001105

3. Feng, G.; Zhu, D.; Guo, S.; Rahman, M. Z.; Jin, Z.; and Shi, C., "A Review on Mechanical Properties and Deterioration Mechanisms of FRP Bars under Severe Environmental and Loading Conditions," *Cement and Concrete Composites*, V. 134, 2022, p. 104758. doi: 10.1016/j.cemconcomp.2022.104758

4. Feng, G. Y.; Guo, S. C.; Zhou, L. L.; Luo, W.; Guo, X.; Jin, Z.; and Zhu, D., "Effects of Surface Characteristics and Alkalinity on the Deterioration of BFRP Bars and BFRP-SSC Interface in Seawater Environment," *Composites Part B: Engineering*, V. 268, 2024, p. 111072. doi: 10.1016/j.compositesb.2023.111072

5. Zhou, R.; Zhou, F.; Du, Y. X.; Liao, B.; Feng, G.; and Zhu, D., "Effect of Seawater on Bond Performance between BFRP Bars and Seawater Sea-Sand Concrete," *Construction and Building Materials*, V. 415, 2024, p. 135050. doi: 10.1016/j.conbuildmat.2024.135050

6. Zhu, D. J.; Zhou, L. L.; and Geng, J. Z., "Effect of Replacement Rate of Sea Sand from Different Regions on Mechanical Properties of Concrete," *Journal of Hunan University (Natural Sciences)*, V. 49, No. 11, 2022, p. 8.

7. Teng, J. G.; Xiang, Y.; Yu, T.; and Fang, Z., "Development and Mechanical Behavior of Ultra-High-Performance Seawater Sea-Sand Concrete," *Advances in Structural Engineering*, V. 22, No. 14, 2019, pp. 3100-3120. doi: 10.1177/1369433219858291

8. Jiang, K.; Wang, X.; Chen, Z.; Ding, L.; Peng, Z.; and Wu, Z., "Effect of Constituent Content on Mechanical Behaviours of Ultra-High Performance Seawater Sea-Sand Concrete," *Construction and Building Materials*, V. 351, 2022, p. 128952. doi: 10.1016/j.conbuildmat.2022.128952

9. Zhu, D. J.; Li, L. F.; and Zhou, L. L., "Composition Design of Ultra-High Performance Seawater Sea-Sand Concrete and Fiber Strengthening and Toughening," *Journal of Hunan University (Natural Sciences)*, V. 50, No. 1, 2023, pp. 128-136.

10. Li, T.; Liu, X.; Zhang, Y.; Yang, H.; Zhi, Z.; Liu, L.; Ma, W.; Shah, S. P.; and Li, W., "Preparation of Seawater Sea Sand High-Performance Concrete (SHPC) and Serving Performance Study in Marine Environment," *Construction and Building Materials*, V. 254, 2020, p. 119114. doi: 10.1016/j.conbuildmat.2020.119114

11. Li, T. Y.; Zhang, Y. M.; and Liu, X. Y., "Research on the Preparation and Durability of Brine Marine Sand High Performance Concrete," *Concrete*, V. 11, 2019, p. 5. (in Chinese)

12. Liu, J. R., "Research on Composite Structure Performance of FRP Bar-Ultra High Performance Seawater Sea Sand Concrete," Shaoxing University, Shaoxing, China, 2021. (in Chinese)

13. GB 50608-2020, "Technical Standard for Fiber Reinforced Polymer (FRP) in Construction," China Architecture & Building Press, Beijing, China, 2020. (in Chinese)

14. GB/T 30022-2013, "Test Method for Basic Mechanical Properties of Fiber Reinforced Polymer Bar," China Architecture & Building Press, Beijing, China, 2013. (in Chinese)

15. Han, S.; Fan, C.; Zhou, A.; and Ou, J., "Simplified Implementation of Equivalent and Ductile Performance for Steel-FRP Composite Bars Reinforced Seawater Sea-Sand Concrete Beams: Equal-Stiffness Design Method," *Engineering Structures*, V. 266, 2022, p. 114590. doi: 10.1016/j.engstruct.2022.114590

16. ASTM D1141-98(2013), "Standard Practice for the Preparation of Substitute Ocean Water," ASTM International, West Conshohocken, PA, 2013.

17. Li, C. S.; Zhan, M. S.; Huang, X. C.; and Zhou, H., "Degradation Behavior of Ultra-High Molecular Weight Polyethylene Fibers under Artificial Accelerated Weathering," *Polymer Testing*, V. 31, No. 7, 2012, pp. 938-943. doi: 10.1016/j.polymertesting.2012.06.009

18. GB/T 50081-2019, "Standard for Test Methods of Concrete Physical and Mechanical Properties," China Architecture & Building Press, Beijing, China, 2019. (in Chinese)

19. ASTM C39/C39M-18, "Standard Test Method for Compressive Strength of Cylindrical Concrete Specimens," ASTM International, West Conshohocken, PA, 2018.

20. GB/T 50152-2012, "Standard for Test Method of Concrete Structures," China Architecture & Building Press, Beijing, China, 2012. (in Chinese)

21. ACI Committee 440, "Building Code Requirements for Structural Concrete Reinforced with Glass Fiber-Reinforced Polymer (GFRP) Bars—Code and Commentary (ACI CODE-440.11-22)," American Concrete Institute, Farmington Hills, MI, 2022, 260 pp.

22. Naaman, A. E., and Jeong, S. M. H., "Structural Ductility of Concrete Beams Prestressed with FRP Tendons," *Non-Metallic FRP Reinforcements for Concrete Structures: Proceedings of the Second International RILEM Symposium (FRPRCS-2)*, L. Taerwe, ed., CRC Press, London, UK, 1995, pp. 379-386.

23. ACI Committee 440, "Guide for the Design and Construction of Structural Concrete Reinforced with Fiber-Reinforced Polymer (FRP) Bars (ACI 440.1R-15)," American Concrete Institute, Farmington Hills, MI, 2015, 88 pp.

24. CSA S806-12, "Design and Construction of Building Structures with Fiber-Reinforced Polymers," CSA Group, Toronto, ON, Canada, 2012.

25. Xue, W.; Peng, F.; and Zheng, Q., "Design Equations for Flexural Capacity of Concrete Beams Reinforced with Glass Fiber-Reinforced Polymer Bars," *Journal of Composites for Construction*, ASCE, V. 20, No. 3, 2016, p. 04015069. doi: 10.1061/(ASCE)CC.1943-5614.0000630

26. Sun, Y. J.; Wu, T.; and Wang, Z., "Analysis on the Flexural Capacity Model of FRP-Reinforced Concrete Beams," *Journal of Xi'an University of Architecture & Technology*, V. 51, No. 1, 2019, p. 8.

APPENDIX

Table A—Calculation formulas

Calculation method	ρ_{fb}	M_{upre}	Δ_{spre}	V_{upre}
GB 50608-2020[13]	$\rho_{fb} = \frac{\alpha_1 f_c \xi_b}{f_f}$, $\xi_b = \frac{\beta_1 \varepsilon_{cu}}{\varepsilon_{cu} + f_{fd}/E_f}$ $f_{cu} \le 50$ MPa, $\alpha_1 = 1.0, \beta_1 = 0.8$ $f_{cu} = 80$ MPa, $\alpha_1 = 0.94, \beta_1 = 0.7$	$M_{upre} \le f_{fe} A_f \left(h_{0f} - \frac{x}{2}\right)$ $x = \begin{cases} \left[\frac{0.14}{1+400(f_{fe}/E_f)} + \frac{\rho_f f_{fe}}{f_c}\right] h_{0f}, \rho_f < 1.5\rho_{fb} \\ \frac{\rho f_{fe}}{\alpha_1 f_c} h_{0f}, \rho_f \ge 1.5\rho_{fb} \end{cases}$ $f_{fe} = \begin{cases} f_{fd}, \rho_f < 1.5\rho_{fb} \\ \left(\frac{\rho}{\rho_{fb}}\right)^{-0.55} f_{fd}, \rho \ge 1.5\rho_{fb} \end{cases}$	$\Delta_{spre} = \frac{0.5 P_s a}{24 B_s}(3 l_0^2 - 4a^2)$ $B_s = \frac{E_f A_f h_0^2}{1.15\psi_f + 0.2 + \frac{6\alpha_{fE}\rho_f}{1+3.5\gamma_f'}}$ $\gamma_f' = [(b_f' - b)h_f']/(bh_{0f})$ $\psi_f = 1.1 - 0.65(f_{tk}/\rho_{te}\sigma_f)$ $\sigma_{fu} = (M_s/0.9A_f h_0)$, $\rho_{te} = (A_f/0.5bh)$, $\rho_f = (A_f/bh_{0f})$, $\alpha_{fE} = E_f/E_c$	$V_u = V_c + V_f$ $V_c = 0.86 f_t b k h_{0f}$ $k = \sqrt{2\rho_f\alpha_{fE} + (\rho_f\alpha_{fE})^2} - \rho_f\alpha_{fE}$ $V_f = A_{fv} f_{fv} h_{0f}/s$, $A_{fv} = nA_{fv1}$ $f_{fv} = \min\{0.004E_{fv}, f_{bend}\}$ $f_{bend} = \left(0.3 + 0.05\frac{r_b}{d_d}\right) f_{fd}$
ACI 440.1R-15[23]	$\rho_{fb} = 0.85\beta_1 \frac{f_c'}{f_{fu}} \frac{E_f \varepsilon_{cu}}{E_f \varepsilon_{cu} + f_{fu}}$ $f_c' \le 28$ MPa, $\beta_1 = 0.85$ $f_c' > 55$ MPa, $\beta_1 = 0.65$ 55 MPa $\ge f_c' > 28$ MPa, $\beta_1 = 0.85 - 0.05(f_c' - 28)/7$	$\rho_f > \rho_{fb}$: $f_f = \sqrt{\frac{(E_f\varepsilon_{cu})^2}{4} + \frac{0.85\beta_1 f_c'}{\rho_f} E_f \varepsilon_{cu}} - 0.5E_f\varepsilon_{cu} \le f_{fu}$ $M_n = \rho_f f_f \left(1 - 0.59\frac{\rho_f f_f}{f_c'}\right) b d^2$ $\rho_f < \rho_{fb}$: $M_n = A_f f_{fu}\left(d - \frac{\beta_1 c}{2}\right)$ $c = \left(\frac{\varepsilon_{cu}}{\varepsilon_{cu} + \varepsilon_{fu}}\right) d$	$\Delta_{spre} = \frac{(P_s a/2)(3 l_0^2 - 4a^2)}{24 E_c I_e}$ $I_e = \frac{I_{cr}}{1 - \gamma\left(\frac{M_{cr}}{M_s}\right)^2\left[1 - \frac{I_{cr}}{I_g}\right]} \le I_g$ $\gamma = 1.72 - 0.72\left(\frac{M_{cr}}{M_s}\right)$ $I_g = \frac{bh^3}{12}$, $I_{cr} = \frac{1}{3} b h_0^3 k^3 + n_f A_f h_0^2 (1-k)^2$	$V_u = V_c + V_f$ $V_c = 0.4\sqrt{f_c'} b_w (kd)$ $V_f = \frac{A_{fv} f_{fv} d}{s}$ $f_{fv} = \min\{0.004E_{ft}, f_{fb}\}$
CSA S806-12[24]	$\rho_{fb} = \frac{\phi_c}{\phi_f}\alpha_1\beta_1 \frac{f_c'}{f_{fu}} \frac{\varepsilon_{cu}}{(\varepsilon_{cu} + \varepsilon_{fu})}$ $\alpha_1 = 0.85 - 0.0015f_c' \ge 0.67$ $\beta_1 = 0.97 - 0.0025f_c' \ge 0.67$ $\phi_c = 0.65$, $\phi_f = 0.75$	$M_r = \begin{cases} \phi_f f_{fu} A_f \left(d - \frac{\beta_1 c}{2}\right), \rho_f < \rho_{fb} \\ \phi_c \alpha_1 f_c' b \beta_1 c\left(d - \frac{\beta_1 c}{2}\right), \rho_f \ge \rho_{fb} \end{cases}$ $c = \frac{\phi_f A_f f_{fu}}{\phi_c \alpha_1 \beta_1 f_c' b}$	$\Delta_{spre} = \frac{(P_s a/2)(3 l_0^2 - 4a^2)}{24 E_c I_e}$ $I_e = \frac{I_{cr}}{1 - \left[1 - \frac{I_{cr}}{I_g}\right]\left(\frac{M_{cr}}{M_a}\right)^2} \le I_g$ $I_{cr} = \frac{1}{3} b (kd)^3 + n_f A_f d^2 (1-k)^2$ $k = \sqrt{2\rho_f n_f + (\rho_f n_f)^2} - \rho_f n_f$	—
Xue et al.[25]	$\rho_{fb} = \frac{\alpha_1\beta_1 f_c}{f_f} \frac{0.0033 E_f}{f_f + 0.0033 E_f}$ $\alpha_1 = 0.9, \beta_1 = 0.7$	$M_{upre} \le \begin{cases} 0.94 f_{fy} A_f h_0, \rho < \rho_{fb} \\ f_{fy} A_f \left(h_0 - \frac{x}{2}\right), \rho \ge \rho_{fb} \end{cases}$ $f_{fy} = \begin{cases} f_f, \rho < \rho_b \\ \left[1 - 0.211\left(\frac{\rho}{\rho_{fb}} - 1\right)^{0.2}\right] f_f, \rho_{fb} < \rho \le 1.5\rho_{fb} \\ \left(\frac{\rho}{\rho_{fb}}\right)^{-0.5} f_f, \rho > 1.5\rho_{fb} \end{cases}$ $x = \frac{f_{fy} A_f}{\alpha_1 f_c \beta_1 b}, f_{fy} = E_f \varepsilon_{cu} \frac{h_0 - x}{x}$	—	—
Present study	$\rho_{fb} = \frac{\alpha_1\beta_1 f_c}{f_f} \frac{0.0025 E_f}{f_f + 0.0025 E_f}$ $\alpha_1 = 0.9, \beta_1 = 0.7$	$M_{upre} \le \begin{cases} 0.94 f_{fy} A_f h_0, \rho < \rho_{fb} \\ \alpha_1 f_c b x\left(h_0 - \frac{x}{2}\right), \rho \ge \rho_{fb} \end{cases}$ $f_{fy} = \begin{cases} f_f, \rho < \rho_{fb} \\ \left[1 - 0.211\left(\frac{\rho}{\rho_{fb}} - 1\right)^{0.2}\right] f_f, \rho_{fb} < \rho \le 1.5\rho_{fb} \\ \left(\frac{\rho}{\rho_{fb}}\right)^{-0.5} f_f, \rho > 1.5\rho_{fb} \end{cases}$ $x = 0.826 c_b \left(\frac{\rho}{\rho_{fb}}\right)^{0.676}, c_b = \left(\frac{\varepsilon_{cu}}{\varepsilon_{cu} + \varepsilon_{fu}}\right) h_0$	$\Delta_{spre} = \frac{0.5 P_s a}{24 B_{spre}}(3 l_0^2 - 4a^2)$ $B_{spre} = \frac{E_s A_s h_0^2}{\frac{\psi_f}{\eta} + \frac{\alpha_E \rho}{\zeta}}$ $\psi_f = 1.1 - 0.65 \frac{f_t}{\rho_{te}\sigma_{fu}} \frac{E_f}{E_s}$ $\sigma_{fu} = \frac{M_s}{0.9 A_f h_0}, \rho_{te} = \frac{A_f}{0.5bh}$ $\alpha_E = \frac{E_f}{E_c}, \eta = 0.98$, $\zeta = 0.01 + 0.4\alpha_E \rho$	—

ACI STRUCTURAL JOURNAL TECHNICAL PAPER

Title No. 123-S48

Mathematical Framework for Computing Polar Moments of Inertia for Use with Traditional 'ACI Commentary Jc Method'

by Hugo Esquivel and Guang Lin

This paper presents a robust mathematical framework for computing centroidal polar moments of inertia in a standardized manner, applicable to both regular- and irregular-shaped sections, for use with the traditional "ACI Commentary Jc Method." The paper also showcases with mathematical rigor why, for over 60 years, the standard (traditional) expressions used to compute polar moments of inertia for planar sections embedded in three-dimensional (3-D) space have been incorrectly derived, and explores the implications of not adopting the correct expressions in design. The mathematical framework for computing polar moments of inertia is developed using advanced calculus, and primitive sections are integrated into the formulation to derive with ease the necessary expressions for the most common sections used in design, namely rectangular, circular, C-shaped, L-shaped, and regular polygon-shaped sections. Finally, a numerical example is provided to demonstrate the practical implementation of the proposed mathematical framework.

Keywords: ACI CODE-318-25; (centroidal) polar moment of inertia; Jc method; slab-column connection; structural design; two-way shear action.

INTRODUCTION

In 1960, Di Stasio and Van Buren[1] proposed a simple but effective method to calculate shear stresses around slab-column connections due to the effect produced by unbalanced moments at the slab-column connection. The method was included in the ACI Building Code of 1963[2] and gained widespread popularity among structural engineers. The method is still used today. Section R8.4.4.2.3 of ACI CODE-318-25,[3] for instance, suggests it as a valid method for calculating shear stresses around slab-column connections. The method is commonly referred to as the "Jc Method."

The method is based on three premises. First, linear theory of elasticity applies in the vicinity of the slab-column connection. In particular, Hooke's law holds and rotations are assumed to be small. Second, the geometry of the slab-column connection does not change significantly during deformation. Third, the connection's horizontal plane remains plane after deformation. Hence, by adhering to these premises, an expression to compute the shear stresses around a slab-column connection can be developed.

For example, consider Fig. 1, which depicts the critical (shear) section of an interior slab-column connection with Cartesian coordinate system xyz. The column is c_1-by-c_2 in cross section and the effective slab depth is d. Because the critical section is located at a distance $d/2$ from the cross section of the column (Section 22.6.4.1, ACI CODE-318-25), it follows that the horizontal dimensions of the critical section are $b_1 = c_1 + d$ and $b_2 = c_2 + d$. Hence, if the aforementioned premises are followed, it is possible to obtain an expression for the shear stress, v_y, evaluated at a point with coordinates $(x, \cdot, z)$ along the perimeter of the critical section. Namely

$$v_y(x,z) = \frac{V_y}{b_0 d} + \frac{\gamma_{vz} M_z}{\bar{I}_z} x - \frac{\gamma_{vx} M_x}{\bar{I}_x} z \tag{1}$$

where V_y is the shear force acting on the critical section (positive if the force acts in the positive y-direction—with the positive y-axis pointing out of the sheet of paper, as illustrated in Fig. 1(a)); b_0 is the perimeter of the critical section; d is the distance from the extreme compression fiber to the centroid of longitudinal reinforcing bars on the tension side of the slab (a fraction of the slab thickness); γ_{vz} and γ_{vx} are the fractions of M_z and M_x that are transferred by shear stresses on the critical section; M_z and M_x are the unbalanced moments acting in the z- and x-direction of the critical section (positive if the moment acts in the positive direction of the axis); $\gamma_{vz} M_z$ and $\gamma_{vx} M_x$ are the torsional moments acting in the z- and x-direction of the critical section; $\bar{I}_z$ and $\bar{I}_x$ are the centroidal polar moments of inertia of the critical section about the z- and x-axis; and x and z are the coordinates of a point along the critical section where the shear stress, $v_y(x,z)$, is to be computed.

For the particular case of Fig. 1, further annotations can be made. The perimeter of the critical section is $b_0 = 2(b_1 + b_2)$, and the fractions γ_{vz} and γ_{vx} (Sections 8.4.4.2.2 and 8.4.2.2.2, ACI CODE-318-25) are

$$\gamma_{vz} = 1 - \frac{1}{1 + \frac{2}{3}\sqrt{\frac{b_1}{b_2}}} \text{ and } \gamma_{vx} = 1 - \frac{1}{1 + \frac{2}{3}\sqrt{\frac{b_2}{b_1}}} \tag{2}$$

and the centroidal polar moments of inertia of the critical section[4] can be determined to be

$$\bar{I}_z = \frac{1}{6} b_1 d^3 + \frac{1}{6} d b_1^3 + \frac{1}{6} b_2 d^3 + \frac{1}{2} d b_2 b_1^2 \tag{3a}$$

$$\bar{I}_x = \frac{1}{6} b_2 d^3 + \frac{1}{6} d b_2^3 + \frac{1}{6} b_1 d^3 + \frac{1}{2} d b_1 b_2^2 \tag{3b}$$

However, in the literature,[1-3,5-20] these expressions are both incorrectly and standardly presented as

ACI Structural Journal, V. 123, No. 3, May 2026.
MS No. S-2024-296.R2, doi: 10.14359/51749378, received October 11, 2025, and reviewed under Institute publication policies. Copyright © 2026, American Concrete Institute. All rights reserved, including the making of copies unless permission is obtained from the copyright proprietors. Pertinent discussion including author's closure, if any, will be published ten months from this journal's date if the discussion is received within four months of the paper's print publication.

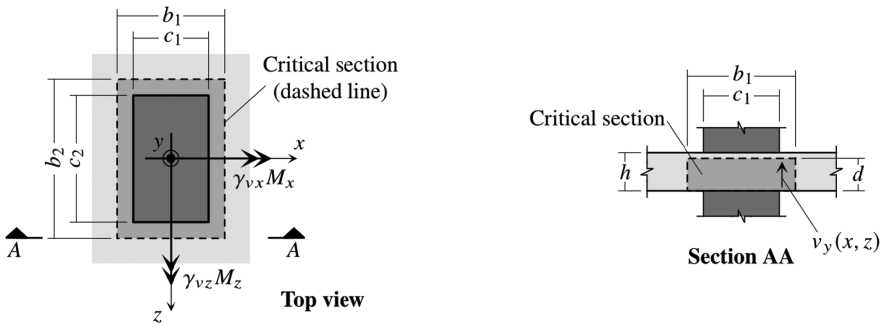

(a) Top view of slab-column connection ***(b) Section view of slab-column connection***

Fig. 1—Typical interior slab-column connection.

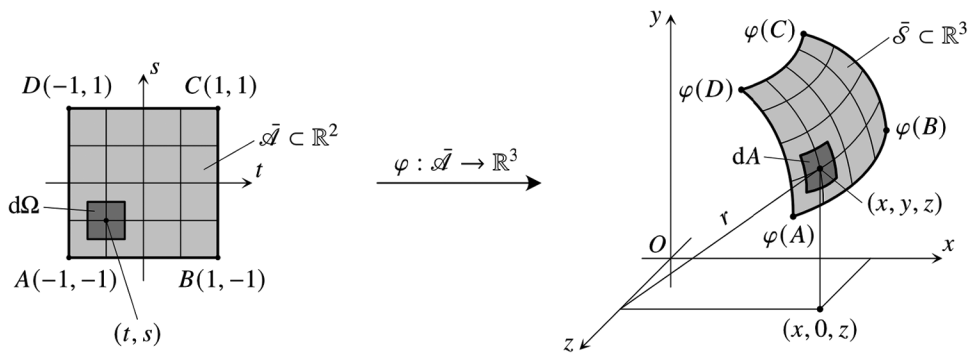

Fig. 2—2-D section—embedded into $\mathbb{R}^3$ by φ.

$$\bar{I}_z = \frac{1}{6}b_1 d^3 + \frac{1}{6}d b_1^3 + \frac{1}{2}d b_2 b_1^2 \tag{4a}$$

$$\bar{I}_x = \frac{1}{6}b_2 d^3 + \frac{1}{6}d b_2^3 + \frac{1}{2}d b_1 b_2^2 \tag{4b}$$

where the contributing terms $\frac{1}{6}b_2 d^3$ and $\frac{1}{6}b_1 d^3$ are unjustifiably neglected. Consequently, one objective of this paper is to rigorously demonstrate why these terms cannot be neglected, and to explore the implications of doing so. A second objective is to present a robust mathematical framework for computing centroidal polar moments of inertia in a standardized manner, applicable to regular- and irregular-shaped sections.

It is important to emphasize that none of the consulted sources[1-3,5-20] provide an explanation for why the contributing terms mentioned previously can be neglected, reinforcing the unacceptability of the approach taken by many authors.

RESEARCH SIGNIFICANCE

The traditional "ACI Commentary Jc Method," outlined in Section R8.4.4.2.3 of ACI CODE-318-25,[3] is widely regarded as the preferred choice for estimating shear stresses around slab-column connections due to its simplicity. However, for over 60 years, the expressions for computing centroidal polar moments of inertia have been incorrectly derived, likely due to a misapplication of Steiner's theorem.[4] This, combined with the absence of a standardized framework for easily computing polar moments of inertia, has led the ACI Building Code to allow designers to approximate circular or regular polygon-shaped sections with square sections of equivalent area (Section 22.6.4.1.2, ACI CODE-318-25). This paper addresses this issue by introducing a robust mathematical framework capable of handling both regular and irregular shapes, enabling the complete rederivation and correction of existing expressions.

POLAR MOMENT OF INERTIA

Let the ambient space be Euclidean and represented with $\mathbb{R}^3$. The selected coordinate system for the space is denoted with *xyz*, as shown in Fig. 2. In structural mechanics, the polar moment of inertia of a two-dimensional (2-D) section about the z-axis[21] is defined as

$$I_z = \int_{\mathcal{S}} r^2(x,y,z)\, \mathrm{d}A \tag{5}$$

where $\bar{\mathcal{S}} \subset \mathbb{R}^3$ is the set of points (x,y,z) comprising the section depicted in Fig. 2 (a closed set); $\mathrm{d}A$ is the area element on $\mathcal{S}$; and r is the shortest distance from the z-axis to $(x,y,z) \in \bar{\mathcal{S}}$, which means that $r^2 : \bar{\mathcal{S}} \to \mathbb{R}$ is the function given by

$$r^2(x,y,z) = x^2 + y^2 \tag{6}$$

For computational purposes, let $\bar{\mathcal{A}} = [-1,\ 1]^2$ be a subset of $\mathbb{R}^2$, and let $\varphi : \bar{\mathcal{A}} \to \mathbb{R}^3$ be a parametrization of $\bar{\mathcal{S}}$ on $\bar{\mathcal{A}}$ given by

$$\varphi(t,s) = (\varphi_1(t,s),\ \varphi_2(t,s),\ \varphi_3(t,s)) \tag{7}$$

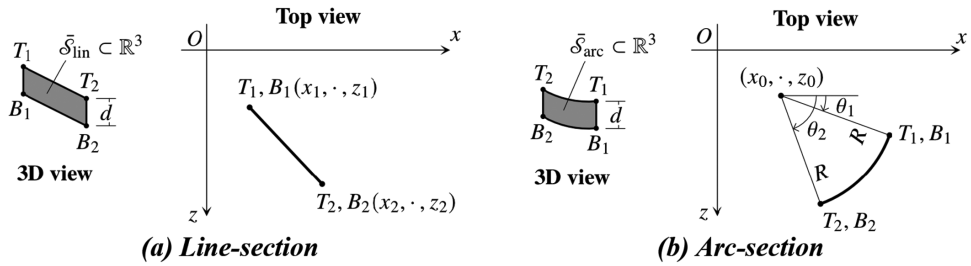

(a) Line-section ***(b) Arc-section***

Fig. 3—Primitive sections in $\mathbb{R}^3$.

where $\varphi_1, \varphi_2, \varphi_3 \colon \overline{\mathcal{A}} \to \mathbb{R}$ are three real-valued functions defined by

$$x = \varphi_1(t,s)\,,\ y = \varphi_2(t,s)\,,\ z = \varphi_3(t,s) \tag{8}$$

Here, $\overline{\mathcal{A}}$ is deliberately taken as the bi-unit square centered at the origin of $\mathbb{R}^2$ in case Eq. (9) is computed with a quadrature rule (for example, the Gauss-Legendre quadrature rule).

Based on the aforementioned setting, Eq. (5) can now be expressed as

$$I_z = \int_{-1}^{1}\int_{-1}^{1} \rho^2(t,s)\,\mathrm{d}\Omega \tag{9}$$

where ρ^2 and $\mathrm{d}\Omega$ are the pullbacks by φ of r^2 and $\mathrm{d}A$, respectively. That is

$$\rho^2(t,s) := \left(\varphi^* r^2\right)(t,s) = r^2(\varphi(t,s)) \text{ on } \overline{\mathcal{A}} \tag{10a}$$

$$\mathrm{d}\Omega := \varphi^*\,\mathrm{d}A = \|\partial_t\varphi \times \partial_s\varphi\|\,\mathrm{d}t\mathrm{d}s \text{ on } \mathcal{A} \tag{10b}$$

where $\|\cdot\|$ is the Euclidean norm on $\mathbb{R}^3$; and $\times$ is the usual vector product on $\mathbb{R}^3$ (the cross product). The symbol ∂ denotes partial derivative. For instance, $\partial_t\varphi$ is the partial derivative of φ with respect to t. In this work, φ is a diffeomorphism between $\mathcal{A}$ and $\mathcal{S}$.

Moreover, if Eq. (10) is expanded, the specific expressions for $\rho^2(t,s)$ and $\mathrm{d}\Omega$ are revealed

$$\rho^2(t,s) = [\varphi_1(t,s)]^2 + [\varphi_2(t,s)]^2 \tag{11a}$$

$$\mathrm{d}\Omega = \sqrt{\{\varphi_1,\varphi_2\}^2 + \{\varphi_2,\varphi_3\}^2 + \{\varphi_3,\varphi_1\}^2}\ \mathrm{d}t\mathrm{d}s \tag{11b}$$

where $\{\varphi_j,\varphi_k\} = \partial_t\varphi_j\partial_s\varphi_k - \partial_t\varphi_k\partial_s\varphi_j$ is the Poisson bracket of φ_j and φ_k for $j,k \in \{1, 2, 3\}$.

Finally, two remarks are in order. The area of $\overline{\mathcal{S}}$ is manifestly given by

$$A = \int_{\mathcal{S}}\mathrm{d}A = \int_{-1}^{1}\int_{-1}^{1}\mathrm{d}\Omega \tag{12}$$

and the centroid of $\overline{\mathcal{S}}$ is the point with coordinates $(\overline{x},\overline{y},\overline{z})$, where

$$\overline{x} = \frac{1}{A}\int_{\mathcal{S}} x\,\mathrm{d}A = \frac{1}{A}\int_{-1}^{1}\int_{-1}^{1}\varphi_1(t,s)\,\mathrm{d}\Omega \tag{13a}$$

$$\overline{y} = \frac{1}{A}\int_{\mathcal{S}} y\,\mathrm{d}A = \frac{1}{A}\int_{-1}^{1}\int_{-1}^{1}\varphi_2(t,s)\,\mathrm{d}\Omega \tag{13b}$$

$$\overline{z} = \frac{1}{A}\int_{\mathcal{S}} z\,\mathrm{d}A = \frac{1}{A}\int_{-1}^{1}\int_{-1}^{1}\varphi_3(t,s)\,\mathrm{d}\Omega \tag{13c}$$

POLAR MOMENTS OF INERTIA OF PRIMITIVE SECTIONS

To construct the most common (critical shear) sections used in design, two primitive sections are considered as follows. The sections are named after how they look from a top view.

Line section

A line section, $\overline{\mathcal{S}}_{lin}$, is depicted in Fig. 3(a). Its vertexes are represented by the points

$$\begin{gathered} T_1\left(x_1,\ \tfrac{1}{2}d,\ z_1\right),\ T_2\left(x_2,\ \tfrac{1}{2}d,\ z_2\right), \\ B_1\left(x_1,\ -\tfrac{1}{2}d,\ z_1\right),\ B_2\left(x_2,\ -\tfrac{1}{2}d,\ z_2\right) \end{gathered} \tag{14}$$

where $x_1, z_1, x_2, z_2 \in \mathbb{R}$ and $d \in \mathbb{R}^+$ are five known numbers (section parameters).

A parametrization of $\overline{\mathcal{S}}_{lin}$ on $\overline{\mathcal{A}}$ produces

$$\varphi_1(t,s) = \frac{1}{2}(x_1 + x_2) + \frac{1}{2}(x_2 - x_1)t \tag{15a}$$

$$\varphi_2(t,s) = \frac{1}{2}ds \tag{15b}$$

$$\varphi_3(t,s) = \frac{1}{2}(z_1 + z_2) + \frac{1}{2}(z_2 - z_1)t \tag{15c}$$

The Jacobian matrix of φ is

$$\mathrm{J}_\varphi = \begin{bmatrix} \partial_t\varphi_1 & \partial_s\varphi_1 \\ \partial_t\varphi_2 & \partial_s\varphi_2 \\ \partial_t\varphi_3 & \partial_s\varphi_3 \end{bmatrix} = \begin{bmatrix} \frac{1}{2}(x_2 - x_1) & 0 \\ 0 & \frac{1}{2}d \\ \frac{1}{2}(z_2 - z_1) & 0 \end{bmatrix} \tag{16}$$

Substitution of Eq. (15) and (16) into Eq. (11) gives

$$\rho^2(t,s) = \left[\frac{1}{2}(x_1 + x_2) + \frac{1}{2}(x_2 - x_1)t\right]^2 + \left[\frac{1}{2}ds\right]^2 \tag{17a}$$

$$\mathrm{d}\Omega = |\partial_s \varphi_2| \sqrt{(\partial_t \varphi_1)^2 + (\partial_t \varphi_3)^2}\ \mathrm{d}t\mathrm{d}s$$

$$= \frac{1}{4} A\ \mathrm{d}t\mathrm{d}s \tag{17b}$$

where $A = b_0 d$ is the area of the section, and $b_0 = \sqrt{(x_2 - x_1)^2 + (z_2 - z_1)^2}$ is the length of the section in the xz-plane.

Consequently, inserting Eq. (17) into Eq. (9) yields the polar moment of inertia of $\overline{\delta}_{\text{lin}}$ about the z-axis

$$I_z = \frac{1}{3} A e^2 + \frac{1}{12} A d^2 \text{ with } e^2 = \det\begin{bmatrix} x_1 + x_2 & x_1 \\ x_2 & x_1 + x_2 \end{bmatrix}$$

$$= (x_1 + x_2)^2 - x_1 x_2 \tag{18}$$

The centroid of $\overline{\delta}_{lin}$ is clearly the point with coordinates

$$(\overline{x}, \overline{y}, \overline{z}) = \left(\frac{1}{2}(x_1 + x_2),\ 0,\ \frac{1}{2}(z_1 + z_2)\right) \tag{19}$$

Arc section

An arc section, $\overline{\delta}_{arc}$, is illustrated in Fig. 3(b). Its vertexes are represented by the points

$$T_1\left(x_0 + R\cos\theta_1,\ \frac{1}{2}d,\ z_0 + R\sin\theta_1\right),$$

$$T_2\left(x_0 + R\cos\theta_2,\ \frac{1}{2}d,\ z_0 + R\sin\theta_2\right) \tag{20a}$$

$$B_1\left(x_0 + R\cos\theta_1,\ -\frac{1}{2}d,\ z_0 + R\sin\theta_1\right),$$

$$B_2\left(x_0 + R\cos\theta_2,\ -\frac{1}{2}d,\ z_0 + R\sin\theta_2\right) \tag{20b}$$

where $x_0, z_0 \in \mathbb{R}$, $R, d \in \mathbb{R}^+$ and $\theta_1, \theta_2 \in [0,\ 2\pi]$ (with $\theta_2 > \theta_1$) are six known numbers.

By letting $\psi = \theta_1 + \theta_2$ and $\phi = \theta_2 - \theta_1$, a parametrization of $\overline{\delta}_{arc}$ on $\overline{\mathcal{A}}$ is realized with

$$\varphi_1(t,s) = x_0 + R\cos\left(\frac{1}{2}\psi + \frac{1}{2}\phi t\right) \tag{21a}$$

$$\varphi_2(t,s) = \frac{1}{2} ds \tag{21b}$$

$$\varphi_3(t,s) = z_0 + R\sin\left(\frac{1}{2}\psi + \frac{1}{2}\phi t\right) \tag{21c}$$

where the Jacobian matrix of the parametrization is

$$\mathrm{J}_\varphi = \begin{bmatrix} \partial_t \varphi_1 & \partial_s \varphi_1 \\ \partial_t \varphi_2 & \partial_s \varphi_2 \\ \partial_t \varphi_3 & \partial_s \varphi_3 \end{bmatrix}$$

$$= \begin{bmatrix} -\frac{1}{2} R\phi \sin\left(\frac{1}{2}\psi + \frac{1}{2}\phi t\right) & 0 \\ 0 & \frac{1}{2} d \\ \frac{1}{2} R\phi \cos\left(\frac{1}{2}\psi + \frac{1}{2}\phi t\right) & 0 \end{bmatrix} \tag{22}$$

Substituting Eq. (21) and (22) into Eq. (11) gives

$$\rho^2(t,s) = \left[x_0 + R\cos\left(\frac{1}{2}\psi + \frac{1}{2}\phi t\right)\right]^2 + \left[\frac{1}{2} ds\right]^2 \tag{23a}$$

$$\mathrm{d}\Omega = |\partial_s \varphi_2| \sqrt{(\partial_t \varphi_1)^2 + (\partial_t \varphi_3)^2}\ \mathrm{d}t\mathrm{d}s = \frac{1}{4} A\ \mathrm{d}t\mathrm{d}s \tag{23b}$$

where $A = b_0 d$ is the area of the section; and $b_0 = R\phi$ is the length of the section in the xz-plane.

Thus, replacing Eq. (23) into Eq. (9) gives the polar moment of inertia of $\overline{\delta}_{arc}$ about the z-axis

$$I_z = \frac{1}{2} \kappa A R^2 + \frac{1}{12} A d^2 \text{ with } \kappa$$

$$= 1 + \cos(2\theta_1, 2\theta_2) + 2\left[2\cos(\theta_1, \theta_2) + \frac{x_0}{R}\right]\frac{x_0}{R} \tag{24}$$

Moreover, inserting Eq. (21) into Eq. (13) prompts the centroid of $\overline{\delta}_{arc}$

$$(\overline{x}, \overline{y}, \overline{z}) = (x_0 + R\cos(\theta_1, \theta_2),\ 0,\ z_0 + R\sin(\theta_1, \theta_2)) \tag{25}$$

The real-valued functions cosi, sini $: \mathbb{R}^2 \to \mathbb{R}$ displayed in Eq. (24) and (25) are given by

$$\mathrm{cosi}(u,v) := \frac{1}{2}\int_{-1}^{1} \cos\left(\frac{1+t}{2}u + \frac{1-t}{2}v\right) \mathrm{d}t = \begin{cases} \frac{\sin v - \sin u}{v - u} & \text{if } u \neq v \\ \cos u & \text{if } u = v \end{cases} \tag{26a}$$

$$\mathrm{sini}(u,v) := \frac{1}{2}\int_{-1}^{1} \sin\left(\frac{1+t}{2}u + \frac{1-t}{2}v\right) \mathrm{d}t$$

$$= \begin{cases} -\frac{\cos v - \cos u}{v - u} & \text{if } u \neq v \\ \sin u & \text{if } u = v \end{cases} \tag{26b}$$

POLAR MOMENTS OF INERTIA OF COMMON SECTIONS

As before, the sections explored in the following are named after how they look from a top view. However, unlike before, the moments of inertia are computed with respect to a z-axis, which passes through the centroid of the section. They are symbolically denoted by $\overline{I}_z$ to distinguish them from the rest.

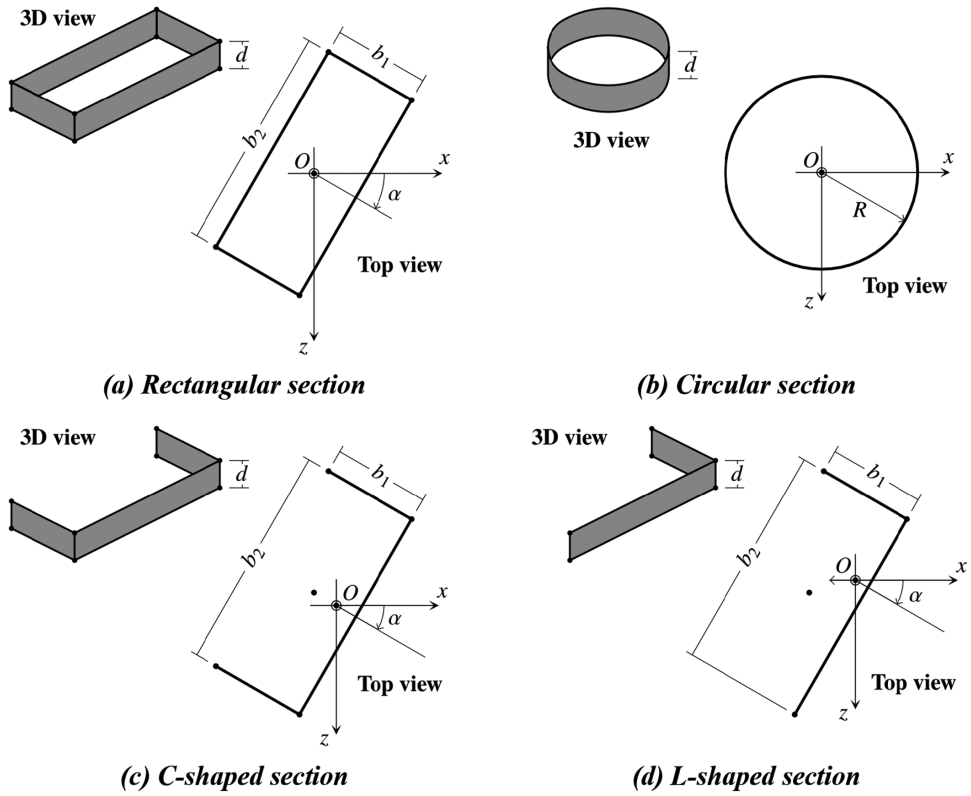

Fig. 4—Common sections in concrete design.

In the following, b_1 and b_2 are two horizontal dimensions characterizing the size of the section in the xz-plane, d is the depth of the section (a dimension parallel to the y-axis), and α is the angle defining the orientation of the section in the xz-plane with respect to the x-axis.

Rectangular section

By definition, a rectangular section is a sequence of four line sections arranged at right angles as in Fig. 4(a). Using Eq. (18) and the principle of moments[21] recursively, it follows that

$$\bar{I}_z = \frac{1}{6}(b_1 + 3\,b_2)d\,b_1^2 - \left[\frac{1}{6}(b_1 + 3\,b_2)d\,b_1^2 - \frac{1}{6}(b_2 + 3\,b_1)d\,b_2^2\right] \times \sin^2\alpha + \frac{1}{12}b_0\,d^3 \tag{27}$$

where $b_0 = 2(b_1 + b_2)$ is the length of the section measured in the xz-plane. As presented, Eq. (27) is the centroidal polar moment of inertia of a rectangular section about the z-axis.

Circular section

A circular section is an arc section with $\theta_1 = 0$ and $\theta_2 = 2\pi$ (Fig. 4(b)). By taking $x_0 = z_0 = 0$ and substituting these into Eq. (24) yields the centroidal polar moment of inertia of a circular section about the z-axis. That is

$$\bar{I}_z = \frac{1}{8}\pi d\,b^3 + \frac{1}{12}\pi b\,d^3 \tag{28}$$

where $b = 2R$ is the diameter of the section; and R is the radius of the section (in the xz-plane).

C-shaped section

A rectangular C-shaped section is depicted in Fig. 4(c). Because the section is comprised by a sequence of three line sections, a recursive implementation of the principle of moments and Eq. (18) and (19) produces

$$\bar{I}_z = \frac{1}{6}(b_1 + 3\mu)d\,b_1^2 - \left[\frac{1}{6}(b_1 + 3\mu)d\,b_1^2 - \frac{1}{12}(b_2 + 6\mu)d\,b_2^2 - \mu\,b_1\,b_2\,d\right]\sin^2\alpha + \frac{1}{12}b_0\,d^3 \tag{29}$$

where $\mu = (b_1\,b_2)/b_0$ is a characteristic length of the section; and $b_0 = 2\,b_1 + b_2$ is the length of the section measured in the xz-plane. Equation (29) is the centroidal polar moment of inertia of a C-shaped section about the z-axis.

It is worth mentioning that the centroid of the section is located $b_2/2$ from the b_1-sides and b_1^2/b_0 from the b_2-side. This follows from a recursive application of Eq. (19) and the principle of moments.

L-shaped section

A rectangular L-shaped section is depicted in Fig. 4(d). Proceeding similarly as before, the centroidal polar moment of inertia of the section can be realized by means of Eq. (18) and (19) and the principle of moments

$$\bar{I}_z = \frac{1}{12}(b_1 + 3\mu)d\,b_1^2 - \left[\frac{1}{12}(b_1 + 3\mu)d\,b_1^2 - \frac{1}{12}(b_2 + 3\mu)d\,b_2^2\right] \times \sin^2\alpha - \frac{1}{4}\mu\,b_1\,b_2\,d\,\sin(2\alpha) + \frac{1}{12}b_0\,d^3 \tag{30}$$

where $\mu = (b_1 b_2)/b_0$ and $b_0 = b_1 + b_2$ is the length of the section measured in the xz-plane. This time the centroid of the section is located $b_2^2/(2b_0)$ from the b_1-side and $b_1^2/(2b_0)$ from the b_2-side.

Regular polygon-shaped section

A regular polygon-shaped section of n sides is considered next with $n \geq 3$. Such a section is made up of a non-intersecting, regular, closed chain of n line sections. For illustrative purposes, Fig. 5(a) depicts a regular polygonal section of $n = 5$ sides (a regular pentagon) inscribed in a circle of radius R and oriented with angle α with respect to the x-axis.

Using Eq. (18) and (19) and the principle of moments recursively, it follows that the centroidal polar moment of inertia of a regular polygon-shaped section about the z-axis is

$$\bar{I}_z = \left[\frac{1}{2}n\sin\left(\frac{1}{2}\theta_n\right) + \frac{1}{6}n\sin\left(\frac{3}{2}\theta_n\right)\right]dR^3 + \frac{1}{6}n \times \sin\left(\frac{1}{2}\theta_n\right)Rd^3 \tag{31}$$

where $\theta_n = 2\pi/n$ is the exterior angle of the polygon in radians. It is noted that this is an expression that does not depend upon the orientation of the section, α.

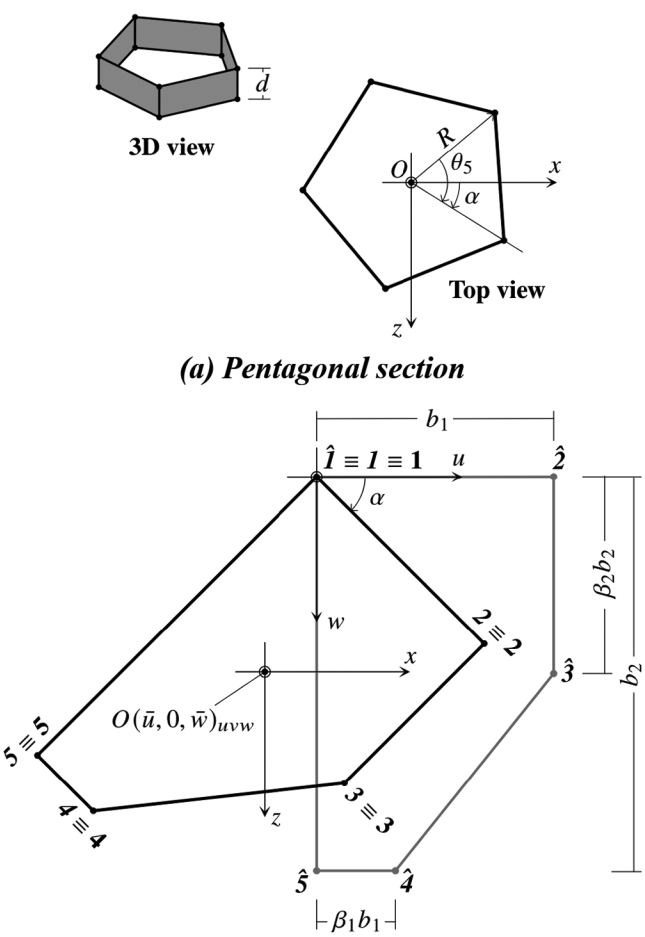

Fig. 5—Less common sections in concrete design.

To test the soundness of Eq. (31), two remarks are in order. First, if $n = 4$, the polygonal section becomes a square of side length $b = \sqrt{2}R$, and so from Eq. (31)

$$\bar{I}_z = \frac{2}{3}db^3 + \frac{1}{3}bd^3 \tag{32}$$

However, this same result could have been obtained from Eq. (27) by setting $b_1 = b_2 = b$.

Second, in the limit a regular polygon of n sides is a circle. So, as n tends to infinity, one should expect that Eq. (31) approaches Eq. (28). This is indeed the case because

$$\begin{aligned} n\sin\left(\frac{1}{2}\theta_n\right) &= n\sin\left(\frac{\pi}{n}\right) \\ &= n\left(\frac{\pi}{n} - \frac{1}{3!}\left(\frac{\pi}{n}\right)^3 + \frac{1}{5!}\left(\frac{\pi}{n}\right)^5 - \frac{1}{7!}\left(\frac{\pi}{n}\right)^7 + \cdots\right) \\ &= \pi\left(1 - \frac{1}{3!}\left(\frac{\pi}{n}\right)^2 + \frac{1}{5!}\left(\frac{\pi}{n}\right)^4 - \frac{1}{7!}\left(\frac{\pi}{n}\right)^6 + \cdots\right) \end{aligned} \tag{33}$$

where the second equality follows from the Taylor series expansion of sine. Thus, $n\sin\left(\frac{1}{2}\theta_n\right) \to \pi$ as $n \to \infty$. Likewise, it can be shown that $n\sin\left(\frac{3}{2}\theta_n\right) \to 3\pi$ as $n \to \infty$. Replacing both these results into Eq. (31) yields Eq. (28) with $b = 2R$.

DISCUSSION

For the typical case where $\alpha = 0$, the centroidal polar moments of inertia displayed in Eq. (27), (29), and (30) reduce to the following expressions. For a rectangular section

$$\bar{I}_z = \frac{1}{6}b_1 d^3 + \frac{1}{6}db_1^3 + \frac{1}{6}b_2 d^3 + \frac{1}{2}db_2 b_1^2 \tag{34}$$

(This is Eq. (3a).) For a C-shaped section

$$\bar{I}_z = \frac{1}{6}b_1 d^3 + \frac{1}{6}db_1^3 + \frac{1}{12}b_2 d^3 + \left(\frac{b_1}{2b_1 + b_2}\right)\frac{1}{2}db_2 b_1^2 \tag{35}$$

For an L-shaped section

$$\bar{I}_z = \frac{1}{12}b_1 d^3 + \frac{1}{12}db_1^3 + \frac{1}{12}b_2 d^3 + \left(\frac{b_1}{b_1 + b_2}\right)\frac{1}{4}db_2 b_1^2 \tag{36}$$

However, in Section R8.4.4.2.3 of ACI CODE-318-25[3] and other sources,[1,2,5-20] Eq. (34) is standardly written without the contributing term $\frac{1}{6}b_2 d^3$, meaning that the centroidal polar moment of inertia is written incorrectly as

$$\bar{I}_z = \frac{1}{6}b_1 d^3 + \frac{1}{6}db_1^3 + \frac{1}{2}db_2 b_1^2 \tag{37}$$

It is believed that Eq. (37) is the result of an incorrect implementation of Steiner's theorem.[4] In their article, Di Stasio and Van Buren[1] appear to have overlooked the fact that the

two side faces parallel to $\gamma_{vz} M_z$ have a definite height equal to d, which also has the potential to contribute significantly to the total polar moment of inertia. Wight and MacGregor[18] offer an insight into why this may have happened—namely, that it is commonly thought that the concept of polar moment of inertia applies only to sections that can be represented on a flat sheet of paper. This statement is far from accurate, for in mechanics the concept of polar moment of inertia is more general and can be extended beyond 2-D space to encompass three-dimensional (3-D) space as well. For example, refer to Eq. (5) for the precise definition of polar moment of inertia in $\mathbb{R}^3$.

The inaccuracies in the literature do not end there. Collins and Mitchell[6] proposed an expression to calculate the centroidal polar moment of inertia of a circular section, defining it as $\bar{I}_z = \frac{1}{2} d b^3 + \frac{1}{6} b d^3$. They did not provide a derivation, nor did they indicate its source. To the best of the authors' understanding, the expression appears to have been derived by approximating a circular section with a circumscribed square section, and then neglecting the dimension b of the side faces perpendicular to $\gamma_{vz} M_z$ and the dimension d of the side faces parallel to $\gamma_{vz} M_z$. However, it should be noted that the correct expression is the one presented in Eq. (28).

Moreover, Section 22.6.4.1.2 of ACI CODE-318-25 permits the designer to approximate a circular or regular polygon-shaped section as a square section of equivalent area. In the following, an asymptotic analysis is pursued to investigate the implications of doing so using the correct expressions for each section.

If a circular section of diameter b and depth d is approximated to a square section of equivalent area, the side length of the square to be used is $\hat{b} = \frac{\sqrt{\pi}}{2} b$. Substituting this $\hat{b}$ as b into Eq. (32) yields

$$\bar{I}_{z,\,\text{approx}} = \frac{1}{12} \pi^{3/2} d b^3 + \frac{1}{6} \sqrt{\pi}\, b d^3 \tag{38}$$

Dividing Eq. (38) by Eq. (28) and simplifying gives

$$\eta := \frac{\bar{I}_{z,\,\text{approx}}}{\bar{I}_z} = \frac{2}{\sqrt{\pi}} \left[\frac{(d/b)^2 + \frac{\pi}{2}}{(d/b)^2 + \frac{3}{2}} \right] \tag{39}$$

To conduct this analysis properly, it is noted that $b = c + d$ is a function of d, where c denotes the diameter of the circular reaction area, such as that generated by a circular column of diameter c. (The dimension b is a function of d because, according to Section 22.6.4.1 of ACI CODE-318-25, the critical section is located at a distance $d/2$ from the reaction's cross section.) If d tends to 0, the ratio η tends to $\frac{2}{3}\sqrt{\pi} \approx 1.18$. If d tends to infinity, η tends to $\frac{2\pi + 4}{5\sqrt{\pi}} \approx 1.16$. If d/b tends to 1 (that is, the case where d and b are of comparable magnitude), η also converges to this limit. These results indicate that the discrepancy between using Eq. (38) and Eq. (28) can range from 16 to 18%, signifying a notable margin of error.

If a regular polygon-shaped section inscribed in a circle of radius R and depth d is approximated to a square section of equivalent area, the side length of the square to be used is $\hat{b} = R\sqrt{\frac{1}{2} n \sin\theta_n}$. Inserting this $\hat{b}$ as b into Eq. (32) gives

$$\bar{I}_{z,\,\text{approx}} = \frac{1}{12} \left[\frac{1}{2} n \sin\theta_n \right]^{3/2} d b^3 + \frac{1}{6} \sqrt{\frac{1}{2} n \sin\theta_n}\, b d^3 \tag{40}$$

where $b = 2R$. Dividing Eq. (40) by Eq. (31) and simplifying produces

$$\eta := \frac{\bar{I}_{z,\,\text{approx}}}{\bar{I}_z} = \frac{2}{\sqrt{n \tan\left(\frac{1}{2}\theta_n\right)}} \left[\frac{(d/b)^2 + \frac{1}{4} n \sin\theta_n}{(d/b)^2 + \frac{1}{2}\cos\theta_n + 1} \right] \tag{41}$$

Similar to the preceding analysis, it is recognized that $b = c + d \sec\left(\frac{1}{2}\theta_n\right)$ is a function of d, where c represents the size of the regular polygon-shaped reaction area inscribed in a circle of diameter c. Thus, if d tends to 0, the ratio η increases asymptotically toward $\frac{2}{3}\sqrt{\pi} \approx 1.18$ as a function of n, starting from $3^{-1/4} \approx 0.760$ when $n = 3$, and taking a value of 1 for $n = 4$. If d tends to infinity, η increases asymptotically towards $\frac{2\pi + 4}{5\sqrt{\pi}} \approx 1.16$ as a function of n, starting from $3^{1/4}(3\sqrt{3} + 2)/12 \approx 0.789$ when $n = 3$, and taking a value of 1 for $n = 4$. Finally, if d/b tends to 1, η also converges to this limit, taking a value of 1 when $n = 4$, but starting from $3^{1/4}(3\sqrt{3} + 8)/21 \approx 0.827$ when $n = 3$. As expected, η approaches the limit values determined for a circular section as n approaches infinity. Interestingly, in the case of an equilateral triangle ($n = 3$), the approximation suggested by the building code results in an underestimation of the polar moment of inertia by up to 24%.

Lastly, the implications of using the traditional expressions versus the correct expressions are investigated next, starting with an asymptotic analysis for the rectangle-shaped sections. Dividing Eq. (37) by Eq. (34) gives

$$\eta := \frac{\bar{I}_{z,\,\text{traditional}}}{\bar{I}_z} = \frac{(d/b_1)^2 + 3(b_2/b_1) + 1}{[(b_2/b_1) + 1](d/b_1)^2 + 3(b_2/b_1) + 1} \tag{42}$$

where $b_1 = c_1 + d$ and $b_2 = c_2 + d$. Hence, if d tends to infinity, the ratio η tends to $\frac{5}{6} \approx 0.833$, indicating that errors of up to 16.7% can be expected if the traditional expression is used. If d tends to 0, the ratio η tends to 1, meaning that when d is sufficiently small, using either the traditional or the correct expression will not make much of a difference. To illustrate these findings, two practical examples are explored. The first example involves a critical section with dimensions $b_1 = 0.565$ m, $b_2 = 0.965$ m, and $d = 0.165$ m, representing a flat slab 0.20 m thick supported by a column with a cross section of $c_1 = 0.40$ m by $c_2 = 0.80$ m. Substituting these values into Eq. (42) yields $\eta = 0.977$, thus

indicating an underestimation of only 2.3%. However, a critical section with dimensions $b_1 = 1.30$ m, $b_2 = 1.70$ m, and $d = 0.90$ m, representing a pad footing 1.00 m thick supporting the same column as mentioned previously, results in an underestimation of approximately 10% ($\eta = 0.896$), which is significant. For mat foundations that are 4.00 m thick, this underestimation can be as high as 15% for the same column.

Similarly, conducting an asymptotic analysis for the C- and L-shaped sections yields the following results. As noted previously, b_1 and b_2 are taken as functions of d, where $b_1 = c_1 + \frac{1}{2}d$ and $b_2 = c_2 + d$ for a C-shaped section, and $b_1 = c_1 + \frac{1}{2}d$ and $b_2 = c_2 + \frac{1}{2}d$ for an L-shaped section. Historically, the traditional expressions for the C- and L-shaped sections have been prescribed by Eq. (35) and (36), respectively, without the contributing term $\frac{1}{12}b_2 d^3$. So, dividing these expressions by Eq. (35) or Eq. (36), as appropriate, gives the ratio η for the section under consideration. Hence, when d tends to infinity, η approaches $\frac{13}{21} \approx 0.619$, regardless of whether the section is C-shaped or L-shaped. Based on these results, it is concluded that errors of up to 38.1% can be expected for both sections. For instance, using the same case scenario of the mat foundation and column cross section mentioned previously, the underestimation can lead to errors as high as 34.5% for the C-shaped section and 37.5% for the L-shaped section. However, if d is taken sufficiently small, there is little difference between using the traditional expression and the correct expression.

NUMERICAL EXAMPLE

To illustrate how Eq. (27) to (31) were derived, consider the five-sided section depicted in Fig. 5(b) with $b_1 = 6$ m, $b_2 = 10$ m, $\beta_1 = \frac{1}{3}, \beta_2 = \frac{1}{2}, \alpha = 45$ degrees, and $d = 2$ m. This shape is relevant in concrete design because it represents the effective critical section of an L-shaped reaction area (Section R22.6.5.2, ACI CODE-318-25[3]).

Let uvw be an auxiliary Cartesian coordinate system. In the uvw system, the coordinates of the unrotated vertexes are (units for the coordinates are omitted for brevity)

$$\hat{1}\,(0,\ \pm 1,\ 0)\,,\ \hat{2}\,(6,\ \pm 1,\ 0)\,,\ \hat{3}\,(6,\ \pm 1,\ 5)\,,$$
$$\hat{4}\,(2,\ \pm 1,\ 10)\,,\ \hat{5}\,(0,\ \pm 1,\ 10)$$

whereas the coordinates of the rotated vertexes are

$$1\,(0,\ \pm 1,\ 0)\,,\ 2\left(3\sqrt{2},\ \pm 1,\ 3\sqrt{2}\right),\ 3\left(\frac{1}{2}\sqrt{2},\ \pm 1,\ \frac{11}{2}\sqrt{2}\right)$$

$$4\left(-4\sqrt{2},\ \pm 1,\ 6\sqrt{2}\right),\ 5\left(-5\sqrt{2},\ \pm 1,\ 5\sqrt{2}\right)$$

To rotate each vertex about the v-axis, the rotation map $R(\alpha): \mathbb{R}^2 \rightarrow \mathbb{R}^2$ (an isometry defined on the uw-plane with α as a parameter) was employed

$$(u, w) = R(\alpha)(\hat{u}, \hat{w}) :\Leftrightarrow$$

$$\begin{bmatrix} u \\ w \end{bmatrix} = \begin{bmatrix} \cos\alpha & -\sin\alpha \\ \sin\alpha & \cos\alpha \end{bmatrix} \begin{bmatrix} \hat{u} \\ \hat{w} \end{bmatrix} \tag{43}$$

It is observed that the section is comprised by a sequence of five line sections—namely: 1-2, 2-3, 3-4, 4-5, and 5-1. Clearly, the lengths of each of these line sections are (that is, the b_0's): 6, 5, $\sqrt{41}$, 2, and 10 m, respectively, and their corresponding areas are (that is, the A's): 12, 10, $2\sqrt{41}$, 4, and 20 m^2.

From Eq. (19), with (x, y, z) replaced by (u, v, w), it follows that the centroids of each line section are (that is, the $(\bar{u}, \bar{v}, \bar{w})$'s)

$$\text{1-2: } \left(\frac{3}{2}\sqrt{2},\ 0,\ \frac{3}{2}\sqrt{2}\right),\ \text{2-3: } \left(\frac{7}{4}\sqrt{2},\ 0,\ \frac{17}{4}\sqrt{2}\right),$$

$$\text{3-4: } \left(-\frac{7}{4}\sqrt{2},\ 0,\ \frac{23}{4}\sqrt{2}\right)$$

$$\text{4-5: } \left(-\frac{9}{2}\sqrt{2},\ 0,\ \frac{11}{2}\sqrt{2}\right),\ \text{5-1: } \left(-\frac{5}{2}\sqrt{2},\ 0,\ \frac{5}{2}\sqrt{2}\right)$$

Note: The values presented as follows are displayed with up to five significant figures for brevity.

By applying the principle of moments,[21] the centroid of the five-sided section, $(\bar{u},\ 0,\ \bar{w})$, can be determined using the previously computed information, where

$$\bar{u} = \frac{(12)\left(\frac{3}{2}\sqrt{2}\right) + (10)\left(\frac{7}{4}\sqrt{2}\right) + (2\sqrt{41})\left(-\frac{7}{4}\sqrt{2}\right) + (4)\left(-\frac{9}{2}\sqrt{2}\right) + (20)\left(-\frac{5}{2}\sqrt{2}\right)}{12 + 10 + 2\sqrt{41} + 4 + 20}$$

$$= -1.3205 \text{ m}$$

$$\bar{w} = \frac{(12)\left(\frac{3}{2}\sqrt{2}\right) + (10)\left(\frac{17}{4}\sqrt{2}\right) + (2\sqrt{41})\left(\frac{23}{4}\sqrt{2}\right) + (4)\left(\frac{11}{2}\sqrt{2}\right) + (20)\left(\frac{5}{2}\sqrt{2}\right)}{12 + 10 + 2\sqrt{41} + 4 + 20}$$

$$= 4.9573 \text{ m}$$

Let xyz be the actual Cartesian coordinate system for the section, such that the origin of the system coincides with $(\bar{u},\ 0,\ \bar{w})$, and the x- and z-axes point in the same direction as the u- and w-axes, respectively. In the xyz-system, the coordinates of the vertexes are

$$1\,(1.3205,\ \pm 1,\ -4.9573)\,,\ 2\,(5.5632,\ \pm 1,\ -0.71466)$$

$$3\,(2.0276,\ \pm 1,\ 2.8209)\,,\ 4\,(-4.3363,\ \pm 1,\ 3.5280)\,,$$

$$5\,(-5.7505,\ \pm 1,\ 2.1138)$$

This follows from taking $(x, y, z) = (u - \bar{u}, v - \bar{v}, w - \bar{w})$. As a result, in the *xyz*-system, the centroid of the five-sided section is $(\bar{x}, \bar{y}, \bar{z}) = (0, 0, 0)$.

From Eq. (18), it follows that the e^2 for line section 1-2 is

$$e_1^2 = (1.3205 + 5.5632)^2 - (1.3205)(5.5632) = 40.039 \text{ m}^2$$

The other e^2's are computed in a similar manner

$$\text{2-3: } e_2^2 = 46.340 \text{ m}^2, \text{ 3-4: } e_3^2 = 14.122 \text{ m}^2$$

$$\text{4-5: } e_4^2 = 76.808 \text{ m}^2, \text{ 5-1: } e_5^2 = 27.219 \text{ m}^2$$

Also from Eq. (18), it follows that the I_z for line section 1-2 is

$$I_{z,1} = \frac{1}{3}(12)(40.039) + \frac{1}{12}(12)(2)^2 = 164.16 \text{ m}^4$$

Likewise, the I_z's for the other line sections are

$$\text{2-3: } I_{z,2} = 157.80 \text{ m}^4, \text{ 3-4: } I_{z,3} = 64.554 \text{ m}^4$$

$$\text{4-5: } I_{z,4} = 103.74 \text{ m}^4, \text{ 5-1: } I_{z,5} = 188.12 \text{ m}^4$$

Therefore, by aggregating all of these I_z's, the centroidal polar moment of inertia of the five-sided section is obtained

$$I_z = \sum_{i=1}^{5} I_{z,i} = 164.16 + 157.80 + 64.554 + 103.74 + 188.12 = 678.38 \text{ m}^4$$

CONCLUSIONS

This paper has presented a robust mathematical framework for computing polar moments of inertia for use with the traditional "ACI Commentary Jc Method," outlined in Section R8.4.4.2.3 of ACI CODE-318-25.[3] The definition of polar moment of inertia for two-dimensional (2-D) sections embedded in three-dimensional (3-D) space was presented, along with the mathematical derivations needed to formulate an expression that is computationally straightforward to implement. Subsequently, the polar moments of inertia for the line and arc sections (two primitive sections) were deduced to obtain the centroidal polar moments of inertia for the most common sections used in design: the rectangular, circular, C-shaped, L-shaped, and regular polygon-shaped sections. Lastly, a numerical example was provided to demonstrate the practical implementation of the proposed mathematical framework.

For over 60 years, the centroidal polar moments of inertia have been consistently derived incorrectly in the literature. The authors believe that one plausible reason for these inaccuracies is the misconception that the concept of polar moment of inertia applies only to sections that can be laid out on a flat sheet of paper. This view is further reinforced by the 2025 edition of the ACI Building Code, which uses the qualifier "analogous" in Section R8.4.4.2.3 to potentially indicate that the concept of polar moment of inertia used in 3-D space is not identical to that used in 2-D space. However, because in mechanics the concept is the same regardless of the dimensionality of the space, the qualifier "analogous" appears unnecessary and erroneous.

The objective of this work was threefold: first, to develop a streamlined mathematical framework for calculating polar moments of inertia for use with the traditional "ACI Commentary Jc Method"; second, to identify and rectify inaccuracies in existing expressions by rigorously rederiving them within the developed mathematical framework; and third, to study the implications of continuing to employ the traditional expressions or approximated sections in design. For example, it was shown that errors up to 18% can be expected if a circular section is approximated to a square section of equivalent area, up to 24% for the case of regular triangular sections, and between 7 and 18% for regular polygonal sections with more than four sides. As a result, the authors do not recommend implementing Section 22.6.4.1.2 of ACI CODE-318-25, not only because it leads to inaccuracies in the design process but also because, as demonstrated in this paper, it is not necessary. In addition, it was shown that for sections sufficiently thick, such as those (critical shear sections) found in mat foundation systems or heavy pad footing systems, the errors between using the traditional expressions and the correct expressions can approach values as high as 15% for rectangle-shaped sections, 34.5% for C-shaped sections, and 37.5% for L-shaped sections. However, for sections sufficiently thin, such as those found in flat floor systems, no significant numerical differences are expected between using the traditional and the correct expressions. In such cases, both the traditional and the correct expressions produce similar results.

Finally, the authors urge the research community to experimentally investigate whether adopting the correct expressions would yield safe designs compliant with current provisions of the ACI Building Code, noting the inverse relationship between shear stresses and polar moment of inertia, and the safety margins that arise from using the traditional expressions to calculate shear stresses around slab-column connections. For further discussion, refer to the Appendix.

AUTHOR BIOS

Hugo Esquivel *is the Lead Structural Engineer at Estructuras del Norte, Barranquilla, Colombia. He is a licensed structural engineer in Colombia with over 15 years of experience designing buildings and bridges. He received his BS from Universidad del Norte, Barranquilla, Colombia, and his MS and PhD from Purdue University, West Lafayette, IN. His research interests include nonlinear structural analysis, uncertainty quantification, and performance-based design.*

Guang Lin *is a Professor in the Department of Mathematics and School of Mechanical Engineering and the Director of Data Science Consulting Service at Purdue University. He received his BS from Zhejiang University, Hangzhou, China; his MS from Peking University, Beijing, China; and his MS and PhD from Brown University, Providence, RI. His research interests include deep learning, uncertainty quantification, large-scale data analysis, and multi-scale modeling.*

ACKNOWLEDGMENTS

The first author would like to express gratitude to Estructuras del Norte—a Colombian structural engineering firm—for their financial support. Part of this work was developed while the first author was an Assistant Professor in the Department of Civil and Environmental Engineering at Universidad de la Costa; their support is gratefully acknowledged.

REFERENCES

1. Di Stasio, J., and Van Buren, M. P., "Transfer of Bending Moment Between Flat Plate Floor and Column," *ACI Journal Proceedings*, V. 57, No. 9, Sept. 1960, pp. 299-314.

2. ACI Committee 318, "Building Code Requirements for Reinforced Concrete (ACI 318-63)," American Concrete Institute, Farmington Hills, MI, 1963, 148 pp.

3. ACI Committee 318, "Building Code for Structural Concrete—Code Requirements and Commentary (ACI CODE-318-25)," American Concrete Institute, Farmington Hills, MI, 2025, 702 pp.

4. Esquivel, H., and Lin, G., "Amending the Traditional 'ACI Commentary *Jc* Method' and Other Sources," *Civil Engineering Journal*, V. 9, No. 11, 2023, pp. 2847-2853.

5. ACI Technical Activities Committee, *ACI Reinforced Concrete Design Handbook: A Companion to ACI 318-19*, 10th edition, American Concrete Institute, Farmington Hills, MI, 2021.

6. Collins, M. P., and Mitchell, D., *Prestressed Concrete Structures*, Response Publications, Ontario, Canada, 1997.

7. Computers & Structures, "Reinforced Concrete Slab Design Manual for ETABS; Release 20," Computers & Structures, Inc., Berkeley, CA, 2022.

8. Clarke, L. A., and Cope, R. J., *Concrete Slabs: Analysis and Design*, CRC Press, London, UK, 1984.

9. Darwin, D., and Dolan, C. W., *Design of Concrete Structures*, 16th edition, McGraw-Hill Education, New York, 2021.

10. Dolan, C. W., and Hamilton, H. R., *Prestressed Concrete: Building, Design, and Construction*, Springer Nature, Cham, Switzerland, 2019.

11. Hanson, N. W., and Hanson, J. M., "Shear and Moment Transfer between Concrete Slabs and Columns," *Bulletin, PCA Research and Development Laboratories*, V. 10, No. 1, 1968, pp. 2-16.

12. Islam, S., "Limit Design of Reinforced Concrete Slabs: Openings and Slab-Column Connections," PhD thesis, University of Canterbury, Christchurch, New Zealand, 1973.

13. Lin, T. Y., and Burns, N. H., *Design of Prestressed Concrete Structures*, third edition, John Wiley & Sons, Inc., New York, 1981.

14. McCormac, J. C., and Brown, R. H., *Design of Reinforced Concrete*, 10th edition, John Wiley & Sons, Inc., Hoboken, NJ, 2015.

15. Naaman, A. E., *Prestressed Concrete Analysis and Design: Fundamentals*, second edition, Techno Press 3000, Ann Arbor, MI, 2004.

16. Nawy, E. G., *Prestressed Concrete: A Fundamental Approach*, fifth edition, Pearson Education, Upper Saddle River, NJ, 2009.

17. Park, R., and Gamble, W. L., *Reinforced Concrete Slabs*, second edition, John Wiley & Sons, Inc., Hoboken, NJ, 1999.

18. Post-Tensioning Institute, *Post-Tensioning Manual*, sixth edition, Post-Tensioning Institute, Farmington Hills, MI, 2006.

19. Wight, J. K., and MacGregor, J. G., *Reinforced Concrete: Mechanics and Design*, sixth edition, Pearson Education, Upper Saddle River, NJ, 2012.

20. Zhou, Y., "Seismic Performance Assessment and Nonlinear Modeling Parameters for Slab-Column Connections," PhD thesis, Texas A&M University, College Station, TX, 2019.

21. Meriam, J. L., and Kraige, L. G., *Engineering Mechanics: Statics*, seventh edition, John Wiley & Sons, Inc., Hoboken, NJ, 2012.

APPENDIX

To ensure structural safety, ultimate shear stresses around slab-column connections must not exceed the connection's design shear strength. In particular, given the ultimate shear stress $v_{uy}(x,z)$ and the nominal shear strength $v_{ny}(x,z)$ at a point $(x, \cdot, z)$ along the critical section, the design objective is to ensure that the following condition is satisfied

$$|v_{uy}(x,z)| \le \phi\, v_{ny}(x,z) \text{ with } \phi = 0.75 \quad \text{(Section 21.2.1, ACI CODE-318-25)} \tag{44}$$

Because the actual ultimate shear stress distribution along the critical section is often difficult to determine (the distribution is generally nonlinear), the ACI Code still permits the use of the theory of elasticity, along with the simplifying assumption that the connection's horizontal plane remains plane after deformation, to estimate the order of magnitude of such stresses (Section 8.4.4.2.3, ACI CODE-318-25). Since the 1960s, ultimate shear stresses have been computed using Eq. (1),[1,2,11] and accordingly, the nominal shear strength $v_{ny}(x,z)$ has been calibrated experimentally based on this equation to serve as a reliable predictor of the connection's shear strength. For instance, according to Sections 8.5.3.1.2, 22.6.1.2, and 22.6.5.2 of ACI CODE-318-25, the nominal shear strength of an interior slab-column connection without shear reinforcement is given by

$$v_{ny}(x,z) = (1.0 \text{ psi})\min\left\{4, 2+\frac{4}{\beta}, 2+\frac{\alpha_s d}{b_0}\right\}\lambda_s\lambda\sqrt{\frac{\min\{f_c', 10 \text{ ksi}\}}{1.0 \text{ psi}}} \tag{45}$$

where β is the ratio of long to short sides of the column; $\alpha_s = 40$ (Section 22.6.5.3, ACI CODE-318-25); d is the effective slab depth (Section 22.6.2.1, ACI CODE-318-25); b_0 is the perimeter of the critical section; f_c' is the slab's specified compressive strength of concrete; $\lambda = 1.0$ is the modification factor for normalweight concrete (Section 19.2.4.3, ACI CODE-318-25); and λ_s is the size effect factor given by

$$\lambda_s = \min\left\{\frac{2}{1+\dfrac{d}{10 \text{ in.}}}, 1.0\right\}$$

As an example, consider a mat foundation 2.00 m thick supporting a bending-dominated column with a cross section of $c_1 = 0.40$ m by $c_2 = 0.80$ m. Figure 1(a) is used as the reference model for this example, including the coordinate system used in the figure. Assume that the mat foundation has a specified compressive strength of $f_c' = 35$ MPa (5000 psi) and an effective depth of $d = 1.90$ m (= 75 in.). Then, $\beta = 0.80/0.40 = 2.0$, $b_1 = c_1 + d = 0.40 + 1.90 = 2.30$ m, $b_2 = c_2 + d = 0.80 + 1.90 = 2.70$ m, $b_0 = 2(b_1 + b_2) = 10.00$ m, and $\lambda_s = 2/(1 + 75/10) = 0.235$ (which is less than 1.0). As a result, the design shear strength for the mat-column connection is

$$\phi v_{ny}(x,z) = (0.75)(1.0 \text{ psi})\min\left\{4, 2+\frac{4}{2.0}, 2+\frac{(40)(1.90)}{10.00}\right\} \times (0.235)(1.0)\sqrt{\frac{5000}{1.0}} = 50 \text{ psi} = 340 \text{ kPa}$$

Moreover, to determine the ultimate shear stress distribution around the mat-column connection, the γ_v-factors are calculated first using Eq. (2)

$$\gamma_{vz} = 1 - \frac{1}{1 + \frac{2}{3}\sqrt{\frac{2.30}{2.70}}} = 0.381 \text{ and}$$

$$\gamma_{vx} = 1 - \frac{1}{1 + \frac{2}{3}\sqrt{\frac{2.70}{2.30}}} = 0.419$$

Then, the centroidal polar moments of inertia about the x- and z-axes are computed using Eq. (34)

$$\bar{I}_z = \frac{1}{6}(2.30)(1.90)^3 + \frac{1}{6}(1.90)(2.30)^3 + \frac{1}{6}(2.70)(1.90)^3 + \frac{1}{2}(1.90)(2.70)(2.30)^2 = 23.1 \text{ m}^4$$

$$\bar{I}_x = \frac{1}{6}(2.70)(1.90)^3 + \frac{1}{6}(1.90)(2.70)^3 + \frac{1}{6}(2.30)(1.90)^3 + \frac{1}{2}(1.90)(2.30)(2.70)^2 = 27.9 \text{ m}^4$$

Given that the column is bending-dominated, assume that the ultimate shear force and ultimate unbalanced moment at the mat-column connection are as follows: V_{uy} = 300 kN, M_{uz} = 250 kN·m, and M_{ux} = −1000 kN·m. Inserting these quantities into Eq. (1) yields the ultimate shear stress at $(x, \cdot, z)$ along the critical section

$$v_{uy}(x,z) = \frac{300}{(10.00)(1.90)} + \frac{(0.381)(250)}{23.1}x - \frac{(0.419)(-1000)}{27.9}z = 15.8 + 4.12x + 15.0z$$

It is apparent that the design condition given by Eq. (44) is critical at the point with coordinates $x = b_1/2$ = 1.15 m and $z = b_2/2$ = 1.35 m, yielding

$$v_{uy}(1.15,\ 1.35) = 15.8 + 4.12(1.15) + 15.0(1.35) = 41 \text{ kPa}$$

Because $|v_{uy}(x,z)| \leq \phi v_{ny}(x,z)$, shear failure is prevented at all points $(x, \cdot, \text{and}, z)$ along the critical section.

Now, if the centroidal polar moments of inertia had been computed using the traditional expressions (Eq. (4)), the following values would have been obtained

$$\bar{I}_{\text{trad},z} = 20.1 \text{ m}^4 \ (= 0.87\,\bar{I}_z) \text{ and}$$
$$\bar{I}_{\text{trad},x} = 25.2 \text{ m}^4 \ (= 0.91\,\bar{I}_x)$$

resulting in a 7% overestimation of v_{uy} at the critical point. Hence, if ϕv_{ny} were only slightly greater than 41 kPa, the design objective specified in Eq. (44) would not have been met, and a redesign of the mat-column connection would have been required.

Before concluding the Appendix, two final remarks are noted. First, although the 7% overestimation noted previously may be marginal (for practical design purposes), the main goal of this paper was to present a robust mathematical framework for computing centroidal polar moments of inertia in a standardized manner, while also correcting long-standing expressions that have been incorrectly derived for over 60 years. The authors firmly believe that any inaccuracies identified in the literature should be reported and subjected to validation by the research community, as such efforts are essential to the continued advancement of knowledge. Second, if modifications to the nominal shear strength formula (Eq. (45)) are deemed necessary, the authors recommend that they be applied to the size effect factor λ_s, which is closely related to the effective depth d of the slab-column connection—the main contributing parameter to the terms unjustifiably neglected by the traditional expressions of polar moments of inertia.

REGISTER TODAY

ACI FOUNDATION CONCRETE INNOVATION FORUM

AUGUST 18-20, 2026, COLUMBUS, OH, USA

Hyatt Regency Columbus 350 N. High St.

The Concrete Innovation Forum is an innovation-focused educational and networking event for concrete professionals. The Forum is your opportunity to connect with representatives from material suppliers, architecture & engineering firms, contractors, academics, top-level executives, and regulatory agencies. You will learn from industry-experts about current trends, emerging technologies, and new product innovations. Build strategic relationships and expand your network.

aci Foundation
Building the Future

ACI STRUCTURAL JOURNAL TECHNICAL PAPER

Title No. 123-S49

Effects of Axial Compression on Shear Strengths of Anchors

by S.-C. Chun, S. Han, S.-H. Yun, M.-G. Kim, J.-H. Lee, C.-H. Park, and I.-H. Kim

The influence of axial compression is not incorporated into the design provisions for concrete breakout or pryout strength of anchors under shear. This study experimentally evaluated the shear capacities of anchors subjected to axial compression on a base plate using 10 large-scale specimens. The test variables included axial compression N*, edge distances from the anchor shaft in the direction of applied shear, edge distances perpendicular to the applied shear, and the compressive strength of concrete. The results showed little difference in crack initiation and propagation with varying axial compression. However, axial compression significantly improved the concrete breakout strength of anchors in shear. The applied axial compression reached up to 2.5 times the mean concrete breakout strength* V_{cbgo}*, as determined by the concrete capacity design (CCD) method, and the average increase in shear strength was approximately 0.6 times the applied compression. In addition, axial compression suppressed concrete pryout failure by preventing the uplift of base plates. Based on the lowest* N/V_{cbgo} *ratio used in the tests, if axial compression of at least 0.5*V_{cbgo} *is applied to a base plate, pryout failure need not be considered.*

Keywords: anchor; axial compression; breakout; pryout; shear.

INTRODUCTION

Chapter 17 of ACI CODE-318-25 (ACI Committee 318 2025) specifies the design strengths of anchors subjected to tension, shear, or a combination of tension and shear. When tension and shear act simultaneously, the nominal tensile and shear strengths are reduced, compared to cases with tension or shear alone. ACI CODE-318-25 requires that the tension-shear interaction satisfy Eq. (1), with the interaction evaluated independently for both concrete and steel failure modes. In contrast, the interaction between compression and shear can enhance the shear strength of anchors. Additionally, for anchors in tension, experimental and theoretical studies have shown increased breakout capacity with lateral pressure (Piccinin et al. 2010, 2012, 2013).

$$\left(\frac{N_u}{\phi N_n}\right)^{\zeta} + \left(\frac{V_u}{\phi V_n}\right)^{\zeta} \leq 1 \tag{1}$$

where ζ is 5/3 or 2 for concrete or steel failure mode, respectively; and the value of ϕ corresponds to the governing failure mode.

Table 22.5.5.1 in ACI CODE-318-25 shows that the shear strengths of compression members, such as columns, are greater than those of flexural members without axial compression. The stress condition in members under compression and shear is similar to that around anchors under compression and shear (Gupta and Collins 2001; Ou and Kurniawan 2015; Shen et al. 2021). Therefore, beneficial effects can also be expected for anchors subjected to compression and shear.

In 2025, Section 17.6.2.7 was introduced in ACI CODE-318 to account for the effect of a compression field on the breakout strength of anchors in tension (Eligehausen et al. 2006). When the distance between the tension resultant of anchors and the compression resultant acting in the concrete is less than $1.5h_{ef}$, the concrete breakout strength increases. Similarly, anchors in shear and compression may also exhibit enhanced breakout strengths due to axial compression compared to the strengths defined in Chapter 17 of ACI CODE-318-25. However, because no research has been reported on anchors subjected to shear with compression acting between the base plate and the concrete, ACI CODE-318-25 includes no provisions for such conditions, except for attachments with shear lugs in Section 17.11.

While ACI 318 does not consider axial compression in the shear design of anchors, ACI CODE-349 (ACI Committee 349 2024) incorporates its effect on the steel strength of anchors: friction between the base plate and concrete is assumed to contribute to the nominal steel strength under shear, using a friction coefficient of 0.40. However, due to the lack of experimental or theoretical evidence, the influence of axial compression is considered only for steel strength, and not for concrete breakout or pryout strength.

If the contribution of axial compression to breakout or pryout strength is quantified, anchors subjected to significant compression—for example, anchors in bearing pads between bridge girders and concrete piers—can be more efficiently designed without compromising the Code-required safety level.

In this study, the shear strengths of anchors installed in uncracked concrete were experimentally evaluated under constant axial compression applied to the base plates.

RESEARCH SIGNIFICANCE

Although axial compression is expected to enhance the shear strength of anchors, its influence is not incorporated into the shear design provisions of Chapter 17 of ACI CODE-318-25 due to the lack of supporting experimental data. This study addresses that gap by presenting test results that demonstrate the significant improvement in anchor shear capacity under combined axial compression and shear. The improved breakout strength reached up to 2.5 times the mean concrete breakout strength calculated using the concrete capacity design (CCD) method, increasing approximately in proportion to 0.6 times the applied compression.

ACI Structural Journal, V. 123, No. 3, May 2026.
MS No. S-2024-344.R3, doi: 10.14359/51749405, received October 3, 2025, and reviewed under Institute publication policies. Copyright © 2026, American Concrete Institute. All rights reserved, including the making of copies unless permission is obtained from the copyright proprietors. Pertinent discussion including author's closure, if any, will be published ten months from this journal's date if the discussion is received within four months of the paper's print publication.

Moreover, axial compression effectively prevented the uplift of base plates, and as a result, concrete pryout failure was not observed. These findings contribute to a better understanding of the favorable effects of axial compression on anchors in shear and can support a rational design approach while maintaining the required safety margins.

DESIGN PROVISIONS OF ANCHORS IN SHEAR AND COMPRESSION

Anchoring to concrete in ACI CODE-318-25

Section 17.7 of ACI CODE-318-25 classifies the strengths of anchors subjected to shear into steel strength, concrete breakout strength, and concrete pryout strength. The steel strength V_{sa} for cast-in headed bolts and hooked bolt anchors can be determined by Eq. (2)

$$V_{sa} = 0.6A_{se,V}f_{uta} \tag{2}$$

where $A_{se,V}$ and f_{uta} are the effective cross-sectional area and tensile strength, respectively, of an anchor in shear.

The nominal concrete breakout strength of an anchor group in shear is calculated in accordance with Eq. (3) and (4), which are based on the CCD method (Fuchs et al. 1995). Equation (4) is the basic concrete breakout strength of a single anchor in shear installed in cracked concrete and includes a safety factor corresponding to the 5% fractile (Fuchs et al. 1995). The mean breakout strength in uncracked concrete can therefore be calculated from Eq. (5). Although Fuchs et al. (1995) did not provide the upper bound of the mean strength on the right-hand side of Eq. (5), this can be approximated by multiplying the upper bound of Eq. (4) by a factor of 1.8. The mean breakout strength of an anchor group, V_{cbgo}, is calculated using Eq. (3), substituting Eq. (5) for ($\psi_{c,V}V_b$)

$$V_{cbg} = \frac{A_{Vc}}{A_{Vco}}\psi_{ec,V}\psi_{ed,V}\psi_{c,V}\psi_{h,V}V_b \tag{3}$$

$$V_b = \left(0.6\left(\frac{l_e}{d_a}\right)^{0.2}\sqrt{d_a}\right)\lambda_a\sqrt{f_c'}(c_{a1})^{1.5} \le 3.7\lambda_a\sqrt{f_c'}(c_{a1})^{1.5} \text{ (MPa)}$$

$$V_b = \left(7\left(\frac{l_e}{d_a}\right)^{0.2}\sqrt{d_a}\right)\lambda_a\sqrt{f_c'}(c_{a1})^{1.5} \le 9\lambda_a\sqrt{f_c'}(c_{a1})^{1.5} \text{ (psi)} \tag{4}$$

$$V_{bo} = \left(1.08\left(\frac{l_e}{d_a}\right)^{0.2}\sqrt{d_a}\right)\lambda_a\sqrt{f_c'}(c_{a1})^{1.5} \le 1.8 \times 3.7\lambda_a\sqrt{f_c'}(c_{a1})^{1.5} \text{ (MPa)}$$

$$V_{bo} = \left(13\left(\frac{l_e}{d_a}\right)^{0.2}\sqrt{d_a}\right)\lambda_a\sqrt{f_c'}(c_{a1})^{1.5} \le 1.8 \times 9\lambda_a\sqrt{f_c'}(c_{a1})^{1.5} \text{ (psi)} \tag{5}$$

where V_{cbg} is the nominal concrete breakout strength in shear of a group of anchors; V_b is the basic concrete breakout strength in shear of a single anchor in cracked concrete; V_{bo} is the mean breakout strength in uncracked concrete; A_{Vc} is the projected concrete failure area for calculation of strength in shear; $A_{Vco} = 4.5(c_{a1})^2$; c_{a1} is the distance from the center of an anchor shaft to the edge of concrete in the direction of the applied shear; $\psi_{ec,V}$, $\psi_{ed,V}$, $\psi_{c,V}$, and $\psi_{h,V}$ are the factors for eccentricity, edge effect, cracking and supplementary reinforcement, and thickness, respectively; l_e and d_a are the load-bearing length and shaft diameter of an anchor, respectively; and λ_a is the reduction factor for lightweight concrete.

The nominal concrete pryout strength of a cast-in anchor group in shear is determined by Eq. (6). Similar to the mean breakout strength V_{cbgo}, the mean pryout strength of an anchor group V_{cpgo} is calculated using Eq. (6) by substituting Eq. (8) for N_b (Fuchs et al. 1995)

$$V_{cpg} = k_{cp}N_{cpg} = k_{cp}\frac{A_{Nc}}{A_{Nco}}\psi_{ec,N}\psi_{ed,N}\,\psi_{c,N}\psi_{cp,N}N_b \tag{6}$$

$$N_b = 10\lambda_a\sqrt{f_c'}h_{ef}^{1.5} \text{ (MPa)}$$
$$N_b = 24\lambda_a\sqrt{f_c'}h_{ef}^{1.5} \text{ (psi)} \tag{7}$$

$$N_{bo} = 13.3\lambda_a\sqrt{f_c'}h_{ef}^{1.5} \text{ (MPa)}$$
$$N_{bo} = 32\lambda_a\sqrt{f_c'}h_{ef}^{1.5} \text{ (psi)} \tag{8}$$

where V_{cpg} is the nominal concrete pryout strength of a group of anchors; N_{cpg} is calculated using N_{cbg} as determined by Eq. (17.6.2.1b) of ACI CODE-318-25; k_{cp} is 1 or 2 for $h_{ef} <$ 65 mm (2.5 in.) or $h_{ef} \ge 65$ mm (2.5 in.), respectively; and N_b and N_{bo} are the basic and mean concrete breakout strength in tension of a single anchor in cracked concrete, respectively.

For attachments with shear lugs, the bearing strength of a shear lug is calculated in accordance with Eq. (9)

$$V_{brg,sl} = 1.7f_c'A_{ef,sl}\psi_{brg,sl} \tag{9}$$

$$\psi_{brg,sl} = 1 + 4\frac{P_u}{A_{bp}f_c'} \le 2.0 \tag{10}$$

where the factored axial force P_u is positive for compression; and $A_{ef,sl}$ and A_{bp} are the effective bearing area of the shear lug and the base-plate area, respectively.

Only the bearing strength of attachments with shear lugs includes the favorable effects of axial compression applied to the base plate, while neither the steel strength, concrete breakout strength, nor concrete pryout strength includes the effects of axial compression in ACI CODE-318-25. Section 17.6.2.7 of ACI 318, first introduced in the 2025 edition, accounts for the effect of a compression field, generated by flexure, on the breakout strength of anchors subjected to tension. When the distance z between the tension resultant of anchors and the compression resultant acting in the concrete is less than $1.5h_{ef}$, the compression field inhibits the formation of the tension breakout cone (Eligehausen et al. 2006), and the concrete breakout strength of anchors in tension can increase according to a modification factor: $\psi_{cm,N} = 2 - z/(1.5h_{ef}) \ge 1.0$.

ACI CODE-349-23

According to Section 17.7.1.2.2 of ACI CODE-349-23 (ACI Committee 349 2024), friction between the base plate and the concrete contributes to the nominal steel strength of an anchor under shear, and the coefficient of friction can be taken as 0.40. If the axial compression exceeds 2.5 times the shear force, the base plate is assumed not to slip, and the anchor is not required to resist the shear force. However, ACI CODE-349-23 does not consider the effects of axial compression on breakout or pryout strength, due to the absence of experimental evidence demonstrating its favorable influence on these failure modes.

SHEAR STRENGTH OF CONCRETE UNDER COMPRESSION

Shear strength of members subject to axial compression

Section 22.5.5.1 of ACI CODE-318-25 calculates the shear strengths of members subjected to compressive forces using Eq. (11)

$$V_c = \left(0.17\lambda\sqrt{f_c'} + \frac{N_u}{6A_g}\right)b_w d \approx \left(1 + \frac{0.17N_u}{V_{co}}\right)V_{co} \text{ (MPa)}$$

$$V_c = \left(2\lambda\sqrt{f_c'} + \frac{N_u}{6A_g}\right)b_w d \approx \left(1 + \frac{0.17N_u}{V_{co}}\right)V_{co} \text{ (psi)} \quad (11)$$

where N_u is positive for compression and negative for tension; and V_{co} (= $0.17\lambda\sqrt{f_c'}b_w d$ MPa [= $2\lambda\sqrt{f_c'}b_w d$ psi]) is the shear strength without compression.

The shear strength of compression members increases by a factor of $(1 + (0.17N_u/V_{co}))$. In both compression members and anchors in compression and shear, axial compressions act perpendicular to the shear force. However, in anchors, the shear force acts locally on the concrete around the anchor shaft, whereas in compression members, the shear force is distributed over the entire section.

Modified Coulomb yield criteria (Nielsen 1999)

Figure 1 shows the modified Coulomb yield criteria (Nielsen 1999), defining sliding failure and separation failure. When only shear force acts without axial compression, Mohr's circle is centered at the origin, as the "pure shear" shown in Fig. 1. If axial compression is applied, this Mohr's circle shifts to the right, increasing the shear stress at which failure occurs, thus enhancing the shear strength. The modified Coulomb yield criteria can explain the enhancement of the shear strength with axial compression.

EXPERIMENTAL PROGRAM

Test variables

Based on the design provisions (ACI Committee 318 2025; ACI Committee 349 2024) and the related studies (Eligehausen et al. 2006; Fuchs et al. 1995), key parameters influencing the breakout and pryout strengths of anchors in shear were selected as test variables: the compressive strength of concrete (f_c'); edge distances from the anchor shaft in the direction of applied shear (c_{a1}), and direction perpendicular to the applied shear (c_{a2}); and axial compression (N). Two design compressive strengths of concrete, 24 and 40 MPa (3500 and 5800 psi), were used, with the concrete mixture proportions summarized in Table 1. The effective embedment depth h_{ef} was designed to achieve the intended failure mode. Axial compressions applied to the base plates were varied up to 2.5 times the mean breakout strength V_{cbgo}, based on the measured compressive strength of concrete.

A total of 10 specimens were tested and categorized into three test series: C24-L-series, C24-T-series, and C40-L-series. In the specimen designation C1-2-N3, "1" is the design compressive strength of concrete (MPa); L and T in "2" represent $c_{a2} \geq 1.5c_{a1}$ and $c_{a2} < 1.5c_{a1}$, respectively; and "3" is the ratio of N to V_{cbgo}.

Specimen design

Two anchors were installed in each specimen, as shown in Fig. 2 for the details of the C40-L-series. Table 2 summarizes the dimensions of the test specimens. Anchor shafts of 60 mm (2.36 in.) diameter were used to prevent steel failure, and their design yield and tensile strengths were 250 MPa (36 ksi) and 400 MPa (58 ksi), respectively. The C24-L- and C40-L-series were designed to induce concrete breakout failure, with an embedment depth h_{ef} of 200 mm (7.9 in.) to prevent pryout failure. Meanwhile, the C24-T-series had a shorter h_{ef} of 100 mm (3.9 in.) and a large front edge distance c_{a1} of 700 mm (27.6 in.), intended to make the pryout strength lower than the breakout strength and thereby promote pryout failure. Furthermore, the base-plate depth for the C24-T-series was only 200 mm (7.9 in.), as shown in Table 2, to increase the likelihood of pryout by inducing

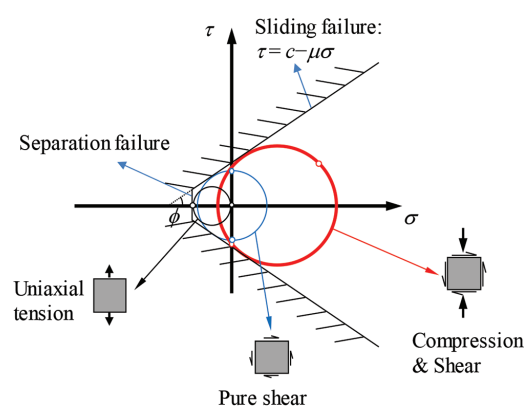

Fig. 1—Modified Coulomb yield (failure) criteria (adapted from Nielsen [1999]).

Table 1—Concrete mixture proportions, kg/m³ (lb/ft³)

Design compressive strength f_c', MPa (psi)	Ordinary portland cement	Water	Sand	Coarse aggregate	High-range water-reducing admixture
24 (3500)	393 (24.5)	174 (10.9)	876 (54.7)	900 (56.2)	3.93 (0.245)
40 (5800)	540 (33.7)	170 (10.6)	733 (45.8)	986 (61.6)	5.40 (0.337)

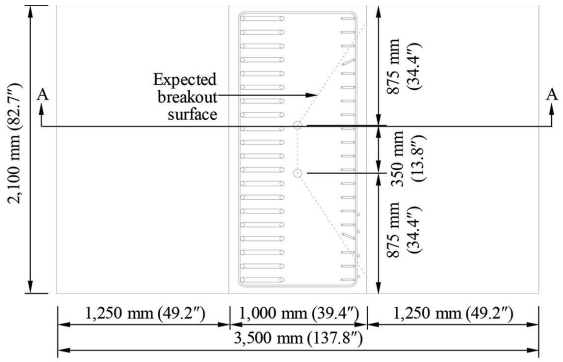

(a) Plan of C40-L-series

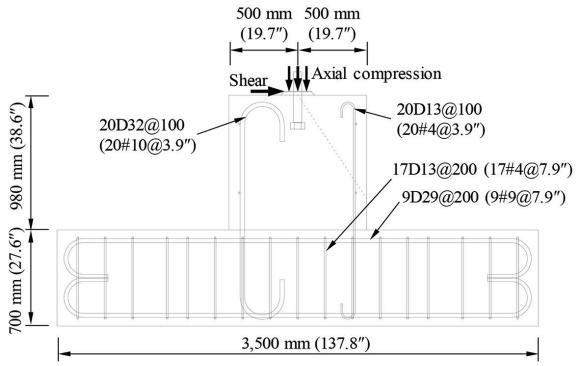

(b) A-A Section of C40-L-series

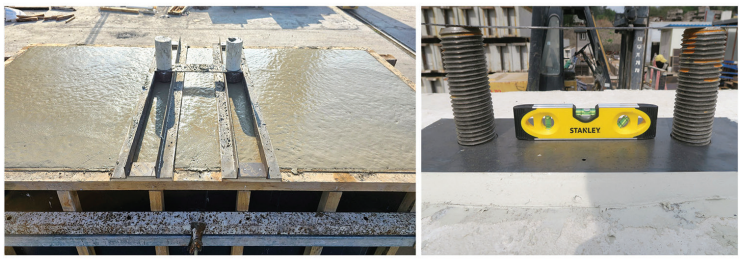

(c) Embedding two anchor bolts and installing a base plate

Fig. 2—Details of C40-L-series.

Table 2—Dimensions of specimens, mm (in.)

Series	Plan				Base plate*		Anchor	Pedestal	Stub	
	B	D	c_{a1}	c_{a2}	b	d	h_{ef}	H_1	H_2	L
C24-L	1400 (55.1)	450 (17.7)	350 (13.8)	600 (23.6)	600 (23.6)	400 (15.7)	200 (7.9)	700 (27.6)	730 (28.7)	2500 (98.4)
C24-T	1400 (55.1)	1400 (55.1)	700 (27.6)	600 (23.6)	600 (23.6)	200 (7.9)	100 (3.9)	1400 (55.1)	780 (30.7)	3500 (137.8)
C40-L-N0.0 C40-L-N2.0	2100 (82.7)	1000 (39.4)	500 (19.7)	875 (34.4)	600 (23.6)	200 (7.9)	200 (7.9)	980 (38.6)	700 (27.6)	3500 (137.8)
C40-L-N0.5 C40-L-N2.5					750 (29.5)					

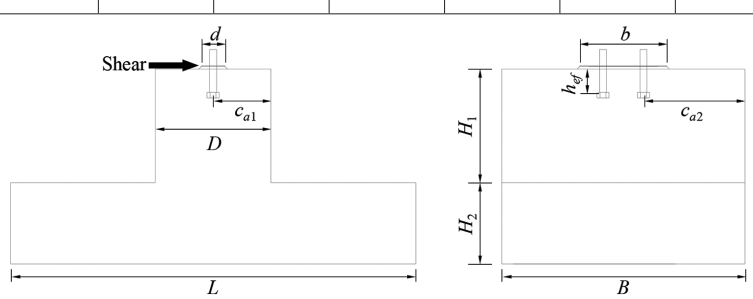

*Thickness of base plates is 5 mm (0.20 in.).

higher tensile forces in the anchor shafts due to the inevitable eccentricity between the applied shear force and resistance, as shown in Fig. 3 (Eligehausen et al. 2006). The base plates were ASTM A36/A36M with a thickness of 5 mm (0.20 in.); Table 2 shows the dimensions.

Table 3 summarizes the concrete compressive strength measured on the test date f_{cm} and the applied axial compression N for each specimen. Each series included one specimen without axial compression ($N = 0$). Table 3 also provides the mean breakout strength V_{cbgo} and the mean pryout strength V_{cpgo}, calculated with f_{cm}. The pedestals and stubs were designed to be sufficiently strong to remain in an elastic state until specimen failure.

Test procedure and instrumentation

Figure 4 presents the test setup. First, the axial compression designated for each specimen was applied to the base plate using two center-hole hydraulic cylinders and a spreader beam. This axial compression was maintained constant using a load-maintaining device, regardless of lateral displacement. A bracket under the spreader beam, shown in Fig. 4, was stiff enough to apply uniform compression on the base plate and prevent bending. After applying the axial compression, the shear force was statically increased using a 2500 kN (562 kip) capacity actuator.

The axial compression force was measured using center-hole load cells installed beneath the hydraulic cylinders.

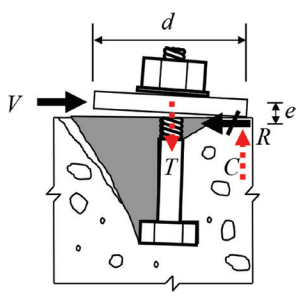

Fig. 3—Mechanism of pryout (adapted from Eligehausen et al. [2006]).

Horizontal displacement at the center of the pedestal face was measured using a linear variable differential transformer (LVDT), as shown in Fig. 4. To measure the crack width and sequence of cracking, 12 Π-shaped displacement transducers with a gauge length of 100 mm (4 in.) were mounted at locations within 50 mm (2 in.) of the base plate, as shown in Fig. 5. Two transducers were located at each side, and eight were positioned in front of the base plate.

TEST RESULTS

Failure modes

Failures of all specimens are shown in Fig. 6. Except for C24-T-N1.3, all specimens exhibited inclined cracks in plan, consistent with the typical concrete breakout of anchors in shear (Fuchs et al. 1995; Eligehausen et al. 2006). C24-T-N1.3 showed local bearing failure in front of the base plate. As the shear load increased, the anchor and base plate rotated due to the inevitable eccentricity, resulting in localized bearing of the base plate on the concrete, as illustrated in Fig. 3. However, uplift of the base plate, implying pryout failure, was not observed in any specimen of the C24-T-series.

Crack initiation and propagation were not significantly influenced by variations in N, c_{a1}, c_{a2}, or f_c'. A few more cracks in the direction of the applied shear were observed in C24-T-N0.6, C40-L-N2.0, and C40-L-N2.5, where relatively high compression forces were applied. All specimens, except C24-T-N1.3, exhibited brittle failure immediately after reaching their maximum loads.

Even in the C24-T-series, designed to induce pryout failure, concrete breakout or local bearing failure was observed instead of pryout failure. When axial compression was applied, pryout did not occur because the compression prevented upward rotation of the base plate. Moreover, even C24-T-N0.0 (where the predicted pryout strength V_{cpgo} was lower than the predicted breakout strength V_{cbgo}, as shown in Table 3) exhibited breakout failure, implying that the pryout strength provision of ACI CODE-318-25 is more conservative than the breakout strength provision. In the subsequent analysis, V_{cbgo} is used as the reference strength for the

Table 3—Test matrix and test results

Specimen ID	f_{cm}, MPa (ksi)	N, kN (kip)	σ_p, MPa (ksi)	V_{cbgo}, kN (kip)	V_{cpgo}, kN (kip)	V_e, kN (kip)	F.M*	N/V_{cbgo}	V_e/V_{cbgo}	V_{cbgo}', kN (kip)	V_e/V_{cbgo}'
C24-L-N0.0	25.1 (3.6)	0	0	260.1 (58.5)	632.6 (142.2)	228.8 (51.4)	CB	0.0	0.88	—	—
C24-L-N1.0	25.1 (3.6)	250 (56.2)	1.04 (151)	260.1 (58.5)	632.6 (142.2)	412.9 (92.8)	CB	1.0	1.59	410.1 (92.2)	1.01
C24-L-N1.9	25.1 (3.6)	500 (112.4)	2.08 (302)	260.1 (58.5)	632.6 (142.2)	439.5 (98.8)	CB	1.9	1.69	560.1 (125.9)	0.78
C24-T-N0.0	25.4 (3.7)	0	0	361.3 (81.2)	281.2 (63.2)	449.7 (101.1)	CB	0.0	1.24	—	—
C24-T-N0.6	25.4 (3.7)	225 (50.6)	1.88 (272)	361.3 (81.2)	281.2 (63.2)	783.8 (176.2)	CB	0.6	2.17	496.3 (111.6)	1.58
C24-T-N1.3	25.4 (3.7)	450 (101.2)	3.75 (544)	361.3 (81.2)	281.2 (63.2)	885.6 (199.1)	B	1.3	2.45	631.3 (141.9)	1.40
C40-L-N0.0	50.5 (7.3)	0	0	652.8 (146.8)	897.3 (201.7)	644.0 (144.8)	CB	0.0	0.99	—	—
C40-L-N0.5	49.7 (7.2)	324 (72.8)	2.16 (313)	647.4 (145.5)	890.1 (200.1)	814.0 (183.0)	CB	0.5	1.26	841.6 (189.2)	0.97
C40-L-N2.0	50.5 (7.3)	1306 (293.5)	10.88 (1578)	652.8 (146.8)	897.3 (201.7)	1450.0 (326.0)	CB	2.0	2.22	1436.2 (322.9)	1.01
C40-L-N2.5	49.7 (7.2)	1619 (363.9)	10.79 (1565)	647.4 (145.5)	890.1 (200.1)	1461.5 (328.6)	CB	2.5	2.26	1618.6 (363.9)	0.90

*F.M means failure mode, and CB and B refer to concrete breakout failure and bearing failure, respectively.

Note: f_{cm} is compressive strength of concrete from 100 x 200 mm (4 x 6 in.) cylinders; N is axial compression; σ_p is bearing pressure (= N/A_{bp}), where A_{bp} is the area of a base plate; V_{cbgo} is mean concrete breakout strength; V_{cpgo} is mean concrete pryout strength; V_e is maximum load; and V_{cbgo}' is breakout strength predicted by Eq. (12).

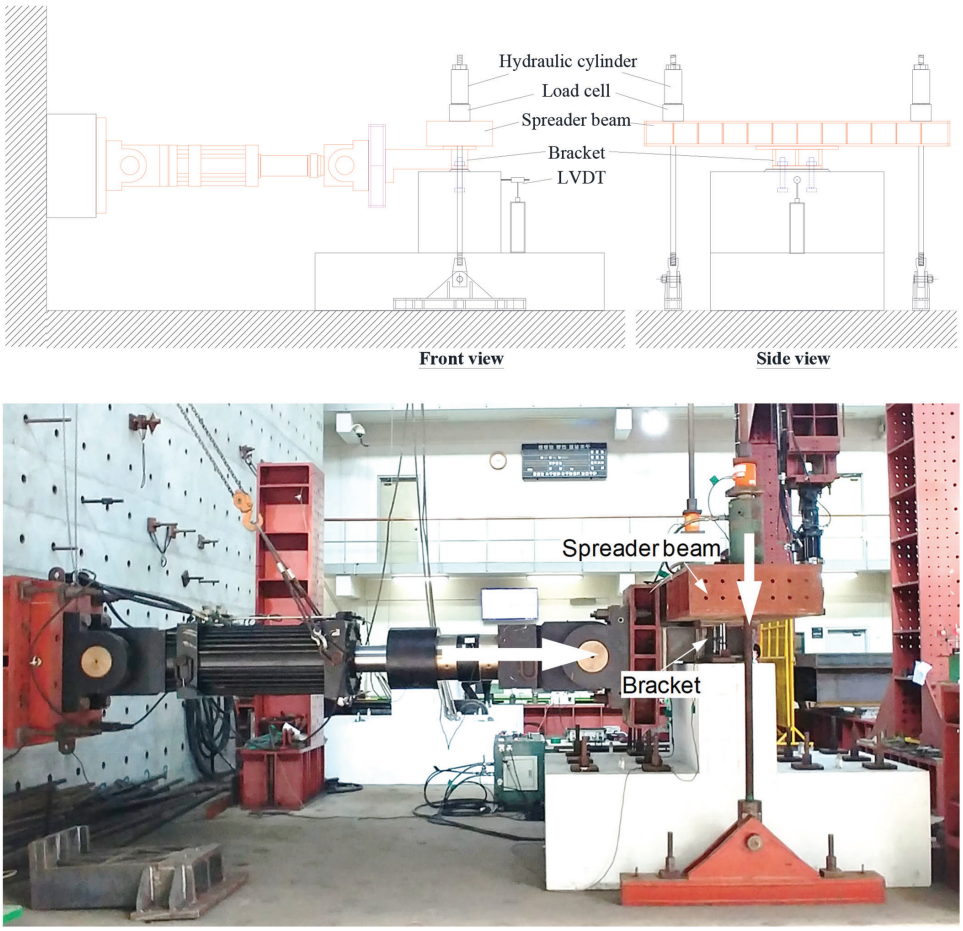

Fig. 4—Test setup.

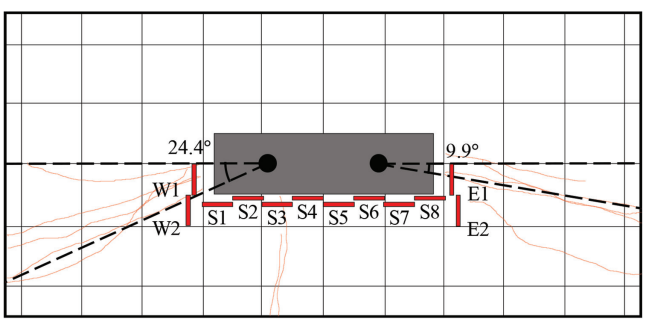

Fig. 5—Cracks observed in C40-L-series and layout of Π-shaped displacement transducers.

C24-T-series, even though V_{cpgo} is lower than V_{cbgo} for the C24-T-series (refer to Table 3).

Figure 5 shows all the cracks observed in the C40-L-series. The largest and smallest crack angles are indicated as dashed lines. These angles ranged from 9.9 to 24.4 degrees, which are lower than the 35 degrees assumed in the CCD method (Fuchs et al. 1995). The load-crack width relationships of C40-L-N0.5 and C40-L-N2.5 are shown in Fig. 7, with the measurement points E1, E2, and W1 defined in Fig. 5. For both specimens, side cracking occurred at maximum load, and the subsequent sudden drop in load indicated brittle failure caused by concrete breakout. There was no notable difference in cracking patterns or post-peak behavior with varying axial compression. As mentioned earlier, specimens subjected to higher axial compression exhibited additional cracks in the direction of applied shear.

Load-displacement relationship and maximum loads

Figure 8 shows the load-displacement responses of the C40-L-series. All specimens exhibited brittle behavior, failing immediately after reaching their peak loads. The maximum loads increased with increasing axial compression. Table 3 summarizes the measured peak loads V_e and failure modes for all specimens. Within each series, the V_e/V_{cbgo} ratio increased as axial compression increased, confirming the beneficial effect of axial compression on concrete breakout strength.

The relationship between maximum load V_e and axial compression N is shown in Fig. 9. Although V_e increased with N, at higher levels of axial compression, the rate of increase diminished. In Fig. 10, both V_e and N are converted to shear stress τ_p and bearing pressure σ_p, respectively, by dividing by the area of the base plate A_{bp}. For the C24-L-series, which used relatively large base plates, the resulting shear stresses were much lower than those of the C24-T- and C40-L-series at similar bearing pressures (refer to the dotted box in Fig. 10). These observations highlight that τ_p and σ_p can be markedly affected simply by changing the base-plate size, even when key parameters, such as c_{a1}, c_{a2}, h_{ef}, and f_c', which govern V_{cbgo} in the CCD method, remain unchanged.

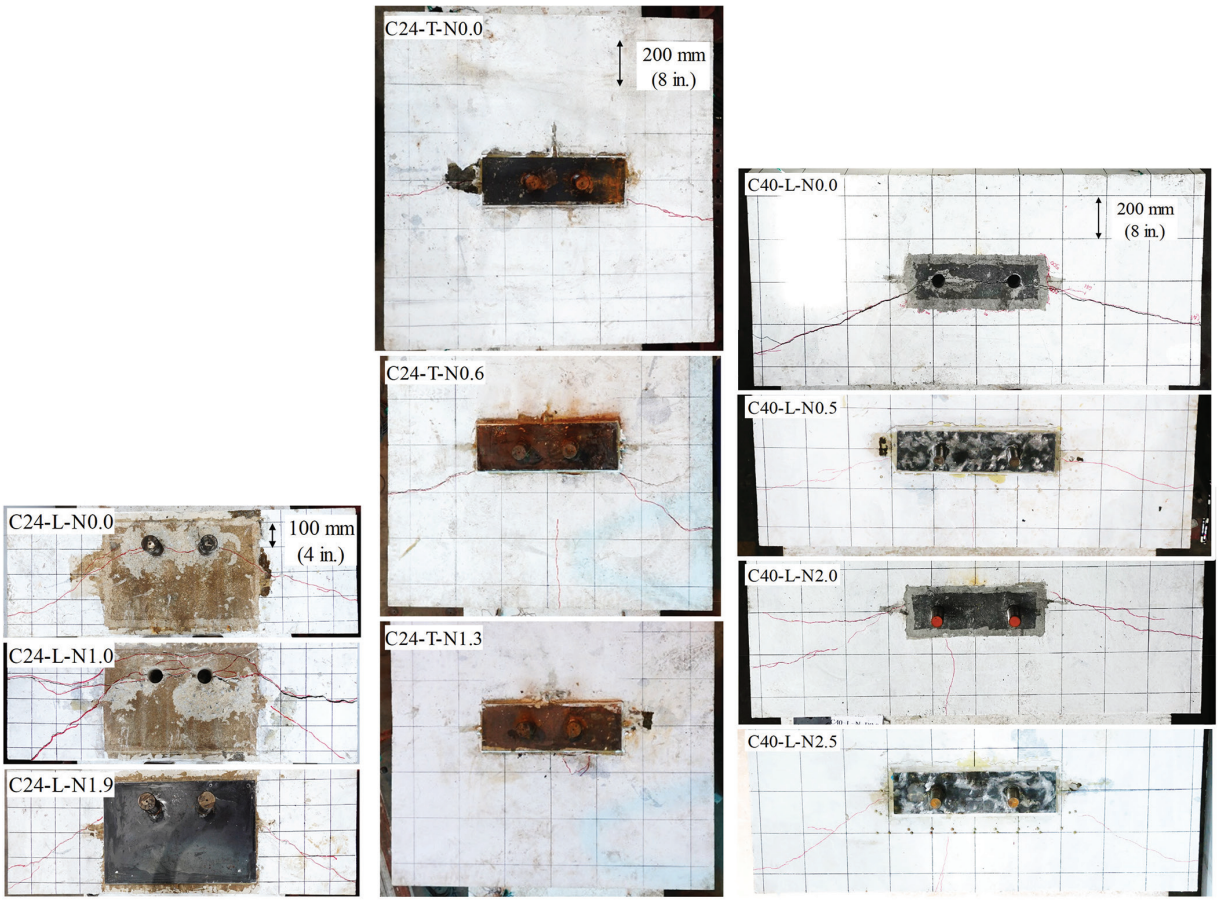

(a) C24-L-series (b) C24-T-series (c) C40-L-series

Fig. 6—Plan views of specimen failures showing breakout crack propagation.

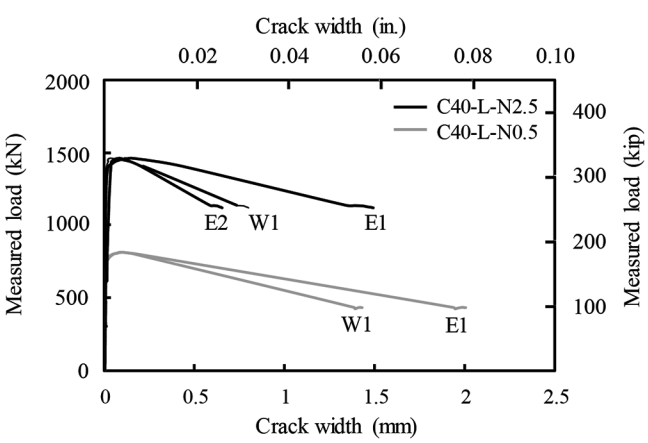

Fig. 7—Load-crack width relationship of C40-L-series.

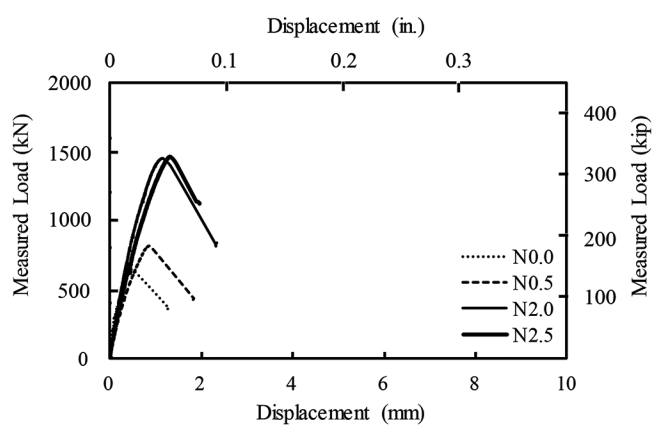

Fig. 8—Load-displacement relationship of C40-L-series.

To address this limitation, a horizontal projected area A_c, as shown in the inset of Fig. 11—defined as the projected area of the failure body perpendicular to A_{Vc}—was used instead of A_{bp}. By dividing the axial compression and maximum shear load by A_c, normal stress σ and shear stress τ were obtained. Their relationship is plotted in Fig. 11. The shear strength increased with increasing normal stress, in agreement with the modified Coulomb yield criteria (Nielsen 1999) introduced in Fig. 1. However, because the cohesion (c) and friction coefficient (μ) parameters of the sliding failure surface vary with the concrete properties, it is difficult to directly apply the modified Coulomb yield criteria to anchor design under shear and compression.

EVALUATION OF CONCRETE BREAKOUT STRENGTH OF ANCHORS IN COMPRESSION AND SHEAR

The experimental results demonstrate that axial compression significantly enhances concrete breakout strength and suppresses pryout failure. The specimens that were expected to fail by pryout instead exhibited breakout failure. Because the lowest N/V_{cbgo} ratio tested in this study is 0.5, it can be concluded that when axial compression of at least $0.5V_{cbgo}$

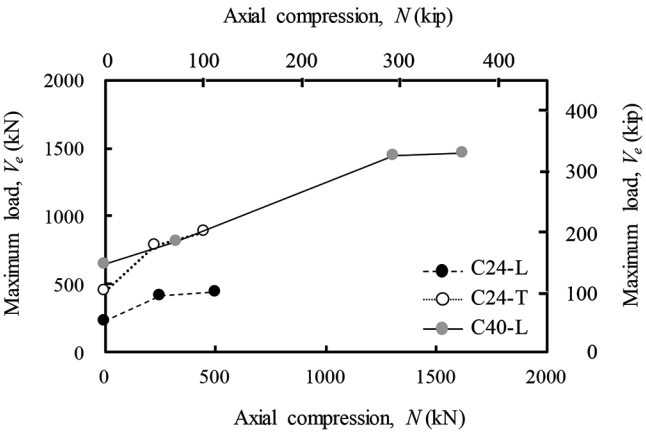

Fig. 9—Maximum load-axial compression relationship.

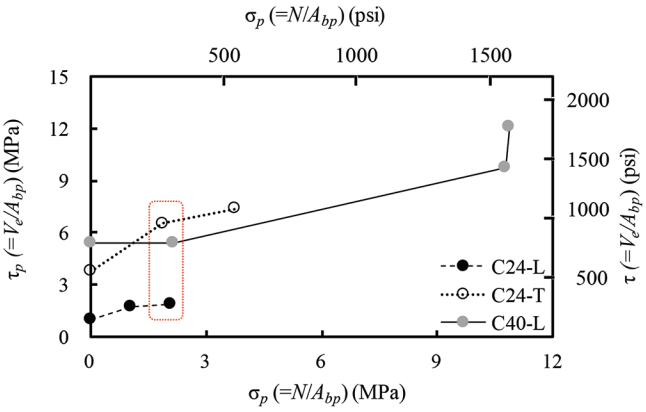

Fig. 10—τ_p-σ_p relationship based on A_{bp}.

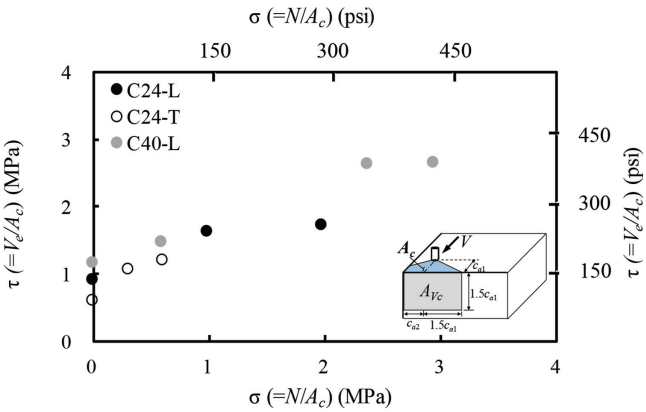

Fig. 11—τ-σ relationship based on A_c.

is applied to the base plate, pryout failure need not be considered.

Because it is difficult to directly evaluate the improvement in shear strength due to axial compression in Fig. 9, both axial compression and maximum shear load were normalized by V_{cbgo} for each specimen, and their relationship is shown in Fig. 12. The V_e/V_{cbgo} ratios are approximately linearly proportional to the N/V_{cbgo} ratios. A trend line based on the specimens with axial compression is expressed by Eq. (12) which is illustrated as a dashed line in Fig. 12. The y-intercept of Eq. (12) was set to 1.0, representing the mean breakout strength V_{cbgo} calculated by the CCD method (Fuchs et al. 1995), which was validated using approximately

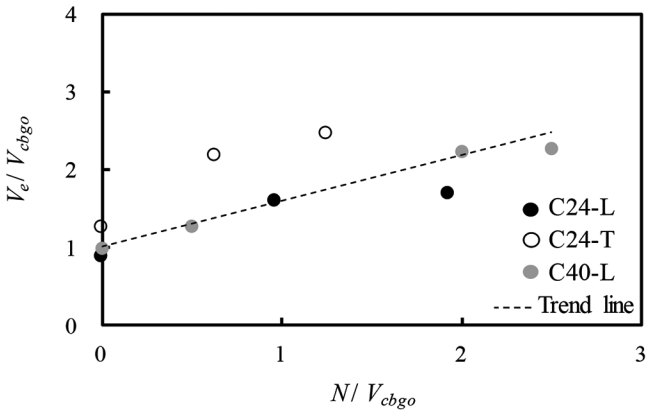

Fig. 12—Maximum loads normalized by V_{cbgo} with varying axial compression normalized by V_{cbgo}.

1200 test results (Fuchs et al. 1995). The enhanced breakout strength due to axial compression increases linearly up to $2.5V_{cbgo}$ when the axial compression reaches $2.5V_{cbgo}$. The 95% confidence interval for the slope of Eq. (12) ranges from 0.31 to 0.88.

$$V_{cbgo}' = V_{cbgo} + 0.6N \tag{12}$$

where V_{cbgo}' is the enhanced mean concrete breakout strength of anchors in shear and compression; and N shall not be taken greater than $2.5V_{cbgo}$.

As shown in Fig. 12, the C24-T-series exhibits greater enhancement in V_e/V_{cbgo} compared to the other series at the same N/V_{cbgo} ratio. This may be attributed to its smaller perpendicular edge distance c_{a2}, as only the C24-T-series had $c_{a2} < 1.5c_{a1}$. In the CCD method, the breakout failure surface is modeled as a polyhedral shape, as shown in Fig. 13(a), with uniform resistance ($f_{1c} = f_{1e}$) across the projected breakout area. However, under combined shear and axial compression, as illustrated in Fig. 13(b), the actual shear resistance near and beneath the base plate (f_{2c}) may be greater than the resistance farther from the base plate (f_{2e}) due to the effects of axial compression. Furthermore, although the CCD method assumes a constant breakout depth of $1.5c_{a1}$, experimental observations show that the depth tends to decrease toward the edges of the breakout surface (Eligehausen et al. 2006), as depicted in Fig. 13(b). As a result, the CCD method yields conservative estimates for the C24-T-series, with $c_{a2} < 1.5c_{a1}$. Consequently, the C24-T-series exhibited greater strength enhancement (V_e/V_{cbgo}) at the same axial load ratio (N/V_{cbgo}) compared to the other series.

Figure 14 compares the predictions from Eq. (12) with the experimental results. The average and coefficient of variation (COV) of the test-to-prediction ratios are 1.08 and 22.2%, respectively. Equation (12) can simply and safely evaluate the enhanced breakout strength of anchors in shear and compression.

CONCLUSIONS

Although Chapter 17 of ACI CODE-318-25 considers the interaction between tension and shear on anchorages, it does not account for the effects of axial compression on anchor

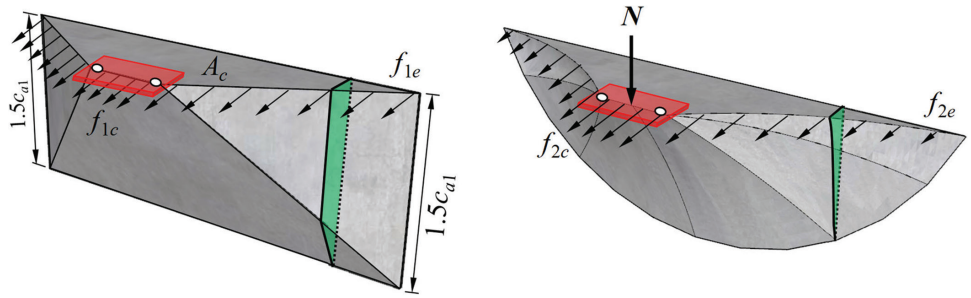

(a) Mathematical model per the CCD method **(b) Experimental observation**

Fig. 13—Shear resistance of breakout surface.

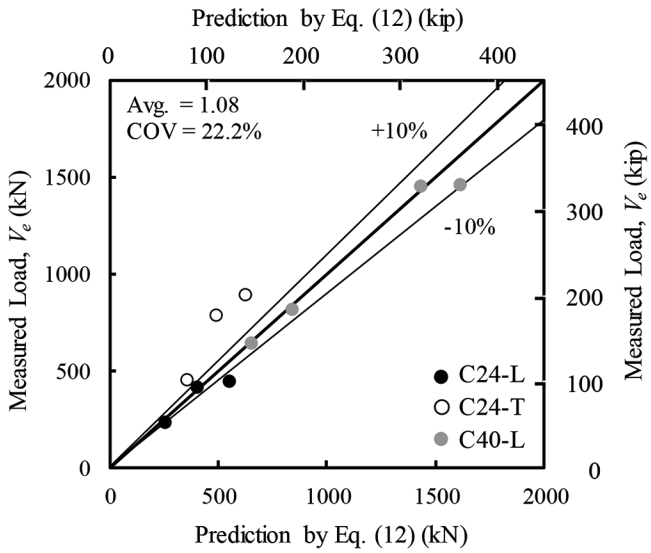

Fig. 14—Comparison of test results and predictions by Eq. (12).

shear strength. The shear capacities of anchors subjected to axial compression through a base plate were experimentally evaluated using 10 large-scale specimens. Based on the test results, the following conclusions are drawn:

1. All specimens except C24-T-N1.3 exhibited typical concrete breakout failure, whereas C24-T-N1.3 experienced local bearing failure in front of the base plate. The initiation and propagation of cracks showed little variation with changes in axial compression, edge distances (both in the direction of and perpendicular to the applied shear), or concrete compressive strength.

2. Axial compression significantly increased the concrete breakout strength of anchors in shear. On average, shear capacity increased by 0.6 times the applied compression, with the improved breakout strength reaching up to 2.5 times the mean breakout strength V_{cbgo} calculated by the concrete capacity design (CCD) method (Fuchs et al. 1995).

3. Axial compression effectively suppressed pryout failure. Even specimens that were expected to fail by pryout instead exhibited breakout failure. Based on the lowest tested N/V_{cbgo} ratio, when axial compression of at least $0.5V_{cbgo}$ is applied to the base plate, pryout failure may be disregarded.

AUTHOR BIOS

ACI member **Sung-Chul Chun** *is a Professor in the Division of Architecture and Urban Design at Incheon National University, Incheon, Republic of Korea. He received his BS, MS, and PhD from Seoul National University, Seoul, Republic of Korea, in 1994, 1996, and 2007, respectively. He is a member of ACI Committees 352, Joints and Connections in Monolithic Concrete Structures, and 408, Bond and Development of Steel Reinforcement. His research interests include steel anchorage to concrete, composite structures, and the rehabilitation of reinforced concrete (RC) structures.*

Sangmin Han *is a Graduate Student in the Division of Architecture and Urban Design at Incheon National University, where he received his BS in 2023. His research interests include anchoring to concrete using reinforcing bars and anchors.*

Sung-Hwan Yun *is a Senior Researcher in the Korea Expressway Corporation Research Institute, Hwaseong, Gyeonggi, Republic of Korea. He received his MS and PhD from Hanyang University, Seoul, Republic of Korea, in 2005 and 2013, respectively. His research interests include repaired/strengthened RC structures and bridge maintenance.*

Mun-Gil Kim *is a Researcher at the Total PC Limited Company, Yeoju, Gyeonggi, Republic of Korea. He received his BS from Mokpo National University, Muan County, South Jeolla Province, Republic of Korea, in 2015, and his MS and PhD from Incheon National University in 2017 and 2022, respectively. His research interests include anchoring to concrete using reinforcing bars and anchors.*

Jong-Han Lee *is a Professor in the Department of Civil Engineering at Inha University, Incheon, Republic of Korea. He received his PhD from the Georgia Institute of Technology, Atlanta, GA, in 2010. His research interests include anchorage in concrete structures and the evaluation of structural performance using field data and numerical analysis.*

Chang-Ho Park *is a Senior Research Fellow at the Korea Expressway Corporation Research Institute. He received his BS from Pusan National University, Busan, Republic of Korea, in 1989, and his MS and PhD from Korea Advanced Institute of Science and Technology, Daejeon, Republic ofKorea, in 1991 and 1997, respectively. His research interests include maintenance and seismic design of bridge structures.*

Ick-Hyun Kim *is a Professor in the School of Architecture and Built Environment at the University of Ulsan, Ulsan, Republic of Korea. He received his PhD from The University of Tokyo, Tokyo, Japan, in 1998. His research interests include nonlinear analysis of concrete structures and seismic design/evaluation of concrete structures.*

ACKNOWLEDGMENTS

This work was supported by the National Research Foundation of Korea (NRF) grant funded by the Korean government (MSIT) (No. 2021R1A2C2010863) and the Korea Expressway Corporation (PJT_0000000000020193).

REFERENCES

ACI Committee 318, 2025, "Building Code for Structural Concrete—Code Requirements and Commentary (ACI CODE-318-25)," American Concrete Institute, Farmington Hills, MI, 702 pp.

ACI Committee 349, 2024, "Nuclear Safety-Related Concrete Structures—Code Requirements and Commentary (ACI CODE-349-23)," American Concrete Institute, Farmington Hills, MI, 273 pp.

Eligehausen, R.; Mallée, R.; and Silva, J. F., 2006, *Anchorage in Concrete Construction*, first edition, Ernst & Sohn, Berlin, Germany, 378 pp.

Fuchs, W.; Eligehausen, R.; and Breen, J. E., 1995, "Concrete Capacity Design (CCD) Approach for Fastening to Concrete," *ACI Structural Journal*, V. 92, No. 1, Jan.-Feb., pp. 73-94.

Gupta, P. R., and Collins, M. P., 2001, "Evaluation of Shear Design Procedures for Reinforced Concrete Members under Axial Compression," *ACI Structural Journal*, V. 98, No. 4, July-Aug., pp. 537-547.

Nielsen, M. P., 1999, *Limit Analysis and Concrete Plasticity*, second edition, CRC Press, Boca Raton, FL, 936 pp.

Ou, Y.-C., and Kurniawan, D. P., 2015, "Effect of Axial Compression on Shear Behavior of High-Strength Reinforced Concrete Columns," *ACI Structural Journal*, V. 112, No. 2, Mar.-Apr., pp. 209-220.

Piccinin, R.; Ballarini, R.; and Cattaneo, S., 2010, "Linear Elastic Fracture Mechanics Pullout Analyses of Headed Anchors in Stressed Concrete," *Journal of Engineering Mechanics*, ASCE, V. 136, No. 6, June, pp. 761-768. doi: 10.1061/(ASCE)EM.1943-7889.0000120

Piccinin, R.; Ballarini, R.; and Cattaneo, S., 2012, "Pullout Capacity of Headed Anchors in Prestressed Concrete," *Journal of Engineering Mechanics*, ASCE, V. 138, No. 7, July, pp. 877-887. doi: 10.1061/(ASCE)EM.1943-7889.0000395

Piccinin, R.; Cattaneo, S.; and Biolzi, L., 2013, "Breakout Capacity of Headed Anchors in Confined Concrete: Experimental Evidence," *ACI Structural Journal*, V. 110, No. 3, May-June, pp. 469-480.

Shen, W.-C.; Hwang, S.-J.; Li, Y.-A.; Weng, P.-W.; and Moehle, J. P., 2021, "Force-Displacement Model for Shear-Critical Reinforced Concrete Columns," *ACI Structural Journal*, V. 118, No. 1, Jan., pp. 241-249.

ACI STRUCTURAL JOURNAL TECHNICAL PAPER

Title No. 123-S50

Interface Shear between Ordinary Concrete and Ultra-High-Performance Concrete with Glass Fiber-Reinforced Polymer Reinforcing Bars

by Yail J. Kim and Ali Alatify

This paper presents the interface shear between ordinary concrete and ultra-high-performance concrete (UHPC) connected with glass fiber-reinforced polymer (GFRP) reinforcing bars. Following ancillary tests on reinforcing bar fracture under in-plane shear loading, concrete-reinforcing bar assemblies are loaded to examine capacities and failure modes as influenced by the size, spacing, and number of reinforcing bars. While the shear behavior of bare reinforcing bars is primarily governed by the orientation of the load-resisting axes in the glass fibers and their volume, the size and spacing of the reinforcement largely control the interface capacity by affecting the load-transfer mechanism from the reinforcing bar to the concrete. The degree of stress distribution affects the load-displacement response of the interface, which is characterized in terms of quasi-steady, kinetic, and failure regions. The primary failure modes of the interface comprise reinforcing bar rupture and concrete splitting. The formation of cracks between the ordinary concrete and UHPC results from interfacial deformations, leading to spalling damage when applied loads exceed service levels. An analytical model is formulated alongside an optimization technique. The capacities of the interface in relation to the reinforcing bar rupture and concrete splitting failure modes are predicted. Furthermore, a machine learning algorithm is used to define a failure envelope and propose practice guidelines through parametric investigations.

Keywords: dowel action; glass fiber-reinforced polymer (GFRP) reinforcement; interface resistance; ultra-high-performance concrete (UHPC).

INTRODUCTION

Ultra-high-performance concrete (UHPC) is deemed a breakthrough solution in contemporary construction and has been implemented for a wide range of purposes, from building facades to bridge joints.[1] Besides its high compressive strength of at least $f_c' = 120$ MPa (17.5 ksi),[2] UHPC is set apart from traditional concrete by three major aspects[3]: homogeneity, packing density, and ductility. Sustainable structures often incorporate UHPC as an additive to conventional concrete elements, such as overlays and built-up components.[4,5] The integration of pre- and post-cast members in a composite system offers many benefits, covering extended longevity, reduced maintenance cost, improved strength, and favorable durability.[6,7] Numerous field applications have been documented around the globe.[8] Royce[9] compiled case studies on the use of UHPC as a closure for precast bulb-tee girders in New York. Shear connectors were epoxy-coated steel reinforcing bars and the compressive strength of UHPC was $f_c' = 97$ MPa (14 ksi) at 12 to 14 hours after casting. Attention was paid to adjusting the camber between neighboring units, and other placement techniques were underscored to facilitate on-site work. Sritharan et al.[10] reported the first application of UHPC overlays for bridge decks in North America. The candidate bridge was constructed in the mid-1960s and, prior to placing UHPC overlays ($f_c' = 124$ MPa [18 ksi]) with a thickness of 38 mm (1.5 in.), the decks were roughened to enhance bond strength. No premature delamination was detected, as confirmed by pull-off tests. Neirinck et al.[11] examined the behavior of a box-girder bridge with UHPC connections and transverse dowel bars in Manitoba, Canada. The 90-day compressive strength of UHPC was $f_c' = 164$ MPa (23.8 ksi) and the diameter and spacing of the steel dowel bars were 16 and 175 mm (0.63 and 7 in.), respectively. Strain gauge readings showed that local tension could cause cracking at the UHPC-girder concrete interface, whereas the installed dowels mitigated exerted stresses. Several laboratory test programs focused on the behavior of ordinary concrete bonded to UHPC to assess adhesion capacity, damage accumulation, and failure characteristics.[12-14]

Among others (notably, load distribution, geometric properties, and connection type), the interface of the aforementioned composite system demands special consideration because connections are a weak link and their capacity is controlled by various interrelated parameters—namely, contact deformations, shear stress distributions, and reinforcement layouts.[4,5] From a structural standpoint, shear friction and dowel action characterize the interfacial resistance of the multi-material system.[15,16] Shear friction originates from forces that preclude slippage between chemically adhered surfaces, while dowel action counteracts in-plane loads parallel to the coupled substrates. In the context of shear friction, simplified laboratory techniques employing push-out specimens are frequently adopted to evaluate interface capacities, stress transfers, and failure modes.[12,17] The dowel action of reinforcing bars elevates substrate stresses and accelerates interfacial failure,[16] highlighting the necessity for a comprehensive analysis of interactions between steel reinforcing bars and ordinary concrete/UHPC substrates.[18,19] In addition, owing to the staged casting of UHPC on existing

ACI Structural Journal, V. 123, No. 3, May 2026.
MS No. S-2024-395.R2, doi: 10.14359/51749317, received October 1, 2025, and reviewed under Institute publication policies. Copyright © 2026, American Concrete Institute. All rights reserved, including the making of copies unless permission is obtained from the copyright proprietors. Pertinent discussion including author's closure, if any, will be published ten months from this journal's date if the discussion is received within four months of the paper's print publication.

concrete members, connection elements are vulnerable to external factors such as moisture and deicing chemicals.[5,20] Accordingly, nonmetallic connectors exemplified by glass fiber-reinforced polymer (GFRP) composites can ameliorate situations where corrosion is highly likely during the service life of such load-bearing members. It is worth noting that, despite the potential of GFRP, no definitive conclusions are currently available on the configuration and arrangement of multiple GFRP connectors encased in concrete. Woltman et al.[21] claimed that the behavior of precast members was independent of the size and spacing of GFRP connectors; on the other hand, Xue et al.[22] argued that these parameters had a significant impact. This controversial issue should be clarified to advance the state of the art in structural concrete.

This paper explores the performance of interface shear between UHPC and ordinary concrete connected by GFRP dowel bars, a topic that has been largely overlooked in the structural concrete field. Emphasis is placed on the implications of varying geometric variables (bar size and spacing) for the failure of the composite interface. Informed by experimental findings, analytical modeling is undertaken together with machine learning technologies to predict interfacial responses and propose practice recommendations.

RESEARCH SIGNIFICANCE

Notwithstanding recent efforts, research on the behavior of ordinary concrete interfaced with UHPC through GFRP connectors is still in its infancy. Because shear friction between these concrete types differs from that of conventional concrete assemblies,[12] prior knowledge may be irrelevant. Specifically, the shear-friction coefficient (μ) stipulated in ACI 318-19[23] is intended to reflect the condition of adjoined concrete surfaces; however, it does not explicitly account for a heterogeneous interface between ordinary concrete and UHPC. In the same manner, the recently released GFRP-related code of ACI CODE-440.11-22[24] lacks information on connections and omits guidance for UHPC application. Elucidating the element-level behavior of GFRP reinforcement interacting with UHPC is a prerequisite for developing provisions as regards nonmetallic connectors in such an emerging load-bearing system, and this study delivers a unique insight. Of interest is the mechanism of interfacial failure that controls the integrity and capacity of the hybrid composite members, leading to practical design guidelines.

EXPERIMENTAL PROCEDURE

An experimental program is delineated to articulate ingredient materials and specimens. Interest centers on investigations at both reinforcing bar and interface levels. Test protocols are outlined in tandem with instrumentation.

Materials

Two concrete types were employed to cast interface specimens: ordinary concrete and UHPC. The specified compressive strength of the ordinary concrete was f_c' = 25 MPa (3630 psi), which was mixed in the laboratory with a water-cement ratio (w/c) of 0.55. The UHPC mixture was a commercial product that contained carbon nanofiber paste. Although specific details cannot be disclosed due to proprietary restrictions, the mixture was formulated with cement, finely graded aggregates, carbon nanofibers, and other admixtures. According to the manufacturer's instructions, the premix dry constituents were blended with the paste diluted by water and the accelerator to create a suspension and were stirred using a high-shear mixer for 12 minutes, until a homogeneous mixture was achieved. The dowel elements connecting the interface of the ordinary concrete and UHPC were composed of ribbed GFRP reinforcing bars. The composite material, consisting of E-glass corrosion-resistant (E-CR) fibers and a vinylester resin, possessed a tensile strength of f_{fu} = 1000 MPa (145 ksi) and an elastic modulus of E_f = 60 GPa (8700 ksi) at a rupture strain of ε_{fu} = 0.017. For practical assessments, three different reinforcing bar sizes were adopted: D10, D16, and D19, equivalent to No. 3, 5, and 6 in the U.S. designation (diameter = 10, 16, and 19 mm [0.3, 0.63, and 0.75 in.]), respectively.

Specimens

The specimens made of the foregoing concrete mixtures were designed to represent an archetypal slab-on-girder system for buildings and bridges—that is, ordinary concrete girders with a UHPC deck. Three blocks (200 mm [8 in.] wide x 200 mm [8 in.] deep x 400 mm [16 in.] long, each) formed a set of specimens, as depicted in Fig. 1(a). The middle block was prepared using UHPC with GFRP reinforcing bars and moisture-cured for 28 days in an environmental chamber at 99% relative humidity and 23°C (73°F). Subsequently, the ordinary concrete side blocks were cast and cured for an additional period of 28 days in the chamber. Given the diverse placement of shear connectors in the field, variable reinforcing bar spacings were considered from 100 to 200 mm (4 to 8 in.), and their performance was comparatively appraised against that of single-reinforcing bar specimens. Table 1 lists the configuration of the assembled specimens based on reinforcing bar diameter and spacing, and each category involved three repetitive sets. The identification code of the test units denotes the size and spacing of the reinforcing bars, as well as the number of repetitions. For instance, D10-0-1 manifests that the interface specimen comprised a single D10 reinforcing bar and was the first replication of its kind, while D19-200-3 symbolizes the third repetition of the category with two D19 reinforcing bars spaced at 200 mm (8 in.).

Testing

Ten cylinders (100 x 200 mm in diameter [4 x 8 in.] in length) were compressed to determine the 28-day strength of the hardened ordinary concrete and UHPC mixtures (five each). Referring to the methodology prescribed in ACI 440.3R-04,[25] the shear strength of the GFRP reinforcing bars was measured. A precut reinforcing bar (300 mm [12 in.] long) was positioned in a fixture with a support spacing of 50 mm (2 in.), and a shearing force was applied (Fig. 1(b)). Regarding the interface test specimens, a total of 36 units were subjected to monotonic loading at a rate of 1 mm/min (0.0394 in./min) until failure (Fig. 1(c)), within the 1.3 mm/min (0.05 in./min) limit set by ACI 440.3R-04.[25] A load cell (bridge resistance = 350 Ω, non-repeatability = ±0.01%, and

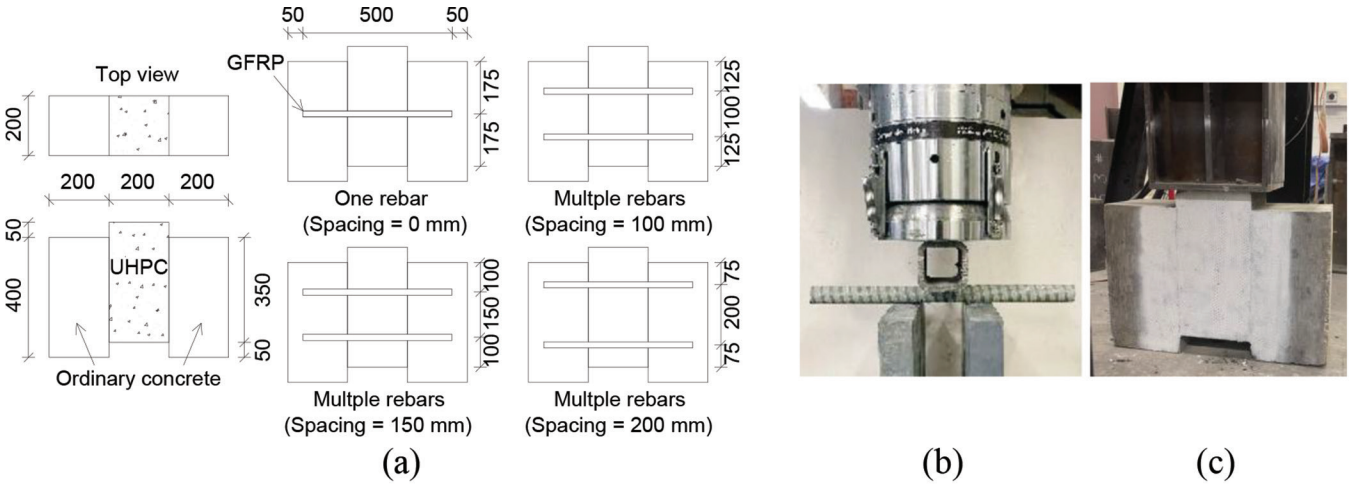

Fig. 1—Experimental details: (a) schematic of specimen categories; (b) reinforcing bar shear test; and (c) interface test. (Note: Units in mm; 1 mm = 0.0394 in.)

nonlinearity = ±0.04%) and a linear potentiometer (resistance = 5 kΩ, repeatability = ±0.002 mm, and linearity = ±0.075%) were used to establish the load-displacement relationship through a stand-alone high-resolution data acquisition system (sampling range is 0.0017 Hz to 14,400 Hz, real-time accuracy is 20 ppm, and maximum data transferring rate is 4800 samples/s) at a sampling rate of 10 Hz.

RESULTS

In this section, test outcomes are expounded on the interfacial responses and failure modes of concrete-reinforcing bar assemblies and the mechanical properties of component elements. The process of interfacial dislocation is visually examined at macro- and micro-scales to understand the integrity of the assemblies subjected to shear loading.

Ancillary test

The compressive strength of the ordinary concrete and UHPC was f_c' = 28.6 MPa (4150 psi) and $f_{c'\text{-}UHPC}$ = 137.4 MPa (20 ksi), respectively, on average (Fig. 2(a)). Figure 2(b) shows the load-displacement relationship of D16 reinforcing bars. Passing through the linear slope at the early stage, a plateau-like pattern was observed until abrupt failure occurred. These transition phases are described in the succeeding segments: 1) when the elastic limit of the GFRP composite was exceeded in shear, the resin matrix gradually impaired and the fibers resisted the applied load (Segment A); 2) the fibers deviating from the longitudinal direction of the reinforcing bar were subjected to axial tension, resulting in the hardening behavior (Segment B); and 3) the fibers finally fractured as the load surpassed the tensile capacity (Segment C). While these sequential procedures were maintained in all specimens, individual responses depended upon the diameter of the reinforcing bars (Fig. 2(c), where selected responses are shown for clarity): the amount of fibers embedded in the resin dominated the elastic limit and the degree of hardening. For that reason, the average shear strength of the D16 and D19 reinforcing bars, calculated by Eq. (1), was 137.4% and 202.1% greater than the capacity of D10, respectively (Fig. 2(d))

$$\tau_u = \frac{P_R}{2A_R} \tag{1}$$

where P_R is the maximum load of the specimen; and A_R is the cross-sectional area of the reinforcing bar.

Load-bearing capacity

Shown in Fig. 3(a) is the ultimate load of the interface specimens. There was a remarkable difference of 129.1% in the capacities between the blocks with single D10 and D16 reinforcing bars (reinforcing bar distance = 0 mm [0 in.]), on average. By contrast, a marginal difference of 11.2% was noted between the average capacities of those with single D16 and D19 reinforcing bars. The observation somewhat diverges from the direct shear capacities recorded in the bare-bar test (Fig. 2(d)); however, it can be attributed to their distinct failure modes demonstrated by the concrete-reinforcing bar assemblies at the interface (further information will be elaborated later). When the number of reinforcing bars increased, the average capacity of the specimens with D10 went up and stabilized (reinforcing bar distance = 100 to 200 mm [4 to 8 in.], Fig. 3(b)). The capacities of the specimens with other reinforcing bars (D16 and D19) ascended as well (Fig. 3(b)); however, flattened trends were not found because the concrete governed the failure in lieu of the reinforcing bars.

Interfacial behavior

Figures 4(a) and (b) exhibit the load-displacement relationship of the specimens with single D10 and D19 reinforcing bars, respectively. On the interfacial behavior pertaining to D10 (Fig. 4(a)), a shift in slope took place at approximately 25 kN (5.6 kip) beyond which the steep response altered to reduced gradients until brittle load drops were noticed (failure region). This implies that the resisting mechanism of the interface changed from the chemical adhesion of the concrete combined with the dowel action of the reinforcing bar (quasi-steady region) to the sliding friction between the concrete substrates accompanied by the infinitesimal shear deformation of the reinforcing bar (kinetic region). In other words, as the interfacial displacement evolved, the

Table 1—Test matrix

Specimen	Reinforcing bar		Ultimate load			Failure mode
	d_b, mm	s, mm	Individual, kN	Average, kN	COV	
D10-0-1	10	0	62.5	66.1	0.137	RR
D10-0-2	10	0	59.4			
D10-0-3	10	0	76.4			
D10-100-1	10	100	129.8	122.9	0.074	RR
D10-100-2	10	100	112.5			
D10-100-3	10	100	126.4			
D10-150-1	10	150	129.4	128.4	0.072	RR
D10-150-2	10	150	137.0			
D10-150-3	10	150	118.7			
D10-200-1	10	200	127.1	130.6	0.084	SC
D10-200-2	10	200	121.8			
D10-200-3	10	200	142.8			
D16-0-1	16	0	146.1	151.4	0.102	RR
D16-0-2	16	0	139.2			
D16-0-3	16	0	168.9			
D16-100-1	16	100	163.7	170.5	0.046	SC
D16-100-2	16	100	168.7			
D16-100-3	16	100	179.0			
D16-150-1	16	150	196.9	204.6	0.033	SC
D16-150-2	16	150	210.1			
D16-150-3	16	150	206.8			
D16-200-1	16	200	228.9	227.9	0.031	SC
D16-200-2	16	200	220.4			
D16-200-3	16	200	234.6			
D19-0-1	19	0	149.7	168.3	0.123	SC
D19-0-2	19	0	190.5			
D19-0-3	19	0	164.8			
D19-100-1	19	100	216.5	213.8	0.068	SC
D19-100-2	19	100	226.9			
D19-100-3	19	100	198.1			
D19-150-1	19	150	208.1	223.8	0.079	SC
D19-150-2	19	150	220.2			
D19-150-3	19	150	243.1			
D19-200-1	19	200	216.3	230.5	0.054	SC
D19-200-2	19	200	235.8			
D19-200-3	19	200	239.5			

Note: 1 mm = 0.0394 in.; 1 kN = 0.225 kip; d_b is reinforcing bar diameter; s is reinforcing bar spacing; RR is rupture of reinforcing bar; SC is splitting of concrete; COV is coefficient of variation.

physical contact between the concrete blocks diminished and the transverse reinforcing bar carried a greater share of the structural demand; thereafter, concrete cracking propagated under the relative motion of the dragging surfaces, entailing a gradual loss of interlocking. Analogous behavior was seen in the D19 specimens (Fig. 4(b)), except for the elevated slope-veering load and the interfacial capacities. The influence of the reinforcing bar spacing is visible in Fig. 4(c). The single-reinforcing bar interface (D19-0) displayed low stiffness, particularly noticeable in the kinetic region. As far as the interface with two reinforcing bars is concerned, precipitous slopes were logged with higher capacities due to the load-sharing feature between the reinforcing bars. Additionally, the enhanced capacities resulting from the widened reinforcing bar spacing point out that the applied shear stress was partly distributed to the concrete between

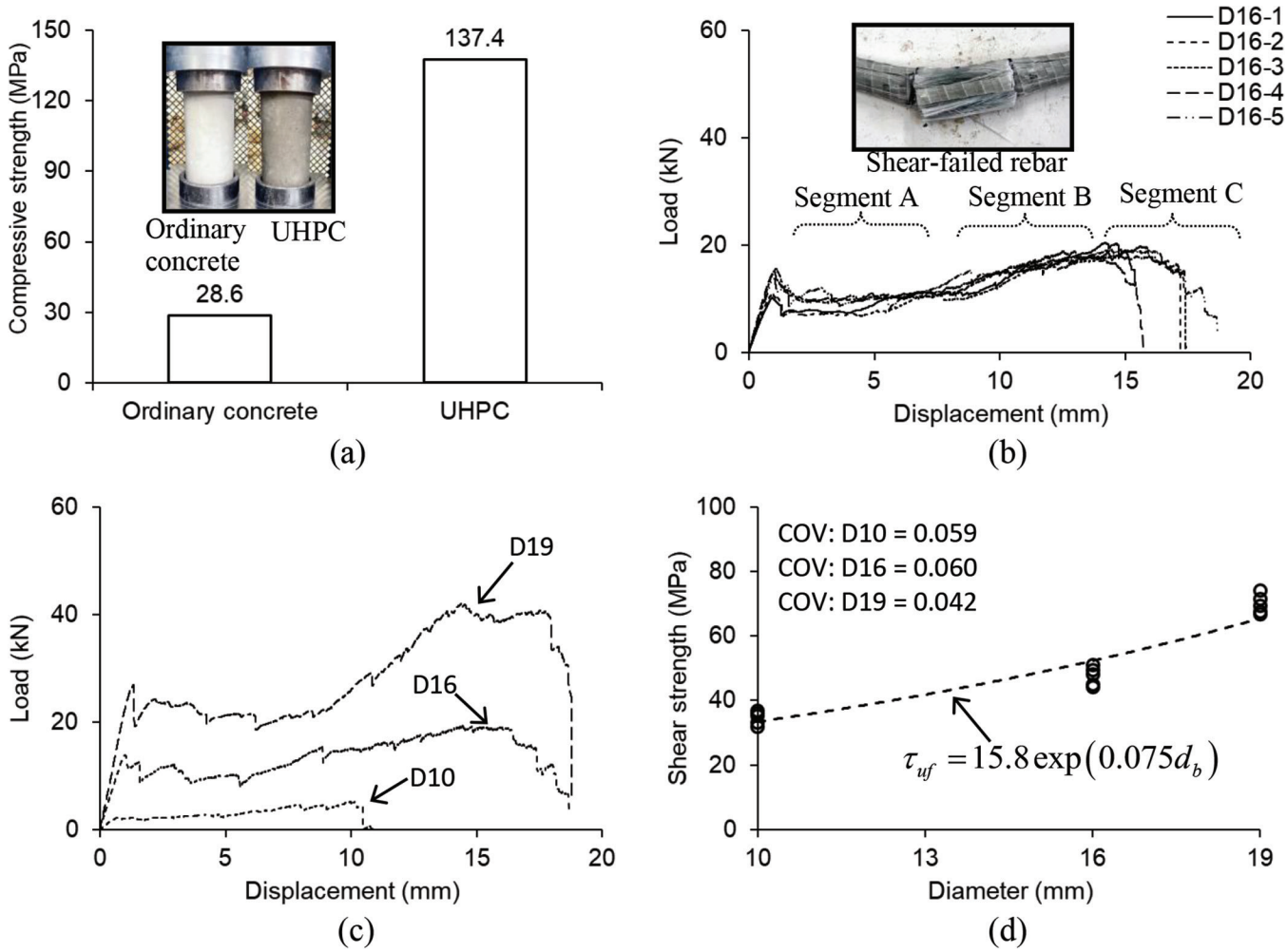

Fig. 2—Ancillary test: (a) compressive strength of ordinary concrete and UHPC; (b) shear resistance of GFRP bars; (c) comparison with respect to reinforcing bar diameter; and (d) diameter-dependent shear strength.

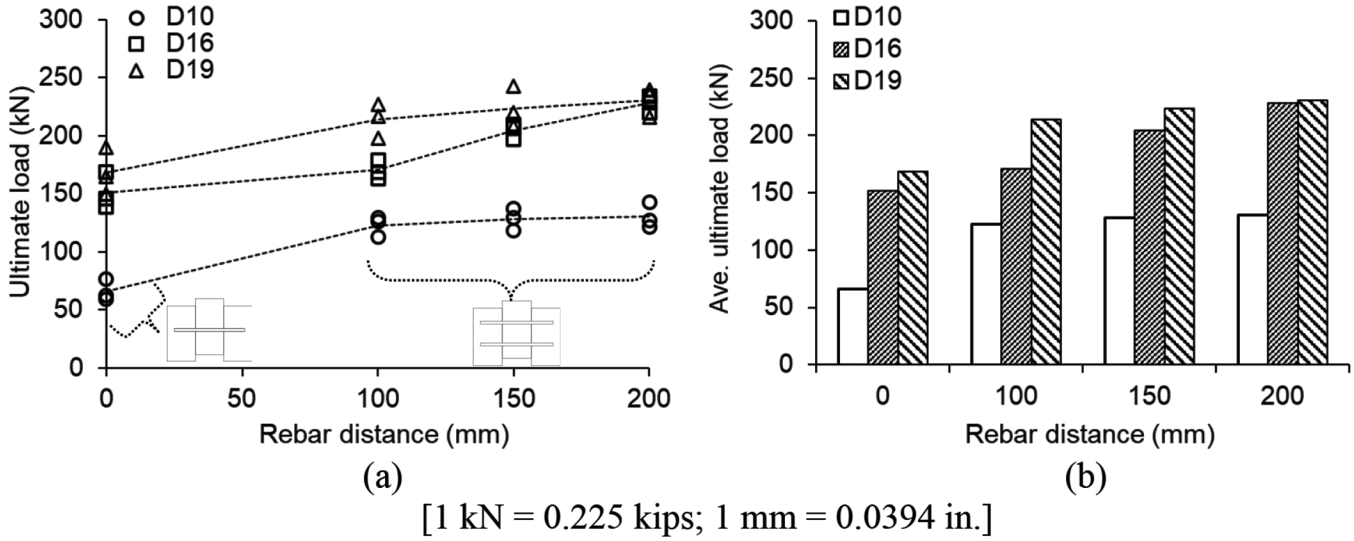

Fig. 3—Interface capacity: (a) individual; and (b) average.

the reinforcing bars, providing evidence for the presence of shear lag along the interface. The displacement of the specimens at peak loads (P_u), distinguishing between the kinetic and failure regions, was contingent upon the size of the reinforcing bars (Fig. 4(d)). In accordance with the regression lines, the characteristic displacement was virtually constant for the D10 specimens; on the contrary, the displacement for the D16 and D19 specimens declined with the enlarged reinforcing bar spacing. It is thus stated that the previously explained stress distribution affected the interface's

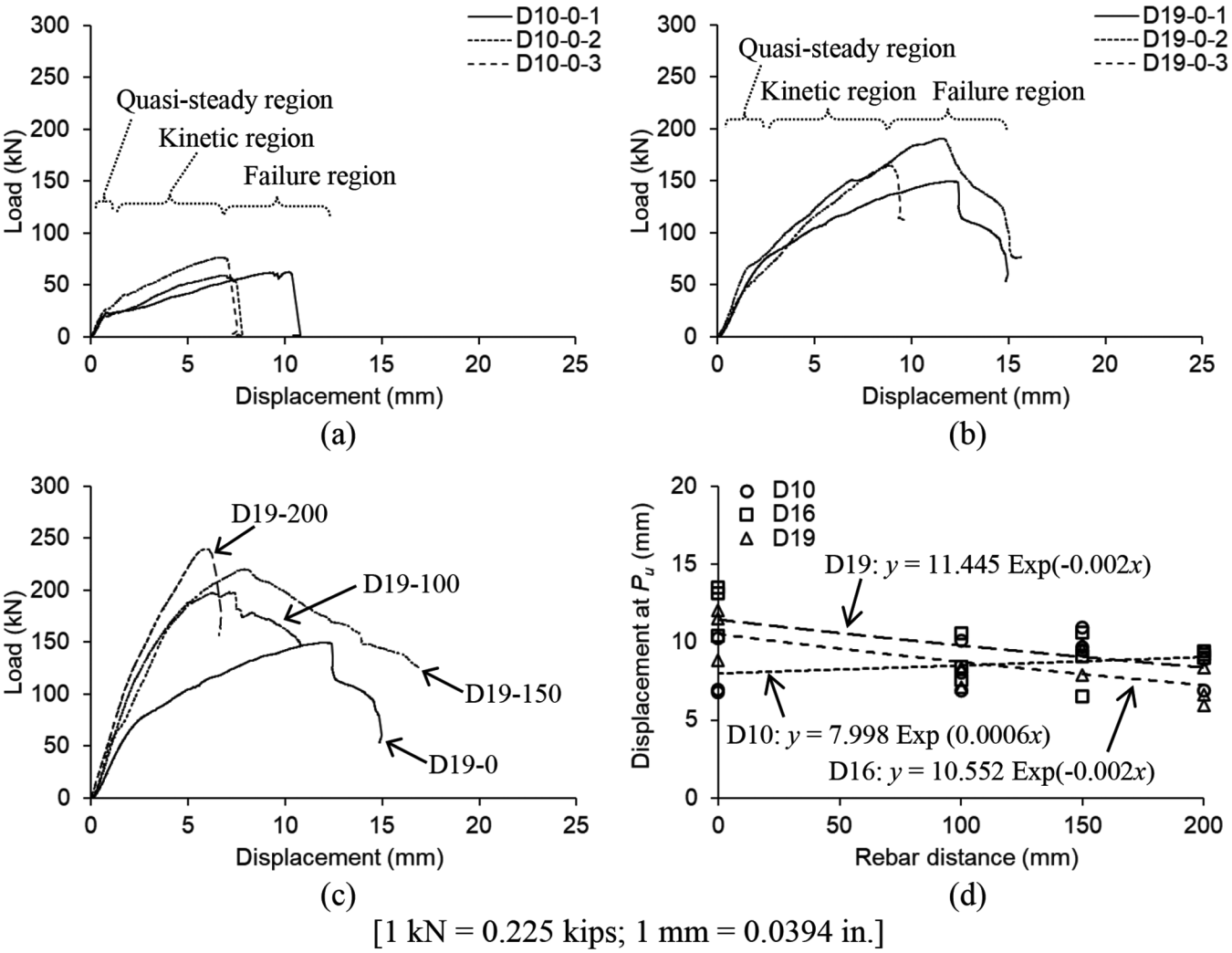

Fig. 4—Interfacial behavior: (a) one D10 reinforcing bar; (b) one D19 reinforcing bar; (c) variable reinforcing bar spacing; and (d) characteristic displacement.

deformability by changing the failure modes of the specimens, as will be described in the next section.

Failure mode

Pictured in Fig. 5 is the failure mode of the interface. Depending upon the size and number of reinforcing bars, two types of failure were recognized: reinforcing bar rupture and concrete splitting. The specimens reinforced with single D10 and D16 reinforcing bars failed by transverse rupture of the reinforcement (D-10-0 and D-16-0, Fig. 5(a)), whereas the specimen with a single D19 reinforcing bar disintegrated by the splitting of the ordinary concrete (D-19-0, Fig. 5(a)) attributable to the amplified cross-sectional resistance of the reinforcing bar. When the strength of the interface was intensified by two D10 reinforcing bars, the locus of failure moved from the reinforcing bar to the concrete as a function of spacing (Fig. 5(b)): the mutual interaction of the reinforcing bars was the main determinant of the raised capacity. For the specimens with two D16 and D19 reinforcing bars, concrete splitting was predominant regardless of the diameter (Fig. 5(c) and (d)). The previously discussed concept with and without the contribution of concrete (interface assemblies versus bare bars) is applicable to these instances; furthermore, the findings corroborate that the size and spacing of the GFRP reinforcing bars played pivotal roles in interfacial failure.

Failure characterization

Macroscopic aspect—Figure 6 renders the sequential snapshots of the interfacial failure, obtained through digital image correlation (DIC) techniques. The color scales belonging to the images merely impart geometric elevations and do not hold any technical meaning. The specimen with a single D10 reinforcing bar revealed apparent interfacial deformations in conjunction with vertical cracking between the ordinary concrete and UHPC under service loadings (25%P_u and 50%P_u, Fig. 6(a)); afterward, the reinforcing bar ruptured (100%P_u, Fig. 6(a)). While interfacial deformations were also detected in the specimen consisting of two D19 reinforcing bars at 25%P_u (Fig. 6(b)), the extent of damage became significant with concrete spalling at 50%P_u and 100%P_u. Clarification appears necessary to avoid confusion about the applied load levels: even if the identical fractional percentage was used for descriptive purposes, the damage to D19-100 at 50%P_u does not necessarily indicate the same level of deterioration as that in D10-0, considering

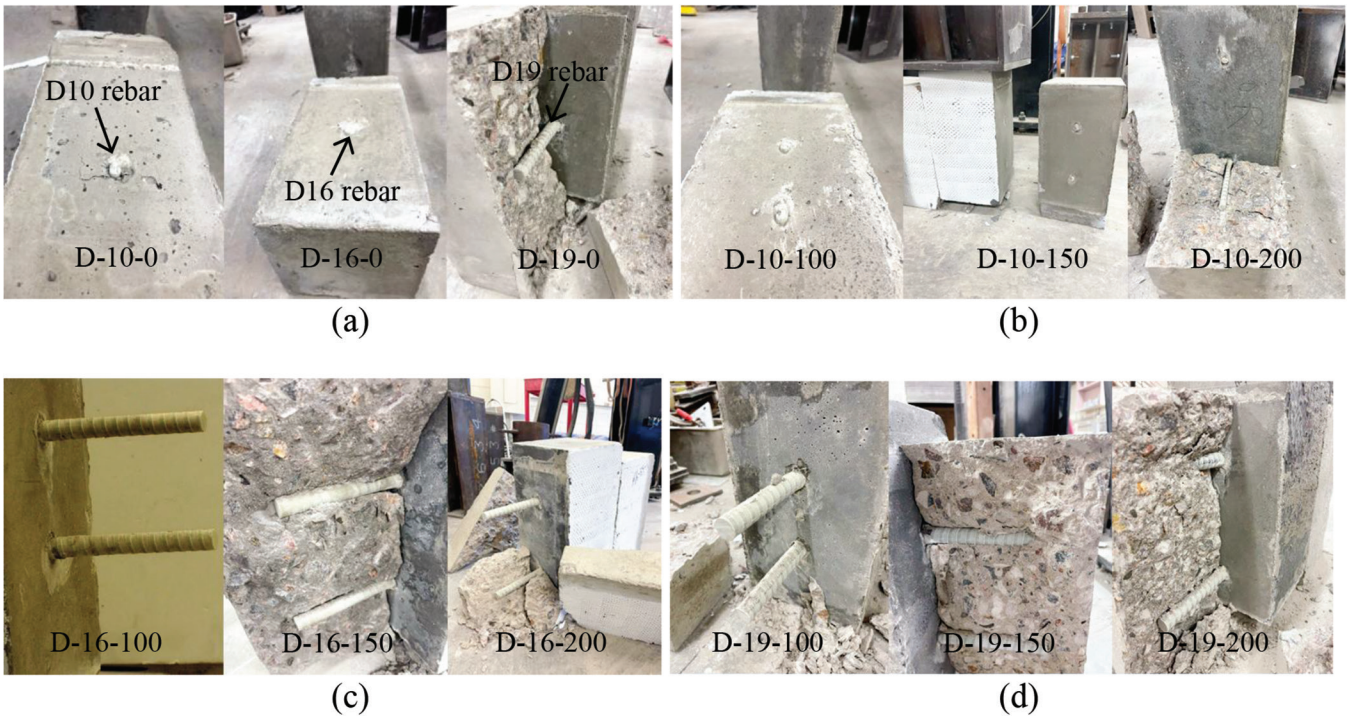

Fig. 5—Failure mode: (a) one reinforcing bar; (b) two D10 reinforcing bars at variable spacing; (c) two D16 reinforcing bars at variable spacing; and (d) two D19 reinforcing bars at variable spacing.

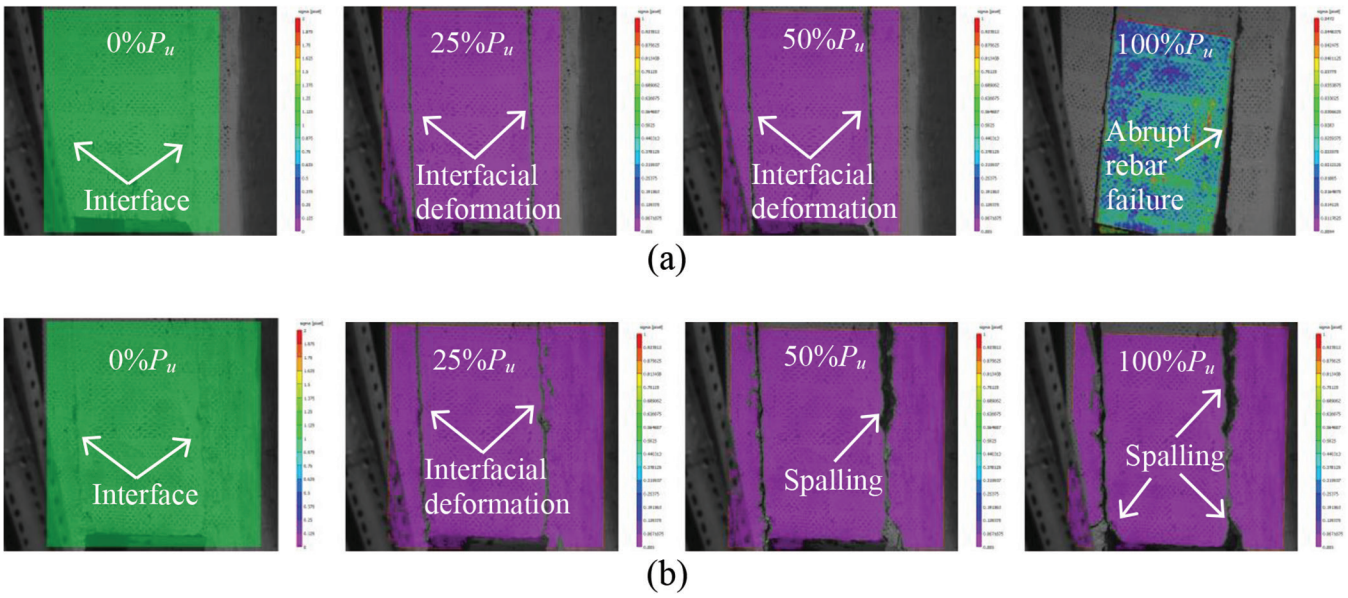

Fig. 6—Macroscopic cracking: (a) D10-0; and (b) D19-100.

their differing ultimate loads (100% P_u = 66.1 kN [14.9 kip] for D10-0 and 213.8 kN [48.1 kip] for D19-100, on average [Table 1]).

Microscopic aspect—As portrayed in Fig. 7, surface scanning was conducted with an optical digital microscope. The fractography of the reinforcing bar demonstrates that transverse fracturing was the primary cause of failure (Fig. 7(a)), substantiated by the existence of bristled fibers randomly dispersed in the radial direction alongside the squashed middle portion. The ordinary concrete plane of D16-0 showed a disturbed region beneath the reinforcing bar (Fig. 7(b)), signifying that the shear stress applied to the reinforcing bar was partially transferred to the concrete and prompted local spalling and microcracking (Fig. 7(b), inset). Likewise, microcracks were discernible where the reinforcing bar intersected the concrete owing to the development of contact stresses (Fig. 7(c)). Although the sturdy adherence of UHPC tore off the near-surface layer of the ordinary concrete (Fig. 7(d)), micro air voids were discovered at the interface (Fig. 7(d), inset), ascribed to the dense formulation of fine particles that inhibit the escape of entrapped air,[26] and these discontinuities could initiate minuscule damage that may progress to a larger scale.

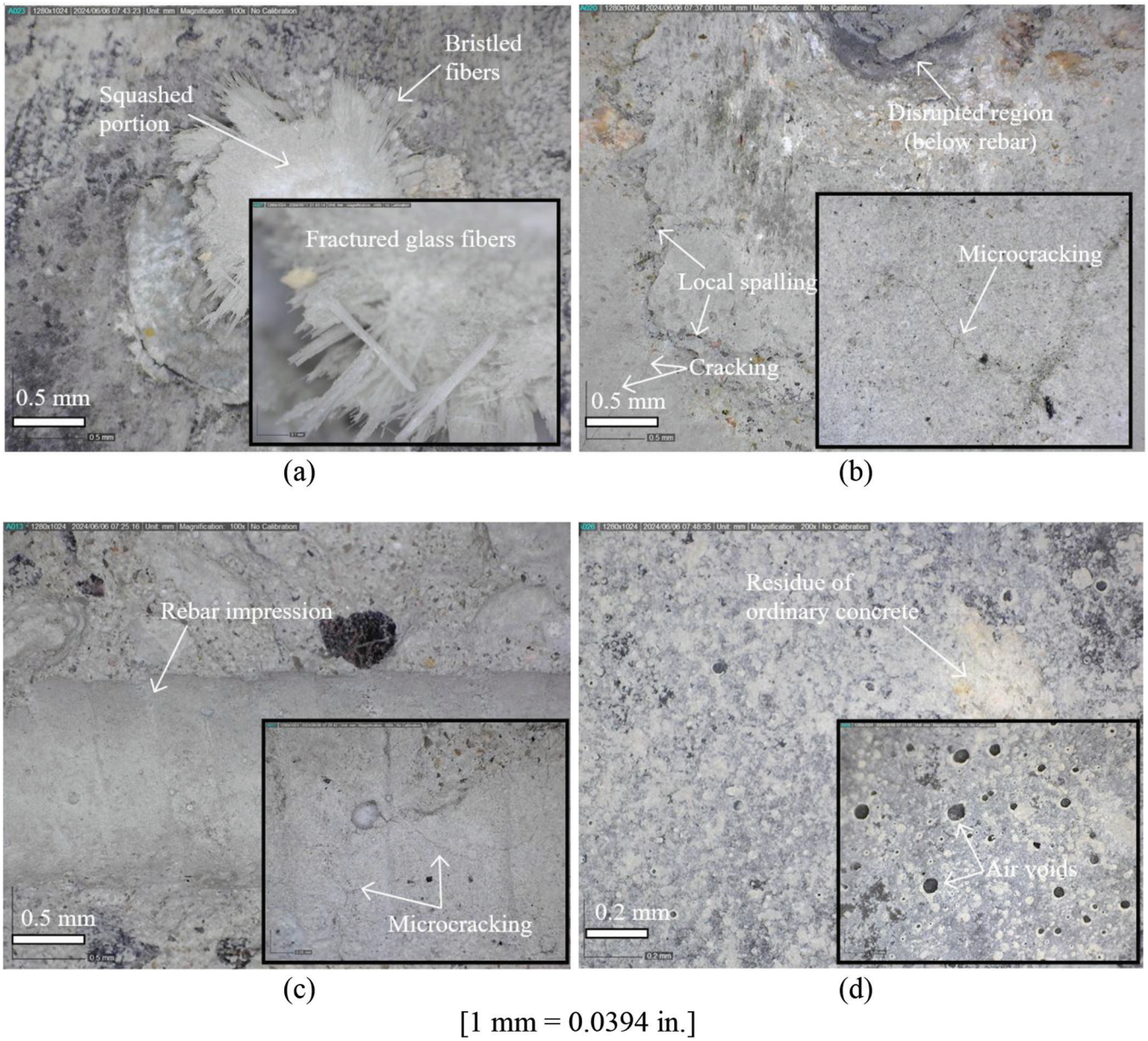

Fig. 7—Microscopic failure characterization (80 to 600× magnification): (a) fractured D16 GFRP reinforcing bar; (b) failed surface of ordinary concrete (D16-0); (c) reinforcing bar impression on ordinary concrete (D19-200); and (d) failed surface of UHPC (D19-200).

MODELING

Analytical modeling is performed to predict the capacity of an interface between ordinary concrete and UHPC linked by GFRP reinforcing bars. Aligning with experimental observations, two failure modes are considered: reinforcing bar rupture and concrete splitting.

Case I: rupture of GFRP

Analytical expression—In compliance with the shear-friction expression of ACI 318,[23] Eq. (2) is proposed

$$V_{RR} = A_{vf}\tau_{fu}\mu = k_1\mu \tag{2}$$

where V_{RR} is the capacity of the interface between the ordinary concrete and UHPC connected by GFRP reinforcing bars; A_{vf} is the total cross-sectional area of the reinforcing bars providing dowel action on each side of the test specimen; τ_{fu} is the shear capacity of the GFRP reinforcing bars (perpendicular to the fiber direction); μ is the effective friction coefficient encompassing the chemical adhesion of the concrete substrates and the dowel resistance of the reinforcing bars; and k_1 is the characteristic resistance. Because of insufficient research, ACI CODE-440.11-22[24] acknowledges that interfacial behavior associated with shear friction is outside its scope.

Calibration and prediction—Figure 8(a) provides the relationship between the characteristic resistance and interfacial capacities of the specimens that failed by transverse rupture of GFRP. Subsequently, the effective friction coefficient (μ) was solved using the generalized reduced gradient (GRG) optimization method[27] and Eq. (3) from Fig. 2(d), resulting in Eq. (4) (Fig. 8(b))

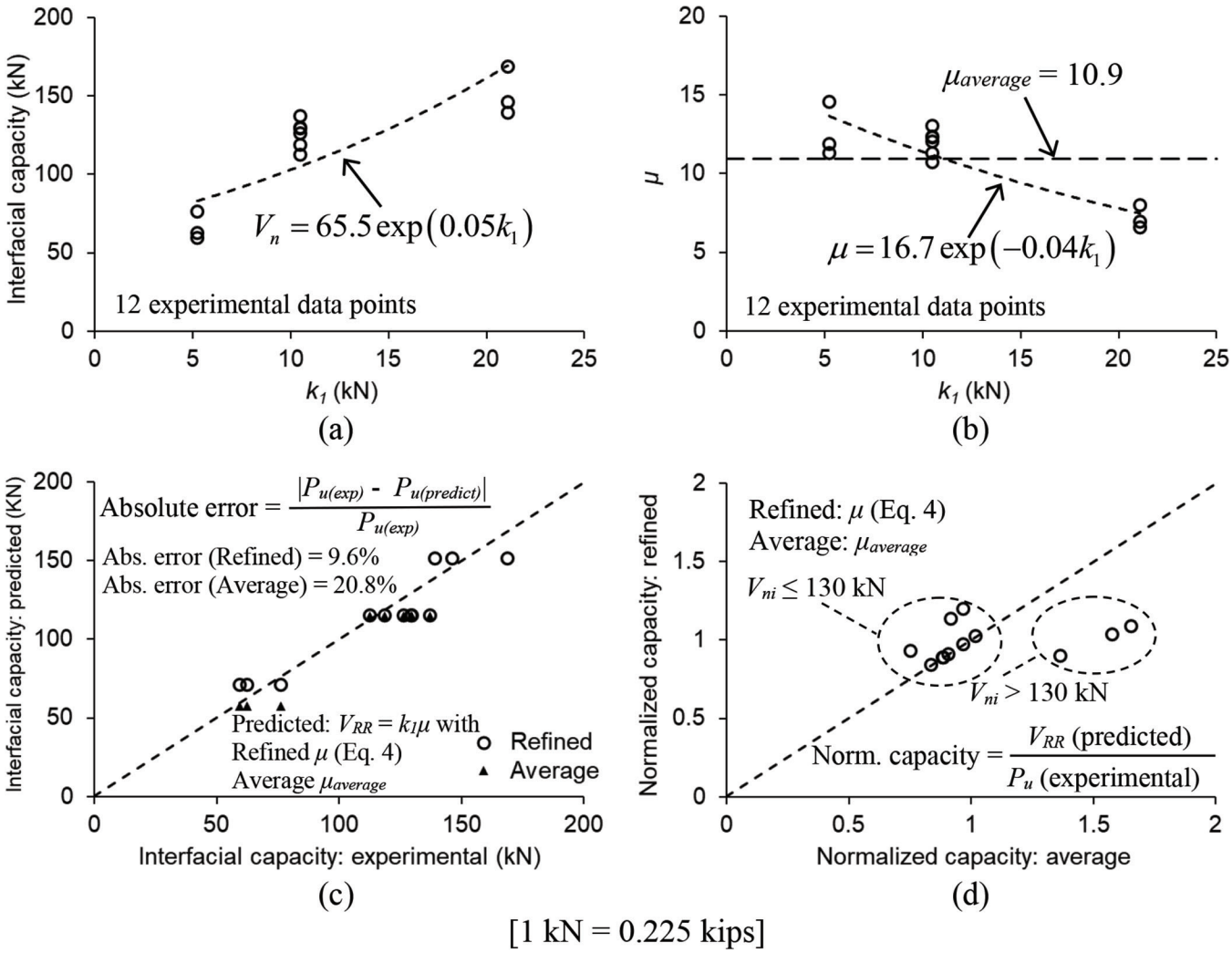

Fig. 8—Analytical modeling for Case I-rupture of GFRP: (a) characteristic resistance (k_1); (b) effective friction coefficient (μ); (c) experimental versus predicted interfacial capacities; and (d) refined versus average effective friction coefficients.

$$\tau_{uf} = 15.8\exp(0.075d_b) \quad (3)$$

$$\mu = 16.7\exp(-0.04k_1) \quad (4)$$

The predicted capacities against their experimental counterparts are plotted in Fig. 8(c). Whereas the refined friction coefficient (Eq. (4)) generated better predictions than the average one ($\mu_{average}$ = 10.9 kN [2.45 kip] in Fig. 8(b)) with absolute average errors of 9.6% and 20.8%, respectively, the approximate coefficient ($\mu_{average}$) was still applicable especially below V_{RR} = 130 kN (29.2 kip) as grouped in Fig. 8(d).

Case II: splitting of concrete

Analytical expression—Equation (5) is derived from modifications to the interfacial capacity model specified in the *fib* Model Code (V_F in Eq. (6))[28]

$$V_{SC} = k_2 A_f (f_c')^{0.5} (f_{c\text{-}UHPC}')^{\alpha} (f_{fu})^{\beta} (s)^{\gamma} \quad (5)$$

$$V_F = k_2 A_s (f_c')^{0.5} (f_{fy})^{0.5} \quad (6)$$

where V_{SC} is the splitting resistance of the concrete subjected to dowel action; k_2 is the bar shape factor (k_2 = 1.6 for circular cross sections[28]); A_f is the cross-sectional area of the reinforcing bars across the interface (A_f means the product of the cross-sectional area of a single reinforcing bar and the total number of reinforcing bars within the length of the considered interface zone); A_s is the cross-sectional area of the dowel bar; f_{fy} is the yield strength of the steel bar (f_{fy} = 414 MPa [60 ksi]); s is the reinforcing bar spacing in mm (the spacing term becomes unity if one reinforcing bar is used: $(s)^{\gamma} = 1$); and α, β, and γ are calibration coefficients.

Calibration and prediction—The calibration coefficients were simultaneously solved using the GRG optimization technique. Two α and β values were separately calibrated for the conditions of a single reinforcing bar and multiple reinforcing bars (α = 0.40 and 0.33 and β = 0.33 and 0.15, respectively, Fig. 9(a) and (b)). Because the $(s)^{\gamma}$ term equals 1 in Eq. (5) for a single reinforcing bar, the identified γ coefficient of 0.25 is applicable to scenarios involving multiple reinforcing bars (Fig. 9(c)). The predicted versus experimental capacities showed an absolute average error of 17.8% (Fig. 9(d)), which is typical in the subject discipline.[15,22] The new expression (Eq. (5)) outperformed the existing one (Eq. (6)), which was developed for steel-concrete assemblies, with an absolute average error of 43.2% (Fig. 9(e)).

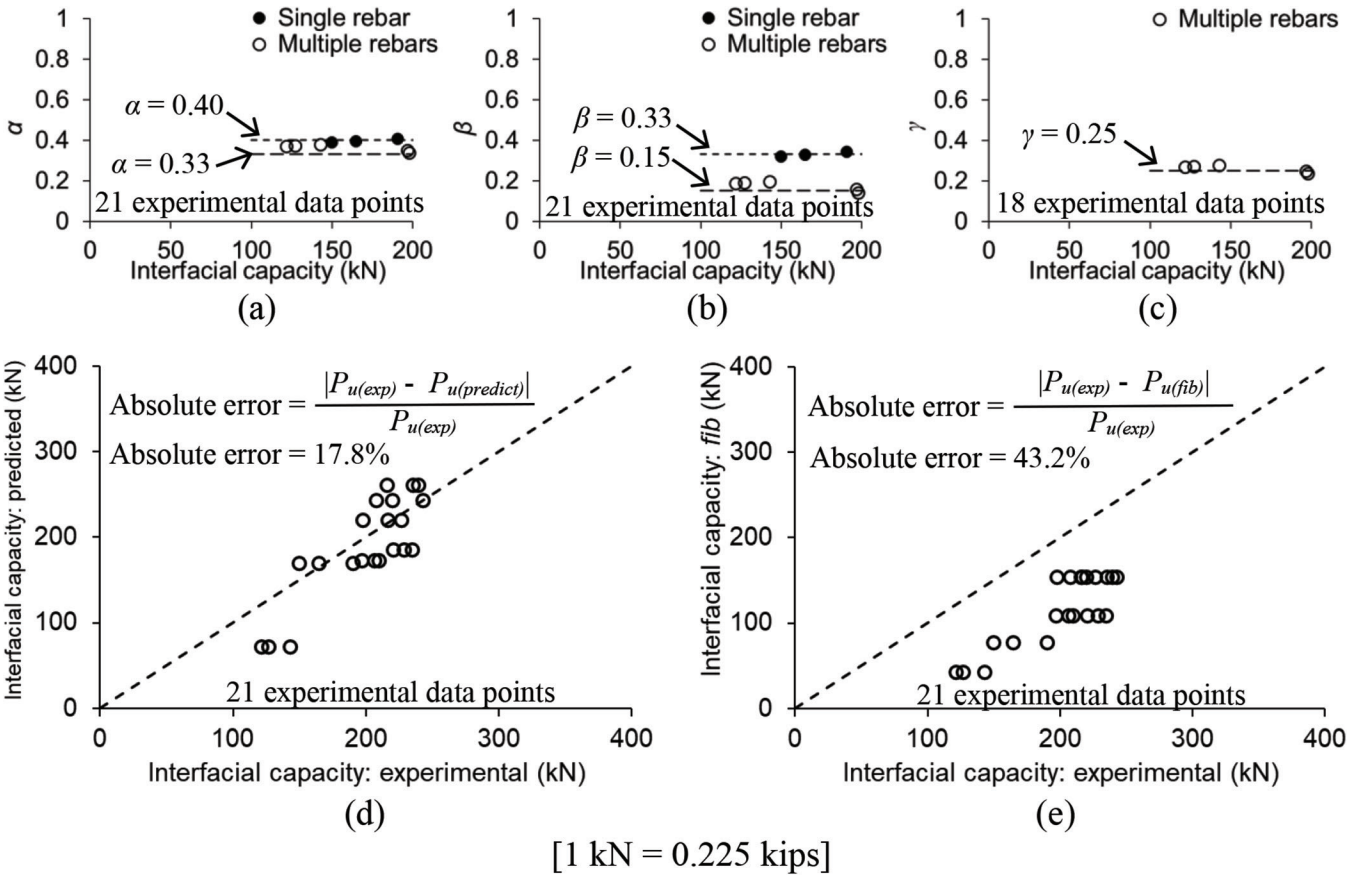

Fig. 9—Analytical modeling for Case II-splitting of concrete: (a) calibration of β *coefficient; (b) calibration of* γ *coefficient; (c) experimental versus predicted capacities; and (d) experimental versus* fib *capacities.*

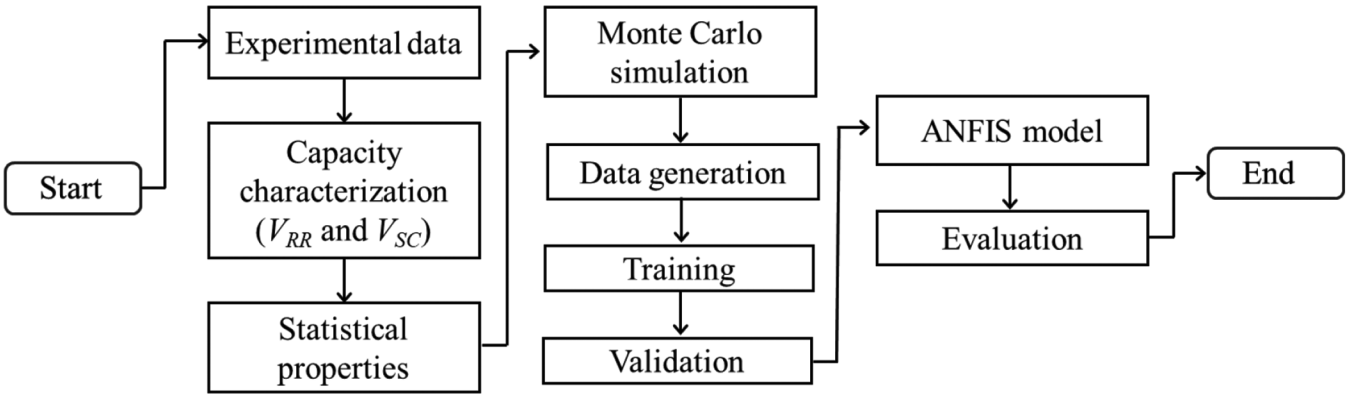

Fig. 10—Flowchart of modeling.

PRACTICAL ASPECTS

To address the limitations of experimental findings induced by a restricted number of specimens, computer simulations are carried out using a machine learning algorithm called the Adaptive Neuro-Fuzzy Inference System (ANFIS) coupled with the Monte Carlo method, which can accommodate potential uncertainties in material and geometric properties, as illustrated in Fig. 10. Solved data are used to propose practice guidelines.

Machine learning

Monte Carlo simulation—Combining the nominal mean values of the experimental program with the statistical properties enumerated in Table 2, random data samples were generated to predict the reinforcing bar rupture (V_{RR}, Eq. (2)) and concrete splitting (V_{SC}, Eq. (5)) terms. The number of samples shifted in relation to the epochs of the supervised machine learning algorithm explicated as follows. The computationally acquired data were then divided into 70% for training and 30% for validating the algorithm.[33]

Adaptive Neuro-Fuzzy Inference System—This hybrid machine learning algorithm is built upon a combination of fuzzy theory and neural networks. Essential concepts are furnished here, while their principles and processing procedures can be referenced elsewhere.[34,35] The algorithm was structured with five layers (Fig. 11(a)).[36] The first layer

Table 2—Statistical properties of simulated parameters

Parameter	Range	COV	Distribution	Reference
Concrete strength	20 MPa $\le f_c' \le$ 50 MPa	0.125	Normal	Nowak and Collins[29]
UHPC strength	120 MPa $\le f_{c\text{-}UHPC}' \le$ 150 MPa	0.06	Lognormal	Abbas[30]
Reinforcing bar diameter	D10 $\le d_b \le$ D19	0.002	Normal	He and Tian[31]
GFRP strength	800 MPa $\le f_{fu} \le$ 1200 MPa	0.05	Normal	He and Tian[31]
Spacing	50 mm $\le s \le$ 200 mm	0.05	Normal	Okeil et al.[32]

Note: 1 MPa = 145 psi; 1 mm = 0.0394 in.

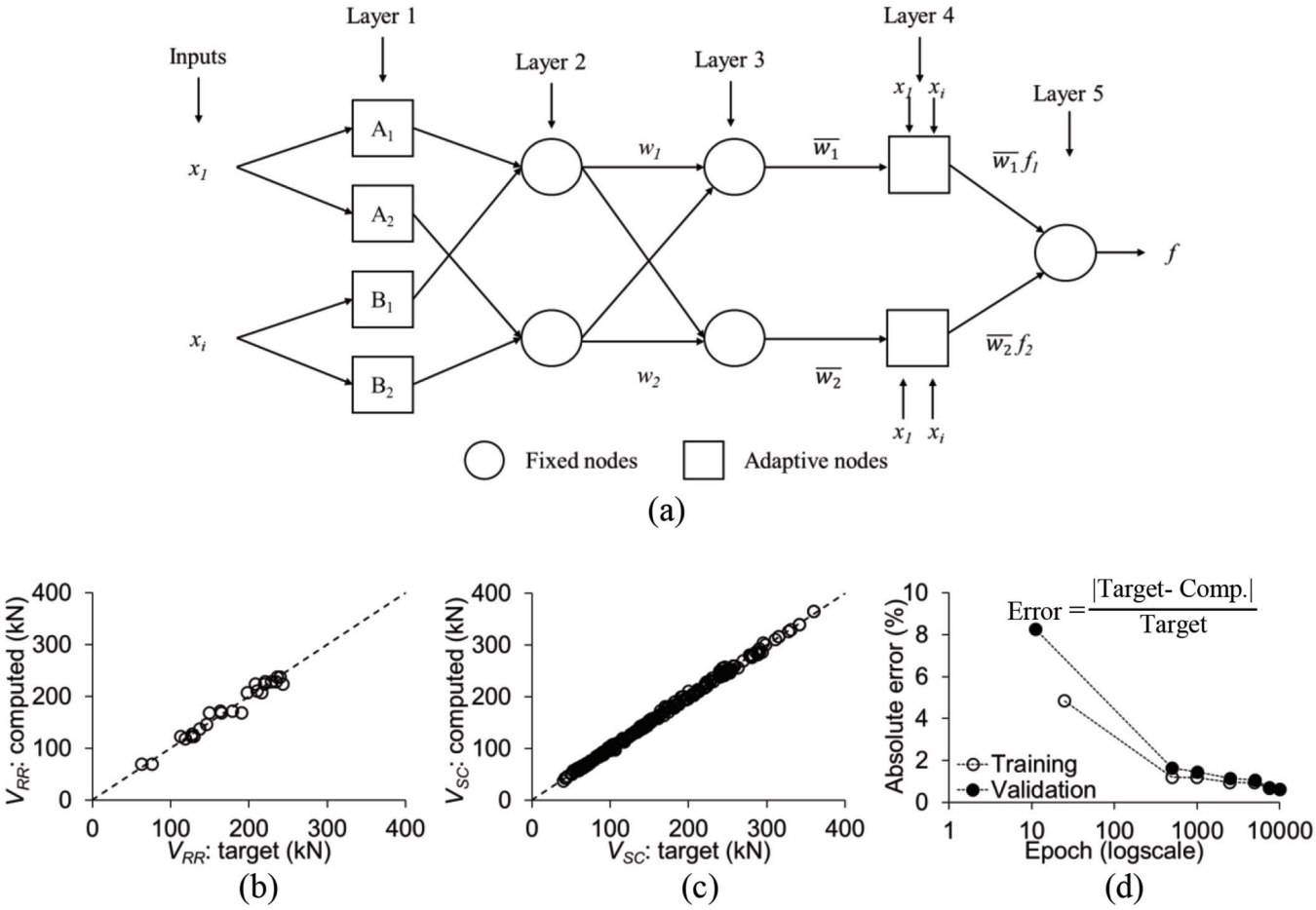

Fig. 11—Machine learning: (a) overview (reproduced from Yosri et al.[36]); (b) training of V_{RR} *at epoch 25; (c) validation of* V_{SC} *at epoch 500; and (d) absolute error of* V_{SC}.

handled input variables constituting Eq. (2) and (5) for fuzzification

$$O_i^1 = \Psi(x_i) \tag{7}$$

where O_i^1 is the output of Layer One for input parameter x_i; and ψ is the membership function with fuzzy c-mean clustering[37]

$$\psi_{ij}(x_i) = \frac{1}{\left(\sum_{k=1}^{c}\left(\frac{\|x_i - c_j\|}{\|x_i - c_k\|}\right)^{\frac{2}{m-1}}\right)} \tag{8}$$

where ψ_{ij} is the membership function of object x_i belonging to cluster i; c is the total number of clusters (15 clusters were chosen after multiple trials); $\|x_i - c_j\|$ is the Euclidean distance between x_i and cluster center c_j; and m is the fuzzification exponent (m = 2).[38] In the second layer, the fixed nodes dealt with outcomes from the preceding layer and created outputs (O_i^2)

$$O_i^2 = w_i = \psi_{A_i}(x_i) \times \psi_{B_i}(x_i) \tag{9}$$

where w_i is the output of the i-th node. The third layer normalized the nodal outputs from the previous layer

$$O_i^3 = \overline{w}_i = \frac{w_i}{\sum w_i} \tag{10}$$

The fourth layer involved the product of the normalized outputs and the characteristic linear function (f_i)

$$O_i^4 = \bar{w}_i f_i = \bar{w}_i \times (p_i x_i + q_i x_i + r_i) \quad (11)$$

where p_i, q_i, and r_i are the consequent parameters concerning input parameters x_i.[39] Next, the last layer computed the overall outputs

$$O_i^5 = \sum \bar{w}_i f_i = \frac{\sum w_i f_i}{\sum w_i} \quad (12)$$

The performance of the V_{RR} and V_{SC} capacities from the model was checked using root mean square errors (RMSE) and iterated until the error was less than 1%. The training and validation outcomes at epochs 25 and 500 are exemplified in Fig. 11(b) and (c), respectively, and the model at epoch 10,000 with an absolute error of less than 0.63% (Fig. 11(d)) was executed for numerical investigations.

Implementation

Figure 12(a) instantiates a failure envelope, proposed to represent the upper bounds of the V_{RR} and V_{SC} terms (Eq. (2) and (5), respectively), through the interfacial capacities of the two-bar specimens at a spacing of 150 mm (6 in.). With an increase in the reinforcing bar diameter, the concrete splitting term (V_{SC}) rose in a linear manner; contrarily, the reinforcing bar rupture term (V_{RR}) reflected slight variations up to a diameter of d_b = 16 mm (0.63 in.), followed by a drop at d_b = 19 mm (0.75 in.). By the same token, failure envelopes are constructed for other parameters such as dowel spacing, albeit omitted due to space limitations. Compared in Fig. 12(b) are the simulated and experimental capacities of the specimens, illustrating reasonable agreement with absolute errors of less than 11.1%. Figures 12(c) and (d) graph the predicted failure envelopes of the single- and multiple-reinforcing bar specimens, respectively. Unlike the specimens with the single reinforcing bars showing a reduced slope beyond d_b = 16 mm (0.63 in.), those with the multiple reinforcing bars exhibited increased slopes driven by the dominance of augmented concrete splitting (V_{SC}) in the interfacial failure. To evaluate the applicability of the proposed equations, random samples were taken from the practical ranges of the constituent variables listed in Table 2. The interfacial capacities from the laboratory-based and random sample-based simulations matched closely, supporting that the calibrated coefficients in Eq. (5) can adequately cover the parameter ranges given in Table 2.

Sensitivity analysis

The results of parametric studies are provided in Fig. 13. Unless otherwise stated, the default properties of the experimental specimens were employed for consistency. The reinforcing bar rupture capacity (V_{RR}) of the single-reinforcing bar interface remained unchanged with the concrete strength varying from f_c' = 20 to 50 MPa (2900 to 7250 psi); however, its concrete-splitting capacity (V_{SC}) steadily went up (Fig. 13(a)). A similar propensity was noted for the multiple-reinforcing bar specimens with higher V_{SC} capacities over 227 kN (51 kip), which controlled the failure envelope of the interface (Fig. 13(b)). When the UHPC strength was increased from $f_{c'\text{-}UHPC}$ = 120 to 150 MPa (17.4 to 21.8 ksi), the capacities of the interface were stable (Fig. 13(c) and (d)). In a similar fashion, the influence of GFRP strength across the spectrum of f_{fu} = 800 to 1200 MPa (116 to 174 ksi) was insignificant for the interfacial capacity (Fig. 13(e) and (f)). These observations signify the importance of ordinary concrete's compressive strength for the interface, while practical options for built-up construction can include UHPC and GFRP materials readily available on the market.

SUMMARY AND CONCLUSIONS

This paper discussed interfacial responses between ordinary concrete and ultra-high-performance concrete (UHPC) connected by glass fiber-reinforced polymer (GFRP) reinforcing bars when subjected to in-plane shear. In line with ancillary testing that shed light on the fracture behavior of the reinforcing bars, concrete-reinforcing bar assemblies were loaded to study load-bearing capacities and failure modes. The size, spacing, and number of the reinforcing bars served as experimental parameters. By means of the analytical model formulated with an optimization technique, the failure of the interface was categorized, and the corresponding capacities were calculated. To expand laboratory findings, a machine learning algorithm was implemented, and sensitivity analysis was conducted. Continued endeavors are required to accomplish the sustainability and economic feasibility of innovative approaches based on nonconventional materials,[29,30] ultimately enabling the cost-effective design of structural concrete, and ensuring the long-term integrity of the interface system under assorted environmental conditions. The following conclusions are drawn:

- The shear response of GFRP bare bars was segmented into three parts, reliant upon the transition of load-resisting axes in the embedded fibers and their quantity. The size and spacing of the reinforcement affected the interfacial capacities of the concrete-reinforcing bar assemblies. A shift of the load-transfer path from the reinforcing bar to the concrete was a decisive factor in determining these capacities.
- The load-displacement relationship of the interface was characterized by the quasi-steady, kinetic, and failure regions. Contrary to the specimens with single reinforcing bars displaying low stiffness, those with multiple reinforcing bars showed improvement through more consistent distribution of applied stresses accompanied by shear lag.
- The rupture of the reinforcing bars and the splitting of the concrete were the two principal failure modes at the interface. From a macroscale perspective, interfacial deformations were responsible for crack formation between ordinary concrete and UHPC, which progressed to spalling damage beyond service load levels. Optical microscopy assisted in uncovering the source of the cracks and the fracture process of reinforcing bars under shear loading, including the presence of discrete microvoids that could accelerate damage growth.
- In applying the analytical model, both refined and approximate friction coefficients (μ) were suitable for predicting the capacity related to the rupture of GFRP (V_{RR}), while specific coefficients (α, β, and γ) were

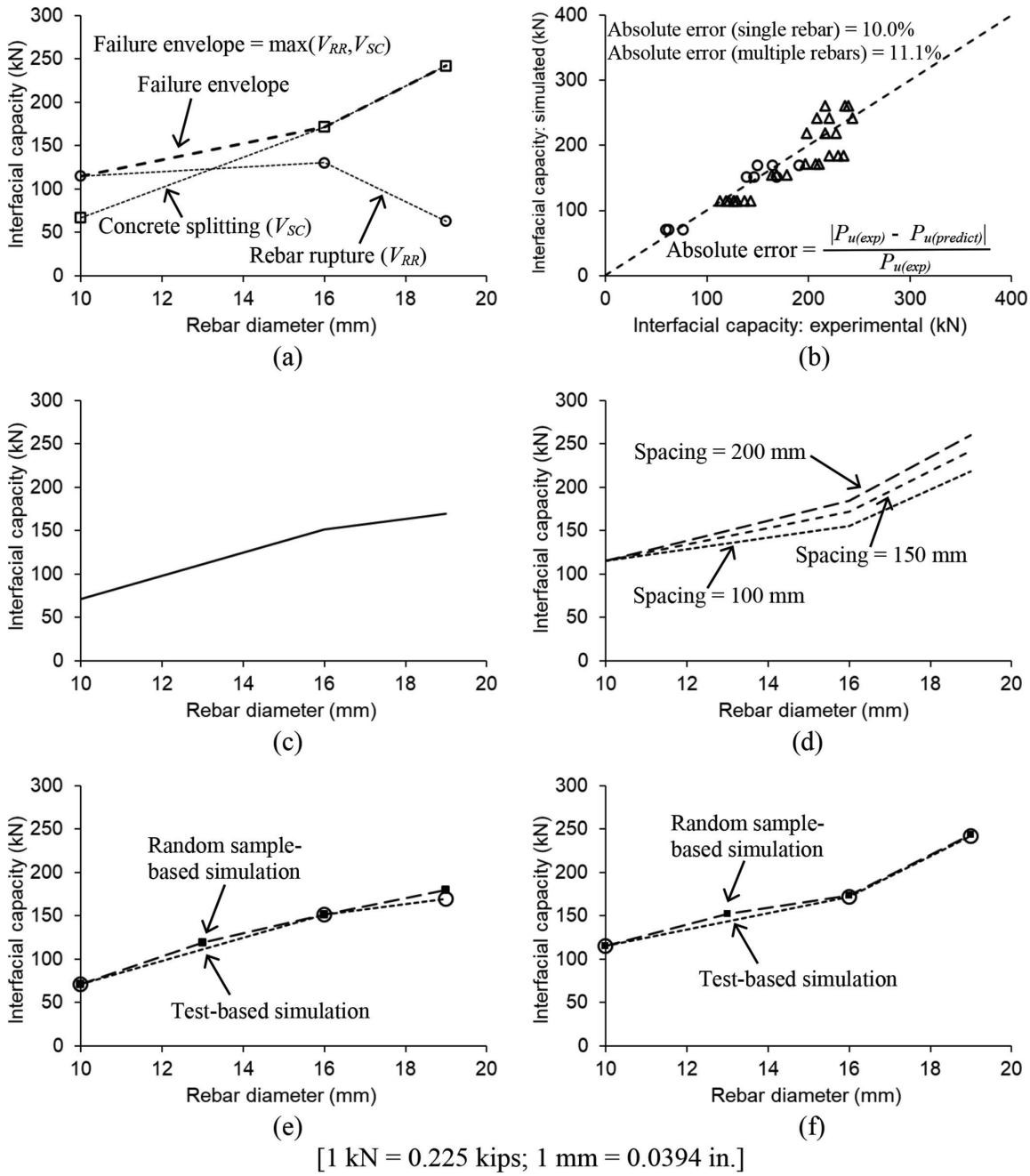

Fig. 12—Simulated interfacial capacity: (a) definition of failure envelope using multiple reinforcing bars with spacing of 150 mm; (b) experimental versus simulated capacities; (c) failure envelope for single-reinforcing bar interface; (d) failure envelope for multiple-reinforcing bar interface; (e) comparison of single-reinforcing bar simulation; and (f) comparison of multiple-reinforcing bar simulation.

necessary for predicting the splitting of the concrete (V_{SC}) with a single reinforcing bar and multiple reinforcing bars.

- Considering the validated machine learning algorithm, a failure envelope was proposed to determine the capacity of the multi-material interface. The established envelope responded sensitively to the strength of ordinary concrete in contrast to the cases of UHPC and GFRP.

AUTHOR BIOS

Yail J. Kim, *FACI, is President of the Bridge Engineering Institute, An International Technical Society, and a Professor in the Department of Civil Engineering at the University of Colorado Denver, Denver, CO. He is past Chair of ACI Committee 345, Concrete Bridge Construction and Preservation, and ACI Subcommittee 440-I, FRP-Prestressed Concrete; and a member of ACI Committees 342, Evaluation of Concrete Bridges and Bridge Elements; 343, Concrete Bridge Design; 377, Performance-Based Structural Integrity & Resilience of Concrete Structures; and 440, Fiber-Reinforced Polymer Reinforcement. He received the ACI Chester Paul Siess Award for Excellence in Structural Research in 2019. His research interests include advanced composite materials for rehabilitation; structural informatics; complex systems; and science-based structural engineering, including statistical, interfacial, and quantum physics.*

Ali Alatify *is an Assistant Professor in the Department of Civil Engineering at Prince Sattam Bin Abdulaziz University, Al-Kharj, Saudi Arabia. He received his BS from Shaqra University, Shaqra, Saudi Arabia, and his MS and PhD from the University of Colorado Denver, respectively. His research interests include composite materials and structural concrete.*

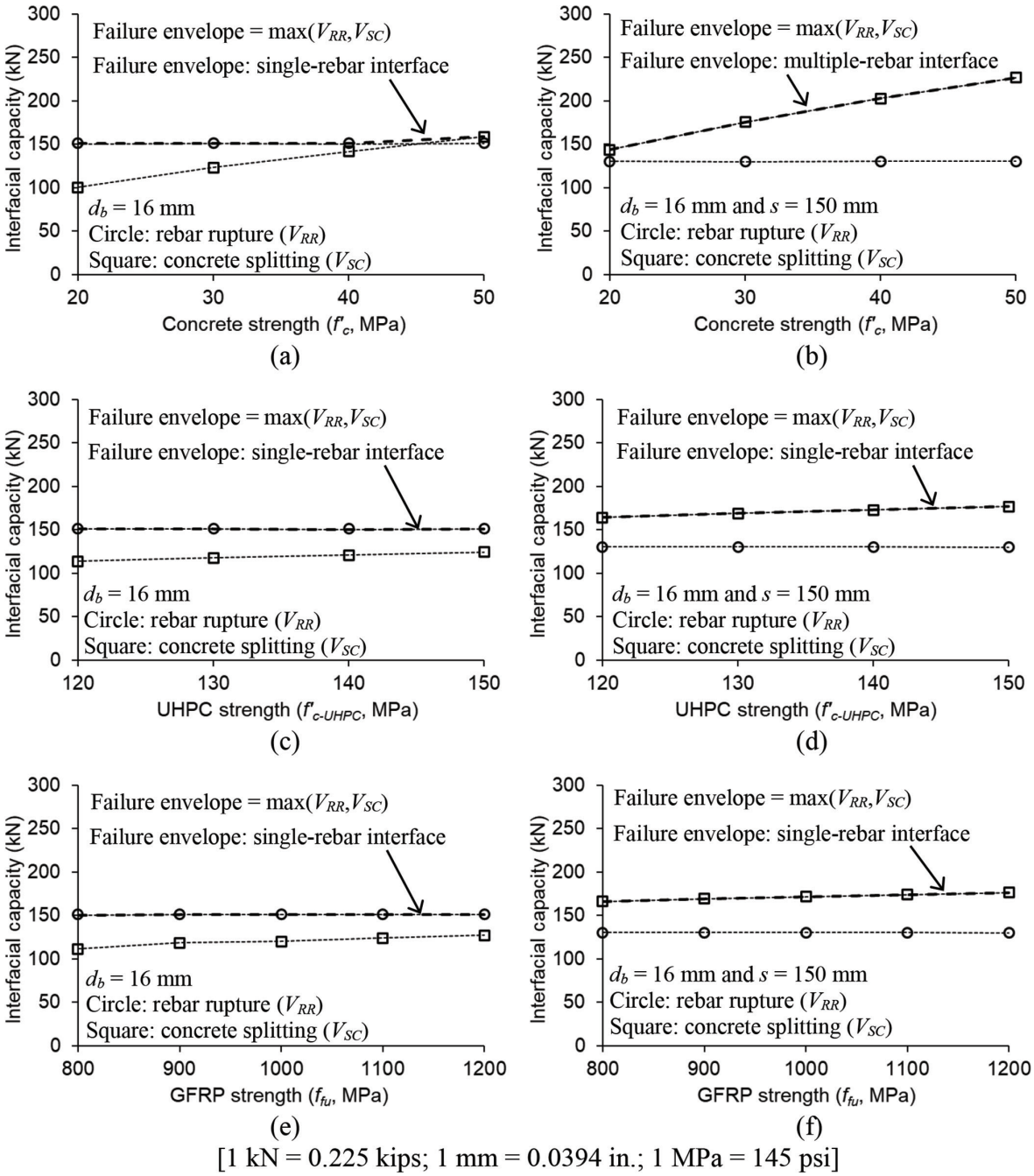

Fig. 13—Parametric study: (a) concrete strength in single-reinforcing bar interface; (b) concrete strength in multiple-reinforcing bar interface; (c) UHPC strength in single-reinforcing bar interface; (d) UHPC strength in multiple-reinforcing bar interface; (e) GFRP strength in single-reinforcing bar interface; and (f) GFRP strength in multiple-reinforcing bar interface.

ACKNOWLEDGMENTS

The authors would like to gratefully acknowledge support from the Government of Saudi Arabia, Prince Sattam Bin Abdulaziz University, the Saudi Arabian Cultural Mission, and the U.S. Department of Transportation through the Center for Transformative Infrastructure Preservation and Sustainability Program. P. Weber at ceEntek and D. Gremel at Owens Corning donated UHPC and GFRP materials, respectively. The technical content presented in this paper is based on the opinion of the authors and does not necessarily represent those of others.

REFERENCES

1. Graybeal, B.; Bruhwiler, E.; Kim, B.-S.; Toutlemonde, F.; Voo, Y. L.; and Zaghi, A., "International Perspective on UHPC in Bridge Engineering," *Journal of Bridge Engineering*, ASCE, V. 25, No. 11, 2020, p. 04020094. doi: 10.1061/(ASCE)BE.1943-5592.0001630

2. AASHTO, "Guide Specifications for Structural Design with Ultra-High-Performance Concrete," American Association of State Highway and Transportation Officials, Washington, DC, 2024.

3. ACI Committee 239, "Ultra-High-Performance Concrete: An Emerging Technology Report (ACI 239-18)," American Concrete Institute, Farmington Hills, MI, 2018, 21 pp.

4. Wu, X.-G., and Han, S.-M., "Interface Shear Connection Analysis of Ultrahigh-Performance Fiber-Reinforced Concrete Composite Girders," *Journal of Bridge Engineering*, ASCE, V. 15, No. 5, 2010, pp. 493-502. doi: 10.1061/(ASCE)BE.1943-5592.0000091

5. Feng, S.; Xiao, H.; Liu, M.; Zhang, F.; and Lu, M., "Shear Behaviour of Interface Between Normal-Strength Concrete and UHPC: Experiment and Predictive Model," *Construction and Building Materials*, V. 342, 2022, p. 127919. doi: 10.1016/j.conbuildmat.2022.127919

6. Abellán-García, J.; Carvajal-Muñoz, J. S.; and Ramírez-Munévar, C., "Application of Ultra-High-Performance Concrete as Bridge

Pavement Overlays: Literature Review and Case Studies," *Construction and Building Materials*, V. 410, 2024, p. 134221. doi: 10.1016/j.conbuildmat.2023.134221

7. Ebrahimpour, A.; Shokrgozar, A.; and Mashal, M., "Field Performance of High-Early-Strength Concrete with Polypropylene Fibers as a Cost-Effective Alternative for Longitudinal Connection Between Bridge Deck Bulb-T Girders," *Journal of Performance of Constructed Facilities*, ASCE, V. 37, No. 3, 2023, p. 04023015. doi: 10.1061/JPCFEV.CFENG-4331

8. Zhou, M.; Lu, W.; Song, J.; and Lee, G. C., "Application of Ultra-High-Performance Concrete in Bridge Engineering," *Construction and Building Materials*, V. 186, 2018, pp. 1256-1267. doi: 10.1016/j.conbuildmat.2018.08.036

9. Royce, M., "Utilization of Ultra-High-Performance Concrete (UHPC) in New York," First International Interactive Symposium on UHPC, Des Moines, IA, 2016, 9 pp.

10. Sritharan, S.; Doiron, G.; Bierwagen, D.; Keierleber, B.; and Abu-Hawash, A., "First Application of UHPC Bridge Deck Overlay in North America," *Transportation Research Record: Journal of the Transportation Research Board*, V. 2672, No. 26, 2018, pp. 40-47. doi: 10.1177/0361198118755665

11. Neirinck, T.; Semendary, A. A.; Murison, E.; and Svecova, D., "Performance of UHPC Shear Keys in Box Girder Bridges-Field and Finite Element Study," *Engineering Structures*, V. 296, 2023, p. 116896. doi: 10.1016/j.engstruct.2023.116896

12. Tian, J.; Jiang, X.; Yang, X.; Ma, M.; and Li, L., "Bonding Performance of the Grooved Interface Between Ultrahigh Performance Concrete and Normal Concrete," *Construction and Building Materials*, V. 336, 2022, p. 127525. doi: 10.1016/j.conbuildmat.2022.127525

13. Feng, S.; Xiao, H.; Liu, M.; Zhang, F.; and Lu, M., "Shear Behaviour of Interface Between Normal-Strength Concrete and UHPC: Experiment and Predictive Model," *Construction and Building Materials*, V. 342, 2022, p. 127919. doi: 10.1016/j.conbuildmat.2022.127919

14. Zhao, L., and Luo, Q., "Evaluating Bonding Strength in UHPC-NC Composite: A Comprehensive Review of Direct and Indirect Characterization Methods," *Construction and Building Materials*, V. 443, 2024, p. 137701. doi: 10.1016/j.conbuildmat.2024.137701

15. Connor, A. B., and Kim, Y. H., "Shear-Transfer Mechanisms for Glass Fiber-Reinforced Polymer Reinforcing Bars," *ACI Structural Journal*, V. 113, No. 6, Nov.-Dec. 2016, pp. 1369-1380.

16. Kottari, A.; Mavros, M.; Murcia-Delso, J.; and Shing, P. B., "Interface Model for Bond-Slip and Dowel-Action Behavior," *ACI Structural Journal*, V. 114, No. 4, July-Aug. 2017, pp. 1043-1053.

17. Bai, M.; Ding, T.; Zhao, Y.; and Zhao, Y., "Shear Performance of New-to-Old Concrete Interface Based on Various Surface Preparation Techniques and Roughness," *Case Studies in Construction Materials*, V. 21, 2024, p. e03549. doi: 10.1016/j.cscm.2024.e03549

18. Guan, D.; Liu, J.; Jiang, C.; Chen, Z.; and Guo, Z., "Shear Behaviour of the UHPC-NSC Interface with Castellated Keys: Effects of Castellated Key Dimension and Dowel Reinforcing Bar," *Structures*, V. 31, 2021, pp. 172-181. doi: 10.1016/j.istruc.2021.01.088

19. Valikhani, A.; Jahromi, A. J.; Mantawy, I. M.; and Azizinamini, A., "Effect of Mechanical Connectors on Interface Shear Strength Between Concrete Substrates and UHPC: Experimental and Numerical Studies and Proposed Design Equation," *Construction and Building Materials*, V. 267, 2021, p. 120587.

20. Zhang, Y.; Zhang, C.; Zhu, Y.; Cao, J.; and Shao, X., "An Experimental Study: Various Influence Factors Affecting Interfacial Shear Performance of UHPC-NSC," *Construction and Building Materials*, V. 236, 2020, p. 117480. doi: 10.1016/j.conbuildmat.2019.117480

21. Woltman, G.; Tomlinson, D.; and Fam, A., "Investigation of Various GFRP Shear Connectors for Insulated Precast Concrete Sandwich Wall Panels," *Journal of Composites for Construction*, ASCE, V. 17, No. 5, 2013, pp. 711-721. doi: 10.1061/(ASCE)CC.1943-5614.0000373

22. Xue, W.; Yan, D.; and Zhang, S., "Push-Out Behavior of GFRP Bolts Shear Connectors in FRP-Concrete Hybrid Beam," *Engineering Structures*, V. 294, 2023, p. 116758. doi: 10.1016/j.engstruct.2023.116758

23. ACI Committee 318, "Building Code Requirements for Structural Concrete (ACI 318-19) and Commentary (ACI 318R-19) (Reapproved 2022)," American Concrete Institute, Farmington Hills, MI, 2019, 624 pp.

24. ACI Committee 440, "Building Code Requirements for Structural Concrete Reinforced with Glass Fiber-Reinforced Polymer (GFRP) Bars—Code and Commentary (ACI CODE-440.11-22)," American Concrete Institute, Farmington Hills, MI, 2023, 266 pp.

25. ACI Committee 440, "Guide Test Methods for Fiber-Reinforced Polymers (FRPs) for Reinforcing or Strengthening Concrete Structures (ACI 440.3R-04)," American Concrete Institute, Farmington Hill, MI, 2004, 23 pp.

26. Wang, R.; Gao, X.; Zhang, J.; and Han, G., "Spatial Distribution of Steel Fibers and Air Bubbles in UHPC Cylinder Determined by X-Ray CT Method," *Construction and Building Materials*, V. 160, 2018, pp. 39-47. doi: 10.1016/j.conbuildmat.2017.11.030

27. Andrei, N., *Modern Numerical Nonlinear Optimization*, Springer Nature, Cham, Switzerland, 2022.

28. *fib*, "fib Model Code for Concrete Structures 2010," International Federation for Structural Concrete, Lausanne, Switzerland, 434 pp.

29. Nowak, A. S., and Collins, K. R., *Reliability of Structures*, second edition, CRC Press, Boca Raton, FL, 2013.

30. Abbas, Y. M., "Shear Behavior of Ultra-High-Performance Reinforced Concrete Beams–Finite Element and Uncertainty Quantification Study," *Structures*, V. 47, 2023, pp. 2365-2380. doi: 10.1016/j.istruc.2022.12.060

31. He, Z., and Tian, G.-W., "Probabilistic Evaluation of the Design Development Length of a GFRP Rod Pull-Out from Concrete," *Engineering Structures*, V. 33, No. 10, 2011, pp. 2943-2952. doi: 10.1016/j.engstruct.2011.06.019

32. Okeil, A.; El-Tawil, S.; and Shahawy, M., "Flexural Reliability of Reinforced Concrete Bridge Girders Strengthened with Carbon Fiber-Reinforced Polymer Laminates," *Journal of Bridge Engineering*, ASCE, V. 7, No. 5, 2002, pp. 290-299. doi: 10.1061/(ASCE)1084-0702(2002)7:5(290)

33. Naser, M. Z., *Machine Learning for Civil and Environmental Engineers: A Practical Approach to Data-Driven Analysis, Explainability, and Causality*, John Wiley & Sons, Inc., Hoboken, NJ, 2023.

34. Singh, H., and Lone, Y. A., *Deep Neuro-Fuzzy Systems with Python: With Case Studies and Applications from the Industry*, Apress, New York, NY, 2020.

35. Dutta, P.; Pal, S.; Kumar, A.; and Cengiz, K., *Artificial Intelligence for Cognitive Modeling: Theory and Practice*, CRC Press, Boca Raton, FL, 2023.

36. Yosri, A.; Farouk, A.; Haruna, S. I.; Deifalla, A. F.; and Shaaban, W. M., "Sensitivity and Robustness Analysis of Adaptive Neuro-Fuzzy Inference System (ANFIS) for Shear Strength Prediction of Stud Connectors in Concrete," *Case Studies in Construction Materials*, V. 18, 2023, p. e02096. doi: 10.1016/j.cscm.2023.e02096

37. Hussain, W.; Merigo, J.; Raza, M.; and Gao, H., "A New QoS Prediction Model Using Hybrid IOWA-ANFIS with Fuzzy C-Means, Subtractive Clustering and Grid Partitioning," *Information Sciences*, V. 584, 2022, pp. 280-300. doi: 10.1016/j.ins.2021.10.054

38. Abdulshahed, A. M.; Longstaff, A. P.; Fletcher, S.; and Myers, A., "Thermal Error Modelling of Machine Tools Based on ANFIS with Fuzzy C-Means Clustering Using a Thermal Imaging Camera," *Applied Mathematical Modelling*, V. 39, No. 7, 2015, pp. 1837-1852. doi: 10.1016/j.apm.2014.10.016

39. Kumar, A.; Arora, H. C.; Kumar, K.; and Garg, H., "Performance Prognosis of FRCM-to-Concrete Bond Strength Using ANFIS-Based Fuzzy Algorithm," *Expert Systems with Applications*, V. 216, 2023, p. 119497. doi: 10.1016/j.eswa.2022.119497

aci® in Your Classroom

Integrate aci® into your classroom!

To support future leaders, ACI has launched several initiatives to engage students in the Institute's activities and programs – select programs that may be of interest to Educators are:

- **Free student membership –** encourage students to sign up
- **Special student discounts on *ACI 318 Building Code Requirements for Structural Concrete*, *ACI 530 Building Code Requirements and Specification for Masonry Structure*, & *Formwork for Concrete* manual.**
- **Access to *Concrete International* –** free to all ACI student members
- **Access to *ACI Structural Journal* and *ACI Materials Journal* –** free to all ACI student members
- **Free sustainability resources –** free copies of Sustainable Concrete Guides provided to universities for use in the classroom
- **Student competitions –** participate in ACI's written and/or team-based competitions
- **Scholarships and fellowships –** students who win awards are provided up to $15,000 and may be offered internships and paid travel to attend ACI's conventions
- **ACI Award for University Student Activities –** receive local and international recognition for your University's participation in concrete-related activities
- **Free access to the *ACI Collection of Concrete Codes, Specifications, and Practices* –** in conjunction with ACI's chapters, students are provided free access to the online ACI Collection
- **ACI online recorded web sessions and continuing education programs –** online learning tools ideal for use as quizzes or in-class study material

https://www.concrete.org/educatorsandresearchers/aciinyourclassroom.aspx

ACI STRUCTURAL JOURNAL TECHNICAL PAPER

Title No. 123-S51

Anchorage Zones Reinforced with Discrete Reinforcing Bars and Continuous Meshes

by Yail J. Kim and Thi Ha

This paper presents the behavior of anchorage zones, also known as end zones, with discrete reinforcing bars and continuous meshes. To examine the implications of various reinforcing schemes on the capacity, cracking, and failure of end zones, 50 block specimens are loaded and their responses are analyzed. Test parameters include the types of reinforcing bar materials (steel and glass fiber-reinforced polymer [GFRP]), and the configurations of the reinforcing bars and steel meshes (single and multiple placements). In terms of load-carrying capacity, the specimens embedded with the GFRP reinforcing bars outperform those with the steel reinforcing bars and meshes by 14.0%. The post-peak load drop of the blocks with steel and GFRP reinforcing bars is analogous, due to distributed axial stresses in the unreinforced concrete region, unlike the abrupt drop observed in the specimens with steel meshes that intersect the concrete in orthogonal directions. While concrete splitting originates from local tension generated near the axial compression, the location of cracking is dominated by the path of stress trajectories related to the number of reinforcing bars, which is not recognized in the case of the mesh specimens. The pattern of the isostatic lines of compression clarifies the development of bursting forces that cause cracking in the concrete. A two-stage analytical model is formulated to predict the magnitude of bursting forces and figure out the effects of several parameters on the response of the end zones. The applicability of existing design expressions is assessed and the need for follow-up research is delineated.

Keywords: anchorage; concentric loading; cracking; end zones; failure; glass fiber-reinforced polymer (GFRP); reinforcing schemes.

INTRODUCTION

Anchorage zones, commonly referred to as end zones, are essential for withstanding prestressing forces in a concrete member. Concentrated axial compression induces local tension in perpendicular directions and causes concrete to split when principal stresses exceed its tensile limit. Adequately designed end zones thus ensure structural integrity for the members under high levels of confining forces. The stress fields in end zones, however, are complex, with a variety of force components; as such, fully comprehending how these zones behave is not a straightforward task.[1] To mitigate cracking in concrete, detailing end zones is important, and reinforcing strategies have gained significance as precasters are reluctant to cast end blocks for economic production.[2] The provisions in the American Association of State Highway and Transportation Officials (AASHTO) Load and Resistance Factor Design (LRFD) Bridge Design Specifications[3] regarding end-zone reinforcement originated from empirical methods based on experimental results and linear analysis.[4,5] Hence, premature spalling and bursting cracks often occur[6] and transportation agencies are eager to seek solutions that can address those problems. Okumus and Oliva[7] evaluated crack-control techniques through finite element modeling. Of interest were the sequence of strand cutting, cross-sectional area of reinforcing bars, location of draped strands, modification of end-zone reinforcements, and debonding of strands. The area of reinforcing bars emerged as the most influential factor with a notable contribution from debonded strands. Steensels et al.[1] examined the effectiveness of several reinforcing bar arrangements and advised placing extra reinforcing bars with larger diameters near the end face of members for the purpose of alleviating spalling cracks, in addition to shear stirrups.

Given the frequent inclusion of vertical reinforcing bars and welded meshes in precasters' shop drawings, researchers attempted to figure out the efficacy of these reinforcing elements.[8,9] For convenience, the end zone of prestressed members was simplified to independent concrete blocks under concentric loading on many occasions.[10-12] Hou et al.[13] developed a numerical model to predict the stress contours of concrete blocks exposed to concentric and eccentric loadings. The profiles of principal stresses changed with the location of axial compression and, as the loaded domain was broadened, the magnitude of bursting stresses abated. The applied loading commenced to deviate from the vertical axis beyond the quarter-length of the loading plate, signifying the importance of near-surface stresses that would govern local tension in the end zones. Zhou et al.[12] tested concrete specimens reinforced with orthogonally placed steel bars. The ramifications of a loading-plate size varying from 10 to 37.5% of the specimen width were assessed. Bursting cracks appeared above the midheight of the blocks and progressed in the diagonal direction. The width of the cracks was correlated with the plate size. According to the proposed strut-and-tie model, stress redistributions after concrete cracking were a dominant consideration in establishing force transfer paths. Cui et al.[14] studied the behavior of rectangular-section concrete with welded meshes. Whereas the resistance of meshes matched that of bent bars, the failure of the welded spots resulted in the brittle failure of the specimens with reduced deformability. Insufficient clarity was stated regarding the meshes' role in ameliorating the cracking response of the sections. Geng et al.[15] loaded

ACI Structural Journal, V. 123, No. 3, May 2026.
MS No. S-2024-413.R2, doi: 10.14359/51749305, received August 24, 2025, and reviewed under Institute publication policies. Copyright © 2026, American Concrete Institute. All rights reserved, including the making of copies unless permission is obtained from the copyright proprietors. Pertinent discussion including author's closure, if any, will be published ten months from this journal's date if the discussion is received within four months of the paper's print publication.

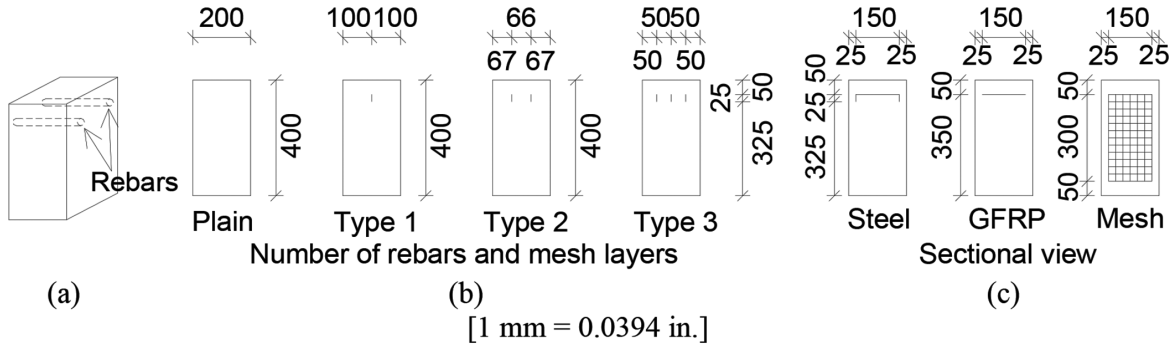

Fig. 1—Various reinforcing schemes for anchorage zones: (a) three-dimensional view; (b) placement of reinforcement; and (c) sectional view.

concrete blocks reinforced with welded meshes to characterize splitting and spalling cracks. The meshes efficaciously confined the concrete and raised the axial capacity of the specimens.

In spite of recent endeavors, there still is a dearth of knowledge on the effects of multiple reinforcing bar placements and the use of steel meshes; particularly, the fundamental failure characteristics and crack-resisting principles of these reinforcing schemes are limitedly known. Along with it, the potential of alternative reinforcing materials exemplified by glass fiber-reinforced polymer (GFRP) composites may be explored to resolve durability matters in concrete structures. This paper aims to investigate the performance of multiple discrete reinforcing bars and continuous meshes in end zones, as well as to ascertain the feasibility of GFRP reinforcing bars that could replace traditional steel reinforcing bars. In fact, no research has been reported on the use of such nonmetallic materials for reinforcing end zones. The focus of the study lies on the load-carrying capacity of end zones with those reinforcements and on the post-peak behavior of the cracked zones to elucidate full-range responses covering elastic and inelastic states. Through analytical modeling, the development of bursting forces and the repercussions of major parameters are expounded in tandem with design aspects.

RESEARCH SIGNIFICANCE

Bursting stresses normal to axial compression prompt cracking in the end-zone concrete. Transverse reinforcement is, therefore, required to preclude the irreversible damage of the disturbed region where beam theory does not apply. Current practices in designing end zones heavily rely upon practitioners' experience and overly conservative design articles.[11] Among many obscure subjects that demand clarification, a thorough understanding of multiple reinforcing bars and meshes embedded in concrete takes precedence to offer a rationale for identifying favorable reinforcing systems in end zones with the intention of refining existing provisions. Additionally, the applicability of noncorrosive GFRP reinforcing bars needs to be discerned for extending the longevity of prestressed concrete structures. By testing a series of specimens possessing a variable number of reinforcing bars and meshes, interactions between the concrete and reinforcing elements are appraised together with post-peak cracking features.

TEST PROCEDURE

The primary segment of the test program consists of material constituents, specimen preparation, and mechanical loading. Monotonic compression is applied to reinforced and unreinforced concrete blocks until failure. Computerized data acquisition systems log their responses and noncontact optical technologies characterize cracking behavior.

Materials

A concrete mixture was designed to achieve a specified compressive strength of f_c' = 25 MPa (3625 psi) with a composition of 354 kg/m^3 (22 lb/ft^3) of cement, 177 kg/m^3 (11 lb/ft^3) of water, 708 kg/m^3 (44 lb/ft^3) of sand, and 1062 kg/m^3 (66 lb/ft^3) of coarse aggregate. In accordance with ASTM C39/C39M-21,[16] moisture-cured cylinders (100 mm [4 in.] in diameter x 200 mm [8 in.] in length) were tested at 28 days and an average strength of 29.8 MPa (4322 psi) was obtained. The size of steel and GFRP reinforcing bars was No. 3 (diameter is 10 mm [0.375 in.] and cross-sectional area is 71 mm^2 [0.11 in.^{2}]). The designation of the steel reinforcing bars was ASTM A572 Grade 60 with a yield strength of f_y = 414 MPa (60 ksi) and an elastic modulus of E_s = 200 GPa (29,000 ksi). The surface-indented GFRP reinforcing bars, comprising ECR (E-glass corrosion-resistant) fibers and a vinyl ester resin, had a tensile strength of f_{fu} = 1000 MPa (145 ksi) with an elastic modulus of E_f = 60 GPa (8700 ksi) at a rupture strain of 1.7%. Welded wire meshes were made of galvanized steel strands (ASTM A653/A653M) with an opening of 25 x 25 mm (1 x 1 in.) and a strand cross-sectional area of 0.81 mm^2 (0.0013 in.^{2}). The nominal yield strength of the mesh was 250 MPa (36 ksi).

Specimens

A total of 50 specimens were cast with various reinforcing layouts (Fig. 1). The dimensions of each block were 200 x 200 x 400 (8 x 8 x 16 in.). The plain concrete without reinforcement served as the control specimen, while others with discrete reinforcement involved between one and three steel and GFRP reinforcing bars positioned at 50 mm (2 in.) from the top surface (Fig. 1(a) and (b)). These reinforcing bars functioned as end-zone reinforcement rather than as other

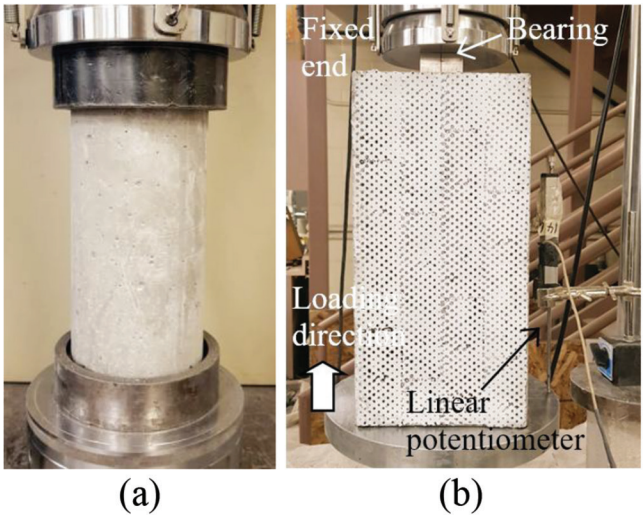

Fig. 2—Test protocol: (a) concrete cylinder; and (b) anchorage zone element.

types of reinforcement, such as shear stirrups. Contrary to the hooked steel reinforcing bars, the non-bendable GFRP reinforcing bars were straight; nonetheless, premature pullout failure was not a concern because the reinforcing bars were subjected to in-plane shear loading. For those with continuous reinforcement, the meshes covered the interior of the block spanning 150 x 300 mm (6 x 12 in.) (Fig. 1(c)). The effective reinforcement ratio of the specimens incorporating the discrete reinforcing elements varied from ρ_{eff} = 0.18 to 0.53%, depending upon the number of embedded reinforcing bars, where ρ_{eff} is defined as the total cross-sectional area of the reinforcement divided by the area of the general zone (the product of the member width and the effective member length that is equal to the member width[17]). The ratio of the specimens with the continuous meshes ranged from ρ_{eff} = 0.014% to 0.043% for one to three layers (only the horizontal strands were taken into account for consistency with the reinforcement ratio of the reinforcing bars). In Table 1, the test matrix of the experimental procedure is presented, showing the types and quantities of the reinforcing bars and meshes, as well as the number of replications: plain represents no reinforcement, S stands for steel reinforcing bars, G for GFRP reinforcing bars, and M for mesh. Five samples for each category were made. For example, S3-2 means the specimen was reinforced with three steel reinforcing bars and was the second repetition of its kind.

Experimental protocol

As mentioned earlier, five cylinders were loaded to determine the 28-day compressive strength of the hardened concrete mixture (Fig. 2(a)). The prepared blocks were placed on top of a circular plate (Fig. 2(b)), and a concentric load was applied at a rate of 1 mm/min (0.0394 in./min) through a rectangular steel bearing plate (50 mm [2 in.] wide x 75 mm [3 in.] long x 30 mm [1.2 in.] thick). A load cell and a linear potentiometer recorded the load and displacement of the specimens, respectively. To study the progression of cracking, digital image correlation (DIC) was employed with a 5-megapixel high-resolution camera and a quad-core computer for processing scanned data.

RESULTS

The results from the experimental program are delineated with an emphasis on the axial strength of concrete members with and without reinforcing elements, the influence of discrete reinforcing bars and continuous meshes, failure aspects, and crack patterns. A comprehensive analysis is undertaken to gauge the practicality of assorted reinforcing schemes in end zones.

Capacity

The load-carrying capacities of the individual specimens are listed in Table 1, depending upon the type of reinforcement, and their average values are charted in Fig. 3(a). The difference between the specimens with the steel reinforcing bars and meshes was 4.5%, whereas the GFRP-reinforced concrete blocks revealed higher capacities than others by up to 14.4%. These observations indicate that the spread mesh configuration was comparable to the case of the discrete reinforcing bars, notwithstanding the differences in reinforcement ratios (0.043% versus 0.53% for the blocks with three mesh layers and reinforcing bars, respectively), and that the nonmetallic composite reinforcing bars were a feasible alternative to the steel reinforcing bars for reinforcing anchorage zones. Figure 3(b) demonstrates the enhanced capacities of the reinforced blocks against the plain ones (increased ratio = reinforced/unreinforced). With an increase in the number of steel reinforcing bars and meshes, the discrepancy between the reinforced and plain specimens went up; for instance, the capacity ratios of the S1 and S3 categories with one and three reinforcing bars were 1.12 and 1.24, respectively. However, the ratio of the GFRP-reinforced blocks remained nearly constant with the number of reinforcing bars: 1.27, 1.32, and 1.33 for one, two, and three reinforcing bars, respectively. This is attributed to the fact that the concrete dominated the failure of the specimens, and the multiple GFRP reinforcing bars did not remarkably impinge upon the reinforcing mechanism; scilicet, the concrete component disintegrated before fully using the high strength of the composite reinforcing bars (to be revisited in the "Failure mode" section).

Figure 3(c) describes the capacities of the specimens normalized by the effective reinforcement ratio (ρ_{eff}) and the strength of the reinforcing bar and mesh (f_y for steel and f_u for GFRP). This analysis considers diverse material properties and reinforcing schemes, contributing to understanding the functionality of these specific constituents. When the number of reinforcing bars and mesh layers was increased, the normalized capacities declined and the steel meshes outperformed other options. Consequently, deploying such uniformly distributed reinforcing elements with an optimal cross-sectional area is a viable solution for anchorage zones, while another possibility could be to sequentially place multiple discrete reinforcing bars in the longitudinal direction of the zones. Even though the high strength of GFRP (f_{fu} = 1000 MPa [145 ksi]) lowered the normalized capacities (Fig. 3(c)), it does not necessarily mean that the performance of the composite was worse: smaller cross-sectional areas

Table 1—Test matrix

ID	Reinforcement		Ultimate load, kN			ID	Reinforcement		Ultimate load, kN		
	Type	No.	Ind.	Ave.	COV		Type	No.	Ind.	Ave.	COV
Plain-1	N/A	0	327.3	327.5	0.073	G2-1	GFRP reinforcing bar	2	449.4	431.8	0.067
Plain-2	N/A	0	334.2			G2-2	GFRP reinforcing bar	2	383.3		
Plain-3	N/A	0	347.8			G2-3	GFRP reinforcing bar	2	455.6		
Plain-4	N/A	0	287.1			G2-4	GFRP reinforcing bar	2	428.7		
Plain-5	N/A	0	341.1			G2-5	GFRP reinforcing bar	2	442.2		
S1-1	Steel reinforcing bar	1	291.4	367.8	0.133	G3-1	GFRP reinforcing bar	3	409.9	437.1	0.036
S1-2	Steel reinforcing bar	1	354.9			G3-2	GFRP reinforcing bar	3	443.2		
S1-3	Steel reinforcing bar	1	374.2			G3-3	GFRP reinforcing bar	3	449.7		
S1-4	Steel reinforcing bar	1	413.7			G3-4	GFRP reinforcing bar	3	439.2		
S1-5	Steel reinforcing bar	1	404.8			G3-5	GFRP reinforcing bar	3	443.6		
S2-1	Steel reinforcing bar	2	390.5	384.6	0.062	M1-1	Steel mesh	1	327.3	354.0	0.089
S2-2	Steel reinforcing bar	2	408.8			M1-2	Steel mesh	1	315.9		
S2-3	Steel reinforcing bar	2	353.7			M1-3	Steel mesh	1	366.8		
S2-4	Steel reinforcing bar	2	365.9			M1-4	Steel mesh	1	392.6		
S2-5	Steel reinforcing bar	2	404.3			M1-5	Steel mesh	1	367.6		
S3-1	Steel reinforcing bar	3	411.6	407.2	0.033	M2-1	Steel mesh	2	386.9	371.7	0.049
S3-2	Steel reinforcing bar	3	398.7			M2-2	Steel mesh	2	356.5		
S3-3	Steel reinforcing bar	3	428.4			M2-3	Steel mesh	2	395.3		
S3-4	Steel reinforcing bar	3	394.2			M2-4	Steel mesh	2	362.6		
S3-5	Steel reinforcing bar	3	403.2			M2-5	Steel mesh	2	357.4		
G1-1	GFRP reinforcing bar	1	423.3	424.3	0.083	M3-1	Steel mesh	3	398.3	381.3	0.031
G1-2	GFRP reinforcing bar	1	365.9			M3-2	Steel mesh	3	385.6		
G1-3	GFRP reinforcing bar	1	449.3			M3-3	Steel mesh	3	378.7		
G1-4	GFRP reinforcing bar	1	393.8			M3-4	Steel mesh	3	378.7		
G1-5	GFRP reinforcing bar	1	439.3			M3-5	Steel mesh	3	365.4		

Note: No. is number; Ind. is individual; Ave. is average; COV is coefficient of variation; 1 kN = 0.225 kip.

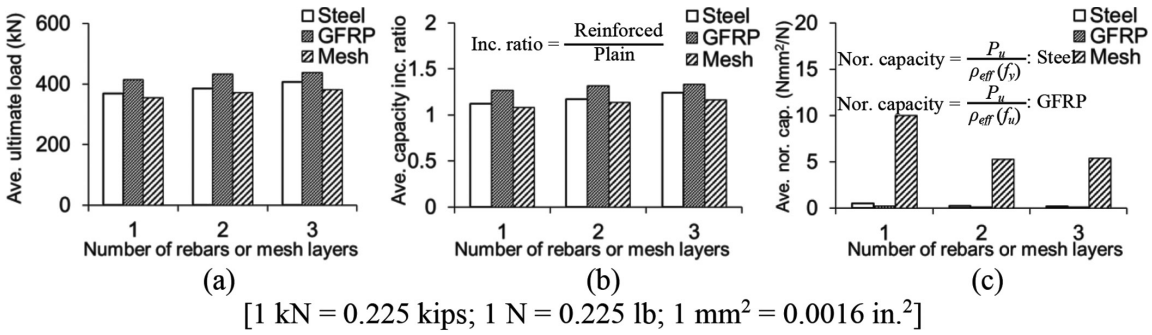

[1 kN = 0.225 kips; 1 N = 0.225 lb; 1 mm^2 = 0.0016 in.^{2}]

Fig. 3—Load-carrying capacity: (a) average ultimate load of test specimens; (b) average increased capacity compared with control capacity; and (c) average normalized capacity.

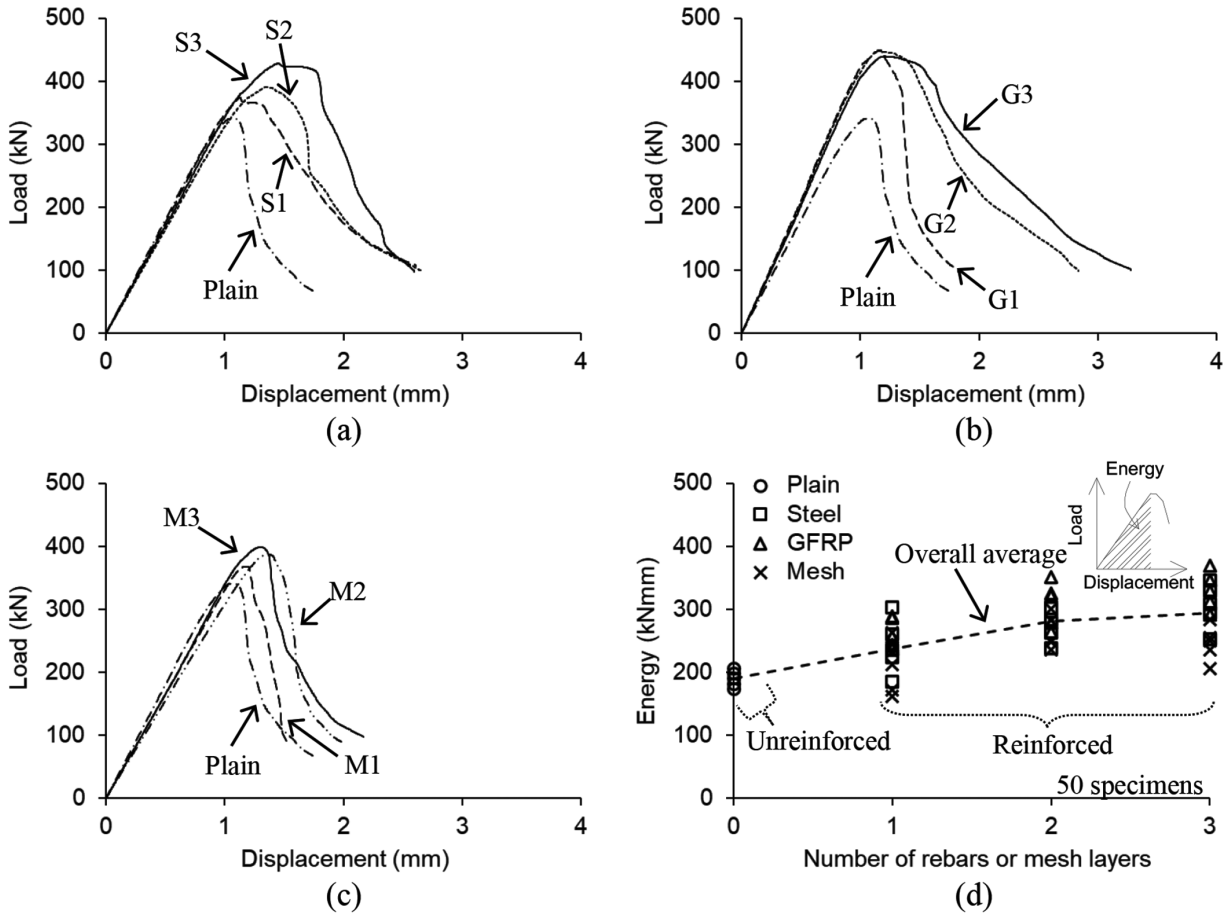

[1 kN = 0.225 kips; 1 mm = 0.0394 in.]

Fig. 4—Load-displacement: (a) steel reinforcing bars; (b) GFRP reinforcing bars; (c) steel meshes; and (d) energy dissipation up to peak loads.

of the GFRP reinforcing bars can achieve equivalent load-bearing capacities to the steel reinforcing bars, as depicted in Fig. 3(a).

Load-displacement

The load-displacement behavior of representative specimens is graphed in Fig. 4(a) to (c). For the blocks with and without steel reinforcing bars (S1 to S3 and plain, Fig. 4(a)), the response ascended linearly until reaching peak loads, and the number of embedded reinforcing bars affected the ultimate loads. The moderate load drops in the post-peak region imply that the applied axial stresses were distributed within the concrete (to be elaborated in the "Analytical Modeling" section), and the reinforcing bars resisted the splitting of the concrete, known as the crack-bridging mechanism.[18] The specimens with the GFRP reinforcing bars manifested analogous responses (Fig. 4(b)). Although the aforementioned independence of the ultimate loads from the number of reinforcing bars was evident, it was influential for the post-peak behavior. A possible explanation is

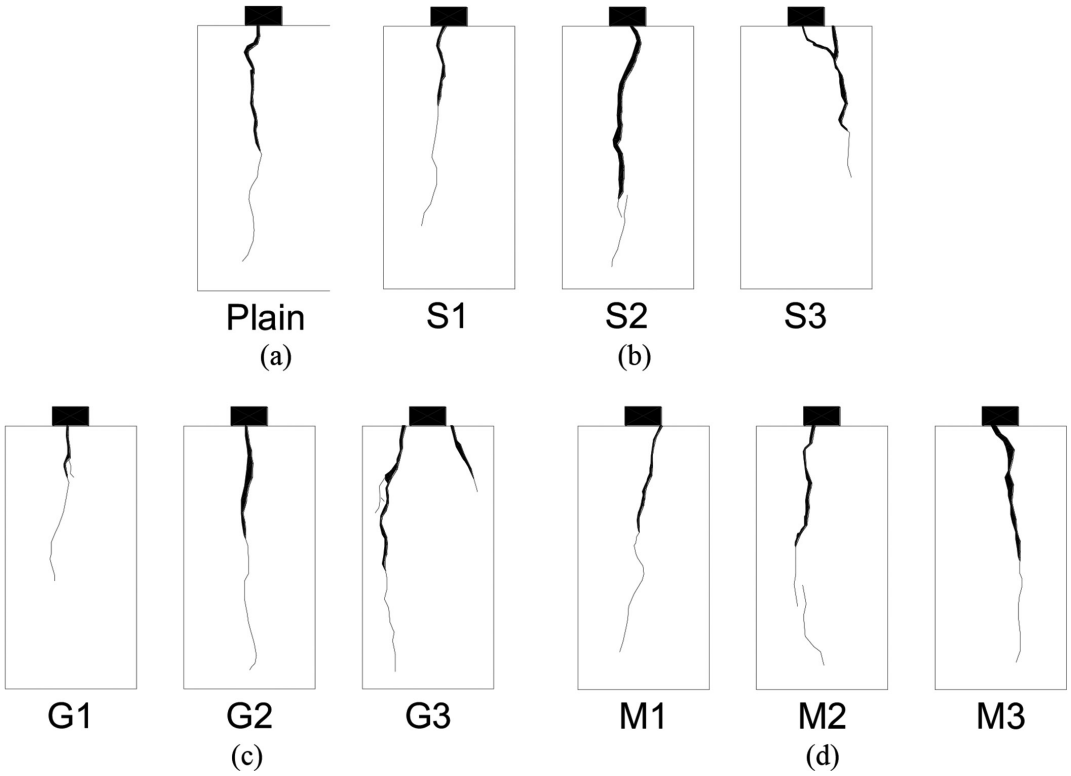

Fig. 5—Failure mode: (a) plain; (b) steel reinforcing bars; (c) GFRP reinforcing bars; and (d) steel meshes.

that the indented surfaces of the multiple GFRP reinforcing bars improved mechanical interlock, thereby delaying the opening of the cracked concrete. The specimens with the meshes exhibited a parallel predisposition (Fig. 4(c)); however, owing to the vertical arrangement of the reinforcement, the post-peak slopes decreased steeply relative to those with the horizontal reinforcing elements (Fig. 4(a) and (b)). Figure 4(d) provides the dissipated energy of the specimens up to the peak loads, calculated by integrating the area under the load-displacement curves (Fig. 4(d), inset). Despite scattering, the reinforced blocks showed higher energy dissipation than the plain blocks, and the energy variation tended to stabilize after the addition of two reinforcing bars and mesh layers. For that reason, ensuring an adequate number of reinforcing bars and mesh layers is salient for concrete members in the end zone.

Failure mode

Plotted in Fig. 5 is the failure mode of the specimens. Regarding plain concrete (Fig. 5(a)), the concentrated compression force induced local tension beneath the loading plate, resulting in a conspicuous separation of the cracked surfaces and ultimately leading to the splitting of the specimen. In line with the control specimen, the cracking of the blocks with one and two steel reinforcing bars initiated below the loading point and intersected the horizontally placed reinforcing bars (S1 and S2, Fig. 5(b)). A combination of static friction and chemical adhesion enabled those reinforcing bars to counteract the horizontal displacement of the concrete.[19] Contrarily, crack formation in the three-reinforcing bar specimens (S3, Fig. 5(b)) shifted away from the loading point because the dispersed reinforcing bars altered the path of stress trajectories. Across the board, inclined cracks were not detected due to the absence of eccentricity in loading. The failure pattern of the GFRP reinforcing bar specimens was akin to their steel counterparts in the context of crack progression (G1 and G2, Fig. 5(c)) and the formation of deviated cracks in the block containing three reinforcing bars (G3, Fig. 5(c)). The cracking adjacent to the quarter points of the upper region in the G3 specimen reaffirms that the three-reinforcing bar placement distributed the applied axial stress outside the immediate loading zone. Furthermore, the consistent cracking of S3 and G3 with the ultimate loads higher than those of the plain concrete (407.2 and 437.1 kN [91.5 and 98.3 kip] versus 327.5 kN [73.6 kip] in Table 1) adduces the potential of GFRP reinforcing bars as reinforcing elements in end zones. On the specimens with meshes (Fig. 5(d)), vertical cracks were observed as in others; by contrast, deviated cracking was not observed in the case with three-mesh layers (M3). This illustrates the practical possibility of coupling meshes and reinforcing bars perpendicular to the loading direction (hybrid reinforcement) to effectively distribute applied stresses across the end-zone concrete.

Evolution of cracking

The sequential images of concrete cracking throughout the post-peak range of the specimens chosen from each category are pictured in Fig. 6. It should be noted that the variation in color contours does not convey technical information; they merely display the relative elevations of the scanned texture. With the axial load continuing beyond the capacity of the

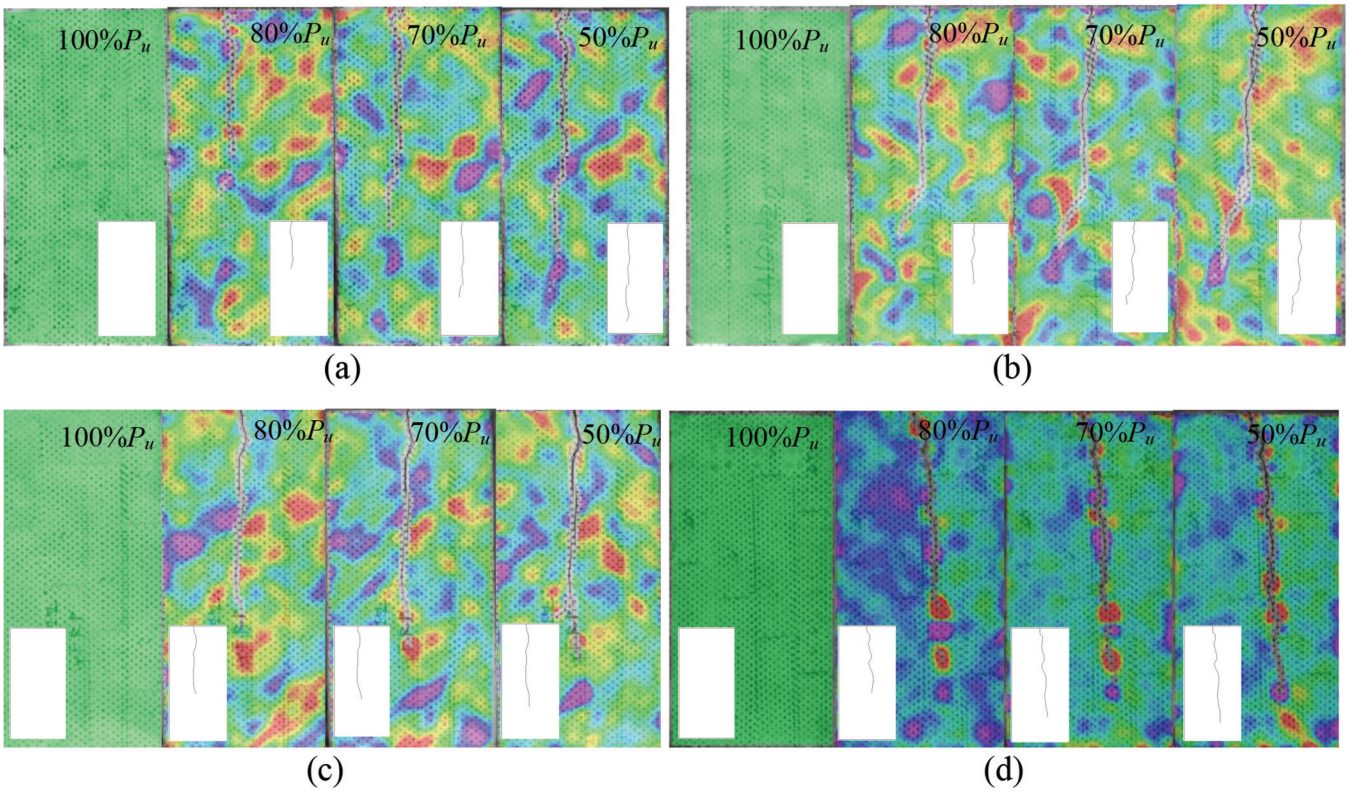

Fig. 6—Progression of cracking depicted by digital image correlation (percentages indicate post-peak load levels): (a) plain; (b) S1; (c) G2; and (d) M3.

plain specimen (Fig. 6(a)), a crack initiated underneath the bearing plate and propagated orthogonally to the principal compressive stress trajectories, which is well documented in deep-beam testing.[20] As the vertical crack advanced, tensile stresses across it accelerated the opening of the concrete: the extended crack may serve as an indirect indicator of diminished stress transfer within the concrete. The cracking appearance in the S1 and G2 specimens was similar to that in the plain specimen (Fig. 6(b) and (c)); nonetheless, their cracking tendencies varied. The low modulus of the nonmetallic reinforcement (E_f = 60 GPa [8700 ksi] for GFRP versus E_s = 200 GPa [27,000 ksi] for steel) was responsible for the expanded crack opening in the GFRP specimen (Fig. 6(c)). From an equilibrium standpoint, the tensile forces of the steel and GFRP reinforcing bars were balanced with the compression resistance of the block in the transverse direction until splitting failure took place. The cracking of the M3 specimen steadily grew with narrow openings (Fig. 6(d)), underscoring the potential advantages of placing continuous meshes in end zones.

Figures 7(a) to (c) show the cracked areas of the specimens in the post-peak domain, quantified by image processing software (the cracked area refers to the portion of the specimen affected by physical cracking). To assist in discussions, the average cracked areas of the test categories were expressed as a percentage relative to the entire area of the concrete block in the loading direction. This method can better characterize the reinforcement's crack-control capabilities than measurements of maximum crack widths, which are inherently random and impractical. Differences were found between the responses of the plain and the S and G specimens; specifically, the increased number of steel and GFRP reinforcing bars corresponded to elongated crack percentages (Fig. 7(a) and (b)). This can be accounted for by the fact that the reinforced specimens with higher capacities (Table 1) incurred more concrete cracking, compared with the P-series control category. In the M specimens (Fig. 7(c)), the crack percentages were markedly reduced and lower than that of the control category because of the distributed mesh layout across the concrete section: consistent with the foregoing specimens, the increased load-bearing capacities of the M1 to M3 specimens were linked to more cracking. The overall post-peak behavior of the S, G, and M specimens is visually assessed in Fig. 7(d) on the basis of their characteristic areas, which were attained by numerically integrating the area under the post-peak load versus crack percentage curves for the examination of cracking tolerance up to $0.5P_u$. Unlike the mesh specimens (M), the disparity between the reinforcing bar specimens (S and G) was modest. To accommodate the uneven ultimate loads of the specimens, the characteristic areas were normalized by the capacities (Fig. 7(e)). The specimens with multiple steel reinforcing bars underwent large crack areas, with the GFRP reinforcing bar and steel-mesh specimens having lesser degrees of cracking.

ANALYTICAL MODELING

A two-stage modeling approach is developed to predict reinforcement responses and bursting forces in the experimental end-zone specimens. The efficiency of discrete reinforcing bars and continuous meshes is detailed and the relevance of a nodal stress limit stipulated in ACI 318-19[17] is

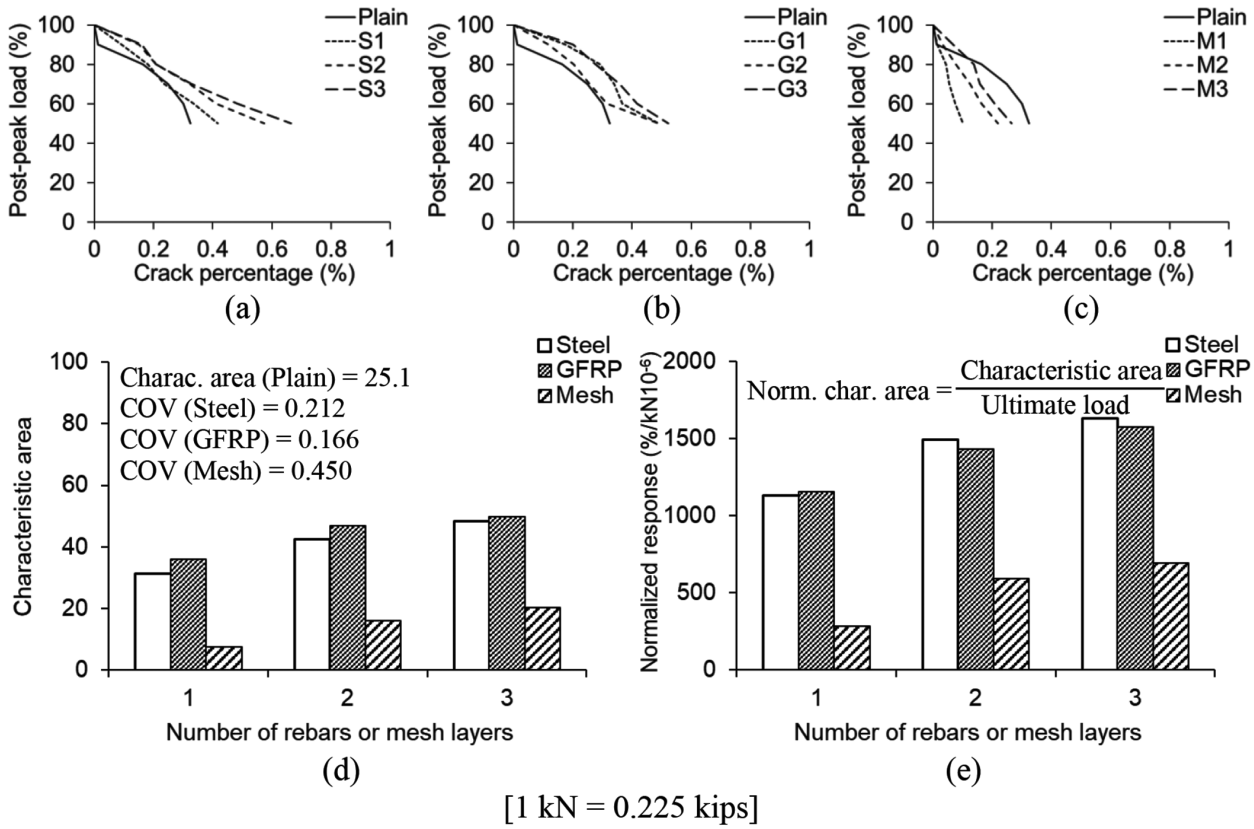

Fig. 7—Crack analysis (average values): (a) steel reinforcing bars; (b) GFRP reinforcing bars; (c) steel meshes; (d) characteristic area; and (e) normalized response.

evaluated. Sensitivity analysis explicates the implications of varying parameters for the behavior of the specimens.

Description

Figures 8(a) and (b) portray the concentrically loaded block models before and after cracking, respectively. The succeeding assumptions were made to facilitate the formulation of the analytical models, which are customary in the theory of elasticity and the strut-and-tie method.[11,17,21,22]

a. In-plane loading is exerted on control and reinforced concrete blocks.

b. Saint-Venant's principle is valid within the disturbed region of the specimens.

c. Reinforcement becomes effective once cracking occurs in the concrete.

d. The distribution of bursting stress along the specimen's height is represented by a resultant force.

e. The location of the resultant bursting force remains unchanged after concrete cracking.

The size of the specimens was appropriate for fully generating a bursting stress profile—that is, the length of the blocks was longer than their width (aspect ratio > 1.0.[23])

Stage I—The first stage of the model is concerned with the specimens until the concrete cracks. The isostatic lines of compression (y, Fig. 8(c)), initially proposed by Guyon,[24] and the transverse stress of the concrete along the loading direction ($\sigma_T(x)$) may be expressed as[11]

$$y = y_i\left[\frac{(h-a)x^2}{h^3}\left(\frac{3}{h^2}x^2 - \frac{8}{h}x + 6\right) + \frac{a}{h}\right] \tag{1}$$

$$\sigma_T(x) = -\frac{3(h-a)P}{2h^4t}(3x^2 - 4hx + h^2) \tag{2}$$

where y_i is the vertical coordinate of the isostatic line of compression at $x = h$; h and a are the width of the specimen and the loading plate, respectively; and P is the concentric load. To account for difficulties in measuring the bursting force of the specimen,[23] Eq. (3) may be used to estimate the force (T_B) up to the cracking of the concrete[25]

$$T_B = \int_{h/3}^{h}\sigma_T(x)t\,dx = \frac{2}{9}P\left(1 - \frac{a}{h}\right) \tag{3}$$

$$P_{cr} = \frac{2ht}{(1 - a/h)}f_t \tag{4}$$

$$f_t = k_1(f_c')^{0.69} \tag{5}$$

where t is the thickness of the specimen; P_{cr} is the cracking load derived from the peak transverse stress[11]; and f_t is the splitting strength of the concrete with k_1 values of 0.214 and 1.38 in metric and U.S. customary units, respectively.

Stage II—Once the load surpasses the cracking load ($P \geq P_{cr}$), the specimen cracks, and the model shifts to the second stage as per the concept of strut-and-tie that is regarded as the standard design method for disturbed or discontinuity

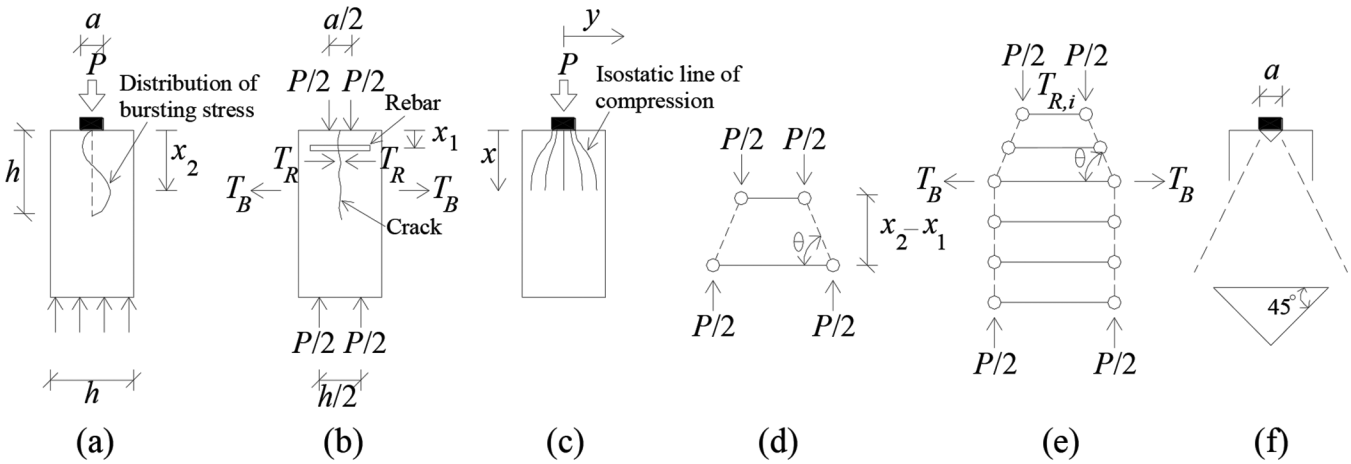

Fig. 8—Model description: (a) before cracking (Stage I); (b) after cracking (Stage II); (c) isostatic lines of compression; (d) strut-and-tie for steel and GFRP reinforcing bars; (e) strut-and-tie for steel meshes; and (f) nodal zone.

regions grounded in a truss-like force transfer mechanism. For the blocks with the steel and GFRP reinforcing bars (Fig. 8(d)), force equilibrium leads to

$$C = \frac{P}{2\sin(\theta)} \tag{6}$$

$$T_B = \frac{P}{2}\cot(\theta) \tag{7}$$

$$\theta = \arctan\left(\frac{(h-a)}{4(x_2-x_1)}\right) \tag{8}$$

where C is the force in the compression strut; θ is the force component angle in degrees; and x_2 and x_1 are the characteristic positions of the reinforcement (Fig. 8(a) and (b)). When the steel meshes are embedded in the specimen (Fig. 8(e)), the horizontal strands counteract the bursting of the concrete.

Force in reinforcement—The reinforcing bar force (T_R) may be equated with the spalling force (T_{sp}) and acquired by $T_R = T_{sp} = 0.02P$, as prescribed in ACI 318-19,[17] in conjunction with Eq. (3) and (7)

$$T_R = \frac{0.09}{\left(1-\frac{a}{h}\right)}T_B \text{ before cracking}$$

$$T_R = \frac{0.04}{\cot\theta}T_B \text{ after cracking} \tag{9}$$

The mesh grids outside the general zone do not interact with horizontal forces in light of the second assumption given previously, which is reasonably acceptable as shown in Fig. 6(d). The spalling force (T_{sp}) is then assumed to be evenly distributed among the individual strands associated with the general zone, which is archetypal in strut-and-tie models

$$\sum_{i=1}^{m} T_{R,i} = T_{sp} \tag{10}$$

$$m = \frac{h-x_1}{s} + 1 \tag{11}$$

where $T_{R,i}$ is the force of the i-th strand; m is the number of the strands in the general zone, including the one at the boundary; and s is the aperture size of the grid.

Nodal resistance—The nodal stress of the concrete underneath the loading plate (σ_{node}, Fig. 8(f)) may be calculated by

$$\sigma_{node} = \frac{P}{A_{node}} \le k_2 f_c' \tag{12}$$

$$A_{node} = \sqrt{\frac{1}{2}}\, a\cos(45° - \theta)t \tag{13}$$

where k_2 is the limit coefficient for design (k_2 = 0.68 for a compression-tension-compression node in the strut-and-tie model[17]).

Predicted response

Plain specimen—Figure 9(a) renders the isostatic lines of compression in the upper part of the symmetric concrete block. The curvilinear trajectory of the isostatic lines gradually rose beyond approximately x = 50 mm (2 in.) and stabilized after x = 150 mm (6 in.). This conformational development points out that the slanted lines were engaged with non-axial force components, creating bursting forces that could split the concrete. As shown in Fig. 9(b), the resultant bursting force (T_B, Eq. (3)) increased linearly with the applied load (P) up to failure. The theoretical cracking load of P_{cr} = 284.9 kN (64.1 kip) was 13% lower than the average ultimate load of P_u = 327.5 kN (73.6 kip). The transition from compressive to tensile stresses is visible in Fig. 9(c). The transverse stress in the tension zone ($\sigma_T(x) > 0$) precipitated the cracking of the plain specimen and the splitting failure was predicted at f_t = 2.23 MPa (323.4 psi). Significant nonlinearity was apparent between the nominal ($\sigma_{nominal} = P/(ta)$) and the transverse ($\sigma_T(x)$) stresses (Fig. 9(d)). The maximum transverse stress in tension was 35.9% of the nominal stress at x = 133 mm (5.2 in.), where the resultant bursting force (T_B) was located.

Reinforced specimen—The behavior of the specimens with the reinforcing bars and meshes is provided in Fig. 10. Prior to the cracking of the concrete ($P \le P_{cr}$), the response of the plain and reinforced blocks was identical (Fig. 10(a));

however, a remarkable increase in the bursting force was computed as soon as the specimen cracked and the force continued to elevate until the load-carrying capacity of the S1 specimen was reached (P_u = 367.8 kN [82.7 kip]). The reduced slope of the load versus bursting force curve after cracking (382 kN [85.9 kip] ≤ T_B ≤ 491 kN [110.4 kip]) is ascribed to the internal forces in the uncracked concrete being directly transferred through the narrow compression struts. Shown in Fig. 10(b) is the stress of the steel reinforcing bars normalized by the yield strength of f_y = 414 MPa (60 ksi). When the number of reinforcing bars was increased, the normalized stress decreased, especially between the one- and two-reinforcing bar cases. This supports the fact that placing at least two reinforcing bars perpendicular to the loading direction is beneficial for lowering stresses, which would preserve the integrity of the end zone exposed to substantial mechanical and environmental distress over the long term. With the inclusion of the GFRP reinforcing bars (Fig. 10(c)), the normalized stresses were noticeably lessened due to the high tensile strength of f_{fu} = 1000 MPa (145 ksi) and it confirms the extended service life of composite-reinforced concrete members.[26] Even if the magnitudes of the normalized stresses were intended to compare the axial resistance of the reinforcing bars solved from the strut-and-tie method, the propensity can be valid under shear loading because the shear strength of the steel reinforcing bars is proportional to their axial strength pursuant to the maximum shear stress theory,[22] which is also acceptable for the GFRP reinforcing bars.[27] Relative to the reinforcing bar specimens, the ones reinforced with the meshes demonstrated considerable stress levels as a result of the strands' small cross-sectional area (Fig. 10(d)); in view of this, attention should be paid to the size and number of such interconnected strands to avert issues anticipated during the functional period of the end zone.

The efficiency of placing multiple reinforcing bars and meshes may be examined by Eq. (14)

$$\psi = \frac{T_R(n)}{T_R(1)} \tag{14}$$

where ψ is the reinforcement efficiency ratio; $T_R(n)$ is the bursting resistance force with n reinforcing bars and mesh layers; and $T_R(1)$ is the resistance force with one reinforcing bar and mesh layer. The steel reinforcing bars and meshes benefited from increasing the number of reinforcing elements (Fig. 10(e)); on the other hand, the efficiency of the multiple GFRP reinforcing bars was nearly constant with only a marginal impact from adding more reinforcing bars, as explained earlier. Figure 10(f) exhibits the growth of the nodal zone stress under the loading plate (Eq. (12)). At the cracking of the specimens when the elastic concrete body transformed into the inelastic truss-like morphology in the strut-and-tie framework, the predicted maximum stress (σ_{node} = 29.5 MPa [4279 psi]) was close to the compressive strength of the concrete (f_c' = 29.8 MPa [4322 psi]) and was 45.3% higher than the ACI stress limit of 20.3 MPa (2944 psi). The proposed two-stage modeling approach can thus be conservatively applied in practice, aligning with the widely accepted notion that strut-and-tie models set a lower bound for the capacity of reinforced concrete members.[28]

Parametric study

The sensitivity of the end-zone specimens to crucial parameters is highlighted in Fig. 11. The default properties of the specimens were those of the plain and S1, G1, and M1 blocks, unless otherwise specified. When the concrete strength (f_c') was increased, the cracking load (P_{cr}) of the plain and reinforced specimens went up linearly (Fig. 11(a)). As far as geometric properties are concerned, the variation of the cracking load was more susceptible to the loaded area ratio (a/h, Fig. 11(b)) than the thickness ratio (t/h, Fig. 11(c)). The reason is that the increased a/h distributed the applied load within the uncracked concrete, allowing the specimen to carry a greater load before the onset of cracking. Figures 11(d) to (f) clarify the consequences of adjusting the geometric properties (a/h and t/h) and loading angle (θ) on the bursting force of the uncracked specimens subjected to a typical service load of $0.3P_{cr}$. In contrast to the t/h and θ situations, the bursting force was contingent upon the a/h ratio because the elastic approach merely handles in-plane stresses (Eq. (3)). After cracking, these trends reshaped and larger force values were predicted from the inelastic strut-and-tie model (Fig. 11(g) to (i)). Given that the failure loads of the steel- and GFRP-reinforcing bar specimens differed (Table 1), the applied load level was taken to be the average ultimate load of the control specimens (P_u = 327.5 kN [73.6 kip], plain) for comparison purposes. The increased cracking load with the enlarged a/h ratio (Fig. 11(b)) led to an appreciable rise in the bursting force after cracking (Fig. 11(g)); in contrast, the effect of the t/h ratio was virtually none (Fig. 11(h)). Misinterpretation of these findings should be avoided to prevent the misconception that the surged bursting force meant expedited failure, as the ability to resist a high bursting force is actually enhanced by retarded cracking; additionally, the modification of the t/h ratio is not insignificant because the widened aspect ratio of the end zone is inherently advantageous for stress control. An exponential drop in the bursting force was noticed with the larger angle (Fig. 11(i)) owing to the reduced horizontal force component (Fig. 8(d)). The stress of the steel and GFRP reinforcing bars declined with the increased effective reinforcement ratio in a like manner (Fig. 11(j)), while the magnitude of the mesh stress was more pronounced up to the point of yielding (Fig. 11(k)). The size of the grid openings played a major role in reinforcement stress (Fig. 11(l)); accordingly, selecting an appropriate mesh size is a critical factor in practice.

Design perspectives

The stress limits of the steel and GFRP reinforcing bars were assigned to be $2/3f_y$ and $0.005E_f$ in compliance with ACI 318-19[17] and ACI CODE-440.11-22,[29] respectively, and the calculated stresses were normalized for assessments (Fig. 12(a)). The rationale for adopting these limits was to preclude cracking in steel-reinforced concrete[17] and to obviate the premature rupture of GFRP reinforcing bars.[29] The evolution of the normalized stresses for the steel and

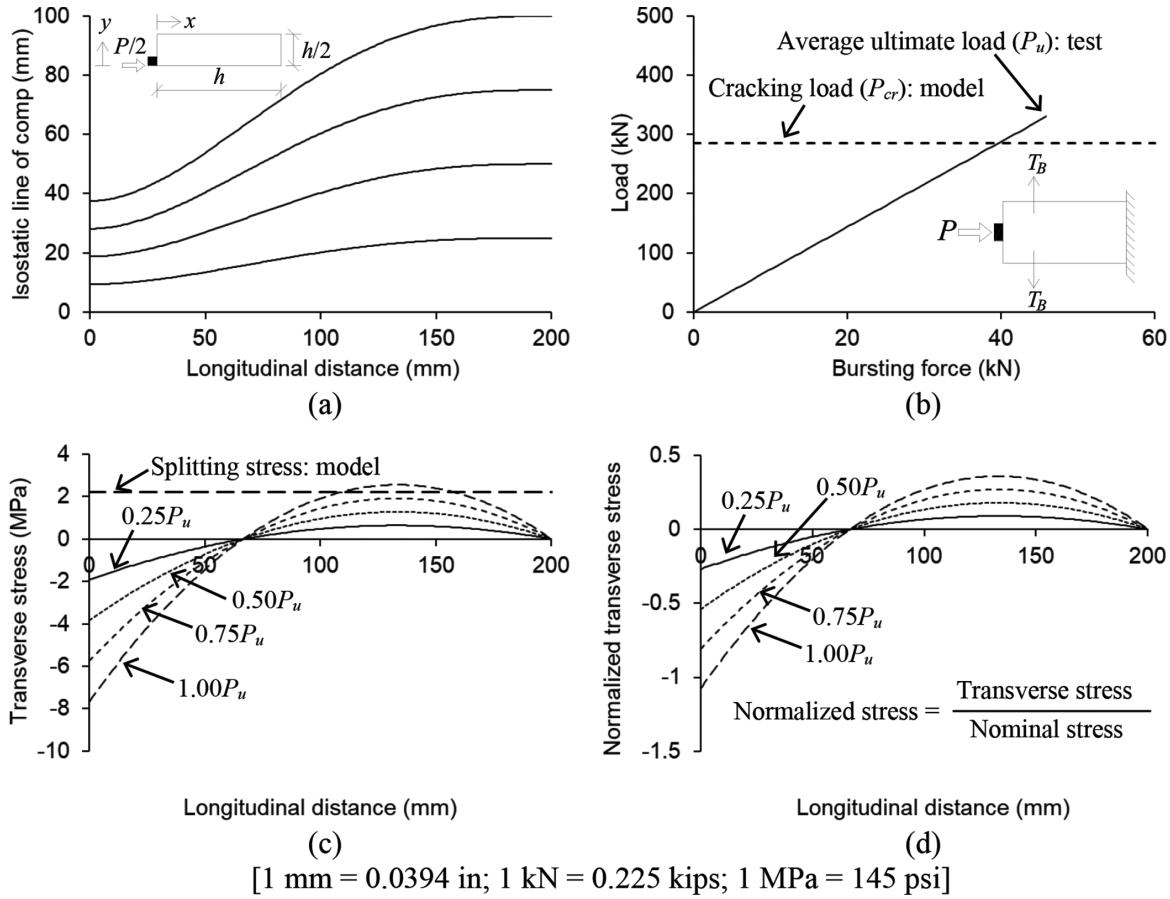

Fig. 9—Plain specimen: (a) isostatic line of compression; (b) bursting force; (c) transverse stress; and (d) normalized transverse stress.

GFRP reinforcing bars was alike, modulated by the effective reinforcement ratio (Fig. 12(a), inset). The stress of the steel meshes was normalized by the yield strength of f_y = 250 MPa (36 ksi), attributable to the scarcity of specific limits in published specifications. The thin mesh strands with effective reinforcement ratios from 0.014 to 0.043% experienced yielding at an applied load of P = 75 kN (16.9 kip), which is equivalent to 0.26P_{cr} (Fig. 12(b)). This fact corroborates the importance of mesh configurations as a reinforcing element for end zones, which warrants extended research to figure out suitable mesh details alongside a stress limit in conformity with those of the reinforcing bars. Figure 12(c) shows the mutual relevance of the steel and GFRP reinforcing bars at the cracking load of P_{cr} = 284.9 kN (64.1 kip), substantiating the validity of both reinforcement types for end-zone applications. The effectiveness of the empirical stress limit of 138 MPa (20 ksi) for nonprestressed end-zone reinforcement, frequently employed by practitioners,[30] is appraised in Fig. 12(d). Even with the conservative approach, the normalized stress of the steel reinforcing bars was maintained at less than 60% of the limit; hence, the empirical limit can justifiably be permitted for controlling stress levels in end zones.

SUMMARY AND CONCLUSIONS

This paper discussed the behavior of anchorage zones with discrete reinforcing bars and continuous meshes. Under monotonic compression, 50 specimens were tested to investigate the effects of different reinforcement types and materials on the capacity, cracking, and failure of the end zones. The practicality of employing nonmetallic glass fiber-reinforced polymer (GFRP) reinforcement was of interest. The two-stage analytical model, formulated with elastic equations and the strut-and-tie method, predicted bursting forces for the plain and reinforced specimens before and after concrete cracking. Parametric studies accounted for significant variables affecting the cracking loads, bursting forces, and reinforcement stresses of the end zones. In a supplementary fashion, design aspects were articulated to evaluate the adequacy of existing expressions and to identify the necessity for new provisions dealing with the unconventional reinforcing elements in end zones. The following conclusions are drawn:

- The load-carrying capacity of the specimens with the GFRP reinforcing bars was 14.0% higher than that of those with the steel reinforcing bars and meshes, although the reinforcement ratio of the mesh blocks was approximately one-tenth the ratio of the others. The capacity of the steel-reinforced specimens was susceptible to the number of reinforcing bars and mesh layers, which was not the case for the GFRP-reinforced specimens.
- The post-peak load drop of the steel- and GFRP-reinforced specimens was comparable because axial

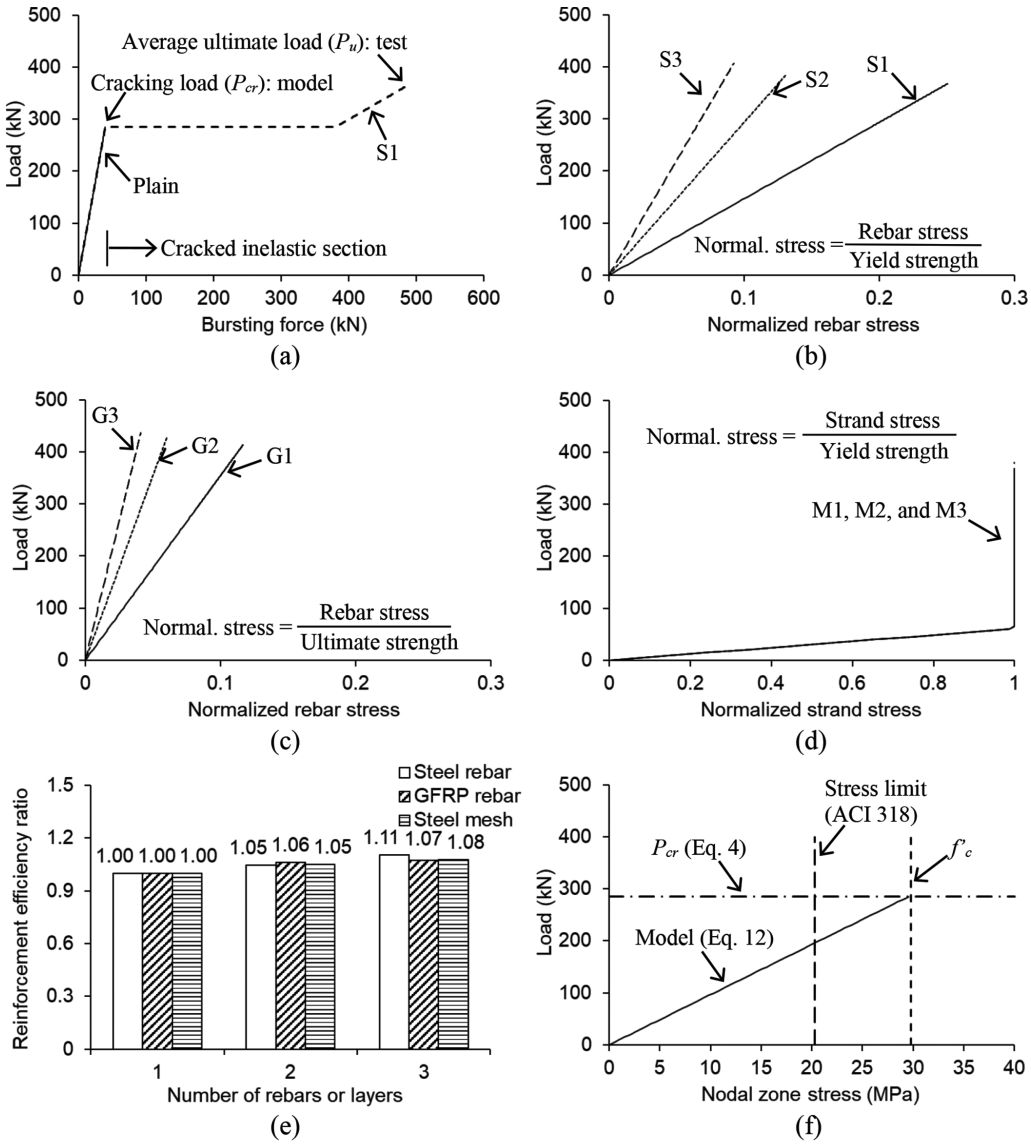

Fig. 10—Specimen with reinforcement: (a) bursting force; (b) normalized stress of steel reinforcing bars; (c) normalized stress of GFRP reinforcing bars; (d) normalized stress of steel meshes; (e) efficiency ratio; and (f) nodal stress up to cracking.

stresses were distributed in the unreinforced concrete zone, whereas the drop was precipitous for the specimens with the meshes that intersected the concrete in orthogonal directions. A combination of these disparate reinforcing elements may be used in practice to complement the weaknesses of each, improving capacity and post-peak failure performance.

- The local tension underneath the axial compression caused the concrete to split. The location of cracking and its pattern changed with the number of embedded reinforcing bars due to alterations in the load path of stress trajectories. This tendency was not recognized in the specimens with the meshes. The low-modulus GFRP reinforcing bars permitted extended crack openings, as opposed to the narrow openings associated with the meshes featuring multilateral layouts in the concrete block.
- Away from the loaded end, the isostatic lines of compression progressively ascended and stabilized, resulting in horizontal bursting forces that cracked the blocks. When the external load was greater than the cracking load ($P > P_{cr}$), the bursting force substantially increased, and at least two reinforcing bars should be placed to effectively manage internal stresses. The size of these end-zone reinforcing bars may not be the same as that of vertical shear reinforcement in concrete beams.
- The loaded area ratio (a/h) and concrete strength (f_c') of the specimens dominated the cracking load, while the contribution of other geometric properties, such as the thickness ratio (t/h), was negligible. The importance of grid size in the meshes was noteworthy for stress development.
- The empirical stress limit of 138 MPa (20 ksi) stated in the AASHTO LRFD Bridge Design Specifications[3] was acceptable for the discrete reinforcing bars in the end

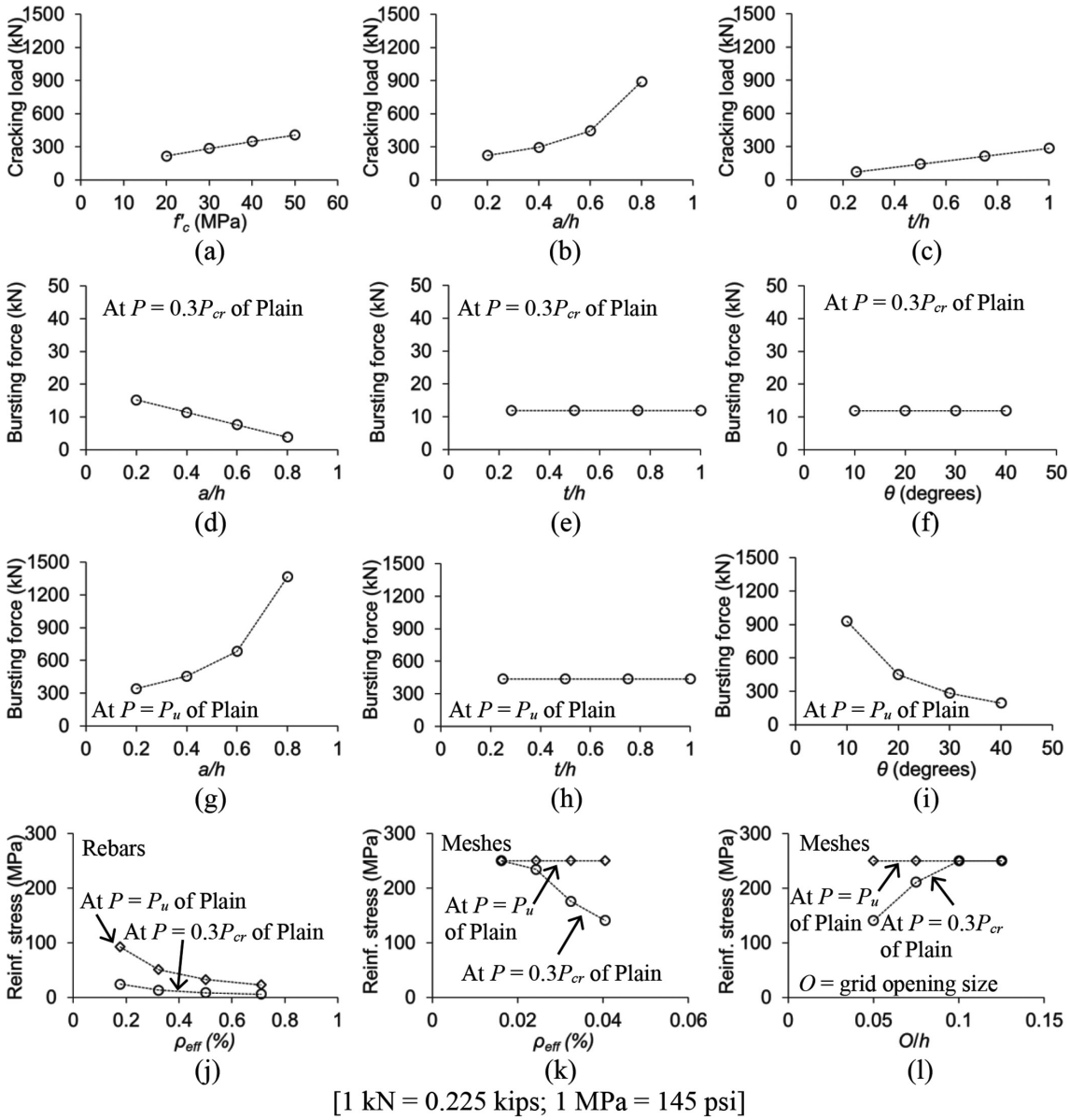

Fig. 11—Parametric study: (a) cracking load with f_c'*; (b) cracking load with* a/h*; (c) cracking load with* t/h*; (d) bursting force before cracking with* a/h*; (e) bursting force before cracking with* t/h*; (f) bursting force before cracking with* θ*; (g) bursting force after cracking with* a/h*; (h) bursting force after cracking with* t/h*; (i) bursting force after cracking with* θ*; (j) reinforcing bar stress with* ρ_{eff}*; (k) mesh stress with* ρ_{eff}*; and (l) mesh stress with* O/h*.*

zone. Further research is necessary on the continuous meshes to establish new design limits. On the whole, the steel and GFRP reinforcing bars performed equally well and the viability of the mesh reinforcement was evinced.

AUTHOR BIOS

Yail J. Kim, *FACI, is President of the Bridge Engineering Institute, an International Technical Society, and a Professor in the Department of Civil Engineering at the University of Colorado Denver, Denver, CO. He is past Chair of ACI Committee 345, Concrete Bridge Construction and Preservation, and ACI Subcommittee 440-I, FRP-Prestressed Concrete. He is a member of ACI Committees 342, Evaluation of Concrete Bridges and Bridge Elements; 377, Performance-Based Structural Integrity and Resilience of Concrete Structures; and 440, Fiber Reinforced Polymer Reinforcement. He received the ACI Chester Paul Siess Award for Excellence in Structural Research in 2019. His research interests include advanced composite materials for rehabilitation, structural informatics, complex systems; and science-based structural engineering, including statistical, interfacial, and quantum physics.*

Thi Ha *is a PhD Student in the Department of Civil Engineering at the University of Colorado Denver. He received his BS in civil engineering from Ho Chi Minh City University of Technology and Education, Ho Chi Minh City, Vietnam, and his MS in civil engineering from Ho Chi Minh City University of Technology, Ho Chi Minh City, Vietnam. His research interests include concrete structures, advanced materials, and computational modeling.*

ACKNOWLEDGMENTS

The authors would like to gratefully acknowledge support from the Colorado Department of Transportation (CDOT). T. Tran and T. Wang were the research manager and the lead panel at CDOT, respectively, who advised this project. The technical content presented here is based on the opinion of the authors and does not necessarily represent those of others.

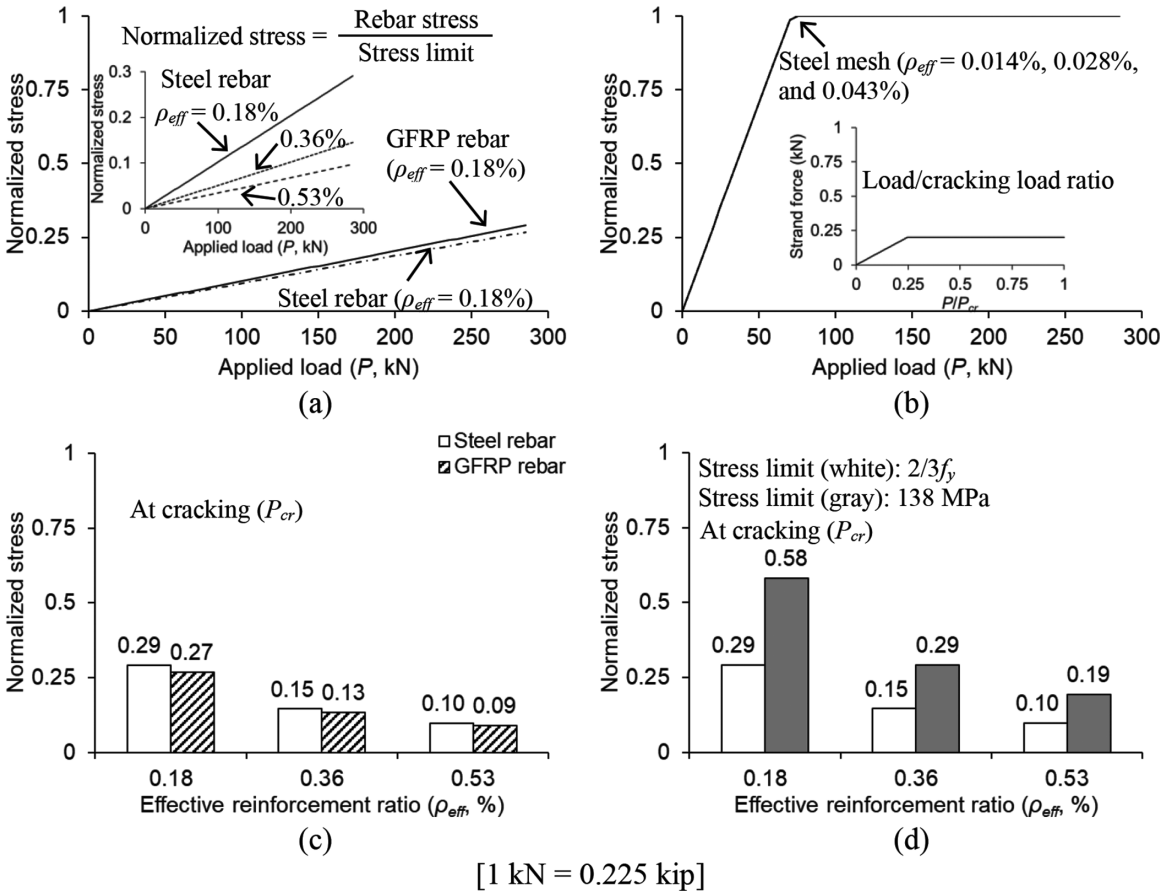

Fig. 12—Design consideration: (a) discrete reinforcing bars; (b) continuous mesh layers; (c) comparison between steel and GFRP reinforcing bars; and (d) alternative stress limit for steel reinforcing bars.

REFERENCES

1. Steensels, R.; Vandoren, B.; Vandewalle, L.; and Degee, H., "Evaluation of End-Zone Detailing of Pre-Tensioned Concrete Girders," *Engineering Structures*, V. 187, 2019, pp. 372-383. doi: 10.1016/j.engstruct.2019.02.068

2. Hiremath, G.; Itani, R.; and Vasishth, U., "Test of Continuous Prestressed Concrete Girders Without End Blocks," *Transportation Research Record: Journal of the Transportation Research Board*, No. 1223, 1989, pp. 73-83.

3. AASHTO, "AASHTO LRFD Bridge Design Specifications," ninth edition, American Association of State Highway and Transportation Officials, Washington, DC, 2020.

4. Burdet, O., "Analysis and Design of Anchorage Zones for Posttensioned Concrete Bridges," PhD dissertation, The University of Texas at Austin, Austin, TX, 1990.

5. Breen, J. E.; Burdet, O.; Roberts, C.; Sanders, D.; and Wollmann, G., "Anchorage Zone Reinforcement for Post-Tensioned Concrete Girders, NCHRP Report 356, Transportation Research Board, Washington, DC, 1994.

6. Srinivasan, S. S.; Rung, M.; and Ferron, R. D., "Factors Affecting Loss in Durability in Prestressed-Concrete Girders with Microcracking," *Journal of Bridge Engineering*, ASCE, V. 25, No. 9, 2020, p. 04020068. doi: 10.1061/(ASCE)BE.1943-5592.0001590

7. Okumus, P., and Oliva, M. G., "Evaluation of Crack Control Methods for End Zone Cracking in Prestressed Concrete Bridge Girders," *PCI Journal*, V. 58, No. 2, 2013, pp. 91-105. doi: 10.15554/pcij.03012013.91.105

8. Tuan, C. Y.; Yehia, S. A.; Jongpitaksseel, N.; and Tadros, M. K., "End Zone Reinforcement for Pretensioned Concrete Girders," *PCI Journal*, V. 49, No. 3, 2004, pp. 68-82. doi: 10.15554/pcij.05012004.68.82

9. Yao, G.; Xiong, X.; and Ge, Y., "Cracking Behavior of Full-Scale Pre-Tensioned Prestressed Concrete Double-Tee Members with Steel-Wire Meshes," *Journal of Building Engineering*, V. 44, 2021, p. 102658. doi: 10.1016/j.jobe.2021.102658

10. Sanders, D. H., and Breen, J. E., "Post-Tensioned Anchorage Zones with Single Straight Concentric Anchorages," *ACI Structural Journal*, V. 94, No. 2, Mar.-Apr. 1997, pp. 146-158.

11. He, Z.-Q., and Liu, Z., "Investigation of Bursting Forces in Anchorage Zones: Compression-Dispersion Models and Unified Design Equation," *Journal of Bridge Engineering*, ASCE, V. 16, No. 6, 2011, pp. 820-827. doi: 10.1061/(ASCE)BE.1943-5592.0000187

12. Zhou, L.; Liu, Z.; and He, Z., "Elastic-To-Plastic Strut-and-Tie Model for Concentric Anchorage Zones," *Journal of Bridge Engineering*, ASCE, V. 22, No. 10, 2017, p. 04017070. doi: 10.1061/(ASCE)BE.1943-5592.0001060

13. Hou, D.-W.; Zhao, J.-L.; Shen, S.-L.; and Chen, J., "Investigation and Improvement of Strut-and-Tie Model for Design of End Anchorage Zone in Post-Tensioned Concrete Structure," *Construction and Building Materials*, V. 136, 2017, pp. 482-494. doi: 10.1016/j.conbuildmat.2017.01.033

14. Cui, M.; Nie, X.; Fan, J.; Li, S.; Liufu, J.; and Huang, Z., "Experimental Study on the Shear Performance of RC Beams Reinforced with Welded Reinforcement Grids," *Construction and Building Materials*, V. 203, 2019, pp. 377-391. doi: 10.1016/j.conbuildmat.2019.01.064

15. Geng, X.; Zhou, W.; and Yan, J., "Reinforcement of Orthogonal Ties in Steel-Fiber-Reinforced Reactive Powder Concrete Anchorage Zone," *Advances in Structural Engineering*, V. 22, No. 10, 2019, pp. 2311-2321. doi: 10.1177/1369433219838085

16. ASTM C39/C39M-21, "Standard Test Method for Compressive Strength of Cylindrical Concrete Specimens, ASTM International, West Conshohocken, PA, 2021, 8 pp.

17. ACI Committee 318, "Building Code Requirements for Structural Concrete (ACI 318-19) and Commentary (ACI 318R-19) (Reapproved 2022)," American Concrete Institute, Farmington Hills, MI, 2019, 624 pp.

18. Drar, A. A. M., and Matsumoto, T., "Fatigue Analysis of RC Slabs Reinforced with Plain Bars Based on the Bridging Stress Degradation Concept," *Journal of Advanced Concrete Technology*, V. 14, No. 1, 2016, pp. 21-34. doi: 10.3151/jact.14.21

19. Chiriatti, L.; Mercado-Mendoza, H.; Apedo, K. L.; Fond, C.; and Feugeas, F., "A Study of Bond Between Steel Rebar and Concrete Under a

Friction-Based Approach," *Cement and Concrete Research*, V. 120, 2019, pp. 132-141. doi: 10.1016/j.cemconres.2019.03.019

20. Mukhtar, F., and Deifalla, A., "Shear Strength of FRP Reinforced Deep Concrete Beams Without Stirrups: Test Database and a Critical Shear Crack-Based Model," *Composite Structures*, V. 307, 2023, p. 116636. doi: 10.1016/j.compstruct.2022.116636

21. Joint ACI-ASCE Committee 445, "Strut-and-Tie Method Guidelines for ACI 318-19—Guide (ACI PRC-445.2-21)," American Concrete Institute, Farmington Hills, MI, 2021, 88 pp.

22. Ugural, A. C., and Fenster, S. K., *Advanced Strength and Applied Elasticity*, third edition, Prentice-Hall, Hoboken, NJ, 1995.

23. Sahoo, D. K.; Singh, B.; and Bhargava, P., "Investigation of Dispersion of Compression in Bottle-Shaped Struts," *ACI Structural Journal*, V. 106, No. 2, Mar.-Apr. 2009, pp. 178-186.

24. Guyon, Y., *Prestressed Concrete*, Contractors Record, London, UK, 1955.

25. Oluokun, F. A., "Prediction of Concrete Tensile Strength From Its Compressive Strength," *ACI Materials Journal*, V. 88, No. 3, May-June 1991, pp. 302-309.

26. Esmaeili, Y.; Eslami, A.; Newhook, J.; and Benmokrane, B., "Performance of GFRP-Reinforced Concrete Beams Subjected to High-Sustained Load and Natural Aging for 10 Years," *Journal of Composites for Construction*, ASCE, V. 24, No. 5, 2020, p. 04020054. doi: 10.1061/(ASCE)CC.1943-5614.0001065

27. Sawpan, M. A., "Effects of Alkaline Conditioning and Temperature on the Properties of Glass Fiber Polymer Composite Rebar," *Polymer Composites*, V. 37, No. 11, 2016, pp. 3181-3190. doi: 10.1002/pc.23516

28. El-Metwally, S., and Chen, W. F., *Structural Concrete: Strut-and-Tie Models for Unified Design*, CRC Press, Boca Raton, FL, 2017.

29. ACI Committee 440, "Building Code Requirements for Structural Concrete Reinforced with Glass Fiber-Reinforced Polymer (GFRP) Bars—Code and Commentary (ACI CODE-440.11-22)," American Concrete Institute, Farmington Hills, MI, 2023, 266 pp.

30. Nawy, E. G., *Prestressed Concrete: A Fundamental Approach*, fifth edition, Prentice Hall, Upper Saddle River, NJ, 2009.

Become a Peer Reviewer for ACI Journals

Peer reviewers help ensure the quality, accuracy, and impact of published concrete research. Your expertise directly supports advancement in the field.

Why Review?

- Shape research that informs codes and practice
- Stay current with new findings and technologies
- Strengthen your professional credentials
- Connect with editors, authors, and industry experts

Areas of Expertise We Seek

- Structural analysis, design, and performance
- Concrete materials, durability, and behavior
- Repair, rehabilitation, and strengthening
- High-performance, sustainable, and low-carbon concrete
- Structural resilience and durability-related performance
- Alternative and non-metallic reinforcement
- Fiber-reinforced concrete
- UHPC and emerging materials
- Performance-based design
- Seismic design and retrofit
- Fire resistance of concrete and masonry
- Testing, evaluation, and condition assessment
- Nondestructive testing and sensing technologies
- Digital tools, modeling, and artificial intelligence

Reviewer Expectations

Technical expertise • Clear, constructive feedback
Timely reviews • Professionalism & confidentiality

How to Join

1. Create an account at **mc.manuscriptcentral.com/aci**
2. Select your areas of expertise
3. Email **journal.manuscripts@concrete.org** to request reviewer status

American Concrete Institute

Always advancing

ACI STRUCTURAL JOURNAL TECHNICAL PAPER

Title No. 123-S52

Confinement Reinforcement of Cyclically Loaded Normal-Strength Concrete Tied Columns under High Axial Loads

by Wen-Cheng Shen and Shyh-Jiann Hwang

In high-rise buildings, lower-story columns must withstand significant seismic shear forces while maintaining sufficient deformation capacity. This capacity is provided through effective confinement using transverse reinforcement. ACI CODE-318-25 specifies that confining reinforcement should be proportional to the applied axial load when the axial load exceeds $0.3A_gf_c'$ and requires all longitudinal bars to be laterally supported with seismic hooks. However, the implementation of seismic hooks at both ends of crossties brings challenges for on-site reinforcement assembly.

This study experimentally investigates full-scale reinforced concrete (RC) column specimens subjected to quasi-static cyclic loading while under a constant high axial load. The objectives are to validate the ACI CODE-318-25 confinement requirements and to evaluate the feasibility of relaxing seismic hook requirements. The results confirm that columns designed in accordance with ACI CODE-318-25 satisfy the required 3% deformation capacity. Furthermore, satisfactory seismic performance can be achieved with crossties incorporating alternating 135-degree and 90-degree hooks, although at the expense of increased confining reinforcement.

Keywords: column; confining reinforcement; crosstie configuration; high axial load; ultimate drift ratio.

INTRODUCTION

Moment-resisting frames are widely used due to their ability to provide open space. Seismic design typically aims to form plastic hinges at beam ends rather than in columns. However, plastic hinges often develop at the bases of first-story columns. In high-rise residential buildings, particularly in densely populated urban areas, lower-story columns are subjected to substantial axial loads. Adequate confinement of these columns is essential to ensure sufficient deformation capacity under lateral loading while maintaining load-bearing capacity. According to ACI 318-11,[1] the design of confining reinforcement in reinforced concrete (RC) columns aims to provide passive confinement to the concrete core after concrete cover spalling, preserving its ultimate compressive strength. However, this design may result in insufficient confinement for columns with large cross sections. To mitigate this deficiency, ACI 318-11[1] specifies minimum confining reinforcement in RC columns. Despite this, strength-based provisions may not ensure sufficient lateral deformation capacity for columns subjected to high axial loads.

Park[2] proposed that moment-curvature analysis provides a more rational framework for evaluating the relationship between confining reinforcement and deformation capacity in RC columns. This analysis indicates that the confining reinforcement requirements specified in ACI 318-11[1] tend to be overly conservative for columns under low axial loads ($P/A_gf_c' \leq 0.36$) but insufficient for those subjected to high axial loads ($P/A_gf_c' > 0.36$). NZS 3101:2006[3] adopted and further developed Park's concept as the basis for its confinement provisions in RC columns. Experimental studies[4,5] further demonstrate that increasing axial load accelerates the degradation of strength and stiffness in RC columns, thereby reducing their seismic performance. Consequently, the amount of confining reinforcement should be proportionally increased with axial load to maintain both strength and ductility under high axial load conditions.

Design standards such as NZS 3101:2006[3] and CAN/CSA-A23.3-04[6] incorporate axial load parameters into their confining reinforcement formulas to account for the reduced deformation capacity of RC columns under high axial loads. In contrast, ACI 318-11[1] does not modify confining reinforcement with respect to axial load variations. A study by Elwood et al.[7] using 145 column test results from the Pacific Earthquake Engineering Research Center[8] (PEER) found that the ACI 318-11[1] confining reinforcement formula failed to provide adequate deformation capacity for tied columns under high axial loads but was overly conservative for low axial loads. In comparison, the NZS 3101:2006[3] and CAN/CSA-A23.3-04[6] confining reinforcement formulas, which account for axial load effects, resulted in improved deformation behavior.

Following a reevaluation of the PEER structural performance database,[8] Elwood et al.[9] proposed a confining reinforcement formula incorporating the axial load ratio (P/A_gf_c') and confinement effectiveness factor (k_n) to ensure columns retain at least 80% of their maximum lateral strength at a drift ratio of 3%. This recommendation was adopted in ACI 318-14,[10] which requires an increased amount of confining reinforcement for columns subjected to high axial loads ($P_u/A_gf_c' > 0.3$) or constructed with high-strength concrete ($f_c' > 70$ MPa [10.15 ksi]) to ensure adequate deformation capacity. Additionally, ACI 318-14[10] further requires that all longitudinal bars around the perimeter of a column core with rectilinear hoops under high axial loads or constructed with high-strength concrete must be laterally supported by the corner of hoops or by seismic hooks, with horizontal spacing between longitudinal bars not exceeding 200 mm (8 in.). ACI 318-19[11] and ACI CODE-318-25[12] retain the confining reinforcement requirements specified

ACI Structural Journal, V. 123, No. 3, May 2026.
MS No. S-2024-415.R2, doi: 10.14359/51749406, received October 8, 2025, and reviewed under Institute publication policies. Copyright © 2026, American Concrete Institute. All rights reserved, including the making of copies unless permission is obtained from the copyright proprietors. Pertinent discussion including author's closure, if any, will be published ten months from this journal's date if the discussion is received within four months of the paper's print publication.

in ACI 318-14[10] for columns in special moment frames. However, during on-site assembly of column reinforcement cages, longitudinal bars and outer hoops are typically secured first, followed by the placement of crossties. The requirement for 135-degree seismic hooks at both ends of the crossties increases the difficulty of reinforcement assembly.

Shen and Hwang[13] investigated the deformation capacity of high-strength RC columns under high axial loads. Their study used high-strength materials, including longitudinal and transverse reinforcement with design yield strengths of 685 and 785 MPa (99.33 and 113.83 ksi), respectively, and concrete with design compressive strengths of 70 and 100 MPa (10.15 and 14.50 ksi). The applied axial load exceeded $0.42A_g f_c'$. The findings indicated that columns in which every alternate longitudinal bar was laterally supported exhibited poor deformation capacity, whereas columns designed in accordance with ACI 318-19[11] achieved the required seismic performance. Moreover, columns with crossties featuring a single seismic hook performed comparably to those with seismic hooks at both ends, indicating potential improvements in on-site constructability. It is noteworthy that normal-strength materials continue to be the predominant choice for RC construction worldwide. Further experimental studies are necessary to evaluate the feasibility of relaxing confining reinforcement requirements for normal-strength RC columns under high axial loads.

This study investigates the seismic response of five full-scale normal-strength RC column specimens subjected to cyclic lateral loading under constant high axial loads. Given the notable differences in confining reinforcement requirements between ACI 318-11[1] and ACI CODE-318-25,[12] their applicability to normal-strength RC columns was evaluated. This study aims to validate the confining reinforcement requirements specified in ACI CODE-318-25[12] and to evaluate the confinement effectiveness in maintaining adequate seismic performance. To mitigate the construction challenges with crossties featuring seismic hooks at both ends, three alternative configurations are proposed: 1) 135- and 90-degree crossties with alternating hook orientations, providing lateral support to every alternate longitudinal bar; 2) 135- and 135-degree crossties, also providing lateral support to every alternate longitudinal bar; and 3) 135- and 90-degree crossties with alternating hook orientations, providing lateral support to all longitudinal bars.

RESEARCH SIGNIFICANCE

Five full-scale normal-strength RC column specimens were constructed to examine their seismic performance. This study focused on evaluating key factors influencing confinement effectiveness including the amount of confining reinforcement and crosstie configuration. The results validate the applicability of the ACI CODE-318-25 confining reinforcement requirements for normal-strength RC columns under high axial loads. Furthermore, when these requirements are satisfied and all longitudinal bars are fully laterally supported, columns incorporating crossties with alternating 135-degree and 90-degree hooks achieve satisfactory seismic performance. This configuration also improves on-site constructability, particularly in cases of reinforcement congestion.

CONFINING REINFORCEMENT DESIGN EQUATIONS

ACI 318-11[1] requires that the amount of confining reinforcement for RC tied columns must satisfy both of the following equations to ensure sufficient deformation capacity under seismic loading conditions

$$\frac{A_{sh}}{s\,b_c} = 0.3\left(\frac{A_g}{A_{ch}} - 1\right)\frac{f_c'}{f_{yt}} \tag{1}$$

$$\frac{A_{sh}}{s\,b_c} = 0.09\frac{f_c'}{f_{yt}} \tag{2}$$

where A_{sh} is the total cross-sectional area of transverse reinforcement including crossties; s is the center-to-center spacing of transverse reinforcement; b_c is cross-sectional dimension of the column core measured to the outside edges of the transverse reinforcement composing area A_{sh}; A_g is gross cross-sectional area of column; A_{ch} is cross-sectional area of a column measured to the outside edges of transverse reinforcement; f_c' is specified compressive strength of concrete; and f_{yt} is specified yield strength of transverse reinforcement. The maximum value of f_{yt} should not exceed 690 MPa (100 ksi).

However, RC columns designed in accordance with the confining reinforcement specified in ACI 318-11[1] have been reported to exhibit inadequate deformation capacity when subjected to high axial loads.[7] To address this issue, ACI 318-14[10] incorporated the recommendations proposed by Elwood et al.,[9] which required an increased amount of confining reinforcement for columns constructed with high-strength concrete or subjected to high axial loads. When either a high-strength concrete ($f_c' > 70$ MPa [10.15 ksi]) or a high axial load ($P_u > 0.3A_g f_c'$) is considered, the required confining reinforcement must not only satisfy the values specified in Eq. (1) and (2) but must also be evaluated using Eq. (3). The final design adopts the maximum confining reinforcement demand calculated from these three equations.

$$\frac{A_{sh}}{s\,b_c} = 0.2\,k_f k_n \frac{P_u}{f_{yt}A_{ch}} \tag{3}$$

where k_f is concrete strength factor; k_n is confinement effectiveness factor; and P_u is factored axial load. The concrete strength factor k_f and confinement effectiveness factor k_n can be calculated according to Eq. (4) and (5)

$$k_f = \frac{f_c'}{175} + 0.6 \geq 1.0 \ (f_c' \text{ in MPa})$$

$$k_f = \frac{f_c'}{25{,}000} + 0.6 \geq 1.0 \ (f_c' \text{ in psi}) \tag{4}$$

$$k_n = \frac{n_\ell}{n_\ell - 2} \tag{5}$$

Table 1—Design parameters

Specimen ID	Longitudinal reinforcement		Transverse reinforcement				Concrete	Axial load
	ρ_ℓ, %	$f_{y\ell}$, MPa	s, mm	$A_{sh}/s\,b_c$, %	f_{yt}, MPa	Crosstie type	f_c', MPa	$\frac{P}{A_g f_c'}$
N1	2.25	464	100	0.73	462		39.6	0.39
N2		485	120	1.02	441	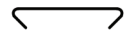	40.4	0.36
N3		464	90	1.27	456	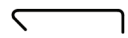	36.2	0.40
N4		464	90	1.27	456	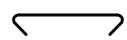	34.5	0.46
N5		464	120	1.02	462	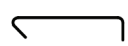	33.8	0.41

Note: 1 MPa = 0.145 ksi; 1 mm = 0.0394 in.

where n_ℓ is number of longitudinal bars laterally supported by the corner of hoops or by seismic hooks that are greater than or equal to 135 degrees.

EXPERIMENTAL PROGRAM

Specimen design

The column specimens in this study were designed to withstand high axial loads and shear forces to evaluate the applicability of ACI CODE-318-25[12] under stringent loading conditions. High axial loads were applied to simulate the behavior of lower-story columns in high-rise buildings, where the axial load demands are high. During seismic loading, the axial forces in columns arise from multi-column frame interaction and vertical ground motion, leading to more complex behavior compared to constant axial load conditions. Ousalem et al.[14] found that columns exhibit lower ductility under constant axial loads than under varying axial loads. On the other hand, if the varied loads include tensile force, the failure mode may shift toward shear-dominated behavior.[15,16] This study focused on evaluating column behavior under constant compressive axial loads. The seismic response of columns subjected to varying axial loads or tensile forces was beyond the scope of this study.

According to ACI CODE-318-25,[12] the required confining reinforcement must be increased to enhance the deformation capacity of columns when the axial load ratio exceeds 0.3. In this study, the applied axial load exceeded this threshold but remained below the maximum axial compressive strength for tied columns ($\phi 0.8 P_0 = 0.52 P_0$; ϕ is strength reduction factor; P_0 is nominal axial strength at zero eccentricity), as specified in ACI CODE-318-25.[12] The column specimens had a height-to-depth ratio (H/h) of 3, which amplifies shear force as the height-to-depth ratio decreased. Cyclic lateral loading was applied using the Multi-Axial Testing System (MATS) at the National Center for Research on Earthquake Engineering (NCREE) in Taipei, Taiwan. The specimens were subjected to double-curvature deformation, generating twice the shear force compared to single-curvature tests.

Each column specimen had cross-sectional dimensions of 600 x 600 mm (23.62 x 23.62 in.) with a clear height (H) of 1800 mm (70.87 in.). Grade 60 steel was used for both longitudinal and transverse reinforcement. The longitudinal reinforcement consisted of 16 uniformly distributed D25 (No. 8) bars, resulting in an area ratio of longitudinal reinforcement of 2.25%. Transverse reinforcement was provided using D13 or D16 (No. 4 or 5) bars arranged at spacing of 100, 120, or 90 mm (3.94, 4.72, or 3.54 in.), corresponding to confining reinforcement ratios (A_{sh}/sb_c) of 0.73%, 1.02%, or 1.27%, respectively. The 0.73% configuration complied with the ACI 318-11[1] requirement based on the greater value of Eq. (1) and (2), whereas the other configurations satisfied ACI CODE-318-25[12] requirement based on the greatest value among Eq. (1), (2), and (3). The specified concrete compressive strength was 30 MPa (4.35 ksi). On the testing day, the actual compressive strength of concrete was determined from the average of three 150 x 300 mm (6 x 12 in.) cylindrical specimens. The axial load ratio for all specimens exceeded 0.36. The design parameters of the column specimen are summarized in Table 1. The detailed reinforcement layouts are illustrated in Fig. 1 and 2. Table 2 presents the provided-to-required ratio (PRR) of the provided confining reinforcement relative to the requirement specified in ACI 318-11[1] and ACI CODE-318-25.[12] This ratio serves as a key indicator of the adequacy of the confining reinforcement in satisfying the confinement demands specified by each Code edition.

To evaluate the necessity of revising the confining reinforcement requirements in ACI 318 (ACI 318-11[1] and ACI CODE-318-25[12]), a comparative study was conducted between Specimens N1 and N2. This comparison aimed to experimentally validate the necessity for increased confining reinforcement and comprehensive lateral support for all longitudinal reinforcement under high axial loads. Specimen N1 was designed following ACI 318-11,[1] which does not account for axial load magnitude in determining confining reinforcement. Consequently, the provided confinement was lower than that required by ACI CODE-318-25.[12] It is worth noting that ACI 318-11[1] does not require lateral support for all longitudinal bars under high axial loads. Instead, it permits a maximum spacing of 350 mm (14 in.) between laterally supported longitudinal bars, which may reduce confinement effectiveness. In Specimen N1, closed hoops provided the lateral support to the corner longitudinal bars, while alternating longitudinal bars were laterally supported by staggered crossties. Each crosstie had a 135-degree seismic hook at one end and a 90-degree bend at the other end, alternating end for end along the longitudinal bars and around the perimeter of the cross section. In contrast, ACI CODE-318-25[12]

Table 2—Provided and required amount of confining reinforcement

Specimen ID	Provided	Required				
		ACI 318-11		ACI CODE-318-25		
	$A_{sh}/s\,b_c$, %	$A_{sh}/s\,b_c$, %	PRR*$_{11}$	n_ℓ	$A_{sh}/s\,b_c$, %	PRR$_{25}$
	(a)	(b)	(c) = (a)/(b)	(d)	(e)	(f) = (a)/(e)
N1	0.73	0.85†	0.86	6	1.33	0.55
N2	1.02	0.91	1.11	16	1.01	1.00
N3	1.27	0.79	1.61	6	1.27	1.00
N4	1.27	0.75	1.69	8	1.24	1.03
N5	1.02	0.73	1.40	10	1.00	1.02

*PRR represents provided-to-required ratio (PRR) of provided and required amount of confining reinforcement.

†Significantly higher concrete compressive strength than specified value results in insufficient PRR.

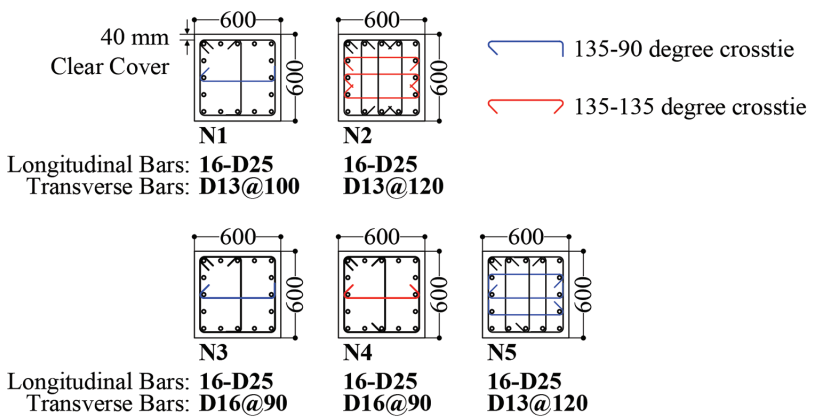

Fig. 1—Specimen cross section.

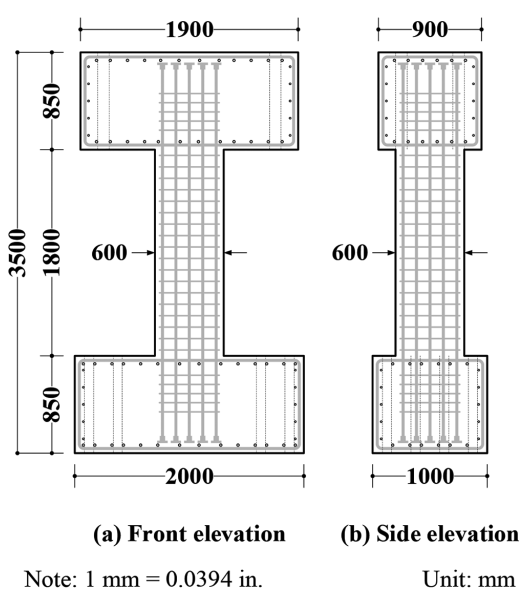

Fig. 2—Geometries of specimens.

requires that when the axial load ratio exceeds 0.3, all longitudinal bars be laterally supported by hoops or seismic hooks to ensure adequate confinement. Specimen N2 was designed in full compliance with ACI CODE-318-25,[12] ensuring that all longitudinal bars were effectively confined by transverse reinforcement.

This study aimed to relax the requirement for crossties with 135-degree seismic hooks at both ends and proposed a concept of increasing the confining reinforcement ratio in accordance with ACI CODE-318-25[12] while providing lateral support to alternating longitudinal bars. This modification was intended to improve on-site constructability without compromising seismic performance. Specimen N3 was designed with a confining reinforcement ratio of 1.27% in accordance with ACI 318-25[12] and maintained the same overall reinforcement layout as Specimen N1. Specimen N4 featured a similar design to Specimen N3 but incorporated crossties with 135-degree seismic hooks at both ends. This variation allowed for a direct comparison of different crosstie configurations while maintaining an identical amount of confining reinforcement.

This study examined the constructability challenges of crossties with seismic hooks at both ends and explored the feasibility of using staggered crossties with a 135-degree seismic hook and a 90-degree bend as an alternative. Specimen N5 was designed to evaluate the seismic performance of this alternative configuration in comparison to Specimen N2. Both specimens complied with ACI CODE-318-25[12] in terms of the required amount of confining reinforcement and provided lateral support to all longitudinal bars. However, Specimen N5 used crossties with alternating 135-degree and 90-degree hook ends. The effective number of longitudinal bars (n_l) laterally supported by the corner of hoops or by

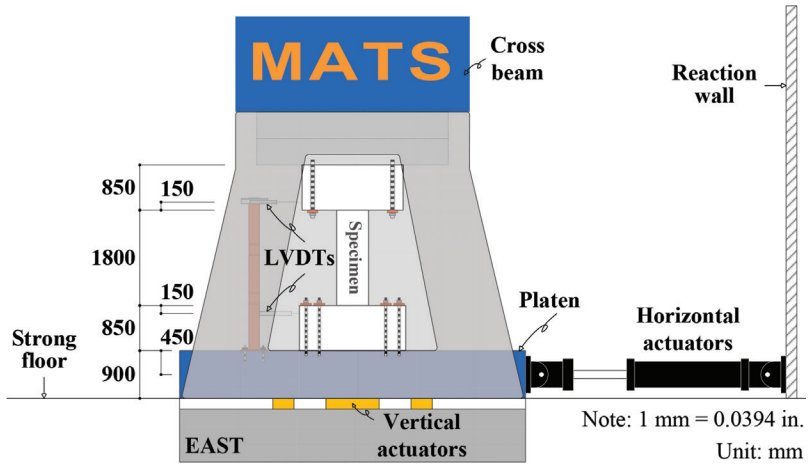

Fig. 3—Test setup.

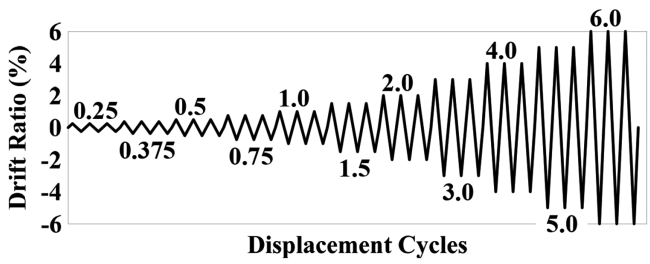

Fig. 4—Loading protocols.

seismic hooks in Specimen N5 was reduced due to the alternative crosstie configuration. Consequently, a slightly higher confining reinforcement was required as a trade-off for the benefit to facilitate construction. All specimens were cast vertically using wooden formwork. Further details regarding the specimen design can be found in the literature.[17]

Test setup

Five full-scale RC column specimens were tested using the MATS at the NCREE in Taipei, Taiwan, as shown in Fig. 3. The MATS has a maximum vertical force capacity of 40 MN (8992 kip) and a horizontal force capacity of 4 MN (899 kip). Each column specimen was subjected to a constant axial load in combination with double-curvature cyclic lateral loading. Once the confining reinforcement and steel and concrete strengths were determined, the magnitude of the applied axial loads was calculated in accordance with Eq. (3), resulting in different axial load ratios among the test specimens. The lateral loading followed the severe test guidelines outlined in ACI 374.1-05.[18] Fully reversed cyclic loading was applied with lateral movements in both forward and backward directions. The target drift ratios were set at 0.25%, 0.375%, 0.5%, and subsequent increments. The drift ratio was defined as the lateral displacement divided by the column clear height. Three loading cycles were performed at each drift level, and the loading protocol is illustrated in Fig. 4. The test was terminated upon the occurrence of either: 1) a sudden loss of axial load-bearing capacity; or 2) an abrupt upward displacement of 20 mm (0.79 in.) in the platen of MATS. Linear displacement transducers were installed to measure lateral displacement throughout the testing process. Additionally, strain gauges were attached to selected longitudinal and transverse reinforcement to capture the strain development during cyclic loading.

EXPERIMENTAL RESULTS AND DISCUSSION

General observations

To monitor crack propagation during testing, blue markers were used to trace cracks formed under positive loading, whereas red markers identified cracks formed under negative loading. Figures 5 through 7 illustrate the crack patterns at different stages: Fig. 5 at the maximum lateral strength, Fig. 6 near the ultimate drift ratio, and Fig. 7 at the final failure condition. The drift ratios shown in Fig. 5 and 6 correspond to the first cycles of the hysteresis responses. For Specimen N1, the maximum lateral strength was recorded at a drift ratio of –1.20%, with compression-induced concrete spalling observed at the upper corners (Fig. 5). As the lateral strength dropped to 80% of its peak value, a central vertical crack widened (Fig. 6), eventually leading to extensive concrete spalling and crushing (Fig. 7). Insufficient confining reinforcement results in hoop detachment from the longitudinal bars, leading to longitudinal reinforcement buckling. Specimen N1 ultimately lost its axial load-bearing capacity during the third cycle of negative loading at a 2.85% drift ratio.

Specimen N2 achieved its maximum lateral strength at a drift ratio of –1.49%. At this stage, concrete spalling occurred at the upper left corner under compression, while extensive cracking developed at the lower left corner (Fig. 5). When the lateral strength degraded to 88% of its peak value, a central vertical crack was observed. As the drift ratio increased, severe concrete crushing and spalling developed at the lower left corner (Fig. 6). By the third cycle at a 4.0% drift ratio, most of the concrete cover had spalled, resulting in longitudinal reinforcement buckling and loss of axial load-bearing capacity (Fig. 7).

For Specimen N3, the maximum lateral strength was achieved at a drift ratio of –1.16%, with minor concrete spalling at the upper corners (Fig. 5). At a drift ratio of 1.84%, the lateral strength had decreased to 80% of its peak value, accompanied by widened inclined cracks and localized concrete crushing and spalling occurred at the corners (Fig. 6). As the drift ratio increased to 2.89%, severe concrete spalling developed while the lateral strength continued

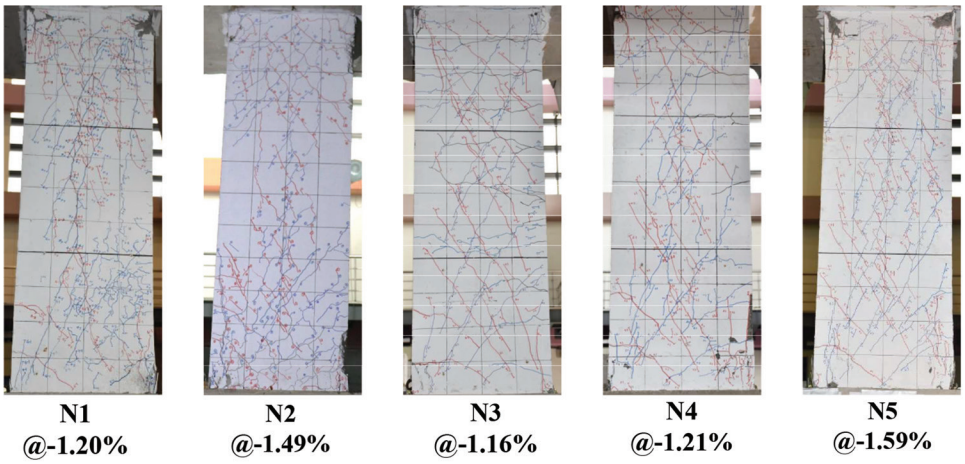

Fig. 5—Crack patterns of specimens at peak load.

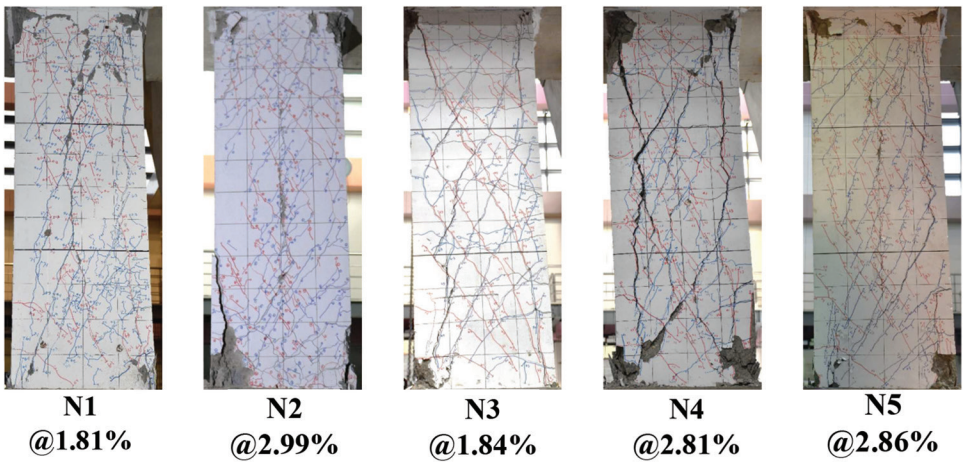

Fig. 6—Crack patterns of specimens near ultimate drift ratio stage.

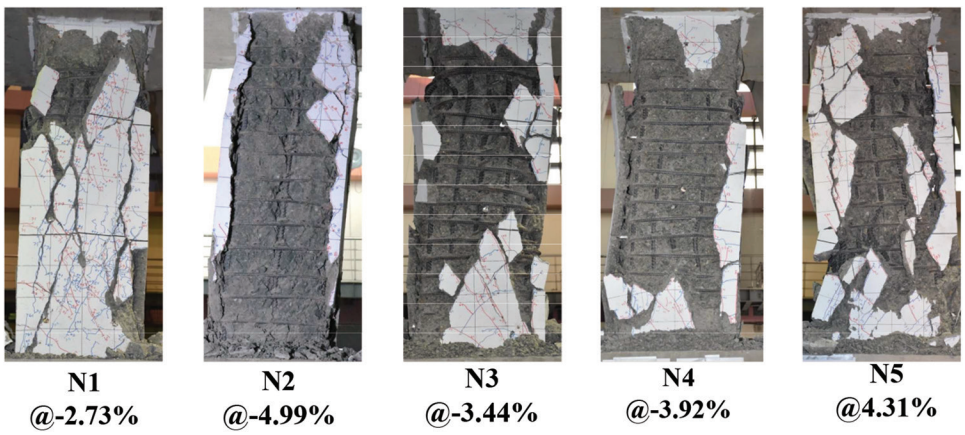

Fig. 7—Crack patterns of specimens at failure.

to degrade. Due to excessive concrete damage and loss of axial load-bearing capacity, the test was terminated before completing the first cycle at a 5.0% drift ratio. Post-test examination revealed hoop detachment and longitudinal bar buckling at both the top and bottom of the column (Fig. 7).

Specimen N4 reached the maximum lateral strength at a drift ratio of –1.21%, with minor concrete spalling at the upper left corner under compression (Fig. 5). When the lateral strength decreased to 80% of its peak value at a drift ratio of 2.81%, severe concrete crushing and spalling occurred at the corners, resulting in concrete cover separation (Fig. 6). The test was terminated after the specimen lost axial load-bearing capacity. Post-test observation revealed that the hoops had detached and longitudinal bar had buckled at both ends of the column specimen (Fig. 7).

Table 3—Summary of test results

Specimen ID	Loading direction	Peak load				Ultimate drift ratio, %
		V_{test} strength, kN	Drift, %	Maximum crack width, mm	Failure mode	
N1	Positive	1814	1.27	0.80	FC*	1.94
	Negative	–1816	–1.20	1.20		–1.75
N2	Positive	1862	1.50	0.40	FC	3.40
	Negative	–1894	–1.49	0.40		–3.04
N3	Positive	1802	1.30	0.55	FC	2.52
	Negative	–1820	–1.16	0.55		–2.23
N4	Positive	1798	1.23	0.50	FC	2.81
	Negative	–1885	–1.21	0.75		–2.30
N5	Positive	1883	1.84	0.55	FC	3.48
	Negative	–1922	–1.59	0.70		–3.07

*Abbreviation "FC" refers to flexural-compression failure mode.

Note: 1 kN = 0.2248 kip; 1 mm = 0.0394 in.

Specimen N5 exhibited the maximum lateral strength at a drift ratio of –1.59%, with concrete spalling at the upper corners due to compression-induced crushing (Fig. 5). As the lateral strength decreased to 80% of its peak value, widespread concrete spalling was observed (Fig. 6). The specimen failed due to extensive spalling of the concrete cover and buckling of the longitudinal reinforcement (Fig. 7), resulting in the loss of axial load-bearing capacity before completing three cycles at a 5.0% drift ratio.

Concrete crushing was observed at the upper corners at the point of the maximum lateral strength in all specimens. This phenomenon may be attributed to the vertical casting of the column specimens, which could have influenced the concrete strength in the compression zones. As the drift ratio increased, progressive concrete crushing led to eventual loss of axial load-bearing capacity. Table 3 summarizes the maximum crack widths observed at peak load for all specimens. Specimen N1 with the lowest amount of confining reinforcement and lateral support provided only to alternating longitudinal bars exhibited the largest crack width. Specimen N2, which fully complied with the confining reinforcement requirements of ACI CODE-318-25[12] and provided full lateral support to all longitudinal bars through transverse reinforcement, showed the smallest crack width. Specimens N3 and N4, which incorporated higher confining reinforcement but provided lateral support only to alternating longitudinal bars, exhibited smaller crack widths than Specimen N1. Specimens N3, N4, and N5 demonstrated comparable crack widths at the maximum lateral strength. However, Specimen N5 reached its maximum lateral strength at a larger lateral drift and maintained a lateral strength plateau compared with the other specimens.

Identification of failure modes

The failure characteristics of the column specimens were identified from the crack patterns shown in Fig. 5 through 7. All specimens failed primarily due to concrete crushing near the flexural-compression zone at peak load, as illustrated in Fig. 5. Figure 6 shows the crack patterns observed after the maximum lateral strength but close to the ultimate drift ratio stage, where the severe concrete crushing occurred at the corners. Although shear cracks were observed at the ends of Specimens N1 and N2, the crack widths did not show significant widening at the ultimate drift ratio stage (Fig. 6). Accordingly, the failure mode was classified as flexural compression rather than flexural shear. Furthermore, the identification of failure characteristics was complemented by the following strength calculations.

The nominal moment strength (M_n) of the column specimens was determined through the cross-sectional analysis. The corresponding flexural strength ($V_{mn} = 2M_n/H$) was calculated under the assumption that the contraflexure point is located at the midheight of the column clear height. The total shear strength (V_n) was evaluated by considering the combined contributions of both the concrete and the transverse reinforcement. The shear strength was estimated using the equation recommended in ASCE/SEI 41-17,[19] which was reconfirmed by ASCE/SEI 41-23.[20] The equation is presented as follows

$$V_n = \alpha_{col}\left(\frac{A_v f_{yt} d}{s}\right) + \left(\frac{0.5\sqrt{f_c'}}{M/Vd}\sqrt{1+\frac{P}{0.5A_g\sqrt{f_c'}}}\right)0.8A_g \ (f_c' \text{ in MPa})$$

$$V_n = \alpha_{col}\left(\frac{A_v f_{yt} d}{s}\right) + \left(\frac{6\sqrt{f_c'}}{M/Vd}\sqrt{1+\frac{P}{6A_g\sqrt{f_c'}}}\right)0.8A_g \ (f_c' \text{ in psi}) \quad (6)$$

where α_{col} is the dimensionless parameter for evaluating the effectiveness of transverse reinforcement in resisting shear forces, with $\alpha_{col} = 1.0$ in this study; A_v is the area of shear reinforcement; d is distance from extreme compression fiber to centroid of tension reinforcement; M/Vd is the largest ratio of moment to shear times effective depth for the column under loadings, but shall not be taken greater than 4 or less than 2; and P is axial force.

The actual yield strengths of the longitudinal and transverse bars listed in Table 1 were used to calculate the nominal moment strength and the shear strength contribution of the transverse reinforcement, respectively. Strain hardening was not considered in these calculations. Table 4 presents the calculated flexural and shear strengths for all specimens. The results indicate that the flexural strength of each specimen was lower than its shear strength, confirming that the failure mechanism was governed by flexure rather than shear. In Table 4, $V_{cal.}$ represents the smaller value of the flexural and shear strengths, while V_{test} denotes the maximum lateral strength recorded in the positive and negative loading directions. The last column in Table 4 shows the ratio of V_{test} to $V_{cal.}$, which ranges from 1.01 to 1.18, indicating that all specimens reached their flexural strength. The shear strength exceeded the maximum lateral strength by at least 12%, reducing the likelihood of shear failure. Strain gauge measurements further confirmed that the outermost longitudinal reinforcement reached its compressive yield strain at the point of the maximum lateral strength.[17] These observations consistently support that the governing failure mechanism was flexural-compression. Consequently, the failure mode was classified as compression-controlled, driven by the combined effects of flexural moment and axial compression force.

Lateral force-drift relationships

All specimens were subjected to high axial loads and cyclic lateral loading, amplifying the P-Δ effect. To correct the hysteresis curve, an equivalent lateral force was determined as the sum of the measured lateral force and the product of the applied axial load and drift ratio.[21] All specimens maintained elastic behavior up to a drift ratio of 0.5% and demonstrated comparable load-displacement responses up to a 1.0% drift ratio. As the drift ratio increased, each specimen reached its maximum lateral strength. Beyond this peak load, most specimens experienced significant strength and stiffness degradation.

The maximum lateral strength of all specimens occurred in the negative loading direction. Table 3 presents the maximum lateral strength in the positive and negative loading directions, along with the corresponding drift ratios, as well as the ultimate drift ratios which are defined as the drift ratios at which the lateral strength degraded to 80% of its peak value. These ultimate drift ratios were determined through linear interpolation. While minor differences were observed in the maximum lateral strength between the positive and negative loading directions, the overall magnitudes were comparable. For instance, Specimen N1 achieved a maximum lateral strength of 1814 kN (407.80 kip) at a drift ratio of 1.27% in the positive loading direction, and –1816 kN (–408.25 kip) at a drift ratio of –1.20% in the negative loading direction. Figures 8 through 10 illustrate the hysteresis loops for each specimen. In these figures, the solid black line represents the load-displacement hysteresis loop (after correction for the P-Δ effect), the dashed gray line represents the hysteresis envelope curve, the red hollow circle (○) marks the maximum lateral strength, the blue cross (+) indicates the ultimate drift ratio, and the green cross (×) denotes the test termination point. (For full-color PDF, visit www.concrete.org.)

According to ASCE/SEI 7-22,[22] a 2% drift ratio is specified as the performance target for the Design Basis Earthquake (DBE), while a 3% drift ratio is specified for the Maximum Considered Earthquake (MCE). ASCE/SEI 7-22[22] defines a structural component as having adequate deformation capacity if its ultimate drift ratio is 3% or higher. In this study, a deformation capacity threshold of 3% was adopted, meaning that columns were required to attain a drift ratio of at least 3% to demonstrate adequate deformation capacity. The hysteresis envelope curves of all specimens are presented

Table 4—Comparisons of calculated strengths and test results

Specimen ID	V_{mn}, kN	V_n, kN	$V_{cal.}$, kN	V_{test}, kN	$\frac{V_{test}}{V_{cal.}}$
N1	1789	2035	1789	1816	1.01
N2	1806	2329	1806	1894	1.05
N3	1703	2647	1703	1820	1.07
N4	1629	2673	1629	1885	1.16
N5	1633	2306	1633	1922	1.18

Note: 1 kN = 0.2248 kip.

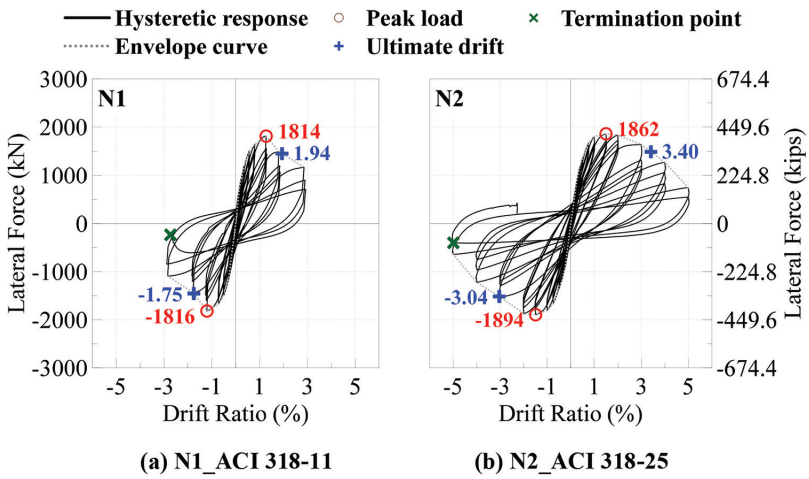

Fig. 8—Hysteresis behaviors of test specimens designed according to different Code versions.

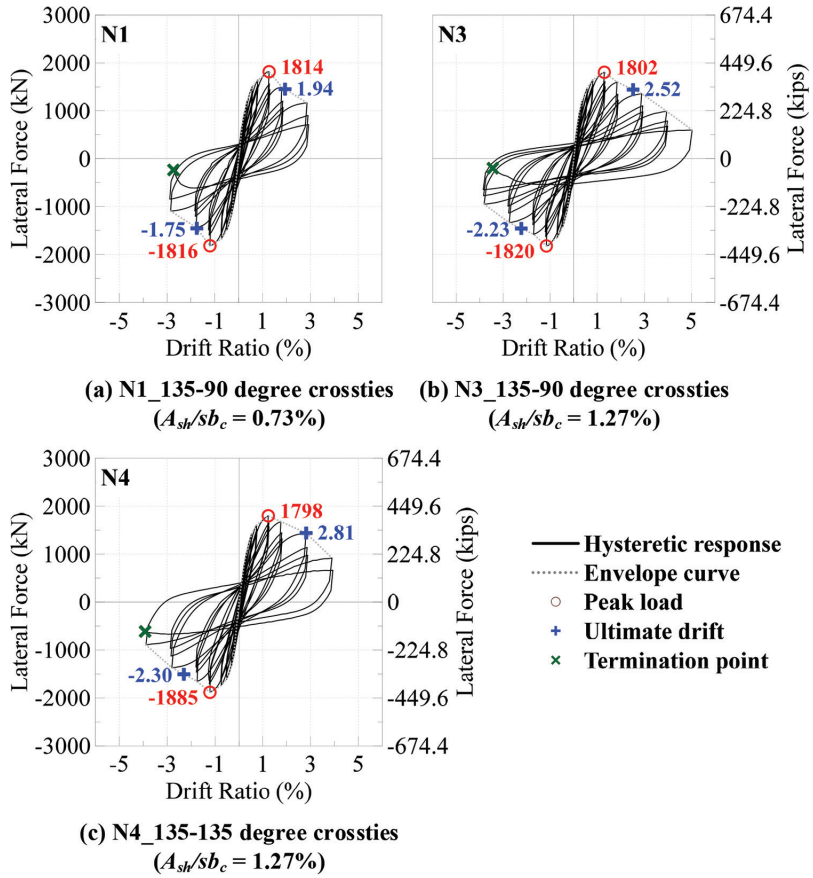

Fig. 9—Hysteresis behaviors of test specimens with alternate lateral support.

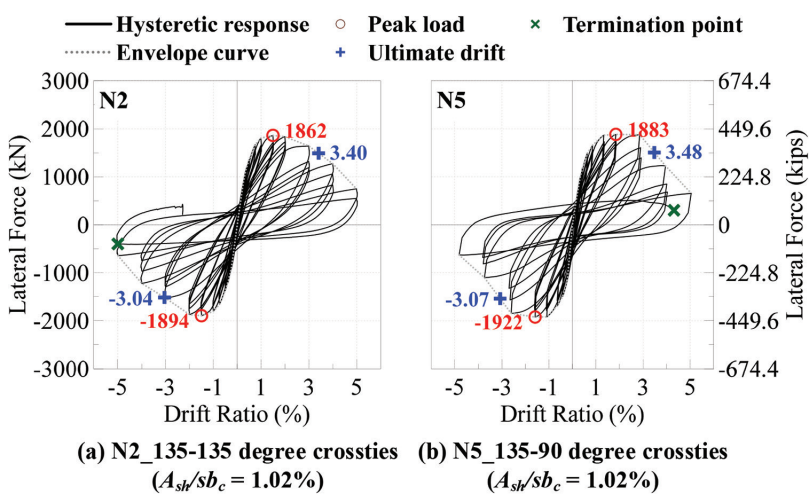

Fig. 10—Hysteresis behaviors of test specimens with full lateral support.

in Fig. 11 for comparison. After reaching the maximum lateral strength, Specimens N1, N3, and N4 exhibited rapid degradation of both strength and stiffness. This deterioration resulted in seismic performance that did not meet the drift ratio target (Fig. 11). The ultimate drift ratios for these specimens did not exceed 3% in either loading direction. In contrast, Specimens N2 and N5 exhibited minimal strength degradation as the drift ratio increased beyond the point of the maximum lateral strength (Fig. 11). Both specimens achieved ultimate drift ratios greater than 3%, demonstrating that the transverse reinforcement effectively preserved its confinement function even after spalling of the concrete cover. A more detailed discussion and comparison of these findings is provided in the subsequent sections.

Discussions on different versions of building codes

Specimens N1 and N2 were tested to evaluate the necessity of the revisions made to the ACI 318 building code (ACI 318-11[1] and ACI CODE-318-25[12]). These specimens differed in the amount of confining reinforcement by approximately 40%, while having similar axial load ratios (0.39 for Specimen N1 and 0.36 for Specimen N2). Before reaching a drift ratio of 1.0%, both specimens exhibited nearly identical load-displacement hysteresis responses, indicating

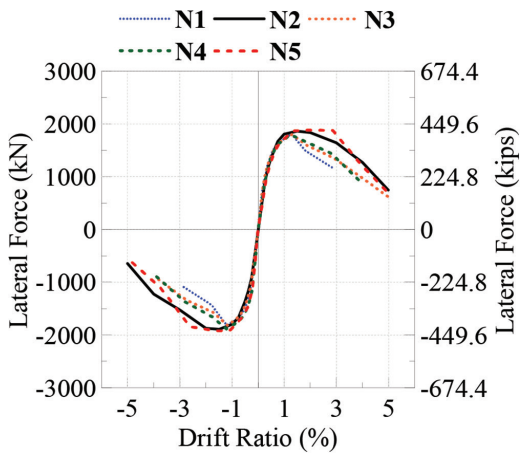

Fig. 11—Hysteresis envelope curves of test specimens.

no significant difference in structural behavior (Fig. 8). However, notable differences appeared at larger drift ratios. Specimen N1 reached its maximum lateral strength at a drift ratio of –1.20%, followed by rapid degradation of both strength and stiffness. Due to insufficient confinement in Specimen N1, the lateral strength had already decreased by 20% when the drift ratio approached 2.0%, as illustrated in Fig. 8(a).

In contrast, Specimen N2 exhibited superior seismic performance, reaching its maximum lateral strength at a drift ratio of –1.49%. At a drift ratio of 2.0%, Specimen N2 experienced less than a 2% reduction in the lateral strength, with significantly slower degradation of strength and stiffness, as shown in Fig. 8(b). This enhanced response is attributed to the adequate amount of confining reinforcement in Specimen N2. On average, the ultimate drift ratio of Specimen N2 was 1.75 times greater than that of Specimen N1. These results confirm that in RC columns subjected to high axial loads, increasing the amount of confining reinforcement and providing lateral support to all longitudinal bars significantly enhances deformation capacity. The findings provide strong experimental validation of the confining reinforcement requirements in ACI CODE-318-25,[12] emphasizing the importance of considering the axial load effects when determining the required confining reinforcement.

Discussion on alternate lateral support

Specimens N1, N3, and N4 were designed with alternate lateral support for longitudinal bars. As illustrated in Fig. 9, the ultimate drift ratios for all three specimens were below 3%, indicating insufficient deformation capacity under high axial load. ACI 318-11[1] did not account for the axial load effects in its design formula for confining reinforcement. In addition, it did not require all longitudinal bars to be laterally supported by crossties with seismic hooks at both ends. As a result, Specimen N1 exhibited poor deformation capacity, achieving ultimate drift ratios of 1.94% and –1.75% in the positive and negative loading directions, respectively. Although Specimen N3 exhibited an ultimate drift ratio over 25% greater than that of Specimen N1, it still failed to reach the 3% deformation capacity threshold, as shown in Fig. 9(a) and (b).

Specimen N3 and N4 incorporated over 70% more confining reinforcement than Specimen N1. As summarized in Table 3, Specimen N3 achieved an average ultimate drift ratio that was 38% higher than that of Specimen N1. However, its deformation capacity remained below the 3% deformation capacity threshold specified by ASCE/SEI 7-22.[22] The limited deformation capacity observed in Specimen N3 can be attributed to the use of crossties with 135-degree seismic hooks at one end and 90-degree hooks at the other end. To address this deficiency, Specimen N4 was designed with crossties featuring 135-degree seismic hooks at both ends, while maintaining the same confining reinforcement ratio as Specimen N3. Both Specimens N3 and N4 satisfied the required amount of confining reinforcement in ACI CODE-318-25.[12] Specimens N3 and N4 exhibited comparable maximum lateral strengths with similar corresponding drift ratios. However, following the maximum lateral strength, both specimens experienced rapid degradation in strength and stiffness, indicating inadequate confinement effectiveness. As a result, neither specimen achieved the 3% deformation capacity requirement, as shown in Fig. 9(b) and (c). Among the three specimens, Specimen N4 using crossties with 135-degree seismic hooks on both ends achieved the highest ultimate drift ratio (2.81% in the positive loading direction and –2.30% in the negative loading direction), as shown in Fig. 9(c). Although this represented an 8% improvement over Specimen N3, the enhancement remained insufficient to meet the 3% deformation capacity threshold.

In summary, even with increased confining reinforcement, RC columns subjected to high axial loads do not achieve the 3% deformation capacity requirement unless all longitudinal bars are fully confined by transverse reinforcement. This finding strongly supports the necessity of ACI CODE-318-25[12] requirement that all longitudinal bars in RC columns subjected to high axial loads must be laterally supported.

Discussion on hooks of crosstie

To evaluate on-site constructability, Specimen N5 was designed to examine the effects of relaxing the requirement for seismic hooks at both ends of the crossties. Its seismic performance was compared with that of Specimen N2, which served as the control specimen. Specimen N2 was configured with the required confining reinforcement in accordance with ACI CODE-318-25[12] and employed crossties with 135-degree seismic hooks at both ends to provide lateral support to all longitudinal bars. The test results for Specimen N2 were consistent with expectations, showing that after reaching the maximum lateral strength, the lateral strength maintained a brief yield plateau before gradually declining, as shown in Fig. 10(a). The ultimate drift ratios in the positive and negative loading directions were 3.40% and –3.04%, respectively.

In contrast, Specimen N5 employed an alternating crosstie configuration with a 135-degree seismic hook at one end and a 90-degree hook at the other end. After reaching its maximum lateral strength, Specimen N5 exhibited a stable lateral strength up to a drift ratio of approximately 2.86%, beyond which rapid strength degradation occurred, as

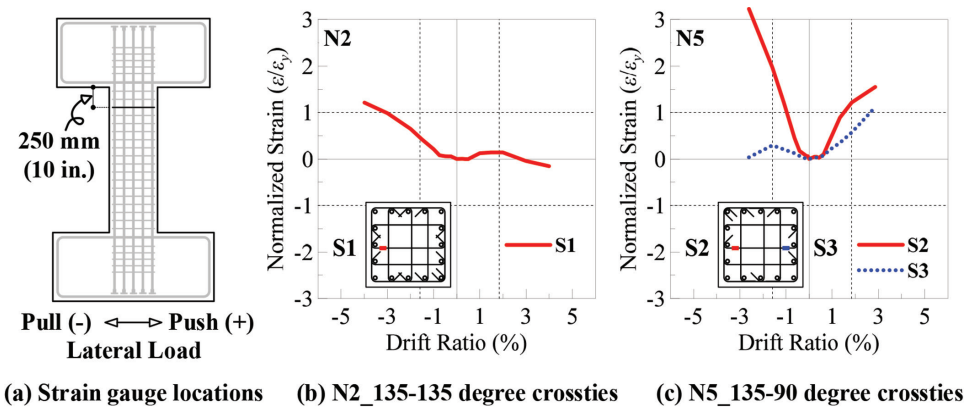

Fig. 12—Normalized strains of crosstie.

shown in Fig. 10(b). Through linear interpolation, the ultimate drift ratios in the positive and negative loading directions exceeded 3%, reaching 3.48% and –3.07%, respectively. These results demonstrate that RC column specimens subjected to high axial loads can achieve adequate deformation capacity even with alternating crosstie hook configurations. This alternative arrangement preserves seismic performance while potentially improving on-site constructability, offering a practical solution for reinforcement detailing in densely reinforced column sections.

The deformations of the crossties in Specimens N2 and N5 are shown in Fig. 12, where strain gauges were installed at the same height, as shown in Fig. 12(a). The maximum tensile strains at each target drift ratio were normalized with respect to the corresponding yield strain. When the loading direction was positive, strain gauges S1 and S2 primarily captured the tensile strain induced by shear forces. In contrast, when the loading direction was reversed, strain gauges S1 and S2 measured the tensile strain resulting from the combined effects of shear forces and confinement. This explains why the tensile strains on the side experiencing both shear forces and confinement were larger than those on the side subjected to shear forces only, as shown in Fig. 12(b) and (c).

In Specimen N2, strain gauge S1 was located at a 135-degree seismic hook end with adjacent hooks also configured as 135-degree seismic hooks, which resulted in lower tensile strain at strain gauge S1. In contrast, strain gauge S2 in Specimen N5 was positioned at a 135-degree seismic hook end but had adjacent 90-degree hook ends, causing the tensile strain to be primarily carried by strain gauge S2 and leading to higher tensile strain. Consequently, the crosstie at the 135-degree seismic hook end in Specimen N5 (strain gauge S2) yielded shortly after drift levels of ±1%, which occurred much earlier than the corresponding crosstie in Specimen N2 (strain gauge S1).

Moreover, the tensile strain recorded at the 135-degree seismic hook end (strain gauge S2) was consistently higher than that at the 90-degree hook end (strain gauge S3), as shown in Fig. 12(c). These results indicate that the confinement effectiveness at the 135-degree seismic hook end is greater than at the 90-degree hook end. Therefore, when columns employ 135- and 90-degree crossties with alternating hook orientations to improve on-site constructability, an increased amount of confining reinforcement is deemed necessary.

Discussion on lateral stiffness

The lateral stiffness at each drift level was evaluated from the envelope of the hysteresis response. It was defined as the slope of the line connecting the maximum lateral strengths from the first cycles in the positive and negative loading directions at given drift level. The stiffness at the *i*-th drift stage was calculated using the following equation

$$K_i = \frac{|P_i^+| + |P_i^-|}{|\Delta_i^+| + |\Delta_i^-|} \tag{7}$$

where P_i^+ and P_i^- denote the maximum lateral strengths at the *i*-th drift stage in the positive and negative loading directions, respectively, and Δ_i^+ and Δ_i^- indicate the corresponding displacements. Figure 13 illustrates the degradation of lateral stiffness throughout the loading history. Specimens N1, N3, and N4, which featured alternate lateral support, exhibited comparable and relatively rapid lateral stiffness degradation, regardless of the increased confining reinforcement. In contrast, slight differences in lateral stiffness degradation were observed between Specimens N2 and N5, both of which provided full lateral support to all longitudinal reinforcement. However, Specimen N2 featuring 135-degree seismic hooks at both ends of the crossties showed better stiffness retention compared to Specimen N5, which used a 135-degree seismic hook at only one end. At the 2.0% drift level, Specimen N2 exhibited the least lateral stiffness degradation, with the ranking from lowest to highest being N2, N5, N4, N3, and N1. Specimen N1 consistently showed the poorest lateral stiffness retention. These findings highlight the importance of full lateral support in enhancing and maintaining lateral stiffness under increasing drift levels. Furthermore, Specimen N5 experienced more rapid degradation in lateral stiffness compared to Specimen N2. As a result, it reached its maximum lateral strength at a larger drift ratio, as reported in Table 3.

CONCLUSIONS

This research conducted quasi-static cyclic tests to evaluate the seismic performance of normal-strength reinforced concrete (RC) column specimens subjected to high

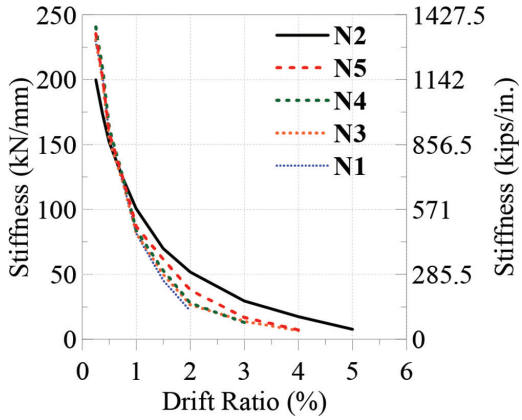

Fig. 13—Stiffness degradation of test specimens.

axial loads. The objective of this study was to evaluate the confining reinforcement requirements of ACI CODE-318-25 and to investigate the feasibility of relaxing the seismic hook requirement. The key test parameters included the amount of confining reinforcement and the crosstie configuration. Specimens were subjected to constant axial load ratios ranging from 0.36 to 0.46. Based on the experimental observations and within the limitations of this study, the following conclusions are proposed:

1. Experimental results confirm that the required amount of confining reinforcement in RC columns should be adjusted proportionally to the applied axial load when it exceeds $0.3A_g f_c'$. Columns subjected to higher axial loads require increased amount of confining reinforcement to achieve desired deformation capacity. The findings validate the essential role of considering axial load effects in determining confining reinforcement requirements specified in ACI CODE-318-25.

2. Test results show that in RC columns subjected to high axial loads, adequate deformation capacity cannot be achieved alone with confining reinforcement unless all longitudinal bars are laterally supported by transverse reinforcement. This emphasizes the importance of complying with both the quantity and detailing requirements specified in ACI CODE-318-25 to enhance column ductility and overall seismic performance.

3. Specimens incorporating crossties with alternating 135-degree and 90-degree hooks to provide lateral support to all longitudinal bars achieved ultimate drift ratios that met the 3% deformation capacity threshold in both loading directions. However, when determining the effective number of confined longitudinal bars (n_l) in accordance with ACI CODE-318-25, only those longitudinal bars laterally supported by 135-degree seismic hooks should be considered. This adjustment necessitates an increase in confining reinforcement to ensure adequate confinement when adopting this crosstie configuration.

4. Specimens employing alternate lateral support for all longitudinal bars exhibited poor lateral stiffness retention even with increased confining reinforcement. In contrast, specimens employing comprehensive lateral support for all longitudinal reinforcement consistently demonstrated slower lateral stiffness degradation than those with alternate lateral support.

5. For those specimens with full lateral support for all longitudinal reinforcement, Specimen N2 featuring 135-degree seismic hooks at both ends of crossties demonstrated better stiffness retention compared to Specimen N5, which incorporated a 135-degree seismic hook at only one end.

6. This study not only validates the confining reinforcement requirements specified in ACI CODE-318-25 but also examines the potential for relaxing the requirement of seismic hooks at both ends of crossties to improve on-site constructability. The findings of this research are consistent with those of previous studies on high-strength RC columns, thereby extending the applicability to normal-strength RC columns.

AUTHOR BIOS

Wen-Cheng Shen *is an Assistant Researcher of the National Center for Research on Earthquake Engineering, Taipei, Taiwan. He received his master's degree from the National Taiwan Ocean University, Keelung, Taiwan. He is currently a PhD Student of civil engineering at National Taiwan University, Taipei, Taiwan. His research interests include seismic evaluation and retrofitting of existing reinforced concrete (RC) structures.*

Shyh-Jiann Hwang, *FACI, is a Professor of civil engineering at National Taiwan University. He received his PhD from the University of California, Berkeley, Berkeley, CA. His research interests include shear behavior of reinforced concrete members and seismic design and retrofitting of RC structures.*

ACKNOWLEDGMENTS

Financial support from Ministry of Science and Technology (MOST) of Taiwan under Grant Number MOST 104-2221-E-002-116- and from National Center for Research on Earthquake Engineering (NCREE) of National Institutes of Applied Research (NIAR) in Taiwan is gratefully acknowledged. The authors also wish to express their appreciation to Tsai W. T. for providing valuable test data. Additionally, the authors thank and acknowledge the NCREE technicians who contributed to this work.

REFERENCES

1. ACI Committee 318, "Building Code Requirements for Structural Concrete (ACI 318-11) and Commentary (ACI 318R-11)," American Concrete Institute, Farmington Hills, MI, 2011, 503 pp.

2. Park, R., "Ductile Design Approach for Reinforced Concrete Frames," *Earthquake Spectra*, V. 2, No. 3, 1986, pp. 565-619. doi: 10.1193/1.1585398

3. NZS 3101.1&2:2006, "Concrete Structures Standard," Standards New Zealand, Wellington, New Zealand, 2006, 754 pp.

4. Watson, S.; Zahn, F. A.; and Park, R., "Confining Reinforcement for Concrete Columns," *Journal of Structural Engineering*, ASCE, V. 120, No. 6, 1994, pp. 1798-1824. doi: 10.1061/(ASCE)0733-9445(1994)120:6(1798)

5. Paultre, P., and Légeron, F., "Confinement Reinforcement Design for Reinforced Concrete Columns," *Journal of Structural Engineering*, ASCE, V. 134, No. 5, 2008, pp. 738-749. doi: 10.1061/(ASCE)0733-9445(2008)134:5(738)

6. CAN/CSA-A23.3-04 (R2010), "Design of Concrete Structures," CSA Group, Toronto, ON, Canada, 2004, 214 pp.

7. Elwood, K. J.; Maffei, J.; Riederer, K. A.; and Telleen, K., "Improving Column Confinement - Part 1: Assessment of Design Provisions," *Concrete International*, V. 31, No. 11, Nov. 2009, pp. 32-39.

8. Berry, M.; Parrish, M.; and Eberhard, M. O., "PEER Structural Performance Database User's Manual (Version 1.0)," Pacific Earthquake Engineering Research Center, University of California, Berkeley, Berkeley, CA, 2004, 43 pp.

9. Elwood, K. J.; Maffei, J.; Riederer, K. A.; and Telleen, K., "Improving Column Confinement - Part 2: Proposed New Provisions for the ACI 318 Building Code," *Concrete International*, V. 31, No. 12, Dec. 2009, pp. 41-48.

10. ACI Committee 318, "Building Code Requirements for Structural Concrete (ACI 318-14) and Commentary (ACI 318R-14)," American Concrete Institute, Farmington Hills, MI, 2014, 520 pp.

11. ACI Committee 318, "Building Code Requirements for Structural Concrete (ACI 318-19) and Commentary (ACI 318R-19) (Reapproved 2022)," American Concrete Institute, Farmington Hills, MI, 2019, 624 pp.

12. ACI Committee 318, "Building Code for Structural Concrete—Code Requirements and Commentary (ACI CODE-318-25)," American Concrete Institute, Farmington Hills, MI, 2025, 702 pp.

13. Shen, W. C., and Hwang, S. J., "Confinement Reinforcement of High-Strength Reinforced Concrete Tied Columns under High Axial Load," *ACI Structural Journal*, V. 120, No. 3, May 2023, pp. 145-155.

14. Ousalem, H.; Kabeyasawa, T.; Tasai, A.; and Ohsugi, Y., "Experimental Study on Seismic Behavior of Reinforced Concrete Columns under Constant and Variable Axial Loadings," *Proceedings of the Japan Concrete Institute*, V. 24, No. 2, 2002, pp. 229-234.

15. Vu, N. S.; Li, B.; and Tran, C. T. N., "Seismic Behavior of Reinforced Concrete Short Columns Subjected to Varying Axial Load," *ACI Structural Journal*, V. 119, No. 6, Nov. 2022, pp. 99-112.

16. Zimos, D. K.; Papanikolaou, V. K.; and Kappos, A. J., "Shear-Critical Reinforced Concrete Columns under Increasing Axial Load," *ACI Structural Journal*, V. 117, No. 5, Sept. 2020, pp. 29-39.

17. Tsai, W. T., "Design of Seismic Confinement of RC Tied Columns," master's thesis, Department of Civil Engineering, National Taiwan University, Taipei, Taiwan, 2016, 276 pp. (in Chinese)

18. ACI Committee 374, "Acceptance Criteria for Moment Frames Based on Structural Testing and Commentary (ACI 374.1-05) (Reapproved 2019)," American Concrete Institute, Farmington Hills, MI, 2005, 9 pp.

19. ASCE/SEI 41-17, "Seismic Evaluation and Retrofit of Existing Buildings," American Society of Civil Engineers, Reston, VA, 2017, 576 pp.

20. ASCE/SEI 41-23, "Seismic Evaluation and Retrofit of Existing Buildings," American Society of Civil Engineers, Reston, VA, 2023, 567 pp.

21. MacRae, G. A., "P-Δ Effects on Single-Degree-of-Freedom Structures in Earthquakes," *Earthquake Spectra*, V. 10, No. 3, 1994, pp. 539-568. doi: 10.1193/1.1585788

22. ASCE/SEI 7-22, "Minimum Design Loads for Buildings and Other Structures," American Society of Civil Engineers, Reston, VA, 2022, 975 pp.

aci Foundation

Building the Future

We're Building the Future

OUR MISSION

We make strategic investments in ideas, research, and people to create the future of the concrete industry.

Through its councils and programs, the ACI Foundation helps to keep the concrete industry at the forefront of advances in material composition, design, and construction.

OUR FOCUS

- Identifying technologies and innovations which provide needed solutions for the concrete industry
- Seeking concrete research projects that further the knowledge and sustainability of concrete materials, construction, and structures
- Supporting our future concrete innovators and leaders by administering fellowships and scholarships
- Helping honorably discharged veterans with our Veterans Rebate for ACI Certification program

www.acifoundation.org

ACI STRUCTURAL JOURNAL TECHNICAL PAPER

Title No. 123-S53

Novel Small-Scale Accelerated Load Test for Assessing Dowel Performance

by Charles A. Donnelly and Julie M. Vandenbossche

Repeated vehicle loading causes a decrease in transverse joint stiffness in concrete pavements due to damage accumulation around dowel bars. The relationship between key design parameters and damage accumulation is not well-established due to limited faulting performance data and a lack of experimental data from expensive full-slab testing. A novel laboratory test setup was developed to characterize damage development caused by repeated vehicle loads. This setup was used to characterize damage for a range of key parameters at a lower cost and level of effort compared to full-scale slab testing. The concept of beam deflection energy, DE_{Beam}, *is also introduced. Experimental results were used to develop a* DE_{Beam} *prediction model. The novel test setup developed in this study enables rapid evaluation of a variety of dowel materials and geometries, and experimental results can be used to improve current faulting prediction performance.*

Keywords: accelerated testing; dowel bars; faulting; performance prediction.

INTRODUCTION

Faulting is a common distress in jointed plain concrete pavements (JPCPs). It is defined as the difference in elevation between the approach and leave slabs (Khazanovich et al. 2004). An effective method to prevent faulting is by increasing joint stiffness through the use of dowel bars. However, dowel performance can decrease over time due to the accumulation of damage to the concrete adjacent to the dowel. This damage develops due to the repeated formation of high bearing stresses between the dowel and surrounding concrete generated as vehicles travel across the transverse joint (Friberg 1938; Marcus 1951). Repeated exposure to high bearing stresses causes fatigue damage in the concrete and introduces looseness around the dowel. Looseness causes a loss in joint stiffness, increasing differential deflections under loading (Teller and Cashell 1959).

Previous studies have evaluated looseness; however, the reduction in joint stiffness caused by repeated vehicle loads is not well-established. Friberg (1938) introduced the modulus of dowel reaction, K, to characterize the stiffness of the dowel-concrete interaction. Static load tests were performed to define a range of K values based on concrete strength, dowel diameter, and applied load (Friberg 1940; Marcus 1951). A significant limitation to these studies is that fatigue damage accumulation from repeated vehicle loading was not considered; the focus was on ultimate load testing. Later studies were performed in which full-scale slab specimens were subjected to repeated vehicle loads. However, only a limited number of replicates were able to be tested (Teller and Cashell 1959; Ciolko et al. 1979). As a result, the relationships between key design and loading parameters and dowel performance have not been established.

A lack of understanding of the fundamental components contributing to the loss of dowel performance has resulted in a number of limitations to the current pavement mechanistic-empirical (ME) faulting prediction model. First, the equations in the pavement ME faulting model that are used to calculate loss of joint performance are empirically derived (Khazanovich et al. 2004). The faulting framework for doweled pavements is coupled to the framework for undoweled pavements due to a lack of mechanistic relationships for dowel performance. This prevented independent adjustment of the faulting prediction between doweled and undoweled pavements (Sachs et al. 2015). Second, the calibration coefficients were determined using field data from both doweled and undoweled pavements due to the insufficient availability of faulting performance data for doweled pavements. Therefore, the calibration coefficients are largely defined by the performance of undoweled pavements (DeSantis et al. 2018). Due to these limitations, the accuracy in predicting faulting is reduced for doweled pavements.

The ability to predict faulting when using alternative dowel materials is significantly impacted by the limitations just defined. Many departments of transportation (DOTs) have considered the use of nontraditional dowel alternatives, including tubular, fiber-reinforced polymer (FRP), and stainless steel dowels (Snyder 2011). These dowels often come with an increased cost and are considered for long-life pavements. The pavement ME faulting model relies on empirically derived relationships from pavements constructed only with conventional epoxy-coated (EC) carbon-steel dowels. Therefore, alternative dowels cannot directly be considered in the current faulting model framework. This prevents agencies from being able to justify the costs associated with the use of these dowels.

There is a need to define the loss of dowel performance as a function of key parameters, such as dowel diameter, dowel stiffness, and applied load. Using currently available experimental processes, this would require a large number of full-scale pavement slabs to be tested (Bruinsma et al. 1995; Khazanovich et al. 2005; Pennsylvania Department of Transportation [PennDOT] 2019). There are no small-scale experimental test setups capable of easily evaluating the loss of performance of various dowels caused by vehicle loads.

The purpose of this study is to develop a novel small-scale laboratory test setup to evaluate damage accumulation

ACI Structural Journal, V. 123, No. 3, May 2026.
MS No. S-2024-430.R3, doi: 10.14359/51749552, received June 6, 2025, and reviewed under Institute publication policies. Copyright © 2026, American Concrete Institute. All rights reserved, including the making of copies unless permission is obtained from the copyright proprietors. Pertinent discussion including author's closure, if any, will be published ten months from this journal's date if the discussion is received within four months of the paper's print publication.

around the dowel due to repeated loads as a function of key design and loading parameters known to affect damage development. The small-scale beam test is designed to replicate bearing stresses around the dowel embedded in the beam that are comparable to those experienced by dowels in full-scale pavement structures under vehicle loading. This laboratory setup is advantageous compared to standard full-slab dowel testing because the cost and labor associated with manufacturing and testing each specimen are greatly reduced, allowing for a larger number of samples to be considered. A series of accelerated loading tests was performed using the test setup to evaluate damage development as a function of key design parameters. Using these results, the concept of beam deflection energy (DE_{Beam}) is introduced to characterize the damage that develops due to repeated vehicle loads. The accelerated load testing results were used to develop a DE_{Beam} prediction equation.

RESEARCH SIGNIFICANCE

Dowels are commonly used in JPCPs; however, the reduction in dowel performance due to damage accumulation is not well-established. This gap in knowledge prevents accurate long-term dowel performance prediction and makes it difficult for state agencies to justify the increased costs associated with alternative dowels. The novel laboratory test developed in this study can be used to better characterize long-term dowel performance without requiring expensive full-slab testing. This is critical because long-term field performance data for long-life dowels are unavailable to date. Additionally, the damage prediction developed using experimental results will be incorporated into the existing faulting model framework to improve faulting prediction and account for nonstandard dowel bars.

EXPERIMENTAL INVESTIGATION

Beam size and load magnitude

The small-scale beam test was designed to replicate the behavior of a dowel subjected to vehicle loads in a full-scale pavement. First, a finite element model of a full-slab system was generated to establish the rotation, deflection, and bearing stresses generated along a dowel subjected to vehicle loads. The full-slab system was designed using the concrete pavement-specific finite element method (FEM) program EverFE (Davids 2003). Second, the small-scale beam test was designed using the general-purpose finite element program Abaqus, so that the deflection and rotation of the pavement surface in the beam test replicated the behavior of the full-slab system (Dassault Systèmes 2013).

Two finite element models were developed. The first was of a full-scale pavement section, and the second was of the beam test. The full-scale model was developed using the two-and-a-half-dimensional (2.5-D) pavement-specific program EverFE to determine the critical bearing stresses that form along the dowel in a full slab. EverFE was selected, in part, because dowels are modeled using independent brick elements, which allows the bearing stresses along the dowel to be calculated (Davids and Turkiyyah 1997). This model consisted of a pavement structure with six 250 mm (10 in.) thick slabs measuring 4.5 x 3.6 m (15 x 12 ft). Dowel diameters of 32 and 38 mm (1.25 and 1.5 in.) were considered in this analysis. The dowels were spaced 30 cm (12 in.) on center along the transverse joint, with the outermost dowels spaced 150 mm (6 in.) from the longitudinal edge of the slab. The modulus of subgrade reaction was 54 MPa/mm (200 psi/in.). The modulus of dowel support, K, was 405 GPa/mm (1.5×10^6 psi/in.) based on values found in the literature (Friberg 1938; Marcus 1951). The elastic modulus of concrete was 28 GPa (4×10^6 psi), and the elastic modulus of steel was 200 GPa (29×10^6 psi). A mesh convergence was performed to determine that an element size of 10 x 12.5 x 12.5 cm (4 x 5 x 5 in.) was sufficient for this analysis.

Several different axle configurations were included in this study to account for the range of vehicle loads present on highways. First, an 80 kN (18 kip) single-axle (SA) and a 160 kN (36 kip) tandem-axle (TA) configuration were considered. These axle configurations and loads correspond to typical vehicles used in the pavement ME design tool (Applied Research Associates, Inc. 2004). In addition, a series of superloads (SL) was considered in this analysis. SLs are characterized by high vehicle weights and unique axle configurations, which have the potential to induce significant damage after just a few load applications. In a previous study, typical SL configurations in Pennsylvania were identified using a series of SL permits provided by PennDOT (Donnelly and Vandenbossche 2021). The SL configurations considered in that analysis are shown in Table 1. Each SL

Table 1—Characteristics of Pennsylvania superloads considered in this study

Vehicle ID	Axle type on trailer, tires per axle	Axle load, kN (kip)	Axle spacing, m (ft)	Distance of outer wheel from lane/shoulder edge, cm (in.)	Gross vehicle weight, kN (kip)
SL1	Tandem, 8	206 (46)	1.6 (5.2)	5 (2)	1646 (360)
SL2	Tridem, 12	241 (54)	1.5 (4.9)	50 (20)	3849 (865)
SL3	Tandem, 8	166 (37)	1.7 (5.6)	5 (2)	2317 (521)
SL4	Single, 4	102 (23)	N/A	60 (24)	2040 (459)
SL5	Tandem, 8	198 (45)	1.8 (5.9)	5 (2)	2361 (531)
SL6	Tandem, 8	187 (42)	1.8 (5.9)	5 (2)	2059 (463)
SL7	Tridem, 12	238 (54)	1.5 (4.9)	50 (20)	3800 (854)
SL8	Single, 4	87 (20)	N/A	60 (24)	2005 (451)
SL9	Tandem, 8	N/A	1.8 (5.9)	5 (2)	N/A
SL10	Tandem, 8	111 (25)	1.8 (5.9)	60 (24)	2079 (467)

Note: N/A is not available.

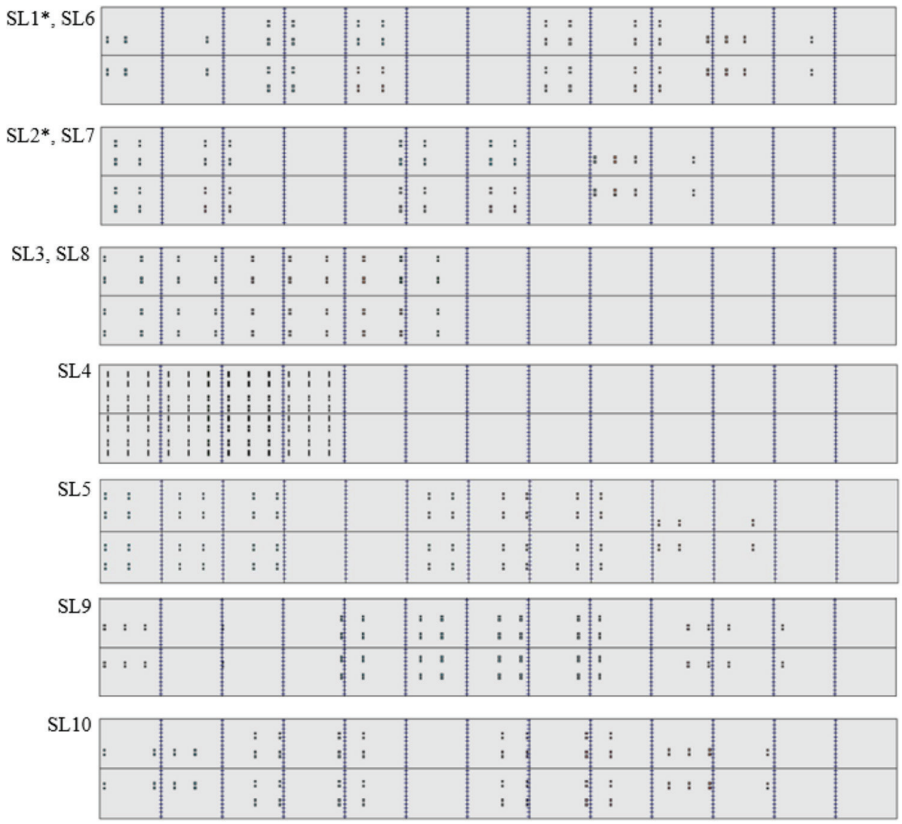

Fig. 1—Superload axle configurations analyzed using EverFE.

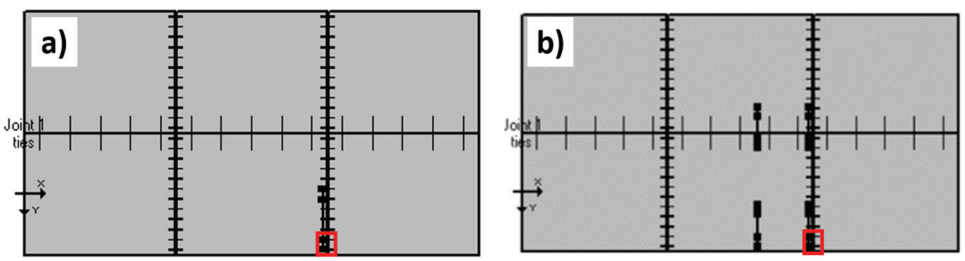

Fig. 2—Example full-slab models for: (a) SA; and (b) SL, with axles placed over critical dowels identified in red. (Full-color PDF can be accessed at www.concrete.org.)

vehicle was modeled using EverFE, as shown in Fig. 1, to find the critical bearing stresses for each dowel at the transverse joint.

Critical bearing stresses for each axle configuration were determined by placing the axle configurations directly above the outermost dowel and adjacent to the transverse joint in the driving lane, as shown in Fig. 2. The bearing stresses were determined along the length of the dowel to determine the critical bearing stress for this axle configuration. SL1, which consisted of 206 kN (46 kip) TAs, generated the greatest bearing stress and was identified as the critical SL. The following load levels were therefore chosen to be included in this laboratory study: a lower load that corresponds to an 80 kN (18 kip) SA, a medium load (ML) level that corresponds to a 160 kN (36 kip) TA, and a high load (HL) level that corresponds to the 206 kN (46 kip) SL.

The critical bearing stresses identified with the EverFE analysis were then used as the target bearing stresses to be imposed in the laboratory doweled beam test. An FEM of the beam was developed using Abaqus. A beam measuring

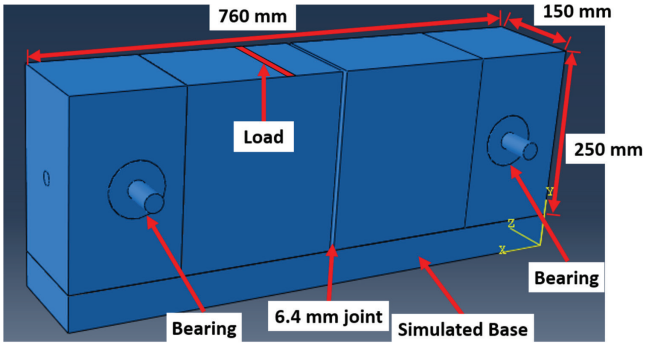

Fig. 3—Schematic of beam model in Abaqus.

760 x 150 x 250 mm (30 x 6 x 10 in.) (length x width x height) was designed with a 6.4 mm (0.25 in.) wide joint at the center of the beam, as shown in Fig. 3. The beam was designed to replicate similar beam tests developed for the evaluation of unbonded concrete overlays (Sachs et al. 2016) and joint performance of concrete pavements

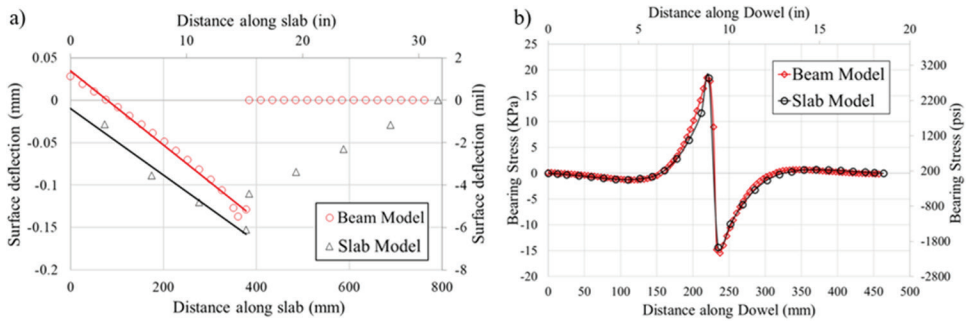

Fig. 4—Example FEM results demonstrating: (a) surface deflections; and (b) that bearing stress profiles along dowel match between full-slab (EverFE) and beam (Abaqus) models.

Table 2—Laboratory loads corresponding to each vehicle

Load ID	Applied load, kN (kip)	Corresponding vehicle load
Low load (LL)	8.9 (2.0)	80 kN (18 kip) SA
Medium load (ML)	13.3 (3.0)	160 kN (36 kip) TA
High load (HL)	17.8 (4.0)	206 kN (46 kip) SL

with fibers (Barman et al. 2019). Restraint conditions were specified such that the resulting rotations, deflections, and bearing stresses were similar between the beam and the full-scale slab. Bearings were placed on each side of the beam to enable the beam to replicate the rotation of the slab that was observed in the full-slab model. The top of the unloaded half of the beam was restrained from rotation and deflection using a vertical clamping system. A line load was specified on the other end of the beam, and the magnitude of the load and distance of the load to the simulated joint were varied until the response (deflection and rotation) of the beam/dowel system replicated that of the slab/dowel system for the axle loads previously defined. A spring interaction with a stiffness of 54 MPa/mm (200 psi/in.) was specified between the base of the beam and the underlying support to replicate the same modulus of subgrade reaction used in the full-slab model. Similarly, the modulus of dowel support, K, was set to 405 GPa/mm (1.5×10^6 psi/in.), which was the same value used in the full-slab model. All material properties for both concrete and steel were identical between the full-scale slab and small-scale beam models.

The model of the beam was constructed using C3D8R elements, which are eight-node linear brick elements with reduced integration. A mesh convergence was performed to ensure sufficient accuracy without requiring extensive computational time. Analyses were run iteratively while refining the mesh in key areas, such as the region of the dowel and surrounding concrete, until changes in the deflection and bearing stress results were deemed negligible.

It was determined that a vertical restraint would be required on the unloaded portion of the beam to replicate these concentrated bearing stresses. With the vertical restraint, the magnitude of the applied line load was adjusted until the bearing stress profile along the length of the dowel matched between the beam and full-slab models. Additionally, it was ensured that the profile of surface deflections on the loaded side of the beam matched between the beam and full-slab models. An example of this is shown in Fig. 4 for a case with a 32 mm (1.25 in.) diameter dowel at an ML level, which is representative of the 160 kN (36 kip) TA. This process was replicated for each of the three load scenarios. The resulting beam loads required to replicate the stress state in the slab along the dowel are shown in Table 2 for each of the three loading scenarios.

Test apparatus, load profile, and data acquisition

The restraint and loading conditions established in the FEM portion of the study were then used to design and fabricate the accelerated dowel test. The test setup is shown in Fig. 5. Bearings were placed on each side of the beam to ensure sufficient rotation of the beam under loading. Each bearing had a calibrated spring torqued to 40 N·m (30 ft·lb), which was established during shakedown testing. A vertical clamp was placed on the unloaded portion of the beam and restrained with four nuts torqued to 20 N·m (15 ft·lb). The clamp provides the restraint required to reflect the boundary conditions in the FEM analysis. Loads were applied to the beam with a 89 kN (20 kip) capacity hydraulic actuator powered by a 230 L (60 gal.) per minute pump. The loading head was machined to ensure a uniform line load was applied across the top surface of the beam, as was applied in the FEM. A 54 MPa/mm (200 psi/in.) modulus of subgrade reaction was simulated using three layers of neoprene vibration- and shock-isolation sheets.

Each specimen was removed from curing conditions once the target compressive strength was obtained. First, the joint was opened and closed prior to initiating the accelerated load testing to simulate joint movement and mobilize the dowel. The joint width was opened from the initial width of 6.4 mm (0.25 in.) to a final width of 12.8 mm (0.5 in.), then closed to the original 6.4 mm (0.25 in.) width. This was performed to ensure the dowel was not bonded to the concrete and that the joint could open and close freely. Next, three layers of the neoprene sheets were placed on a steel platform. The neoprene sheets were positioned in a manner that eliminated seams between sheets and staggered seams between layers. This ensures uniform support is provided beneath the beam. The vertical clamp was then placed on the unloaded side of the beam, and the four nuts were tightened to 20 N·m (15 ft·lb) of torque using a calibrated torque wrench. This ensures uniform and repeatable tightening across the vertical clamp. Next, the bearings were fixed to the beam using a 20 mm (0.75 in.) diameter threaded rod, which ran through

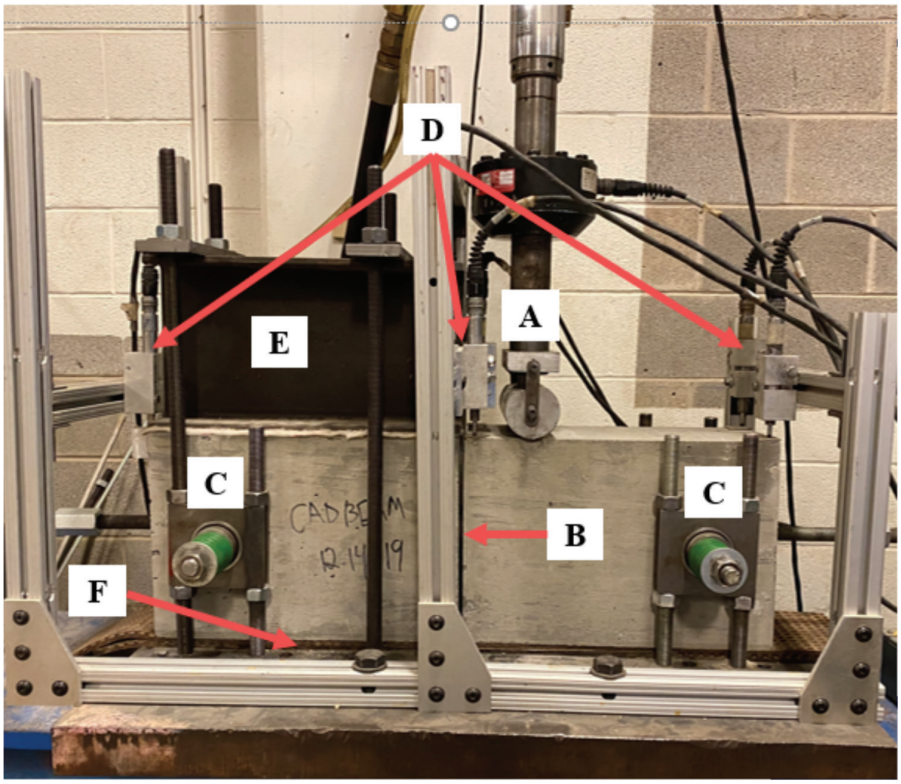

Fig. 5—Accelerated loading dowel test setup consisting of: (a) loading head; (b) simulated joint; (c) bearings; (d) deflection sensors; (e) vertical restraint on unloaded side; and (f) simulated subgrade.

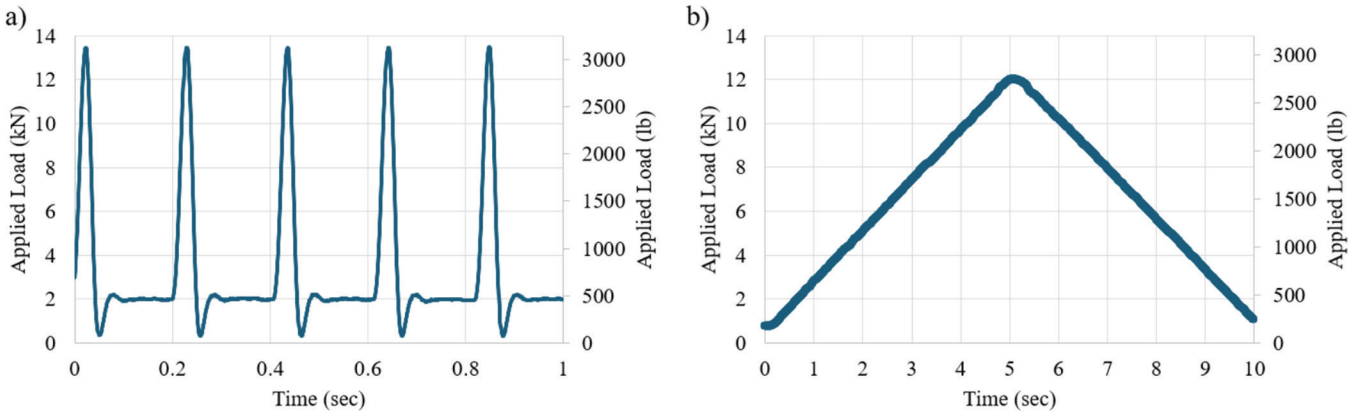

Fig. 6—Loading profiles for: (a) dynamic; and (b) static loading.

a polyvinyl chloride (PVC) pipe cast into the beam on each side of the joint. Calibrated springs maintained equal pressure between the bearing and the specimen. Each spring was compressed by torquing the nuts on the threaded rod to 40 N·m (30 ft·lb).

Lastly, linear variable differential transducers (LVDTs) were positioned to record surface deflections during testing. The LVDTs were fixed in an LVDT frame fabricated from 80/20 aluminum stock. The frame was mounted independently of the load frame to minimize vibration during testing. The frame also ensured that the spacing was maintained between the LVDTs for all tests. Polished aluminum contact plates were epoxied to the surface of the beam prior to testing to ensure that the LVDT remained in constant contact with a smooth surface, as opposed to with the concrete surface. Each LVDT was mounted to the frame, and the vertical position was adjusted until the LVDT output was ±0.125 mm (5 mil) from the midpoint of the reading range. The loading head on the actuator was lowered into position, and the LVDTs were zeroed.

Once the beam was properly secured into the loading apparatus, the accelerated load testing was initiated. The accelerated load testing consisted of two loading profiles, as shown in Fig. 6. These profiles are for an ML case; however, the loading frequency remains the same for HL and low load (LL) cases. The dynamic load simulates a vehicle traveling across a joint at 56 km/h (35 mph). The load profile consists of a haversine wave with a peak load of 8.9, 13.3, or 17.8 kN (2.0, 3.0, or 4.0 kip), depending on the vehicle load simulated. A sustained load of 2 kN (500 lb) was maintained between load cycles to ensure the loading head remained in constant contact with the surface of the beam. The duration

of the loading period was 0.04 seconds, with a rest period of 0.16 seconds, resulting in a total loading rate of 5 Hz. The dynamic loading rate was determined through shakedown testing to ensure the beam would be able to fully rebound after each load was applied prior to the application of the subsequent load. This ensured that load signals did not overlap. A total of two million dynamic loads were applied to each specimen.

Periodically during testing, the dynamic loading was paused to apply static loads. The magnitude of the static load was equal to the magnitude of the dynamic load and consisted of a linear load applied at a rate of 0.1 Hz. Ten consecutive static loads were applied at each collection interval to ensure repeatable results. A rest period of 30 seconds was placed between each static load to allow the simulated subgrade to fully rebound and prevent overlap of the loading signals. Loads and deflections were recorded at 1064 Hz to ensure the resolution of the deflection curves was sufficient. A 28-channel controller was used for controlling the actuator and data acquisition.

Sample fabrication

The 760 x 150 mm (30 x 6 in.) beams were cast using custom-fabricated forms. The thickness of the beams was 150, 200, or 250 mm (6, 8, or 10 in.). An acrylic joint board was placed in the center of the beam, 380 mm (15 in.) from each end, to form a 6.4 mm (0.25 in.) wide joint. The purpose of the joint was to prevent aggregate interlock from occurring and to ensure that the load was transferred only through the dowel. Spanning the two halves of the beam was a 310 mm (12.25 in.) long dowel with the center of the dowel located along the center of the length of the form. The dowel was placed at middepth and laterally centered (75 mm [3 in.] from each side) at mid-beam. Each side of the dowel was fixed to a steel chair with flexible plastic zip ties to ensure the dowel remained properly aligned during casting. A 19 mm (0.75 in.) diameter Schedule 40 PVC pipe was cast 90 mm (15 in.) away from each end, at middepth and perpendicular to the long axis of the beam, to facilitate rotation of the beam at these points.

Prior to placement, the dowels were coated with SAE 30 motor oil, which served as bond-breakers during construction. Each dowel was fully submerged in the oil before being stood on end so that its axis along the dowel was vertical. The dowel was held in this orientation for 30 seconds to allow excess oil to freely drip off the dowel before the dowel was placed in the forms. The motor oil was not applied to the following four specimens because they were the first fabricated and tested: 32EC 250 ML a, 32EC 250 HL a, 38EC 250 ML a, and 38EC 250 HL a. These specimens were coated with form release oil instead of the motor oil; however, it was determined that this form release oil did not provide sufficient lubrication to work as a debonding agent. As a result, it was not possible to open and close these joints prior to the accelerated load testing.

The beams were cast in the laboratory according to ASTM C192/C192M-15 (2015). The mixture design used, shown in Table 3, was selected because it represents a typical paving mixture design with a target compressive strength at the time of testing of 38 MPa (5500 psi). One beam and six to eight 100 x 200 mm (4 x 8 in.) cylinders were cast from each batch of concrete. The compressive strength was measured when the specimen age was 11 days to ensure consistent strength between replicates, and the elastic modulus was measured for most specimens (ASTM C39/C39M-23 [2023]; ASTM C469/469M-22 [2022]). During each cast, concrete was placed in the beams in two lifts. A shaft vibrator was used to eliminate entrapped air voids around the dowel and bearings. Special care was taken to ensure proper consolidation was achieved around the dowel without misaligning the dowel. The target air content was 6 ± 1% with a target slump of 7.6 ± 1.3 cm (3 ± 0.5 in.). Slump and air tests were performed according to ASTM C143/C143M-20 (2020) and ASTM C231/C231M-10 (2010), respectively. All specimens were demolded after 24 hours and cured according to ASTM C192/C192M-15.

Table 3—Mixture design used to cast each load specimen

Material	Weight, kg/m^3 (lb/yd^3)	Volume fraction
Coarse aggregate	1139 (1918)	0.42
Fine aggregate	640 (1078)	0.24
Cement	374 (630)	0.12
Water	157 (265)	0.16
Air content (6%)	—	0.06
High-range water-reducing admixture	88.0 mL per 50 kg of cement (2.5 oz. per 100 lb of cement)	
Water reducer	75.0 mL per 50 kg of cement (2.3 oz. per 100 lb of cement)	
Air entrainer	48.9 mL per 50 kg of cement (3.3 oz. per 100 lb of cement)	

Experimental design

Loss of dowel performance was evaluated as a function of key design and loading parameters, including dowel type, dowel diameter, beam thickness, and load magnitude. A range of dowel designs was considered based on typical materials and diameters used in the field. It was critical that this study include a range of dowel stiffnesses to capture the response when using alternate dowel designs and materials. Three types of dowels were included: solid, EC steel; solid FRP; and EC tubular zinc-galvanized steel dowels (ET).

Dowels with varying stiffnesses were considered in this study. To account for differences in material and dowel design, the concept of equivalent dowel diameter is used. The equivalent dowel diameter, d_{eq}, is calculated for a given dowel by determining the diameter of a solid steel dowel spaced at 30.5 cm (12 in.), which results in the same bearing stress under an applied load. This is calculated using Eq. (1), which is based on the work of Friberg (1938).

$$d_{eq} = \frac{30}{DowelSpace}\sqrt[7]{\frac{d_o^3 \cdot E_{dowel} \cdot \left[\left(d_o\right)^4 - \left(d_i\right)^4\right]}{E_{steel}}} \quad (1)$$

Table 4—Properties of dowels considered in this study

Dowel type	Outer diameter, mm (in.)	Tubular dowel inner diameter, mm (in.)	I, cm^4 (in.^{4})	E, GPa (psi)	Equivalent diameter, mm (in.)
FRP	32 (1.25)	—	5.0 (0.11)	53.8 (7.8 × 10^6)	26 (1.04)
EC	25 (1.0)	—	2.0 (0.05)	200.0 (2.9 × 10^7)	25 (1.00)
ET	34 (1.38)	28 (1.12)	4.1 (0.10)	200.0 (2.9 × 10^7)	32 (1.27)
EC	32 (1.25)	—	5.0 (0.11)	200.0 (2.9 × 10^7)	32 (1.25)
ET	41 (1.63)	35 (1.37)	7.2 (0.17)	200.0 (2.9 × 10^7)	37 (1.47)
EC	38 (1.5)	—	10.3 (0.24)	200.0 (2.9 × 10^7)	38 (1.50)

Table 5—Experimental design for accelerated load study

		Dowel diameter, mm (in.)					
Beam thickness, cm (in.)	Load	25 (1)	32 (1.25)		34 (1.32)	38 (1.5)	41 (1.63)
15 (6)	Low	—	—	—	—		
	Medium	EC	FRP	EC	—		
	High	—	—	—	—		
20 (8)	Low	—	—	EC	—		
	Medium	EC	—	EC	ET		
	High	—	—	EC	—		
25 (10)	Low			—	—	—	—
	Medium			EC	—	EC	ET
	High			EC	—	EC	—

Note: Cells with unrealistic dowel diameter/beam thickness combinations are shaded.

where d_{eq} is the equivalent dowel diameter (mm); *DowelSpace* is the spacing between dowels in the transverse joint (cm); E_{dowel} is the elastic modulus of the dowel (GPa); d_o is the outer diameter of the dowel (mm); d_i is the inner diameter of the dowel (mm); and E_{steel} is the elastic modulus of steel, equal to 200 GPa (29 × 10^6 psi). The measured diameters, elastic moduli, and equivalent dowel diameters for each dowel considered in this study are reported in Table 4.

The following three levels of beam thickness were chosen to correspond to typical highway pavement slab thicknesses: 150, 200, and 250 mm (6, 8, and 10 in.). The thickness of the pavement is typically a consideration when selecting the diameter of the dowel for a JPCP. For example, a 38 mm (1.5 in.) dowel would not be installed in a 150 mm (6 in.) JPCP. Therefore, the various pavement thickness-dowel diameter combinations that would not typically be constructed were eliminated from the experimental design. Additionally, it was deemed unnecessary to test each dowel/thickness combination at each of the three load levels described in Table 2, as this would result in an excessively large experimental design. Based on this, a partial factorial design was developed, resulting in a total of 13 combinations of dowel types and diameters, beam thicknesses, and load levels for inclusion in this study; they are presented in Table 5.

A total of 45 beams were tested in this study. A minimum of two replicates were tested for each combination of factors based on the experimental design presented in Table 5. Additional replicates were tested for several specimens to ensure consistent results. A list of the specimens tested in this study is presented in Table 6. The specimen ID details the combinations of factors tested for each specimen. The first cluster denotes the outer diameter of the dowel in mm and the type of dowel tested (EC, ET, or FRP). The second number is the beam thickness in mm, followed by the load magnitude (LL, ML, or HL). Lastly, the replicate number is denoted alphabetically. For example, the ID "25EC 150 ML a" denotes the first replicate of a 25 mm (1 in.) diameter EC dowel, 150 mm (6 in.) thick beam, and medium load (ML) corresponding to 160 kN (36 kip) TA.

RESULTS AND DISCUSSION

Deflection energy

The concept of beam deflection energy (DE_{Beam}) was developed to quantify the increase in damage accumulation due to repeated vehicle loads throughout the duration of loading. DE_{Beam} is based on the concept of the endurance index (EI), developed to quantify the performance of transverse cracks in jointed reinforced concrete pavements (Raja 1991). The EI is found by calculating the ratio of the area under the plot of load transfer efficiency (LTE) versus the logarithm of the number of applied loads to the area under the plot of LTE = 100% versus the logarithm of the number of applied loads. In this study, DE_{Beam} is defined as the cumulative total deflection area under the loaded and unloaded portions of the beam throughout cyclic loading. To find DE_{Beam}, first, the loaded and unloaded beam slopes are used to determine the area under the loaded and unloaded portions of the beam. This is depicted in Fig. 7. The deflections are normalized to the deflection of the unloaded bearing to

Table 6—Specimen description

Specimen ID	Beam thickness, mm (in.)	Dowel diameter, mm (in.)	Dowel type	Load level	Date cast
25EC 150 ML a	150 (6)	25 (1)	EC	ML	8/12/2021
25EC 150 ML b					12/1/2021
25EC 150 ML c					6/14/2022
25EC 150 ML d					3/14/2023
25EC 200 ML a	200 (8)	25 (1)	EC	ML	8/5/2021
25EC 200 ML b					9/10/2021
25EC 200 ML c					7/20/2022
25EC 200 ML d					2/2/2023
32EC 150 ML a	150 (6)	32 (1.25)	EC	ML	8/17/2021
32EC 150 ML b					6/1/2022
32EC 200 LL a	200 (8)	32 (1.25)	EC	LL	7/6/2021
32EC 200 ML a	200 (8)	32 (1.25)	EC	ML	6/8/2021
32EC 200 ML c					8/26/2021
32EC 200 ML d					10/7/2021
32EC 200 ML e					1/6/2022
32EC 200 ML f					5/26/2022
32EC 200 ML g					3/1/2023
32EC 200 ML h					4/19/2023
32EC 200 HL a	200 (8)	32 (1.25)	EC	HL	6/8/2021
32EC 200 HL b					9/30/2021
32EC 200 HL c					3/20/2023
32FRP 200 ML a	200 (8)	32 (1.25)	FRP	ML	3/24/2022
32FRP 200 ML b					4/21/2022
34ET 200 ML a	200 (8)	34 (1.32)	ET	ML	10/25/2021
34ET 200 ML b					6/23/2022
32EC 250 ML a	250 (10)	32 (1.25)	EC	ML	3/4/2021
32EC 250 ML b					10/28/2021
32EC 250 ML c					1/27/2022
32EC 250 ML d					3/30/2022
32EC 250 ML e					7/13/2022
32EC 250 HL a	250 (10)	32 (1.25)	EC	HL	3/4/2021
32EC 250 HL b					7/19/2021
32EC 250 HL c					9/16/2021
32EC 250 HL d					3/3/2022
32EC 250 HL e					8/1/2022
38EC 250 ML a	250 (10)	38 (1.5)	EC	ML	3/4/2021
38EC 250 ML b					7/27/2021
38EC 250 ML c					2/16/2022
38EC 250 HL a	250 (10)	38 (1.5)	EC	HL	3/4/2021
38EC 250 HL b					5/27/2021
38EC 250 HL c					10/14/2021
38EC 250 HL d					2/2/2022

Table 6 (cont.)—Specimen description

Specimen ID	Beam thickness, mm (in.)	Dowel diameter, mm (in.)	Dowel type	Load level	Date cast
41ET 250 ML a	250 (10)	41 (1.63)	ET	ML	9/2/2021
41ET 250 ML b					11/18/2021
41ET 250 ML c					3/17/2022

Note: Specimens in bold were cast without greasing dowel; EC denotes solid epoxy-coated dowels, FRP denotes solid fiber-reinforced polymer dowels, and ET denotes epoxy-coated tubular dowels; LL denotes low load corresponding to 8.9 kN (2.0 kip) SA, ML denotes medium load corresponding to 13.3 kN (3.0 kip) TA, and HL denotes high load corresponding to 17.8 kN (4.0 kip) SL.

Table 7—DE_{Beam} at two million loads for each specimen

	DE_{Beam} at two million cycles									
Case \ Replicate	Average	Standard deviation	a	b	c	d	e	f	g	h
32EC 150 ML	1184	122	1258	1267	1006	1203	—	—	—	—
25EC 200 ML	1053	91	1107	1139	936	1029	—	—	—	—
32EC 150 ML	963	—	1046	880	—	—	—	—	—	—
32EC 200 LL	548	—	548	—	—	—	—	—	—	—
32EC 200 ML	955	136	946	—	1028	1095	1109	841	937	733
32EC 200 HL	1309	303	1268	1630	1029	—	—	—	—	—
32FRP 200 ML	1328	—	1197	1459	—	—	—	—	—	—
34ET 200 ML	1007	—	1024	990	—	—	—	—	—	—
32EC 250 ML	867	111	756	1019	848	937	777	—	—	—
32EC 250 HL	1258	171	1371	1438	1323	1040	1119	—	—	—
38EC 250 ML	613	32	595	649	595	—	—	—	—	—
38EC 250 HL	1024	137	912	917	1072	1196	—	—	—	—
41ET 250 ML	785	67	851	787	717	—	—	—	—	—

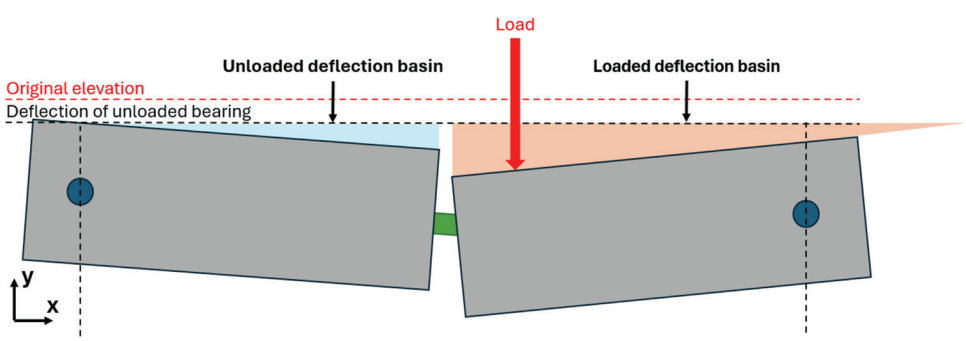

Fig. 7—Loaded and unloaded deflection basins illustrated for beam specimen.

remove any effects of differential settling of the beam under loading. The total deflection basin is calculated by summing the unloaded and loaded deflection basins. DE_{Beam} is found by integrating the total deflection with respect to the logarithm of the number of applied cycles, as shown in Eq. (2)

$$DE_{Beam} = \int_{\mathrm{Log1}}^{\mathrm{Log}N} (Basin_{Loaded} + Basin_{Unloaded}) d(\mathrm{Log}N) \quad (2)$$

where DE_{Beam} is the beam deflection energy; N is the number of applied loads; $Basin_{Loaded}$ is the deflection basin under the loaded portion of the beam, as shown in Fig. 7; and $Basin_{Unloaded}$ is the deflection basin under the unloaded portion of the beam, as shown in Fig. 7.

DE_{Beam} was determined at each of the test intervals defined in Table 3 for the 45 specimens tested, and the average and standard deviation of DE_{Beam} across replicates for a given combination of factors were then calculated. The ultimate DE_{Beam} is defined as the DE_{Beam} calculated at two million loads and is provided in Table 7 for each specimen. Plots of the average DE_{Beam} versus the logarithm of load cycles are shown in Fig. 8 to 18 for groupings of design and load parameters. Visual inspection of the figures indicates that outer dowel diameter, equivalent dowel diameter, and load magnitude may be significant factors that affect DE_{Beam}.

Slab thickness—Based on the trends shown in Fig. 9, beam thickness does not appear to significantly affect DE_{Beam} for the range of beam thicknesses and dowel diameters

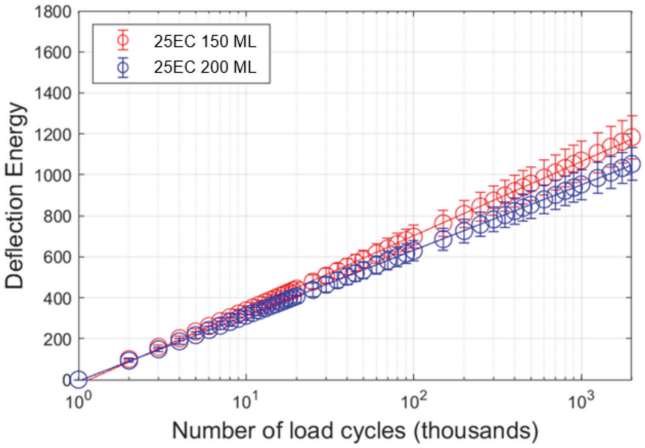

Fig. 8—Average DE_{Beam} *for 25 mm (1.0 in.) diameter EC dowels in 150 and 200 mm (6 and 8 in.) beams with ML magnitude.*

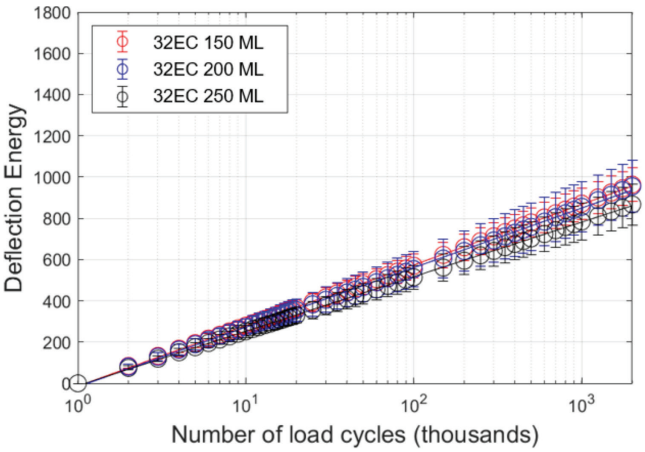

Fig. 9—Average DE_{Beam} *for 32 mm (1.25 in.) diameter EC dowels in 150, 200, and 250 mm (6, 8, and 10 in.) beams with ML magnitude.*

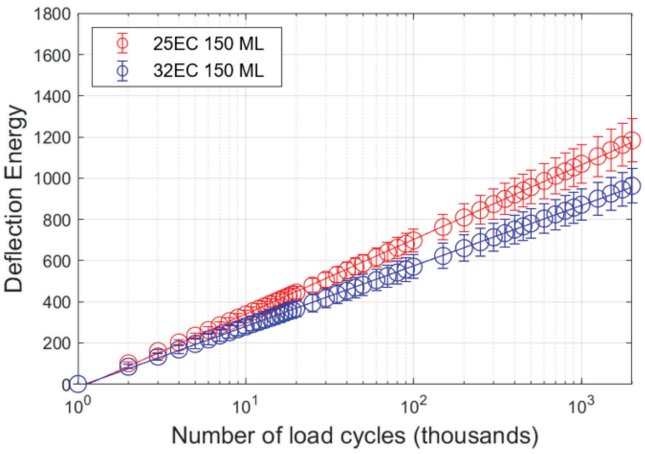

Fig. 10—Average DE_{Beam} *for 25 and 32 in. (1 and 1.25 in.) diameter EC dowels in 150 mm (6 in.) beams with ML magnitude.*

considered in this analysis. While Fig. 9 shows a slight difference in performance between the 150 and 200 mm (6 and 8 in.) beams with 25 mm (1 in.) diameter dowels, this may in part be due to the limited number of replicates tested.

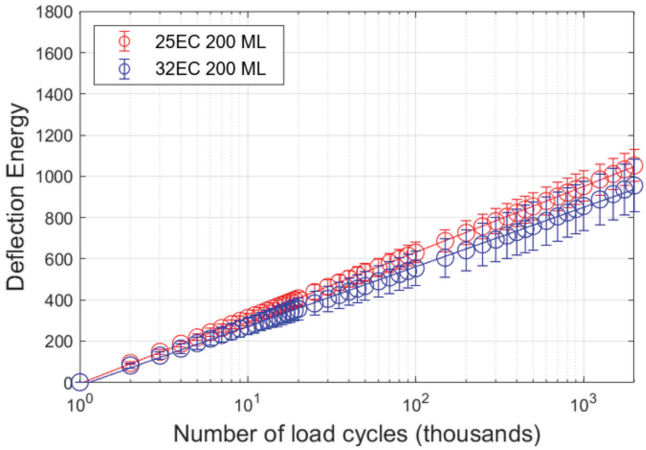

Fig. 11—Average DE_{Beam} *for 25 and 32 mm (1 and 1.25 in.) diameter EC dowels in 200 mm (8 in.) beams with ML magnitude.*

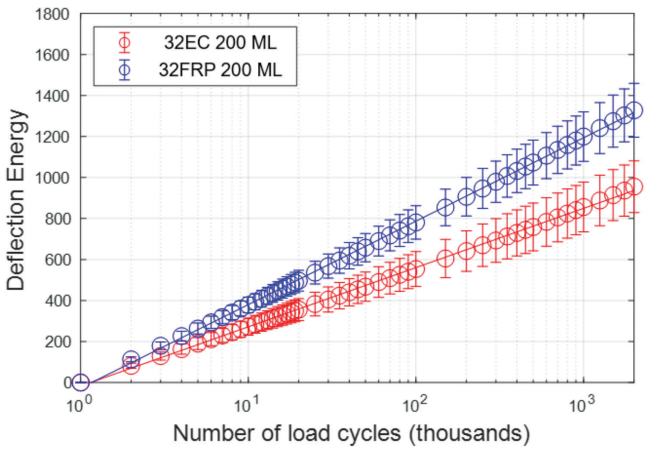

Fig. 12—Average DE_{Beam} *for 32 mm (1.25 in.) EC (*d_{eq} *= 32 mm [1.25 in.]) and FRP (*d_{eq} *= 26 mm [1.04 in.]) dowels in 200 mm (8 in.) beams with ML magnitude.*

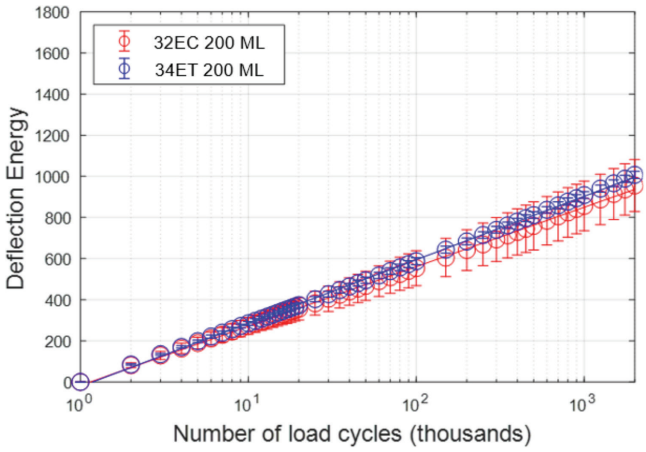

Fig. 13—Average DE_{Beam} *for 32 mm (1.25 in.) diameter EC (*d_{eq} *= 32 mm [1.25 in.]) and 34 mm (1.32 in.) diameter ET (*d_{eq} *= 32 mm [1.27 in.]) dowels in 200 mm (8 in.) beams with ML magnitude.*

A statistical analysis, which will be discussed subsequently, did not indicate any statistical significance when comparing results with different beam thicknesses.

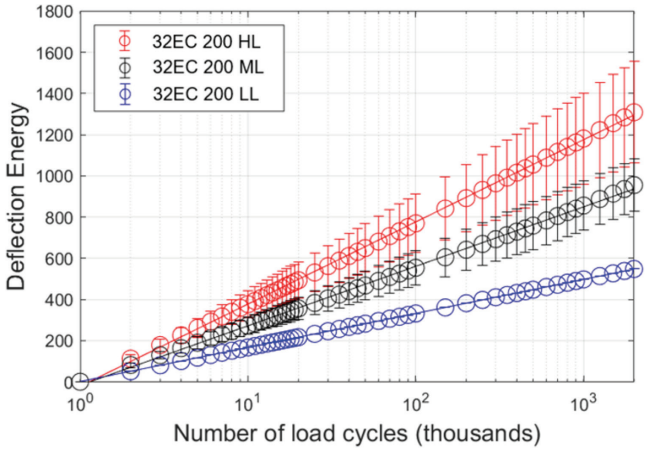

Fig. 14—Average DE_{Beam} *for 32 mm (1.25 in.) diameter EC dowels in 200 mm (8 in.) beams with LL, ML, and HL magnitudes.*

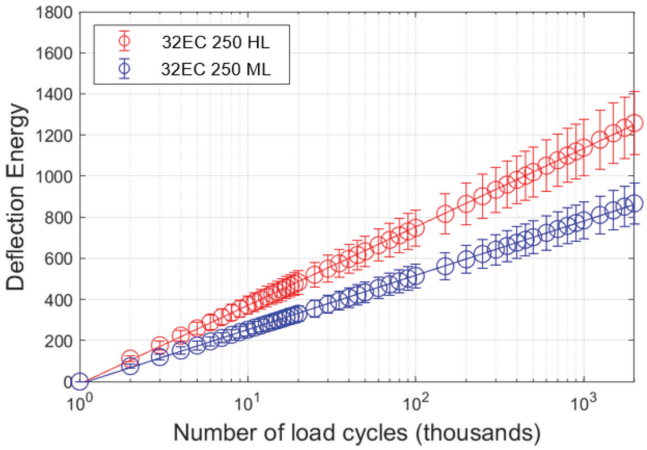

Fig. 15—Average DE_{Beam} *for 32 mm (1.25 in.) diameter EC dowels in 250 in. (10 in.) beams with ML and HL magnitudes.*

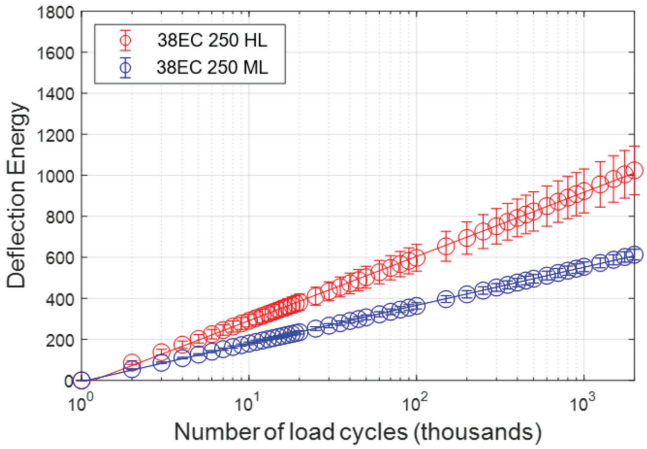

Fig. 16—Average DE_{Beam} *for 38 mm (1.5 in.) diameter EC dowels in 250 mm (10 in.) beams with ML and HL magnitudes.*

Dowel diameter and stiffness—For EC dowels, decreases in DE_{Beam} with increasing dowel diameter were observed after two million cycles when load magnitude remained constant, as seen in Fig. 10, 11, and 17. Increasing the dowel diameter from 25 to 32 mm (1 to 1.25 in.) resulted in a 19%

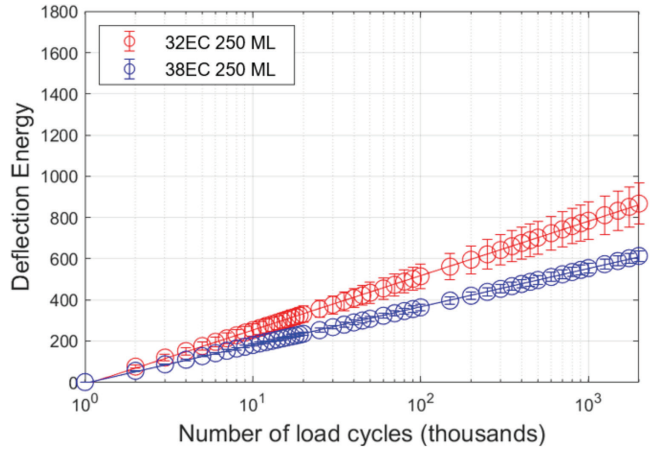

Fig. 17—Average DE_{Beam} *for 32 and 38 mm (1.25 and 1.5 in.) diameter EC dowels in 250 in. (10 in.) beams with ML magnitude.*

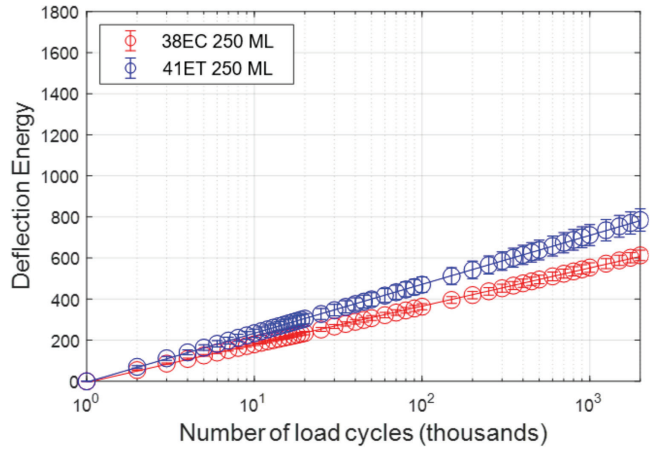

Fig. 18—Average DE_{Beam} *for 38 mm (1.5 in.) EC (*d_{eq} *= 38 mm [1.5 in.]) and 41 mm (1.63 in.) ET (*d_{eq} *= 37 mm [1.47 in.]) dowels in 250 mm (10 in.) beams with ML magnitudes.*

reduction in average DE_{Beam} after two million load cycles. Increasing the dowel diameter from 32 to 38 mm (1.25 to 1.5 in.) resulted in a 36% reduction in average DE_{Beam} after two million load cycles. Increasing the dowel diameter from 34 to 41 mm (1.32 to 1.63 in.) resulted in a 22% reduction in average DE_{Beam} after two million load cycles. This is explained by the increase in stiffness achieved with larger-diameter ET dowels. To further evaluate the effect of dowel stiffness, the effect of equivalent dowel diameter is evaluated. The average DE_{Beam} for 32 mm (1.25 in.) FRP dowels (d_{eq} = 26 mm [1.04 in.]) was 39% higher than the average DE_{Beam} for 32 mm (1.25 in.) EC dowels after two million load cycles with the ML magnitude. The average DE_{Beam} is comparable throughout testing for 34 mm (1.32 in.) ET dowels (d_{eq} = 32 mm [1.25 in.]) and 32 mm (1.25 in.) EC dowels (stiffness = 3.6×10^5 kN·mm [3.2×10^6 lb·in.]). Interestingly, the average DE_{Beam} for 41 mm (1.63 in.) ET dowels (d_{eq} = 37 mm [1.47 in.]) was 28% higher than the average DE_{Beam} for 38 mm (1.5 in.) EC dowels after two million load cycles with the ML magnitude. This suggests that relating the stiffness of dowel bars is effective for most diameters of dowels considered in the study. The slight difference in d_{eq}

for the larger-diameter dowels appears to have a more significant effect. This could be in part due to the limited number of 41 mm (1.63 in.) ET dowels tested in this study.

Load magnitude—Load magnitude significantly affected DE_{Beam} throughout testing, as shown in Fig. 14 and 16. For 32 mm (1.25 in.) EC dowels in a 200 mm (8 in.) beam, increasing the load magnitude from the LL (80 kN [18 kip] SA) to the ML (160 kN [36 kip] TA) resulted in a 74% increase in DE_{Beam} after two million load cycles. For 32 mm (1.25 in.) EC dowels in a 200 mm (8 in.) beam, increasing the load magnitude from the ML (160 kN [36 kip] TA) to the HL (206 kN [46 kip] SL) resulted in a 37% increase in DE_{Beam} after two million load cycles. Similarly, increasing the load magnitude of 38 mm (1.5 in.) EC dowels in a 250 mm (10 in.) beam, from the ML (160 kN [36 kip] TA) to the HL (206 kN [46 kip] SL), resulted in a 67% increase in DE_{Beam} after two million load cycles.

To confirm the trends visually identified in Fig. 8 to 18, two-way hypothesis testing was performed. The significance between different levels of load magnitude, dowel diameter, beam thickness, and dowel stiffness was tested using Fisher's least significant difference (LSD) method. The null hypothesis is that the average ultimate DE_{Beam} is equal for each pair evaluated. The pairwise testing results are shown in Table 8. The confidence level is 95%, and comparisons that are statistically significant are identified in bold.

No comparison between the beam thicknesses evaluated in this study is found to be statistically significant, which supports the trends observed in the DE_{Beam} plots. However, this could be due to the larger number of dowels tested in 200 and 250 mm (8 and 10 in.) thick beams. Several comparisons between dowel diameters were found to be significant. Significant comparisons occur between pairs of dowels with large differences in diameters, such as the 25 and 38 mm (1 and 1.5 in.) dowels, 25 and 41 mm (1 and 1.63 in.) dowels, and 32 and 38 mm (1.25 and 1.5 in.) dowels. The effect of equivalent dowel diameter is found to be statistically significant. For example, DE_{Beam} for 32 mm (1.25 in.) FRP (d_{eq} = 26 mm [1.04 in.]) versus 38 mm (1.5 in.) EC is statistically different; however, DE for 8.3×10^4 kN·mm (7.3×10^5 lb·in.) 32 mm (1.25 in.) FRP versus 3.6×10^5 kN·mm (3.2×10^6 lb·in.) 32 mm (1.25 in.) EC is not statistically different. However, these results may be affected by the fact that some dowel types were tested with both ML and HL magnitudes. Therefore, the confounding effects of stiffness and load magnitude may prevent direct comparisons between levels of dowel diameter and dowel stiffness. This is one explanation for why the pronounced visual difference in performance between 32 mm (1.25 in.) FRP versus 32 mm (1.25 in.) dowels did not prove to be statistically significant.

To eliminate the effect of load magnitude on the comparisons between dowel diameter and dowel stiffness, pairwise comparisons were made using data filtered to only include results from specimens loaded at the ML level, which corresponds to a 160 kN (36 kip) TA. Similar to the previous analysis, the significance between different levels of dowel diameter and dowel stiffness is evaluated using Fisher's LSD method. The null hypothesis is that the average ultimate DE_{Beam} is equal for each pair evaluated. The pairwise

Table 8—Pairwise comparison results from hypothesis testing of different parameters for DE_{Beam}

		p-value	
Parameter	Comparison	All specimens	Medium load only
Beam thickness, mm (in.)	150 versus 200 (6 versus 8)	0.620	—
	150 versus 250 (6 versus 10)	0.142	—
	200 versus 250 (8 versus 10)	0.156	—
Dowel diameter, mm (in.)	25 versus 32 (1 versus 1.25)	0.494	**0.040**
	25 versus 34 (1.25 versus 1.32)	0.538	0.368
	25 versus 38 (1 versus 1.5)	**0.026**	**0.000**
	25 versus 41 (1 versus 1.63)	**0.035**	**0.003**
	32 versus 34 (1.25 versus 1.32)	0.775	0.783
	32 versus 38 (1.25 versus 1.5)	**0.038**	**0.001**
	32 versus 41 (1.25 versus 1.63)	0.057	0.058
	34 versus 38 (1.32 versus 1.5)	0.384	**0.009**
	34 versus 41 (1.32 versus 1.63)	0.287	0.123
	38 versus 41 (1.5 versus 1.63)	0.688	0.180
Equivalent dowel diameter, mm (in.)	26 versus 25 (1.04 versus 1.00)	0.228	**0.030**
	26 versus 32 (1.04 versus 1.25)	0.068	**0.000**
	26 versus 37 (1.04 versus 1.47)	**0.009**	**0.000**
	26 versus 38 (1.04 versus 1.50)	**0.009**	**0.000**
	25 versus 32 (1.00 versus 1.25)	0.319	**0.001**
	25 versus 37 (1.00 versus 1.47)	**0.028**	**0.000**
	25 versus 38 (1.00 versus 1.50)	**0.021**	**0.000**
	32 versus 37 (1.25 versus 1.47)	0.072	**0.048**
	32 versus 38 (1.25 versus 1.50)	0.057	**0.000**
	37 versus 38 (1.27 versus 1.50)	0.675	0.080
Load	LL versus ML	0.058	—
	LL versus HL	**0.005**	—
	ML versus HL	**0.002**	—

Note: Bold font indicates comparisons that are statistically significant.

testing results are shown in the last column of Table 8. The confidence level is 95%, and comparisons that are statistically significant are identified in bold. These results indicate that d_{eq} is significant for all comparisons between d_{eq} levels except for the comparison between 41 mm (1.63 in.) ET (d_{eq} = 37 mm [1.47 in.]) and 38 mm (1.5 in.) EC (d_{eq} = 38 mm [1.5 in.]). When evaluating outer dowel diameter, it is determined that differences in dowel diameter are not significant when multiple equivalent dowel diameter values were evaluated for the same outer dowel diameter. For example, 32 and 41 mm (1.25 and 1.63 in.) diameter dowels were not found to be statistically significant, which is likely because the stiffness of the 32 mm (1.25 in.) diameter dowels varied significantly between the FRP (d_{eq} = 26 mm [1.04 in.]) and EC (d_{eq} = 32 mm [1.25 in.]) dowels. The equivalent dowel diameter incorporates the dowel diameter and material parameters, and these results indicate that the equivalent dowel diameter is a more comprehensive metric for evaluating average DE_{Beam}.

Increasing the dowel diameter results in decreases in the DE_{Beam} standard deviation when the load magnitude is held constant. For the 250 mm (10 in.) beams tested with the ML magnitude (160 kN [36 kip] TA), the DE_{Beam} standard deviation for the 38 mm (1.5 in.) EC was 71% lower than for the 32 mm (1.25 in.) EC specimens after two million load applications. Similarly, for the 250 mm (10 in.) beams tested with the HL magnitude (206 kN [46 kip] SL), the DE_{Beam} standard deviation for the 38 mm (1.5 in.) EC was 20% lower than for the 32 mm (1.25 in.) EC specimens after two million load applications. These results indicate that increasing dowel diameter minimizes variability between replicates, which could be due to a decrease in the effect of concrete flaws. Larger-diameter dowels distribute the bearing stress over a greater surface area of the concrete, thereby bridging across flaws such as small cracks or voids that may be present in the concrete. Where a smaller-diameter dowel is present, applied loads may result in lower stress concentrations at flaws. Any variation in flaw size or frequency between replicates would be more pronounced if the dowel diameter is smaller. These results clearly show that one effect of increasing dowel diameter is the decrease in the variability in DE_{Beam} results.

DOWEL DAMAGE PREDICTION

The results from the accelerated load testing were used to develop a dowel damage model, which accounts for loss of dowel performance due to repeated vehicle loading. The DE_{Beam} calculated for the laboratory specimens is used as the damage parameter in this model. The analysis of the experimental results demonstrated that the parameters significant for predicting DE_{Beam} include dowel diameter, applied load, dowel bending stiffness, and number of load cycles. The load transferred through the dowel is determined based on the load applied in the laboratory. This is calculated assuming that 10% of the load is transferred through the simulated base layer, which is consistent with the current design procedure (Applied Research Associates, Inc. 2004). Half of the remaining load is assumed to transfer through the dowel, which is equal to 45% of the applied load.

Dowel stiffness is accounted for using β, which is the relative stiffness of the dowel embedded in the concrete, as defined by Friberg (1938). This is calculated using Eq. (3) and (4)

$$\beta = \sqrt[4]{\frac{K \cdot d}{4 \cdot E_{dowel} \cdot I}} \tag{3}$$

$$K = \frac{E_{PCC}}{h_{PCC}} \tag{4}$$

where β is the relative stiffness of the dowel embedded in concrete (mm^{-1}); K is the modulus of dowel reaction (GPa/mm); d is the diameter of the dowel (mm); E is the modulus of elasticity of the dowel (MPa); I is the moment of inertia of the dowel (mm^4); E_{PCC} is the elastic modulus of the dowel (GPa); and h_{PCC} is the slab thickness (mm). The concrete elastic modulus for each specimen was measured prior to testing. For each specimen, DE_{Beam} is calculated at 49 discrete times throughout the loading test, which results in 2205 total data points.

A database of the calculated DE_{Beam} for each specimen was constructed. Multiple linear regression was used to develop the DE_{Beam} prediction model shown in Eq. (5). This equation is in the form of a stepwise function to ensure the model does not predict a negative DE_{Beam}

$$DE_{Beam} = \begin{cases} a_1 \cdot \log(x+1) + a_2 \cdot \log(x+1) \cdot \dfrac{\log(Load \cdot 4.448 \times 10^{-3})}{\beta \cdot 25.4} + a_3 \cdot \dfrac{\log(x+1)}{\beta \cdot 25.4} & \text{if } Load \geq 4.0 \\ \dfrac{Load}{4.0} \cdot \left(a_1 \cdot \log[x+1] + a_2 \cdot \log[x+1] \cdot \dfrac{\log[Load \cdot 4.448 \times 10^{-3}]}{\beta \cdot 25.4} + a_3 \cdot \dfrac{\log[x+1]}{\beta \cdot 25.4} \right) & \text{if } Load < 4.0 \end{cases} \tag{5}$$

where DE_{Beam} is the beam deflection basin; x is the number of applied loads; $Load$ is the magnitude of the load transferred through the dowel (kN); β is the dowel constant (mm^{-1}); and a_1, a_2, and a_3 are the regression coefficients equal to 592.8, 353.3, and –1256.6, respectively. The adjusted R^2 is 0.82, and the root mean square error (RMSE) is equal to 192. The measured versus predicted DE_{Beam} is shown in Fig. 19.

CONCLUSIONS

In this study, a novel accelerated beam test for characterizing dowel performance was developed. The beam test replicates the behavior of a section of a transverse joint of a jointed plain concrete pavement (JPCP). The range of parameters evaluated in this study reflected typical pavement design and loading conditions for a conventional JPCP. The concept of beam deflection energy, DE_{Beam}, was introduced to characterize the damage development to the concrete around the dowel due to the application of repeated vehicle loads. DE_{Beam} was calculated as a function of the area

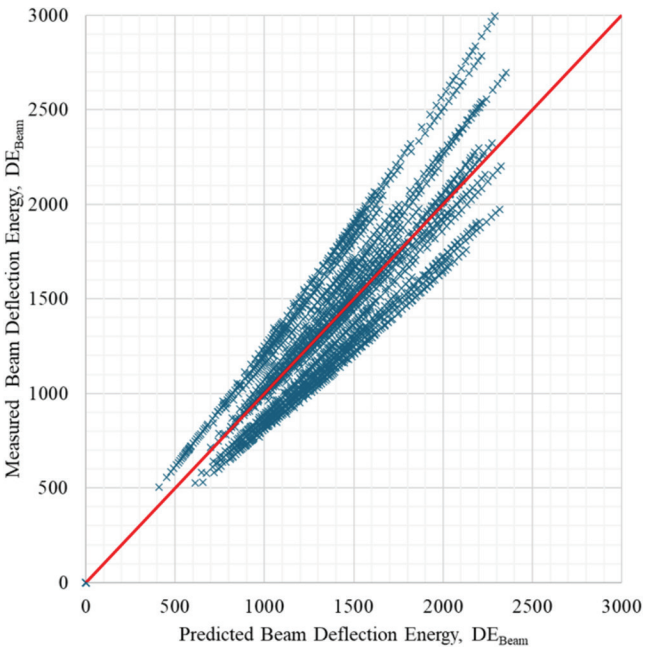

Fig. 19—Measured versus predicted DE_{Beam} *values.*

of the total beam slope versus the logarithm of the number of load cycles for each specimen.

An analysis was performed to identify the effects of key design and loading parameters. Beam thickness is not a significant parameter that affects DE_{Beam} for the range of parameters considered in this study. Dowel diameter was found to be significant when comparing specimens with large differences in diameter. Increasing dowel stiffness resulted in decreases in DE_{Beam}. The effect of dowel diameter varies depending on the material of the dowel, as explained by the effect of equivalent dowel diameter, d_{eq}. For example, 32 mm (1.25 in.) epoxy-coated (EC) dowels and 32 mm (1.25 in.) fiber-reinforced polymer (FRP) dowels (d_{eq} = 26 mm [1.04 in.]) resulted in statistically different DE_{Beam} after two million load cycles. Even though these specimens had the same dowel diameter, the stiffness varied due to differences in material. These results support the implementation of equivalent dowel diameter as a predictor of damage development instead of the measured outer dowel diameter, because equivalent dowel diameter captures the effects of both diameter and material selection.

The experimental results were used to develop a predictive dowel damage equation that accounts for key design and loading parameters. The predictive equation has an adjusted R^2 of 0.82. Using this tool, the performance of a range of standard and alternative dowel designs can be evaluated. This predictive equation can be implemented into the existing faulting model framework to improve performance prediction for the range of dowel designs currently on the market. The products from this research will enable pavement engineers to directly account for the long-term performance of pavements constructed with standard or alternative dowels.

AUTHOR BIOS

Charles A. Donnelly *is a Postdoctoral Researcher at Texas A&M University, College Station, TX. He received his BS, MS, and PhD in civil engineering from the University of Pittsburgh, Pittsburgh, PA. His research interests include concrete materials and concrete pavement laboratory analysis and performance modeling.*

Julie M. Vandenbossche *is a Professor in the Department of Civil and Environmental Engineering at the University of Pittsburgh. She received her BS and MS from Michigan State University, East Lansing, MI, and her PhD from the University of Minnesota, Minneapolis, MN. Her research interests include concrete materials and the design, analysis, and rehabilitation of concrete pavements.*

REFERENCES

Applied Research Associates (ARA), Inc. 2004, "Guide for Mechanistic-Empirical Design of New and Rehabilitated Pavement Structures," Final Report NCHRP 1-37A, Transportation Research Board, Washington, DC.

ASTM C39/C39M-23, 2023, "Standard Test Method for Compressive Strength of Cylindrical Concrete Specimens," ASTM International, West Conshohocken, PA, 8 pp.

ASTM C143/C143M-20, 2020, "Standard Test Method for Slump of Hydraulic-Cement Concrete," ASTM International, West Conshohocken, PA, 4 pp.

ASTM C192/C192M-15, 2015, "Standard Practice for Making and Curing Concrete Test Specimens in the Laboratory," ASTM International, West Conshohocken, PA, 8 pp.

ASTM C231/C231M-10, 2010, "Standard Test Method for Air Content of Freshly Mixed Concrete by the Pressure Method," ASTM International, West Conshohocken, PA, 10 pp.

ASTM C469/C469M-22, 2022, "Standard Test Method for Static Modulus of Elasticity and Poisson's Ratio of Concrete in Compression," ASTM International, West Conshohocken, PA, 6 pp.

Barman, M.; Vandenbossche, J. M.; and Janssen, D. J., 2019, "Small-Scale Joint Performance Test for Concrete Pavements," *ACI Structural Journal*, V. 116, No. 6, Nov., pp. 109-119.

Bruinsma, J. E.; Raja, Z. I.; Snyder, M. B.; and Vandenbossche, J. M., 1995, "Factors Affecting the Deterioration of Transverse Cracks in JRCP," Research Report No. RC-1427, Michigan Department of Transportation and Great Lakes Center for Truck Transportation Research, University of Michigan, University of Michigan Transportation Research Institute, Ann Arbor, MI, 238 pp.

Ciolko, A. T.; Nussbaum, P. J.; and Colley, B. E., 1979, "Load Transfer of Dowel Bars and Starlugs," PCA R&D Serial No. 1354, American Cement Association, Washington, DC, 39 pp.

Dassault Systèmes, 2013, "Abaqus Analysis User's Manual (Version 6.13)," Vélizy-Villacoublay, France.

Davids, B., 2003, "EverFE Theory Manual (Version 2.24)," University of Maine, Orono, ME.

Davids, W. G., and Turkiyyah, G. M., 1997, "Development of Embedded Bending Member to Model Dowel Action," *Journal of Structural Engineering*, ASCE, V. 123, No. 10, Oct., pp. 1312-1320. doi: 10.1061/(ASCE)0733-9445(1997)123:10(1312)

DeSantis, J.; Vandenbossche, J.; and Sachs, S., 2018, "Investigation of Faulting Models used for Concrete Pavement and Concrete Overlays," *Proceedings of the 9th International Delft University of Technology (DUT) Workshop on Research and Innovations for Design of Sustainable and Durable Concrete Pavements*, Potsdam, Germany.

Donnelly, C., and Vandenbossche, J., 2021, "Establishing Effects of Superloads on Doweled Jointed Plain Concrete Pavements," *Proceedings of the 12th International Conference on Concrete Pavements (ICCP)*, A. Amirkhanian and E. Skelton, eds., Minneapolis, MN, pp. 381-387.

Friberg, B., 1938, "Design of Dowels in Transverse Joints of Concrete Pavements," *Proceedings of the American Society of Civil Engineers*, ASCE, V. 64, No. 9.

Friberg, B. F., 1940, "Design of Dowels in Transverse Joints of Concrete Pavements," *Journal of the American Society of Civil Engineers*, ASCE, V. 105, No. 1, Jan., pp. 1076-1095.

Khazanovich, L.; Darter, M. I.; and Yu, H. T., 2004, "Mechanistic-Empirical Model to Predict Transverse Joint Faulting," *Transportation Research Record: Journal of the Transportation Research Board*, V. 1896, No. 1, Jan., pp. 34-45.

Khazanovich, L.; Yut, I.; Tompkins, D.; and Schultz, A., 2005, "The Second Generation of Minnesota Accelerated Loading Facility - Minne-ALF-2," *Proceedings of the 8th International Conference on Concrete Pavements*, Colorado Springs, CO, pp. 1013-1029.

Marcus, H., 1951, "Load Carrying Capacity of Dowels at Transverse Pavement Joints," *ACI Journal Proceedings*, V. 48, No. 10, Oct., pp. 169-184.

PennDOT, 2019, "Determining Structural Adequacy of Dowel Bars Used in Concrete Pavement," PA Test Method No. 642, Pennsylvania Department of Transportation, Harrisburg, PA, 10 pp.

Raja, Z. I., 1991, "Factors Affecting Deterioration of Transverse Cracks in Jointed Reinforced Concrete Pavement (JRCP)," PhD dissertation, Michigan State University, East Lansing, MI, 354 pp.

Sachs, S.; Vandenbossche, J. M.; and Snyder, M. B., 2015, "Calibration of National Rigid Pavement Performance Models for the Pavement Mechanistic–Empirical Design Guide," *Transportation Research Record: Journal of the Transportation Research Board*, V. 2524, No. 1, Jan., pp. 59-67. doi: 10.3141/2524-06

Sachs, S.; Vandenbossche, J. M.; Alland, K.; DeSantis, J.; and Khazanovich, L., 2016, "Effects of Interlayer Systems on Reflective Cracking in Unbonded Overlays of Existing Concrete Pavements," *Transportation Research Record: Journal of the Transportation Research Board*, V. 2591, No. 1, Jan., pp. 33-41. doi: 10.3141/2591-06

Snyder, M. B., 2011, "Guide to Dowel Load Transfer Systems for Jointed Concrete Roadway Pavements," National Concrete Pavement Technology Center, Iowa State University, Ames, IA, 40 pp.

Teller, L. W., and Cashell, H. D., 1959, "Performance of Doweled Joints Under Repetitive Loading," Highway Research Board Bulletin No. 217, 42 pp.

NEW Symposium Publications from ACI

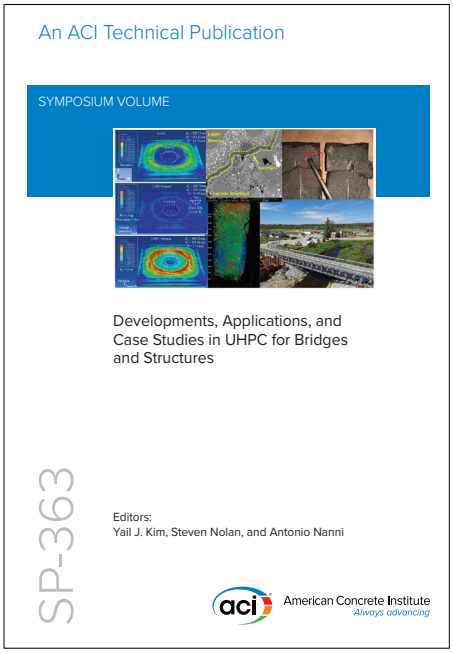

SP-363: Developments, Applications, and Case Studies in UHPC for Bridges and Structures

Ultra-high-performance concrete (UHPC) is a state-of-the-art cementitious composite. Since the concept of this novel concrete mixture emerged in the 1990s, significant advancements have been made with numerous benefits such as high strength, flowability, high post-cracking tensile resistance, improved durability, reduced maintenance, and extended longevity. Currently, UHPC is employed around the globe alongside recently published practice guidelines. Although numerous research projects were undertaken to examine the behavior of UHPC-incorporated structures, there still are many gaps to be explored.

Available in PDF format: $69.50
(FREE to ACI members)

SP-364: Serviceability and Performance Evaluation of Concrete Bridges and Structures: Analysis, Design, and Construction

Serviceability is considered a critical factor in the management of concrete bridges and structures. Typical components for evaluating the serviceability limit state include cracking, deflection, and vibration. Additionally, to ensure the adequate performance of load-bearing members, proper evaluation methodologies should be adopted. Although numerous research projects have been undertaken to examine the serviceability and performance assessment of concrete bridges and structures, significant endeavors are still required to address unexplored challenges.

Available in PDF format: $69.50
(FREE to ACI members)

American Concrete Institute
+1.248.848.3700 • www.concrete.org

ACI STRUCTURAL JOURNAL TECHNICAL PAPER

Title No. 123-S54

Seismic Design of Intermediate Precast Group-Coupled Shear Walls

by Won-Jun Lee, Deuckhang Lee, Min-Su Kim, and Xianze Jin

*As modern industrial and residential buildings become larger and longer, the use of precast concrete (PC) has been essential in current practice. A PC lateral force-resisting system has inevitable discrete joints between precast components, which are considered one of its major concerns in structural integrity and emulative seismic performances comparable to monolithic connections. It can be overcome through code-compliant joint details and tight connection quality under capacity design philosophy, for which suitable emulative design methods also need to be adopted. This study aims to investigate various design options based on the so-called degree-of-coupling (DOC) in vertical wall-to-wall connections in lateral seismic design of an intermediate precast coupled shear wall system. To this end, a flexible and cost-effective lateral design method is proposed by addressing a simple but reasonable factor (*G*). To verify the proposed approach, an experimental campaign and robust analytical studies were conducted. Especially in the experimental program, several precast coupled shear walls with semi-emulative and fully emulative connection details in wall-to-wall vertical connections were tested under cyclic loading. On this basis, it appeared that an existing design process of precast coupled shear wall systems can be simplified, providing reasonable accuracy and design flexibility for engineers toward cost-effective intermediate precast shear wall systems.*

Keywords: coupled shear wall; *G*-factor; group coupling; intermediate precast structural wall; precast concrete; vertical connection.

INTRODUCTION

One of the critical factors emphasized in the contemporary construction industry is the integration of multiple attributes, such as rapid construction, cost-effectiveness, sustainability with low carbon emissions, and robust structural connections capable of withstanding diverse external threats.[1-5] To this end, so-called ESG (environmental, social, and governance) management and off-site construction (OSC) strategy have been quickly implemented in recent years. However, traditional reinforced concrete (RC) or cast-in-place (CIP) construction methods cannot fully satisfy those key agendas due to several inherent disadvantages in terms of heavy formwork, construction noise, dust, long construction duration, and subsequent safety issues.[5-9] As a result, precast concrete (PC) method is increasingly gaining attention as an inevitable and viable alternative. Active research on precast shear walls has been conducted,[1-10] and more detailed progress in precast shear wall systems can be found in Singhal et al.[11]

Particularly in South Korea, most multi-story buildings employ bearing walls as lateral force-resisting systems (LFRS), where PC shear walls are commonly adopted for exterior continuous walls in underground parking and core walls in superstructure, as presented in Fig. 1(a) and (b), respectively. However, such a prefabricated system possesses an obvious weakness in its joints between individual precast components compared to RC shear walls with monolithic connections, which is particularly critical in lateral design under seismic and wind loads.[12-16] To this end, emulative (or code-compliant) seismic connection details are required to achieve enough degree of coupling (DOC) or composite action between individual precast wall panels and segments.[17,18] The current ACI 318-19[19] presents ordinary, intermediate, and special precast shear wall systems, while the KDS 41 20 10 (Korea Design Standard – Precast Concrete Building)[20] currently allows only two possible design options for precast shear walls: intermediate and special shear wall systems. For intermediate precast concrete shear walls, which are expected to be widely used as an LFRS in practice, the new ACI-PCI CODE-319[21] code preannounces significant changes in code provisions on this system compared to ACI 318-19, as summarized in Fig. 2. Notably, the code distinguishes between ductile and strong connections, which can coexist within a certain precast joint or shear wall system. For ductile connections, yielding is permitted only in the steel reinforcements, and the code requires substantially high overstrength of $1.5S_y$ for the anchorage length of yielding reinforcements and all other stresses induced by coexisting forces for non-yielding elements at the joint. Strong connections, on the other hand, are required to be designed to withstand the probable strength (S_e) estimated at $1.25f_y$ of the yielding part, which can be simply assumed to be $1.25S_y$. Note that S_y is the yield strength of connection based on f_y of the connected part for moment, shear, torsion, and axial force according to ACI 318-19[19] and ACI-PCI CODE-319,[21] and f_y is the specified yield strength of reinforcement. Furthermore, ACI-PCI CODE-319[21] states that for both the ductile and strong connections, the required strength need not exceed the load combination E_{mh}, which accounts for the system overstrength (Ω_o).[21] PC shear walls inevitably involve both horizontal (wall-to-foundation or wall-to-wall) and vertical (wall-to-wall) joints in their seismic design, resulting in a high level of design complexity due to required overstrength and chosen level of DOC. This study aims to simplify the lateral strength design of precast coupled shear wall systems considering the effect of the DOCs provided in the vertical joints of precast shear wall systems to be fully code-compliant or emulative system. To

ACI Structural Journal, V. 123, No. 3, May 2026.
MS No. S-2024-474.R1, doi: 10.14359/51749491, received August 7, 2025, and reviewed under Institute publication policies. Copyright © 2026, American Concrete Institute. All rights reserved, including the making of copies unless permission is obtained from the copyright proprietors. Pertinent discussion including author's closure, if any, will be published ten months from this journal's date if the discussion is received within four months of the paper's print publication.

(a) Underground parking (b) PC bearing walls

Fig. 1—Typical precast concrete projects in multi-story building.

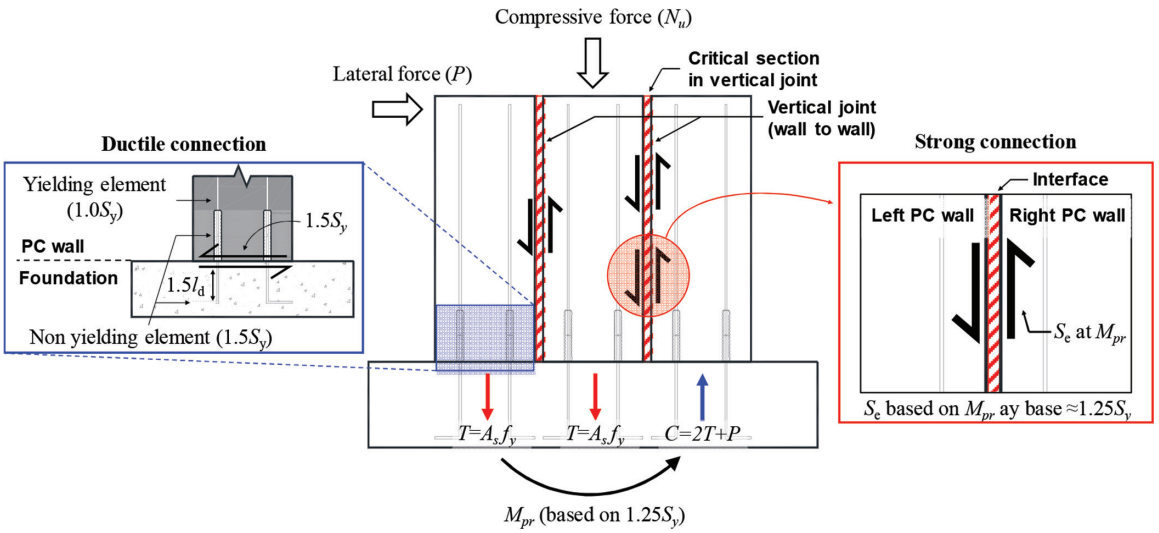

Fig. 2—Code-compliant design of intermediate precast shear wall system.

this end, a simple factor reflecting the effect of the DOCs on lateral strength of PC coupled shear wall system, defined as group coupling factor (*G*-factor), is to be addressed for more economical and better practical design.

RESEARCH SIGNIFICANCE

This study presents a simple approach for quick and flexible design of PC coupled shear wall systems with multiple vertical connections detailing under intermediate precast shear wall systems specified in the current design codes. By addressing group coupling design strategy by addressing *G*-factor, this study simplifies the design process under emulative and capacity design principles, which is crucial for seismic performance. The proposed method quantifies composite action in a simple manner, and on this basis, unnecessary overstrength and over-design like excessive reinforcement details can be avoided and can guarantee to be fully code compliant. Experimental and analytical studies were conducted to verify its reasonable and reliable accuracy in lateral strength design of a precast coupled shear wall system.

COUPLING ACTION IN PRECAST CONCRETE COMPOSITE SHEAR WALL

Effect of DOC

Figure 3 shows typical lateral responses of PC coupled shear walls depending on various DOC from zero to maximum (that is, from non-coupling to full-coupling, and partial coupling between them).[17,18] A PC coupled shear wall system inevitably has discrete connections at interfaces between precast wall panels or at interface of wall-to-foundation in both the vertical and horizontal directions, respectively. The higher DOC (that is, interface shear strength) in the vertical joints between precast individual shear wall panels is provided, the higher lateral strength and stiffness but adversely the lower deformation capacity are subsequently anticipated at the same load level.[17,18,22-24] In other words, when PC coupled shear wall is designed to be fully composite or full coupled (that is, full coupling strength [FCS]), it could exhibit equivalent and emulative lateral performances to that of RC shear wall with monolithic connections. However, as presented in Fig. 2 and 3, cumbersome seismic details are required to satisfy substantially high overstrength to coexisting shear force at the

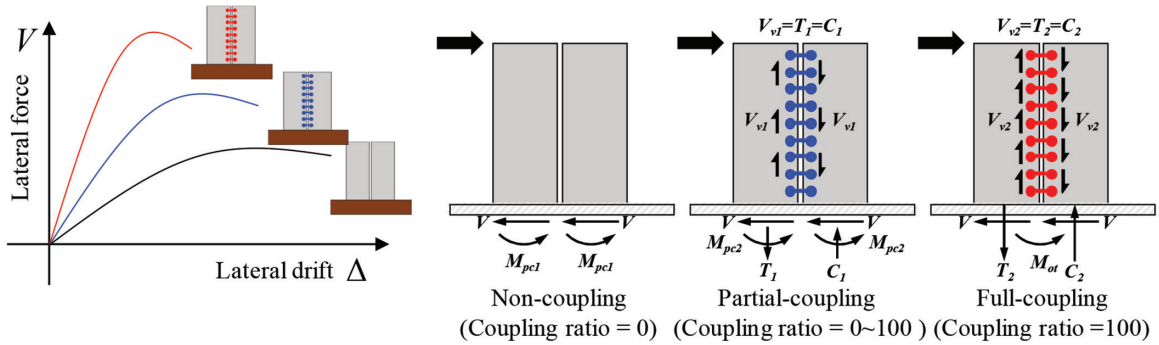

Fig. 3—Effect of level of DOC in lateral design of precast shear wall systems.

precast vertical connections (that is, interfaces) according to the ductile and strong connections specified in ACI 318 and ACI-PCI 319 codes. On the other hand, as another extreme case, if no connecting reinforcement in shear is provided at vertical wall-to-wall connections (that is, non-coupling strength [NCS]), the lowest lateral strength and stiffness, but economically-effective design is possible by avoiding any seismic detail in vertical precast joints, for which design strength (ϕR_n) should be greater than required strength (U) without coupling action. In addition, as semi-emulative cases, there are partially coupled shear wall systems (that is, partial coupling strength [PCS]). This method can be a good alternative but is hard to adopt in practice due to unclear design methodology (that is, not fully code-compliant) and limited experimental evidence.

Coupling design methods

As explained, the degree-of-coupling (DOC or coupling ratio) significantly influences the overall structural response of a precast shear wall system, and the key design component is the capacity design of shear in vertical connections at the interface between adjacent PC wall panels following the strong connection required in Clause 18.5.4 and Commentary R18.5.5.1 of ACI-PCI CODE-319 (refer to Fig. 2). That said, there are four possible coupling design options: 1) NCS; 2) FCS; 3) PCS; and 4) group coupling strength (GCS). In any case, the following relationship should be satisfied

$$\phi M_n \geq U \tag{1}$$

where ϕ is the strength reduction factor; and M_n is the nominal flexural strength.

For better understating, this study introduces an actual field project of PC bearing wall system as an example.[25] As shown in Fig. 4, substantial numbers of PC walls are available along the West-East direction, thus it is quite common that those walls are designed to be as non-coupled precast shear walls (that is, NCS, with no seismic detail between wall-to-wall vertical connection) to satisfy the required strength (U). As shown in Fig. 5(a), this non-coupled precast shear wall system is the simplest form, where each PC shear wall panel resists design lateral force through the sum of flexural actions of individual PC panels. When the same PC segments are used in design, the non-coupling strength (NCS, $M_{n,NCS}$) can be easily estimated as the product of the flexural strength of individual PC shear wall and the total number of PC shear walls in the system as follows

$$M_n = M_{n,NCS} = \sum_{i=1}^{n_{pc}} M_{n,unit,i} = n_{pc} M_{n,unit} \tag{2}$$

where $M_{n,unit}$ is the nominal flexural strength of an individual precast shear wall; and n_{pc} is the total number of individual PC shear wall units involved in LRFS, where $M_{n,unit}$ can be estimated by using the general strength model presented in Cardenas et al.[26] as follows

$$M_{n,unit} = 0.5(A_{s,unit} f_y + N_u)(l_w - c) \tag{3a}$$

$$c = \frac{(A_{s,unit} f_y + N_u) l_w}{2 A_{s,unit} f_y + 0.85 f_c \beta_1 l_w b} \tag{3b}$$

where $A_{s,unit}$ is the area of longitudinal reinforcements under tension within a precast wall panel across the wall-foundation connection; N_u is the axial compression force acting on a precast wall panel; l_w and b are the length and thickness of a precast wall panel, respectively; c is the depth of the neutral axis; and β_1 is the coefficient for the depth of the equivalent compressive stress block.

Meanwhile, along the N-S direction in Fig. 4, only the limited numbers of PC walls can be used in lateral design to overturning moment, and thus much greater lateral flexural strength and stiffness are required for individual members when the NCS is taken. Note that the interface shear strength at the base is almost the same regardless of DOC. Therefore, some DOC action between the precast shear walls needs to increase the lateral strength along the N-S direction, as shown from Fig. 5(b) to (d), and the shear design of the vertical wall-to-wall connections is surely a dominant factor to achieve a proper level of composite action and subsequent emulative performances in the system level, which usually relies on the interface shear or shear friction strength. According to Clause 18.5 of ACI-PCI CODE-319, for the shear design of vertical connections in the intermediate precast structural walls, as presented in Fig. 2, substantially high overstrength (so-called S_e) is required to all coexisting forces (usually, shear force) when the primary reinforcements reach the probable strength (M_{pr}) at the critical section (at base) regardless of the type of splicing methods used in the connection, where M_{pr} is the moment strength at joint faces estimated with $1.25f_y$ with or without axial force. For

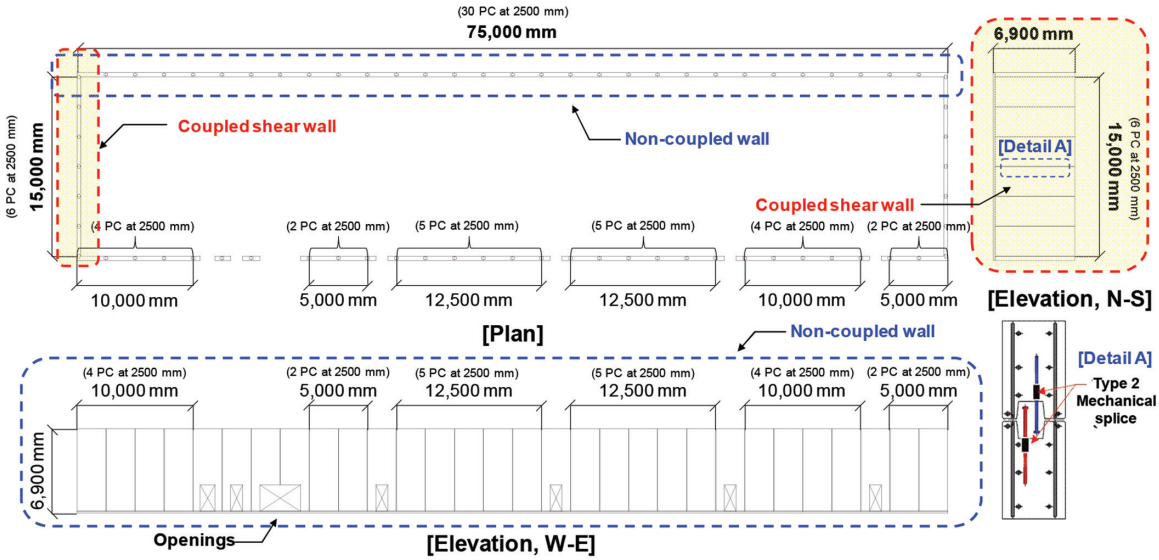

(a) Project details

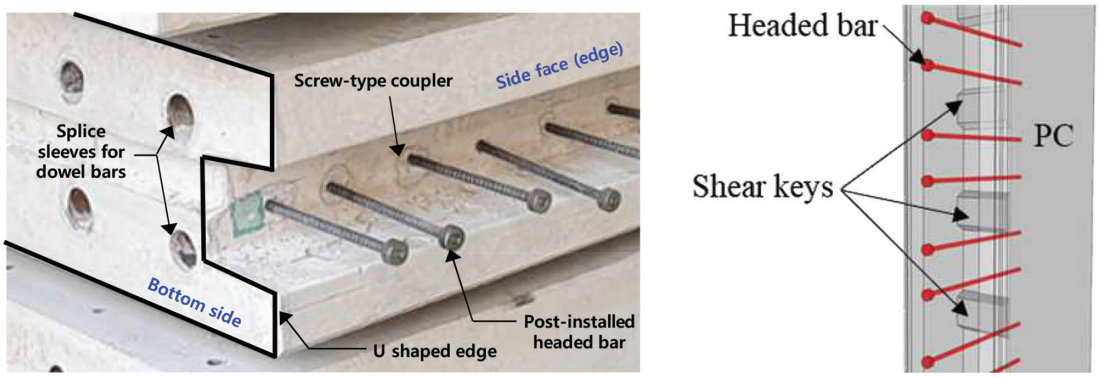

(b) Seismic connection detail

Fig. 4—Example project of precast shear wall system.

example, when the flexure of the primary reinforcements at the critical section (that is, wall-to-foundation base connection; refer to Fig. 2 and 5) is chosen as a governing mechanism, at which the coexisting shear (for example, wall-to-wall connections; refer to Fig. 2 and 3) should be taken at higher or equal to 1.25 times the expected shear force estimated at the nominal flexural strength of the base by using the specified yield strength of the primary reinforcements (that is, strong connection refer to the Clause 18.5.6 and Commentary R18.5.5.1 specified in ACI-PCI CODE-319), and the reinforcement details at the wall base including its anchorage length should be greater than 1.5 times the nominal flexural strength estimated at the base by using the specified yield strength of the primary reinforcements (that is, $1.5S_y$ in ductile connection; refer to Clause 18.5.5 of ACI-PCI CODE-319 or Clause 18.5.2.2 of ACI 318-19).[21] For this reason, under the FCS option, it is almost impossible to design the vertical connections subjected to interface shear in a precast coupled shear wall due to heavy amounts of shear connectors (that is, beyond the maximum shear strength allowed in ACI 318 Code; refer to Table 5 later) and relevant seismic details required to satisfy the overstrength (that is, S_e for coexisting design forces of strong connection in vertical connections and $1.5S_y$ for any non-yielding part in ductile connection at the yielding location). This can be demonstrated as shown in Fig. 5(b) as follows

$$M_n = M_{n,FCS} = \sum T \times jd_{FCS} = n_{FCS} A_s f_y \times jd_{FCS} \quad (4)$$

where n_{FCS} is the number of PC wall panels under tension contributing to full coupling action (for example, n_{FCS} = 5.0 in Fig. 5(b)); A_s is the total area of longitudinal tension reinforcements provided in a precast wall panel across wall-foundation connection; jd_{FCS} is the length of moment lever arm involved with full coupling action; and the accumulated tension ($\sum T$) at the critical section (highlighted in Fig. 5(b)) is the vertical interface shear demand (V_{vu}) for full coupling action. This implies that very high shear strength is necessary for the vertical connections between PC walls greater than or equal to 1.25 times V_{vu} ($=\sum T$), and it also indicates that its implementation becomes more challenging

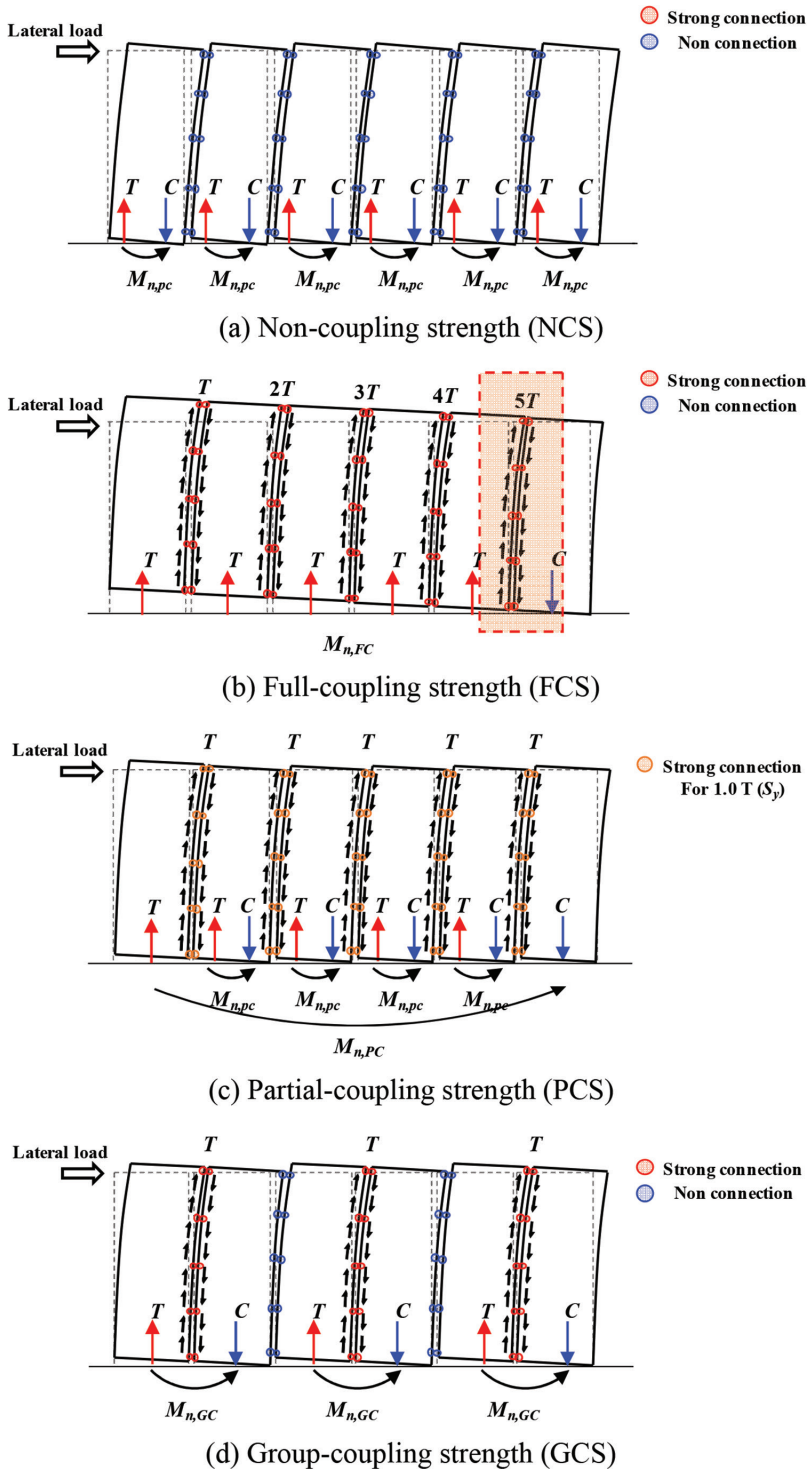

Fig. 5—Various coupling strength design approaches.

as the wall aspect ratio (wall heigh to length, h_w/l_w) decreases or number of involved PC wall panels increases.

Zhang et al.[17,18] proposed a PCS method for precast coupled shear walls, as presented in Fig. 5(c), as an alternative design method between NCS and FCS. This approach maximizes the coupling moment by using actual shear strength provided in vertical connections. But this method is hard to be code-compliant and somewhat tricky to be applied in practices, and no clear experimental evidence is available at this moment. The lateral flexural strength based on PCS approach can be approximately expressed as follows

$$M_n = M_{n,PCS} = V_{vn} jd_{PCS} + n_{NCS} M_{n,unit} \tag{5}$$

where V_{vn} is the shear strength provided in the vertical connections of a partially-coupled shear wall system, which is less than that required for FCS but provided the same in all the vertical connections between PC wall panels; jd_{PCS} is the length of moment lever arm involved with partial coupling action (refer to Fig. 5(c)); and n_{NCS} is the number of PC wall panels not involved in partial coupling action (for example, $n_{NCS} = 4.0$ in Fig. 5(c)).

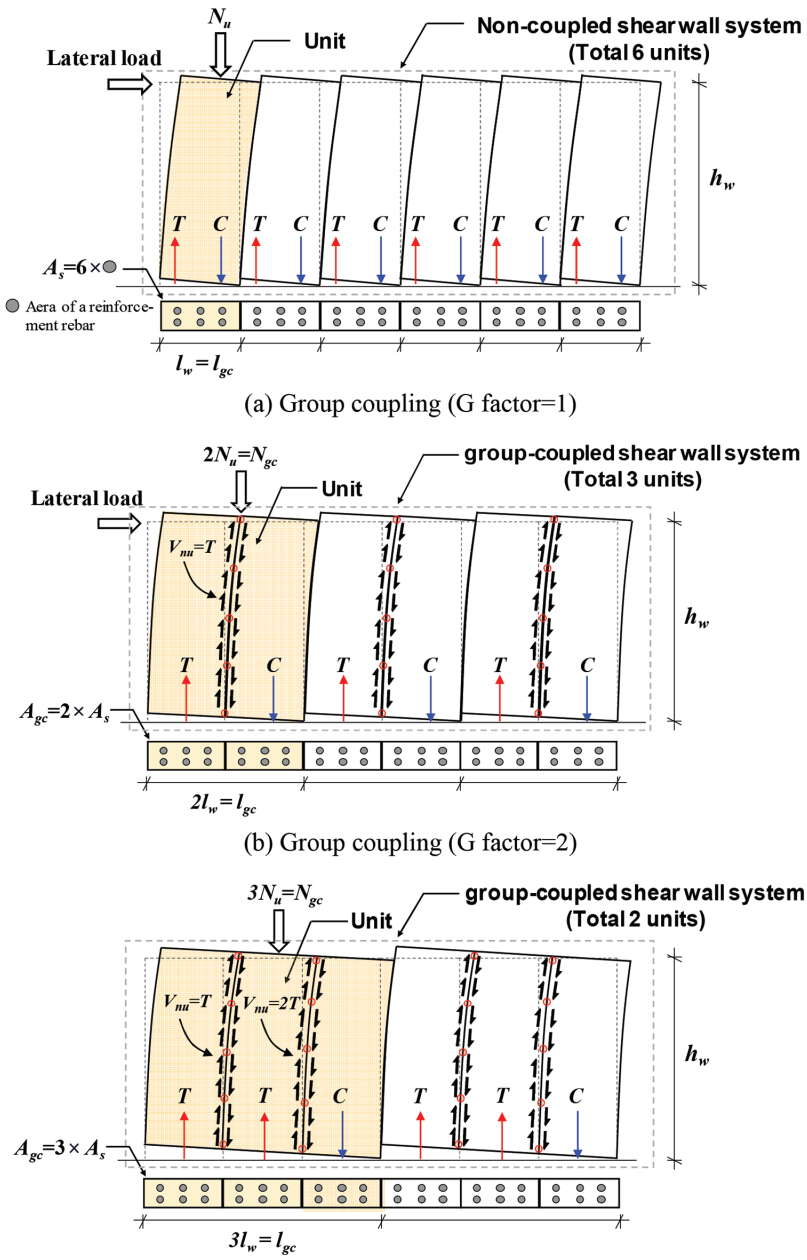

Fig. 6—Various design strategy in group coupling method.

In summary, the aforementioned three design options have some of their own limitations. To be code-compliant and economically feasible, the GCS method is presented in the following section as a good and quick design alternative.

GCS approach

Figure 5(d) shows the GCS approach, where a certain number of individual PC panels are grouped (chosen) to be coupled as a single fully coupled shear wall (that is, unit wall), but there is no connection between each group-coupled precast wall. This certain chosen number is defined as group coupling factor (*G*-factor). Figure 6 addresses descriptive examples to explain how the GCS is effectively used in the seismic design of six individual PC walls along the N-S direction previously presented in Fig. 4, where high seismic design force is expected because only the limited number of PC wall panels are available. When the *G* value is chosen to be 1.0 (refer to Fig. 6(a)), the GCS ($M_{n,GCS}$) is exactly the same with the NCS ($M_{n,NCS}$) estimated from Eq. (2). When the *G* value is taken to be 2.0, for example, two individual PC wall panels are chosen to be fully coupled to form a single group-coupled shear wall, and it results in a total of three group coupled-shear walls contributing to the lateral strength of the system, as shown in Fig. 6(b). To be code-compliant as the strong connection specified in ACI-PCI CODE-319, shear strength greater than the accumulated tension force ($V_{vn} \geq \sum T$) times overstrength factor estimated approximately at $1.25S_y = 1.25A_sf_y$ needs to be provided at the vertical joints, where A_s is the total area of longitudinal connecting reinforcements passing through the wall-to-foundation interface in the tension zone within a group-coupled shear wall. When the *G*-factor is chosen to

be 3.0, three PC wall panels are fully coupled as a single composite shear wall, and subsequently total two strong group-coupled precast walls are available in the system, as shown in Fig. 6(c). Therefore, to guarantee the full coupling action within a group-coupled precast wall, vertical shear strength (V_{vn}) greater than the flexural tension of the reinforcements ($V_b = \Sigma T$) times overstrength factor, at $2.0 \times 1.25S_y = 2.5A_sf_y$ needs to be provided at vertical joints, and it means the required shear strength of the vertical connection between walls can be simply expressed in a general form as a function of G-factor as follows

$$V_{vn} = \alpha S_y(G - 1)/\phi_s \tag{6}$$

where ϕ_s is the strength reduction factor for shear (=0.75); and α is the capacity design factor to address overstrength, which is taken to be 1.25 for the strong connection of intermediate precast shear wall and 1.0 for ordinary precast shear wall, respectively. Note that, in the context of the GCS method, the definition of a unit, as previously expressed in Eq. (2), undergoes a modification. For instance, as illustrated in Fig. 6(b), when the G value is taken as 2.0, a single unit contains two PC wall segments. Similarly, when $G = 3.0$ in Fig. 6(c), the PC unit is defined as a group-coupled precast wall comprising three PC wall segments. This new definition of the unit based on the group coupling factor, G, alters the total flexural strength of the group coupled shear wall system ($M_{n,GCS}$) based on Eq. (3) as follows

$$M_{n,GCS} = 0.5(A_{gc}f_y + N_{gc})(l_{gc} - c_{gc}) \times n_{gc} = M_{n,unit} \times n_{gc} \tag{7}$$

where A_{gc}, N_{gc}, l_{gc}, and c_{gc} are the total area of the longitudinal reinforcements, axial compression, length, and depth of the neutral axis of a group-coupled PC shear wall unit (refer to Fig. 6), respectively, and n_{gc} is the number of group-coupled PC shear walls units within the system. Those can be estimated by multiplying the G-factor to unit values, as $A_{gc} = G \times A_s$, $N_{gc} = G \times N_u$, $l_{gc} = G \times l_w$, $c_{gc} = G \times c$, and $n_{gc} = n_{pc}/G$. In addition, $M_{n,unit}$ is the flexural strength of a group-coupled PC shear wall unit. The GCS can then be simply expressed by using the G-factor and NCS expressed in Eq. (2) as follows

$$\begin{aligned} M_{n,GCS} &= 0.5(GA_{pc}f_y + GN_{pc})(Gl_{pc} - Gc_{pc}) \times \frac{n_{pc}}{G} \\ &= Gn_{pc}0.5(A_{pc}f_y + N_{pc})(l_w - c) = GM_{n,NCS} \end{aligned} \tag{8}$$

As explained earlier, when the G-factor is 1.0, the GCS converges to the NCS. On this basis, this simple linear relationship between the GCS and NCS by using the G-factor as follows

$$\phi M_{n,GCS} = \phi GM_{n,NCS} \geq M_u \tag{9}$$

Then, the required G-factor for a simplified design can be finally estimated as follows

$$G_{req} \geq \frac{M_u}{\phi M_{n,NCS}} \tag{10}$$

From Eq. (10), the required value of the group-coupling factor (G_{req}) can be easily estimated by using all the known design values (that is, M_u and $M_{n,NCS}$), and all the required overstrength can be easily addressed to a group-coupled PC shear wall unit to be a fully code-compliant as the intermediate precast structural walls, as previously presented in Eq. (6). Thus, the proposed GCS method can facilitate quick and flexible capacity-based lateral design as an economically feasible design option for precast coupled shear wall systems.

EXPERIMENTAL PROGRAM

This study conducts experimental verifications on the proposed group coupling strength model. To this end, the lateral strengths of existing seismic test results reported in the authors' own studies[17,18] are used in this section. A total of three test specimens were used in the verification, and their dimensional details and material properties are summarized in Fig. 7 and Table 1, respectively. The first two letters (NS or CS) of the specimen title indicate non-coupled and coupled shear wall specimens, respectively, and their last number (2 or 3) denotes the number of individual precast wall panels in the test specimens. All the test specimens, except for the vertical connection details of the NS2 specimen (that is, not fully coupled shear wall), were designed fully satisfactory to the intermediate precast shear wall system specified in Clauses 18.5 and 14.2.2.4 of ACI 318-19 and ASCE 7-22, respectively.[17,18] Note that the public discussion version of ACI-PCI CODE-319 has not been released at that time. According to those Code provisions, the non-yielding parts in the ductile connection of intermediate precast shear walls were designed to have overstrength greater than at least $1.5S_y$. Figure 7(a) shows the details of the NS2 specimen with a CIP cap beam on the top of two PC wall units, and its shear (or coupling) strength was set approximately to be $1.0S_y$. The cap beam of the NC2 specimen was designed with a height of 600 mm (23.62 in.) and a thickness of 350 mm (13.78 in.). It was reinforced with a total of 12-D19 (No. 6) bars as longitudinal reinforcement, and D13 (No. 4) bars were arranged as shear reinforcement at 100 mm (3.94 in.) spacing. Thus, it indicates that the lateral peak strength of the NS2 specimen is expected to be PCS estimated from Eq. (5), while its post-peak residual strength is then expected to approach the NCS ($G = 1.0$) presented in Eq. (2) after shear damage of the cap beam, as a coupling beam connecting two PC wall panels. This is because there is 5 mm (0.20 in.) gap (that is, no shear connection) along the vertical joint between two adjacent PC wall panels, and limited shear strength was provided by the cap beam approximately to be $1.0S_y$, which can be estimated according to ACI 318-19 as follows

$$V_{vn} = 0.17\sqrt{f_c'}\,b_w d + \frac{A_v f_{vy} d}{s} \tag{11}$$

where b_w and d are the width and effective depth of the CIP cap beam; and A_v, f_{vy}, and s are the area, yield strength, and spacing of shear reinforcements, respectively. More details can be found in Zhang et al.[17]

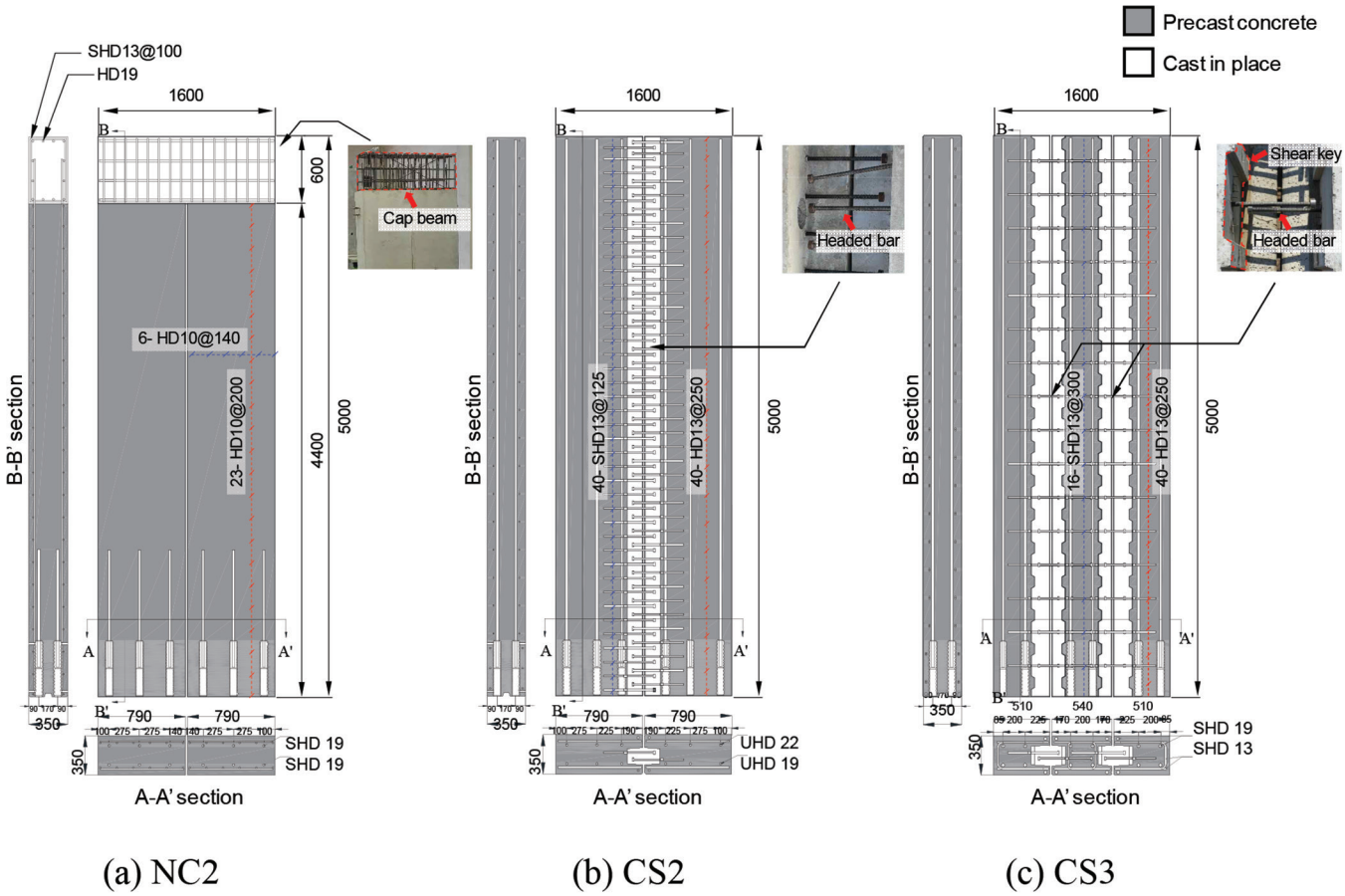

Fig. 7—Dimensional details of test specimens.

Table 1—Section and material properties of test specimens

ID	G-factor	f_c', MPa	f_y, MPa	b_{pc}, mm	l_{pc}, mm	A_{pc}, mm^2	N_{pc}, kN	$M_{n,NCS}$, kN·m ①	M_{test}, kN·m ②	②/①
NC2	1	48.6	550	350	790	1719	800	1360.6	2328.3 (1494.8)*	1.71 (1.09)
CS2	2	48.6	690	350	790	2020.8	800	1470.2	2956.8	2.01
CS3	3	42.0	550	350	530	1146.0	533	733.3†	2317	3.15

*Flexure strength of NC2 specimen after decoupling (noncoupling strength, NCS).

†$M_{n,NCS}$ of CS3 specimen is total flexure strength for each PC wall (three walls).

Note: 1 kN = 0.2248 kip; 1 mm = 0.03937 in.; 1 mm^2 = 0.00155 in.^{2}; 1 kN·m = 7.375 kip·ft.

Figure 7(b) illustrates the details of the CS2 specimen, which has a strong connection between two PC wall panels, and subsequently, its expected strength should be the FCS estimated by using Eq. (4) (or GCS with G = 2.0 from Eq. (7)). D13 (No. 4) reinforcements with a headed bearing anchor were used in the vertical connection of the CS2 specimen with 125 mm (4.92 in.) spacing (that is, $\rho_v = A_v/b_w s$ = 0.29%). Its details can be found in Fig. 4(b), where asymmetric headed bars are to be composite with CIP concrete. Note that no intentionally roughness and shear key was introduced along the side faces (edges) of all the PC wall segments, and this means that the shear friction coefficient (μ) is to be 0.6 for the interfaces between PC wall panels and CIP concrete according to shear friction design provision specified in ACI 318-19 (Clause 22.9.4.2)[19] as follows

$$V_{vn} = \mu A_{vf} f_{yt} \tag{12}$$

where μ is the coefficient of shear friction, which is taken to be 0.6 for no intentionally roughened condition according to Clause 22.9.4.2 in ACI 318-19[16]; and A_{vf} and f_{yt} are the total area across interface and specified yield strength of interfacial shear reinforcement, respectively.

As shown in Fig. 7(c), three PC unit walls are involved in CS3 specimen, where the strong connections were addressed in the vertical joints between PC wall panels to have the code-compliant overstrength estimated at the base with its probable strength (M_{pr}—that is, $1.25S_y$). Thus, its expected strength should be satisfactory to the FCS estimated by using Eq. (4) (or GCS with G = 3.0 from Eq. (7)), for which HD13 (No. 4) reinforcing bars were be placed at 300 mm (11.81 in.) (that is, $\rho_v = A_v/b_w s$ = 0.12%) and shear keys with 300 mm (11.81 in.) spacing and 30 mm (1.18 in.) amplitude were provided in the vertical connection of the CS3 specimen. Thus, its shear friction coefficient (μ) can be adopted to be 1.0. Cyclic lateral loading tests were conducted on each

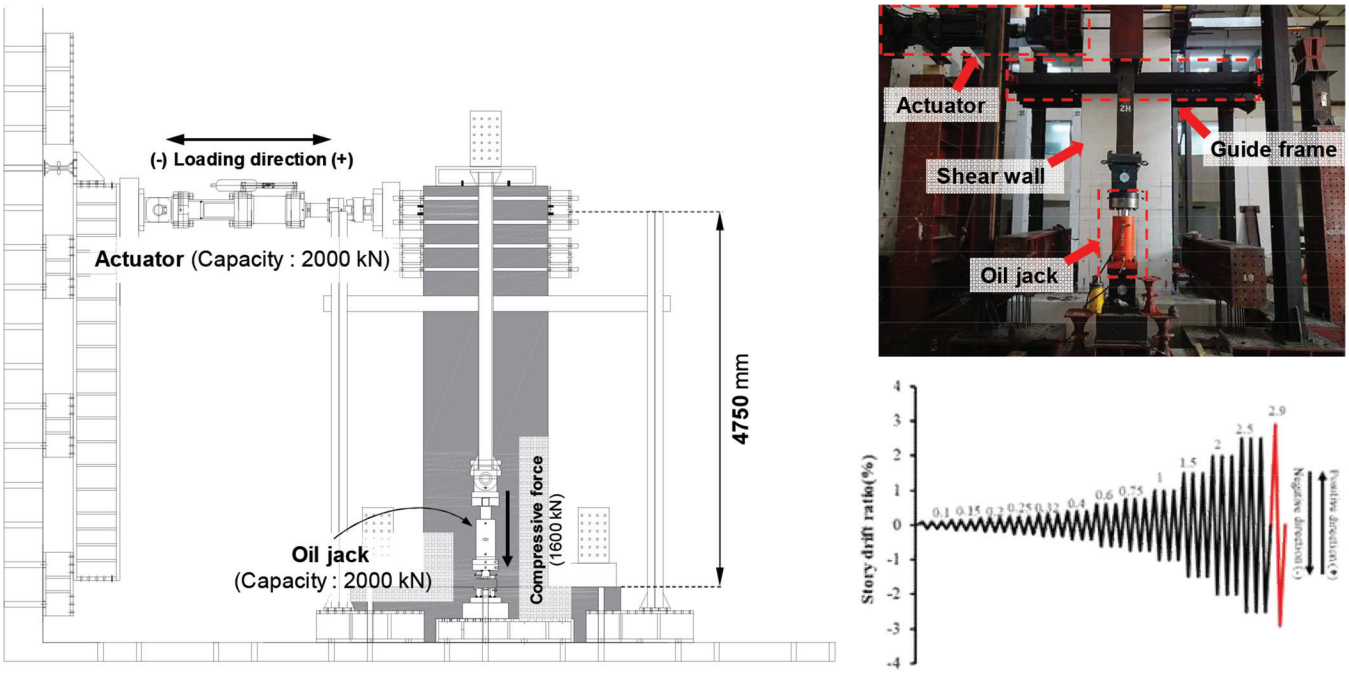

Fig. 8—Experimental setup.

specimen. The NS2 and CS2 specimens were originally from Zhang et al.,[17,18] while the CS3 specimen was additionally tested to verify the *G*-factor proposed in this study. All the test specimens had the same total height, width, and thickness of 5000 mm (16.4 ft), 1600 mm (5.3 ft), and 350 mm (13.8 in.), respectively.

Figure 8 illustrates the experimental setup and loading protocols. In the CS2 and CS3 specimens, the lateral loading actuator with a maximum capacity of 2000 kN (450 kip) was installed at a height of 4750 mm (15.6 ft) from the base. For the NS2 specimen, the actuator was positioned at a height of 4150 mm (15.4 ft) from the base. An axial load of approximately 1600 kN (360 kip) was applied using a centrally located oil jack. In addition, guide frames were installed to prevent out-of-plane displacement of the specimen. As presented in Table 1, M_{test} is the test results, and $M_{n,NCS}$ is the non-coupling strength of the test specimens estimated from Eq. (2).

Figure 9 shows the cyclic responses of the test specimens, where the blue line indicates the NCS of each test specimen, while the red line represents the calculated flexural strengths considering the coupling effect, where the GCS is equal to the FCS for all the test specimens. It shows that the NS2 specimen exhibited the peak strength clearly lower than the FCS, as shown in Fig. 9(a). As expected, its strength eventually converged to the NCS with no coupling action. In contrast, the CS2 and CS3 specimens with strong connections according to ACI 318-19 and ACI-PCI CODE-319 showed the FCS (or GCS), as presented in Fig. 9(b) and (c), respectively. Except for the NS specimen, as presented in Fig. 10, a strong correlation between the normalized experimental results ($M_{test}/M_{n,NCS}$) and *G* values of the test specimens (CS2 and CS3), means that $M_{n,GCS}$ is equal to $GM_{n,NCS}$, as expressed in Eq. (8). Note again that the residual strength of the NC2 specimen after decoupling was taken as the NCS in the comparison made in Fig. 9. As presented, the red dashed line indicates the linear relationship between the lateral strength of test specimens and *G*-factor, as described in Eq. (8) and (10). (Note: Full-color PDF can be accessed at www.concrete.org.)

As presented, the red dashed line indicates the linear relationship between the lateral strength of test specimens and *G*-factor, as described in Eq. (8) and (10). The peak strength of the NC2 specimen demonstrated a greater degree of composite action than that predicted by the linear relationship observed in the other specimens (CS2 and CS3) because of the partial composite action provided by the cap beam in the NC2 specimen, while its post-peak strength after decoupling was aligned well with the linear relation, expressed in Eq. (8).

ANALYTICAL VERIFICATIONS

Test results on the coupled precast shear walls available in literature are limited, and thus this study conducts nonlinear analyses of various coupled PC shear wall systems for more detailed and systematic verifications. First, nonlinear sectional analyses of a very large precast shear wall system located in the W-E direction, previously presented in Fig. 4(a), was conducted by using Response-2000.[27] The nonlinear sectional analysis results were compared with those calculated by using Eq. (9). The length of the target precast wall (l_{tot}) is 75,000 mm (246.0 ft), and its thickness is 350 mm (17.7 in.). The concrete compressive strength (f_c') and yield strength (f_y) of the flexural reinforcements are set to be 35 and 500 MPa (5.07 and 72.5 ksi), respectively. Each precast shear wall unit in the system has a width (l_w) of 2500 mm (8.2 ft), thickness (b) of 350 mm (17.7 in.), flexural reinforcement area (A_s) of 6735 mm^2 (10.44 in.^{2}), and is assumed to carry no axial force (N_u). These parameters are summarized in Table 2. Figure 11 and Table 3 compare the sectional analysis results with the *G*-factor, where $M_{n,R2K}$ represents the flexural strengths obtained from the section

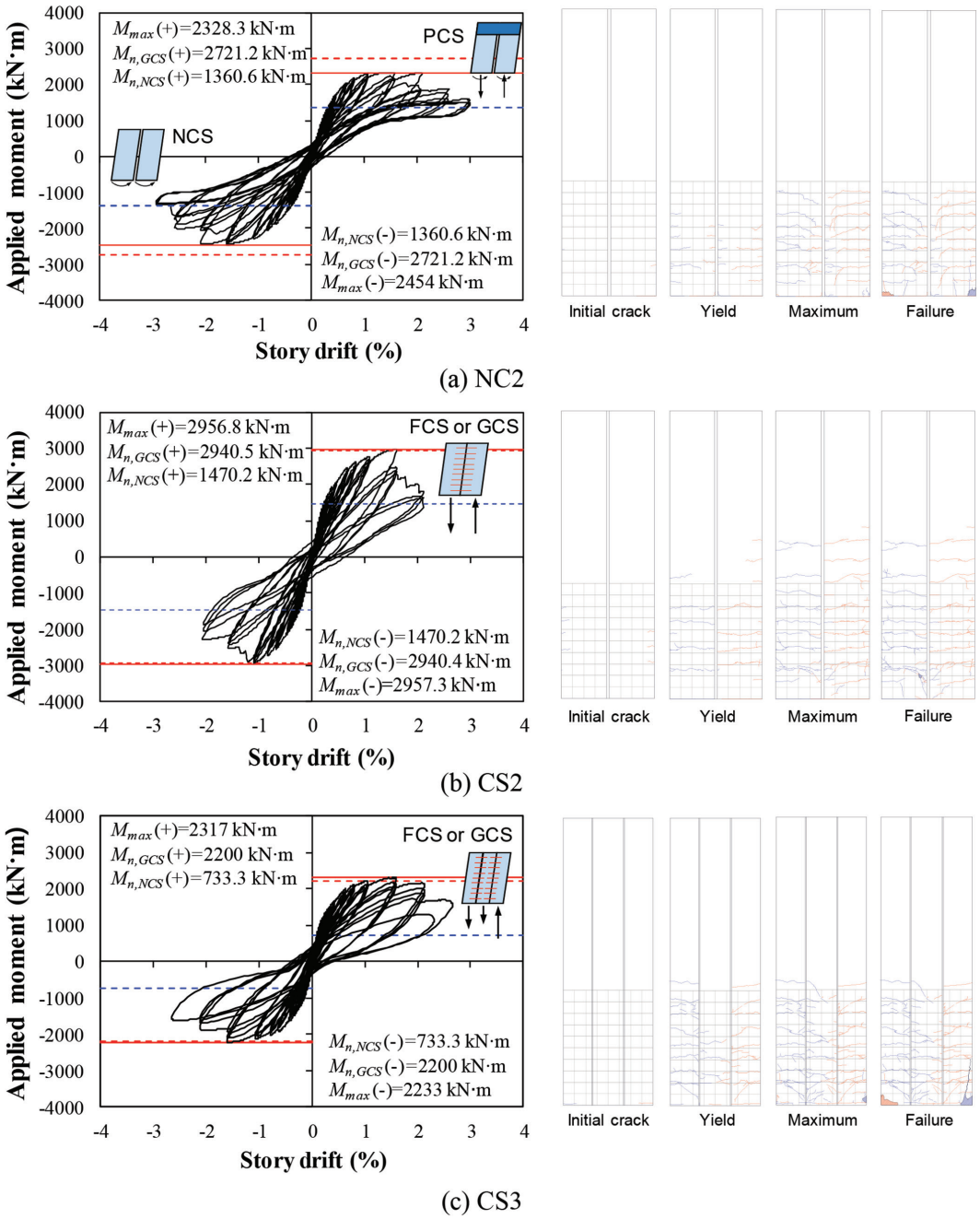

Fig. 9—Cyclic responses of test specimens.

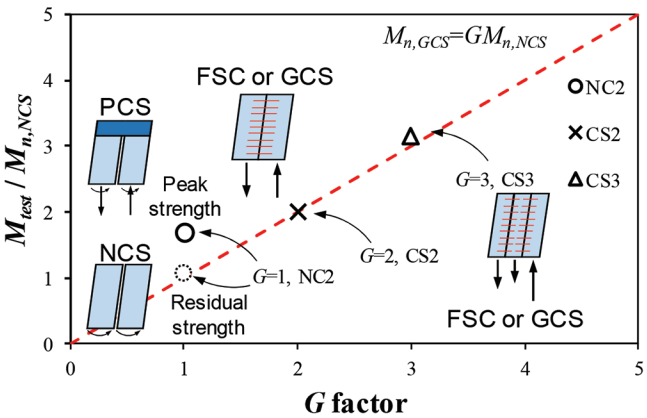

Fig. 10—Verification of proposed method by using experimental results.

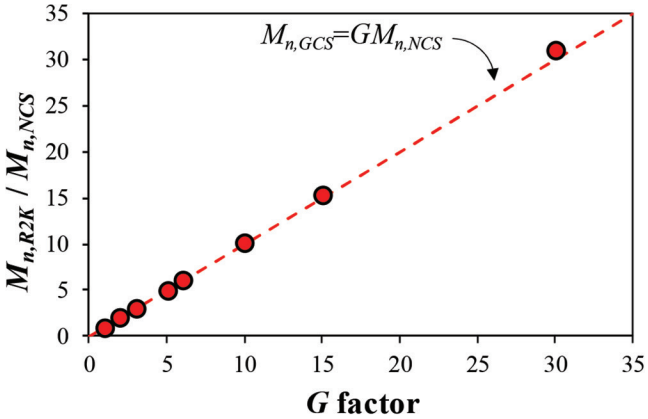

Fig. 11—Verification of proposed method by using section analysis.

Table 2—Summary of analytical studies

Analysis methods	f_c', MPa	f_y, MPa	b, mm	h_w/l_w	$A_{s,unit}$, mm^2
Sectional analysis (Response 2000, R2K)	35	500	350	—	6735
NLFEA (Vector 2 – Basic 4.4)	35	500	350	2.7*	6735

*Aspect ratio of systems (h_w/l_{tot}) ranges from 0.225 to 0.45.

Note: 1 MPa = 0.145 ksi; 1 kN = 0.2248 kip; 1 mm = 0.03937 in.; 1 mm^2 = 0.00155 in.^{2}

Table 3—Section analysis results

Case	n_{pc}	G-factor	$M_{n,NCS}$, kN·m, ①	$M_{n,R2K}$, kN·m, ②	②/①
1	30	1	113,058.0	113,058.0	1.00
2		2		226,636.5	2.00
3		3		340,379.0	3.01
4		5		570,284.4	5.04
5		6		684,622.0	6.06
6		10		1,147,649	10.15
7		15		1,728,989	15.29
8		30		3,505,387	31.01

Note: 1 kN = 0.2248 kip; 1 mm = 0.03937 in.; 1 mm^2 = 0.00155 in.^{2}; 1 kN·m = 7.375 kip·ft.

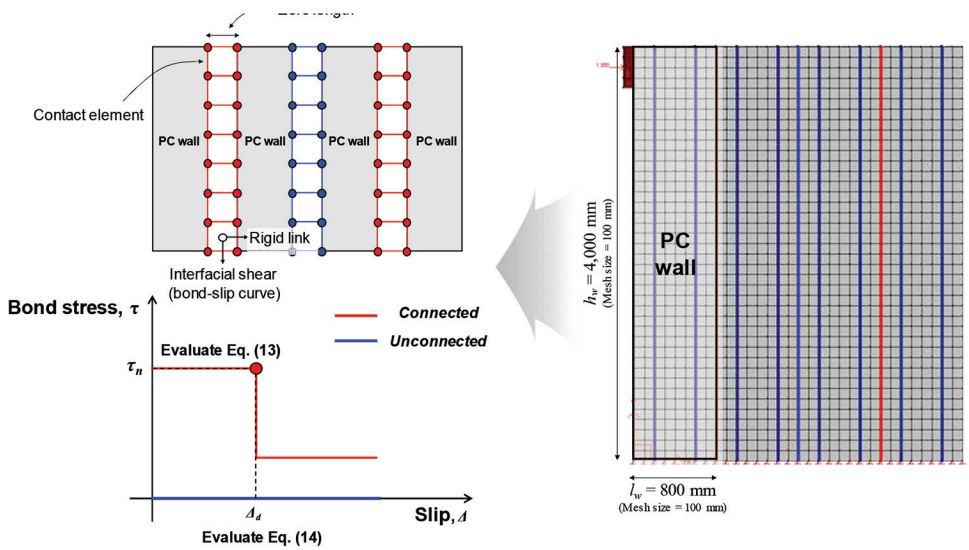

Fig. 12—Nonlinear modeling of vertical connection and coupling effect.

analysis. It shows that the red dashed line representing the GCS closely aligns with the linear function between the NCS and the G-factor presented in Eq. (9). This is consistent with findings from the experimental study.

Robust nonlinear finite element analyses (NLFEA) were conducted on the Vector 2 (v4.4 basic) software platform,[28] and the analysis results were compared with those calculated from Eq. (9) to verify the GCS approach by using the G-factor. The constitutive model of concrete used in the analysis was based on Hognestad[29] and the elastic-plastic model was adopted for that of reinforcements.[30-32] Figure 12 shows the modeling strategy of the vertical joints in the finite element analysis, where the contact elements provided in Vector 2 (v4.4 Basic) were adopted, for which bond-slip curve was used to simulate the interface shear responses as follows

$$\tau_n = \frac{V_{vn}}{A} \tag{13}$$

where τ_n is the shear strength in stress level provided in vertical connection; V_{vn} can be estimated from Eq. (11) or (12) depending on seismic details addressed for coupling action; and A is the contact area of vertical connection. According to Zhang et al.,[17,18] the expected threshold slip (Δ_d) between PC wall segments shown in Fig. 12 can be estimated through the theorem of similar triangles (refer to example 4.5.3.1 in PCI Design Handbook[33]) as follows

$$\Delta_d = \frac{\Delta}{h_o} l_w = 0.015 \times 1000 = 15.0\,\text{mm}\ (0.59\ \text{in.}) \tag{14}$$

where Δ/h_o is the drift ratio at the peak, which is taken to be 1.5% based on the test results in this study; and l_w is the length of an individual PC wall panel (=1.0 m [3.3 ft]). The same sectional properties of a PC wall unit were used in

Table 4—Finite element analysis results

Specimen ID	n_{pc}	G-factor	$M_{n,NCS}$, kN·m ①	$M_{n,FEA}$, kN·m ②	②/①	K_{NCS}†, kN/mm ③	K_{FEA}, kN/mm ④	③/④
6N1G	6	1	3738	3923.8	1.05	151.4	151.4	1.00
6N2G		2		7766.1	2.08		581.1	3.84
6N3G		3		11,391.2	3.05		933.0	6.56
6N6G		6		21,023.6	5.62*		1734.4	11.45
8N1G	8	1	4984	5490	1.10	201.3	201.3	1.00
8N2G		2		10,217.1	2.05		793.2	3.94
8N4G		4		19,956.5	4.00		1861.0	9.25
8N8G		8		31,710.8	6.36*		2711.5	13.47
10N1G	10	1	6230	6306	1.01	253.5	253.5	1.00
10N2G		2		12,902.5	2.07		985.1	3.89
10N5G		5		29,765.1	4.78		2734.4	10.79
10N10G		10		43,956.3	7.05*		3853.7	15.20
12N1G	12	1	7476	7733.0	1.03	283.4	283.4	1.00
12N2G		2		15,782.2	2.11		1156.5	4.08
12N3G		3		23,081.0	3.09		2063.2	7.28
12N4G		4		29,159.3	3.90		3117.3	11.00
12N6G		6		41,872.2	5.60*		3589.2	12.67
12N12G		12		61,769.4	8.26*		4831.8	17.05

*Failure mode of results is horizonal shear failure at base.

†K_{NCS} is stiffness of analysis result with no composite action considered (that is, G = 1.0).

Note: 1 kN = 0.2248 kip; 1 mm = 0.03937 in.; 1 mm^2 = 0.00155 in.^{2}; 1 kN·m = 7.375 kip·ft.

NLFEA, as presented in Table 2. In addition, static lateral loading (monotonic and cyclic) was applied at the top of the shear wall system and nonlinear analyses were conducted with variables including the number of walls (n_{pc}), G-factors, and the magnitude of coupling strength at vertical connections, which are listed in Table 4. In Table 4, the first two letters indicate the number of precast shear walls used in the precast coupled shear wall system, the latter two letters represent the G-factor, and $M_{n.NCS}$ and $M_{n,FEA}$ denote the NCS obtained from Eq. (2) and flexural strengths obtained from the NLFEA, respectively. Figures 13(a) to (d) present the NLFEA results of the monotonic (M) and cyclic (C) loading for the 6N, 8N, 10N, and 12N series, respectively, while Fig. 13(e) shows the monotonic loading (M) for each analysis series. The analysis results indicate that the lateral strength showed a very marginal variation in the lateral strength between monotonic and cyclic loading; however, the specimens subjected to cyclic loading exhibited a brittle failure mode due to strength degradation, where the lateral responses of the various group-coupled shear wall systems listed in Table 4 shows increasing trends in both the lateral strength and stiffness as the G value increases. This trend can be plotted against the G-factor in Fig. 14, where the ratio between the GCS to NCS (that is, $M_{n,GCS}/M_{n,NCS}$) shows obvious linear relation against the G-factor. For analysis models with full coupling assumptions, such as 8N8G, 10N10G, and 12N12G, horizontal shear failure is expected from the NLFEA results at the base before reaching their GCS. It indicates heavy coupling (shear) reinforcements are required to obtain the FCS, and FCS cannot be guaranteed when the G value is greater than a certain value due to shear failure. In addition, the G value cannot be greater than 4.0 due to the maximum shear friction strength allowed in the Clause 22.9.4 of ACI 318-19 presented in Table 5. On this basis, the applicability of the proposed group coupling strength method is clearly affirmed, and it also appeared that the G-factor can be used for simplified and cost-effective design of a coupled precast shear wall system.

DESIGN EXAMPLE

To illustrate how the proposed group coupling design method can be applied in practical design, a precast shear wall system aligned in the E-W direction of Fig. 4(a) is chosen as an example. The design base shear and corresponding overturning moment are assumed at 5558.2 kN and 38,351.5 kN·m, respectively, and those were determined through equivalent lateral force (ELF) analysis with the response modification factor (R) of 4.0 as an intermediate precast bearing wall system. More details can be found in the Appendix and Lee and Kang.[25] A single wall ID with several elements was used in finite element modeling and subsequently guarantees the conservative estimation of the base shear force due to smaller fundamental period of the target building, which induces high lateral stiffness and corresponding higher seismic design forces. Three design options: the NCS, FCS, and GCS expressed in Eq. (2), (3), and (12), respectively, were considered in its flexural strength design in the lateral direction, and the

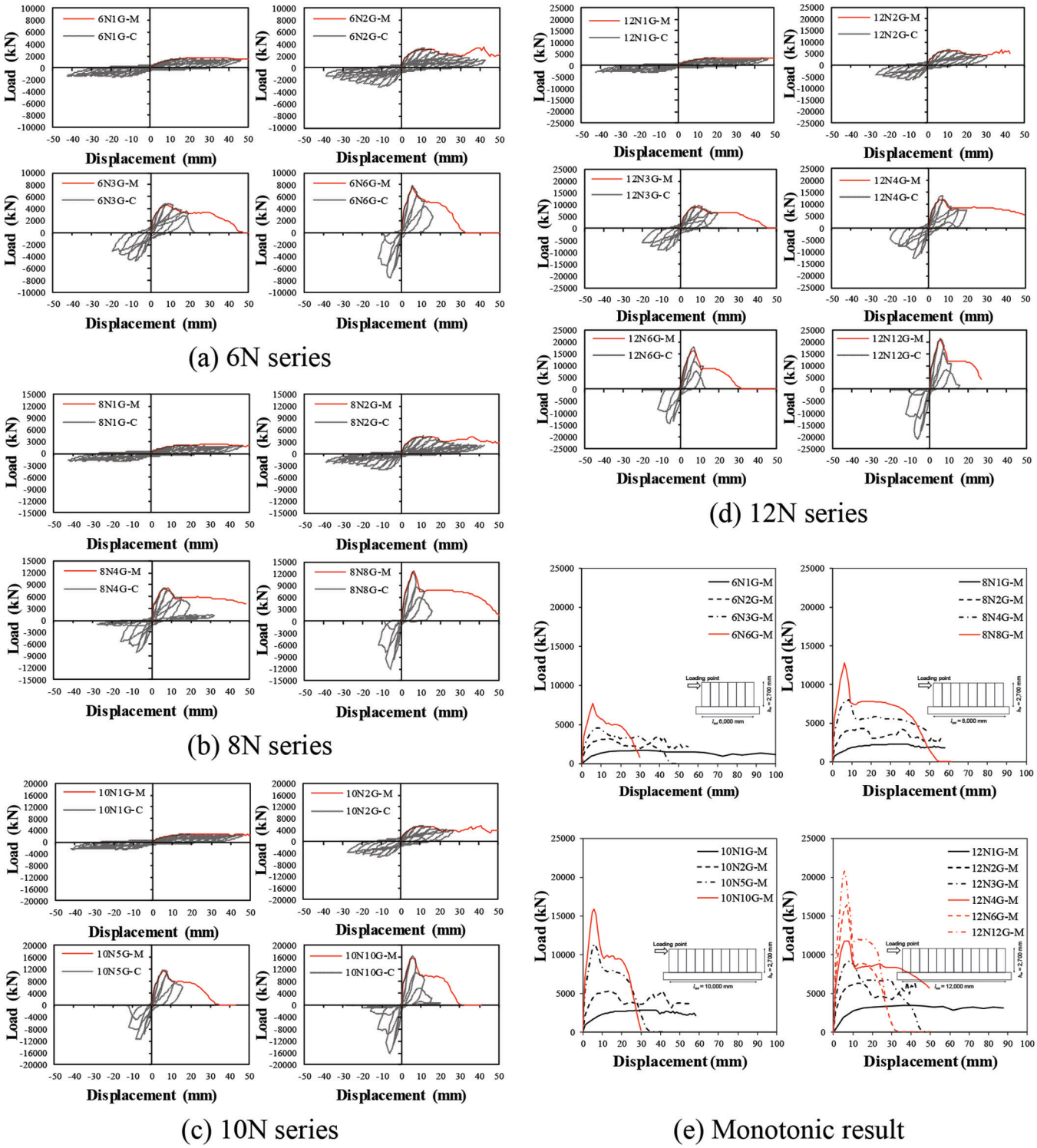

Fig. 13—Analysis result of NLFEA.

design outcomes are summarized in Table 6. For the shear design at the base, the shear friction strength in Eq. (12) was adopted for a simplified design, and thus all the three methods provide the same shear strength, where its allowable limits specified in Table 22.9.4.4 of ACI 318-19 are also presented in Table 5. Seismic details addressed in wall-to-wall connection are based on Zhang et al.,[17] Lee et al.,[12] and Lee and Kang[25] in Fig. 4(b) (that is, headed anchor connection), which fully meet all other detailing requirements including overstrength specified in the Clauses 18.5.2 (precast intermediate structural walls) specified in ACI-PCI CODE-319. As presented in Table 6 and Fig. 14, in the case of the NCS (that is, $G = 1.0$), the total sum of the flexural strength of individual PC wall segments was insufficient to meet the required demand in overturning moment. Note that no shear connecting reinforcement (that is, $V_{vu} = 0$) is required in vertical wall-to-wall connections when the NCS is taken as a design method. Meanwhile, for the FCS, two D16 (No. 5) shear friction reinforcements with 20 mm spacing (2-D16@20 mm or 2-No. 5@0.8 in.) were

provided in all the wall-to-wall vertical connections, and the nominal shear strength required for full composite action exceeded the maximum allowable shear friction strength specified in ACI 318-19 (refer to Table 6), finally making the design impractical in terms of economically effective design and structural performances. In contrast, for the GCS, based on Eq. (14), the required number for the group-coupled walls can be calculated as follows

$$G_{req} \geq \frac{M_u}{\phi M_{n,NCS}} = \frac{38,351.5}{19,219.9} = 1.99 \quad (15)$$

This indicates that the design can be quickly done when the G value is chosen to be 2.0 (>1.99). To satisfy the required overstrength ($1.25S_y$) at the probable moment strength (M_{pr}) of the base for wall-to-wall connections as a strong connection of the intermediate precast structural wall system specified in ACI-PCI CODE-319 and ASCE 7-22 for the response modification factor (R) of 4.0 as intermediate precast shear wall in the bearing wall systems according to Table 12.2-1 of ASCE 7-22, the required interface shear strength in the vertical connections within a group-coupled wall can be computed from Eq. (6) as follows

$$V_{vn} = \alpha S_y(G-1)/\phi_s = 1.25 \times 6735 \times 500 \times (2-1)/0.75 = 5612.5 \text{ kN} \quad (16)$$

where S_y is the shear force of wall-to-wall vertical connection estimated at the yielding of the base connection. On this basis, the required area and corresponding number of shear friction reinforcements between walls can be estimated by using D16 (No. 5) reinforcements (A_s = 198.1 mm^2 [0.31 in.^{2}])

$$A_{vf} = V_{vn}/\mu f_{yt} = 5612.5 \text{ kN}/(0.6 \times 400 \text{ MPa}) = 23,385.4 \text{ mm}^2 \quad (17a)$$

$$n = A_{vf}/A_{v,D13} = 23,385.4/(198.1 \times 2) \approx 60 \quad (17b)$$

$$s = h_w/n = 6900/60 = 115 \text{ mm} \approx 100 \text{ mm} \quad (17c)$$

Thus, two D16 shear friction reinforcements with 100 mm spacing (or 2 No. 5@4in.) were enough to be code-compliant.

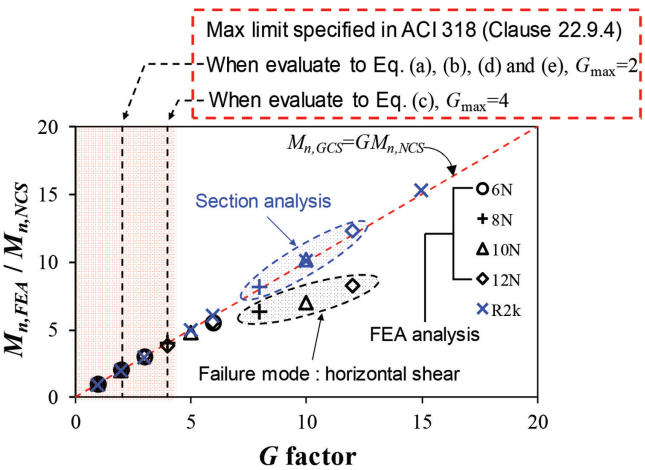

Fig. 14—Correlation between G-factor and analysis results.

CONCLUDING REMARKS

This study investigated the effect of degree-of-coupling (DOC) and various coupling methods on lateral performances of precast coupled shear wall systems, and the group coupling strength approach was newly proposed as design method and its accuracy and applicability were verified in detail. On this basis, following conclusions can be drawn:

1. This study classifies the lateral resistance mechanism of precast concrete shear wall shear system based on the degree of coupling: non-coupling strength (NCS), full coupling strength (FCS), partial coupling strength (PCS), and group coupling strength (GCS). Among those design options, it

Table 5—Maximum shear strength specified in ACI 318-19 (Table 22.9.4.4)

Condition	Maximum interface shear strength		Reference
Normalweight concrete placed monolithically or placed against hardened concrete intentionally roughened to full amplitude of approximately 6 mm	Least of (a), (b), and (c)	$0.2f_cA_c$	(a)
		$(3.3 + 0.08f_c)A_c$	(b)
		$11A_c$	(c)
Other cases	Lesser of (d) and (e)	$0.2f_cA_c$	(d)
		$5.5A_c$	(e)

Note: A_c is area of concrete section resisting shear transfer, mm^2; 1 kN = 0.2248 kip.

Table 6—Summary of design example

Case	G_{req}	V_{vu}, kN	V_{vn}, kN ①	Detail of vertical joint	$V_{vn,max}$, kN ②	ϕM_n, kN·m ③	M_u, kN·m ④	① < ② and ③ > ④
NCS	1	0	0	—	14,731	19,219.9	38,315	N.G.*
GCS	2	4209.3	5612	2-D16@100		38,527.9		O.K.
FCS	6	21,046.8	28,062	2-D16@20		95,047.0		N.G.†

*Design flexural strength (ϕM_n) is not satisfied required strength.

†Normal shear strength (V_{vn}) exceeds maximum shear strength listed in Table 5.

‡This value is $\phi M_{n,NCS}$.

Note: 1 kN = 0.2248 kip; 1 mm = 0.03937 in.; 1 kN·m = 7.375 kip·ft.

appears that the GCS is a simple and flexible design approach as a code-compliant method.

2. It was found that the GCS exhibited a clear linear relationship with the *G*-factor and the NCS, based on which simplified strength design is possible. In addition, the *G*-factor highlights the significant impact of the GCS on achieving code compliance.

3. Experimental studies were conducted to validate the proposed GCS approach with the *G*-factor. The experimental program included cyclic lateral loading tests on two specimens comprising two individual shear walls, and another specimen comprising three individual shear walls. On this basis, it is confirmed that the test results showed a consistent relationship between GCS and NCS described by the *G*-factor.

4. Analytical verifications were also performed by using an example structure of precast building frame system. Nonlinear analysis by using sectional analysis and finite element analysis were conducted to examine the relationships among the GCS, *G*-factor, and the shear demand for possible coupling action. The analytical results present a very consistent response with the experimental findings, where the GCS exhibited a linear relationship with the NCS and *G*-factor.

5. According to quick design example, it can be confirmed that the NCS approach may provide insufficient lateral strength when the number of individual walls is limited. While the FCS approach can fully satisfy the required lateral strength, it is not always a feasible option because the shear friction strength to be provided in vertical connections is inevitably limited by the maximum allowable level specified in the current shear design provision.

6. In contrast, the GCS approach provides design flexibility with fully code-compliant design, and its applicability is clearly affirmed. On this basis, it can suggest that the *G*-factor can be effectively used for the simplified and cost-efficient design of precast coupled shear wall systems.

AUTHOR BIOS

Won-Jun Lee *is a PhD Student in the Department of Global Smart City at Sungkyunkwan University (SKKU), Suwon, Korea. His research interests include the seismic analysis and design of precast concrete structures.*

ACI member **Deuckhang Lee** *is an Associate Professor in the School of Civil, Architectural Engineering, and Landscape Architecture & Department of Global Smart City at SKKU. He has previously served as Associate Professor at Chungbuk National University (CBNU), Korea; an Assistant Professor at Nazarbayev University (NU), Kazakhstan; and a Postdoctoral Researcher at the University of Illinois at Urbana-Champaign (UIUC), Urbana, IL. He is a member of ACI Committee 550, Precast Concrete Structure, and ACI Subcommittees 445-E, Shear and Torsion – Torsion; and 445-F, Shear and Torsion – Interface Shear. His research interests include seismic response analysis and design of precast and prestressed concrete buildings.*

Min-Su Kim *is a PhD Student in the Department of Architectural Engineering at CBNU. His research interests include the seismic analysis and design of precast concrete shear wall systems.*

Xianze Jin *is a PhD Student in the Department of Architectural Engineering at CBNU. His research interests include the nonlinear modeling and analysis of reinforced and precast concrete structures.*

ACKNOWLEDGMENTS

This work was supported by the National Research Foundation of Korea (NRF) grant funded by the Korea government (MSIT) (No. RS-2023-00209647).

REFERENCES

1. Han, S. J.; Lee, D. H.; and Kim, K. S., "Web-Shear Capacity of Prestressed Composite Inverted Multi-Tee Slabs," *ACI Structural Journal*, V. 118, No. 3, May 2021, pp. 295-304.

2. Kim, J. H.; Lee, D. H.; Choi, S. H.; Jeong, H. S.; and Kim, K. S., "Seismic Performance of Precast Multi-Span Frame System Integrated by Unbonded Tendons," *ACI Structural Journal*, V. 119, No. 5, Sept. 2022, pp. 193-206.

3. Maya, L. F.; Zanuy, C.; Albajar, L.; Lopez, C.; and Portabella, J., "Experimental Assessment of Connections for Precast Concrete Frames Using Ultra High Performance Fibre Reinforced Concrete," *Construction and Building Materials*, V. 48, 2013, pp. 173-186. doi: 10.1016/j.conbuildmat.2013.07.002

4. Jaillon, L., and Poon, C. S., "Sustainable Construction Aspects of Using Prefabrication in Dense Urban Environment: A Hong Kong Case Study," *Construction Management and Economics*, V. 26, No. 9, 2008, pp. 953-966. doi: 10.1080/01446190802259043

5. Zhang, D. C.; Fleischman, R.; and Lee, D. H., "Verification of Diaphragm Seismic Design Factors for Precast Concrete Office Buildings," *Earthquakes and Structures*, V. 20, No. 1, 2021, pp. 13-27.

6. Yee, A. A., "Social and Environmental Benefits of Precast Concrete Technology," *PCI Journal*, V. 46, No. 3, 2001, pp. 14-19. doi: 10.15554/pcij.05012001.14.19

7. López-Mesa, B.; Pitarch, Á.; Tomás, A.; and Gallego, T., "Comparison of Environmental Impacts of Building Structures within Situ Cast Floors and with Precast Concrete Floors," *Building and Environment*, V. 44, No. 4, 2009, pp. 699-712. doi: 10.1016/j.buildenv.2008.05.017

8. Sebaibi, N., and Boutouil, M., "Reducing Energy Consumption of Prefabricated Building Elements and Lowering the Environmental Impact of Concrete," *Engineering Structures*, V. 213, No. 1, 2020, p. 110594. doi: 10.1016/j.engstruct.2020.110594

9. He, J. X.; Xu, Z. D.; Zhang, L. Y.; Lin, Z. H.; Hu, Z. W.; Li, Q. Q.; and Dong, Y. R., "Shaking Table Tests and Seismic Assessment of a Full-scale Precast Concrete Sandwich Wall Panel Structure with Bolt Connections," *Engineering Structures*, V. 278, No. 1, 2023, p. 115543. doi: 10.1016/j.engstruct.2022.115543

10. Hu, Z. W.; Xu, Z. D.; Zhang, L. Y.; He, J. X.; Chen, Z. H.; Miao, Q. S.; and Li, W. F., "Full-Scale Shaking Table Test on a Precast Sandwich Wall Panel Structure with a High-Damping Viscoelastic Isolation and Mitigation Device," *Engineering Structures*, V. 329, No. 1, 2025, p. 119797. doi: 10.1016/j.engstruct.2025.119797

11. Singhal, S.; Chourasia, A.; Chellappa, S.; and Parashar, J., "Precast Reinforced Concrete Shear Walls: State of the Art Review," *Structural Concrete*, V. 20, No. 3, 2019, pp. 886-898. doi: 10.1002/suco.201800129

12. Lee, D. H.; Zhang, W.; Kang, S. M.; and Kang, T. H. K., "Seismic Performance of Precast Shear Wall Systems and Connection Details for Underground Structures," *Journal of Structural Engineering*, V. 149, No. 6, 2023, pp. 433-447. doi: 10.1061/JSENDH.STENG-11888

13. Zhang, W.; Kim, S. H.; Lee, D. H.; Zhang, D.; and Kim, J., "Seismic Performance of Self-Sustaining Precast Wide Beam-Column Connections for Fast Construction," *Computers and Concrete*, V. 32, No. 3, 2023, p. 339.

14. Xu, G.; Wang, Z.; Wu, B.; Bursi, O. S.; Tan, X.; Yang, Q.; and Wen, L., "Seismic Performance of Precast Shear Wall with Sleeves Connection Based on Experimental and Numerical Studies," *Engineering Structures*, V. 150, 2017, pp. 346-358. doi: 10.1016/j.engstruct.2017.06.026

15. Wu, D.; Liang, S.; Shen, M.; Guo, Z.; Zhu, X.; and Sun, C., "Experimental Estimation of Seismic Properties of New Precast Shear Wall Spatial Structure Model," *Engineering Structures*, V. 183, 2019, pp. 319-339. doi: 10.1016/j.engstruct.2018.12.096

16. Zhang, R., and Li, A., "Experimental Study on the Performance of Damaged Precast Shear Wall Structures after Base Isolation," *Engineering Structures*, V. 228, 2021, p. 111553. doi: 10.1016/j.engstruct.2020.111553

17. Zhang, W.; Lee, D. H.; Lee, W. J.; Kim, M. S.; and Park, J. Y., "Effect of Cast-in-Place Beams on Seismic Performance of Precast Shear Walls," *ACI Structural Journal*, V. 120, No. 1, Jan .2023, pp. 89-102.

18. Zhang, W.; Lee, D. H.; and Zhang, D., "Effect of Interfacial Shear on Seismic Performance of Precast Concrete Shear Walls," *ACI Structural Journal*, V. 120, No. 1, Jan. 2023, pp. 269-284.

19. ACI Committee 318, "Building Code Requirements for Structural Concrete (ACI 318-19) and Commentary (ACI 318R-19) (Reapproved 2022)," American Concrete Institute, Farmington Hills, MI, 2019, 623 pp.

20. MOLIT, (Ministry of Land, Infrastructure and Transport), "Korean Design Standard 41 20 10 (KDS 41 20 10), Precast Concrete Buildings" Korea Concrete Institute, Sejong, Korea, 2025. (in Korean)

21. Joint ACI-PCI Committee 319, "Structural Precast Concrete—Code Requirements and Commentary (ACI/PCI CODE-319-25)," American Concrete Institute, Farmington Hills, MI, 2025, 296 pp.

22. Mei, C.; Zhao, Z.; Zhang, Y.; Wang, D. M.; and Wu, C., "Performance Evaluation and Shear Resistance of Modular Prefabricated Two-Side Connected Composite Shear Walls," *KSCE Journal of Civil Engineering*, V. 25, No. 8, 2021, pp. 2936-2950. doi: 10.1007/s12205-021-2394-6

23. Zhang, W., and Lee, D. H., "Effect of Mechanical Splice to Seismic Performance of Precast Column-Foundation Connection," *ACI Structural Journal*, V. 121, No. 5, Sept. 2024, pp. 133-146.

24. Wang, D.; Zhang, Y.; and Chen, H., "Seismic Performance Assessment of New Dry Assembled Prefabricated Composite Shear Wall System with Beam-Only Connection," *Structural Design of Tall and Special Buildings*, V. 29, No. 8, 2020, pp. 1-17. doi: 10.1002/tal.1729

25. Lee, D. H., and Kang, S. M., "Safe Seismic Design of Intermediate Precast Shear Wall System," *Journal of Structural Engineering*, V. 150, No. 9, 2024, pp. 1-14. doi: 10.1061/JSENDH.STENG-13322

26. Cardenas, A. E.; Hanson, J. M.; Corley, W. G.; and Hognestad, E., "Design Provisions for Shear Walls," *ACI Structural Journal*, V. 70, No. 3, Mar. 1973, pp. 221-230.

27. Bentz, E. C., "Sectional Analysis of Reinforced Concrete Members," University of Toronto, Toronto, ON, Canada, 2000, 310 pp.

28. Wong, P. S.; Vecchio, F. J.; and Trommels, H., *Vector2 & Formworks User's Manual*, second edition, University of Toronto, Toronto, ON, Canada, 2013, 318 pp.

29. Hognestad, E., "A Study on Combined Bending and Axial Load in Reinforced Concrete Members," University of Illinois Urbana-Champaign, Champaign County, IL, 1951, pp. 43-46.

30. Lee, D. H., "Dual Potential Capacity Model for Deep Reinforced Concrete Members Strengthened by Fiber-Reinforced Polymer Composites," *ACI Structural Journal*, V. 121, No. 6, Nov. 2024, pp. 33-46.

31. Park, M. K. and Lee, D. H., "Dual Potential Capacity Model for FRP-Reinforced Concrete Members Failed in Shear," *ACI Structural Journal*, V. 122, No. 1, Jan. 2025, pp. 77-89.

32. Kim, K. S., and Lee, D. H., "Nonlinear Analysis Method for Continuous Post-Tensioned Concrete Members with Unbonded Tendons," *Engineering Structures*, V. 40, No. 1, 2012, pp. 487-500. doi: 10.1016/j.engstruct.2012.03.021

33. Precast/Prestressed Concrete Institute, "PCI Design Handbook: 8th Edition, Precast and Prestressed Concrete," Precast/Prestressed Concrete Institute, Chicago, IL, 2017.

APPENDIX A

Table A1—Seismic design parameter

Design parameter	Value
Risk Category II	$I_e = 1.0$
S_S	2.0
S_1	1.0
Site class	D
F_a	1.0
F_v	1.7
$S_{MS} = F_a S_S$	2.0
$S_{M1} = F_v S_1$	1.7
$S_{DS} = 2/3 S_{MS}$	1.33
$S_{D1} = 2/3 S_{M1}$	1.13
Seismic design category	C
Basic seismic force-resisting system	Bearing wall system
Wall type	Intermediate precast structural wall
R	4.0
Ω_0	2.5
C_d	4
$C_s = S_{DS}/(R/I_e)$	0.3325
W	16,716.5 kN
$V = C_s W$	5558.2 kN

ACI STRUCTURAL JOURNAL TECHNICAL PAPER

Title No. 123-S55

Innovative Reinforced Concrete Deep Beam Analysis Using Improved Strut-and-Tie Method

by Ali H. Alqarni, Hayder A. Rasheed, and Krishna Ghimire

In this study, a detailed innovative procedure is devised to recover the full response of reinforced concrete (RC) deep beams using an improved strut-and-tie method (STM) based on ACI 318 rules. The load-deflection curve is described by two critical response levels represented by the yield and ultimate points. The STM is used to determine the nodal displacements under a unit load and compute the yield and ultimate load in the strut-and-tie model as the minimum force needed to realize each loading stage from all truss elements. Once the critical load at the two stages is determined, the elongation, strain, and stress of each element in the truss is extracted, thus avoiding the need to approximate the nonlinear strain profile across the depth. Also, two solution strategies using the secant and tangent stiffness are formulated, and their results are successfully compared to the experimental response of seven deep beams with a wide range of shear span-depth ratios. The failure modes reported experimentally perfectly match the failure member indicated by this improved analysis.

Keywords: deep beams; nonlinear response; reinforced concrete (RC) analysis; strut-and-tie method (STM).

INTRODUCTION

Deep beams are commonly used in a variety of structural systems, such as high-rise buildings, pile caps, foundations, and bridge-transfer girders. Deep beams typically carry the loads from structural columns above. The term "deep beam" specifically refers to a reinforced concrete (RC) beam where the shear span, a, does not exceed three times the total depth of the beam, h ($a/h \leq 3.0$). On the other hand, if $a/h > 4.0$, the beam is then classified as a shallow beam. For the intermediate cases, where $3.0 < a/h \leq 4.0$, the beam is considered to be in a transition zone. This is a unique state where the beam cannot be definitively classified as either deep or shallow and thus requires a more complex analysis for strength and deflection characteristics.[1] Numerous experimental studies on RC deep beams have demonstrated that their behavior deviates significantly from the predictions of classical beam theory. This is due to the nonlinear strain distribution across the beam's depth, particularly when subjected to concentrated or eccentric loads in the disturbed regions (D-regions). In addition, it is observed in these studies that the first mode of failure is typically governed by shear deformation, especially for deeper members. Accordingly, the major cracks observed were shear cracks.[2-8]

Despite extensive research, the complete load-deflection behavior of RC deep beams remains an area of active investigation. Deep beams inherently have high shear stresses and noticeable shear deformation. As a result, beam theory based on the Bernoulli-Navier hypothesis is not applicable. The methods most commonly used in the analysis of beams include: 1) the theory of the Bernoulli-Navier beam with an assumption that all transverse shear strain is negligible because the plane cross section is assumed to remain plane and perpendicular to the mid-surface axis after deformation; and 2) the theory of Timoshenko's first-order shear deformation, which is an expansion of the Bernoulli-Navier beam theory and takes into account the transverse shear deformation.[2] In 1997, Norris et al.[3] tested a deep beam that had a/h = 2.25, where the shear span a is measured from the applied load to the beam support, and h is the total depth. The beam was subjected to four-point bending and it was found that the failure mode was controlled by shear. Also, in 2002, Aguilar et al.[4] examined four beams with a/h = 1.0 subjected to monotonic loads. It was observed that flexural failure occurred for Specimens ACI-I and STM-I, while the STM-H and STM-M specimens failed by shear compression. In 2004, Pham and Al-Mahaidi[9] examined 18 rectangular RC beams with a constant shear ratio of a/h = 2.7. The results showed that control beams showed yielding of tension steel followed by the crushing of concrete in compression. In 2005, Salami et al.[5] examined 19 RC beams. Each beam had a shear span-depth ratio ranging from 0.5 to 1.5, effective depth ranging from 400 to 1400 mm (15.7 to 55.1 in.), and lateral reinforcement ratio ranging from 0 to 0.8%. All beams experienced a shear-dominated failure. In 2011, Kim et al.[6] experimentally investigated deep RC beams under bending and axial compression. The authors concluded that the failure mode occurred in concrete crushing before shear failure when a/h decreases with an increase in axial compression. In 2015, Zhu et al.[7] tested a few RC deep beams subjected to three-point bending. The researchers found that the B2T3-1 specimen exhibited yielding of the tension steel, while B2T3-2 was controlled by yielding of stirrups. In 2022, Raheem and Rasheed[8] tested an RC beep beam with a/h = 1.5 subjected to three-point bending. The authors found the failure mode was controlled by the crushing of the horizontal strut.

The RC deep beams exhibit behavior similar to that of a truss, featuring two axial member types that encompass four distinct elements: 1) horizontal compression concrete struts; 2) diagonal or inclined concrete struts; 3) horizontal steel tension ties; and 4) vertical steel tension ties.[8] In a study on the shear capacity of RC deep beams, approximately 36% of previous studies used the strut-and-tie model,

ACI Structural Journal, V. 123, No. 3, May 2026.
MS No. S-2024-477.R3, doi: 10.14359/51750571, received October 6, 2025, and reviewed under Institute publication policies. Copyright © 2026, American Concrete Institute. All rights reserved, including the making of copies unless permission is obtained from the copyright proprietors. Pertinent discussion including author's closure, if any, will be published ten months from this journal's date if the discussion is received within four months of the paper's print publication.

approximately 30% used numerical models (finite element method [FEM]), approximately 18% used artificial intelligence models, approximately 8% applied upper-bound plasticity models, 5% adopted the shear panel method, and the remaining 3% used other mechanical models.[10] In 2001, Sanad and Saka[11] estimated the ultimate shear strength of simply supported deep beams subjected to two-point loads using four different approaches outlined in the ACI method, truss method, Mau-Hsu method, and neural network method. The investigators compared the findings with experimental results. The ACI method had the highest average error of 41%, and the STM showed approximately 11% error compared with the experiments. On the other hand, the neural network method had the smallest average error of 1.6%. Tan and Cheng,[12] in their work from 2001 to 2006, introduced a comprehensive strut-and-tie model applicable to both prestressed and nonprestressed deep beams, regardless of the presence of web reinforcement. The model is based on the assumption that the stress field remains consistent across the width and length of the strut. Additionally, it was assumed that the nodal zone experiences a hydrostatic stress condition.[13-15] According to the ACI Code, the angle between any inclined strut and any tie must be between 25 and 65 degrees while the applied load exists within 2*h* from the support's face under eccentric loads or the clear span not exceeding 4*h* under concentric loads.[1] Several studies have been conducted by using the STM. In 2006, Tan and Cheng[12] investigated the size effect on deep beam shear strength using the finite element and strut-and-tie models. It has been found that the size effect is mainly due to the misapplication of the steel beam shear-transfer concept to concrete beams. The revised STM predictions are validated with 36 case studies, confirming their accuracy and consistency.[16] In 2013, Gandomi et al.[13] used an empirical model to predict the RC deep beam shear strength. The authors concluded that the genetic-simulated annealing (GSA)-based machine learning model provides a reliable estimate for the shear strength of deep beams, outperforming both ACI and CSA models significantly. Moreover, the proposed GSA-based formula for shear strength is straightforward. In 2016, Chou et al.[14] predicted the shear strength of deep beams by using nature-inspired metaheuristic support vector regression. The researchers found that the ACI method had the highest root-mean-square error, at 2.396, followed by the CSA method, baseline support vector regression (SVR), GSA-based model, and smart artificial firefly colony algorithm (SFA) and least-squares SVR (SFA LS-SVR). In 2018, Ismail et al.[15] developed a unified procedure for using an STM for RC deep beam design and for predicting the strength and size needed. Ultimately, the study concludes that the strut-and-tie model's safety provisions and effectiveness factors drawn from Eurocode 2, ACI 318-14, and the *fib* Model Code 2010 do not assure sufficient protection for RC deep beams without shear reinforcement, even when safety factors are taken into account. In 2022, Raheem and Rasheed[8] proposed a first attempt to capture deep beam response by approximating the strain profile using Timoshenko's first-order shear deformation correction.

This paper aims to recover the load-deflection characterization of RC deep beams without any need to approximate the strain profile across the depth. Rather, it computes the strain and stress in each member through finding the member elongation. Iterations are followed until convergence at the key limit points using the uniaxial stress-strain behavior of steel and concrete. The methodology proposed herein is confirmed through comparisons with experimental results from specimens with a wide range of a/h ratios. Furthermore, the model accurately predicts the load-deflection response and failure mode of various deep beams.

RESEARCH SIGNIFICANCE

This study develops an innovative procedure for the full nonlinear analysis of RC deep beams using the STM without the need to approximate the nonlinear strain distribution across the depth. The proposed procedure was proven to be applicable to the full range of shear span-depth ratios by closely matching the load-deflection response curves and failure modes of seven deep beams tested in the literature. This successful outcome is a positive step toward objectively analyzing deep beams for standard design programs in the future.

ANALYTICAL ASSUMPTION

The present analysis procedure is based on the following assumptions:

1. The height of the horizontal strut (y_c) is taken at the ultimate capacity as suggested by ACI 318-19[1]; by ignoring the compression steel, refer to Eq. (1), (3), and (11) that follow.

2. The depth of the inclined strut (W_c) is taken as the minimum of the two depths at the end connecting nodes as suggested by ACI 318-19[1]; refer to Fig. 1 and Eq. (12) through (15) that follow.

3. The horizontal tie is modeled using steel only because the load levels calculated at yield and above (ultimate) admit exccessive cracking along the horizontal tie, causing no surrounding concrete contribution due to tension stiffening.[16]

4. The full load-deflection response of the RC deep beams is assumed to be bilinear and, thus, controlled by the yield and ultimate points only, as implemented in an earlier study.[8]

5. The topology of the truss depends on the truss height (j_d) and the number of bays in the shear span. It is important to note that these two parameters must sustain the strut angle (θ) between 25 and 65 degrees, as suggested by ACI 318-19.[1]

6. Concrete in compression behaves in a nonlinear fashion ending at a crushing strain of $\varepsilon_{cu} = 0.003$, as implemented by ACI 318-19.[1]

7. The vertical tie is modeled using steel only at the yield and ultimate stages. While the surrounding concrete works in conjunction with the steel in vertical ties within the post-cracking load levels, the effective area of concrete confinement reduces rapidly for vertical ties near the yield point (fully cracked tension zone). Therefore, such concrete contribution to the vertical area of ties is neglected at yield and ultimate loads, where severe cracking is anticipated.

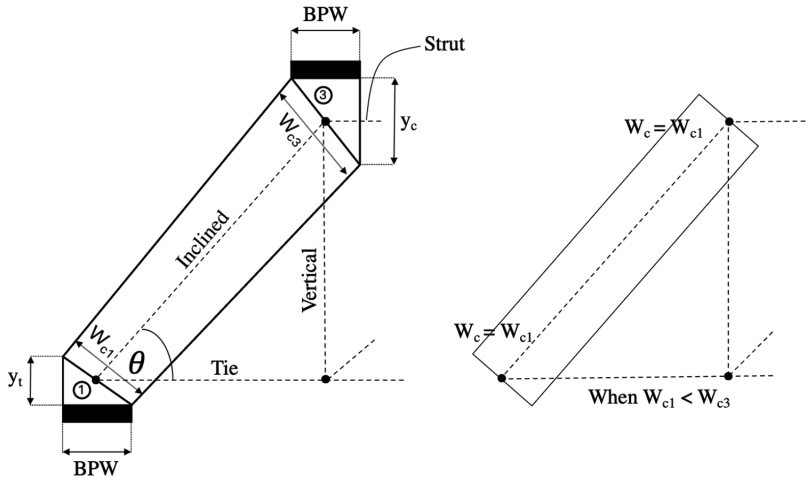

Fig. 1—Nodal zone of beam specimen to determine inclined strut width.

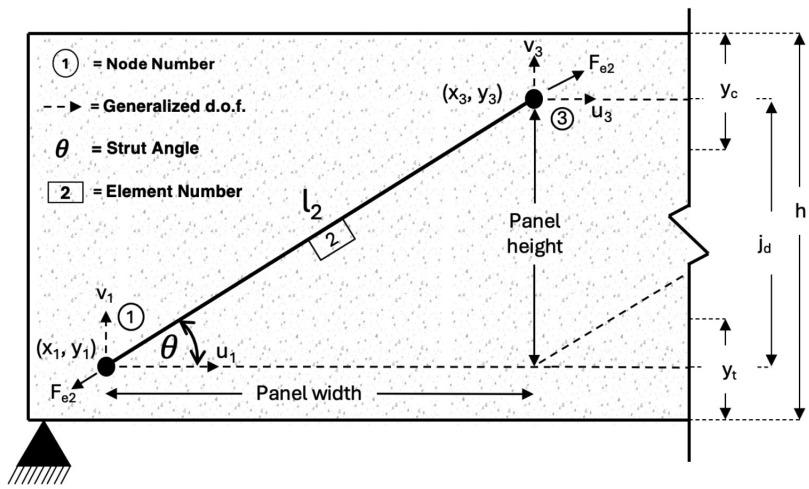

Fig. 2—Generalized two-dimensional (2-D) truss element in deep beam.

TRUSS TOPOLOGY AND ANALYSIS

To determine yield and ultimate load points, a truss analogy approach is employed. This section details the steps involved in calculating internal forces and deflections using this method.

Truss model response—Define the geometry of the truss by identifying node numbers and their x- and y-coordinates as well as element numbers, length, orientation, and type (for example, strut or tie) within the truss (refer to Fig. 2).

Topology of model—It is essential to ascertain that the diagonal elements in a statically determinate truss are in compression (struts), while the vertical connecting elements are in tension (ties). For simply supported deep beams under gravity load, the upper chord elements are in compression (struts), while the lower chord elements are in tension (ties).

$$j_d = (y_3 - y_1) = h - 0.5y_t - 0.5y_c \tag{1}$$

$$y_t = 2[h - d] \tag{2}$$

Find y_c by using the force equilibrium equation

$$0.85f_c'\beta_s b_w y_c = A_s f_y, \text{ where } \beta_s = 1 \tag{3}$$

$$\text{orientation of strut angle} = \tan^{-1}\left(\frac{j_d}{\text{panel width}}\right) \tag{4}$$

The direction cosines for the element are calculated as

$$\cos(\theta) = c = \frac{(x_3 - x_1)}{l_2} = \frac{\text{panel width}}{l_2} \tag{5}$$

$$\sin(\theta) = s = \frac{(y_3 - y_1)}{l_2} = \frac{j_d}{l_2} \tag{6}$$

The standard truss element stiffness matrix K in global coordinates is

$$K = \frac{EA}{l_2}\begin{vmatrix} c^2 & cs & -c^2 & -cs \\ cs & s^2 & -cs & -s^2 \\ -c^2 & -cs & c^2 & cs \\ -cs & -s^2 & cs & s^2 \end{vmatrix} \tag{7}$$

Initial elastic moduli—Every strut element is initially assigned a concrete elastic modulus (E_c)

$$E_c = 4700\sqrt{f_c'} \text{ (SI units, } E_c \text{ and } f_c' \text{ in MPa)} \tag{8}$$

$$E_c = 57\sqrt{f_c'} \text{ (U.S. units, } E_c \text{ in ksi and } f_c' \text{ in psi)} \quad (9)$$

Every tie element is initially assigned a steel elastic modulus (E_s), typically = 200 GPa (29,000 ksi) or a close value reported experimentally.

Element cross-sectional area—In the truss structure, accurate computation of the member areas is essential, as it allows for the straightforward calculation of stress, elongation, strain, and deflection once the axial forces acting on each truss member have been determined.

I—Horizontal ties area

$$A_s = \text{Number of bars} \times A_{bar} \quad (10)$$

II—Horizontal struts area

$$A_{hst} = y_c b \quad (11)$$

III—Diagonal struts area (Fig. 1)

$$W_c = \min(W_{c1}, W_{c3}) \quad (12)$$

$$W_{c1} = BPW\sin\theta + y_t\cos\theta \quad (13)$$

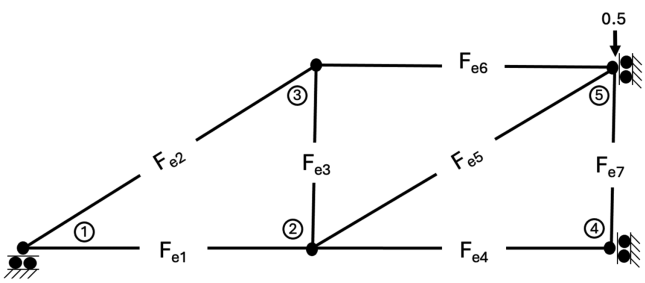

Fig. 3—Truss internal forces subjected to unit load.

$$W_{c3} = BPW\sin\theta + y_c\cos\theta \quad (14)$$

$$A_{dst} = W_c b \quad (15)$$

IV—Vertical ties area

$$A_{v-st} = \text{Number of stirrup legs} \times A_{bar} \quad (16)$$

$$A_{s_{vt}} = \left(\frac{\text{bay length}}{\text{stirrup spacing}} + 1\right) A_{v-st} \quad (17)$$

Internal member forces—The internal element force due to a unit applied force can be computed after finding the nodal displacements and the elongation in the element (Fig. 3).

$$F_{e2} = \frac{A_{c_2}E_c}{l_2}[c \quad s \quad -c \quad -s]\begin{Bmatrix} u_1 \\ v_1 \\ u_3 \\ v_3 \end{Bmatrix} \quad (18)$$

PROGRESSIVE STEPS AT KEY ANALYSIS POINTS

Material properties

Material behavior (concrete in compression)—According to ACI, the behavior of concrete under compressive stress can be described as nearly linear up to a strain level corresponding to $0.45f_c'$. Beyond this point, it is nonlinear and takes nearly a parabolic shape until the ultimate unconfined cylinder stength (f_c'). Then, a softening linear branch may be extended to concrete crushing failure. The relationship in the linear region can be expressed as Fig. 4

$$\sigma_c = E_c\varepsilon_c \text{ for } 0 < \varepsilon_c \leq 0.45\frac{f_c'}{E_c} \quad (19)$$

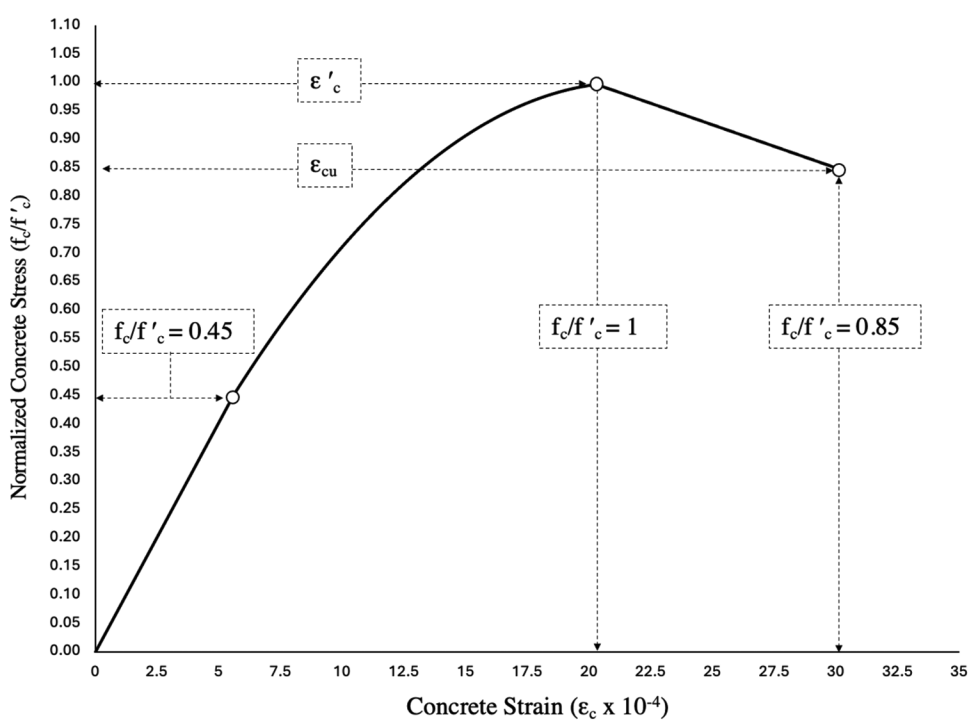

Fig. 4—Normalized stress-strain curve for concrete in compression.

In the nonlinear stage, Hognestad's parabola may be used for computing the stress-strain relationship in concrete (Fig. 4)

$$\sigma_c = f_c'\left[2\frac{\varepsilon_c}{\varepsilon_c'} - \left(\frac{\varepsilon_c}{\varepsilon_c'}\right)^2\right] \text{ for } 0.45\frac{f_c'}{E_c} < \varepsilon_c \leq \varepsilon_c' \quad (20)$$

where ε_c' is the strain corresponding to f_c'.

The softening branch of the curve connects the peak point (ε_c', f_c') to the failure point (ε_{cu}, $0.85f_c'$), as shown in Fig. 4.

$$\sigma_c = f_c' - 0.15f_c'\left[\frac{\varepsilon_c - \varepsilon_c'}{\varepsilon_{cu} - \varepsilon_c'}\right] \text{ for } \varepsilon_c' < \varepsilon_c \leq \varepsilon_{cu} \quad (21)$$

Material behavior (steel)—Steel behaves similarly in compression and tension. It has three distinct stages: the linear-elastic stage, the flat plateau, and the strain-hardening stage. The steel may be modeled to have a bilinear curve. The elastic stage is characterized by a constant modulus of elasticity, denoted as E_s. The inelastic stage may be replaced with a hardening line having a slope of approximately 1 to 6% of E_s, based on an equivalent area under that line to that of the actual stress-strain curve (Fig. 5).

Computing yield load and deflection—The minimum load at which steel in tension yields, P_y, is calculated by determining the load corresponding to the yielding of each individual tension member. Once all the yield loads are calculated, the smallest of these loads is considered as P_y for the entire structure. This is because the structural member with the lowest yield load will be the first to cause that yielding.

$$\text{Horizontal ties } P_{y(1,4)} = \frac{f_y A_s}{F_{e1}} \text{ and } \frac{f_y A_s}{F_{e4}} \quad (22)$$

$$\text{Vertical ties } P_{y(3,7)} = \frac{f_{yv} A_{s_{vt}}}{F_{e3}} \text{ and } \frac{f_{yv} A_{s_{vt}}}{F_{e7}} \quad (23)$$

$$\text{Diagonal struts } P_{u(2,5)} = \frac{0.85f_c' A_{dst}}{F_{e2}} \text{ and } \frac{0.85f_c' A_{dst}}{F_{e5}} \quad (24)$$

$$\text{Horizontal strut } P_{u(6)} = \frac{0.85f_c' A_{hst}}{F_{e6}} \quad (25)$$

$$P_y = \min(P_{y1}, P_{y3}, P_{y4}, P_{y7}),\ P_u = \min(P_{u2}, P_{u5}, P_{u6}) \quad (26)$$

$$\text{If } P_y < P_u \text{ yielding happens before ultimate failure, otherwise no yield stage} \quad (27)$$

Note that zero-force members are assigned a very high value of P_y to avoid division by zero. Also, it is important to note that the critical horizontal tie force at yielding typically gives the critical P_y value. It is also established that the maximum deflection at yielding occurs at Node 4 under a unit load, specifically at v_4 (Fig. 3). It is important to note here that the displacement v_4 (under a unit load) varies along the nonlinear analysis by virtue of using the effective (secant) or incremental (tangent) moduli in concrete and steel. These moduli are adjusted after every iteration in which the elongation, strain, stress, and modulus are updated. Therefore, the maximum deflection Δ_y can be expressed as

$$\Delta_y = P_y v_4 \quad (28)$$

Once P_y and Δ_y are evaluated, the actual elongation (e), strain (ε), and stress (σ) can be calculated for all elements to allow for correcting Δ_y in subsequent iterations, if any.

Computing ultimate load and deflection—To calculate the complete load-deflection response, two different approaches are employed: the secant and tangent approaches. The secant approach is simpler to formulate, but the tangent approach is computationally more efficient.

Secant approach: The first step is to import the cross-sectional area and secant modulus of elasticity from the last

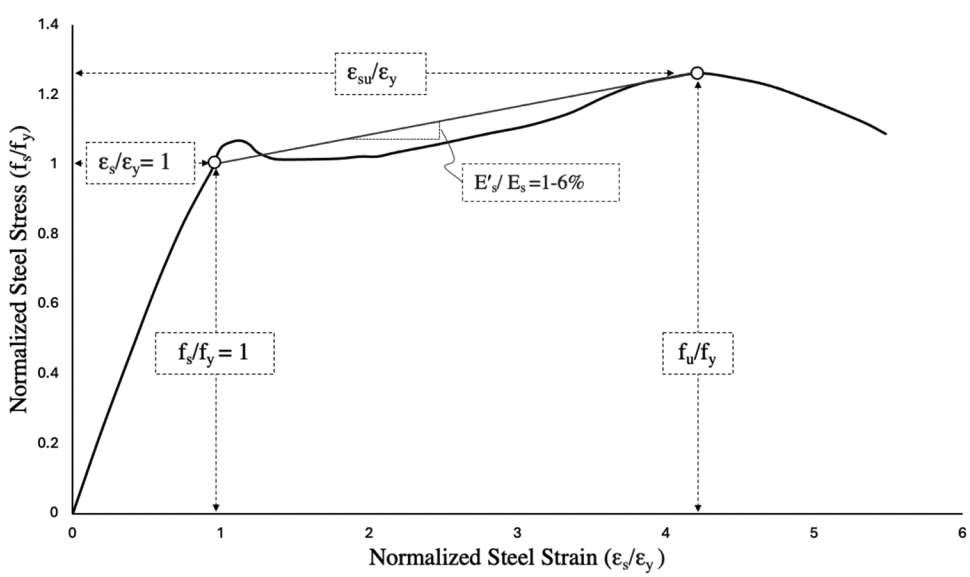

Fig. 5—Normalized stress-strain curve for steel.

converged iteration of the yield stage, if any, for each element and calculate the first estimate of the total ultimate force using the truss nodal displacements under a unit load after defining all elements' area, modulus of elasticity, and length. The maximum displacement typically occurs at the midpoint (v_4) (Fig. 3). To determine the overall ultimate load P_u, the ultimate load is calculated for each individual element. The minimum of these values controls the overall capacity.

$$\text{Horizontal ties } P_{u4} = A_s \frac{f_u = f_y + E_s'(\varepsilon_{su} - \varepsilon_y)}{F_{e4}} \tag{29}$$

when element 4 yields first.

$$\text{Vertical ties } P_{u(3,7)} = A_{svt} \frac{f_u = f_y + E_s'(\varepsilon_{su} - \varepsilon_y)}{F_{e3,7}} \tag{30}$$

On the other hand, $P_{u(2,5)}$ for the diagonal struts and $P_{u(6)}$ for the horizontal strut are computed from Eq. (24) and (25).

Once all element ultimate forces are obtained, the value of P_u is determined by

$$P_u = \min(P_{u1}, P_{u2}, P_{u3}, P_{u4}, P_{u5}, P_{u6}, P_{u7}) \tag{31}$$

Furthermore, it has been determined that the peak deflection is observed at node 4—namely, at v_4 under a unit load. It is important to note here that the displacement v_4 (under a unit load) varies along the nonlinear analysis by virtue of using the effective (secant) or incremental (tangent) moduli in concrete and steel. These moduli are adjusted after every iteration in which the elongation, strain, stress, and modulus are updated. Thus, the actual peak ultimate deflection Δ_u may be denoted as

$$\Delta_u = P_u v_4 \tag{32}$$

Once P_u and Δ_u are computed, the actual elongation (e), strain (ε), and stress (σ) can be evaluated for all elements to allow for correcting Δ_u in subsequent iterations.

Tangent approach: In this step, the ultimate stress (σ_u) and strain (ε_u) are calculated for all steel and concrete elements by adding incremental stress ($\Delta\sigma_u$) and strain ($\Delta\varepsilon_u$) to yield stress (σ_y) and strain (ε_y).

$$\text{Horizontal ties } \Delta P_{u1,4} = \begin{cases} E_s\left(\dfrac{\varepsilon_y - \varepsilon_{1,4}}{F_{e1,4}}\right)A_s & \text{if } E_{1,4} = E_s \\ E_s'\left(\dfrac{\varepsilon_{su} - \varepsilon_{1,4}}{F_{e1,4}}\right)A_s & \text{if } E_{1,4} = E_s' \end{cases} \tag{33}$$

$$\text{Vertical ties } \Delta P_{u3,7} = \begin{cases} E_s\left(\dfrac{\varepsilon_y - \varepsilon_{3,7}}{F_{e3,7}}\right)A_{svt} & \text{if } E_{3,7} = E_s \\ E_s'\left(\dfrac{\varepsilon_{su} - \varepsilon_{3,7}}{F_{e3,7}}\right)A_{svt} & \text{if } E_{3,7} = E_s' \end{cases} \tag{34}$$

where $\varepsilon_{su} = 0.05$.

$$\text{Diagonal struts } \Delta P_{u2,5} = \begin{cases} \dfrac{0.85f_c' - \sigma_{2,5}}{F_{e2,5}} A_{dst}, \text{ if } \varepsilon_{2,5} \le \dfrac{0.45f_c'}{E_c} \\ \sigma_{2,5} = E_c\varepsilon_{2,5} \\ \dfrac{0.85f_c' - \sigma_{2,5}}{F_{e2,5}} A_{dst}, \\ \sigma_{2,5} = f_c'\left[2\dfrac{\varepsilon_{2,5}}{\varepsilon_c'} - \left(\dfrac{\varepsilon_{2,5}}{\varepsilon_c'}\right)^2\right] \text{ if } \varepsilon_{2,5} > \dfrac{0.45f_c'}{E_c} \end{cases} \tag{35}$$

$$\text{Horizontal struts } \Delta P_{u6} = \begin{cases} \dfrac{0.85f_c' - \sigma_6}{F_{e6}} A_{hst}, \quad \text{if } \varepsilon_{2,5} \le \dfrac{0.45f_c'}{E_c} \\ \sigma_6 = E_c\varepsilon_6 \\ \dfrac{0.85f_c' - \sigma_6}{F_{e6}} A_{hst}, \\ \sigma_6 = f_c'\left[2\dfrac{\varepsilon_6}{\varepsilon_c'} - \left(\dfrac{\varepsilon_6}{\varepsilon_c'}\right)^2\right] \qquad \text{if } \varepsilon_6 > \dfrac{0.45f_c'}{E_c} \end{cases} \tag{36}$$

Once all element ultimate force increments are obtained, the value of P_u is determined by

$$\Delta P_u = \min(\Delta P_{u1}, \Delta P_{u2}, \Delta P_{u3}, \Delta P_{u4}, \Delta P_{u5}, \Delta P_{u6}, \Delta P_{u7}) \tag{37}$$

$$P_u = P_y + \Delta P_u \tag{38}$$

Furthermore, it has been determined that the peak incremental deflection is observed at node 4—namely, at v_4 under a unit load. Thus, the actual peak ultimate deflection Δ_u may be denoted as

$$\delta\Delta_u = \Delta P_u v_4 \tag{39}$$

$$\Delta_u = \Delta_y + \delta\Delta_u \tag{40}$$

ITERATIVE FORCE-DISPLACEMENT COMPUTATIONS

To automate the iterations in the yield and ultimate stages, the elongation (e), strain (ε), and stress (σ) are evaluated for each element, as shown in the following. Then, the values of load and deflection are recalculated using Eq. (27), (31) or (37), and (38) and Eq. (28), (32) or (39), and (40), respectively. For steel members, such as elements 1,3,4,7, the

actual strain (ε_s) and stress (σ_s) can be calculated using the following equations, where the subscript s denotes steel

$$\varepsilon_{s1,3,4,7} = \frac{e_{s1,3,4,7}P_{y,u}}{l_{1,3,4,7}} \tag{41}$$

$$\sigma_{s1,3,4,7} = \begin{cases} E_s\varepsilon_{s1,3,4,7} & \text{if } \varepsilon_{s1,3,4,7} < \varepsilon_y \\ f_y + E_s'\left(\varepsilon_{s1,3,4,7} - \varepsilon_y\right) & \text{if } \varepsilon_{s1,3,4,7} \geq \varepsilon_y \end{cases} \tag{42}$$

For concrete members, such as elements 2,5,6, the actual strain (ε_c) and stress (σ_c) can be calculated using the following equations, where the subscript c denotes concrete

$$\varepsilon_{c2,5,6} = \frac{e_{c2,5,6}P_{y,u}}{l_{2,5,6}} \tag{43}$$

$$\sigma_{c2,5,6} = \begin{cases} E_c\varepsilon_{c2,5,6} & \text{if } \varepsilon_{c2,5,6} \leq \dfrac{0.45f_c'}{E_c} \\ f_c'\left[2\dfrac{\varepsilon_{c2,5,6}}{\varepsilon_c'} - \left(\dfrac{\varepsilon_{c2,5,6}}{\varepsilon_c'}\right)^2\right] & \text{if } \dfrac{0.45f_c'}{E_c} < \varepsilon_{c2,5,6} \leq \varepsilon_c' \\ f_c' - 0.15f_c'\left[\dfrac{\varepsilon_{c2,5,6} - \varepsilon_c'}{\varepsilon_{cu} - \varepsilon_c'}\right] & \text{if } \varepsilon_c' < \varepsilon_{c2,5,6} \leq \varepsilon_{cu} \end{cases} \tag{44}$$

For the secant approach, $E_s = \frac{\sigma}{\varepsilon}$

For the tangent approach, $E_t = \frac{\Delta\sigma}{\Delta\varepsilon}$

This process is iterative. After updating element moduli, the unit load truss analysis is repeated, and the remaining steps are repeated until convergence.

PREDICTING FAILURE MODES

Structural failure modes in RC deep beams can be broadly classified into three types: 1) flexural failure; 2) shear failure; and 3) flexural-shear failure. A flexural failure occurs primarily in the horizontal tie or the horizontal strut where the tensile reinforcement elongates to its maximum practical steel strain $\varepsilon_{su} = 0.05$, before other structural members reach their failure limits. Otherwise, the horizontal strut reaches $\varepsilon_{cu} = 0.003$ before flexural steel ruptures, while other shear-dominated members (diagonal strut and vertical tie) are lightly stressed. Shear failure can occur in diagonal members or vertical ties. Diagonal members fail due to excessive loads, while vertical ties fail due to the development and widening of shear cracks that extend to the compression zone. The flexural-shear failure takes place when both the flexural and shear members compete to have stress levels nearing failure at approximately the same load levels.

CURRENT TREATMENT FOR INTRODUCTION OF SHEAR CRACKS

In RC deep beams, a shear crack typically initiates before the horizontal steel tie reinforcing bar starts yielding. This is observed in the four experiments that follow (DB-1.00, DB-1.25, DB-1.4, and DB-1.50), which represent deeper beams. This is signified by the early yielding of the vertical ties prior to the main flexural reinforcement, indicating the initiation of the shear crack. Truss members have uniform stress and strain distribution. Therefore, applying the post-yield modulus (E_s') to the entire vertical tie upon localized yielding within the shear crack is unrealistic, as it would result in excessive deflections. The vertical tie yields across the small width of the shear crack, while the rest of the vertical tie is unyielded (having E_s) due to the confinement of the intact surrounding concrete. Accordingly, the effective steel modulus for the vertical tie crossing a shear crack is expressed as follows; refer to Fig. 6

$$E_{seff_vt} = \frac{E_s(L - W_{sc}) + E_s'W_{sc}}{L} \tag{45}$$

$$\text{when } W_{sc} \ll L, E_{seff_vt} \approx E_s \tag{46}$$

In this version of the analysis, the vertical tie is maintained to have an elastic modulus (E_s) after the initiation of a shear crack. The steel rupture within the crack width is traced through an energy-equivalent approach due to the constant strain-or-stress captured by the vertical tie member as follows; refer to Fig. 6

$$\text{Energy under elastic line} = \frac{1}{2}E_s\varepsilon_s^2 \tag{47}$$

$$\text{Energy under bilinear curve} = \frac{1}{2}E_s\varepsilon_y^2 + f_y(\varepsilon_{s_{adj}} - \varepsilon_y) + \frac{1}{2}E_s'\,(\varepsilon_{s_{adj}} - \varepsilon_y)^2 \tag{48}$$

Equating the aforementioned terms and solving for ε_{sadj}, which would eventually indicate vertical tie rupture when it reaches ε_{su}

$$\varepsilon_{s_{adj}} = \varepsilon_y\left[-\left(\frac{E_s}{E_s'} - 1\right) + \sqrt{\left(\frac{E_s}{E_s'} - 1\right)^2 - \left(1 - \frac{E_s}{E_s'}\left(1 + \left(\frac{\varepsilon_s}{\varepsilon_y}\right)^2\right)\right)}\right] \tag{49}$$

APPLICATIONS AND DISCUSSION

Seven examples were examined using this new procedure, with the prediction results showing excellent agreement compared with the experimental outcomes. The specimens exhibited a range of shear span-depth ratios, from a/h = 1.00 to a/h = 2.70. The deep beams were named DB-1.00 to DB-2.70, where "DB" designates the phrase "deep beam" and "1 to 2.7" indicates the a/h ratio. Both three-point and four-point bending setups were used in the experiments, as shown in Fig. 7. The beam's dimensions and reinforcement details are listed in Table 1, while the material properties are presented in Table 2.

DB-1.00, as tested by Aguilar et al.,[4] exhibited a compressive strength of 28.27 MPa (4.10 ksi). The yield strength of

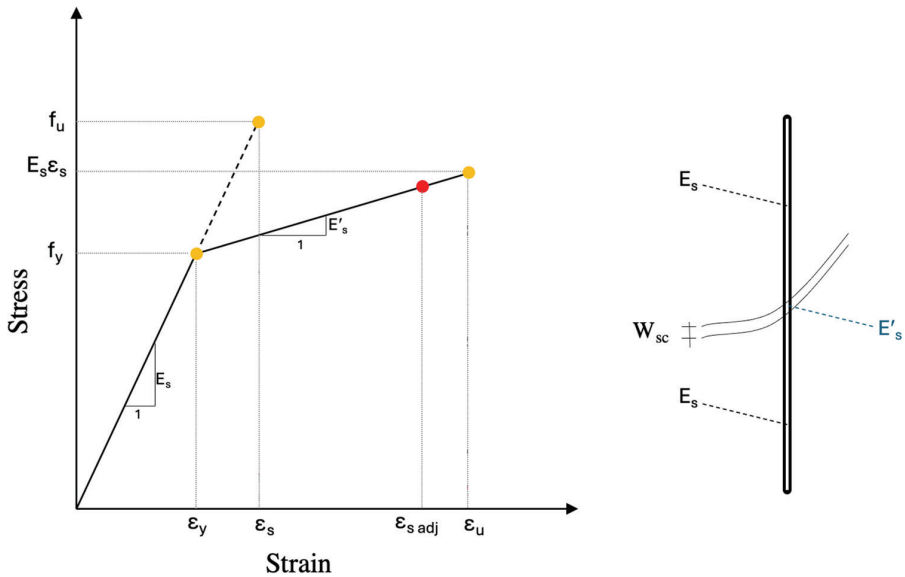

Fig. 6—Treatment of shear crack prediction and analysis.

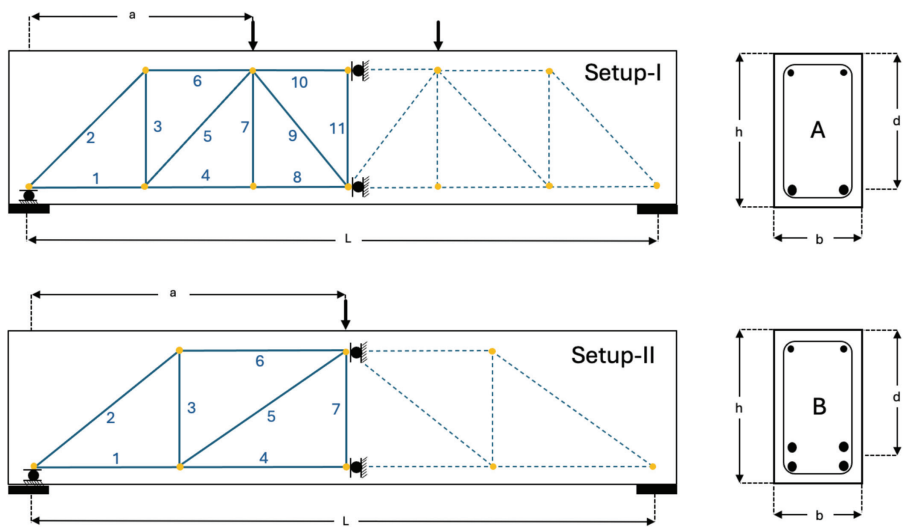

Fig. 7—Experimental setups showing numbered elements and solid lines representing analyzed trusses.

the main reinforcing bars was 420 MPa (60.91 ksi), while the yield strength of the stirrups was 450 MPa (65.26 ksi). Four critical points were identified using the proposed method. The first point marks the stage at which the vertical ties reach their yield strain before the horizontal ties. The second point reveals the yield load being measured from the horizontal ties. The third point indicates that the critical horizontal strut reached the ultimate design point. The final point indicates the failure point. According to the experimental results described by Aguilar et al.,[4] the failure mode observed was classified as shear compression. The predicted versus experimental comparisons are summarized in Tables 3 through 5 and Fig. 8.

DB-1.25, as tested by Jin et al.,[17] showed a compressive strength of 43.6 MPa (6.32 ksi). The yield strength of the main reinforcing bars was 456 MPa (66.13 ksi), while the stirrups had a yield strength of 406 MPa (58.88 ksi). The yield load was identified from the horizontal ties after the vertical ties had yielded, indicating the initiation of a diagonal crack. The authors observed that the failure mode occurred due to shear compression, confirming the predicted failure mode in the inclined strut member; refer to Tables 3 through 5 and Fig. 9.

DB-1.40, as tested by Zhu et al.,[7] exhibited a compressive strength of 45 MPa (6.52 ksi). The yield strength of both the main reinforcing bars and stirrups was 560 MPa (81.22 ksi). The analysis of the DB-1.4 specimen has three critical points. The first point was where the vertical ties yield. The second point was where the horizontal ties yield. The predicted failure mode was anticipated to occur in the horizontal ties at the third point. Zhu et al.[7] confirmed that the failure mode indeed happened in the tension bars. This is due to the extremely low flexural reinforcement ratio; refer to Tables 3 through 5 and Fig. 10.

DB-1.50, as tested by Tan et al.,[18] exhibited a compressive strength of 48.03 MPa (6.96 ksi). The yield strength of the main reinforcing bars was 504.8 MPa (73.2 ksi), while the yield strength of the stirrups was 375.2 MPa (54.4 ksi). Tan et al.[18] found that the failure mode was initiated by vertical flexural cracks in the constant moment region,

Table 1—Beam dimensions and reinforcement details in mm

Name	Setup	L	a	h	b	Reinforcement		
						Top	Bottom	Stirrups
DB-1.00 (STM-H)[4]	I	4470	915	915	305	2Φ25	6Φ25 (B)*	Φ10@152
DB-1.25 (S-0.942-I)[18]	I	1500	375	300	100	2Φ12	4Φ18 (B)	Φ6@60
DB-1.40 (B2T3-1)[7]	II	820	410	280	150	2Φ6	2Φ12 (A)	Φ6@220
DB-1.50 (E-1.62-5.38)[19]	I	2500	750	500	110	2Φ6	2Φ20 (A)	Φ10@300
DB-2.00 (B0)[9]	I	850	300	150	100	2Φ8	2Φ10 (A)	Φ8@75
DB-2.25(C48)[3]	I	1220	458	203	127	2Φ10	2Φ16 (A)	Φ6@205
DB-2.70 (control beam)[5]	I	2300	700	260	140	2Φ12	3Φ12 (A)	Φ10@125

*Skin reinforcements (2Φ10) are placed 406 mm below top surface of beam.

Note: 1 in. = 25.4 mm.

Table 2—Material parameters details in MPa

Name	Concrete		Steel			
	E_c	f_c'	f_y	f_{yv}	f_u	f_{uv}
DB-1.00 (STM-H)[4]	24,989.68	28.27	420.00	450.00	700.00	720.00
DB-1.25 (S-0.942-I)[18]	31,034.24	43.60	456.00	406.00	593.00	590.00
DB-1.40 (B2T3-1)[7]	31,528.56	45.00	560.00	560.00	620.00	620.00
DB-1.50 (E-1.62-5.38)[19]	31,643.95	45.00	504.80	375.20	N/A	N/A
DB-2.00 (B0)[9]	30,094.68	41.00	485.00	550.00	595.00	640.00
DB-2.25(C48)[3]	28,395.16	36.50	420.00	420.00	N/A	N/A
DB-2.70 (control beam)[5]	32,460.64	47.70	504.00	334.00	599.00	483.00

Note: 1 ksi = 6.90 MPa; N/A means that values were not mentioned in paper.

Table 3—Strain unity check and predicted failure modes

Beam	Strain unity check				Predicted failure mode
	$\frac{\varepsilon_{hst-u}}{\varepsilon_{cn}^{*}}$	$\frac{\varepsilon_{ht-u}}{\varepsilon_{sn}^{\dagger}}$	$\frac{\varepsilon_{ist-u}}{\varepsilon_{cn}^{*}}$	$\frac{\varepsilon_{vt\,adj-u}^{\ddagger}}{\varepsilon_{sn}^{\dagger}}$	
DB-1.00	**1.00**	0.05	**1.00**	0.80	Inclined strut failure
DB-1.25	0.50	0.06	**1.00**	0.08	Inclined strut failure
DB-1.40	0.64	**1.00**	0.40	0.09	Horizontal tie failure
DB-1.50	**1.00**	0.09	0.27	0.05	Horizontal strut failure
DB-2.00	**1.00**	0.26	0.19	0.03	Horizontal strut failure
DB-2.25	0.38	0.10	0.14	**1.00**	Vertical tie failure
DB-2.70	**1.00**	0.36	0.27	0.02	Horizontal strut failure

*ε_{cn} = 0.003.

†ε_{sn} = 0.05.

‡$\varepsilon_{vt\,adj-u}$ = adjusted by Eq. (49).

Note: Bold values indicate location of attaining failure level.

which propagated upward and outward, leading to a ductile collapse by crushing of the compression zone. This is due to the relatively long constant moment region compared to the shear span. The moment in the constant moment region is indeed constant and symmetric. However, because the constant moment region is very long compared to the shear span, the deflection increase in the constant moment region is very high, leading to a lot of flexural cracks along that region, causing tension stiffening to wear out quickly and the failure to initiate in the horizontal strut. With the small shear span at both ends and the long constant moment region, the behavior was dominated by pure bending (refer to Fig. 11), and the experimental failure mode matched the predicted failure mode; refer to Tables 3 through 5 and Fig. 12.

DB-2.00, as tested by Kadhim and Özakça,[19] demonstrated a compressive strength of 41 MPa (5.94 ksi). The yield strength of the main reinforcing bars was 485 MPa (70.34 ksi), while the yield strength of the stirrups was 550 MPa (79.77 ksi). Kadhim and Özakça[19] described the failure mode as a flexural failure, with concrete crushing occurring after the steel bars had yielded (Mode 1). As illustrated in the plot that follows, the proposed method predicted the failure mode to occur in the horizontal strut. This is attributed to the fact that both the flexural and shear

Table 4—Predicted versus experimental failure modes

Name	Experimental failure mode	Predicted failure mode
DB-1.00 (STM-H)[4]	Shear compression	Inclined strut failure
DB-1.25 (S-0.942-I)[18]	Shear compression	Inclined strut failure
DB-1.40 (B2T3-1)[7]	Tension bar failure	Horizontal tie failure
DB-1.50 (E-1.62-5.38)[19]	Flexural failure	Horizontal strut failure
DB-2.00 (B0)[9]	Concrete crushing failure	Horizontal strut failure
DB-2.25(C48)[3]	Shear failure	Vertical tie failure
DB-2.70 (control beam)[9]	Concrete crushing failure	Horizontal strut failure

Table 5—Loads and displacements comparison details in kN and mm

Name	Experimental results				Predicted results			
	P_y	Δ_y	P_u	Δ_u	P_y	Δ_y	P_u	Δ_u
DB-1.00 (STM-H)[4]	2159.1	15.38	2578.3	33.60	2047.5	15.32	2625.2	37.55
DB-1.25 (S-0.942-I)[18]	405.88	6.19	422.37	7.19	463.85	6.88	466.99	7.89
DB-1.40 (B2T3-1)[7]	169.89	2.45	199.07	16.35	164.64	2.66	211.82	19.29
DB-1.50 (E-1.62-5.38)[19]	344.50	9.22	347.74	11.44	357.4	9.46	372.50	12.93
DB-2.00 (B0)[9]	51.45	4.52	49.48	15.85	51.33	4.56	57.64	15.41
DB-2.25(C48)[3]	104.94	5.34	103.33	8.22	97.77	4.89	100.64	8.83
DB-2.70 (control beam)[9]	99.47	12.22	107.78	50.70	102.08	12.48	116.45	55.90

Note: 1 kip = 4.45 kN; 1 in. = 25.4 mm.

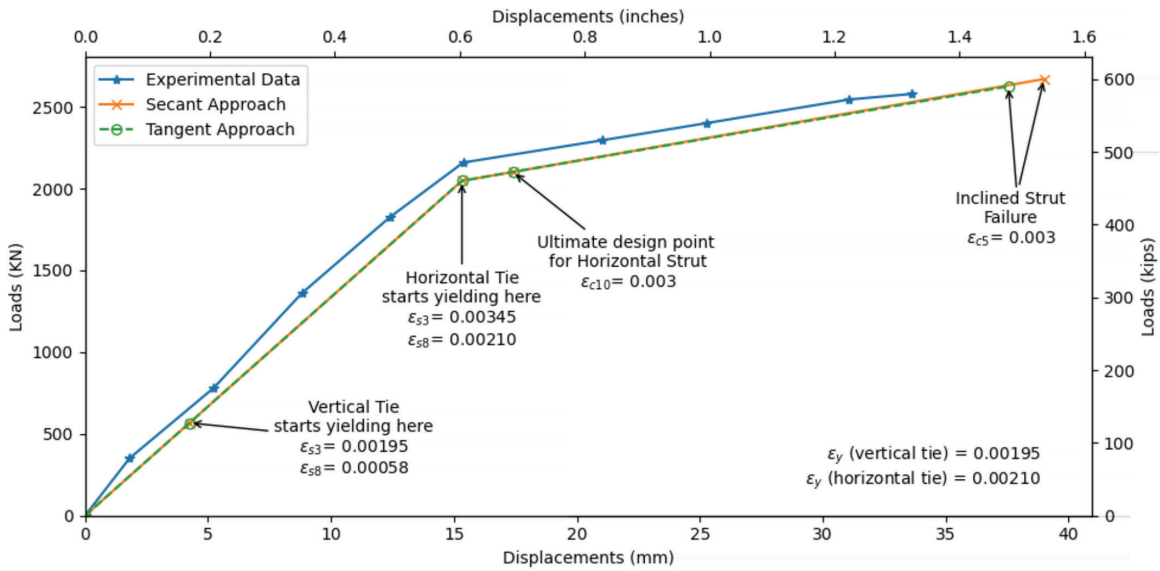

Fig. 8—Load-displacement curve of Specimen DB-1.00.

reinforcement ratios are large and the yield strength of the shear reinforcement is high; refer to Tables 3 through 5 and Fig. 13.

DB-2.25, as tested by Norris et al.,[3] exhibited a compressive strength of 36.5 MPa (5.29 ksi). The yield strength of both the main reinforcing bars and the stirrups was 420 MPa (60.91 ksi). Norris et al.[3] observed that the shear beam (C48) failed due to shear, while the proposed methods predicted that the failure occurred in the vertical ties, which is also classified as a shear failure. This failure was caused by the low shear reinforcement ratio; refer to Tables 3 through 5 and Fig. 14.

DB-2.70, as tested by Pham and Al-Mahaidi,[9] demonstrated a compressive strength of 47.7 MPa (6.91 ksi). The yield strength of the main reinforcing bars was 504 MPa (73.09 ksi), while the yield strength of the stirrups was 334 MPa (48.44 ksi). The investigators stated that the control beam experienced failure due to standard steel yielding, which was subsequently followed by concrete crushing. This failure mode happened due to the relatively long constant moment region compared to the shear span, as well as the large shear-to-flexural reinforcement ratio. The proposed method predicted the failure mode to occur in the horizontal strut, which reached the maximum concrete crushing strain (refer to Fig. 15).

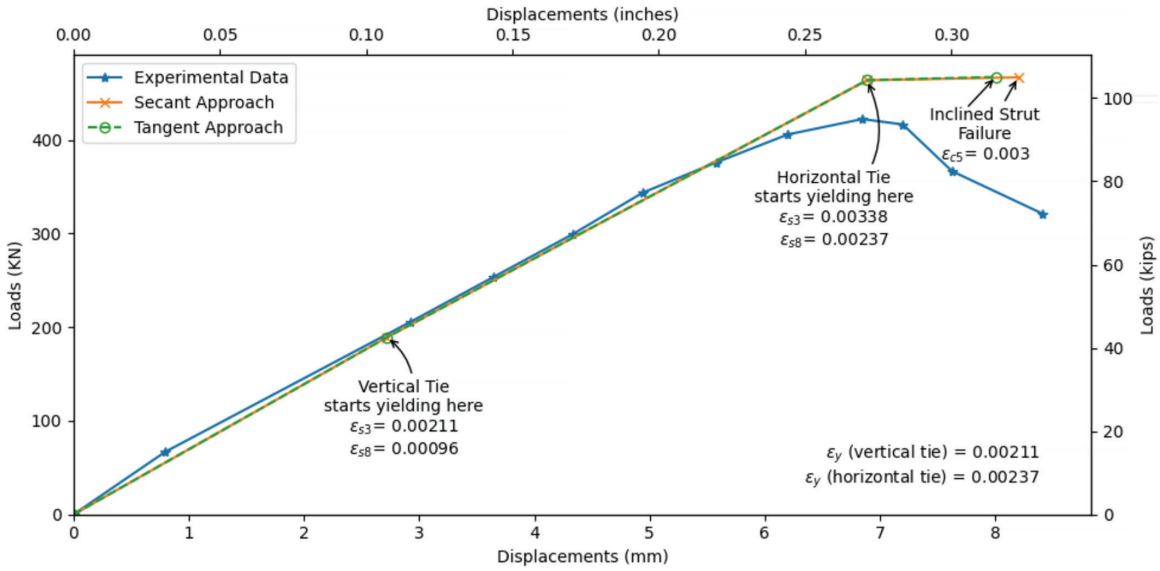

Fig. 9—Load-displacement curve of Specimen DB-1.25.

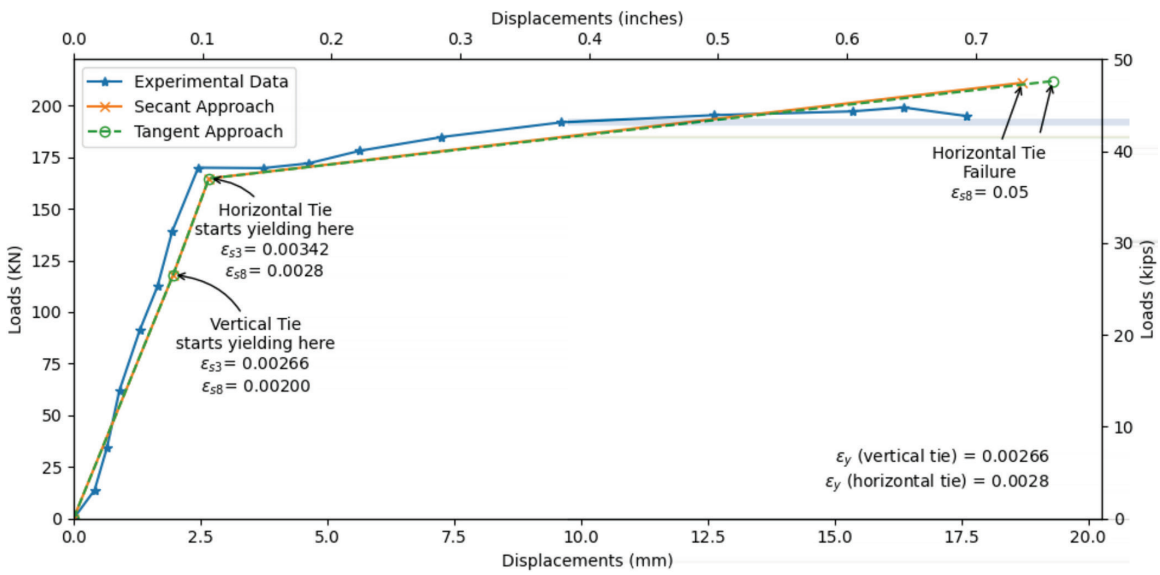

Fig. 10—Load-displacement curve of Specimen DB-1.40.

Table 3 summarizes the strain unity checks in the critical flexural and shear members, confirming the failure modes depicted by analysis. It is relevant to mention that the strain unity checks are simply ratios of the member strain from analysis at the ultimate stage divided by the corresponding ultimate strain of that specific member. This helps the reader judge which members dominate the failure mode.

Table 4 presents a comparison between the experimental and predicted failure modes for the seven RC deep beam tests examined. The experimental failure modes, such as flexural failure, shear compression, and concrete crushing failure, are shown alongside the predicted modes based on the analytical model. The predicted failure modes, including horizontal strut failure, inclined strut failure, horizontal tie failure, and vertical tie failure closely align with the experimental observations, indicating excellent agreement between the theoretical predictions and actual experimental outcomes. This agreement highlights the reliability of the predictive model in capturing the structural failure behavior of RC deep beams

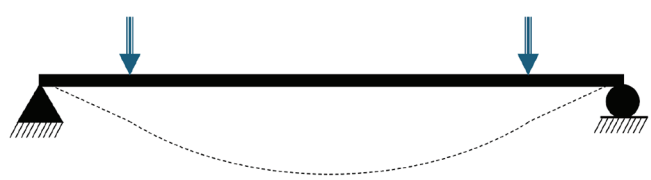

Fig. 11—Flexural behavior in beams with long constant moment region and short shear spans.

across various shear span-depth ratios.[20] Furthermore, the failure mode in the proposed method is determined through iterative processes. The secant approach requires 25 to 30 iterations to converge, while the tangent approach converges after three to eight iterations, demonstrating the efficiency of the tangent approach in achieving convergence for the ultimate stages. The tangent approach is superior to the secant approach when it comes to convergence speed due to a mathematical advantage inherent to the tangent formulation. This is simply due to the tangent to the nonlinear curve

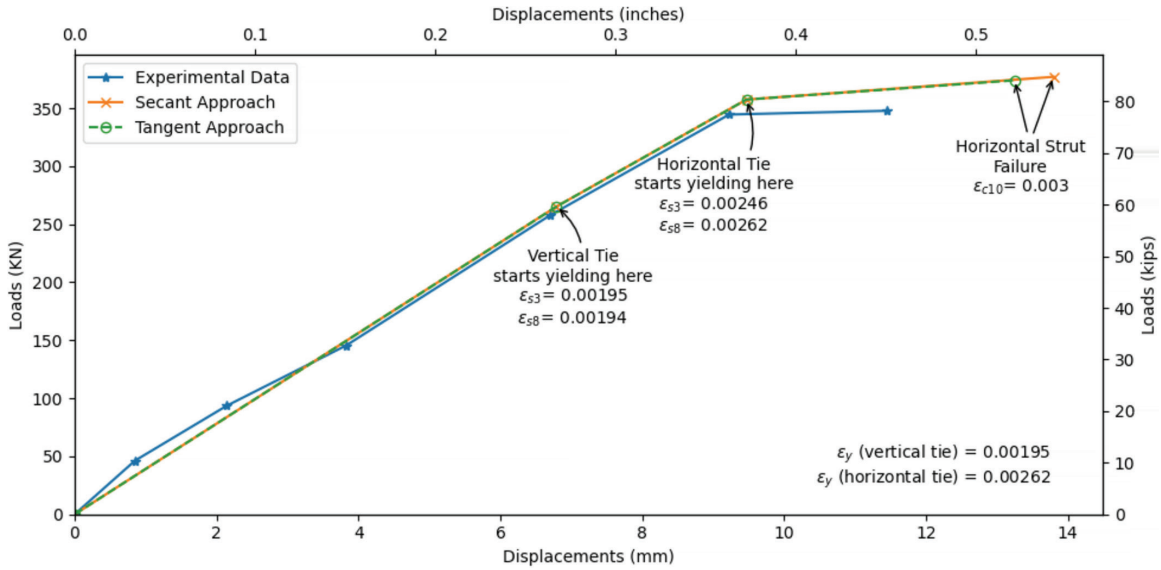

Fig. 12—Load-displacement curve of Specimen DB-1.50.

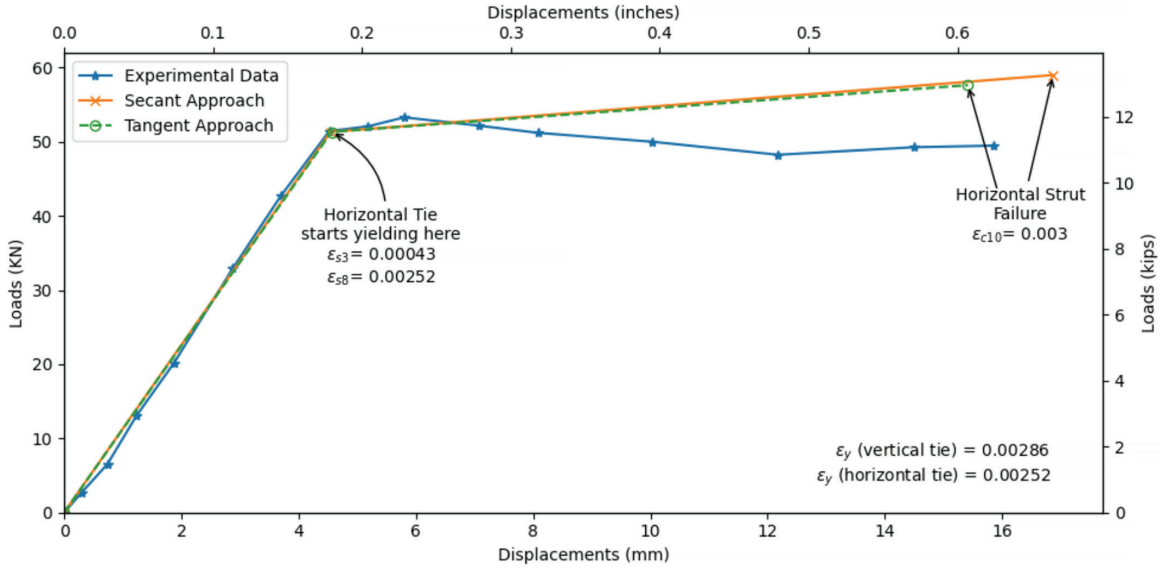

Fig. 13—Load-displacement curve of Specimen DB-2.00.

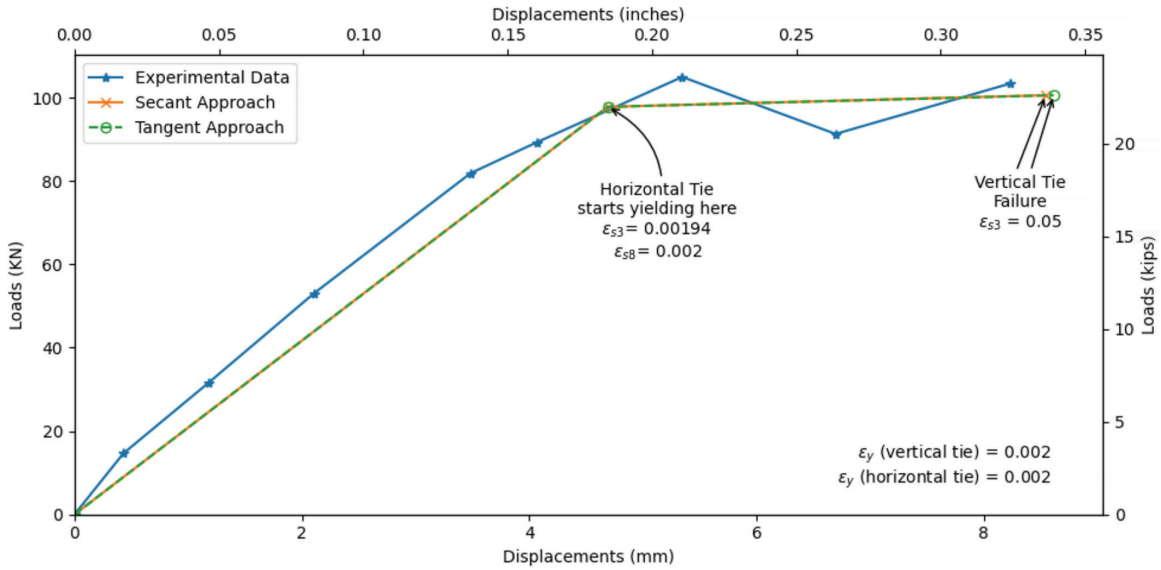

Fig. 14—Load-displacement curve of Specimen DB-2.25.

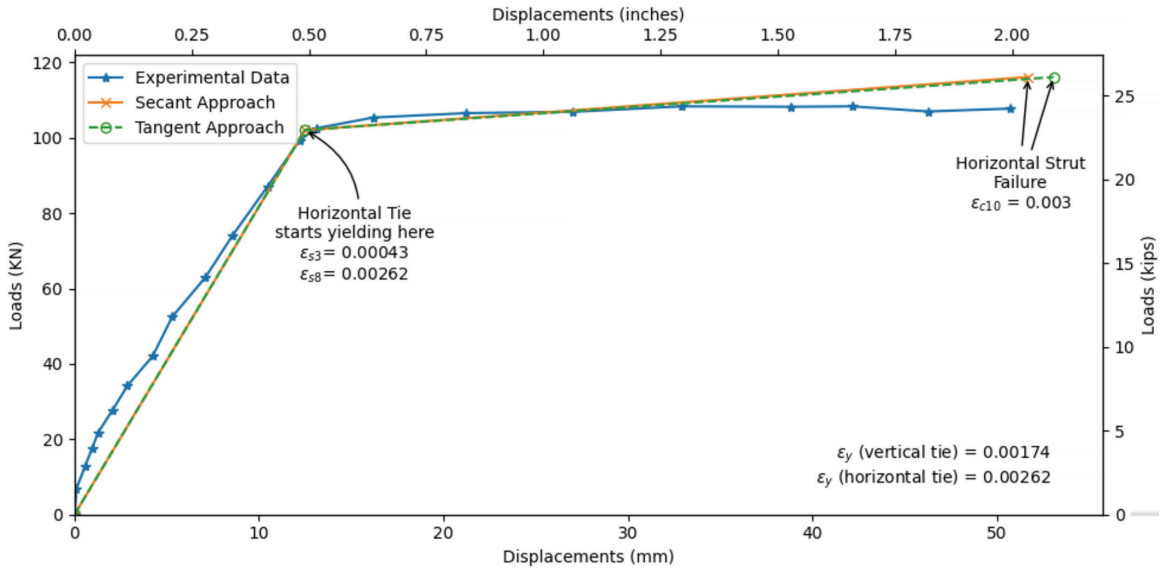

Fig. 15—Load-displacement curve of Specimen DB-2.70.

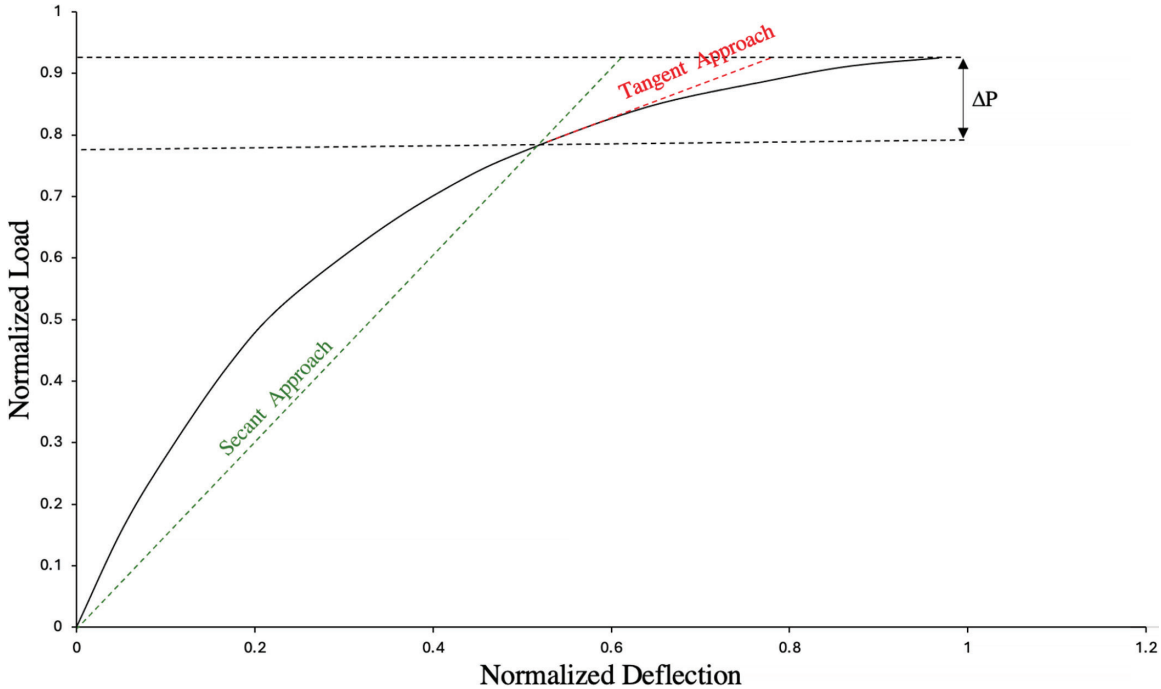

Fig. 16—Tangent and secant approach comparison.

reaching the correct solution by Newton-Raphson iteration much faster than the unguided secant formulation; refer to Fig. 16. It is clear from the aforementioned graph that the tangent red line reaches much closer to the correct point on the curve than the secant line when extended by a load increment of ΔP (for a full-color version of this paper, refer to www.concrete.org).

CONCLUSIONS

In this paper, an innovative truss analysis of reinforced concrete (RC) deep beams is formulated and presented by using the strut-and-tie method (STM). The following conclusions can be drawn based on the predicted results described previously:

1. The secant and tangent approaches exhibit a high degree of correlation with the experimental data, providing accurate load and deflection estimates at the yield and the ultimate points of both vertical and horizontal ties. Moreover, the secant approach requires a greater number of iterations in comparison to the tangent approach.

2. Yield points are directly influenced by the horizontal ties in Specimens DB-2.00, DB-2.25, and DB-2.70, while in Specimens DB-1.00, DB-1.25, DB-1.40, and DB-1.50, the vertical ties yielded before the horizontal ties, indicating the formation of diagonal cracks. Conversely, the ultimate points are primarily determined by which element reaches its maximum strain first, with ε_{su} = 0.05 for steel and ε_{cu} = 0.003 for concrete. The predicted failure modes show excellent agreement with the experimental failure modes.

3. The study investigates two distinct experimental configurations: the three-point bending and the four-point bending tests. Both methods demonstrate high precision in measuring the complete response. Additionally, this study explores two different beam reinforcement layouts, each featuring either one or two layers of bottom steel reinforcement.

4. This study highlights the development of a systematic yet innovative approach in accurately analyzing RC deep beams that lends itself to direct programming and automation.

It is also important to state herein that this method does not currently address uniform loading cases, nor does it implement horizontal skin reinforcement in the models. These features will be implemented in a future study.

AUTHOR BIOS

ACI member **Ali H. Alqarni** *is an Assistant Professor in the Department of Civil and Construction Engineering, College of Engineering, Imam Abdulrahman Bin Faisal University, Dammam, Saudi Arabia. He received his BS in construction engineering from Imam Abdulrahman Bin Faisal University; his MS in civil engineering from the University of Dayton, Dayton, OH; and his PhD in civil engineering from Kansas State University, Manhattan, KS. His research interests include the nonlinear analysis of concrete deep beams reinforced with conventional steel and glass fiber-reinforced polymer (GFRP) bars.*

Hayder A. Rasheed, *FACI, is a Professor of structural engineering at Kansas State University. He received his PhD from The University of Texas at Austin, Austin, TX, in 1996. He is a member of ACI Committees 440, Fiber-Reinforced Polymer Reinforcement; and 441, Reinforced Concrete Columns. His research interests include the behavior of reinforced/prestressed concrete and advanced composites.*

ACI member **Krishna Ghimire** *is a Teaching Associate Professor of civil engineering at Kansas State University. He is a member of ACI Committees 311, Inspection of Concrete; 408, Bond and Development of Steel Reinforcement; and 437, Strength Evaluation of Existing Concrete Structures.*

ACKNOWLEDGMENTS

The first author is thankful to the Deanship of Scientific Research at Imam Abdulrahman Bin Faisal University, Saudi Arabia, for the financial support provided through the scholarship program of the university.

NOTATION

A = area
a = shear span
b = width
d = depth
E = modulus of elasticity
F = axial force
f = stress
h = height
J_d = height of truss
K = global stiffness
L = length
P = load
W = depth of connecting nodes
Wsc = width of shear crack
y_c = depth of horizontal strut from compression fiber
y_t = depth of horizontal tie from tension fiber
β_s = effective depth factor of beam section in compression side
ε = strain
Φ = steel diameter
v = node deflection under one unit load
θ = strut angle

Subscripts

$_c$ = concrete
$_{cr}$ = cracking
$_{dst}$ = diagonal strut
$_e$ = element
$_{hst}$ = horizontal strut
$_s$ = steel
$_{st}$ = stirrups
$_{svt}$ = vertical steel ties
$_u$ = ultimate
$_{vt}$ = vertical tie
$_y$ = yielding
$_1$ to $_7$ = element numbers

REFERENCES

1. ACI Committee 318, "Building Code Requirements for Structural Concrete (ACI 318-19) and Commentary (ACI 318R-19) (Reapproved 2022)," American Concrete Institute, Farmington Hills, MI, 2019, 624 pp.

2. Wang, C. M., "Timoshenko Beam-Bending Solutions in Terms of Euler-Bernoulli Solutions," *Journal of Engineering Mechanics*, ASCE, V. 121, No. 6, 1995, pp. 763-765.

3. Norris, T.; Saadatmanesh, H.; and Ehsani, M. R., "Shear and Flexural Strengthening of R/C Beams with Carbon Fiber Sheets," *Journal of Structural Engineering*, ASCE, V. 123, No. 7, 1997, pp. 903-911.

4. Aguilar, G.; Matamoros, A. B.; Parra-Montesinos, G.; Ramírez, J. A.; and Wight, J. K., "Experimental Evaluation of Design Procedures for Shear Strength of Deep Reinfoced Concrete Beams," *ACI Structural Journal*, V. 99, No. 4, July-Aug. 2002, pp. 539-548.

5. Salami, M.; Kobayashi, H.; and Unjoh, S., "Experimental and Analytical Study on RC Deep Beams," *Asian Journal of Civil Engineering*, V. 6, No. 5, 2005, pp. 487-499.

6. Kim, H. S.; Lee, M. S.; and Shin, Y. S., "Structural Behaviors of Deep RC Beams under Combined Axial and Bending Force," *Procedia Engineering*, V. 14, 2011, pp. 2212-2218.

7. Zhu, W.; François, R.; Cleland, D.; and Coronelli, D., "Failure Mode Transitions of Corroded Deep Beams Exposed to Marine Environment for Long Period," *Engineering Structures*, V. 96, 2015, pp. 66-77.

8. Raheem, M. M., and Rasheed, H. A., "Novel Truss Analogy Model to Predict Full Response of Reinforced Concrete Deep Beams," *ACI Structural Journal*, V. 119, No. 4, July 2022, pp. 97-108.

9. Pham, H., and Al-Mahaidi, R., "Experimental Investigation Into Flexural Retrofitting of Reinforced Concrete Bridge Beams Using FRP Composites," *Composite Structures*, V. 66, No. 1-4, 2004, pp. 617-625.

10. Abbood, I. S., "Strut-and-Tie Model and Its Applications in Reinforced Concrete Deep Beams: A Comprehensive Review," *Case Studies in Construction Materials*, V. 19, 2023, Article No. e02643.

11. Sanad, A., and Saka, M. P., "Prediction of Ultimate Shear Strength of Reinforced-Concrete Deep Beams Using Neural Networks," *Journal of Structural Engineering*, ASCE, V. 127, No. 7, 2001, pp. 818-828.

12. Tan, K. H., and Cheng, G. H., "Size Effect on Shear Strength of Deep Beams: Investigating with Strut-and-Tie Model," *Journal of Structural Engineering*, ASCE, V. 132, No. 5, 2006, pp. 673-685.

13. Gandomi, A. H.; Alavi, A. H.; Mohammadzadeh Shadmehri, D.; and Sahab, M. G., "An Empirical Model for Shear Capacity of RC Deep Beams Using Genetic-Simulated Annealing," *Archives of Civil and Mechanical Engineering*, V. 13, No. 3, 2013, pp. 354-369.

14. Chou, J.-S.; Ngo, N.-T.; and Pham, A.-D., "Shear Strength Prediction in Reinforced Concrete Deep Beams Using Nature-Inspired Metaheuristic Support Vector Regression," *Journal of Computing in Civil Engineering*, ASCE, V. 30, No. 1, 2016, p. 04015002.

15. Ismail, K. S.; Guadagnini, M.; and Pilakoutas, K., "Strut-and-Tie Modeling of Reinforced Concrete Deep Beams," *Journal of Structural Engineering*, ASCE, V. 144, No. 2, 2018, p. 04017216.

16. Nayal, R., and Rasheed, H. A., "Tension Stiffening Model for Concrete Beams Reinforced with Steel and FRP Bars," *Journal of Materials in Civil Engineering*, ASCE, V. 18, No. 6, 2006, pp. 831-841.

17. Jin, L.; Zhang, J.; Song, B.; Li, D.; Li, P.; and Du, X., "Effect of Stirrups on Shear Performance of Geometrically-Similar Reinforced Concrete Deep Beams: An Experimental Study," *Engineering Structures*, V. 295, 2023, Article No. 116883.

18. Tan, K.-H.; Kong, F.-K.; and Teng, S., and Guan, L., "High-Strength Concrete Deep Beams with Effective Span and Shear Span Variations," *ACI Structural Journal*, V. 92, No. 4, July-Aug. 1995, pp. 395-405.

19. Kadhim, S., and Özakça, M., "Flexural Performance of RC Beams Externally Strengthened with a Single-Layer of Basalt Fiber Reinforced Polymer Sheets," *Composites and Advanced Materials*, V. 31, 2022, 17 pp.

20. Alqarni, A. H., "Comprehensive Treatment of Strut-And-Tie Approach across Concrete Deep Beams Reinforced with Different Systems," dissertation, Kansas State University, Manhattan, KS, 2025.

ACI STRUCTURAL JOURNAL TECHNICAL PAPER

Title No. 123-S56

Optimized Slant Shear Interface between Steel-Fiber Concretes

by Aaron Nzambi, Victória Seixas, and Dênio Oliveira

This study investigated the shear bond behavior, with and without optimized interfaces, between conventional and geopolymer steel fiber-reinforced concretes. Sixteen prismatic and eight cylindrical composite specimens were cast with interface inclination angles of 45 and 27 degrees, respectively. In prisms, the inclined interface area was varied: eight were optimized by 50% to balance compressive and shear stresses, allowing a more accurate determination of cohesion and friction coefficients under steel fiber effects. Fiber volume fractions of 0.0, 0.5, 1.0, and 1.5% were tested, and the influence of epoxy at the interface was also assessed. Optimized prisms exhibited adhesive failure along the interface, matching the internal friction angle, whereas non-optimized prisms showed cohesive failure with a friction angle deviating from the interface. Increasing fiber content improved performance, especially when combined with epoxy. A new bond shear strength model is proposed, incorporating friction, cohesion, and fiber effects.

Keywords: geopolymer concrete; interface; shear strength; slant shear; steel fiber.

INTRODUCTION

The growing demand for concrete, combined with the global push for sustainable materials to reduce CO_2 emissions, has driven research into low-carbon alternatives that minimize the environmental impacts associated with clinker and carbon steel production. Among these alternatives, geopolymer concrete (GPC) and steel fibers have emerged as environmentally friendly solutions to reduce portland cement and steel consumption in the construction industry.

Geopolymer concrete, first introduced in the 1970s,[1-4] is produced by activating aluminosilicate-rich precursors—such as blast-furnace slag, fly ash, or metakaolin—with alkaline solutions, typically sodium hydroxide (NaOH) and sodium silicate (Na_2SiO_3). The effectiveness of NaOH depends on its molar concentration; literature[2] indicates that concentrations between 5 and 16 mol are required to break precursor bonds and form a three-dimensional aluminosilicate gel network.

GPC exhibits low porosity, high resistance to chemical attack and fire, and excellent compressive strength. However, it generally has a lower modulus of elasticity compared to conventional concrete (CC). The addition of steel fibers enhances its mechanical performance and durability, improving ductility, toughness, and steel-concrete bond,[5] while also increasing residual strength, reducing crack propagation, and boosting flexural, shear, and punching resistance.[2,6,7] These improvements make steel fiber-reinforced geopolymer concrete (SFRGPC) an attractive choice for a range of applications, from industrial floors to large structural elements. Moreover, studies indicate that incorporating steel fibers into repair materials can improve the bond interface between substrate and overlay.[8,9] However, further research is needed to fully understand their role in enhancing surface roughness and their influence on stress states and failure modes in old-to-new concrete bonding.

Bond performance between substrate and repair materials—whether or not a bonding layer (for example, epoxy adhesive) is used—is typically evaluated through adherence tests.[10-15] Achieving high bond strength is essential for ensuring monolithic structural behavior.[16] The strength of concrete-to-concrete interfaces is influenced by several factors, including specimen geometry, shear plane inclination, stiffness differences between concretes, interface treatment (surface roughness), and the presence or absence of bonding agents.[13,17] Various testing methods exist, classified according to the type of stress at the bond interface (shear or tensile). The selection of the test method must reflect the expected in-service stress conditions. For example, failure may occur vertically under load in direct or pure shear tests, or along an inclined plane in oblique shear tests—commonly referred to as slant shear tests (SSTs)—which combine compressive and shear stresses at the interface. The SST, along with the splitting tensile test, remains one of the most widely used approaches for bond strength evaluation.

Slant shear test

The SST, originally proposed by Kriegh et al.[18-21] as the Arizona Composite-Cylinder Test, evaluates shear strength at inclined interfaces, typically 30 degrees to the vertical (Fig. 1(a)), representative of stress directions in bridge joints.[25] The method applies combined compressive and shear stresses under axial loading to assess bonding materials such as structural epoxies. Variations have been used in precast element (Fig. 1(b)) evaluation[23] and prismatic specimens[26] (Fig. 1(c)), with standards ASTM C882/C882M[27] and BS EN 12615[24] later formalizing the procedure, and recent ASTM updates[22] extending it to bonded and unbonded interfaces.

In SST, cohesive failure occurs within the concrete adjacent to the interface, while adhesive failure occurs along the bond line. Failure mode depends on interface angle.[28,29]

ACI Structural Journal, V. 123, No. 3, May 2026.
MS No. S-2025-033.R4, doi: 10.14359/51749306, received August 23, 2025, and reviewed under Institute publication policies. Copyright © 2026, American Concrete Institute. All rights reserved, including the making of copies unless permission is obtained from the copyright proprietors. Pertinent discussion including author's closure, if any, will be published ten months from this journal's date if the discussion is received within four months of the paper's print publication.

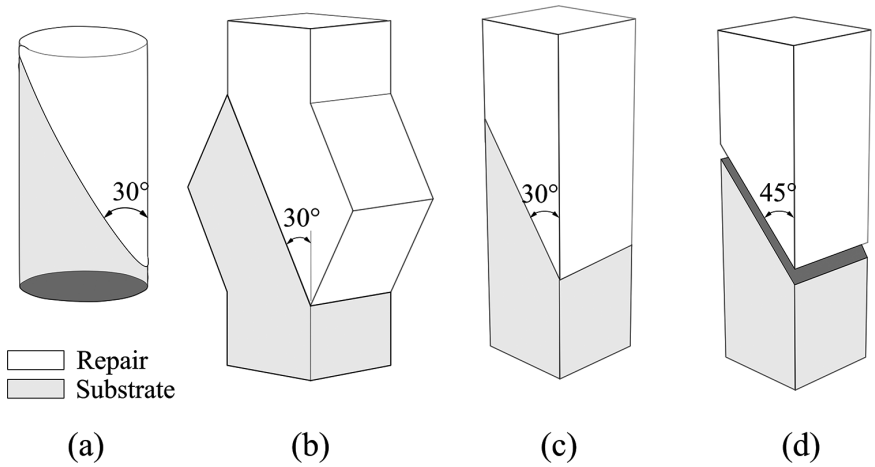

Fig. 1—Typical SST specimen models: (a) ASTM C882/C882M model[22]; (b) model used by Diaz[23]; (c) BS EN 12615[24] model; and (d) proposed model.

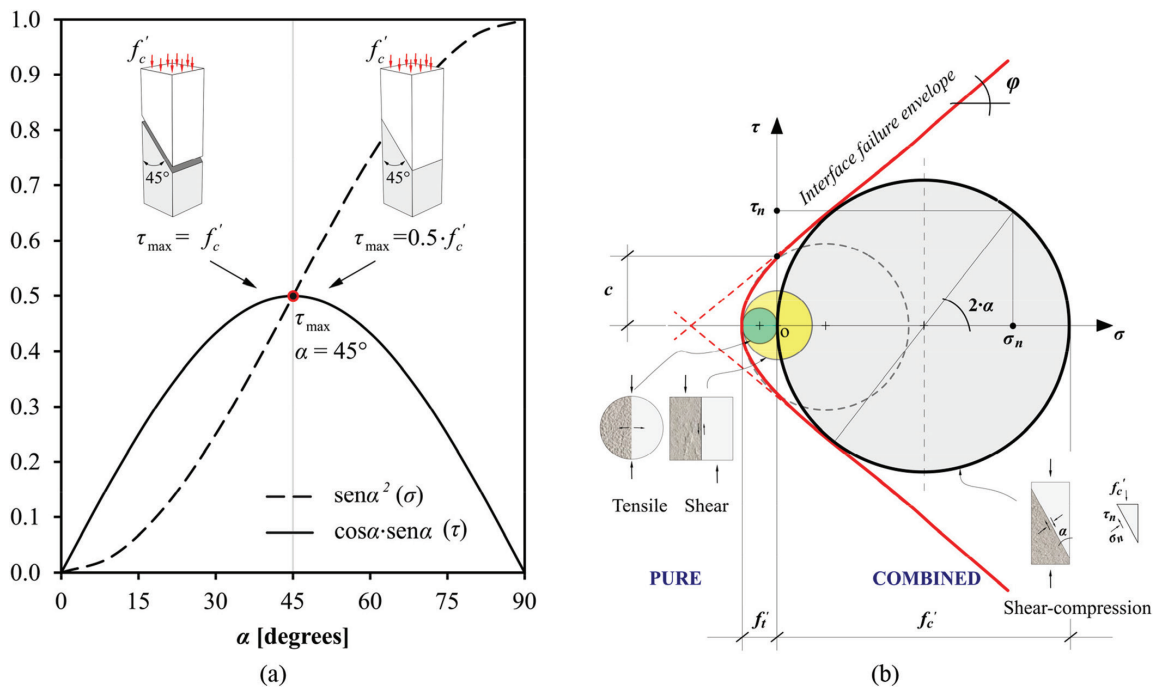

Fig. 2—(a) Induced failure assumed at interface; and (b) stress state at interface for several test methods.

Higher angles increase compressive stress influence, approaching the compressive strength of the weaker material. Surface roughness enhances friction and mechanical interlock, which can shift the fracture plane away from the interface,[30,31] potentially increasing strength but masking actual interface stress states. Differences in modulus of elasticity also influence results; GPC, for example, has a lower modulus but higher compressive strength than conventional concrete.[2]

Cohesive failure typically occurs in the material with lower compressive strength, limiting uniform stress distribution. Saldanha et al.[32] found geometry modification alone insufficient to force adhesive failure, requiring reinforcement to control cracking.

This study evaluated bond strength between CC substrates and GPC repairs with 0.5, 1.0, and 1.5% steel fibers using a modified prismatic SST. The 45-degree interface had a 50% reduced area from grooves (Fig. 1(d)) to align the internal friction angle with the interface angle, balancing compressive and shear stresses (Fig. 2(a)). While SST is not pure shear ($\sigma_n \neq 0$, Fig. 2(b)), this "optimized slant shear" approach enabled uniform stress distribution, improving assessment of fiber roughness, epoxy bonding, and stiffness effects. Results for grooved prisms were compared to non-grooved prisms and 27-degree cylindrical specimens, with friction and cohesion coefficients proposed and validated against AASHTO LRFD,[33] ACI 318,[34] CSAA23.3,[35] Eurocode 2,[36] and *fib* Model Code.[37]

RESEARCH SIGNIFICANCE

Cohesive failure in concrete-to-concrete bonds is considered satisfactory in the SST. However, it may reflect a greater influence of compressive stresses, altering the shear failure plane inclination relative to the internal friction angle, which

Table 1—Mixture proportions and mechanical properties of concrete

Mixture ID	Grade	Mixture proportion, kg/m³ (proportion by weight)									Slump, mm	Mechanical properties at 28 days			
		Cement	Small aggregate	Coarse aggregate	Steel fiber	Active silica	Water	Chemical admixture	Metakaolin	Alkaline solution		No. Samples	f_c, MPa (CoV)	f_t, MPa (CoV)	E_c, GPa (CoV)
Old concrete															
$CC_{0.0}$	C30	365 (1.00)	838 (2.30)	984 (2.70)	—	7.3 (0.02)	183 (0.50)	7.3 (0.02)	—	—	202	6	27.6 (9%)	3.1 (8%)	29.4*
$SFRC_{0.5}$					39.3				—	—	145	6	28.5 (1%)	2.8 (4%)	29.9*
$SFRC_{1.0}$					78.5				—	—	160	6	28.1 (7%)	3.3 (14%)	29.7*
$SFRC_{1.5}$					117.8				—	—	120	6	26.2 (14%)	4.9 (3%)	28.6*
New concrete															
$GPC_{0.0}$	C30	—	958 (2.30)	1125 (2.70)	—	8.3 (0.02)	42 (0.10)	8.3 (0.02)	417 (1.00)	334 (0.80)	135	9	35.8 (16%)	3.1 (22%)	20.3 (14%)
$SFRGPC_{0.5}$		—			39.3						125	9	39.3 (12%)	4.1 (20%)	20.5 (16%)
$SFRGPC_{1.0}$		—			78.5						100	9	37.4 (4%)	4.8 (6%)	18.7 (13%)
$SFRGPC_{1.5}$		—			117.8						110	9	34.2 (2%)	4.0 (14%)	18.3 (12%)

*Calculated from expression $E_c = 5600\sqrt{f_c}$, according to ABNT NBR 8522-1:2021.[38]

Note: CC is conventional concrete (portland cement + aggregates + water); SFRC is steel fiber-reinforced concrete (CC mixture + steel fibers); GPC is geopolymer concrete (metakaolin + aggregates + alkaline solution + water); SFRGPC is steel fiber-reinforced geopolymer concrete (GPC mixture + steel fibers).

can affect the friction and cohesion coefficients in design models. To address this, the Optimized Slant Shear Interface Test (OSSIT) was developed, aiming to align the internal friction angle with the desired bond surface. This modification enables a more accurate determination of friction and cohesion coefficients, while isolating and highlighting the influence of steel fibers on bond performance and interface behavior.

EXPERIMENTAL INVESTIGATION

The experimental program was conducted at the Laboratory of the Graduate Program in Civil Engineering of the Federal University of Pará. A total of 24 specimens were cast: 16 prismatic and eight cylindrical. Eight main concrete mixtures were prepared: four conventional concrete mixtures, used as the old concrete (substrate), and four geopolymer concrete mixtures, used as the new concrete (repair). The steel fiber content was varied at 0.0%, 0.5%, 1.0%, and 1.5% by volume. All specimens were tested under compressive loading using the SST method.

Materials and concrete properties

Table 1 summarizes the compositions and mechanical properties of the mixtures. The conventional concrete used CP II-F-32 portland cement as the binder, while the geopolymer concrete employed metakaolin (Table 2) activated with a 16 M solution of sodium hydroxide and neutral sodium silicate.[5] Aggregate proportions were kept constant. Small aggregate consisted of local sand (fineness modulus 2.63, maximum size 1.18 mm) and coarse aggregate was gravel (fineness modulus 3.69, maximum size 9.5 mm) (Fig. 3). Hooked-end steel fibers[41,42] with a length of 60 mm, diameter of 0.90 mm, tensile strength of 1160 MPa, and modulus of elasticity of 210 GPa were added at different volume fractions. Active silica and a high-range water-reducing admixtures ensured workability. For each mixture, nine cylindrical specimens (Ø100 x 200 mm) were tested for compressive strength,[43] tensile strength,[44] and modulus of elasticity.[38] Geopolymer concrete exhibited compressive strength gains of 31 to 38% compared to conventional concrete, particularly with fiber contents of 0.5% and 1.5%.

Table 2—Physical and chemical properties of metakaolin[39]

Physical and chemical properties	Typical value	Limit value
SiO_2	57.0%	44.0 to 65.0%
Al_2O_3	34.0%	32.0 to 46.0%
CaO + MgO	< 0.1%	< 1.5%
SO_3	< 0.1%	< 1.0%
Na_2O	< 0.1%	< 0.5%
Fe_2O_3	2.0%	—
TiO_2	1.5%	—
Humidity	0.5%	< 2.0%
Fire loss	3.0%	< 4.0%
Residue #325	6.0%	< 10.0%
BET Specific surface area	230,000 cm²/g	150,000 cm²/g
Specific mass	2.56 g/cm³	—

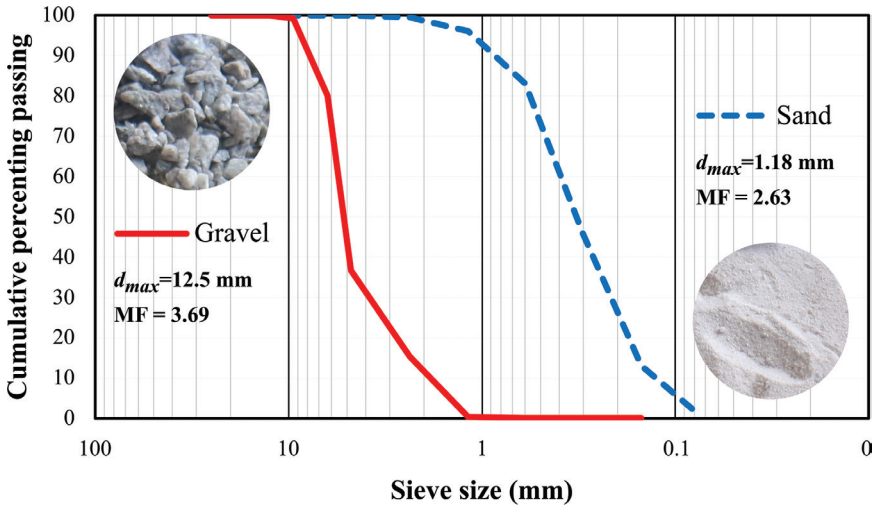

Fig. 3—Tested particle size distribution of aggregates.[40]

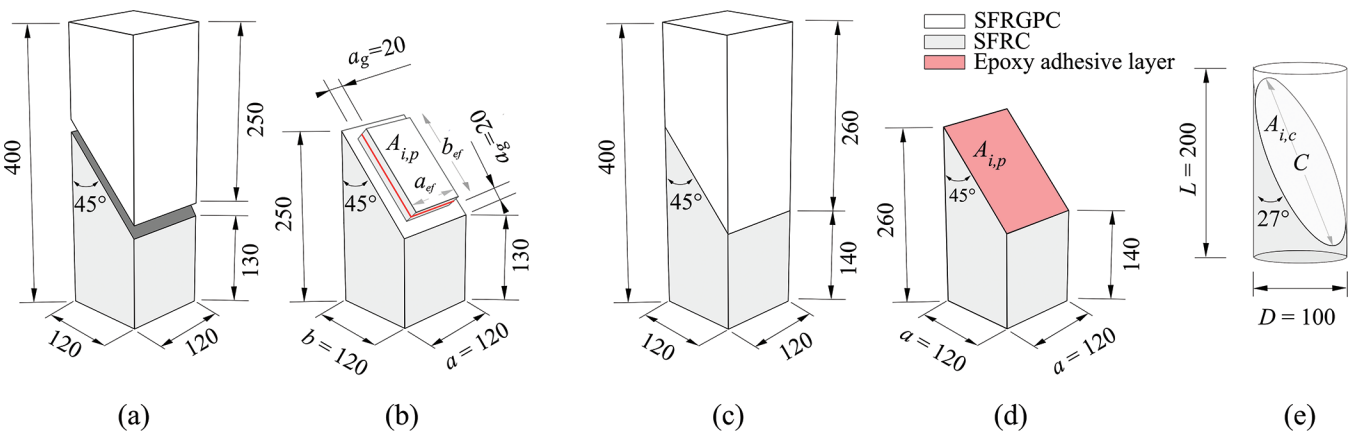

Fig. 4—Characteristics and dimensions of specimens: (a) composite concrete prism with grooves; (b) details of reduced bonding surface ($A_{i,p}$ = 10,376.00 mm^2), $A_{i,p} = a_{ef}b_{ef}$, $a_{ef} = a - (2a_g)$, $b_{ef} = \sqrt{a^2 + b^2} - (2a_g)$; (c) composite concrete prism without grooves; (d) details of bonding surface ($A_{i,p}$ = 20,365.00 mm^2), $A_{i,p} = a^2/\sin\alpha$; and (e) composite cylindrical specimen ($A_{i,c}$ = 17,562.05 mm^2), $A_{i,p} = [\pi(D/2)(C/2)]$.

It also showed higher tensile strength and lower modulus of elasticity, indicating greater ductility.

Specimen characteristics

Figures 4(a) to (e) illustrate the specimen configurations. The optimized prismatic specimens with grooves in the interface contour were designated as GP, and the unoptimized prisms were designated as UGP. Conventional concrete was cast first; after 28 days, the geopolymer concrete was placed. Curing was carried out at room temperature[45] under 85% relative humidity. For prisms, the old concrete surfaces were chipped to expose the fibers before placing the repair mixture. In each fiber ratio group, one prism received a two-part epoxy adhesive (Table 3) layer on the bond surface prior to repair casting. Figures 5(a) to (c) show the bond surface preparation[46] steps.

Test setup

The tests were conducted on a servo-controlled universal testing machine (closed circuit) with a capacity of 2000 kN, as shown in Fig. 6. The setup consisted of a fixed base, an actuator, and two steel plates fixed to the specimen ends—square plates (120 x 120 mm, 18 mm thick) for prisms and circular plates (100 mm diameter, 18 mm thick) for cylinders. The procedure started by adjusting the mobile platform height and applying an initial load of 0.50 to 1.00 kN to ensure proper seating without damaging the specimen. Loading was applied at a displacement rate of 0.05 mm/min until failure. Load and displacement data were recorded using software, and subsequent data analysis and graph generation were performed. This setup ensured controlled loading conditions, accurate measurement of responses, and reliable characterization of the bond strength in both prism and cylinder specimens.

Ultimate bond strength and normal stresses

As shown in Fig. 7(a), the compressive strength of composite specimens (f_c') is determined by Eq. (1), dividing the applied load (F) by the specimen's cross-sectional area. The bond strength (f_b) at the inclined concrete-to-concrete interface is calculated following ASTM C882/C882M[22] (Eq. (2)), while normal stresses are obtained from Eq. (3) and (4). Austin et al.[28] recommends including cohesion in interface shear bond strength. AASHTO LRFD,[33] CSAA23.3,[35]

(a) (b) (c)

Fig. 5—Substrate surface roughness: (a) partially chipped; (b) exposed fibers; and (c) partially slotted.

Table 3—Properties of epoxy adhesive (from manufacturer data sheet)

Properties	Description
Color	A: white; B: gray
Appearance	medium viscosity (fluid)
Density	~1.5 kg/l (A+B) (23°C)
Mixture ratio	A:B = 2:1 (parts by weight)
Curing time	24 hours (initial); 7 days (final)
Compressive strength	60 MPa (1 day); 80 MPa (7 days) (23°C)
Flexural strength	~50 MPa (7 days)
Bond strength to concrete	3.8 MPa (7 days); 18.4 MPa (14 days)
Bond strength to steel	12 MPa (3 days)
Application temperature	Min. +10°C / Max. +60°C
Pot life	1 kg: 45 minutes (23°C)

Eurocode 2,[36] and *fib* Model Code[37] incorporate cohesion and friction coefficients (Table 4), whereas ACI 318[34] omits friction, yielding conservative results. Tensile strength for composite cylinders (Fig. 7(b)) follows Eq. (5).[44,47] None of these codes account for steel fiber effects.

$$f_c' = F/A_c \tag{1}$$

$$f_b = F/A_i \tag{2}$$

$$\tau_v = f_b \cos(\alpha) \tag{3}$$

$$\sigma_v = f_b \sin(\alpha) \tag{4}$$

$$f_{ct}' = \frac{F}{A_t} = \frac{2 \cdot F}{\pi \cdot D \cdot L} \tag{5}$$

where f_c' is compressive strength of composite specimen; F is failure load; A_c is area; A_i is area of the inclined plane; f_b is shear bond strength; σ_n and τ_n are normal compressive and shear stresses acting on the bond interface, respectively; τ_u is bond shear strength; α is angle between the bond interface and the longitudinal axis; c is cohesion strength; f_{ctd} is design concrete tensile strength ($f_{ctd} = f_{ct}/\gamma_c$); f_{ct} is concrete tensile strength, ($f_{ct} = 0.3 \cdot f_{ck}^{2/3}$); f_{ct}' is concrete tensile strength of composite specimen; γ_c is concrete safety factor; μ is coefficient of friction; and f_{ck} is characteristic compressive strength of concrete.

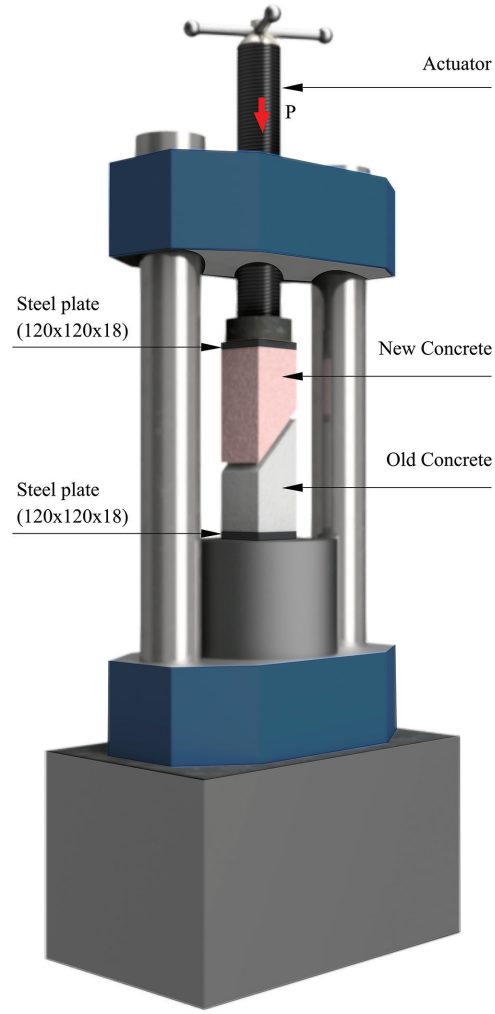

Fig. 6—Slant shear test setup illustration.

RESULTS AND DISCUSSIONS

Direct tensile analysis

The tensile bond strengths of the cylindrical composite specimens (f_{ct}') were 2.7 MPa (coefficient of variation [CoV] = 17%), 2.7 MPa (CoV = 15%), 2.9 MPa (CoV = 22%), and 3.1 (CoV = 9%) for fiber contents of 0.0%, 0.5%, 1.0%, and 1.5%, respectively. No strength increase was observed between the mixtures without fibers and those with 0.5% fibers, nor was there a significant difference between the 1.0 and 1.5% fiber contents. However, all composite specimens achieved average tensile bond strengths above 2.1 MPa at 28 days, classifying them as excellent quality according to

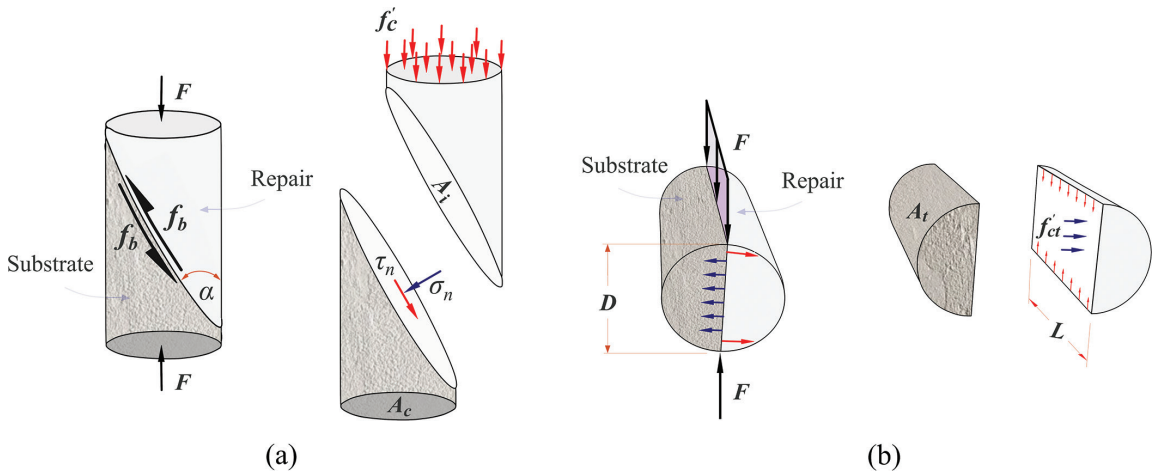

Fig. 7—Details of stress distributions at interface: (a) in oblique compression; and (b) in indirect tensile.

Table 4—Design codes' bond shear strengths without shear reinforcement and intentionally roughened

Codes	Design shear strength	Parameter values	
		Cohesion coefficient c	Friction coefficient μ
AASHTO- LRFD[33]	$\tau_n = c + \mu\sigma_n$	1.65 MPa	1.0
ACI 318[34]	$\tau_{nh} \leq 0.56$ MPa	0.56 MPa	—
CSAA23.3[35]	$\tau_r = \lambda\phi_c(c + \mu\sigma) \leq 0.25\phi_c f_{ck}$	0.50 MPa	1.0
Eurocode 2[36]	$\tau_{RD} = cf_{ctd} + \mu\sigma_n \leq 0.5\nu f_{cd}$	0.45 MPa	0.70
fib MC 2010[37]		0.40 MPa	0.70

Note: Except for ACI 318,[34] limits imposed by standards were not considered when comparing results to assess studied parameters, friction, and cohesion. λ is coefficient for lightweight concrete; ϕ_c is strength-reduction factor for concrete, $\phi_c = 0.65$; $\nu = 0.55\cdot(30/f_{ck})^{1/3} < 0.55$; $f_{cd} = f_{ck} / \gamma_c$, $\gamma_c = 1.5$.

ACI 546.3R,[48] with the 1.5% fiber mixture showing a 15% gain compared to the 0.0% mixture.

Slant shear analysis

Table 5 presents the SST results for the ultimate failure loads (F_u), the ultimate shear force at the interface ($V_u = F_u\cdot\cos\alpha$); the vertical stresses (f_c'); the bond strengths (f_b); the ultimate normal stresses (τ_u and σ_u); the ultimate load displacement (δ_{Fu}) and maximum displacement (δ_{max}); and the failure mode.

Failure loads and bond strengths

Figure 8 compares strength gains across specimens. Regardless of epoxy use, optimized prisms (GP) achieved 20 to 30% lower load capacity than non-optimized prisms (UGP) for 0.0% and 0.5% fiber contents. With epoxy and 1.0% fibers, UGP showed a 151% gain over GP. However, higher load capacity does not necessarily mean higher bond stress, since stress depends on load and failure surface area. For example, $PSGA_{1.0}$ and $PSA_{1.0}$ reached the same shear stress (17 MPa) despite different loads due to the 50% reduced area in optimized prisms.

Figure 9 shows GP failing by adhesive shear at 45 degrees, while UGP failed cohesively in compression. UGP did not exceed the ACI 546.3[48] qualitative limit of 21 MPa. Cylindrical specimens performed worse, partly due to fiber settlement during casting and slower curing. Epoxy improved strength by 16 to 53% in GP and 15 to 23% in UGP.

Displacements

Figures 10(a) to (d) present the displacement curves for GP with and without epoxy, by steel fiber content. GP specimens showed similar behavior, with average displacements at failure load (δ_{Fu}) and maximum displacement (δ_{max}) of 2.46 and 3.26 mm, respectively. For UGP, Fig. 11(a) to (d), δ_{Fu} and δ_{max} were 3.58 and 4.69 mm, representing increases of 46% and 44% compared to GP, indicating compression in these specimens and corresponding gains in failure load. Cylindrical specimens (CS) showed δ_{Fu} and δ_{max} of 1.63 and 1.90 mm. Despite their lower strengths, the curves revealed post-cracking resistance with gradual load reduction, influenced by steel fibers (Fig. 12(a) to (d)). Even mixtures without fibers exhibited smoother displacement curves, attributed to the lower modulus of elasticity of geopolymer concrete, particularly evident in prismatic specimens.

Analysis of concrete envelope and cracking maps

Figures 13(a) to (d) present the concrete failure envelopes for the lowest compressive and tensile strengths of the control full cylindrical specimens. A Coulomb-type failure envelope was identified for each steel fiber content in the four CC-GPC mixture combinations. GP showed higher resistance than UGP and cylindrical specimens, even with critical cracks at the interface. Steel fibers around the bond surface acted as reinforcement, providing a bridging effect and increasing stress capacity through enhanced ductility and bond efficiency.

Table 5—Experimental results of slant shear tests

ID.	Interface				F_u, kN	V_u, kN	f_c', MPa	Bond strength		Normal stresses		Displacements		Failure mode
	α, deg	Roug.	Cont.	Epoxy				A_i, mm^2	f_b, MPa	τ_u, MPa	σ_u, MPa	δ_{Fu}, mm	δ_{max}, mm	
$PSGA_{0.0}$	45	C	Gd	Yes	267.2	188.9	18.6	10,376	25.8	18.2	18.2	1.95	2.24	AF+CR
$PSG_{0.0}$				No	262.2	185.4	18.2	10,376	25.3	17.9	17.9	2.98	3.50	AF
$PSGA_{0.5}$				Yes	298.8	211.3	20.8	10,376	28.8	20.4	20.4	2.92	3.91	AF
$PSG_{0.5}$				No	257.8	182.3	17.9	10,376	24.8	17.6	17.6	2.37	3.02	AF
$PSGA_{1.0}$				Yes	250.1	176.8	17.4	10,376	24.1	17.0	17.0	1.75	3.59	AF
$PSG_{1.0}$				No	333.1	235.5	23.1	10,376	32.1	22.7	22.7	2.45	3.06	AF
$PSGA_{1.5}$				Yes	262.5	185.6	18.2	10,376	25.3	17.9	17.9	3.01	3.70	AF
$PSG_{1.5}$				No	172.0	121.6	11.9	10,376	16.6	11.7	11.7	2.26	3.09	AF
$PS_{0.0}$			—	No	314.3	222.2	21.8	20,365	15.4	10.9	10.9	3.31	4.07	CF+CR
$PSA_{0.0}$				Yes	325.4	230.1	22.6	20,365	16.0	11.3	11.3	2.37	2.62	CF+CR
$PS_{0.5}$				No	331.7	234.5	23.0	20,365	16.3	11.5	11.5	4.29	5.66	CF+CR
$PSA_{0.5}$				Yes	380.5	269.1	26.4	20,365	18.7	13.2	13.2	3.60	5.19	CF+CRS
$PS_{1.0}$				No	414.9	293.4	28.8	20,365	20.4	14.4	14.4	3.28	4.49	CF+CR
$PSA_{1.0}$				Yes	508.5	359.6	35.3	20,365	25.0	17.7	17.7	3.05	4.29	CF+CS
$PS_{1.5}$				No	367.1	259.6	25.5	20,365	18.0	12.7	12.7	3.96	4.83	CF+CS
$PSA_{1.5}$				Yes	348.9	246.7	24.2	20,365	17.1	12.1	12.1	4.81	6.39	CF+CI
$CS_{0.0}$	27	S		No	188.1	167.6	23.9	17,562	10.7	9.5	4.9	1.34	1.37	AF
$CS_{0.0}$					191.0	170.2	24.3	17,562	10.9	9.7	4.9	1.13	1.24	AF
$CS_{0.5}$					137.3	122.3	17.5	17,562	7.8	7.0	3.5	2.19	2.69	AF
$CS_{0.5}$					168.2	149.9	21.4	17,562	9.6	8.5	4.3	1.47	1.72	AF
$CS_{1.0}$					60.2	53.6	7.7	17,562	3.4	3.1	1.6	1.32	1.33	AF
$CS_{1.0}$					73.8	65.8	9.4	17,562	4.2	3.7	1.9	1.50	1.66	AF
$CS_{1.5}$					171.7	153.0	21.9	17,562	9.8	8.7	4.4	2.24	2.55	AF
$CS_{1.5}$					146.8	130.8	18.7	17,562	8.4	7.4	3.8	1.81	2.62	AF

Note: α is angle between bond interface and longitudinal axis; Roug. is roughness; Cont. is contour; C is chipped; S is slotted; Gd is Grooved. Specimen notation: PS is Prism specimen; G is Groove; A is Adesive; CS is Cylindrical specimen; and number in subscript refers to volumetric rate of steel fiber; AF is adhesive failure; CF is cohesive failure; AF+CR is adhesive failure and crushing of repair concrete; CF+CR is cohesive failure and crushing of repair concrete; CF+CR is cohesive failure and cracks at repair; CF+CS is cohesive failure and cracks at substrate; CF+CI cohesive failure and cracks at interface; CF+CRS is cohesive failure and cracks at repair and substrate.

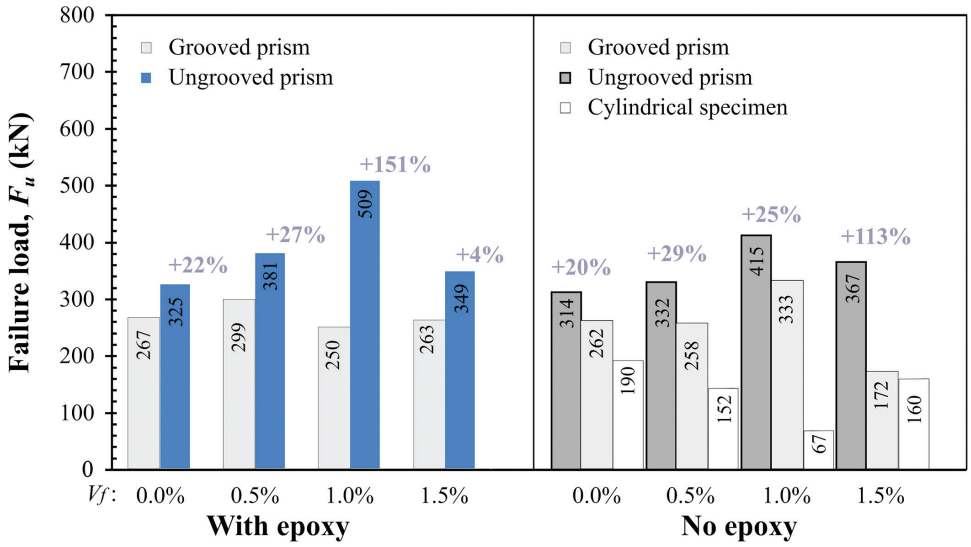

Fig. 8—Comparison of oblique shear failure loads.

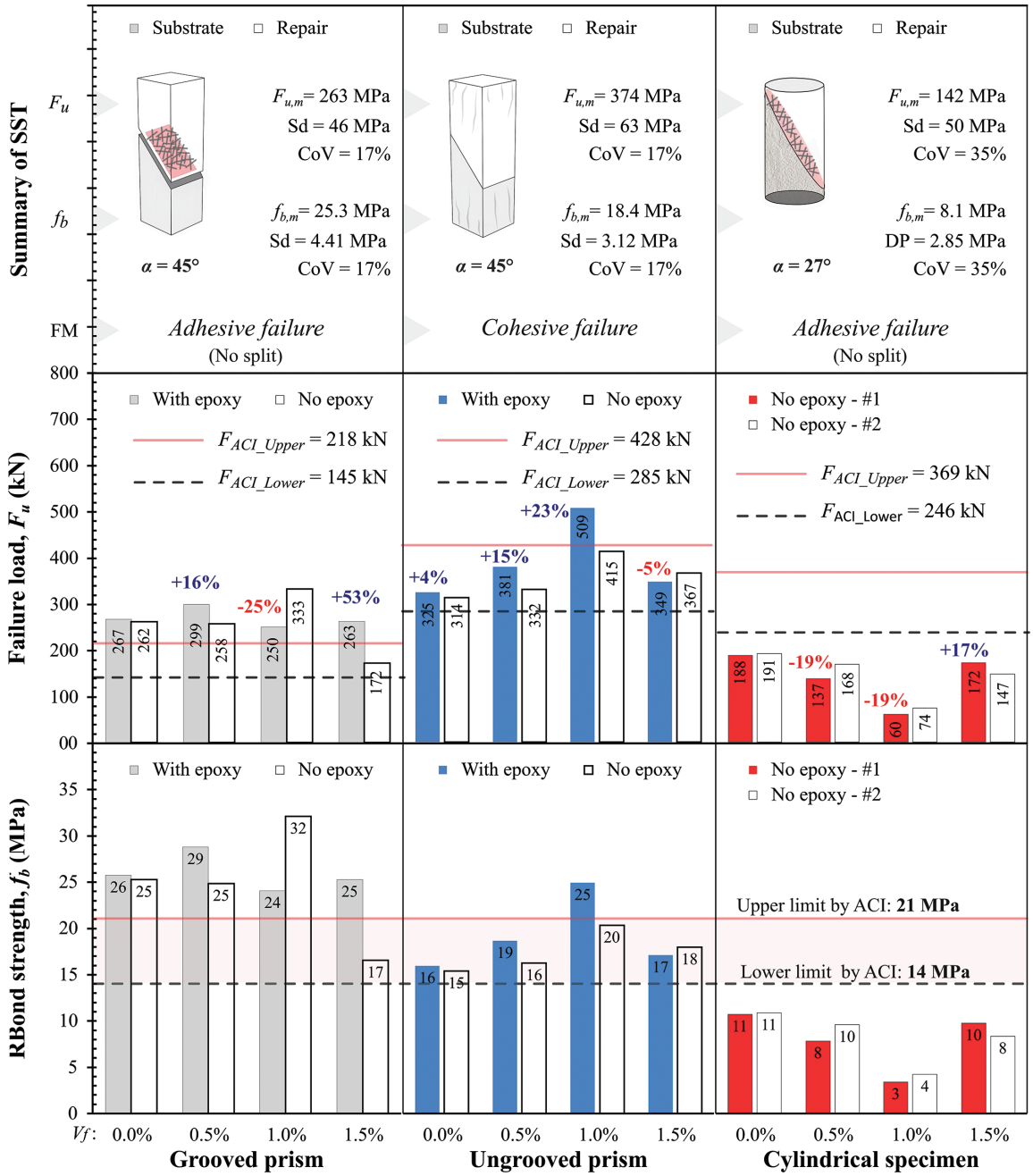

Fig. 9—Analysis of loads and failure modes.

No epoxy effect was observed for CC/GPC composites without fibers (V_f = 0.0%). At V_f = 0.5%, epoxy improved monolithicity, especially in $PSGA_{0.5}$ and $PSGA_{1.5}$ (GP + epoxy). UGP specimens exhibited cohesive failure outside the bond plane. Cylindrical specimens typically failed at the interface and in compression, except $CS_{1.0}$, which failed at the interface before reaching substrate stress levels. At V_f = 1.5%, except for GP + epoxy, performance was similar to fiberless mixtures, indicating no significant fiber effect, with results mainly influenced by the failure plane angle.

Influence of internal friction angle on failure mode

The internal friction angle at interface failure (ϕ) was calculated using Coulomb's theory, based on the compressive and tensile strengths of each composite specimen. As shown in Fig. 14, GP failed at the interface with an average ϕ of 44 degrees, confirming the observed failure mode and highlighting the steel fibers' contribution to post-cracking shear behavior. This reinforces the feasibility of using fiber-reinforced geopolymer concrete for repairs, as it can shift abrupt shear failures toward more ductile responses.

In contrast, UGP exhibited an average ϕ of 51 degrees, a 16% increase over GP, supporting the premise that failure planes with angles >45 degrees tend toward compression (cohesive failure). Cylindrical specimens showed similar behavior, with an average ϕ of 43 degrees, nearly 60% higher than the interface angle of 27 degrees. These failed at the interface due to low strength and in compression due to post-cracking adherence from interface roughness and steel fibers.

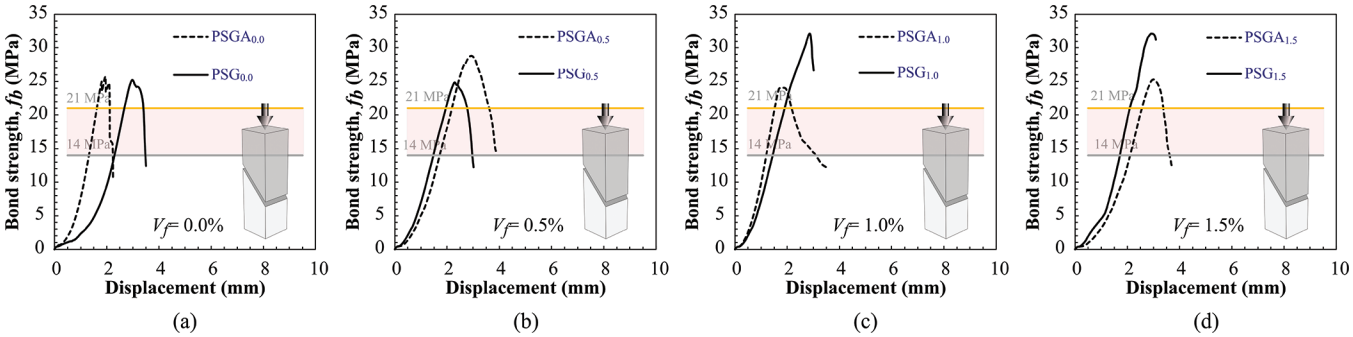

Fig. 10—Bond strength versus displacement curves in grooved prisms: (a) V_f *= 0.0%; (b)* V_f *= 0.5%; (c)* V_f *= 1.0%; and (d)* V_f *= 1.5%.*

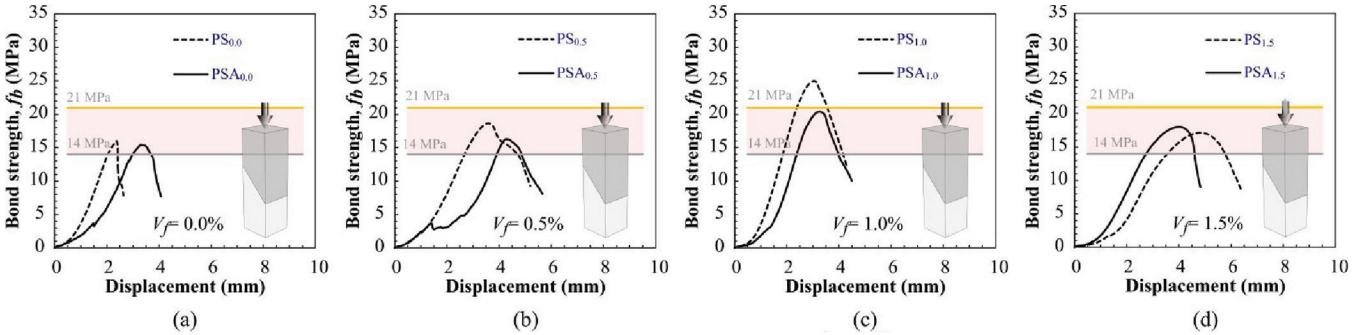

Fig. 11—Bond strength versus displacement curves in ungrooved prisms: (a) V_f *= 0.0%; (b)* V_f *= 0.5%; (c)* V_f *= 1.0%; and (d)* V_f *= 1.5%.*

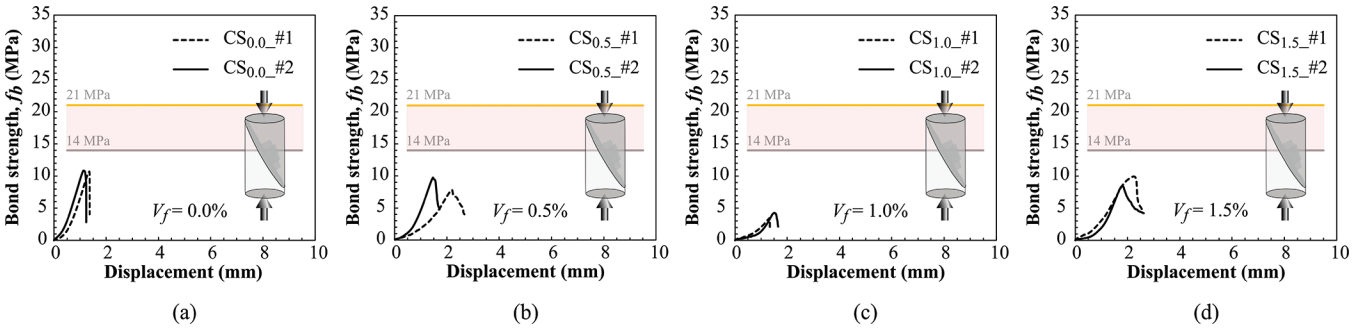

Fig. 12—Bond strength versus displacement curves in cylindrical specimens: (a) V_f *= 0.0%; (b)* V_f *= 0.5%; (c)* V_f *= 1.0%; and (d)* V_f *= 1.5%.*

Proposed model for bond shear strength in steel fiber-reinforced concrete

Based on the results discussed in the previous sections, a model was proposed for calculating the bond shear strength of steel fiber-reinforced concrete with intentionally roughened surfaces (Eq. (6)). The failure criterion assumed tangential stress equal to vertical compressive stress. The cohesion coefficient was defined as $c = f_c'/\tau_u$, derived from the linear regression curves in Fig. 15. GP showed c = 1.0, while UGP and cylindrical specimens had coefficients of 0.5 and 0.4, respectively—values consistent with CSAA23.3[35] and *fib* Model Code[37] for rough surfaces

$$\tau_p = c_r f_{ctd} + [\phi\mu\sigma_n] + F_f \tag{6}$$

where c_r is cohesion coefficient proposed by the linear regression method, equal to 0.50 MPa for prism and 0.40 MPa for cylinder; f_{ctd} is design concrete tensile strength; ϕ is shear strength reduction factor,[34] equal to 0.85; μ is coefficient of friction, equal to 1.00 for prism and 1.50 for cylinder; σ_n is compressive normal stress acting on the bond interface; and F_f is a parameter that considers the effect of the steel fiber at the interface, $F_f = V_f(l_f/d_f)$.

For the friction coefficient, the adopted criterion was the ratio between the internal friction angle (ϕ) and the bond surface inclination angle (α), yielding 1.0 for prismatic specimens [((44/45) + (51/45))/2] and 1.5 for cylindrical specimens (43/27). With a 45-degree surface plane, normal stress components are equal; therefore, a shear reduction factor ϕ = 0.85 (ACI 318[34]) was applied to avoid underestimating shear strength. The fiber contribution at the interface was incorporated through parameter F_f.

Analyzing and comparing the experimental results with the predictions from design codes and the proposed equation (Fig. 16(a) to (d)), using the lower compressive strength of the fiber-reinforced concrete (SFRC mixture) between

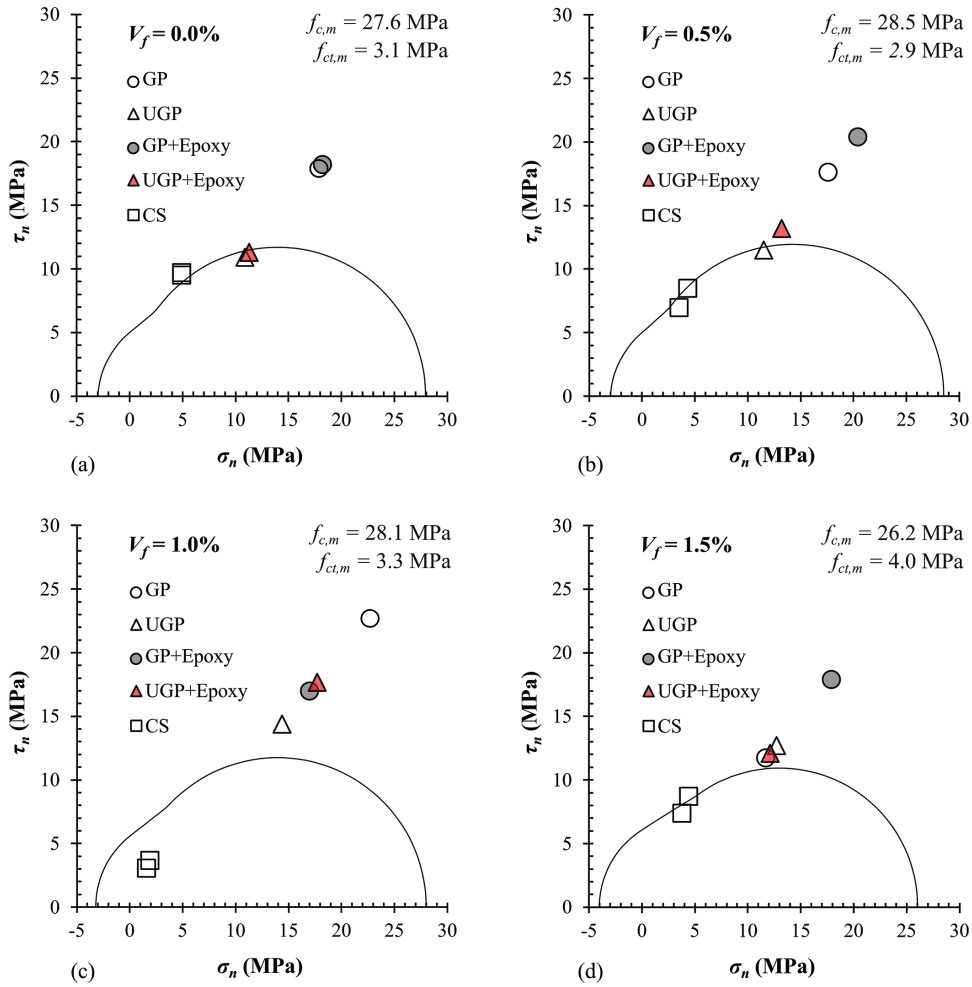

Fig. 13—Concrete failure envelopes: (a) V_f *= 0.0%; (b)* V_f *= 0.5%; (c)* V_f *= 1.0%; and (d)* V_f *= 1.5%.*

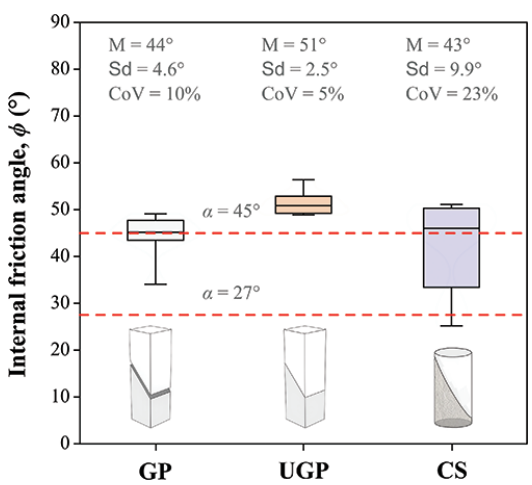

Fig. 14—Comparison of internal friction angles between composite specimens.

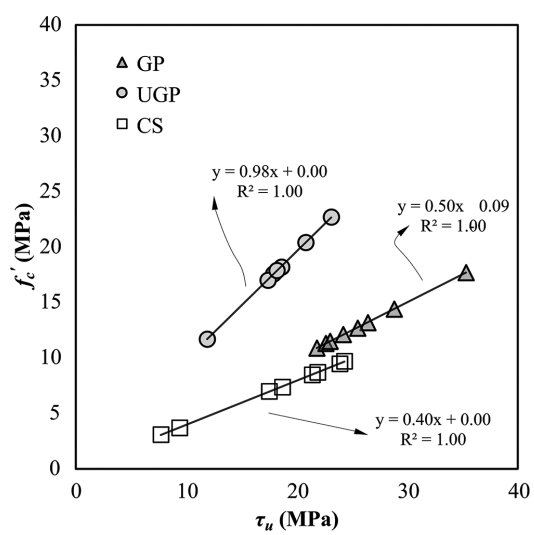

Fig. 15—Cohesion assessment by correlating f_c' *and* τ_u.

repair and substrate, it was observed that both the AASHTO LRFD[33] and the proposed model provided the most accurate predictions, with average ratios of 1.04 and 1.05, respectively. However, the AASHTO LRFD showed a higher CoV of 22%, compared to only 8% for the proposed model.

ACI 318[34] was found to be extremely conservative for models without shear reinforcement. CSAA23.3,[35] Eurocode 2,[36] and *fib* Model Code[37] were also conservative, with CoVs ranging from 25 to 30%.

The proposed model was further validated using the experimental results from Youm et al.[12] for rough surfaces, adopting the compressive strength of ultra-high-performance concrete with fiber (UHPC mixture), as shown in Table 6 and Fig. 17. In this case, the proposed equation achieved

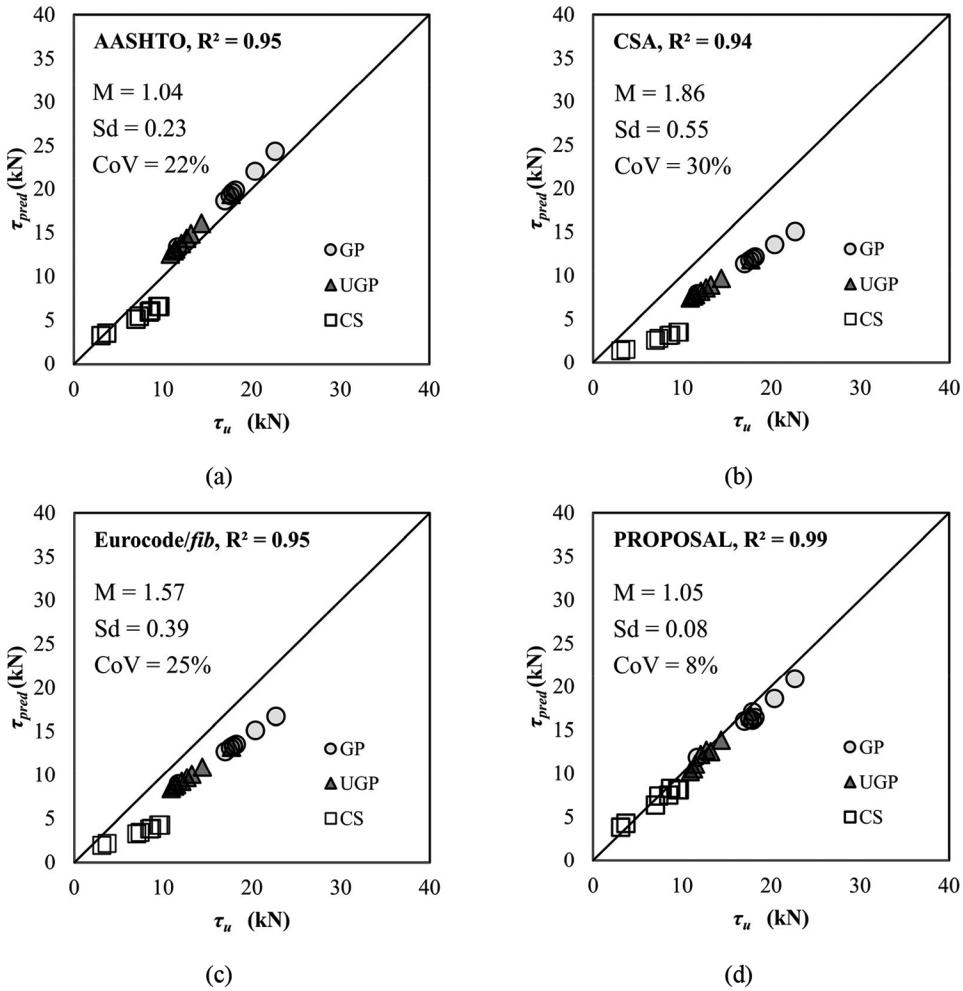

Fig. 16—Comparison between τ_{pred} *and* τ_u*: (a) AASHTO; (b) CSA A23.3; (c) Eurocode/*fib*; and (d) proposal.*

an average ratio of 1.17 and a CoV of 10%, compared to 1.42 and 22% for AASHTO LRFD. Although CSA A23.3[35] includes a reduction factor for concrete strength, it still proved more conservative than the Eurocode and *fib* Model Code.

Overall, the evaluation method developed in this study—based on linear regression correlating vertical and shear stresses, and on the direct relationship between the internal friction angle and the bond plane—proved satisfactory. The proposed equation is applicable to fiber-reinforced concretes across a wide strength range, from 30 to 160 MPa.

CONCLUSIONS

This study investigated the influence of steel fibers on the bond shear strength between old conventional concrete (CC) and new metakaolin-based geopolymer concrete (GPC). Optimizing the bond interface area by 50% promoted adhesive failure with a balanced distribution of compressive and shear stresses. This configuration aligned the internal friction angle with the bond surface inclination, enabling a more accurate determination of friction and cohesion coefficients for both prismatic and cylindrical specimens, while also highlighting the fiber effect.

A new bond shear strength calculation model was proposed, incorporating these parameters and the steel fiber contribution. Validation against literature results showed good correlation, with an average ratio of 1.17 and a coefficient of variation of 10%, outperforming existing design models, which were generally conservative and more scattered.

Geopolymer repair concrete also demonstrated superior mechanical performance in terms of compressive and tensile strength. Additionally, using structural adhesive at the fiber-reinforced concrete interface tended to enhance bonding.

Although based on a limited experimental program and validation dataset, the proposed Optimized Slant Shear Interface Test (OSSIT) and calculation model satisfactorily addressed a critical limitation of the slant shear test—namely, the difficulty of obtaining reliable friction and cohesion parameters without the predominance of compressive stresses—while also providing a consistent method for assessing bond performance.[49]

AUTHOR BIOS

Aaron Nzambi *is a Collaborating Professor in the Graduate Program in Construction Processes and Urban Sanitation at the Federal University of Pará, Pará, Brazil, where he received his BS, MSc, and PhD in 2018, 2020, and 2025, respectively. His research interests include steel-concrete adherence, steel fiber-reinforced concrete, new materials, and structural reinforcement.*

Table 6—Validation of model with the experimental results obtained by Youm et al.[12]

ID.	f_c, MPa		Test results		Shear strength ratio (τ_u/τ_{pred})					
	NSC	UHPC	τ_u, MPa	σ_u, MPa	τ_u/τ_{ASH}	τ_u/τ_{ACI}	τ_u/τ_{CSA}	τ_u/τ_{Euro}	τ_u/τ_{fib}	τ_u/τ_{prop}
50RA	30.4	106.2	17.05	14.31	1.07	30.45	1.77	1.42	1.44	1.07
50RH	29.9	162.8	15.82	13.28	1.06	28.25	1.77	1.32	1.35	1.00
60RA	30.4	106.2	14.43	8.33	1.45	25.77	2.51	1.84	1.89	1.34
60RH	29.9	162.8	12.85	7.42	1.42	22.95	2.50	1.63	1.70	1.19
70RA	30.4	106.2	7.18	2.61	1.69	12.82	3.55	1.87	1.98	1.21
70RH	29.9	162.8	8.84	3.22	1.82	15.79	3.66	1.79	1.91	1.22
				Mean	1.42	22.67	2.63	1.64	1.71	1.17
				Standard deviation	0.31	7.01	0.83	0.23	0.26	0.12
				Coefficient of variation	0.22	0.31	0.31	0.14	0.15	0.10

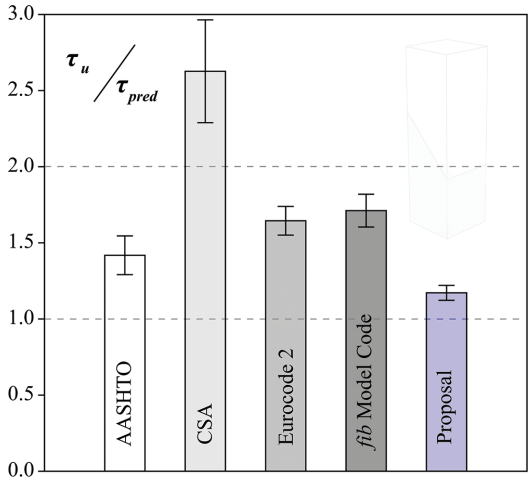

Fig. 17—Comparison of experimental[12] and theoretical bond shear strength results.

Victória Seixas *received his MSc in structures and civil construction from the Federal University of Pará in 2024. His research interests include reinforced concrete structures and new materials.*

Dênio Oliveira *is a Professor at Federal University of Pará, where he received his BS in 1995. He received his MSc and PhD from the University of Brasília, Brasília, Brazil, in 1998 and 2003, respectively, and his Post PhD from Imperial College of London, London, UK, in 2007. His research interests include reinforced concrete structures with emphasis to shear and torsion, besides structural strengthening and new materials*

ACKNOWLEDGMENTS

The authors thank the Institute of Ecological Research in Amazon (IPEAM) and Amazon Foundation for the Support of Studies and Research (FAPESPA) for all support to develop this and others researches in the Amazon.

DATA AVAILABILITY STATEMENT

All data, models, and code generated or used during the study appear in the published paper.

REFERENCES

1. Davidovits, J., "Properties of Geopolymer Cements," *Proceedings of the First International Conference on Alkaline Cements and Concretes*, Kiev, Ukraine, 1994, pp. 131-149.

2. Azevedo, E.; Oliveira, D.; and Nzambi, A., "Geopolymer Flat Slabs with Synthetic Coarse Aggregate under Punching," *ACI Structural Journal*, V. 121, No. 4, July 2024, pp. 161-172. doi: 10.14359/51740573

3. Singh, B.; Ishwarya, G.; Gupta, M.; and Bhattacharyya, S. K., "Geopolymer Concrete: A Review of Some Recent Developments," *Construction and Building Materials*, V. 85, 2015, pp. 78-90. doi: 10.1016/j.conbuildmat.2015.03.036

4. Topark-Ngarm, P.; Chindaprasirt, P.; and Sata, V., "Setting Time, Strength, and Bond of High-Calcium Fly Ash Geopolymer Concrete," *Journal of Materials in Civil Engineering*, ASCE, V. 27, No. 7, 2015, pp. 1-7. doi: 10.1061/(ASCE)MT.1943-5533.0001157

5. Nzambi, A. K. L. L.; dos Santos, M. C. M.; and de Oliveira, D. R. C., "Pull-Out Tests of Headed Studs Embedded in Steel Fiber–Reinforced Geopolymer Concrete," *Journal of Structural Design and Construction Practice*, V. 30, No. 3, 2025, p. 05025006. doi: 10.1061/JSDCCC.SCENG-1794

6. Banthia, N., and Gupta, R., "Influence of Polypropylene Fiber Geometry on Plastic Shrinkage Cracking in Concrete," *Cement and Concrete Research*, V. 36, No. 7, 2006, pp. 1263-1267. doi: 10.1016/j.cemconres.2006.01.010

7. Sorelli, L. G.; Meda, A.; and Plizzari, G. A., "Steel Fiber Concrete Slabs on Ground: A Structural Matter," *ACI Structural Journal*, V. 103, No. 4, July-Aug. 2006, pp. 551-558. doi: 10.14359/16431

8. Zanotti, C.; Banthia, N.; and Plizzari, G., "Towards Sustainable Repairs: Substrate-Repair Interface Mode-I Fracture Analysis," *International Journal of Sustainable Materials and Structural Systems*, V. 1, No. 3, 2014, pp. 265-281. doi: 10.1504/IJSMSS.2014.062768

9. Zanotti, C.; Banthia, N.; and Plizzari, G., "A Study of Some Factors Affecting Bond in Cementitious Fiber Reinforced Repairs," *Cement and Concrete Research*, V. 63, 2014, pp. 117-126. doi: 10.1016/j.cemconres.2014.05.008

10. Ju, Y.; Shen, T.; and Wang, D., "Bonding Behavior between Reactive Powder Concrete and Normal Strength Concrete," *Construction and Building Materials*, V. 242, 2020, p. 118024. doi: 10.1016/j.conbuildmat.2020.118024

11. Alameri, I., and Oltulu, M., "Bond Strength Between Concrete Substrate and Reinforced Polyester Composites," *Journal of Materials Engineering and Performance*, V. 30, No. 1, 2021, pp. 56-65. doi: 10.1007/s11665-020-05295-7

12. Youm, H.; Lim, W.; Hong, S.; and Joh, C., "Interface Shear Strength between Ultra-High-Performance Concrete and Normal-Strength Concrete," *ACI Structural Journal*, V. 118, No. 2, Mar. 2021, pp. 287-298. doi: 10.14359/51729350

13. Santos, P. M. D., and Júlio, E. N. B. S., "Factors Affecting Bond between New and Old Concrete," *ACI Materials Journal*, V. 108, No. 4, July-Aug. 2011, pp. 449-456. doi: 10.14359/51683118

14. Diab, A. M.; Abd-Elmoaty, A.-E. M.; and Tag Eldin, M. R., "Slant Shear Bond Strength between Self *Compacting* Concrete and Old Concrete," *Construction and Building Materials*, V. 130, 2017, pp. 73-82. doi: 10.1016/j.conbuildmat.2016.11.023

15. Ceia, F.; Raposo, J.; Guerra, M.; Júlio, E.; and de Brito, J., "Shear Strength of Recycled Aggregate Concrete to Natural Aggregate Concrete Interfaces," *Construction and Building Materials*, V. 109, 2016, pp. 139-145. doi: 10.1016/j.conbuildmat.2016.02.002

16. Beaupre, D., "Bond Strength of Shotcrete Repair," *Shotcrete Magazine*, V. 1, No. 2, 1999, pp. 12-15.

17. Clímaco, J. C. T. S., and Regan, P. E., "Evaluation of Bond Strength between Old and New Concrete in Structural Repairs," *Magazine of Concrete Research*, V. 53, No. 6, 2001, pp. 377-390. doi: 10.1680/macr.2001.53.6.377

18. Kriegh, J. D.; Nordby, G. M.; and Eubank, T. C., "Progress Report to the Arizona State Highway Department on the Use of Epoxy Resins in

Reinforced Concrete," Department of Civil Engineering, The University of Arizona, Tucson, AZ, 1961.

19. Kriegh, J. D.; Nordby, G. M.; and Endebrock, E. G., "The Use of Epoxy Resins in Reinforced Concrete—Static Load Tests - Part 1," Final Report 1, Arizona Highway Department, Engineering Research Laboratories, Phoenix, AZ, Jan. 1962.

20. Kriegh, J. D., and Endebrock, E. G., "The Use of Epoxy Resins in Reinforced Concrete--Static Load Tests - Part IT," Final Report No. 2, Arizona Highway Department, Engineering Research Laboratories, Phoenix, AZ, Jan. 1963.

21. Kreigh, J. D., "Arizona Slant Shear Test: A Method to Determine Epoxy Bond Strength," *ACI Journal Proceedings*, V. 73, No. 7, July 1976, pp. 372-373.

22. ASTM C882/C882M-23, "Standard Test Method for Bond Strength of Bonding Systems Used with Concrete by Slant Shear," ASTM International, West Conshohocken, PA, 2023, 6 pp. doi: 10.1520/C0882_C0882M-23

23. Diaz, B. E., "The Technique of Glueing Precast Elements of the Rio-Niteroi Bridge," *Materiales de Construcción*, V. 8, No. 1, 1975, pp. 43-50. doi: 10.1007/BF02538956

24. BS EN 12615, "Products and Systems for the Protection and Repair of Concrete Structures – Test Methods – Determination of Slant Shear Strength," British Standard Institution, London, UK, 1999.

25. Knab, L. I., and Spring, C. B., "Evaluation of Test Methods for Measuring the Bond Strength of Portland Cement Based Repair Materials to Concrete," *Cement, Concrete and Aggregates*, V. 11, No. 1, 1989, pp. 3-14. doi: 10.1520/CCA10096J

26. Tabor, L. J., "Evaluation of Resin Systems for Concrete Repair," *Magazine of Concrete Research*, V. 30, No. 105, 1978, pp. 221-225. doi: 10.1680/macr.1978.30.105.221

27. ASTM C882/C882M-20, "Standard Test Method for Bond Strength of Epoxy-Resin Systems Used with Concrete by Slant Shear," ASTM International, West Conshohocken, PA, 2020, 4 pp.

28. Austin, S.; Robins, P.; and Pan, Y., "Shear Bond Testing of Concrete Repairs," *Cement and Concrete Research*, V. 29, No. 7, 1999, pp. 1067-1076. doi: 10.1016/S0008-8846(99)00088-5

29. Hu, B.; Li, Y.; and Liu, Y., "Dynamic Slant Shear Bond Behavior between New and Old Concrete," *Construction and Building Materials*, V. 238, 2020, p. 117779. doi: 10.1016/j.conbuildmat.2019.117779

30. Momayez, A.; Ramezanianpour, A. A.; Rajaie, H.; and Ehsani, M. R., "Bi-Surface Shear Test for Evaluating Bond between Existing and New Concrete," *ACI Materials Journal*, V. 101, No. 2, Mar.-Apr. 2004, pp. 99-106. doi: 10.14359/13045

31. Zanotti, C., and Randl, N., "Are Concrete-Concrete Bond Tests Comparable?" *Cement and Concrete Composites*, V. 99, 2019, pp. 80-88. doi: 10.1016/j.cemconcomp.2019.02.012

32. Saldanha, R.; Júlio, E.; Dias-da-Costa, D.; and Santos, P., "A Modified Slant Shear Test Designed to Enforce Adhesive Failure," *Construction and Building Materials*, V. 41, 2013, pp. 673-680. doi: 10.1016/j.conbuildmat.2012.12.053

33. AASHTO-LRFD, "Bridge Design Specifications," American Association of State Highway and Transportation Officials, Washington, DC, 2012, 1661 pp.

34. ACI Committee 318, "Building Code Requirements for Structural Concrete (ACI 318M-19) and Commentary (ACI 318R-19) (Reapproved 2022)," American Concrete Institute, Farmington Hills, MI, 2019, 628 pp.

35. CSA A23.3-04, "Design of Concrete Structures," Canadian Standards Association, Mississauga, ON, Canada, 2004, 214 pp.

36. EN 1992-1-1, "Design of Concrete Structures: Part 1–1: General Rules and Rules for Buildings," European Committee for Standardization, Brussels, Belgium, March 2010, 259 pp.

37. *fib*, "*fib* Model Code for Concrete Structures 2010," Fédération Internationale du Béton, Lausanne, Switzerland, 2013, 434 pp.

38. ABNT NBR 8522-1:2021, "Concreto endurecido - Determinação dos módulos de elasticidade e de deformação Parte 1: Módulos estáticos à compressão," Associação Brasileira de Normas Técnicas, Rio de Janeiro, Brazil, 2021.

39. ABNT NBR 15894-1:2010, "Metacaulim para uso com cimento Portland em concreto, argamassa e pasta Parte 1: Requisitos," Associação Brasileira de Normas Técnicas, Rio de Janeiro, Brazil, 2010.

40. ABNT NBR 17054:2022, "Agregados - Determinação da composição granulométrica - Método de ensaio," Associação Brasileira de Normas Técnicas, Rio de Janeiro, Brazil, 2022.

41. ASTM A820/A820M-22, "Standard Specification for Steel Fibers for Fiber-Reinforced Concrete," ASTM International, West Conshohocken, PA, 2022, 4 pp. doi: 10.1520/A0820_A0820M-22

42. ABNT NBR 15530:2019, "Fibras de aço para concreto — Requisitos e métodos de ensaio," Associação Brasileira de Normas Técnicas, Rio de Janeiro, Brazil, 2019.

43. ABNT NBR 5739:2018, "Concreto – Ensaios de compressão de corpos de prova cilíndricos - Método de ensaio," Associação Brasileira de Normas Técnicas, Rio de Janeiro, Brazil, 2018.

44. ABNT NBR 7222:2011, "Concreto e argamassa — Determinação da resistência à tração por compressão diametral de corpos de prova cilíndricos," Associação Brasileira de Normas Técnicas, Rio de Janeiro, Brazil, 2011.

45. ABNT NBR 5738:2016, "Concreto-Procedimento para moldagem e cura de corpos de prova," Associação Brasileira de Normas Técnicas, Rio de Janeiro, Brazil, 2016.

46. Tayeh, B. A.; Abu Bakar, B. H.; Megat Johari, M. A.; and Voo, Y. L., "Mechanical and Permeability Properties of the Interface between Normal Concrete Substrate and Ultra-High Performance Fiber Concrete Overlay," *Construction and Building Materials*, V. 36, 2012, pp. 538-548. doi: 10.1016/j.conbuildmat.2012.06.013

47. ASTM C496/C496M-17, "Standard Test Method for Splitting Tensile Strength of Cylindrical Concrete Specimens," ASTM International, West Conshohocken, PA, 2017, 5 pp. doi: 10.1520/C0496_C0496M-17

48. ACI Committee 546, "Guide to Materials Selection for Concrete Repair (ACI 546.3R-14)," American Concrete Institute, Farmington Hills, MI, 2014, 72 pp.

49. Ghamarpoor, R.; Jamshidi, M.; and Mohammadpour, M., "Achieving Outstanding Mechanical/Bonding Performances by Epoxy Nanocomposite as Concrete–Steel Rebar Adhesive Using Silane Modification of Nano SiO_2," *Scientific Reports*, V. 13, No. 1, 2023, p. 9157. doi: 10.1038/s41598-023-36462-0

NEW Symposium Publications from ACI

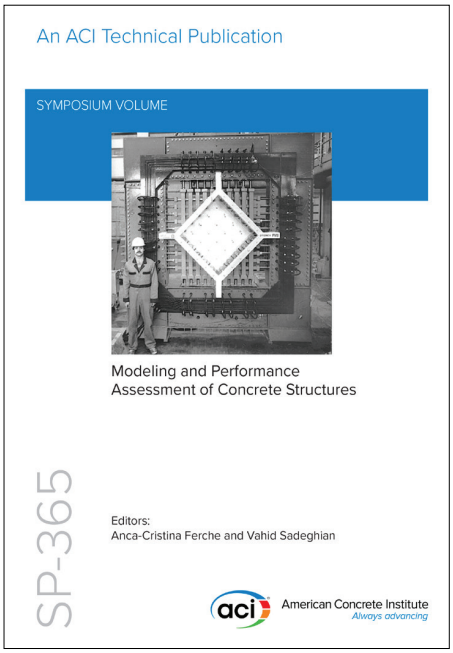

SP-365: Modeling and Performance Assessment of Concrete Structures

The papers cover different aspects related to modeling and performance assessment of concrete structures including developments of the Modified Compression Field Theory, finite element modeling of punching shear in slabs, behavior and modeling of steel fiber-reinforced concrete members subjected to torsion, modeling of concrete structures subjected to impact loading, behavior and modeling of slender walls, modeling of concrete frame elements, behavior and modeling of GFRP reinforced members, crack-based assessment of concrete structures, and advancements in modeling deterioration mechanisms and repaired concrete structures.

Available in PDF format: $69.50
(FREE to ACI members)

SP-366: A Vision for the Future of Corrosion Resistant Structures - A Special Session Honoring Professor Carolyn Hansson

Professor Carolyn Hansson's remarkable journey began in England, during the turbulence of the Second World War. Carolyn was raised in a nurturing environment by parents who instilled in her a deep respect for learning and perseverance. These values would guide her through an exceptional academic and professional life. This Special Publication celebrates more than 60 years of Professor Hansson's contributions as a scientist, educator, and mentor. The papers collected here reflect not only the lasting relevance of her work but also its future promise. Her vision stands as both a mirror to the past and a beacon for innovations yet to come in corrosion-resistant construction.

Available in PDF format: $69.50
(FREE to ACI members)

American Concrete Institute
+1.248.848.3700 • www.concrete.org

ACI STRUCTURAL JOURNAL TECHNICAL PAPER

Title No. 123-S57

Seismic Behavior of External Socket Connections for Reinforced Concrete Columns

by Julio A. Samayoa, Giorgio T. Proestos, and Mervyn J. Kowalsky

This study uses six large-scale experimental tests to investigate the seismic behavior of external socket connections for reinforced concrete columns. The tests evaluated the effects of key design parameters, including socket height and grout strength, on the performance of these connections under reverse cyclic lateral loads. The results indicate that socket height significantly affects whether the plastic hinge forms in the column above the connection or inside the socket and influences the required strength of the structural components. Shorter socket heights required higher grout strengths and increased shear capacity to avoid undesirable failure modes. Three primary failure modes were observed: grout crushing, shear failure, and flexural failure above the socket. Regardless of socket height, all tests showed that external socket connections effectively protect adjoining structural members by limiting plastic strain demands. These findings provide valuable insights into optimizing the design and performance of external socket connections in seismic regions.

Keywords: accelerated bridge construction; external socket connection; large-scale tests; reinforced concrete column, seismic design; seismic performance.

INTRODUCTION

Accelerated bridge construction (ABC) is an innovative approach to bridge design and construction, offering numerous benefits such as reduced construction timelines, minimized traffic disruption, and improved material quality. The Federal Highway Administration[1] recognizes ABC as a critical tool for enhancing work-zone safety, reducing environmental impacts, and mitigating weather-related delays during construction. A key component of ABC is the connection between prefabricated elements, which critically impacts the overall structural performance of bridges, especially in seismic regions. Among various connection types, socket connections in reinforced concrete (RC) structures have shown promise as a viable ABC alternative in moderate and high seismic zones.[2-9]

In a socket connection, a precast column is embedded into a voided opening within elements such as a cap beam or foundation, and the gap is filled with cast-in-place concrete or grout, eliminating the need for additional reinforcement. Socket connections are classified as either internal or external, with the location of the void serving as the main difference. Figure 1 shows an elevation view of both internal and external socket connections. External sockets, as shown in Fig. 2, provide advantages over internal sockets. They simplify the construction of adjoining members by reducing steel congestion in the cap beam or foundation and allow for smaller cap beam cross sections because the void is external to the structural element. These characteristics make external sockets more practical for use in cap beams, in addition to their established application in footings for internal socket connections.

Accurate assessment of external socket connections requires the determination of various design parameters, including socket height (*Hs*), the thickness of the external socket wall (*tw*), and grout strength (*fg′*), which is the strength of the material used to connect the column and socket. *Hs* must be sufficient to develop the full plastic moment of the column. Traditionally, socket height is normalized as a fraction of the column diameter (*Dc*). Studies on internal socket connections with *Hs* ranging from 1.0 to 1.5*Dc* have been shown to be sufficient to develop the plastic hinge in the column just outside the cap beam or foundation, maintaining structural integrity during the test.[3,10-14] Studies investigating plastic hinge relocation in repaired columns[15,16] show functional similarities to external socket connections and demonstrate that a repair height exceeding 0.9*D* effectively shifts the plastic hinge formation above the repaired region. While some experimental work has been conducted, there is limited understanding of the fundamental behavior of socket connections, resulting in little guidance for their design.

Understanding the seismic behavior of external socket connections requires both analytical modeling and large-scale experimental testing. Analytical modeling is essential for evaluating the interaction between *Hs*, *tw*, *fg′*, and F_{CIS}, which is the strength of the concrete in the portion of the column that lies within the socket. While the development of an analytical model is beyond the scope of this paper, the selection of *Hs*, *tw*, and the material strengths for the experimental program was guided by analytical evaluations.[17]

This paper presents a large-scale experimental investigation of external socket connections for RC columns. The objectives of this study are to evaluate the influence of socket height (*Hs*) and the material strengths of different socket components (for example, grout strength) on seismic performance, and to identify characteristic failure mechanisms and performance limit states. Six full-scale tests were conducted to quantify the effects of these parameters using performance indicators such as lateral column deformation and hysteretic energy dissipation. The results contribute

ACI Structural Journal, V. 123, No. 3, May 2026.
MS No. S-2025-056.R1, doi: 10.14359/51749376, received September 22, 2025, and reviewed under Institute publication policies. Copyright © 2026, American Concrete Institute. All rights reserved, including the making of copies unless permission is obtained from the copyright proprietors. Pertinent discussion including author's closure, if any, will be published ten months from this journal's date if the discussion is received within four months of the paper's print publication.

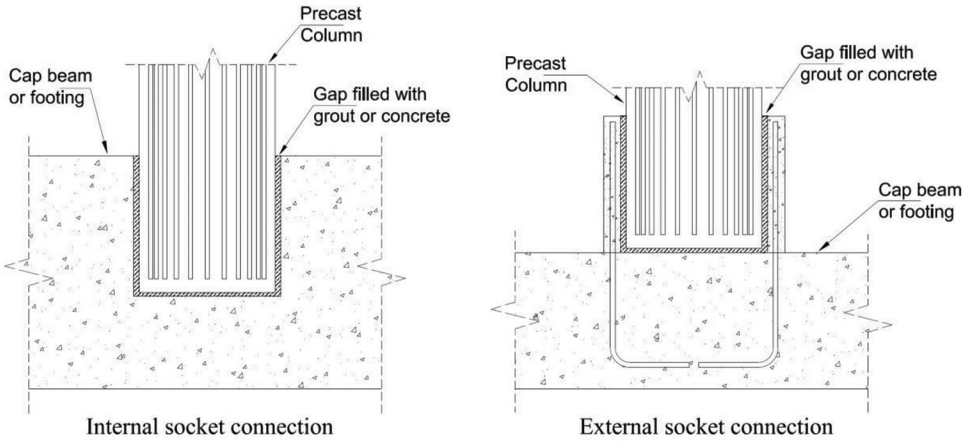

Fig. 1—Elevation view of internal and external socket connection.

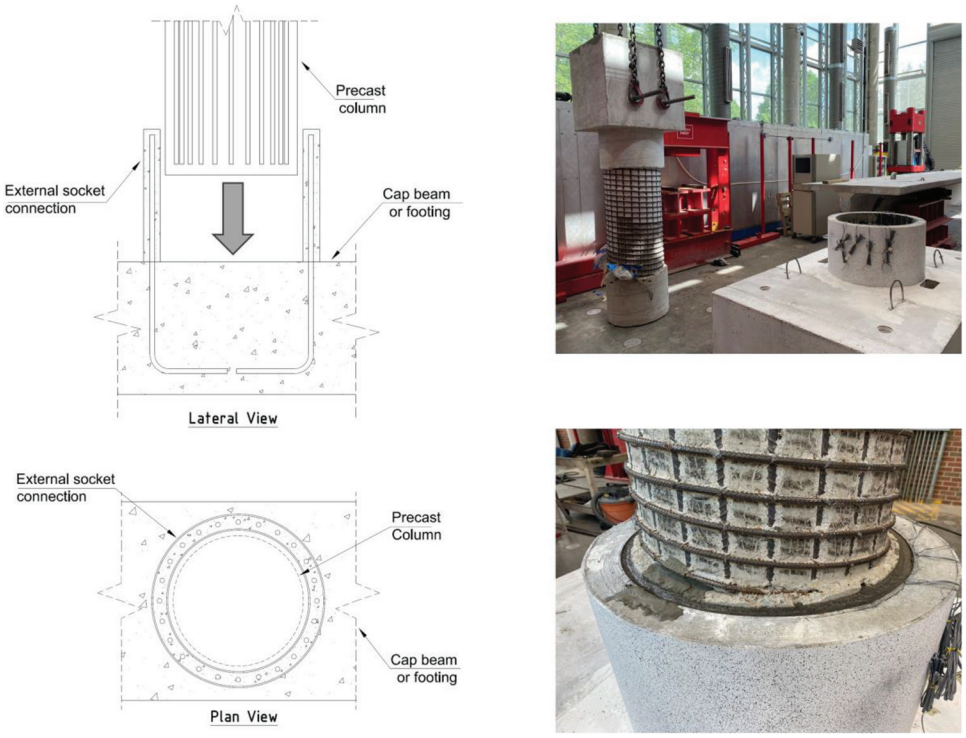

Fig. 2—External socket connection.

to a more comprehensive understanding of the behavior of external socket connections under seismic loading. It is important to note that this study is limited to an experimental program aimed at characterizing the seismic behavior of external socket connections and identifying their failure modes and performance limit states. The analytical modeling work that guided the selection of design parameters for the specimens is not presented in this document, nor does this paper provide prescriptive design equations or guidelines. These aspects are beyond the scope of the current work and will be addressed in future studies.

RESEARCH SIGNIFICANCE

This study enhances the understanding of external socket connections for RC columns, which is particularly important for performance-based seismic design. Through six large-scale tests, the research establishes a relationship between *Hs*, the material strength of the connection components, and failure modes. The results demonstrate how *Hs*, fg', and F_{CIS} influence the mechanisms that contribute to column displacement, strain demands in the plastic hinge region, and column energy dissipation. Additionally, the findings identify failure mechanisms, including grout crushing, flexural, and shear failure of the column. This research supports the broader implementation of ABC techniques while ensuring the structural integrity of external socket connections in earthquake-prone regions.

EXPERIMENTAL PROCEDURE

Six large-scale circular RC columns were tested at the Constructed Facilities Laboratory at North Carolina State University (NCSU). All specimens had a column height of 2290 mm. Table 1 presents the design variables considered in the large-scale tests, including column diameter, socket

Table 1—Design variables and average concrete strength of structural components

Test	Column diameter, mm	Socket height, % *Dc*	Column—outside socket, MPa	Column—inside socket, MPa	Socket wall, MPa	Gap-filling material, MPa
SJS 1	610	1.0	41.6	41.6	89.2	54.4
SJS 2	610	0.75	41.6	41.6	65.6	45.0
SJS 3	610	0.85	41.6	68.8	83.5	63.0
SJS 4	610	0.85	41.6	57.0	83.5	67.0
SJS 5	457	0.85	46.7	46.7	96.5	71.2
SJS 6	457	0.85	46.7	63.4	96.5	68.9

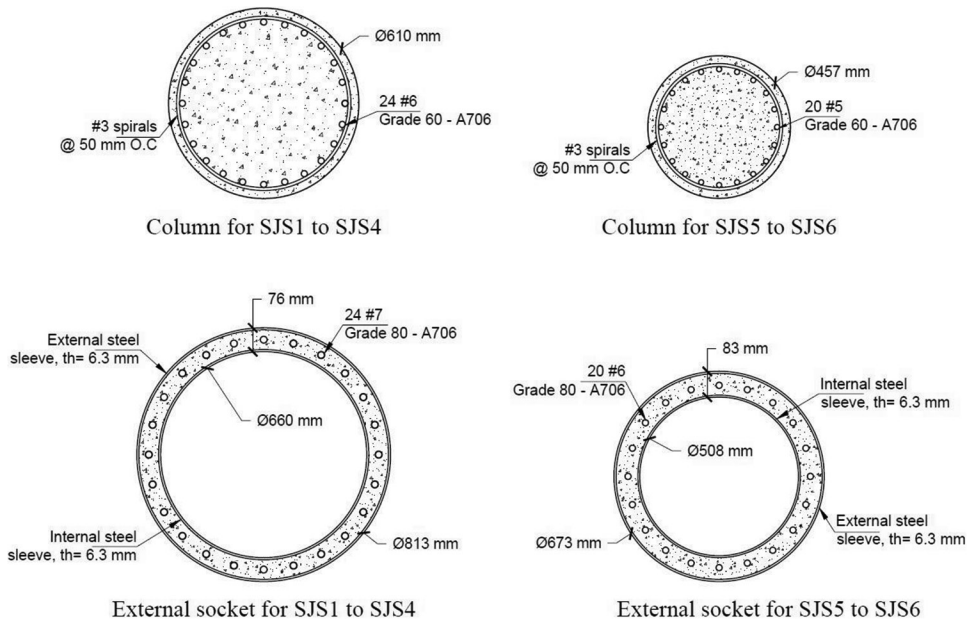

Fig. 3—Plan view of column and external socket reinforcement.

height-to-column diameter ratio, and material strengths for the different connection components. Concrete and grout compression tests were performed on 100 x 200 mm cylinders in accordance with ASTM C39/C39M.[18] ASTM C39 was selected for testing the grout material because, in most cases, coarse aggregate was included in the grout mixture, making it the more appropriate standard for evaluating compressive strength. An axial load ratio of 5% of the design axial column capacity was applied to all specimens. This value was chosen to maintain consistency with previous tests conducted at NCSU and to facilitate direct comparison between RC columns with external socket connections and conventional RC columns.

Specimens SJS 1 to SJS 4 had a diameter of 610 mm, resulting in a height-diameter ratio of 3.62. The longitudinal reinforcement consisted of 24 Grade 60-A706 No. 6 (19 mm nominal diameter) steel bars, corresponding to a reinforcement ratio (ρl) of 2.34%. The transverse reinforcement consisted of No. 3 (10 mm nominal diameter) steel spirals spaced at 50 mm intervals, resulting in a volumetric reinforcement ratio (ρs) of 1.04%. The concrete cover to the outside of the longitudinal steel was 25 mm. The longitudinal reinforcement of the external socket wall for these specimens consisted of 24 Grade 80-A706 No. 7 (22 mm nominal diameter) steel bars. The external and internal steel sleeves, fabricated from A36 steel with a thickness of 6.3 mm, were used to provide confinement and shear capacity to the external socket wall, while also serving as formwork during construction. The socket wall thickness, *tw*, was 76 mm, and the gap between the column and the external socket was 25 mm.

Specimens SJS 5 and SJS 6 had a diameter of 457 mm, resulting in a height-diameter ratio of 5.0. These columns also included a 25 mm concrete cover to the outside of the longitudinal steel, with longitudinal reinforcement consisting of 20 Grade 60-A706 No. 5 (16 mm nominal diameter) steel bars, corresponding to a reinforcement ratio (ρl) of 2.4%. The transverse reinforcement consisted of No. 3 (10 mm nominal diameter) steel spirals spaced at 50 mm intervals, resulting in a volumetric reinforcement ratio (ρs) of 1.3%. The longitudinal reinforcement of the external socket wall for these specimens consisted of 20 Grade 60-A706 No. 6 (19 mm nominal diameter) steel bars. The external and internal steel sleeves enclosing the concrete were made of A36 steel with a thickness of 6.3 mm. The *tw* was 83 mm, and the gap between the column and the external socket was 25 mm.

The footing and cap beam for all specimens were designed as capacity-protected components, using identical detailing.

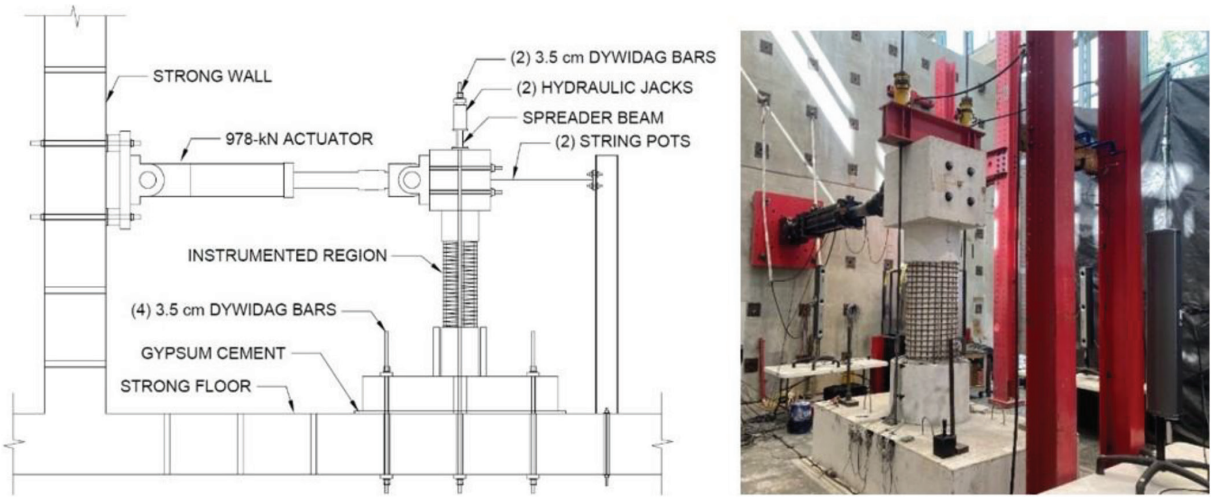

Fig. 4—Experimental test setup.

Figure 3 illustrates the reinforcement details for the RC column and the external socket.

Test setup and instrumentation

The large-scale specimens were subjected to lateral load using a 978 kN hydraulic actuator with a 101.6 cm stroke, anchored to a strong wall with a steel plate. The specimens were positioned at midstroke. A spreader beam with two 445 kN hydraulic jacks above the cap beam was used to apply the 5% constant axial load throughout the test. A self-regulated axial load system was used, considering a third jack located in a universal testing machine in a force-controlled mode.[19]

To optimize surface contact and increase friction, gypsum cement was cast between the footing and the strong floor. Additionally, the foundation was post-tensioned to the strong floor using four bars with a diameter of 3.5 cm, each stressed to 452.3 kN.

Specimen displacement was measured using two string potentiometers placed at the center and edge of the cap beam to monitor the potential twisting of the specimen. The longitudinal bars in the external socket wall were instrumented with 12 strain gauges to measure the strains in the reinforcement and the strains transmitted to the footing or cap beam.

An active infrared motion tracking system was used to capture the displacement response of the RC columns. This system used 288 light-emitting diode (LED) markers placed on exposed reinforcement at the plastic hinge regions to measure the three-dimensional displacement history of the longitudinal bars and spirals. This instrumentation facilitated the determination of axial and bending strain in the column reinforcement and the shear deformation of the specimens. Additionally, digital image correlation (DIC) was employed to monitor displacements and strains in the external socket sleeve. Figure 4 illustrates the test setup.

Loading protocol

The specimens were subjected to a reverse cyclic unidirectional quasi-static force applied at the top of the column. Positive force and displacement values represented a push to the north, while negative values signified a pull to the south.

The loading protocol for the six large-scale tests included a single cycle at 25%, 50%, 75%, and 100% of the theoretical first yield force. In the plastic range, three cycles were applied at increasing increments of displacement ductility. Displacement ductility one was calculated by extrapolating the experimentally measured first yield displacement to the nominal moment capacity of the cross section, as expressed in Eq. (1). In Eq. (1), M_y' is the theoretically calculated first yield moment of the column section. Note that the experimentally measured first yield displacement for the system contains numerous deformation components, including shear and flexural deformation of the column, strain penetration of the column longitudinal steel into the portion of the column embedded in the socket, rocking of the column within the socket, socket shear deformation, and socket rotation.

$$\mu_1 = \frac{M_N}{M_y'}\Delta_y' \tag{1}$$

To calculate the displacement at any given ductility level n, the displacement corresponding to ductility one was multiplied by n, as shown in Eq. (2).

$$\mu_n = n\mu_1 \tag{2}$$

To distinguish cycles at each displacement ductility, a superscript c is placed after the displacement ductility level (μ_n^c), where c indicates the first, second, or third cycle at that displacement ductility.

The experimental tests continued until the recorded force dropped by approximately 40% from the maximum value observed during the experiment. Further loading beyond a 40% reduction of strength would not have provided additional insight and may have also compromised the safety of the test setup. Figure 5 presents an example of the loading protocol.

EXPERIMENTAL RESULTS AND DISCUSSION

Global response and associated failure modes

The experimental tests were categorized according to the observed failure modes identified through direct observations

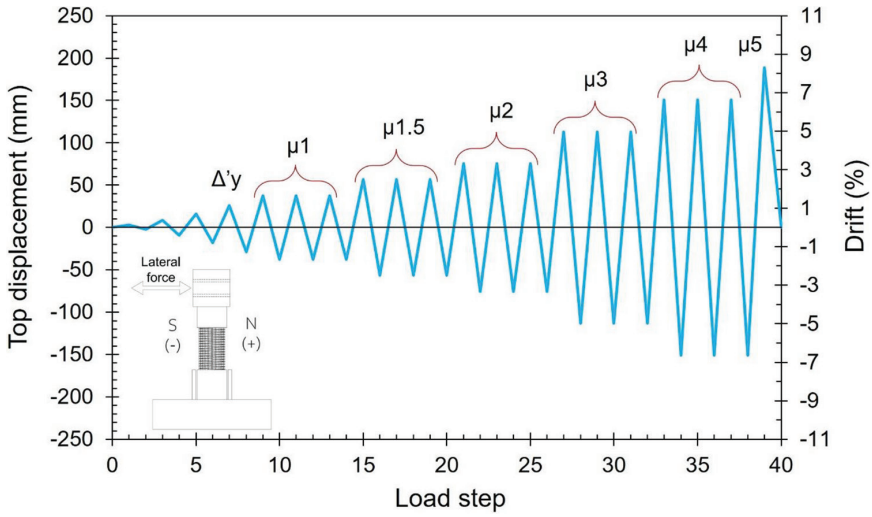

Fig. 5—Example of loading protocol for large-scale tests.

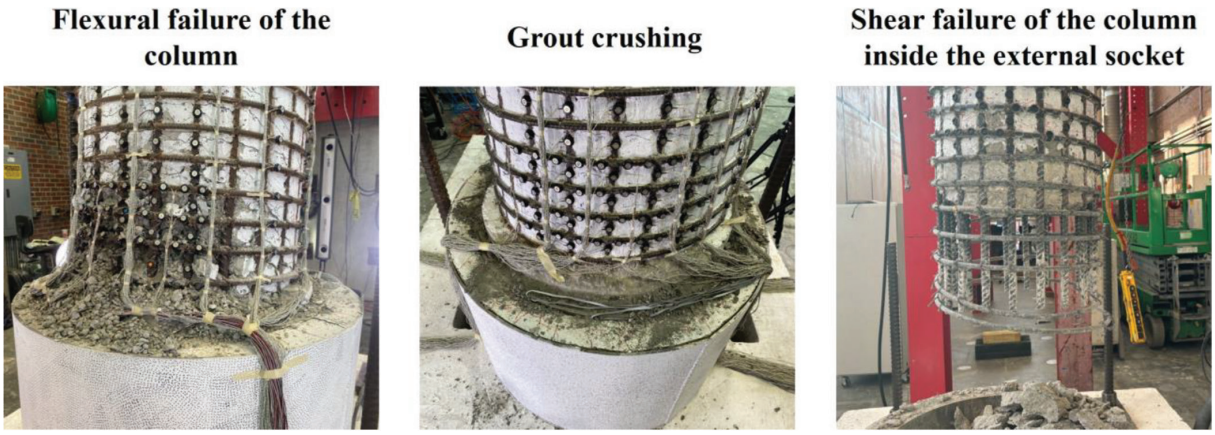

Fig. 6—Failure mechanisms of experimental tests.

during testing, post-test inspections, and corroborative data analysis. The failure mechanisms considered were: 1) fracture of the longitudinal reinforcing bars above the interface of the external socket connection; 2) grout crushing, characterized by extensive compressive damage at the interface of the connection; and 3) shear failure in the portion of the column embedded within the external socket connection. The latter was confirmed post-test by lifting the column to inspect internal damage. These failure mechanisms are illustrated in Fig. 6.

In all tests, the external socket wall sustained no significant damage, showing only minor radial cracks in the concrete and grout before loading to the first yield force. Similarly, the footing remained free from visible damage, acting as a capacity-protected element.

The global response of the six large-scale tests was measured through moment-displacement response, which illustrates stiffness, ductility, and strength degradation. Figure 7 presents the measured moment-displacement response for all six tests while also comparing the response with a theoretical prediction of a cast-in-place (CIP) column, using the same material properties as those in the experimental tests. There was no CIP column test, as the behavior of such columns is well established in the literature, thus allowing for the comparison to be done from a theoretical prediction of CIP column behavior. Table 2 summarizes the global response and failure modes for specimens SJS 1 through SJS 6 to complement the visual data.

The flexural failure mode was observed in specimens SJS 1 and SJS 6, both of which exhibited similar behavioral trends, as shown in Fig. 7. In both tests, the columns reached their nominal moment capacity, and the longitudinal reinforcement fractured outside the external socket connection, consistent with the expected behavior of a CIP column.

Grout crushing was the predominant failure mode in specimens SJS2, SJS3, and SJS4. As shown in Fig. 7, a pattern was identified in which a lower fg' led to increased column rocking and reduced displacement ductility before failure, defined as a reduction of more than 40% from the maximum lateral force. In contrast, higher fg' resulted in a response similar to a flexural failure of the column. The socket height also influenced the fg' required to achieve flexural failure; smaller socket heights require higher fg', whereas larger socket heights reduce this requirement. Specimen SJS2, which combined the lowest fg' with an Hs of $0.75Dc$, exhibited the lowest displacement ductility because grout crushing initiated at an earlier applied displacement. By comparison, SJS4, with the highest fg' and a socket height of $0.85Dc$, achieved the largest displacement ductility among the three specimens before reaching the 40% strength degradation

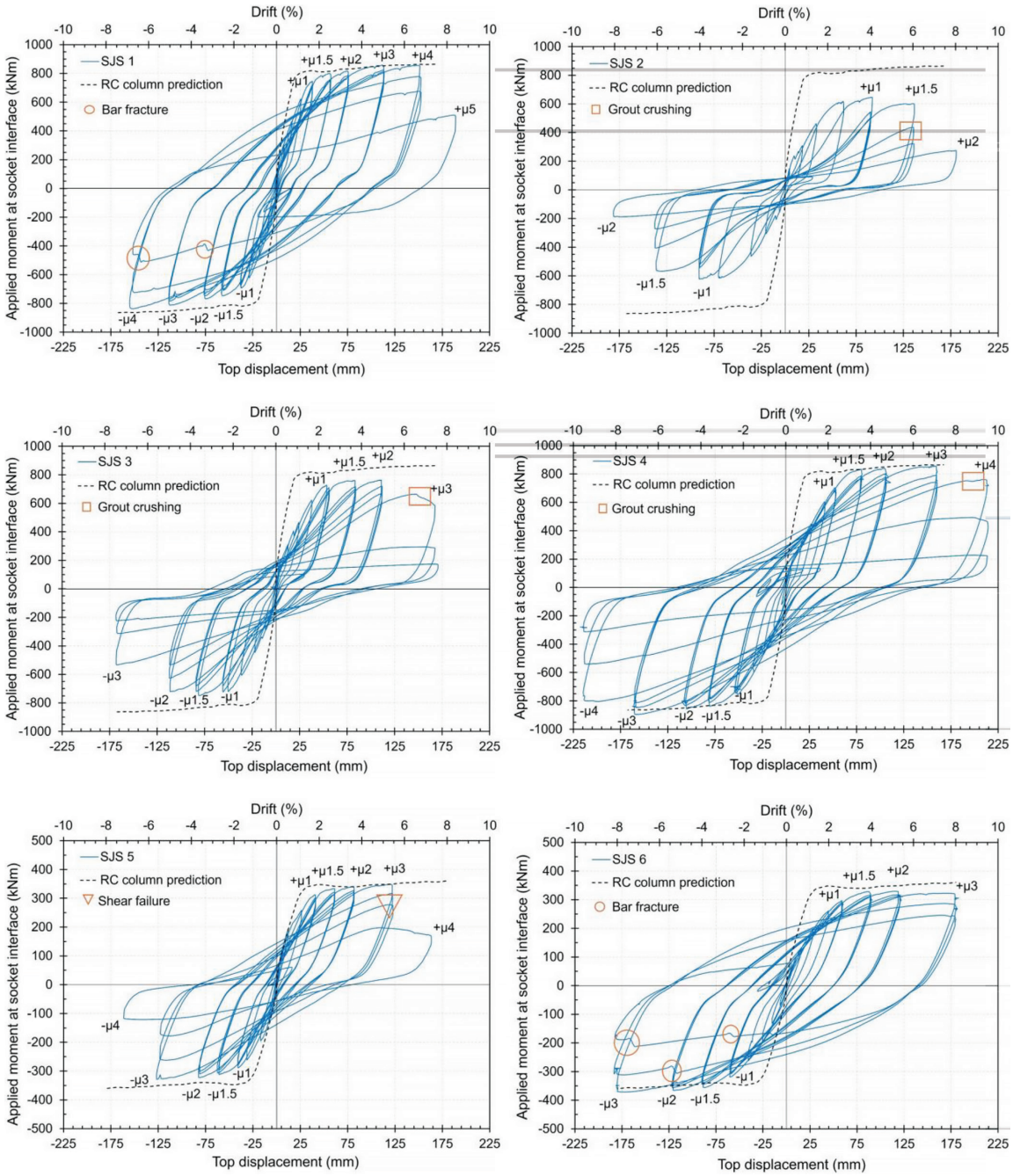

Fig. 7—Measured moment-displacement response at column base (interface of external socket).

threshold. However, grout crushing initiated in SJS4 after reaching the nominal column capacity, making it a transition case between flexural failure and grout crushing. The influence of fg' is further demonstrated by comparing SJS3 and SJS4, which were both constructed with the same socket height of $0.85Dc$; the lower fg' of SJS3 resulted in reduced displacement capacity and earlier grout crushing compared with SJS4.

The shear failure mode on the column occurring inside the external socket was observed in specimen SJS 5. As shown in Fig. 7, its global response initially followed a pattern similar to flexural failure of the column until reaching displacement ductility three, at which point shear failure occurred in the portion of the column embedded in the external socket, leading to increased rocking of the column.

Axial strains and associated failure modes

Strain profiles were developed to visualize the distribution of axial strains along the column height. These profiles were generated by calculating the strains between each marker placed on the extreme longitudinal bars of the RC columns. The strain profiles represent the first cycles of each ductility increment, considering both loading directions. "Pushing Cycles" indicates strain profiles when the applied force pushed the column toward its north direction, while "Pulling Cycles" indicates when the force pulled the column toward its south direction.

Figures 8, 9, and 10 present the strain profiles of the extreme longitudinal bar on the north side of each specimen, along with images of column damage at failure. This allows for a direct comparison between the strain profiles

Table 2—Summary of global response of test SJS 1 to SJS 6

Test	Column nominal capacity, kNm	Peak moment of column, kNm	Failure mode (reached limit state)	Ductility at limit state	Drift at limit state
SJS 1 (1.0*Dc*)	811.9	858.1	Flexural failure of column; bar fracture	$-\mu_4^3$	6.6%
SJS 2 (0.75*Dc*)	811.9	645.9	Grout crushing	$+\mu_{1.5}^2$	5.9%
SJS 3 (0.85*Dc*)	811.9	762.8	Grout crushing	$+\mu_3^1$	4.9%
SJS 4 (0.85*Dc*)	811.9	856.5	Grout crushing	$+\mu_4^1$	6.9%
SJS 5 (0.85*Dc*)	344.8	348.0	Shear failure of column inside external socket	$+\mu_3^3$	5.3%
SJS 6 (0.85*Dc*)	344.8	368.4	Flexural failure of column; bar fracture	$-\mu_3^2$	7.8%

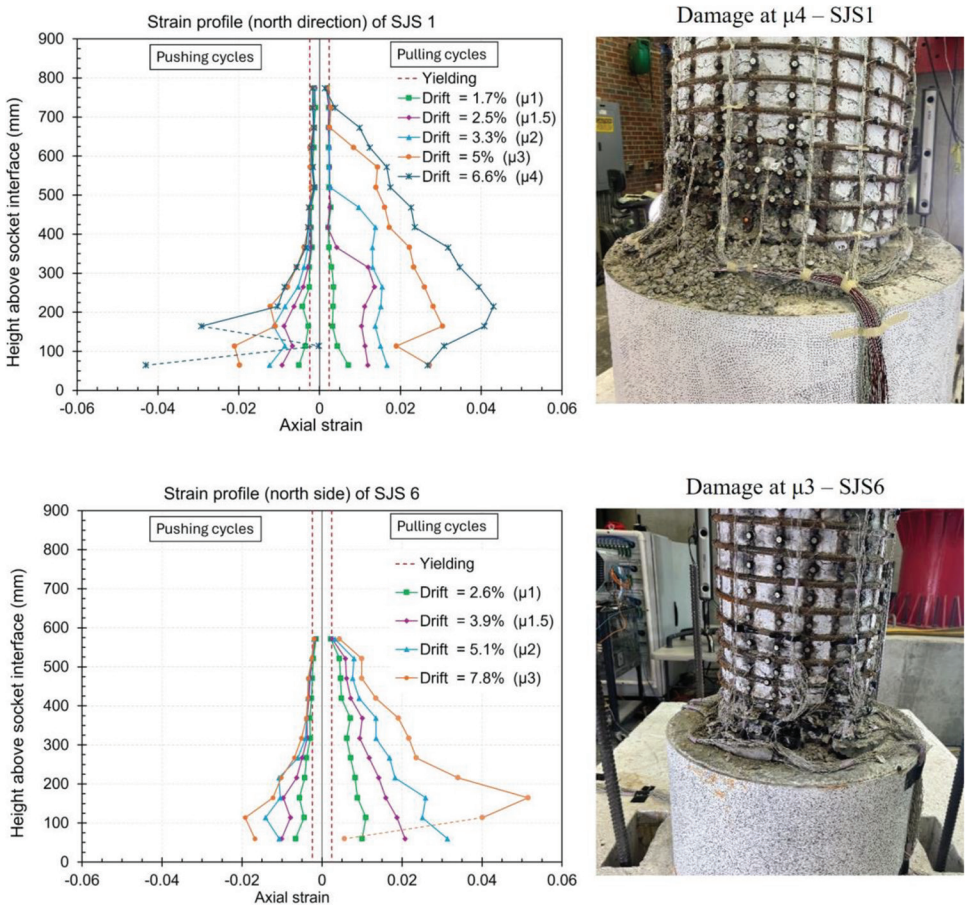

Fig. 8—Strain profile and damage at limit state for tests with flexural failure of column (SJS 1 and SJS 6).

and the observed damage patterns. The dashed lines indicate data points where LED markers were no longer visible to the camera due to concrete crushing or other obstructions. Figure 8 represents tests that exhibited flexural failure of the column. In both tests, significant tension and compression strains developed in the longitudinal bars before failure. For SJS 1, the strain reached 4.5% before bar buckling occurred, followed by fracture in the subsequent cycle. Similarly, in SJS 6, the strain reached 5.0% before buckling and fracture. These results confirm that the plastic hinge is fully developed above the external socket interface.

Figure 9 depicts tests with grout crushing failure. In SJS 2, the longitudinal bars reached yielding at the predicted yield displacement. At higher ductility levels, the column experienced rocking, causing a reduction in strain demand on the bars. In SJS 3 and SJS 4, the bars reached maximum strains of 1.6% and 4.0%, respectively, before grout crushing occurred, leading to column rocking and a reduction in reinforcement strains. This behavior prevented the full development of the plastic hinge above the external socket connection.

Figure 10 illustrates the test in which shear failure occurred within the portion of the column embedded in the external socket. The tension strains in the longitudinal bars reached 2.5% before shear failure initiated, leading to grout splitting and subsequent rocking of the column. This behavior further prevented the full development of the plastic hinge above the external socket connection.

In addition to material strains within the column, Fig. 11 presents the strains measured in the external socket reinforcement along the north direction. The external socket connections effectively confined plastic strains to the column, preventing them from extending into the foundation

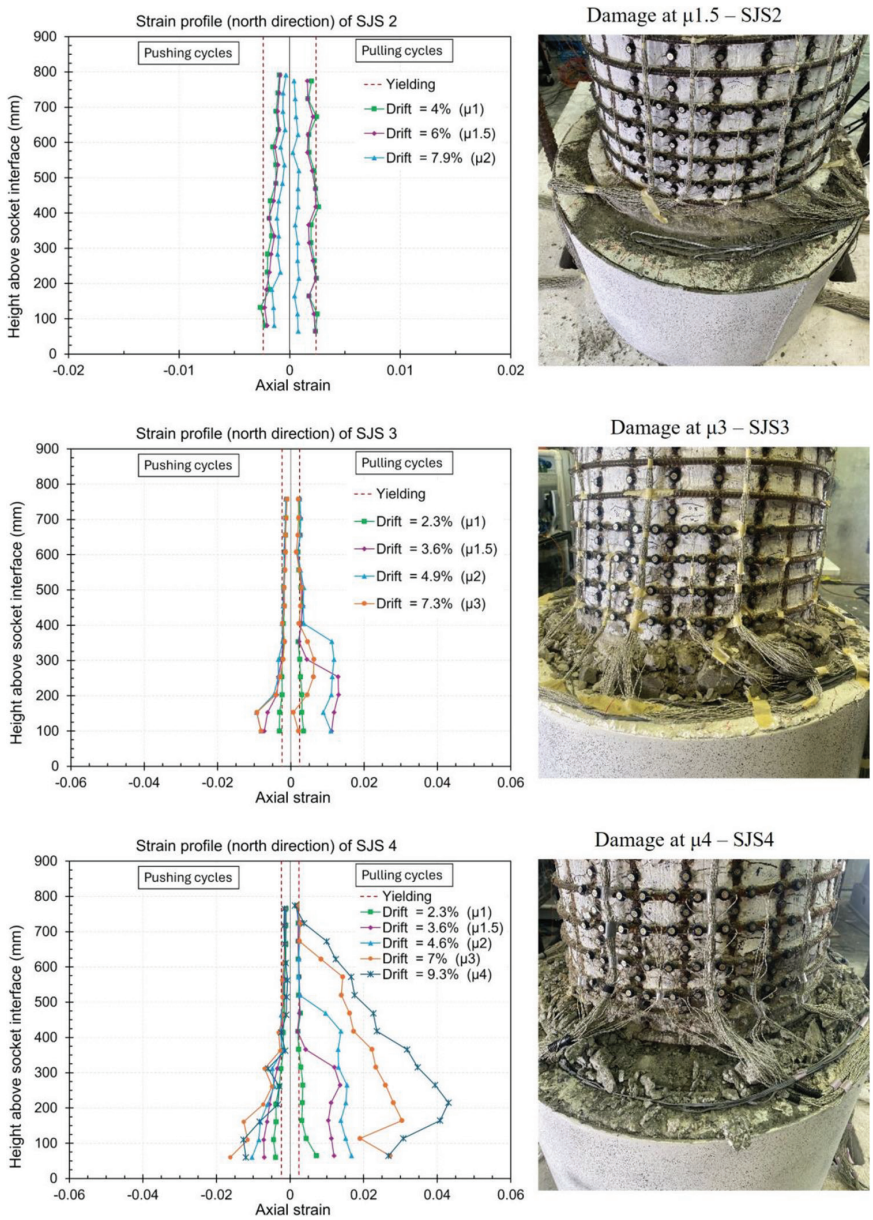

Fig. 9—Strain profile and damage at limit state for tests with grout crushing (SJS 2, SJS 3, and SJS 4).

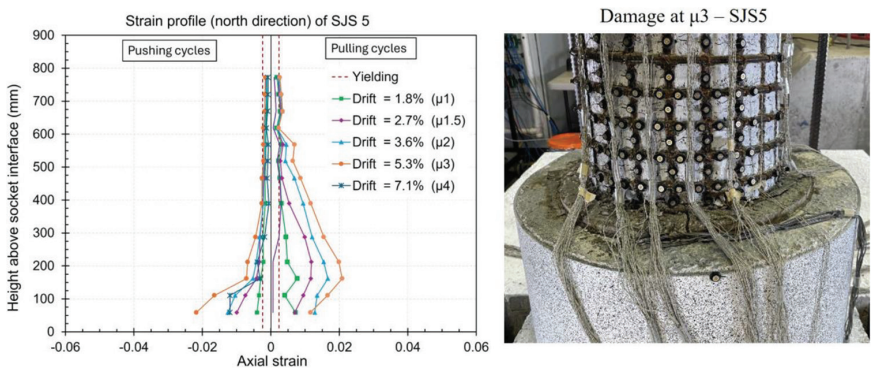

Fig. 10—Strain profile and damage at limit state for tests with shear failure of column within external socket (SJS 5).

or cap beam. Throughout all tests, the external socket wall and footing sustained no visible damage, confirming their role as capacity-protected elements. This was demonstrated by the strain measurements in the external socket wall, where the reinforcing bars remained below the yield point in all specimens, regardless of failure mode.

Figure 12 presents the circumferential strains on the external socket sleeve, representing the hoop forces acting around its circumference for all large-scale tests. These

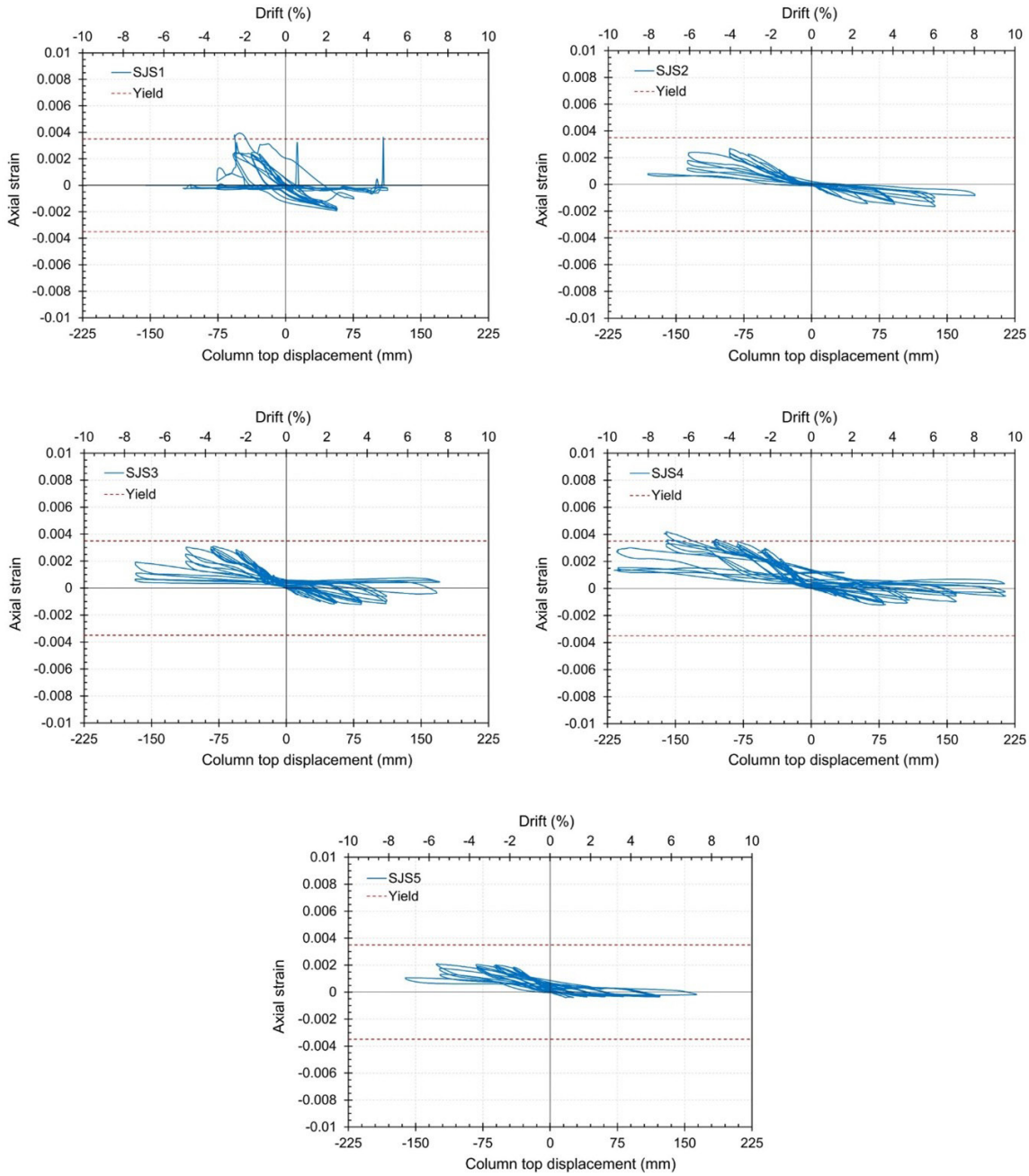

Fig. 11—Axial strains of external socket reinforcement.

strains were monitored to evaluate their contribution to the connection's behavior. In SJS 1, SJS 2, SJS 3, and SJS 4, circumferential strains exceeded the yield strain at the top third of *Hs*, with maximum values of approximately 0.45% for SJS 1, 1% for SJS 2 and SJS 3, and 0.6% for SJS 4. The rest of the socket remained elastic in all cases. This localized inelastic deformation correlated with the visible damage observed during testing but did not compromise the overall integrity of the sleeve.

In contrast, for SJS 5 and SJS 6, circumferential strains remained below the yield strain across the entire *Hs*. No visible damage was observed on the sleeves, confirming that they did not experience significant inelastic deformation.

Hysteretic damping and associated failure modes

Hysteretic damping is a crucial parameter for understanding how structures dissipate energy during large inelastic deformations, which is particularly important for evaluating their seismic performance. For this study, hysteretic damping was calculated using Jacobsen's area-based method.[20] This approach involves determining the ratio of the area enclosed by the force-displacement hysteresis loop for each cycle of each ductility displacement to the total elastic energy stored in the same loop.

Figure 13 illustrates the hysteretic damping across all cycles at different ductility levels for the six large-scale tests, along with a comparison to a similar CIP column test conducted at NCSU.[19,21] As expected, damping generally increased with higher ductility levels, indicating greater

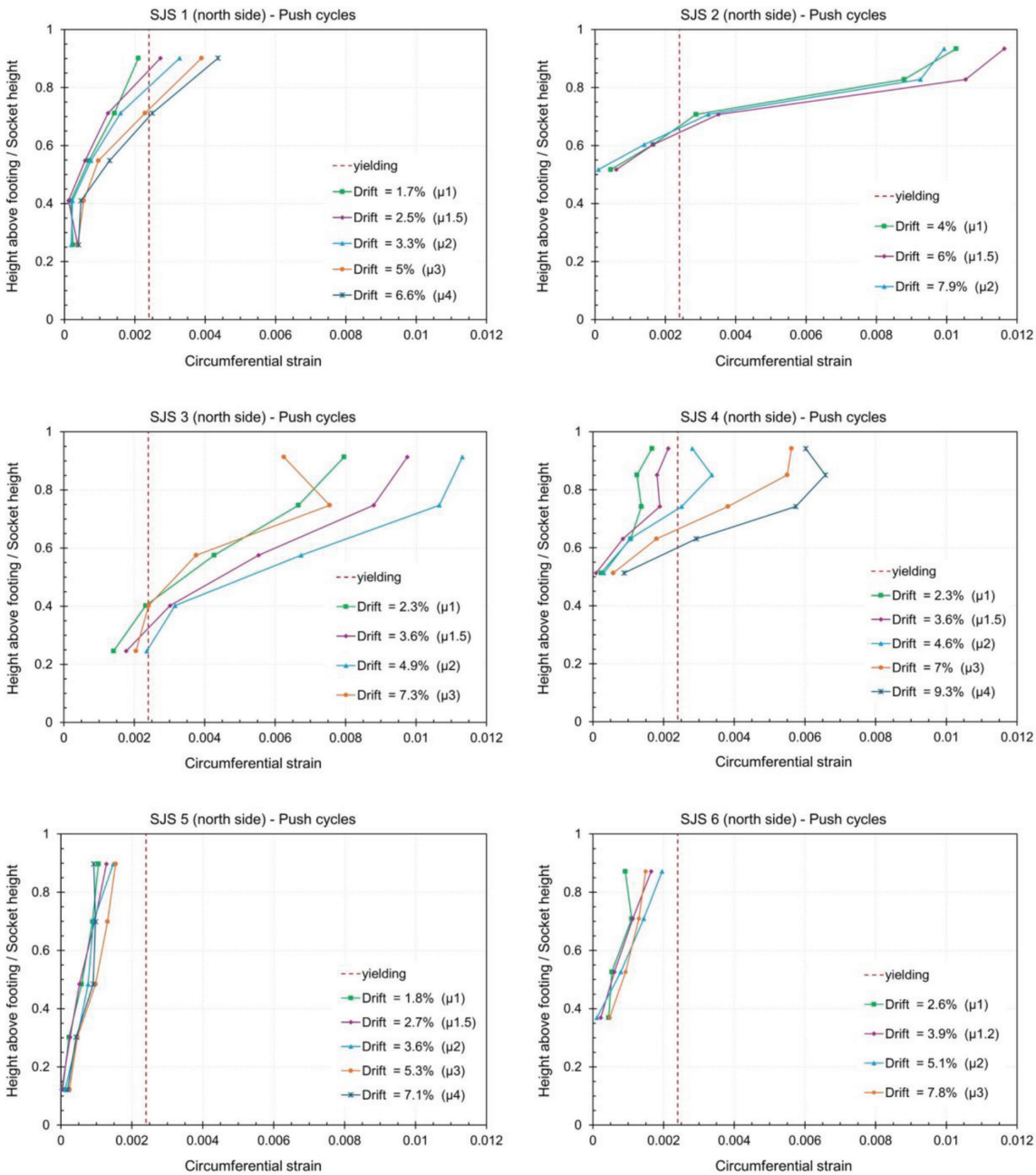

Fig. 12—Horizontal axial strains on external socket sleeve.

energy dissipation as inelastic deformations progressed. The damping values were consistent across all tests when compared at the same ductility levels, regardless of the observed failure mode. Columns with external socket connections showed approximately 5% higher hysteretic damping than the CIP column, although the overall trend of increasing damping with ductility remained similar for both systems. This increase in damping may be attributed to the formation of initial cracks in the socket wall and grout, which enhances energy dissipation.

Despite all specimens exhibiting similar hysteretic damping values during inelastic cycles, the sources of energy dissipation varied across the different failure modes. In specimens SJS 1 and SJS 6, which exhibited flexural failure, energy dissipation during inelastic cycles was primarily attributed to the progression of flexural damage in the column. For specimens with grout crushing failure, energy dissipation was mainly due to increased friction during rocking and progressive damage to the grout, while the contribution from column damage was less significant. In specimens with shear failure on the column, energy dissipation before shear failure was primarily due to column damage, similar to flexural failure. However, after shear failure occurred, energy dissipation was mainly attributed to increased friction during rocking and progressive damage to both the grout and the portion of the column embedded in the socket where the shear failure occurred.

Displacement components and associated failure modes

The total lateral displacement of the column results from multiple components, including column flexural deformation,

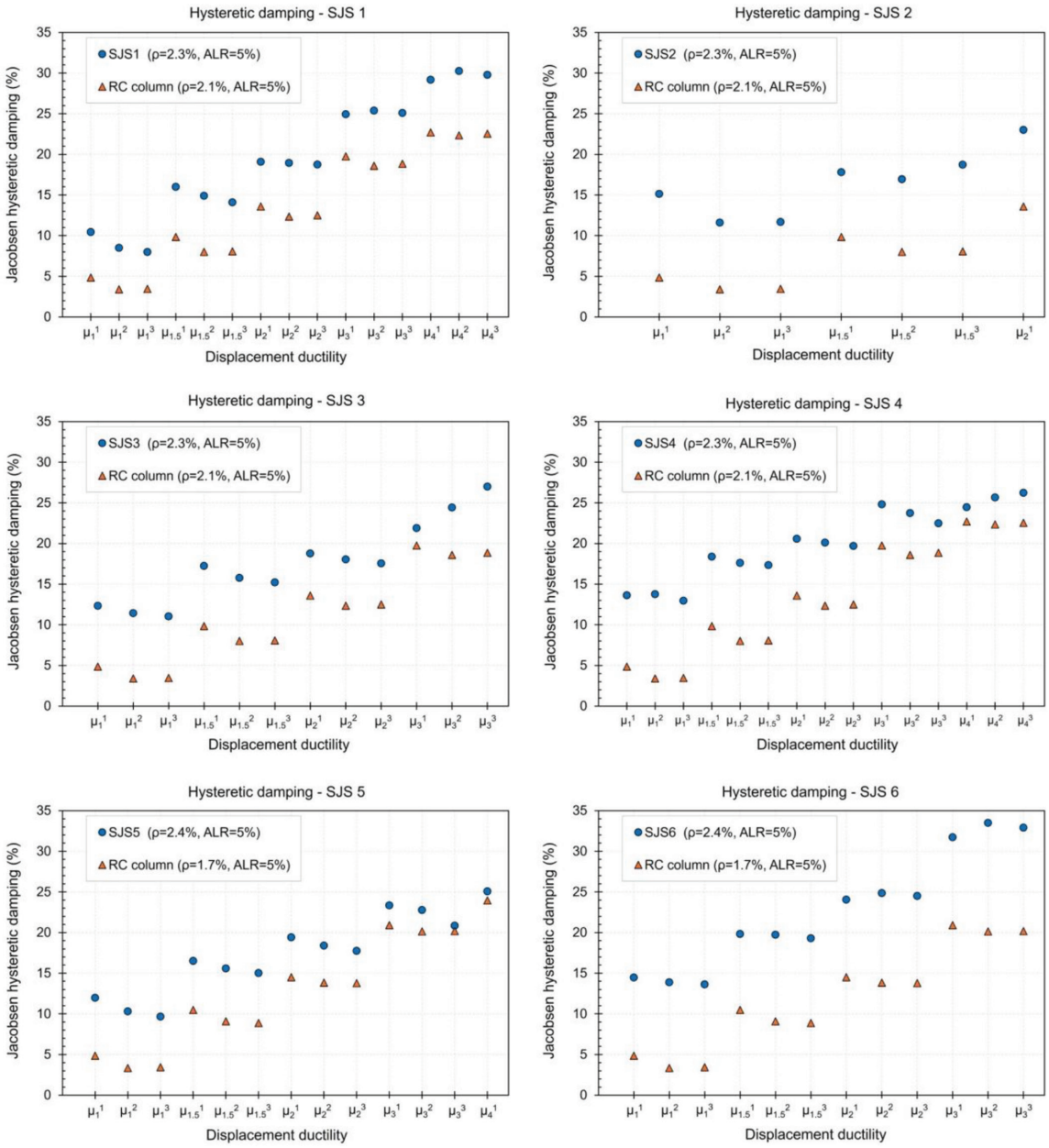

Fig. 13—Hysteretic damping for all cycles of each ductility displacement.

rotation due to strain penetration of the longitudinal bars, rocking of the column, shear deformation of the socket, and rotation of the external socket connection. Isolating these components provides a detailed understanding of the system's global behavior under cyclic loading.

The flexural displacement component was calculated using the second theorem of the moment-area method, which relates the curvature distribution along the column height to flexural deformation.[22] Curvature was determined using strains measured from the three most extreme reinforcing bars on each side of the column. Assuming plane sections remain plane, the strain distribution across the column cross section was treated as linear, and the slope of this line provided the curvature. The moment-area method was then applied to calculate flexural displacements for the first cycle of each ductility displacement in both loading directions.

Strain penetration and rocking displacements were derived by tracking the vertical change in position (slip) of LED markers placed at the bottom of the column on the three extreme bars on each side. The initial marker positions were recorded as a baseline, and the change in position during testing was used to calculate the slip. A line was fit to the slip data to determine the rotation angle due to strain penetration and rocking. This angle was multiplied by the column height measured from the interface of the external socket to determine the displacement component. In this study, strain penetration and rocking are not separated and are treated together as a single displacement component.

The shear displacement component was calculated using LED markers placed on the west side of the column, positioned at intervals of 50 mm along the height. Shear strains for each interval were multiplied by the interval height to compute the shear displacement, summing contributions to

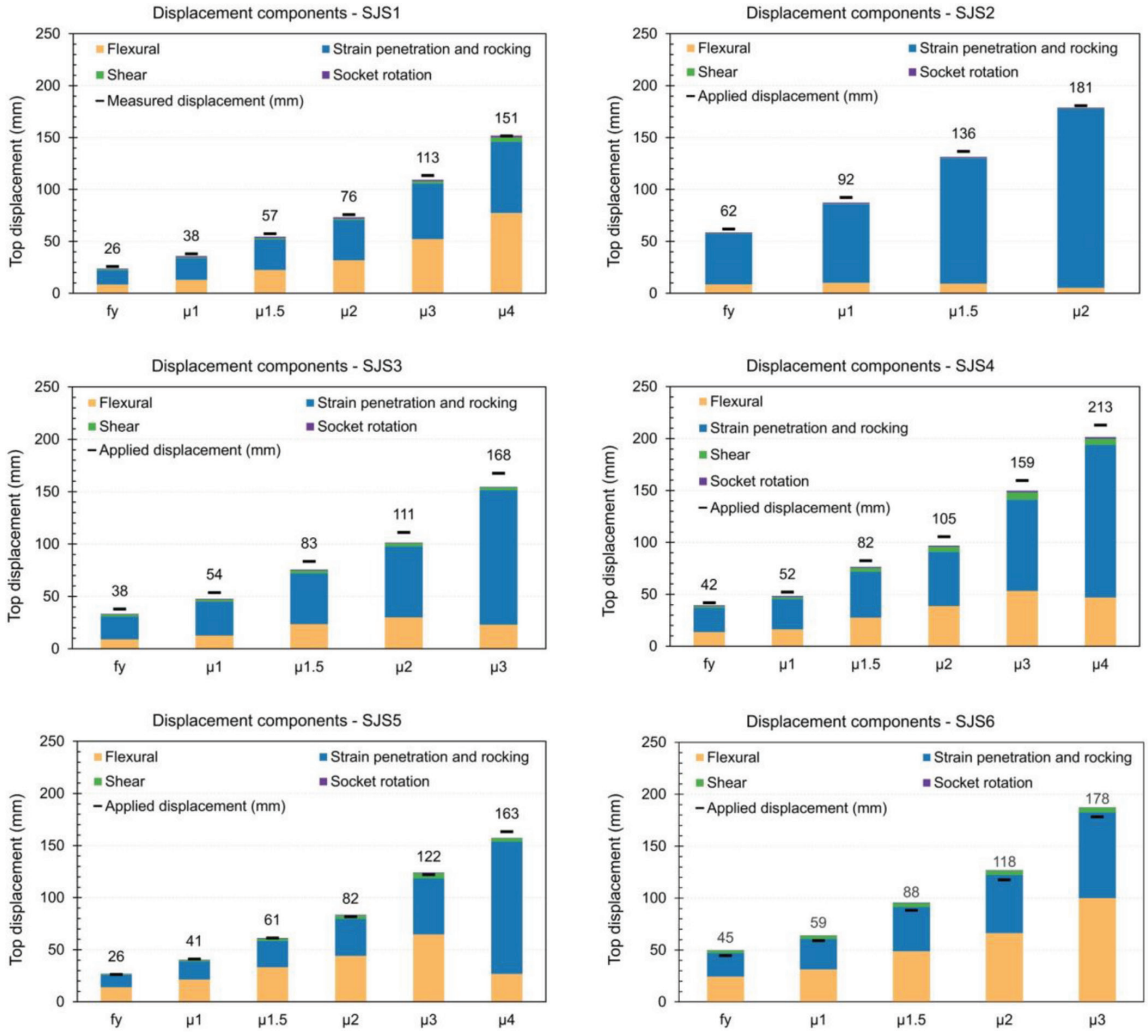

Fig. 14—Displacement components for each ductility displacement for pushing cycles.

the top of the instrumented region. Beyond the instrumented region, it was assumed that the last measured shear strain remained constant up to the top of the column.

Displacement resulting from socket rotation was calculated using DIC software to analyze the rotation of the socket region. The socket rotation was considered to influence column displacement up to the *Hs*, and the rotation angle was multiplied by this height to obtain the displacement component.

Figure 14 illustrates the contributions of flexural deformation, strain penetration, rocking, shear deformation, and socket rotation, compared to the measured displacement at each ductility level for pushing cycles in the six large-scale tests. While some discrepancies due to calculation and instrumentation errors were observed, the results demonstrate that the calculated displacement components align well with the measured displacements. This analysis illustrates how various displacement components contribute to the overall response and how their distribution varies across different failure mechanisms.

For flexural failure of the column, deformation was significantly influenced by column flexure. In SJS 1, flexural deformation accounted for approximately 40% of the total displacement, while strain penetration and rocking contributed approximately 50%. In SJS 6, flexural deformation made up about 50% of the total displacement, with strain penetration and rocking contributing approximately 45%, as shown in Fig. 14. These contributions differ from those in CIP columns, where flexural displacement typically dominates at 65% and strain penetration accounts for about 30%. The results highlight that strain penetration and rocking play a more significant role in the displacement of columns with socket connections.

For grout failure, strain penetration and rocking were the primary contributors to deformation. As shown in Fig. 14, displacement behavior in these specimens was largely governed by rocking and strain penetration, which accounted for approximately 90% of the total displacement in SJS 2, 65% in SJS 3, and 55% in SJS 4. In contrast, flexural displacements contributed only 5%, 25%, and 30%, respectively. These results indicate that when grout crushing is the governing failure mode, rocking and strain penetration dominate the total displacement, significantly reducing the influence of flexural deformation compared to CIP columns. Additionally, as grout strength increased, the contribution of rocking decreased, while the flexural component of displacement became more prominent, shifting the behavior closer to that of a flexural failure.

For shear failure within the column inside the external socket, flexural deformation was a major contributor to displacement before failure occurred. After the onset of shear failure, strain penetration and rocking became the dominant displacement mechanisms. As shown in Fig. 14, the overall displacement behavior of SJS 5 was initially governed by flexural deformation, strain penetration, and rocking. Before shear failure of the column inside the external socket, flexural displacement accounted for approximately 50% of the total displacement, while strain penetration and rocking contributed around 45%. However, after shear failure occurred, the flexural component was reduced to approximately 15%, while strain penetration and rocking increased to approximately 80% of the total displacement. These results indicate that when shear failure governs the response, strain penetration and rocking become the primary displacement mechanisms, significantly influencing the overall behavior of the column within the socket connection.

Implications for design of external socket connections

The experimental results provided critical insights into the behavior of external socket connections under seismic loads. Socket height proved to be a key design variable, as it significantly influenced socket connection material stress demands, shear forces within the socket, and ultimately system failure modes. Shorter socket heights increased stress demands on the grout and shear forces on the embedded portion of the column, necessitating higher grout strengths and greater shear capacity to achieve a flexural failure mechanism, which is the desired outcome for design. Additionally, both the socket height and the material strengths of the grout and column concrete played a crucial role in determining the failure mode, whether it be flexural failure, grout crushing, or shear failure within the socket. Optimizing these parameters is essential to ensure the column develops a full plastic hinge above the socket interface while maintaining the structural integrity of the connection. The tests confirmed that properly designed sockets can achieve behavior comparable to CIP columns while effectively preventing plastic strain demands from transferring into the adjoining member. Ensuring that the socket remains elastic helps mitigate damage to the foundation or cap beam.

In terms of mechanisms that contributed to column deformation, strain penetration and rocking were the dominant displacement components, accounting for more than 65% of the total displacement, particularly for shorter sockets. This contrasts with CIP columns, where strain penetration typically contributes around 35% of the total displacement. These findings highlight the importance of considering both socket height and material properties when designing external socket connections to achieve a desirable failure mechanism and improve seismic performance in external socket connections.

CONCLUSIONS

The six large-scale tests provided an evaluation of the performance of external socket connections, highlighting the combined influence of socket height and material strengths on their behavior and design. The ability of the connection to develop the full plastic moment in the column at the socket interface depended not only on socket height but also on the material strength of the socket components. Additionally, grout strength and the concrete strength of the embedded portion of the column played a crucial role in determining the failure mode.

A critical finding from the experimental tests was the inverse relationship between socket height, grout strength, and the shear force acting on the column within the socket connection. Shorter socket heights increased stress demands on the grout and shear forces on the embedded portion of the column, requiring higher grout strengths and greater shear capacity to prevent an undesired failure mode. In contrast, longer socket heights reduced shear forces on the embedded portion of the column and allowed for lower grout strengths without compromising the connection's performance. This inverse relationship is an essential design consideration for engineers optimizing socket connections based on material properties and force demands. Furthermore, the experimental results demonstrated that external socket connections effectively protected the adjoining structural members by confining plastic strains to the column, regardless of socket height or failure mechanism.

The study also highlighted differences in energy dissipation and contributors to system deformation compared to cast-in-place (CIP) columns. External socket connections exhibited higher elastic damping, attributed to early cracking in the grout and socket walls. Additionally, displacement components were dominated by strain penetration and rocking, particularly for shorter socket heights, contrasting with CIP columns, where flexural deformations typically govern response.

The experimental tests successfully established the practical limits of external socket connections and provided a deeper understanding of the failure modes associated with different socket heights and material strengths. These failure modes included grout crushing, shear failure within the portion of the column embedded in the connection, and flexural failure, depending on the specific combination of design parameters. The desired outcome is a flexural failure of the column above the external socket connection. The findings highlight the importance of proper design to ensure that external socket connections can achieve performance comparable to CIP columns, making them a viable option for seismic applications.

Future research should focus on extending this experimental work through the development of analytical models capable of capturing the interaction between socket height, grout strength, and socket wall thickness, thereby enabling parametric investigations beyond the tested configurations. Analytical models will support the formulation of design equations and practical guidelines for external socket connections. Additionally, more studies are needed to assess the performance of these connections under different axial load ratios, boundary conditions, and effects such as cyclic degradation with shake table tests. This will ensure the reliable implementation in design practice.

AUTHOR BIOS

ACI member **Julio A. Samayoa** *is a Postdoctoral Researcher at North Carolina State University (NCSU), Raleigh, NC, where he received his PhD. He received his BS from Universidad Centroamericana José Simeón Canas, San Salvador, El Salvador, and his MS from the University of Bologna, Bologna, Italy. His research interests include accelerated bridge construction, seismic behavior, and structural design.*

ACI member **Giorgio T. Proestos** *is an Associate Professor at NCSU. He received his BASc in engineering science, his MASc, and his PhD from the University of Toronto, Toronto, ON, Canada, in 2012, 2014, and 2018, respectively. He is Chair of ACI Subcommittee 445-F, Interface Shear, and Secretary of ACI Committee 445, Shear and Torsion. He received the ACI Chester Paul Seiss Award in 2018 and the ACI Design Award in 2017.*

ACI member **Mervyn J. Kowalsky** *is the Christopher W. Clark Distinguished Professor at NCSU. He is Chair of ACI Committee 341, Performance-Based Seismic Design of Concrete Bridges, and a member of ACI Committees 213, Lightweight Aggregate and Concrete; 374, Performance-Based Seismic Design of Concrete Buildings; and 439, Steel Reinforcement. He received the ACI Structural Research Award in 2002 and the ACI Wason Medal for Materials Research in 2021. His research interests include the seismic behavior, analysis, and design of structural systems.*

ACKNOWLEDGMENTS

This project was funded by the Alaska Department of Transportation and Public Facilities. Their support is gratefully acknowledged. The authors sincerely appreciate the support and contributions from the faculty, students, and technical staff at the Constructed Facilities Laboratory at North Carolina State University.

NOTATION

Dc	=	column diameter
fg'	=	grout strength
F_{CIS}	=	strength of concrete in portion of column that lies within socket
Hs	=	socket height
M_n	=	nominal moment capacity
M_y'	=	theoretically calculated first yield moment
tw	=	wall thickness
$\Delta y'$	=	experimentally measured first yield displacement
μ	=	ductility
ρl	=	longitudinal steel ratio
ρs	=	transverse volumetric steel ratio

REFERENCES

1. Culmo, M. P., "Accelerated Bridge Construction: Experience in Design, Fabrication and Erection of Prefabricated Bridge Elements and Systems," Federal Highway Administration, Washington, DC, 2011.

2. Saiidi, M. S.; Mehraein, M.; Shrestha, G.; Jordan, E.; Itani, A.; Tazarv, M.; Sanders, D.; Murphy, T. P.; Reno, M. L.; and Pohll, M. N., "Proposed AASHTO Seismic Specifications for ABC Column Connections," Transportation Research Board, Washington, DC, 2020. doi: 10.17226/2580310.17226/25803

3. Restrepo, J. I.; Matsumoto, E. E.; and Tobolski, M. J., *Development of a Precast Bent Cap System for Seismic Regions*, National Academies Press, Washington, DC, 2011. doi: 10.17226/1448410.17226/14484

4. Fulmer, S. J.; Kowalsky, M. J.; and Nau, J. M., "Grouted Shear Stud Connection for Steel Bridge Substructures," *Journal of Constructional Steel Research*, V. 109, 2015, pp. 72-86. doi: 10.1016/j.jcsr.2015.02.009

5. Marsh, M. L.; Stanton, J. F.; Wernli, M.; Eberhard, M. O.; Garrett, B. E.; and Weinert, M. D., *Application of Accelerated Bridge Construction Connections in Moderate-to-High Seismic Regions*, National Academies Press, Washington, DC, 2011. doi: 10.17226/1457110.17226/14571

6. Culmo, M. P., "Connection Details for Prefabricated Bridge Elements and Systems," Report No. FHWA-IF-09-010, Federal Highway Administration, Washington, DC, 2009.

7. Tazarv, M., and Saiidi, M. S., "Design and Construction of Precast Bent Caps with Pocket Connections for High Seismic Regions," University of Nevada, Reno, Reno, NV, 2015.

8. Wang, Z.; Li, T.; Qu, H.; Wei, H.; and Li, Y., "Seismic Performance of Precast Bridge Columns with Socket and Pocket Connections Based on Quasi-Static Cyclic Tests: Experimental and Numerical Study," *Journal of Bridge Engineering*, ASCE, V. 24, No. 11, 2019, p. 04019105. doi: 10.1061/(ASCE)BE.1943-5592.0001463

9. Canha, R. M. F.; Ebeling, E. B.; De Cresce El Debs, A. L. H.; and El Debs, M. K., "Analysing the Base of Precast Column in Socket Foundations with Smooth Interfaces," *Materials and Structures*, V. 42, No. 6, 2009, pp. 725-737. doi: 10.1617/s11527-008-9416-4

10. Mehrsoroush, A., and Saiidi, M. S., "Cyclic Response of Precast Bridge Piers with Novel Column-Base Pipe Pins and Pocket Cap Beam Connections," *Journal of Bridge Engineering*, ASCE, V. 21, No. 4, 2016, p. 04015080. doi: 10.1061/(ASCE)BE.1943-5592.0000833

11. Motaref, S.; Saiidi, M. S.; and Sanders, D. H., "Seismic Response of Precast Bridge Columns with Energy Dissipating Joints," University of Nevada, Reno, NV, 2011.

12. Mohebbi, A.; Saiidi, M. S.; and Itani, A. M., "Shake Table Studies and Analysis of a Precast Two-Column Bent with Advanced Materials and Pocket Connections," *Journal of Bridge Engineering*, ASCE, V. 23, No. 7, 2018, p. 04018046. doi: 10.1061/(ASCE)BE.1943-5592.0001247

13. Haraldsson, O. S.; Janes, T. M.; Eberhard, M. O.; and Stanton, J. F., "Seismic Resistance of Socket Connection between Footing and Precast Column," *Journal of Bridge Engineering*, ASCE, V. 18, No. 9, 2013, pp. 910-919. doi: 10.1061/(ASCE)BE.1943-5592.0000413

14. Haraldsson, O. S.; Janes, T. M.; Eberhard, M. O.; and Stanton, J. F., "Precast Bent System for High Seismic Regions – Laboratory Tests of Column-to-Footing Socket Connections," University of Washington, Seattle, WA, 2013.

15. Wu, R.-Y., and Pantelides, C. P., "Rapid Repair and Replacement of Earthquake-Damaged Concrete Columns Using Plastic Hinge Relocation," *Composite Structures*, V. 180, 2017, pp. 467-483. doi: 10.1016/j.compstruct.2017.08.051

16. Rutledge, S. T.; Kowalsky, M. J.; Seracino, R.; and Nau, J. M., "Repair of Reinforced Concrete Bridge Columns Containing Buckled and Fractured Reinforcement by Plastic Hinge Relocation," *Journal of Bridge Engineering*, ASCE, V. 19, No. 8, 2014, p. A4013001. doi: 10.1061/(ASCE)BE.1943-5592.0000492

17. Samayoa, J. A.; Proestos, G. T.; and Kowalsky, M. J., "External Pocket and Socket Connections for the Seismic Design of Alaska Bridges," Alaska Department of Transportation and Public Facilities, Juneau, AK, 2024.

18. ASTM C39/C39M-24, "Standard Test Method for Compressive Strength of Cylindrical Concrete Specimens," ASTM International, West Conshohocken, PA, 2024. doi: 10.1520/C0039_C0039M-24

19. Goodnight, J. C.; Feng, Y.; Kowalsky, M. J.; and Nau, J. M., "The Effects of Load History and Design Variables on Performance Limit States of Circular Bridge Columns - Volume 1," North Carolina State University, Raleigh, NC, 2015.

20. Jacobsen, L. S., "Damping in Composite Structures," *Proceedings of the 2nd World Conference on Earthquake Engineering*, 1960.

21. Goodnight, J. C.; Feng, Y.; Kowalsky, M. J.; and Nau, J. M., "The Effects of Load History and Design Variables on Performance Limit States of Circular Bridge Columns - Volume 2: Experimental Observations," North Carolina State University, Raleigh, NC, 2015.

22. Priestley, M. J. N.; Calvi, G. M.; and Kowalsky, M. J., *Displacement-Based Seismic Design of Structures*, second edition, IUSS Press, Pavia, Italy, 2007.

ACI STRUCTURAL JOURNAL TECHNICAL PAPER

Title No. 123-S58

Seismic Performance of Precast Concrete Full-Scale Wide Beam-Column Connections with Emulative Detailing

by Seon-Hoon Kim, Deuckhang Lee, Wei Zhang, and Thomas H.-K. Kang

Precast concrete (PC) moment-resisting frame systems with wide beam sections have been increasingly adopted in the construction industry due to their advantages in reducing the span length of PC slabs perpendicular to wide beam members and improving the constructability of precast construction. To further facilitate fast-built construction, this study introduces a novel PC wide beam-column connection system, where the solid panel zone is prefabricated and integrated into the PC column, allowing the upper floor to be quickly constructed without delay due to the curing time of cast-in-place concrete. Meanwhile, the current ACI 318-19 Code imposes strict allowable limits on the width of wide beams and complex reinforcement details as part of a seismic force-resisting system to effectively transfer forces into the joint, considering the shear lag effect. To address this, two full-scale PC wide beam-column test specimens were carefully designed, fabricated, and tested to explore the impact of large beam width and simplified reinforcement details beyond the code limit. The seismic performance was evaluated in terms of lateral strength, deformation capacity, stiffness degradation, failure mechanism, and energy dissipation. Based on the evaluation, the proposed PC wide beam-column connections demonstrated equivalent, or even better, seismic performance than the reinforced concrete control specimen. Additionally, it was found that the presence of corbels can mitigate the shear lag effect in PC wide beam-column connections, and that the current effective beam width limit imposed by ACI 318-19 is conservative for PC wide beam-column connections with corbels.

Keywords: effective beam width; emulative detailing; precast concrete; seismic performance; strong connection; wide beam.

INTRODUCTION

The construction industry is witnessing a transformation from on-site construction to off-site construction (OSC).[1-3] Compared to traditional cast-in-place (CIP) wet construction, which is susceptible to external environmental factors such as weather conditions, OSC methods offer distinct advantages, including cost reduction, waste minimization, and shorter construction duration, while significantly enhancing energy efficiency.[1-5] The precast moment-frame system has undergone significant technological advancements in recent years, with various precast concrete (PC) wide beam systems being increasingly adopted in the construction of residential, large-scale logistics, and industrial buildings in South Korea, as illustrated in Fig. 1. These precast structures usually require large PC slabs with a net span length over 10 m (32.8 ft), where excessive deflection inevitably becomes a critical issue in practice.[6-8] Therefore, PC wide beams have been implemented to reduce the span length of PC slabs in the transverse direction, as illustrated in Fig. 2(a). This approach enhances overall building performance and economic feasibility. To ensure structural integrity and emulative behavior of the PC wide beam-column connection, CIP concrete for the panel zone is simultaneously placed together with the topping layer of the PC wide beam. Additionally, in accordance with ACI 318-19 (R18.6.2),[9] transverse reinforcement may need to be placed through the column perpendicular to the loading direction (that is, the beam axis) to confine the longitudinal reinforcement of beam members extending beyond the column width, as shown in Fig. 2(b). However, this conventional connection detail inevitably compromises the advantages of PC construction in terms of construction speed and efficiency, as the upper floor cannot be erected until the CIP concrete in the joint panel zone is fully cured. To facilitate rapid precast construction, this study proposes an alternative reinforcement detail, as depicted in Fig. 2(c), in which the solid panel zone is prefabricated together with the lower PC column. In this detail, the confinement of beam longitudinal reinforcement can be sufficiently achieved by transverse reinforcement located in the outer part of the PC beam, avoiding the need for transverse bars penetrating through the column core as in Fig. 2(b). This allows the upper PC column to be directly positioned onto the PC joint, facilitating the construction process. Furthermore, this connection detail reduces the number of temporary supports during the PC component assembly.[10]

Nonetheless, the seismic performance of a PC wide beam-column connection system has not yet been experimentally examined to the authors' knowledge. Existing studies[11-17] indicate that the shear lag effect between the wide beam and column can significantly impact joint shear performance, and subsequently the seismic performance of a building. Therefore, the width of wide beams of a special moment frame is strictly limited in Section 18.6.2 of ACI 318-19,[9] and the longitudinal reinforcement of the beam passing outside the column is also recommended to be effectively confined by transverse reinforcement, as illustrated in Fig. 3 (from Fig. R18.6.2 in ACI 318-19).

The effective beam width ($b_{w,eff}$) is also specified in several international building codes, such as NZS 3101,[18] Eurocode 8,[19] and NCSE.[20] As summarized in Table 1, the key influencing parameters on the effective beam width ($b_{w,eff}$)

ACI Structural Journal, V. 123, No. 3, May 2026.
MS No. S-2025-070.R2, doi: 10.14359/51749377, received August 27, 2025, and reviewed under Institute publication policies. Copyright © 2026, American Concrete Institute. All rights reserved, including the making of copies unless permission is obtained from the copyright proprietors. Pertinent discussion including author's closure, if any, will be published ten months from this journal's date if the discussion is received within four months of the paper's print publication.

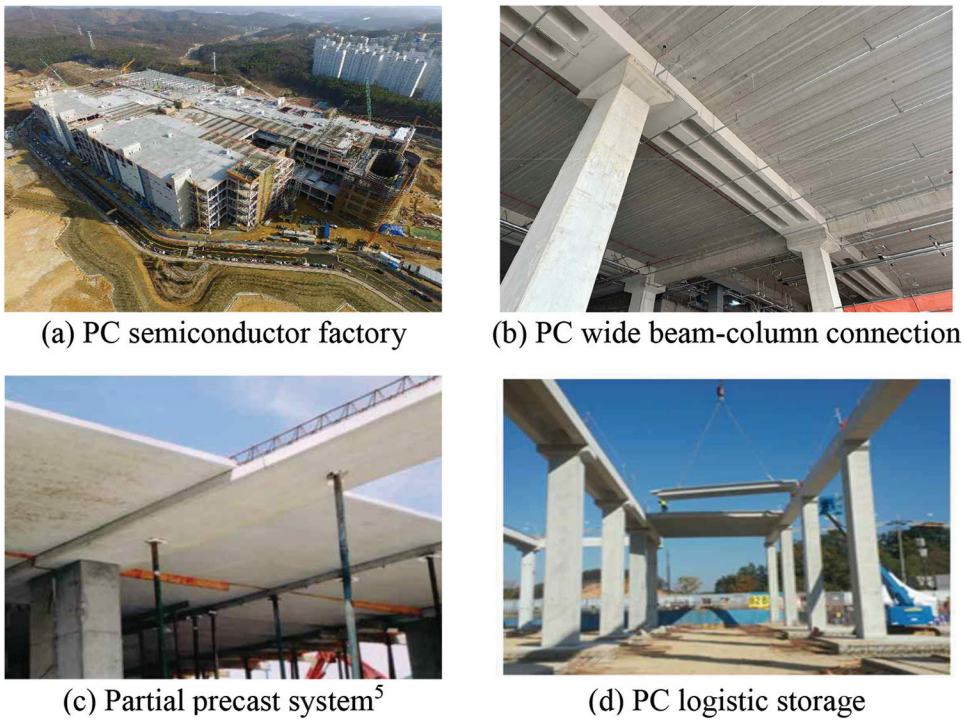

Fig. 1—Application of PC wide beam-column system.

are set by dimensional properties, such as the column width (b_c), column depth (h_c), and beam height (h_b). However, it is noteworthy that the equations for the maximum effective width of wide beams given in these codes are predominantly based on the empirical results of conventionally reinforced concrete (RC) specimens.[21] Test results of the PC wide beam-column connection specimens are very limited, especially the results from full-scale test specimens. Therefore, it is necessary to conduct realistic seismic testing on full-scale specimens of the PC wide beam-column connection systems. To this end, two full-scale PC wide beam-column connections with different effective beam widths and an RC wide beam-column connection as the control specimen were designed to be code-compliant and tested under reversed cyclic loadings. Their seismic performance was then evaluated in terms of load-carrying capacity, deformation capacity, stiffness degradation, failure mechanism, and energy dissipation capacity.

RESEARCH SIGNIFICANCE

PC wide beam-column connection systems have been increasingly adopted in building construction to take advantage of reducing the span length of PC slabs and improving constructability. However, there is an issue regarding the shear lag effect and the complex shear reinforcement details due to the wide width of beam members. The maximum effective width of wide beams specified in current codes is predominantly based on the empirical results of RC test specimens, while test results of PC wide beam-column connection specimens are very limited in the literature. This study conducts full-scale reversed cyclic tests of PC wide beam-column connections, providing a valuable starting point for updating the seismic details required in the code for PC wide beam-column connection systems.

Table 1—Effective width of wide beam limited by design codes

Codes	Equations for $b_{w,eff}$	Key parameters
ACI 318-19[9]	Min ($b_c + 1.5h_c$; $3b_c$)	b_c, h_c
NZS 3101[18]	Min ($b_c + 0.5h_c$; $2b_c$)	b_c, h_c
Eurocode 8[19]	Min ($b_c + h_b$; $2b_c$)	b_c, h_b, h_c
NCSE[20]	$b_c + h_b$	b_c, h_b

Notes: b_c is column width; h_c is column depth; and h_b is beam height.

EXPERIMENTAL PROGRAM

Test specimens

Two full-scale test specimens of PC wide beam-column connections were designed, fabricated, and tested, as depicted in Fig. 4. The first PC specimen is designated as PC-A, where A represents "Accepted as code-compliant system" because the beam width (b_w) of the PC-A specimen was 2400 mm (94.5 in.), the column width (b_c) was 900 mm (35.4 in.), and the column depth (h_c) was 1000 mm (39.4 in.), which satisfied the maximum effective beam width limit specified in ACI 318-19 (that is, $b_{w,eff} = \text{Min}[b_c + 1.5h_c, 3b_c]$). For the second PC specimen, the column size was intentionally reduced, with both the width and height being 800 mm (31.5 in.), while the same beam width of 2400 mm (94.5 in.) was used. The beam width in the second PC specimen was larger than the maximum effective beam width specified in ACI 318-19; therefore, it was designated as PC-N, where N represents "Non-code-compliant system." In addition, to facilitate fast-built construction, the panel zone at the beam-column joint was cast together with the lower PC column, so that the upper PC column of the second floor could be immediately placed onto the joint panel zone of the lower PC column without delay due to the curing time of the topping CIP concrete. This feature can be distinguished

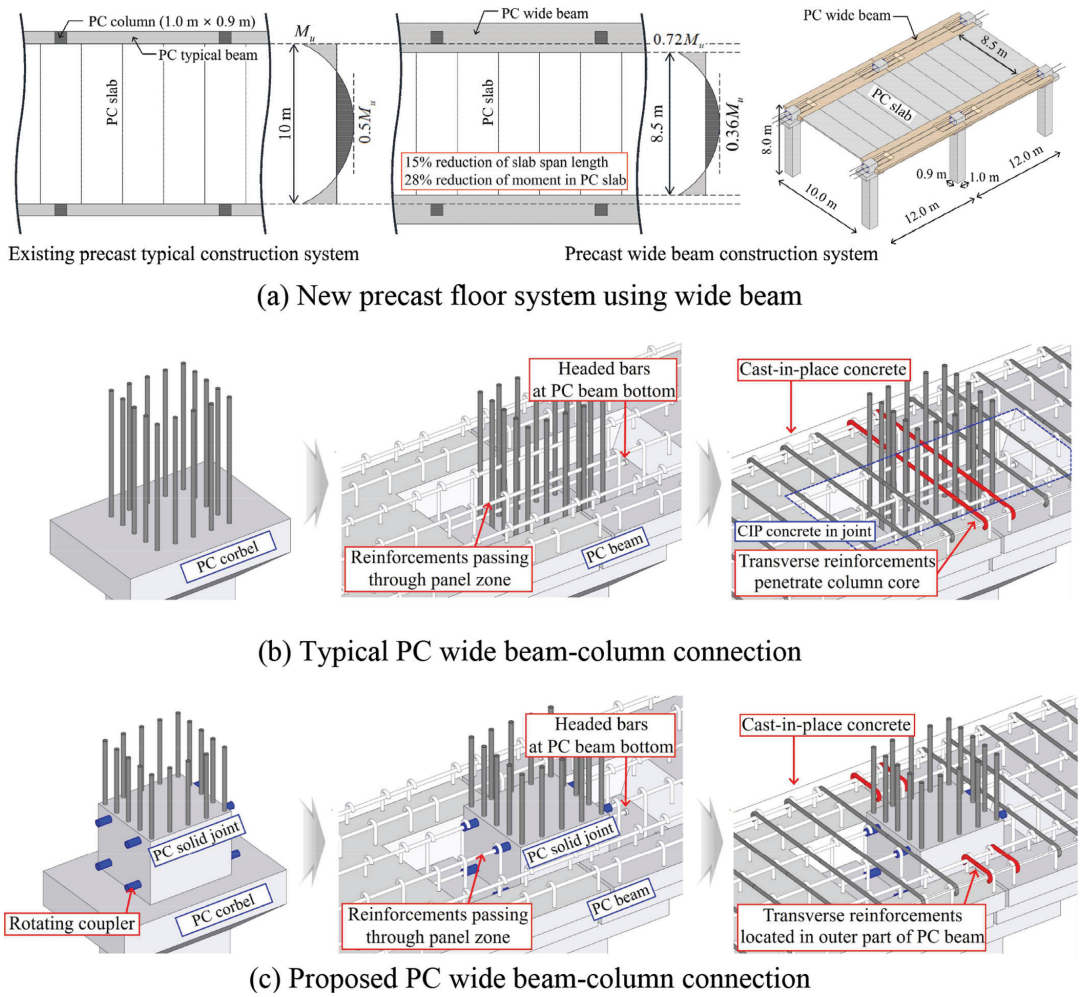

Fig. 2—Description of novel framing system by using precast wide beam. (Note: Units in m; 1 m = 3.28 ft.)

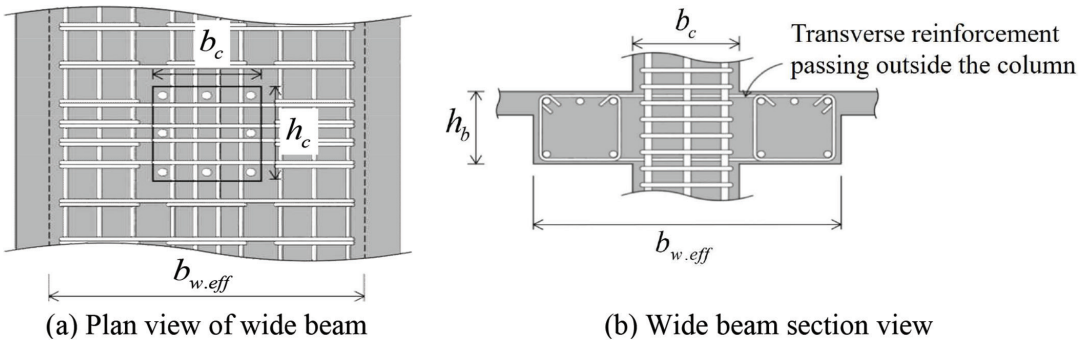

Fig. 3—Maximum effective width and reinforcement detail in ACI 318-19.

by comparing the details depicted in Fig. 2(a) and (b). In this way, the lower and upper PC columns can be quickly connected through grouting-type mechanical splices, as shown in Fig. 4.

As mentioned, because the solid panel zone is prefabricated and integrated with the precast column, an embedded grout-filled splice sleeve system is used to secure a tight connection between the PC columns and half-PC wide beams with different sizes of reinforcing bars (refer to Fig. 5 for details). The proposed horizontal splice connection system includes steel tubes, vertical polyvinyl chloride (PVC) pipes, and connecting reinforcing bars with threaded ends (refer to Fig. 4 and 5, as well as Appendix A). For the "strong connection" specified in Section 18.9.2.2 of ACI 318-19, as presented in Fig. 5(c), two different sizes of reinforcing bars are spliced at the precast beam-column connection. To this end, the PVC pipes, which have inlet and outlet for grouting, were installed in the precast factory and connected to the horizontal steel tubes. The larger reinforcing bars were then inserted into the steel tubes pre-installed in the solid panel zone to be grouted, which were tightly connected again by using screw-type rotating couplers with the smaller-sized beam reinforcement. To secure the bond performance between reinforcing bars inside the steel tubes, non-shrink

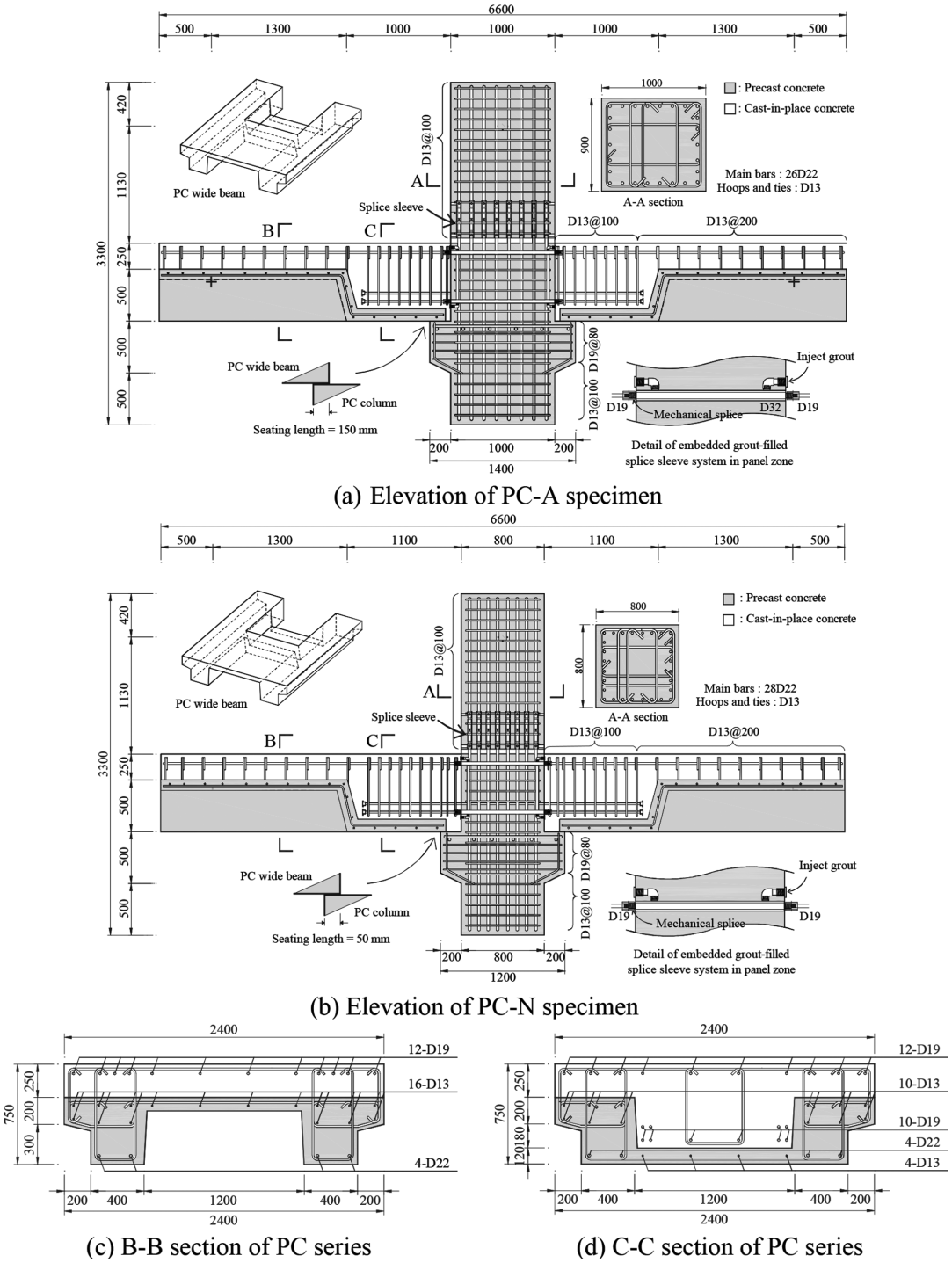

Fig. 4—Dimensional details of PC specimens. (Note: Units in mm; 1 mm = 0.039 in.)

high-strength grout was carefully injected. Note that only the top and bottom bars passing through the column width were spliced. Other longitudinal reinforcing bars outside the column were continuously placed with no splices.

The size of the reinforcing bars in the solid panel zone of the column was D32 (No. 10), much larger than that of the longitudinal reinforcing bars in the wide beams—that is, D19 (No. 6). As presented in Fig. 5(c), the strong precast connection requirement of ACI 318-19 is fully satisfied, such that the larger reinforcing bars in the panel zone can remain elastic, and yielding is limited to the smaller size of beam reinforcement. For the purpose of stable and safe assembly of PC wide beams, the lower PC column was precast with a corbel, which had a seating length of 150 mm (5.9 in.) for a PC wide beam on either side of the column.

For PC wide beams, a non-prismatic precast section was adopted, with a U-shaped section used near the PC column so that the bottom beam bars connected to the column can be developed to their yield strength (refer to Fig. 4(d)), while a double-tee section was applied 1000 mm (39.4 in.) away from the column face and for the remaining length of the beam to reduce its self-weight (refer to Fig. 4(c)). The total thickness of the wide beams (h_b) was 750 mm (29.5 in.),

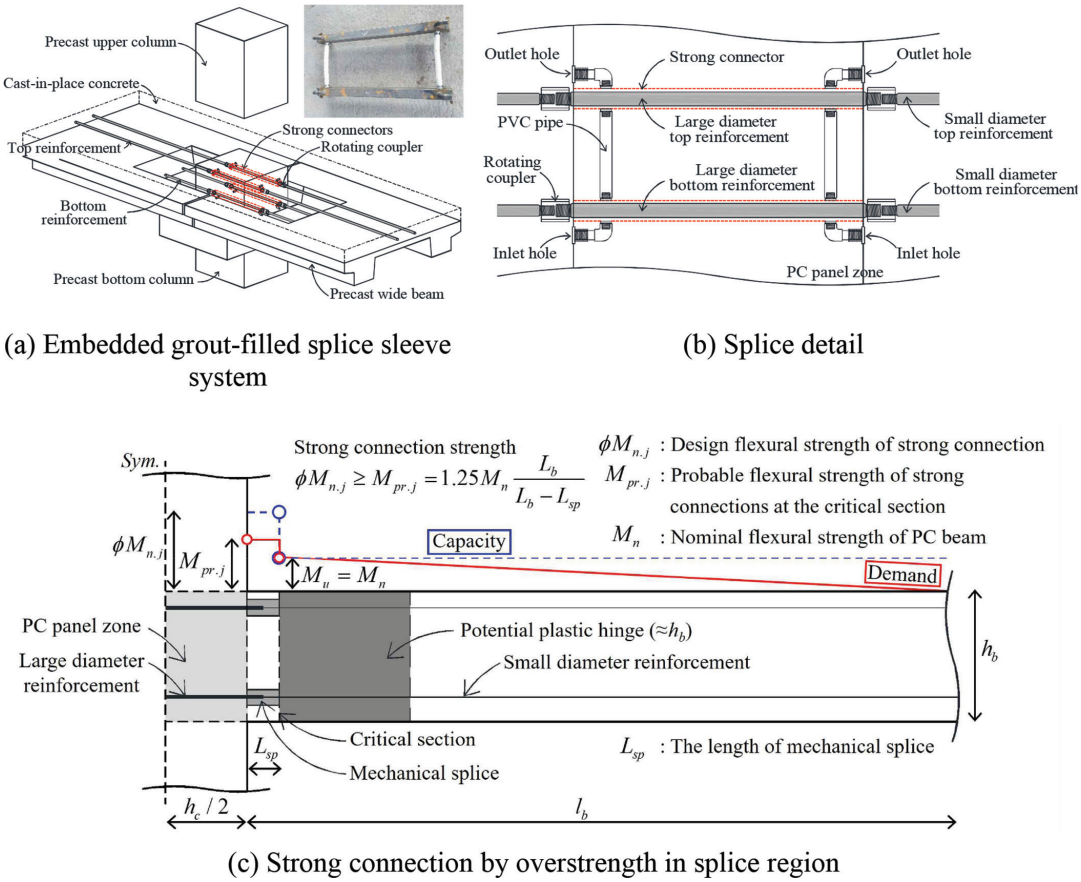

Fig. 5—Strong connection principle (as per ACI 318-19, Section 18.9.2.2).

with the PC section being 500 mm (19.6 in.) thick and the topping CIP layer being 250 mm (9.8 in.) thick.

An RC wide beam-column connection specimen was also tested for comparison purposes, as presented in Fig. 6. The RC specimen had similar material properties and dimensions to the PC-A specimen, except for the presence of a corbel. Therefore, it was designated as RC-A. In addition, the RC-A specimen had similar reinforcement details to the PC-A specimen, from which the emulation level can be examined. It should also be noted that the beam section of the RC-A specimen was set into a prismatic solid cross section. According to Fig. 3 from Commentary R18.6.2 of ACI 318-19, the beam longitudinal reinforcement passing outside the column is supposed to be engaged with closed transverse reinforcement, which is not easy to follow for precast wide beam-column connections. To this end, this study applied alternative reinforcement details, as presented in Fig. 2(c) and 4. As presented in Fig. 6, all the beam reinforcement was properly enclosed by the transverse reinforcement and fully continuous with no lap splice.

Some key design parameters are summarized in Table 2, including the reinforcement details, effective beam width ($b_{w,eff}$), beam-to-column flexural strength ratio (M_r), joint depth-to-bar diameter ratio (h_c/d_b), and percentage of wide beam reinforcement anchored in column core of the test specimens. Both the PC-A and RC-A specimens had the beam width equal to the maximum effective beam width specified by ACI 318-19, while this was not the case for the PC-N specimen with the smaller column size. ACI 318-19 requires that the flexural strength of columns in part of the special moment frame be at least 1.2 times that of beams framing into it (that is, $M_r \geq 1.2$). All the test specimens satisfied the strong column-weak beam requirement. The minimum joint (horizontal) depth requirement is also specified in ACI 318-19 to control bar slip along the panel zone, which was satisfied for all the test specimens. Because the embedded reinforcing bars in the solid panel zone were high-strength (Grade 600 MPa [87 ksi]) bars, the ratio of joint depth-to-bar diameter (h_c) should be at least $26d_b$. In summary, both the PC-A and RC-A specimens fully satisfied all the dimensional and strength requirements for beam-column connections in the special moment frame. Only the PC-N specimen had a greater width for the precast wide beam than the maximum effective beam width.

Figure 7 shows the fabrication process of the PC test specimens. The customized formworks were first erected for casting PC beam and column components in a local precast factory, and these were steam-cured as shown in Fig. 7(a). After 14 hours of steam curing, the PC components were moved to the factory yard for assembly. As mentioned previously, the upper PC column can be directly placed onto the lower PC column with the solid panel zone and quickly connected by using typical grout-filled splice sleeves, as shown in Fig. 7(b). After that, the beam longitudinal reinforcing bars were connected to the embedded splice system using rotating couplers, as presented in Fig. 5(b) and 7(c). Finally, the topping CIP concrete layer was cast and cured in natural conditions, as shown in Fig. 7(d) and (e). After

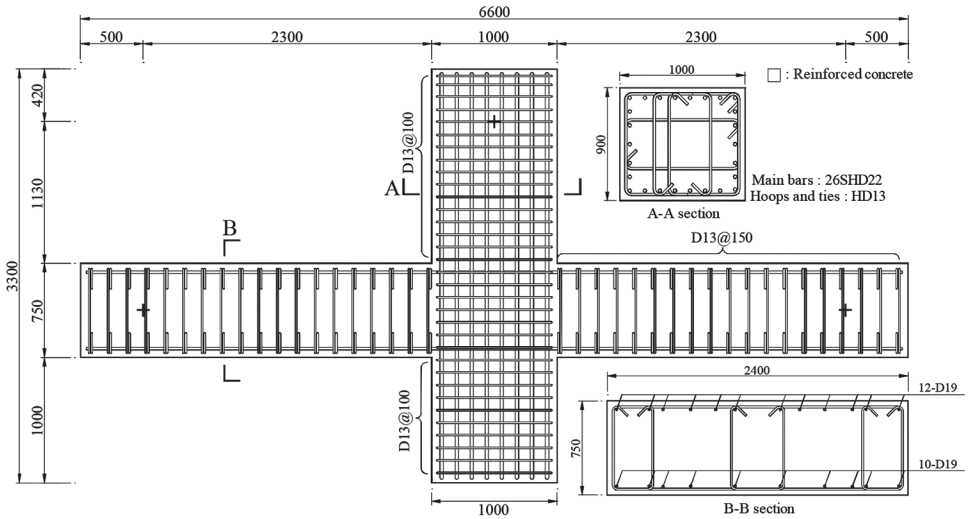

Fig. 6—Dimensional details of RC specimen. (Note: Units in mm; 1 mm = 0.039 in.)

Table 2—Key design parameters of test specimens

Specimen	Longitudinal reinforcement			$b_{w,eff}$*, mm	Beam width criteria	M_r†	h_c/d_b‡	Percentage of wide beam reinforcement anchored in column core	
	Beam								
	Top	Bottom	Column					Top, %	Bottom, %
PC-A	12D19	10D19	26D22	2400	Code compliant	1.69	52.3	16.6	20.0
PC-N	12D19	10D19	28D22	2000	Non-code compliant	1.64	41.8	16.6	20.0
RC-A	12D19	10D19	26D22	2400	Code compliant	1.74	52.3	16.6	20.0

*Maximum effective beam width requirement: $b_{w,eff} = \text{Min}\ (b_c+1.5h_c;\ 3b_c)$.

†Minimum column flexural strength requirement: $M_r = \Sigma M_c/\Sigma\ M_b \geq 1.2$.

‡Minimum joint depth requirement: $h_c/d_b \geq 20$ and 26 for Grades 60 and 80, respectively.

Note: 1 mm = 0.039 in.; for joint shear design parameters, refer to Table 6.

28 days of natural curing, the test specimens were then moved to the laboratory for testing. Note that the RC test specimens were fabricated on the same day as the casting of the CIP concrete of the PC test specimens.

Material properties

Cylinder and cube samples of concrete and grouting materials were tested on the day of testing, respectively. The average value of three samples is taken as the compressive strength of concrete (f_c'), as listed in Table 3. The concrete compressive strengths of the PC columns and beams were measured at 63.9 and 48.8 MPa (9265 and 7076 psi), respectively, while that of the CIP concrete was 25.2 MPa (3654 psi). The cube strength of the grouting material was 61.4 MPa (8903 psi). For the reinforcement, a series of tensile tests were conducted to measure their yield and tensile strengths (f_y and f_u), which are summarized in Table 4. Type 2 mechanical splice couplers, in accordance with ACI 318-19, were used for the test specimens.

Test setup and loading protocol

Figure 8 shows the test setup for the full-scale wide beam-column connection specimens. The bottom of the PC column was pinned to a steel base, which was fixed to the strong floor, and the ends of the precast wide beams were also connected to the steel bases through hinge supports. Lateral loading was applied to the top of the column through an actuator with a 5000 kN (1124.0 kip) capacity, mounted on a reaction wall, and the effective height (h_{eff}) between the loading point and base support of the column was 3070 mm (10.0 ft). The effective length (L_b) between the left and right supports of the beam members was 5600 mm (18.4 ft). Displacement control was used. The loading protocol recommended in ACI 374.1-05(19)[22] was adopted, where the target drift ratio gradually increases from 0.2% to 6.0%, with three cycles repeated at each drift level, as shown in Fig. 8(b). If there was no significant strength degradation (that is, no more than a 15% post-peak strength drop) at a drift ratio of 6.0%, an extra loading cycle was applied up to 7.0%. To simulate gravity loads typical of real buildings, an axial load equal to 10% of the column's nominal axial strength (that is, $0.1 f_c'A_g$) was applied, as shown in Fig. 8(c). The locations of the linear variable differential transformers (LVDTs) are presented in Fig. 8(c). LVDT 1 was positioned to measure the horizontal displacement of the test specimens, while LVDTs 2 to 5 were installed to measure the opening of the beam-column interfaces. LVDTs 6 to 8 were used to monitor any rigid body movement of the steel bases, which allowed for the adjustment of the target displacement of the lateral loading during testing. To evaluate the shear lag effect and plastic hinge length of the wide beam-column connections, strain gauges were attached to the longitudinal reinforcement of the beams. The locations of the gauges and the corresponding strain responses are presented Fig. 9.

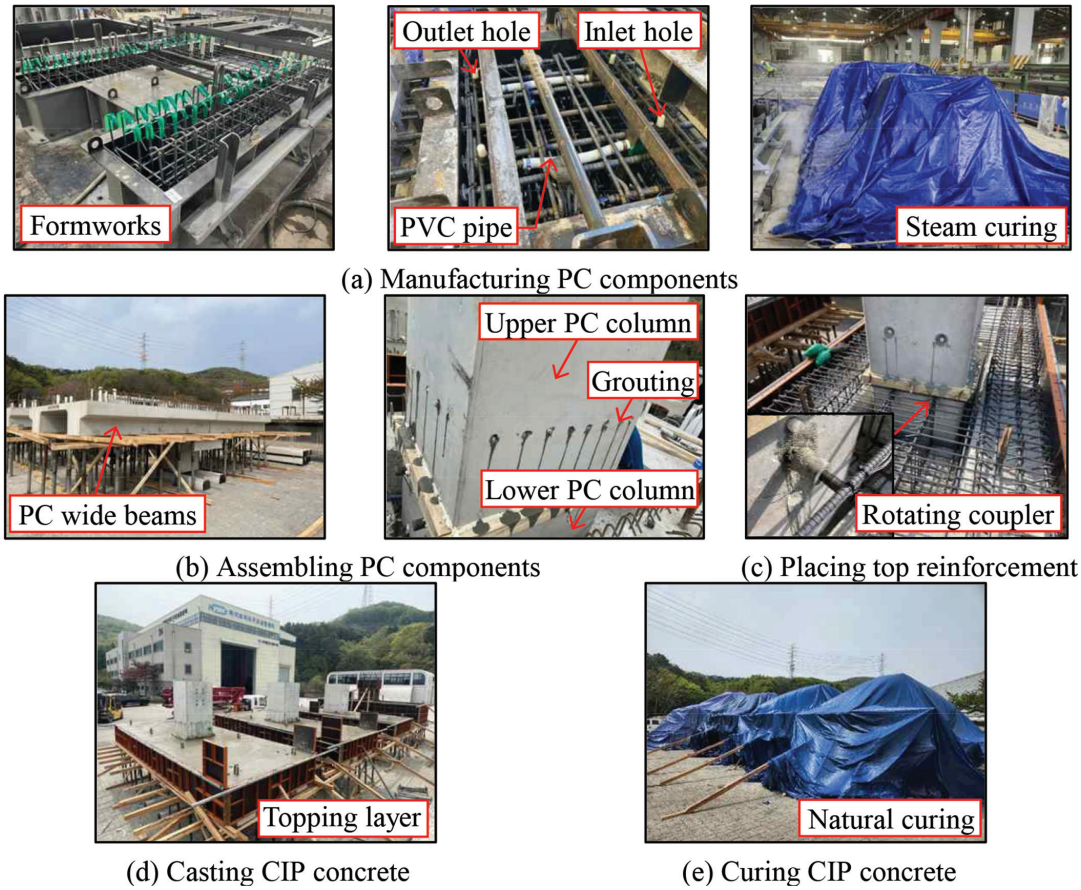

Fig. 7—Fabrication process of test specimens.

Table 3—Joint shear strength of test specimens

Specimens	f_c', MPa	A_j, mm^2	V_{jn}, kN	V_{col}, kN	V_{ju1}, kN	V_{ju2}, kN	V_{jn}/V_{ju1}	V_{jn}/V_{ju2}
PC-A	63.9	900,000	11,942.6	1135.1	3645.3	4891.8	3.276	3.178
PC-N	63.9	640,000	8492.5	1078.2	3905.3	2075.6	2.174	2.226
RC-A	25.2	900,000	7499.8	781.6	2423.6	2372.2	3.094	3.161

Note: V_{jn} is joint shear strength (Eq. (3)); V_{col} is tested peak force (P_{test}); V_{ju1} is joint shear demand (Eq. (4)); V_{ju2} is joint shear demand (Eq. (5)); 1 MPa = 0.145 ksi; 1 mm^2 = 1.55 × 10^{-3} in.^{2}; 1 kN = 0.225 kip.

Table 4—Material properties of concrete and cement grout

Specimen	Compressive strength f_c', MPa		
	Column	Grout	Beam (PC/CIP)
PC-A, PC-N	63.9	61.4	48.8 / 25.2
RC-A	25.2	—	— / 25.2

Note: 1 MPa = 0.145 ksi.

TEST RESULTS

Lateral load-story drift relationship

Figure 10 shows the lateral load-drift responses of the test specimens under reversed cyclic loadings. Backbone curves were obtained by connecting the peak points of the overall cyclic loops. The yielding point was then determined using the equal energy approach,[23] as illustrated by the schematic plot in Fig. 10. Meanwhile, the ultimate point was defined as a 15% strength drop compared to the peak point. All the key event points such as yielding, peak strength, and ultimate points were marked on the backbone curves. To evaluate the load-carrying capacity of the test specimens, their nominal strength (P_n) was calculated for the PC and RC specimens, as follows:

$$P_n = (M_{bp} + M_{bn})\frac{L_b}{h_{eff}}/(L_b - h_c + s_l) \text{ for PC specimen} \quad (1)$$

$$P_n = (M_{bp} + M_{bn})\frac{L_b}{h_{eff}}/(L_b - h_c) \text{ for RC specimen} \quad (2)$$

where M_{bp} and M_{bn} are the nominal beam flexural strengths under positive and negative bending moments, respectively; L_b and h_{eff} are the effective lengths of the beam and column, respectively (refer to Fig. 8); h_c is the column depth; and s_l is the seating length of the precast beams on the corbel of PC column. With the nominal strengths (estimated from Eq. (1) and (2)), the backbone curves extracted from the test results can be normalized as the overstrength index (that is P/P_n), as shown in Fig. 10(d). Some of the key test results

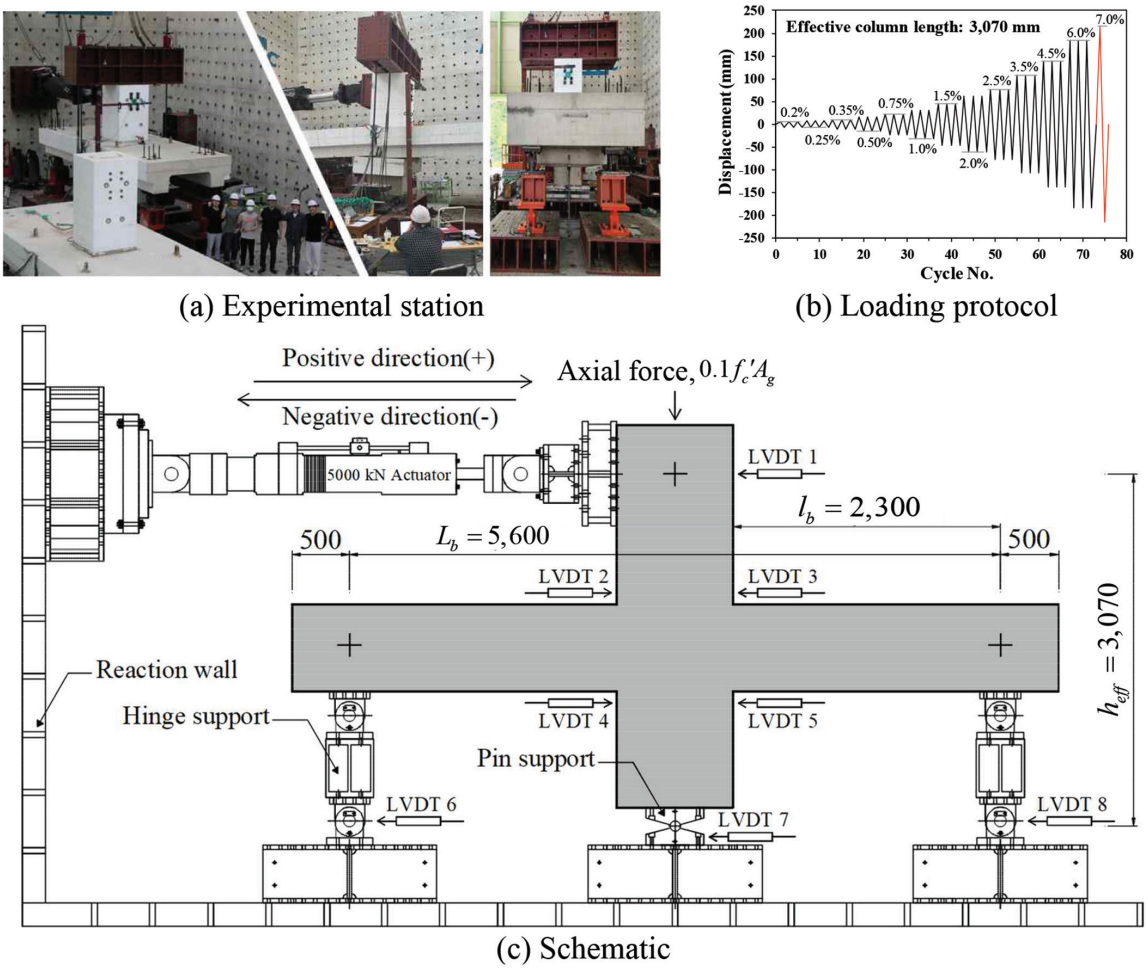

Fig. 8—Test setup and loading protocol. (Note: Units in mm; 1 mm = 0.039 in.)

(that is, load-carrying capacity, deformation capacity, and stiffness) obtained from the lateral load-story drift curves are summarized in Table 5. It appears that the PC-A and RC-A specimens showed a similar overstrength level, while the PC-N specimen showed the lowest margin of overstrength. This is because the PC-N specimen had a smaller column size, which induced a smaller effective beam width, subsequently leading to a smaller effective force transferred to the joint region. Regarding deformation capacity, the RC-A specimen had the lowest ultimate drift ratio. It reached a 15% strength drop at a 6% drift ratio, while both the PC-A and PC-N specimens sustained more than a 6% drift ratio. The ultimate drift ratios of all the test specimens were greater than the collapse prevention (CP) drift level (that is, 4% drift ratio) specified in ASCE/SEI 41,[24] which demonstrates that the wide beam-column connection specimens in this study had sufficient deformation capacity. Additionally, the PC specimens showed comparable hysteretic behavior to the RC specimen with monolithic connection details. In Appendix B, the test results were evaluated in detail using the acceptance criteria outlined in ACI 374.1 for moment frame systems based on structural testing. The overall seismic performance of all test specimens was found to be compliant with these criteria.

Table 5—Mechanical properties of reinforcement

Reinforcement	Yield strength f_y, MPa	Tensile strength f_u, MPa	f_y/f_u
D13	442.7	559.1	1.29
D16	461.7	563.6	1.22
D19	435.1	558.6	1.28
D22	454.5	554.9	1.22
D32	632.7	771.7	1.21

Note: 1 MPa = 0.145 ksi.

Joint shear and failure modes

The failure modes of the wide beam-column connections can be significantly affected by the joint shear strength, as described in ACI 352R.[25] For the beam flexure-dominant mechanism of moment-resisting frames, the joint shear strength (V_{jn}) should be greater than the joint shear demand (V_{ju}). Based on the recommendations of ACI 318, the nominal joint shear strength (V_{jn}) of the beam-column connections can be estimated as follows

$$V_{jn} = 0.083\gamma\sqrt{f_c'}A_j \tag{3}$$

where γ is a coefficient that accounts for the confinement effect provided by the beams framing into the joint. In this study, the PC prototype structure's beam-column joint is

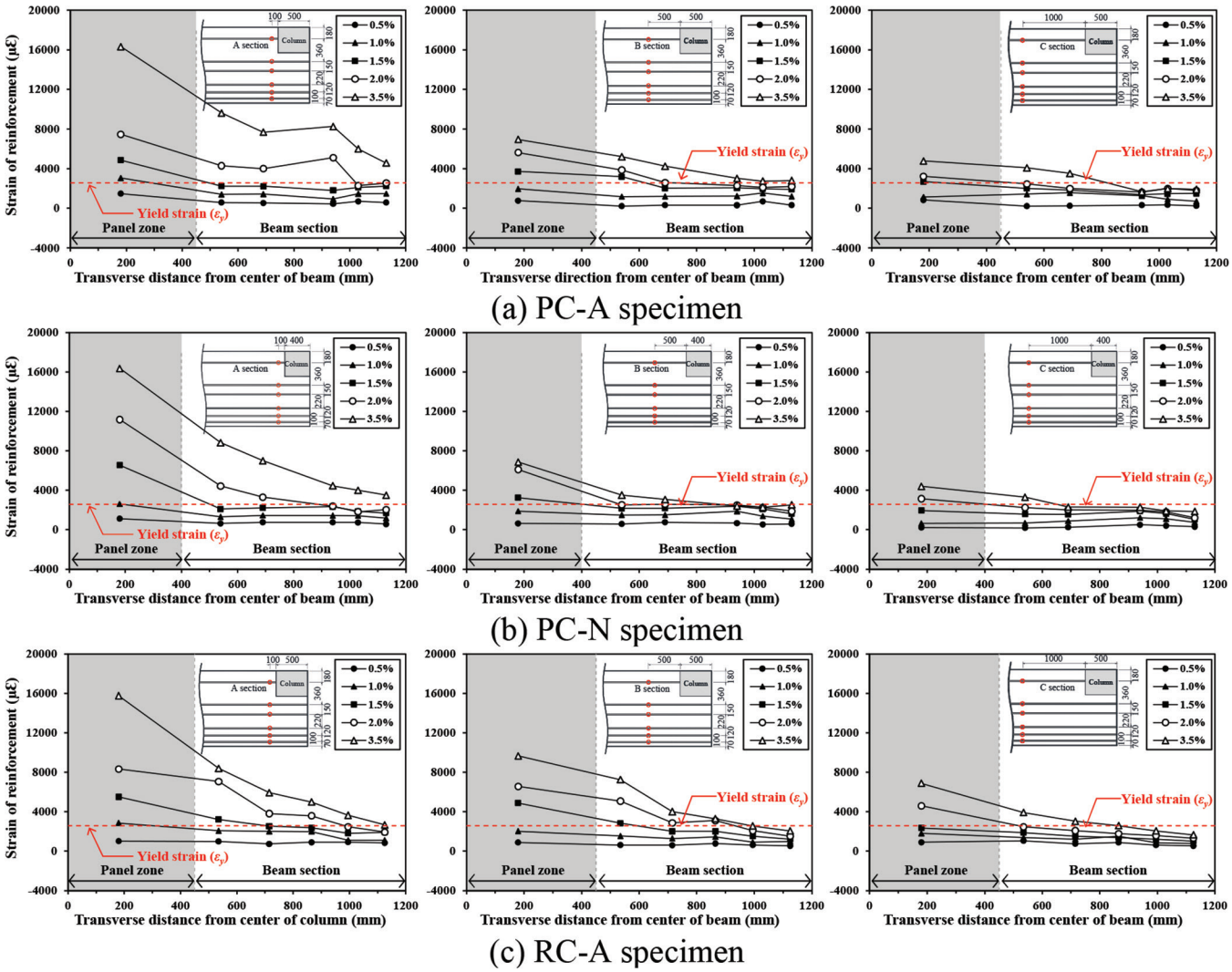

Fig. 9—Strain responses of longitudinal reinforcement.

effectively confined on two opposite vertical faces; therefore, γ is taken as 20; f_c' is the measured compressive strength of concrete; and A_j is the effective joint area as specified in ACI 352R, and for wide beam-column connections, it is taken as equal to the cross-sectional area of the column. The joint shear demand (V_{ju}) can be estimated by assuming the beam flexural yielding occurs at the joint panel zone, as follows

$$V_{ju1} = \alpha(M_{bp} + M_{bn})/0.8h_b - V_{col} \quad (4)$$

$$V_{ju2} = \alpha(C + T) - V_{col} \quad (5)$$

where α is the multiplier to account for strain hardening only, which can be taken as 1.15 (not 1.25); h_b is the beam height and $0.8h_b$ is approximated to the length of moment lever arm at the ultimate limit state; and V_{col} is the shear force of column members, which can be taken to be the lateral force obtained from test results. On this basis, the joint shear can be examined, along with the joint shear obtained based on the peak lateral load times h_{eff}, and the results are presented in Table 6. It can be seen that the joint shear strength (V_{jn}) is sufficiently larger than the corresponding demands (V_{ju}) for all the test specimens. This is expected because of application of the "strong connection" principle (refer to Fig. 5(c)). To examine the failure mechanism of the test specimens, their failure modes are presented in Fig. 11. It shows that multiple flexural cracks were concentrated in the beam for all the test specimens, indicating that they were dominated by the beam flexural mechanism during cyclic loadings. Note that, for the PC specimens, the panel zone was covered by a pair of wings attached to a precast concrete beam, as presented in Fig. 5(a). Severe damage was mostly concentrated in the concrete covers of the PC beams, not the panel zone (that is, column core). The main difference in damage patterns between the PC and RC specimens is that the PC specimens exhibited a clear opening gap at the ends of the PC wide beams at the midpoint of the connection, while the RC-A specimen experienced more severe diagonal shear damage outside the column core region. The reason for this phenomenon is that a large portion of the joint shear resistance was transferred by the wide beam wrapping around the column core.

Strain responses

To investigate the strain responses of the longitudinal reinforcement in wide beams, three gauge groups (Group A,

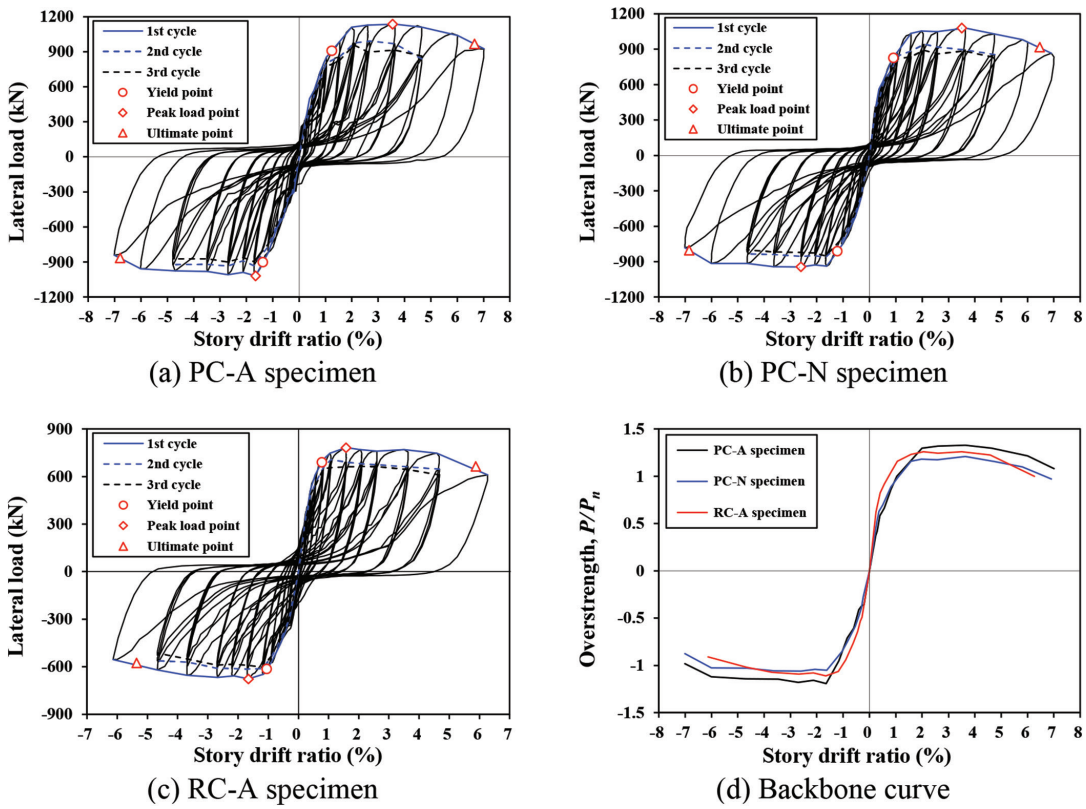

Fig. 10—Lateral load-story drift responses of test specimens. (Note: 1 kN = 0.225 kip.)

Table 6—Key test results

Specimen	Load-carrying capacity			Deformation capacity			Stiffness		
	Test strength P_{test}, kN	Nominal strength P_n, kN	P_{test}/P_n	Yield drift ratio θ_y, %	Ultimate drift ratio θ_u, %	Ductility μ	k_y, kN/mm	k_u, kN/mm	k_y/k_u
PC-A	1135.1 (–1018.8)	854.2 (–854.2)	1.33 (1.19)	1.24 (–1.37)	6.65 (–6.78)	5.36 (4.95)	23.82 (21.41)	4.72 (4.16)	5.05 (5.15)
PC-N	1078.2 (–943.8)	890.5 (–890.5)	1.21 (1.06)	0.90 (–1.21)	6.45 (–6.85)	7.17 (5.66)	29.83 (21.71)	4.62 (3.81)	6.46 (5.70)
RC-A	781.6 (–676.9)	610.1 (–610.1)	1.28 (1.11)	0.77 (–1.04)	5.87 (–5.35)	7.62 (5.14)	28.98 (19.14)	3.69 (3.50)	7.85 (5.47)

Note: 1 kN = 0.225 kip; 1 kN/mm = 5.7101 kip/in.; numbers in parenthesis denote negative direction values; k_y is yield stiffness; k_u is ultimate stiffness.

Group B, and Group C) were attached to the bars of each test specimen. These strain gauge groups were positioned 100, 500, and 1000 mm (3.93, 19.69, and 39.37 in.) away from the column face. Figure 9 illustrates the strain responses. All test specimens exhibited a similar strain response pattern, with the strain magnitudes decreasing as the location of the strain gauges moved farther from the column face. All gauge groups recorded strain values exceeding the yield strain (that is, $\varepsilon_y = f_y/E_s$), and a plastic hinge formed approximately within the beam depth (h_b) from the column face. Additionally, the strain values showed a clear declining trend along the beam width. Specifically, the longitudinal reinforcing bars near the beam center exhibited the largest strain magnitudes, while those closer to the edge of the beam showed the smallest strains. This result clearly demonstrates the shear lag effect in wide beams.[26-28] Furthermore, the presence of a corbel in the joint appeared to mitigate the shear lag effect, as indicated by the strain responses of Group A (that is, the location within the corbel's seating length). The RC-A specimen displayed a more pronounced decline in strain distribution along the beam width compared to the PC-A specimen, which lacked a corbel. Regarding the effective beam width, the strain responses along the beam width for the PC-N specimen were quite similar to those of the RC-A specimen, although slightly steeper than the PC-A specimen. This difference was due to the smaller column size and consequently smaller effective beam width in the PC-N specimen. It appears that the effect of the reduced effective beam width in the PC specimens on the strain distribution is marginal. Overall, these results suggest that the current effective beam width limit specified by ACI 318-19 may be too stringent for wide PC beam-column connections with a corbel(s).

Energy dissipation capacity

The energy dissipation capacity of a building structure reflects its inherent resistance to earthquake-induced vibrations, serving as a key seismic performance index.[29-34] For

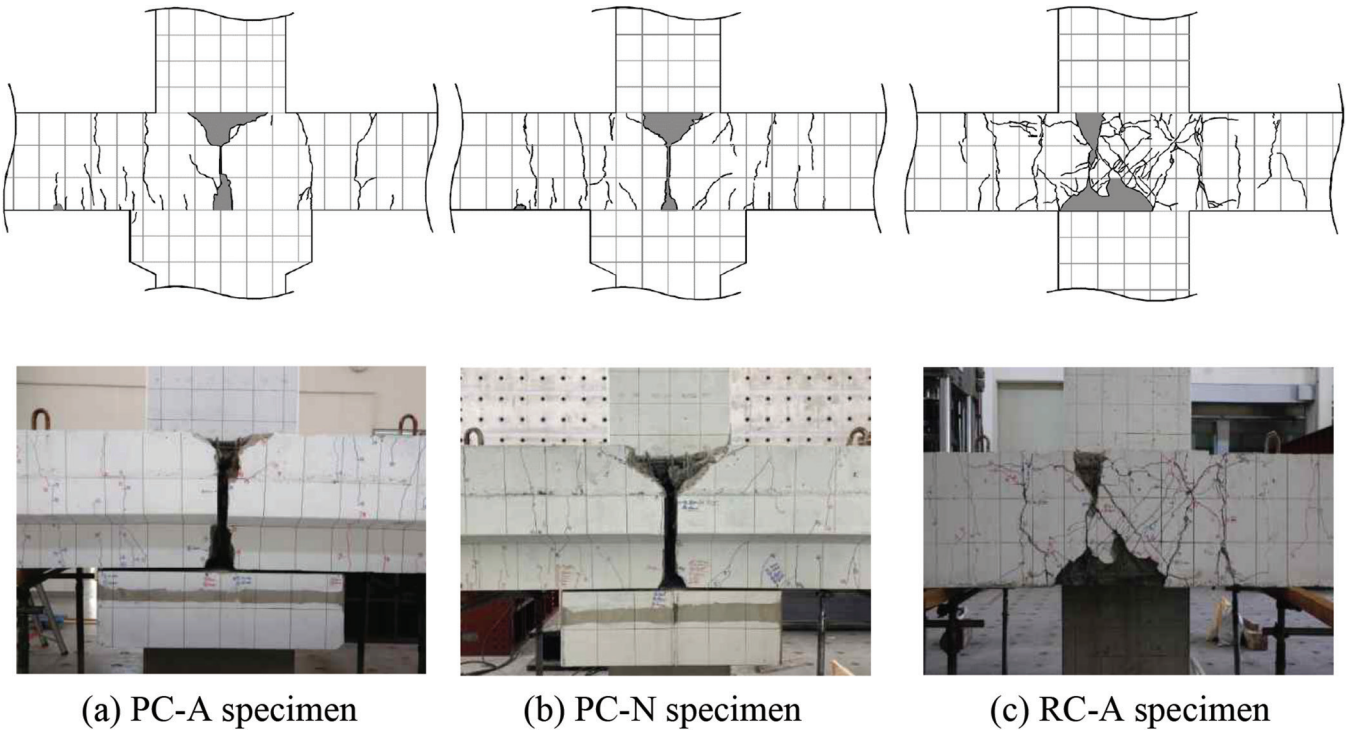

Fig. 11—Damage and crack patterns at ultimate state.

beam-column connections, this capacity is primarily associated with the inelastic deformation of beam hinges during multiple significant displacement reversals. The dissipated energy (E_I) is represented by the enclosed area of the cyclic loops. Based on this, the equivalent viscous damping ratio (ξ_{eq}) corresponding to the dissipated energy can also be calculated as follows

$$\xi_{eq} = \frac{1}{4\pi}\frac{E_I}{E_{so}} \tag{6}$$

where E_{so} reflects the maximum strain energy at the target drift of each cyclic loop, which can be taken to be the integral area of the secant line from origin to target drift. Finally, the cumulative energy dissipation of all cyclic loops and the corresponding equivalent viscous damping (ξ_{eq}) for the three test specimens were calculated, as shown in Fig. 12. The results indicate that the PC and RC specimens exhibited similar cumulative energy dissipation during the early loading stage. However, the PC specimens demonstrated significantly greater cumulative energy dissipation than the RC specimen when the drift ratio exceeded 3.5% (that is, post-peak stage), as shown in Fig. 12(a). This is because the PC specimens experienced more gradual post-peak strength degradation than the RC specimen, due to the application of the strong connection principle, as illustrated in Fig. 5(c). Regarding the equivalent viscous damping ratios, the PC-A specimen showed a notably higher damping ratio, reaching up to 9.2%, while the PC-N and RC-A specimens exhibited similar hysteretic behavior. Based on these findings, it is confirmed that the proposed PC wide beam-column connection system is comparable to a monolithic reinforced concrete system with similar details and dimensions. Therefore, it can be used as a code-compliant seismic force-resisting system. Additionally, the test results suggest that the maximum effective beam width limit for PC connections (that is, $b_c + 1.5h_c$) is too conservative. Therefore, future studies should consider modifying the maximum effective width limit for precast connections by accounting for the dimensions of the corbel and column.

CONCLUSIONS

In this study, a precast concrete (PC) wide beam-column connection featuring fast-built construction was developed and designed as part of a seismic force-resisting system (SFRS). To examine its seismic performance, two full-scale PC wide beam-column connection test specimens with different column sizes and consequently different effective beam widths, along with one reinforced concrete (RC) wide beam-column connection as a control specimen, were fabricated and tested under reversed cyclic loading. Based on the results, the following conclusions can be drawn:

1. The PC wide beam-column connections with a code-compliant effective beam width (that is, the PC-A and RC-A specimens) demonstrated slightly better load-carrying capacity, in terms of overstrength capacity relative to their nominal strength, compared to the specimens with a smaller effective beam width (that is, the PC-N specimen). However, no significant difference was observed in overall seismic performance between the specimens.

2. According to ACI 318-19, beam longitudinal reinforcement passing outside the column needs to be enclosed by transverse confinement reinforcement. However, this detail is impractical for precast wide beam-column connections. To address this issue, a simplified alternative reinforcement detail was implemented in the PC specimens, in which transverse reinforcement was placed only in the outer regions of

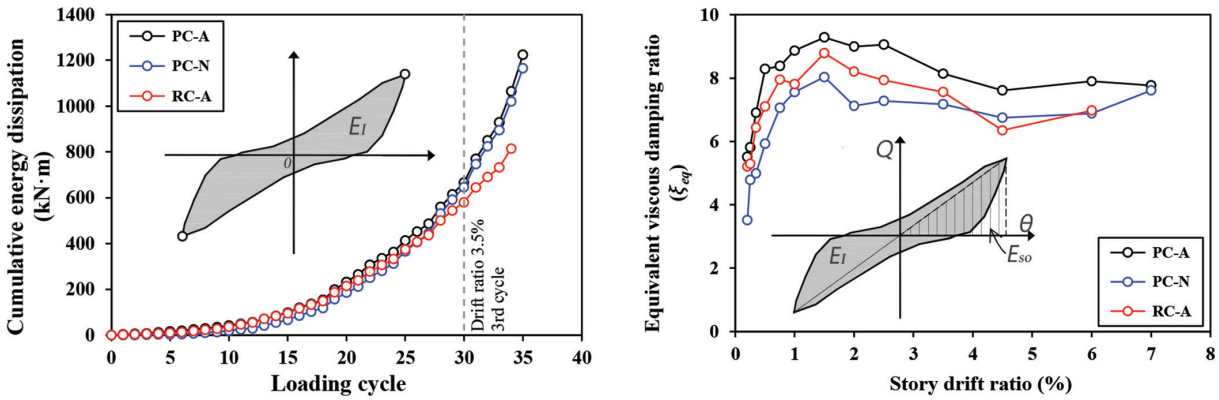

(a) Cumulative energy dissipation (b) Equivalent viscous damping ratio

Fig. 12—Energy dissipation and equivalent viscous damping ratio.

the wide beam, avoiding the panel zone. Its effectiveness was experimentally validated.

3. Compared to the PC connections, the RC connection exhibited lower deformation capacity and greater stiffness degradation due to the larger degree of concrete damage outside the column core region. This was because a portion of the joint shear force demand was transferred by the wide beam, while the opening gap between PC wide beams on top of the large corbel at the midpoint of the connection helped alleviate damage to the PC wide beam around the PC joint panel zone.

4. The strain responses indicated that the presence of a corbel can mitigate the shear lag effect in PC wide beam-column connections. The impact of the reduced effective beam width on strain distribution was more pronounced at locations beyond the corbel. The current maximum effective beam width specified by ACI 318-19 appears to be conservative for PC wide beam-column connections with a corbel(s). Therefore, it is recommended that the influences of both the corbel and column size on the shear lag effect be considered when designing PC wide beam-column connections as part of the SFRS. Future numerical and analytical studies are planned to examine the effects of corbel presence and column size on the shear lag phenomenon, with the goal of developing refined guidelines for determining the effective beam width in such precast systems.

5. The PC and RC wide beam-column connections demonstrate comparable seismic performance regardless of their different seismic details, including lateral strength, stiffness, and energy dissipation. Full-scale testing confirms that the PC wide beam-column connections presented in this study can be effectively used in practice as an emulative precast SFRS.

AUTHOR BIOS

Seon-Hoon Kim *is a PhD Student in the Department of Global Smart City at Sungkyunkwan University (SKKU), Suwon, Korea. His research interest is the seismic analysis and design of precast moment frame systems.*

ACI member **Deuckhang Lee** *is an Associate Professor in the School of Civil, Architectural Engineering, and Landscape Architecture; and the Department of Global Smart City at SKKU. He is a member of ACI Committee 550, Precast Concrete Structure, and ACI Subcommittees 445-E, Shear and Torsion – Torsion, and 445-F, Shear and Torsion – Interface Shear. His research interests include seismic response analysis and design of precast and prestressed concrete buildings.*

Wei Zhang *is an Assistant Professor in the College of Civil and Architectural Engineering at North China University of Science and Technology, Tangshan, China. He received his PhD in architectural engineering from CBNU. His research interests include smart construction, shear, and seismic responses of reinforced concrete structures.*

Thomas H.-K. Kang, *FACI, is a Professor of Structural Engineering and the Interdisciplinary Program of Artificial Intelligence at Seoul National University. He is a member of ACI Committees 352, Joints and Connections in Monolithic Concrete Structures, and 423, Prestressed Concrete; Joint ACI-PTI Committee 320, Post-Tensioned Concrete Code; and Joint ACI-ASME Committee 359, Concrete Containments for Nuclear Reactors. He received the ACI Wason Medal for Most Meritorious Paper in 2009 and the ASCE's T.Y. Lin Award in 2025 on a paper published in the* ACI Structural Journal. *His research interests include the design and behavior of reinforced, prestressed, and precast concrete structures.*

ACKNOWLEDGMENTS

This work was supported by the National Research Foundation of Korea (NRF) grant funded by the Korea government (MSIT) (No. RS-2023-00209647), by the Institute of Information & Communications Technology Planning & Evaluation (IITP) grant funded by the MSIT (No. RS-2021-II211343), and the Institute of Engineering Research at Seoul National University.

REFERENCES

1. Zhang, W.; Lee, D. H.; Kim, S. H.; and Zhang, D., "Seismic Performance of Precast Concrete Wide Beam-Column Connections under Ductile Connection Principle," *ACI Structural Journal*, V. 122, No. 2, Mar. 2025, pp. 1-12.

2. Zhang, W.; Kim, S. H.; Lee, D. H.; Zhang, D.; and Kim, J., "Seismic Performance of Self-Sustaining Precast Wide Beam-Column Connections for Fast-Built Construction," *Computers and Concrete*, V. 33, No. 3, 2023, pp. 339-349.

3. Zhang, W.; Lee, D. H.; Kim, S. H.; Ju, H. J.; and Lee, C. J., "Seismic Performance of Precast Wide Beam-Column Connections with Asymmetrical Anchorage Reinforcement Details," *Engineering Structures*, V. 275, 2023, pp. 1-17. doi: 10.1016/j.engstruct.2022.115237

4. Memon, S. A.; Zain, M.; Zhang, D.; Rehman, S. K. U.; Usman, M.; and Lee, D. H., "Emerging Trends in the Growth of Structural Systems for Tall Buildings," *Journal of Structural Integrity and Maintenance*, V. 5, No. 3, 2020, pp. 155-170. doi: 10.1080/24705314.2020.1765270

5. Bozzo, L., "A Prestressed Partially Precast System," *Concrete International*, V. 30, No. 2, Feb. 2008, pp. 35-38.

6. Huang, R. Y. C., and Kuang, J. S., "Predicting Strength of Exterior Wide Beam–Column Joints for Seismic Resistance," *Journal of Structural Engineering*, ASCE, V. 146, No. 2, 2020, p. 04019209. doi: 10.1061/(ASCE)ST.1943-541X.0002488

7. Kim, J. H.; Choi, S. H.; Han, S. J.; Jeong, H.; Lee, J. Y.; and Kim, K. S., "Effect of Reinforcing Details on Seismic Behavior of RC Exterior Wide Beam-Column Joint," *Earthquakes and Structures*, V. 25, No. 4, 2023, pp. 283-296.

8. Kim, J. H.; Jang, B. S.; Choi, S. H.; Lee, Y. J.; Jeong, H. S.; and Kim, K. S., "Experimental Study on Lateral Behavior of Precast Wide Beam-Column Joints," *Earthquakes and Structures*, V. 21, No. 6, 2021, pp. 653-670.

9. ACI Committee 318, "Building Code Requirements for Structural Concrete (ACI 318-19) and Commentary (ACI 318R-19) (Reapproved 2022)," American Concrete Institute, Farmington Hills, MI, 2019, 624 pp.

10. Kim, S. H.; Lee, D. H.; Kim, Y. K.; Lee, S. W.; Yeo, U. Y.; and Park, J. E., "Seismic Performance Evaluation of Dry Precast Concrete Beam-Column Connections with Special Moment Frame Details," *EESK Journal of Earthquake Engineering*, V. 27, No. 5, 2023, pp. 203-211. doi: 10.5000/EESK.2023.27.5.203

11. Kuang, J. S.; Behnam, H.; and Huang, Q., "Effective Beam Width of Reinforced-Concrete Wide Beam-Column Connections," *Proceedings of the Institution of Civil Engineers. Structures and Buildings*, V. 170, No. 5, 2017, pp. 336-353. doi: 10.1680/jstbu.15.00124

12. LaFave, J. M., and Wight, J. K., "Reinforced Concrete Wide-Beam Construction vs. Conventional Construction: Resistance to Lateral Earthquake Loads," *Earthquake Spectra*, V. 17, No. 3, 2001, pp. 479-505. doi: 10.1193/1.1586185

13. Benavent-Climent, A., "Seismic Behavior of RC Wide Beam-Column Connections under Dynamic Loading," *Journal of Earthquake Engineering*, V. 11, No. 4, 2007, pp. 493-511. doi: 10.1080/13632460601064814

14. Benavent-Climent, A.; Cahís, X.; and Vico, J. M., "Interior Wide Beam-Column Connections in Existing RC Frames Subjected to Lateral Earthquake Loading," *Bulletin of Earthquake Engineering*, V. 8, No. 2, 2010, pp. 401-420. doi: 10.1007/s10518-009-9144-3

15. Gentry, T. R., and Wight, J. K., "Wide Beam-Column Connections under Earthquake-Type Loading," *Earthquake Spectra*, V. 10, No. 4, 1994, pp. 675-703. doi: 10.1193/1.1585793

16. LaFave, J. M., and Wight, J. K., "Reinforced Concrete Exterior Wide Beam-Column-Slab Connections Subjected to Lateral Earthquake Loading," *ACI Structural Journal*, V. 96, No. 4, July-Aug. 1999, pp. 577-585.

17. Quintero-Febres, C. G., and Wight, J. K., "Experimental Study of Reinforced Concrete Interior Wide Beam-Column Connections subjected to Lateral Loading," *ACI Structural Journal*, V. 98, No. 4, July-Aug. 2001, pp. 572-582.

18. NZS 3101:2006, "The Design of Concrete Structures," Standards New Zealand, Wellington, New Zealand, 2006.

19. EN 1998-1, "Eurocode 8: Design of Structures for Earthquake Resistance Part 1: General Rules, Seismic Actions and Rules for Buildings," European Committee for Standardization, Brussels, Belgium, 2004.

20. Committee for the Development of Seismic Codes, "Norma de Construccion Sismo rresistente (NCSE-02)," Spanish Ministry of Construction, Madrid, 2002.

21. Fadwa, I.; Ali, T. A.; Nazih, E.; and Mirzabagheri, S., "Reinforced Concrete Wide and Conventional Beam–Column Connections Subjected to Lateral Load," *Engineering Structures*, V. 76, 2014, pp. 34-48. doi: 10.1016/j.engstruct.2014.06.029

22. ACI Committee 374, "Acceptance Criteria for Moment Frames Based on Structural Testing and Commentary (ACI 374.1-05) (Reapproved 2019)," American Concrete Institute, Farmington Hills, MI, 2005, 9 pp.

23. Park, R., "Ductility Evaluation from Laboratory and Analytical Testing," *Proceedings of the 9th World Conference on Earthquake Engineering*, V. 8, 1988, pp. 605-616.

24. ASCE/SEI 41-17, "Seismic Evaluation and Retrofit of Existing Buildings," American Society of Civil Engineers, Reston, VA, 416 pp.

25. Joint ACI-ASCE Committee 352, "Recommendations for Design of Beam-Column Connections in Monolithic Reinforced Concrete Structures (ACI 352R-02)," American Concrete Institute, Farmington Hills, MI, ACI, 2002, 37 pp.

26. Eom, T. S.; Park, H. G.; Hwang, H. J.; and Kang, S. M., "Plastic Hinge Relocation Methods for Emulative PC Beam–Column Connections," *Journal of Structural Engineering*, ASCE, V. 142, No. 2, 2016, p. 04015111. doi: 10.1061/(ASCE)ST.1943-541X.0001378

27. Hwang, H. J.; Eom, T. S.; and Park, H. G., "Bond-Slip Relationship of Beam Flexural Bars in Interior Beam-Column Joints," *ACI Structural Journal*, V. 112, No. 6, Nov.-Dec. 2015, pp. 827-837.

28. Kim, J. H.; Choi, S. H.; Han, S. J.; Hwang, J. H.; Jeong, H.; and Kim, K. S., "Effect of Beam Elongation Phenomenon on Lateral Load Resistance of RC Frame," *Journal of Building Engineering*, V. 65, 2023, p. 105764. doi: 10.1016/j.jobe.2022.105764

29. Fan, J. J.; Wu, G.; Feng, D. C.; Zeng, Y. H.; and Lu, Y., "Seismic Performance of a Novel Self-Sustaining Beam-Column Connection for Precast Concrete Moment-Resisting Frames," *Engineering Structures*, V. 222, 2020, p. 111096. doi: 10.1016/j.engstruct.2020.111096

30. Kim, J. H.; Lee, D. H.; Choi, S. H.; Jeong, H.; and Kim, K. S., "Seismic Performance of Precast Multi-Span Frame System Integrated by Unbonded Tendons," *ACI Structural Journal*, V. 119, No. 5, Sept. 2022, pp. 193-206.

31. Lee, D. H.; Kang, T. H.-K.; Ju, H.; Moon, S. W.; and Yang, I. S., "Seismic Performance of RC Column-Foundation Connections with Combo-Type Mechanical Splices," *ACI Structural Journal*, V. 116, No. 5, Sept. 2019, pp. 173-186.

32. Zhang, W.; Lee, D. H.; Lee, W. J.; Kim, M. S.; and Park, J. Y., "Effect of Cast-In-Place Beams on Seismic Performance of Precast Shear Walls," *ACI Structural Journal*, V. 120, No. 1, Jan. 2023, pp. 89-102.

33. Feng, F.; Jiang, K.; Hwang, H. J.; and Yi, W. J., "Earthquake Response of Low-Rise RC Moment Frame Structures according to Energy Dissipation Ratio of Beam-Column Joints," *Journal of Structural Integrity and Maintenance*, V. 3, No. 1, 2018, pp. 33-43. doi: 10.1080/24705314.2018.1426171

34. Kim, S. H.; Cho, J.; Oh, H. K.; Choi, S. D.; Yeo, U. Y.; and Lee, D. H., "Seismic Performance Evaluation of Dry Precast Concrete Beam-Column Connections with Intermediate Moment Frame Details," *EESK Journal of Earthquake Engineering*, V. 27, No. 3, 2023, pp. 129-137. doi: 10.5000/EESK.2023.27.3.129

APPENDIX A—DETAILED PHOTOS OF CONNECTORS, COUPLERS AND SPLICES, AS WELL AS STRONG CONNECTION SYSTEM

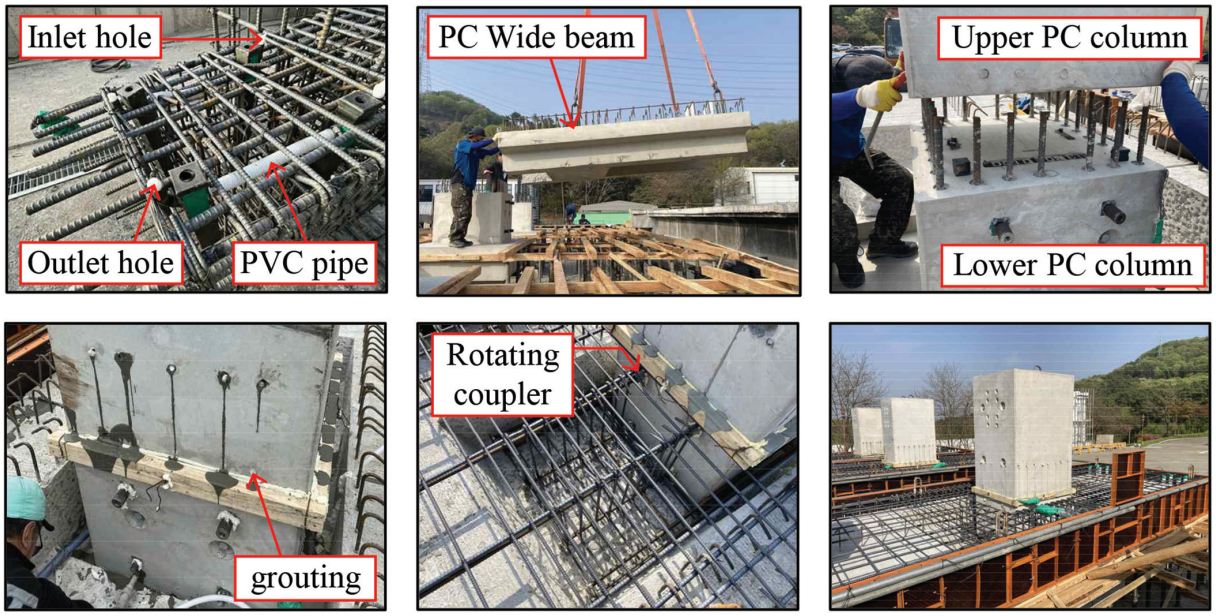

Fig. A1—Details of embedded grout-filled splice sleeve system.

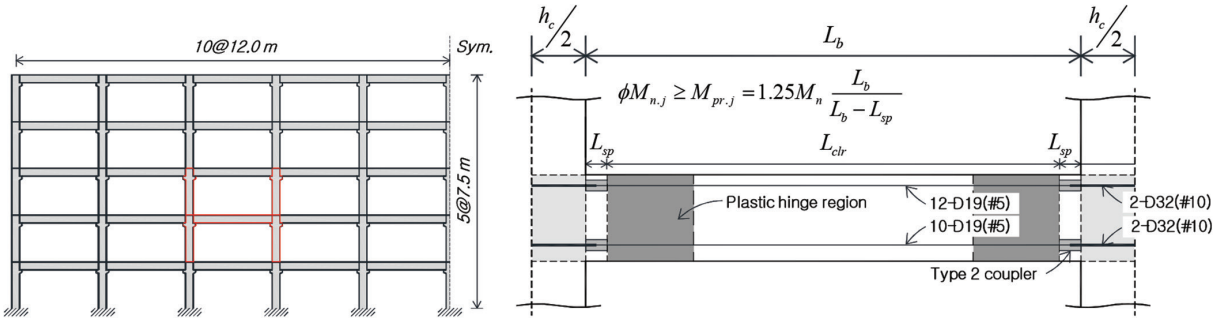

(a) Prototype structure

$H_c = 7.5\,\text{m}$

$h_c = 1.0\,\text{m}$

$L_b = 11.0\,\text{m}$

$L_{sp} = 100\,\text{mm}$

$L_{clr} = L_b - 2L_{sp} = 10.8\,\text{m}$

$f_c' = 45\,\text{MPa}$

1) Positive flexural moment of beam

$M_{n+} = 742.3\,\text{kN}\cdot\text{m} \quad \phi M_{n+.j} = 1{,}113.3\,\text{kN}\cdot\text{m}$

$$M_{pr+.j} = 1.25(742.3)\left(\frac{11.0}{10.8}\right) = 945.1\,\text{kN}\cdot\text{m}$$

2) Negative flexural moment of beam

$M_{n-} = 1{,}173.9\,\text{kN}\cdot\text{m} \quad \phi M_{n-.j} = 1{,}662.2\,\text{kN}\cdot\text{m}$

$$M_{pr+.j} = 1.25(1{,}173.9)\left(\frac{11.0}{10.8}\right) = 1{,}494.5\,\text{kN}\cdot\text{m}$$

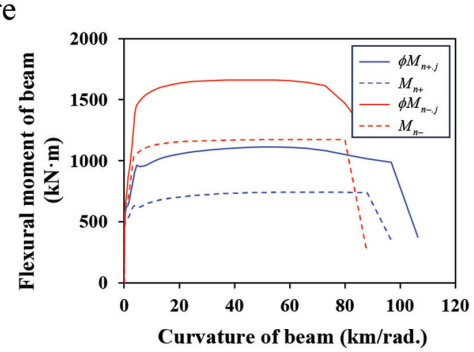

(b) Calculation of strong connection (Response 2000)

Fig. A2—Details of strong connection for PC specimen. (Note: 1 m = 3.28 ft; 1 mm = 0.039 in.; 1 MPa = 0.145 ksi; 1 kN = 0.225 kip; 1 kN·mm = 0.73756 kip·in.)

APPENDIX B—EVALUATION OF TEST RESULTS BASED ON ACI 374.1 ACCEPTANCE CRITERIA

Table B1—Evaluation of test specimens based on ACI 374.1 criteria

Specimen		PC-A	PC-N	RC-A
ACI 374.1 9.1.1 or ASCE/SEI 41	P_n, kN	854.2 (–854.2)	890.5 (–890.5)	610.1 (–610.1)
	Δ_v, %	0.98 (–1.01)	1.04 (–1.24)	0.95 (–0.97)
	Δ_{CP}*, %	4.0	4.0	4.0
	Acceptance criteria	Not passed	Not passed	Not passed
ACI 374.1 9.1.2	P_{max}, kN	1135.1 (–1018.9)	1012.5 (–1027.9)	781.7 (–677.0)
	λP_n, kN	1190.7 (–1190.7)	1196.4 (–1196.4)	1151.0 (–1151.0)
	Acceptance criteria	Passed	Passed	Passed
ACI 374.1 9.1.3(1)	$P_{3.5\%\ 3rd\ cycle}$, kN	913.2 (–872.4)	821.4 (–829.9)	643.8 (–550.7)
	$0.75P_{max}$, kN	851.3 (–764.1)	759.3 (–770.9)	586.2 (–507.7)
	Acceptance criteria	Passed	Passed	Passed
ACI 374.1 9.1.3(2)	$E_{i.3.5\%\ 3rd\ cycle}$†, kN·m	50.4	64.9	36.6
	$E_{t.\ 3.5\%\ 3rd\ cycle}$‡, kN·m	386.3	370.8	266.1
	Energy dissipation ratio β	0.134	0.175	0.137
	Acceptance criteria	Passed	Passed	Passed
ACI 374.1 9.1.3(3)	$K_{s.3.5\%\ 3rd\ cycle}$§, kN/mm	2.54 (2.83)	2.92 (3.24)	2.76 (2.34)
	$0.05K_I$‖, kN/mm	2.04 (2.43)	2.72 (1.71)	2.45 (1.71)
	Acceptance criteria	Passed	Passed	Passed

*Story drift ratio corresponding to CP performance level specified in ASCE/SEI 41.

†Energy dissipated during third cycle at 3.5% drift ratio.

‡Idealized energy, calculated as area of circumscribing parallelograms defined by initial stiffness and peak lateral resistances in positive and negative directions.

§Secant stiffness from a drift ratio of –0.35% to a drift ratio of 0.35%.

‖Initial stiffness of test specimens.

Note: 1 kN = 0.225 kip; 1 kN/mm = 5.7101 kip/in.; 1 kN·mm = 0.73756 kip·in.; numbers in parenthesis denote negative direction values.

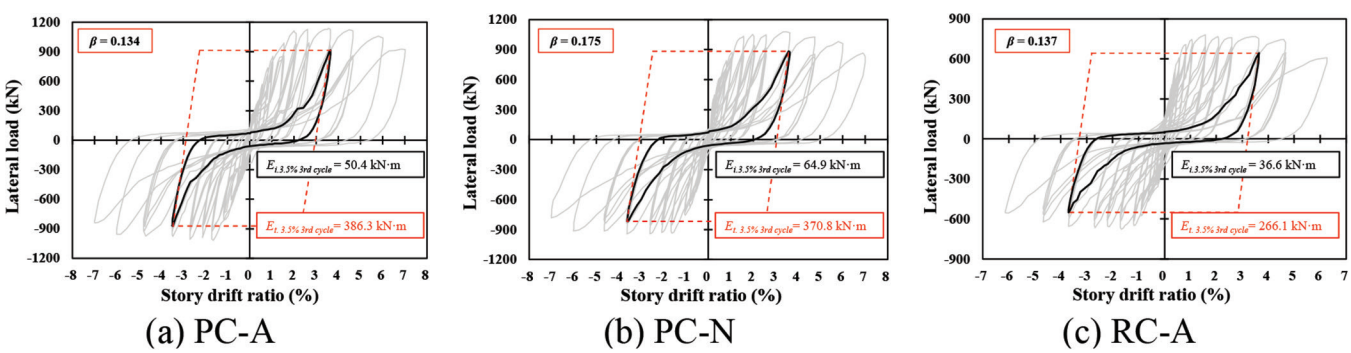

Fig. B1—Energy dissipation evaluation of test specimens based on ACI 374.1 criteria. (Note: 1 kN = 0.225 kip.)

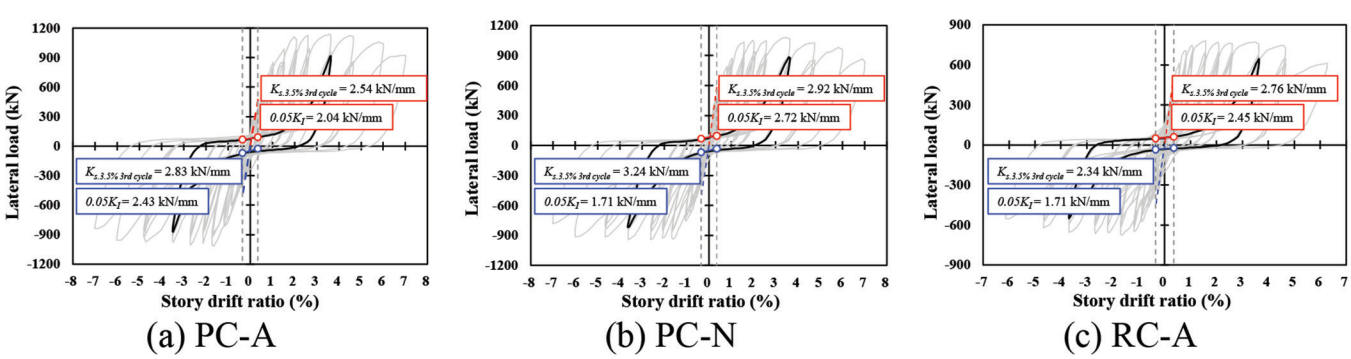

Fig. B2—Secant stiffness evaluation of test specimens based on ACI 374.1 criteria. (Note: 1 kN = 0.225 kip.)

ARE YOU A RESEARCHER?

SIGN UP FOR ORCID TODAY!

1. Register
2. Use your ORCID ID
3. Share

ORCID provides a digital identifier that distinguishes you from every other researcher and, through integration in key research workflows such as manuscript and grant submission, supports automated linkages between you and your professional activities, ensuring that your work is recognized.

ORCID services are FREE and it's as easy as **1-2-3**.

WWW.ORCID.ORG

ACI STRUCTURAL JOURNAL TECHNICAL PAPER

Title No. 123-S59

Component Model-Based Method for Damage Assessment of Reinforced Concrete Structures Subjected to Blast Loads

by Ren Jiang

Traditional analytical models have commonly been employed to assess the progressive collapse performance of building structures subjected to seismic loads. However, little research has addressed the effect of initial damage to adjacent components following the failure of a key component under explosion loads. In this paper, a damage assessment method for reinforced concrete (RC) structures was proposed based on a component analytical model, accounting for damage to adjacent members resulting from close-in explosive scenarios. The reliability of the proposed analytical model was validated through comparison with experimental results in the existing literature. Besides comparing the damage levels of a five-story RC frame with those predicted by the proposed component models, the proposed assessment method based on components for predicting the damage degree of RC frames was validated to be reliable under a close-in explosion. The results indicated that the proposed analytical model could offer the advantage of not requiring a complex modeling process or the consideration of safety concerns associated with field explosion testing by comparing to numerical models of equivalent accuracy and experimental results.

Keywords: analytical model; damage assessment; explosion load; progressive collapse; reinforced concrete (RC) structure.

INTRODUCTION

In recent years, disasters caused by accidental explosions and car bomb attacks have occurred, usually in daily life, resulting in a large number of property losses and casualties. The shock waves caused by the explosions have led to different levels of damage to building structures. Moreover, the damage to the local load-bearing members of the building structure caused by the explosion loads will further cause damage to the surrounding members, which caused the collapse of the building structures and aggravated the degree of the disaster. In building structures, reinforced concrete (RC) structures have better blast resistance performance compared to other buildings, which is widely favored by many scholars around the world. Therefore, RC structures have become the main research object in the field of blast resistance and progressive collapse of building structures.

To date, there have been extremely few test studies on the collapse resistance performance of RC structures under explosion loads. For example, when RC structures were attacked by explosion loads (Shi and Jiang 2024), the structural column has occurred serious damage, and adjacent joints and beams to the key columns accumulated different degrees of damage. Meanwhile, the test results showed that the structural column to the adjacent members can conduct the axial compression and tension forces (Shi et al. 2021). A typical 4 x 4 span RC frame (Sasani 2008; Sasani and Sagiroglu 2008, 2010; Sasani et al. 2011;) has suffered severe damage under blast loads, and the side deformation of the middle column caused different damage to adjacent members. As a result, the damage of the columns in RC structures caused by explosion loads can lead to the bearing capacity degradation and deformation of adjacent components, which can accumulate the damage of buildings in RC.

Once building structures have been subjected to explosion loads, the extent of damage should be confirmed as soon as possible. Extensive scholars have researched the dynamic behaviors of RC structures, including test study (Lu et al. 2017; Ren et al. 2016; Gao et al. 2013; Yi et al. 2007, 2008; Jiang et al. 2025a,b), numerical analysis (Qian et al. 2015; Jiang et al. 2025c,d), and theoretical analysis (Jian and Zheng 2014; Lu et al. 2018; Xu and Wang 2021; Izzuddin et al. 2008; Zhu et al. 2020; Yu and Tan 2014). For most of the experimental cases, Gao et al. (2013) analyzed the damage behaviors of the three-story RC frames under the field-explosion loads. Crawford et al. (2012) investigated the damage modes on the four-story RC frame under explosion loads. Additionally, some scholars (Yi et al. 2007, 2008) conducted experiments on the collapse performance of RC buildings subjected to explosion loads. However, the limited data in the aforementioned experiment were not enough to support the need for assessing the degree of damage to building structures.

Considering the field explosion tests security and few experimental data, numerical simulation methods have been used to study the collapse resistance behaviors of RC structures. Izzuddin et al. (2008) presented a method for evaluating damage to buildings under removal-column scenarios. Vlassis et al. (2008) put forward a method for the removal of the bottom column in buildings. Pham et al. (2015) presented an effective analysis approach for the dynamic behavior of RC frames, which was validated through a series of tests. Shi et al. (2010) presented an initial velocity analysis method for simulating the initial damage to buildings subjected to explosion loads. Li and Hao (2013) proposed a static condensation method that can be used to simulate the dynamic behaviors of building structures. Shi et al. (2022b) presented an assessment method for the degree of damage of the RC frame using concrete substructures, and the accuracy of the presented method was verified under explosion scenarios. Although the previous investigation results can assess the levels of damage for the RC structures under explosion scenarios, considering the complex modeling establishment

ACI Structural Journal, V. 123, No. 3, May 2026.
MS No. S-2025-105.R3, doi: 10.14359/51749496, received October 8, 2025, and reviewed under Institute publication policies. Copyright © 2026, American Concrete Institute. All rights reserved, including the making of copies unless permission is obtained from the copyright proprietors. Pertinent discussion including author's closure, if any, will be published ten months from this journal's date if the discussion is received within four months of the paper's print publication.

and loading process of the numerical model, these numerical models have lower computational efficiency in the analysis against the collapse of buildings in RC.

Simplified analytical models were recognized as an effective method for investigating the collapse mechanism of building structures. Existing research (Shi et al. 2022b and Jiang et al. 2025) illustrated that the force-versus-displacement curves derived from pushdown static loading have usually been used to represent the against collapse process of RC structures, including the axial resistance (AR) mechanism of the structural column, the compressive arch action (CAA) and tensile catenary action (TCA) mechanism of the beam. For example, the research on the analytical model for calculating the CAA load-bearing capacity of RC structures was presented by Park (1965), which has been validated to predict the against collapse capacity of RC structures (Su et al. 2009). Lu et al. (2018) presented a CAA simplified model for beam-slab substructure, which can accurately estimate the CAA resistance and corresponding deformation in the against collapse analysis of buildings in RC. Xu and Wang (2021) presented a simplified model for calculating the reverse arch mechanism and CAA mechanism of RC substructures, which is beneficial to analyze the against collapse capacity of buildings in RC. Zhu et al. (2020) presented a simplified model to estimate the CAA resistance of slabs based on a three-hinged arch mechanism. Yu and Tan (2014) proposed a simplified theoretical model to calculate the resistance deformation relationship of the double-span beam substructures. Jian and Zheng (2014) presented a theoretical model for the collapse performance of substructures under static pushdown loading, and the simplified model was validated by test results. Kang et al. (2020) presented a calculation model for predicting the resistance and deflection of a beam-slab substructure. Wang and Kang (2019) presented a theoretical model for predicting the resistance of RC beams before and after longitudinal reinforcement fracture scenarios. Zhang et al. (2020) presented calculation formulas for the resistance and corresponding deflection of buildings in RC. More importantly, Campione (2021) presented a theoretical model for calculating the anti-collapse capacity of RC substructures under static pushdown loading, including the resistance of columns and beams in the CAA and TCA stages. Even though the aforementioned simplified models can properly calculate the against collapse mechanism of RC structures in the field of seismic, these cannot properly consider the initial damage to buildings in RC under explosion loads. Therefore, it is necessary to further perfect knowledge of the collapse resistance performance of RC structures by considering the blast damage to adjacent components.

RESEARCH SIGNIFICANCE

Traditional analytical models have commonly been employed to assess the progressive collapse resistance of building structures subjected to seismic loads. However, there is a scarcity of research addressing the effect of initial damage to adjacent structural members following the failure of a key structural component under blast loads. Meanwhile, considering the field explosion tests, security, and a few experimental data, there is a lack of a simplified analytical model for analyzing the collapse resistance performance of RC structures under blast loads. To resolve these issues, a component-based analytical model for assessing the degree of damage in RC buildings under explosion loads, grounded in the principle of energy conservation, is proposed. The analytical models are expressed in terms of forces and displacements, derived from calculation formulas corresponding to different stages of collapse resistance. The accuracy of the simplified analytical model for calculating the collapse resistance capacity of RC columns and beams was validated as follows. Besides, the reliability of the proposed component-based analytical model was confirmed by comparing its results with the damage assessment of a five-story RC frame subjected to explosive loads.

PROPOSED DAMAGE ASSESSMENT METHOD

According to the work of Shi et al. (2022b), the collapse resistance mechanisms of RC frame can be classified into three categories, as exhibited in Fig. 1. The first phase was the AR mechanism, which ends when the RC column in the building failed; the second phase was the CAA mechanism, which ends when the plastic hinge was observed at beam ends; the third phase was the TCA mechanism, which ends when building structures lost their collapse resistance capacity.

According to the existing literature (Shi et al. 2022b), there is no consideration of the RC slabs in building structures, and the RC frame can be divided into many beam-column substructures, and then the substructure model can be further divided into one column and double-span beam substructure without column, as exhibited in Fig. 2. Notably, the double-span beam substructure without column is symmetric about the joint; thus, the resistance of the double-span beam substructure is twice that of a single beam under the same joint displacement scenarios. In this section, the simplified component analytical models for the column and double-span beam substructures, without a column, under pushdown static loading are as follows.

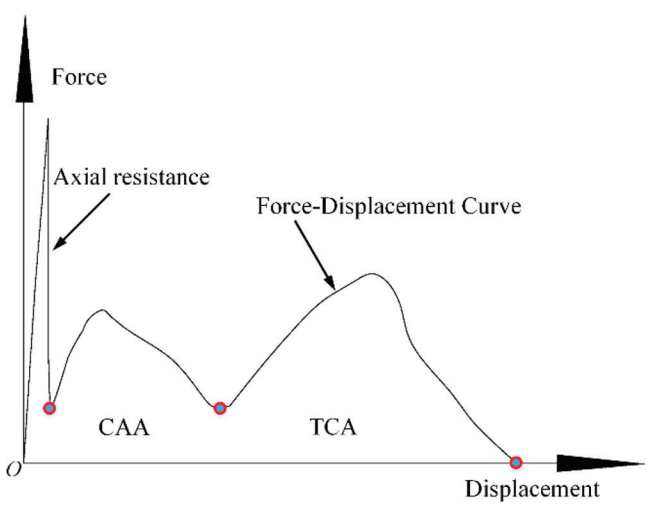

Fig. 1—Force-displacement curve of RC structure.

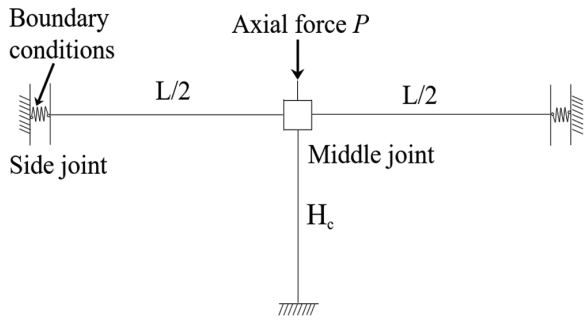

Fig. 2—Substructure simplified model.

Analytical model of RC column

Analytical model of undamaged RC column—The analytical formulas for the resistance and corresponding deflection of RC column proposed by Campione (2021) are exhibited as follows.

1. The resistance in the elastic stage can be decided by Eq. (1)

$$p_{c1} = \left[(B-\delta)^2 \cdot E_c + \frac{A_f}{n} \cdot E_f\right] \cdot \varepsilon \qquad 0 \le \varepsilon \le \varepsilon_y \quad (1)$$

where $n = 15$, which can be decided in ACI 318 (2019).

2. The resistance in the plastic stage can be decided by Eq. (2)

$$p_{c2} = (B-\delta)^2 \cdot f_c + A_f \cdot f_y \qquad \varepsilon_{co} \le \varepsilon \le \varepsilon_{cc} \quad (2)$$

with $\varepsilon_{co} = 0.002$, and $\varepsilon_{cc} = 0.0035$.

3. The column resistance in the residual strength can be calculated by Eq. (3)

$$p_{c3} = \beta \cdot A_f \cdot f_y \qquad \varepsilon \ge \varepsilon_c \quad (3)$$

where concrete strength is f_c; concrete elastic modulus is E_c; strength of the reinforcing bar is f_y; area of reinforcing bar is A_f; the width of the column section is B; ε_c is the failure strain of concrete; and β is the reduction factor of steel bars.

Analytical model of RC column after explosion

In practical engineering, once explosion loads are applied to an RC column, the stiffness and deflection of the RC column can deteriorate. A damaged analytical model for calculating the resistance degradation and corresponding deflection of an RC column is proposed. The main procedures are listed as follows.

1. According to the given parameters of the RC column, the overpressure (P) and impulse (I) curves presented by Shi et al. (2008) can calculate the critical equivalent damage degree (that is, γ) of each column in building structures, when the degree of damage values of the column are respectively 0.2, 0.5, and 0.8. The P and I calculation formulas of RC column under explosion loads can be decided by Eq. (4) to (6), respectively.

$$\begin{cases} P_0(0.2)=1000\left[\begin{array}{l} 0.007\exp\left(\frac{\rho_s}{0.01}\right)+0.069\left(\frac{\rho}{0.01}\right) \\ +0.034\exp\left(\frac{f_c'}{30}\right)-0.835\ln\left(\frac{H}{4.0}\right)+\left(\frac{h_c}{0.6}\right)^{1.804} \\ +0.067\ln\left(\frac{B}{0.6}\right)-0.168 \end{array}\right] \\ I_0(0.2)=1000\left[\begin{array}{l} 0.053\exp\left(\frac{\rho_s}{0.01}\right)+0.107\left(\frac{\rho}{0.01}\right) \\ +0.021\exp\left(\frac{f_c'}{30}\right)+\left(\frac{H}{4.0}\right)^{-0.207} \\ +1.203\exp\left(\frac{h_c}{0.6}\right)-0.943\ln\left(\frac{B}{0.6}\right)-2.686 \end{array}\right] \end{cases} \quad (4)$$

$$\begin{cases} P_0(0.5)=1000\left[\begin{array}{l} 0.143\ln\left(\frac{\rho_s}{0.01}\right)+0.320\left(\frac{\rho}{0.01}\right) \\ +0.063\exp\left(\frac{f_c'}{30}\right)+\left(\frac{H}{4.0}\right)^{-1.390} \\ +2.639\left(\frac{h_c}{0.6}\right)+0.318\ln\left(\frac{B}{0.6}\right)-2.271 \end{array}\right] \\ I_0(0.5)=1000\left[\begin{array}{l} 0.837\left(\frac{\rho_s}{0.01}\right)+0.036\left(\frac{\rho}{0.01}\right) \\ +0.235\exp\left(\frac{f_c'}{30}\right)+\left(\frac{H}{4.0}\right)^{-0.274} \\ +2.271\exp\left(\frac{h_c}{0.6}\right)-0.998\ln\left(\frac{B}{0.6}\right)-5.286 \end{array}\right] \end{cases} \quad (5)$$

$$\begin{cases} P_0(0.8)=1000\left[\begin{array}{l} 0.062\ln\left(\frac{\rho_s}{0.01}\right)+0.238\left(\frac{\rho}{0.01}\right)+0.291\ln\left(\frac{f_c'}{30}\right) \\ -1.676\ln\left(\frac{H}{4.0}\right)+2.439\ln\left(\frac{h_c}{0.6}\right)+0.210\ln\left(\frac{B}{0.6}\right)+1.563 \end{array}\right] \\ I_0(0.8)=1000\left[\begin{array}{l} 3.448\left(\frac{\rho_s}{0.01}\right)-0.254\left(\frac{\rho}{0.01}\right)+1.200\left(\frac{f_c'}{30}\right) \\ -0.521\left(\frac{H}{4.0}\right)+6.993\left(\frac{h_c}{0.6}\right)-2.759\left(\frac{B}{0.6}\right)-2.035 \end{array}\right] \end{cases} \quad (6)$$

In the aforementioned formulas, $P_0(\gamma)$ is the asymptote of pressure, expressed in kPa; $I_0(\gamma)$ is the impulse asymptote, expressed in kPa·ms; f_c' is concrete compression strength, measured in MPa; ρ_s is the ratio of stirrup to longitudinal reinforcement ratio; ρ is the reinforcement ratio of longitudinal bars; H is the height of column, B is the width of column, and h_c is the column depth. The units of H, B, and h_c are all meters.

2. The P-I diagram of a column in RC frame corresponding to the degree of damage 0.2, 0.5, and 0.8 could be calculated as

$$(P-P_0)(I-I_0) = 12(P_0/2 + I_0/2)^{1.5} \quad (7)$$

where I and P are, respectively, the impulsive and reflected overpressure of explosion loads; and I_0 and P_0 are the impulse asymptote and overpressure asymptote, respectively.

3. According to the TM-1500 (1990) and UFC 4-340-02 (2008) manual, the maximum P and I applied on column in RC frame can be calculated under a given explosion scenario.

4. The damage index (γ_i) of an RC column can be determined using linear interpolation methods. According to Shi et al. (2010), the degree of damage to an RC column after the explosion mainly manifests as the degradation of the strength and stiffness of the longitudinal bars and concrete materials. The stiffness and strength calculation formulas of an RC column subjected to explosion loads are as follows

$$f_c' = K_Y \cdot f_c\,(1 - \gamma) \tag{8}$$

$$E_c' = K_E \cdot E \cdot (1 - \gamma) \tag{9}$$

$$\varepsilon_{sp}' = \varepsilon_{sp} \cdot (1 - \gamma) \tag{10}$$

$$f_y' = f_y \cdot (1 - \gamma) \tag{11}$$

where f_c' and E' represent the axial compression strength and elastic modulus of the RC column after the explosion, respectively; K_E and K_Y are correction coefficients; and f_y' and ε_y' represent the yield strength and strain of the steels after the explosion.

4. According to the parameters of the post-blast column (Eq. (8) to (11)), the resistance and corresponding deflection of the post-blast column can be calculated by that of the calculation formulas (Eq. (1) to (3)). Meanwhile, the solution procedures for the column analytical model is expressed in Fig. 3.

It should be noted that if γ_i is less than 0.2, the force and deformation degradation of the column is not considered, and it is assumed to be elastic. If γ_i of the column is greater than 0.8 the RC column is assumed to lose the collapse resistance capacity. Also, the collapse analysis of the substructure is controlled by the deflection to the middle joint (that is, δ) in the AR stage, which is the axial deformation of a RC column. Therefore, the failure strain of a column is $\varepsilon = \delta/H$, where H is the height of the column. The initial AR applied to the column cannot be considered in the calculation formula as follows. More detailed information can be found in Campione (2021).

ANALYTICAL MODEL OF DOUBLE-SPAN BEAM SUBSTRUCTURE

Analytical model of undamaged double-span beam substructure

The simplified formulas for the resistance and corresponding deflection of an undamaged double-span beam substructure without a column proposed by Campione (2021) are as follows. For the cross section of a beam with height h and width b, the inertia moment of a beam is I ($I = bh^3/12$). The yield flexural moment of the rectangular beam is $M_P = 0.9 \cdot d \cdot A_s \cdot f_y$, where d is the effective section height of the beam.

1. The resistance and corresponding deformation of the beam at first crack appearance can be listed as follows

$$P_{ct} = (4 \cdot M_{ct})/L \tag{12}$$

$$w_{ct} = (P_{ct} \cdot L^3)/(192 \cdot E \cdot I) \tag{13}$$

where M_{ct} represents the moment when cracks appear; and I represents the effective inertia moment of the beam section. M_{ct} can be decided by the following formula

$$M_{ct} = ((b \cdot h^2)/6) \cdot f_{ct} \tag{14}$$

where f_{ct} is the concrete strength corresponding to the first cracking of the beam.

2. The resistance and corresponding deformation formulas of the beam in the elastic-plastic stage can be calculated as follows

$$P_u = (8 \cdot M_p)/L \tag{15}$$

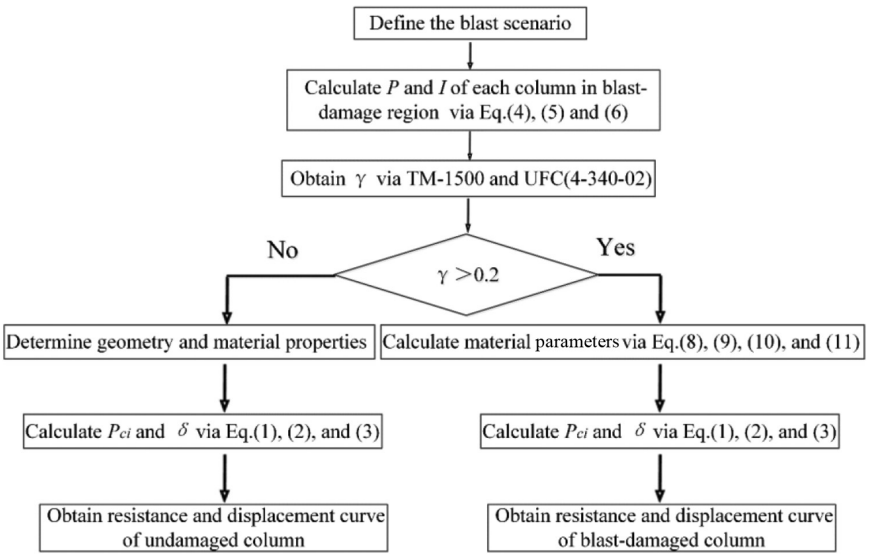

Fig. 3—Procedure for column analytical model.

$$w_u = (P_u \cdot L^3)/(192 \cdot E \cdot 0.3I) \quad (16)$$

3. The resistance and corresponding deformation formulas of the beam can be calculated as follows

$$w_{uc} = w_u + (\theta_u - \theta_y) \cdot l_p \cdot L/2 \quad (17)$$

where l_p is the plastic hinge length, which can be calculated as follows

$$l_p = 0.5 \cdot d_0 + 0.2\sqrt{d_0} \cdot (L/(4 \cdot d_0)) \quad (18)$$

where d_0 denotes the diameter of the reinforcing bar.

According to Jian and Zheng (2014), the reinforcing bar strain is $10\varepsilon_y$, and the corresponding curvature of the bar is yield θ_y and ultimate θ_u. The calculation formulas can be calculated as follows

$$\theta_y = \varepsilon_y/(d_0 - 0.33 \cdot x_{cy}) \quad (19)$$

$$\theta_u = 10 \cdot \varepsilon_y/(d_0 - 0.4 \cdot x_{cu}) \quad (20)$$

where ε_y denotes the corresponding yield strain of the longitudinal bars.

4. The resistance and deformation of beam in the CAA stage ending could be expressed as follows

$$P_{cc} = 2 \cdot \xi \cdot f_c \cdot x_{cu} \cdot \sin(\arctan(2L/d_0)) \quad (21)$$

The softening coefficient (ξ) can be expressed as follows

$$\xi = 1/(1 + 0.66 \cdot (2 \cdot d_0/L)) \quad (22)$$

$$x_{xu} = (A_s \cdot f_y)/(0.8 \cdot 0.85 \cdot b \cdot f_c) \quad (23)$$

The deflection of the beam can be decided by the following formula

$$w_{ucc} = w_{uc} + \varepsilon_{cu}\sqrt{d_0^2 + \left(\frac{L}{2}\right)^2} \cdot \sin\left(\arctan\frac{2 \cdot L}{d_0}\right) \quad (24)$$

where ε_{cu} is the strain of concrete. More details can be found in Campione (2021).

5. The peak resistance and corresponding deformation of beam at the TCA stage can be calculated as follows

$$P_{ucatenary} = A_s \cdot f_y \cdot \sin(\arccos(1 - (2 \cdot u)/L)) \quad (25)$$

$$w_{ucantanary} = w_{cc} + \sqrt{w_{uc}^2 + u \cdot L - u^2} - w_{uc} \quad (26)$$

The calculation formula for the horizontal deflection of the beam (u) caused by TCA effect is as follows

$$u = \varepsilon_{uy} \cdot (L/2) \quad (27)$$

where the corresponding ultimate strain (ε_{uy}) in the TCA stage represents the failure of the longitudinal bars.

Analytical model of double-span beam substructure after explosion

Once explosion loads acting on RC structures, the column of structure induced by blast loads can generate the axial tensile force on adjacent components (Shi and Jiang 2024), further causing the stiffness and deflection degradation of beams in building structures. In this paper, the initial damage of beams can be presented by the joint deformation (δ) after explosion—that is, the axial deformation of the column to the adjacent joint. The initial damage index λ of the beam (Cui et al. 2015) is decided as the ratio of the column axial deformation and the half of the beam height as follows

$$\lambda = \frac{\delta}{h/2} \quad (28)$$

where δ represents the maximum deflection of the column; and h represents the height of the beam section.

The initial damage to the beam after the explosion mainly manifests as the degradation of the stiffness and strength of the longitudinal bars and concrete materials (Shi et al. 2008). The strength and stiffness calculation formulas for the concrete and longitudinal bars of the post-blast beam are obtained as follows

$$f_b' = K_Y \cdot f_c(1 - \lambda) \quad (29)$$

$$E_b' = K_E \cdot E \cdot (1 - \lambda) \quad (30)$$

$$\varepsilon_y' = \varepsilon_y \cdot (1 - \lambda) \quad (31)$$

$$\varepsilon_{uy}' = \varepsilon_{uy} \cdot (1 - \lambda) \quad (32)$$

$$f_{by}' = f_y \cdot (1 - \lambda) \quad (33)$$

where f_b' and E_b' represent the against compressive strength and concrete modulus of the damaged beam after explosion, respectively; and f_{by}', ε_y', and ε_{uy}' represent the yield strength, yield strain, and maximum strain of the bars in beam after explosion, respectively.

According to the parameters of the post-blast beam (Eq. (29) to (33)), the resistance and corresponding deflection of the post-blast beam can be defined by the calculation formulas (Eq. (12) to (27)). Notably, considering the symmetry of the double-span beam substructure, the resistance of the single beam is half that of the double-span beam substructure under the same joint deformation. Meanwhile, the solution procedures of the beam analytical model is expressed in Fig. 4.

PROPOSED ASSESSMENT METHOD FOR DAMAGE DEGREE OF RC STRUCTURE

According to the energy conservation, the resistance versus displacement diagrams derived from the aforementioned analytical model can be transferred to the equivalent pseudo-static curves. The failure displacement and corresponding equivalent resistance of the beam and column in pseudo-static curves can be obtained (Shi et al. 2022a). In

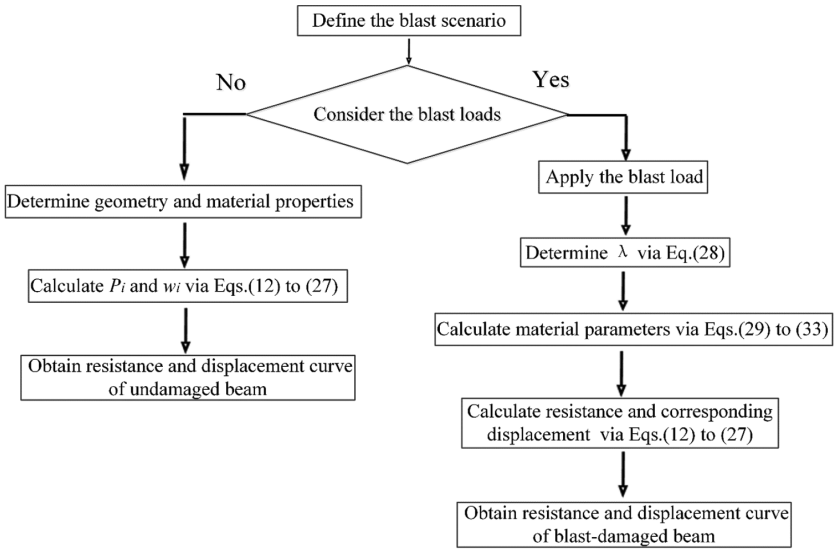

Fig. 4—Procedure for beam analytical model.

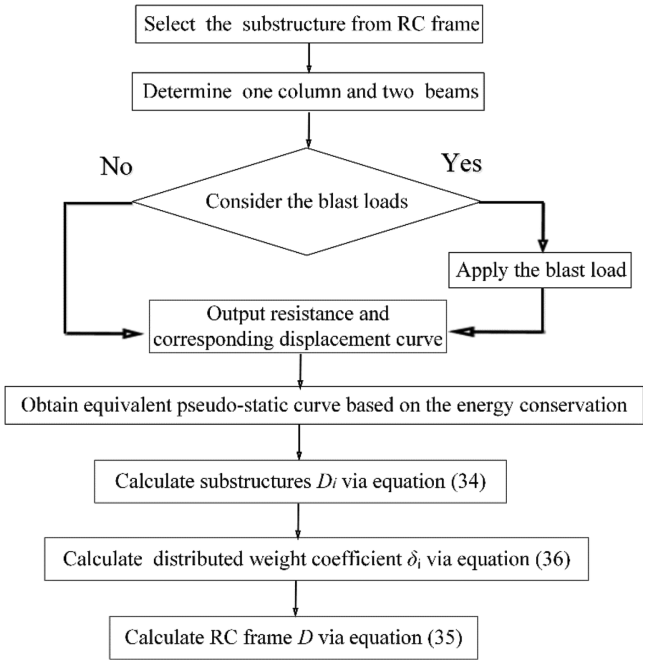

Fig. 5—Assessment degree of damage flowchart of RC frame.

the paper, the damage index D_i of each substructure in the frame structure (refer to Fig. 2) is determined by calculating the equivalent resistance and corresponding displacement of both the column and beam in pseudo-static curves as follows

$$D_i = 1 - \frac{F_{cr} \times S_{cr} + F_{br} \times S_{br}}{F_{cu} \times S_{cu} + F_{bu} \times S_{bu}} \tag{34}$$

where F_{cr} and F_{br} represent the equivalent residual resistance of a column and beam after the explosion, respectively; S_{cr} and S_{br} represent the equivalent residual displacement of a column and beam after the explosion, respectively. Meanwhile, F_{cu} and F_{bu} represent the equivalent ultimate resistance of the undamaged column and beam, respectively; and S_{cu} and S_{bu} represent the equivalent ultimate displacement of the undamaged column and beam, respectively.

The D value of a frame structure is calculated by Eq. (35), and the weight coefficient for each substructure can be decided by Eq. (36). Notably, the assessment of the degree of damage procedures flowchart of the frame in RC is expressed in Fig. 5

$$D = \delta_1 \times D_1 + \delta_2 \times D_2 + \cdots\cdots + \delta_i \times D_i + \cdots\cdots + \delta_n \times D_n \tag{35}$$

where δ_i represents the coefficient of each substructure as follows

$$\delta_i = \frac{\Delta Q_i}{\sum_1^n \Delta Q_i} \tag{36}$$

$$\Delta Q_i = \left(F_{cu,i} \times S_{cu,i} - F_{cr,i} \times S_{cr,i}\right) + \left(F_{bu,i} \times S_{bu,i} - F_{br,i} \times S_{br,i}\right) \tag{37}$$

where $\delta_1 + \delta_2 + \cdots + \delta_i \cdots + \delta_n = 1$; and n indicates the amount of substructures. It should be noted that ΔQ_i represents the difference in energy absorbed by each substructure before and after the explosion. Afterwards, the residual deformation (that is, $S_{cr,i}$ and $S_{br,i}$) of the explosion-damaged column and beam and ultimate deformation (that is, $S_{cu,i}$ and $S_{bu,i}$) of the undamaged column and beam can be obtained from the force versus displacement diagrams, respectively. The equivalent ultimate resistance (that is, $F_{cu,i}$ and $F_{bu,i}$) of the undamaged column and beam and the equivalent residual resistance (that is, $F_{cr,i}$ and $F_{br,i}$) of the damaged column and beam can be used, which are obtained from the force displacement diagrams, respectively.

COMPARISON AND VERIFICATION OF PROPOSED ANALYTICAL MODEL

To verify the accuracy of the aforementioned component analytical models, the resistance and corresponding deformation for the RC substructure based on the proposed component analytical model will be contrasted with test results. In this section, the pushdown static analysis needs to be conducted for both the undamaged RC column and

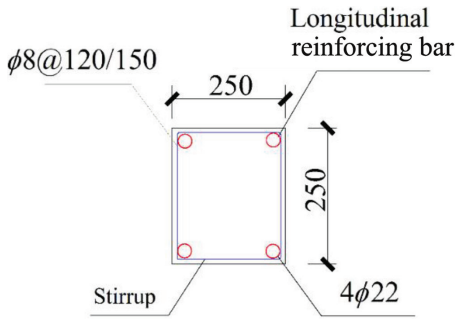

Fig. 6—Cross section of test RC column.

double-span beam substructure and the damaged RC column and two-span beam substructure induced by the explosion.

Collapse analysis of analytical model of RC beam

Description of RC column—The authors (Shi et al. 2022b) carried out seven RC columns to investigate the performance of degradation for the bearing capacity of a RC column under explosion scenarios. In the section, the test case of both Z3A2 and Z3A4 are used to confirm the proposed analytical model. The geometric dimensions and material parameters of the studied RC column can be found in the literature (Shi et al. 2022b), as exhibited in Fig. 6. The explosive (that is, 21 kg TNT) is a height of 1.5 m far away from the ground, and the distance from the explosive to the tested column is 1.5 m. Because the equivalent TNT explosive acting on the front surface of the tested column was not uniformly distributed, thus the surface of the tested column is separated into five equal regions (Shi et al. 2008). Afterward, the average explosion loads acting on the column surface (that is, pressure and impulse) are calculated by the scale distance ($Z = R/M^{1/3}$). More details can be found in Shi et al. (2022b).

Validation of column analytical model

According to the proposed analytical model, the average reflected overpressure (16.974 MPa) and impulse (1017.346 kPa·ms) on the studied column are recorded in the equivalent P versus I curves when the degree of damage of a RC column equaled 0.2, 0.5, and 0.8. Therefore, the degree of damage to the studied column is determined to be 0.52.

Figure 7 exhibits the resistance and corresponding deformation curves of the studied column under blast loads. The figure illustrates that the force versus displacement curves between the proposed analytical model and the experimental results exhibited a similar same. More carefully, the experimental results of the studied column are slightly greater than those of the proposed model. This is because the proposed analytical model neglects the strain rate effects of materials. Besides, the peak value of the Z3A2 is smaller than that of the Z3A4. The main reason is that the axial precompression force acting on the Z3A4 column is slighter than that of the Z3A2 column, causing the concrete element of the Z3A4 entering a plastic stress state earlier. Besides, the residual resistance of the tested column is significantly greater than that of the analytical model. This illustration is that, once the concrete element of the tested column has been deleted,

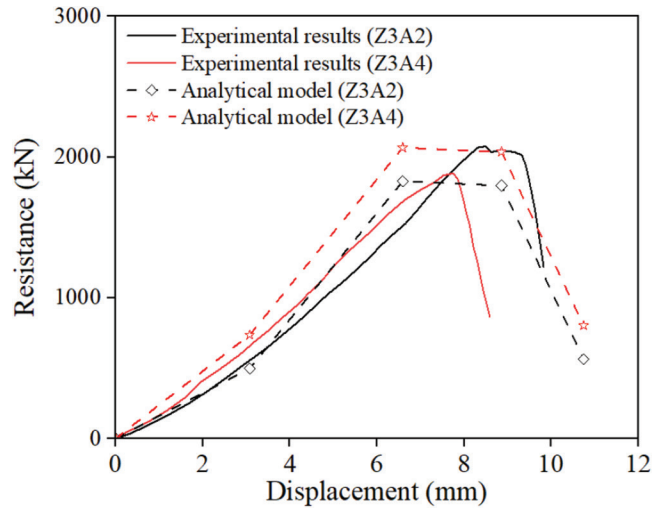

Fig. 7—Force-displacement curves of blast-damage column.

the residual resistance and deformation of the reinforced bars in the column are not further recorded in the experiment loading. The aforementioned result illustrates that the proposed analytical models might properly predict the collapse performance of the RC column.

Collapse analysis of analytical model of RC beam

Description of double-span beam substructure—The reliability for the proposed analytical model of RC column is demonstrated by analyzing the against collapse capacity of the RC column under explosion loads. Meanwhile, to further investigate the accuracy for the proposed analytical model of beam in RC, the collapse resistance performance of the analytical model is confirmed by extracting the test results (Shi and Jiang 2024).

The authors carried out six RC substructures with column (that is, named RCS) and a double-span beam substructure without column experiments to investigate the explosion loads on the against collapse performance effects of buildings in RC. The analysis process of the studied substructure consists of the blast dynamic test and pushdown static test. For the blast dynamic case, the initial axial force (341.2 kN) was first acting on the RC column, and then explosion loads were added to the middle column of substructure. After that, the explosion-damaged column was removed from the damaged substructure. For the pushdown static case, the damaged double-span beam substructures and undamaged double-span beam substructure were conducted under the joint displacement-control. More details on the geometric dimensions and material parameters of the studied RC substructure can be found in Shi and Jiang (2024).

Validation of beam analytical model

Regarding the undamaged double-span beam substructure (that is, the RC substructure without column) as an example, the reliability of the analytical model of the beam was investigated by comparing with experimental results.

Figure 8 shows the force-versus-displacement curves derived from test results and analytical models. As can be observed, the analytical model for the undamaged substructure agrees with the experimental results. However, the

resistance at the CAA stage ending obtained from the analytical model is 11.8% smaller than the experimental results. Once the concrete cracks appeared, the concrete elements in the analytical model were deleted in the CAA softening stage. Furthermore, the peak resistance at the TCA stage ending obtained from the model is 5.8% more than the test results. This is because the tensile stress in beams is transmitted to the steel reinforcement through the bonding stress in the TCA stage, causing a significant increase in the stress of the longitudinal bar at the cracking interface. Besides, the displacement of the analytical model has some slight differences. This is because the resistance deflection curves of the substructure are not only determined by the reinforcements and concrete materials properties, but also the arrangement of the reinforcing bar and the sizes of the specimen.

The authors (Shi and Jiang 2024) have investigated the collapse resistance performance of RC substructure with columns under explosion scenarios. The test results of the substructures studied (including RCS 1, RCS 2, RCS 3, and RCS 6) are selected for comparison with the proposed analytical model. The damage index of the experimental substructure is exhibited in Table 1.

Figure 9 shows the comparisons between the proposed analytical models and test results. In these cases, the resistance versus deformation curves trend of the double-span beam substructure obtained by the simplified analytical model agrees with that of the experimental results. However, it is easy to find that the resistance in the CAA and TCA stage ending are a slight difference between the proposed models and test results. This is because the simplified theoretical formulas in the CAA softening stage neglect the strain rate effects of materials. Also, the strain hardening of the tension steels in the TCA stage is not considered in the simplified models; thus, the stress value of longitudinal bars at cracking is higher than that of longitudinal bars between cracks.

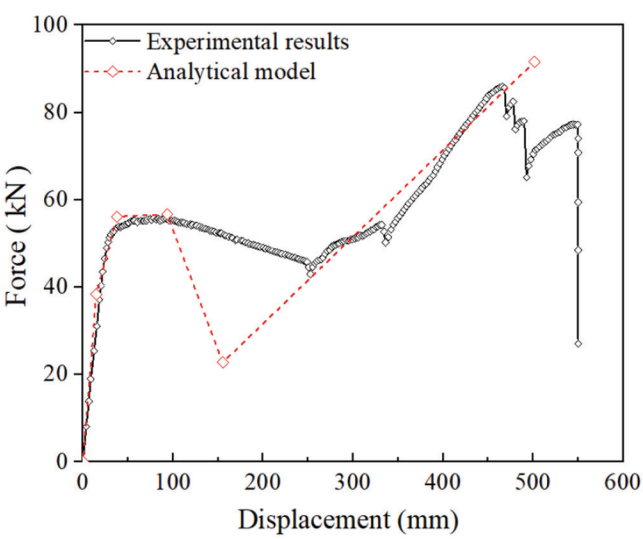

Fig. 8—Force-displacement diagrams of undamaged substructure.

Table 1—Damage index of tested substructures

Test specimen	RCS 1	RCS 2	RCS 3	RCS 6
Displacement, mm	10.2	33.9	29.4	4.6
λ_i	0.08	0.27	0.24	0.04

VERIFICATION OF DAMAGE DEGREE OF RC FRAME

To prove the method based on components for assessing the degree of damage of RC frame, the collapse resistance analysis needs to be conducted on both undamaged RC column and beam and explosion-damaged RC column and beam, and the damage degree for the components in the blast-damaged region will be compared with that of the studied frame.

Description of studied frame

The aforementioned research has verified the collapse capacity of the column and beam under explosion loads using the proposed analytical model, but there was a lack of test investigation on the collapse resistance of RC frame. Therefore, the studied RC frame in the literature (Shi et al. 2022a) is selected for verification and comparison. The physical dimension of studied RC frame is exhibited in Fig. 10. More details on concrete and reinforcing bar materials are exhibited in Tables 2 and 3, respectively. The distance between the explosive (200 kg) and the front surface of the column and the height away from the ground are 3 m and 1 m, respectively. More information on the studied RC frame is found in Shi et al. (2022a).

Assessment of damage degree of RC frame

According to the literature (Shi et al. 2022a), other columns of the RC frame (that is, the damage index of column is lower than 0.2) need to be considered the initial damage except for the bottom-story and second-story middle column. Afterward, the maximum P and I of the column is recorded in the critical curves, as exhibited in Fig. 11. The γ value of the bottom-floor and second-floor middle column are respectively decided as 0.73 and 0.39 based on the theoretical formulas of RC column in the aforementioned.

Figure 12 shows the resistance displacement curves of the bottom column and beam in the RC frame derived from the simplified analytical model. It is worth mentioning that the initial axial force (that is, the four-story adjacent components weight located on the upper of the column) of the structural column was added. According to energy conservation, the pseudo-static diagrams (that is, the red dotted line) of the column can be gained from resistance versus displacement diagrams. (Note: Full-color PDF can be accessed at www.concrete.org.) The failure displacement and axial bearing capacity of the analytical model derived from the intact column in the pseudo-static diagram are 21.1 mm and 5450.3 kN, respectively, as exhibited in Fig. 12(a). The residual resistance of the explosion-damaged column is 1716.2 kN when the failure displacement reaches 20.6 mm, as exhibited in Fig. 12(b). As can be observed by Fig. 12(c), the AR can be obtained as 93.3 kN when the joint displacement of the undamaged substructure in the pseudo-static curves reaches 1.41 m. Besides, the equivalent residual resistance in the simplified analytical model is 70.2 kN when the displacement of the explosion-damaged substructure

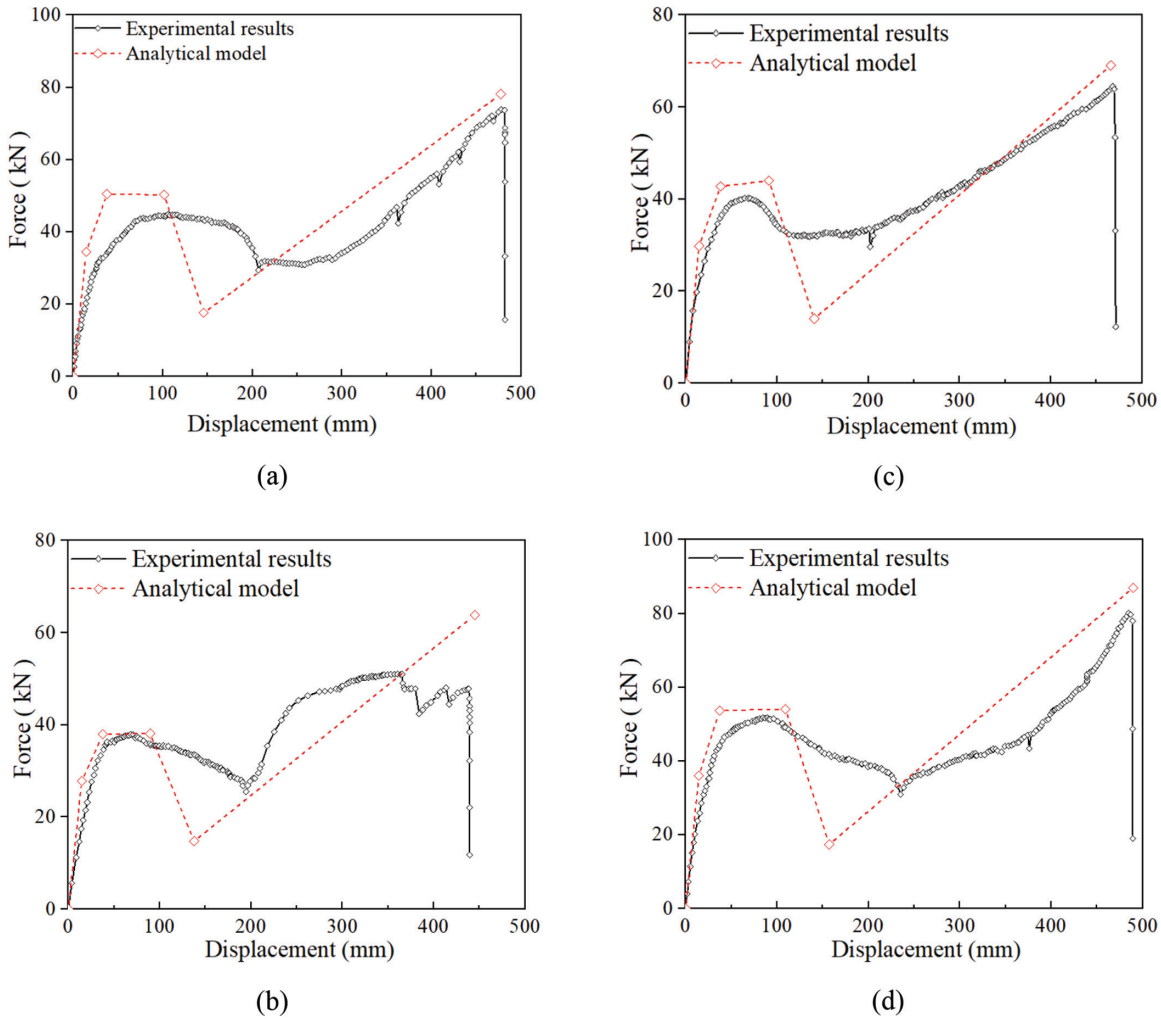

Fig. 9—Resistance deformation diagrams of blast-damaged substructures: (a) DBS 1; (b) DBS 2; (c) DBS 3; and (d) DBS 6.

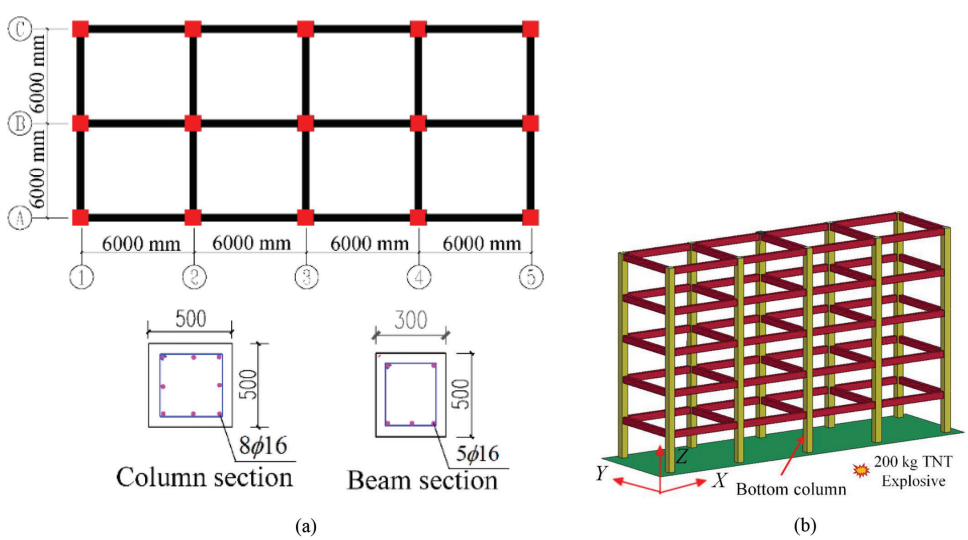

Fig. 10—Schematic diagram of RC frame structure under blast loads.

approaches 1.39 m, as exhibited in Fig. 12(d). Thus, the damage value of the analytical model is calculated as 0.461 by Eq. (34), which indicates that this bottom substructure exhibits middle degree damage.

As can be observed in Fig. 13, the resistance and corresponding displacement curves of the analytical model

Table 2—Concrete material properties

Density, kg/m^3	Concrete grade	Element size, mm	Failure principal strain	Failure shear strain
2450	C40	50	0.15	0.9

Table 3—Mechanical characteristics of bars

Yield strength of longitudinal steel, MPa	Ultimate strength of longitudinal steel, MPa	Yield strength of hoop reinforcing bar, MPa	Ultimate strength of hoop reinforcing bar, MPa	Young's modulus	Poisson's ratio
400	520	300	420	2.0×10^5	0.3

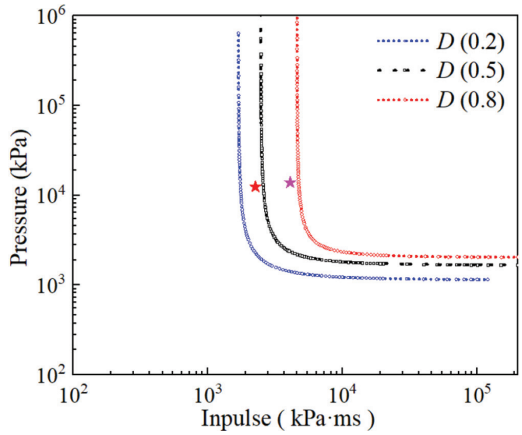

Fig. 11—Pressure and impulse curve for studied column.

derived from the undamaged and explosion-damaged second-story substructure are gained under the pushdown static loading. Compared with Fig. 13(a), the resistance of the second-layer substructure is distinct from that of the first-layer substructure (refer to Fig. 12(c)). This is because the initial resistance applied on the joint of the second-layer substructure is lower than that of the bottom substructure. Notably, there is no consideration of the resistance of the column in the second-floor substructure. The main reason is that the second-floor column has lost the collapse-resistant capacity with the failure of the bottom-floor column. The ultimate resistance of the undamaged substructure reaches 90.5 kN when the failure displacement is up to 1.40 m in the analytical models. The equivalent resistance of the damaged substructure is 86.5 kN when the failure displacement approaches 1.39 m, as exhibited in Fig. 13(b). Hence, the damage values of the second-floor substructure in the analytical model are calculated to be 0.051 based on the formula (Eq. (34)), which is lower than the D_1 of the first-floor substructure. Because the second-floor substructure is far away from the explosive charge compared with the bottom substructure. Afterward, the weight coefficient of the bottom-floor structure and second-floor structure are decided as 0.946 and 0.054 based on Eq. (36), respectively. As a result, the D value of the aforementioned substructures in the RC frame is calculated as 0.439 based on Eq. (35).

Using the proposed component assessment method, the damage derived from the component analytical models is compared with that of the RC frame model (that is, 0.401) in the literature (Shi et al. 2022a). The aforementioned result shows that the damage degree difference between the component analytical models in the blast-damaged region and the studied frame is 9.48%, which might be acceptable in engineering structures. Therefore, the damage degree of components in the explosion-damaged zone might be used to predict that of the RC frame model. Besides, the proposed component analytical models do not need to establish complex numerical models and consider the safety of explosion experiments.

CONCLUSIONS

In this study, a component-based analytical model was proposed to evaluate damage levels in reinforced concrete (RC) structures under the principle of energy conservation. Additionally, the collapse resistance capacity of RC structures can be expressed by forces and displacements derived from the analytical model. The key findings can be described as follows:

1. An assessment method using a component-based analytical model for evaluating the degree of damage in RC structures was proposed. The accuracy of the method was validated by comparing the damage assessment results of a five-story RC frame subjected to explosion loads with those obtained from the component-based analytical models.

2. The analytical model expressions, derived from forces and corresponding deflections, might accurately predict the collapse resistance capacity of RC structures under close-in explosion scenarios. The reliability of the proposed analytical component model was confirmed through comparison with test results.

3. Compared with numerical models and experimental results, the proposed component-based analytical models offer the advantage of not requiring the development of a complex numerical model or the consideration of safety concerns associated with explosion experiments.

Notably, the boundary conditions at the beam ends of the proposed component analytical models are assumed to be fixed. Besides, the aforementioned research is mainly applicable to RC structures under close-in explosion scenarios and situations when the deflect of joint is relatively small. Therefore, the above research is necessary to further explore the effect of various boundary conditions and real explosion scenarios in RC structures on the theoretical formulas, especially when the building structures are damaged under a far-field explosion, to enhance the model's accuracy in the future.

AUTHOR BIOS

Ren Jiang *is an Associate Professor in the School of Civil Engineering and Architecture at East China Jiaotong University, Nanchang, China. His research interests include reinforced concrete (RC) structures and precast concrete structures design, particularly in the field of progressive collapse and explosion resistance.*

ACKNOWLEDGMENTS

This research was supported from the National Natural Science Foundation of China under Grant No. 52568074, the Natural Science Foundation of Jiangxi Province of China under Grant No. 20242BAB25307, and the Youth Science and Technology of Department of Transportation of Jiangxi Province under Grant No. 2025QN002.

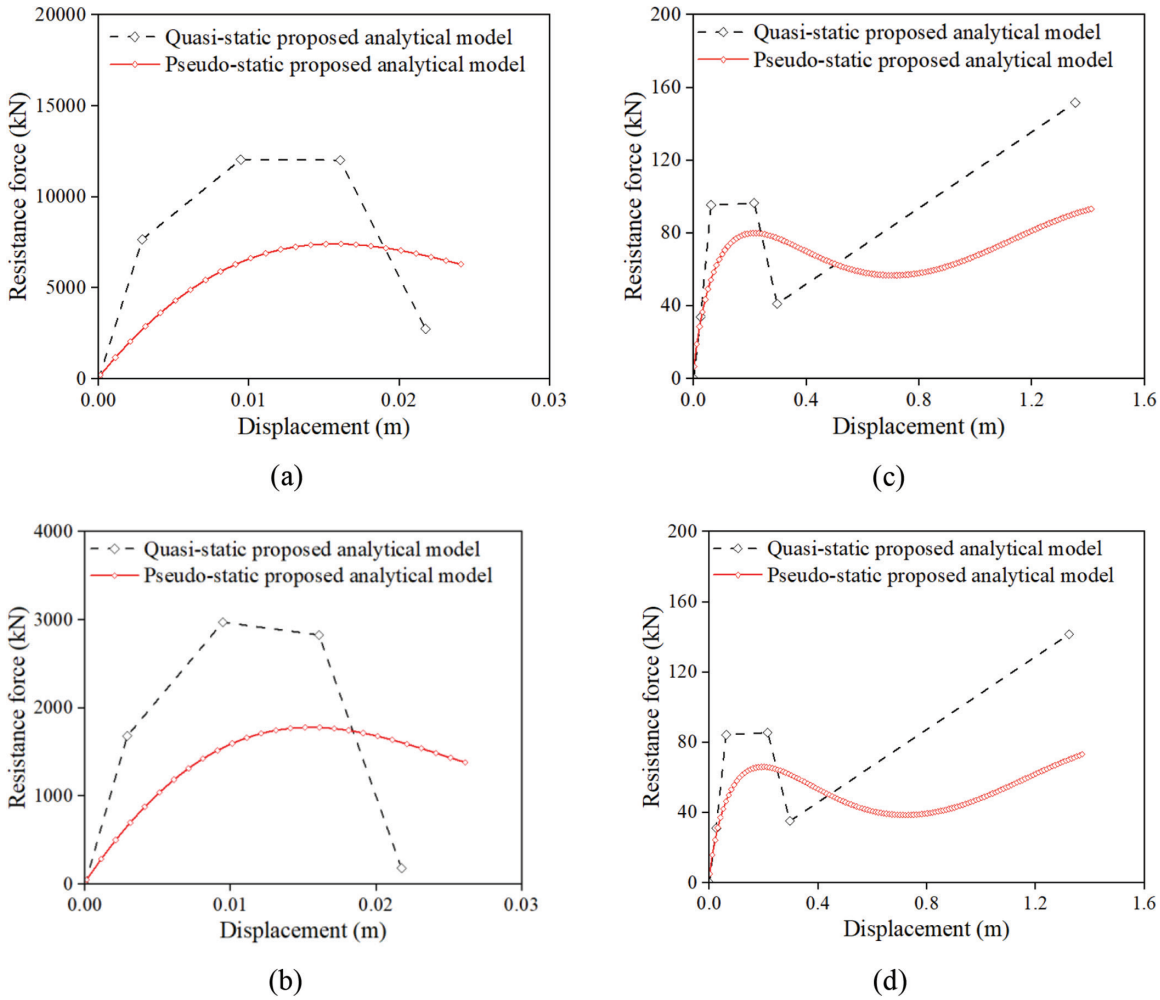

Fig. 12—Bottom substructure: (a) force-displacement curves of undamaged column; (b) force-displacement curves of damaged column; (c) resistance displacement diagrams of undamaged substructure; and (d) resistance displacement diagrams of damaged substructure.

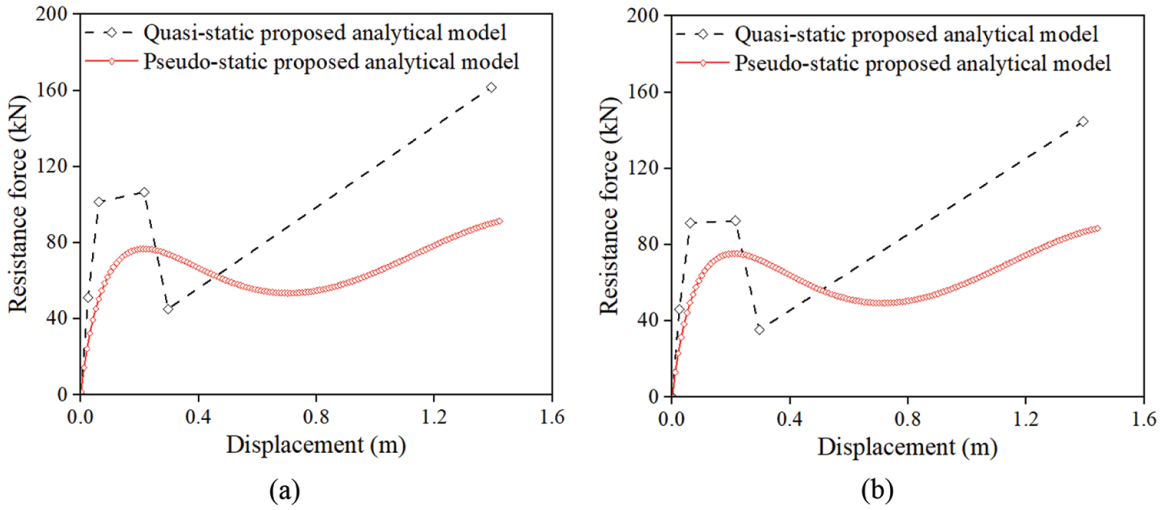

Fig. 13—Second floor substructure: (a) resistance displacement diagrams of undamaged substructure; and (b) resistance displacement diagrams of blast-damaged substructure.

REFERENCES

ACI Committee 318, "Building Code Requirements for Structural Concrete (ACI 318-19) and Commentary (ACI 318R-19) (Reapproved 2022)," American Concrete Institute, Farmington Hills, MI, 2019, 624 pp.

Campione, G., 2021, "Effect of Progressive Collapse of Central Column on the Push-Down Response of Two-Span Beam-Column Substructures," *Engineering Structures*, V. 248, pp. 113119. doi: 10.1016/j.engstruct.2021.113119

Crawford, J. E.; Wu, Y.; and Choi, H. J., 2012, "Use and Validation of the Release K&C Concrete Material Model in LS-DYNA," Karagozian and Case Structural Engineers, Burbank, CA, July.

Cui, J.; Shi, Y. C.; Li, Z. X.; and Chen, L., 2015, "Failure Analysis and Damage Assessment of RC Columns Under Close-In Explosions," *Journal of Performance of Constructed Facilities*, ASCE, V. 29, No. 5, pp. B4015003. doi: 10.1061/(ASCE)CF.1943-5509.0000766

Gao, C.; Zong, Z. H.; and Wu, J., 2013, "Experimental Study on Progressive Collapse Failure of RC Frame Structures Under Blast Loading," *Tumu Gongcheng Xuebao*, V. 46, No. 7, pp. 9-20. (in Chinese)

Izzuddin, B. A.; Vlassis, A. G.; Elghazouli, A. Y.; and Nethercot, D. A., 2008, "Progressive Collapse of Multi-Story Buildings Due to Sudden Column Loss-Part I: Simplified Assessment Framework," *Engineering Structures*, V. 30, No. 5, pp. 1308-1318. doi: 10.1016/j.engstruct.2007.07.011

Jian, H., and Zheng, Y., 2014, "Simplified Models of Progressive Collapse Response and Progressive Collapse-Resisting Capacity Curve of RC Beam-Column Substructures," *Journal of Performance of Constructed Facilities*, ASCE, V. 28, No. 4, p. 04014008. doi: 10.1061/(ASCE)CF.1943-5509.0000492

Jiang, R.; Shi, Y. C.; and Cui, J., 2025c, "A Novel Beam-Column Component Macro Model for Degradation Mechanism Analysis of RC Structures Subjected to Blast Loading," *Journal of Performance of Constructed Facilities*, V. 39, No. 3, p. 04025014. doi: 10.1061/JPCFEV.CFENG-4867

Jiang, R.; Shi, Y. C.; Zhong, B.; and Zhuang, H. Y., 2025d, "Numerical Investigation on Degradation Mechanism of Reinforced Concrete Structures Under Close-In explosion load," *Advances in Structural Engineering*, No. 9, pp. 1610-1626. doi: 10.1177/13694332251313865

Jiang, R.; Shi, Y. C.; and Zhuang, H. Y., 2025b, "Experimental Comparative Study on the Progressive Collapse Mechanism of ALP Method and Blast-Induced Concrete Substructures," *Materials and Structures*, V. 58, No. 10, pp. 345. doi: 10.1617/s11527-025-02867-8

Jiang, R.; Shi, Y. C.; Zhuang, H. Y.; and Zhang, J., 2025a, "Experimental and Numerical Investigation on Collapse Mechanism of Reinforced Concrete Substructures Subjected to Explosion Loads," *Journal of Structural Engineering*, V. 151, No. 12, p. 04025207. doi: 10.1061/JSENDH.STENG-14833

Kang, S. B.; Wang, S.; and Gao, S., 2020, "Analytical Study on One-Way Reinforced Concrete Beam-Slab Sub-Structures Under Compressive Arch Action and Catenary Action," *Engineering Structures*, V. 206, p. 110032. doi: 10.1016/j.engstruct.2019.110032

Li, J., and Hao, H., 2013, "Numerical Study of Structural Progressive Collapse Using Substructure Technique," *Engineering Structures*, V. 52, pp. 101-113. 10.1016/j.engstruct.2013.02.01610.1016/j.engstruct.2013.02.016

Lu, X. Z.; Lin, K. Q.; Li, Y.; Guan, H.; Ren, P.; and Zhou, Y., 2017, "Experimental Investigation of RC Beam-Slab Substructures Against Progressive Collapse Subject to an Edge-Column Removal Scenario," *Engineering Structures*, V. 149, pp. 91-103. doi.org/10.1016/j.engstruct.2016.07.039

Lu, X.; Lin, K.; Li, C.; and Li, Y., 2018, "New Analytical Calculation Models for Compressive Arch Action in Reinforced Concrete Structures," *Engineering Structures*, V. 168, pp. 721-735. doi: 10.1016/j.engstruct.2018.04.097

Park, R., 1965, "The Lateral Stiffness and Strength Required to Ensure Membrane Action at the Ultimate Load of a Reinforced Concrete Slab and Beam Floor," *Magazine of Concrete Research*, V. 16, No. 40, pp. 139-152. doi: 10.1680/macr.1965.17.50.29

Pham, X. D.; Tan, K. H.; and Yu, J., 2015, "A Simplified Approach to Assess Progressive Collapse Resistance of Reinforced Concrete Framed Structures," *Engineering Structures*, V. 101, pp. 45-57. doi: 10.1016/j.engstruct.2015.06.051

Qian, K.; Li, B.; and Ma, J. X., 2015, "Load-Carrying Mechanism to Resist Progressive Collapse of RC Buildings," *Journal of Structural Engineering*, ASCE, V. 141, No. 2, p. 04014107. doi: 10.1061/(ASCE)ST.1943-541X.0001046

Ren, P.; Li, Y.; Lu, X.; Guan, H.; and Zhou, Y., 2016, "Experimental Investigation of Progressive Collapse Resistance of One-Way Reinforced Concrete Beam-Slab Substructures under a Middle-Column-Removal Scenario," *Engineering Structures*, V. 118, pp. 28-40. doi: 10.1016/j.engstruct.2016.03.051

Sasani, M., 2008, "Response of a Reinforced Concrete Infilled-Frame Structure to Removal of Two Adjacent Columns," *Engineering Structures*, V. 30, No. 9, pp. 2478-2491. doi: 10.1016/j.engstruct.2008.01.019

Sasani, M.; Kazemi, A.; Sagiroglu, S.; and Forest, S., 2011, "Progressive Collapse Resistance of an Actual 11-Story Structure Subjected to Severe Initial Damage," *Journal of Structural Engineering*, ASCE, V. 137, No. 9, pp. 893-902. doi: 10.1061/(ASCE)ST.1943-541X.0000418

Sasani, M., and Sagiroglu, S., 2008, "Progressive Collapse Resistance of Hotel San Diego," *Journal of Structural Engineering*, ASCE, V. 134, No. 3, pp. 478-488. doi: 10.1061/(ASCE)0733-9445(2008)134:3(478)

Sasani, M., and Sagiroglu, S., 2010, "Gravity Load Redistribution and Progressive Collapse Resistance of 20-Story Reinforced Concrete Structure Following Loss of Interior Column," *ACI Structural Journal*, V. 107, No. 6, Nov.-Dec., pp. 636-644.

Shi, Y. C.; Hao, H.; and Li, Z. X., 2008, "Numerical Derivation of Pressure-Impulse Diagrams for Prediction of RC Column Damage to Blast Loads," *International Journal of Impact Engineering*, V. 35, No. 11, pp. 1213-1227. doi: 10.1016/j.ijimpeng.2007.09.001

Shi, Y. C.; Hu, Y.; Chen, L.; Li, Z. X.; and Xiang, H. B., 2022a, "Experimental Investigation Into the Close-In Blast Performance of RC Columns with Axial Loading," *Engineering Structures*, V. 268, p. 114688. doi: 10.1016/j.engstruct.2022.114688

Shi, Y. C.; Jiang, R.; Li, Z. X.; and Ding, Y., 2022b, "A Substructure Based Method for Damage Assessment of RC Frame Structures under Close-In Explosion," *Engineering Structures*, V. 272, pp. 115017. doi: 10.1016/j.engstruct.2022.115017

Shi, Y. C., and Jiang, R., 2024, "Experimental Investigation on Progressive Collapse Performance of RC Substructures Under Blast Loading," *Structures*, V. 70, pp. 107803. doi: 10.1016/j.istruc.2024.107803

Shi, Y. C.; Jiang, R.; Li, Z. X.; and Ding, Y., 2021, "A New Macromodel of Beam-Column Joints for Progressive Collapse Analysis of Reinforced Concrete Structures Under Blast Loading," *International Journal of Structural Stability and Dynamics*, V. 22, No. 1, p. 2250008. doi: 10.1142/S0219455422500080

Shi, Y. C.; Li, Z. X.; and Hao, H., 2010, "A New Method for Progressive Collapse Analysis of RC Frames Under Blast Loading," *Engineering Structures*, V. 32, No. 6, pp. 1691-1703. doi: 10.1016/j.engstruct.2010.02.017

Su, Y. P.; Tian, Y.; and Song, X., 2009, "Progressive Collapse Resistance of Axially-Restrained Frame Beams," *ACI Structural Journal*, V. 106, No. 5, Sept.-Oct., pp. 600-607.

Sun, J. S.; Jia, Y. S.; Yao, Y. K.; and Xie, X. Q., 2020, "Experimental Investigation of Stress Transients of Blasted RC Columns in the Blasting Demolition of Buildings," *Engineering Structures*, V. 210, pp. 110417. doi: 10.1016/j.engstruct.2020.110417

TM5-1300, 1990, "To Resist the Effect of Accidental Explosions," Department of the Army, Navy and the Air Force, Washington, DC.

UFC 4-340-02, 2008, "Structures to Resist the Effects of Accidental Explosions," Department of the Army, Navy and the Air Force, Washington, DC, May 12.

Vlassis, A. G.; Izzuddin, B. A.; Elghazouli, A. Y.; and Nethercot, D. A., 2008, "Progressive Collapse of Multi-Story Buildings Due to Sudden Column Loss-Part II: Application," *Engineering Structures*, V. 30, No. 5, pp. 1424-1438. doi: 10.1016/j.engstruct.2007.08.011

Wang, S., and Kang, S. B., 2019, "Analytical Investigation on Catenary Action in Axially-Restrained Reinforced Concrete Beams," *Engineering Structures*, V. 192, pp. 145-155. doi: 10.1016/j.engstruct.2019.05.008

Xu, W. L., and Wang, L. C., 2021, "Analytical Models for Reverse Arch and Compressive Arch Action in Horizontally Restrained Unbonded Prestressed RC Beam-Column Sub-Assemblages," *Engineering Structures*, V. 228, pp. 111529. doi: 10.1016/j.engstruct.2020.111529

Yi, W. J.; He, Q. F.; and Xiao, Y., 2007, "Experimental Study on Collapse Resistance of Reinforced Concrete Frame Structure," *Journal of Building Structures*, V. 28, No. 5, pp. 104-109. (in Chinese)

Yi,, W. J.; He,, Q. F.; and Xiao,, Y., Kunnath; and Sashi, K., 2008, "Experimental Study on Progressive Collapse-Resistant Behavior of Reinforced Concrete Frame Structures," *ACI Structural Journal*, V. 105, No. 4, July-Aug., pp. 433-439.

Yu, J., and Tan, K. H., 2014, "Analytical Model for the Capacity of Compressive Arch Action of Reinforced Concrete Sub-Assemblages," *Magazine of Concrete Research*, V. 66, No. 3, pp. 109-126. doi: 10.1680/macr.13.00217

Zhang, Q.; Zhao, Y. G.; Kolozvari, K.; and Xu, L., 2020, "Simplified Model for Assessing Progressive Collapse Resistance of Reinforced Concrete Frames under an Interior Column Loss," *Engineering Structures*, V. 215, pp. 110688. doi: 10.1016/j.engstruct.2020.110688

Zhu, Y. J.; Wang, J. J.; Nie, X.; Pan, X. B.; and Fan, J. S., 2020, "Structural Performance of Slabs in Composite Box Girder Considering Compressive Membrane Action," *Engineering Structures*, V. 212, pp. 110457. doi: 10.1016/j.engstruct.2020.110457

ACI STRUCTURAL JOURNAL TECHNICAL PAPER

Title No. 123-S60

Post-Cracking Shear Capacity of Precast Hollow-Core Floor Units

by Mohamed Mostafa, Richard S. Henry, and Kenneth J. Elwood

Precast concrete hollow-core floor units have been shown to sustain cracking to their unreinforced webs near the end support during earthquakes. Post-cracking shear strength is essential to maintain gravity loads following earthquakes. This paper presents the results of an experimental program that examined the post-cracking shear capacity of 12 full-scale hollow-core floor units. Variables included different support seating lengths, shear span-depth ratios, and loading protocols. Results showed that cracking in the unreinforced webs of hollow-core floor units can reduce shear capacity by at least 60% relative to uncracked strength. Additionally, reduced support seating length markedly decreased post-cracking shear strength: 30 mm (1.2 in.) seating provided no residual capacity, while 50 and 100 mm (2 and 4 in.) lengths retained approximately 50% and 100% of the calculated uncracked section capacity, respectively. The findings from this study provide a basis to quantify the residual capacity of web-cracked hollow-core floor units, which can be used in post-earthquake structural assessments.

Keywords: hollow core; post-cracking behavior; precast concrete; prestressed concrete; residual shear strength; seismic assessment; shear failure; web cracking.

INTRODUCTION

Precast concrete floor units that incorporate hollow cores to reduce weight without significant loss of strength or stiffness are structurally efficient and cost-effective. In addition to their structurally efficient cross section and high strength-to-weight ratio, precast concrete hollow-core floor units offer speed of installation and a reduction in site labor and formwork, making them preferred in some applications to cast-in-place concrete flooring.[1-3] Precast hollow-core floor units are typically prefabricated with extruded zero-slump concrete and reinforced only with prestressing strands in the longitudinal direction. The extrusion process used to manufacture hollow-core floor units contributes to the competitiveness of these floor units, where material waste and manufacturing labor time are reduced. However, this production method does not allow for the installation of transverse shear reinforcement into the floor units. Due to the absence of shear reinforcement, hollow-core units are designed to support gravity loads based on the uncracked section capacity. Therefore, any cracking in their webs can severely weaken their load-bearing capacity, potentially leading to the collapse of the floor.

Hollow-core floor units have been observed to sustain inclined cracks in their unreinforced webs near the support when subjected to earthquake-induced deformations, as illustrated in Fig. 1, at deformations corresponding to approximately 0.6% interstory drift,[4-6] significantly lower than the typical design drifts for buildings subjected to seismic demands. Such observations raise concerns that existing buildings with precast hollow-core flooring in areas with moderate to high seismic activity (for example, Wellington and Christchurch in New Zealand) may already have cracked webs due to prior earthquakes causing interstory drifts that exceeded the 0.6% threshold for cracking the units.

The susceptibility of hollow-core floor units to sustain damage due to earthquake actions has been realized and extensively investigated since the mid-1990s, as summarized in Corney et al.[7] and Puranam et al.[8] Laboratory investigations revealed that inclined web cracks in hollow-core floor units due to deformation compatibility between the hollow-core floor units and the supporting structure during earthquakes can propagate through the depth of the section, appearing as transverse cracks at the top and bottom of the unit.[9-11] Moreover, numerous studies have been conducted on hollow-core floor units subjected to flexural and shear actions as part of investigations into their gravity-load behavior.[12-18] However, most of these tests were stopped shortly after reaching peak shear strength (that is, almost immediately after web cracking) and do not provide sufficient information regarding the post-cracking residual shear capacity. Recognizing the importance of understanding the post-cracking behavior, a study by Hernández et al.[19] investigated the effects of using fiber-reinforced concrete on the post-cracking web-shear response of hollow-core floor units with the intent of providing reliable residual shear strength. However, little attention was given to investigating the post-cracking behavior of conventional unreinforced hollow-core floor units in the Hernández et al.[19] study.

While the uncracked shear capacity of hollow-core floor units is relatively well-studied, there is little information regarding the post-peak and post-cracking behavior of these floor units to quantify the residual gravity load-carrying capacity of cracked hollow-core floor units. The lack of information on the residual capacity of hollow-core floor units has hindered the ability to assess the risk posed by cracked hollow-core floor units and to ensure that life safety requirements are met during and after earthquakes. Consequently, the New Zealand Seismic Assessment Guidelines for Concrete Buildings[20] state that "unreliable load paths…may result in gravity load support for units beyond

ACI Structural Journal, V. 123, No. 3, May 2026.
MS No. S-2025-118.R2, doi: 10.14359/51749308, received August 24, 2025, and reviewed under Institute publication policies. Copyright © 2026, American Concrete Institute. All rights reserved, including the making of copies unless permission is obtained from the copyright proprietors. Pertinent discussion including author's closure, if any, will be published ten months from this journal's date if the discussion is received within four months of the paper's print publication.

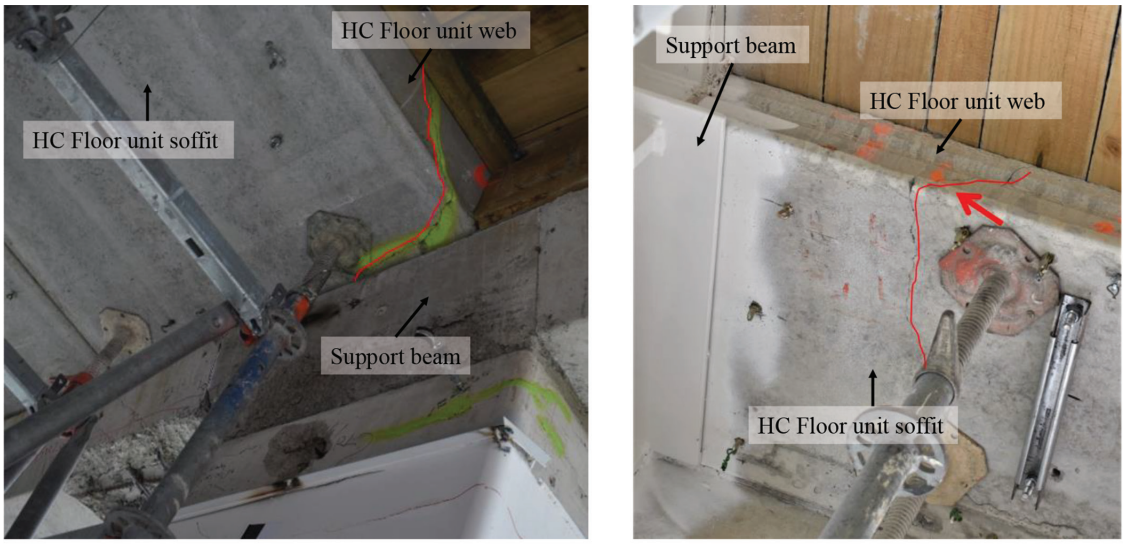

(a) Web cracking observed close to the support

(b) Web cracking observed about 400 mm aways from the support

Fig. 1—Examples of hollow-core floor unit web cracking observed in post-earthquake structural reconnaissance.

the drifts indicated by [the guidelines]; however, such load paths cannot be reliably calculated."

An experimental campaign was conducted to investigate the post-cracking residual shear strength of full-scale concrete hollow-core floor units. The tested floor units were loaded well beyond the peak shear strength to investigate their post-cracking response and explore the influence of different support seating lengths, shear span-depth ratios, and loading protocols. The recorded responses were compared to the estimated uncracked section capacity calculated by commonly used design standards, such as ACI 318-19,[21] European design standards for hollow-core floor units (BS EN 1168:2005+A3:2011),[22] and the New Zealand Concrete Structures Standard (NZS 3101.1&2:2006),[23] to quantify the residual shear capacity of cracked hollow-core units.

RESEARCH SIGNIFICANCE

Hollow-core floor units have been observed to sustain web cracking at low levels of earthquake shaking. While the uncracked shear strength of hollow-core floor units is well understood, little information is available regarding the post-cracking response and residual gravity load-carrying capacity of cracked hollow-core floor units. Quantifying the post-cracking shear strength is essential to assessing the gravity load-bearing capacity of hollow-core floor units following earthquakes. This study experimentally evaluated the residual shear capacity of web-cracked hollow-core floor units, providing data that can be used in post-earthquake structural assessments.

DESCRIPTION OF EXPERIMENTAL PROGRAM

Testing of the post-cracking web-shear behavior of 12 full-scale hollow-core floor units was conducted in two phases. The first series of tests focused on the influence of support seating lengths on the post-cracking residual shear capacity of the floor units, and the second series focused on the influence of shear span-depth ratios on the floor units' post-cracking response. All the hollow-core units were 200 mm (7.9 in.) deep, manufactured using the extrusion method, and designed according to the New Zealand Concrete Structures Standard.[23]

Test setup and instrumentation

Earthquake-induced web cracking in hollow-core units can vary in location, crack angle, and initiation point. A typical three-point bending test setup was used to induce the inclined web-shear cracking, which was considered a suitable proxy for earthquake-cracked webs and allowed for testing under controlled loading conditions (that is, repeatable and comparable between tests). Furthermore, as with most component-level laboratory testing, the experimental campaign focused on the response of individual floor units in isolation. However, in reality, the concrete topping and load sharing between adjacent units may contribute to the post-cracking response of these floor units, and, depending on the connection detail, the connection may also contribute to the post-cracking response of these floors. It was a deliberate choice of methodology to quantify the post-cracking response of individual bare hollow-core floor units, being the main component contributing to the post-cracking residual gravity load capacity. The conscious choice of testing the units in isolation was due to the following:

1. Longitudinal cracking between adjacent hollow-core floor units observed in earthquake-damaged floors resulting from the rotation and elongation of the supporting frame during an earthquake[4,5,24,25] can compromise and reduce the load-sharing effect.

2. Delamination between the cast-in-place topping and the precast hollow-core units is also likely to occur.[26-28] Therefore, its contribution is unreliable.

3. In New Zealand, most of the existing building stock specified connection details had the units seated on the supporting beam ledge with no reinforcement going into the units. However, in cases where the connection included reinforcement that extended into the units, it may provide a

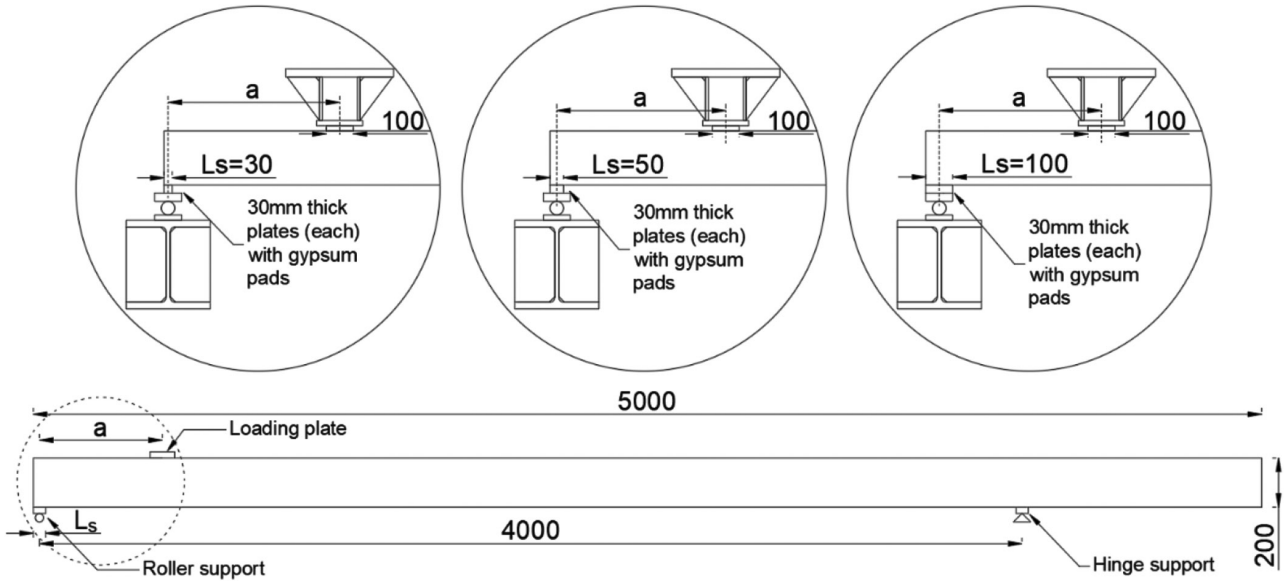

Fig. 2—Schematic for test setup. (Note: All dimensions in mm; 1 mm = 0.0394 in.)

favorable effect. Thus, the critical condition (that is, no reinforcement extending through the units) was tested.

In buildings, hollow-core floor units are typically supported at the very end of the unit with a relatively short seating length (a typical specified seating length of 50 mm [2 in.], with in-place conditions often resulting in less than 30 mm [1.2 in.] seating length[29]). Having the hollow-core floor units supported at the end of the unit, where the prestressing strands are not fully developed, on a relatively short seating length is also considered the most unfavorable condition for the web-shear capacity of hollow-core units. Therefore, the tested units were supported at the very end of the unit to recreate this critical condition.

A typical beam shear test setup was adopted using the arrangement illustrated in Fig. 2. The specimens were simply supported with a span of 4 m (13.1 ft) during testing. Hollow-core units with a total length of 5 m (16.4 ft) were used so that two tests could be performed on a single floor unit by rotating the unit 180 degrees after one end of the unit was tested. The choice of a 4 m (13.1 ft) central span followed the full-scale testing recommendation of the European standard for the design of hollow-core floor units[22] to allow comparisons between available test data. The support nearest to the load application point consisted of two 30 mm (1.2 in.) thick plates to have sufficient thickness to distribute the bearing stress so that the support was effective over the entire seating length provided (L_s). A gypsum-based plaster mixture was used as a bedding material to compensate for the unevenness of the hollow-core floor unit soffit in the transverse direction and to maintain uniform load distribution. The specimens were subjected to a monotonic concentrated load applied by means of an actuator connected to a steel loading frame at a distance equal to the shear span a, measured from the center of the support to the center of the loading beam (Fig. 2). The 500 kN (112,404.5 lb) hydraulic actuator was operated in displacement control with a 0.2 mm/min (0.008 in./min) loading rate.

Instrumentation was designed to capture the load-deformation response, potential support movements, prestressing strands slippage, and crack widths. The force exerted on the units was measured using a load cell connected to the actuator. Deformations of the units were recorded by measuring the vertical displacement at the loading location using two draw-wire transducers at the bottom of the units. The vertical displacement values at the loading location were corrected for support settlements, which were measured using linear variable displacement transformers (LVDTs). Prestressing strand pull-in during testing was measured for five strands using LVDTs. Finally, crack width measurements were collected using digital image correlation (DIC) on one side and a grid of displacement gauges placed on the other side of the unit, as shown in Fig. 3.

Test variables

The first series included six units, where the support seating length (L_s) was varied between 30, 50, and 100 mm (1.2, 2, and 4 in.), with two tests conducted for each support seating length variation. The shear span (a) was fixed for this first series of tests, with the actuator load applied at a shear span of 500 mm (20 in.), which corresponds to a shear span-depth ratio (a/d) of 2.5. The choice of a shear span-depth ratio of 2.5 followed the full-scale testing recommendation of the European standard for the design of hollow-core floor units.[22] The six tests in the first series were all loaded monotonically well beyond the peak shear force to deformations in excess of $L/200$ (20 mm [0.8 in.]) to study the post-cracking response of the hollow-core floor units.

The second series of tests included a further six units, where the shear span-depth ratio varied between 1.5, 2.5, and 3.5. The support seating length was fixed for this series, with a 50 mm (2 in.) support seating length used. The choice of a 50 mm (2 in.) support seating length was driven by the fact that 50 mm (2 in.) was the most commonly specified seating length for existing hollow-core flooring systems in New Zealand.[29] Two tests were conducted for each shear span-depth variation.

Because this study was motivated by earthquake-induced damage, the effect of opening and closing of the web

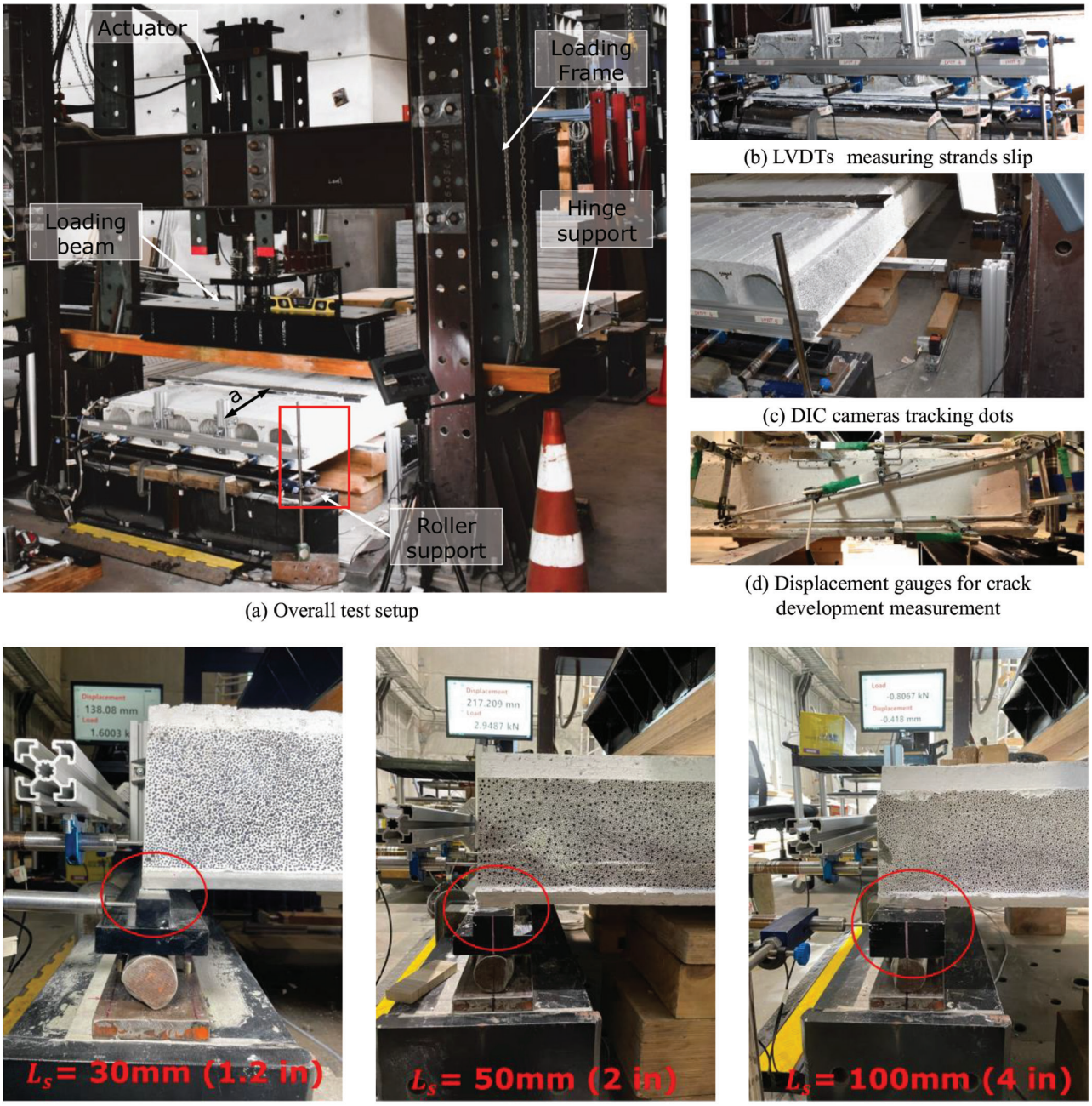

(a) Overall test setup

(b) LVDTs measuring strands slip

(c) DIC cameras tracking dots

(d) Displacement gauges for crack development measurement

(e) Different support seating lengths investigated

Fig. 3—Test setup, instrumentation, and support conditions.

cracking was simulated through loading cycles in some of the tests conducted in this second series of tests. The first cyclic protocol (Cyclic1) consisted of a quasi-static cyclic loading protocol (modified from the loading procedure described in BS EN 1168:2005[22]), where the load was removed from the specimen after cracking at peak force, and three cycles of repeated loading were applied at amplitudes of 50, 75, and 85% of the observed residual force maintained from the monotonic test. Following the cyclic loading, a final monotonic push up to deformations in excess of $L/200$ (20 mm [0.8 in.]) was performed. The second cyclic loading (Cyclic2) was a quasi-static cyclic loading protocol where the load was removed from the specimen upon cracking at peak force, and then a monotonic push up to failure was applied.

Table 1 summarizes the details of each test. The test units in each series were labeled according to their support seating length (30, 50, or 100), shear span-depth ratio (1.5, 2.5, or 3.5), test repeat (A or B), and loading type (Monotonic, Cyclic1, or Cyclic2).

Test specimens

The cross section of the hollow-core units tested is shown in Fig. 4. The unit contained seven 12.7 mm (0.5 in.) diameter prestressing strands with an area of 98.6 mm^2 (0.153 in.^{2}) per strand. All prestressing strands were seven-wire, low-relaxation type with a tensile ultimate capacity of 1840 MPa (266.9 ksi). Prior to casting the concrete, the strands were stressed to 67% of their ultimate strength, corresponding to a jacking stress of approximately 1230 MPa (178.4 ksi).

Table 1—Summary of test unit variations

	Test name	Support seating length L_s	Shear span-depth ratio a/d	Loading type
Series One	HC-30-2.5A-M	30 mm	2.5	Monotonic
	HC-30-2.5B-M			
	HC-50-2.5A-M	50 mm		
	HC-50-2.5B-M			
	HC-100-2.5A-M	100 mm		
	HC-100-2.5B-M			
Series Two	HC-50-1.5A-M	50 mm	1.5	Monotonic
	HC-50-1.5B-C1			Cyclic1
	HC-50-2.5A-C1		2.5	Cyclic1
	HC-50-2.5B-C2			Cyclic2
	HC-50-3.5A-M		3.5	Monotonic
	HC-50-3.5B-M			

Note: 1 mm = 0.0394 in.

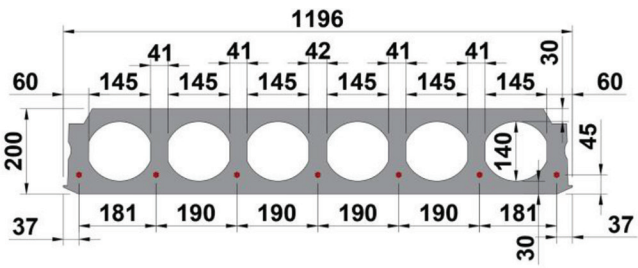

Cross-section Geometrical Properties

$A_g =$	$132 \times 10^3\ mm^2$
$b_w =$	$290\ mm$
$I =$	$636 \times 10^6\ mm^4$
$S =$	$4.25 \times 10^6\ mm^3$
$Y_c =$	$98\ mm$
$W =$	$330\ kg/m'$

Fig. 4—Hollow-core floor unit cross-section nominal geometry and section properties. (Note: All dimensions in mm; 1 mm = 0.0394 in.)

The concrete used in hollow-core floor units requires a high early strength (typically 30 MPa [4.35 ksi] after 24 hours, in New Zealand) to resist the prestressing force when releasing the prestressing strands and cutting the units to their specified lengths. To achieve this, a design compressive strength of 45 MPa (6.5 ksi) was specified, but it is noted that the 28-day strength typically exceeds the specified concrete strength by a significant margin.[20] The specified maximum size of coarse aggregates was 10 mm (0.4 in.).

MATERIAL TESTING

The shear strength of hollow-core units largely depends on the tensile strength of the concrete in the webs. Hollow-core manufacturers typically test standard cylinders for quality control. However, due to the extrusion manufacturing process and cross-section geometry with thin-walled elements, significant differences can result between the actual strength of the concrete in the hollow-core units and the measured cylinder strength.[30] Therefore, the concrete properties were assessed using drilled cylindrical cores and rectangular beams extracted from the hollow-core unit webs. The tensile strength of the concrete was assessed by conducting splitting and flexural tensile strength tests on the drilled cores and extracted webs, respectively, in accordance with NZS 3112.2:1986,[31] ASTM C496/C496M-17,[32] and ASTM C78-09.[33] Additionally, the concrete compressive strengths were assessed using the drilled cores according to NZS 3112.2:1986.

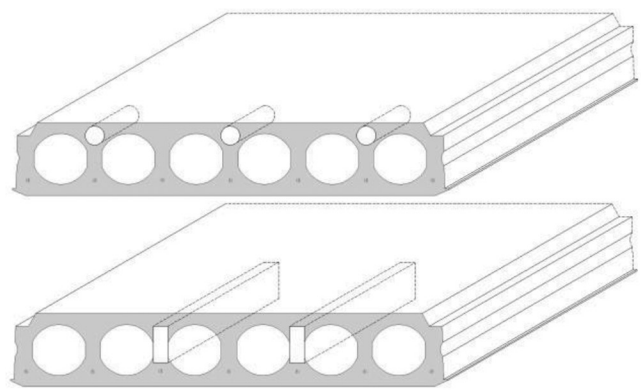

Fig. 5—Schematic showing location of material samples extraction from tested hollow-core units.

A total of 85 samples (36 cores for splitting tensile strength, 24 rectangular beams for flexural tensile strength, and 25 cores for compressive strength) were extracted and tested. Cylindrical cores (54 x 108 mm [2.12 x 4.25 in.]) were extracted from the top region of the webs, and rectangular beams (web width x 100 mm high [3.94 in.] x 350 mm long [13.8 in.]) were sawn out from the webs of each tested hollow-core unit end, as shown in Fig. 5.

The compressive and tensile strengths obtained from the extracted material samples are summarized in Table 2. The mean measured compressive and tensile strengths of the hollow-core units tested were approximately 70 and 6.2 MPa (10.15 and 0.9 ksi), respectively. It is noted that previous research on the properties of hollow-core units in New Zealand[10,11] reported a similar range of concrete strength to that measured herein. The relatively high concrete strength

Table 2—Summary of material test results

	Measured strengths, MPa				
	Mean	Maximum	Minimum	Standard deviation	Coefficient of variation
Compressive strength	68.68	79.63	43.86	5.10	8.00%
Splitting tensile strength	6.14	7.69	3.71	0.79	12.84%
Modulus of rupture	6.30	8.16	4.81	0.83	15.69%

Note: 1 MPa = 0.145 ksi.

values observed can be attributed to the mixture design and manufacturing process, in which the concrete used in hollow-core units requires a high early strength (typically 30 MPa [4.35 ksi] after 24 hours) to resist the prestressing force when cutting the units to their specified lengths.

SHEAR STRENGTH ACCORDING TO EXISTING STANDARDS

To quantify the gravity-load resistance of a web-cracked hollow-core floor, the post-cracking residual capacity was compared to the calculated uncracked full-section capacity. The estimated uncracked section capacity was calculated by commonly used design standards, including the American "Building Code Requirements for Structural Concrete" (ACI 318-19), European design standard for hollow-core floor units (BS EN 1168:2005), and the New Zealand Concrete Structures Standard (NZS 3101.1&2:2006). Design standards distinguish between the shear strength estimated at a cracked section in flexure (flexural-shear) and an uncracked section (web-shear) of prestressed concrete members. The web-shear strength is most relevant as a benchmark of the tests reported due to the setup with all units ultimately failing in web-shear. The New Zealand Concrete Structures Standard (NZS 3101.1&2:2006) uses essentially the same expression as ACI 318-19, with a minimal difference due to rounding in the coefficient for unit conversion. According to ACI 318-19, the web-shear strength, V_{cw}, can be calculated using Eq. (1), where f_c' is the specified concrete compressive strength in MPa; f_{pc} is the corresponding longitudinal prestress at the neutral axis in MPa; λ is a factor for lightweight concrete, taken as 1 herein; and A_{cv} is the effective shear area in mm^2.

$$V_{cw} = (0.29\lambda\sqrt{f_c'} + 0.3f_{pc})A_{cv} \tag{1}$$

The European standard (BS EN 1168:2005) for precast hollow-core floor units provides a simplified expression to calculate the design shear resistance V_{Rdc}, as shown in Eq (2), where I is the second moment of area in mm^4; b_w is the width of the cross section at the centroidal axis in mm; S is the first moment of area above and about the centroidal axis in mm^3; f_{ctd} is the design concrete tensile strength in MPa; β is a reduction factor referred to transfer length of prestressing, taken as 0.9 as per BS EN 1168:2005; α_1 is a factor to account for the degree of prestressing in transmission ($\alpha_1 \leq 1.0$); and σ_{cp} is the concrete compressive stress in MPa at the centroidal axis due to prestressing, in the area where the prestressing force is fully introduced.

$$V_{Rdc} = 0.8\frac{Ib_w}{S}\sqrt{(f_{ctd})^2 + \beta\alpha_1\sigma_{cp}f_{ctd}} \tag{2}$$

When calculating the uncracked web-shear strength using the design standards expressions, the shear strength was calculated at a section of half the depth of the floor unit (d/2) from the support face. The effective prestress force was assumed to be 80% of the prestress after initial losses. Finally, the specified material properties were used for all calculations. The calculated web-shear strength was 98.4 kN (22,121.2 lb) and 101.4 kN (22,795.627 lb), according to ACI 318-19 and NZS 3101.1&2:2006, respectively. A web-shear strength of 112 kN (25178.6 lb) was calculated following the simplified expression presented in BS EN 1168:2005.

EXPERIMENTAL RESULTS

All test units were loaded well beyond the peak shear force, where inclined web-shear cracking occurred, to study the post-cracking behavior of the hollow-core units. The measured response of the tested units is represented by the load-deflection responses, where the deflections are the recorded displacements at the loading location relative to the supports. Figure 6 demonstrates an example of the recorded load-deflection responses relative to the calculated uncracked section capacity as a gauge of the post-cracking residual capacity and shows the observed damage state just after cracking (left images) and almost at the end of the test (right images).

Key performance metrics from the measured response of each test unit are summarized in Table 3, including the peak uncracked shear strength (V_{ult}), post-cracking residual shear strength at a deflection of 20 mm (0.8 in.) (L/200) (V_{res}), the ratio of the observed post-cracking residual shear strength to the observed peak uncracked shear strength (V_{res}/V_{ult}), and the ratio of the observed post-cracking residual shear strength to the calculated section design capacity (V_{res}/V_{calc}). In addition, the ratio of the observed uncracked shear strength to the calculated section design capacity (V_{ult}/V_{calc}) is also reported, where the section capacities (V_{calc}) were calculated according to NZS 3101.1&2:2006, ACI 318-19, and BS EN 1168:2005. It should be noted that test unit HC-50-2.5B-M was excluded from the analysis because it did not sustain the targeted inclined web cracking, and the test concluded with complete anchorage failure of the prestressing strands.

Uncracked shear strength

The tested units exhibited a mostly linear response prior to reaching the peak shear strength, based on the stiffness of the uncracked unit, followed by a sudden drop in strength upon

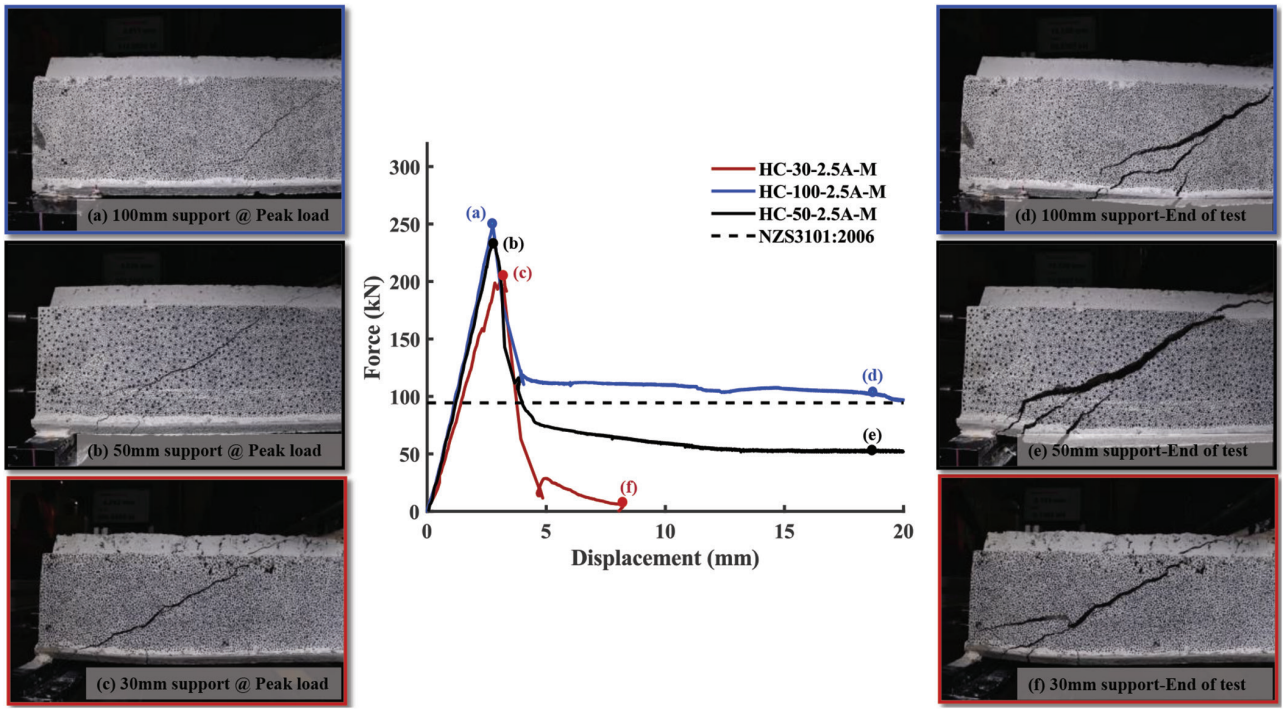

Fig. 6—Example of measured response relative to calculated capacity and observed damage states. (Note: 1 mm = 0.0394 in.; 1 kN = 224.81 lb.)

Table 3—Summary of shear test results

No.	Test name	V_{ult}, kN	V_{res}, kN	V_{res}/V_{ult}	V_{res}/V_{calc}		V_{ult}/V_{calc}	
					ACI 318-19	BS EN 1168:2005	ACI 318-19	BS EN 1168:2005
1	HC-30-2.5A-M	158.2	0.0	0.00	0.00	0.00	1.61	1.41
2	HC-30-2.5B-M	179.3	0.0	0.00	0.00	0.00	1.82	1.60
3	HC-100-2.5A-M	220.2	84.4	0.38	0.86	0.75	2.24	1.97
4	HC-100-2.5B-M	270.6	111.0	0.41	1.13	0.99	2.75	2.42
5	HC-50-2.5A-M	204.8	45.8	0.22	0.47	0.41	2.08	1.83
6	HC-50-2.5A-C1	204.4	0.0	0.00	0.00	0.00	2.08	1.83
7	HC-50-3.5A-M	168.5	0.0	0.00	0.00	0.00	1.71	1.50
8	HC-50-3.5B-M	185.8	0.0	0.00	0.00	0.00	1.89	1.66
9	HC-50-2.5B-C2	155.1	17.4	0.11	0.18	0.16	1.58	1.38
10	HC-50-2.5B-M	192.2	113.0	0.59	1.15	1.01	1.95	1.72
11	HC-50-1.5A-M	224.2	58.7	0.26	0.60	0.52	2.28	2.00
12	HC-50-1.5B-C1	275.2	45.7	0.17	0.46	0.41	2.80	2.46

Note: 1 kN = 224.81 lb.

web-shear cracking (for example, Fig. 6). Three specimens (HC-100-2.5B-M, HC-50-3.5B-M, and HC-50-2.5B-C2) sustained flexural cracks that initiated in the soffit of the unit at a location close to the loading position prior to achieving the peak load capacity, followed by stiffness degradation when the load-carrying capacity increased again. Nevertheless, the peak shear strength in these units was still governed by the formation of web-shear cracking.

Reducing the support seating length for specimens with the same shear span (2.5*d*) resulted in a reduction in the uncracked section shear strength. The mean shear strength for the units with a 100 mm (4 in.) support seating length (HC-100-2.5A/B-M) was 245 kN (55,078.2 lb). In the case of specimens with a 50 mm (2 in.) support seating length (HC-50-2.5A/B-M), the mean shear strength was 199 kN (44,737 lb), equating to a 19% reduction in shear strength when compared to the specimens with a 100 mm (4 in.) support seating length. As for the specimens with a 30 mm (1.2 in.) support seating length (HC-30-2.5A/B-M), the observed mean shear strength was 169 kN (37,992.7 lb), equating to a 31% reduction in the observed shear strength

compared to the specimens with a 100 mm (4 in.) support seating length.

The results also show that smaller shear spans resulted in higher shear strengths for specimens with the same support seating length (50 mm [2 in.]). The mean shear strength for the specimens with a 1.5*d* shear span (HC-50-1.5A-M and HC-50-1.5B-C1) was 250 kN (56,202.2 lb). In the case of specimens with a shear span of 2.5*d* (HC-50-2.5A/B-M), the mean shear strength was 199 kN (44,737 lb), a reduction of 20% in shear strength when compared to the specimens with a shear span of 1.5*d*. As for the specimens with a shear span of 3.5*d* (HC-50-3.5A/B-M), the observed mean shear strength was 177 kN (39,791.2 lb), a 29% reduction in the observed shear strength compared to the specimens with a 1.5*d* shear span.

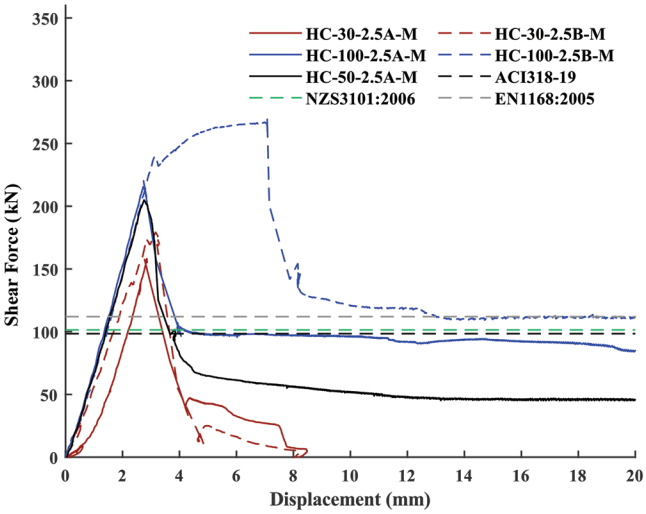

*Fig. 7—Measured response of monotonically tested units with fixed shear span of 2.5*d *and varying support seating lengths. (Note: 1 mm = 0.0394 in.; 1 kN = 224.81 lb.)*

Post-cracking residual shear strength

The results showed that the support seating length also substantially affected the residual shear strength of hollow-core floor units with web cracking. Specimens with a 30 mm (1.2 in.) support seating length (HC-30-2.5A/B-M) completely lost the ability to resist gravity loads after web cracking, with no stable residual strength maintained, as shown by the load-displacement response in Fig. 7. On the other hand, the observed mean residual shear strength for specimens with a 100 mm (4 in.) support seating length (HC-100-2.5A/B-M) was almost equivalent to 100% of the calculated uncracked section design capacity and approximately 40% of the peak uncracked shear strength. HC-100-2.5B-M initially sustained a flexural crack near the loading location, followed by stiffness degradation, which led to larger unit displacement prior to reaching the peak load, at which point the unit sustained a web-shear crack, leading to an abrupt and sudden drop in strength, as shown in Fig. 7. The photos in Fig. 8 show the flexural cracking observed before reaching the peak shear strength and the observed web-shear cracking directly after reaching the peak shear strength.

The unit with a 50 mm (2 in.) support seating length (HC-50-2.5A-M) maintained a residual strength of approximately 50% of the calculated uncracked section design capacity, as shown in Fig. 7. When comparing the response of units with 30, 50, and 100 mm (1.2, 2, and 4 in.) seating lengths,

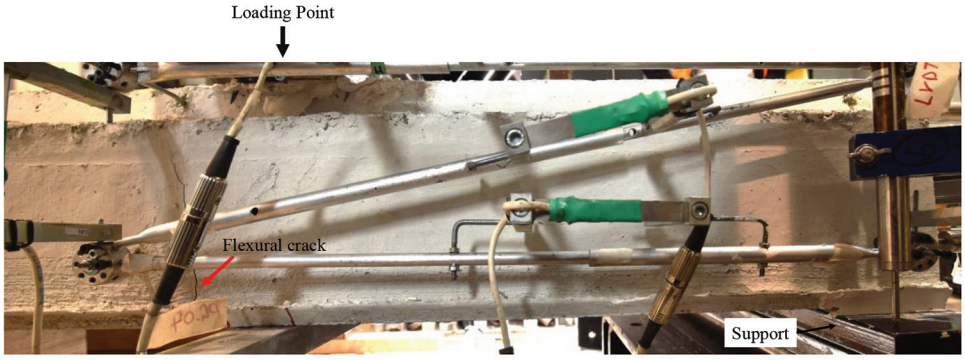

(a) damage observed directly before peak shear strength

(b) damage observed directly after peak shear strength

Fig. 8—Observed damage state in test HC-100-2.5B-M.

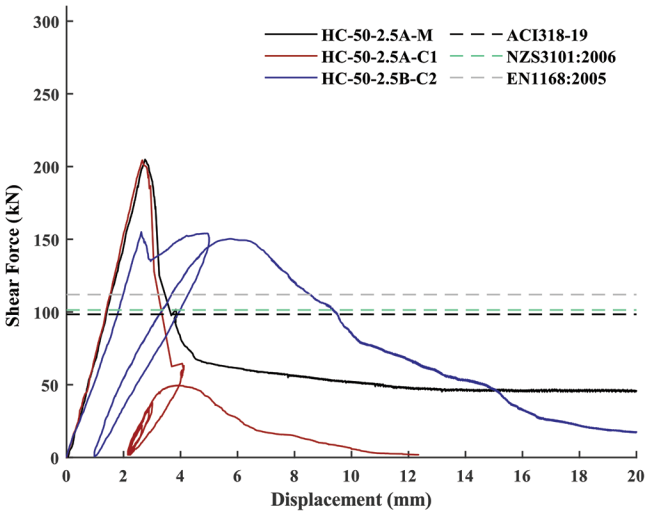

*Fig. 9—Comparison of measured response of units with 50 mm support seating length and shear span of 2.5*d *with different loading protocols. (Note: 1 mm = 0.0394 in.; 1 kN = 224.81 lb.)*

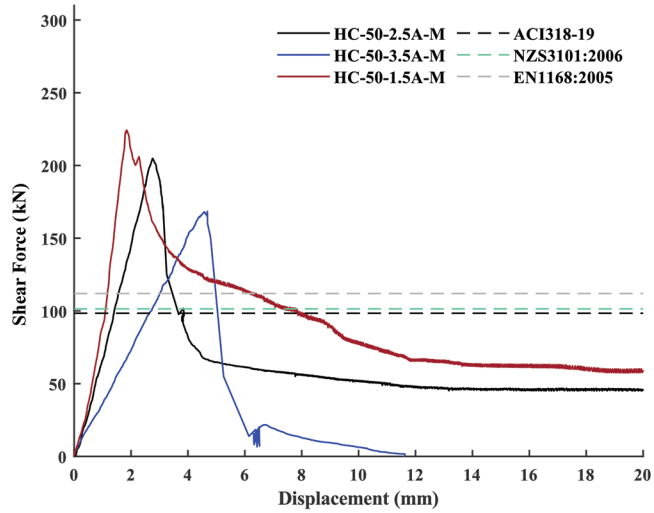

Fig. 10—Comparison of measured response of units with 50 mm support seating length with different shear spans. (Note: 1 mm = 0.0394 in.; 1 kN = 224.81 lb.)

it was noted that shorter support seating lengths negatively affected the post-cracking shear response. This was particularly notable for the shorter seating length (30 mm [1.2 in.]), where a sudden failure occurred, compared to the units with 50 and 100 mm (2 and 4 in.) seating lengths, which exhibited a more stable post-cracking response.

Another factor that notably impacted the hollow-core units' residual gravity load capacity after web cracking was the opening and closing of the web cracks during cyclic loading, as shown by the load-displacement responses in Fig. 9. Specimen HC-50-2.5A-C1 lost all gravity load-carrying ability after subjecting the specimen to three incremental loading cycles after initial web cracking. Specimen HC-50-2.5B-C2 sustained a residual load less than 20% of the calculated uncracked section capacity, where the load was removed from the specimen upon cracking at peak force, and then a monotonic push up to failure was applied. When comparing the response of the specimens with varying cyclic loading (HC-50-2.5A-C1, HC-50-2.5B-C2) to the specimen with the same boundary conditions but subjected to monotonic loading (HC-50-2.5A-M), the negative effect of repeated opening and closing of the web cracks on the residual gravity load-carrying capacity was identified.

The main influence of the shear span on the post-cracking shear response was observed in the rate of strength degradation, as shown by the load-displacement responses in Fig. 10. Units with a 1.5*d* shear span exhibited a more gradual strength degradation compared to those with a 2.5*d* shear span. Units with a 3.5*d* shear span (HC-50-3.5A/B-M) were observed to rapidly lose all ability to resist gravity loads after the formation of web-shear cracking. This observation might be attributed to the sudden release of the accumulated internal strain energy in these units. Units with a 3.5*d* shear span were deformed almost double those with a 2.5*d* and 1.5*d* before the principal tensile stress reached the concrete tensile strength at the critical section. This sudden release of the large accumulated internal strain energy associated with the web-shear crack opening could have affected the mechanisms that provide residual shear strength. Specimen HC-50-1.5B-C1 was subjected to three incremental loading cycles after initial web cracking, but these cycles did not appear to have a significant impact on the post-cracking response when compared to the specimen with the same boundary conditions that was monotonically loaded (HC-50-1.5A-M). This observation can be attributed to the direct load transfer to the support when the load is applied close to the support.

Failure profiles

Figures 11 and 12 show the cracking profiles of the exterior webs on both sides of the unit observed at the end of each test. The cracks were accurately traced using spatially calibrated images taken on both sides of each tested unit using digital single-lens reflex (DSLR) cameras and plotted on the same image for comparison. An average cracking profile was deduced by plotting a straight line at the mean position and angle of cracking. The average cracking line was centered at the unit's midheight between the traced cracks. Then, the average cracking angle was obtained from the mean of straight lines plotted approximately parallel to the slope of each traced web crack at the midheight level of the floor unit. The observed crack angles ranged from 24 to 65 degrees, which is consistent with earthquake-induced crack angles.[34]

EVALUATION OF EXPERIMENTAL RESULTS

Uncracked shear strength

When comparing the measured uncracked shear strength to the calculated web-shear capacity according to different standards (refer to Table 3), the test strengths exceeded the design strengths by a considerable margin. The minimum uncracked shear strength from the tests was approximately 50% higher than the calculated shear strength, and the maximum was approximately 160% higher than the calculated shear strength.

Reducing the support seating length was observed to result in a reduced hollow-core unit shear strength. A comparison

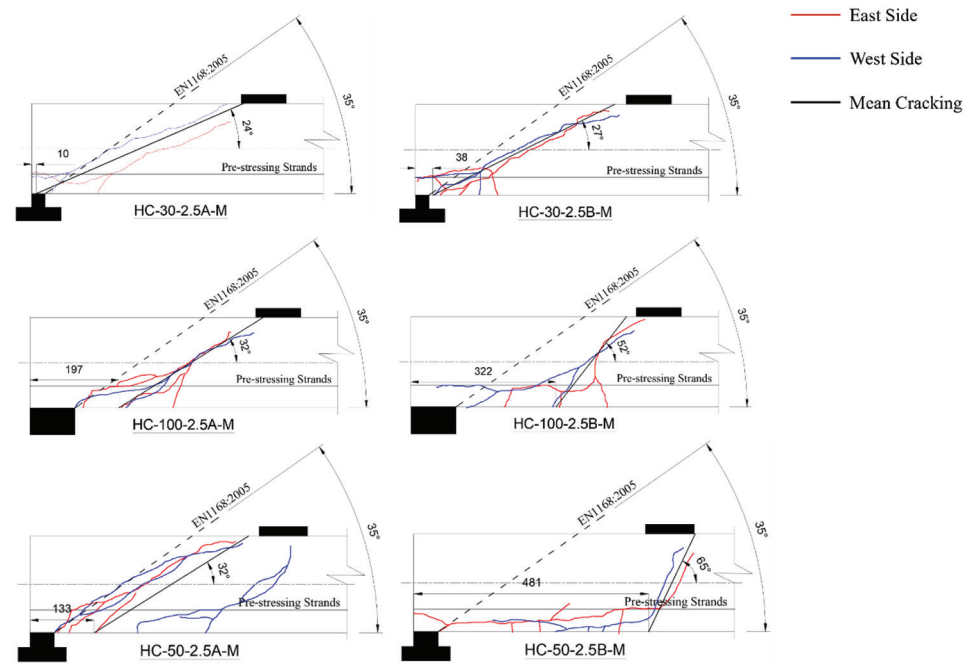

Fig. 11—Cracking profiles for first test set observed at end of each test.

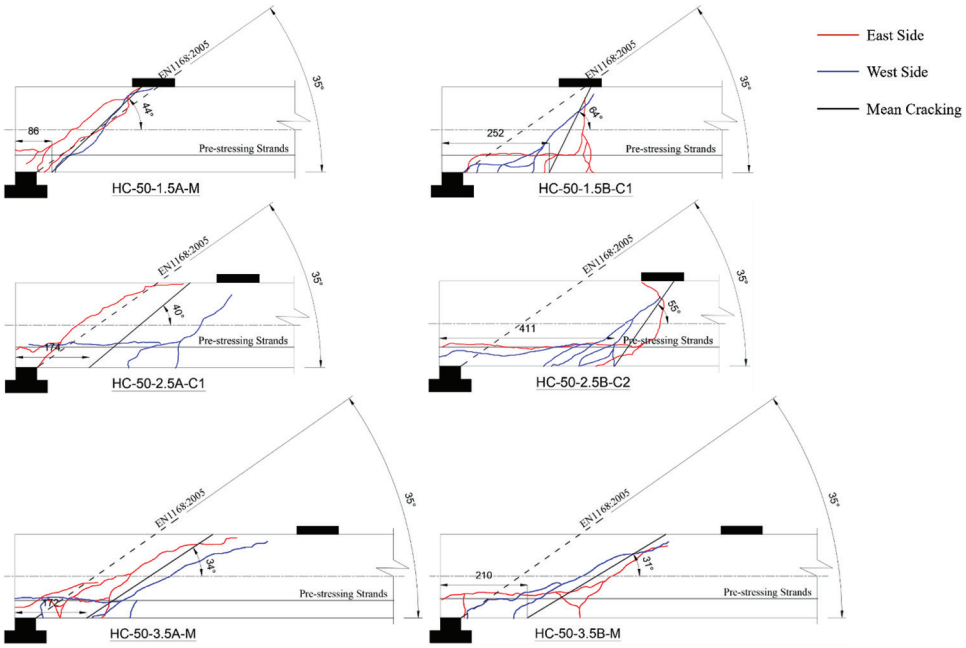

Fig. 12—Cracking profiles for second test set observed at end of each test.

of the measured peak shear strength to the calculated shear strength according to ACI 318-19, NZS 3101.1&2:2006, and BS EN 1168:2005 for tests with the same shear span (2.5*d*) and varying support seating length is shown in Fig. 13. When comparing the ratio of the measured uncracked shear strength with the calculated shear strength, on average, units with a 50 mm (2 in.) support seating length were approximately 40% lower than those with a 100 mm (4 in.) support seating length. Furthermore, test units with a 30 mm (1.2 in.) support seating length were approximately 30% lower than those with a 50 mm (2 in.) support seating length. The difference in the observed shear strength for specimens with different support seating lengths can be partly attributed to shifting the critical section for shear relative to the end of the unit. A larger support seating length shifts the critical section for shear further into the unit, where a slightly higher level of prestressing force is developed. Because the critical section for shear is within the transfer length of the prestressing strands, the resulting shear strength of the unit can be sensitive to small variations in the seating length.

Increasing the shear span-depth ratio led to a decrease in the ratio of the measured-to-calculated uncracked shear strength. A comparison of the measured-to-calculated shear strength for test units with the same support seating length (50 mm [2 in.]) and varying shear span is shown in Fig. 14. When comparing the specimens with a shear span

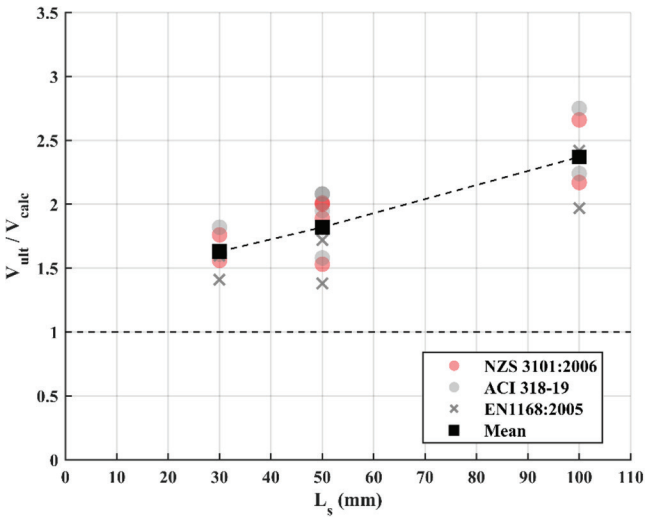

Fig. 13—Influence of support seating length on ratio of measured-to-calculated shear strength calculated according to different design standards. (Note: 1 mm = 0.0394 in.)

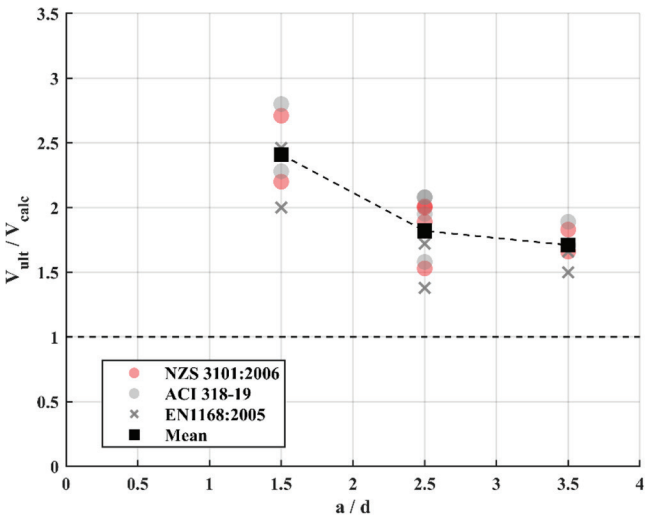

Fig. 14—Influence of different shear span-depth ratios on ratio of measured-to-calculated shear strength calculated according to different design standards.

of 2.5 to those of 1.5, on average, specimens with a shear span of 2.5*d* had approximately a 70% lower observed-to-calculated shear strength ratio than those with a 1.5*d* shear span. Specimens with a 3.5*d* shear span were approximately 12% less than those with a 2.5*d* shear span. The large difference between specimens with a shear span of 1.5*d* and 2.5*d* can be attributed to the arching action that develops when the load is applied close to the support. This effect has been shown[35] to be almost negligible for prestressed members with a shear span greater than 2.4*d*.

Post-cracking residual shear strength

The ability of web-cracked hollow-core floor units to carry gravity loads and the reduction in their shear capacity were quantified by comparing the post-cracking residual capacity of the units to the calculated uncracked full-section capacity. Figure 15 shows the measured post-cracking residual shear strength as a ratio of the mean calculated uncracked shear

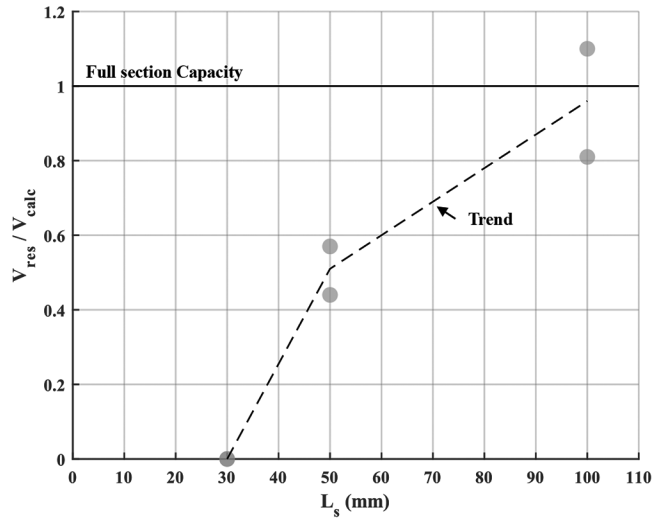

Fig. 15—Effect of different support seating lengths on observed residual shear strength. (Note: 1 mm = 0.0394 in.)

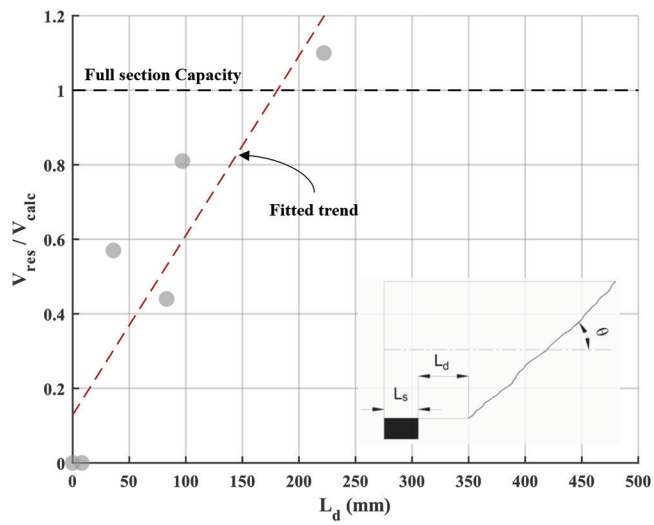

Fig. 16—Effect of cracking location on observed residual shear strength. (Note: 1 mm = 0.0394 in.)

strength according to ACI 318-19, NZS 3101.1&2:2006, and BS EN 1168:2005 for test units with different support seating lengths. Based on the results in Fig. 15, it is evident that reduced support seating length can significantly impair the post-cracking residual shear strength, where floor units with a 30 mm (1.2 in.) support seating length had zero post-cracking residual shear strength and floor units with 50 and 100 mm (2 and 4 in.) seating lengths maintained post-cracking shear strength of approximately 50% and 100% of their design capacity, respectively. Such observation is critical for post-earthquake structural assessment, as many existing hollow-core floor units are expected to sustain web cracking during earthquakes[5,6] and are expected to be left with less than the specified 50 mm (2 in.) seating length due to construction tolerances[29] and even less following an earthquake due to support ledge spalling.[7,8] Based on the test results discussed in this paper, web-cracked hollow-core floor units with seating less than 50 mm (2 in.) should be temporarily supported and retrofitted or repaired without delay after an earthquake.

Another factor that notably impacted the ability of the hollow-core floor units to resist gravity loads after web cracking was the crack location. The relationship between the location of the mean cracking profile (refer to Fig. 11 and 12) and the observed residual shear strength is plotted in Fig. 16. There is a clear trend: the further the web crack was from the support, the higher the post-cracking shear strength. Such observation is considered positive, as some hollow-core floor units in earthquake-damaged buildings were observed to sustain transverse cracking in the soffit further away from the support (400 mm [15.7 in.] away from the support),[36] which raised concerns regarding the efficacy of some of the already installed retrofits that are at the support (for example, supplemental seating angles).[34] The results shown in Fig. 16 provide some confidence that web cracking further away from the support is less of a concern. Web cracking can occur near the support within the transfer region, where the prestressing strands are not fully developed. The residual gravity load capacity depends on the strands' anchorage. The ability of the strands to sustain tensile forces is a necessary component to maintain equilibrium due to bending moments resulting from gravity loads and can affect the post-cracking gravity capacity of hollow-core floors.

The location of the mean cracking profile was defined as the distance between the intersection of the mean crack with the bottom of the floor unit and the face of the support at the end of the unit, as this is where the crack can be visibly observed in damaged structures where only the soffit of the units is exposed. Specimens subjected to cyclic loading upon cracking and specimens with a shear span of 3.5*d* were not included in Fig. 15 and 16. Only the monotonically loaded test units were included in Fig. 15 and 16, as these results are more relevant to post-earthquake gravity load-carrying capacity.

CONCLUSIONS

This study presented the results of an experimental program that examined the post-cracking residual shear capacity of 12 full-scale 200 mm (7.9 in.) deep extruded precast concrete hollow-core floor units. The parameters investigated in this study included the support seating length, shear span-depth ratios, and loading protocols. The tested floor units were loaded to deformations well beyond the peak shear strength to investigate the post-cracking shear response. To quantify the reduction in shear capacity of cracked hollow-core units, the floor units' recorded responses were compared to the estimated uncracked section capacity calculated by design standards. Based on the test results and the observations discussed in this paper, the following conclusions were drawn:

1. Cracking of the unreinforced webs of the precast hollow-core floor unit reduced the residual gravity load-carrying capacity by at least 60% of its ultimate strength, and in some cases, no reliable residual capacity could be maintained.

2. Shorter support seating lengths significantly reduced the gravity load-carrying capacity of hollow-core floor units with web cracking. Specimens with a 30 mm (1.2 in.) support seating length had no stable post-cracking residual shear capacity. Meanwhile, specimens with 100 and 50 mm (4 and 2 in.) support seating lengths maintained a post-web-cracking residual strength of almost 100% and 50% of the calculated uncracked section capacity, respectively.

3. The poor residual capacity of units with short seating lengths (<50 mm [2 in.]) is critical for post-earthquake structural assessment, as many existing hollow-core floor units have been installed with less than 50 mm (2 in.) seating and are expected to sustain web cracking following an earthquake. Therefore, hollow-core floor units that have sustained web cracking should be supported immediately and retrofitted or repaired after an earthquake.

4. The cracking location affects the gravity load-carrying capacity of hollow-core floor units with web cracking. Generally, the further the web cracking was from the support, the greater the hollow-core unit residual capacity. Therefore, transverse cracking observed on the soffit in existing floor units away from the support (>200 mm [7.9 in.]) is less of an immediate concern for repair and retrofit purposes. However, careful borescoping is recommended to ensure there are no web cracks closer to the support that are not visible on the soffit.

5. Cyclic loading, causing repeated opening and closing of the web cracks, can substantially degrade the hollow-core floor units' ability to resist gravity loads, leading to a complete loss of shear capacity. Further investigations for units under cyclic conditions that are more consistent with those expected during earthquakes are recommended to confirm this conclusion.

The results from the experimental campaign discussed in this study provide a basis for quantifying the risk posed by web-cracked hollow-core floor units in areas of high seismicity and provide insights that can aid in quantifying whether cracked precast hollow-core floor units meet life safety requirements following an earthquake. This information can be used to develop guidance for post-earthquake structural assessments.

AUTHOR BIOS

Mohamed Mostafa *is a PhD Candidate at the University of Auckland, Auckland, New Zealand. His research interests include seismic assessment, strengthening, and design of reinforced concrete structures.*

ACI member **Richard S. Henry** *is an Associate Professor at the University of Auckland, where he received his BE and PhD. He is a member of ACI Subcommittee 318-H, Seismic Provisions. His research interests include the seismic design of reinforced and precast concrete structures.*

Kenneth J. Elwood, *FACI, is a Professor at the University of Auckland. He received his BASc from The University of British Columbia, Vancouver, BC, Canada; his MS from the University of Illinois Urbana-Champaign, Champaign, IL; and his PhD from the University of California, Berkeley, Berkeley, CA. He is a member of ACI Committee 369, Seismic Repair and Rehabilitation. His research interests include the seismic assessment of existing concrete buildings.*

ACKNOWLEDGMENTS

This investigation was supported by the Building Research Association of New Zealand (BRANZ) under Grant No. LR13069 and partly funded through the ReCast Floors project through the University of Auckland, sponsored by BRANZ, EQC (now the Natural Hazards Commission Toka Tū Ake), and Concrete NZ. In addition, this project was partially supported by QuakeCoRE, a New Zealand Tertiary Education Commission-funded Centre. The support received is gratefully acknowledged.

REFERENCES

1. *fib*, "Special Design Considerations for Precast Prestressed Hollow Core Floors: Guide to Good Practice," *fib* Bulletin No. 6, International Federation for Structural Concrete, Lausanne, Switzerland, 2000, 180 pp.

2. *fib*, "Seismic Design of Precast Concrete Building Structures: State-of-Art Report," *fib* Bulletin No. 27, International Federation for Structural Concrete, Lausanne, Switzerland, 2003, 262 pp.

3. Park, R., "A Perspective on the Seismic Design of Precast Concrete Structures in New Zealand," *PCI Journal*, V. 40, No. 3, May-June 1995, pp. 40-60. doi: 10.15554/pcij.05011995.40.60

4. Mostafa, M.; Hogan, L.; and Elwood, K. J., "Seismic Performance of Hollow-Core Floors with Modern Detailing: A Case Study," *Journal of the Structural Engineering Society of New Zealand Inc.*, V. 35, No. 1, Apr. 2022, pp. 86-100.

5. Büker, F.; Parr, M.; De Francesco, G.; Hogan, L. S.; Bull, D. K.; Elwood, K. J.; Liu, A.; and Sullivan, T. J., "Seismic Damage Observations of Precast Hollow-Core Floors from Two Full-Scale Super-Assembly Tests," *Journal of the Structural Engineering Society of New Zealand Inc.*, V. 35, No. 1, Apr. 2022, pp. 125-147.

6. Mostafa, M.; Hogan, L.; Stephens, M. T.; Olsen, M. J.; and Elwood, K. J., "A Detailed Damage Investigation of an Instrumented Ductile Reinforced Concrete Building Following the M-7.8 Kaikoura Earthquake," *Earthquake Spectra*, V. 40, No. 3, Aug. 2024, pp. 2179-2209. doi: 10.1177/87552930231218750

7. Corney, S. R.; Puranam, A. Y.; Elwood, K. J.; Henry, R. S.; and Bull, D., "Seismic Performance of Precast Hollow-Core Floors: Part 1—Experimental Data," *ACI Structural Journal*, V. 118, No. 5, Sept. 2021, pp. 49-63. doi: 10.14359/51732821

8. Puranam, A. Y.; Corney, S. R.; Elwood, K. J.; Henry, R. S.; and Bull, D., "Seismic Performance of Precast Hollow-Core Floors: Part 2—Assessment of Existing Buildings," *ACI Structural Journal*, V. 118, No. 5, Sept. 2021, pp. 65-77.

9. Liew, H. Y., "Performance of Hollowcore Floor Seating Connection Details," master's thesis, University of Canterbury, Christchurch, New Zealand, 2004, 140 pp.

10. Jensen, J., "The Seismic Behaviour of Existing Hollowcore Seating Connections Pre and Post Retrofit," master's thesis, University of Canterbury, Christchurch, New Zealand, 2006, 292 pp.

11. Woods, L. J., "The Significance of Negative Bending Moments in the Seismic Performance of Hollow-Core Flooring," master's thesis, University of Canterbury, Christchurch, New Zealand, 2008, 294 pp.

12. Walraven, J. C., and Mercx, W. P. M., "The Bearing Capacity of Prestressed Hollow Core Slabs," *HERON*, V. 28, No. 3, 1983, pp. 1-46.

13. Yang, L., "Design of Prestressed Hollow Core Slabs with Reference to Web Shear Failure," *Journal of Structural Engineering*, ASCE, V. 120, No. 9, Sept. 1994, pp. 2675-2696. doi: 10.1061/(ASCE)0733-9445(1994)120:9(2675)

14. Pisanty, A., "The Shear Strength of Extruded Hollow-Core Slabs," *Materials and Structures*, V. 25, No. 4, May 1992, pp. 224-230. doi: 10.1007/BF02473067

15. Tawadrous, R., and Morcous, G., "Shear Strength of Deep Hollow-Core Slabs," *ACI Structural Journal*, V. 115, No. 3, May 2018, pp. 699-709.

16. Truderung, K. A.; El-Ragaby, A.; Mady, M.; and El-Salakawy, E., "Shear Capacity of Dry-Cast Extruded Precast, Prestressed Concrete Hollow-Core Slabs," *PCI Journal*, V. 64, No. 4, July-Aug. 2019, pp. 71-83. doi: 10.15554/pcij64.4-01

17. de Lima Araújo, D.; Sales, M. W. R.; Silva, R. P. M.; Antunes, C. F. M.; and Ferreira, M. A., "Shear Strength of Prestressed 160 mm Deep Hollow Core Slabs," *Engineering Structures*, V. 218, Sept. 2020, Article No. 110723. doi: 10.1016/j.engstruct.2020.110723

18. Jonsson, E., "Shear Capacity of Prestressed Extruded Hollow-Core Slabs," *Nordic Concrete Research*, V. 7, 1988, pp. 167-187.

19. Hernández, E.; Matthews, B.; Granello, G.; and Palermo, A., "Post-Cracking Web-Shear Response of Hollow Core Slabs with Low Steel Fiber-Volume Fractions," *ACI Structural Journal*, V. 119, No. 6, Nov. 2022, pp. 53-66.

20. NZSEE, SESOC, and Concrete NZ Learned Society, "Technical Proposal to Revise the Engineering Assessment Guidelines: Part C—Section C5: Concrete Buildings," New Zealand Society for Earthquake Engineering, Wellington, New Zealand, 2018, 252 pp.

21. ACI Committee 318, "Building Code Requirements for Structural Concrete (ACI 318-19) and Commentary (ACI 318R-19) (Reapproved 2022)," American Concrete Institute, Farmington Hills, MI, 2019, 624 pp.

22. BS EN 1168:2005+A3:2011, "Precast Concrete Products — Hollow Core Slabs," British Standards Institution, London, UK, 2005, 84 pp.

23. NZS 3101.1&2:2006, "Concrete Structures Standard," Standards New Zealand, Wellington, New Zealand, 2017, 754 pp.

24. Fenwick, R. C., and Megget, L. M., "Elongation and Load Deflection Characteristics of Reinforced Concrete Members Containing Plastic Hinges," *Bulletin of the New Zealand Society for Earthquake Engineering*, V. 26, No. 1, 1993, pp. 28-41. doi: 10.5459/bnzsee.26.1.28-41

25. Fenwick, R.; Bull, D.; and Gardiner, D., "Assessment of Hollow-Core Floors for Seismic Performance," Research Report 2010-02, University of Canterbury, Christchurch, New Zealand, 2010, 164 pp.

26. Matthews, J., "Hollow-Core Floor Slab Performance Following a Severe Earthquake," PhD thesis, University of Canterbury, Christchurch, New Zealand, 2004, 523 pp.

27. Lindsay, R., "Experiments on the Seismic Performance of Hollow-Core Floor Systems in Precast Concrete Buildings," master's thesis, University of Canterbury, Christchurch, New Zealand, 2004, 340 pp.

28. MacPherson, C., "Seismic Performance and Forensic Analysis of a Precast Concrete Hollow-Core Floor Super-Assemblage," master's thesis, University of Canterbury, Christchurch, New Zealand, 2005, 342 pp.

29. Puranam, A.; Filippova, O.; Pastor-Paz, J.; Stephens, M.; Elwood, K. J.; Ismail, N.; Noy, I.; and Opabola, E., "A Detailed Inventory of Medium to High-Rise Buildings in Wellington's Central Business District," *Bulletin of the New Zealand Society for Earthquake Engineering*, V. 52, No. 4, 2019, pp. 172-192. doi: 10.5459/bnzsee.52.4.172-192

30. *fib*, "Quality Assurance of Hollow Core Slab Floors," International Federation for Structural Concrete, Lausanne, Switzerland, 1992, 30 pp.

31. NZS 3112.2:1986, "Methods of Test for Concrete: Part 2: Tests Relating to the Determination of Strength of Concrete," Standards New Zealand, Wellington, New Zealand, 1986, 22 pp.

32. ASTM C496/C496M-17, "Standard Test Method for Splitting Tensile Strength of Cylindrical Concrete Specimens," ASTM International, West Conshohocken, PA, 2017, 5 pp.

33. ASTM C78-09, "Standard Test Method for Flexural Strength of Concrete (Using Simple Beam with Third-Point Loading)," ASTM International, West Conshohocken, PA, 2009, 4 pp.

34. Büker, F., "Experimental Evaluation of the Seismic Performance of Hollow-Core Floors and Retrofits," PhD thesis, University of Auckland, Auckland, New Zealand, 2023, 491 pp.

35. Hawkins, N. M.; Kuchma, D. A.; Mast, R. F.; Marsh, M. L.; and Reineck, K.-H., "Simplified Shear Design of Structural Concrete Members," NCHRP Report 549, Transportation Research Board, Washington, DC, 2005, 64 pp.

36. Henry, R. S.; Dizhur, D.; Elwood, K. J.; Hare, J.; and Brunsdon, D., "Damage to Concrete Buildings With Precast Floors During The 2016 Kaikoura Earthquake," *Bulletin of the New Zealand Society for Earthquake Engineering*, V. 50, No. 2, 2017, pp. 174-186.

NOTES:

ACI STRUCTURAL JOURNAL TECHNICAL PAPER

Title No. 123-S61

Comprehensive Multi-Metric Comparison of One-Way Shear Models for Reinforced Concrete Beams without Shear Reinforcement

by Amir Mofidi, Sara Mirzabagheri, Kourosh Nasrollahzadeh, and Shahryar Rahnamayan

The ACI 318-19 provisions for one-way shear strength (V_c) in reinforced concrete (RC) members were majorly modified for the first time since 1963. The ACI 318-19 equation addresses certain previously identified limitations of the well-known $V_c = 0.17\lambda\sqrt{f_c'}b_w d$ equation for members without shear steel reinforcement, incorporating factors such as size effect and the influence of longitudinal reinforcement ratio. This study takes a multi-metric approach to evaluate the accuracy and safety of ACI 318-19's one-way shear relationship for RC members without stirrups. ACI 318-19 predictions are compared against those of its predecessor and other state-of-the-art models, using a database of experimental results gathered by ACI Committee 445 and DAfStb. This study shows that the ACI 318-19 equation significantly improved accuracy and safety over ACI 318-14 provisions. One-way shear predictions of ACI 318-19 for RC members without shear reinforcement are generally comparable to existing models, though certain aspects may benefit from continued development and refinement.

Keywords: accuracy; building code; multi-metric comparative study; one-way shear; Pareto analysis; safety; statistical tests.

INTRODUCTION

Significant concerns related to the safety and accuracy of ACI 318-14 one-way shear relationship prompted the development of a new one-way shear design model for reinforced concrete (RC) beams without stirrups for ACI 318-19 (Belarbi et al. 2017; Frosch et al. 2017). These concerns were primarily related to the size effect, the differing one-way shear failure mechanisms in RC beams with and without steel stirrups, and the unconservative predictions for lightly reinforced members without transverse shear reinforcement (Belarbi et al. 2017; Reineck 2017). The one-way shear equation of ACI 318-19 for RC beams without transverse reinforcement is developed to address these concerns. In addition, the effect of axial stress on V_c is added to the basic one-way shear relationship in ACI 318-19. In parallel with using the newly added one-way shear equation for members with and without shear reinforcement, the previously used expression in ACI 318-14, $V_c = 0.17\lambda\sqrt{f_c'}\,b_w d$ (in SI units), may still be used in members with the minimum shear reinforcement. Meanwhile, the one-way shear relationship for prestressed concrete (PC) members remained unchanged in ACI 318-19.

While many researchers reported that the ACI 318-14 one-way shear equation was not producing safe or accurate results, particularly in the aforementioned cases (for example, Belarbi et al. [2017]), the extent of ACI 318-19 one-way shear equation's impact on accuracy and safety still warrants further investigation. To date, no published comprehensive, precise, and transparent study has thoroughly compared the accuracy and safety of existing and past ACI one-way shear equations with other state-of-the-art models in literature.

Kuchma et al. (2019) introduced the new ACI 318-19 one-way shear equation for non-prestressed concrete members and conducted a statistical evaluation comparing the accuracy and safety of the new provisions against those in ACI 318-14. However, their study focused on the ACI 318 past and present provisions and did not include other one-way shear models in literature. Meanwhile, until now, most comparative studies on different one-way shear strength models—for example, Park and Choi (2017), Cladera et al. (2017), Frosch et al. (2017), and Kuchma et al. (2019)—among others, are based on comparing the mean and coefficient of variation (CoV) of the strength ratio (SR) equal to $V_{c\ exp}/V_{c\ cal}$ ratio, where $V_{c\ exp}$ is the experimental shear strength and $V_{c\ cal}$ is the predicted shear strength. While this approach offers insight into whether the model tends to overestimate or underestimate predictions on average and highlights variations in the predictions, it has its limitations. This approach does not offer an ample and comprehensive statistical evaluation of the overall accuracy and safety of the predicted results.

It is important to note that CoV should be used with caution when the data does not follow a normal distribution, as outliers and skewness can distort its interpretation (Arachchige et al. 2020). As can be seen in Fig. 1, when testing the SR distribution for ACI 318-19 predictions, it is evident that the data distribution is not normal. When applying the Shapiro-Wilk normality test (Shapiro and Wilk 1965) on the ACI 318-19 predictions, the calculated probability value (P-value) is much smaller than 0.05, which rejects the null hypothesis that the data follow a normal distribution. Figure 1 shows that the data set has a moderate positive skewness with a longer right tail and includes a few high outliers. The data set has positive skewness, meaning many values cluster around the lower end, with a long right tail. However, CoV expresses variability relative to the the mean, assuming the mean is a relevant central reference point, which is not true in skewed distributions. This means that the produced CoV for one-way shear models may be misleading.

ACI Structural Journal, V. 123, No. 3, May 2026.
MS No. S-2025-121.R3, doi: 10.14359/51749319, received August 25, 2025, and reviewed under Institute publication policies. Copyright © 2026, American Concrete Institute. All rights reserved, including the making of copies unless permission is obtained from the copyright proprietors. Pertinent discussion including author's closure, if any, will be published ten months from this journal's date if the discussion is received within four months of the paper's print publication.

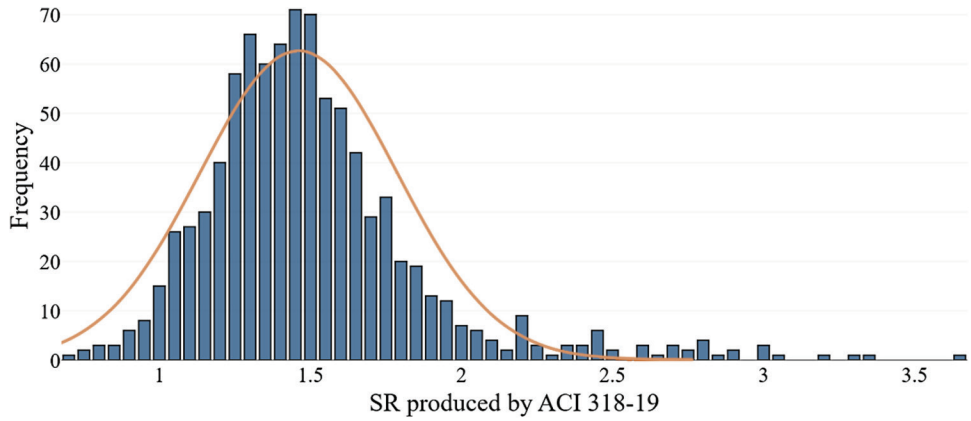

Fig. 1—SR distribution for ACI 318-19 predictions versus normal distribution curve.

Meanwhile, in design equations, the mean value is intentionally set higher than one by the model developers as a safety measure. Such safety margins may obscure different forms of prediction model errors, including systematic (bias) errors and model calibration errors, among others. Systematic errors are observed where the model consistently overpredicts or underpredicts across all test cases. A safety margin can mask underpredictions, making a biased model appear more reliable. Model calibration errors can be concealed by incorporating additional safety margins, resulting in an apparent improvement in the model's performance. A model that does not correctly capture one-way shear behavior, might still pass validation if a conservative correction factor is included in the model. Meanwhile, a model may be overfitted to a specific data set, leading to poor generalization in real-world applications.

To this end, a multi-metric approach, based on several relevant statistical metrics and tests, that provides a comprehensive understanding of the existing one-way shear models' performance, error distribution, outlier effects, and variation explanation is essential. Aguilar et al. (2022) provided a multi-metric approach in comparing the results of the ACI 318-19 one-way shear relationship with those of the ACI 318-14 code, in addition to six proposals that have been submitted for possible inclusion in ACI 318-19. Aguilar et al. (2022) highlighted the limitations of relying exclusively on mean and CoV, and incorporate additional measures such as P_{5th}, percentage of unconservative predictions, R^2, root mean square error (RMSE), Kolmogorov-Smirnov (D_{ks}, D_{kss}) distances, and percentages of acceptable predictions. While their chosen statistical approach was sound, their reproduced predictions of certain proposed models did not match those reported by the model developers in the literature at times. For example, the reproduced CoV of SR by Aguilar et al. (2022) of RC members without shear reinforcement for the Cladera et al. (2017) model was 0.26. However, the reported CoV for these members in Cladera et al. (2017) was equal to 0.17. Similarly, the reproduced CoV by Aguilar et al. (2022) of RC members without shear reinforcement for Park and Choi (2017) model was 0.23. However, the reported CoV for such members in Park and Choi (2017) was equal to 0.18.

In the safety evaluation of shear strength prediction models for concrete members, Collins (2001) proposed the demerit points classification (DPC) approach, which has been adopted by other researchers such as Perumalla and Laskar (2020) to examine the safety performance of one-way shear design equations. The DPC approach classifies SR distribution into seven predefined safety intervals: SR < 0.5 (extremely dangerous), 0.5 to 0.65 (dangerous), 0.65 to 0.85 (low safety), 0.85 to 1.30 (approximately safe), 1.30 to 2.00 (conservative), and SR > 2.00 (extremely conservative). Each class is assigned a certain demerit point value equal to 10, 5, 2, 0, 1, and 2, respectively. The overall safety rating of a model is then computed as a weighted average of the percentages of predictions falling within each class, multiplied by their respective demerit points. This approach highlights the importance of placing higher penalties on unsafe and over conservative predictions compared to safe predictions. However, this method has some limitations including: 1) abrupt changes in scoring at the boundary of classes lead to increased sensitivity to small changes in SR near the boundaries; and 2) SR predictions from 0.85 to 1.0 are not penalized despite such predictions may indicate unsafe performance.

In this investigation, a comprehensive multi-metric comparative (CMMC) study is provided that evaluates the accuracy and safety of ACI 318-19 one-way shear equation for RC members without shear reinforcement versus the state-of-the-art in literature. The featured models include ACI 318-19; ACI 318-14 simplified; ACI 318-14 detailed; Eurocode 2 (2005); CSA A23.3:2024; JSCE (2007); Choi and Park (2023) model proposed for KDS 14 20 22; and one-way shear models such as Tureyen and Frosch (2003), Cladera et al. (2017), Reineck (2017), and Li et al. (2017). These models will hereafter be referred to as ACI 318-19, ACI 318-14S, ACI 318-14D, EC2, CSA, JSCE, PCH, TFR, CLD, RNK, and LI, respectively.

RESEARCH SIGNIFICANCE

A new comprehensive multi-metric comparative analysis is conducted on one-way shear relationships in design standard codes, including ACI 318-19, ACI 318-14S, ACI 318-14D, and eight additional one-way shear design models in literature. The study highlights improvements in the ACI 318-19 one-way shear relation for RC beams without shear reinforcement compared to those of ACI 318-14 and evaluates the accuracy and safety levels of the ACI 318-19 model relative to existing standard codes and models.

MULTI-METRIC COMPARATIVE STUDY

The novelty of this study lies in its systematic ranking of recognized one-way shear strength models based on the newly proposed CMMC methodology. Unlike the previous comparative studies, which did not provide a methodology to rank the prediction models and did not assess the accuracy of the reproduced model predictions of the investigated one-way shear relations, this study provides a logical and transparent methodology for comparison of the existing models. The predictions of the studied models were replicated and confirmed independently using original sources and, where possible, directly confirmed with the original model authors, assuring the validity of comparative results. Two rounds of CMMC investigation were adopted to analyze the selected one-way shear models. In each round, the models were compared in three categories: accuracy, safety, and statistical tests while ranked with respect to several performance indicators. A detailed description of the newly proposed methodology, scoring system, and applied statistical measures is provided in "Methodology of Multi-Metric Comparative Study" section.

DATABASE FOR ONE-WAY SHEAR STRENGTH OF RC BEAMS

In the last decades, ACI Committee 445, in collaboration with DAfStb, has gathered inclusive refined databases for the shear tests on structural concrete members. Details of the extensive work on data gathering, filtration, and presentation of the data sets have been provided in Reineck et al. (2013). For consistency in the experimental test data used, the ACI-DAfStb database of 892 shear tests of slender reinforced concrete beams without stirrups has been used in this research, which comprises rigorous filtering criteria developed by ACI Committee 445 and DAfStb. The database has not been modified to avoid introducing bias. The scope of this study is limited to the evaluation and comparison of shear-strength prediction models, without manipulation of the reference database.

In addition, to evaluate the possibility of uneven distribution due to using different testing equipment and loading protocols, a statistical analysis of database distribution was conducted. The database is comprised of 102 separate studies, in the form of published articles, contributing a total of 892 specimens. The mean number of specimens per study is 8.75, with a standard deviation of 10.0. Notably, 88 out of 102 studies (86.3%) fall within one standard deviation of the mean, which indicates a rather well-balanced data contribution. The largest individual contribution consists of 64 specimens, while the smallest is 1; however, such extremes are uncommon.

Regarding specimen sizes, it is noteworthy that the available test data may overrepresent beams with small depths relative to those found in real structures. As can be seen in Fig. 2, 33% of the beams in the data set have an effective depth smaller than 250 mm. To address this concern, at the end of Round 1 of the CMMC study, a comparative study was conducted on accuracy and safety of the models using only 596 RC beams with $d \geq 250$ mm. Similarly, to prevent failure in flexure, laboratory specimens often feature higher longitudinal reinforcement ratios than real-life RC beams (Fig. 2). In addition, the available experimental data are dominated by rectangular sections (93% rectangular cross sections), while T- and I-shaped beams are more common in real life. Figure 2 presents the distribution of d, f_c', ρ_w, and b_w in the database of RC beams without steel stirrups under point load.

METHODOLOGY OF MULTI-METRIC COMPARATIVE STUDY

As mentioned earlier, two rounds of CMMC studies were conducted on the model predictions of one-way shear models under investigation. Similar comparative studies were conducted on each round with the following multi-metric comparative study configuration.

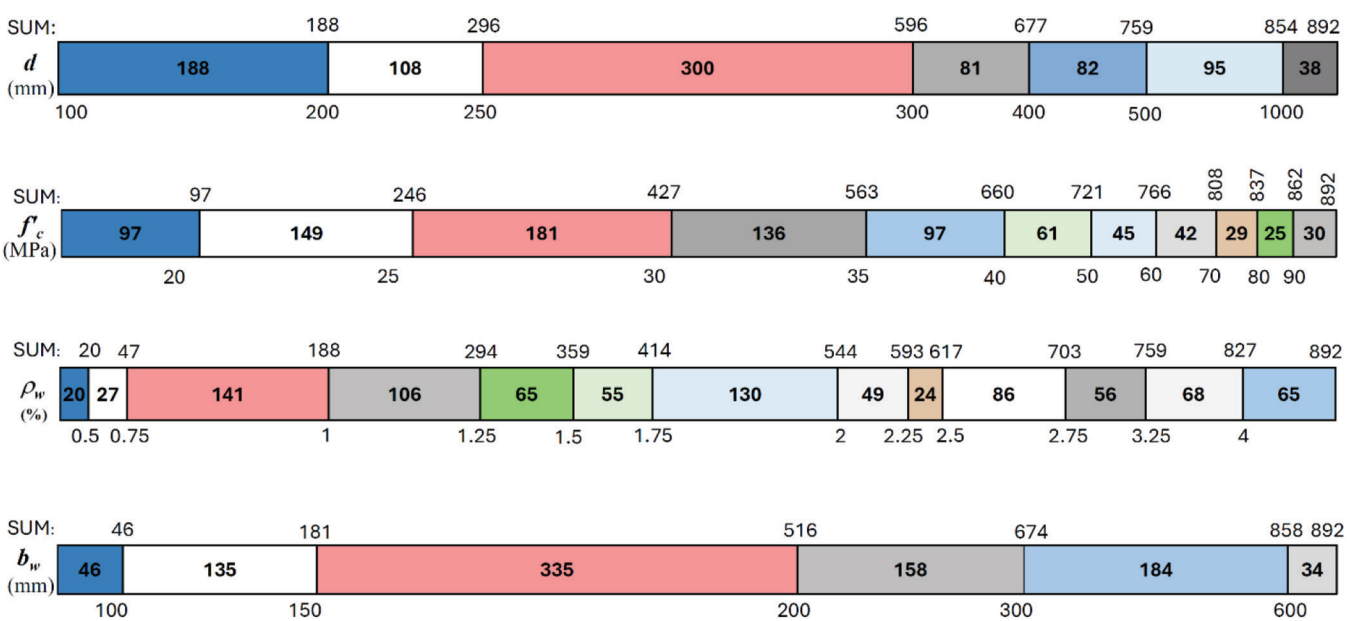

Fig. 2—Distribution of beam parameters in 892-member database of RC beams without steel stirrups under point load.

Multi-metric comparative study configuration

In the first step of the proposed CMMC methodology, the authors established the comparative study configuration, which remained consistent throughout the study. To achieve this, different statistical metrics, tests, and analyses were carefully selected to maximize statistical and safety insights while minimizing overlap among the metrics. These were then divided into three comparison categories, including: 1) accuracy assessment; 2) safety assessment; and 3) statistical tests. The predictions were then ranked for each metric in each comparison category and received scores based on their ranks on each metric. A performance-based comparison was conducted in terms of accuracy (scores gathered in category 1), safety (scores gathered in category 2), combined accuracy and safety (accumulated scores in categories 1 and 2), and overall performance (overall scores received in categories 1 to 3). Based on the results of each category, a Pareto front analysis (Ibrahim et al. 2024) was conducted to classify the models into hierarchical club levels. Lastly, an independent bottom half statistical analysis from the previously mentioned comparative study steps was conducted on the model predictions. Both rounds of comparative studies benefited from an almost similar methodology which included the aforementioned three comparison categories, scoring system, and performance-based comparison, except that, in Round 2 presented in Appendix B*, the safety measures for all models were unified to the same level. The Pareto front and bottom half analysis was only conducted in Round 1.

It should be noted that no weighting was explicitly given to the evaluation metrics in this study. This is because the underlying SR data are not normally distributed, and the use of the raw magnitudes of each metric in the scoring framework might bias the comparisons. Instead, a systematic equal weight ranking scheme was thus adopted, with each measure contributing equally to the total score. Models were scored linearly by rank, with Rank 1 assigned 11 points and Rank 11 assigned one point. This approach places greater emphasis on relative performance than on absolute values and ensures that no single metric has a disproportionate influence on the overall assessment. Assigning weights affects scores in scalar methods but does not influence ranking or Pareto dominance, as dominance is determined through metric-by-metric comparison rather than any weighted sum.

Chosen metrics for each comparison category are introduced as follows:

Accuracy assessment—As mentioned earlier, the use of mean and CoV values of the produced SRs by the prediction models might not provide complete insight into accuracy of the prediction models. In this article, in addition to the deviation-based metrics (for example, CoV), error-based metrics and correlation-based metrics were also used for a more thorough comparative study.

Deviation-based metrics: CoV has been conventionally employed to assess the variability and consistency among the SR results. CoV, as the ratio of standard deviation over mean, treats all deviations relative to mean in the same way (Rainio et al. 2024). It does not penalize larger errors more than smaller errors, beyond what is inherent in the standard deviation calculation, unlike metrics such as mean absolute error (MAE) and normalized root mean square error (NRMSE).

Error-based metrics: The chosen error-based metrics in this study are as follows:

1. MAE is a metric that calculates the average magnitude of the absolute errors between the predicted and actual values, which measures actual error rather than a simple ratio, providing an absolute error value. MAE is calculated as follows

$$\text{MAE} = \frac{1}{n}\sum\left|V_{c\,exp} - V_{c\,cal}\right| \tag{1}$$

where n is the number of specimens in the data set.

2. NRMSE provides a standardized way to evaluate model performance across different data sets. NRMSE penalizes large errors more heavily than MAE because it squares the errors before averaging, thereby amplifying the impact of larger deviations relative to smaller ones. NRMSE is calculated as follows

$$\text{NRMSE} = \frac{\sqrt{\dfrac{\Sigma\left(V_{c\,exp} - V_{c\,cal}\right)^2}{n}}}{\overline{V}_{c\,exp}} \tag{2}$$

where $\overline{V}_{c\,exp}$ is the mean experimental shear strength of concrete specimens in the data set.

3. Root mean squared logarithmic error (RMSLE) measures the relative error between predicted and actual values on a logarithmic scale. RMSLE is used when the target variable is skewed (Hyndman and Athanasopoulos 2018). RMSLE is calculated using Eq. (3) as follows

$$\text{RMSLE} = \sqrt{\frac{1}{n}\sum\left(\log(V_{c\,cal}+1) - \log(V_{c\,exp}+1)\right)^2} \tag{3}$$

4. Mean absolute percentage error (MAPE) quantifies the accuracy of a prediction model by measuring the average percentage deviation of the predicted values from the actual values. MAPE normalizes errors by actual values, making it useful when comparing data sets of different scales. MAPE in percentage is calculated using Eq. (4).

$$\text{MAPE} = \frac{100}{n}\sum\left|\frac{V_{c\,exp} - V_{c\,cal}}{V_{c\,exp}}\right| \tag{4}$$

Correlation-based metrics: The coefficient of efficiency E has been widely used to evaluate the performance of prediction models. Nash and Sutcliffe (1970) defined E as a replacement for the coefficient of determination (R^2), which is insensitive to additive and proportional differences between the model predictions and experimental values (Willmott 1984). It should be noted that E ranges from minus infinity to 1.0, with higher values indicating better agreement and can be calculated as follows

*The Appendix is available at **www.concrete.org/publications** in PDF format, appended to the online version of the published paper. It is also available in hard copy from ACI headquarters for a fee equal to the cost of reproduction plus handling at the time of the request.

$$E = 1.0 - \frac{\sum(V_{c\,exp} - V_{c\,cal})^2}{\sum(V_{c\,exp} - \overline{V}_{c\,exp})^2} \quad (5)$$

The index of agreement (d) provides a refined normalized measure of model fit by considering both systematic and unsystematic errors. This index ranges between 0 and 1, where a value of 1 signifies a perfect match between model predictions and observed data. Similar to NRMSE, the d index penalizes large errors more than small errors.

$$d = 1.0 - \frac{\sum(V_{c\,exp} - V_{c\,cal})^2}{\sum(|V_{c\,exp} - \overline{V}_{c\,exp}| + |V_{c\,cal} - \overline{V}_{c\,exp}|)^2} \quad (6)$$

Safety assessment—As mentioned earlier, the predictions for one-way shear models need to strike a balance between safety and accuracy to provide reliable results (Reineck 2017). During the accuracy assessment, this study aimed to evaluate the models solely based on their prediction errors. However, despite these efforts, the safer models may still be penalized for the intentionally included safety margins in their predictions. To credit the models for their safety, a separate safety assessment was conducted in this study to compare the models exclusively based on their safety performance. The following safety-related statistical measures were used in this study as follows:

Mean of SR: The mean is a safety metric in the safety assessment by considering the models producing higher means as safer prediction models.

Failure probability: This metric is calculated based on the percentage of model predictions of each model leading to SR < 1 across all predictions for the test specimens in the database.

Probability of failure of design using 0.75 reduction factor: This metric evaluates the percentage of predictions with SR less than 0.75 (ACI 318's φ factor for shear).

Percentage of suitable predictions (PSP): This metric measures the percentage of model predictions with an SR falling between 1 and 1.25. A higher PSP value signifies a model's ability to balance safety and efficiency.

P_{5th}: This is a statistical measure that represents the value below which 5% of the data in a data set falls. A higher P_{5th} in Model A compared to Model B may suggest that Model A predictions are more conservative than Model B.

Statistical tests—In addition to the aforementioned statistical accuracy and safety metrics, separate statistical tests have been considered to provide a more in-depth comparative analysis.

Two-sample Kolmogorov-Smirnov test (KS test): This test is a non-parametric statistical test used to compare whether two independent data sets (experimental results versus predictions in this study) come from the same underlying distribution (Simard and L'Ecuyer 2011). The KS test computes the maximum absolute difference (D) between the cumulative distribution functions (CDFs) of the experimental and predicted data sets as follows

$$D = \max\left|CDF(V_{c\,exp}) - CDF(V_{c\,cal})\right| \quad (7)$$

A smaller D value in Model A than that of Model B, when both are compared to the same experimental results, suggests that the experimental and predicted distributions in Model A are closer than those in Model B.

Friedman Mean Rank Analysis: This approach, developed by Milton Friedman (Friedman 1937), is often used in model comparisons on data sets that do not follow a normal distribution when the goal is to evaluate relative performance across multiple prediction models without testing for statistical significance. As a part of this method, ranks are assigned separately to all model predictions for each test specimen based on the proximity of the prediction to the experimental result. The mean ranks over all specimens are then computed for each model to assess which model performs best on average across all specimens. The model with the lowest mean rank is considered superior based on mean rank analysis.

Pareto front analysis: Using the results gathered in the three categories of comparison studies, a Pareto front analysis is conducted in Round 1. This method is a structured way to classify prediction models based on multiple competing criteria. Instead of selecting just one best model, it groups models into performance clubs, ensuring that the highest-ranked models in the top club are not dominated in all categories by any other model. The models are ranked based on accuracy, safety, and statistical tests comparison, and then grouped into performance tiers using a non-dominated sorting approach. Models that were not outperformed (dominated) by any other model in all three criteria were placed in the top club. The remaining models are re-evaluated, and if a model was dominated across all three criteria by another remaining model, it was placed in a lower club. This process continued iteratively, ensuring that each club contained models that were only dominated by those in higher clubs but not by others within the same or lower levels.

Bottom-half statistical analysis: An independent bottom-half statistical comparison is performed in Round 1 to evaluate model predictions in the lower half of the SR distribution, where the risks of failure are higher. In this process, the cumulative probability distribution was developed for each model by calculating the CDF of the experimental data and each model's predictions. An optimizer was used to adjust the model parameters, minimizing the difference between the model's predicted CDF and the observed CDF. Once the optimization process was completed, the bottom half of the distribution was analyzed, and the bottom half mean and CoV were calculated as a measure of the model's consistency and accuracy.

In the CMMC methodology, statistical measures were chosen carefully to avoid overlapping while providing a complete comparative framework. Each statistical measure was chosen to capture a specific aspect of model performance. In this regard, CoV captures consistency in prediction, while MAE and NRMSE quantify absolute errors, with NRMSE putting greater emphasis on large deviations. RMSLE and MAPE provide scale-independent and relative measures of error, respectively, beneficial for different beam sizes.

Table 1—List of used statistical metrics, tests, and analyses in this study

Metric/analysis	Category
Coefficient of variation (CoV)	Accuracy – Deviation-based
Mean absolute error (MAE)	Accuracy – Error-based
Normalized root mean square error (NRMSE)	Accuracy – Error-based
Root mean squared logarithmic error (RMSLE)	Accuracy – Error-based
Mean absolute percentage error (MAPE)	Accuracy – Error-based
Efficiency coefficient (E)	Accuracy – Correlation-based
Index of agreement (d)	Accuracy – Correlation-based
Mean strength ratio (SR)	Safety – Central tendency
Fifth percentile (P_{5th})	Safety – Lower-tail
Failure probability (SR < 1)	Safety – Reliability
Probability SR < 0.75	Safety – Reliability
Percentage of suitable predictions (PSP)	Safety – Balanced measure
Kolmogorov-Smirnov (KS) test	Statistical test – Distributional
Friedman rank analysis	Statistical test – Ranking
Pareto front analysis	Statistical evaluation – Hierarchical club levels
Bottom-half analysis	Statistical evaluation – Lower-bound

Meanwhile, E measures accuracy of predictions to reduce error in comparison with the observed mean, and d measures how prediction and observation agreement compare to potential error. For safety, mean SR, P_{5th}, failure probability, and PSP quantify conservatism or underprediction risks in different manners. Finally, the KS test and Friedman rank compare distributional agreement and rank models specimen-by-specimen, respectively. Together, with Pareto front and bottom-half statistical analyses, they offer a well-rounded measure of accuracy, safety, and statistical consistency beyond the conventional mean and CoV approach.

Table 1 provides a summary of all the accuracy and safety metrics, and statistical tests and analyses used in this study.

One-way shear model result reproduction

Following the selection of the studied models and establishment of the comparative study methodology, the selected model predictions were reproduced by the authors. The results were subsequently compared with existing model predictions reported in the literature. In cases where discrepancies were identified between the reproduced predictions in this study and those found in literature, the model developers were contacted to help clarify the reasons behind these differences. This process was iterated until the discrepancies were resolved and the authors could confirm the reported statistics of each model in the literature. Once accurate model predictions were established, the multi-metric comparison steps were conducted as outlined earlier. Details of the model equations are provided in Appendix A[†]. A flowchart summarizing the steps taken in this study is presented in Fig. 3.

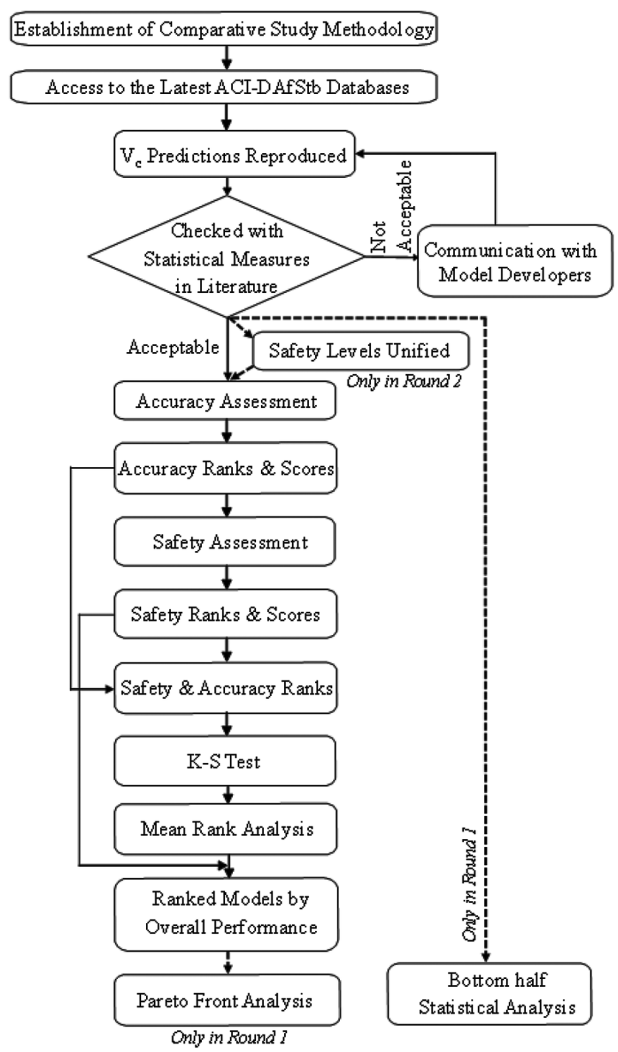

Fig. 3—CMMC methodology procedural steps in model predictions, comparisons, and rankings.

[†]The Appendix is available at **www.concrete.org/publications** in PDF format, appended to the online version of the published paper. It is also available in hard copy from ACI headquarters for a fee equal to the cost of reproduction plus handling at the time of the request.

COMPARATIVE STUDY RESULTS AND DISCUSSIONS

Figures 4(a) to (c) reveal the normalized shear stress for each specimen, calculated from predicted and experimental V_c, plotted against the logarithm of effective depth, where normalized shear stress is equal to $V_c/(b_w \cdot d \cdot \sqrt{f'_c})$. As can be seen in Fig. 4(a), normalized shear stress conservatively decreases with changes in effective depth for ACI 318-19 predictions. This is not the case for the ACI 318-14D and ACI 318-14S predictions where the normalized shear stress remains rather unchanged. In case of ACI 318-14S, the normalized shear stress is equal to 0.17 for all specimen when SI units are considered; therefore, the datapoints were not added to Fig. 4(a). When examining the size effect in other models (Fig. 4(a) to (c)), the CSA, JSCE, RNK, CLD, and PCH predictions appear to capture the experimentally observed trend more accurately. In addition, Fig. 4(a) to (c) show that, for beams with $d \geq 250$ mm, model predictions by ACI 318-19, CSA, JSCE, RNK, CLD, and PCH consider the size effect with a reasonably conservative approach.

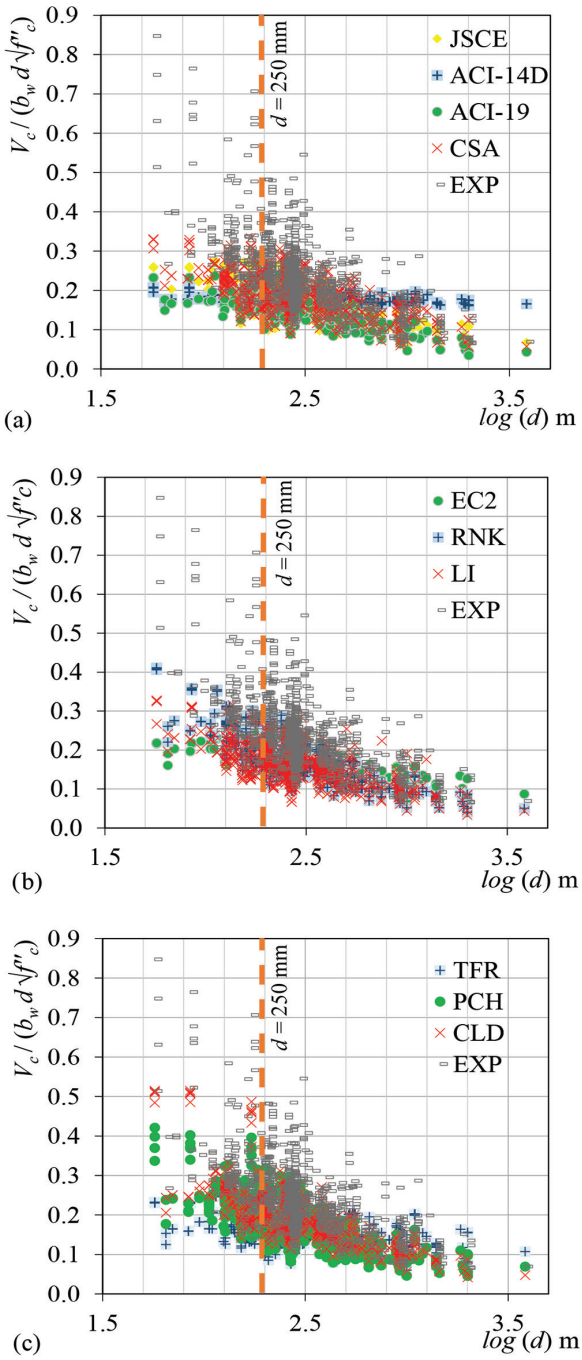

Fig. 4—(a)Normalized shear stress produced by ACI 318-19, ACI 318-14, CSA, JSCE, and experimental results versus logarithms of effective depth of specimens; (b) normalized shear stress produced by EC2, RNK, LI, and experimental results versus logarithms of effective depth of specimens; and (c) normalized shear stress produced by CLD, TFR, PCH, and experimental results versus logarithms of effective depth of specimens.

Further, the following sections present a comparison of the ACI 318-19 one-way shear equation for RC beams without transverse shear reinforcement based on CMMC methodology with other design equations and models available in the literature.

Round 1: comparative study in original safety level

Accuracy assessment—In this section, the accuracy metrics for the ACI 318-19 design equation and other selected design equations and models are computed and presented in Table 2. Each model is ranked based on its performance across the evaluated metrics, with lower values of mean (only when SR > 1), CoV, MAE, NRMSE, RMSLE, and MAPE indicating better accuracy, similar to higher values of E and d. In the next step, the models were ranked and scored for their performance on each accuracy metric. To provide a comprehensive assessment, overall accuracy scores across all eight metrics were considered for each model to compare the accuracy of the models. It should be noted that in the presentation of the calculated values, where applicable, up to three decimals were chosen, only when needed to break the ties.

This section discusses the results presented in Table 2, highlighting the strengths and limitations of the ACI 318-19 shear equations in accuracy comparisons with other models.

Mean: ACI 318-19 has picked a more conservative approach in terms of the mean when compared to the rest of the models, except for the ACI 318-14S equation. In accuracy comparisons, the lowest means are rewarded, which are the CSA, CLD, and PCH models with means equal to 1.228, 1.245, and 1.331, respectively.

CoV: ACI 318-19 one-way shear equation CoV was considerably improved (0.247) when compared to those of ACI 318-14S (0.387) and ACI 318-14D (0.338). The best one-way shear models in terms of CoV are PCH, CLD, and LI with CoVs equal to 0.134, 0.189, and 0.203, respectively.

MAE: In terms of absolute errors produced, ACI 318-19 did not improve significantly when compared to ACI 318-14 equations. ACI 318-19 was ranked ninth in MAE comparisons (MAE = 32.65 kN) higher than ACI 318-14D (MAE = 32.92 kN) and ACI 318-14S (MAE = 35.36 kN). It should be noted that MAE of the top three ranked models in MAE comparisons are below 25 kN, with the best model (CSA) reaching an MAE equal to 18.25 kN. This could be because ACI 318-19, ACI 318-14D, and ACI 318-14S produced a significant number of outliers (outliers defined here, as

Table 2—Accuracy assessment results, Round 1

Model	ACI-19	ACI-14S	ACI-14D	EC2	CSA	JSCE	PCH	TFR	RNK	CLD	LI
Mean	1.483	1.514	1.356	1.354	1.228	1.343	1.331	1.456	1.370	1.245	1.457
CoV	0.247	0.387	0.338	0.275	0.220	0.245	0.134	0.274	0.214	0.189	0.203
MAE	32.65	35.36	32.92	24.22	18.25	24.33	26.84	27.85	29.43	22.92	30.62
NRMSE	0.533	0.826	0.784	0.398	0.328	0.409	0.448	0.425	0.503	0.418	0.472
RMSLE	0.187	0.198	0.176	0.152	0.114	0.145	0.130	0.179	0.151	0.114	0.173
MAPE	30.85	32.53	29.71	24.05	17.70	22.97	23.65	29.35	24.94	19.01	29.37
E	0.791	0.500	0.549	0.884	0.921	0.877	0.853	0.868	0.814	0.872	0.837
d	0.932	0.913	0.921	0.969	0.979	0.963	0.951	0.966	0.938	0.961	0.950
Mean, rank	10	11	6	5	1	4	3	8	7	2	9
CoV, rank	7	11	10	9	5	6	1	8	4	2	3
MAE, rank	9	11	10	3	1	4	5	6	7	2	8
NRMSE, rank	9	11	10	2	1	3	6	5	8	4	7
RMSLE, rank	10	11	8	6	1	4	3	9	5	2	7
MAPE, rank	10	11	9	5	1	3	4	7	6	2	8
E, rank	9	11	10	2	1	3	6	5	8	4	7
d, rank	9	11	10	2	1	4	6	3	8	5	7
Accuracy scores	23	8	23	62	84	65	62	45	43	73	40
Accuracy rank	9	11	9	4	1	3	4	6	7	2	8

specimens with SR > 1.75), totaling 144, 182, and 120, respectively. A model with a CoV close to that of ACI 318-19 (CoV = 0.247) is JSCE model with CoV = 0.245. However, JSCE produced a much smaller number of outliers (79) than the ACI 318-19 (144). While the two models show a close CoV, the MAE of JSCE is 24.33 kN, compared to 32.65 kN for the ACI 318-19, which puts the JSCE model in the fourth MAE rank. This highlights the importance of incorporating additional metrics, such as MAE, in comparative studies.

NRMSE: This metric penalizes large errors. If, for example, SR > 2 is considered a large error in predictions, ACI 318-19 and ACI 318-14S produced 68 and 99 large errors in the 892-specimen database. This puts them in the ninth and 11th NRMSE ranks with NRMSEs equal to 0.533 and 0.826, respectively. Although this result shows a great improvement in terms of the produced NRMSE of the ACI 318-19 versus ACI 318-14S equation, there is room for improvement. For example, JSCE with a close CoV to ACI 318-19 produced 44 large errors with an NRMSE equal to 0.409 (NRMSE Rank 3). The NRMSE of the top rank model (CSA), with 23 large errors, was equal to 0.328.

RMSLE: ACI 318-19 was ranked 10th in RMSLE comparisons (RMSLE = 0.187) after ACI 318-14S (RMSLE = 0.198). The best models in RMSLE comparisons are CSA, CLD, and PCH with RMSLEs between 0.114 and 0.130.

MAPE: This metric shows the average percentage error between actual and predicted values. The results of MAPE comparison show that the ACI 318-19 stands in rank 10 with MAPE = 30.85%, which is a slight improvement when compared to ACI 318-14S with MAPE = 32.53%. ACI 318-19 did not show much improvement when compared to MAPE produced by ACI 318-14D (MAPE = 29.71%). The top-ranked models in MAPE comparisons were CSA, CLD, and JSCE with MAPEs equal to 17.70%, 19.01%, and 22.97%, respectively.

Efficiency coefficient: ACI 318-19 showed a significant improvement in terms of E when compared to the ACI 2014 equations. At the ninth rank, ACI 318-19's E is equal to 0.872, which is much closer to the top rank model in E comparisons (CSA with E equal to 0.921) than ACI 318-14S and ACI 318-14D with E values equal to 0.500 and 0.549.

Index of agreement: Similar to E comparisons, ACI 318-19 showed improvements in d metric compared to the ACI 318-14 equations, however, the ACI 318-19 equation ranks ninth among other models. The top ranks in the d comparisons belong to CSA, EC2, and TFR with d values equal to 0.979, 0.969, and 0.966, respectively.

After the models were ranked according to each metric, scores were assigned to all models for each accuracy metric, as presented in Table 2. In addition, the accuracy performance of the one-way shear models is illustrated in Fig. 5 using a radar chart based on their ranks in each metric. A larger covered area signifies superior model performance in terms of accuracy (Fig. 5).

According to the results of this study, several distinguishing properties can be highlighted for the top-ranked models in the accuracy assessments, including low CoV, small absolute errors in MAE and NRMSE, and mean predictions that are closely greater than SR = 1 without being excessively conservative. Models such as CSA and CLD also demonstrate strong performance on other statistical metrics, including MAPE, RMSLE, and correlation-based metrics, indicating fair predictive capacity rather than calibration of the model for one statistical metric.

Safety assessment—As stated, five safety measures were used to assess the safety of the chosen one-way shear

models for RC beams without shear reinforcement. Table 3 presents the calculated results for each metric. After calculating the safety metric values, the models were ranked for each metric, as can be seen in Table 3. The overall safety scores of the models on the featured safety metrics were used to evaluate the overall performance of the models as a safety assessment.

Mean: The conservative approach of ACI 318 one-way shear models is rewarded here, as the ACI 318-14S and ACI 318-19 are ranked first and second with Means equal to 1.514 and 1.483. The third rank in the Mean comparison is the LI model.

Failure probability: The percentages of the predictions with SR < 1 are compared in this section. ACI 318-19 is ranked third with 3.14% after PCH and LI with 1.46% and 2.69% failure probability, respectively. This represents a significant improvement in the ACI 318-19 one-way shear equation compared to ACI 318-14S and ACI 318-14D, where the earlier equations resulted in 17.60% and 17.94% of predictions with SR < 1, respectively.

Two of the reported issues corresponded to ACI 318-14 provisions were the high number of unconservative predictions for: 1) RC members with low longitudinal reinforcement; and 2) for beams with large depth.

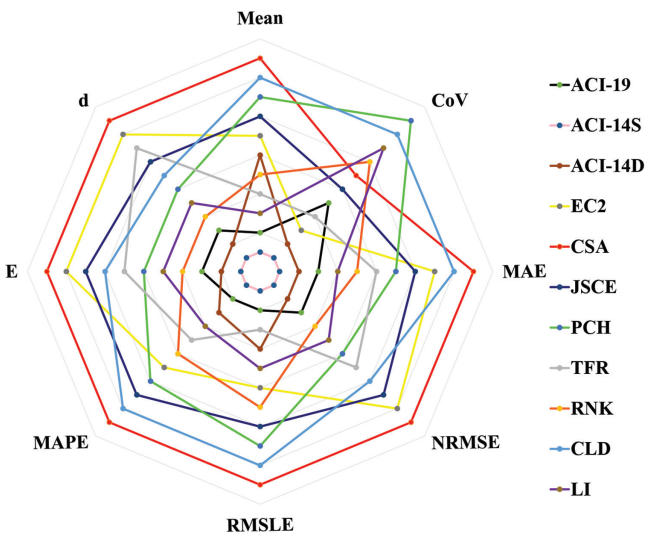

Fig. 5—Radar chart of accuracy metrics, Round 1.

The failure probability of ACI 318-19 for RC members without shear reinforcement and $\rho_w < 0.01$ was equal to 12.9%—that is, 13 out of 125 specimens with such criteria. These numbers were 70.4% and 73.6% for ACI 318-14D and ACI 318-14S equations, respectively. This puts the ACI 318-19 equation in third place after PCH and RNK with 5.6% and 8.0% failure probability for such specimens, respectively. Further, the failure probability of RC members without shear reinforcement with a depth greater than 500 mm, based on ACI 318-19 provisions, was found to be 2.7%. This corresponds to 5 predictions with SR < 1 out of 188 experimental specimens meeting these criteria. These numbers were 48.9% and 47.9% for ACI 318-14D and ACI 318-14S equations, respectively. This puts the ACI 318-19 equation in third place after PCH and LI models with 1.1% and 2.1% failure probability for such members, respectively. It is evident that the equation introduced in ACI 318-19 has addressed the limitations observed in ACI 318-14 regarding the prediction of one-way shear strength in RC members without shear reinforcement for members with low longitudinal reinforcement ratios and/or large effective depths.

It should be noted that only the ranks and scores corresponding to the percentage of predictions with SR < 1 across the entire database were considered in the comparative study's scoring.

Probability of failure of design using a 0.75 reduction factor: ACI 318-19 is ranked fourth in this metric, with SR < 0.75 percentage equal to 0.224%, which is equal to two specimens out of 892. This is a great improvement when compared to ACI 318-14S and ACI 318-14D with 7.063% (63 specimens) and 6.614% (59 specimens), respectively. The top-ranked model in the SR < 0.75 metric is PCH, with no SR predictions below 0.75, followed by RNK and JSCE models, both with 0.112% (one specimen).

PSP: The percentage of SR predictions between 1 and 1.25, considered as suitable predictions, is compared in this section. In this metric, ACI 318-19 was ranked last due to the conservative approach chosen. Only 18.39% of

Table 3—Safety assessment results, Round 1

Model	ACI-19	ACI-14S	ACI-14D	EC2	CSA	JSCE	PCH	TFR	RNK	CLD	LI
Mean	1.483	1.514	1.356	1.354	1.228	1.343	1.331	1.456	1.370	1.245	1.457
Failure probability, %	3.14	17.60	17.94	7.96	12.00	4.48	1.46	7.17	4.48	8.18	2.69
<0.75, %	0.224	7.063	6.614	0.897	0.224	0.112	0	1.233	0.112	0.561	0.336
PSP, %	18.39	21.52	25.11	34.64	53.81	39.35	32.96	22.09	31.05	50.00	19.51
P_{5th}	1.041	0.692	0.700	0.955	0.924	1.006	1.076	0.923	1.006	0.947	1.057
Mean rank	2	1	6	7	11	8	9	4	5	10	3
Failure probability, %	3	10	11	7	9	4	1	6	4	8	2
<0.75	4	11	10	8	4	2	1	9	2	7	6
PSP rank	11	9	7	4	1	3	5	8	6	2	10
P_{5th} rank	3	11	10	6	8	4	1	9	5	7	2
Safety scores	37	18	16	28	27	39	43	24	38	26	37
Safety rank	4	10	11	6	7	2	1	9	3	8	4

the ACI 318-19 SR predictions are between 1 and 1.25. This is a downgrade when compared to ACI 318-14S and ACI 31814D, with PSP equal to 21.52% and 25.11%. In fact, 78.47% of the ACI 318-19 predictions produce SR > 1.25, and 16.14% of the ACI 318-19 predictions lead to SR > 1.75. The top three ranked models in PSP comparisons were CSA, CLD, and JSCE, with PSP values equal to 53.81%, 50.00%, and 39.35%, respectively.

***P_{5th}*:** ACI 318-19 is ranked third in this metric, with P_{5th} equal to 1.041, after PCH and LI models with P_{5th} values equal to 1.076 and 1.057, respectively. This is considered a great improvement in ACI 318-19 when compared to ACI 318-14S and ACI 318-14D with P_{5th} values equal to 0.692 and 0.700, respectively. The large number of predictions with SR < 1 in ACI 318-14S and ACI 318-14D was the reason behind the low P_{5th} values of ACI 318-14 models. This major issue is addressed in ACI 318-19.

The overall safety ranking, as presented in Table 3. The results of the safety rankings provide an insight into the relative safety considerations adopted in the development of each model. From the results of this study, it appears that there is an inherent trade-off between optimizing accuracy and ensuring safety. For example, in the case of CSA equation, where the model performs well in accuracy (Rank 1), in terms of safety the model does not get ranked high (Ranks 7). In contrast, models such as PCH, JSCE, RNK, ACI 318-19, and LI (Safety Ranks 1 to 4) adopt a calibration closer to $P_{5th} = 1$, which shifts the predictions toward a relatively safer side. This difference in target safety levels is a choice that has been intentionally adopted by the model developers. The overall safety performance of the one-way shear models is illustrated in the form of a radar chart, as shown in Fig. 6.

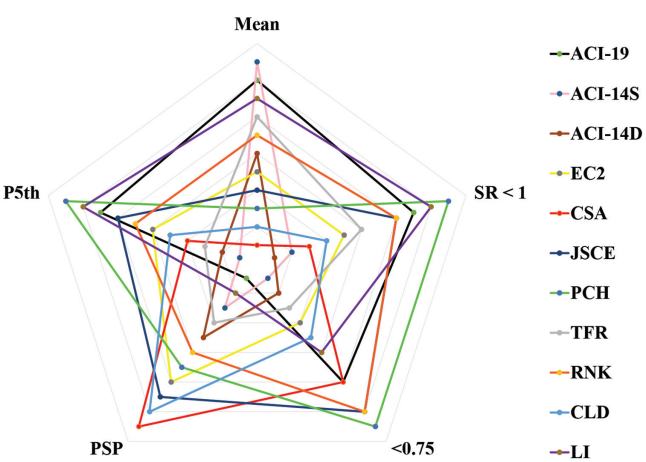

Fig. 6—Radar chart of safety metrics, Round 1.

Statistical tests—Two statistical tests were examined in this section.

KS test: In this test, ACI 318-19 was ranked ninth (D = 0.240), which indicates that eight other models, including ACI 318-14D produced prediction data sets that match the experimental data set more closely (Table 4). In this test, the first three ranks belong to CSA, CLD, and PCH models with D values equal to 0.128, 0.131, and 0.173, respectively.

Friedman mean rank analysis: As mentioned earlier, this test is a non-parametric statistical test used to compare three or more related groups when the assumption of normality is violated. In this test, ACI 318-19 was ranked last with an average rank of 8.19. This means that, on average, for each prediction for the test data in the experimental data set, there have been seven models that predicted V_c with a closer prediction than that of ACI 318-19. The top-performing models in this test were CSA and CLD, both achieving average ranks of 3.32.

The overall performance of the models across two statistical tests can be found in Table 4.

Summary of comparative study in original safety level—As previously mentioned, evaluating the overall performance of the models requires a comprehensive multi-metric comparative study considering both accuracy and safety comparisons simultaneously. Table 5 provides the overall ranking of the models based on accuracy assessment, safety assessment, and statistical tests, and the combinations of these three categories. The top three models in combined accuracy and safety are CSA, PCH, and JSCE. Although ranked ninth, ACI 318-19 score is closer to the top-ranked models, such as EC2, than those at the bottom of the ranking table—that is, ACI 318-14 equations (Table 5).

When considering accuracy, safety, and statistical test scores, the ranks mainly stayed the same as when combined accuracy and safety were considered. The only difference is that the second place is jointly shared between PCH and JSCE when accuracy, safety, and statistical test scores are considered (Table 5).

Pareto front analysis—In Pareto analysis, the rankings of three different categories, including accuracy, safety, and statistical tests, are considered separately (that is, combined ranks are not considered). Following the Pareto front analysis on the model ranks based on the previously mentioned categories, the following results were extracted: Tier 1: CSA, PCH,

Table 4—Statistical test results, Round 1

Model	ACI-19	ACI-14S	ACI-14D	EC2	CSA	JSCE	PCH	TFR	RNK	CLD	LI
D for K-S test	0.240	0.243	0.219	0.206	0.128	0.192	0.173	0.256	0.207	0.131	0.224
Average prediction rank for Friedman mean rank analysis	8.19	7.78	6.63	5.15	3.32	5.15	5.51	7.78	6.15	3.32	7.01
K-S test rank	9	10	7	5	1	4	3	11	6	2	8
Friedman test rank	11	9	7	3	1	3	5	9	6	1	8
Statistical test scores	4	5	10	16	22	17	16	4	12	21	8
Statistical tests rank	10	9	7	4	1	3	4	10	6	2	8

Table 5—Summary of Round 1 scores and rankings

Model	ACI-19	ACI-14S	ACI-14D	EC2	CSA	JSCE	PCH	TFR	RNK	CLD	LI
Accuracy scores (out of 88)	23	8	23	62	84	65	62	45	43	73	40
Accuracy ranking	9	11	9	4	1	3	4	6	7	2	8
Safety scores (out of 55)	37	18	16	28	27	39	43	24	38	26	37
Safety ranking	4	10	11	6	7	2	1	9	3	8	4
Statistical tests scores (out of 22)	4	5	10	16	22	17	16	4	12	21	8
Statistical tests ranking	10	9	7	4	1	3	4	10	6	2	8
Accuracy + safety, scores	60	26	39	90	111	104	105	69	81	99	77
Accuracy + safety, ranking	9	11	10	5	1	3	2	8	6	4	7
Accuracy + safety + statistical test scores	64	31	49	106	133	121	121	73	93	120	85
Accuracy + safety + statistical test ranking	9	11	10	5	1	2	2	8	6	4	7

Table 6—Bottom-half analysis

Model	ACI-19	ACI-14S	ACI-14D	EC2	CSA	JSCE	PCH	TFR	RNK	CLD	LI
Bottom-half mean	1.450	1.360	1.320	1.293	1.170	1.270	1.310	1.400	1.319	1.220	1.410
Bottom-half CoV	0.172	0.287	0.280	0.166	0.128	0.134	0.107	0.200	0.144	0.139	0.156
Bottom-half CoV, rank	8	11	10	7	2	3	1	9	5	4	6

and JSCE; Tier 2: RNK, CLD and EC2; Tier 3: LI and TFR, and Tier 4: ACI 318-19, ACI 318-14S, and ACI 318-14D.

It should be noted that in Tier 1, PCH, CSA, and JSCE one-way shear models were not able to dominate each other based on the distinct ranks in the accuracy, safety, and statistical tests categories, as shown in Table 5. In Tier 2, RNK model was outperformed by PCH and JSCE, which caused the model to be transferred to Tier 2. Similarly, CLD model was dominated by CSA. Meanwhile, EC2 was dominated by PCH and JSCE, which relegated the model to Tier 2. In Tier 3, LI model was dominated by RNK, PCH and JSCE, whereas TFR model was dominated by CLD, EC2, JSCE, PCH, and RNK. In Tier 4, ACI 318-19 was dominated by RNK, LI, PCH, and JSCE. Similarly, the ACI 318-14D model was dominated by RNK, LI, PCH, CSA, CLD, and JSCE. Further, ACI 318-14S equation was dominated by all other models except ACI 318-19, ACI 318-14D, and TFR .

Bottom half analysis—As mentioned earlier, bottom half analysis required a slight optimization in the models to minimize the difference between the model's predicted CDF and the observed CDF. Due to this slight optimization, the results of this analysis were presented separately from the comparative study of the model predictions in their original form. Table 6 presents the results of the bottom-half analysis, summarizing the mean and CoV of the lower 50% of model SR predictions. The top three rankings are held by the PCH, CSA, and JSCE models, respectively.

Accuracy and safety assessments on RC beams with $d \geq 250$ mm—To address the concerns related to excessive presence of small size specimens in the database, accuracy and safety assessments were conducted on the RC beams in the database with $d \geq 250$ mm. The results of this study can be found in Tables 7 through 9. These results reveal that while there are slight changes in the accuracy and safety rankings, the overall performance of the models did not change significantly. When combined accuracy and safety scores were compared, the only difference between rankings using the complete database and that using the database of larger beams with $d \geq 250$ mm was the swapped ranks of JSCE and PCH models in Ranks 2 and 3 (Tables 7 through 9).

Round 2 comparisons of the selected one-way shear models for RC beams without transverse shear reinforcement are provided in Appendix B.

CONCLUSIONS

Benefiting from the proposed comprehensive multi-metric comparative (CMMC) study, the ACI 318-19 one-way shear equation for reinforced concrete (RC) specimens without shear reinforcement was evaluated versus the state-of-the-art in literature. Predictions from ACI 318-19 and 10 other models for 892 RC beams without shear reinforcement were carefully reproduced to ensure accuracy. A new multi-metric comparative study was conducted on model predictions considering three major categories, including: 1) accuracy assessment; 2) safety assessments; and 3) statistical tests. Each category comprised distinct metrics and tests used to rank and score the models. The results of these evaluations were ranked for each category to evaluate the position of the ACI 318-19 equation among the one-way shear models studied. In the second round of comparative studies, the models benefited from a similar safety margin, considering their fifth percentile (P_{5th}) equal to one. From the results of this study, the following conclusions can be drawn:

- The results of this study show that the ACI 318-19, CSA 23.3:24, Japan Society of Civil Engineers (JSCE), Cladera et al. (2017) (CLD), Reineck (2017) (RNK), and Choi and Park (2023) (PCH) models were able to provide a more reliable representation of the size effect

Table 7—Accuracy assessment results of beams with $d \geq 250$ mm, Round 1

Model	ACI-19	ACI-14S	ACI-14D	EC2	CSA	JSCE	PCH	TFR	RNK	CLD	LI
Mean	1.436	1.249	1.194	1.264	1.153	1.270	1.332	1.325	1.370	1.230	1.419
CoV	0.206	0.324	0.282	0.219	0.185	0.200	0.127	0.220	0.197	0.182	0.193
MAE	39.27	42.51	39.56	27.61	19.90	27.76	33.65	30.95	36.46	28.00	36.72
NRMSE	0.502	0.797	0.757	0.365	0.296	0.376	0.428	0.383	0.476	0.395	0.441
RMSLE	0.169	0.162	0.143	0.125	0.089	0.121	0.131	0.144	0.149	0.110	0.163
MAPE	28.61	28.90	26.26	20.68	14.03	19.85	23.90	24.84	25.21	18.36	28.00
E	0.783	0.453	0.507	0.885	0.924	0.878	0.843	0.874	0.805	0.866	0.832
d	0.930	0.907	0.916	0.969	0.980	0.964	0.948	0.968	0.935	0.959	0.949
Mean, rank	11	4	2	5	1	6	8	7	9	3	10
CoV, rank	7	11	10	8	3	6	1	9	5	2	4
MAE, rank	9	11	10	3	1	4	5	6	7	4	8
NRMSE, rank	9	11	10	2	1	3	6	4	8	5	7
RMSLE, rank	11	9	6	4	1	3	5	7	8	2	10
MAPE, rank	10	11	8	4	1	3	5	6	7	2	9
E, rank	9	11	10	2	1	3	6	4	8	5	7
d, rank	9	11	10	2	1	4	7	3	8	5	6
Accuracy scores	21	17	30	67	86	65	52	51	36	68	35
Accuracy rank	10	11	9	3	1	4	5	6	7	2	8

Table 8—Safety assessment results of beams with $d \geq 250$ mm, Round 1

Model	ACI-19	ACI-14S	ACI-14D	EC2	CSA	JSCE	PCH	TFR	RNK	CLD	LI
Mean	1.436	1.249	1.194	1.264	1.153	1.270	1.332	1.325	1.370	1.230	1.419
Failure probability, %	4.36	25.17	25.84	10.57	15.27	5.87	1.51	10.74	3.69	8.72	3.19
<0.75, %	0.336	10.570	9.899	1.342	0.336	0.168	0	1.846	0	0.839	0.503
PSP, %	20.64	26.34	30.37	42.28	64.60	45.97	31.71	29.03	29.87	51.34	20.81
P_{5th}	1.011	0.635	0.648	0.908	0.885	0.984	1.100	0.874	1.020	0.945	1.056
Mean rank	1	8	10	7	11	6	4	5	3	9	2
Failure probability, %	4	10	11	7	9	5	1	8	3	6	2
<0.75	4	11	10	8	4	3	1	9	1	7	6
PSP rank	11	9	6	4	1	3	5	8	7	2	10
P_{5th} rank	4	11	10	7	8	5	1	9	3	6	2
Safety scores	36	11	13	27	27	38	48	21	43	30	38
Safety rank	5	11	10	7	7	3	1	9	2	6	3

Table 9—Summary of Round 1 scores and rankings of beams with $d \geq 250$ mm

Model	ACI-19	ACI-14S	ACI-14D	EC2	CSA	JSCE	PCH	TFR	RNK	CLD	LI
Accuracy + safety, scores	57	28	43	94	113	103	100	72	79	98	73
Accuracy + safety, ranking	9	11	10	5	1	2	3	8	6	4	7

in one-way shear behavior compared to ACI 318-14 models. Meanwhile, these models were able to provide a consistent trend, for RC beams larger than 250 mm, when compared to the experimental results.

- The coefficient of variation (CoV) for the strength ratio (SR) predicted by the ACI 318-19 one-way shear equation shows a marked improvement at 0.247, compared to 0.387 for ACI 318-14S and 0.338 for ACI 318-14D. Among all evaluated models, the top-ranked models, based on CoV, are PCH, CLD, and Li et al. (2017) (LI) models, with CoVs of 0.134, 0.189, and 0.203, respectively.
- As the accuracy assessment results of this study showed, CoV can be misleading when the data are skewed and not normally distributed and may lead to distorted interpretations of model variability. For example, although the Eurocode 2 (EC2) model ranked ninth in terms of

CoV, it secured the fourth overall position in accuracy during the first round of comparisons.

- In terms of error-based metrics, ACI 318-19 showed improvements over ACI 318-14S and ACI 318-14D; however, the model is not among the top-ranked models.
- ACI 318-19 is ranked third with 3.14% predictions with SR < 1 after PCH and LI models with 1.46% and 2.69% failure probability, respectively. This represents a significant improvement in the ACI 318-19 one-way shear equation compared to ACI 318-14S and ACI 318-14D, with 17.60% and 17.94% of predictions with SR < 1, respectively.
- ACI 318-19 is ranked fourth for SR < 0.75 percentage equal to 0.224%, which is equal to two specimens out of 892. This is a considerable improvement when compared to ACI 318-14S and ACI 318-14D with 7.063% (63 specimens) and 6.614% (59 specimens), respectively.
- In comparison of percentage of suitable predictions (PSP) values, ACI 318-19 was ranked last due to the conservative approach chosen. Only 18.39% of the ACI 318-19 predictions of SR are between 1 and 1.25. The top three ranked models in PSP comparisons were CSA, CLD, and JSCE with PSP values equal to 53.81%, 50.00%, and 39.35%, respectively.
- The overall safety ranking indicates that ACI 318-19 is the fourth model (shared with LI) after PCH, JSCE, and RNK models at the first to third ranks, respectively.
- In terms of combined accuracy, safety, and statistical assessments comparisons, ACI 318-19 has shown considerable improvement over ACI 318-14 equations. However, the model needs improvements to reach top-ranked one-way shear models.
- Considering only specimens with effective depths larger than 250 mm did not affect the overall ranking of the models when combined accuracy and safety rankings were considered, except that JSCE model exchanged ranks with PCH model in Ranks 2 and 3.
- Unifying the safety margins to $P_{5th} = 1$ in the second round of comparisons caused individual slight shifts in rankings but did not result in a drastic change in the overall model rankings.

AUTHOR BIOS

ACI member **Amir Mofidi** *is an Associate Professor in the Department of Engineering at Brock University, St. Catharines, ON, Canada. He received his MSc from Concordia University, Montreal, QC, Canada, and his PhD from the University of Quebec, Montreal, QC, Canada. He completed a 7-year postdoctoral period at McGill University, Montreal, QC, Canada. He is a member of ACI Committee 440, Fiber-Reinforced Polymer Reinforcement, focusing on the shear rehabilitation of concrete members and the application of advanced composites in concrete structures.*

Sara Mirzabagheri *is an Assistant Professor in the Department of Engineering at Pa.C Islamic Azad University, Parand, Iran. She received her MSc and PhD from Tarbiat Modares University, Tehran, Iran. She completed her first postdoctoral fellowship at Lakehead University, Thunder Bay, ON, Canada, and her second postdoctoral fellowship at Brock University. Her research interests include experimental and numerical modeling of reinforced concrete (RC) structures, rehabilitation of concrete members, and application of green concrete.*

Kourosh Nasrollahzadeh *is an Associate Professor in the Department of Civil Engineering at K. N. Toosi University of Technology, Tehran, Iran. He received his BSc and MSc from the University of Tehran, Tehran, Iran, and his doctoral degree in structural engineering from the University of the Ryukyus, Nishihara, Japan. He completed his JSPS postdoctoral research fellowship at the University of Tokyo, Tokyo, Japan. His research interests include seismic retrofitting of RC structures by fiber-reinforced polymer (FRP) and reliability analysis.*

Shahryar Rahnamayan *is Professor and Chair of Engineering at Brock University. He received his BSc and MSc in software engineering and PhD in systems design engineering from the University of Waterloo, Waterloo, ON, Canada. With over 18 years of research experience, he has published more than 250 papers on machine learning, optimization, and imaging, amassing over 10,000 citations. He directs the Nature-Inspired Computational Intelligence (NICI) Lab at Brock University.*

ACKNOWLEDGMENTS

The authors extend their sincere gratitude to A. Cladera, K.-K. Choi, R. J. Frosch, E. Bentz, and S.-J. Hwang for their valuable assistance to the authors in ensuring the accurate reproduction of their respective one-way shear model predictions.

REFERENCES

ACI Committee 318, 2014, "Building Code Requirements for Structural Concrete (ACI 318-14) and Commentary (ACI 318R-14)," American Concrete Institute, Farmington Hills, MI, 520 pp.

ACI Committee 318, 2019, "Building Code Requirements for Structural Concrete (ACI 318-19) and Commentary (ACI 318R-19) (Reapproved 2022)," American Concrete Institute, Farmington Hills, MI, 624 pp.

ACI Committee 445 and German Committee for Structural Concrete (DAfStb), *ACI-DAfStb Databases with Shear Tests for Evaluating Relationships for the Shear Design of Structural Concrete Members without and with Stirrups*.

Aguilar, V.; Barnes, R. W.; and Nowak, A. S., 2022, "Comparative Assessment of Shear Strength Equations for Reinforced Concrete," *Practice Periodical on Structural Design and Construction*, ASCE, V. 27, No. 2, pp. 1-11. doi: 10.1061/(ASCE)SC.1943-5576.0000666

Arachchige, C. N. P. G.; Prendergast, L. A.; and Staudte, R. G., 2020, "Robust Analogs to the Coefficient of Variation," *Journal of Applied Statistics*, V. 49, No. 2, pp. 268-290. doi: 10.1080/02664763.2020.1808599

Belarbi, A.; Kuchma, D. A.; and Sanders, D. H., 2017, "Proposals for New One-Way Shear Equations for the 318 Building Code," *Concrete International*, V. 39, No. 9, Sept., pp. 29-32.

Choi, K. K., and Park, H. G., 2023. "Presentation on the Revision of Shear and Torsion Design Standards for the 2026 reversion of Concrete Structure Standards KDS 14 20," Korea Concrete Institute, 2023 Fall KCI Conference, Nov. 1-3, Phoenix, Jeju, South Korea. (in Korean)

Cladera, A.; Marí, A.; Bairán, J. M.; Oller, E.; and Ribas, C., 2017, "One-Way Shear Design Method Based on a Multi-Action Model," *Concrete International*, V. 39, No. 9, Sept., pp. 40-46.

Collins, M. P., 2001, *Evaluation of Shear Design Procedures for Concrete Structures*, CSA Group, Toronto, ON, Canada, 148 pp.

CSA A23.3:24, 2024, "Design of Concrete Structures," CSA Group, Toronto, ON, Canada.

Eurocode 2 (European Committee for Standardization), 2005, "Design of Concrete Structures-Concrete Bridges—Design and Detailing Rules," EN 1992-2:2005 (E), European Committee for Standardization, Brussels, Belgium, 408 pp.

Friedman, M., 1937, "The Use of Ranks to Avoid the Assumption of Normality Implicit in the Analysis of Variance," *Journal of the American Statistical Association*, V. 32, No. 200, pp. 675-701. doi: 10.1080/01621459.1937.10503522

Frosch, R. J.; Yu, Q.; Cusatis, G.; and Bažant, Z. P., 2017, "A Unified Approach to Shear Design," *Concrete International*, V. 39, No. 9, Sept., pp. 47-52.

Hyndman, R. J., and Athanasopoulos, G., 2018, *Forecasting: Principles and Practice,* second edition, OTexts Publishing, Monash University, Melbourne, Australia, 382 pp.

Ibrahim, A., Bidgoli, A. A., Rahnamayan, S., and Deb K., 2024, "A Novel Pareto-optimal Ranking Method for Comparing Multi-Objective Optimization Algorithms," *arXiv*:2411.17999, 13 pp.

Japan Society of Civil Engineers (JSCE), 2007, "Standard Specifications for Concrete Structures-2007; Part 5 Design," Tokyo, Japan, 469 pp.

Kuchma, D. A.; Wei, S.; Sanders, D. H.; Belarbi, A.; and Novak, L. C., 2019, "Development of the One-Way Shear Design Provisions of ACI 318-19 for Reinforced Concrete," *ACI Structural Journal*, V. 116, No. 4, July, pp. 285-295.

Li, Y. A.; Hsu, T. T. C.; and Hwang, S. J., 2017, "Shear Strength of Prestressed and Non-prestressed Concrete Beams," *Concrete International*, V. 39, No. 9, Sept., pp. 53-57.

Nash, J. E., and Sutcliffe, J. V., 1970, "River Flow Forecasting through Conceptual Models Part I—A Discussion of Principles," *Journal of Hydrology*, V. 10, pp. 282-290.

Park, H. G., and Choi, K. K., 2017, "Unified Shear Design Method of Concrete Beams Based on Compression Zone Failure Mechanism," *Concrete International*, V. 39, No. 9, Sept., pp. 59-63.

Perumalla, M., and Laskar, A., 2020, "Evaluation of Design Methods for Prestressed Concrete Members with Stirrups Using a New Traditional Shear Database," *Structures*, V. 23, pp. 621-634. doi: 10.1016/j.istruc.2019.10.021

Rainio, O.; Teuho, J.; and Klén, R., 2024, "Evaluation Metrics and Statistical Tests for Machine Learning," *Scientific Reports*, V. 14, No. 1, p. 6086. doi: 10.1038/s41598-024-56706-x

Reineck, K.-H., 2017, "Proposal for ACI 318 Shear Design," *Concrete International*, V. 39, No. 9, Sept., pp. 65-70.

Reineck, K.-H.; Bentz, E. C.; Fitik, B.; Kuchma, D. A.; and Bayrak, O., 2013, "ACI-DAfStb Database of Shear Tests on Slender Reinforced Concrete Beams without Stirrups," *ACI Structural Journal*, V. 110, No. 5, Sept.-Oct., pp. 867-876.

Shapiro, S. S., and Wilk, M. B., 1965, "An Analysis of Variance Test for Normality (Complete Samples)," *Biometrika*, V. 52, No. 3-4, pp. 591-611. doi: 10.1093/biomet/52.3-4.591

Simard, R., and L'Ecuyer, P., 2011, "Computing the Two-Sided Kolmogorov–Smirnov Distribution," *Journal of Statistical Software*, V. 39, No. 11, pp. 1-18. doi: 10.18637/jss.v039.i11

Tureyen, A. K., and Frosch, R. J., 2003, "Concrete Shear Strength: Another Perspective," *ACI Structural Journal*, V. 100, No. 5, Sept.-Oct., pp. 609-615.

Willmott, C. J., 1984. "On the Evaluation of Model Performance in Physical Geography," *Spatial Statistics and Models*, pp. 443-460.

ACI STRUCTURAL JOURNAL TECHNICAL PAPER

Title No. 123-S62

Long-Term Field Monitoring and Analysis of Post-Tensioned Flat Slab System

by Kwanwoo Yi, Ah Sir Cho, and Thomas H.-K. Kang

This study presents a comprehensive field investigation into the long-term behavior of unbonded post-tensioned (PT) concrete flat slabs using Smart Strands embedded with fiber Bragg grating (FBG) sensors. The monitoring program was conducted in a real-world building in Seoul, Korea, spanning over 5 and a half years and capturing continuous prestressing force and deflection measurements at multiple slab locations. Results revealed that approximately 5% of nominal strength of tendon prestress losses occurred within the first year, stabilizing thereafter, and that deflection patterns were significantly influenced by slab position and construction activities. Comparison with analytical models showed strong alignment, with ACI CODE-318-25 time-dependent coefficients accurately predicting long-term deflections after the early-age period. This study contributes valuable long-term data, validating design codes and guidelines and enhancing understanding of the time-dependent behavior of PT concrete structures.

Keywords: deflection; long-term monitoring; optical fiber; prestressed concrete; prestress loss; smart tendon; unbonded post-tensioned concrete flat slab.

INTRODUCTION

Post-tensioned (PT) concrete structures have become integral to modern construction due to their ability to span greater distance while maintaining structural integrity. However, the long-term performance of these structures depends significantly on maintaining adequate prestressing forces throughout their service life. Prestress losses, resulting from concrete shrinkage, creep, steel relaxation, and other factors, can compromise structural safety and serviceability when not properly accounted for in design or monitored during service. While theoretical models exist to predict these losses, field validation data from actual structures remains limited, especially over extended periods under real-world loading and environmental conditions.

The accurate measurement of prestressing forces in PT structures has traditionally relied on electrical resistance strain gauges (ERSGs), which often suffer from durability issues and limited sensing capabilities. Recent advancements in optical fiber sensing technology, particularly fiber Bragg grating (FBG) sensors embedded within "Smart Strands," have opened new possibilities for long-term monitoring. These Smart Strands replace the steel core wire of conventional seven-wire strands with carbon fiber-reinforced polymer (CFRP) core housing optical sensors, enabling continuous strain measurement along the tendon length without compromising structural performance (Fig. 1).

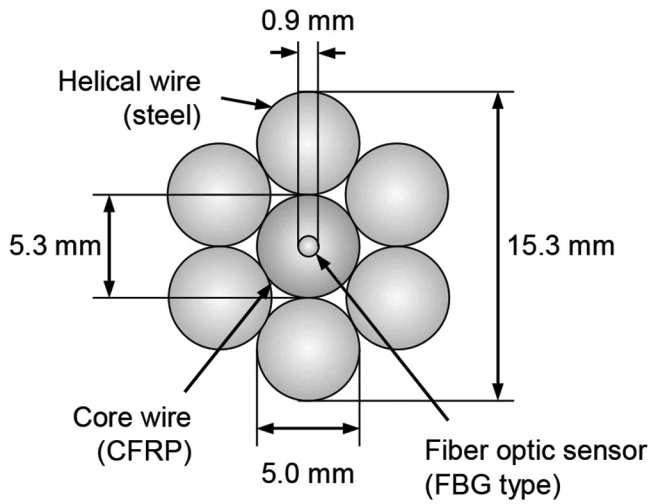

Fig. 1—Cross section of Smart Strand.[1] (Note: 1 mm = 0.039 in.)

Previous research has demonstrated the effectiveness of Smart Strands in laboratory settings and limited field applications. Kim et al.[2] used FBG-embedded Smart Strands to monitor short-term prestress losses during tensioning and anchoring processes, while Jeon et al.[3] applied similar technology to analyze friction losses in PT tendons. Additionally, studies by Jeon et al.[1] and Kim et al.[4] highlighted the critical importance of temperature compensation in optical fiber sensing systems for accurate strain measurement in field applications. However, comprehensive long-term monitoring data from operational buildings remains scarce, particularly regarding the simultaneous measurement of prestressing forces and structural deflections over several years.

Concurrently, the long-term deflection behavior of PT structures has received considerable attention in laboratory studies. Extensive laboratory studies conducted between 1964 and 2024,[5-27] resulting total of 139 specimens, have provided valuable insights into the long-term deflection and prestress loss behavior of PT concrete (Table 1). While steel tendons remain predominant, alternative materials such as CFRP, glass fiber-reinforced polymers (GFRP), and basalt fiber-reinforced polymers (BFRP) have shown promising

ACI Structural Journal, V. 123, No. 3, May 2026.
MS No. S-2025-166.R2, doi: 10.14359/51749492, received August 12, 2025, and reviewed under Institute publication policies. Copyright © 2026, American Concrete Institute. All rights reserved, including the making of copies unless permission is obtained from the copyright proprietors. Pertinent discussion including author's closure, if any, will be published ten months from this journal's date if the discussion is received within four months of the paper's print publication.

Table 1—Data set of long-term deflection of prestressed concrete

Source	Specimen type	Number of specimens	Testing time, days	Final-to-initial deflection ratio		Predicted-to-measured final deflection ratio	
				Min	Max	Min	Max
Breckenridge and Bugg[6]	I-beam*	8	2555	1.44	2.46	1.13	1.39
	I-beam*	14	2555	1.33	2.68	1.07	1.32
	Hollow-box*	8	2555	1.60	2.32	1.01	1.26
Branson et al.[7]	Rectangular beam*	3	180	1.96	2.05	—	—
	T-beam†	6	180	1.26	2.15	—	—
	I-beam†	5	560	0.01	0.28	—	—
Anderson et al.[8]	I-beam†	12	270	N/A	N/A	N/A	N/A
Chiu et al.[9]	Rectangular beam (1 data missing)	6	210	2.24	3.20	0.65	0.90
Braimah et al.[10]	T-beam	4	651	1.16	1.47	1.71	2.18
Zou[11]	Rectangular beam	6	270	1.67	3.36	0.68	1.38
Xue et al.[12]	Composite beam	2	360	2.96	3.14	0.66	0.70
Radnić and Matešan[13]	Shell	1	360	2.75	2.75	0.76	0.76
Fornůsek et al.[14]	Rectangular beam (data missing)	1	360	N/A	N/A	N/A	N/A
Terrasi et al.[15]	Circular pole (2 data missing)	5	6023	2.29	3.30	0.82	1.19
Singh[16]	Rectangular-shape-like beam*	9	500	N/A	N/A	N/A	N/A
Zawam et al.[17]	Rectangular beam	9	300	1.25	2.02	0.97	1.58
Cao et al.[18]	Box girder	2	470	1.63	1.97	1.26	1.52
Cao et al.[19]	Composite beam	2	420	1.82	2.53	0.82	1.14
Sovják et al.[20]	Rectangular beam	1	2555	5.00	5.00	0.60	0.60
Al-Negheimish et al.[21]	Hollow core slab	4	730	1.84	2.15	1.22	1.40
Zawam et al.[22]	Rectangular beam	6	300	1.23	1.87	1.05	1.59
Yang et al.[23]	I-beam	6	1350	1.38	2.09	1.28	1.95
Cao et al.[24]	Box girder	4	470	1.83	2.36	0.77	0.99
Li et al.[25]	Rectangular beam	8	170	1.30	1.52	1.09	1.27
Shi et al.[26]	T-beam*	4	300	1.00	1.18	—	—
Cao et al.[27]	Box girder	3	558	1.64	4.40	0.53	1.41
This study	Flat slab (field test)	6	2062	2.53	3.40	0.78	1.04
	Total number of specimens:	145			Mean:	1.167	
					Standard deviation:	0.329	

*Specimens without external loading, causing growing camber included.

†Specimens with concrete topping during test included.

Note: Specimens lacking sufficient data or subjected to additional loading during test were excluded from metric calculations; specimens with upward deflection due to excessive prestressing at initial loading stage were excluded for calculating metrics.

performance with reduced prestress losses compared to conventional steel.[9,10,19] Prestress loss was typically highest in the early period (first 30 to 90 days), then stabilized. Higher initial prestressing forces resulted in greater absolute losses but often improved deflection control.[25]

The deflection multiplier, defined as the ratio of long-term deflection to initial elastic deflection, was collected across the study as a key indicator of time-dependent behavior in PT concrete (Fig. 2). After excluding data lacking sufficient detail or involving secondary loading or unloading, a total of 88 data points were collected. Multiplier values varied widely, usually ranging from 1.47 for CFRP systems[9] to 3.1 for composite beams with steel prestress,[11] with typical values falling between 2.0 and 3.0 for steel systems. Several studies[18,26] reported that cracked members exhibited significantly higher deflection multipliers, up to 18% greater, compared to uncracked members. Additionally, the rate of deflection development was most rapid during the initial 3

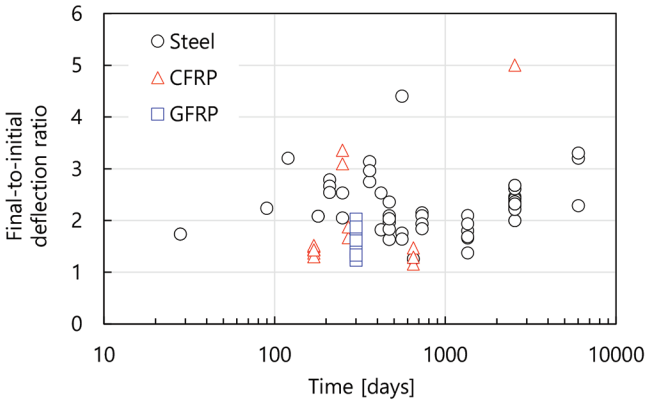

Fig. 2—Final-to-initial deflection ratio of prestressed concrete.

to 6 months, accounting for up to 80% of the total deflection, after which it tended to stabilize. This pattern was consistently observed in both small-scale beams[18] and large bridge models.[26]

Laboratory findings consistently indicate that prestress losses are highest during the initial months after tensioning before stabilizing, with deflection multipliers typically ranging from 1.5 to 3.0 depending on the prestressing material and structural configuration. Despite extensive laboratory research, there is a notable gap in long-term field monitoring data from operational buildings. The Precast/Prestressed Concrete Institute (PCI) provision[5] provides guidance for predicting long-term deflections in prestressed concrete (PC), but these provisions are primarily for precast PC rather than in-place PT structures.

Addressing this gap, this study presents comprehensive monitoring data from a real-world building in Seoul, Korea, where two Smart Strands with embedded FBG sensors were installed to monitor prestressing forces continuously for up to 5 and a half years. Simultaneous deflection measurements were conducted at six locations across two floors, providing unprecedented data regarding the long-term behavior of PT flat slabs under actual building conditions. This study also aims to analyze the data using computational tools and to validate existing prediction models. It is the authors' perspective that this study may further enhance the knowledge and practical usage of guidelines regarding the long-term behavior of PT structures.

RESEARCH SIGNIFICANCE

This study provides unprecedented long-term field data on prestressing force and deflection behavior in unbonded PT concrete structures, addressing a critical gap in existing literature. By using Smart Strands with embedded FBG sensors, it demonstrates the feasibility of continuous, accurate monitoring under real-world conditions. The validated correlation between measured and predicted performance enhances confidence in the analysis method and ACI CODE-318-25 provision. These findings offer valuable insights for improving serviceability predictions, optimizing maintenance strategies, and advancing structural health monitoring technologies, thereby contributing to more durable, efficient, and resilient PT concrete systems in modern construction.

TARGET BUILDING AND MONITORING METHOD

Target building

The target building for this study was a real-world office building constructed in Seoul, Korea (Fig. 3). This structure was selected to examine the long-term behaviors of PT slabs from installation to actual in-service conditions. The building features a flat slab structure with each column having a rectangular drop panel. The story height was 3.9 m (12.8 ft), with a slab thickness of 210 mm (8.3 in.) and drop panel thickness of 190 mm (7.5 in.). Each slab had a square shape with spans of approximately 10 m (32.8 ft). For the slab and column, the concrete strengths were set at 35 and 45 MPa (5075 and 6525 psi), respectively. Main and distribution reinforcement consisting of 12.7 mm (0.5 in.) diameter bars with a yield strength of 500 MPa (72.5 ksi) was placed at 250 mm (9.84 in.) spacing at the bottom of the slab. At the top of the slab, 12.7 mm (0.5 in.) diameter bars with a yield strength of 500 MPa (72.5 ksi) and 15.9 mm (0.625 in.) diameter bars with a yield strength of 600 MPa (87.0 ksi) were alternately placed at 250 mm (9.84 in.) spacing for main and distribution reinforcement. The unbonded single-strand post-tensioning method was implemented for the entire slab structure from the third to 36th floors. The tendons were arranged in a banded configuration in the north-south direction and distributed in the east-west direction. Non-encapsulated tendons were used, except for the smart tendon, because encapsulated tendons are not required in Korea (Fig. 4).

Prestressing force monitoring method

To measure the prestressing forces within the PT slab, optical sensors using FBG system were employed. This system, developed by the Korea Institute of Civil Engineering and Building Technology (KICT),[28] allowed for internal stress monitoring of the tendons (Fig. 4 and 5). For these measurements, Smart Strands were fabricated where the center wire of the standard seven-wire strand was replaced with carbon fiber steel containing optical fiber.[1-4,29] These modified strands exhibited the same strength as conventional 1860 MPa (270 ksi) low-relaxation strands, reaching an ultimate strain of approximately 0.012. The fiber-optic strands were installed on the 13th floor of the building, consisting of one 13 m (42.7 ft) strand and one 55 m (180.4 ft) strand. The 13 m (42.7 ft) strand contained one sensor, while the 55 m (180.4 ft) strand had five sensors positioned at the center of each span. For the jacking procedure, the 13 m (42.7 ft) strand was tensioned in a single step due to its shorter length, whereas the 55 m (180.4 ft) strand required a three-step loading process. The prestressing forces were measured during the initial jacking and continuously monitored over an extended period to evaluate the long-term performance of the system.

Deflection monitoring method

Deflection measurements were conducted at six specific points across the 13th and 14th floors, where the concrete pouring of the 13th floor began in December 2015. The measurement points were strategically positioned to capture data from three different slab configurations on each floor:

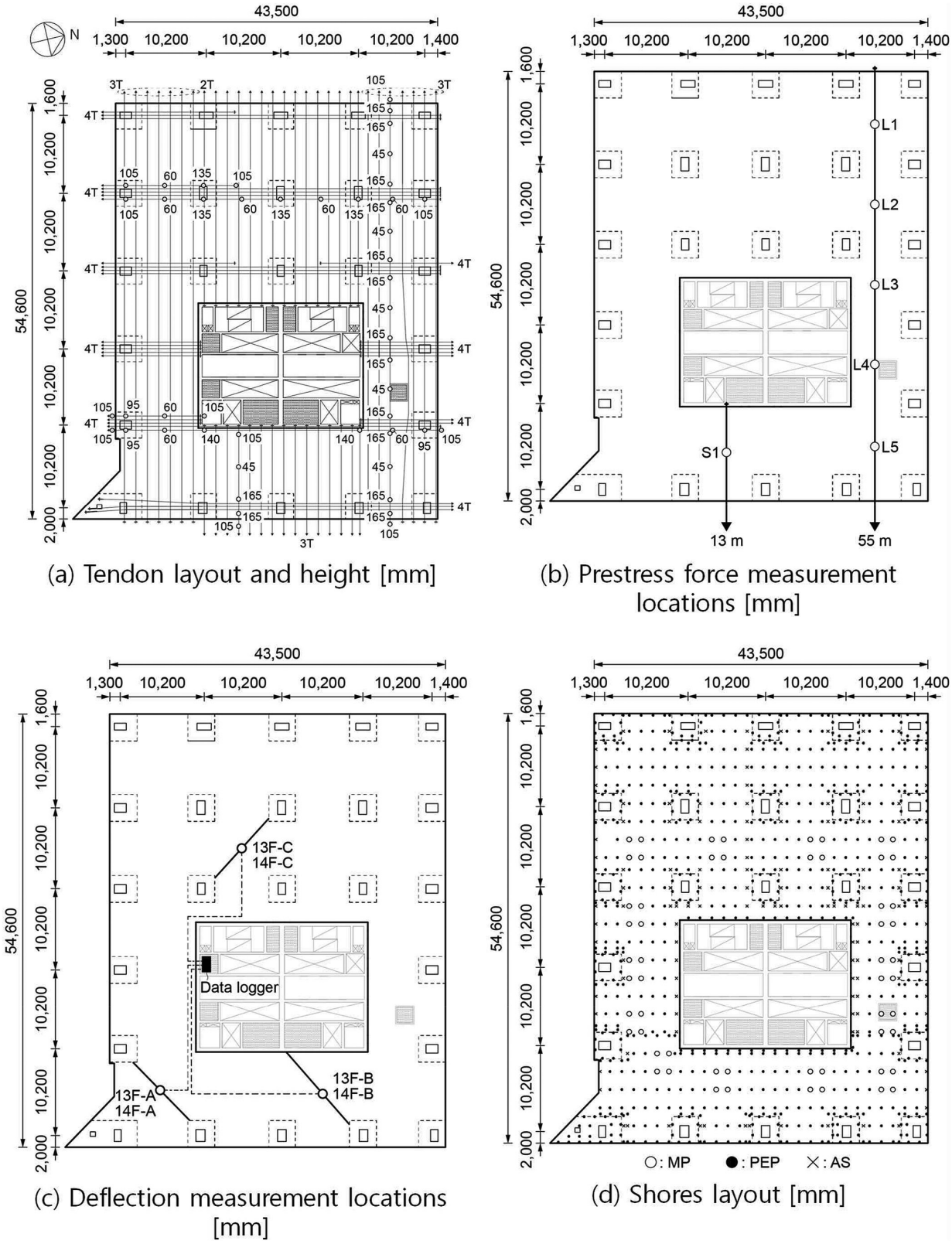

(a) Tendon layout and height [mm]

(b) Prestress force measurement locations [mm]

(c) Deflection measurement locations [mm]

(d) Shores layout [mm]

Fig. 3—Monitoring locations and construction plan. (Note: 1 mm = 0.039 in.)

corner slabs (designated as A), edge slabs (designated as B), and interior slabs (designated as C). This arrangement allowed for comprehensive comparison of deflection behavior across various slab positions within the structure. The deflection measuring equipment consisted of a specialized setup using steel wires suspended between drop panels (Fig. 6). The wires were pretensioned with springs and turnbuckles to prevent sagging due to temperature fluctuations during the extended measurement period. Linear variable differential transformers (LVDTs) with 100 mm

(3.94 in.) measurement capacity were installed to record the deflection values. Data collection began immediately after the concrete formwork was removed and continued for approximately 5 and a half years, providing a comprehensive record of deflection behavior through various construction stages and into the building's operational life.

Construction method

The construction sequence was carefully documented as it significantly impacts deflection behavior. The construction of Nth floor consisted of three distinct stages: concrete pouring on the Nth floor slab, shoring removal on the (N-3)th floor slab, and post-tensioning jacking on the Nth floor slab (Fig. 7 and Table A1 of Appendix A*). Each cycle, consisting of these three steps, took approximately 12 days. Because shores were placed on three consecutive floors during the construction of a new floor, the effect of shoring, transferring construction loads downward, was significant for three cycles per floor, lasting a total of approximately 37 days (three 12-day cycles plus 1 additional day).

The building employed three types of shoring systems to support the slabs during construction: PERI's Prop (PEP) shores (steel) distributed across the entire slab, Alu Shoring (AS) shores (aluminum) positioned near drop panels, and Multi Prop (MP) shores (copper) arranged in groups of four to support the center of each slab where maximum deflection was anticipated. Material properties of shores are summarized in Table 2.

PRESTRESSING FORCE MONITORING

Initial prestressing force measurements

The prestressing force measurements during the jacking process provided valuable insights into the behavior of tendons (Fig. 8 and 9). For the 13 m (42.7 ft) strand (designated as S1), prestress of approximately 50% of the nominal strength was applied, corresponding to 135 kN (30,349 lbf). For the 55 m (180.4 ft) strand, the monitoring system demonstrated the effects of tendon curvature and friction inside the sheathing. The five sensors (designated L1 through L5) showed a gradient of prestressing forces, with higher values near the stressing end (L5) at 204 kN (45,861 lbf) and lower values toward the fixed end (L1) at 165 kN (37,094 lbf). This gradient became particularly pronounced once the jacking force exceeded 60 kN (13,489 lbf), indicating the threshold where friction effects began to significantly influence force distribution.

At the stressing end of the 55 m (180.4 ft) strand, the maximum jacking force measured was approximately 80% (204 kN [45,861 lbf]) of the nominal tensile strength. After strand release and seating, this value decreased to approximately 77% (196 kN [44,063 lbf]), representing an anchor set loss of approximately 3% of the nominal tensile strength. This loss corresponded to an anchorage slip of approximately 3 mm (0.12 in.), which is within acceptable limits for post-tensioning systems. Notably, the sensors at positions L1 through L4 did not register any significant change after jacking force removal, indicating that the anchorage slip effects were localized to the stressing end.

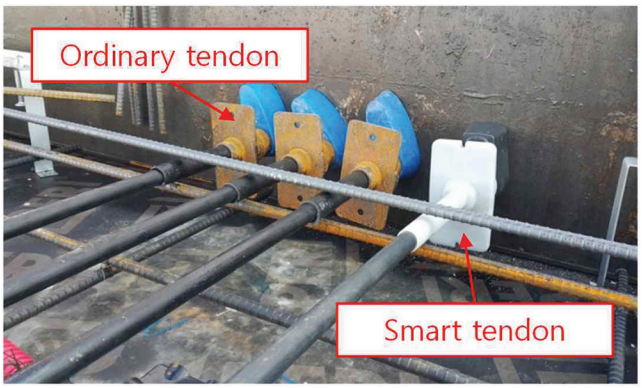

Fig. 4—Ordinary and smart tendons.

Long-term prestressing force monitoring

To evaluate the time-dependent behavior of tendons, prestressing forces were continuously monitored following the initial jacking operations (Fig. 10). For the 55 m (180.4 ft) strand, data was collected for approximately 3 months before an unfortunate disconnection of the fiber terminated the measurements in April 2016.

The measurements from the 55 m (180.4 ft) strand showed similar trends across all five sensing points over time. All five sensors indicated a decrease in prestressing force after 1 month by approximately 3% of nominal strength. From the second month onward, all sensors showed a slight increase by 1% of nominal strength, which continued thereafter. The decrease in prestressing force may be attributed to concrete shrinkage resulting in decreased total tendon length, while the increase in prestressing force may be attributed to shore removal resulting in increased deflection of the slab. An interesting phenomenon was observed between points L5 and L4, where the force magnitudes became nearly identical after approximately 2 months. This convergence was attributed to force redistribution, albeit slight, within the two-span section containing these points after the removal of shoring supporting the slab. This observation highlighted the dynamic nature of prestressing force distribution in response to structural support conditions.

More comprehensive long-term data was obtained from the 13 m (42.7 ft) strand (S1), which provided continuous measurements over a 6-year period (Fig. 11). The long-term behavior of this tendon provided valuable insights into the time-dependent performance of the unbonded PT system. A notable observation from the long-term monitoring was the correlation between prestressing force fluctuations and ambient temperature variations. In the summer season when ambient temperatures ranged from 20 to 30°C (68 to 86°F), the measured prestressing force was approximately 46 to 39% of the nominal strength. In the winter season when temperatures ranged from –5 to 10°C (23 to 50°F), the measured prestressing force was approximately 42 to 44% of the nominal strength. The optical fiber measurements exhibited high sensitivity to temperature changes, showing

*The Appendix is available at **www.concrete.org/publications** in PDF format, appended to the online version of the published paper. It is also available in hard copy from ACI headquarters for a fee equal to the cost of reproduction plus handling at the time of the request.

Fig. 5—Tendon jacking and seating process.

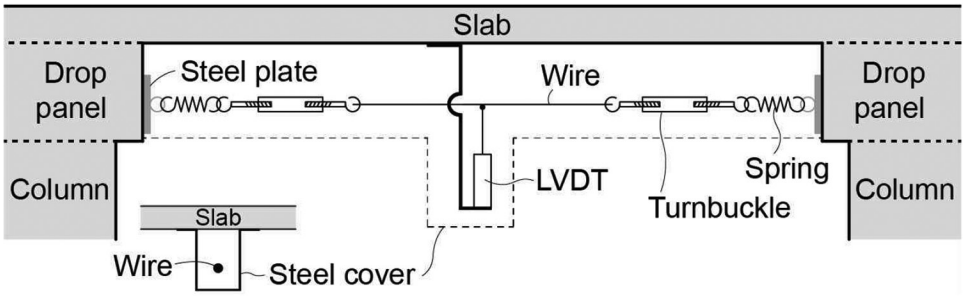

Fig. 6—Deflection monitoring device.

Table 2—Properties of shores

Type	Weight, kg	Elastic modulus, MPa	Creep coefficient
MP	18.8	200,000	2.0
PEP	19.2	69,999	2.0
AS	17.9	69,999	2.0

Note: 1 kg = 2.2 lb; 1 MPa = 0.145 ksi.

cyclic variations that corresponded to seasonal temperature patterns.

Therefore, temperature calibration of the measurements was required to monitor actual prestressing force variations over the long term. Equation (1), suggested from the previous study,[3] was used to calibrate the optical sensor.

$$\varepsilon = \frac{1}{1-p_e}\left(\frac{\Delta\lambda}{\lambda_B} - (\alpha+\xi)\Delta T\right) \quad (1)$$

where ε is prestressing tendon strain; p_e is photo-elastic coefficient; $\Delta\lambda$ is λ-λ_B, λ is measured wave length, λ_B is base wave length at the start of the measurement; ΔT is T-T_B, T is measured temperature, T_B is base temperature at the start of the measurement; α is thermal expansion coefficient of concrete; and ξ is coefficient ranging from $6 \cdot 10^{-6}$ to $11 \cdot 10^{-6}$/°C ($1.08 \cdot 10^{-5}$ to $1.98 \cdot 10^{-5}$/F). In this study, α was neglected because the actual building was considered restrained against thermal expansion, and $6.2 \cdot 10^{-6}$/°C ($1.12 \cdot 10^{-5}$/F) was used for ξ, regarding the previous study by Jeon et al.[3]

When calibrated, the prestressing force showed a similar trend to the 55 m (180.4 ft) strand for the first 4 months, decreasing by approximately 2% of the nominal strength. However, after that period, the prestressing force rapidly decreased, and after 1 year, the force decreased by approximately 5% of the nominal strength. This was attributed to factors affecting prestressing force, including concrete shrinkage, concrete creep, and stress relaxation.[30-32] Subsequently, the prestressing force showed minor variations, remaining at approximately 43% of the nominal strength for 5 years. This result indicated that in actual concrete building, most of the prestressing force loss may occur within a year after tendon jacking. Overall, the prestressing force monitoring program provided unprecedented insights into the behavior of PT tendons in an actual building environment. The results demonstrated its ability to maintain effective prestressing forces over an extended period, which is essential for the long-term serviceability of PT structures.

DEFLECTION MONITORING AND ANALYSIS

Deflection monitoring results

Deflection data was collected over approximately 5 and a half years from six measurement points across the 13th and 14th floors of the building. These measurement points represented three different slab configurations: corner slabs (A), edge slabs (B), and interior slabs (C). The monitoring began immediately after the removal of concrete formwork and continued through various construction stages and into the building's operational period.

The deflection measurements revealed distinct patterns corresponding to the construction sequence (Fig. 12). When

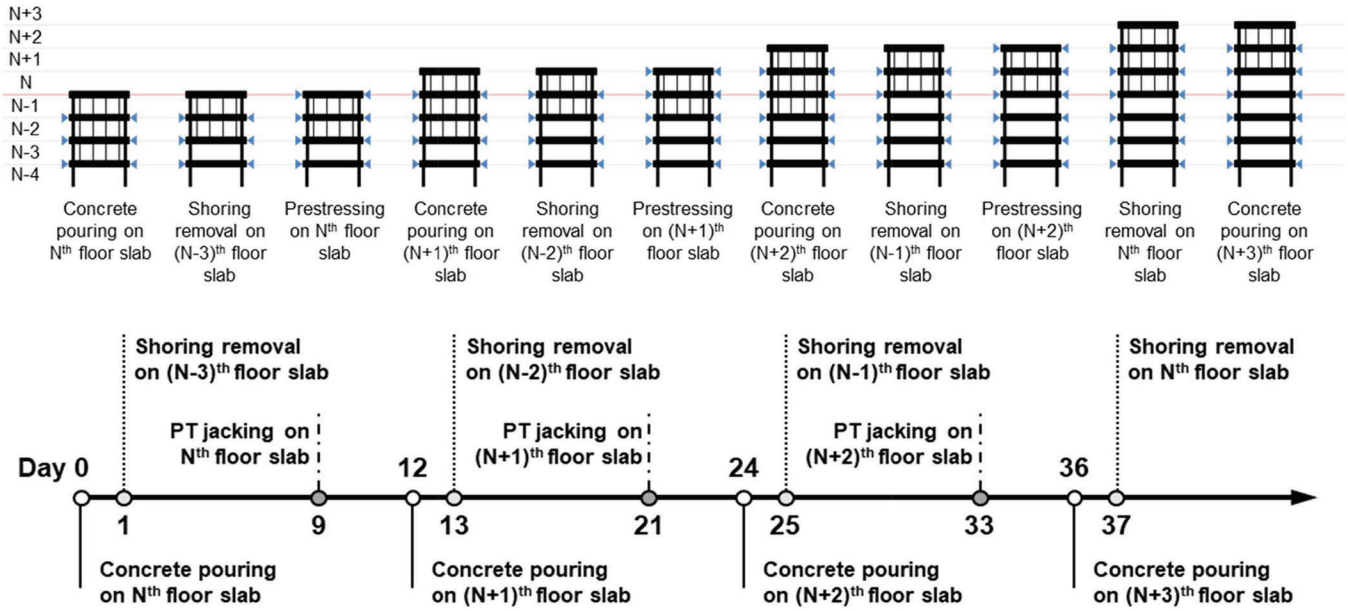

Fig. 7—Planned construction timeline (refer to Appendix A for actual elapsed time).

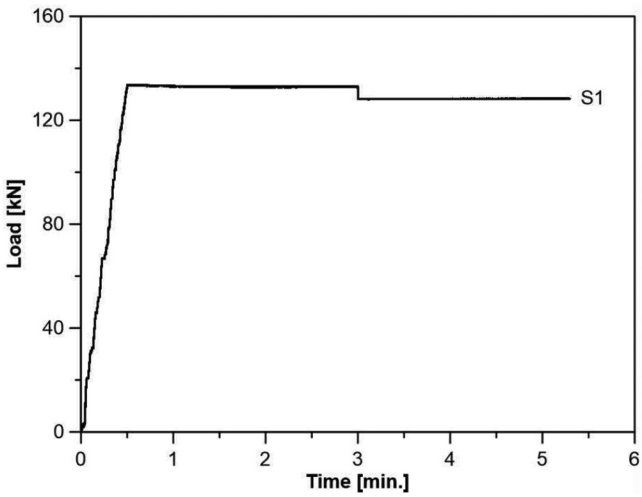

Fig. 8—Prestressing force of short tendon. (Note: 1 kN = 0.2248 kip.)

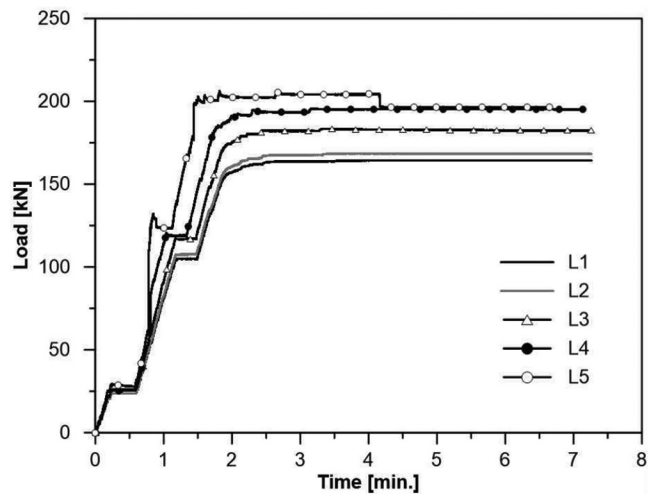

Fig. 9—Prestressing force of long tendon. (Note: 1 kN = 0.2248 kip.)

the prestressing strands were jacked (PT jacking on 13th, 14th, and 15th floor in Fig. 12), a noticeable decrease of approximately 1 to 2 mm (0.039 to 0.079 in.) in deflection was observed. This same effect occurred when strands were jacked on multiple floors above, as shores transferred the construction load downward. When concrete was placed on up to three stories above (concrete pouring on 14th, 15th, and 16th floor in Fig. 12), the floor deflection increased by approximately 3 to 4 mm (0.118 to 0.157 in.), as shores transferred the not-yet-hardened concrete load to the slab. The removal of shores supporting the floor (removal of shores on 11th and 12th floor in Fig. 12) resulted in increased deflection by 4 to 5 mm (0.157 to 0.197 in.). Conversely, when shores on the floor that were transferring loads from above were removed (removal of shores on 13th floor in Fig. 12), the deflection decreased significantly by approximately 10 mm (0.394 in.).

After the complete removal of all shores associated with the slab, the resulting deflection was designated as the short-term deflection value, recording approximately 10 to 15 mm (0.394 to 0.591 in.) of deflection recovery from the maximum values recorded. The short-term deflection varied by location, where interior slabs with all four edges constrained demonstrated significantly smaller deflection (7.5 mm [0.295 in.] for 13F-C) compared to corner or edge slabs (13.0 mm [0.512 in.] for 13F-A).

To demonstrate the advantages of deflection control in PT slabs compared with RC slabs, the measurement results were compared with field-monitored data from an RC slab constructed by the same contractor in Korea (Fig. 13). The RC slab had a story height of 2750 mm (108 in.), slab thickness of 300 mm (11.8 in.), and a span of approximately 10 m (32.8 ft). Deflection measurements were taken at two locations, designated RC-A and RC-B.[33,34]

During the construction stage, all slabs showed similar maximum deflection values: 13F-A (PT) recorded 23.3 mm (0.92 in.) on day 27, while RC-A and RC-B reached 24.0 and 21.0 mm (0.94 and 0.83 in.) on days 21 and 26, respectively.

Given that the same contractor executed both projects, construction control conditions were likely similar. However, the deflection recovery differed notably between slab types. On day 57, 13F-A recovered to 12.3 mm (0.48 in.), reflecting an 11.0 mm (0.43 in.) recovery. In contrast, RC-A and RC-B deflections were 20.0 and 18.2 mm (0.79 and 0.72 in.) on days 59 and 66, yielding recoveries of only 4.0 and 2.8 mm (0.16 and 0.11 in.), respectively. This limited recovery in the RC slabs resulted in larger initial deflections at the time of occupancy and a more rapid increase in deflection over time. After 300 days, RC-A exhibited a deflection of 36.9 mm (1.45 in.), whereas 13F-A reached only 24.1 mm (0.95 in.), indicating a 34.7% reduction in deflection for the PT slab. Despite having a thicker slab and similar span, the RC slab exhibited significantly greater deflection, clearly indicating the superior deflection control performance of the PT slab.

The deflection at each location grew as time passed (Fig. 14). The increased deflection after the removal of shores was designated as long-term deflection. Because no shores were associated with the slab, the deflection was only affected by time and additional loads. The long-term deflection, early after short-term deflection, for approximately 180 days, increased drastically due to insufficient stiffness and the loads attributed to finishing materials. After that, the sag increased gradually over time. Unlike the slabs located at the corners or edges (A and B), the inner slab with all four constrained edges (C) witnessed the smallest deflection results. This was attributed to boundary conditions of the slabs, with C locations having higher flexural stiffness. Each measurement reached maximum deflection of 32.8, 34.0, 19.7, 45.1, 43.8, and 32.2 mm (1.29, 1.39, 0.78, 1.78, 1.72, and 1.27 in.) for 13F-A, 13F-B, 13F-C, 14F-A, 14F-B, and 14F-C after 5 and a half years of use (Table 3). The growing nature of long-term concrete deflection was attributed to concrete shrinkage and creep.

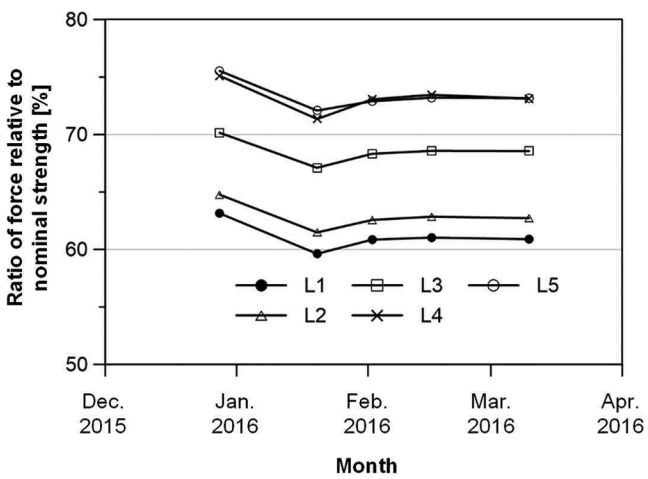

Fig. 10—Short-term prestressing force measurement for long tendon.

Differences in deflection behavior were observed between floors at the same plan locations due to variations in construction and service loads, construction schedules, material properties, and long-term environmental conditions (Fig. 14 and Table 3). For example, the design concrete strengths were 45 MPa (6.53 ksi) for the first through 12th floors and 35 MPa (5.08 ksi) for the 13th floor and above, indicating greater stiffness in the lower floors. In addition, construction took place during winter, when strength development is particularly sensitive to curing conditions. The primary objective of this study is to demonstrate that short- and long-term deflections of PT slabs can be accurately predicted when construction processes and initial deflections, respectively, are characterized with a high degree of accuracy.

Short-term deflection analysis

Short-term deflection was predicted using specialized PT slab design software. The model included the same dimensions as the actual building, including the target slab with columns, drop panels, and PT tendons. In the analysis with self-weight, the maximum deflection was observed at the corner slab, which is the same location as 13F-A or 14F-A. To reduce modeling and computing time, a partial model of the corner slab was designed (Fig. 15 and 16). Partial modeling required proper division of the compartments and appropriate boundary conditions for the cutouts. For the two

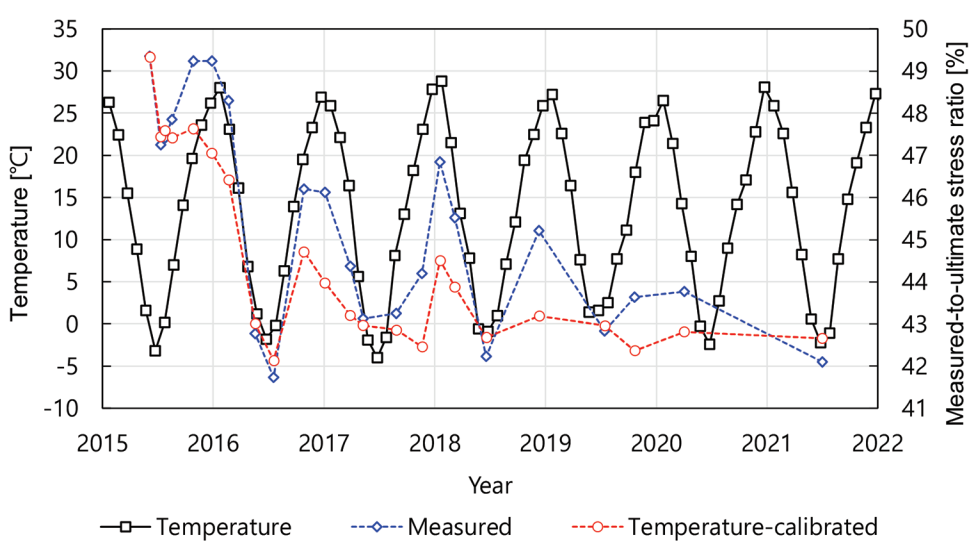

Fig. 11—Long-term prestressing force measurement for short tendon. (Note: [°C x 9/5] + 32 = °F.)

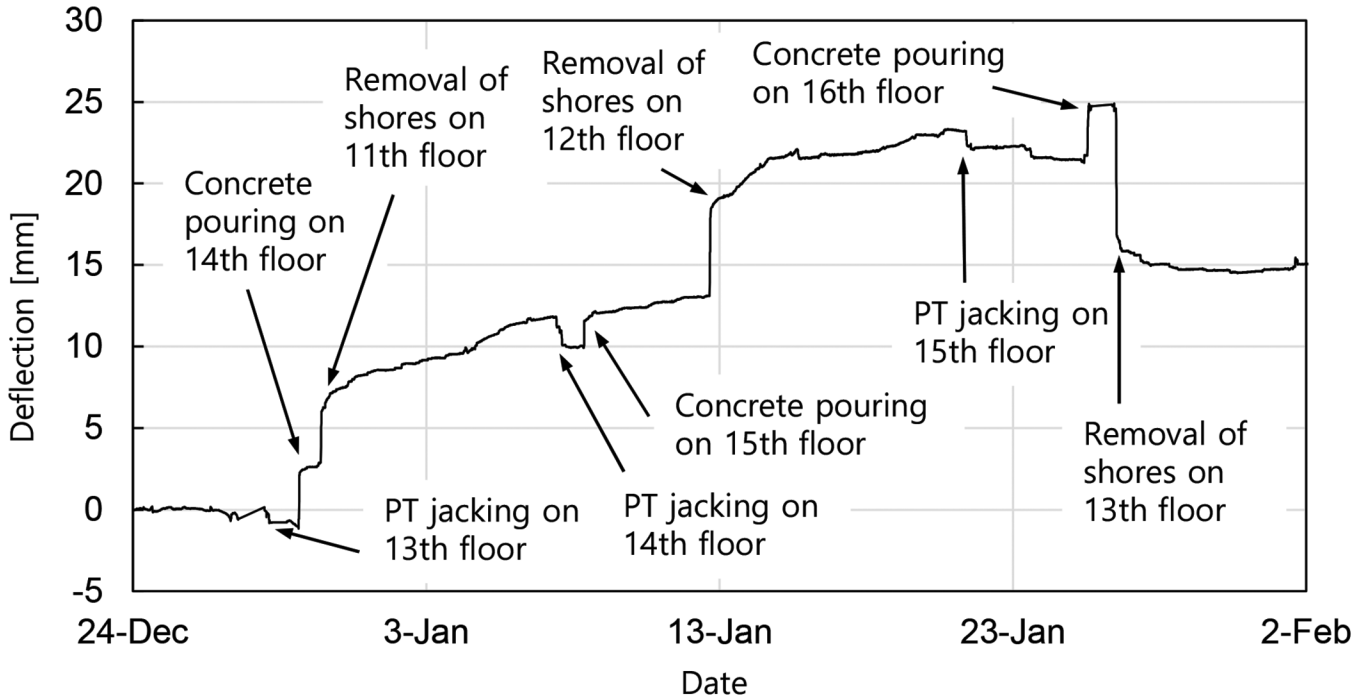

Fig. 12—Short-term deflection measurement. (Note: 1 mm = 0.039 in.)

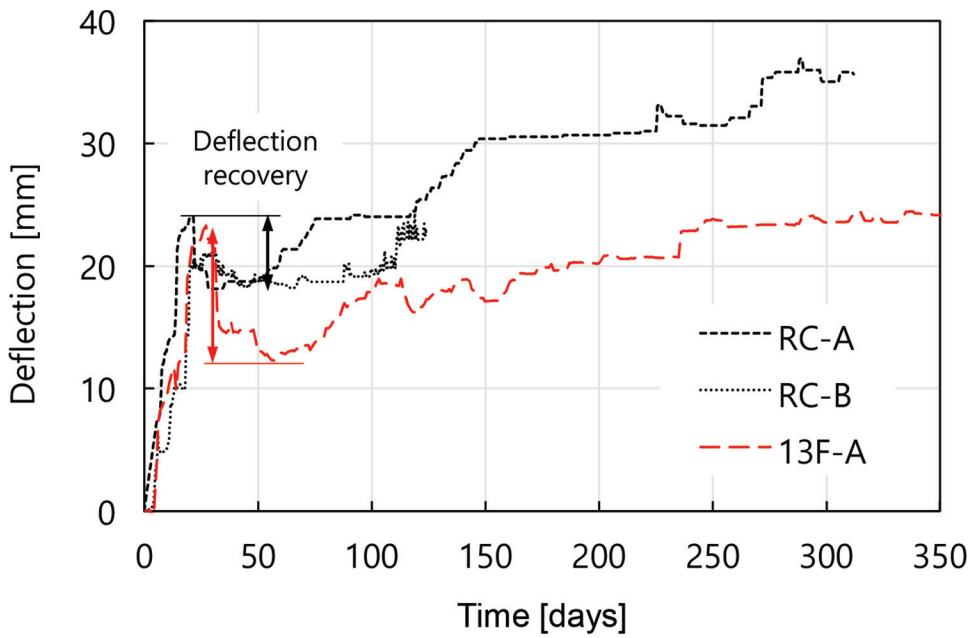

Fig. 13—Comparison of deflections in field-monitored PT and RC slabs (Note: 1 mm = 0.039 in.)

sides where the slab continues, displacement was allowed in the Z direction while rotation was fixed only along the edge of X-X or Y-Y.

The analysis results of the whole and partial models were compared. The two models showed similar deflections for each load combination. When only self-weight was considered, the whole slab model exhibited 9.12 mm (0.359 in.) deflection, while the partial slab model showed 9.11 mm (0.359 in.). When prestressing was added, the whole slab model showed 4.56 mm (0.180 in.) deflection, compared to 4.63 mm (0.182 in.) for the partial slab model. The differences were 0.01 mm (0.0004 in.) under self-weight and 0.07 mm (0.003 in.) with prestressing. As the partial slab model successfully represented the full slab behavior, it was used for the remaining prediction analyses throughout this study.

The analysis incorporated detailed information about the construction sequence, shoring arrangement, concrete strength development, and elastic modulus evolution. In ADAPT, shoring was expressed as a circular pillar with a diameter of 100 mm (3.94 in.). The unit weight was input by dividing the total weight by the volume of the circular column. The elastic modulus was set as 200,000 MPa (29,008 ksi) for MP shores and 70,000 MPa (10,153 ksi) for PEP and AS shores. The strength of the circular column was calculated automatically according to the elastic modulus.

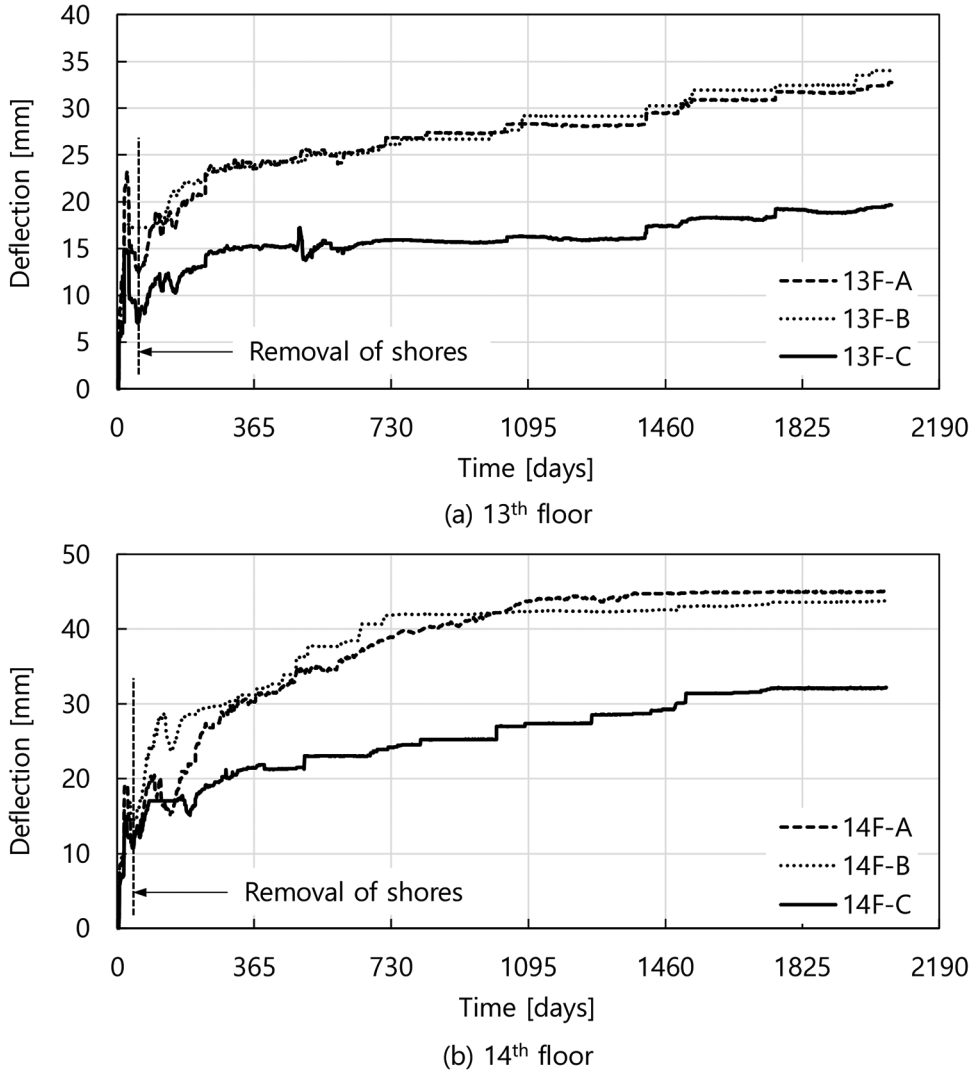

Fig. 14—Long-term deflection measurement (Note: 1 mm = 0.039 in.)

Table 3—Maximum deflection at measurement locations

Measurement location	Maximum deflection, mm
13F-A	32.8
13F-B	34.0
13F-C	19.7
14F-A	45.1
14F-B	43.8
14F-C	32.2

Note: 1 mm = 0.039 in.

To accurately represent early-age concrete properties, equivalent concrete age was calculated considering actual curing temperatures during construction, using the approach developed by Hansen and Pedersen (Eq. (2) and (3)).[35] This adjustment was particularly important as construction occurred during winter months with low ambient temperatures

$$t_e = \sum_0^t \exp\left[\frac{E_a}{R}\left(\frac{1}{T_s} - \frac{1}{T_a}\right)\right] \cdot \Delta t \ \text{[days]} \tag{2}$$

$$E_a = \begin{cases} 33.5 & (T_a \geq 20°\text{C}) \\ 33.5 + 1.47(20 - T_a) & (T_a < 20°\text{C}) \end{cases} \text{[KJ/mol]} \tag{3}$$

where t_e is the equivalent age; E_a is the apparent activation energy; R is the gas constant (8.314 J/molK); T_s is the reference temperature (293K); and T_a [K] is the concrete temperature during the time Δt days.

The curing rates using the reference temperature of 20°C (68°F) were derived for temperatures ranging from 1 to 80°C (33.8 to 176°F). At the reference temperature, the curing rate is 100%. According to the Korea Meteorological Administration (KMA),[36] the representative temperature during January 2016 was 0°C (32°F). The first 2 days were set at 20°C (68°F) because thermal curing was performed until the formworks were demolded. After demolding, 0°C (32°F) was input for the remaining period. The equivalent age is the product of the curing rate and the duration. The cumulative equivalent age represents the equivalent age up to the specified date.

The equivalent age was used to derive concrete compressive strength at early age, using Eq. (4) to (7).[37] For the slab

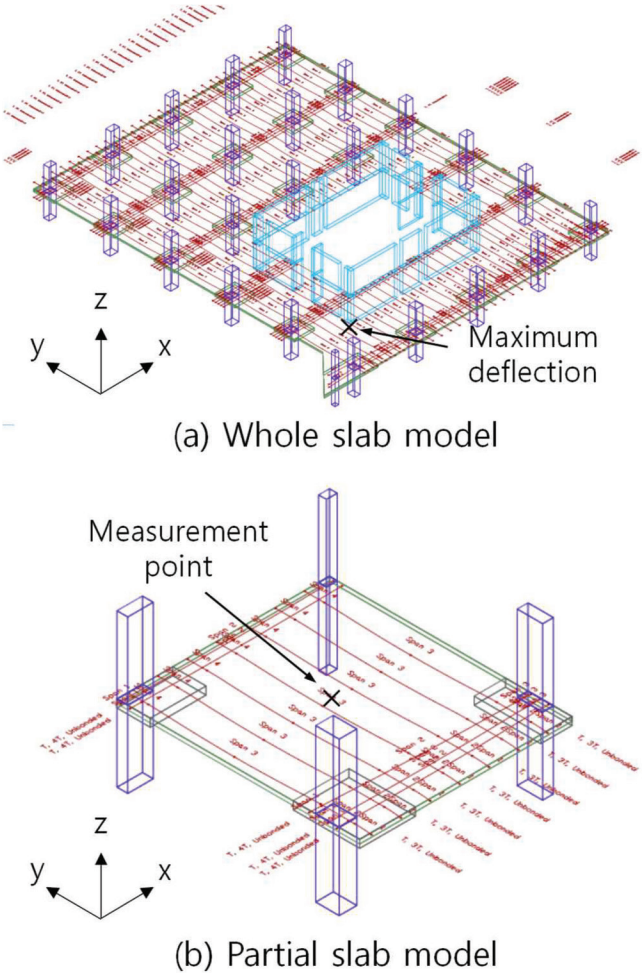

Fig. 15—Slab deflection analysis models.

and column, design strengths were set at 35 and 45 MPa (5075 and 6525 psi), respectively

$$f_{cu}(t_e) = \beta_{cc}(t_e) f_{cu} \tag{4}$$

$$\beta_{cc}(t_e) = \exp\left[\beta_{sc}\left(1 - \sqrt{\frac{28}{t_e}}\right)\right] \tag{5}$$

$$f_{cu} = f_c' + \Delta f \tag{6}$$

$$\Delta f = \begin{cases} 4 \text{ [MPa]} & (f_c' < 40) \text{ [MPa]} \\ 4 + 0.1(f_c' - 40) \text{ [MPa]} & (40 \le f_c' \le 60) \text{ [MPa]} \\ 6 \text{ [MPa]} & (f_c' > 60) \text{ [MPa]} \end{cases} \tag{7}$$

where f_{cu} is the average compressive strength of concrete at the age of 28 days; Δf is the correction factor for concrete strength; $\beta_{cc}(t_e)$ is the correction coefficient according to equivalent age for concrete strength development; and β_{sc} is the influence coefficient on dry shrinkage according to cement type. In this study, 0.35 was used for β_{sc} of moist

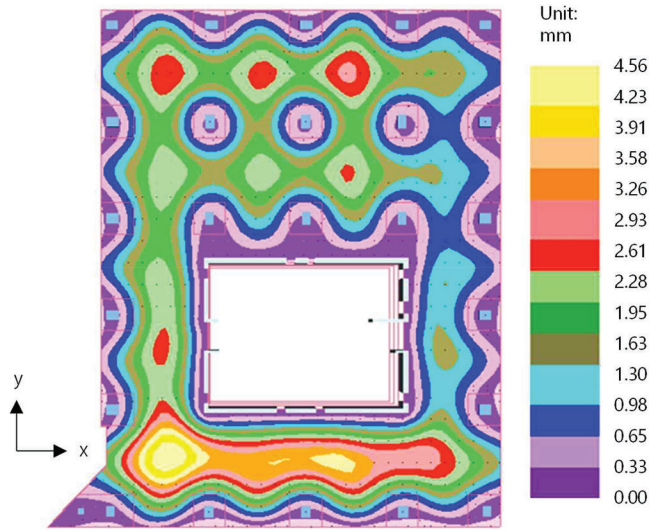

Fig. 16—Slab deflection analysis results. (Note: 1 mm = 0.039 in.)

cured ordinary portland cement, 0.15 was used for β_{sc} of steam cured ordinary portland cement, and 1 MPa is 145 psi.

The elastic modulus was calculated using an equation proposed for typical Korean concrete by Hong et al. (Eq. (8))[38]

$$E_c(t_e) = k_1 \sqrt{f_{cu}(t_e)} \text{ [MPa]} \tag{8}$$

where $E_c(t_e)$ is the elastic modulus of concrete at equivalent age; f_c' is the specified compressive strength of concrete; k_1 is the constant depending on the type of concrete (4050 for ordinary portland cement was used in this study, and the constant is 48,600 for f_{cu} in unit of psi); and 1 MPa is 145 psi.

The concrete properties derived from equivalent age were used as inputs for the analysis. The analytical results demonstrated that deflection changes corresponded directly to construction activities (Fig. 17). When tendons were jacked, deflection decreased; when concrete was poured on upper floors or shores were removed, deflection increased. The model predicted that in the final stage, when all shoring above the slab was removed, approximately 62% of the maximum deflection would be recovered, resulting in a short-term deflection of 11.3 mm (0.445 in.). Comparison between measured and predicted deflection for monitoring points 13F-A and 14F-A showed good agreement, particularly for short-term deflection values. Usually, the difference between the analysis and the measurement was no more than 5 mm (0.20 in.). While the analysis predicted immediate deflection recovery upon shore removal, the actual measurements showed a more gradual recovery process spanning approximately 20 days. This difference was attributed to the time-dependent elastic recovery characteristics of concrete. For 14F-A, between days 30 and 40, the measurement was significantly lower compared to the analysis, because the LVDT in the measurement reached its temporary maximum measurement capacity. The device was adjusted after it was found that the temporary LVDT had reached its stroke limit. Given that the analysis was based on elastic behavior of concrete, the close correlation between analytical and

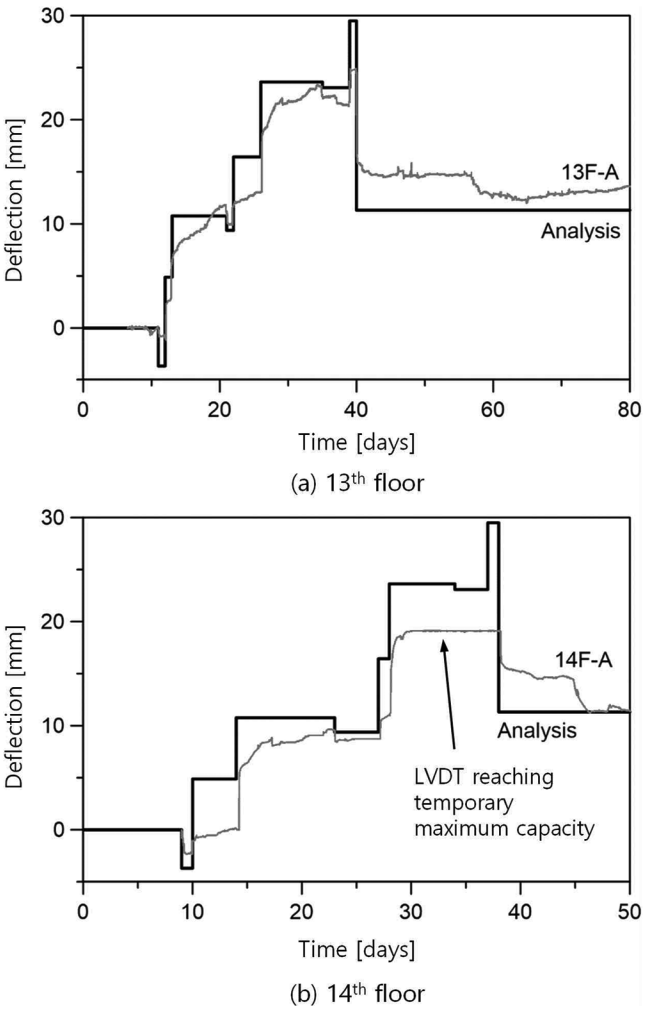

Fig. 17—Short-term deflection analysis results (Note: 1 mm = 0.039 in.)

measured results confirmed that the PT system effectively minimized concrete cracking, allowing the assumption of uncracked elastic behavior to remain valid.

Long-term deflection analysis

ACI CODE-318-25[39] provides equation of increasing long-term deflection over the duration of sustained loading for reinforced concrete (RC). The long-term deflection is proportional to the initial deflection and can be expressed by using the Eq. (9) and (10)[37,39]

$$\Delta_L = \Delta_i(1 + \lambda_\Delta) \tag{9}$$

$$\lambda_\Delta = \frac{\xi}{1 + 50\rho'} \tag{10}$$

where Δ_L is the long-term deflection; Δ_i is the initial deflection; λ_Δ is the amplification factor; ξ is the time-dependent coefficient; and ρ' is the compression steel ratio.

The ACI CODE-318-25 suggests that ξ may increase up to 2 at maximum after 60 months for RC system. However, it does not offer equivalent guidance for PT systems, as PT behavior is influenced by additional variables not present in RC, such as concrete stiffness at the time of prestressing, long-term prestress loss, and the presence of concrete topping in precast systems. Due to these complexities, alternative methods are recommended to estimate long-term deflection in PT members. One commonly adopted approach is the use of multipliers from the PCI provision,[5] which are derived through rational procedures developed by Martin.[40]

However, it is important to note that this method may not be directly applicable to in-place PT construction. The PCI multipliers are tailored for precast systems and are based on assumptions such as prestressing being applied before the concrete reaches its 28-day strength and the use of pretensioning methods. These multipliers are applied to both the initial deflection or camber at the time of prestressing and the deflection from superimposed loads. While this method is appropriate for precast elements, where deflection can be easily monitored and managed in a controlled environment, it poses challenges for cast-in-place construction.

In on-site PT construction, the self-weight of freshly cast slabs is typically supported by shores, transferring loads to lower floors. As a result, the true deflection due to the member's own stiffness cannot be measured accurately until all shores, including formwork, shoring, and adjustable props, are removed, usually a few weeks after initial concrete placement or prestressing. Therefore, the step-by-step application of deflection multipliers, as outlined in the PCI provision, becomes impractical for on-site PT. Considering that both ACI CODE-318-25 and the PCI provision are based on the same underlying logic for deriving their multipliers, it may be more appropriate to use the ACI CODE-318-25 provisions for estimating long-term deflection in PT systems, especially because shores are typically removed and sustained loads applied only after the concrete has fully developed its stiffness.

To assess the validity of applying RC-based multipliers to PT systems, long-term deflections of both RC and PC specimens were predicted using the deflection coefficient specified for RC in ACI CODE-318-25 (Table 4). The RC dataset was obtained from the study by Nguyen et al.,[41] which included 217 specimens subjected to sustained loading durations ranging from 88 to 3052 days. The PC dataset included 145 specimens from previous studies under laboratory condition[6-27] and this study; however, data with insufficient information, such as missing initial deflection measurements, or growing upward deflection caused by the absence of external load were excluded, resulting in 94 usable data points for analysis. The comparison showed no significant difference between the prediction accuracy for RC and PC specimens (Fig. 18). The average predicted-to-measured deflection ratio was 1.168 for the RC dataset and 1.167 for the PC data set, with corresponding standard deviations of 0.324 and 0.329, respectively. These closely aligned results suggest that applying RC deflection coefficient to PC systems remains a valid and reasonable approach.

The ACI CODE-318-25 time-dependent coefficient was applied to predict the long-term deflection at six measurement locations (Fig. 19). Based on the design conditions, a ρ' value of 0.005 was used in the calculations. Initial deflection values were taken as 12.9, 7.6, 13.3, 16.5, and 12.2 mm (0.5, 0.3, 0.52, 0.65, and 0.48 in.) for 13F-A, 13F-C, 14F-A,

14F-B, and 14F-C, respectively, corresponding to the measured deflection at 60 days after concrete placement, the point when shores were removed and construction loads transitioned to service loads. Due to a measurement error at 13F-B, the initial deflection of 13F-A, exhibiting a similar behavior, was substituted.

When compared to measured values, the ACI 318-25 predictions overestimated deflections with high variability during the first 180 days after shore removal. During this early period, the predicted deflections were up to approximately 50% higher than the measurements: 49.6, 29.4, 44.1, 56.9, 36.8, and 52.2% for 13F-A, 13F-B, 13F-C, 14F-A, 14F-B, and 14F-C, respectively. This overestimation is attributed to the rapid increase in deflection caused by early-stage creep, shrinkage, and steel relaxation, which also introduces high variability in the measured data.

After 180 days, prediction errors decreased significantly as the rate of deflection slowed, leading to more stable measurements. The maximum error between predicted and measured deflections beyond 180 days was 18.7%, 15.6%, 20.0%, 27.2%, 10.7%, and 24.0%, respectively. The largest discrepancies typically occurred between 1 and 2 years after concrete placement. By the final day of measurement, approximately 5 years after casting, deflections had stabilized and prediction errors further decreased to 4.2%, 0.2%, 2.2%, 22.3%, 0.5%, and 0.1%.

While predictions closely aligned with measurements at most locations toward the end of the monitoring period, 14F-A remained an exception, showing a relatively large error. This discrepancy may be due to a possible error in the initial deflection measurement at 14F-A. To minimize such measurement errors, stricter control of measurement device settings, construction loads, and support removal procedures may be necessary. As specified in ACI CODE-318-25, long-term deflection is directly proportional to the initial deflection, making accurate measurement of the latter critical. Although 14F-A exhibited similar long-term deflection behavior to 14F-B, its recorded initial deflection was 19.4% lower, suggesting inconsistency in measurement and complicating accurate long-term prediction.

In summary, the ACI CODE-318-25 time-dependent coefficient generally provided reasonable long-term deflection predictions for field-measured PT flat slab, especially after the early high-variability period. Accurate measurement of initial deflection was found to be crucial, as errors in this parameter significantly affect long-term predictions. The design process for long-term deflection of the flat slab, following the studies by Bischoff[42] and by Bischoff and Scanlon[43] based on the ACI CODE-318-25 multiplier, is further elaborated in Appendix B.

Table 4—Time-dependent coefficients in ACI CODE-318-25

Sustained load duration, months	Time-dependent coefficient
3	1.0
6	1.2
12	1.4
60	2.0

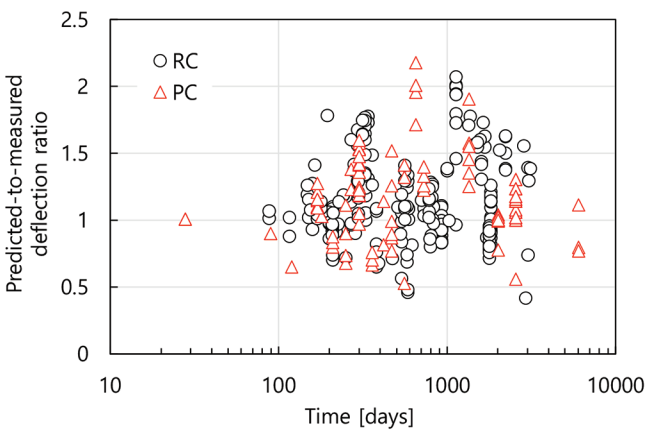

Fig. 18—Predicted-to-measured deflection ratio.

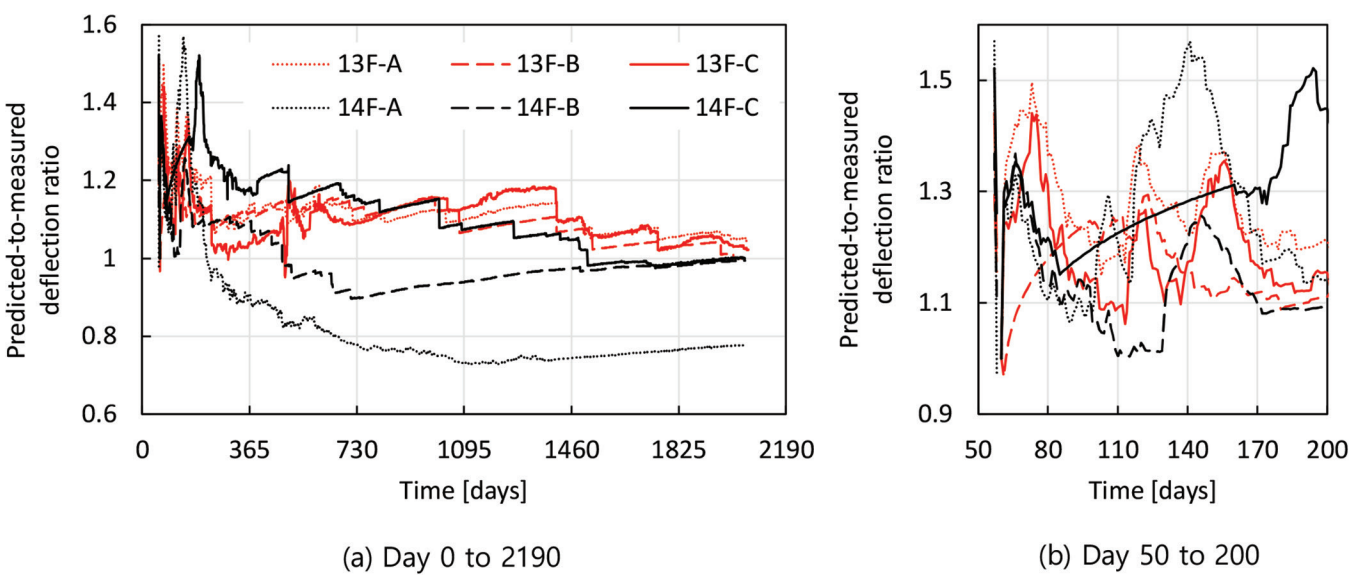

Fig. 19—Predicted-to-measured deflection ratio over time.

CONCLUSIONS

This study presented a comprehensive investigation of prestressing force behavior and deflection characteristics in an unbonded post-tensioned (PT) flat slab system over a remarkably long monitoring period of approximately 5 and a half years. The research used Smart Strands with embedded fiber Bragg grating (FBG) sensors for force monitoring and a linear variable differential transformer (LVDT)-based system for deflection measurements in an actual building environment, providing valuable insights that bridge the gap between theoretical models and real-world performance.

Several significant findings emerged from the prestressing force monitoring program. The Smart Strand monitoring system effectively captured both short-term and long-term prestressing force variations, demonstrating its viability for practical field applications. Initial prestressing force measurements revealed the gradient effects of tendon curvature and friction, with forces decreasing from the stressing end toward the fixed end, a phenomenon that became pronounced once jacking forces exceeded 60 kN (13,500 lbf) in case of single strand tendon. After temperature calibration, the long-term prestressing force monitoring showed that most prestress losses (approximately 5% of nominal strength) occurred within the first year after jacking, with forces subsequently stabilizing at around 43% of nominal strength for the remaining 5 years (for short tendon). The correlation between prestressing force fluctuations and ambient temperature variations underscored the importance of proper temperature compensation in optical fiber sensing systems for structural health monitoring.

The deflection monitoring program provided equally valuable insight. Deflection behavior showed clear responses to construction activities, with measurable changes corresponding to prestressing operations, concrete pouring, and shore removal. Slab position significantly influenced deflection magnitude, with interior slabs demonstrating substantially smaller deflections compared to corner or edge slabs due to enhanced boundary constraints. The comparison between measured and predicted short-term deflection showed good agreement, validating the analytical approach based on elastic uncracked behavior and confirming that the PT system effectively minimized concrete cracking. Long-term deflection analysis using the ACI CODE-318-25 time-dependent coefficient initially overestimated deflections by up to 50% during the first 180 days but achieved remarkable accuracy after this period, with final prediction errors as low as 0.1 to 4.2% for most measurement locations after 5 years. The deflection coefficient approach in ACI CODE-318-25, originally developed for reinforced concrete (RC), proved suitable for PT systems with similar prediction accuracy, providing a practical method for estimating long-term deflection in PT structures.

These findings have significant implications for the design and maintenance of PT concrete structures. The observed stabilization of prestressing forces after the first year suggests that design considerations should focus particularly on early-age behavior when estimating long-term performance. Although some measurement and calibration errors may remain, the ACI 318-25 time-dependent coefficient offers a reliable method for predicting long-term deflections in PT slabs, especially after the initial period of high variability. Smart Strand technology with FBG sensors demonstrates promising potential for continuous monitoring of prestressing forces in critical infrastructure, enabling more proactive maintenance strategies. The demonstrated influence of slab position on deflection magnitude highlights the importance of considering boundary conditions in design calculations to prevent excessive deflection in corner and edge slabs.

In conclusion, this extensive field monitoring program provides valuable insights into the long-term behavior of PT concrete structures under actual service conditions, contributing valuable data to bridge the gap between laboratory research and practical applications while validating existing design approaches for predicting long-term performance.

AUTHOR BIOS

Kwanwoo Yi *is a former MS Student of structural engineering at Seoul National University, Seoul, Korea, where he received his BS and MS. His research interests include the design and behavior of reinforced, prestressed, and post-tensioned concrete structures.*

Ah Sir Cho *is an Assistant Professor at Dongyang Mirae University, Seoul, Korea. He received his BS and PhD from Seoul National University. His research interests include the design and behavior of reinforced, prestressed, and post-tensioned concrete structures.*

Thomas H.-K. Kang, *FACI, is a Professor of Structural Engineering and the Interdisciplinary Program of Artificial Intelligence at Seoul National University. He is a member of ACI Committees 352, Joints and Connections in Monolithic Concrete Structures, and 423, Prestressed Concrete; Joint ACI-PTI Committee 320, Post-Tensioned Concrete Code; and Joint ACI-ASME Committee 359, Concrete Containments for Nuclear Reactors. He received the ACI Wason Medal for Most Meritorious Paper in 2009 and the ASCE's T.Y. Lin Award in 2025 on a paper published in the* ACI Structural Journal. *His research interests include the design and behavior of reinforced, prestressed, and precast concrete structures.*

ACKNOWLEDGMENTS

This research received long-term support from numerous organizations and individuals, including the Samsung C&T Corporation (Y.-N. Kim, Y.-W. Cho, M. J. Seo, and B.-K. Jeon), the Korea Institute of Civil Engineering and Building Technology (Y.-H. Park), the National Research Foundation of Korea (No. RS-2021-NR060085), the Total PS Co., Ltd. (K. N. Jeong), the Institute of Construction and Environmental Engineering at Seoul National University (S. Park), the Korea Concrete Institute (H.-G. Park, S.-J. Jeon, C. Kim, and H.-J. Hwang), the Institute of Information & Communications Technology Planning and Evaluation (IITP) grant (No. RS-2021-II211343, MSIT), and the Post-Tensioning Institute (M. Vejvoda).

REFERENCES

1. Jeon, S.-J.; Park, S. Y.; and Kim, S. T., "Temperature Compensation of Fiber Bragg Grating Sensors in Smart Strand," *Sensors (Basel)*, V. 22, No. 9, 2022, p. 3282 doi: 10.3390/s220932822.

2. Kim, S.-H.; Park, S. Y.; Kim, S. T.; and Jeon, S.-J., "Analysis of Short-Term Prestress Losses in Post-tensioned Structures Using Smart Strands," *International Journal of Concrete Structures and Materials*, V. 16, No. 1, 2022, pp. 1-15. doi: 10.1186/s40069-021-00488-3

3. Jeon, S.-J.; Park, S. Y.; Kim, S.-H.; Kim, S. T.; and Park, Y., "Estimation of Friction Coefficient Using Smart Strand," *International Journal of Concrete Structures and Materials*, V. 9, No. 3, 2015, pp. 369-379. doi: 10.1007/s40069-015-0112-9

4. Kim, S.-H.; Park, S. Y.; and Jeon, S.-J., "Long-Term Characteristics of Prestressing Force in Post-Tensioned Structures Measured Using Smart Strands," *Applied Sciences*, V. 10, No. 12, 2020, p. 4084. doi: 10.3390/app10124084

5. Precast/Prestressed Concrete Institute (PCI), *Bridge Design Manual*, third edition, Chicago, IL, 2014.

6. Breckenridge, R. A., and Bugg, S. L., "Effects of Long-Time Loads on Prestressed Concrete Beams," *PCI Journal*, V. 9, No. 6, 1964, pp. 75-89. doi: 10.15554/pcij.12011964.75.89

7. Branson, D. E.; Meyers, B. L.; and Kripanarayanan, K. M., "Time-Dependent Deformation of Noncomposite and Composite Prestressed Concrete Structures," Department of Civil Engineering, University of Iowa, Iowa City, IA, 1970.

8. Anderson, T. C.; Houdeshell, D. M.; and Gamble, W. L., "Construction and Long-Term Behavior of 1/8th Scale Prestressed Concrete Bridge Components," University of Illinois, Urbana, IL, 1972.

9. Chiu, H.-S.; Chern, J.-C.; and Chang, K.-C., "Long-Term Deflection Control in Cantilever Prestressed Concrete Bridges II: Experimental Verification," *Journal of Engineering Mechanics*, ASCE, V. 122, No. 6, 1996, pp. 495-501. doi: 10.1061/(ASCE)0733-9399(1996)122:6(495)

10. Braimah, A.; Green, M. F.; and Soudki, K. A., "Long-Term Behavior of CFRP Prestressed Concrete Beams," *PCI Journal*, V. 48, No. 2, 2003. doi: 10.15554/pcij.03012003.98.107

11. Zou, P., "Long-Term Deflection and Cracking Behavior of Concrete Beams Prestressed with Carbon Fiber-Reinforced Polymer Tendons," *Journal of Composites for Construction*, ASCE, V. 7, No. 3, 2003, pp. 187-193. doi: 10.1061/(ASCE)1090-0268(2003)7:3(187)

12. Xue, W.; Ding, M.; He, C.; and Li, J., "Long-Term Behavior of Prestressed Composite Beams at Service Loads for One Year," *Journal of Structural Engineering*, ASCE, V. 134, No. 6, 2008, pp. 930-937. doi: 10.1061/(ASCE)0733-9445(2008)134:6(930)

13. Radnić, J., and Matešan, D., "Testing of Prestressed Concrete Shell Under Long-Term Load and Unload," *Experimental Mechanics*, V. 50, No. 5, 2010, pp. 575-588. doi: 10.1007/s11340-009-9242-9

14. Fornůsek, J.; Konvalinka, P.; Sovják, R.; and Vítek, J. L., "Long-Term Behaviour of Concrete Structures Reinforced with Pre-Stressed GFRP Tendons," *WIT Transactions on Modelling and Simulation*, V. 48, 2009, pp. 535-545. doi: 10.2495/CMEM090481

15. Terrasi, G. P.; Meier, U.; and Affolter, C., "Long-Term Bending Creep Behavior of Thin-Walled CFRP Tendon Pretensioned Spun Concrete Poles," *Polymers*, V. 6, No. 7, 2014, pp. 2065-2081. doi: 10.3390/polym6072065

16. Singh, M., "Long Term and Short Term Deflection of GFRP Prestressed Concrete Slabs," The University of Manitoba, 2014.

17. Zawam, M.; Soudki, K.; and West, J. S., "Effect of Prestressing Level on the Time-Dependent Behavior of GFRP Prestressed Concrete Beams," *Journal of Composites for Construction*, ASCEV, V. 21, No. 4, 2017, p. 04017001. doi: 10.1061/(ASCE)CC.1943-5614.0000783

18. Cao, G.; Han, C.; Dai, Y.; and Zhang, W., "Long-Term Experimental Study on Prestressed Steel–Concrete Composite Continuous Box Beams," *Journal of Bridge Engineering*, ASCE, V. 23, No. 9, 2018, p. 04018067. doi: 10.1061/(ASCE)BE.1943-5592.0001269

19. Cao, G. H.; Zhang, S.; Zhang, W.; and Peng, X. R., "Long-Term Deflection Test and Theoretical Analysis on Cracked Prestressed Concrete Box Beams," *KSCE Journal of Civil Engineering*, V. 22, No. 2, 2018, pp. 688-695. doi: 10.1007/s12205-017-1295-1

20. Sovják, R.; Havlásek, P.; and Vítek, J., "Long-Term Behavior of Concrete Slabs Prestressed with CFRP Rebars Subjected to Four-Point Bending," *Construction and Building Materials*, V. 188, 2018, pp. 781-792. doi: 10.1016/j.conbuildmat.2018.08.084

21. Al-Negheimish, A. I.; El-Sayed, A. K.; Khanbari, M. O.; and Alhozaimy, A. M., "Long-Term Deflection of Prestressed SCC Hollow Core Slabs," *Construction and Building Materials*, V. 189, 2018, pp. 181-191. doi: 10.1016/j.conbuildmat.2018.08.116

22. Zawam, M.; Soudki, K.; and West, J. S., "Factors Affecting the Time-Dependent Behaviour of GFRP Prestressed Concrete Beams," *Journal of Building Engineering*, V. 24, 2019, p. 100715. doi: 10.1016/j.jobe.2019.02.007

23. Yang, M.; Jin, S.; and Gong, J., "Concrete Creep Analysis Method Based on a Long-Term Test of Prestressed Concrete Beam," *Advances in Civil Engineering*, V. 2020, No. 1, 2020, p. 3825403. doi: 10.1155/2020/3825403

24. Cao, G.; Zhang, W.; Hu, J.; and Peng, X., "Long-Term Performance of Prestressed Concrete Continuous Box Girders in the Natural Environment," *Canadian Journal of Civil Engineering*, V. 47, No. 7, 2020, pp. 856-864. doi: 10.1139/cjce-2018-0447

25. Li, X.; Deng, J.; Wang, Y.; Xie, Y.; Liu, T.; and Rashid, K., "RC Beams Strengthened by Prestressed CFRP Plate Subjected to Sustained Loading and Continuous Wetting Condition: Time-Dependent Prestress Loss," *Construction and Building Materials*, V. 275, 2021, p. 122187. doi: 10.1016/j.conbuildmat.2020.122187

26. Shi, J.; Wang, X.; Wu, Z.; Wei, X.; and Ma, X., "Long-Term Mechanical Behaviors of Uncracked Concrete Beams Prestressed with External Basalt Fiber-Reinforced Polymer Tendons," *Engineering Structures*, V. 262, 2022, p. 114309. doi: 10.1016/j.engstruct.2022.114309

27. Cao, G.; Shen, J.; Yang, L.; Li, K.; and Li, Z., "Experimental and Modeling Study on Long-Term Deformation of Three-Span Prestressed Concrete Continuous Box-Girder Bridge Model after Cracking," *Journal of Bridge Engineering*, V. 29, No. 10, 2024, p. 04024073. doi: 10.1061/JBENF2.BEENG-6725

28. Korea Institute of Civil Engineering and Building Technology (KICT), "Development of Smart Prestressing and Monitoring Technologies for Pre-Stressed Concrete Bridges," Goyang-si, Republic of Korea, 2013.

29. Jeon, S.-J.; Shin, H.; Kim, S.-H.; Park, S. Y.; and Yang, J.-M., "Transfer Lengths in Pretensioned Concrete Measured Using Various Sensing Technologies," *International Journal of Concrete Structures and Materials*, V. 13, No. 1, 2019, p. 43 doi: 10.1186/s40069-019-0355-y

30. Ebrahimi Motlagh, H. R., and Rahai, A., "Prediction of Long-Term Prestress Loss in Prestressed Concrete Beam with Corrugated Steel Web," *International Journal of Civil Engineering*, V. 20, No. 11, 2022, pp. 1309-1325. doi: 10.1007/s40999-022-00731-2

31. Han, W.; Tian, P.; Lv, Y.; Zou, C.; and Liu, T., "Long-Term Prestress Loss Calculation Considering the Interaction of Concrete Shrinkage, Concrete Creep, and Stress Relaxation," *Materials (Basel)*, V. 16, No. 6, 2023, p. 2452. doi: 10.3390/ma16062452

32. Youakim, S. A.; Ghali, A.; Hida, S. E.; and Karbhari, V. M., "Prediction of Long-Term Prestress Losses," *PCI Journal*, V. 52, No. 2, 2007, pp. 116-130. doi: 10.15554/pcij.03012007.116.130

33. Park, H.-G.; Hwang, H.-J.; Hong, G.-H.; Kim, Y.-N.; and Kim, J.-Y., "Slab Construction Load Affected by Shore Stiffness and Concrete Cracking," *ACI Structural Journal*, V. 108, No. 6, Nov.-Dec. 2011, pp. 679-688. doi: 10.14359/51683366

34. Hwang, H.-J.; Park, H.-G.; Hong, G.-H.; Kim, J.-Y.; and Kim, Y.-N., "Time-Dependent Deflection of Slab Affected by Construction Load," *ACI Structural Journal*, V. 113, No. 3, May-June 2016, pp. 557-566. doi: 10.14359/51687943

35. Hansen, P. F., and Pedersen, E. J., "Maturity Computer for Controlled Curing and Hardening of Concrete," *Nordisk Betong*, V. 1, No. 19, 1977, pp. 19-34.

36. Korea Meteorological Administration, Climate Statistics Analysis, Seoul, Korea 2025.

37. The Architectural Institute of Korea (AIK), Korean Building Code and Commentary (KBC), 2016.

38. Hong, G.-H.; Park, H.-G.; Eum, T.-S.; Mihn, J.-S.; and Kim, Y.-N., "Evaluation of Strength and Stiffness Gain of Concrete at Early-Ages," *Journal of the Korea Concrete Institute*, V. 22, No. 2, 2010, pp. 237-245. doi: 10.4334/JKCI.2010.22.2.237

39. ACI Committee 318, "Building Code for Structural Concrete—Code Requirements and Commentary (ACI CODE-318-25)," American Concrete Institute, Farmington Hills, MI, 2025, 704 pp.

40. Martin, L. D., "A Rational Method for Estimating Camber and Deflection of Precast Prestressed Members," *PCI Journal*, V. 22, No. 1, 1977, pp. 100-108. doi: 10.15554/pcij22.1-04

41. Nguyen, N.-M.; Wang, W.-C.; and Cao, M.-T., "Early Estimation of the Long-Term Deflection of Reinforced Concrete Beams Using Surrogate Models," *Construction and Building Materials*, V. 370, 2023, p. 130670. doi: 10.1016/j.conbuildmat.2023.130670

42. Bischoff, P. H., "Computing Deflections Using ACI CODE-318-19 and Beyond, Part 4," *Concrete International*, V. 47, No. 5, May 2025, pp. 62-65.

43. Bischoff, P. H., and Scanlon, A., "Effective Moment of Inertia for Calculating Deflections of Concrete Members Containing Steel Reinforcement and Fiber-Reinforced Polymer Reinforcement," *ACI Structural Journal*, V. 104, No. 1, Jan.-Feb. 2007, pp. 68-75.

NOTES:

NOTES:

NOTES:

NOTES:

NOTES:

ACI STRUCTURAL JOURNAL

The American Concrete Institute (ACI) is a leading authority and resource worldwide for the development and distribution of consensus-based standards and technical resources, educational programs, and certifications for individuals and organizations involved in concrete design, construction, and materials, who share a commitment to pursuing the best use of concrete.

Individuals interested in the activities of ACI are encouraged to explore the ACI website for membership opportunities, committee activities, and a wide variety of concrete resources. As a volunteer member-driven organization, ACI invites partnerships and welcomes all concrete professionals who wish to be part of a respected, connected, social group that provides an opportunity for professional growth, networking, and enjoyment.

American Concrete Institute